

Sheffield Hallam University

Synthesis and drug development of small molecule inhibitors of PTP1B

WOOTTON, Timothy Luke

Available from the Sheffield Hallam University Research Archive (SHURA) at:

<http://shura.shu.ac.uk/33738/>

A Sheffield Hallam University thesis

This thesis is protected by copyright which belongs to the author.

The content must not be changed in any way or sold commercially in any format or medium without the formal permission of the author.

When referring to this work, full bibliographic details including the author, title, awarding institution and date of the thesis must be given.

Please visit <http://shura.shu.ac.uk/33738/> and <http://shura.shu.ac.uk/information.html> for further details about copyright and re-use permissions.

Synthesis and drug development of small molecule inhibitors of PTP1B

Timothy Luke Wootton

A thesis submitted in partial fulfilment of the requirements of
Sheffield Hallam University
for the degree of Doctor of Philosophy

December 2023

Candidate Declaration

I hereby declare that:

1. I have not been enrolled for another award of the University, or other academic or professional organisation, whilst undertaking my research degree.
2. None of the material contained in the thesis has been used in any other submission for an academic award, unless otherwise clearly stated.
3. I am aware of and understand the University's policy on plagiarism and certify that this thesis is my own work. The use of all published or other sources of material consulted have been properly and fully acknowledged.
4. The work undertaken towards the thesis has been conducted in accordance with the SHU Principles of Integrity in Research and the SHU Research Ethics Policy.

The word count of the thesis is 63,028.

Name	Timothy Luke Wootton
Award	Doctor of Philosophy (PhD)
Date of submission	December 2023
Faculty	Health, Wellbeing and Life Sciences
Director of studies	Dr Daniel M. Allwood

Abstract

PTP1B (Protein tyrosine phosphatase 1B) is a member of the PTP (Protein tyrosine phosphatase) family of proteins and has previously been identified as a potential therapeutic target for numerous high-profile disease states, including obesity, type II diabetes, Alzheimer's disease and certain cancers including breast cancer. This work focuses on a means of treatment of metabolic syndrome (obesity, type II diabetes, and hypertension), by synthesising potential specific small molecule inhibitors of PTP1B that are impermeable to the blood brain barrier (BBB).

Herein, druggable target sites of PTP1B were investigated computationally, to assist in the identification of possible PTP1B inhibitors, for subsequent synthesis and testing. This initially entailed the virtual docking of databases of commercially available compounds, downloaded from ZINC. The main database used, contained over 870,000,000 'drug-like' compounds as defined by Lipinski's rule of 5, which resulted in 1822 computational active site hits. The process of identifying a potential hit was comprised of two stages. Initially the software used (CrossMiner) classified a molecule as a hit if a Tanimoto ratio score of ≥ 0.7 was obtained. These initial hits then underwent visual scrutiny by which any of these 'hits' that predominately resided outside of the active site pocket or had motifs located within the protein were discounted and not considered true hits. The remaining computational hits were then plotted in pharmaceutically relevant chemical space, and molecules of interest were selected for further investigation based upon chemical space location, physiochemical properties, binding mode and ease of synthesis.

This computational work led to an initial compound library of benzodioxanes being synthesised and tested. The main driving force behind the functionalisation and modification of the initial hit compound was the ease of synthetic conversion in addition to desirable changes from computational docking studies.

The potential synthesised inhibitors were then tested for PTP activity against PTP1B and TCPTP *via* a yeast-based inhibitory assay where the growth rate of the co-transformed yeast cells correlates to PTP inhibitor activity. For BBB permeability assessment, a commercially available kit was utilised, that used a synthetic BBB mimic membrane.

Future work aims to develop the most promising hit into a potential lead compound, thus contributing to a possible future treatment for the comorbidities of obesity.

Table of Contents:

Candidate Declaration	i
Abstract	ii
Acknowledgements	x
Abbreviations and symbols	xii
Chapter 1: Introduction	1
1.1. Metabolic syndrome.....	1
1.1.1. Obesity	1
1.1.2. Hypertension	5
1.1.3. Non-alcoholic fatty liver disease	5
1.1.4. Type II diabetes	6
1.2. Relevant Biological Processes	7
1.2.1. Glucose regulation.....	7
1.2.2. Insulin Signalling	8
1.2.3. Leptin signalling.....	10
1.3. Target for therapeutic intervention.....	13
1.3.1. PTP insulin mediated effect.....	13
1.3.2. PTP leptin mediated effect.	14
1.3.3. Overarching review.....	15
1.4. Protein tyrosine phosphatase family	16
1.4.1. PTP catalytic mode of action	20
1.4.2. PTP1B:	22
1.4.3. PTP1B target sites.....	22
1.4.3.1. Active site.....	23
1.4.3.2. Allosteric site	27
1.4.3.3. Disordered region.....	30
1.5. Animal models of PTP1B deletion.....	32
1.5.1. Genome wide	33
1.5.2. Central Nervous System tissue specific.....	34
1.5.3. Peripheral tissue specific	35
1.6. Blood Brain Barrier permeability	38
1.7. Summary and aims.....	40
Chapter 2: <i>In silico</i> PTP1B inhibitor database screen	41
2.1 Overview:	42
2.2 Background:	42

2.2.1	Molecular three-dimensionality	42
2.2.2	Hit identification parameters.....	44
2.2.3	Computational studies justification.....	45
2.2.4	PTP1B regions targeted.....	45
2.2.5	Computational methodology overview.....	46
2.2.5.1	Docking studies.....	46
2.2.5.2	Chemical space plotting.....	47
2.2.5.3	Example hit selection	47
2.3	Results and discussion:	47
2.3.1	Active site pharmacophore construction.....	48
2.3.2	Active site database screening.....	53
2.3.2.1	Drug-like database screen.	54
2.3.2.2	“Shard” database screen.	59
2.3.3	Allosteric site pharmacophore construction.....	60
2.3.4	Allosteric site database screening.	64
2.3.4.1	Drug-like database screening.	64
2.3.4.2	“Shard” database screening.....	68
2.4	Conclusion:	69
Chapter 3: Biological assay development.....		70
3.1.	Overview.....	71
3.2.	Background.....	71
3.2.1.	Means of assessing PTP inhibition.....	71
3.2.2.	Yeast-based inhibition assay.....	73
3.2.3.	Blood Brain Barrier assay	77
3.3.	Results and discussion	78
3.3.1.	Yeast assay verification	78
3.3.1.1.	Selection of yeast strain	78
3.3.1.1.1.	Doubling times.....	79
3.3.1.1.2.	Growth curves:	82
3.3.1.1.3.	% change in doubling times:.....	87
3.3.1.1.4.	Justification in strain selection.....	89
3.3.2.	Yeast based inhibition assay testing.....	89
3.3.2.1.	Known inhibitions and assay verification.....	89
3.3.2.1.1.	Growth curves of known inhibitors.....	92
3.3.2.1.2.	% change in doubling time.....	105
3.3.2.1.3.	EC ₅₀ values.....	118

3.4.3.	Blood brain barrier assay.....	120
3.4.3.1.	Permeability rate.....	120
3.4.3.2.	Concentration of acceptor and donor wells.....	120
3.4.3.3.	% of total input in acceptor plate wells.....	121
3.4.3.4.	Known PTP inhibitors.....	123
3.6.	Conclusion.....	127
Chapter 4: Benzodioxane synthesis and PTP1B inhibitor development		128
4.1	Overview:.....	128
4.2	Background:.....	128
4.2.1	Tetrahydronaphthalene synthesis investigation	128
4.2.2	Design of alternatives to tetrahydronaphthalene	130
4.2.3	Justification of benzodioxane	130
4.2.4	Previous examples of benzodioxane containing pharmaceuticals	133
4.2.5	Literature procedures for benzodioxane synthesis	135
4.3	Results and Discussion:.....	137
4.3.1	Initial synthesis of the benzodioxane core.....	137
4.3.2	Substrate scope of dibrominated precursor compounds	139
4.3.3	First wave of benzodioxane synthesis.....	140
4.3.4	Biological inhibition data for initially synthesised benzodioxanes	145
4.3.4.1	Initial screen	145
4.3.4.2	Investigation of potential inhibitor compound 16	148
4.3.4.2.1	PTP1B activity.....	148
4.3.4.2.2	TCPTP activity	150
4.3.4.2.3	PTP activity comparison.....	152
4.3.4.2.4	Computational modelling.....	154
4.3.4.2.5	Calculated EC ₅₀ values.....	156
4.3.5	Attempted alternative synthesis pathways to benzodioxane precursors.....	157
4.3.6	Formation of potential benzodioxane active site inhibitors	159
4.3.7	Identification of computationally designed hit compounds.....	161
4.3.7.1	Initial screen of targeted benzodioxanes	161
4.3.7.2	Investigation of potential inhibitor compound 30	164
4.3.7.3	Investigation of potential inhibitor compound 30a	169
4.3.7.3.1	PTP selectivity	172
4.3.8	Optimisation of compound 20 synthesis.....	182
4.3.9	Modification of compound 30a	183
4.3.9.1	Altering aromatic diol precursor of 30a.....	183

4.3.9.2	Utilising alternative dibrominated precursor compounds	184
4.3.9.2.1	Proposed mechanism for compound 43 formation	187
4.3.9.2.2	Alternative synthesis route for compound 45 formation	189
4.3.9.3	Reactions to yield compound 30a derivatives.....	191
4.3.10	Synthesis of second wave of compound 30a derivatives.	192
4.3.11	Attempted unsuccessful procedures for other compound 30a derivatives.	195
4.3.11.1	Further modification of compound 30a.	195
4.3.11.2	Attempted substitution reactions with compound 45	197
4.3.11.3	Hydrolysis of compound 59	198
4.3.12	Biological testing of compound 30a derivatives.....	200
4.3.12.1	PTP activity compound 30a derivatives	201
4.3.12.2	BBB permeability comparison.....	204
4.3.13	Compound 55 activity investigation	206
4.3.13.1	PTP1B activity.....	206
4.3.13.2	TCPTP activity	208
4.3.13.3	PTP activity comparison.....	210
4.3.13.4	Computational binding mode	213
4.4	Conclusion:	223
Chapter 5: Spirocyclic dihydropyrazole synthesis and PTP1B active site inhibitor development.....		223
5.1	Overview:	224
5.2	Background:	224
5.2.1	Justification for synthesis and biological testing	224
5.2.1.1	Computational studies	224
5.2.1.2	Molecular three-dimensionality	225
5.2.1.3	Known spirocyclic pharmaceuticals.....	225
5.2.2	Literature procedures for 5,6-spirocyclic dihydropyrazole synthesis	226
5.2.3	Utilised synthesis route	228
5.2.4	Investigation into alkene incorporation into for spirocycle synthesis	228
5.2.5	Proposed mechanism of formation	230
5.3	Results and Discussion:.....	231
5.3.1	Spirocyclic formation optimisation with model substrate	231
5.3.2	Sulfonyl hydrazone	234
5.3.2.1	Synthesis.....	234
5.3.2.2	Biological testing	235
5.3.3	Spirocyclic substrate scope.....	238

5.3.3.1.	Sulfonyl hydrazone altered spirocycle synthesis.....	238
5.3.3.2.	Biological testing of initial wave of spirocycles.....	240
5.3.3.3.	Alkene altered spirocycle synthesis.	243
5.3.3.4.	Biological testing of selected examples from the alkene substrate scope	246
5.3.3.5.	Hit compound 78 PTP inhibitor investigation.....	247
5.3.3.5.1.	PTP1B based dose response screen.....	247
5.3.3.5.2.	TCPTP based dose response screen.....	249
5.3.3.5.3.	EC ₅₀ comparison.....	252
5.3.3.5.4.	Computational binding mode investigation.....	253
5.3.3.5.5.	BBB permeability.....	255
5.3.3.6.	Unsuccessful spirocycle formations.....	257
5.3.4.	Metal free carbon-carbon bond formation.....	258
5.3.4.1.	Synthesis.....	258
5.3.4.2.	Proposed mechanism.....	259
5.3.4.3.	Prior literature on alternative synthesis methods.....	260
5.3.4.4.	Biological testing of compound 89.....	261
5.3.5.	Spirocyclic dihydropyrazole synthetic utility.....	262
5.3.5.1.	Successful functionalisation reactions.....	262
5.3.5.2.	Unsuccessful functionalisation reactions.....	264
5.3.5.3.	Biological testing of compounds 91-97.....	268
5.3.6.	One-pot synthesis of compound 62.....	270
5.3.7.	Spirocycle hit biological data comparison.....	270
5.3.7.1.	Yeast-based PTP activity.....	271
5.3.7.1.1.	PTP1B inhibitory activity.....	271
5.3.7.1.2.	TCPTP inhibitory activity.....	273
5.3.7.2.	BBB permeability.....	275
5.4.	Conclusion:.....	277
5.5.	Important comments:.....	278
Chapter 6: Conclusions and Future direction.....		278
6.1.	Conclusions.....	279
6.2.	Future direction.....	283
Chapter 7: Methodology.....		286
7.1.	General Experimental Details.....	287
7.2.	Chemical Synthesis.....	288
7.2.1.	Synthesis of LZP25 and precursors: 1-5.....	288

Procedure A: for synthesis of 1	288
General procedure B: for synthesis of 2 and 3	289
Procedure C: for synthesis of 4	291
Procedure D: for synthesis of 5	292
7.2.2. Synthesis of Benzodioxane precursors: 6, 9-15, 24, 34-37	293
General procedure E: for synthesis of 6	293
General procedure F: for synthesis of 9-15	293
General procedure B.1: for synthesis of 24	297
General procedure G: for synthesis of 34 and 35	298
General procedure G.1: for synthesis of 36 and 37	299
7.2.3. Synthesis of Benzodioxanes: 7, 8, 16-23, 38-46 and 52	301
General procedure H: for synthesis of 7 and 52	301
General procedure H.1: for synthesis of 7	301
General procedure H.2: for synthesis of 7	301
General procedure I: for synthesis of 8, 16-19, 21, 40-42 and 46	303
General procedure I.1: for synthesis of 20, 22, 23 and 46	303
General procedure I.2: for synthesis of 38, 39 and 41-45	304
Procedure J: for synthesis of 45 and 45a	318
7.2.4. Hydrolysis of benzodioxane esters: 25-32, 47-51	320
General procedure K: for synthesis of 25 – 31 and 48-51	320
General procedure K.1: for synthesis of 32 and 47	320
7.2.5. Continued synthesis of benzodioxanes: 33, 53-60	330
General procedure L: for synthesis of 33 and 53	330
General procedure M: for synthesis of 33 and 54	331
Procedure N: for synthesis of 55	332
Procedure O: for synthesis of 56	333
Procedure O.1: for synthesis of 56	334
Procedure P: for synthesis of 57	335
Procedure Q: for synthesis of 58	336
Procedure R: for synthesis of 59	337
Procedure C.1: for synthesis of 60	338
7.2.6. Synthesis of sulfonylhydrazones: 61, 63-67 and 68.1-68.8	339
General Procedure S: for synthesis of 61, 63-66	339
General Procedure S.1: for synthesis of 67	342
7.2.7. Synthesis of spirocyclic dihydropyrazoles: 62, 69-86	343
General procedure T: for synthesis of 62, 69-86	343

7.2.8. Synthesis of alkenes for spirocycle synthesis: 87 and 88	356
General procedure U: for synthesis of 87 and 88	356
General procedure T.1: for synthesis of 89 and 90	358
Procedure V: for synthesis of 91	360
Procedure W: for synthesis of 92	361
Procedure W.1: for synthesis of 93	362
Procedure X: for synthesis of 94	363
Procedure Y: for synthesis of 95 and 96	364
Procedure Z: for synthesis of 97	366
7.3. Computational studies	367
7.3.1. Database screening	367
7.3.2. Docking studies	367
7.4. Biological methodologies	368
7.4.1. Yeast cell transformation	368
Frozen-EZ Yeast Transformation II™ kit protocol:	368
Preparation of Competent cells:	368
Transformation:	369
Single Colony purification:	370
7.4.2. Yeast cell maintenance	370
Plate composition:	370
Growth media composition:	370
Short-term yeast cell storage:	371
Long-term yeast cell storage:	371
7.4.3. Yeast growth curves	372
Growth curve setup:	372
Growth curve experiment:	372
6.4.3.1. Doubling time calculations:	373
6.4.3.2. EC₅₀ calculation	374
7.4.4. Blood Brain Barrier (BBB) Permeability assay	374
BBB assay protocol:	375
BBB data analysis:	376
7.4.5. Spot Plate assay	378
8. References	379
Appendix	393

Acknowledgements

Firstly, I would like to thank my entire supervisor team comprised of Dr Daniel Allwood, Dr Nicola Aberdein and Dr Alessandra Princivalle, for the opportunity to work with you on this research project, during the course of which you all provided useful intellectual insight and research direction. This was especially useful during the covid-19 pandemic where the weekly paper review meetings provided purpose and direction for the project despite being out of the laboratory for the majority of a year. Additionally, I would also again like to thank Dr Nicola Aberdein and Dr Alessandra Princivalle in particular for teaching me, as a chemist, how to plan, conduct and write about biological experiments which from the content of this thesis was a key aspect.

I would also like to give additional thanks to my DoS, Dr Daniel Allwood for being a primary contributor to the scientist I am today. For having an input in my chemistry development as far back as the second year of my undergraduate degree. But especially during my final undergraduate year project and master's level project where the independent laboratory and chemistry skills learnt were foundational at the start of my PhD and developed further through the duration of the project. For this I am grateful.

Another academic whom I would also like to thank is Dr Susan Campbell for proving pivotal knowledge and expertise with regards to the setup, utilisation and maintenance of the yeast based inhibition assay, the use of which was a major aspect of this work.

For the kind donation of the plasmids used for the yeast cell transformations I would like to express gratitude towards Professor Anthony C. Bishop from Amherst College, Department of Chemistry, Amherst, Massachusetts.

Thanks to the technical team at Sheffield Hallam University, with particular thanks for Mick for your assistance with fixing the Xevo when it chose not to play ball which was far more often than I would have liked. Additionally, I would like to thank the technicians who maintained the NMR so a thank you to Andy, Dan, and Adam, for keeping the liquid nitrogen and helium levels topped up.

I could not have a list of acknowledgements without mentioning my fellow PhD students. That despite whatever went on in the laboratory that day, the office would remain a surprising light-hearted and dare, I say a fun place to be. Well mostly, thesis writing really tested that statement. So, thank you to all the PhD students whom I have had the pleasure

of sharing a drink with over the years, this PhD could not have been done alone, without the support and banter of the great friends I have made along the way during my PhD.

Finally, I would like to give a big thank you to my family for providing support and believing in me throughout my entire PhD even during the hard times when no matter what I tried, nothing worked. But special thanks go to my Mum for all the above and for being a proof-reader for my thesis and I cannot thank you enough for this, as it is a slog even for me, the author.

Abbreviations and symbols

Ac	acetyl group
ade2-1	mutations in adenine biosynthesis pathway genes
Arg	argine
Ala	alanine
ars	autonomously replicating sequence
Asn	asparagine
ASAP+	atmospheric solids analysis probe, positive mode
Asp	aspartic acid
<i>app</i>	apparent
atm	atmosphere
ATP	adenosine triphosphate
ATR	attenuated total reflectance
Akt	protein kinase B
Alb-Cre-PTP1B ^{-/-} mice	hepatic PTP1B deficient mice
ANOVA	analysis of variance
<i>aq</i>	aqueous
BBB	blood brain barrier
BMI	body mass index
Bn	benzyl
Boc	tert-butyloxycarbonyl
BP	blood pressure
br	broad
Bz	benzoyl
C	permeability rate constant
CAD	coronary artery disease
can1-100	nonsense allele of CAN1 gene (Canavanine resistance mutation)
<i>cat.</i>	catalytic amount
CCDC	Cambridge Crystallographic Data Centre
cen	stable yeast vector
conc	concentrated
COSY	correlation spectroscopy
CIS	cytokine-inducible SH2-containing protein
cLogP	calculated partition coefficient
CNS	central nervous system
CSA	cross sectional area
Cys	cysteine
d	doublet
ddd	doublet of doublet of doublets
DCM	dichloromethane
dd	doublet of doublets
DEPT	distortionless enhancement by polarisation transfer
DIPA	<i>N,N</i> -diisopropylamine

DMAP	4-dimethylaminopyridine
DMF	<i>N,N</i> -dimethylformamide
DMSO	dimethylsulfoxide
DSP	dual-specificity phosphatase
dq	doublet of quartets
1,2-DCE	1,2-dichloroethane
<i>d</i> ₆	Deuterated DMSO
EC ₅₀	half maximal effective concentration
ER	endoplasmic reticulum
eNOS	endothelial NO synthase
<i>ee</i>	enantiomeric excess
ESI+	electrospray ionisation, positive mode
ET	endothelin
<i>et al.</i>	<i>et alia</i> (and others)
Et	ethyl
equiv.	equivalent
FabH	β-ketoacyl-acyl carrier protein synthase III
FDA	United States Food and Drug Administration
FTIR	Fourier transform infrared
FOSL2	FOS-like antigen 2
Fsp ³	fraction of sp ³ -hybridised atoms
Gal	galactose
GCGR	glucagon receptor
GDP	gross domestic product
<i>G. hanburyi</i>	<i>Garcinia. hanburyi</i>
Gln	glutamine
Glu	glutamic acid
GLUT	glucose transporter
Gly	glycine
GPCR	G-protein-coupled receptor
GS	glutamine synthetase
H-bond	hydrogen bond
HC(X) ₅ R.	unique signature motif of PTPs
HePTP	haematopoietic protein tyrosine phosphatase
HEPES	zwitterionic sulfonic acid buffering agent
HFD	high fat diet
His	histidine
HMBC	heteronuclear multiple bond correlation
HRMS	high resolution mass spectroscopy
HMQC	heteronuclear multiple quantum correlation
hr(s)	hour(s)
<i>h</i> ₆ -DMSO	non-deuterated DMSO
IC ₅₀	half maximal inhibitory concentration
IKKβ	one of three subunits of IκB kinase

Ile	isoleucine
IMS	industrial methylated spirit
InsRb	insulin receptor
<i>in vacuo</i>	under reduced pressure
IR	infrared spectroscopy
IRE	inositol-requiring enzyme
IRS	insulin receptor substrate
<i>J</i>	coupling constant
JAK	janus tyrosine kinase
JNK	c-Jun N-terminal kinase
KO ^t Bu	potassium tert-butoxide
LAR	leukocyte common antigen-related receptor protein tyrosine phosphatases
leu	leucine
L-DOPA	levodopa
LepRb	leptin receptor
Leu	leucine
LG	leaving group
LogP	partition coefficient
Lyp	lymphoid-specific tyrosine phosphatase
Lys	lysine
m	multiplet
MAPK	mitogen-activated protein kinase
MC4R	melanocortin 4 receptor
Me	methyl group
Met	methionine
micro	microbiological
Min(s)	minute(s)
mRNA	messenger ribonucleic acid
MTBE	methyl tert-butyl ether
MW	molecular weight
n	number of biological replicates
NAFLD	non-alcoholic fatty liver disease
NASH	non-alcoholic steatohepatitis
NF- κ B	nuclear factor kappa-light-chain-enhancer of activated B cells
NMR	nuclear magnetic resonance
NO	nitric oxide
ns	not significant
ObRb	long isoform of leptin receptor
OD	optical density
OD _A	absorbance of acceptor well solution
OD _E	the absorbance of the equilibrium standard
org	organic

PAMPA	parallel artificial membrane permeability assay
PBS	phosphate buffered saline
PCC	pyridinium chlorochromate
PDB	Protein Data Bank
PD-LID	parkinson's disease levodopa-induced dyskinesia
Ph	phenyl group
pH	potential of hydrogen
Phe	phenylalanine
pNP	p-nitrophenyl
pNPP	p-nitrophenyl phosphate
PMBBB	permeability membrane blood brain barrier assay
POMC	pro-opiomelanocortin
Pro	proline
PI3-K	phosphatidylinositol-4,5-bisphosphate 3-kinase
Pt	part
PTP	protein tyrosine phosphatase
PTPR	receptor-type protein tyrosine phosphatases
PTP1B	protein tyrosine phosphatase 1B
pTyr	phosphorylated tyrosine residue
PVH	paraventricular nucleus of the hypothalamus
q	quartet
quin	quintet
R	receptor
R _f	retention factor
RT	room temperature
RPTP	transmembrane receptor-like protein
RTK	receptor tyrosine kinase
s	singlet or strong
sat.	saturated
S/B	signal to background ratio
SC	synthetic complete supplement mixture
Sept	septet
Ser	serine
SHP	Src homology region 2 domain-containing phosphatase
SMK1	meiosis-specific mitogen-activated protein
S/N	signal to noise ratio
snRNP	small nuclear ribonucleoproteins
SOC	suppressors of cytokine signalling
Sol.	solution
SGLT2	sodium-glucose co-transporter type 2
STAT	signal transducer and activator of transcription
Std.	standard deviation
Sub	substrate
S _N 1	nucleophilic substitution unimolecular

S _N 2	nucleophilic substitution bimolecular
t	triplet or time of experimental run in hours
TBAF	tetra-n-butylammonium fluoride
TCPTP	T-cell protein tyrosine phosphatase
td	triplet of doublets
T _d	doubling time
TDAE	tetrakis(dimethylamino)ethylene
TFAA	trifluoroacetic anhydride
THF	tetrahydrofuran
Thr	threonine
TIID	Type II diabetes
TLC	thin-layer chromatography
TMSA	total molecular surface area
TNF	plasma tumour necrosis factor
ToF	time of flight
Trp	tryptophan
Ts	tosyl group
Tyr	tyrosine
w	weak
UA	ursolic acid
ura	uracil
USD	United States Dollar
UV	ultra-violet
U1 snRNP	U1 spliceosomal RNA
V _A	initial volume in cm ³ of the acceptor well
Val	valine
V _D	initial volume in cm ³ of the donor well
VHR	vaccinia H1-related phosphatase
<i>via</i>	by means of
<i>v</i> _{max}	the frequency of maximum power
vs	versus
YNB	yeast nitrogen base
YPD	yeast extract peptone dextrose
ZINC	ZINC is not commercial
5-HT	serotonin receptor
α	alpha
&	and
Å	Angstrom(s)
~	approximately
β	beta
δ	chemical shift
cm	centimetres
°C	degrees Celsius

g	gram(s)
>	greater than
Hz	hertz
κ	kappa
-/-	knockout
kDa	kiloDalton(s)
<	less than
≤	less than or equal too
L	litre(s)
M	molar
MHz	megahertz
μg	microgram(s)
mg	milligram(s)
μmol	micromole(s)
mmol	millimole(s)
mol %	mole percent
mL	millilitre(s)
μL	microlitres(s)
-	minus or knockout or 'to'
ng	nanogram
nm	nanometre
nM	nanomolar
ppm	parts per million
π	pi
±	plus, minus
:	ratio of two combined components
λ	wavelength

Chapter 1

Introduction

1.1. Metabolic syndrome

Metabolic syndrome can be defined as the combination of three disease states: obesity, type II diabetes (TIID) and high blood pressure (hypertension), all of which are comorbidities of each other, due to interlinked biological processes. Resultant effects of metabolic syndrome include enlarged waist circumference due to increased adipose tissue, abnormal cholesterol levels circulating in the blood stream, impaired glucose regulation. Which contributes to elevated blood glucose levels and cardiovascular issues, including a greater likelihood of strokes and heart disease. ^{1,2}

1.1.1. Obesity

Obesity can be defined as excessive or abnormal accumulation of fat, which presents a risk to health. This often leads to other health complications such as cardiovascular issues, liver steatosis, and type II diabetes (TIID). Obesity-associated type II diabetes causes glucose dysregulation. In part due to the elevated glucose formation in the liver *via* gluconeogenesis and glycogenolysis pathways, and a decreased uptake of glucose into the skeletal muscle cells. ³ Gluconeogenesis is the pathway by which glucose is formed from non-hexose precursors such as glycerol, lactate and pyruvate, whereas glycogenolysis is the breakdown of glycogen into glucose, this occurs in the liver. Both processes contribute to the elevation of blood glucose levels. ³

To reduce excess fat content and improve glucose homeostasis, a common treatment prescribed for obesity is a reduced-calorie diet in conjunction with an exercise plan. ⁴ However the most successful alternative treatment for obesity currently is gastric bypass surgery. This is an expensive and invasive procedure that requires long term post operative lifestyle changes, but patients can on average lose 25% of their initial body weight through loss of adipose after 6-12 months, in conjunction with improved diet and exercise. ⁵

As of 2023, there are currently five FDA approved prescription weight-loss drugs, these are Bupropion-naltrexone (Contrave), Orlistat (Xenical), Phentermine-topiramate (Qsymia), Semaglutide and Setmelanotide. The components of the first three examples are shown below in **Figure 1**. These drugs operate by making the individual feel full quicker, resulting in less food uptake and, over time weight loss. The exception to this is Orlistat which instead operates by decreasing fat absorption by as much as 30% which contributes to weight loss. ⁶ It has been found that taking one of these drugs for a year can

result in a total body weight loss of 3% to 12% more than that lost with lifestyle changes alone. ⁶

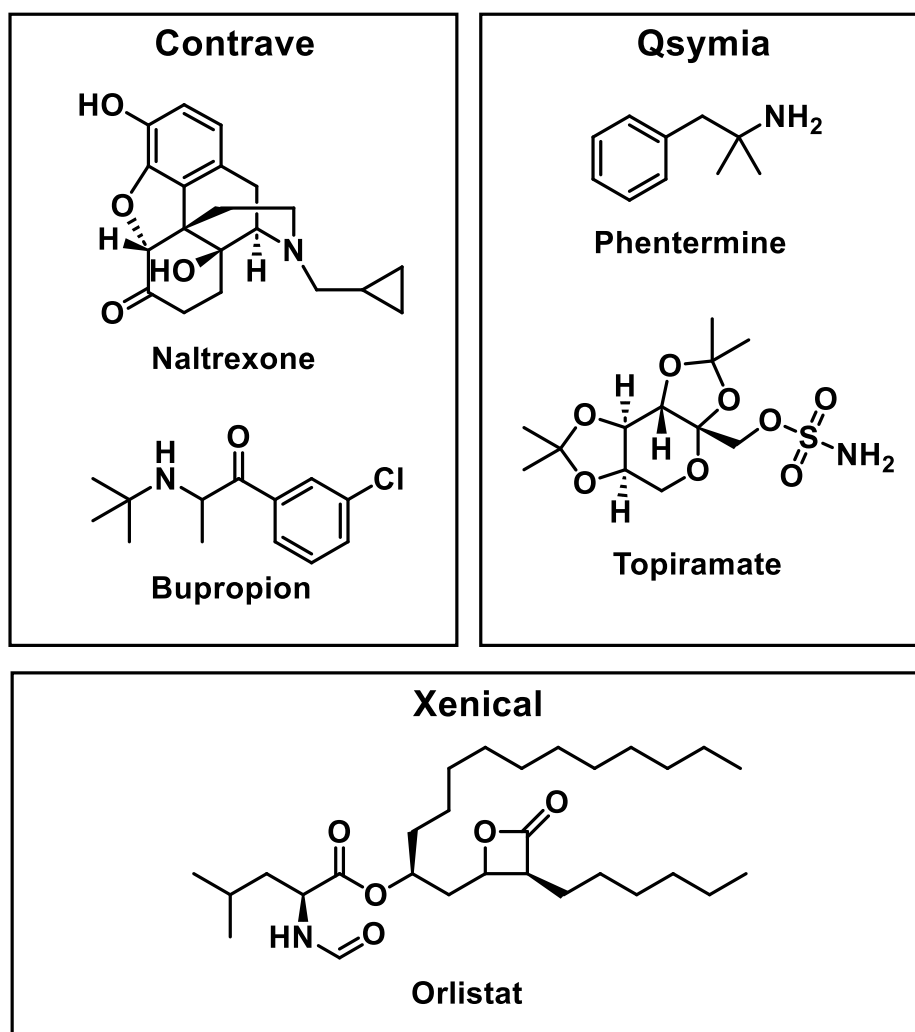


Figure 1: Chemical structures, of current pharmaceutical products for type II diabetic treatment with the commercial name stated above each drug composition.

However, for any significant effect to be observed with weight loss, all these treatments need to be conducted in parallel to regular exercise. Furthermore, once the patient has been taken off the medicine, regaining fat often occurs unless the change in lifestyle remains. ⁶ Common side-effects of these orally administered drugs include nausea, headache, constipation, stomach-ache, potential increase in blood pressure, and insomnia. ⁶ Hence new more effective pharmaceutical intervention with a less invasive administration route are needed with increased potency and fewer side effects.

A sixth drug, Lorcaserin, was approved for weight loss but after being in clinical use for eight years, was later withdrawn, due to a potential link of patients having an increased risk of developing cancer from long term use. ⁶

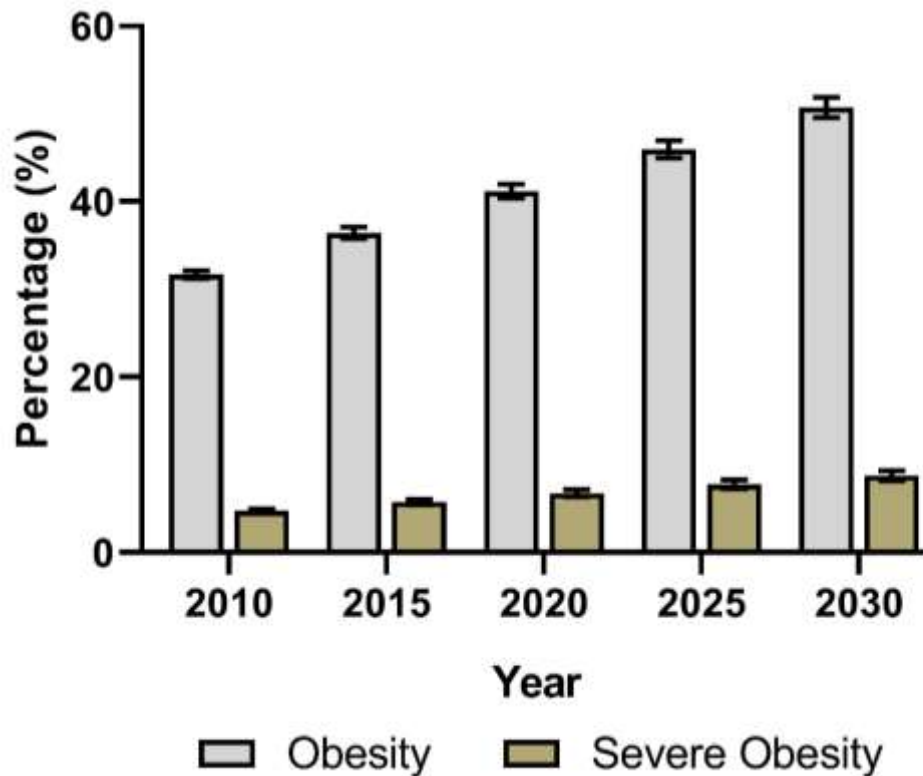


Figure 2: Linear progression of the percentage of the U.S. population classified as obese or severely obese. Data used obtained from publication by W. Dietz *et al.* ⁷ where obesity is defined as a BMI > 30 and severely obese is classified as having a BMI >40.

A study conducted by W. Dietz *et al.* in 2008 predicted that by 2030, 51% of U.S. adults could be obese (BMI >30), if the linear trend at that time was maintained. This would be an increase of over 20% in a 22-year period. Up from ~30% of U.S. adults being obese in 2008. ⁷ The results are also illustrated above in **Figure 2**.

Additionally, data collected from the Active Lives Adult Survey estimated that in England between November 2020 – 2021, 25.3% of all adults aged 18 years and over were obese. This was an increase from 22.7% in 2015 – 2016 to 24.4% in 2019 - 2020. Additionally, a large variance in local authorities was observed with the upper range of adult obese percentages ranging from 10.5 - 40.3%. ⁸ The difference in the proportion of the population of a local authority which are obese means that for England, local targeted intervention of the regions with higher obesity rate would be more effective in lowering the national average.

Furthermore, the Health Survey for England in the calendar year of 2021 estimated that approximately 25.9% of adults in England are obese with an additional 37.9% being considered overweight, with men being statistically more likely to be overweight or obese

than women, 68.9% and 59% respectively. The age range of people 45-74 were statistically the most obese with 41% classified as obese and approximately an additional 31.3% being overweight. ⁹

The link between lower socio-economic status and obesity is well documented in the literature, ¹⁰ predominantly in countries classified as developed such as the UK and U.S. For example, in the UK it was found that the obesity of adults in the most deprived regions was near double that of the least deprived regions, at 36% compared to 20% respectively in 2018-2019. With regards to obesity in children the gap between the most deprived and least deprived areas widens, with an increase from 8.5% in 2006-2007 to 13.9% in 2018-2019, were a continuing upward trend predicted. ¹⁰

The underlying physiological cause of increased fat accumulation and latterly obesity is primarily resultant of an energy imbalance between consumed and expended calories for an individual. The increase is due to numerous reasons including greater availability and affordability of high energy-dense food. Hence the socio-economic status of an individual has a significant effect on their ability to achieve the balance needed to reduce likelihood for developing obesity. ^{11,12}

The excess of calories consumed is not the only environmental factor which contributes to the expression of the phenotype obesity as the types of food consumed can also contribute. Refined carbohydrates may cause inflammation in the body, as the resultant spike in blood glucose triggers an inflammatory response. Chronic inflammation can cause the upregulation of the hormone leptin. This over expression can contribute to increased leptin resistance. Interfering in leptin receptor signalling has been shown to impair the biological function of leptin predominantly in the hypothalamus where it controls the body's appetite suppression and weight control. Reduced leptin sensitivity therefore can contribute to increased food uptake and weight gain. ¹³

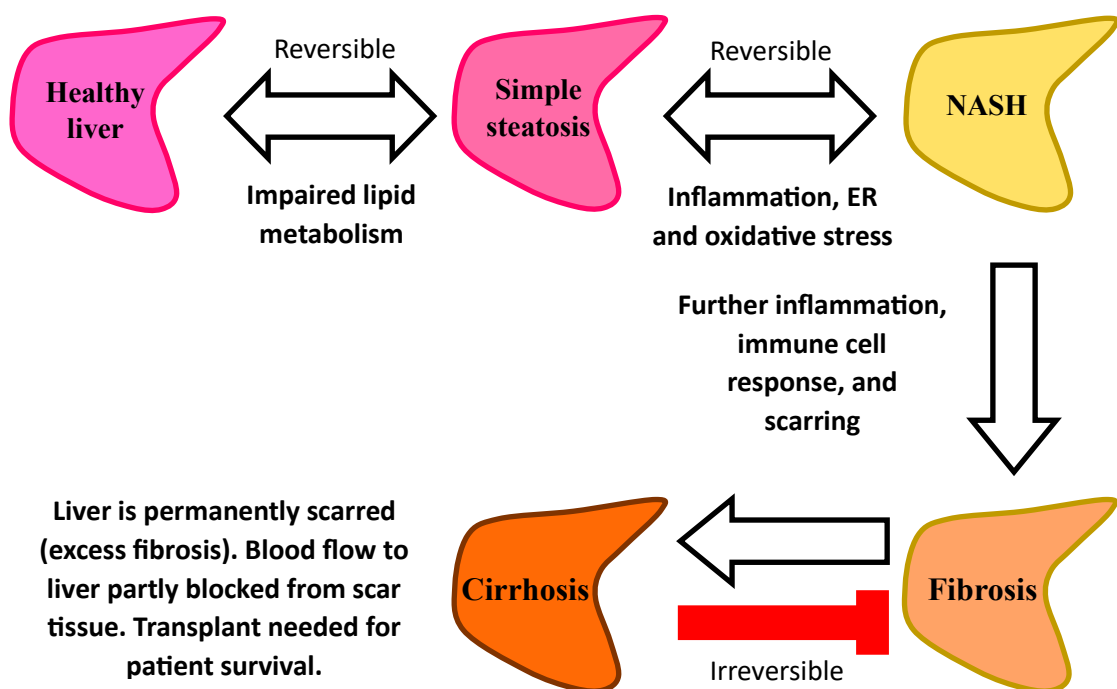
Environmental factors are not the only contributing factor to energy imbalance, as a persons' genetics can also play a pivotal role in the susceptibility to accumulate fat. The most commonly implicated gene is MC4R, (melanocortin 4 receptor). Altered MC4R are found in a small fraction (<5%) of obese people, and its reduced activity causes individuals to feel extremely hungry and become obese because of consistent overeating (hyperphagia). ¹⁴

1.1.2. Hypertension

As mentioned previously the resultant spike in blood glucose levels caused by the consumption of refined carbohydrates can trigger an inflammatory response, and also an immune response, activating T-cells which migrate to the capillary system and the kidney causing inflammation and hypertension. Chronic inflammation can lead to damage in the lining of the blood vessels (endothelial cells) and artery wall stiffening, both of which increase blood pressure.¹⁵ Weight gain has been linked to causing hypertension by the narrowing of blood vessels due to increased cholesterol levels. A higher blood pressure has also been shown to precede the weight gain thus is another contributing factor. Hence this relationship of weight gain and hypertension is a downward spiral of continuous feedback.¹⁶

1.1.3. Non-alcoholic fatty liver disease

Non-alcoholic fatty liver disease (NAFLD) is an umbrella term for a range of liver conditions in which an excessive build-up of fat in the liver occurs, and any resultant damage is due to this and not excessive alcohol consumption.



Scheme 1: Progression of non-alcoholic fatty liver disease (NAFLD). NASH: Non-alcoholic steatohepatitis¹⁷⁻¹⁹

The stages of NAFLD are illustrated above in **Scheme 1**. When an increased amount of adipose tissue collects in the liver and remains untreated in the early onset stages, this results in the liver becoming inflamed. When persistent, the inflammation causes scarring

of tissue around the liver and nearby blood vessels, but normal function can occur.¹⁷⁻¹⁹ This stage is called fibrosis; however, this can further develop into cirrhosis in the most extreme cases. After years of inflammation, the liver damage is permanent, resulting in liver failure. The inflammation caused by NAFLD also contributes to cardiovascular issues and obesity in the manner stated above. The onset of NAFLD is primarily contributed by obesity and T2DM. Visceral fat that encompasses organs is an important risk factor for the onset of NAFLD. An accumulation of ectopic fat (fat stored within normally lean locations e.g. liver), and visceral obesity leads to a dysfunction of the adipose tissue with impaired production of adipocytokines. This upregulates the formation of pro-inflammatory cytokines which over time can cause liver damage and scarring as stated above. T2DM and NAFLD as disease states often coexist, where 60% of T2DM patients also exhibit NAFLD. This link is in part due to the sustained elevated blood glucose level and glucose dysregulation which is synonymous with T2DM.¹⁷⁻¹⁹

1.1.4. Type II diabetes

Another comorbidity of obesity which also simultaneously promotes weight gain is T2DM. Type II diabetes onset occurs in-part due to insulin resistance which leads to elevated fatty acids in the plasma, causing decreased glucose transport into the muscle cells, and subsequently contributing to elevated hepatic glucose production. The resultant effect is upregulation of insulin products leading to hyperinsulinemia, which is sustained elevated blood insulin levels. Ultimately a proportion of the excess blood glucose is stored as fat in the body, again leading to weight gain.²⁰

The link between obesity and T2DM is well established, and they are involved in a self-perpetuating loop. One study found that 86% of patients with type II diabetes were overweight or obese. Of this 52% were obese, and 8.1% were classified as morbidly obese.²¹ The development of T2DM occurs due to a multitude of factors including increased consumption of foods containing high levels of sugar and/or simple or refined carbohydrates, reduced physical activity and obesity which can cause increased insulin resistance, all of which contribute to a sustained elevated blood glucose level. It is this poor control of the body's glucose levels which primarily result in the onset of T2DM.^{21,22}

Obesity and its related comorbidities such as T2DM and fatty liver disease exert a significant financial cost on global healthcare organisations. In the year 2015, \$ 1.3 trillion (USD) was spent globally on T2DM, equalling approximately 12% of the total

health resource expenditure at this time, or 1.8% of the total global GDP. This is projected to rise to \$ 2.1-2.5 billion by 2030, equalling 2.2% of total global GDP. ^{23,24}

People aged between 35 to 64 living with T1D are up to two times more likely to die prematurely than healthy individuals. ²⁵ Between January 2006 and December 2010 in the UK, approximately 60% of 97,689 patients with T1D were admitted to hospital at least once during the 4-year study period. In another study undertaken between 2004 to 2012 (England), there was an increase in people with diabetes being admitted to hospital due to emergencies. ²⁶ Hence, with the increasing financial pressure, action needs to be taken globally, to prevent future costs and preventable deaths.

1.2. Relevant Biological Processes

1.2.1. Glucose regulation

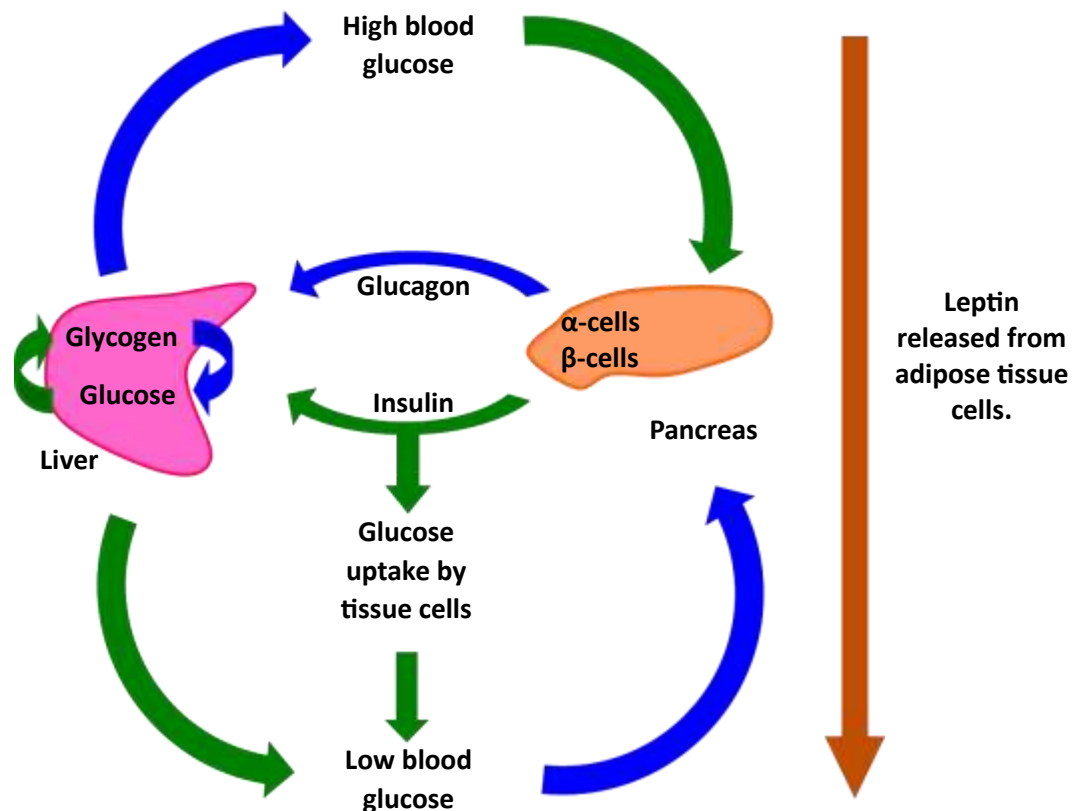


Figure 3: Depiction of how glucose homeostasis is maintained. Blue = glucagon's role in increasing blood glucose level. Green = insulin's effect on blood glucose level. Orange = leptin's effect on the body's glucose regulations. ³¹⁻³³

Blood glucose levels are maintained in a narrow range, normally between 4.0 to 5.4 mM/L when fasting and can peak up to 7.8 mM/L 2 hours after eating. This is primarily maintained by two hormones: glucagon and insulin. ²⁷

G-protein-coupled receptors (GPCRs) monitor and play a key role in maintaining blood glucose homeostasis. GPCRs span cell membranes to relay signals. Once activated a cascade of responses is triggered inside the cell, and the required biological response occurs.^{28,29} Of the approximately 370 different nonsensory GPCRs present in the human body, around 90% are present in the brain and have been found to play pivotal roles in appetite control.³⁰

As demonstrated in **Figure 3** above, glucagon is released from the pancreatic α -cells when blood glucose concentration decreases below the ideal range, often due to exercise. The glucagon binds its receptor (GCGR), on the surface of liver cells,³¹ which triggers glycogenolysis, a breakdown of glycogen stored inside the liver cells into glucose. This results in an influx of glucose into the bloodstream, raising the concentration and returning it back to the ideal range.^{27,31,32}

When levels of blood sugar rise outside the normal range, insulin is released from pancreatic β -cells. Blood glucose levels are normalised *via* two means. Firstly, the liver (independent of insulin) transfers glucose into liver cells with the GLUT1 transporter and then converts more glucose into glycogen by the process, glycogenesis. Additionally, insulin causes about 2/3 of body cells, primarily muscle and adipose tissue cells, to take up glucose from the blood through the insulin-regulated glucose transporter (GLUT4). This causes glucose to be metabolised and utilised as energy, thus reducing blood glucose and maintaining glucose homeostasis.³³

Another dietary hormone which contributes to glucose homeostasis is leptin; primarily produced in white adipose tissues and secreted into the circulation. Leptin lowers blood glucose levels in a similar way to insulin, particularly in hyperglycaemic models where high blood glucose levels are present, such as obesity and T1DM. This is achieved by suppressing production of glucagon, increasing glucose uptake, and reducing net hepatic glucose output which is defined as the summative total output of all the liver's glucose-related processes.^{28,33}

1.2.2. Insulin Signalling

The actions of insulin are mediated by its $\alpha_2\beta_2$ glycoprotein transmembrane receptor (InsRb), which is a member of the receptor tyrosine kinase (RTK) family of cell surface receptors. Of the 90 unique tyrosine kinases identified in the human genome, 58 encode for tyrosine kinase protein receptors.^{34,35}

Insulin exerts its biological function by binding to the extracellular α chains of the InsRb. This induces a structural change, facilitating autophosphorylation of specific tyrosine residues Tyr-1146, Tyr-1150, Tyr-1151 in the cytoplasmic portion of the β subunit. Tyrosine phosphorylation increases the catalytic activity of the receptor and generates recruitment sites for downstream signalling proteins, such as the insulin receptor substrates (IRS), as shown below in **Figure 4**.^{34,36-39}

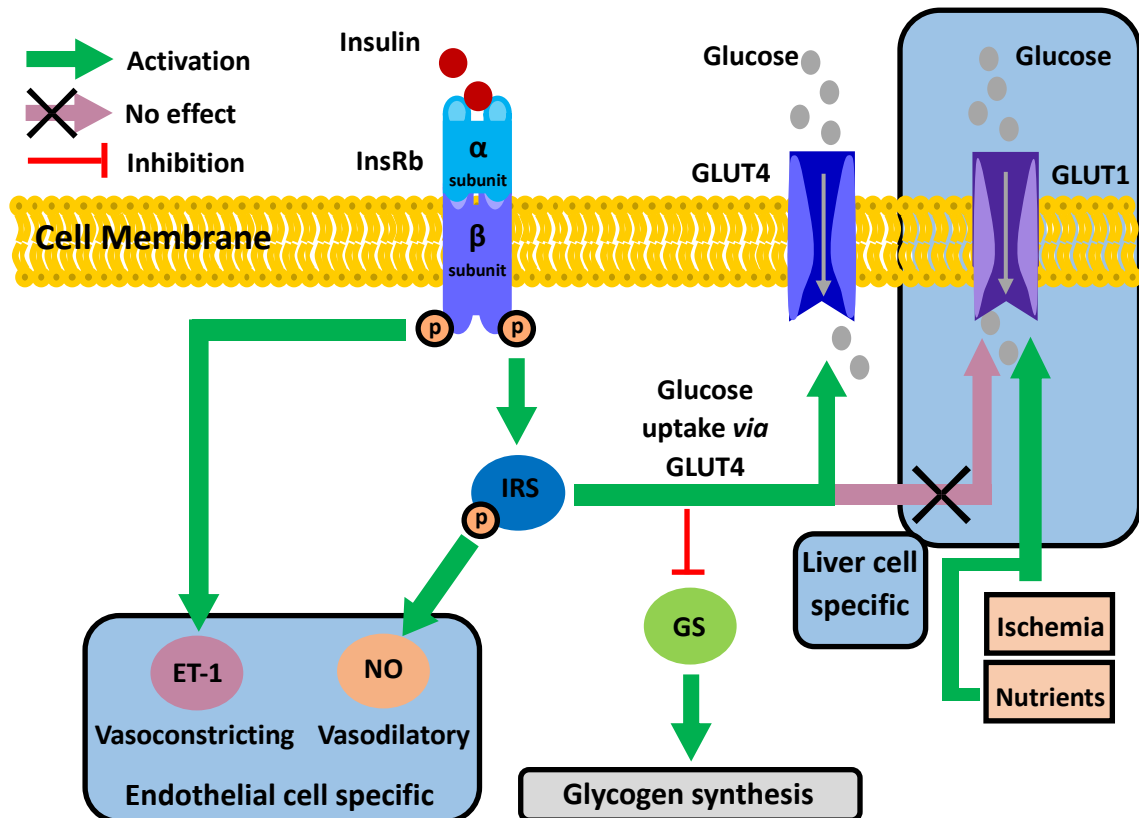


Figure 4: Key biological signalling pathways affected or propagated due to insulin binding. GS: glutamine synthetase, GLUT: Glucose transporter, IRS: Insulin receptor substrate, ET-1: Endothelin-1, NO: Nitric oxide. P: phosphorylated Tyr residue.^{34,36-50}

For the majority of the body's cells including skeletal muscle, adipose and endothelial cells, the glucose transporter GLUT4 is the primary means of glucose absorption into cells for energy production *via* ATP synthesis. In endothelial cells specifically insulin binding also has both direct and indirect effects on the diameter of blood vessels and hence blood pressure. With regards to liver cells, glucose uptake is not dependent or triggered by insulin secretion directly. Instead of GLUT4 being used to transport glucose into liver cells, GLUT1 is utilised. GLUT1 depends on blood glucose concentration (nutrients) and ischemia (decreased blood flow and oxygen level).^{34,36-50}

The immediate effector, insulin receptor substrate (IRS) is activated by tyrosine phosphorylation and are utilised to propagate intracellular signalling. This results in the activation of the glucose transporter GLUT4. GLUT1 which enables uptake of glucose in liver cell operates, independently to the action of insulin. ^{34,36-47}

GLUT1 expression is mainly regulated by blood glucose concentration, cell signalling mechanisms and ischemia which is characterised by decreased blood flow and oxygen concentration. In hypoglycaemic states, there is an upregulation of GLUT1 in tissues such as brain where it helps in providing a major source of energy. ^{34,36-47}

The activation of IRS due to insulin binding to the insulin receptor (InsRb) also downregulates glutamine synthetase (GS) thus leading to an increase in the formation of glycogen which is produced and stored in the liver for future use. As shown above in **Figure 3** glycogen is converted into glucose *via* glycogenolysis and released into the bloodstream raising the blood glucose level when concentration below ideal range.

As demonstrated in **Figure 4**, insulin mediates its actions on blood vessels by stimulating the release of nitric oxide (NO) by endothelial cells. Phosphatidylinositol-4,5-bisphosphate 3-kinase (PI3-K) branch of insulin signalling results in the phosphorylation of P13K's Ser-1177 and subsequent activation of endothelial NO synthase (eNOS) stimulating NO production which induces vasodilation. Conversely, mitogen-activated protein kinase (MAPK) branch stimulates the production of endothelin-1 (ET-1) resulting in vasoconstriction. Both these processes of endothelial vasodilation and vasoconstriction are insulin mediated, this is a contributing factor for the common link between cardiovascular issues and T1DM as stated above. ⁴⁸⁻⁵⁰

Therefore, any effect resulting in glucose dysregulation predominately due to impaired insulin sensitivity would exert a greater effect in the periphery tissues.

1.2.3. Leptin signalling

Leptin is a 16-kDa protein hormone, which is secreted by adipocytes and is involved in the regulation of appetite suppression as well as other cardiometabolic responses to obesity, as stated above. Plasma leptin concentration increases in proportion to body fat mass and regulate food intake and energy expenditure to maintain body fat stores. ^{38,51-53}

Insulin, glucocorticoids, FOS-like antigen 2 (FOSL2), and leptin itself, include the main hormones which regulate the expression of leptin. FOSL2 is a key transcription factor

that controls leptin expression in adipocytes. Circulating leptin levels provide an indication of adiposity and is proportionate to body fat mass.^{38,51-53} The central nervous system (CNS), particularly the hypothalamus, is the predominant leptin target and is the main site for implementing leptin's anti-obesity action including control of appetite, energy expenditure and metabolism. Leptin exerts its biological action through binding to and activating predominantly the long form of leptin receptor (LepRb).

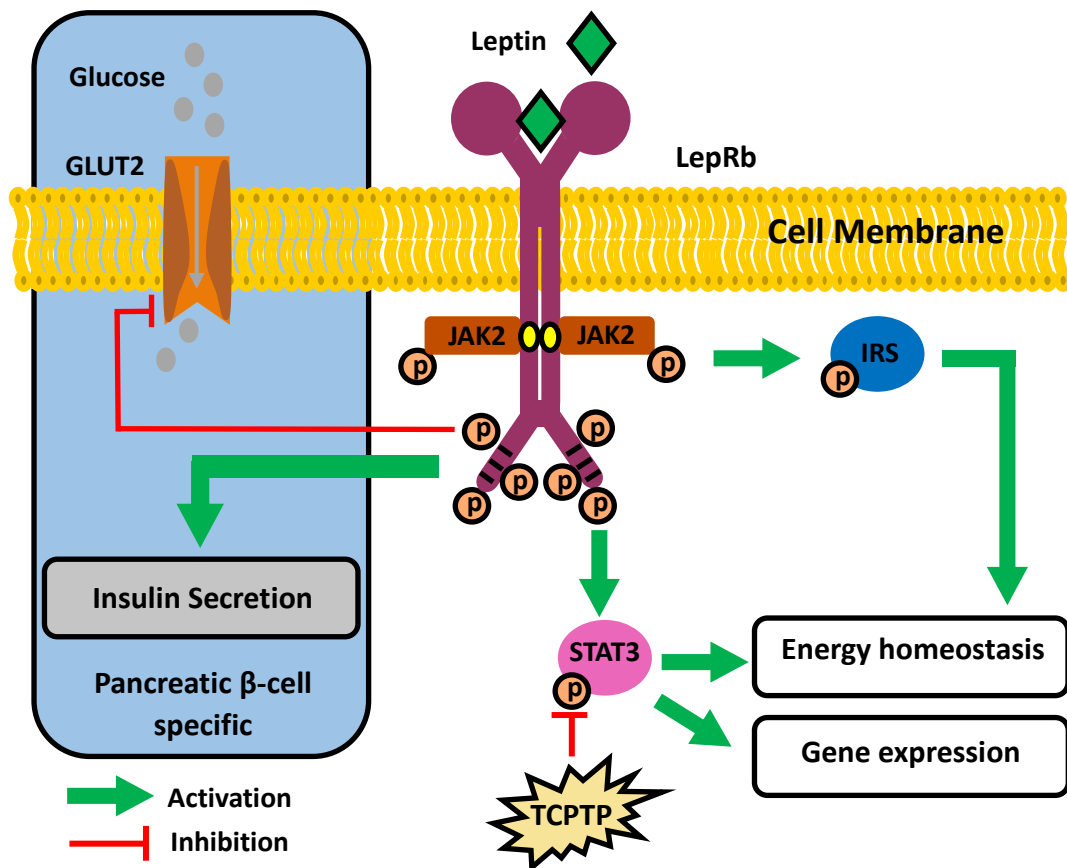


Figure 5: Signalling pathway induced *via* the binding of the dietary hormone leptin. STAT proteins are latent cytoplasmic transcription factors activated by various extracellular signalling proteins. Gene expression denotes reduced fatty acid synthesis and increased fatty acid oxidation.^{40,62,98}

As shown above in **Figure 5**, upon leptin binding to the leptin receptor (LepRb) its biological action is induced. Intracellularly, the LepRb does not have an intrinsic tyrosine kinase domain, therefore it binds cytoplasmic kinases, mainly Janus tyrosine kinase (JAK2). Like other cytokine receptors, the LepRb contains a highly conserved, proline-rich box1 and two, less conserved, box2 motifs. Box1 and box2 motifs are considered important in recruiting and binding JAKs. These resultant activated JAKs subsequently transphosphorylate each other, as well as other specific tyrosine residues (Tyr-985, Tyr-1138 and Tyr-1077) of the leptin receptor, providing docking sites for downstream

molecules such as STATs (signal transducer and activator of transcription protein), which result ultimately in leptin's function.^{32-36,53}

The JAK-STAT signalling pathway self-regulates its suppressors. Suppressors of cytokine signalling (SOCS) molecules provide negative feedback by inhibiting JAK and STAT activation and phosphorylation. The SOCS family includes eight family members, SOCS1–7 and cytokine-inducible SH2-containing protein (CIS).^{32,34-36,53}

In addition to controlling appetite suppression, leptin also has a direct effect on blood glucose levels (see **Figure 3**). Leptin is able to suppress the production of glucagon, which inhibits net hepatic glucose output, and increases glucose uptake in skeletal muscle and brown adipose tissue *via* the hypothalamic–sympathetic nervous system axis and β -adrenergic mechanism, thus leptin is involved in multiple mechanisms for the reduction of blood glucose levels.^{33,54}

However as shown in **Figure 5**, leptin binding to the long form of the LepRb (ObRb) can also have an indirect effect of raising blood glucose levels by down regulating the biosynthesis and subsequent release (exocytosis) of insulin into the bloodstream from pancreatic β -cells.^{55,56}

Several signalling pathways are involved in this inhibitory role of leptin in terms of insulin secretion. Leptin also inhibits glucose transport *via* down regulating glucose transporter 2 (GLUT-2), therefore reducing the amount of glucose available for metabolism. Leptin itself is upregulated in response to food consumption.^{55,56}

Leptin directly affects the pancreatic β -cell gene expression leads and has bearing on the β -cell mass by altering proliferation, apoptosis, and cell growth.⁵⁶ The regulation of β -cell mass is essential for the response of the pancreas to increase insulin demand, when required such as in an obese model. The proliferative, antiapoptotic, and proapoptotic effects of leptin are known to regulate mass of pancreatic β -cells.⁵⁶

Interestingly, insulin can stimulate leptin secretion from adipose tissue, resulting in a hormonal regulatory feedback loop called the adipo-insular axis. Dysfunction of this plays an important role in the development and exacerbation of hyperinsulinemia and type II diabetes.^{55,56}

In order to prevent overexpression of the primary hormones related to glucose regulation and appetite suppression; insulin and leptin, the body has in place a negative feedback

loop, to control the hormonal activity, this can provide a means for therapeutic intervention.

1.3. Target for therapeutic intervention

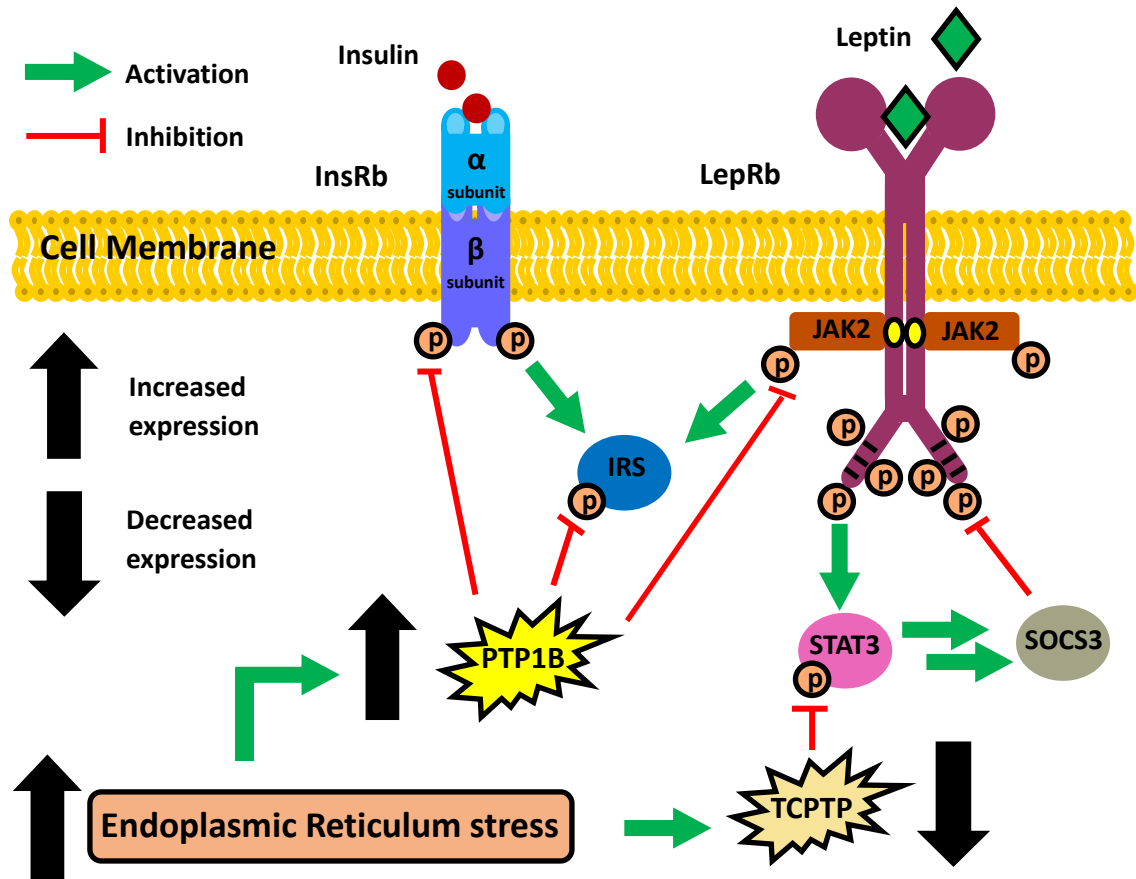


Figure 6: Downregulation of insulin and leptin signalling by PTP1B. Insulin exerts its biological function predominantly in peripheral tissue, whereas leptin's main biological target sites are present in central tissue. Protein tyrosine phosphatase 1B (PTP1B), T-Cell Protein tyrosine phosphatase (TCPTP).^{40-50,57}

An important link between the insulin and leptin signalling pathways is the involvement of protein tyrosine phosphatases (PTPs). Specifically, PTP1B (protein tyrosine phosphatase 1B) which in both cases operates to prevent the over expression of these hormones, by dephosphorylating the specific tyrosine residues of the InsRb, and the LepRb recruited JAK2 and IRS. These are essential for the biological binding of insulin or leptin and the subsequent downstream signalling. As demonstrated in **Figure 6**.^{40-50,57}

1.3.1. PTP insulin mediated effect.

With regards to the insulin biological pathway specifically, PTP1B prevents the overexpression of insulin by dephosphorylating specific Tyr residues. This deactivates

both the insulin receptors and the signalling proteins IRS, thus having a two-fold effect of downregulating insulin. In terms of skeletal muscle and adipose tissue predominantly, the prevention of over absorption of glucose in the cells, is achieved by downregulating this signalling pathway that leading to glucose uptake. This is achieved with PTP1B as shown in **Figure 6**.^{40-47,57}

However, for endothelial cell specifically the effect of PTP1B upregulation goes beyond just glucose uptake, (as shown previously in **Figure 4**) in that reducing the effect of insulin binding prevents the over expression of ET-1 and NO synthesis. Both ET-1 and NO are key in controlling the diameter of blood vessels. This imbalance in endothelial cells is a factor that leads to obesity derived cardiovascular issues including hypertension by blood vessel constriction.⁴⁸⁻⁵⁰

1.3.2. PTP leptin mediated effect.

As with insulin, PTP1B exerts its biological effect on leptin signalling by dephosphorylating specific Tyr residues of the recruited IRS and JAK2. This reduces the downstream signalling effect of leptin which leads to in part, to impaired appetite control. Two additional proteins involved in leptin regulation, are suppressor of cytokine signalling 3 (SOCS3), which is activated by signal transducer and activator of transcription 3 (STAT3), and T-Cell protein tyrosine phosphatase (TCPTP).^{32,34-36,53}

SOCS3 operates in a similar manner to PTP1B in terms of leptin downregulation. As SOCS3 also dephosphorylates the same phosphorylated Tyr residues of the recruited JAK2 motif, and the specific Tyr residues of the LepRb itself which become phosphorylated as a result of JAK2 recruitment and activation. Hence like PTP1B, SOCS3 also limits the biological response of leptin binding.^{32,34-36,53}

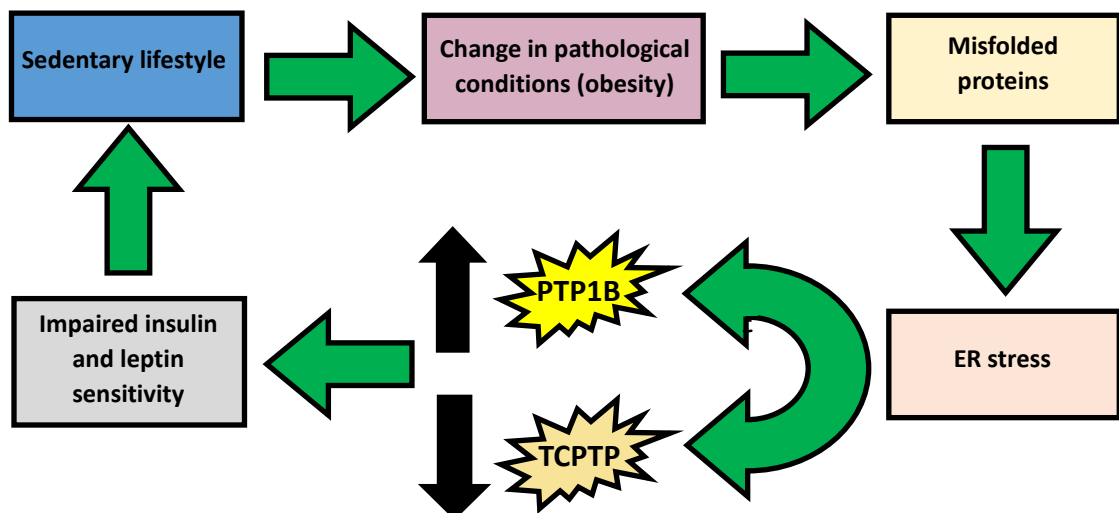
TCPTP operates more downstream in leptin signalling pathway by downregulating STAT3. STAT3 is activated by the phosphorylation LepRb itself and is involved in maintaining energy homeostasis. Hence a downregulation of TCPTP due to increased ER stress triggers an increase proportion of phosphorylated STAT3 which causes increased SOCS3 activity thus adding to dysregulation of energy homeostasis and gene expression.

Both protein tyrosine phosphatases operate in a similar manner to each other by dephosphorylating their respective signalling proteins reducing the respective subsequent signalling.

However, in terms of leptin signalling PTP1B and TCPTP biological effects both collectively contribute to energy homeostasis as shown in **Figure 6**. PTP1B operation reduced the effect of leptin section as the dephosphorylation of the activated JAK2 Tyr residues reduces leptin binding. Whereas TCPTP attenuates the leptin induced STAT3 signalling pathway which subsequently triggers a lesser response of SOCS3 meaning a greater proportion of LepRb is active as fewer are dephosphorylated. However, the reduced activity caused by STAT3 again leads to contribution of energy homeostasis impairment.^{32,34-36,53}

1.3.3. Overarching review

PTP1B is anchored to the cytosolic face of the endoplasmic reticulum (ER) and serves as an enzyme with multiple functions. Due to this fact ER stress is a contributing factor in the up regulation of PTP1B.^{40,41,44,46} ER stress is the result of the accumulation of misfolded/unfolded proteins. Which is caused by changes in nutrients and energy status of pathological conditions such as obesity which overwhelms the capacity of ER leading to the condition termed as endoplasmic reticulum stress (ER stress). Where it has been shown in mice models that increased ER stress simultaneously down regulates the expression of TCPTP and upregulates that of PTP1B.⁵⁸ A simple depiction of this is shown in **Scheme 2**.



Scheme 2: Generalised overview of the effect of a sedentary lifestyle and the ultimate effect on leptin and insulin signalling.

ER stress results in a reduction in glucose uptake into cells *via* GLUT2 and GLUT4 and a decrease in glycogen formation. As PTP1B dephosphorylates a greater proportion of the active InsRb, LepRb and IRS (see **Figure 6**), a reduction in insulin and leptin

sensitivity is observed, resulting in a sustained elevated blood glucose levels and an increased delay in fullness after eating. Insulin's reduction in sensitivity is due to the glucose transporter protein (GLUT4) not being activated by the downstream effects of IRS-1 and IRS-2 (see **Figure 4**). But as GLUT1 operation is not dependent on insulin signalling, hepatocytes are still able to uptake glucose. However, under increased PTP1B activity glucose is incorrectly metabolised in the liver, and not stored as glycogen. Further resulting in the impairment of glucose homeostasis. ^{40,41,44,46,59}

The effects of PTP1B upregulation in response to increased ER stress, on the insulin and leptin signalling pathways. With regards to insulin the effect on the majority of the body's cells (such as skeletal muscle, adipose), is that the activity of GLUT4 is impaired resulting in reduced uptake of glucose into these cells, causing a reduced metabolism rate of glucose and a sustained elevated blood glucose level because of this. But for endothelial cells specifically, an increase in blood pressure and endothelial dysfunction is observed, due to a reduced NO bioavailability.

Hence in summary obesity contributes to an impairment of glucose and appetite regulation *via* up regulation of PTP1B and down regulation of TCPTP due to increased ER stress, which both contribute to insulin and leptin insensitivity. This is why PTPs have the potential to provide means for therapeutic intervention for this metabolic syndrome.

1.4. Protein tyrosine phosphatase family

The protein Tyrosine Phosphatase (PTP) family includes in excess of 100 members, with numerous and differing physiological functions throughout the body. ⁶⁰⁻⁶² PTPs are defined by containing the unique signature motif HC(X)₅R. This superfamily of proteins can be subdivided into two general groups. These are the tyrosine specific PTPs that dephosphorylate tyrosine residues present in protein substrates (Classical PTPs). Which can be subdivided again into Tyrosine-specific PTPs comprising receptor-like PTPs and non-transmembrane PTPs. The second main category of PTPs is the DSPs (dual-specificity phosphatases) that dephosphorylate protein substrates on tyrosine, serine, and threonine residues, as well as lipid substrates. ^{63,64}

The catalytic domain of classical PTPs comprises approximately 280 residues and is defined by several short sequence motifs, in particular the signature sequence that functions as a phosphate-binding loop at the active site.

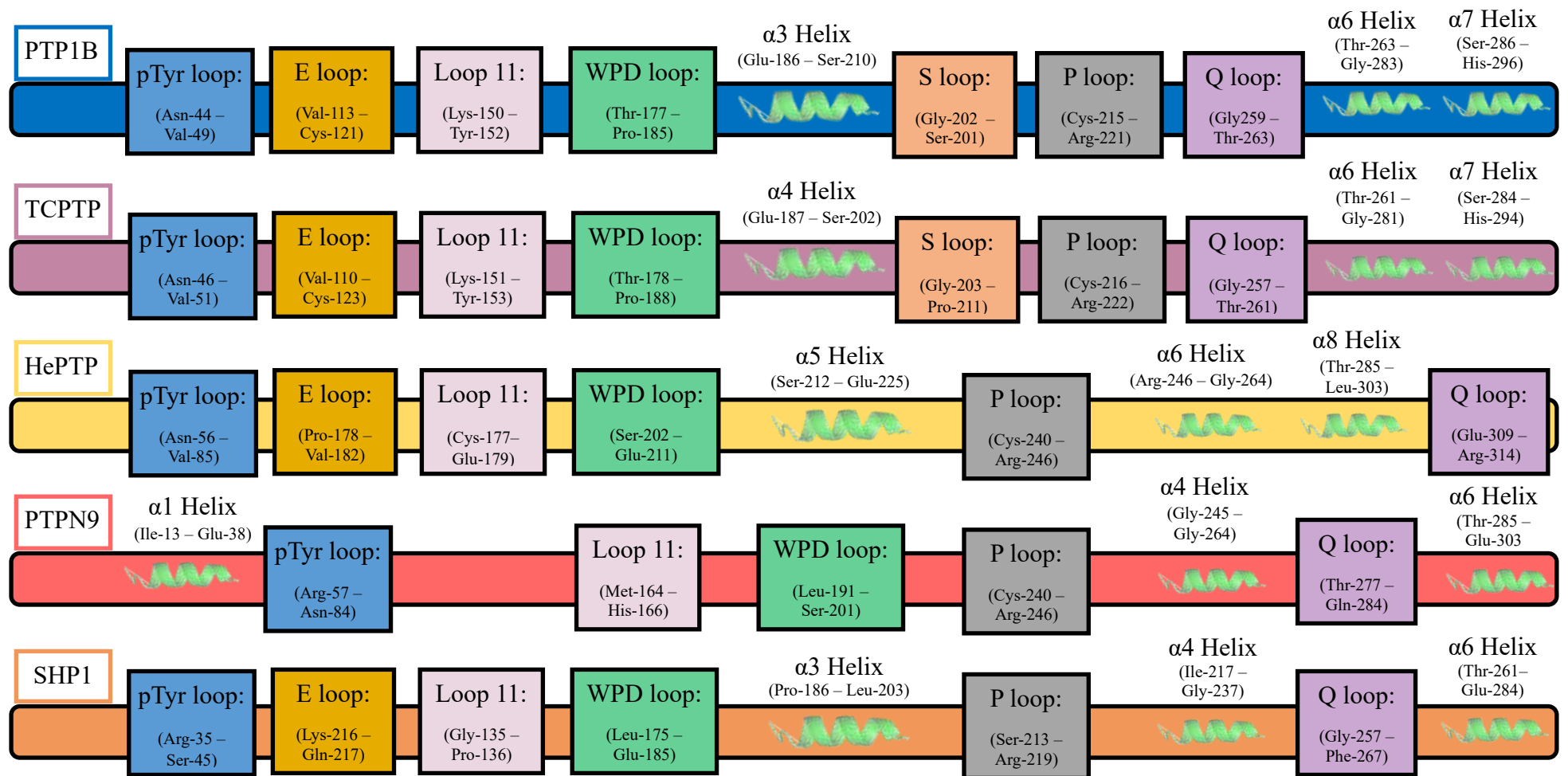


Figure 7: Illustration of PTPs demonstrating the similarities and differences in protein sequence and structure of catalytic domains. ^{61,65-74}

The classical PTPs include transmembrane receptor-like proteins (RPTPs) which exert signalling through ligand-controlled protein tyrosine dephosphorylation. The other subcategory are non-transmembrane, cytoplasmic PTPs, and are characterised by regulatory sequences that neighbour the catalytic domain and control activity. These non-catalytic sequences control subcellular distribution, thereby indirectly regulating activity by limiting access to particular substrates at specific subcellular locations. ^{63,64}

There are approximately 65 genes that encode the heterogeneous group of phosphatases called dual specificity phosphatases or DSPs. These enzymes are less conserved than the classical PTPs and have reduced sequence similarity between each other apart from the cysteine-containing signature motif. Generally, DSPs share the same catalytic mechanism as the classical PTPs, but the composition of the DSP active site allows them to accommodate phosphoserine and phosphothreonine residues as well as phosphotyrosine residues in proteins. Giving them greater biological activity than classical PTPs which can only exert their biological function of Tyr residues. ^{63,64}

Despite the underlying biological function of, the major subfamily of PTPs being comparable to one another, the key structural motifs can vary significantly or be structurally similar, This is demonstrated in **Figure 7**, where specific structural features involved in biological function or integral to a druggable target site are highlighted. ^{61,65-74}

The main structural features of the five PTP shown above in **Figure 7** that are shared are essential for the catalytic activity of Tyr dephosphorylation and these are the pTyr loop, loop 11, WPD loop, P loop and the Q loop. The primary biological binding site is denoted as the active / catalytic site or P loop and in the majority of PTPs the cysteine residue is key for substrate turn over. This is true for all of the five PTPs shown in **Figure 7**, apart from SHP 1 as its P loop is flanked by a serine and an arginine residue rather than a cysteine and an arginine residue. Despite this difference Src homology region 2 domain-containing phosphatase-1 (SHP1) is still capable of dephosphorylating and therefore is able to deactivate a number of kinases as part of its biological function. ^{61,65-74}

Key differences between the selected PTPs shown in **Figure 7** concern the number, order and positions of the α helices present in the protein structure. These are of interest not for contribution towards biological function, but instead potential alternative means of down regulation or inhibition of the PTP. This is because the helix at the C-terminus, which is about 20Å away from the active site in PTP1B, and the two-encompassing helices in terms of physical positioning create a hydrophobic pocket. This provide an alternative means for inhibition, due to the distribution of the WPD loop *via* loop 11, this is discussed further below.

The function and primary location of the five PTPs shown in **Figure 7** are as follows: PTP1B as discussed above is a major negative regulator for both the insulin and leptin receptor signalling pathways and is bound to the cytoplasmic surface of the endoplasmic reticulum.⁴⁸ TCPTP, is an expressed non-receptor type tyrosine phosphatase, and as stated above is also involved in the leptin signalling pathway but in fact exerts the opposite effect to PTP1B when maintaining energy homeostasis.⁷⁵

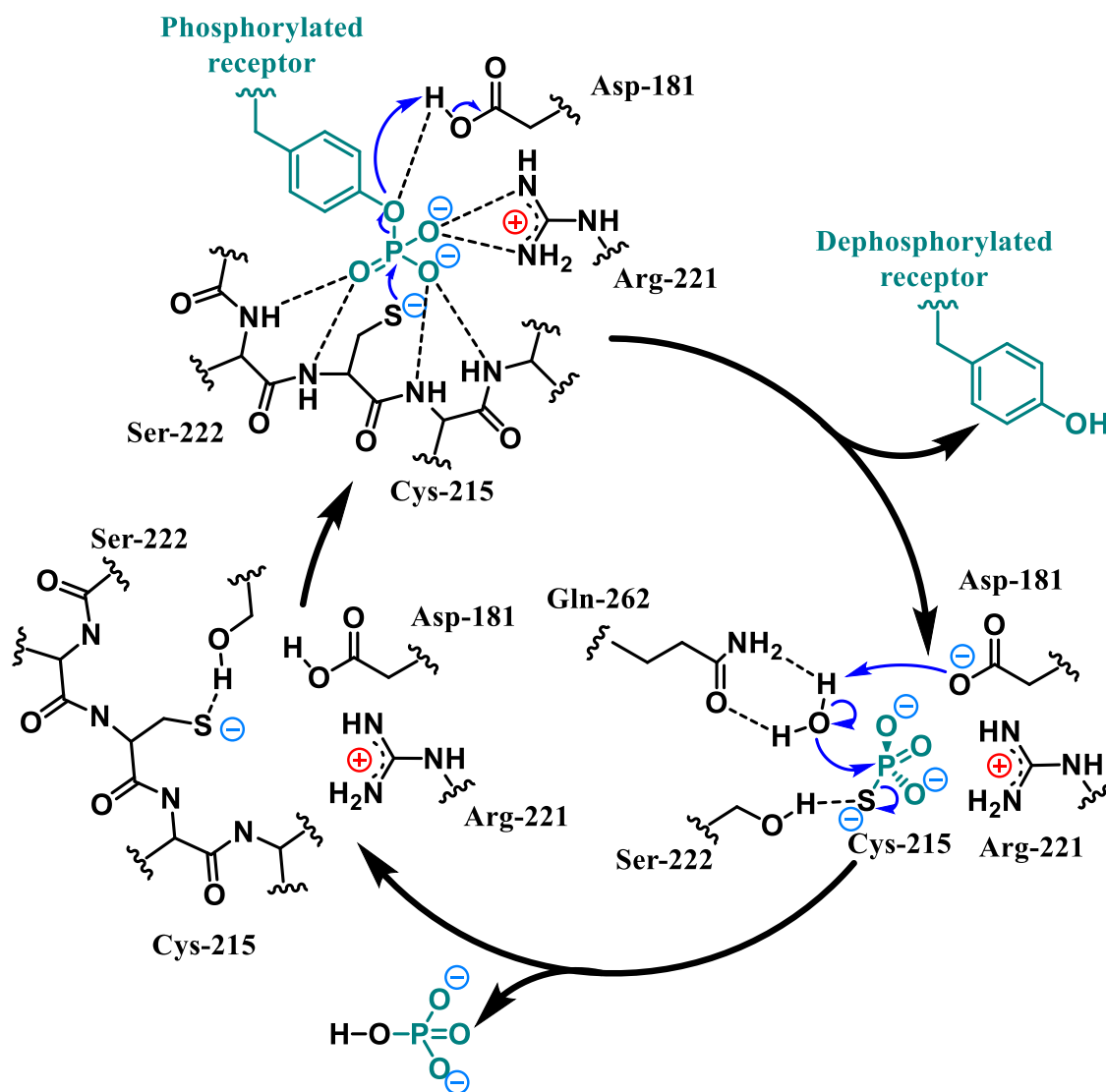
HePTP (haematopoietic protein tyrosine phosphatase) functions is as a negative regulator of p38 MAP kinases (mitogen-activated protein kinases) in T-cells, p38 MAP kinase plays an essential role in regulating many cellular processes including inflammation, cell differentiation, cell growth and death. Therefore, potentially HePTP may also play a role in obesity onset due to its involvement in inflammation.⁷⁶

PTPN9 (Protein Tyrosine Phosphatase Non-Receptor Type 9) function is the negative regulation of the paracrine vasoprotective activity of bone-marrow derived pro-angiogenic cells.⁷⁷

The final of the five PTPs shown in **Figure 7** is the most different both structurally and operationally. SHP1 is a component of U1 snRNP and is required for mRNA splicing and has been linked to several types of autoimmune and neurodegenerative diseases.⁷⁸

The primary reason for discussing other members of the PTP family which are not all related to the onset or as a means for potential treatment of metabolic syndrome is to demonstrate that despite the wide range of biological functions carried out by this superfamily, a significant number exert their function *via* dephosphorylation of Tyr residues using a structurally similar catalytic site of action. Hence why developing a selective inhibitor for any PTP is challenging, but imperative to ensure the desired result without additional off-target effects. This is particularly poignant when considering a

PTP1B over TCPTP selective inhibitor. Specifically, PTP1B's sequence in its catalytic domain is 74% identical with TCPTPs and the two enzymes possess near superimposable active sites. ⁶⁷ TCPTP has different biological functions from PTP1B as demonstrated above in **Figure 6**. Hence leading to off-target effects if a non-specific active site inhibitor is used *in vivo*, which is clearly undesirable for pharmaceuticals.



Scheme 3: Catalytic cycle of PTP1B's active site in 'normal' physiological conditions.

1.4.1. PTP catalytic mode of action

Scheme 3 shows the general catalytic cycle of non-transmembrane tyrosine specific PTPs active site which causes the biological function in 'normal' physiological conditions. In this process a specific tyrosine phosphorylated receptor is reduced to a phenol (dephosphorylated) and hydrogen phosphate is produced as a by-product. ^{43,79-81} The specified residues shown in **Scheme 3** denote the surrounding residues of PTP1B's active

site specifically but the overall process involving Cys, Arg and Asp residues is the same for all non-transmembrane tyrosine specific PTPs, only the sequence number may differ.

PTP1B can only bind to the 'activated' InsRb due to the resultant conformational change, caused by insulin binding as mentioned previously. After PTP1B has bound,³⁸ a localised conformational change is induced in which the WPD loop containing Phe-182 moves 5.5 Å into the catalytic site, contributing to a hydrophobic pocket that buries the pTyr of the substrate. This conformational change positions the side chain of Asp-181 enabling it to act as a general acid to facilitate protonation of the phenolic oxygen atom of the tyrosyl leaving group. Cleavage of the scissile bond yields a Cys-215 thiol-phosphate intermediate and releases the free substrate protein product (dephosphorylated insulin receptor).³⁹

It is important to note that the PTP1B tyrosine residues Tyr-66, Tyr-152 and Tyr-153 are essential for controlling the activity of PTP1B as, when these residues are phosphorylated by the InsRb tyrosine kinase PTP1B, binding affinity towards IRK (insulin receptor kinase) increases. Furthermore, these tyrosine residues remain phosphorylated after completion of the catalytic cycle, increasing that PTP1B's future activity towards subsequent insulin receptor kinases. Currently it is not fully understood how PTP1B's Tyr residues (Tyr-66, Tyr-152 and Tyr-153) become dephosphorylated, which would reduce the PTP1B activity. A prominent theory, is that PTP1B modulates its own tyrosine phosphorylation state, thereby providing a mechanism for regulating its own enzymatic activity, by undergoing some form of auto-dephosphorylation, probably *via* an intermolecular mechanism to return to its basal state. Thus, it is plausible that insulin stimulation may result in impaired PTP1B activity in physiological conditions.⁸²

In addition, insulin stimulation also causes down regulation of PTP1B due to phosphorylation of PTP1B residue Ser-50 by Akt (Protein kinase B, a serine/threonine-specific protein kinase). The following PTP1B residues Ser-50, Tyr-46, Arg-47, Asp-48 and Val-49 play important roles in stabilising substrates in the catalytic site of PTP1B. Thus, it is plausible that phosphorylation at Ser-50 may alter the ability of PTP1B to engage and dephosphorylate its substrates. Since Akt is a downstream effector of insulin and leptin action and as PTP1B acts at upstream sites to inhibit these hormones' action, the ability of Akt to impair PTP1B function may also contribute to positive feedback mechanism.^{35,82}

1.4.2. PTP1B:

PTP1B is one member of the Protein Tyrosine Phosphatase family, and as demonstrated above is a plausible target for inhibition as a means of obesity, TIID and comorbidities treatment.⁶⁰⁻⁶²

PTP1B is a non-transmembrane tyrosine phosphatase and intracellular protein which is widely expressed throughout the body including the brain, liver, skeletal muscle, and adipose tissue. As a tyrosine-protein phosphatase, PTP1B's main function is the dephosphorylation of intracellular tyrosine residues.⁶⁰⁻⁶²

Protein Tyrosine Phosphatase 1B (PTP1B) has two well defined druggable targets for small molecule inhibitors. As displayed in **Figure 8** these are the active or catalytic site and the allosteric site which is a druggable pocket ~ 20 Å away from the catalytic site.

^{60,79,83,84}

1.4.3. PTP1B target sites

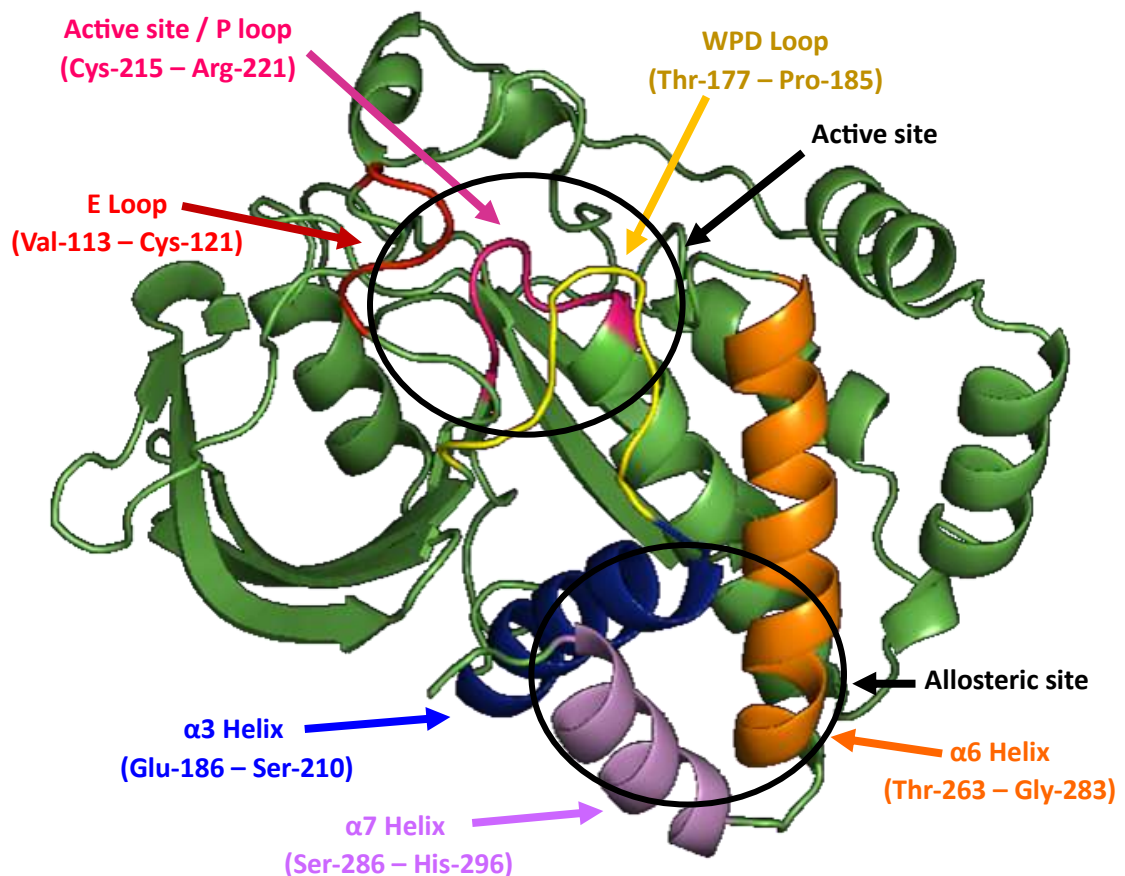


Figure 8: Crystal structure of PTP1B. PTP1B residues that are key either for binding or biological function are also highlighted.^{42,92,115}

The two target sites (active and allosteric) are structurally very different. With the active site being a narrow channel where the main binding feature, which induces the biological function is the cysteine residue (Cys-215) at its base. Additionally, the conformation of the WPD loop is also a major factor in the ability for substrates to bind to this site.⁶⁰ Whereas the allosteric site is a hydrophobic pocket located on the C-terminal domain of PTP1B encompassed by helices α 3, α 6 and α 7.^{60,79,84}

1.4.3.1. Active site

Initial literature focused on targeting the active site of PTP1B as a means of therapeutic intervention for TIID and related comorbidities. But due to the chemical nature of this target, namely the Cys-215, initial inhibitors contained highly charged chemical groups such as phosphate group (PO_4^{2-}), as seen with 1BZJ in **Figure 9**. Hence, these exhibited low oral bioavailability and limited drug development potential, due to these compounds not functioning in an *in vivo* setting. As the formal charge present impede them entering into cells effectively. Therefore, alternative strategies were needed to create clinically relevant inhibitors, that were still active and able to effectively outcompete the biological targets.^{60,85}

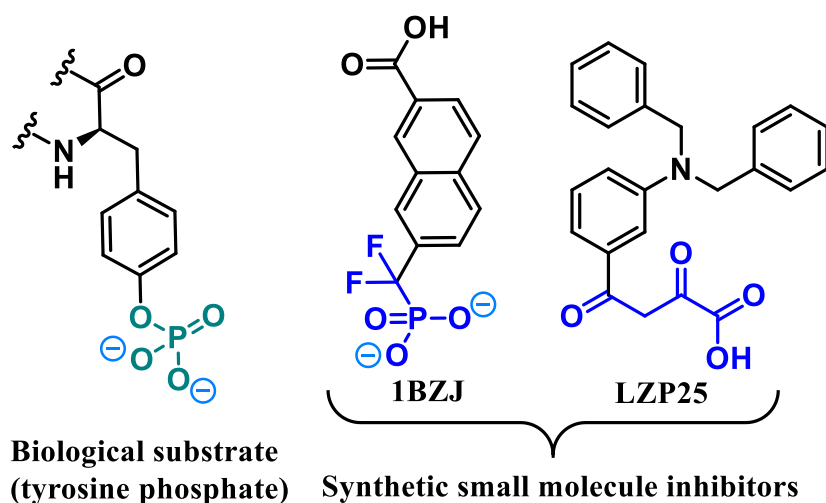


Figure 9: Structures of previous synthesis active site inhibitors. Key structural motifs for binding of both the biological substrate and inhibitors have been highlighted (bind to Cys-215 at the base of the active site).^{42,86,115}

LZIP25 (**Figure 9**)⁸⁶ attempted to overcome the bioavailability and cell permeability issues by utilising a functional group with a similar size and polarity to the phosphate group (PO_4^{2-}), but with the inclusion of a reduced number of formal charges. As at physiological pH carboxylic acids are charged. Hence if successful, overcoming arguably the main inabilities of previous inhibitors of PTP1B's active site.⁸⁶

Kinetic Analysis of PTP1B Inhibition calculated an IC_{50} value for LZP25 (aryl diketoacid) of $20 \pm 5 \mu\text{M}$.⁸⁶ The selectivity of LZP25 for PTP1B was also examined against a panel of PTPs including cytosolic PTPs, HePTP, SHP2, and Lyp, the receptor-like PTPs, LAR and PTPR, and the dual specific phosphatase, VHR. In terms of IC_{50} LZP25 displayed at least three-fold selectivity for PTP1B over all PTPs examined⁸⁶, however the fact that TCPTP was overlooked is interesting when investigating the selectivity of PTP1B active site inhibitors, due to the extensive structural similarities.

However, when the mammalian cell membrane permeability of LZP25 was investigated, it was found to have poor penetration. S. Lui *et al.*⁸⁶ proposed that the carboxylic acid may contribute to the poor permeability and that by removing the acid functional group with a piperazine linker, LZP25 cellular permeability may improve. This was shown to be the case.⁸⁶

Additionally, another contributing factor that the authors did not mention could be the molecules cross sectional area (CSA) which for its size is fairly large, as CSA in addition to overall Log P also contributes to a molecules permeability. LZP25 did not make it to clinical trial testing.

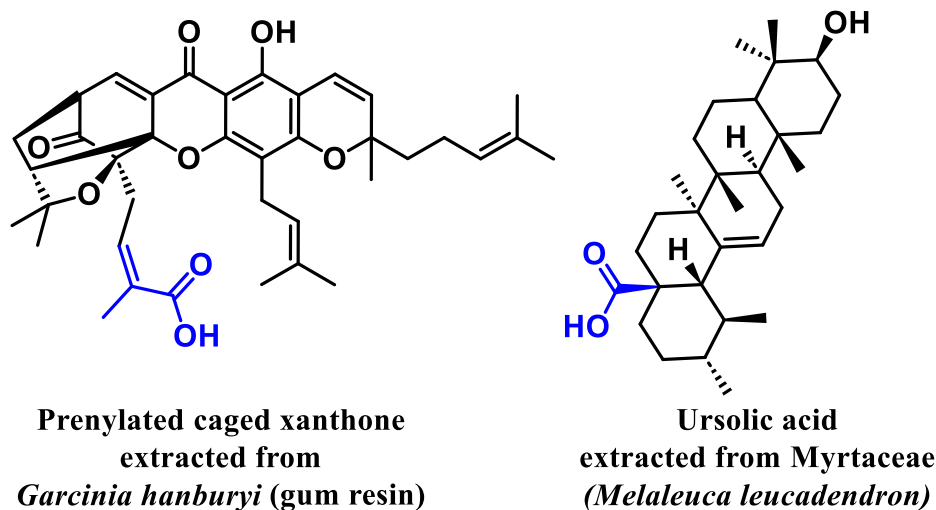


Figure 10: Structures of naturally occurring active site inhibitors. Key structural motifs for binding have been highlighted (bind to Cys-215, at the base of the active site).⁸⁷⁻⁸⁹

In terms of naturally occurring active site inhibitors, examples are shown in **Figure 10**. The prenylated caged xanthone is one of the predominant metabolites of the yellow gum resin (derived from *G. hanburyi*). They are known to have numerous therapeutic benefits, including anti-inflammatory activity.^{87,88}

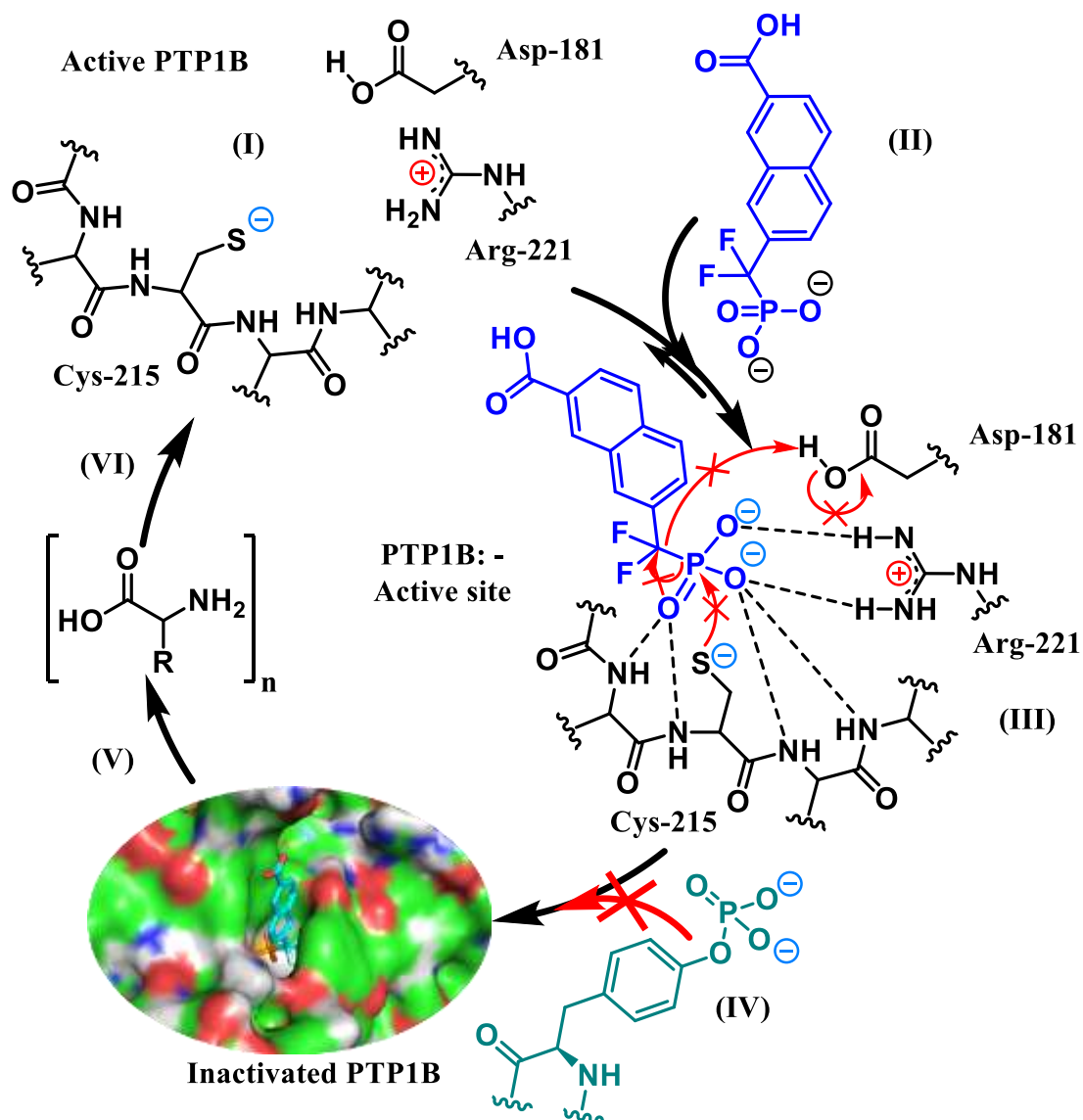
As discussed above, proinflammatory proteins such as NF- κ B, activate PTP1B which leads to the suppression of glucose regulation. Therefore, these prenylated caged xanthenes being anti-inflammatory also may have a positive impact on the knock-down of proinflammatory proteins, thus improving glucose regulation and appetite control, *via* a primary and secondary effect of PTP1B downregulation.^{87,88}

Ursolic acid (UA) is a natural product extracted from *Melaleuca leucadendron* (Myrtaceae) and has been recorded as a component of Jamu, an Indonesian medicinal tonic.^{89,90} UA an established non-specific PTP active site inhibitor that can bind to PTP1B as well as TCPTP which is the closest family member in terms of catalytic site structure. The affinity of ursolic acid between PTP1B and TCPTP is also comparable, when comparing IC₅₀ values, but a lower concentration for half maximum inhibitory effect is observed towards PTP1B. With IC₅₀ values being: 2.3 μ g / mL for PTP1B, and 3.1 μ g / mL for TCPTP.^{89,90}

Due to ursolic acid's lack of selectivity, in its unmodified state it would make a poor choice of lead compound for PTP1B inhibitor drug discovery. Both because of the structural similarities between PTP1B and TCPTP and their differing physiology functions this non-selectivity between the two PTPs is a common issue, in terms of reaching clinical trials.

The binding positions of all the aforementioned active site inhibitors are comparable to not only each other but also the biological substrates. Therefore, it is imperative that the inhibitors are able to outcompete the biological substrates in order to function, by physically blocking the PTP1B site of catalytic action.

The mechanism of PTP1B inhibition by active sites inhibitors is demonstrated in **Scheme 4** below. Since the active site is where the catalytic function of PTP1B occurs, all active site inhibitors are inherently competitive. This may be an issue as over time the body will inevitably upregulate the biological substrate, thus out competing the small molecular inhibitor, if the dosage is kept constant. This could be avoided by targeting another target site of PTP1B thus enabling the inhibitor to be non-competitive.



Scheme 4: Active site inhibitor mechanism of action. ⁸⁷⁻⁸⁹

I: Active site of PTP1B is unbound and active. II: Competitive active site inhibitor binds. III: Biological dephosphorylation mechanism is unable to break the P-C(F₂) bond, so the inhibitor remains bound. IV: PTP1B active site inhibitor is unable to be dephosphorylated so remains bound to be active site. V: PTP1B remains inactive until inhibitor unbinds (if reversible) or is broken down to respective amino acids by protein degradation. VI: PTP1B reformed by protein anabolism. The known inhibitor used within this figure is denoted as 1BZJ as has been discussed above. ⁸⁷⁻⁸⁹

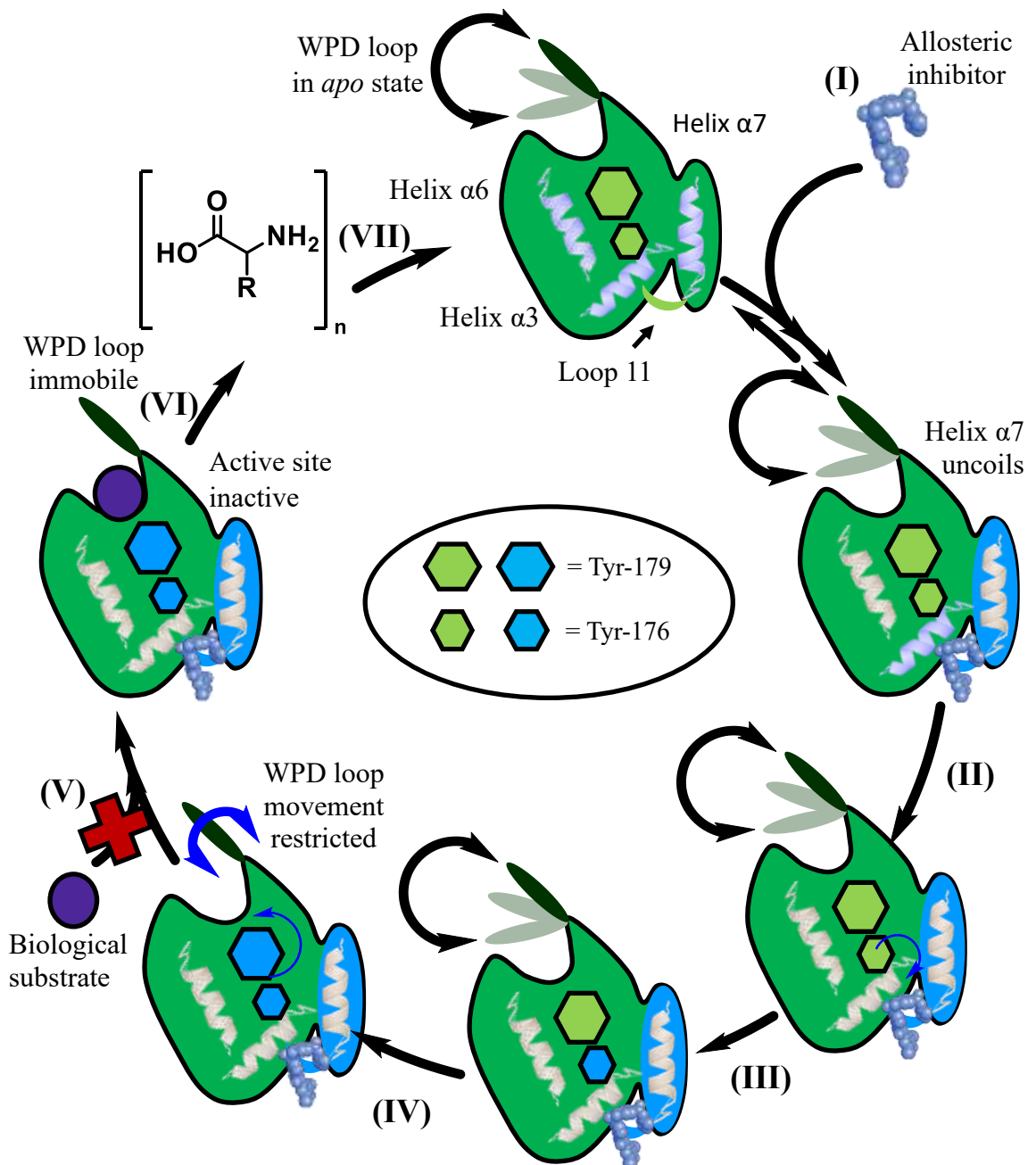
1.4.3.2. Allosteric site

One such alternative druggable target is PTP1B's allosteric site, which is a hydrophobic pocket located at the C-terminal domain of the protein.^{83,84,86}

Intrinsically due to the nature of allosteric inhibitors, they are non-competitive, hence upregulation of the biological substrate will have a lesser impact on the effectiveness of a small molecular allosteric inhibitor long-term (constant dose dependent).⁶⁰

Allosteric site inhibition is achieved by disrupting the catalytic mechanism of PTP1B shown in **Scheme 3**. In normal physiological conditions the WPD loop is in an *apo* state, which means that it is dynamic, and not fixed to either the 'open' or 'closed' conformation, thus allowing the biological substrate to bind, and be turned over by the active site. As it is the closing of the WPD loop that triggers the dephosphorylation process. Binding of an allosteric inhibitor which causes a conformational change, resulting in the WPD loop being restricted to a single 'open' position thus deactivating PTP1B.^{60,83}

The stages of allosteric inhibitor inhibition as shown in **Scheme 3** is outlined as follows. I: Allosteric inhibitor binds. II: Allosteric inhibitor binding induces a conformational rearrangement in helix $\alpha 7$. III: The triangular interaction among helix $\alpha 7$, helix $\alpha 3$, and loop 11 is disrupted, which results in helix $\alpha 3$ being pulled outwards, promoting an interaction between Ser-190 with Tyr-176. IV: This deviation of Tyr-176 repels the hydrophobic interactions with Trp-179 resulting in the downward movement of the WPD loop, causing a H-bond to be formed between Asp-181 and Glu115. V: The formation of this H-bond constrains the WPD loop to its open conformation inactivating PTP1B catalytic function. VI: Inactive PTP1B broken down to respective amino acids by protein degradation. VII: PTP1B reformed by protein anabolism.⁸⁷⁻⁸⁹



Scheme 5: Allosteric site inhibitor mechanism of action. ⁸⁷⁻⁸⁹

The mechanism of action for allosteric inhibitors is depicted above in **Scheme 5**, and summarised here: When an allosteric inhibitor binds to the hydrophobic pocket present on PTP1B C-terminus (allosteric site) a conformational rearrangement in helix $\alpha 7$ occurs. This interrupts the triangular interaction among helices $\alpha 7$, $\alpha 3$, and loop 11, resulting in helix $\alpha 7$ exerting a force that pulls helix $\alpha 3$ outward.^{83,84,86}

This conformational change results in Ser-190 interacting with Tyr-176. The subsequent repulsion of Trp-179, leads to the downward movement of the WPD loop, resulting in the formation of a H-bond between Asp-181 and Glu-115. The formation of this H-bond constrains the WPD loop to its open conformation. With the WPD loop remaining in the open position the biological substrate is still able to bind to PTP1B's active site but will not undergo dephosphorylation, thus inactivating PTP1B.^{29,60,62,82-84}

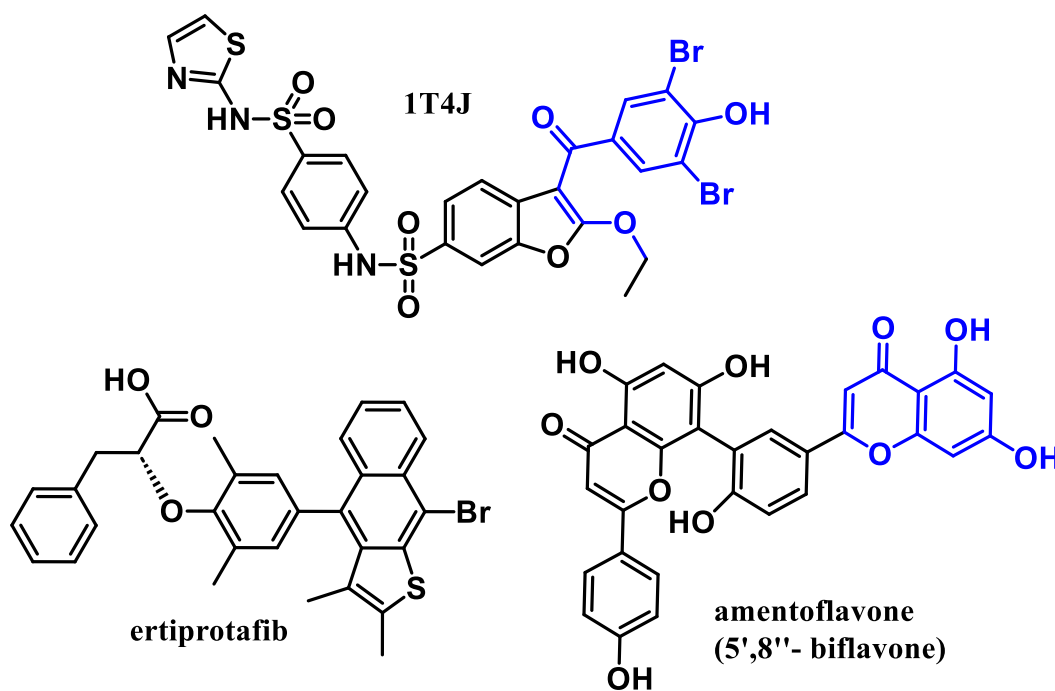


Figure 11: Known allosteric inhibitors^{29,60,62,82-84} from the literature. 1T4J^{29,60,62,82-84} and ertiprotafib are synthetic allosteric PTP1B inhibitors. Amentoflavone^{91,92} naturally occurring compound.

With regards to allosteric inhibitors, in the current literature a number of synthetic and natural small molecule allosteric inhibitors share similar functional groups; this can be seen when comparing 1T4J and amentoflavone in **Figure 11** above.^{91,92}

Interestingly the binding mode of 1T4J and amentoflavone are comparable due to shared functional groups. Where the right terminal benzene ring possesses two electron withdrawing groups *meta* to each other along with a carbonyl and an ether group in very

similar positions when bound. Specifically, the hydroxyl groups hydrogen bond with the amine present in helix $\alpha 3$, with the carbonyl in both cases again forming a hydrogen bond with Asn-131. The aromatic ring present also π -stacks with the benzene present in Phe-196, therefore, it is logical to presume that this structural motif is required for binding and thus induce the configurational changes needed to inactivate PTP1B's active site. Leading to the desired therapeutic effect of improving glucose homeostasis, leptin sensitivity and hepatic steatosis. ^{91,92}

The other allosteric inhibitor shown in **Figure 11** is ertiprotafib which was the first reported PTP1B inhibitor to reach clinical trials. However, in 2022 ertiprotafib failed phase II clinical trials due to undesirable side effects. ^{93,94}

1.4.3.3. Disordered region

There is also a third, binding region of PTP1B in addition to the active and allosteric sites. This is a poorly defined disordered region of the protein and so is less favourable for targeted drug synthesis. However, there are known inhibitors of PTP1B that operate by binding to this relatively un-investigated disordered region of PTP1B. ^{60, 95-97}

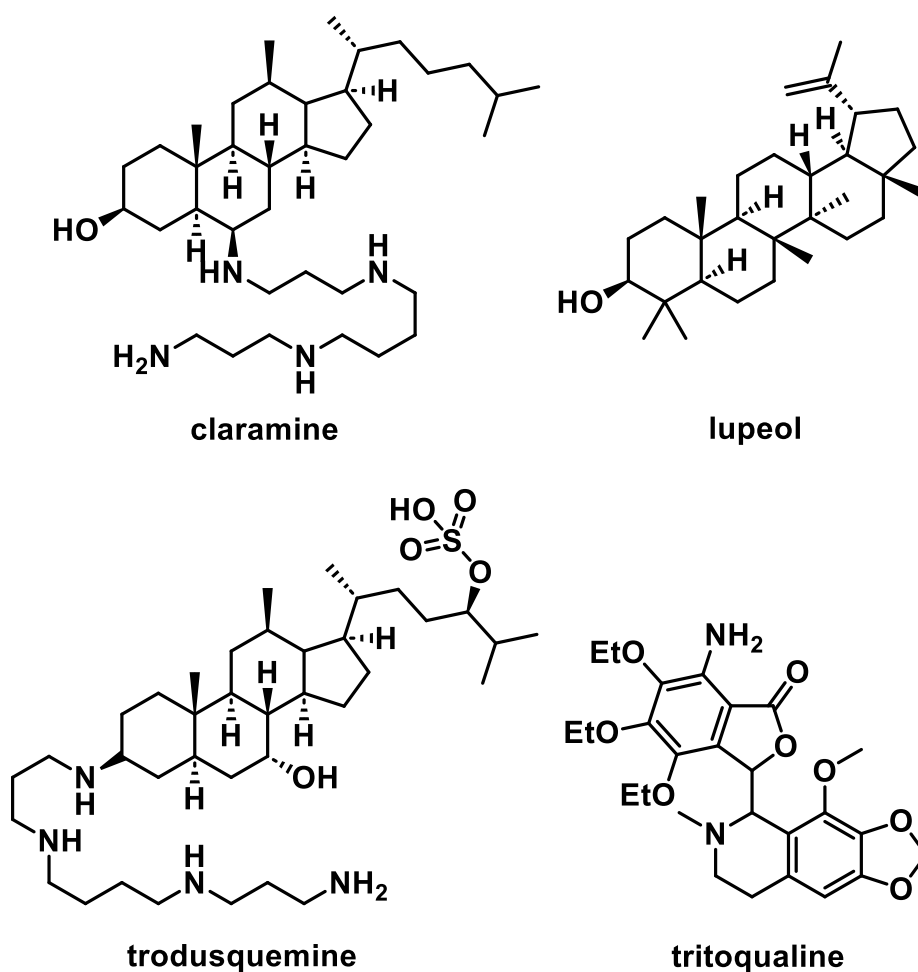


Figure 12: Known disordered region inhibitors, from the literature, and lupeol. Lupeol, is a known PTP1B inhibitor with an unknown binding position.^{60, 95-97}

These include the natural product trodusquemine, and its simplified synthetic analogue claramine⁹⁴, in addition to triterpene lupeol (Lupeol)⁹⁵ which is a natural product obtained from the Caribbean fruit Myrtaceae (*Pimenta racemosa var. ozuca*). (**Figure 12**).

Trodusquemine was originally isolated from the dogfish shark (*Squalus acanthias*) but has been synthesised chemically, for easier investigation.⁹⁶

Trodusquemine and claramine both display selectivity towards PTP1B over TCPTP,⁹⁷ but both are also BBB permeable thus discounting them for the treatment of type II diabetes and comorbidities. A disordered region binder that reached but did not surpass phase I clinical trials is tritoqualine.⁹⁷ Tritoqualine was investigated for the treatment of obesity, TIID, and cancer. Tritoqualine is a synthetic product whose primary pharmaceutical use is as a histidine decarboxylase inhibitor, for the treatment of urticaria, a type of itchy rash.⁹⁷

Figure 12 above also shows the structure of triterpene lupeol, has been found to be a potent non-competitive inhibitor of PTP1B, $IC_{50} = 5.6 \mu\text{M}$.⁹⁵ Therefore, lupeol cannot be bound to the active site due to being non-competitive. Because of this T. Jin *et al.*⁶⁰ proposed that lupeol and other active triterpene compounds (such as betulin), must operate *via* the allosteric site, and inhibit PTP1B by the mechanism shown above in **Scheme 5**. But since lupeol shares more structural similarities with claramine and trodusquemine than with the known allosteric inhibitors, as shown in **Figure 11**. It is possible that these triterpene compounds may instead bind to the same or another poorly defined disordered region of PTP1B, rather than the allosteric site. But future work would be needed to confirm either way.

1.5. Animal models of PTP1B deletion

To demonstrate the potential therapeutic effect of PTP1B inhibition on individuals with metabolic syndrome, numerous *in vivo* mouse model studies have been conducted. These demonstrated that when the mice are deficient in PTP1B the normal effects of a high fat diet, on body weight, glucose regulation and hepatic steatosis are substantially improved as a result. This further illustrates the utility PTP1B has as a therapeutic target, for obesity and related comorbidities.^{43,60,62,98}

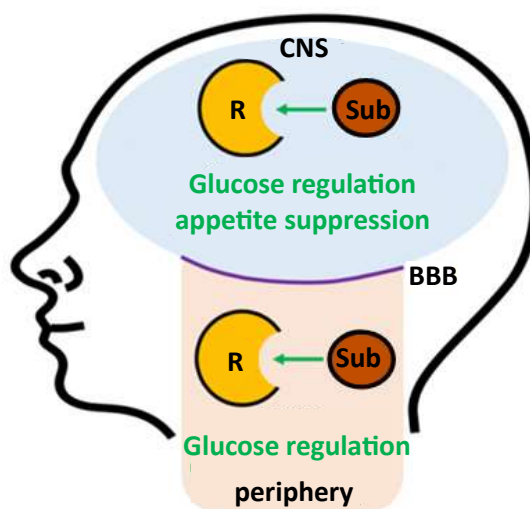


Figure 13: Effects of leptin and insulin binding to their corresponding receptors. CNS (primarily leptin) and periphery (primarily insulin) receptors (R). BBB: Blood Brain Barrier, Sub: substrate (leptin / insulin).^{40,43,59,62,81,98-102}

A brief summary of insulin and leptin's biological function is shown in **Figure 13**. The biological result of insulin and leptin binding to their corresponding receptors differs based on the location of the binding. For example, the majority of the biological action of leptin is expressed in the hypothalamus. As mentioned previously this is where the majority of the LepRb receptors are located. For individuals suffering from metabolic syndrome their insulin and leptin sensitivity is often impaired due to the upregulation of PTP1B, hence why PTP1B inhibition or knockout can improve insulin and leptin sensitivity. However, the location where PTP1B is more active dictates whether the result is biological improvement or side effect. Because of this difference in tissue response, numerous studies have been conducted on tissue specific PTP1B deletion.^{40,43,59,62,81,98-102}

1.5.1. Genome wide

Genome wide deletion of PTP1B, has numerous positive benefits on subject mice including increased leptin sensitivity, improved glucose regulation, and protection from obesity and T1D. It has also been recorded that the subject mice have a reduced fat pad and become leaner when compared to control mice. This is due to increased energy expenditure and a lower consumption of food on both a chow (3.4% fat) and a 55% fat high fat diet (HFD).^{59,81,98,101,103}

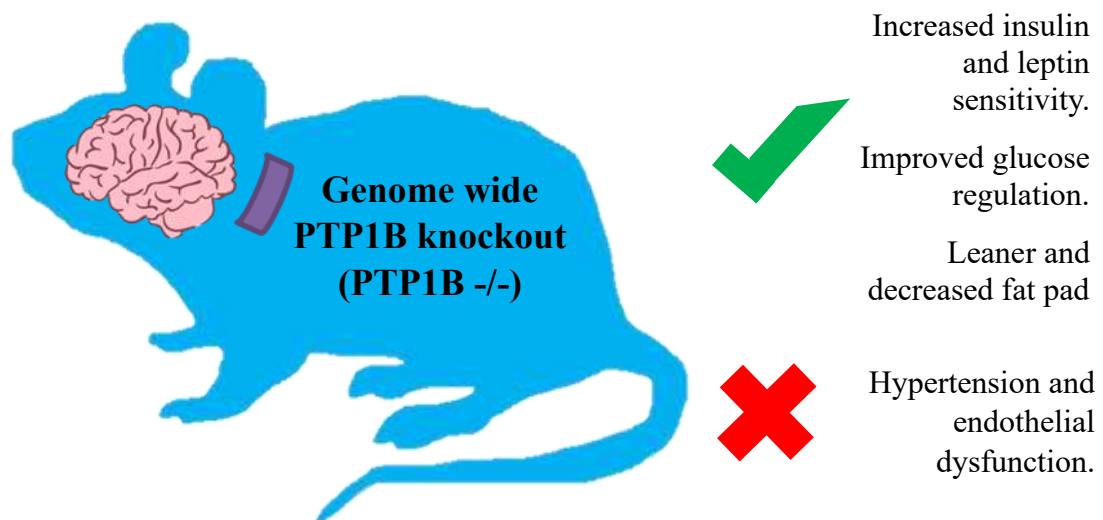


Figure 14: Biological effect *in vivo* on mice with genome wide PTP1B deletion. Compared against control unaltered mice.^{59,81,98,101,103}

Where the green tick denotes positive results, and the red cross corresponds to negative effects.

But as illustrated in **Figure 14** the aforementioned benefits of genome wide deletion or inhibition of PTP1B are outweighed by the resultant cardiovascular consequences. PTP1B deletion in the whole body leads to an increase in heart rate and endothelial dysfunction which subsequently leads to increased blood pressure (BP) in the subject PTP1B^{-/-} mice when compared to controls.⁹⁸ Endothelial dysfunction is a type of non-obstructive coronary artery disease (CAD) where large blood vessels on the heart's surface constrict, without the presence of heart artery blockages. This negative impact of endothelial function leads to the apoptosis of endothelial cells which may result in loss of blood supply to the extremities, leading to potential limb loss.^{59,81,98,101,103}

Due to the target patient group, negative cardiovascular effects caused by treatment would prevent any potential drug approvals. Hence subsequent studies were conducted on tissue specific PTP1B deletion to determine which tissue(s) specific PTP1B deletion / inhibition results in off target side effects including a negative cardiovascular response.

1.5.2. Central Nervous System tissue specific

Neuronal PTP1B^{-/-} mice demonstrate improved glucose homeostasis and are hypersensitive to leptin, despite exhibiting elevated leptin levels when compared to control mice. This results in reduced food intake and increased energy expenditure in neuronal PTP1B^{-/-} mice, as with genome wide PTP1B deletion. Previous work found that the body mass and adiposity of subject mice is primarily operated through actions of PTP1B present in the brain, as neuronal PTP1B regulates adipocyte leptin production and is presumed essential for the development of leptin resistance.^{48,101}

Pro-opiomelanocortin (POMC) neurons have also been specifically investigated in relation to obesity as POMC neurons are mainly located in the arcuate nucleus of the hypothalamus and the *nucleus tractus solitarius* of the brainstem.¹⁰⁴ The hypothalamus is the region of the brain where the majority of leptin's anti-obesity effect originates from.^{39,51,105} POMC neurons release α -melanocortinmelanocortin stimulation hormone (α -MSH) which activates melanocortin 4 receptors (MC4R) on the surface of neurons in the paraventricular nucleus of the hypothalamus (PVH) and brainstem. In doing so this inhibits appetite and increases energy expenditure.¹⁰⁶

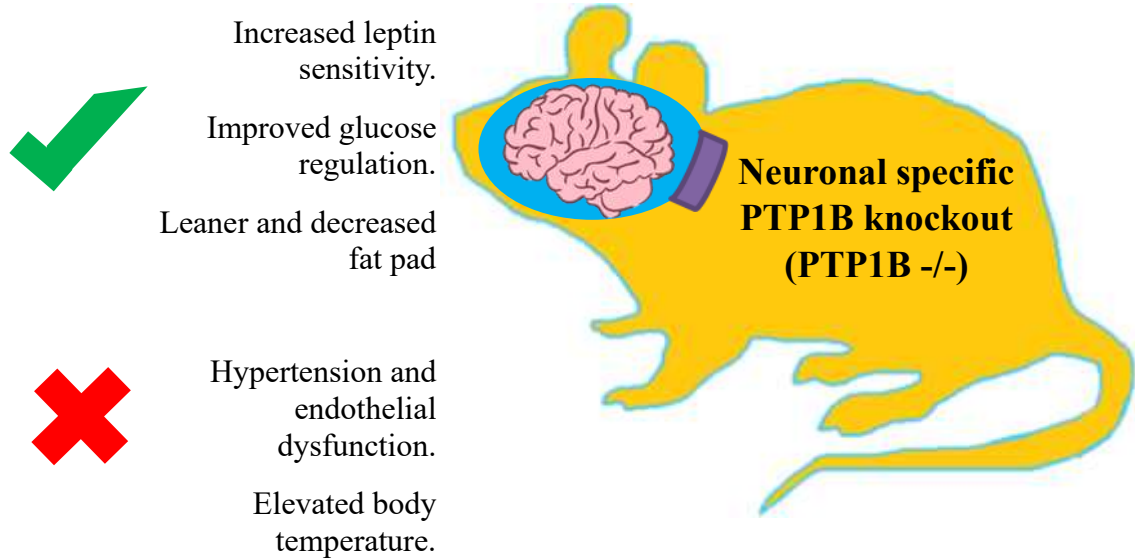


Figure 15: Biological effect *in vivo* on mice with neuronal specific PTP1B deletion. Compared against control unaltered mice. ^{45,59,101}

Where the green tick denotes positive results, and the red cross corresponds to negative effects.

As with whole body and neuronal PTP1B deletion, POMC-PTP1B deletion also results in reduced body fat and increased energy expenditure as evidenced by a decrease in feed efficiency and an increase in oxygen consumption. ^{45,59,101} However POMC-PTP1B deletion also induces a 2.5-fold increase in plasma tumour necrosis factor α (TNF- α) levels, which result in increased endothelial dysfunction in addition to hypertension and elevated body temperature of the subject mice. ¹⁰¹ Hypertension as a result of POMC-PTP1B-/- depends on the activation of the transcription nuclear factor κ B (NF- κ B) and its upstream regulator κ B kinase β (IKK β), in POMC neurons. As PTP1B is a negative regulator of both NF- κ B and IKK β , deletion of PTP1B in these specific neurons results in a higher blood pressure and heart rate. ¹⁰¹

The positive and negative effects present due to neuronal specific PTP1B knockout (PTP1B-/-) are highlighted above in **Figure 15**.

1.5.3. Peripheral tissue specific

Below the effect of specific PTP1B deletion on certain key types of peripheral tissues is discussed.

The brain is the primary PTP1B site that affects fat content of model mice *via* leptin induced appetite suppression. However, liver PTP1B also plays an important role in glucose and lipid metabolism, independent of alterations in adiposity. Previous studies

have demonstrated that liver PTP1B deletion (Alb-Cre-PTP1B^{-/-} mice) results in improved insulin sensitivity, glucose regulation and has a lipid lowering effect, thus potentially protecting the PTP1B-deficient mice from non-alcoholic fatty liver disease. Furthermore, unlike with POMC-PTP1B deletion, endothelial function is not impaired, in fact the opposite is demonstrated. As liver PTP1B deletion impairs endoplasmic reticulum (ER) stress which induce IRE1 signalling. This improves endothelial function, protecting against hypertension, and reduces apoptosis of endothelial cells. ^{34,44,98,102}

Diabetes induces macrovascular endothelial dysfunction *via* endothelial ER stress and PTP1B-mediated apoptosis. Therefore, it was theorised that by inhibiting or removing endothelial PTP1B, the subject mice could be protected against hypertension and apoptosis of endothelial cells caused by endothelial dysfunction. ¹⁰¹

Endothelial-specific deletion of PTP1B as well as pharmacological inhibition protected aortic rings from ER stress mediated endothelial dysfunction. S. Legeay *et al.*, determined this was due to the contribution of the p38/JNK-apoptosis pathway in ER stress-mediated endothelial dysfunction, as endothelial PTP1B was identified as a major regulator of endothelial cell viability in conduit vessels. Thus, endothelial PTP1B^{-/-} is a potential target for the management of macrovascular diseases in diabetics. ¹⁰¹

Muscle-specific PTP1B^{-/-} mice exhibited increased muscle glucose uptake, improved systemic insulin sensitivity, and enhanced glucose tolerance. ⁸¹ So like liver PTP1B, muscle PTP1B also plays a major role in regulating insulin action and glucose homeostasis, independent of adiposity, as fat content was comparable to control mice. But despite the increase in glucose into the muscle no effect on weight gain was observed compared to controls. ⁸¹

M. Delibegovic *et al.* found that the observed improvements of insulin sensitivity in skeletal muscle PTP1B^{-/-} mice was independent of changes in tissue triglycerides and/or adipokines, despite the muscle triglycerides being increased in skeletal muscle PTP1B^{-/-} on both chow and high fat diets over controls. Furthermore, no effect on cardiovascular was observed when compared to controls. ⁸¹

Both chow-fed and HFD adipose PTP1B^{-/-} mice displayed enlarged adipocytes, despite having similar body weight, adiposity and glucose homeostasis compared to control mice. Additionally, HFD adipose PTP1B^{-/-} mice exhibited increased circulating glucose and

leptin levels, in addition to reduced leptin sensitivity and increased basal lipogenesis compared to controls.¹⁰⁷

Insulin-stimulated InsRb phosphorylation is unchanged in the adipose tissue of PTP1B^{-/-} mice, therefore adipose PTP1B is a minor regulator of glucose homeostasis, unlike other peripheral tissues. Hence selective deletion of adipose PTP1B has no drastic beneficial or negative effect on the subject mice.¹⁰⁷

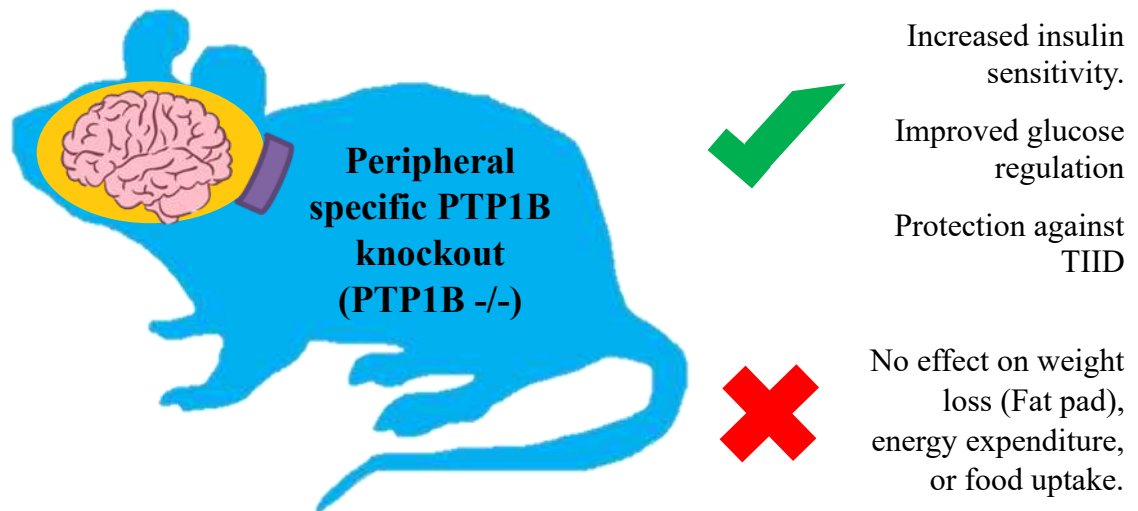


Figure 16: Biological effect *in vivo* on mice with peripheral tissue specific PTP1B deletion. Compared against control unaltered mice.^{45,81,98,101,102,106,107}

Where the green tick denotes positive results, and the red cross corresponds to negative effects.

Therefore, as shown above in **Figure 16**, inhibition of PTP1B specifically in the peripheral tissues provides a tangible means for treatment of metabolic syndrome, by reducing cardiovascular endothelial dysfunction and improving the glucose homeostasis for diabetics. As neuronal PTP1B knock-out is the cause of the negative cardiovascular side effects.^{45,101,106}

1.6. Blood Brain Barrier permeability

Because of the above demonstrated *in vivo* study results conducted on rats any potential PTP1B inhibitor needs to selectively only downregulate PTP1B in the periphery tissues. One way to enable this is to design small molecule inhibitors that are poorly permeable or impermeable to the blood brain barrier (BBB). The presumed biological effect of BBB permeable and impermeable PTP1B inhibitors are illustrated shown below in **Figure 17**.

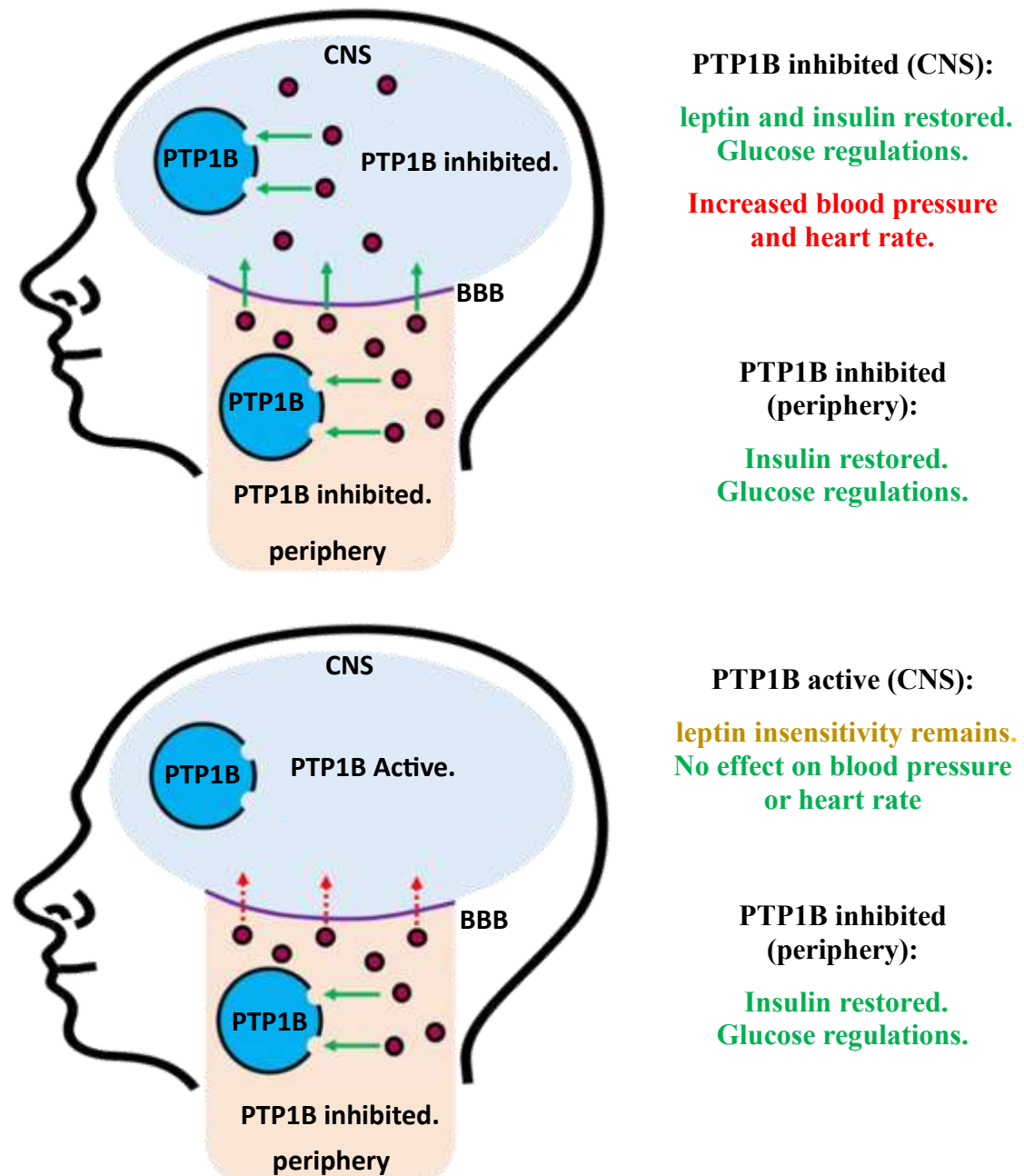


Figure 17: Comparing BBB permeable to BBB impermeable PTP1B inhibitors. Resultant insulin and leptin mediated effects due to use of PTP1B inhibitor that is BBB permeable (top) or BBB impermeable (bottom).^{59,98}

As mentioned above a periphery tissue specific PTP1B inhibitor is the target for obesity, T2DM and related comorbidities treatment, as inhibition in this manner does not exhibit any negative cardiovascular side effects. Since the target patient group for this potential medication already displays obesity induced hypertension, any potential therapeutic intervention that also increases heart rate and blood pressure would not receive approval. A plausible way to achieve peripheral specific PTP1B inhibitors is to develop inhibitors which are impermeable to the BBB, in addition to selectivity towards PTP1B.

One way to obtain a PTP1B inhibitor that is impermeable to the body's blood brain barrier is by designing it specifically with this in mind. BBB permeability is known to be dependent in part on lipophilicity and the compound's cross-sectional area (CSA).¹⁰⁸

A measure of a compound's lipophilicity is its LogP. The LogP value is a constant defined as, relative dissolved distribution between an organic and an aqueous layer. For several classes of CNS active substances, it has been found that blood-brain barrier penetration is optimal when the LogP values are in the range of 1.5-2.7, with the mean value of 2.1.¹⁰⁹ Therefore, designing a compound, that has a LogP outside of this range would increase its likelihood of poor permeability. However, any potential small molecule inhibitor also needs to be able to enter periphery cells, in order to exert its biological effect *in vivo*. It has been shown that drugs with good cell permeability exhibit moderate LogP values. The Lipinski rule of five that is used to evaluate the oral bioavailability of compounds. From this a moderate LogP within the range of $-0.5 < \text{LogP} < 5$ results in substances with good absorption.¹¹⁰ As such the theoretical ideal LogP range for blood brain barrier impermeable small molecule inhibitors is between $-0.5 < \text{LogP} < 1.4$ or $2.8 < \text{LogP} < 5$.

With regards to cross-sectional area, generally the larger the CSA the less permeable the molecule is to the BBB; however this does not mean that small molecules are inherently BBB permeable as other factors place an important role as discussed above with lipophilicity.

1.7. Summary and aims.

The primary aims of this work are outlined as follows: designing, synthesising and optimising inhibitors for the enzyme Protein Tyrosine Phosphatase 1B (PTP1B) that are impermeable to the BBB.

PTP1B poses a very attractive potential target for the therapeutic intervention of obesity and related comorbidities such as type II – diabetes, as previous studies have shown PTP1B downregulation can result in both improved glucose regulation and leptin re-activation, and protection against developing obesity when even on a high fat diet.

To date, no inhibitor of PTP1B has successfully progressed past phase II clinical trials irrespective of the target site of PTP1B being bound. The major contributing factors to the lack of success of previous small-molecule inhibitors are selectivity, chemical properties, and adverse side-effects.

Such off-target effects could be limited by developing an inhibitor that has a low BBB permeability to prevent neuronal PTP1B inhibition which leads to cardiovascular issues, and also PTP selectivity towards PTP1B over other family members.

Computational studies were planned to aid in the identification, design, and development of PTP1B inhibitors. Specifically, utilising database screening against the two defined druggable target sites of PTP1B and docking studies to better understand how molecules potentially bind, and what protein residues are involved.

For PTP1B inhibition effectiveness a preexisting yeast based inhibitory assay was selected with the aim of optimising, and then deploying to determine potency of potential inhibitors towards both PTP1B and TCPTP. Subsequent hit compounds then had their BBB permeability assessed *via* a commercially available synthetic BBB permeability assay.

It was envisaged that these results from these biological assays would feed back into subsequent development of potential PTP1B inhibitor design and operate as an iterative cyclic process. Until a compound was found to be sufficiently selective towards PTP1B over TCPTP, potent and poorly BBB impermeable then further work would be conducted such as animal modes would be conducted in the future. The overarching cyclic nature of this work is illustrated below in **Figure 18**.

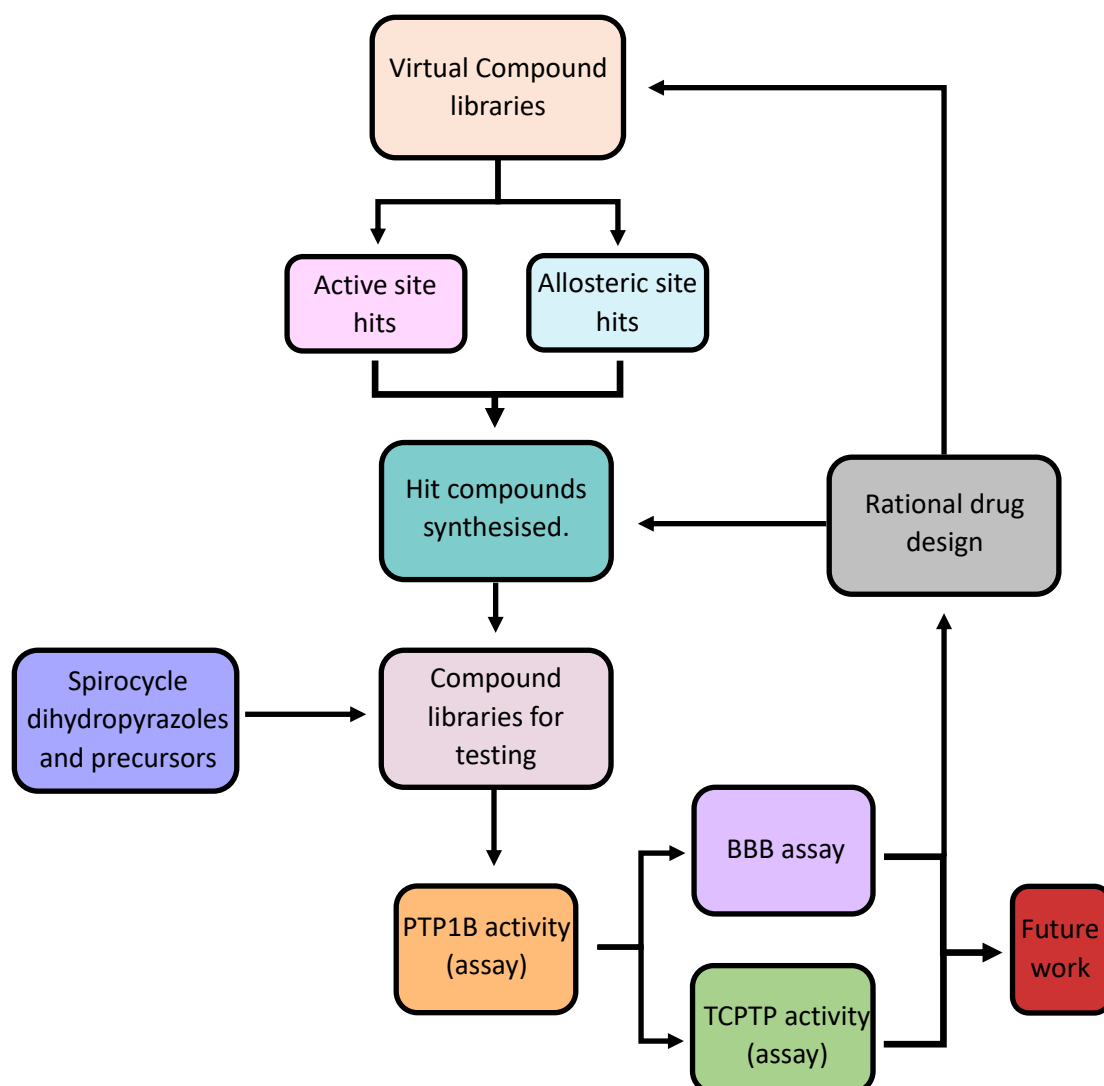


Figure 18: Iterative drug design process of this project.

Hence a peripheral tissue specific small molecule inhibitor that is selective towards PTP1B would be the ideal therapeutic intervention for obesity and comorbidities and is the desired aim of this work.

From the computationally determined potential hit compounds, the selection for which core structures would be further investigated through synthesis and testing were based upon weighing up the following factors: The substrate's binding potential and mode derived from computational modelling, ease of synthesis and accessibility of compounds. All of these factors contributed to the latterly shown core structures which compound libraries for testing were based upon. But the key driving factor was the ease of synthesis as pursuing a computationally perfect inhibitor which has limited proof of synthetic success may not have been the best use of limited time and resources.

Chapter 2

*In silico PTP1B inhibitor
database screen*

2.1 Overview:

Herein justification for the screening of a compound library of ‘drug-like’ spirocyclic dihydropyrazoles is stated in addition to a refined database of screening hits. A database of “shards” (compounds with molecular weight < 200 Da) and of drug-like molecules (according to Lipinski rule of 5) ¹¹⁰ were screened separately against both the active and allosteric target sites of protein tyrosine phosphatase 1B (PTP1B) to identify classes of potential PTP1B inhibitors. These were subsequently synthesised and developed into a hit or lead compound for PTP1B inhibition and thus provide potential means of therapeutic treatment of type II-diabetes (TIID) and related co-morbidities.

2.2 Background:

2.2.1 Molecular three-dimensionality

Molecular three-dimensionality plays a key role in the relative success of potential medicinal small molecule progressing through the numerous stages of clinical trials and becoming licenced pharmaceutical compounds. This is highlighted by F. Lovering ¹¹¹ as shown in **Figure 19**, where mean values with trend line are shown.

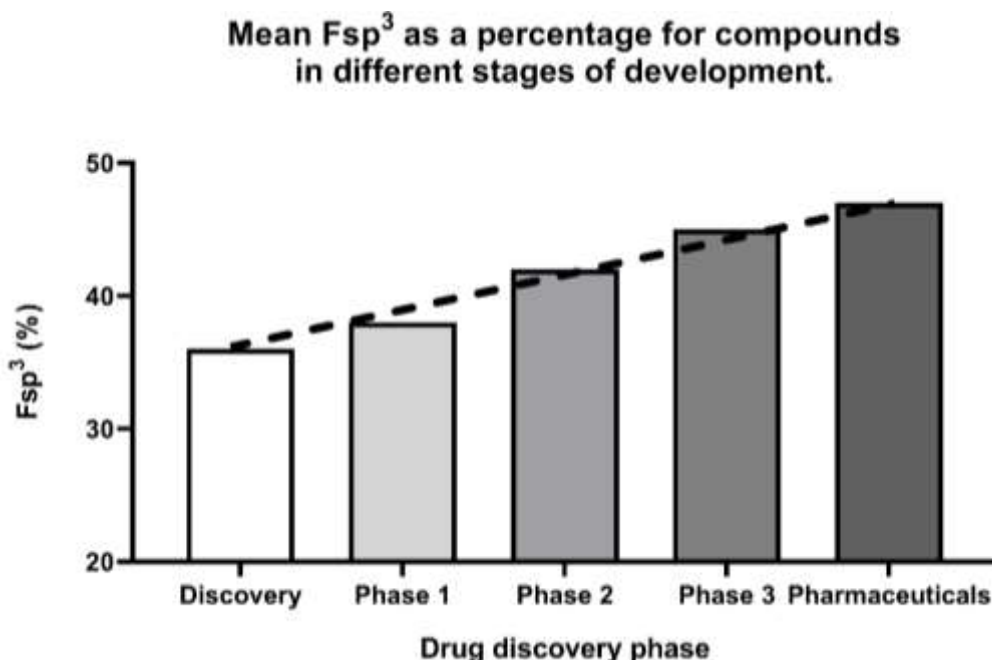


Figure 19: Graphical demonstration of the trend between molecular three-dimensionality and compound success in clinical trials. Modified from F. Lovering et al., ¹¹¹ n = 2.2 million, Phase 1 n = 376, Phase 2 n = 591, Phase 3 n = 188, Drugs n = 1179. n numbers are unrelated to each other, instead denote sample size used to investigate the mean Fsp³-hybridised atoms present, at each stage of the drug discovery process.

A trend between a compound's fraction of sp^3 -hybridised atoms and its progression through the clinical trials is apparent as the mean percentage fraction of sp^3 hybridized atoms of compound in stage 3 clinical trials was found to be 47% up from 38% at the initial discovery stage. This is a substantial increase hence why more three-dimensional compounds due to a higher proportion of sp^3 -hybridised atoms are desirable in pharmaceutical studies as statically such compounds have a greater likelihood of progressing further through clinical trials.

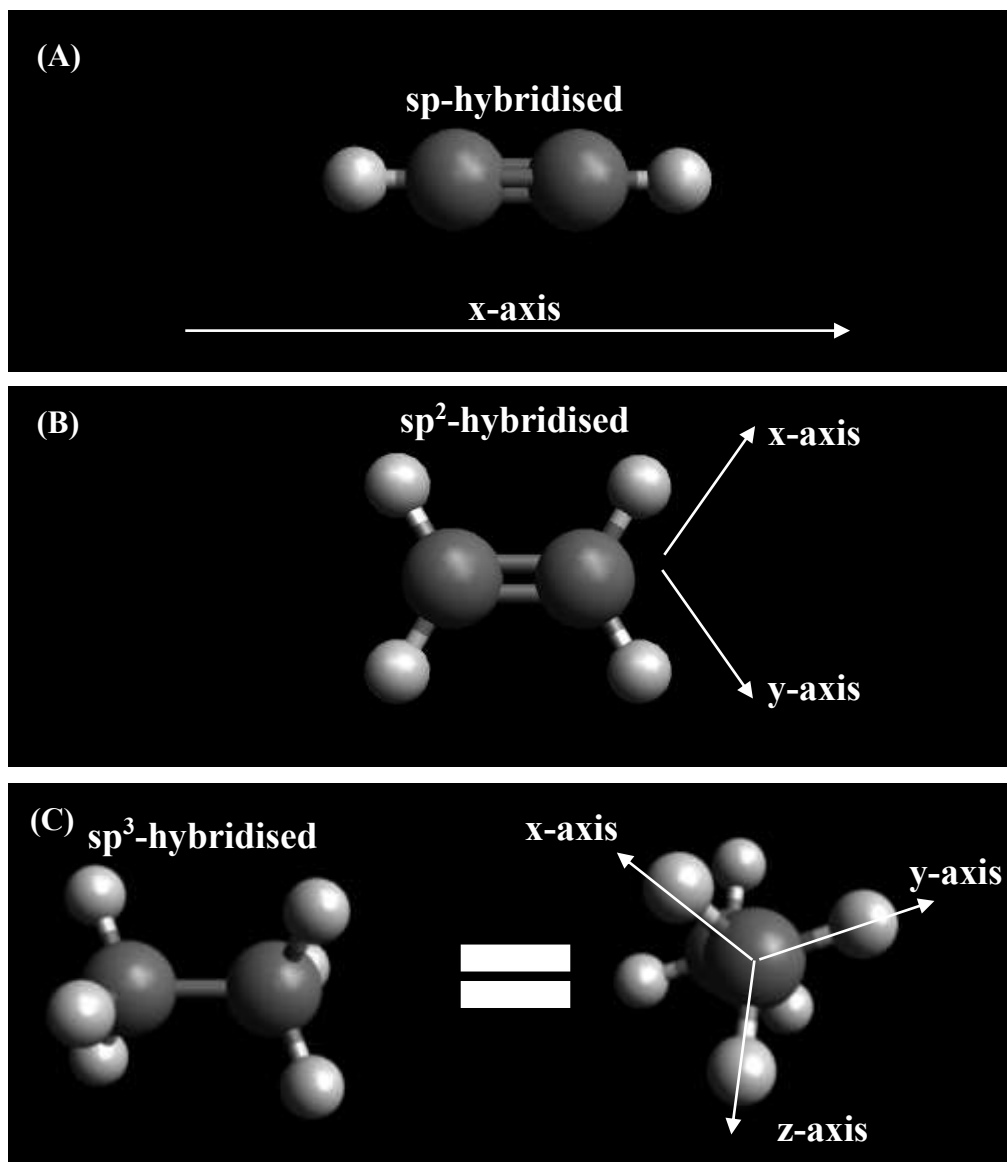


Figure 20: Visualization of how the hybridized state effects the number of dimensions a compound can exert an effect on. (A): sp -hybridised compounds have one exit vector, engages in one dimension (x-axis). (B): sp^2 -hybridised compounds have two exit vectors, engages in two dimensions (x, and y-axis). (C): sp^3 -hybridised compounds have three exit vectors, engages in all dimensions (x, y, and z-axis).

This is partly due to selectivity of the compounds being tested. As shown in **Figure 20**, generally more three-dimensional compounds, such as sp³-hybridised compounds possess a greater amount of ‘chemical information’. Therefore, are able to interact in the third dimension, and so possess increasing selectivity. Thus resulting in fewer side effects, hence desirable for pharmaceutical research.

2.2.2 Hit identification parameters.

When conducting the computational database screen using the software CrossMiner 2022 3.0,¹¹² the potential hit compounds were initially identified using their Tanimoto ratio score, which was calculated in terms of similarity to the designed pharmacophore. These identified potential hit compounds were then inspected to check that both their spatial positioning and three-dimensionality are viable within the target binding site. These phase 2 computational hits (see **Scheme 6** below) from both druggable target sites were taken forward for synthesis and subsequent biological testing. The Tanimoto ratio or coefficient is a measure of similarity between two parties (the pharmacophore and the compound from the database screen). The numerical number is derived from the ratio of the number of features common to both molecules to the total number of features. The range is 0 to 1 inclusive, where the greater the number, the more shared features¹¹²

These initial Phase 1 hits then underwent visual inspection as a mean of hit ratification. Meaning that any ‘hits’ that predominately resided outside of the defined target region such as the active site pocket, or had motifs located within the protein itself were discounted and not considered true hits. These Phase 2 hits were taken forward and plotted into ‘drug-like’ relevant chemical space.

Database screening is the process by which a library of relevant compounds is virtually screened against a predetermined pharmacophore comprised of identified key structural and functional motifs essential for binding. Pharmacophore features for the target site of the protein of interest are designed based on the crystal structure of the defined target region and the bound chemical structure of different known previous inhibitors.

Numerous structurally different previous known inhibitors were investigated. So multiple different binding modes were incorporated into the pharmacophore design for each potential binding site. This resulted in a more informed pharmacophore thus in theory more relevant structures of potential hit compounds for that specific target site.

2.2.3 Computational studies justification.

Conducting database screening of compounds for the drug discovery process, has both positive and negative attributes. The key benefit to computationally screening a database of compounds against a potential therapeutic target is the ability to narrow down or identifying a new compound class of possible inhibitors, thus reducing the number of compounds actually being synthesised and tested, saving time and resources. However, database screening that utilises pharmacophores based on structurally similar compounds can result in stagnation in terms of chemical space. Chemical space is a concept in cheminformatics and can be defined as the set of every possible chemical compound, that could be synthesised based upon the normal valency rules. The location of each compound in chemical space is based upon physicochemical properties.¹¹³ As the resultant hit compounds from the screen will more likely have similar functional and structural properties, thus exist in a similar region of chemical space, potentially resulting in any of the same selectivity / off-target issues of the previously published inhibitors. Specifically with regards to PTP1B inhibitors, new regions of chemical space may need to be explored in order to obtain a PTP1B inhibitor that can successfully pass phase II clinical trials.

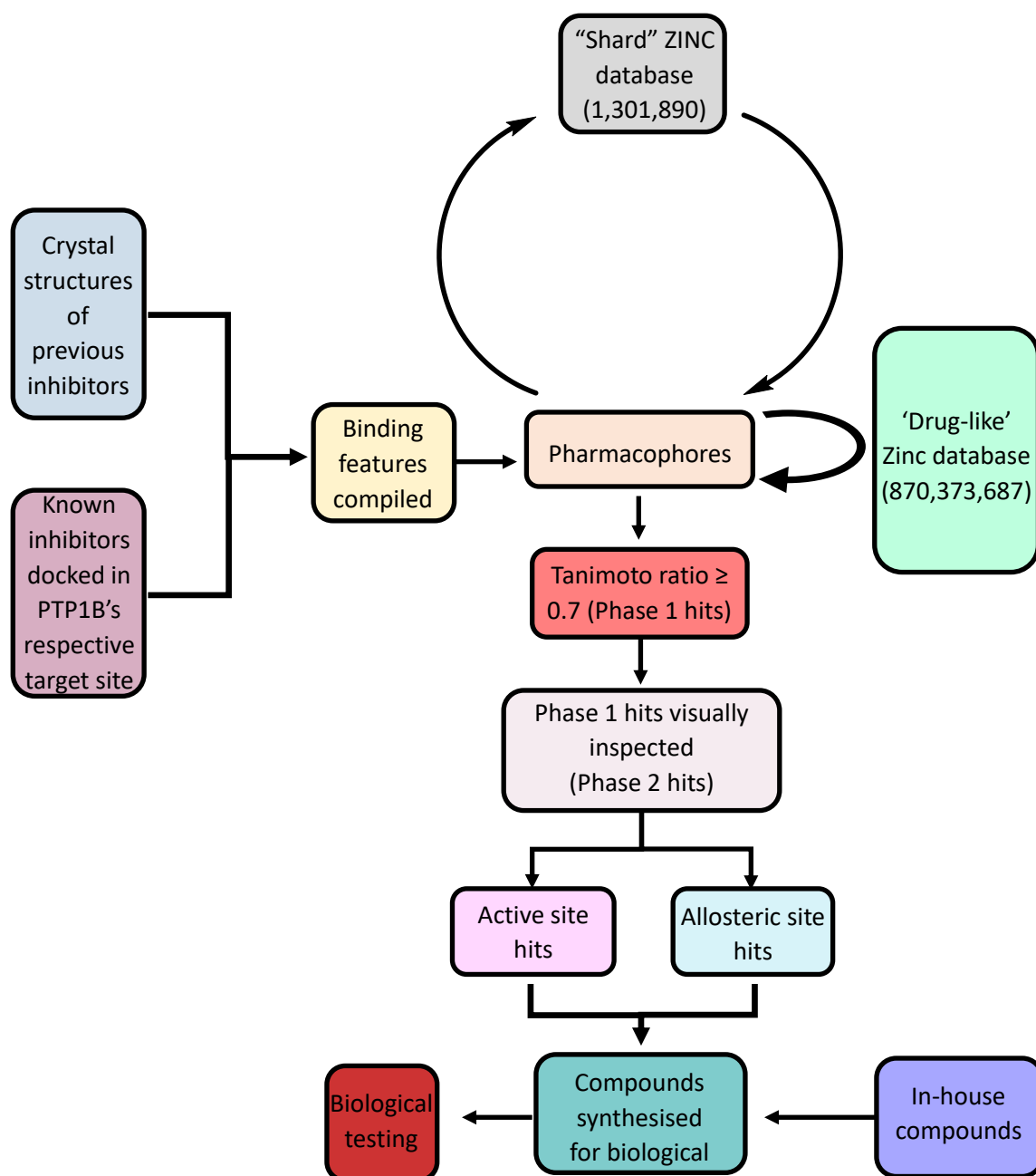
2.2.4 PTP1B regions targeted.

The initial identification and development of potential PTP1B inhibitors was conducted and informed with the database screening results of the two well defined druggable target sites of PTP1B, the active / catalytic site and the allosteric site.

In addition to the *de novo* hits identified computationally; additional in-house compounds synthesised for another publication were incorporated into the compound library for screening due to them possess the desired three-dimensionality for pharmaceuticals as stated above.

In summary, database screening is a powerful initial tool for identifying and / or refining potential inhibitors of therapeutic targets. But care needs to be taken to ensure that the new inhibitors being designed, synthesised, and tested are not mere rehashed versions of previous inhibitors, as this would result in the same downsides being replicated. So, consideration of hit results is needed to ensure that the most optimal results are taken forward. A summary of the planned workflow for this computational aspect of this project is illustrated below in **Scheme 6**.

2.2.5 Computational methodology overview



Scheme 6: Flow diagram of the *in silico* studies conducted for the selection of core structures for synthesis and testing.

2.2.5.1 Docking studies

When conducting docking studies on the Phase 2 active and allosteric site hits (discovered by database screening as shown in **Scheme 6**), two pieces of software were predominantly used. These were PyRx and PyMol. PyRx was the software which tried to slot the substrates into a defined region of the target protein (PTP1B), either the active or allosteric site. The most probable binding modes according to binding affinity (kcal/mol)

were subsequently investigated visually with another piece of software PyMol. Here the positioning and likelihood of proposed interactions were visually scrutinised to determine validity of results, in the same manner as discussed above, in addition to the interactions distance between possible substrate and protein motifs. It is important to note that it did not occur with each Phase 2 hit and only those of initial interest as discussed below.

2.2.5.2 Chemical space plotting

Here the software used for the plotting of the Phase 2 hits of both the active and allosteric site was DataWarrior. The selection for three-dimensional chemical space axis was based upon the parameters known to be linked to ‘drug-likeness’ as defined by Lipinski’s rule of 5, where cLogP was chosen as the common factor due its additional link to blood brain barrier permeability.

2.2.5.3 Example hit selection

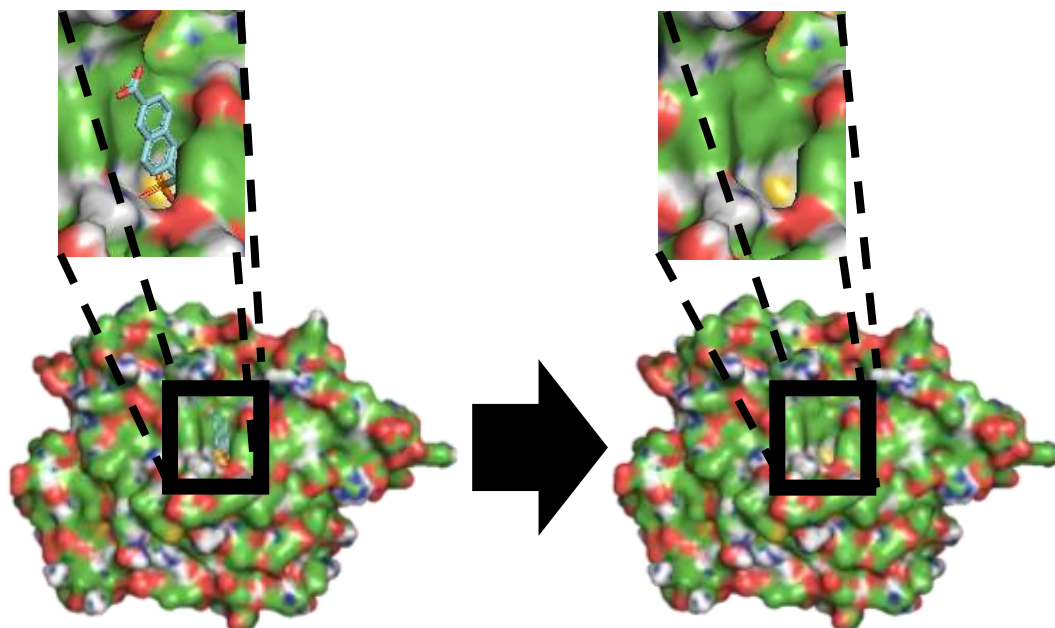
In the following section the examples hits shown below were chosen to cover different regions of chemical space enable comparisons of differing physicochemical properties and possess core structures that either can be considered easy synthetic targets post modification or are of synthetic interest due to be more novel, inherently three-dimensional and therefore can also be considered more ‘drug-like’.

2.3 Results and discussion:

As mentioned prior the identification of hits were based upon two stages; computational database screen where a Tanimoto ratio score ≥ 0.7 denotes an initial hit. The phase 1 hits from the ZINC drug-like database yielded in excess of 16,300 active site and 6,200 allosteric site hits. The second stage involved visible inspection to check spatial positioning is both viable for the physical constraints of the target site and for sufficient three-dimensionality. The final result of these two stages of investigation from the ZINC drug-like database resulted in 1822 active site hits and 731 allosteric site hits. The process by which these hit compounds were obtained is demonstrated below.

2.3.1 Active site pharmacophore construction.

Before a database of compounds can be virtually screened against a biological target site the pharmacophore must be defined, in terms of structure and chemical binding.



Scheme 7: Crystal structure of PTP1B with the active site defined in the closed conformation.

As shown above in **Scheme 7**, a known inhibitor was computationally removed from the co-crystalline structure (obtained from the protein data bank (PDB) ^{80,114,115}) leaving the protein's binding site empty and in the structural conformation for binding. In the case for **Scheme 7** it is the active / catalytic domain that has been defined in its closed conformation. As mentioned previously in Chapter 1 (section 1.4) due to the WPD loop of PTP1B being in constant flux or in an *apo* state between two conformations (open and closed), ^{60,83} it is important to acknowledge which conformation of the active site is being utilised. When the biological substrate or a known inhibitor is bound to the active site of PTP1B it is in its closed conformation, hence why this structural conformation is employed for the pharmacophore design.

With the target site defined, docking studies were conducted using Pyrx¹¹⁶ and PyMol¹¹⁷ software in tandem with known previously published binding modes of PTP1B active site inhibitors.^{80,86,89,115,118} In order to determine shared key functional and structural motifs essential for binding. As a collective, these features can be defined as the pharmacophore. This was conducted for both PTP1B's active and allosteric sites separately. These were utilised for the respective database screening.

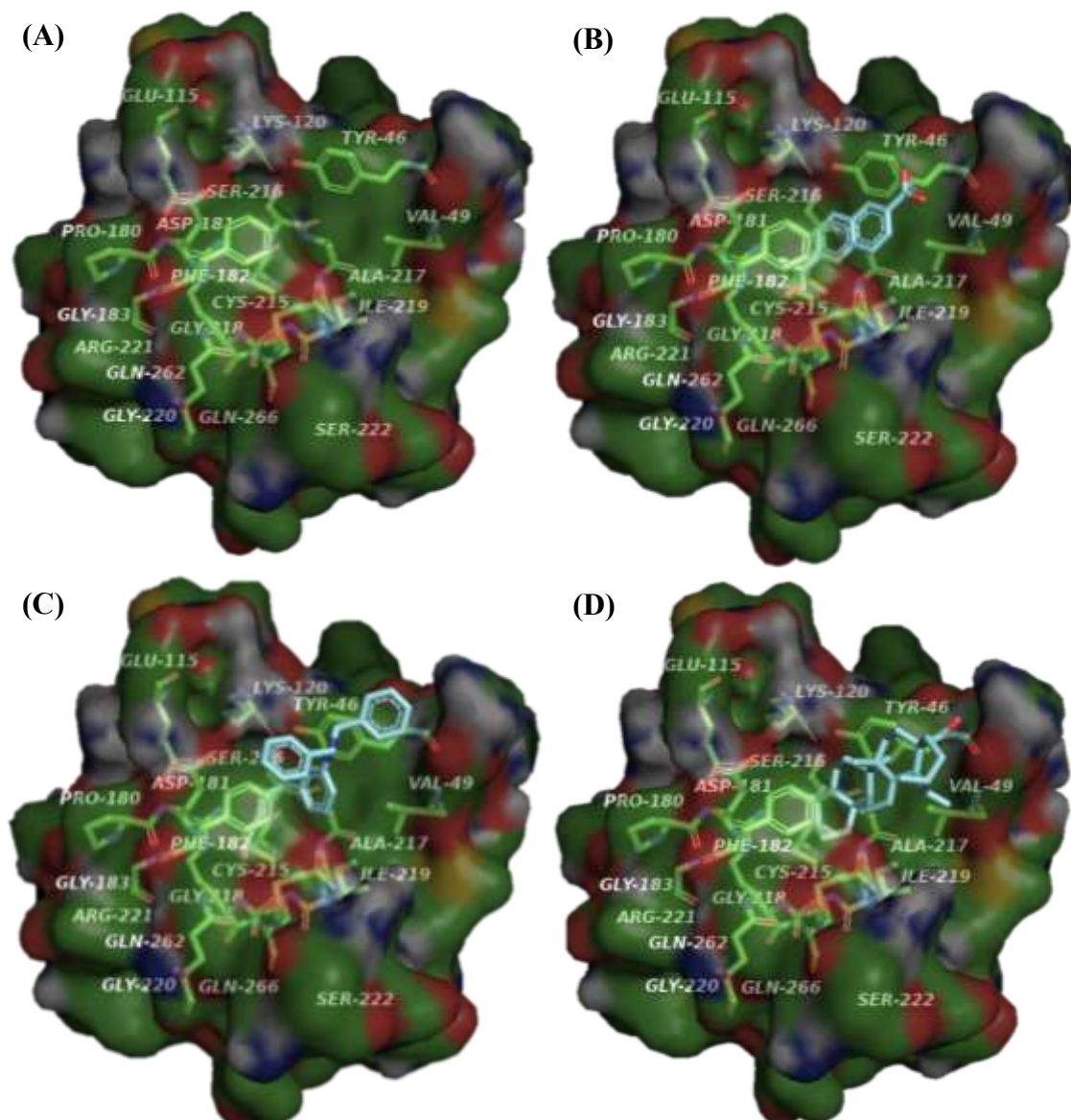


Figure 21: Binding modes of known inhibitors in PTP1B closed active site. (A) Empty active site in the closed conformation. (B) Crystal structure of the active site inhibitor 1BZJ bound in PTP1B. (C) Crystal structure of the active site inhibitor LZP25 in the PTP1B active site. (D) Computationally favoured docked position of ursolic acid in the PTP1B active site.^{80,86,89,115,118}

The docking study results utilise the algorithm, docking root mean square deviation (RMSD) as a means of ranking potential ligand-target site binding modes.

Figure 21 above and **Figure 22** below demonstrate the binding modes of three established known inhibitors of PTP1B's active site in the closed conformation. These have either been obtained from previously reported co-crystalline structures as for IBZJ and LZP25.^{80,86,118} Or from previously published computational modelling data (ursolic acid)⁸⁹, in conjunction with computational modelling done during this PhD work. From this the optimum positioning and protein residues involved in binding could be computationally predicted, to best inform PTP1B active site pharmacophore for database screening.

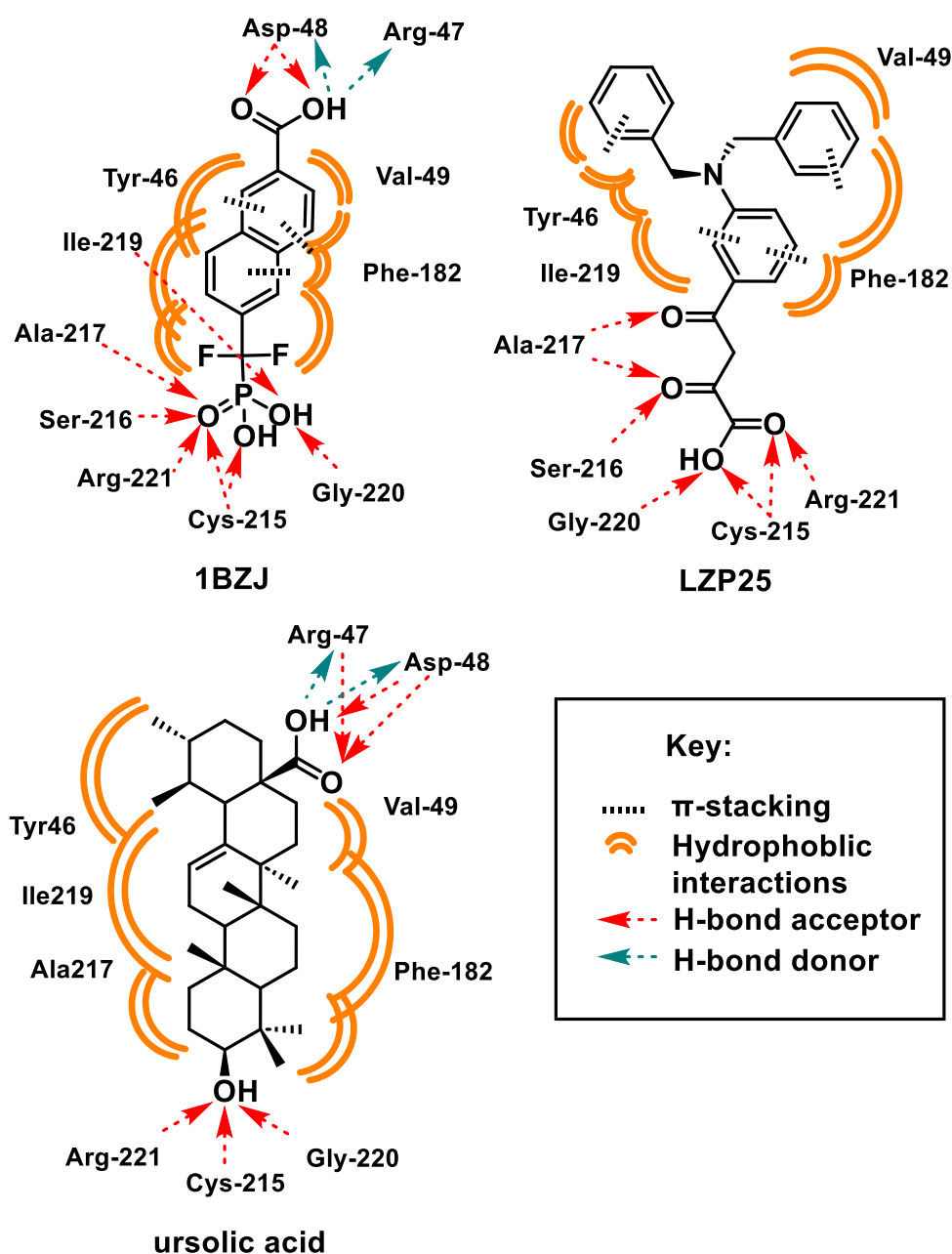


Figure 22: Two-dimensional representation of known PTP1B active site inhibitors with protein interactions labelled.^{80,86,117,118}

As shown in **Figure 21B** and **Figure 22** the key structural motif for 1BZJ's binding is the most akin to the biological substrate, as both utilise phosphoric acids to bind with PTP1B's Cys-215 and surrounding residues. Specifically, for 1BZJ the phosphoric acid hydrogen bonds with Ile-219, Gly-220 and Cys-215 *via* the OH's and Cys-215, Arg-221 and Ser-216 hydrogen bond *via* the carbonyl motif. In all these cases the hydrogen bonding is predominantly hydrogen accepting in terms of the inhibitor. The diaromatic region also undergoes π -stacking and hydrophobic interactions with Phe-182 and Tyr-46. Hydrophobic interactions can be defined as the energetic preference of nonpolar molecular surfaces to interact with other nonpolar molecular surfaces resulting in the displacement of water molecules from the interacting surfaces.¹¹⁹ Finally, the carboxylic acid of 1BZJ can act as both a hydrogen bond donor and acceptor with Arg-47 and Asp-48. When 1BZJ was computationally modelled in PTP1B's active site with the software Pyrx¹¹⁶ and Pymol,¹¹⁷ the computationally optimum binding mode aligned with the known crystal structure binding position obtained from the PDB,^{80,114,118} thus supporting the relevance of the utilised computational modelling software.^{80,114,118}

However the binding position of LZP25 shown in **Figure 21C** and **Figure 22** which was determined to be the optimum position from computational studies slightly differs from the co-crystallisation structure presented in the literature.⁸⁶ In theory based on the proximity and positioning of the left-hand sided benzene ring of LZP25 in **Figure 22**, to Phe-182, better π -stacking would appear to occur. Hence why both computational modelling and real-world crystallography data needs to be used collectively to obtain the most relevant results. Regardless of binding position the PTP1B active site residues and the interactions involved with LZP25 are the same for both the computational docking studies and published co-crystallisation data. As with the known inhibitor IBZJ, a significant part of LZP25 binding to the active site is *via* Cys-215 and the surrounding residues, as Gly-220, Cys-215 and Arg-221 hydrogen bond with the carboxylic acid motif. With regards to the two additional carbonyls of LZP25, hydrogen bonds are formed with Ser-216 and Ala-217. Additional interactions again include π -stacking and hydrophobic interactions of Tyr-46 and Phe-162 with the three benzene rings present.

The final of the three known inhibitors whose interactions with PTP1B's active site was used to inform the database screening pharmacophore was ursolic acid. But unlike with the prior two known inhibitors no literature example of ursolic acid being co-crystallized with PTP1B could be found, hence a previous paper⁸⁹ that utilised computational docking

studies to predict ursolic acid binding position was used in conjunction with in-house computational modelling.

When comparing the structural composition of ursolic acid to 1BZJ and LZP25 a key difference is the lack of π -stacking motifs present in ursolic acid, meaning that the hydrophobic interactions between PTP1B and ursolic acid are not only extensive but also key for binding. As with the prior two examples hydrogen bonding between PTP1B residues Cys-215, Gly-220, and Arg-221 with ursolic acid is probable to occur, in addition to, hydrogen bonding of Arg-47 and Asp-48 with ursolic acid hydrogen bond accepting functional groups is also likely to occur, based on other inhibitor interactions.

However, the proposed computational binding mode of the previously published work,⁸⁹ and the findings from this work differ, with the prior literature proposing a binding position where the ursolic acid is flipped 180° from the position shown in **Figure 21D** and **Figure 22** resulting in the carboxylic acid instead forming hydrogen bonds with the Cys-215 residue.

From this work this proposed binding position was not the most computationally favourable according to Pyrx¹¹⁶ but also was not present in any of the top 8 modes (computationally most probable). Without actual real-world crystallography data of ursolic acid being co-crystallized with PTP1B's active site, the definitive binding mode cannot be stated.

All the aforementioned crystallography and computational docking study data was hence compiled, and with the essential PTP1B active site residues for binding identified, the pharmacophore used for all PTP1B active site database screening was constructed and is shown below in **Figure 23**.

The pharmacophore formation and resultant database screening was conducted in CSD-CrossMiner 2022.3.0¹¹²

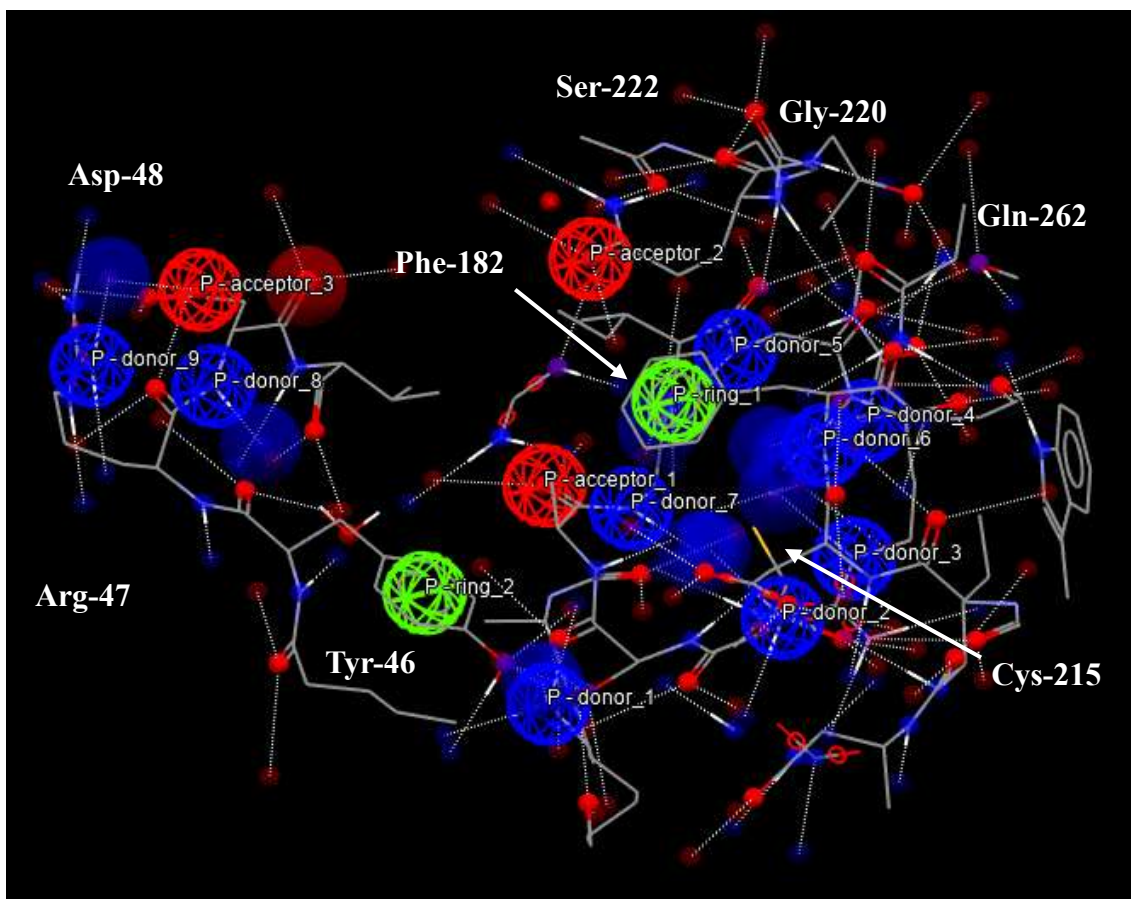


Figure 23: Structural features of pharmacophore used for PTP1B closed active site database screening. P – ring denotes aromatic π -stacking. P – ring 1: Phe-182, P – ring 2: Tyr-46. P – acceptor, protein residue that can act as a hydrogen bond acceptor. P – acceptor 1: Ala-217, P – acceptor 2: Ile-217, P – acceptor 3: Arg-47. P – donor, protein residue that can act as a hydrogen bond donor. P-donor 1: Lys-120, P-donor 2: Glu-115, P-donor 3: Asp-181, P-donors 4 & 6: Arg-221, P-donor 5: Gln-262, P-donor 7: Gln-218, P-donor 8: Arg-47, P-donor 9: Asp-48.^{80,86,89,118}

2.3.2 Active site database screening.

With the PTP1B active site pharmacophore computationally determined, database screening of this druggable target could then occur. Two different databases of compounds were selected and downloaded from ZINC¹²⁰. The ZINC database is a collection of commercially available chemical compounds specifically compiled for use in virtual screening. The two databases screened were comprised of 870,373,687 entries considered ‘drug-like’ according to Lipinski’s rule of 5,¹¹⁰ and a ‘shard’ database comprised of 1,301,890 entries at or below 200 Daltons in molecular weight.

These two compound databases were selected for different reasons. Firstly the ‘drug-like’ database was conducted to identify a new class of potential PTP1B active site inhibitors that exist in a different region of chemical space than the above showcased known PTP1B active site inhibitors. But also remaining in theory pharmaceutically relevant by adhering

to Lipinski's rule of 5, which has been considered the gold standard in terms of chemical properties for orally bioavailable pharmaceutical compounds. Instead, the "shard" database was carried out to identify potential functional groups that could be incorporated into the substrate scope after a hit compound had been identified from biological testing. The "shard" database is defined as any commercially available compound present in the ZINC database with a molecular weight equal or less than 200 Daltons. Where an alternative would have been a fragment database screen which comprises of compounds up to a molecular weight of 250 Daltons and a LogP of 3.5 or below.

2.3.2.1 Drug-like database screen.

From the 'drug-like' database, 1822 hits were ultimately identified and a select few are illustrated below in **Figure 24**. These potential hit compounds were three-dimensionally mapped in chemical space based upon relevant chemical properties, with the open-source software DataWarrior¹²¹ see **Figure 25** below, for example hit structures and chemical space positions.

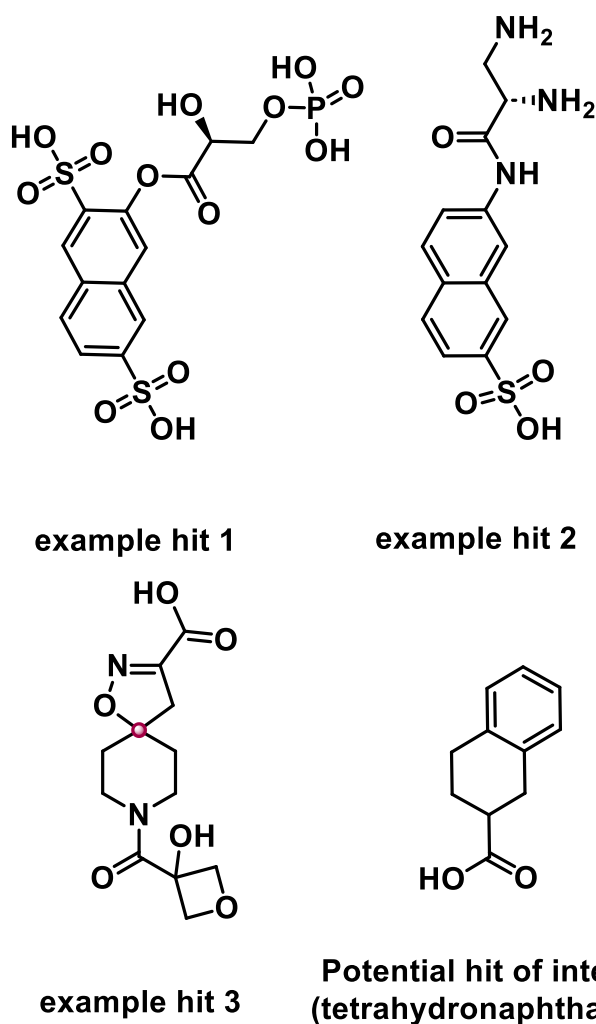


Figure 24: Chemical structures of example hits found *via* computational database screening, for the active site of PTP1B.

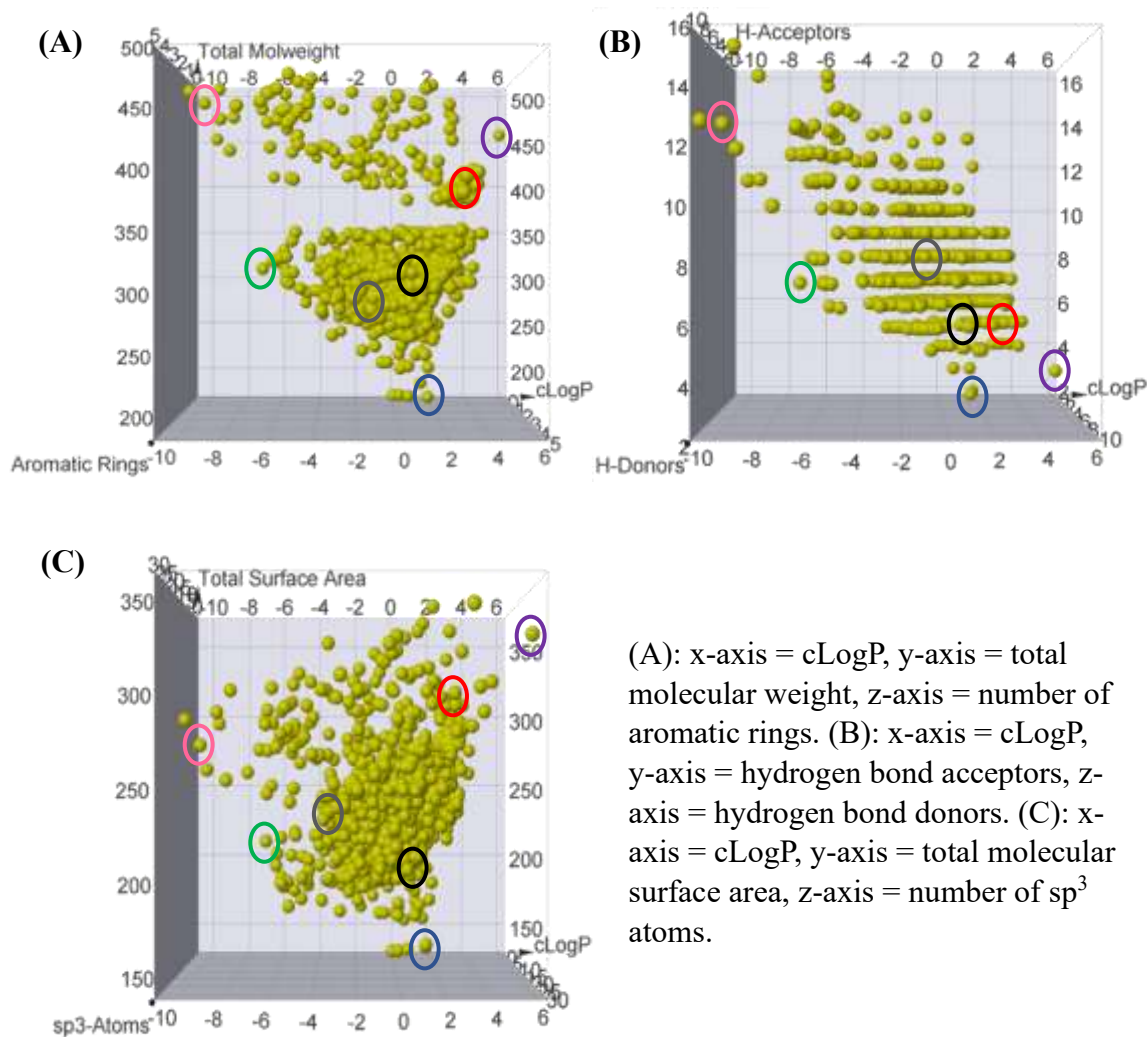


Figure 25: Three-dimensional chemical space maps of PTP1B's active site 'drug-like' database hits. 1BZJ = black, LZP25 = red, ursolic acid = purple, example hit 1 = pink, example hit 2 = green, example hit 3 = grey, potential hit of interest = blue.

The chemical properties chosen for chemical space mapping were selective either for their relation to Lipinski's rule of 5 (cLogP, H-bond acceptor/donor, molecular weight), the chemical composition of the target site (H-bond acceptor/donor, number of aromatic rings), hit selectivity (number of sp^3 atoms) and / or blood brain barrier permeability relation (cLogP and total molecular surface area). By investigating the positions of the known inhibitors in chemical space based upon these physicochemical properties, and knowing the structure of PTP1B's active site a new informed compound family of potential inhibitors was selected. Positioning of this hit of interest is indicated with a blue oval as shown in **Figure 25** above.

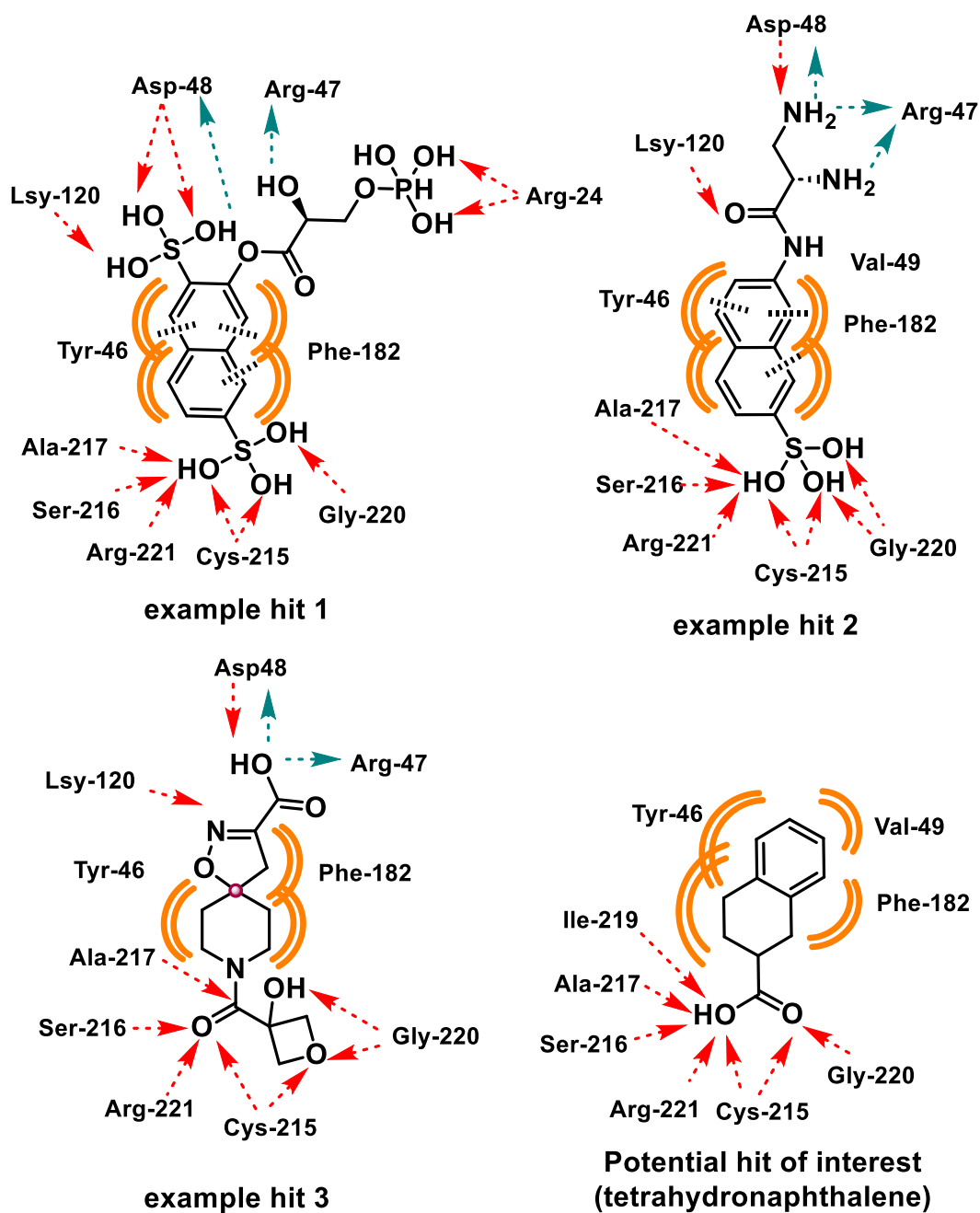


Figure 26: Chemical structures and predicted interactions of example hits and proposed modified hit for synthesis with PTP1B's active site.

Table 1: Physicochemical values of PTP1B active site inhibitors and example hits.

Compound	cLogP	MW	Aromatic rings	H - acceptors	H - donors	Total molecular surface area	sp ³ -atoms
1BZJ	1.0819	301.161	2	5	2	187.5	4
LZP25	2.8429	387.434	3	5	1	303.96	4
ursolic acid	6.0021	456.708	0	3	2	337.87	29
Example hit 1	-9.7609	478.387	2	13	10	275.87	17
Example hit 2	-6.7727	312.369	2	7	6	212.13	8
Example hit 3	-0.8593	283.303	0	6	2	191.61	13
Potential hit of interest	1.8094	176.214	1	2	1	137.64	5

Numerical values of interest for the known inhibitors and of the example hits of are summarised above in **Table 1**, along with the chemical structures and proposed binding modes of the example active site database screen hits shown above in **Figure 26**.

As mentioned previously, one of the aims of the ‘drug-like’ database screen was to identify potential PTP1B active site inhibitors that occupy a different region of chemical space to known inhibitors as a means of attempting to avoid the selectivity issues of these previous inhibitors that failed to progress past phase-II of clinical trials. Example hits 1, 2, 3 and the potential hit of interest have been highlighted in the above **Figure 25**, **Figure 26** and **Table 1** as these potential hits exist in different regions of chemical space and as specifically shown in **Figure 26**, have extensive binding potential to PTP1B’s active site, based on computational modelling.

BBB impermeability is an important aspect for this work, the cLogP value is important when selecting the potential hit for synthesis. For several classes of CNS active substances, Hansch and Leo found that blood-brain barrier penetration is optimal when the LogP values are in the range of 1.5-2.7, with the mean value of 2.1.¹⁰⁹ But in addition to BBB permeability general cell permeability is an important consideration for any potential pharmaceutical compound.

As stated above, drugs with good cell permeability exhibit moderate cLogP value in the range of $-0.5 < \text{cLogP} < 5$ for substances with good cell permeability.¹¹⁰ Therefore the theoretical ideal cLogP value for BBB impermeability while maintaining good peripheral cell permeability is expected to be within $-0.5 < \text{cLogP} < 1.4$ or $2.8 < \text{cLogP} < 5$.

However, as shown in **Table 1** both example hits 1 and 2 are very hydrophilic (water soluble) in term of their cLogP values. For blood brain barrier (BBB) impermeability, hydrophilicity is a desirable trait, but it has been shown that drugs with good cell permeability exhibit a moderate cLogP value in the range of $-0.5 < \text{cLogP} < 5$.¹⁰⁹ So in theory based on cLogP values alone the example hits 1 and 2 are both too hydrophilic to cross the cell's phospholipid bilayer, thus minimising the *in vivo* effect on PTP1B or in the yeast cell-based inhibition assay that was utilised for testing. Hence despite their high theoretical potential for PTP1B inhibition, their hydrophilicity justifies why no further investigation was conducted.

As with the previous two examples (1 and 2) the potential hit of interest (structure shown above in **Figure 26**) was selected for occupying a different region of chemical space to the previous inhibitors but while still possessing means of PTP1B active site binding. This was explicitly done to try and prevent the same main downsides as the previous inhibitors including poor PTP selectivity and BBB permeability. Additionally, to the profile of this tetrahydronaphthalene being narrow also enabling this compound to in theory be able to bind with the Cys-215 residue at the base of PTP1B active site.

The final example hit highlighted above in **Figure 25**, **Figure 26** and **Table 1** is example hit 3 which is a 5,6-spirocyclic. In general, spirocyclic compounds are desirable synthetic targets for drug-discovery due to being highly three-dimensional, thus often have greater selectivity. Therefore, utilised as core structures and subsequently functionalised in pharmaceutical and drug discovery research. Numerous spirocyclic containing licenced pharmaceuticals are present in the literature, examples are exhibited in Chapter 5 (section 5.2.1.3). Specifically the core of this computational hit was of interest not only for existing in a different region of chemical space (**Figure 25**) to other hit compounds and the known inhibitors, but also for still possessing the ability for hydrophobic interactions without the need for aromatic π -stacking (proposed interactions shown in **Figure 26**).

2.3.2.2 “Shard” database screen.

As mentioned previously, a supplementary shard database screen was conducted in conjunction with the ‘drug-like’ database screen, to provide additional information on potential structural motifs required for binding. Selected results with proposed interactions with PTP1B’s active site from the shard screen are shown in **Figure 27**.

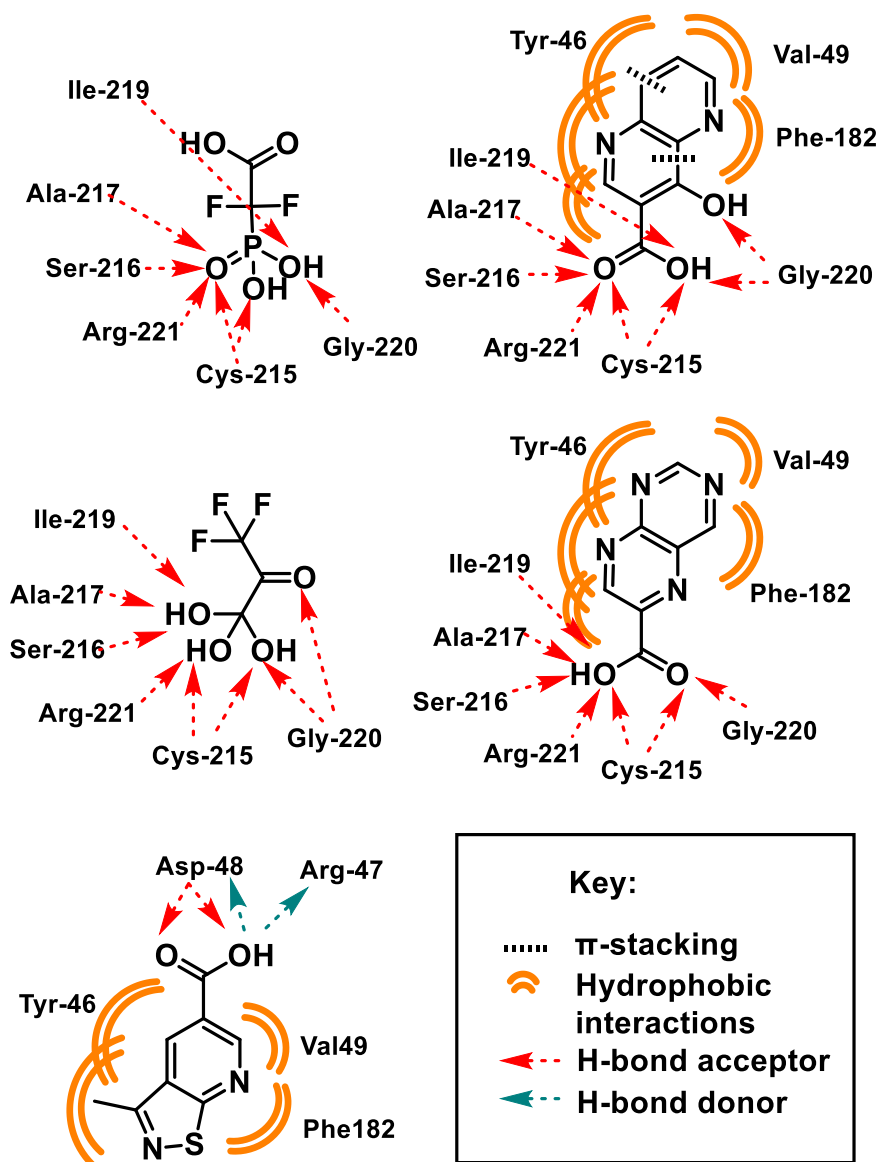


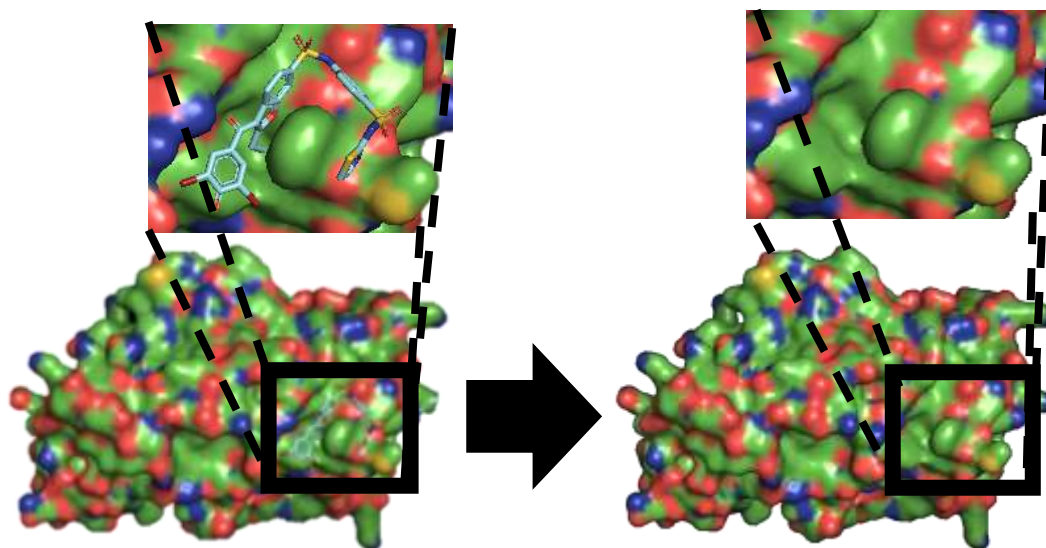
Figure 27: Example structures and proposed interactions of shard database screen hits for PTP1B active site.

From the shard database screen (comprised of 1,301,890 molecules) with PTP1B’s active site pharmacophore (see **Figure 23**) a total of 108 hits were identified. The aim of the shard database screen was to identify other functional groups that are able to bind to the regions in interest of the PTP1B active site for subsequent incorporation into the

compound library of benzodioxanes for biological activity testing and enhance our knowledge of the closed active site of PTP1B.

2.3.3 Allosteric site pharmacophore construction.

With a starting core motif selected for synthesis and testing against PTP1B active site inhibition, the same process of computational database screening was subsequently tested on PTP1B another well-defined druggable target, the allosteric site.



Scheme 8: Co-crystallisation structure of a known inhibitor bound to an allosteric site located at the C-terminus of the protein PTP1B.

Here the known inhibitor (1T4J) can be computationally removed leaving a defined, static conformation of the allosteric site for computational studies.¹¹²

As shown above in **Scheme 8**, as before a known inhibitor can be computationally removed from the co-crystalline structure (obtained from the PDB^{114,118}) leaving the protein's target site empty and in the structural conformation for binding.

As with determining the active site's pharmacophore, numerous known PTP1B allosteric site inhibitors^{86,114,118} from the literature that have been co-crystallized in PTP1B's allosteric site were investigated to determine shared key functional and structural motifs essential for binding. As a collective, these features could then be defined as the pharmacophore and utilised for the respective database screening of PTP1B allosteric site.

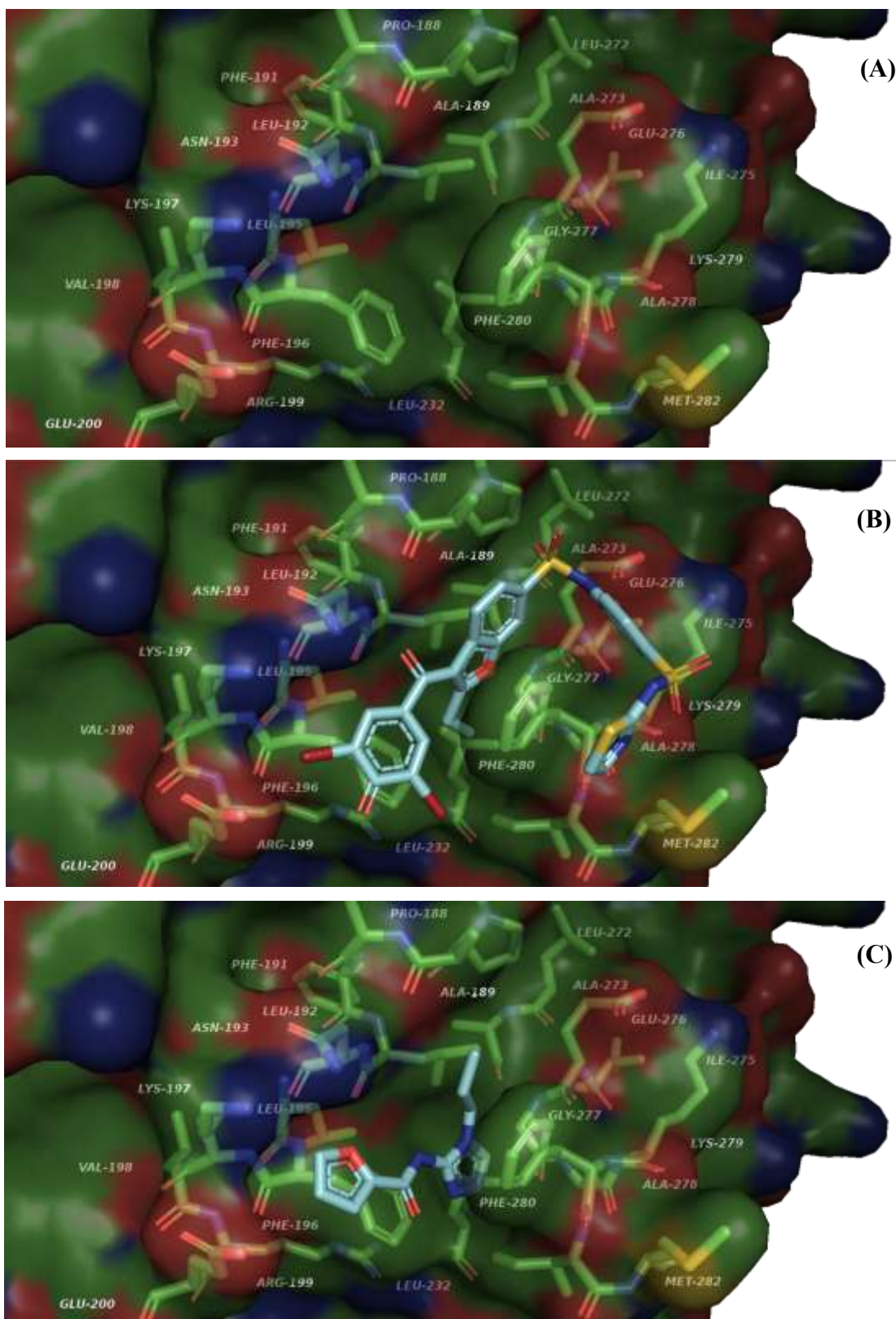


Figure 28: Binding modes of known inhibitors in PTP1B allosteric site. (A): Empty defined PTP1B allosteric site (B): Known allosteric inhibitor 1T4J bound to PTP1B. (C): Known allosteric inhibitor 5QDT bound to PTP1B. ^{114,118,208}

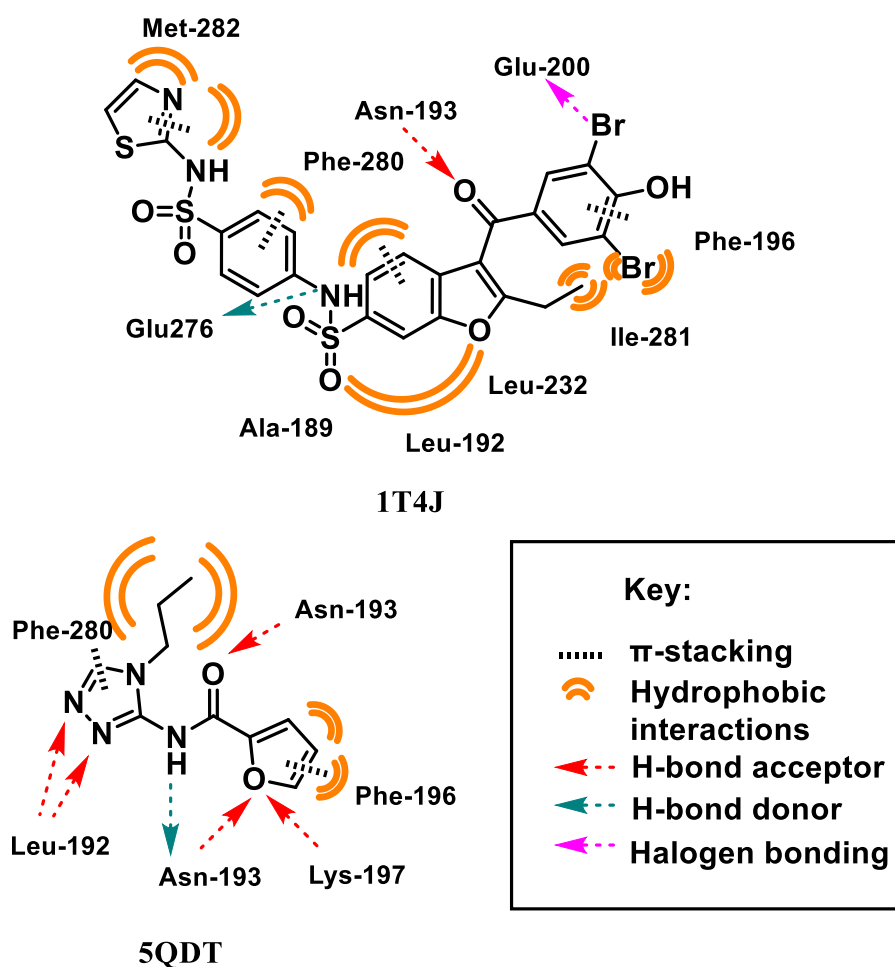


Figure 29: Two-dimensional representation of known PTP1B active site inhibitors with protein interactions labelled.^{114,118,208}

PTP1B's allosteric site is a hydrophobic pocket located at the C- terminus of the protein, as such the binding modes of allosteric site inhibitors contained extensive hydrophobic and π -stacking interactions. This is shown to be the case with both known inhibitors 1T4J and 5QDT in **Figure 28** and **Figure 29** above.

The known allosteric site inhibitor 1T4J is an unsaturated compound comprised of four aromatic rings, which enable extensive hydrophobic interactions to occur with the following allosteric site residues: Phe-196, Ile-281, Leu-232, Leu-192, Ala-189, Phe-280 and Met-282, as shown above in **Figure 28B** and **Figure 29**. π -stacking also occurs between the aforementioned 4 aromatic rings and the two allosteric site phenylalanine residues (Phe-196 and Phe-280). Additional interactions include a halogen bond between one of the bromines present on the substrate and the residue Glu-200, and limited hydrogen bonding between the carbonyl motif of the substrate and Asn-193 (residue acts as the donor), and the substrates NH acting as a hydrogen bond donor with Glu-276. Firstly, 5QDT's amide motif can act as both a hydrogen bond donor to Asn-193 and as an

acceptor with Asn-193, the oxygen present in the furan ring can also act as a hydrogen bond acceptor with Asn-193 and Lys-197. Finally, two of the nitrogen atoms of the triazole act as hydrogen bond acceptors with the residue Leu-192.

Due to 5QDT's smaller molecular structure (see **Figure 28C** and **Figure 29**), this known inhibitor has fewer hydrophobic interactions with the aforementioned residues that interact with 1T4J, but 5QDT's 2 aromatic motifs can still π -stack and form hydrophobic interactions with both Phe-196 and Phe-280. However, 5QDT is able to form a greater number of hydrogen bonding interactions with the surrounding residues than 1T4J.

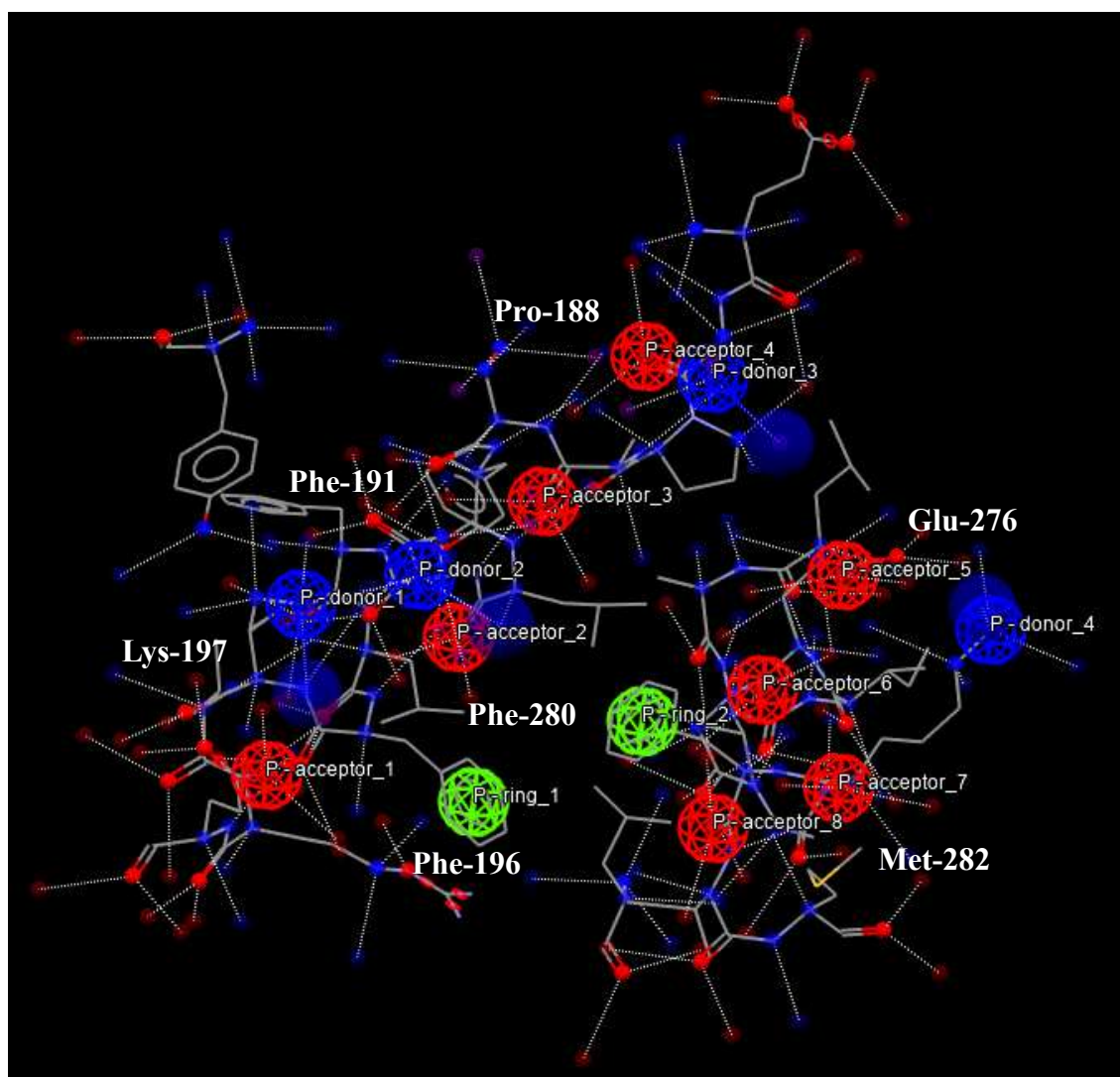


Figure 30: Structural features of pharmacophore used for PTP1B allosteric site database screening. P – ring denotes aromatic π -stacking. P – ring 1: Phe-196, P – ring 2: Phe-280. P – acceptor, protein residue that can act as a hydrogen bond acceptor. P – acceptor 1: Lys-197, P – acceptor 2: Asn-193, P – acceptor 3: Leu-192, P – acceptor 4: Pro-188, P – acceptor 5: Glu-276, P – acceptors 6 & 7: Phe-280, P – acceptor 9: Ile-281. P – donor protein residue that can act as a hydrogen bond donor. P – donor 1: Leu-195, P – donor 2: Val-274, P – donor 3: Pro-188, P – donor 4: Lys-279. ^{112,118,208}

As with the active site known inhibitors, the aforementioned crystallography and computational docking study data of the two allosteric site inhibitors and the composition of the allosteric site were hence compiled and key residues identified to form the pharmacophore used for all PTP1B allosteric site database screening shown above in **Figure 30**.

The pharmacophore formation and resultant database screening was conducted in CSD-CrossMiner 2022.3.0 ¹¹²

2.3.4 Allosteric site database screening.

As with PTP1B active site, PTP1B allosteric site's pharmacophore was computationally screened against the two aforementioned databases download from ZINC ¹²⁰, these are the 'drug-like' and shard databases.

2.3.4.1 Drug-like database screening.

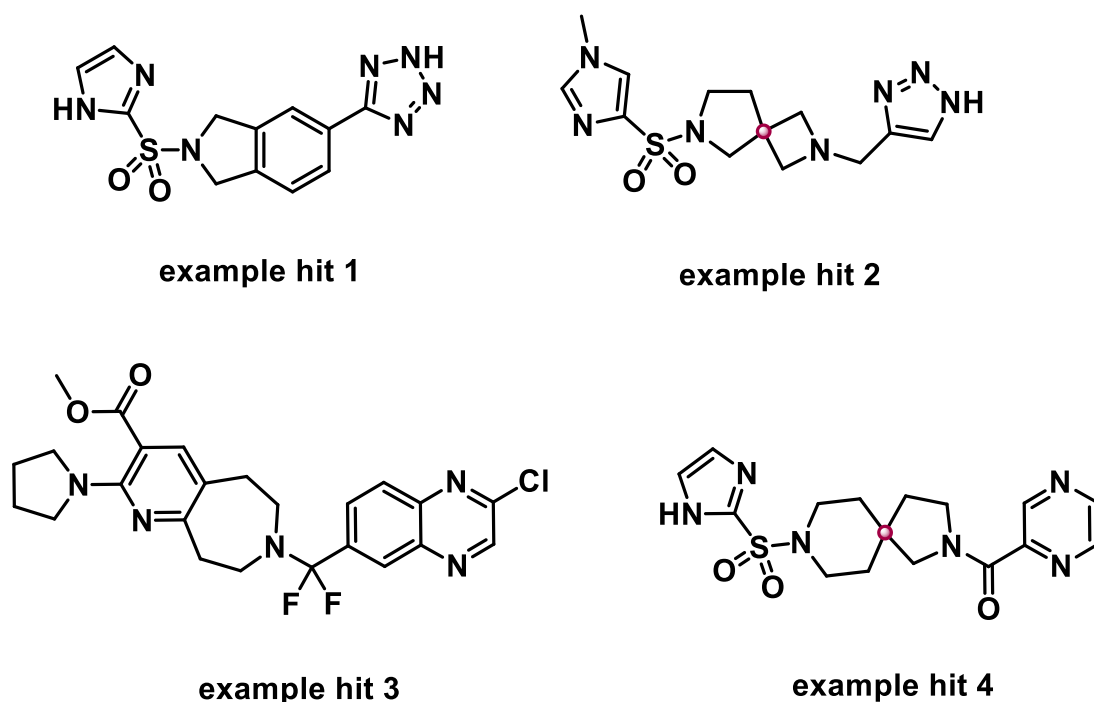
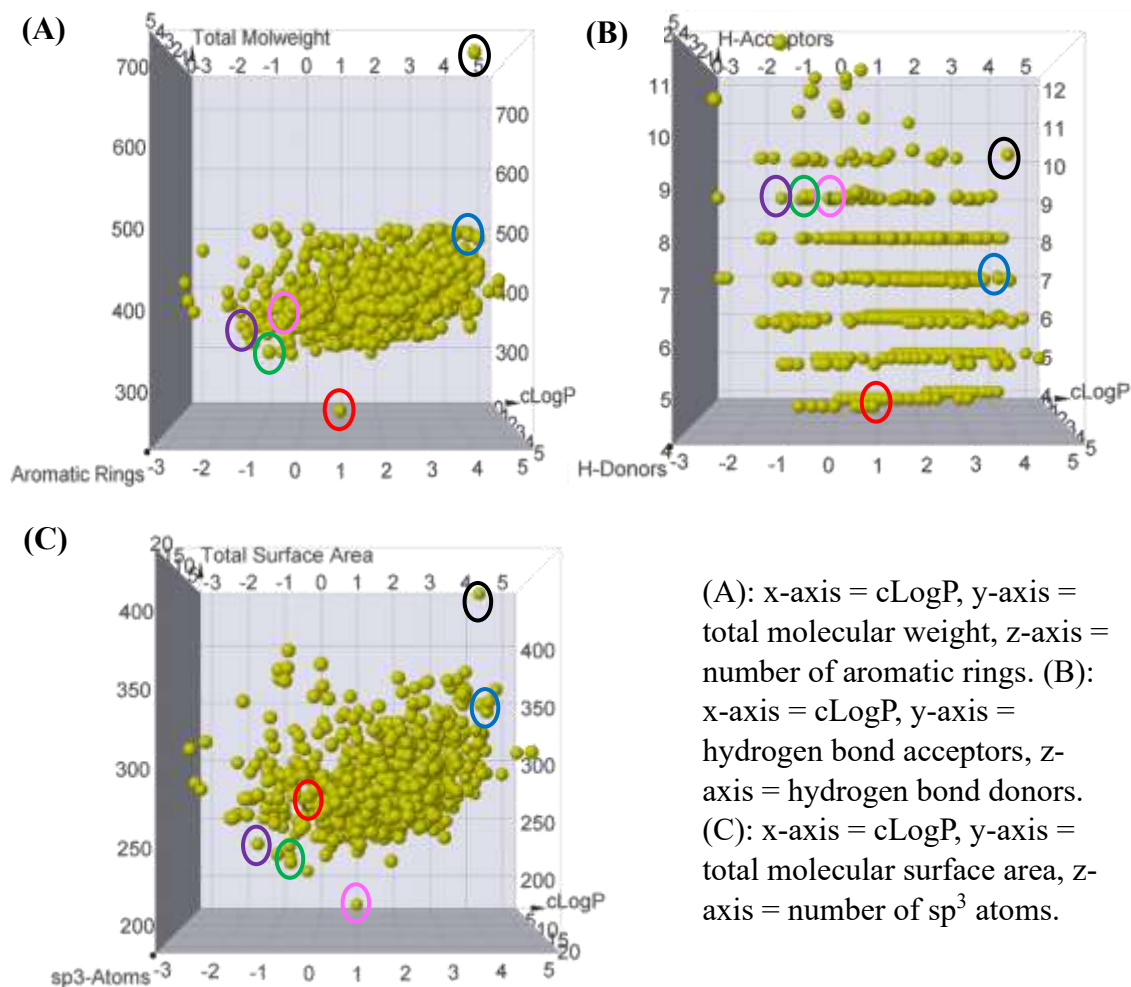


Figure 31: Chemical structures of example hits found with computational database screening, of the allosteric site of PTP1B.



(A): x-axis = cLogP, y-axis = total molecular weight, z-axis = number of aromatic rings. (B): x-axis = cLogP, y-axis = hydrogen bond acceptors, z-axis = hydrogen bond donors. (C): x-axis = cLogP, y-axis = total molecular surface area, z-axis = number of sp³ atoms.

Figure 32: Three-dimensional chemical space maps of the PTP1B's allosteric site 'drug-like' database hits. 1T4J = black, 5QDT = red, example hit 1 = green, example hit 2 = purple, example hit 3 = blue, example hit 4 = pink.

From the 'drug-like' database, 731 hits were identified for the allosteric site and a select few are illustrated above in **Figure 31**. Again, these potential hit compounds were three-dimensionally mapped in chemical space based upon relevant chemical properties, with the open-source software DataWarrior¹²¹ see **Figure 32** above.

The same plotting parameters used for the active site results were again utilised and investigated for the allosteric site hits for the same aforementioned reasons. By investigating the positions of the known inhibitors in chemical space based upon these physicochemical properties and knowing the structure of PTP1B's allosteric site a new compound class of potential inhibitors, located in a different region of chemical space could potentially be identified. See **Figure 32** above, where the known inhibitors along with example hits have been circled in numerous chemical space regions where cLogP is a constant parameter.

The structures of the example hits are shown below in **Figure 33** and their respective physicochemical properties (calculated in DataWarrior¹²¹) demonstrated in **Table 2** below.

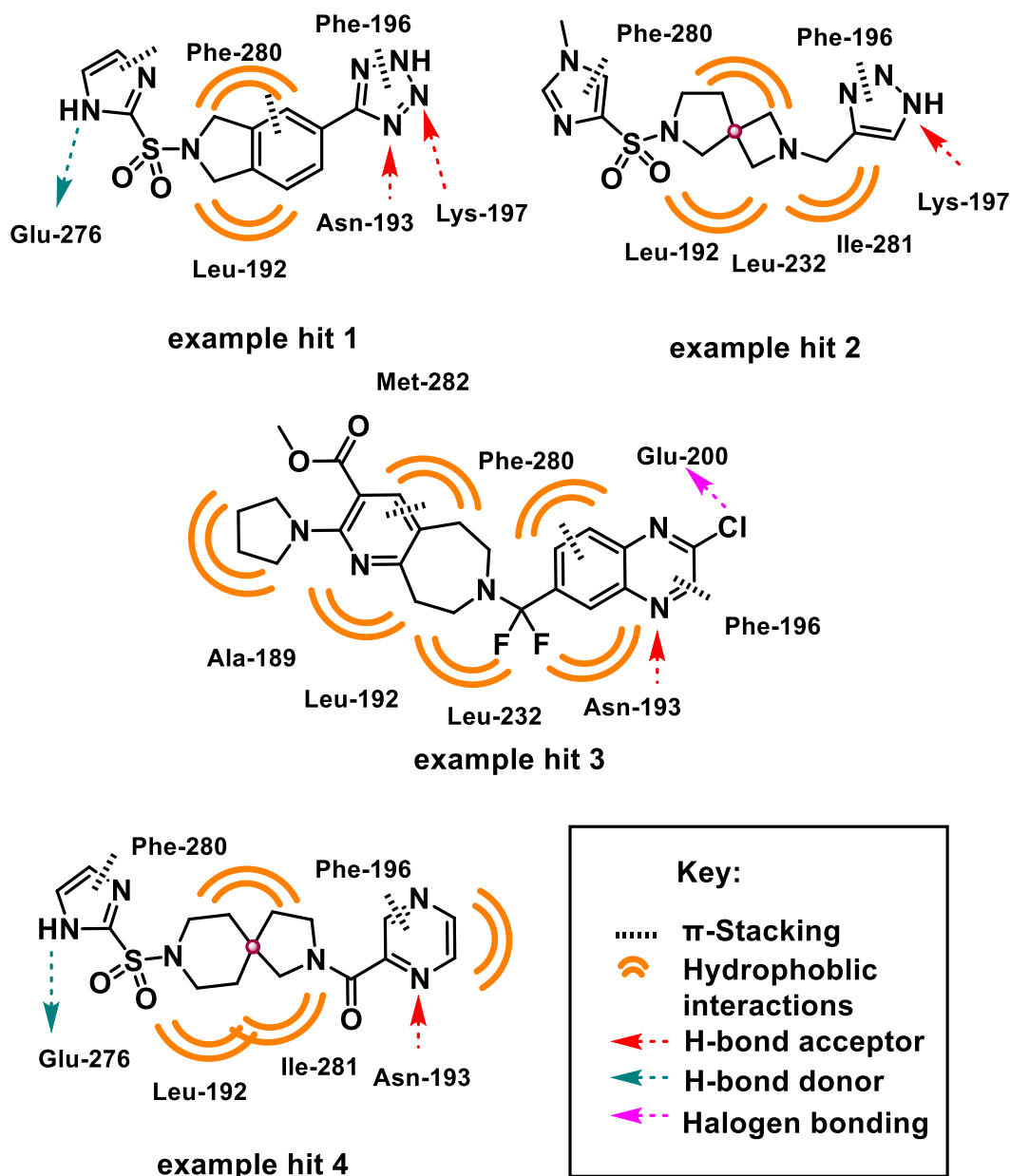


Figure 33: Chemical structures and computationally predicted interactions of example hits with PTP1B's allosteric site.

Table 2: Physicochemical values of PTP1B allosteric site inhibitors and example hits.

Compound	cLogP	MW	Aromatic rings	H - acceptors	H - donors	Total molecular surface area	sp ³ -atoms
1T4J	4.2049	741.457	4	10	2	439.05	5
5QDT	0.9787	220.231	2	6	1	209.85	3
Example hit 1	-0.8095	317.332	3	9	2	219.86	3
Example hit 2	-1.4789	337.407	2	9	1	235.48	10
Example hit 3	4.2159	487.937	3	7	0	346.12	12
Example hit 4	-0.2416	376.44	2	9	1	265.53	9

The primary factor for selecting the example hits from the allosteric site ‘drug-like’ database screen was cLogP value, binding potential, and three-dimensionality. As stated, before the theoretical ideal cLogP value ranges for BBB impermeable drug-like molecules is $-0.5 < \text{LogP} < 1.4$ and $2.8 < \text{LogP} < 5$, of the example hits shown only example hit 3 and 4 fall into one of these cLogP ranges. It is not surprising that the majority of the 731 total ‘drug-like’ hits have negative cLogP values due to the highly hydrophobic nature of the target site, and as stated previously hydrophobic compounds are generally more BBB permeable. When comparing example hit 3 and example hit 4, on paper example hit 3 is more hydrophobic, from cLogP values. The incorporation of halogen species in example hit 3 can form additional interactions (halogen bond) with another allosteric site residue (Glu-200), this may result in a stronger interaction with the allosteric site. Due to both example hits 3 and 4 containing 2 aromatic systems enabling both π -stacking and hydrophobic interactions with Phe-196 and Phe-280, and additional hydrophobic interactions with Ala-189, Leu-192, Leu-232 and Met-282.

Another contributing factor to BBB permeability is the molecules cross-sectional area (CSA). Molecules with a smaller CSA are generally more BBB permeable, meaning that compounds with lower three-dimensionality, such as those containing a significant number of unsaturated motifs (e.g., aromatic rings) are often more BBB permeable due to being flatter thus having a smaller CSA. Additionally, as previously stated more two-dimensional compounds are considered less ‘drug-like’ as they are more likely to be involved in cross-selectively off-target binding, which is undesirable for potential pharmaceutical products.

This is why the incorporation of a 5,6-unsaturated cyclic motif into example hit 4 is potentially desirable as it still enables the same aforementioned hydrophobic interactions, and π -stacking (to a lesser extent with adjoining aromatic rings) with PTP1B allosteric site but with a substantial increase in the compounds CSA thus in theory reducing its BBB permeability when compared to a comparable two-dimensional molecule, such as example hit 1.

2.3.4.2 “Shard” database screening.

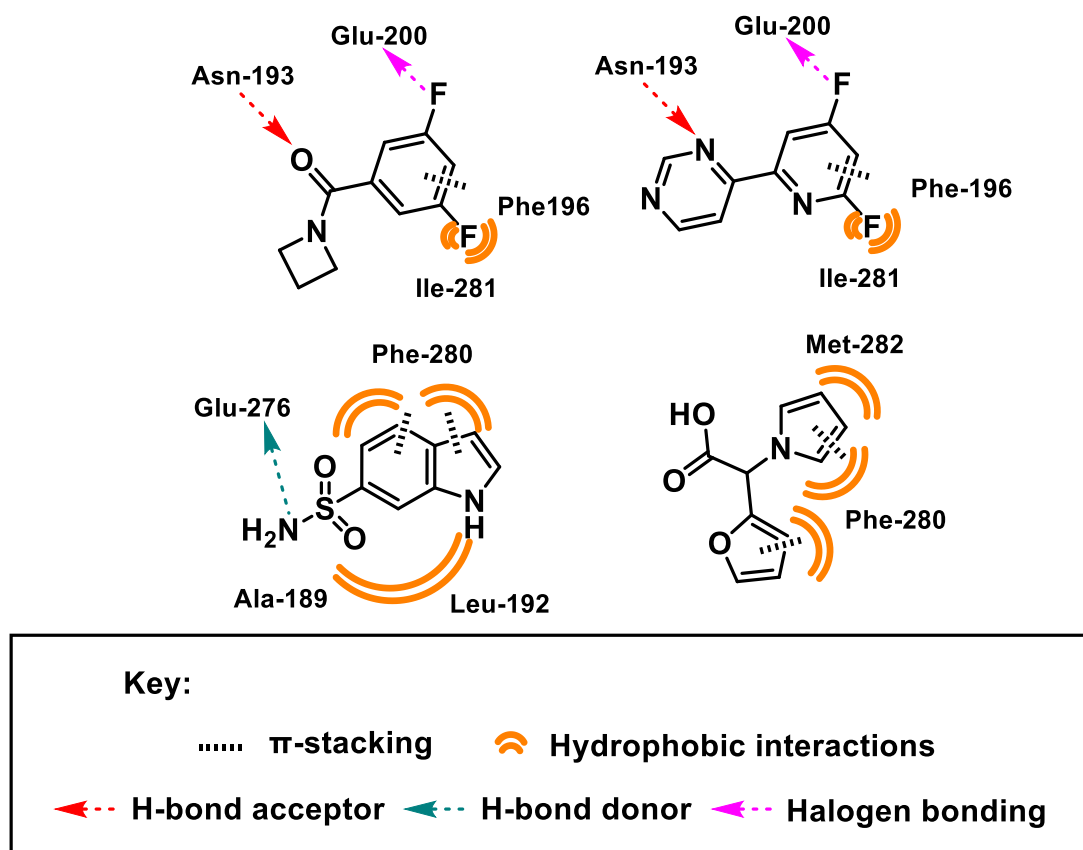


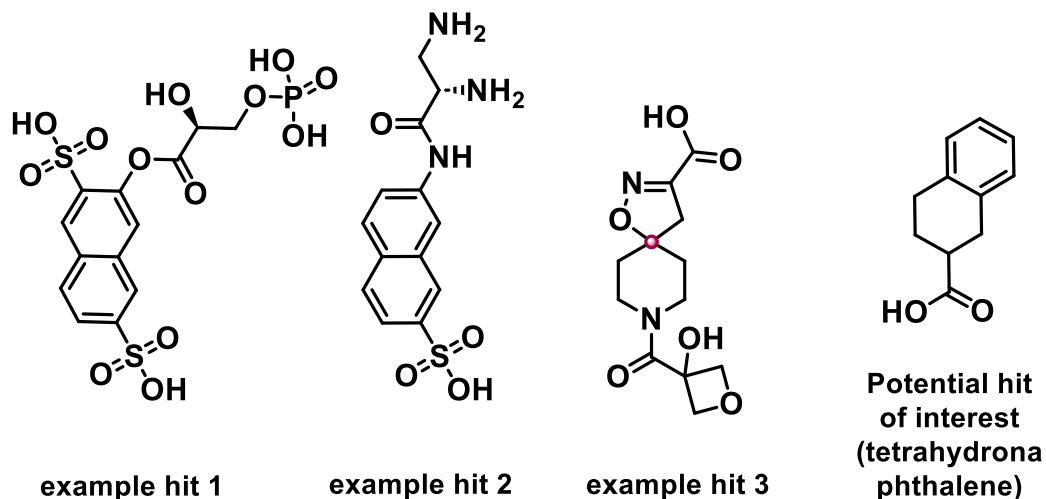
Figure 34: Example structures and proposed interactions of shard database screen hits for PTP1B allosteric site.

Before a potential PTP1B allosteric site inhibitor was fully designed a shard base database screen was conducted using the previously stated pharmacophore (**Figure 30**). Once again, example hits from this database screen are shown above in **Figure 34**. As with the active site version, the shard database allosteric site screen was conducted as an attempt to identify additional substrate motifs that can interact with PTP1B allosteric site residues and therefore provide additional structural information on allosteric site binding. However, of the over 14 million compounds screened only 24 hit molecules were acquired, which was fewer than expected but the same trend of fewer allosteric site hits

in the ‘drug-like’ screen also occurred. All the 24 shard hits contained preidentified motifs for binding found from the ‘drug-like’ database screen, but these results do support the expected binding modes of substrates and again bind in a comparable manner to the crystallography data of the two known allosteric site inhibitors, supporting the relevance of the pharmacophore used and of the computational software.

2.4 Conclusion:

Active site: Example hits



Allosteric site: Example hits

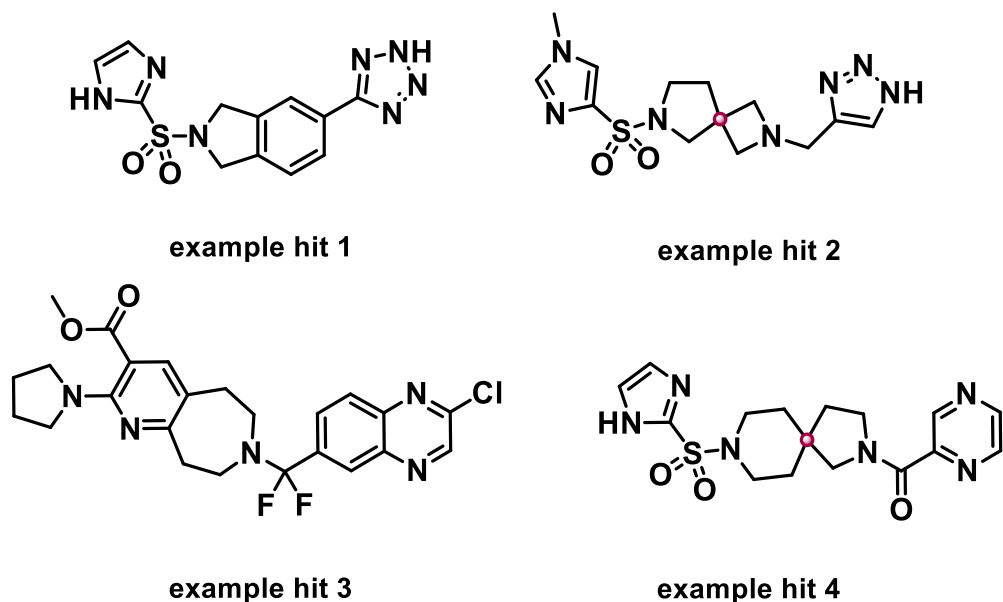


Figure 35: Structures of computationally found example hits for both of the druggable targets of PTP1B.

Above the rationale and reasoning behind the conducted database screening for both PTP1B's active and allosteric site has been explained and the results summarised. The pharmacophore used for both the active and allosteric site were derived from co-crystallisation data and prior literature computational studies of known PTP1B inhibitors which was compiled to gain a well-informed computational model with key binding residues and modes identified prior to screening.

With regards to the selection and future investigation of the database hits the key thread of blood brain barrier (BBB) impermeability and chemical space location were the main driving forces. The subsequent design of the modified hits designed for synthesis to target one of PTP1B's well defined druggable sites were hence based on these hits of interest to, in theory, design an optimal PTP1B inhibitor for synthesis and subsequent testing.

With a pharmacophore, and subsequent ZINC drug-like and "shard" database screen results in hand for both the active and allosteric site of PTP1B, the example hits for both druggable targets are shown in **Figure 35**. The active site was selected as the initial target for investigation for the finding and developing a new core structure of PTP1B inhibition. All subsequent allosteric site inhibitor work was allocated to future work to be conducted outside this PhD project, but with the groundwork demonstrated within this Chapter as a starting point. With target compounds in hand, the means of biologically testing these potential PTP1B inhibitors when synthesised needed to be chosen, validated, and developed from preexisting methodologies in the literature.

Chapter 3

Biological assay development

3.1. Overview

This Chapter explores and justifies the selection of the chosen biological assays used to identify potential new PTP inhibitors with the specific interest in activity, potency, PTP selectivity and blood brain barrier permeability. All these parameters were investigated with the combined use of the below discussed assays, which had the produced data ratified as valid prior to potential inhibitor testing.

3.2. Background

3.2.1. Means of assessing PTP inhibition

In the current literature there are numerous *in vitro* methods¹²²⁻¹²⁶ that can be used for the screening and identification of potential PTP inhibitors, and a few different examples are briefly mentioned below before the utilised assay is discussed.

One example from the literature of an *in vitro* assay for the investigation of PTP inhibition is an enzymatic assay where p-nitrophenyl phosphate (pNPP) is used as a substrate.^{122,123} This method works by measuring the production of p-nitrophenyl (pNP) over 30 minutes at 37 °C. pNP is the dephosphorylated product of pNPP and can be monitored by a multi-mode microplate reader (such as the Spectra Max M3) at 405 nm. As the quantity of pNP produced is directly proportional to the dephosphorylation potential of a proposed PTP inhibitor, a lower subsequent concentration of pNP indicates lower PTP inhibition. The benefits to this and similar enzymatic methods is that with them being conducted at a physiological temperature of 37 °C the results can be considered somewhat biologically relevant. Furthermore, with an overall experiment time of only 40 minutes (10 minutes incubation prior to the 30 minutes of monitoring), and the fact multiple compounds can be tested in tandem this methodology can provide fast turnover of results. However, if this enzymatic assay protocol utilises the full length of PTP1B further kinetic and / or mutational assays would need to be conducted in addition to determine the biological site of action. As mentioned previously in Chapter 1 (section 1.4.3) PTPs have numerous potential known binding sites. Additionally, this assay type provides no indication of general cell permeability, so the permeability of any potential hit compounds would need to be investigated later *via* another assay.

As previously mentioned, the absorbance of pNP to dephosphorylation is a linear relationship at approximately 5–500 μM , so coloured small molecules of interest could absorb light at similar frequencies (around 405 nm), leading to potentially false negative results, i.e., apparent decreased activity (dephosphorylation) of the PTP, when in reality the small molecule is in fact a hit, but as it absorbs at a similar wavelength to pNP thus a false negative result occurs. Relatively high concentrations of recombinant PTPs (in the mid nanomolar range) are also typically required to produce sufficient pNP so that the signal to background (S/B) and signal to noise (S/N) ratios are significantly low enough to gain relevant and repeatable results.¹²⁴

Another example of an *in vitro* assay for the investigation of PTP inhibition is a biochemical inhibition assay which works by monitoring a change in fluorescence intensity. The fluorogenic protein phosphatase substrates used in this assay have a low fluorescence in the phosphorylated state, but post dephosphorylation fluorescence greatly increases.¹²⁴ The authors of this methodology¹²⁴ stated that the fluorescence emission of the dephosphorylated products can be measured over a wider range of concentrations (approximately 10 nM to >100 μM) than the above enzymatic assay with superior S/N and S/B ratios, thus contributing to the production of highly reproducible results, while requiring a lower concentration of recombinant PTPs. Additionally, up to a 1536-well format, can be deployed allowing for efficient dose response testing of large compound libraries of candidate inhibitors, and because this assay works on emission rather than absorption the likelihood of the small molecules of interest themselves providing negative results is significantly reduced than for the above pNPP enzymatic assay. This assay can also be used to investigate any specific recombinant PTP that is available, supporting the discovery of specific PTP inhibitors *via* testing with multiple PTPs. But again, if the entire protein (full length) structure of recombinant PTP was used further kinetic and / or mutational assays would need to be conducted in addition to determine the region of the PTP which the potential inhibitor interacts with, as mentioned above. Furthermore, buffers containing sulfonic acids such as HEPES, could compete with inhibitor binding at the active site, and therefore cannot be deployed in this assay, and as with the above pNP assay no information on general cell permeability is acquired, so again the permeability of any potential hit compounds would need to be investigated later with a different assay.¹²⁴

Additionally, as previously stated the operational range of this fluorescence-based assay was stated to be 10 nM to >100 μM . As the paper stated concentrations greater than 100 μM could be investigated it implies that such concentrations have not been tested and that it would be reasonable to expect that beyond a certain concentration the relationship between the resultant fluorescence and test compound concentration is no longer linear and may ultimately plateau. Thus, depreciating the results of this assay at higher concentrations. But this is only speculative and would need to be investigated to determine.

3.2.2. Yeast-based inhibition assay

Despite the fluorescence-based assay providing an overall sound means of selective PTP inhibition testing at low concentration with the nano molar range preferred. Another *in-vitro* methodology was deployed for all potential PTP inhibitor testing which could operate in the desired manner at higher concentrations in the micro molar range. This is a yeast (*Saccharomyces cerevisiae*) based assay in which specific PTP plasmid comprised of the respective active site is transcribed into wild type yeast cells.^{125,126}

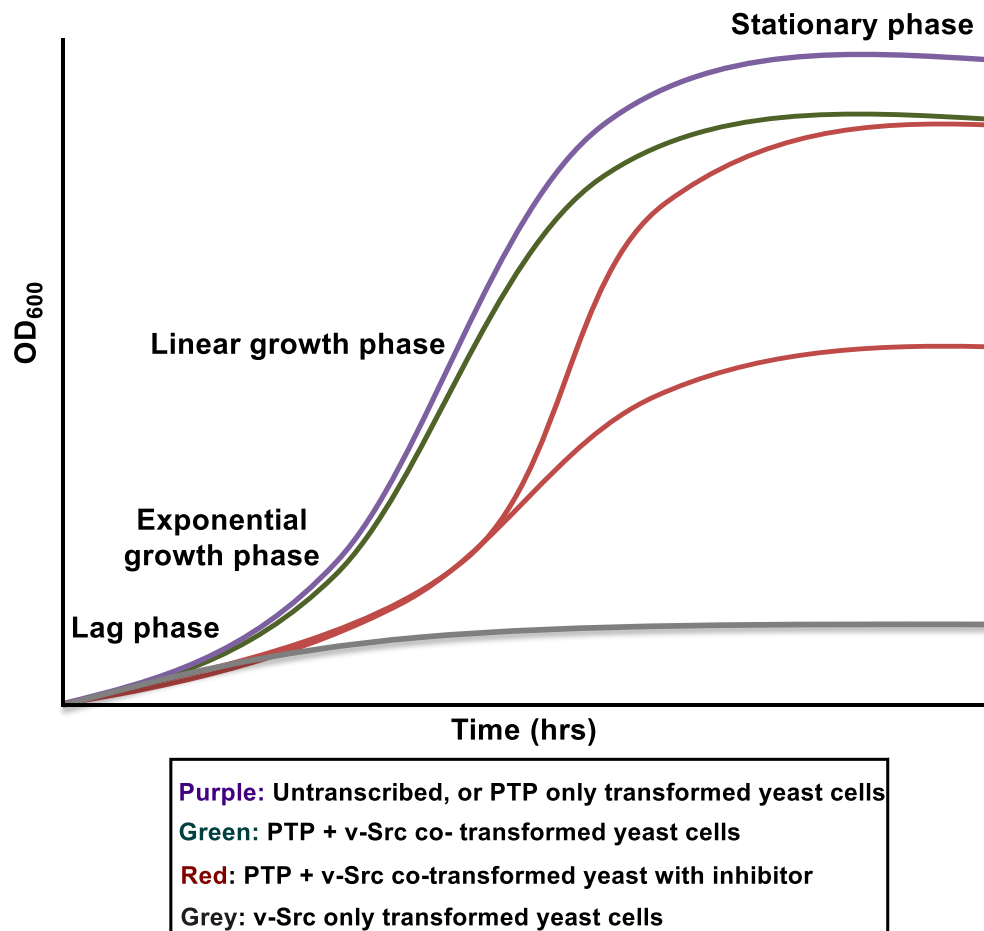


Figure 36: Example growth profiles of differently transcribed yeast cells. Explanation of how the utilised yeast-based assay tests for PTP inhibition.^{127,128}

Due to this any activity exerted upon the PTP can be presumed with high certainty to occur *via* the active site as that is the only known binding domain present in the transformed yeast cell.

This reason, paired with the in-house expertise of yeast-based inhibitory assays and the availability of the required plasmids for transcription, are the main contributing factors as to why this yeast-based inhibition assay was utilised.

The assay operates by linking the growth rate of the yeast cells, measured as a doubling time (T_d) of the exponential growth phase to the activity of the PTP plasmid transcribed into the yeast cell. This is achieved with the addition of the oncogenic plasmid v-Src to wild type *Saccharomyces cerevisiae* which harshly limits the proliferation of the yeast cells, by phosphorylating numerous yeast proteins, including SMK1. SMK1 is a MAP kinase that controls spore wall assembly and SH2-binding proteins.^{127,128} As many unicellular eukaryotes including *Saccharomyces cerevisiae* lack intact phosphotyrosine signalling pathways required for the self-dephosphorylation of the specific spore wall remodelling pathway. This distribution severely reduces the cell's ability to divide, multiply and proliferate exponentially, hence why the example growth profile of v-Src only transcribed yeast has no exponential growth phase, as shown above in **Figure 36**.

^{127,128}

However, when a plasmid containing a biologically active, site of a PTP, is co-expressed with v-Src, the growth rate is mostly restored and the same growth profile of a lag, exponential growth, linear growth, stationery and death phase, is seen as with the untransformed wild type yeast as shown above in **Figure 36**. This is because the PTP is able to dephosphorylate what the v-Src phosphorylated in-part restoring the specific spore wall remodelling pathway and enabling the yeast cells to proliferate at a rate that is more comparable to the untransformed or PTP only transcribed yeast cells.

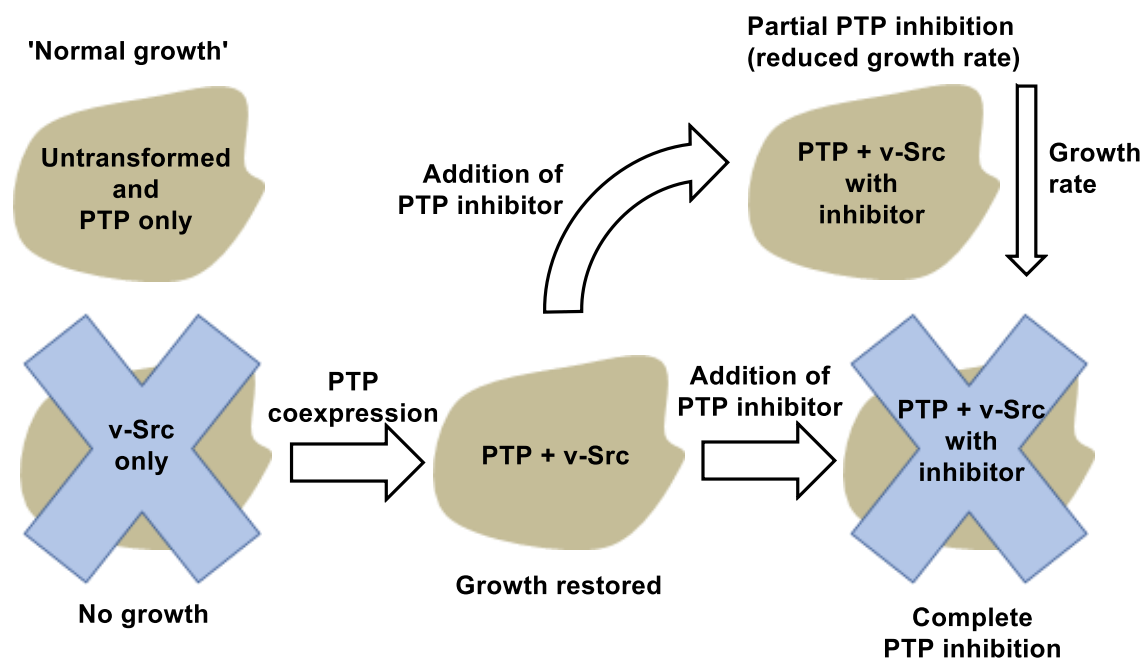


Figure 37: Illustration of the effect on growth rate when plasmid(s) are incorporated. Explanation of how the utilised yeast-based assay tests for PTP inhibition. ^{125,126}

As shown above in **Figure 37**, when a PTP active site inhibitor is added specifically to the PTP + v-Src transcribed yeast, a decrease in the doubling time (growth rate during the exponential phase), is observed because with the PTP being inhibited it is less able to dephosphorylate the proteins phosphorylated by v-Src, so the spore wall process and thus the yeasts ability to divide and multiply is hindered. By measuring the exponential growth phase, doubling time (T_d) of yeast cells after transcription with a PTP and v-Src plasmids, the effect of transcription of the growth profile of the yeast cells can be investigated, by comparing to untransformed native yeast cells. Furthermore, the activity of a potential small molecule inhibitor can also be determined and ranked against other known inhibitors or hit compounds for effectiveness and selectivity by comparing the percentage change in T_d 's between different PTPs.

For this the percentage change in doubling time (compared against the respective biological replicate base growth) was used in order to gain a more accurate representation of the effect the small molecule of interest exerts as the base growth of different biological repeats of the same transcribed yeast cells can be significantly different. See methodology Chapter 7 (section 7.4.2.1) for equations used.

It is important to note that PTP inhibition is only linked to the yeast's growth rate when the plasmid v-Src is co-transcribed, meaning when a known inhibitor is added to yeast

that just expresses a PTP plasmid no significant effect on growth rate should occur, if an effect is observed it is due to an off-target effect, potentially toxicity related.

Figure 36, above shows two different potential example growth profiles for a PTP + v-*Src* transcribed yeast with the addition of a PTP active site inhibitor (red line). Both of these lines have a comparable exponential growth phase and hence would be considered comparable PTP inhibitors. As the duration and timing of the subsequent growth phases (linear growth and stationary phases) the final absorbance value, and the prior lag phase does not have necessarily have a direct correlation to the potency of the small molecule inhibitor. It is any significant change in the exponential growth phase that is of interest as this is what the T_d values are derived from.

It would be logical to presume that a lower final absorbance value denotes fewer yeast cells thus corresponding to a more potent or effective PTP inhibitor. However, this may not always be the case, as other unrelated factors affect the final yeast cell number. These include unknown off-target toxicity effect that the compound being tested may exert on yeast cells generally. The length of the lag phase of the base growth of that biological replicate (base growth means for example a PTP + v-*Src* yeast cell culture without the addition of the compound of interest), also affects the final absorbance value as a longer lag phase often means a lower final OD₆₀₀ value (absorbance) after the 47.5 hr long experiment has concluded. Finally, it had been observed that at higher concentrations certain compounds result in the yeast cells clumping together and partly crashing out of the growth media, drastically reducing the OD₆₀₀ value and thus giving the appearance in growth curves of a high positive effect (PTP inhibition) or complete cell death. An example image of this can be found in the appendix (section 1.8).

Hence why the doubling time and thus the exponential growth phase was the measure of PTP inhibition as the length of the lag phase does not affect the resultant T_d measure of the exponential phase, as the time frame used is not rigid so for each biological repeat the time points that provide a linear line when absorbance is in the log scale is used to calculate the T_d values. Furthermore, this is the way the effectiveness of potential PTP inhibitors has been determined in the past literature.^{125,126}

Before the assay could be validated or any potential small molecule inhibitors tested the type of yeast strain to be used in this assay was first investigated by transcribing and comparing the growth profiles and doubling time values of two sets of different yeast

strains, these were YMK23 and YSC1, all additional information on these strains is present in the Chapter 7 Methodology (section 7.4).

3.2.3. Blood Brain Barrier assay

As mentioned previously numerous times the permeability of potential PTP1B inhibitors through the blood brain barrier (BBB) is comparatively as important to clinical success as potency and selectivity towards PTP1B over other PTP family members. Therefore, in addition to just identifying and developing PTP1B specific potent inhibitors, the BBB permeability of found hit compounds also was investigated *via* means of a commercially available synthetic BBB membrane parallel artificial membrane permeability assay (PAMPA) kit.

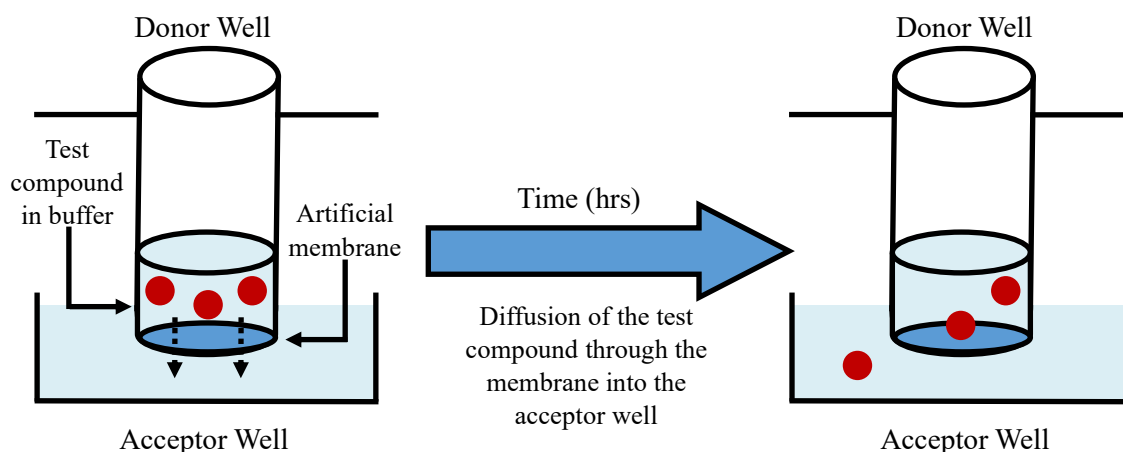


Figure 38: Illustration of the utilised BBB PAMPA assay operation. ¹²⁹⁻¹³¹

This kit utilises a synthetic membrane that mimics the physicochemical properties of the mammalian blood brain barrier *in vivo*. So, the results obtained should give a good indication into hit compound permeability through the BBB or at least maintain the same trends and provide means for hit compound permeability ranking so these results can be feed into subsequent choices for further hit compound development.

As demonstrated above in **Figure 38**, the basic premise of how this assay functions are that a compound of interest at a set concentration in a predominantly PBS based solution is added to the donor well which is able to feed into the acceptor well which contains only PBS. The compound is only able to travel from the donor well to the acceptor well is through the synthetic BBB membrane, hence after x hours the concentration of the test compound in the acceptor well is indicative of the compounds BBB permeability. ¹²⁹⁻¹³¹

Another way in which this assay provides means for BBB permeability compound ranking is with the calculation of the permeability rate (cm/s) for each compound of interest, known inhibitors and provided permeability controls, *via* the use of equilibrium standards and the equation stated in Chapter 7 Methodology (section 7.4.4). So, the larger the permeability rate, the faster the compound traverses the membrane and thus more permeable to the BBB it is. ¹²⁹⁻¹³¹

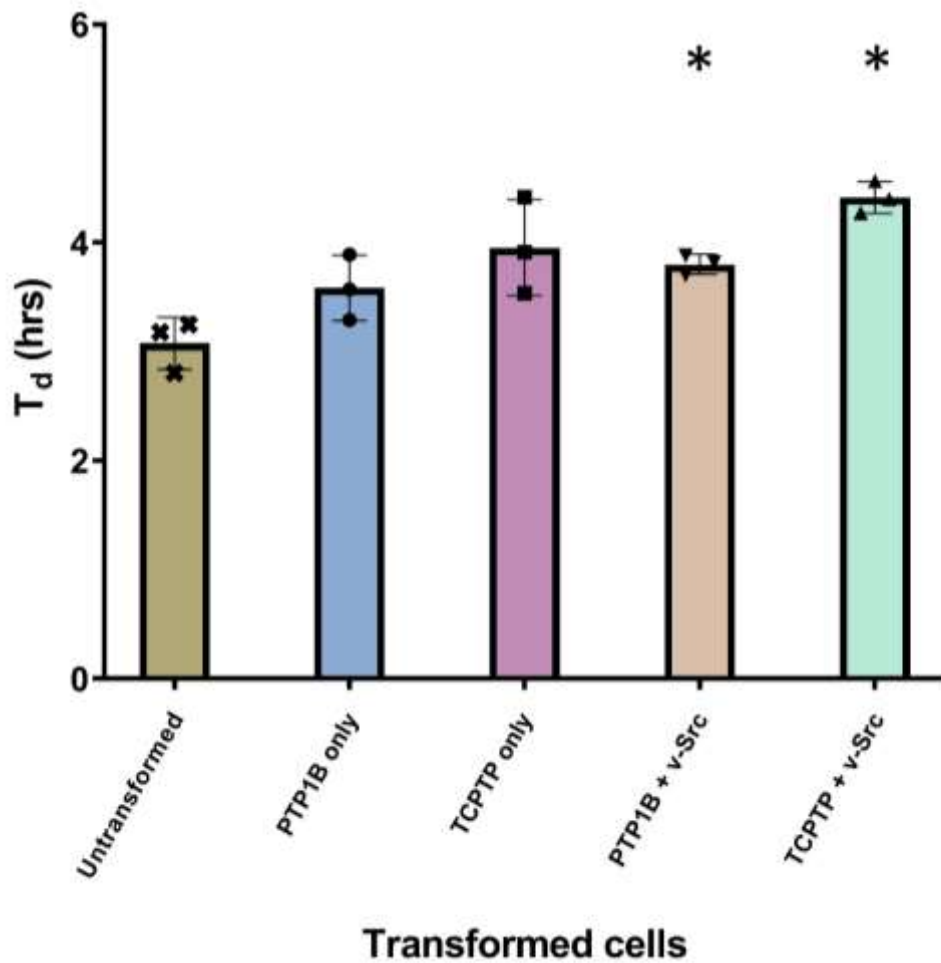
3.3. Results and discussion

3.3.1. Yeast assay verification

3.3.1.1. Selection of yeast strain

After all required combinations of plasmids had been transcribed into both yeast strains, YMK23 and YSC1, initial comparison of the two strains was based upon resultant cell viability. Post single colony purification, a single colony from these plates was picked and plated onto the corresponding knock-out media plate after left to grow at 30 °C for approx. 48hrs. Visually all transcribed cells had comparable growth / coverage to each other apart from for TCPTP based double knockouts (TCPTP + v-Src) for each strain as this had lesser final growth than the other altered cells. But all modified cells had a final growth less than the corresponding untransformed yeast strain. This was not surprising as transcribing cells does often negatively affect doubling time or the growth rate of the yeast cells. Once sufficient growth had occurred all plated cells were stored at -20 °C, and regardless of yeast strain base or plasmid composition all yeast cells remained viable on the original plate for up to 4 weeks. As a means of more accurately comparing the two different yeast strains multiple 48-hour growth cycles were conducted and statistically compared to better inform the choice of yeast strain taken forward for all subsequent yeast assay PTP inhibition experiments.

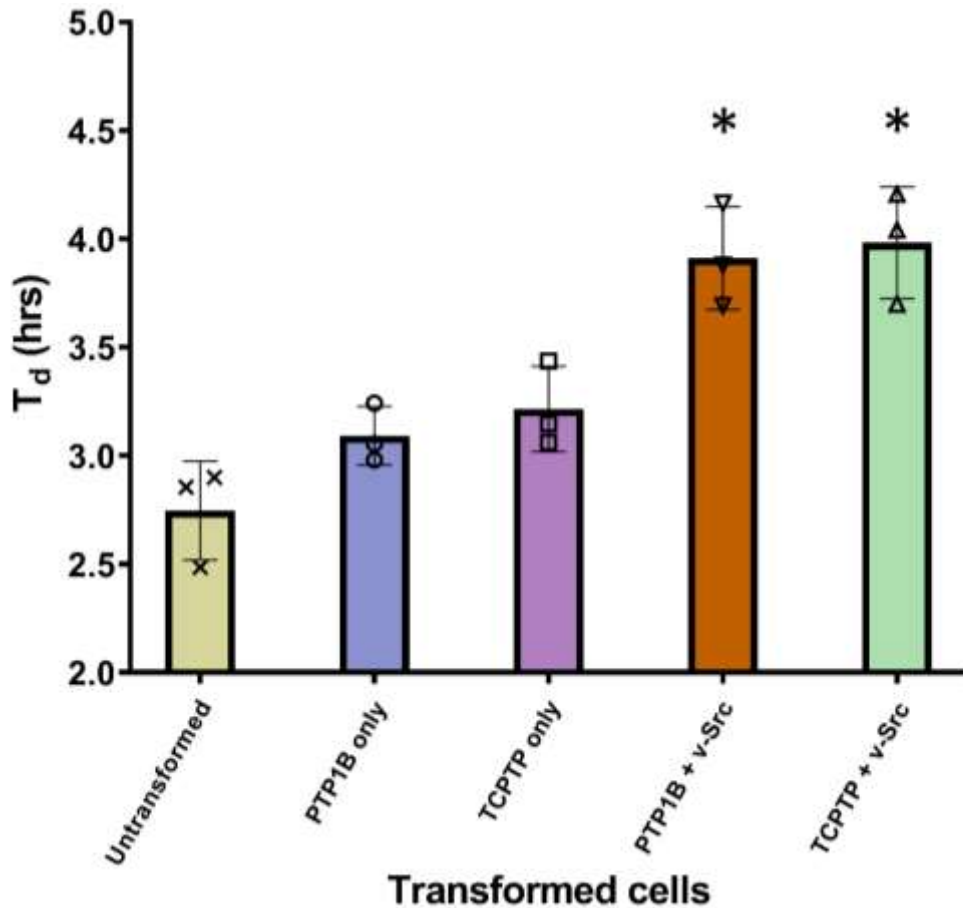
3.3.1.1.1. Doubling times



Transformed cells	PTP1B only	TCPTP only	PTP1B + v-Src	TCPTP + v-Src
p value	ns	ns	<0.050	<0.005

Figure 39: Initial doubling time (T_d) data for all transformations of the YMK23 strain, $n=3$ for each transformation. Mean and individual biological points \pm standard deviation plotted. Data is normally distributed according to a Shapiro-Wilk test. Used a parametric t-test with Welch's corrections. * p value ≤ 0.050 vs untransformed cells.

Figure 39 above and below in **Figure 40**, the initial investigation results are shown where three biological replicates (single colony) each with three to five mechanical replicates for each were conducted. As shown in **Figure 39**, YMK23 transformations the sole inclusion of the plasmids encoded for PTP1B or TCPTP did not cause a significant effect on the growth rate when compared to the untransformed yeast. A significant effect is observed when comparing untransformed YMK23 cells with cells transcribed either of the PTPs with v-Src. The most significant of which being the co-transcription of TCPTP and v-Src.



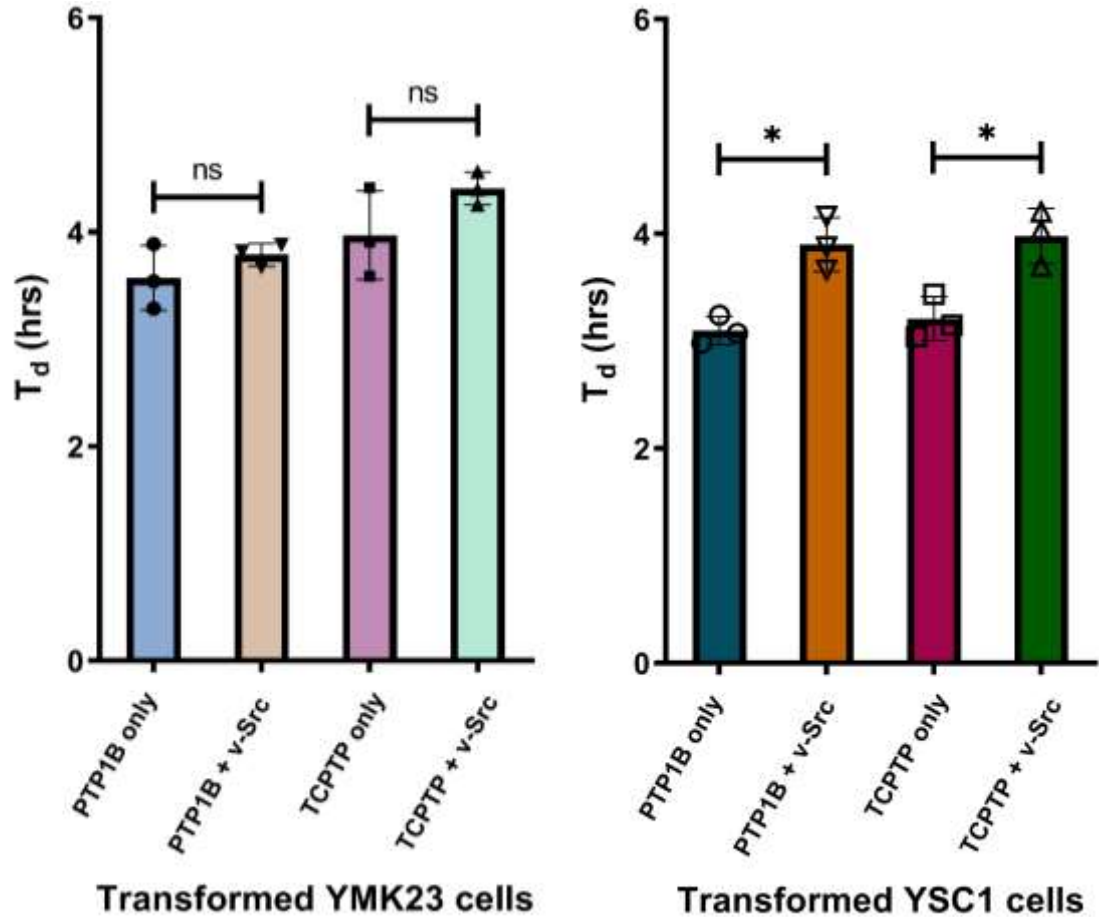
Transformed cells	PTP1B only	TCPTP only	PTP1B + v-Src	TCPTP + v-Src
p value	ns	ns	<0.050	<0.050

Figure 40: Initial doubling time (T_d) data for all transformations of the YSC1 strain, $n=3$ for each transformation. Mean and individual biological points \pm standard deviation plotted. Data is normally distributed according to a Shapiro-Wilk test. Used a parametric t-test with Welch's corrections. * p value ≤ 0.050 vs untransformed cells.

As with YMK23, the YSC1 based transformations (**Figure 40**), also did not cause a significant effect on the growth rate when the sole inclusion of the plasmids encoded for either PTP1B or TCPTP, when compared against the corresponding untransformed yeast. However, a significant effect is again observed when comparing untransformed YSC1 cells with cells transcribed with either of the PTPs + v-Src. A more significant but comparable effect on growth rate occurred when PTP1B + v-Src were co-expressed in YSC1 cells, than when PTP1B + v-Src was co-expressed into YMK23 cells when compared against respective untransformed cell growth.

As well as comparing the effect on the growth of the yeast strains with the addition of plasmids to untransformed growth it is also relevant to compare the corresponding single PTP transcribed cells to the corresponding co-transcribed PTP + v-Src. As treated PTP

only transcribed cells are used as a control for assessing actual PTP inhibition so that an increase in T_d for PTP + v-Src co-transcribed cells when treated is due to PTP inhibition and not off-target effects. Hence ideally the base growth of PTP1B and PTP1B + v-Src for example will not be significantly different to each other.



Transformed cells	PTP1B based	TCPTP based
p value: YMk23	ns	ns
p value: YSC1	<0.050	<0.050

Figure 41: Comparing the initial doubling time (T_d) data for all transformations of the YMk23 and YSC1 strains, $n=3$ for each transformation. Mean and individual biological points \pm standard deviation plotted. Data is normally distributed according to a Shapiro-Wilk test. Used a parametric t-test with Welch's corrections. * p value \leq 0.050, PTP only vs corresponding PTP + v-Src.

Above **Figure 41** (left) demonstrates that for the YMk23 strain there is no significant difference in the transformed cell doubling time between the addition of only a PTP plasmid or the addition of a PTP plasmid in conjunction with the v-Src plasmid regardless of the PTP included. With the doubling time of PTP1B + v-Src transformed cells do not have significantly different T_d values to the PTP1B only cells, this heavily

implies that the PTP1B plasmid in YMK23 based cells does effectively restore growth which was initially downregulated due to the v-Src plasmid presence. The ability of the PTP to rescue the growth of the PTP + v-Src double transcribed cells is an important aspect of this assay's functionality, in identifying and ranking potential PTP inhibitors as a greater rescue in terms of T_d of the exponential growth phase specifically, the better the down regulation of PTP can be determined.

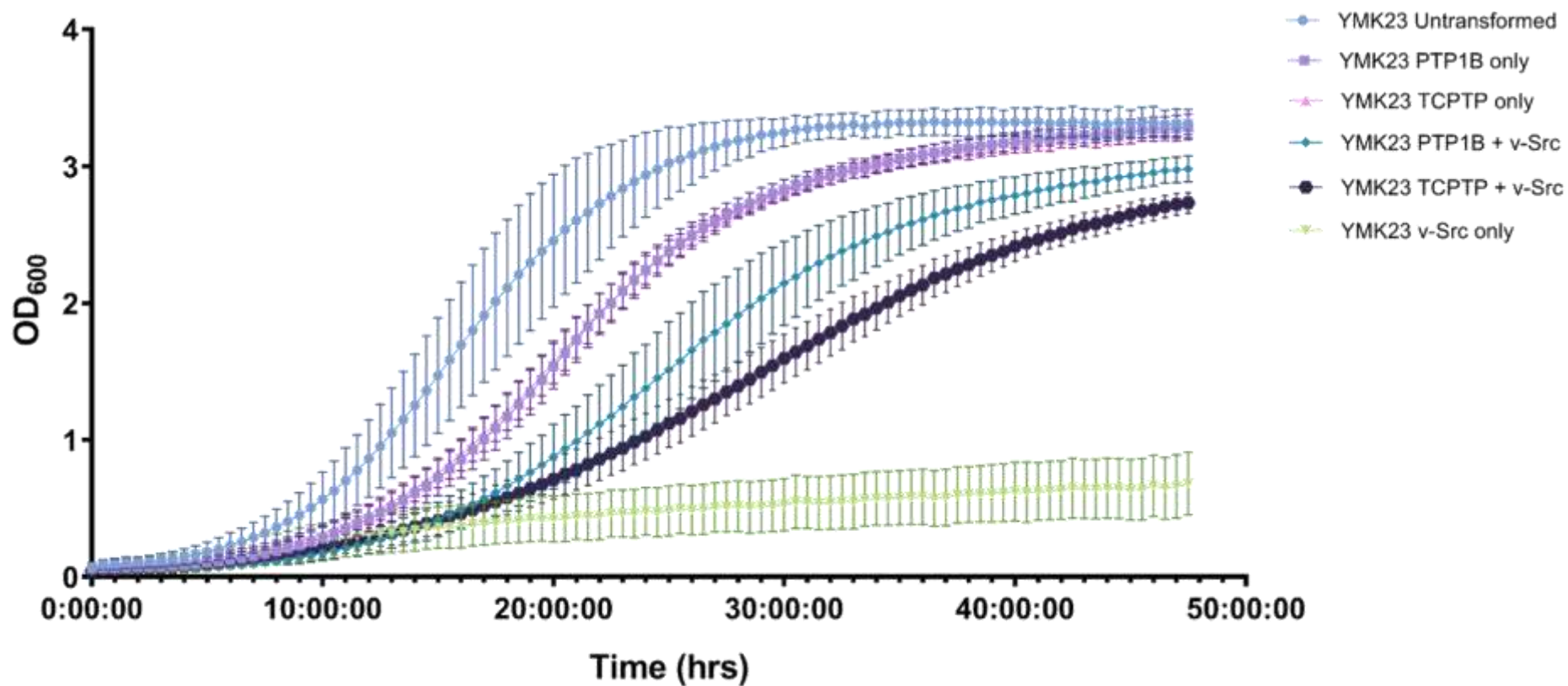
However, in **Figure 41** (right) with regards to the YSC1 strain-based transformations both versions of PTP + v-Src co-transcribed cells had a significantly higher T_d value than their respective single PTP transcribed counterpart. This implies that both the PTP1B and TCPTP plasmids are less capable of reverting the negative effect on the growth rate, namely the exceptional phase caused by the v-Src plasmids in the YSC1 strain than they are able to in the YMK23 strain. Meaning that in YSC1 based cells from this work the spore-wall process and therefore the mechanism for yeast duplication is still significantly impaired due to v-Src transcription even when co-transcribed with a PTP plasmid.

3.3.1.1.2. Growth curves:

In addition to assessing the doubling time of the exponential growth phase, the effect of plasmid incorporation on the overall 47.5-hour growth profile was also investigated. Both in terms of sole plasmid incorporation and the ability for the PTP plasmid to rescue the growth when co-transformed with the v-Src plasmid. The growth profile results of both yeast strains were fed into the selection of the plasmid to use when testing, potential hits.

When statistical analysis was conducted on yeast growth curve data, 2-way ANOVA was conducted where the column factor was the source of variance used to investigate significant difference. This is true for all growth curves when 2-way ANOVA is stated as statistical test used in this and all for all growth curve data present in this thesis and appendix.

This lessened ability the PTPs appear to exert in the restoration of the exponential growth phase of the PTP + v-Src co-transcribed cells in the YSC1 strain cells is unfortunate. As the incorporation of only a PTP plasmid in YSC1 cells did not have a significantly different effect on the overall growth profile or the exponential growth phase of the yeast cells when compared to untransformed YSC1 hence the overall growth profile of the yeast is maintained. The differences between in the resultant YMK23 and YSC1 growth profiles after a 47.5-hour period are shown below in **Figure 42** and **Figure 43**.

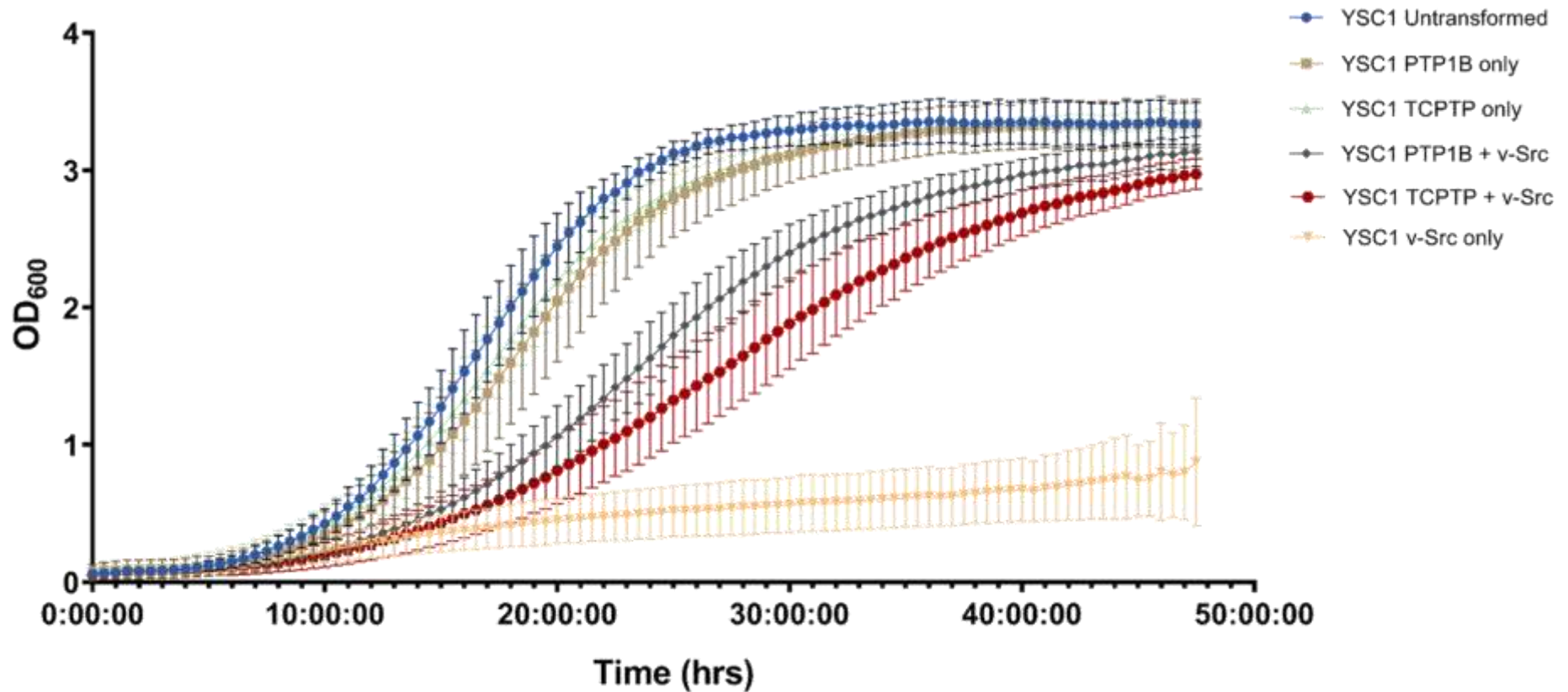


Cells	PTP1B only	TCPTP only	PTP1B + v-Src	TCPTP + v-Src	v-Src only	Cells	PTP1B based	TCPTP based
P value	<0.0001 *	<0.0001 *	<0.0001 *	<0.0001 *	<0.0001 *	P value	<0.0001 *	<0.0001 *

Figure 42: YMk23 strain-based yeast growth curves of a 47.5-hour period for all utilised transformations. $n=3$ for each transformation. Mean points \pm standard deviation plotted. Data is normally distributed according to a Shapiro-Wilk test. Used a 2-way ANOVA where column factor was source of variance. * p value ≤ 0.050 vs untransformed cells or PTP only vs corresponding PTP + v-Src.

When 2-way ANOVA statistical tests were conducted on the YMK23 transformations where the source of variance was the column factor, all transformation resulted in a significant change in the overall growth profile of the cell as shown above in **Figure 42**, when compared to the untransformed version. However, despite this the T_d values may not necessarily be significantly different (**Figure 39**). This statistical significance can be explained by the involvement of two factors. Firstly, the incorporation of any plasmid combination in YMK23 cells results in an elongated lag phase which resulted in the subsequent growth phases occurring later than in the untransformed counterpart, thus contributing to the significant difference in overall growth curves observed.

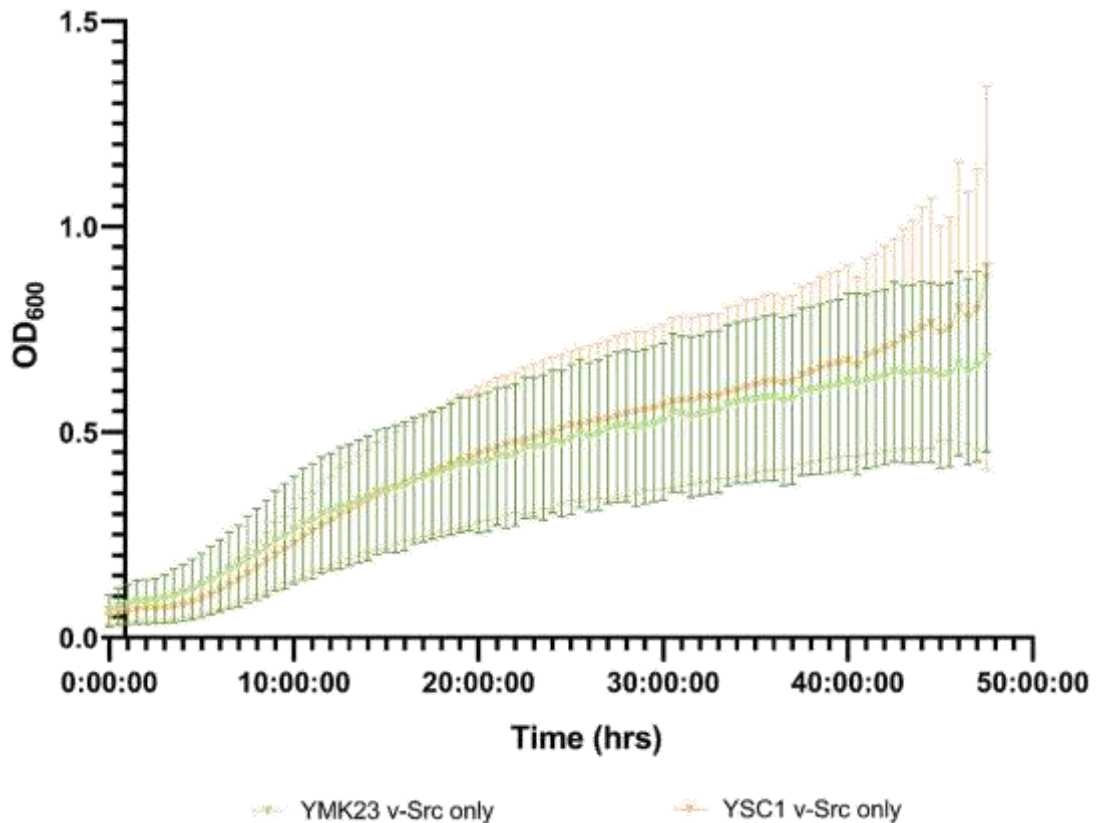
It is important to note that all the transformations of YMK23 apart from v-*Src* only (**Figure 42**) exhibited the same four stages of growth shown above in **Figure 36** as expected. The second noticeable factor is the variation in the growth profiles of the biological replicates. As with the single inclusion of only a PTP plasmid the standard deviation, for each recorded time point are very small and hence the error bars do not overlap with YMK23 untransformed, unlike with the YSC1 counterparts. As shown in **Figure 43** the growth profile for the untransformed cells and the YSC1 PTP only cells are either not significantly different (PTP1B) or only slightly significantly different (TCPTP). Once further studies and additional biological replicates were conducted the statistical difference between YMK23 untransformed cells and the PTP1B or TCPTP only transcribed YMK23 cells diminished, this is shown and discussed in the appendix (section 1.4).



Cells	PTP1B only	TCPTP only	PTP1B + v-Src	TCPTP + v-Src	v-Src only	Cells	PTP1B based	TCPTP based
P value	ns	<0.050 *	<0.0001 *	<0.0001 *	<0.0001 *	P value	<0.0001 *	<0.0001 *

Figure 43: YSC1 strain-based yeast growth curves of a 47.5-hour period for all utilised transformations. $n=3$ for each transformation. Mean points \pm standard deviation plotted. Data is normally distributed according to a Shapiro-Wilk test. Used a 2-way ANOVA where column factor was source of variance. * p value ≤ 0.050 vs untransformed cells or PTP only vs corresponding PTP + v-Src.

As with YMK23, both versions of PTP + v-Src YSC1 based cells and v-Src only YSC1 cells had significantly different growth profiles than the untransformed YSC1 cells, as seen in **Figure 43**. This was again expected for v-Src only transcribed cells. Furthermore, again all the expected transformation exhibited the four stages of yeast growth, with the exception being v-Src only. The corresponding growth profiles of the YMK23 and YSC1 cells were then compared.



P value	ns
---------	----

Figure 44: v-Src only transcribed yeast cell growth curves of a 47.5-hour period for both utilised strains. n=3 for both strains Mean points \pm standard deviation plotted. Data is normally distributed according to a Shapiro-Wilk test. Used a 2-way ANOVA where column factor was source of variance. * p value \leq 0.050.

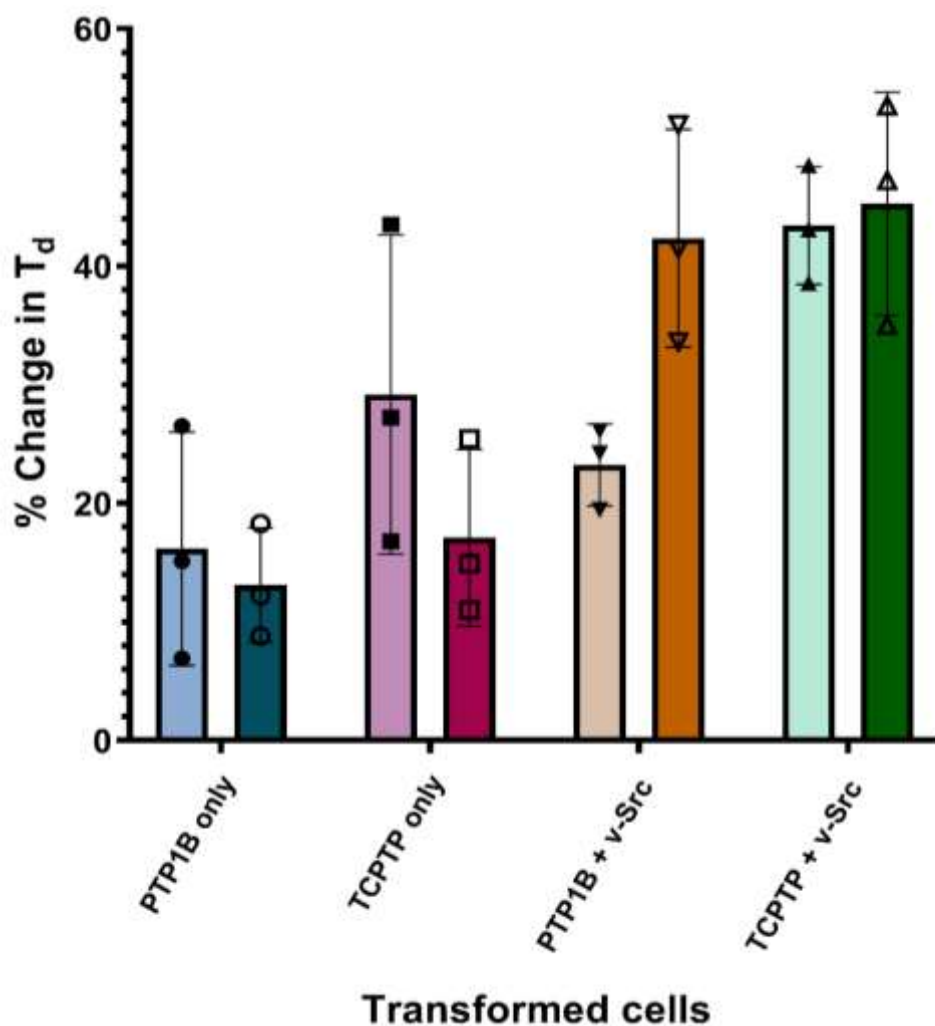
The comparison of the resultant growth profiles of YMK23 and YSC1 with the transcription of v-Src plasmid only is also an important factor when selecting the yeast strain to use, this is shown in **Figure 44**. In terms of v-Src only transcription initially both YMK23 and YSC1 growth profiles were comparable until the last 10 hours (~38-48 hrs) when YSC1 v-Src had a sizable uptick in growth with an upward projection in growth in the subsequent hours after the 40-hour mark. The ideal growth profile for v-Src only cells is demonstrated by YMK23 as the v-Src plasmid operates as a positive control for

complete PTP inhibition, a slight curve followed by a plateau is better for visualising successful PTP inhibitors by growth profiles. Therefore, in terms of v-Src only transcribed cells YMK23 is the preferred yeast strain for use in this PTP inhibitory assay. The statistical comparison of the rest of the transformation for both yeast strains can be found in the appendix (section 1.3).

Furthermore, the growth profile of YMK23 transcribed with the v-Src plasmid only in **Figure 44** also supports the previous assertion that the plasmids exert their respective effects to a greater extent in the YMK23 strain than the YSC1 strain, as with v-Src specifically the uptick in growth of YSC1 v-Src transcribed suggests that the yeast cell itself can recover its own growth rate to some extent and therefore potentially cause uncertainty of any potential inhibitor result with regards to the extent of the rescued growth rate due to PTP inhibition. Additionally, the greater the potential effect a PTP inhibitor can exert the better the comparisons which can be drawn when ranking potential inhibitors in terms of rescued growth rate *via* T_d values.

3.3.1.1.3. % change in doubling times:

As the untransformed growth rates for the two yeast strains, YMK23 and YSC1, are not the same due to biological differences the mechanical repeat values were again averaged, resulting in three biological repeats and the percentage change in T_d values were calculated for each transformation against the averaged T_d of the corresponding untransformed cells of that yeast strain, to enable relevant comparison between the two yeast strains, the result of which is shown below in **Figure 45**.



Transformation	PTP1B only	TCPTP only	PTP1B + v-Src	TCPTP + v-Src
P value	ns	ns	ns	ns

Figure 45: Comparison of the effects on the % change in the doubling time (T_d) value of YMK23 and YSC1 cells post transcription of plasmids. $n=3$ for each transformation, mean and individual points \pm standard deviation plotted. Used non-parametric Mann-Whitney t-test for statistical analysis. * p value ≤ 0.050 , YMK23 vs YSC1. Left = YMK23 and Right = YSC1 based transformed cells.

As mentioned previously, ideally the incorporation of the PTP plasmid would only have a limited effect on the exponential growth phase since the primary means by which PTP1B inhibition will later be measured, is the growth rate (T_d) of the treated cells, however the growth rate of the altered cells do not matter to a great extent as long as the cells remain viable as the primary measure of PTP inhibitor activity measure is the percentage change in T_d value, as this enables more relevant comparison between compounds and biological repeats due to the range of growth rates the untreated transcribed cells can produce.

However, due to the data being converted to a % change to enable cross yeast strain comparison, any statistical analysis conducted needs to be conducted using non-parametric tests even if the data is normally distributed. Such tests including the deployed Mann-Whitney t-tests require a greater number of biological replicates to demonstrate significance than the parametric counterparts. This means that with a biological n number of 3, no statistical significance between the corresponding transformation of the YMK23 and YSC1 strains are shown (**Figure 45**). In order to achieve significance a greater n number would need to be obtained. Regardless, the % change in T_d values do still provide insight into yeast strain selection. As there is a clear trend that in the YSC1 strain double transcription of both PTP1B and v-Src has a greater effect of increasing the T_d of the cells than appears to occur in the YMK23 version, thus supporting what was stated earlier in that the PTP1B plasmid is able to better recover the exponential growth phase of the yeast from the effect of the co-expression with v-Src in the YMK23 strain. But to confirm this with regards to % change in T_d more biological repeats would be needed.

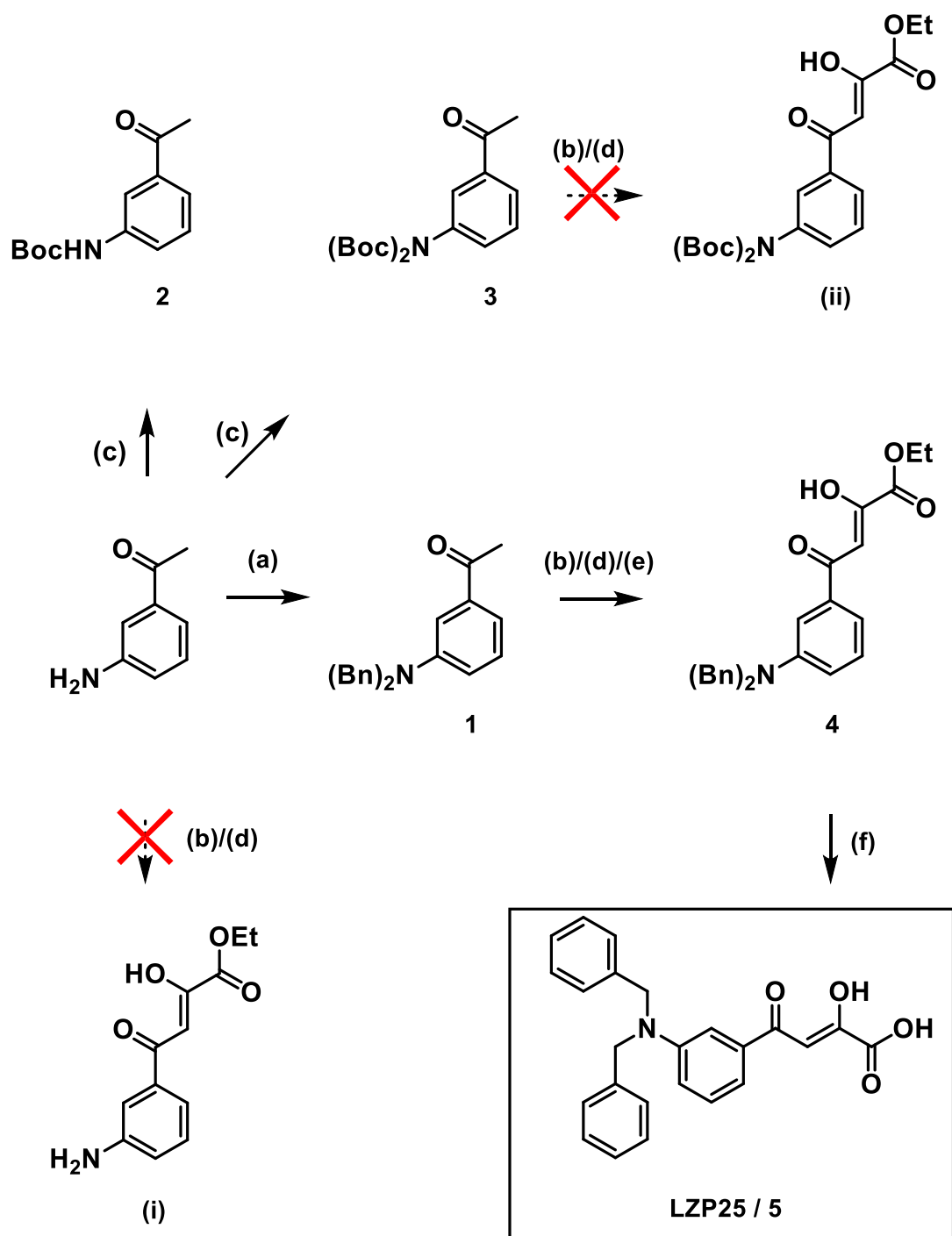
3.3.1.1.4. Justification in strain selection

As discussed above, both yeast strains, YMK23 and YSC1 possess different beneficial attributes for use within an PTP inhibitory assay post incorporation of plasmids. However, overall, from this preliminary data the strain YMK23 was selected and taken forward for all subsequent yeast-based inhibition assay runs. This is primarily due to that when transcription of a single PTP plasmid into YMK23 has a lesser or non-significant effect on the exponential growth phase (thus T_d) when compared to the corresponding PTP + v-Src co-transcribed YMK23 yeast (**Figure 41**). Demonstrating near complete growth restoration. Also, the biological effect of plasmid transcription such as inhibited growth with v-Src in YMK25 is enhanced when compared to the corresponding YSC1 version. Enhanced knock-down in growth due to v-Src and the subsequent rescue of growth with PTP plasmid co-transcription is imperative for the identification of PTP inhibitors.

3.3.2. Yeast based inhibition assay testing.

3.3.2.1. Known inhibitions and assay verification.

Despite the yeast assay being based upon prior literature^{125,126} the results obtained needed to be proven valid. This was achieved with the use of two known active site PTP inhibitors, specifically two of the compounds utilised in the formation of the PTP1B active site pharmacophore in Chapter 2 (section 2.3.1), ursolic acid and LZP25.

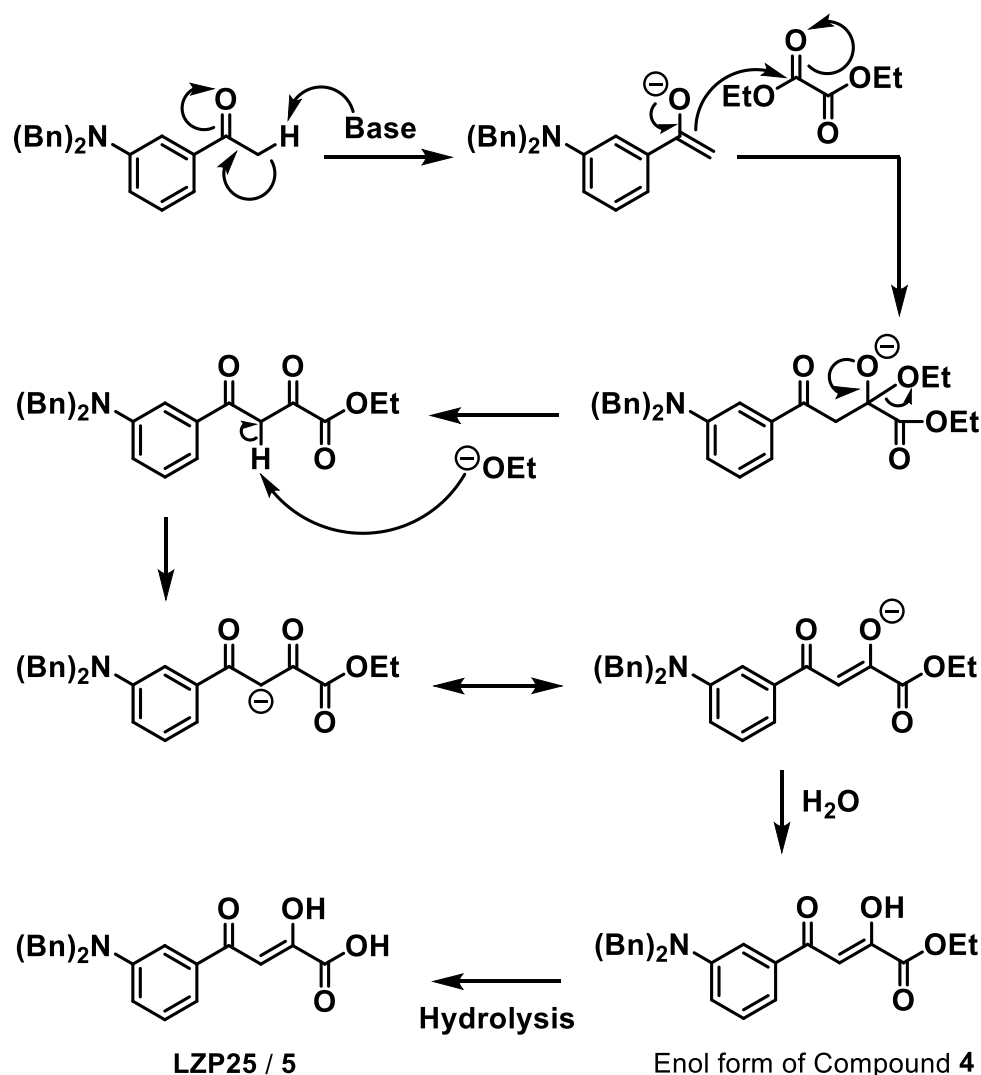


Scheme 9: Synthesis scheme to form known active site PTP1B inhibitor LZP25.

(a): 1-(3-aminophenyl)ethan-1-one (1.0 equiv.), DMF, Cs₂CO₃ (2.0 equiv.), BnBr (2.0 equiv.), 60 °C, 77% compound **1**. (b): Aromatic methyl ketone (1.0 equiv.), toluene, KOtBu (2.0 equiv.), diethyl oxalate (2.0 equiv.), 0 °C to RT, 0% for compound **4**, (i) and (ii). (c): 1-(3-aminophenyl)ethan-1-one (1.0 equiv.), DCM, NEt₃ (2.0 equiv.), DMAP (*cat.*), (Boc)₂O (2.2 equiv.), RT, formed compound **2** (5%) and **3** (76%) in parallel. (d): Aromatic methyl ketone (1.0 equiv.), THF, NaH (2.0 equiv.), MeOH (*cat.*), diethyl oxalate (2.0 equiv.), added 30 minutes later, RT to reflux (75 °C), 0% for compound **4**, (i) and (ii). (e): Compound **1** (1.0 equiv.), THF anhydrous, diethyl oxalate (2.0 equiv.), NaOMe (2.0 equiv.), N₂ atm, RT, 58%, compound **4**. (f) Compound **4** (1.0 equiv.), MeOH:DCM (1:1), LiOH.H₂O (1.5 equiv.), RT, 91% for LZP25 / compound **5**.¹³²⁻¹³⁵

Ursolic acid is commercially available and hence for this purpose it was purchased and tested in accordance with the aforementioned YMK23 yeast-based inhibition assay. However, the other selected PTP1B active site inhibitor chosen (LZP25), is not commercially available, so was synthesised *via* the linear synthesis shown above in **Scheme 9**.¹³²⁻¹³⁵

After some method alternations predominantly with the second step of converting compound **1** to **4**, LZP25 / compound **5** was successfully formed *via* a three-step linear synthesis from 1-(3-aminophenyl)ethan-1-one with an overall yield of 41%.



Scheme 10: Proposed mechanism for the mixed Claisen condensation synthesis step to form compound **4**.¹³⁶

As demonstrated in **Scheme 10** above the proposed mechanism of the mixed Claisen condensation style synthesis step is based upon prior literature¹³⁶ and from the experimental results the keto form of compound **4** appears to predominately tautomerism

into the enol form, with the reverse keto form being minimal. Hence the enol form of compound **3** is the major structural isomer, and this structure is illustrated above in **Scheme 9**.

With regards to the unsuccessful attempts to form compound **4** *via* (b) or (d) as seen in **Scheme 9**, it is proposed that the conditions utilised are not favourable for the initial dehydration step, shown in **Scheme 10**, as compound **4** was recovered and the reaction was unable to go to a form of completion from looking at the thin-layer chromatography (TLC) results despite being allowed an extended reaction time.

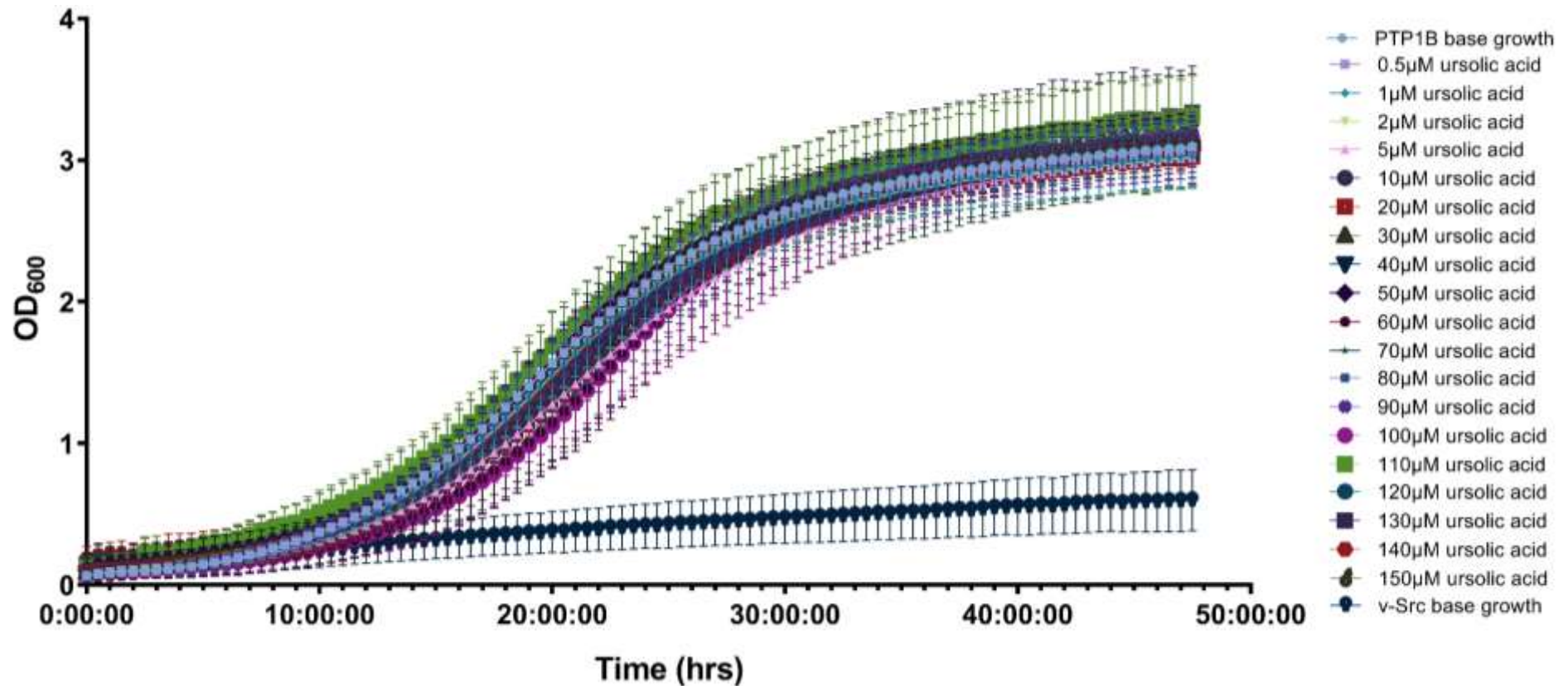
Once LZP25 had been synthesised and fully characterised, the yeast-based inhibition assay validity was subsequently verified by use of the two aforementioned known active site PTP inhibitors.

3.3.2.1.1. Growth curves of known inhibitors

As previously stated, above PTP inhibition only is related to the yeast cells growth rate when the PTP plasmid is co-expressed with the v-Src plasmid meaning any apparent effect of a PTP inhibitor on growth rate in PTP only cells are not indicative for PTP inhibition. The reason for also assessing the effect of ursolic acid or any known or potential inhibitor in PTP only expressed cells is as a means of control, to provide evidence that any change in the growth profile or in T_d from inhibitor addition is predominantly due to PTP inhibition and not off target effects such as general yeast cell toxicity or the clumping and crashing out of cells from solution. Both of which could affect both the growth profile and T_d values.

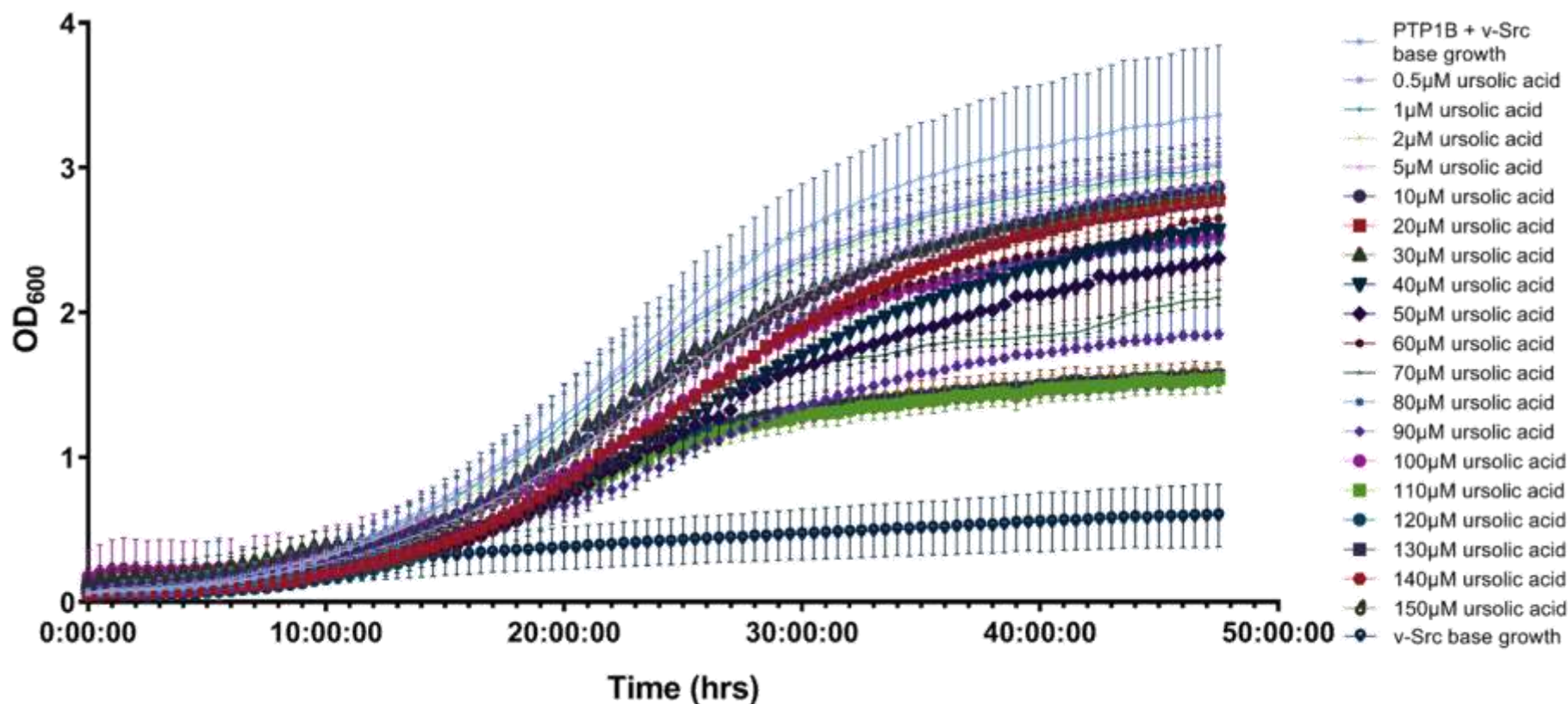
3.3.2.1.1.1. Ursolic acid PTP1B based.

As demonstrated in **Figure 46**, no concentration of ursolic acid tested caused a significant effect on the overall growth profile of the PTP1B only expressed YMK23 yeast cells. This result is as expected since here PTP1B inhibition does not correlate to growth rate.



μM	0.5	1	2	5	10 *	20 *	30	40 *	50	60 *	70	80 *	90	100 *	110	120	130	140	150
p value	ns	ns	ns	ns	<0.050	<0.050	ns	<0.050	ns	<0.050	ns	<0.010	ns	<0.010	ns	ns	ns	ns	ns

Figure 46: Growth profiles of PTP1B only yeast cells with the addition of ursolic acid. $n=7$ for 0.5-20 and 40 μM $n=6$ for rest of concentrations in PTP1B only cells, $n=13$ for v-*Src* base growth. Mean points \pm standard deviation plotted. Data is normally distributed according to a Shapiro-Wilk test. Used a 2-way ANOVA where column factor was source of variance. * p value ≤ 0.050 vs control.



μM	0.5	1	2	5 *	10 *	20 *	30 *	40 *	50 *	60 *	70 *	80 *	90 *	100 *	110 *	120 *	130 *	140 *	150 *
p value	ns	ns	ns	<0.050	<0.010	<0.001	<0.050	<0.001	<0.001	<0.005	<0.0001	<0.050	<0.0001	<0.050	<0.0001	<0.0001	<0.0001	<0.0001	<0.0001

Figure 47: Growth profiles of PTP1B + v-Src yeast cells with the addition of ursolic acid. n=7 for 0.5-20 and 40 μM n=6 for rest of concentrations in PTP1B + v-Src cells, n=13 for v-Src base growth. Mean points \pm standard deviation plotted. Data is normally distributed according to a Shapiro-Wilk test. Used a 2-way ANOVA where column factor was source of variance. * p value \leq 0.050 vs control.

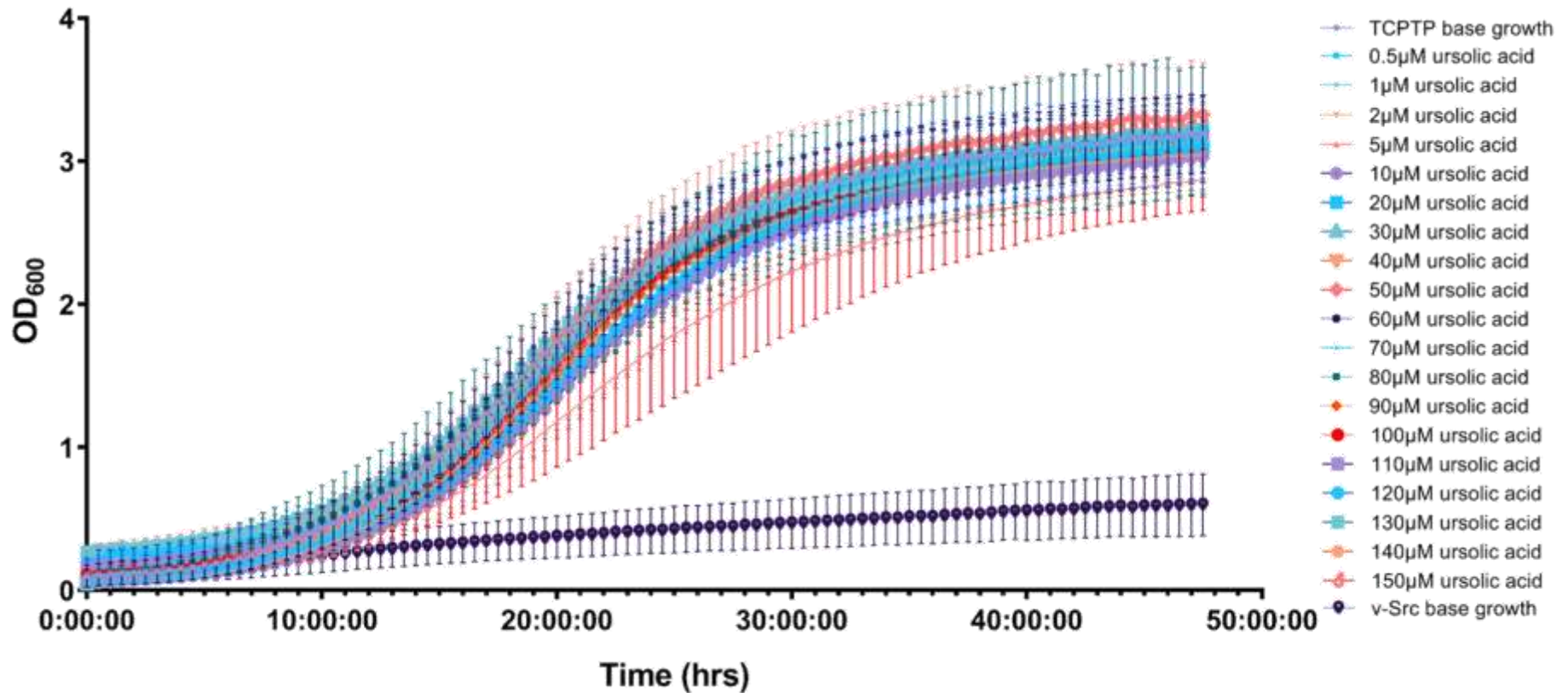
Unlike with **Figure 46**, **Figure 47** shows a clear dose dependent response trend for the addition of ursolic acid, in terms of the overall growth profile but more importantly with regards to the exponential growth phase. This is the desired result, as with the PTP + v-Src transcribed cells the inhibition of PTP is directly related to the growth rate or doubling time value of the yeast where greater the increase in doubling time the more effective the PTP inhibition. Ursolic acid has a significant overall effect on the growth profile of PTP1B + v-Src co-transcribed cells (**Figure 47**) from 5 μM , whereas for PTP1B only cells (**Figure 46**), a significant effect was not observed at the maximum concentration investigated of 150 μM .

As mentioned in the introduction a lower final absorbance value of the growth profile is not necessarily indicative of greater effect in terms of PTP inhibition, and the primary measure is the % change in doubling time.

3.3.2.1.1.2. Ursolic acid TCPTP based.

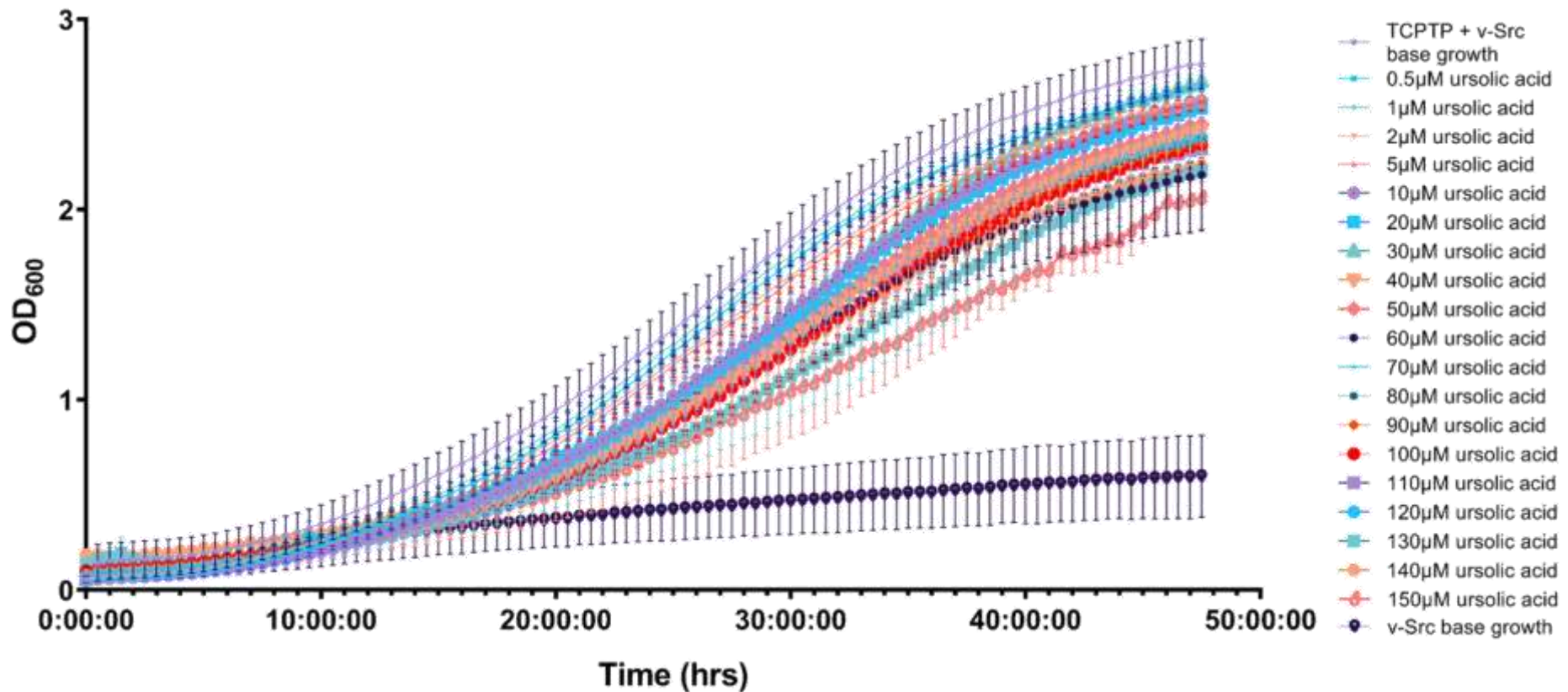
Figure 48 shows that as with PTP1B only (**Figure 46**), TCPTP only growth profiles overall are not affected by the incorporation of a known PTP inhibitor at any concentration tested. This is the desired result as any witnessed affect would be due to external effects to TCPTP inhibition. The only exception is that at 5.0 μM an increase in the growth rate of the exponential growth phase occurs, this is because three of the six biological repeats have consistently lower absorbance values throughout the experiment than the other biological repeats, the reason for this is unknown but overall ursolic acid appears to have no significant effect on the growth rate or profile of TCPTP only yeast cells.

As with **Figure 47** and PTP1B + v-Src transcribed cells, TCPTP + v-Src transcribed cells also overall exhibited the expected general dose dependent change in the exponential growth phase and overall growth profile due to the addition of ursolic acid. However, to a lesser effect than was witnessed in the PTP1B + v-Src transcribed cells (**Figure 47**). As shown below in **Figure 49**, the lowest ursolic acid concentration that had a significant overall effect on the growth profile of TCPTP + v-Src transcribed cells was 0.5 μM . However, at higher concentrations such as 120 μM no significant effect on the overall growth profile was observed the reason why is unknown but it thought to be contributed to the greater degree of variability in the base TCPTP + v-Src transcribed cells than in the untreated PTP1B + v-Src transcribed cells.



μM	0.5	1	2	5 *	10	20	30	40	50	60	70	80	90	100	110	120	130	140	150	
p value	ns	ns	ns	<0.010	ns	ns	ns	ns	ns	ns	ns	ns	ns	ns	ns	ns	ns	ns	ns	ns

Figure 48: Growth profile of TCPTP only yeast cells with the addition of ursolic acid. n=7 for 0.5-20 and 40 μM n=6 for rest of concentrations in TCPTP only cells, n=13 for v-Src base growth. Mean points ± standard deviation plotted. Data is normally distributed according to a Shapiro-Wilk test. Used a 2-way ANOVA where column factor was source of variance. * p value ≤ 0.050 vs control.



µM	0.5 *	1	2*	5 *	10 *	20 *	30 *	40 *	50 *	60 *	70 *	80 *	90	100 *	110	120	130 *	140 *	150 *
p value	<0.050	ns	<0.050	<0.010	<0.010	<0.005	<0.050	<0.001	<0.005	<0.005	<0.005	<0.005	ns	<0.050	ns	ns	<0.050	<0.050	<0.005

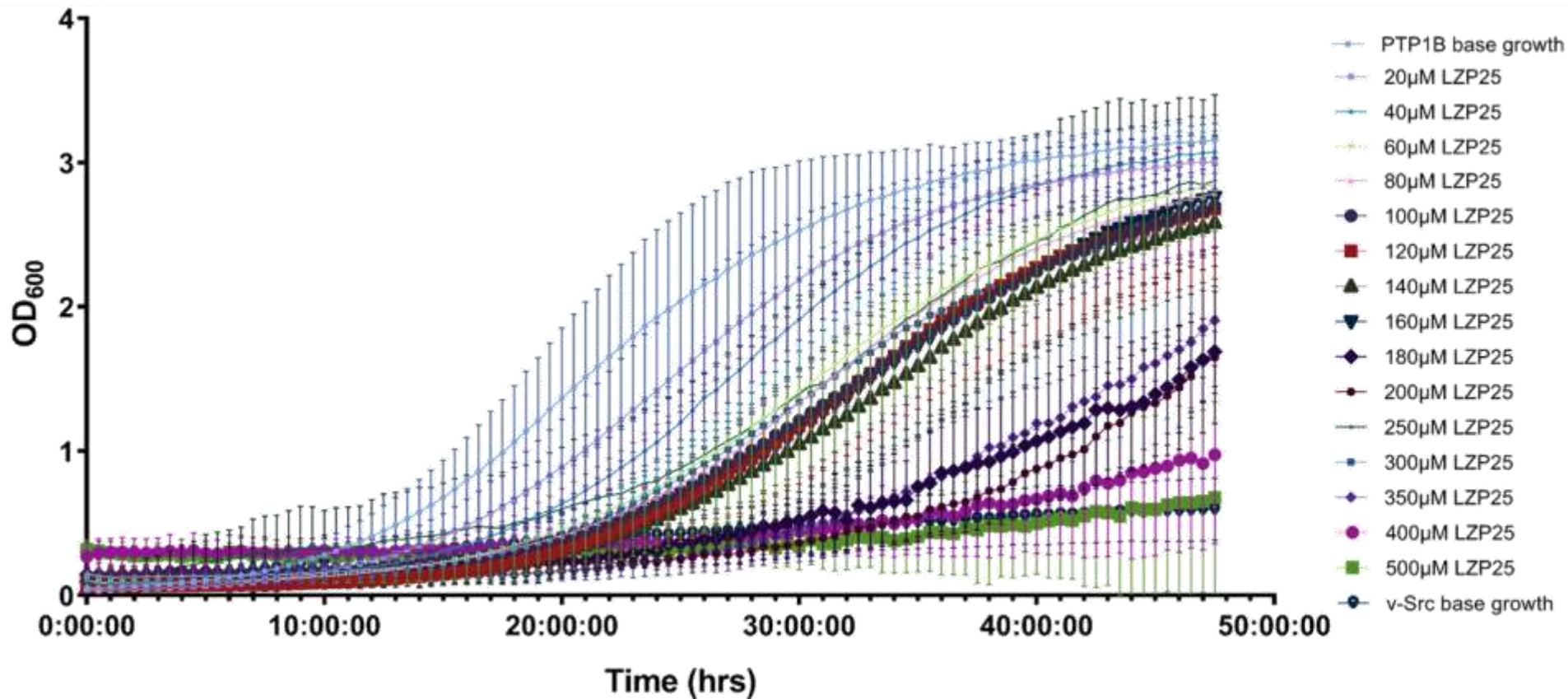
Figure 49: Growth profile of TCPTP + v-Src yeast cells with the addition of ursolic acid n=7 for 0.5-20 and 40 µM n=6 for rest of concentrations in TCPTP only cells, n=13 for v-Src base growth. Mean points ± standard deviation plotted. Data is normally distributed according to a Shapiro-Wilk test. Used a 2-way ANOVA where column factor was source of variance. * p value ≤ 0.050 vs control

3.3.2.1.1.3. LZP25 PTP1B based.

When LZP25 was deployed to further assess the robustness of the yeast-based inhibition assay the growth profile result were different than when ursolic acid was deployed, possible reasoning for this is described below. But the inhibitory activity of LZP25 is still demonstrated from this assay.

As shown below in **Figure 50**, when LZP25 was added to PTP1B only YMK23 transcribed yeast cells over a range of 20 – 500 μM it would appear that the inclusion of LZP25 results in a semi-dose dependent increase in T_d , which is not desirable since PTP inhibition is not related to growth. Hence other contributing factors are at play. These factors are most likely not limited too but include the following three; extended lag phase, less accurate correlation between absorbance and number of cells and clumping of cells.

In terms of the presence of an extended lag phase this factor is predominantly apparent at concentrations of 300 μM and below, as with the addition of LZP25 at these concentration the growth of the yeast cells is delayed from approximately 2 hours to in excess of 15 hours at the higher aforementioned concentrations the reason for this is unknown, but this delay has two main effects which significantly affect the growth profile of the yeast but not necessarily the exponential growth rate. Firstly, despite the exponential phase being delayed the resultant growth rate during this phase may not be significantly different and as such when looking at the T_d and % change in T_d values for PTP1B only cells no significance or a lesser than expected significance maybe found, as with regards for the operation of this assay and its ability to determine PTP inhibition it is not when the exponential growth phase starts but the T_d of this phase itself. Furthermore, on that vein an extended lag phase will also result in a lower final absorbance value after the 47.5-hour experiment as in real terms a lesser amount of yeast growth has elapsed, hence is not indicative of PTP inhibition as previously stated.



μM	20	40 *	60 *	80 *	100 *	120 *	140 *	160 *	180 *	200 *	250 *	300 *	350 *	400 *	500 *
p value	ns	<0.050	<0.005	<0.001	<0.001	<0.001	<0.001	<0.005	<0.0001	<0.0001	<0.0001	<0.0001	<0.0001	<0.0001	<0.0001

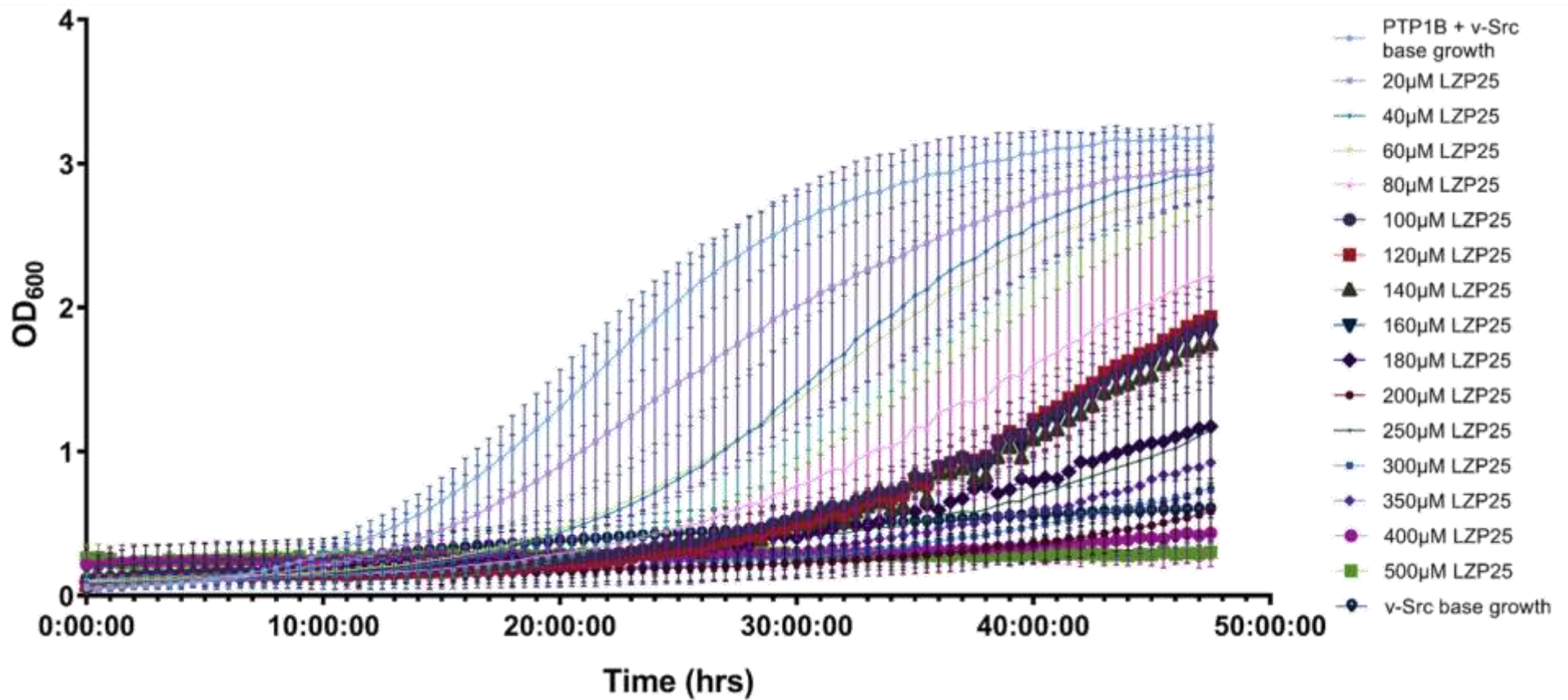
Figure 50: Growth profile of PTP1B only yeast cells with the addition of LZP25 n=6 for all concentrations in PTP1B only cells, n=13 for v-Src base growth. Mean points \pm standard deviation plotted. Data is normally distributed according to a Shapiro-Wilk test. Used a 2-way ANOVA where column factor was source of variance. * p value \leq 0.050 vs control.

The second potentially identified contributing factor to the significant change in PTP1B only growth curves are due to the colouration of LZP25 and of the resultant solution, which at higher concentrations is a dark orange in colour. The wavelength of light used for measuring the growth rate of yeast of 600nm is not the optimum wavelength of light in terms of LZP25 absorbance, but the darker colourisation may result in a false positive result in terms of relative cell number. For concentrations 400 and 500 μM , this would certainly explain the significantly higher starting absorbance value when the same volume of stock overnight cell solution was seeded into these corresponding wells as with all other concentrations.

The third possible contributing factor is that at higher concentrations of LZP25 after the 47.5-hour growth experiment clumps of cells were seen to crash out of solution. This would have the effect of lowering the absorbance values and thus the apparent number of cells, this reduction in measurable cell count results in the apparent effect of cell death. This occurred to the greatest extent at 400 and 500 μM , but there was also some evidence of it at 200 – 350 μM , in addition to a substantially extended lag phase.

Below **Figure 51** shows the resultant growth profiles of YMK23 PTP1B + v-Src transcribed yeast cells with the addition of LZP25 ranging from 20 to 500 μM . Without the control PTP1B only cell data shown in **Figure 50** it would be presumed that the significant changes in both the overall growth profile and exponential growth phase is solely due to PTP1B inhibition by the known inhibitor LZP25. However, as stated above there are other presumed factors associated with LZP25 use as the inhibitor in the yeast assay. But these aforementioned other factors effect on the growth profile could be considered comparable in both transformations of yeast, PTP1B only and PTP1B + v-Src. Meaning any additional effect witnessed in the PTP1B + v-Src transformation where PTP1B inhibition is attributed to the T_d of the exponential growth phase, can be considered as being due to PTP1B inhibition.

When comparing the resultant growth curves of PTP1B only (**Figure 50**) with PTP1B + v-Src (**Figure 51**) with the addition of LZP25 it is clear that for all concentrations particularly at 40 μM and above, a significantly greater deviation in both the overall growth profile and more importantly the exponential growth phase rate (T_d) in the PTP1B + v-Src cells than the PTP1B cells, thus supporting that the LZP25 does indeed inhibit the PTP1B and hence cause a drop in growth. This is demonstrated more clearly to be the case below with the % change in T_d data being graphically presented.



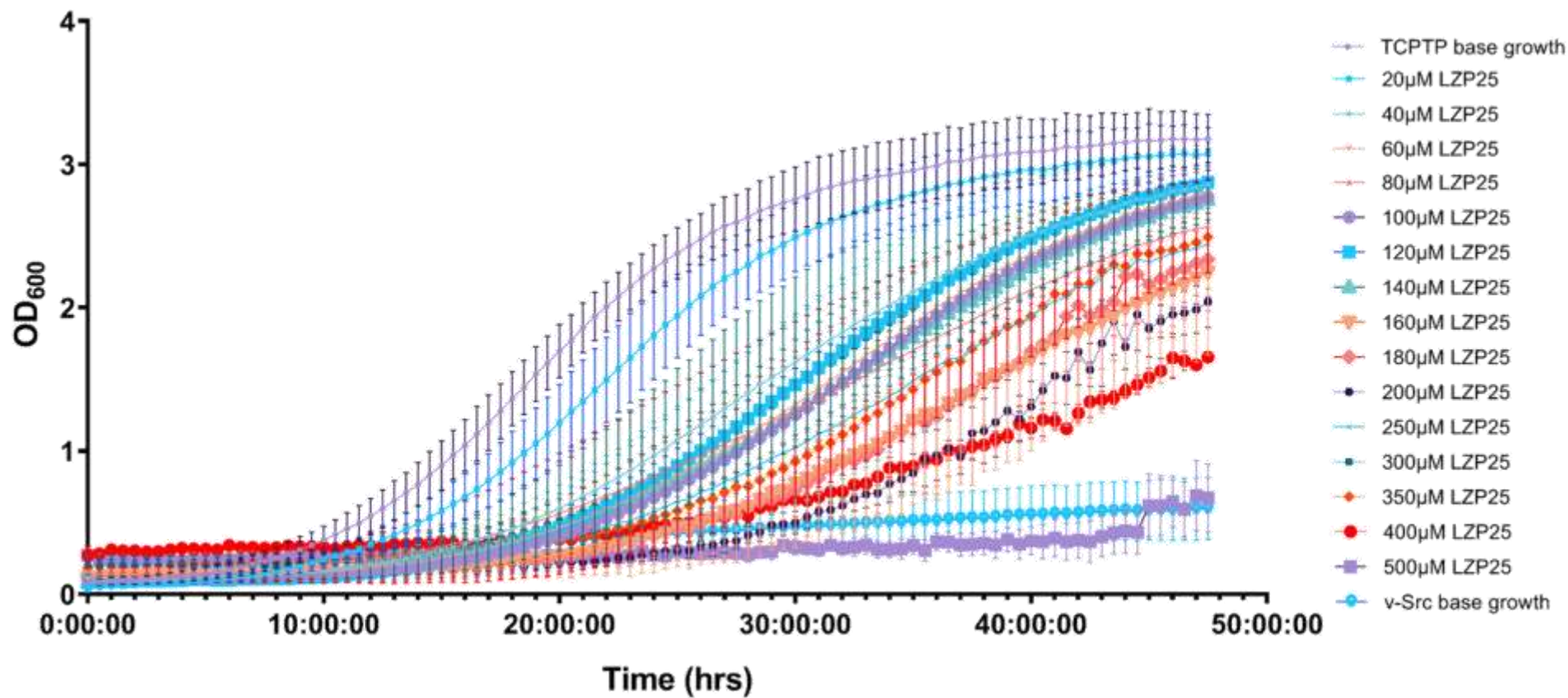
μM	20	40 *	60 *	80 *	100 *	120 *	140 *	160 *	180 *	200 *	250 *	300 *	350 *	400 *	500 *
p value	ns	<0.001	<0.001	<0.0001	<0.0001	<0.0001	<0.0001	<0.0001	<0.0001	<0.0001	<0.0001	<0.0001	<0.0001	<0.0001	<0.0001

Figure 51: Growth profile of PTP1B + v-Src yeast cells with the addition of LZP25 n=6 for all concentrations in PTP1B + v-Src cells, n=13 for v-Src base growth. Mean points \pm standard deviation plotted. Data is normally distributed according to a Shapiro-Wilk test. Used a 2-way ANOVA where column factor was source of variance. * p value \leq 0.050 vs control.

3.3.2.1.1.4. LZP25 TCPTP based.

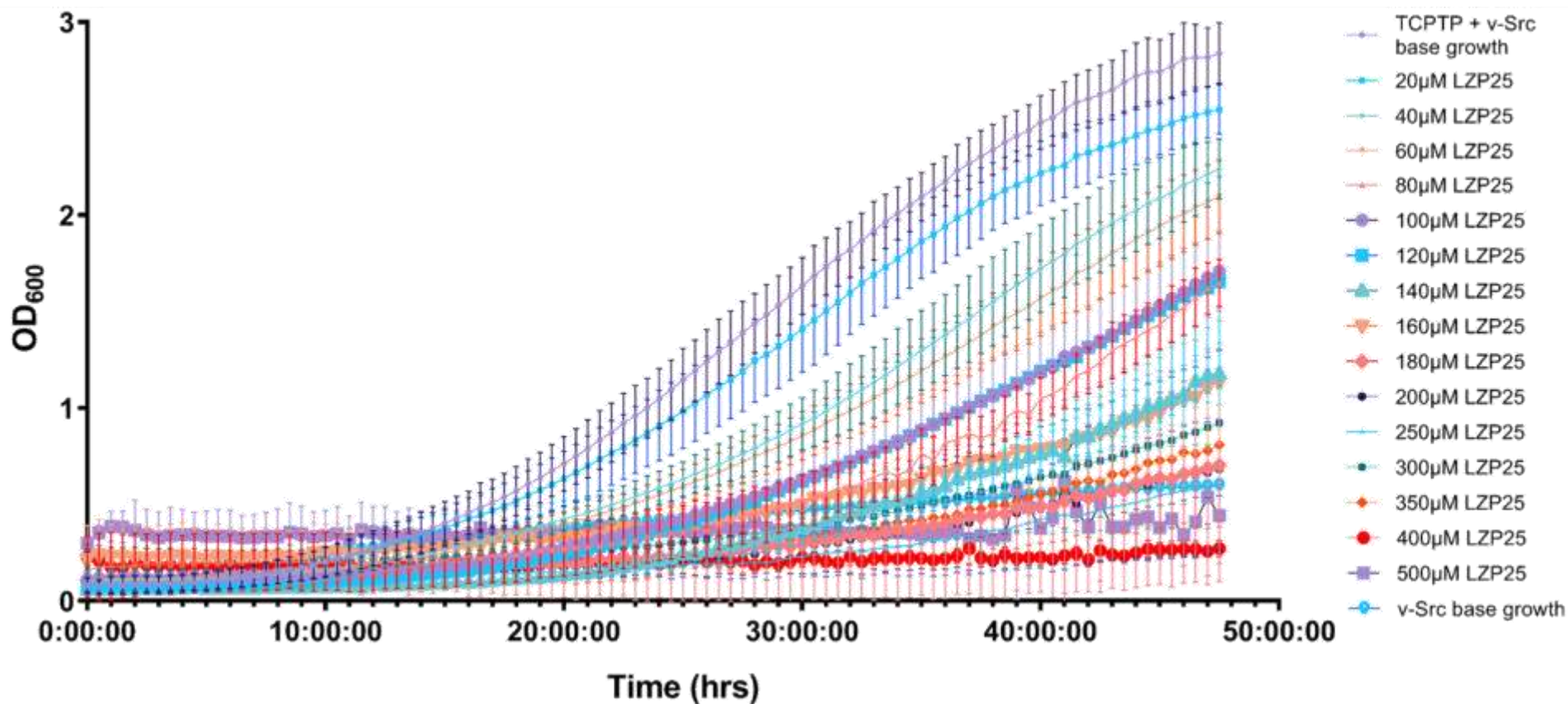
As with ursolic acid, LZP25 was also tested to investigate its ability to inhibit TCPTP. Once again this involved the addition of LZP25 to both the control, TCPTP only transcribed cells and TCPTP + v-Src cells.

As with PTP1B only cells (**Figure 50**) when LZP25 was added to TCPTP only cells, a significant change in the overall growth profile for all concentrations investigated occurred, and a significant effect on the exponential growth phase for all concentrations where T_d can be measured above and including 40 μM (40 - 350 μM) was also significant. This can once again potentially be attributed to the additional factors mentioned previously, extended lag phase, less accurate correlation between absorbance and number of cells and clumping of cells. However again as with the PTP1B based cells, there is also a greater effect exerted on the TCPTP + v-Src cells than the TCPTP only cells as shown in **Figure 52** and **Figure 53**.



μM	20 *	40 *	60 *	80 *	100 *	120 *	140 *	160 *	180 *	200 *	250 *	300 *	350 *	400 *	500 *
p value	<0.050	<0.001	<0.0001	<0.001	<0.0001	<0.0001	0.0003	<0.0001	<0.0001	<0.0001	<0.0001	<0.0001	<0.0001	<0.0001	<0.0001

Figure 52: Growth profile of TCPTP only yeast cells with the addition of LZP25 n=6 for all concentrations in TCPTP only cells, n=13 for v-Src base growth. Mean points \pm standard deviation plotted. Data is normally distributed according to a Shapiro-Wilk test. Used a 2-way ANOVA where column factor was source of variance. * p value ≤ 0.050 vs control.



μM	20	40 *	60 *	80 *	100 *	120 *	140 *	160 *	180 *	200 *	250 *	300 *	350 *	400 *	500 *
p value	ns	<0.0001	<0.0001	<0.0001	<0.0001	<0.001	<0.0001	<0.0001	<0.0001	<0.0001	<0.0001	<0.0001	<0.0001	<0.0001	<0.0001

Figure 53: Growth profile of TCPTP + v-Src yeast cells with the addition of LZP25 n=6 for all concentrations in TCPTP + v-Src cells, n=13 for v-Src base growth. Mean points \pm standard deviation plotted. Data is normally distributed according to a Shapiro-Wilk test. Used a 2-way ANOVA where column factor was source of variance. * p value \leq 0.050 vs control.

When comparing the resultant growth curves of TCPTP only (**Figure 52**) with TCPTP + v-Src (**Figure 53**) with the addition of LZP25 it is again apparent that for all concentrations 40 μ M and above a greater deviation in both the overall growth profile and more importantly the exponential growth phase rate (T_d) in the TCPTP + v-Src cells is observed, supporting that the LZP25 does also inhibit TCPTP which causes a drop in growth. This is again illustrated more clearly below with the % change in T_d data graphically presented.

After the growth profiles had been investigated the key region of yeast growth, the exponential growth phase was investigated and compared with the calculation of T_d and latter % change in T_d .

3.3.2.1.2. % change in doubling time

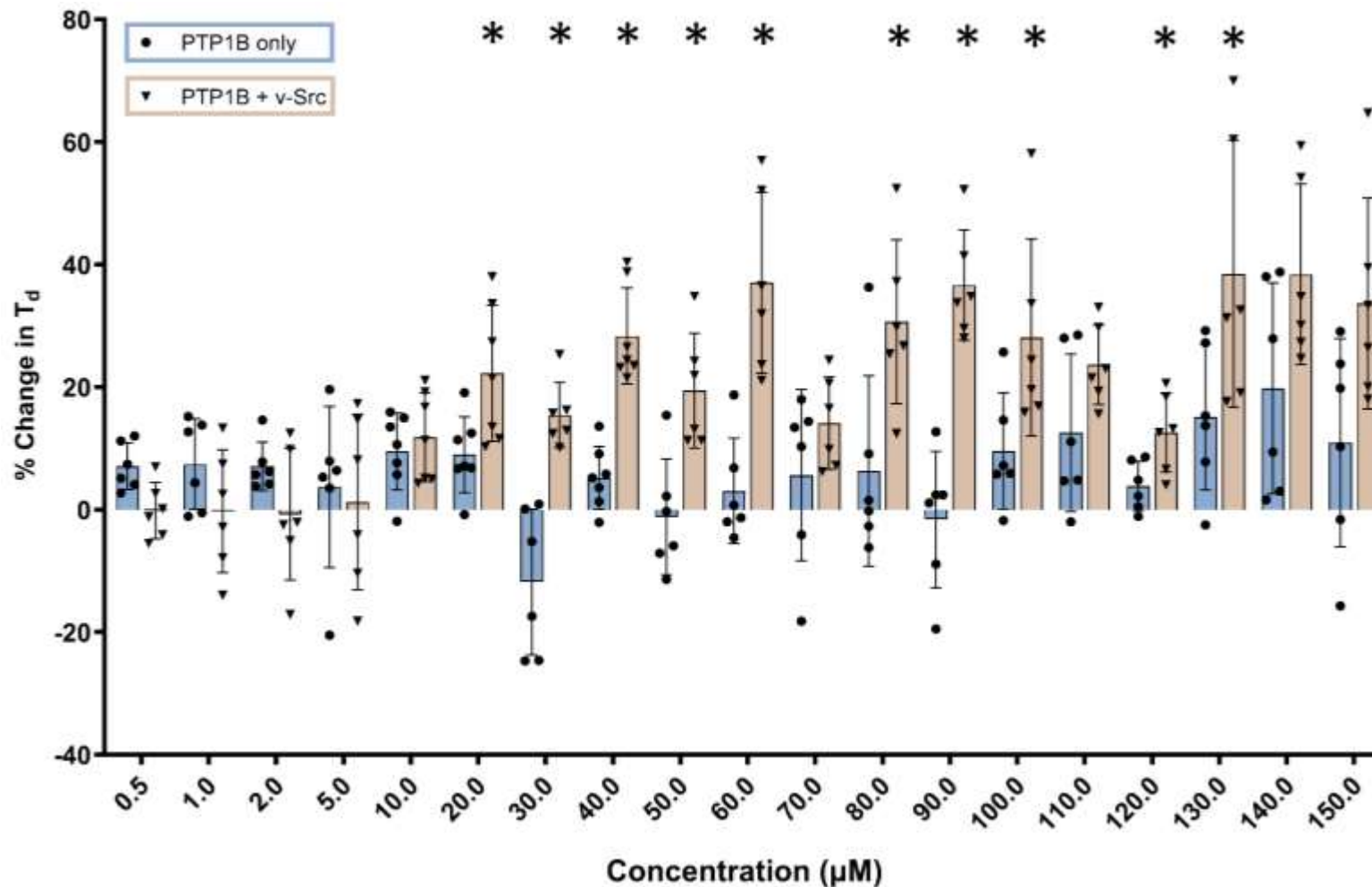
All the T_d values which were converted to % change in T_d are shown in the attached appendix (section 1.6). The reason for the utilisation of % change is as stated previously allows comparison between different cell lines and biological repeats or different compounds tested on different days and hence the base growth rate for the specifically used colony can differ. Additionally, all statistical P values for % change in T_d were calculated with the Welch's parametric unpaired t-test.

3.3.2.1.2.1. Ursolic acid

As mentioned previously the primary way PTP inhibition was assessed is by investigating the change in the doubling time of the exponential growth phase when compared against the corresponding base or untreated cells. A significant increase in T_d in PTP + v-Src co-transcribed cells is indicative of PTP inhibition. In order to enable comparison of results between different experiments the effect on growth rate was calculated as a percentage change in T_d . The active side inhibitory results of both known inhibitors towards PTP1B and TCPTP is demonstrated below.

3.3.2.1.2.1.1. PTP1B based.

As illustrated in **Figure 54**, overall, for the concentrations tested the % change in T_d is significantly higher in the PTP1B + v-Src cells when compared against PTP1B only cells.



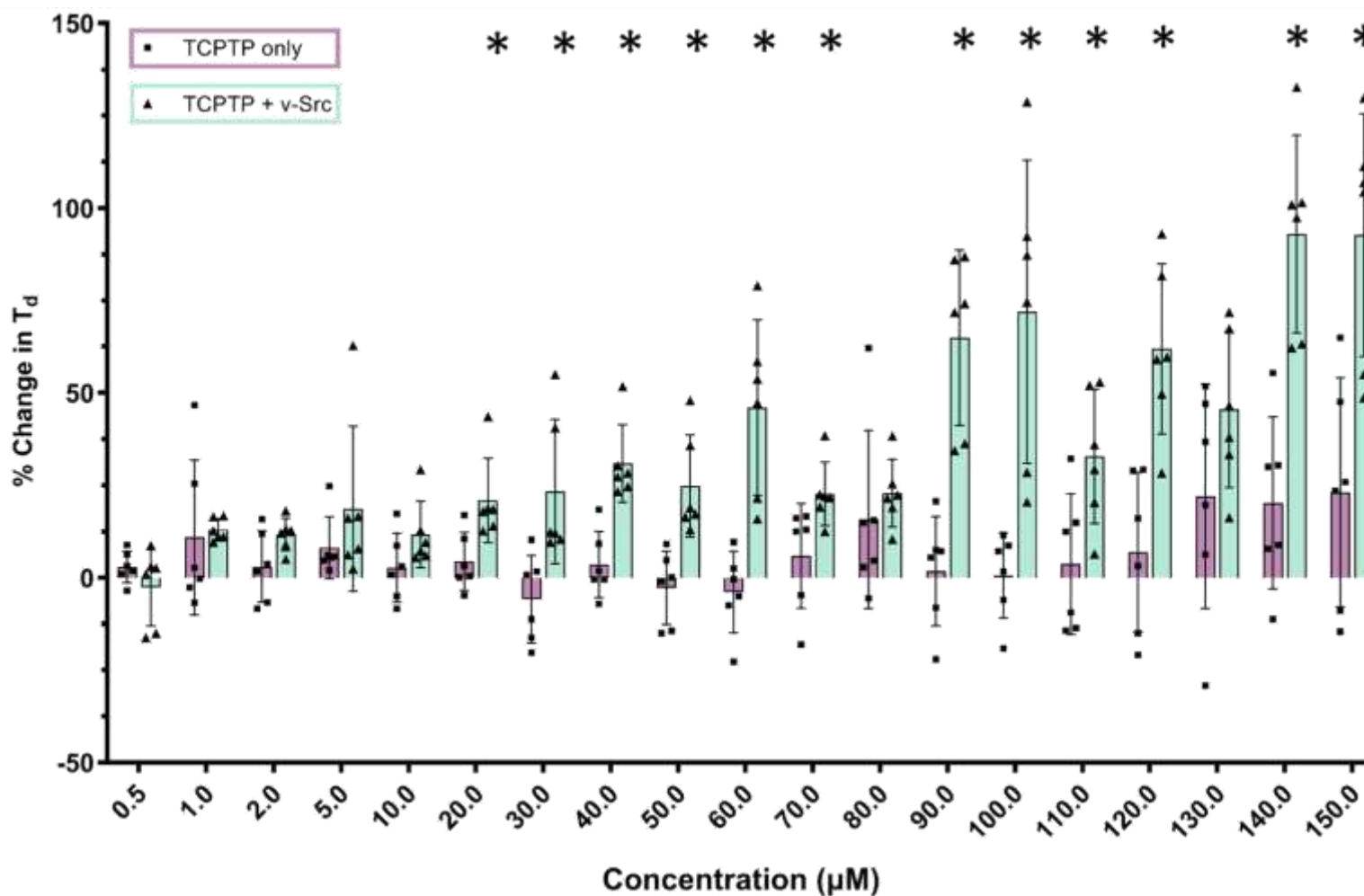
μM	p value
0.5	ns
1	ns
2	ns
5	ns
10	ns
20	<0.050
30	<0.005
40	<0.001
50	<0.050
60	<0.001
70	ns
80	<0.050
90	<0.005
100	<0.050
110	ns
120	<0.050
130	<0.050
140	ns
150	ns
Overall *	<0.005

Figure 54: Comparison of % change in doubling time (T_d) of PTP1B only and PTP1B + v-Src transformed yeast cells in the presence of ursolic acid at 0.5-150 μM . $n=7$ for 0.5-20 and 40 μM $n=6$ for rest of concentrations tested in both transformations, mean and individual points \pm standard deviation plotted. Used non-parametric Mann-Whitney t-test for statistical analysis. * p value ≤ 0.050 vs control.

From **Figure 54** above the lowest concentration of ursolic acid to cause significantly higher effect on growth rate in the PTP1B + v-Src cells when compared to the control PTP1B only cells were 20 μM , indicating PTP1B inhibition. This is also the case for all subsequent higher concentrations apart from 70, 110 and 140 μM , this non-significance is partly due to the increased range of % change observed in the PTP1B only cells at these concentrations. A drop in the effect of ursolic acid in the PTP1B + v-Src cells is also observed at 70 μM , due to three biological repeats being lower than effect based upon the neighbouring concentration results, the reason for this is not known. But the overall theme is an upward trend in the % change in T_d in PTP1B + v-Src cells with increasing concentration of ursolic acid where the effect is consistently significantly higher than the % change in T_d for the PTP1B only cells for the same ursolic acid concentration. Therefore, the addition of ursolic acid into PTP1B only and PTP1B + v-Src had the desired effects on the % change by producing a dose dependent response on PTP1B inhibition in the PTP1B + v-Src cells, and not in the PTP1B only control cells. As shown in the appendix (section 1.6.1), the T_d values for ursolic acid addition in PTP1B only cells are not significantly different when compared to the corresponding base PTP1B only cells for all concentrations apart from (110, 130 and 140 μM), meaning overall the ursolic acid has no significant effect on growth rate, which it should not in these cells as PTP inhibition is not linked to growth rate. However, again shown in the appendix (section 1.6.1) the addition of ursolic acid to PTP1B + v-Src cells significantly increases T_d values when compared against the corresponding biological replicate base growth rate all concentrations tested above and including 20 μM . Hence ursolic acid is successfully inhibiting PTP1B as evidenced by the significant increase in doubling times (T_d), where generally a higher concentration results in a greater increase.

3.3.2.1.2.1.2. TCPTP based.

As well as determining PTP selectivity of potential developed inhibitors ursolic acid was also deployed in the TCPTP based version of the inhibitory assay and the % change in T_d for both TCPTP only and TCPTP + v-Src were calculated. This is another reason why ursolic acid and LZP25 were selected for assay validation as both are non-specific PTP inhibitors, so can act as positive controls in both the PTP1B and the TCPTP based cells. Results shown below in **Figure 55**, for the effect on TCPTP based cells upon the addition of ursolic acid.



μM	p value
0.5	ns
1	ns
2	ns
5	ns
10	ns
20	<0.010
30	<0.005
40	<0.005
50	<0.005
60	<0.005
70	<0.050
80	ns
90	<0.005
100	<0.005
110	<0.005
120	<0.005
130	ns
140	<0.005
150	<0.010
Overall *	<0.0001

Figure 55: Comparison of % change in doubling time (T_d) of TCPTP only and TCPTP + v-Src transformed yeast cells in the presence of ursolic acid at 0.5-150 μM . $n=7$ for 0.5-20 and 40 μM $n=6$ for rest of concentrations tested in both transformations, mean and individual points \pm standard deviation plotted. Used non-parametric Mann-Whitney t-test for statistical analysis. * p value ≤ 0.050 vs control.

Again, overall, when looking at all concentrations of ursolic acid tested, the % change in T_d in TCPTP + v-Src was significantly higher than for TCPTP only cells, again demonstrating that the ursolic acid is having the desired effect of inhibiting the PTP, which in this case is specifically TCPTP. As was seen in **Figure 54** with PTP1B + v-Src, the lowest concentration of ursolic acid which is required to inhibit TCPTP significantly is 20 μ M as seen above in **Figure 55**. Once again, every subsequent higher concentration of ursolic acid also exerted a significantly higher % change in T_d in the TCPTP + v-Src cells over TCPTP only cells as expected with the only exception being 80 μ M. This is due to a single biological replicate in the TCPTP only cells which had a resultant % change of 62%. This value is not only substantially larger than the rest of the biological replicates but also of the six biological repeats of the TCPTP + v-Src cells at 80 μ M. However, this potential outlier was not found to be anomalous and hence is included in all statistical analysis and the presented average value.

An upward trend in the % change in T_d in TCPTP + v-Src cells is apparent in **Figure 55** with regards to increasing the concentration of ursolic acid where the effect is consistently significantly higher than for the % change in T_d for the TCPTP only cells for the same ursolic acid concentration. But as was witnessed with PTP1B + v-Src at 70 μ M and also exclusively with TCPTP + v-Src at 80 μ M no significant difference between the % change in T_d is observed between TCPTP only and TCPTP + v-Src due to an apparent drop-in activity in TCPTP + v-Src at these two concentrations.

It would be logical to perhaps presume that the stock ursolic acid solution used to create a resultant concentration of 70 μ M in the wells for testing was incorrectly created. This is a possibility but since the PTP1B and TCPTP based yeast experiments were ran on separate occasions with freshly created stock solutions the likelihood that this is the primary reason is less likely but still possible.

The appendix (section 1.6.1) again contains and demonstrates that the T_d values for ursolic acid addition in TCPTP only cells are not significantly different when compared to the corresponding base TCPTP only cells for all concentrations apart from (140 μ M), showing that overall ursolic acid has no significant effect on growth rate. This is as expected as cells transcribed with just a PTP plasmid should not have an effect, as PTP inhibition is not linked to growth rate. Again, as shown in the appendix (section 1.6.1) the TCPTP + v-Src cells when comparing the T_d values with ursolic acid addition, to the corresponding biological replicate base growth rate are significantly higher for all

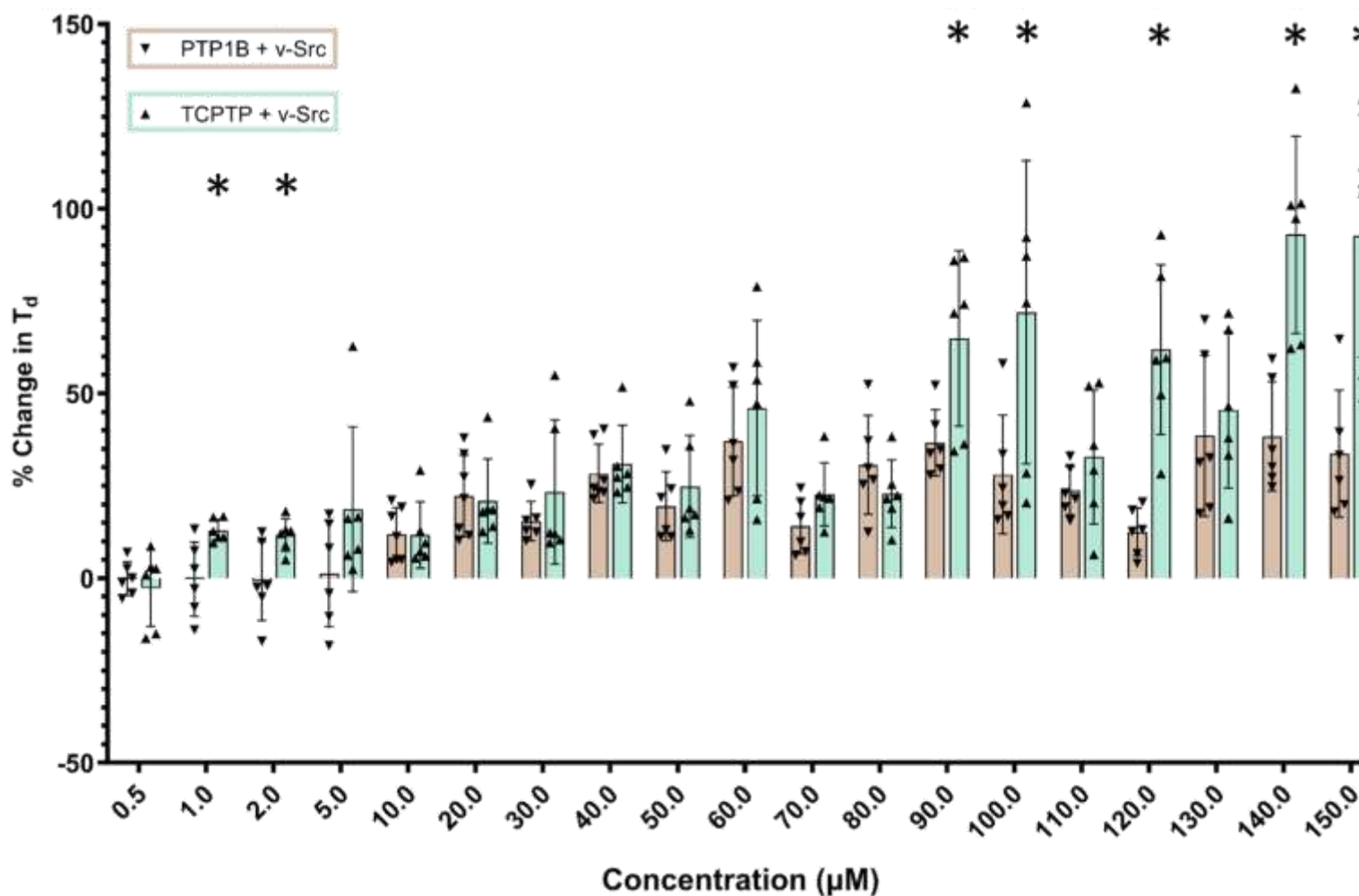
concentrations above and including 20 μM , meaning ursolic acid is successfully inhibiting TCPTP as evidenced by the significant increase in doubling times (T_d), where generally a higher concentration results in a greater increase.

3.3.2.1.2.1.3. Comparing PTP inhibitory activity.

Figure 56 below is comparing the effect on the % change of T_d in both PTP + v-Src double transcribed yeast cells, as an illustration of the activity ursolic acid exerts on both PTP1B and TCPTP separately. This means inhibition selectivity can be assessed for this known inhibitor to determine if ursolic acid is specific towards either of these structurally similar PTPs.

From the statistical non-parametric t-test conducted, the % change in T_d is significantly greater in TCPTP + v-Src then PTP1B + v-Src at the following concentrations: 1, 2, 90, 100, 110, 120, 140 and 150 μM . However, despite this fact and the % change being consistently higher in TCPTP + v-Src overall for all concentrations tested there is no statistical difference between the ability of ursolic acid to inhibit either PTP1B or TCPTP overall, meaning the suspected selectivity towards TCPTP from the results in **Figure 56**, is not significant. Despite this the trend of ursolic acid exerting a greater effect on TCPTP particularly at the higher concentrations tested (90 – 150 μM) agrees with prior literature^{89,90} which as stated previously in the introductory Chapter 1 (section 1.4.3.1) found ursolic acid to have a higher IC_{50} value for TCPTP over PTP1B. So, the fact that the same trend of ursolic acid exerting a greater effect on inhibiting TCPTP then PTP1B despite not being significant is beneficial when demonstrating the validity of the assay results.

Further investigation of ursolic acid at higher concentrations was planned however due to the high lipophilicity of this compound, attempted incorporation of ursolic acid at concentrations greater than 150 μM resulted in ursolic acid crashing out of solution, this was more common with higher concentration, 150 μM was the highest concentration where this phenomenon did not occur.



μM	p value
0.5	ns
1	<0.050
2	<0.050
5	ns
10	ns
20	ns
30	ns
40	ns
50	ns
60	ns
70	ns
80	ns
90	<0.050
100	<0.050
110	ns
120	<0.005
130	ns
140	<0.005
150	<0.010
Overall	ns

Figure 56: Comparison of % change in doubling time (T_d) of PTP1B + v-Src and TCPTP + v-Src transformed yeast cells in the presence of ursolic acid at 0.5-150 μM . n=7 for 0.5-20 and 40 μM n=6 for rest of concentrations tested in both transformations, mean and individual points \pm standard deviation plotted. Used non-parametric Mann-Whitney t-test for statistical analysis. * p value ≤ 0.050 , PTP1B + v-Src vs TCPTP + v-Src cells.

3.3.2.1.2.2. LZP25

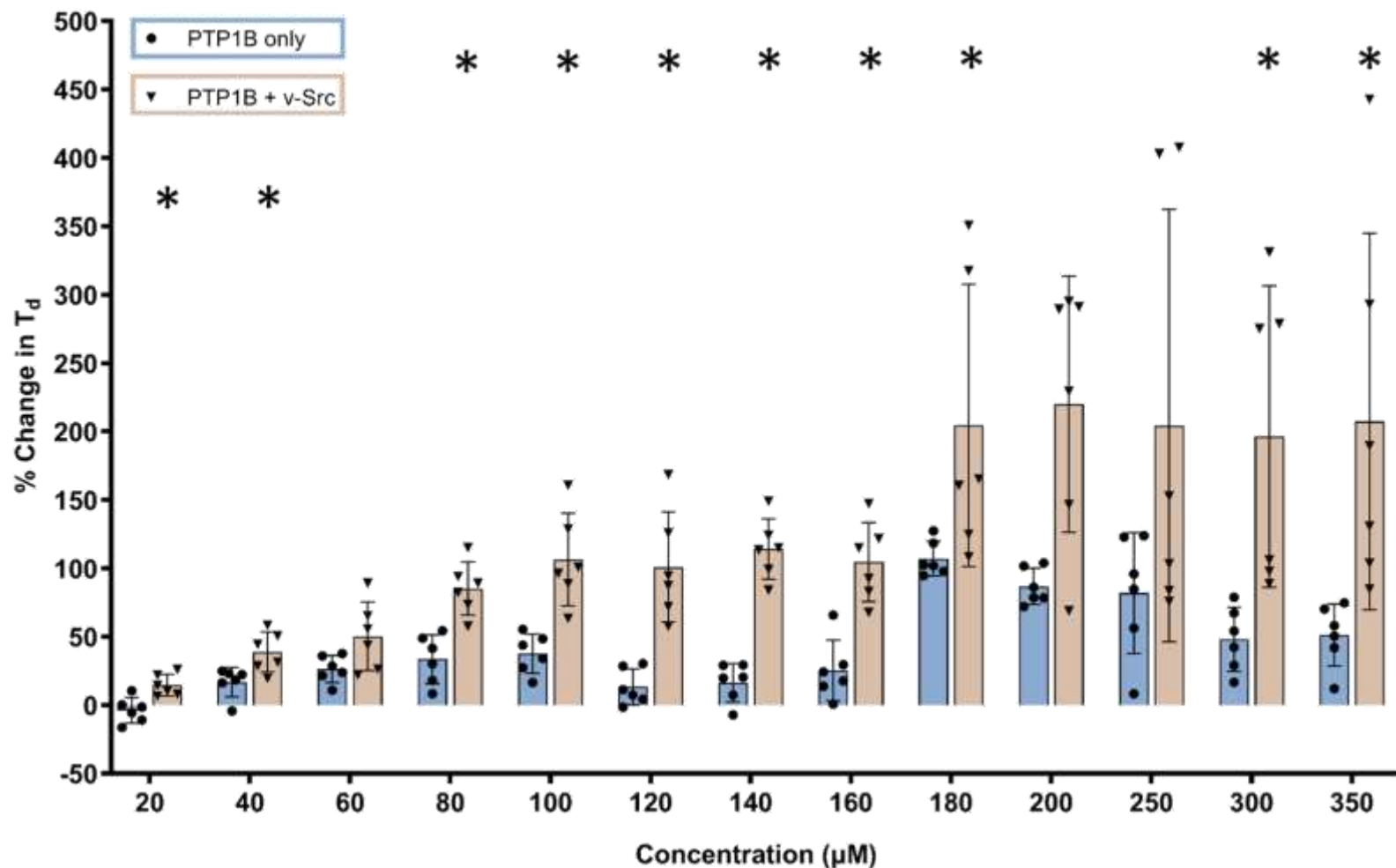
LZP25 is a known PTP inhibitor that is not commercially available, so was synthesised as outlined above in **Scheme 9**.

3.3.2.1.2.2.1. PTP1B based.

As illustrated in **Figure 57** overall for the concentrations tested, the % change in T_d is significantly higher in the PTP1B + v-Src cells when compared against PTP1B only cells.

The lowest concentration of LZP25 to have a significantly higher effect on growth rate in the PTP1B + v-Src cells when compared to the control PTP1B only cells is at 20 μM . This is also the case for all subsequent higher concentrations apart from 200 and 250 μM , this non-significance is partly due to the increased range of % change observed in the PTP1B + v-Src cells at these concentrations. The concentrations of 400 and 500 μM were also tested, however due to the additional proposed aforementioned reasons, predominantly an extended lag phase and the clumping and subsequent crashing out of cells, the T_d cannot be measured at these concentrations as no exponential phase is present.

But the overall theme is an upward trend in the % change in T_d in PTP1B + v-Src cells with increasing concentration of LZP25 where the effect is consistently significantly higher than the % change in T_d for the PTP1B only cells for the same LZP25 concentration. Therefore, the addition of this inhibitor into PTP1B only and PTP1B + V-Src exhibits the desired effect on the % change in a fairly consistent dose dependent manner on PTP1B inhibition in the PTP1B + v-Src cells, and this has been shown to be the case despite the added disruption caused by other contributing factors. As shown in the appendix (section 1.6.2), the T_d values for LZP25 addition in PTP1B only cells is not significantly different when compared to the corresponding base PTP1B only cells for the concentrations 20, 120 and 140 μM , meaning LZP25 had no significant effect on growth rate, which it should not in these cells as PTP inhibition is not linked to growth rate. However, again shown in the appendix (section 1.6.2) the addition of LZP25 to PTP1B + v-Src cells significantly increases T_d values when compared against the corresponding biological replicate base growth rate all concentrations tested where T_d could be measured (20 - 350 μM . Hence LZP25 is successfully inhibiting PTP1B as evidenced by the greater significant increase in doubling times (T_d), than was seen in PTP1B only cells when a significant change in T_d was observed.



Concentration (µM)	p value
20	<0.050
40	<0.050
60	ns
80	<0.005
100	<0.005
120	<0.005
140	<0.005
160	<0.005
180	<0.050
200	ns
250	ns
300	<0.005
350	<0.005
Overall *	<0.005

Figure 57: Comparison of % change in doubling time (T_d) of PTP1B only and PTP1B + v-Src transformed yeast cells in the presence of LZP25 at 20-350 μM . $n=6$ for all concentrations tested in both transformations, mean and individual points \pm standard deviation plotted. Used non-parametric Mann-Whitney t-test for statistical analysis. * p value ≤ 0.050 vs control.

3.3.2.1.2.2.2. TCPTP based.

PTP selectivity of potential developed inhibitors is of interest so LZP25 was also deployed in the TCPTP based version of the inhibitory assay and the % change in T_d for both TCPTP only and TCPTP + v-Src were calculated. Results shown below in **Figure 58**, for the effect on TCPTP based cells upon the addition of LZP25.

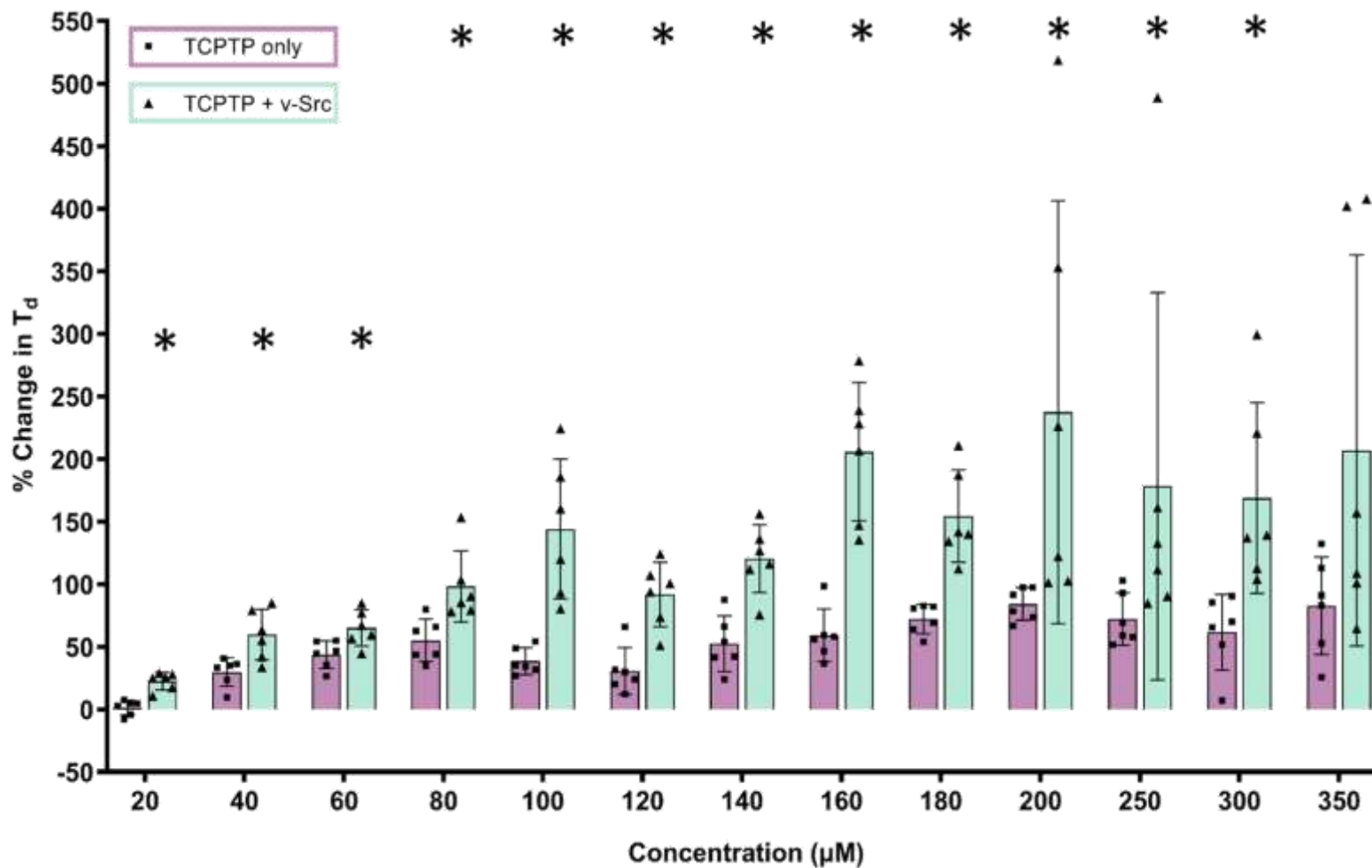
Again, overall, when looking at all concentrations of LZP25 tested, the % change of T_d in TCPTP + v-Src was significantly higher than for TCPTP only cells, again demonstrating that LZP25 is having the desired effect of inhibiting TCPTP. As was seen in **Figure 57** with PTP1B + v-Src, the lowest concentration of LZP25 which is required to inhibit TCPTP significantly is 20 μ M as seen in **Figure 58**. Once again, every subsequent higher concentration of LZP25 also exerted a significantly higher % change in T_d in the TCPTP + v-Src cells over TCPTP only cells up to 350 μ M.

An upward trend in the % change in T_d in TCPTP + v-Src cells is apparent in **Figure 58** due to increasing concentration of LZP25 where the effect is consistently significantly higher than for the % change in T_d for the TCPTP only cells for the same ursolic acid concentration.

As shown in appendix (section 1.6.2) the T_d values for LZP25 addition in TCPTP only cells are significantly different when compared to the corresponding base TCPTP only cells for all concentrations in the range 40 - 350 μ M. This significant uptick in T_d is not indicative of PTP inhibition as highlighted previously with ursolic acid as growth rate (T_d) is only linked to PTP inhibition when a PTP plasmid is co-expressed with the plasmid, v-Src. Instead, this significance is probably due to a combination of factors highlighted and proposed earlier but including the colouration of LZP25 and the resultant clumping of yeast cells particularly at the higher concentrations investigated.

When comparing the resultant T_d values in TCPTP + v-Src cells with the addition of LZP25 to the corresponding biological replicate base growth rate, a significant increase all concentrations tested was observed excluding 400 and 500 μ M, as T_d cannot be calculated.

In summary, as the % change in T_d for TCPTP + v-Src cells is significantly higher than for TCPTP only cells at all concentration investigated, this supports the notion that LZP25 is successfully inhibiting TCPTP as evidenced by the significant increase in doubling times (T_d), where generally a higher concentration results in a greater increase.



Concentration (µM)	p value
20	<0.005
40	<0.050
60	<0.050
80	<0.001
100	<0.005
120	<0.005
140	<0.005
160	<0.005
180	<0.005
200	<0.005
250	<0.005
300	<0.005
350	<0.005
Overall *	<0.001

Figure 58: Comparison of % change in doubling time (T_d) of TCPTP only and TCPTP + v-Src transformed yeast cells in the presence of LZP25 at 20-350 μ M. $n=6$ for all concentrations tested in both transformations, mean and individual points \pm standard deviation plotted. Used non-parametric Mann-Whitney t-test for statistical analysis. * p value ≤ 0.050 vs control.

3.3.2.1.2.2.3. Comparing PTP inhibitory activity.

Shown below in **Figure 59**, is the comparison of the effect on the % change of T_d in both PTP + v-Src double transcribed yeast cells, and therefore the potency of LZP25 in terms of PTP1B and TCPTP inhibition can be assessed for this known inhibitor as a means of determining if LZP25 is specific towards either of these structurally similar PTPs.

From the statistical non-parametric t-test conducted the % change in T_d is not significantly different overall and for each concentration tested individually between PTP1B + v-Src and TCPTP + v-Src the only concentration where this is not the case is 160 μ M. As TCPTP + v-Src is significantly greater (p value <0.010), due to a substantial increase in activity from the prior concentration. However, when looking at the lower concentrations specifically (20 – 100 μ M) the effect due to TCPTP + v-Src is on average higher for each of these concentrations individually than PTP1B + v-Src, but as stated previously this difference in activity is not significant.

Therefore, unlike ursolic acid, which is specific towards TCPTP, LZP25 statistically exerts a comparable inhibitory effect on both PTPs investigated, PTP1B and TCPTP.

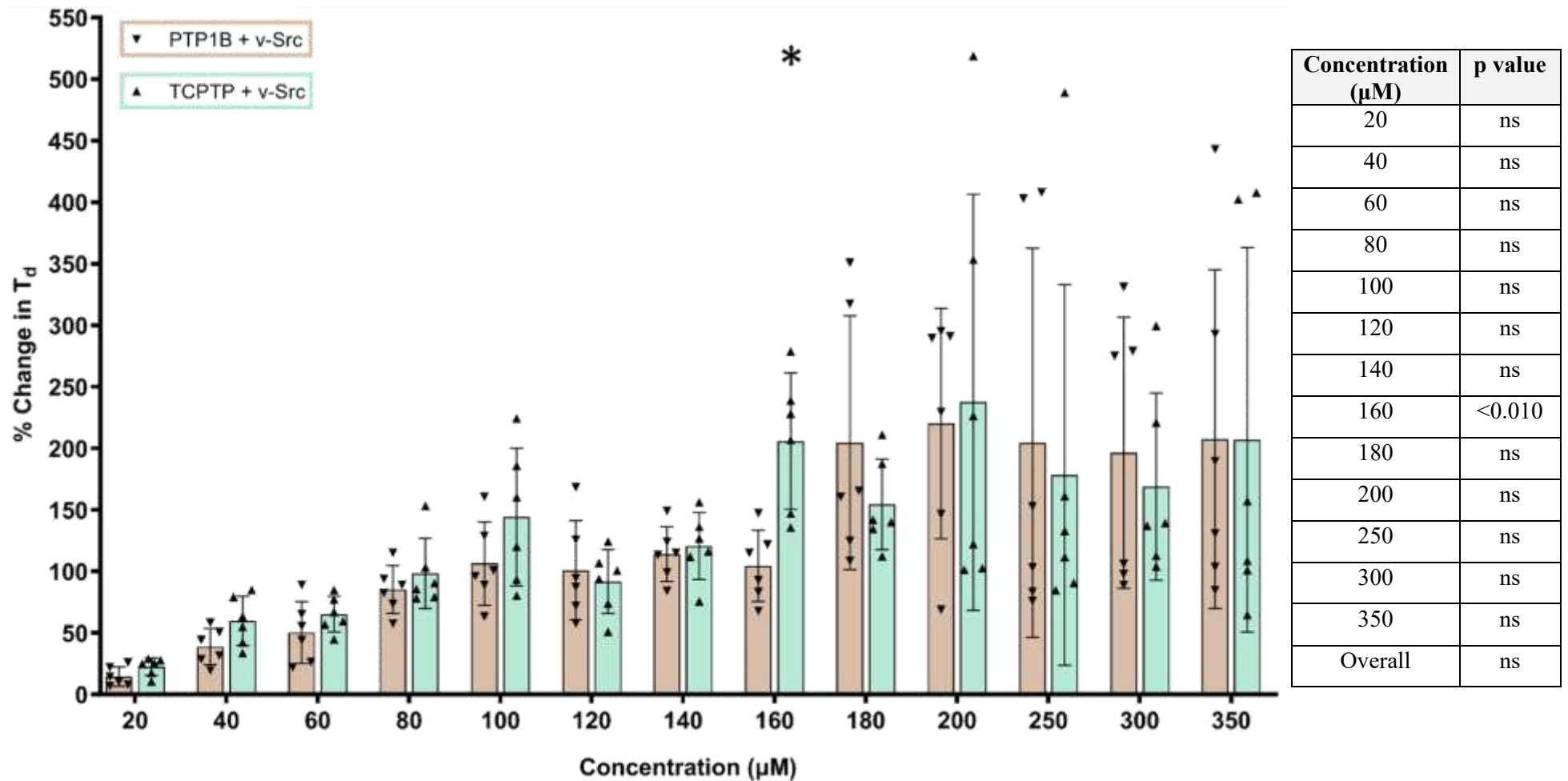


Figure 59: Comparison of % change in doubling time (T_d) of PTP1B + v-Src and TCPTP + v-Src transformed yeast cells in the presence of LZP25 at 20-350 μM . $n=6$ for all concentrations tested in both transformations, mean and individual points \pm standard deviation plotted. Used non-parametric Mann-Whitney t-test for statistical analysis. * p value ≤ 0.050 , PTP1B + v-Src vs TCPTP + v-Src cells.

It may have been noted that a different concentration range was investigated for both known inhibitors, ursolic acid and LZP25, the reasoning for this is described in the appendix (section 1.7), but briefly put the solubility of these compounds in the resultant DMSO and water-based growth media is the key driving factor.

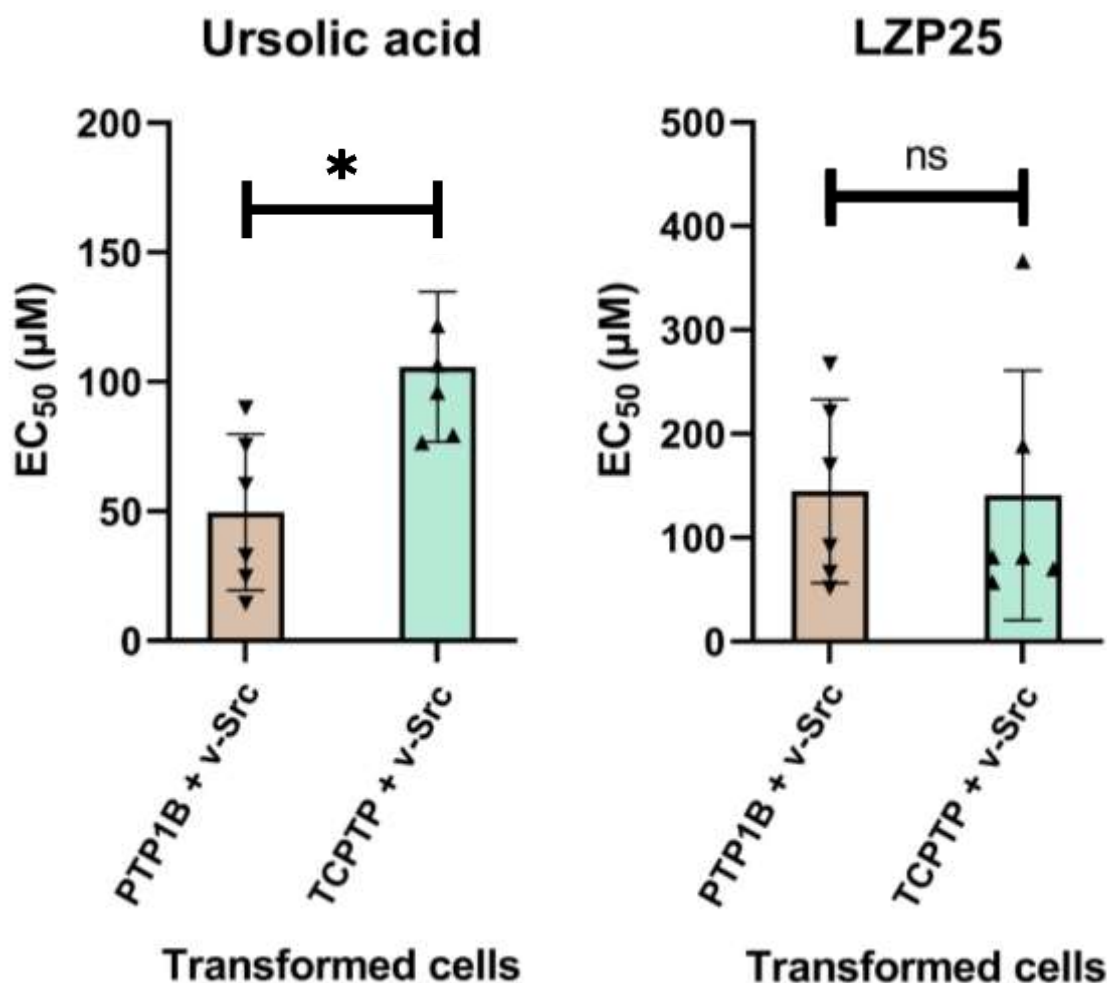
3.3.2.1.3. EC_{50} values

Another means of assessing the potency of PTP inhibition is with the calculation of IC_{50} values. However, due to how this assay functions IC_{50} values cannot be calculated, as this requires a numerical value for 100% PTP inhibition. For this assay that is denoted by the growth profile for v-Src only yeast cells as this is the expected result for an inhibitor which completely inhibits a PTP in PTP + v-Src cells thus resulting in v-Src activity not being at all downregulated so the disfunction of the spore wall synthesis process is at its most prevalent. This translates to severely reduced growth rate, as shown with the v-Src growth profile of **Figure 44**. However, the v-Src growth profile does not contain an exponential growth phase hence a T_d value cannot be assigned to 100% PTP inhibition. A plausible alternative could be the assigning the difference in final absorbance value (OD_{600}) of the base untreated PTP + v-Src growth profile and the v-Src growth curve after the 47.5-hour experiment as '100% inhibition', thus making the concentration which achieves half this decrease in final absorbance value the IC_{50} for that compound. However, as previously stated numerous times PTP inhibition is not the sole contributing factor to the final absorbance value, hence also cannot be used.

An alternative related means of potency investigation is EC_{50} , which is defined as half the concentration of a compound which causes its maximum effect. As growth rate is the means of assessing activity, the maximum effective of each compound is the highest recorded % change in T_d values for each of the PTP + v-Src transcribed cells. Hence EC_{50} values can be calculated, the means of how is explained within the Chapter 7 Methodology (section 7.4.2.2).

EC_{50} is a measure of a compound's potency, in this case its ability to inhibit a PTP, having a smaller EC_{50} means that a compound is more potent as it requires a lower dose to achieve the maximum biological effect. EC_{50} is not necessarily a measure of overall desirability of a potential pharmaceutical, as other factors in addition to potency are relevant. Hence a compound with a low EC_{50} which is considered highly potent may only exert a minimal biological effect which may not be sufficient. Also, selectivity or the potential for off-target side effects would need to be considered. Ideally a potential

inhibitor will possess a high biological effect (% change in T_d), a low EC_{50} value (potency) and only do so towards the desired target, which in this case is PTP1B with minimal activity in TCPTP.



Compound	Ursolic acid	LZP25
p value	<0.010	ns

Figure 60: Comparison of EC_{50} values of ursolic acid and LZP25 for PTP1B and TCPTP active site inhibition. $n=6$ for all both types of transformed cells. Mean and individual points \pm standard deviation plotted. Used non-parametric Mann-Whitney t-test for statistical analysis. * p value ≤ 0.05 for PTP1B + v-Src vs TCPTP + v-Src.

The calculated EC_{50} values for both known inhibitors are shown in **Figure 60**. As stated previously ursolic acid exerts a greater biological effect in TCPTP over PTP1B, and this is shown in **Figure 60**, with the EC_{50} value for TCPTP being significantly greater (<0.010) than for PTP1B, and LZP25 is again non-specific with the EC_{50} values for both PTP1B and TCPTP inhibition being not significantly different, despite one biological

replicate for TCPTP being significantly different to the rest but is not classified as an outlier (used ROUT).

3.4.3. Blood brain barrier assay

From the biological assay selection, four different parameters are of interest. These are hit effectiveness, potency, selectivity, and permeability through the BBB. The yeast-based assay fulfils the first three objectives, and the fourth can be achieved with a commercially available synthetic BBB assay which was introduced above. Again, as with the yeast assay before this kit was used the results produced were assessed to confirm if this commercial kit provided reliable results.

The comparison and statistical analysis of the provided permeability rate data of the permeability controls from the manufacturer and the acquired in-house data is shown and discussed in the appendix (section 1.9.4). The in-house data for all permeability controls was comparable with there being no significant difference with the medium permeability results to the manufacturers.

3.4.3.1. Permeability rate

The permeability rate results for all controls and known inhibitors at both RT and the more physiologically relevant temperature of 37 °C can be found in the appendix (section 1.9.4.4). It was determined that presenting the data from the synthetic BBB permeability assay as a percentage of the inputted concentration present in the acceptor well was easier to demonstrate. The permeability results conducted in-house at two separate occasions at RT were comparable and in the case of the medium control not significantly different from that of the provided manufacturers data, supporting the correct function of this assay.

3.4.3.2. Concentration of acceptor and donor wells

To assess a compounds permeability, the absorbance values of the acceptor and donor well contents were recorded at the respective optimum wavelength (found in the appendix section 1.9). From these absorbance values the concentrations from both RT and 37 °C assay results were calculated with calibration curves (appendix 1.9) to determine concentrations.

These concentration results found in the appendix (section 1.9) were as expected, based upon the permeability rate results. As for each permeability control a significantly greater concentration was present in the acceptor well after 24 hours at 37 °C than at RT.

Furthermore, the proportionality of the acceptor well concentration between the permeability controls was also maintained with the permeability rates. For example, the expected result of the medium control concentration in the acceptor well, being six times greater than that of the low permeability control was witnessed, in terms of both permeability rate and concentration in acceptor well (appendix section 1.9).

It is important to note that the initial concentration of each permeability control was 500 μ M, and the total recovered concentration was not significantly different from this with the only exception being LZP25 at 37 $^{\circ}$ C (appendix section 1.9.3.5).

3.4.3.3. % of total input in acceptor plate wells

In order to easily compare the relative permeability of the controls, known inhibitors and latterly hit compounds to each other, the concentration values were converted into a percentage of input concentration (a percentage of 500 μ M), so non-parametric t-test where also subsequently conducted to assess significance, as shown below.

As demonstrated in **Figure 61** below, at 37 $^{\circ}$ C a statistically significant greater amount of all the provided permeability controls permeated through the synthetic BBB membrane into the acceptor well due to an increased permeability rate (cm/s) at 37 $^{\circ}$ C than at RT. The concentration present in the acceptor and donor wells are also displayed graphically in the appendix (section 1.9.3). With regards to the medium and high permeability controls a significantly lesser amount remained in the donor well after the 24 hrs at 37 $^{\circ}$ C than at RT. For the low permeability control no significance was observed due to a smaller amount being able to permeate through the membrane at either temperature.

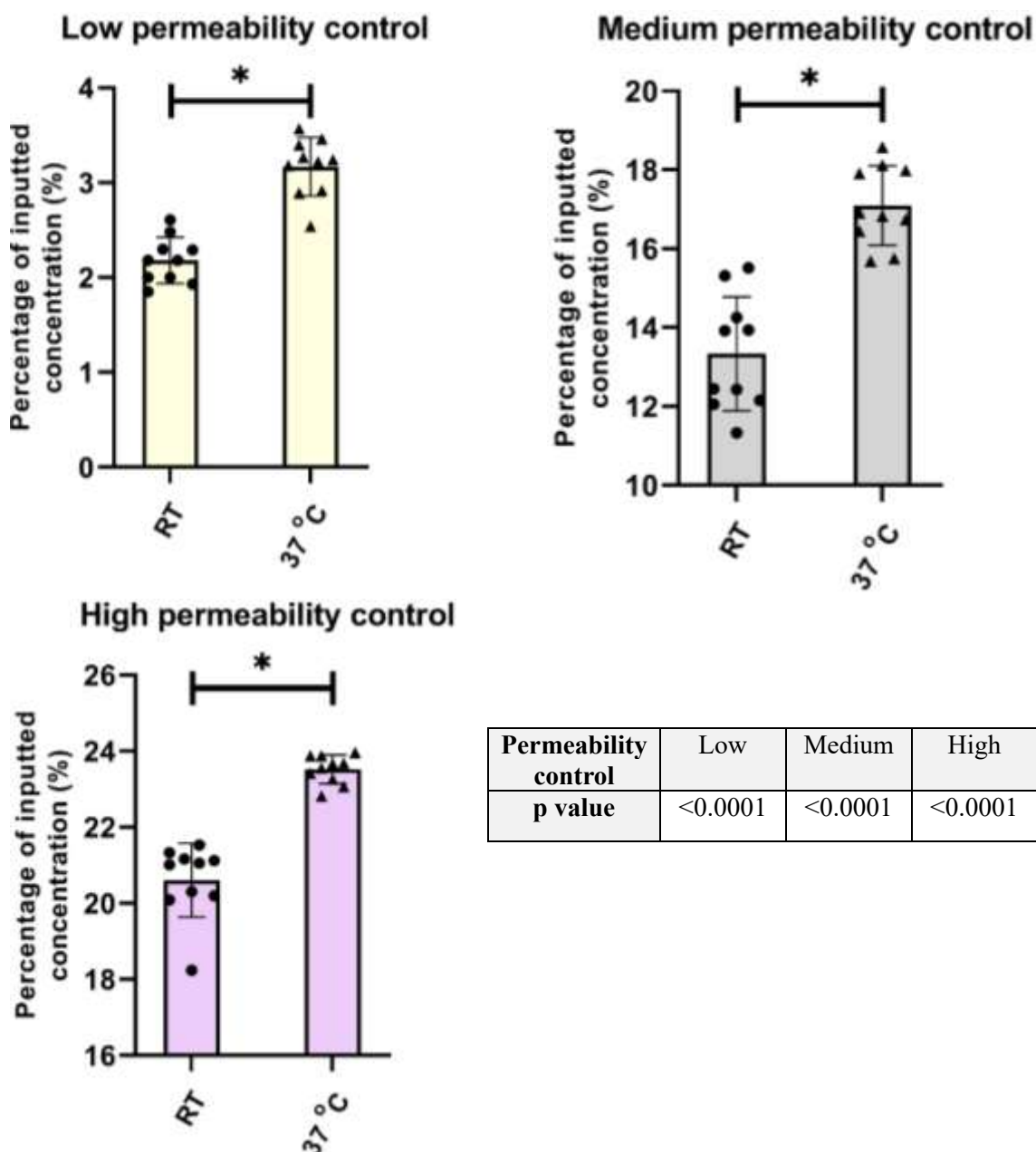
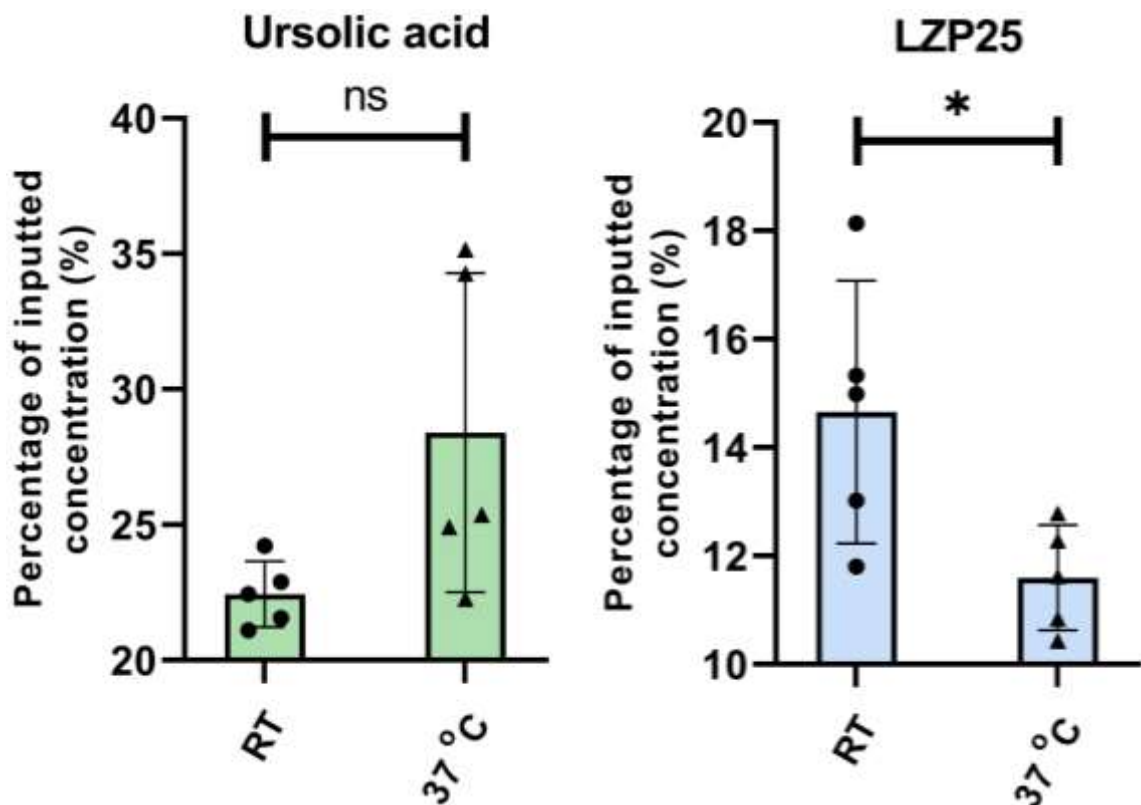


Figure 61: The percentage of the inputted concentration in the BBB assay acceptor well after 24 hrs at RT or 37 °C. of permeability controls n=10 for all compounds tested. Mean and individual points \pm standard deviation plotted. Used non-parametric Mann-Whitney t-test for statistical analysis. * p value \leq 0.050.

Once the provided permeability controls were sufficiently investigated (predominantly present in the appendix section 1.9) thus verifying the validity of the assay's results. The two aforementioned known inhibitors were also tested at both RT and 37 °C over a 24-hour period to provide additional means of comparison for the subsequently identified PTP inhibitor compounds. The results from this are shown below in **Figure 62**.

3.4.3.4. Known PTP inhibitors.

The two known inhibitors utilised for blood brain barrier permeability assessment were once again ursolic acid and LZIP25 which are both non-selective active site PTP inhibitors. As before with the permeability controls, the known inhibitors were assessed upon their calculated permeability rate, concentration present in both the acceptor and donor well post experiment (appendix section 1.9) and % of total inputted concentration, 500 μ M was present in the acceptor well (**Figure 62**).



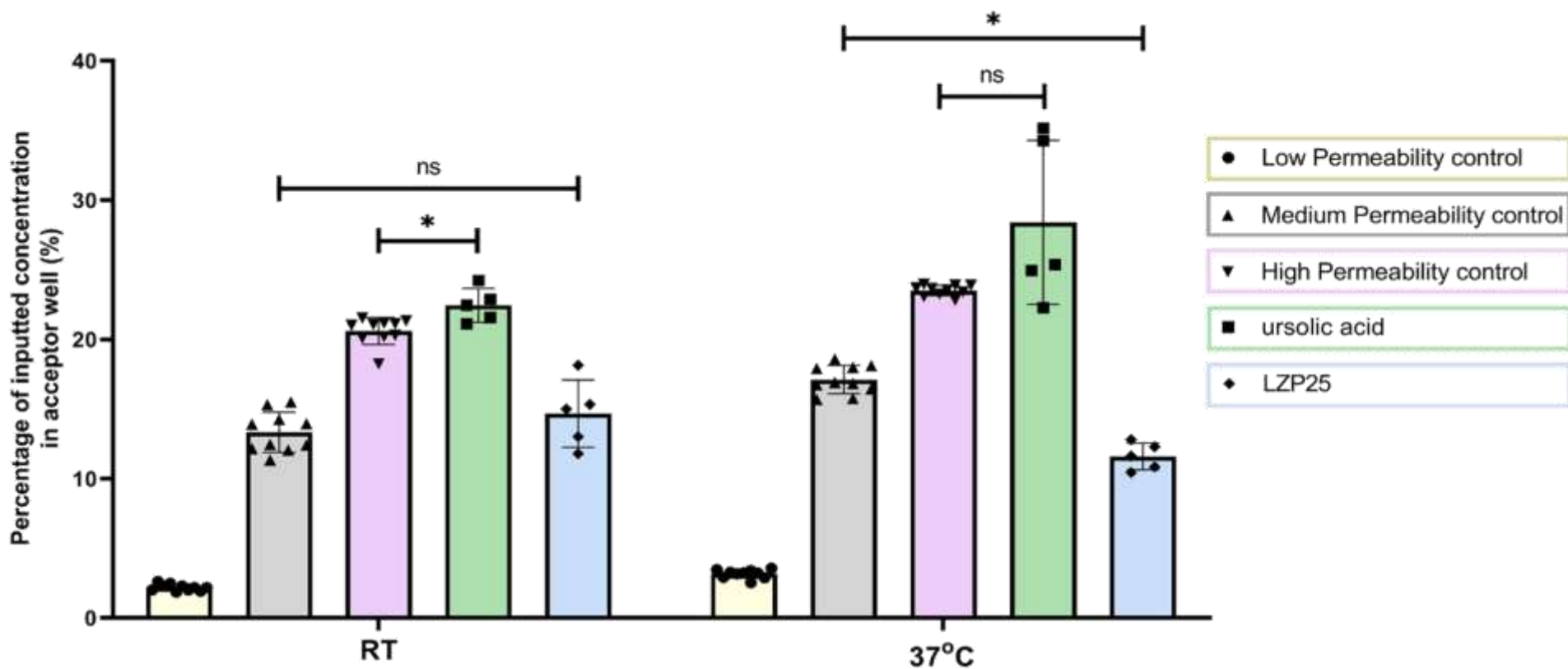
Known inhibitor	Ursolic acid	LZIP25
p value	ns	<0.050

Figure 62: The percentage of the inputted concentration in the BBB assay acceptor well after 24 hrs at RT or 37 °C. of two known PTP inhibitors n=5 for both compounds and temperatures. Mean and individual points \pm standard deviation plotted. Used non-parametric Mann-Whitney t-test for statistical analysis. * p value \leq 0.050, RT vs 37°C.

Figure 62 shows that on average ursolic acid is more permeable at 37 °C than RT but again due to the large range of experimental results at 37 °C there is no significant difference. However, unlike the three permeability controls and ursolic acid, LZIP25 appears to be significantly less permeable through the synthetic membrane after 24 hours at 37 °C than RT (p value <0.050).

However as shown in the appendix (section 1.9) approximately 33 μM of the LZP25 inputted (500 μM total) was not recovered after the 24-hour experiment at 37 °C. As discussed in the appendix (section 1.9) the absorbance and thus the concentration of the stock LZP25 solution used was verified to be correct. Hence at 37 °C is partial diffusion through the synthetic membrane resulting in a fraction of LZP25 remaining within the membrane is thought to of occurred. One way to provide evidence for this could be by running fresh DMSO:PBS through the membrane after the experiment had concluded to determine if any of the unaccounted LZP25 is subsequently collected. Regardless even if this was the case it would not affect the present permeability results from LZP25 as the concentration which fully diffused through the membrane and ultimately ended in the acceptor well is the measure of permeability.

When comparing ursolic acid to LZP25 as shown in **Figure 62** above and **Figure 63** below the expected result of ursolic acid being significantly more permeable to the synthetic BBB membrane than LZP25 was obtained at both temperatures (p value <0.010 at both temperatures). This prediction was predominantly based on the cLogP of the two compounds with the calculated LogP values for ursolic acid (6.0021) being over two-fold larger than the cLogP of LZP25 (2.8429), this increase in cLogP denotes the increased lipophilicity of ursolic acid and therefore suspected increased BBB permeability. The expected proportionate permeability of the two known inhibitors being obtained further demonstrates the relevance of this assay's results in predicting BBB permeability.



Known inhibitor (Temperature of comparison)	Ursolic acid (RT)	LZP25 (RT)	Ursolic acid (37°C)	LZP25 (37°C)
p values vs medium permeability control	<0.001	ns	<0.001	<0.001
p values vs high permeability control	<0.010	<0.001	ns	<0.001

Figure 63: The percentage of the inputted concentration in the BBB assay acceptor well after 24 hrs at RT or 37 °C. of permeability controls (n=10) and known PTP inhibitors (n=5). Mean and individual points ± standard deviation plotted. Used non-parametric Mann-Whitney t-test for statistical analysis. * p value ≤ 0.050.

As shown in **Figure 63** at both temperatures investigated ursolic acid has a greater average percentage of total 500 μM in the acceptor well than the high permeability control, at RT this difference is significant. So ursolic acid can be considered as very BBB permeability relatively speaking. This supports what was said previously in Chapter 2 (section 2.3.4.1) in that lipophilicity and having a small cross-sectional area in one dimension promotes BBB permeability as ursolic acid is itself very lipophilic and in one plane relatively flat and thus a lower cross-sectional area. Both of which are linked to BBB permeability and thus a higher permeability rate for ursolic acid was expected and further supports the relevance of the produced data.

Whereas LZP25 is more comparable to the medium permeability control and is the only example to date where the permeability rate is lower when the kit was run at 37 °C to RT, and this is also significant meaning that increasing the temperature does not necessarily increase permeability as was thought prior to this point.

In summary as shown in **Figure 63** at both temperatures the permeability of ursolic acid is greater than that of the higher permeability control at both temperatures, and LZP25 is comparable to the medium permeability control. Due to this, ursolic acid is significantly more permeable than LZP25 at both temperatures investigated, this result is as predicted, when looking at the cLogP values of both known inhibitors as ursolic acid is a more lipophilic compound with a higher cLogP which is a factor that contributes to BBB permeability. From the permeability of the known inhibitors through the synthetic BBB membrane more relevant comparisons can be made and target permeabilities set for the subsequent hit compounds identified and discussed in the subsequent Chapters 4 and 5.

3.5. Conclusion

Herein this Chapter explores and explains the biological assays utilised for the identification and assessment of potential PTP1B inhibitors with the overall aim of identifying a potent, effective PTP1B specific inhibitor that also has a low permeability to the blood brain barrier (BBB). With regards to the yeast-based inhibition assay, from the two investigated strains the YMK23 variant was selected for all subsequent assay runs predominantly due to the increased ability the PTP plasmids had in rescuing the growth profile of yeast cells in the co-transcribed YMK23 due to v-Src plasmid incorporation. Which disrupts the spore wall process and thus slows cell division. With the aid of two known PTP inhibitors, validation for the yeast-based inhibition assay resulted was provided hence supporting with sufficient confidence that any identified hit compounds possessed genuine PTP inhibitory activity. The other assay utilised for the assessment of BBB permeability was a commercially available kit, where the in-house results for the provides permeability controls obtained were comparable to the results provided by the manufacturer and the two in-house runs were also to each other, hence this supported the reliability of the assay data. Once again, the same two known PTP inhibitors were tested to provide means of comparison to the subsequently acquired hits outlined in the subsequent Chapter 4 and Chapter 5.

Chapter 4

*Benzodioxane synthesis and
PTP1B active site
inhibitor development*

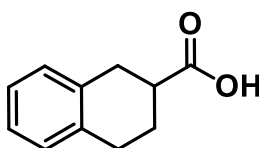
4.1 Overview:

As demonstrated in Chapter 2 (section 2.3.2), a potential family of PTP1B active site inhibitors identified from database screening and computational modelling are tetrahydronaphthalenes. However, this fused ring system is more synthetically challenging than the proposed alternative, benzodioxanes. This Chapter initially computationally compares, the binding potential and physicochemical properties of the original tetrahydronaphthalene hits to comparable benzodioxanes. This was done to support the notion that this structural alternation would not prevent biological function. Subsequently the results from the synthesis, optimisation, and testing of benzodioxanes are discussed. The iterations of the benzodioxanes synthesised and tested were directly led by the previous biological data to improve the attributes of the initial biological benzodioxane hit. The synthetic challenges of downstream benzodioxane synthesis and isolatable yield are also discussed herein, and how these synthetic steps were optimised, to produce sufficient product for testing.

4.2 Background:

4.2.1 Tetrahydronaphthalene synthesis investigation

The original identified hit core structure, tetrahydronaphthalene (tetralin) was a partially hydrogenated derivative of naphthalene comprised of a carbon based dicyclic fused ring system. As shown in **Figure 64**, with the specific hit identified it appeared that the benzene ring and the carboxylic acid, three atoms away where essential for binding to PTP1B active site, hence the saturated carbon ring acts more as a spacer for the other motifs to bind.

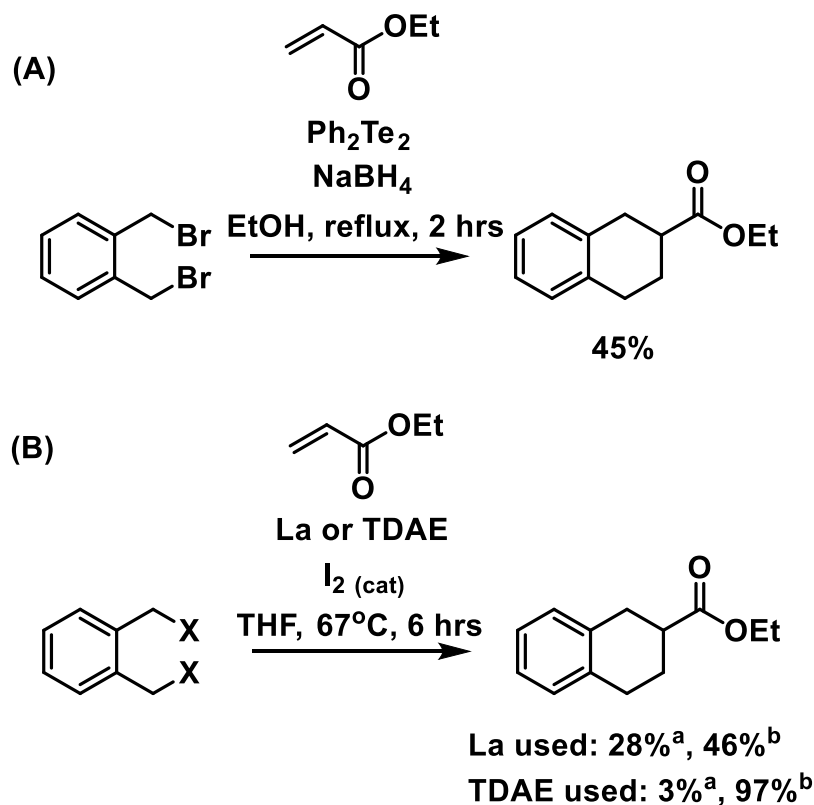


**Original hit of interest
(tetrahydronaphthalene)**

Figure 64: Structure of the original identified potential active site PTP1B hit from a drug-like computational database screen.

However, the literature procedures attempted by master's students to form tetralin based compounds were found to not provide the sufficient yield required for subsequent functionalisation and biological testing. Literature procedures with reported isolated yields are demonstration in **Scheme 11** below. It is important to note that all synthetic

work conducted on the formation of benzodioxanes, and precursors was completed solely by the author of this thesis.



Scheme 11: Literature procedures for tetrahydronaphthalene formation.

(A): di-haloxylylene (5.0 mmol, 1.0 equiv.), Ph_2Te_2 (5.0 mmol, 1 equiv.), NaBH_4 (10.5 mmol, 2.1 equiv.), ethyl acrylate (50.0 mmol, 10.0 equiv.).¹³⁷ (B): La (1.5 mmol, 1.5 equiv.), di-haloxylylene (1.0 mmol, 1.0 equiv.), I_2 (0.04 mmol cat), ethyl acrylate (5.0 mmol, 5.0 equiv.).¹³⁹ (B): TDAE (0.6 mmol, 1.1 equiv.), di-haloxylylene (0.5 mmol, 1.0 equiv.), I_2 (0.08 mmol cat), ethyl acrylate (2.0 mmol, 4.0 equiv.).¹³⁸ TDAE: Tetrakis(dimethylamino)ethylene. ^a X = Cl, ^b X = Br

As shown in **Scheme 11** (A)¹³⁷ a moderate yield of the tetrahydronaphthalene product was reported in the literature but the ethyl acrylate is required to be in excess of 10.0 molar equivalents, making it undesirable compared to alternative methodologies. A superior synthesis route to form tetrahydronaphthalenes was found. **Scheme 11** (B) has an excellent reported yield of 97% when the optimum reaction conditions were utilised.^{138,139} It is important to note that when TDAE was used the paper reported a significant drop in yield when di-chloroxylylene was utilised instead of a di-bromoxylylene (97% to 3% isolated yield). Additionally, when the stoichiometry of TDAE was lowered to 1.0 equiv. the observed yield again dropped to 69%. Such a yield would have been sufficient for the needs of this project, however as mentioned above the master's students were unable to achieve such a yield and only could obtain minimal yields. This lack of reaction success is in part due to the complexity of this chemistry and of the reaction components required

to form tetrahydronaphthalenes, so alternative similar structures with a simpler synthesis pathway were investigated.

4.2.2 Design of alternatives to tetrahydronaphthalene

Removal of the saturated ring of tetrahydronaphthalene leaving phenylpropanoic acids as bases of the initial compound library screen were postulated, due the saturated ring primary acts as a spacer with minimal binding contribution in itself. However, it was thought that the increased degrees of freedom possessed by the carboxylic acid in the phenylpropanoic acid may in fact hinder the binding potential to the PTP1B active site. From the computational studies the bicyclic ring system was thought to may lock the carboxylic acid into a preferential position for PTP1B active site binding than if more degrees of freedom and potentially lower energy position were available.

Therefore, another alternative to tetrahydronaphthalene was needed which maintained the key structural features and binding potential while simultaneously being able to be synthesised from a more procedurally simple synthetic route which yielded greater amounts of product. Benzodioxanes were found to fit the required criteria.

4.2.3 Justification of benzodioxane

Benzodioxane can be defined as a compound which contains a benzene ring fused to a dioxane ring, in which the positioning of the two oxygen atoms results in three structural isomers of the benzodioxane motif. As demonstrated below in **Figure 65**.

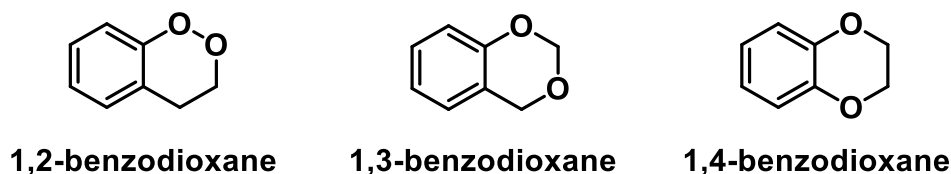


Figure 65: Structures of the three isomeric benzodioxanes.

Initial investigation into whether benzodioxanes are a relevant alternative target core structure for the initial PTP1B active site inhibitor compound library was conducted using docking studies to predict positioning and potential binding interactions with the relevant protein residues, the findings from this are illustrated below in **Figure 66**.

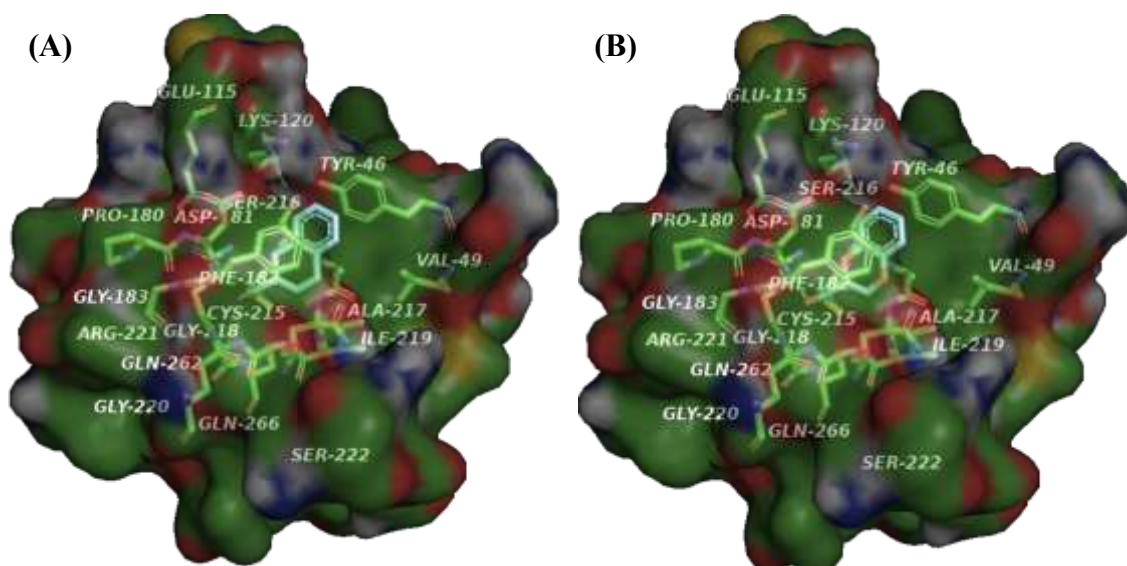
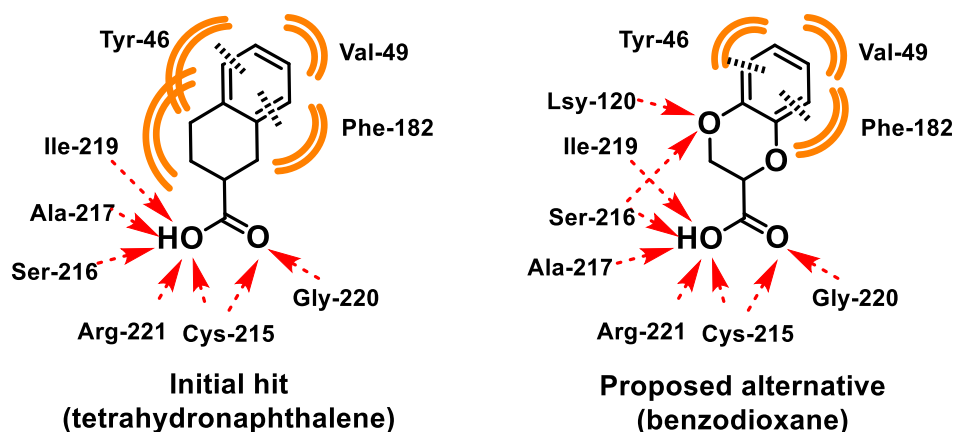


Figure 66: Theoretical binding positions of tetrahydronaphthalene hit (A) and benzodioxane modified hit (B), in PTP1B's active site.

Figure 66 and **Figure 67** demonstrate that both the initial tetrahydronaphthalene hit and benzodioxane modified hit can form hydrogen bonds with the following protein residues *via* the carboxylic acid: Gly-220, Cys-215, Arg-221 and Ser-216. The diaromatic region also undergoes π -stacking and hydrophobic interactions with Phe-182 and Tyr-46. Additionally, for the benzodioxane the cyclic oxygen closer to the carboxylic acid may be able to accept hydrogen bonds from the residues Lys-120 and Ser-216.



Key:

..... π - Stacking Hydrophobic interactions
 H-bond acceptor

Figure 67: Chemical structures and computationally predicted interactions of tetrahydronaphthalene and benzodioxane with the active site of PTP1B.

From the computational docking results highlighted in **Figure 66**, it appears that the potential binding positions of both are near identical with the main impact of the oxygens is the potential reduction in hydrophobic interactions provided by the saturated ring of tetralin. However, a theoretical additional benefit of the benzodioxane motif over the tetrahydronaphthalene is the two extra hydrogen bond acceptor positions due to the oxygen addition into the cyclic system which could enable further protein-substrate interactions such as with the residues Lys-120 and Ser-216, enabling a stronger bound position and thus potentially a more potent inhibitor.

The other important aspect in verifying the validity of benzodioxanes as synthetic targets is the physicochemical properties of this core structure as these and hence Lipinski's rule of five ¹¹⁰ as stated previously are important considerations when designing pharmaceutical compounds and in particular cLogP for this project as low BBB permeability is essential.

Table 3: Physicochemical values of identified tetrahydronaphthalene hit and the proposed modified benzodioxane version.

Compound	cLogP	MW	Aromatic rings	H - acceptors	H - donors	Total molecular surface area
Tetrahydronaphthalene (original hit)	1.8094	176.214	1	2	1	137.64
Benzodioxane (Modified hit)	1.1706	180.159	1	4	1	130.12

As previously stated, the theoretical ideal cLogP value for BBB impermeability while maintaining good peripheral cell permeability is expected to be within $-0.5 < \text{cLogP} < 1.4$ or $2.8 < \text{cLogP} < 5$.

The cLogP of the potential tetrahydronaphthalene hit was 1.8094 (as shown in **Table 3** above), therefore the addition of two oxygen atoms *para* to each other in the aliphatic ring was proposed as the initial substrate to be synthesised and investigated for biological testing, as the resultant cLogP of the designed benzodioxane was 1.1706 (as shown in **Table 3** above), and thus within the theoretical desired cLogP range for permeability.

The inclusion of the oxygens into the aliphatic ring which enable a more procedurally simple synthetic pathway as the formation of carbon-oxygen bonds are well established in the literature as being easier to perform than the respective carbon-carbon bond

formation. From the physicochemical data the oxygen addition may also in theory enable better general cell permeability and importantly decreased BBB permeability due to resulting in a decrease in cLogP. Thus, meaning benzodioxanes are not only a viable alternative to tetrahydronaphthalene but also may be an improved version.

Herein the synthesis, optimisation, subsequent functionalisation, and biological testing of 1,4-benzodioxanes for implementation as potential PTP1B inhibitors are presented.

4.2.4 Previous examples of benzodioxane containing pharmaceuticals

Despite 1,4-dioxane's simple structure, this versatile template has widely been employed in the design of molecules over the last couple of decades in numerous pharmaceutically active compounds. The diverse range of bioactivity and disease states treated by 1,4-dioxane containing drug molecules is shown below in **Figure 68**.

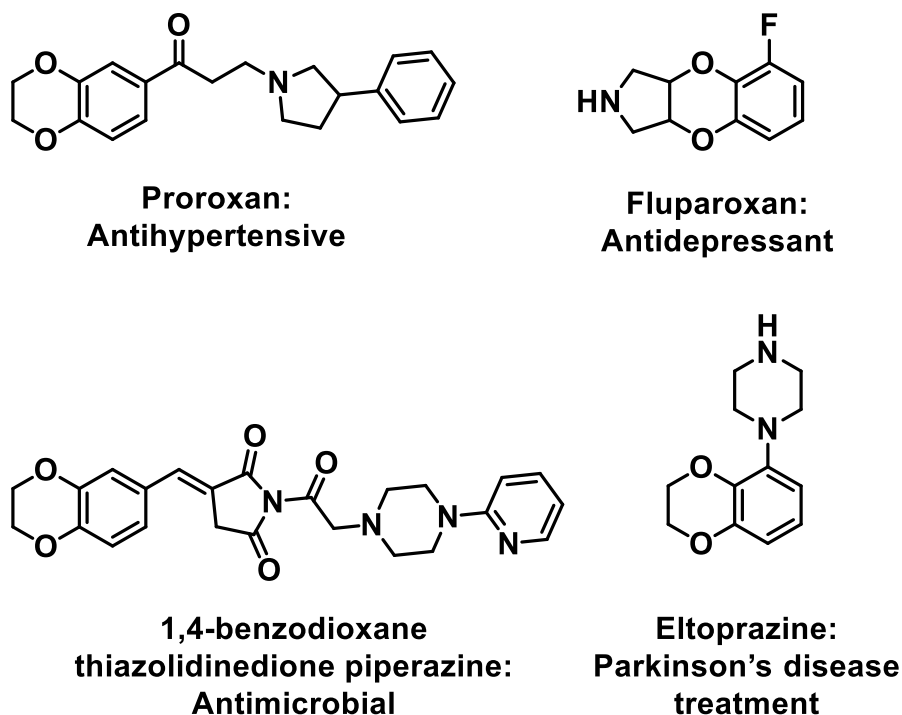


Figure 68: Structures of biologically active 1,4-benzodioxane drug molecules. ¹⁴⁰⁻¹⁴⁴

Proroxan is a non-selective α -adrenoblocker and has been used as an antihypertensive and in the treatment of Ménière's disease, motion sickness, and allergic dermatitis. ^{140,141} Ménière's disease is a disorder characterised by hearing loss, tinnitus and disabling vertigo. ¹⁴⁰ Proroxan was developed in the 1970s at the Institute of Toxicology of the USSR Ministry of Health. In addition to its antihypertensive function, Proroxan use has

also been shown to cause a decrease in alcohol and drug consumption in patients, the mode of action for this side-effect is currently unknown.^{140,141} Another older example is Fluparoxan which is a potent α_2 -adrenergic receptor antagonist that demonstrates excellent selectivity over the α_1 -adrenergic receptor and was patented as an antidepressant by Glaxo in the early 1980s.¹⁴² But despite its selectivity the development was discontinued by Glaxo, when the compound failed to demonstrate a significant clinical advantage over existing therapies.

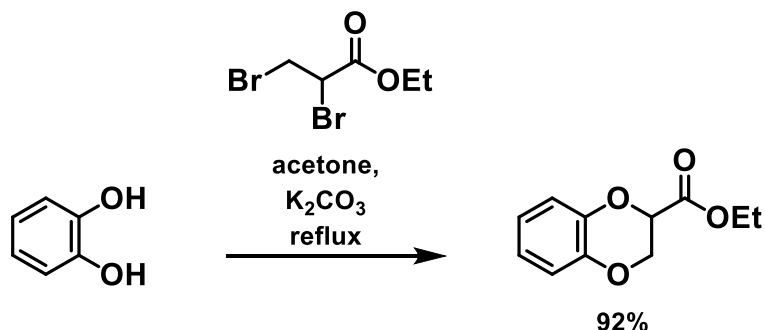
More recent examples of benzodioxane including compounds currently undergoing investigation are Eltoprazine and the currently unnamed 1,4-benzodioxane thiazolidinedione piperazine derivative, structures shown above in **Figure 68**.

Originally Eltoprazine, was created by Duphar in the 1980s and deployed as a 5-HT_{1A/B} receptor partial agonist, to treat pathological aggression.¹⁴³ Subsequently, this drug is now currently undergoing clinical development for the treatment of Parkinson's disease levodopa-induced dyskinesia (PD-LID). In advanced stages of Parkinson's disease, the conversion of L-DOPA into dopamine is upregulated, and this abnormally released dopamine is suspected to contribute to the development of L-DOPA-induced dyskinesias. It has been shown in animal models of dopamine depletion that activation of 5-HT_{1A} and 5-HT_{1B} receptors block L-DOPA-induced dyskinesias, hence why Eltoprazine, is currently undergoing clinical investigations for Parkinson's disease treatment.¹⁴³

The final example shown in **Figure 68**, is a 1,4-benzodioxane thiazolidinedione piperazine derivative, and this compound has been shown in 2019 to possess antimicrobial properties by acting as a FabH inhibitor.¹⁴⁴ β -Ketoacyl-acyl carrier protein synthase III (FabH) is essential for the synthesis of bacterial fatty acid. Importantly for both Gram-positive and Gram-negative bacteria FabH has a highly conserved structure, which is sufficiently different from human fatty acid synthesis counterpart. Hence, why FabH has become the most attractive antibacterial target.¹⁴⁴ This 2019 publication did computational docking studies and biological testing but did not state whether this or a related compound is currently undergoing clinical trials.

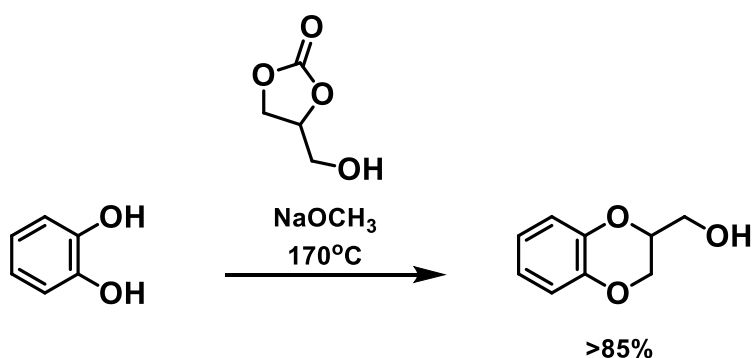
4.2.5 Literature procedures for benzodioxane synthesis

Numerous different methodologies for the synthesis of 1,4-benzodioxanes are presented in the literature of a few varying examples are shown in the below **Schemes 12-15**.¹⁴⁵⁻¹⁴⁷



Scheme 12: A literature synthesis of benzodioxane, from catechol and a dibromoalkane.¹⁴⁰⁻¹⁴⁴

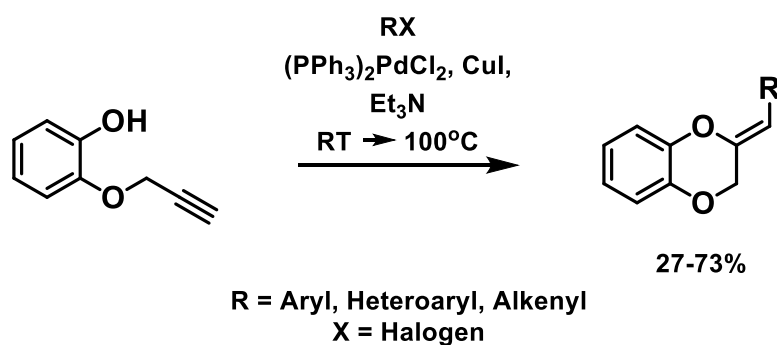
The synthesis route for benzodioxanes demonstrated in **Scheme 12**, is an extremely procedurally simple route using well established synthesis techniques where a number of catechol derivatives along with precursor alkenes are cheaply commercially available, enabling potentially a quick method for creating a sizable compound library. However, the stereochemistry configuration at the ester bearing carbon, is not controlled so forms a racemic mixture which can be problematic for pharmaceutical investigation. Additionally, the formation of halogenated waste is often considered a downside in terms of resultant disposal and potential environmental harm, thus why more modern methodologies are aiming to be more ‘Green’ by not forming halogenated wastes and reducing or removing the need for organic solvents. Such a method is shown below in **Scheme 13**.



Scheme 13: Solvent free synthesis of (2,3-dihydrobenzodioxin-2-yl) methanol.¹⁴⁵

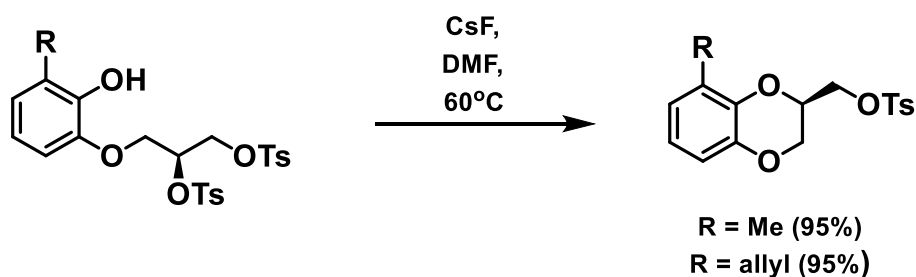
As with the method shown in **Scheme 12**, **Scheme 13** also utilises a basic intermolecular cyclisation reaction involving catechol but is considered ‘green’ by predominantly being a solvent free reaction as the glycerol carbonate is a highly reactive alkylating agent for

phenolic compounds while simultaneously acting as the reaction solvent. This does result in a greater stoichiometry of a two-fold excess, but this would not be considered detrimental if this excess glycerol carbonate could be reused for subsequent reactions. A main downside to this reaction could be the high reaction temperature of 170 °C required, which is close to three times the required temperature of the reaction shown in **Scheme 12**, as the synthetic community is generally moving away from harsh reaction conditions. But the procedure in **Scheme 13** is certainly one of interest and has further promise.



Scheme 14: Palladium catalysed intramolecular synthesis of 1,4-benzodioxanes.¹⁴⁶

Another procedurally different method to acquire 1,4-benzodioxanes is the palladium catalysed intramolecular reaction shown above in **Scheme 14**. This procedure stereoselectively forms the (*Z*) isomer and electron-withdrawing groups present in aryl halide moieties resulting in higher isolated yields when compared to electron-donating groups. However, based on the computational data presented in Chapter 2 (section 2.3.2) the alkene position in **Scheme 14** would be saturated. This could be achieved with a subsequent reaction however this additional linear synthesis step would reduce the overall procedural yield unless the alkyne motif could be substituted out for an alkene as if so, that would negate the need for an additional step. Furthermore, when comparing the 2-(prop-2-yn-1-yloxy)phenol starting material for **Scheme 14** to catechol, the commercial cost for purchase is far greater and less available. This additional cost could be circumvented by synthesizing 2-(prop-2-yn-1-yloxy)phenol from catechol but again additional linear synthesis step reduces overall yield. This in conjunction with the need of a palladium catalyst is why this methodology, despite merits was not deployed for the synthesis of the 1,4-benzodioxane compound library shown later in this Chapter.



Scheme 15: Intramolecular nucleophilic substitution synthesis of 1,4-benzodioxanes.¹⁴⁷

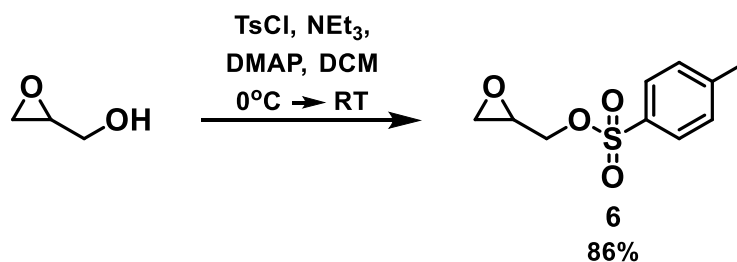
The fourth and final literature procedure for the synthesis of 1,4-benzodioxanes is shown above in **Scheme 15** and is another example of an intramolecular synthesis route. This methodology has numerous benefits over **Scheme 14**, including higher isolated yields, not requiring a catalyst or co-catalyst, and operating at a lower reaction temperature. Additionally, the resultant product is enantiopure with the shown isomeric product having an ee in excess of 99%, in both cases. However, again this procedure has some downsides one of which is that only electron donating methyl or allyl R groups were reported¹⁴⁷ meaning that if this method is unable to accommodate electron donating groups subsequent functionalisation or synthesising a chemically broad compound library could be more challenging. Furthermore, as with **Scheme 14**, the acquisition of the starting material for **Scheme 15** may provide additional challenges over using catechol or catechol derivatives, as **Scheme 15** starting material does not appear to be commercially available and also needs to be isomerically pure to obtain the isomerically pure product.

As demonstrated above, the synthesis of 1,4-benzodioxanes is fairly well documented in the literature with a wide range of synthetic procedures being able to yield 1,4-dibenzodioxanes. However, the benzodioxanes synthesised within this Chapter predominately utilised a method based upon that shown above in **Scheme 12**, due to using commercially cheap and available starting materials.

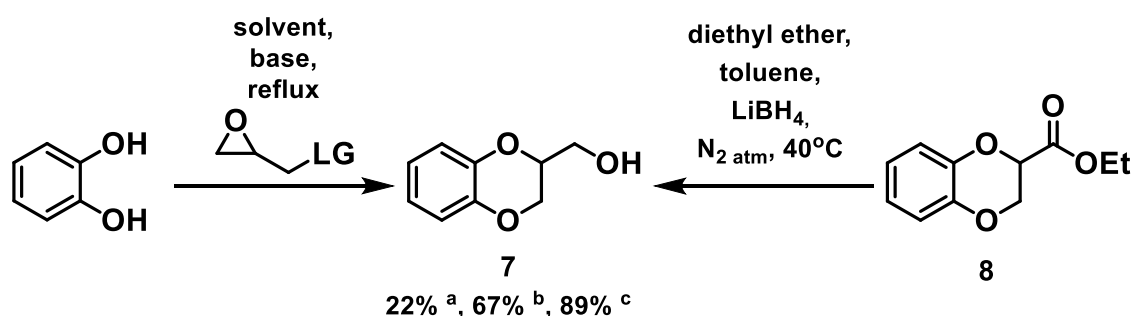
4.3 Results and Discussion:

4.3.1 Initial synthesis of the benzodioxane core

The initial 1,4-benzodioxane synthesised as part of this work was (2,3-dihydrobenzo[b][1,4]dioxin-2-yl)methanol (compound **7**), whose formation was optimised by altering reaction components and conditions. The different synthetic methodologies for this compound's synthesis and required precursors is shown below in **Scheme 16** and **Scheme 17**^{145,148-150}

**Scheme 16:** Formation of compound **6**

Glycidol (1.0 equiv.), DCM, 0 °C, Et₃N (2.0 equiv.), DMAP (0.15 equiv.), TsCl (1.0 equiv.), RT. ¹⁴⁷

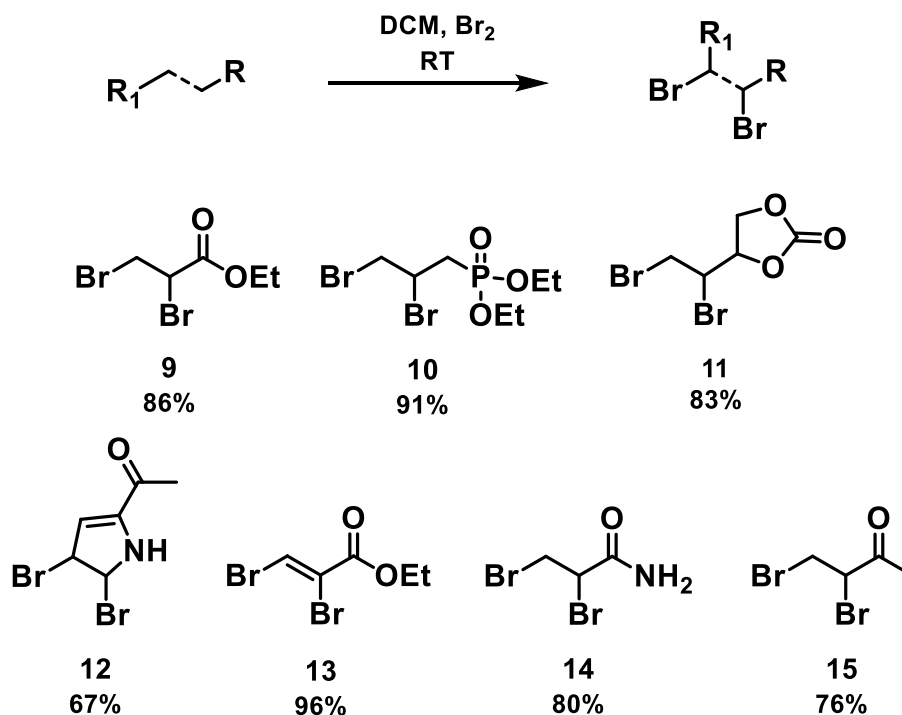
**Scheme 17:** Formation of compound **7**

^a Catechol (1.0 equiv.), Cs₂CO₃ (2.0 equiv.), acetone, after 5 minutes epichlorohydrin (1.0 equiv.) added, reflux until completion. ¹⁴⁷ ^b Catechol (1.0 equiv.), K₂CO₃ (2.0 equiv.), acetone, after 5 minutes compound **6** (1.0 equiv.) added, reflux until completion. ¹⁵¹ ^c Compound **8** (1.0 equiv.), LiBH₄ (1.1 equiv.), ethyl ether, toluene, N₂ atm, 40 °C. ¹⁴⁷ LG = Cl ^a or Ts (compound **6**) ^b

The initial reaction conditions utilised a literature procedure which yielded isolated compound **7** at 22%, this was enhanced by substituting epichlorohydrin with the tosylate containing epoxide product (compound **6**), synthesis shown above in **Scheme 17**. Compound **6** was synthesised by a known literature procedure. ¹⁵¹ When compound **6** was used a significant increase in the isolated yield for compound **7** of 67% was found. It is important to note that when K₂CO₃ was used in conjunction with epichlorohydrin, or Cs₂CO₃ with compound **6** no significant change in yield was observed. The primary reason for utilising K₂CO₃ with compound **6** was availability at that time. The postulated reason for the enhanced yield when using compound **6** over epichlorohydrin, is that the tosylate motif acts as a better leaving group than the Cl anion. However, the greatest isolated yield for compound **7** was *via* the literature procedure from the corresponding ester (compound **8**, synthesis shown below in **Scheme 20**). ¹⁴⁹

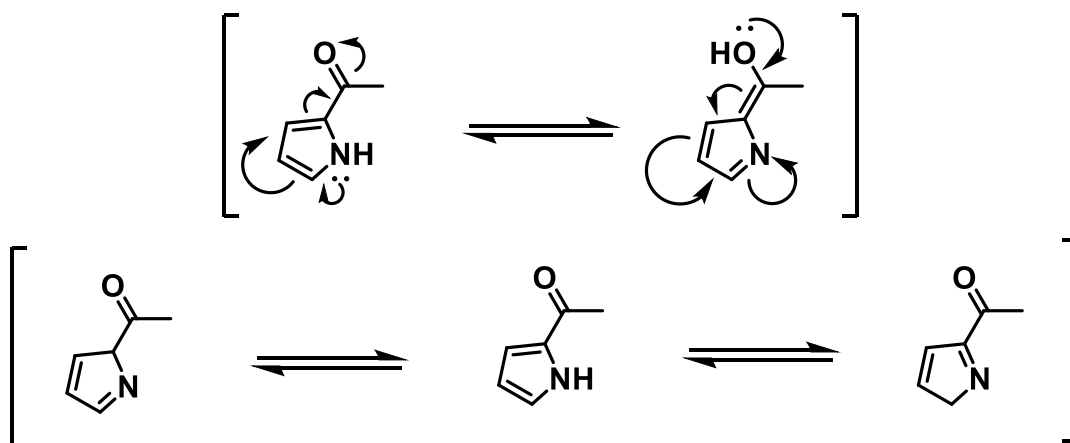
4.3.2 Substrate scope of dibrominated precursor compounds

As shown above in **Scheme 12**, another means for the synthesis of 1,4-benzodioxanes is *via* aromatic diols with dibrominated compounds, the synthesis and substrate scope of which is shown below in **Scheme 18**.



Scheme 18: Reaction conditions and substrate scope for dibrominated compounds. Alkene or Alkyne (1.0 equiv.), DCM, cooled to 0 °C, Br₂ (l) (1.0 equiv.), RT. ^{145,148}

As shown above in **Scheme 18**, the literature procedure ¹⁵² used, produced good to excellent isolated yields (67 – 96%) on all unsaturated starting materials with linear alkenes working better than the cyclic alkenes. With regards to compound **12** a lesser isolated yield of 67% could in part be due to evidence of subsequent bromination at the remaining double bond present in compound **12** and starting material in the resultant reaction mixture. But only trace amounts of the secondary brominated version of compound **12** were observed, meaning additional factors are resulting in the reduced yield when compared to the other brominated compound shown in **Scheme 18**.

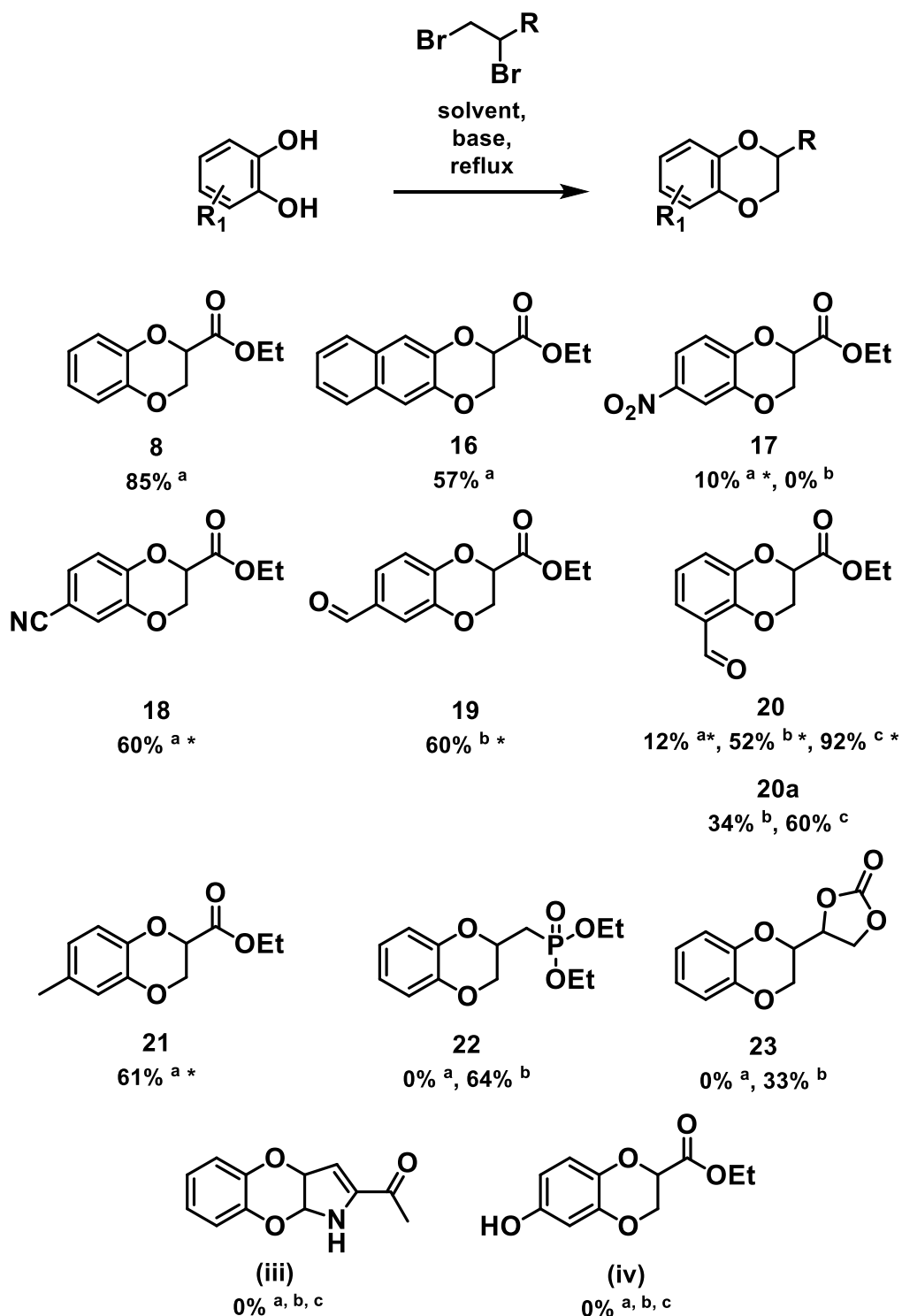


Scheme 19: Tautomer structures of the precursor to compound **12**.

Potentially the increased stability of the starting material for compound **12** could also contribute to the lesser isolated yield as it is able to form an additional resonance form due to the nitrogen's lone pair being able to conjugate with the neighbouring alkenes (shown in **Scheme 19**). In addition, aromatic stability, may also to a greater extent contribute to the compound's stability through the shunting of electron density around the ring. Therefore, limiting reactivity. Another noteworthy observation from the results presented in **Scheme 18** above is that the reaction involving an alkyne resulted in the highest isolated yield of 96% and no additional bromination products of compound **13** were observed. Possibly the increased electron density of the alkyne motif over that of alkenes is a contributing factor to apparent favouritism of the reaction conditions to alkynes as an isolated yield 10% lower was observed for the corresponding alkene alternative (compound **8**, isolated yield of 86%).

4.3.3 First wave of benzodioxane synthesis

With the range of α,β -dibrominated compounds acquired (**Scheme 18**) they were initially reacted with primarily catechol and a select range of commercially available catechol derivatives. As shown below in **Scheme 20** the highest isolated yield obtained with the literature conditions discussed above in **Scheme 12**, was by reacting catechol with the dibromoalkene compound **8**, with an isolated yield of 86%. Additionally, with catechol having a plane of symmetry in between the diol of the compound perpendicular to the page only one structural isomer was found to form. This is also the case for compounds **16**, **22** and **23**. For the rest of the benzodioxanes illustrated in **Scheme 20**, the ratio of structural isomers has been identified and is stated in the footer, with the proposed major structural isomer illustrated where applicable. ^{145,153}



Scheme 20: Initial 1,4-benzodioxane compound library.

Aromatic diol (1.0 equiv.), base (2.0 equiv.), solvent, after 10 mins a dibrominated product (compound 9-15) (1.0 equiv.) added, reflux until completion. ^a Acetone and K₂CO₃ used, ^b Acetone and Cs₂CO₃ used, ^c EtOAc and Cs₂CO₃ used.

* Mix of two structural isomers isolated major illustrated. ¹⁴⁹ Structural isomer product ratios: compound 17 - 3:1, compound 18 - 2:1, compound 19 - 2:1, compound 20 - 2.5:1, compound 21 - 1:1. Note: compound 20a yields shown are for single shown structural isomer, compound 20 yields are for the pure mixture of structural isomer products.

One experimental observation with regards to the synthesis of compound **17**, is that when the 2.0 equiv. of K_2CO_3 (base) was added in a single addition prior to compound **9**, no observable amount of the desired product was obtained only starting materials. However, when the K_2CO_3 (base) was added in two 1.0 equiv. additions, with the second being added 10 minutes later in conjunction with compound **9**, the isolated yield of 10% for compound **17** (as shown in **Scheme 20**) was obtained. The reason why this occurs is not known, but this alteration in methodology was carried forward for all subsequent reactions, it is also important to note that when this alteration in base addition was conducted on the synthesis of compounds **8** and **16**, no difference in yield was observed when the original method of adding the 2.0 equiv. of K_2CO_3 (base) at once was used.

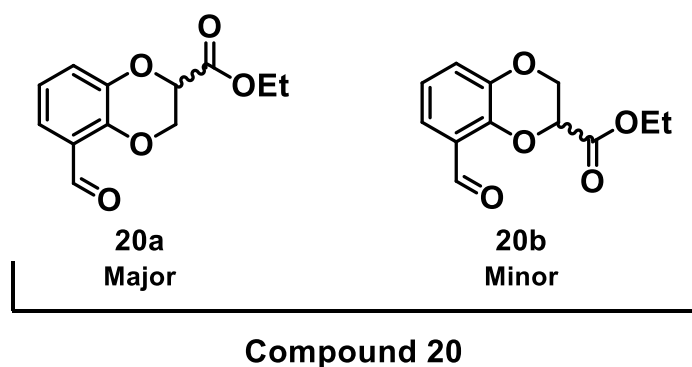


Figure 69: Structures of both resultant structural isomers of compound **20**.

An example demonstrating the two structural isomers that can form from the procedure outlined in **Scheme 20**, is shown above in **Figure 69**. It is important to note that for each structural isomer of benzodioxane formed two enantiomers are also formed. Separation of enantiomers also did not occur, meaning that the inhibitory response results shown throughout this Chapter below could be greater if a single enantiomer of the tested structural isomer hit was isolated and tested.

The variations in the reaction conditions shown in **Scheme 20**, were based on the NMR yield results from the optimisation investigation specifically for the formation of compound **20**, as the hydrolysis product of this (compound **30**) was the first benzodioxane compound to be identified as having PTP inhibitory biological activity. The optimisation data is shown later in this Chapter in **Table 7**, and the biological activity data in section 4.3.4. It was found that the optimised conditions for the synthesis of compound **20**, was found to be suboptimal for all of the other benzodioxanes shown in **Scheme 20**, and instead the reaction conditions akin to the literature method of acetone with a group 2 metal carbonate as a base at 60 °C were superior for compounds **8**, **16-19** and **21-23**.

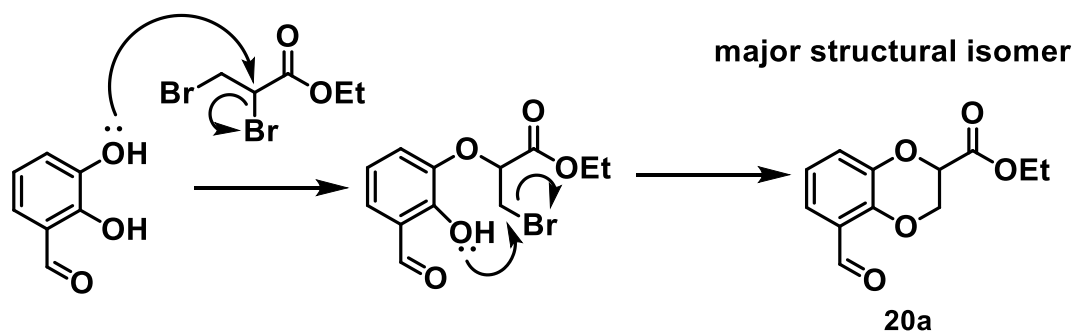
With regards to why the formation of compounds **(iii)** and **(iv)** failed, the reason may be partly due to electronic factors. For compound **(iii)** the carbon atoms directly bonded to the bromines in compound **12** may not be electropositive enough to enable the attack from the aromatic diol. Alternatively, or additionally compound **12** like its precursor, may possess increased stability from resonance forms contributed to the nitrogen lone pair. However, for the failed formation of compound **(iv)** it is postulated to be due to the additional *meta*-aromatic alcohol being present, thus resulting in the reaction with multiple brominated alkanes causing an inseparable mixture of products. One way to form compound **(iv)** by selectively protecting the *meta*-alcohol *via* the protection of the diol first as a cyclic acetal, thus then allowing protection of the lone OH and the subsequent selective deprotection of the diol, but this would result in an overall poor reaction yield caused by an increased linear synthesis pathway.

With regards to the structural isomers that form, it appears that the electronic effect of the 'R' group present on the aromatic diols has on the closest OH is the primary factor in not only which structural isomer is the major product but also the resultant ratio of the two. With compound **17** which has the most electron withdrawing 'R' group of an NO₂. Which is conjugated with the *para* OH, therefore in theory the *meta* OH (to the NO₂) would be more favourable for attach the bromoalkane of compound **9**. Despite this a 3:1 ratio in the favour of initial attack at the *para* site was found, this would explain why a lower isolated yield of 10% was observed due to the greater electron density at that position. However, with compound **18** which contains another *meta* directing group (cyano) an isolated yield of 60% was observed, potential due to CN being less electron withdrawing than NO₂. This was the same for compound **19** whose 'R' group are in the same position but again is less electron withdrawing, also here the carbonyl is *ortho* / *para* directing and so conjugates with the *meta* OH. A structural isomer ratio of 2:1 is observed but again the *para* OH in both the precursor for compounds **18** and **19** appears be more likely to initially react due to being more electron dense than the *meta* OH.

When the aldehyde is moved an atomic position closer to the OHs (compound **20**) the ratio between the two structural isomers increases compared to compound **19** at 2.5:1, as the closer OH to the aldehyde is more electron withdrawn in compound **20** than with compound **19**. So again, the now *meta* OH (one further from the aldehyde 'R' group) is more favourable to react initially so the stated major isomer shown in **Figure 69**, is correct

and this is supported by two-dimensional HMBC NMR data. This observation informed the proposed mechanism of 1,4-benzodione *via* this method, shown below in **Scheme 21**.

Additionally, when an electron donating 'R' group (Me) containing aromatic diol was utilised in this reaction to form compound **21**, a structural isomer ratio of 1:1 was observed. It was expected that the reverse would have occurred with instead the OH closer to the methyl group being more likely to react first with the bromoalkane, but instead it appears that for the precursor of compound **21** no inherent selectivity is present. Potentially if a more electron donating group was utilised (such as an ether) the above-mentioned reaction favour may have occurred, but this was not the case for the precursor for compound (**iv**), where the 'R' group was a more electron donating OH group.



Scheme 21: Proposed mechanisms for benzodioxane synthesis cyclisation step with aromatic diol and dibromoalkane.

The mechanism for the formation of 1,4-benzodioxanes are very similar regardless of if the deprotonated catechol is reacting with a dibromoalkane, epichlorohydrin or compound **6**. As the process is initiated by one of oxygen anions of the aromatic diol which attacks the more electron withdrawn carbon forming an O-C bond. For the reaction involving a dibrominated product (compounds **9-15**) the second oxygen attached the other carbon adjacent to the other bromine atom thus cyclising to form the benzodioxane. There is an additional step for the formation of compound **7**, in that after the initial attack by the aromatic diol the epoxide ring reforms *via* the ejection of the leaving group (LG), subsequently enabling the cyclisation and formation of the benzodioxane which contains a primary alcohol.

However, when the symmetry of the aromatic diol ring is broken by the addition of 'R' group(s), multiple structural isomers can form. The electronic effects of the 'R' group(s) is a major determining factor in which OH is favoured for the initial attack and thus which structural isomer is major as stated above. Illustrated in **Scheme 21** above is the proposed

mechanism of the formation of the major structural form of compound **20a**, where the OH *meta* from the aldehyde is favoured for the initial attack as a greater proportion of electron density will be pulled from the *ortho* OH towards the aldehyde. So, the most electron dense aromatic OH will attack the least electron dense carbon of dibrominated product (compound **9-15**). The C-Br adjacent to the ester functional group will be less electron dense so more electronically active thus potentially preferentially attacked over the less sterically hindered but more electron dense C-Br to form primarily the structural isomer shown in **Scheme 21b**.

4.3.4 Biological inhibition data for initially synthesised benzodioxanes

4.3.4.1 Initial screen

The first set of compounds tested for PTP1B active site binding were precursors to the computationally found target carboxylic acid containing benzodioxanes and are from **Scheme 16**, **Scheme 17**, **Scheme 18** and **Scheme 20** above.

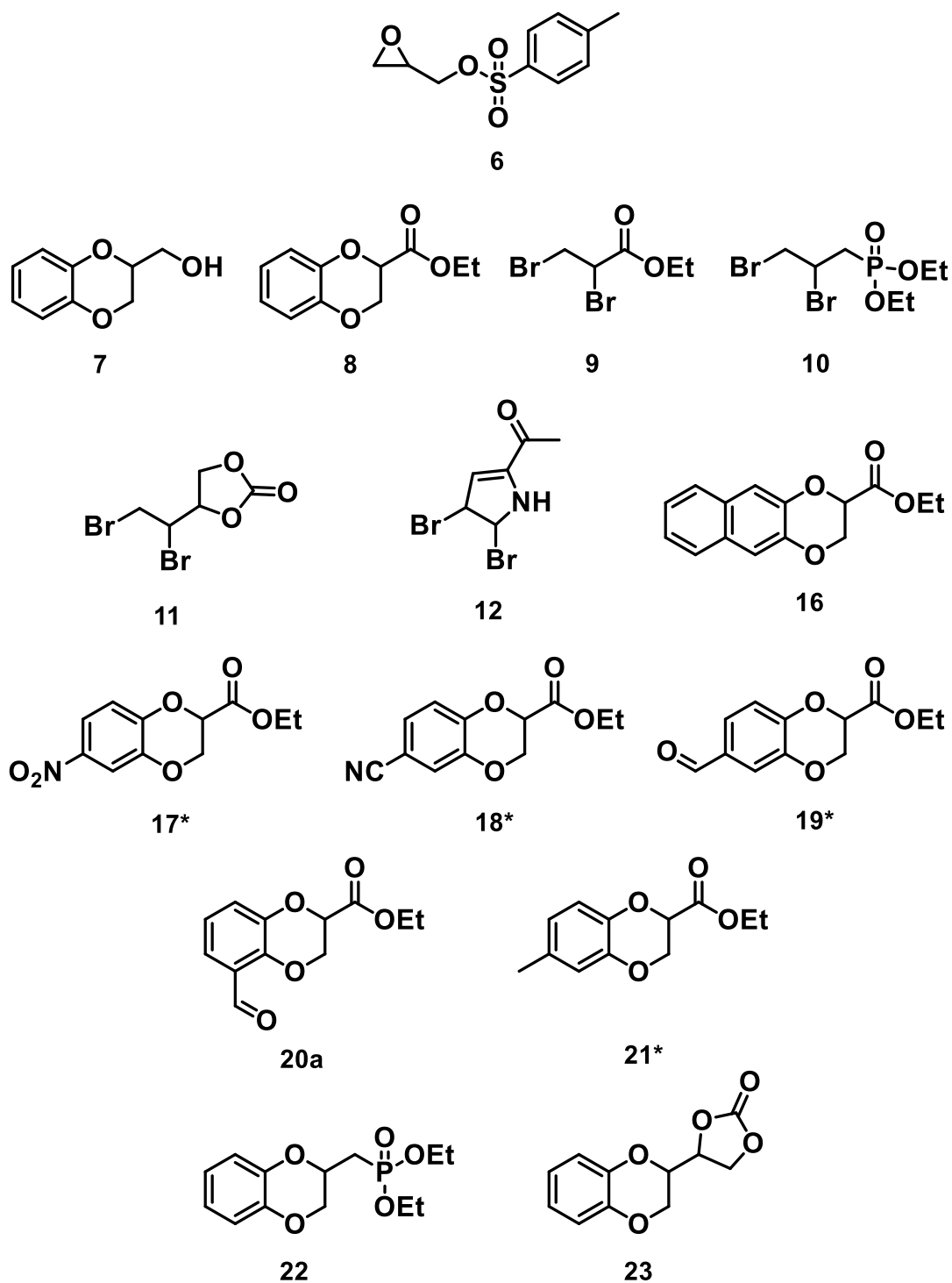
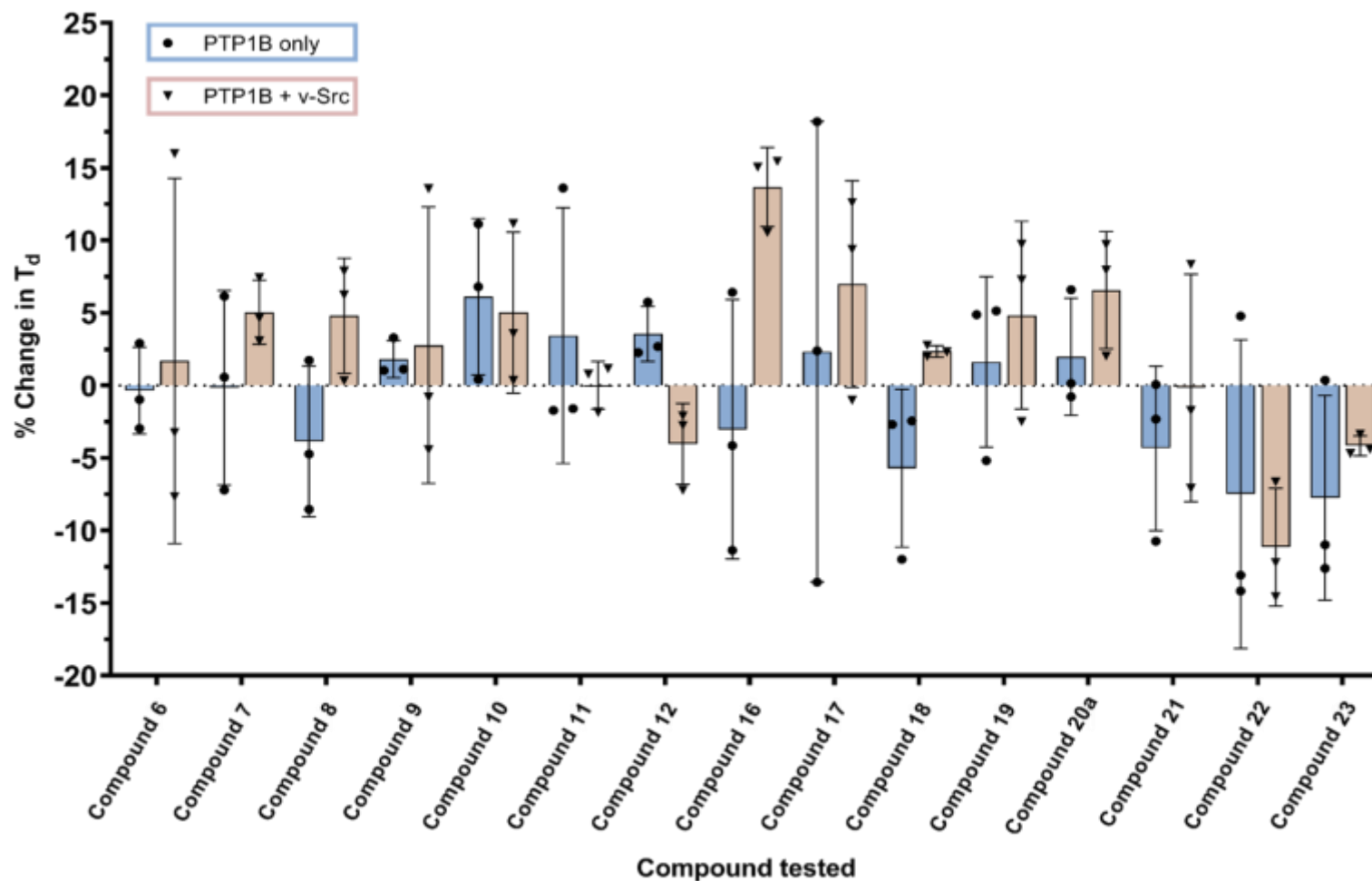


Figure 70: Initial compounds tested for PTP1B inhibitory activity.

* Mix of two structural isomers utilised major illustrated. For ratios see Methodology chapter.



Compound	p value
6	ns
7	ns
8	ns
9	ns
10	ns
11	ns
12	ns
16	ns
17	ns
18	ns
19	ns
20a	ns
21	ns
22	ns
23	ns

Figure 71: Comparison of % change in doubling time (T_d) of PTP1B only and PTP1B + v-Src transformed yeast cells in the presence of synthesised compounds **6-12** and **16-23** at 100 μ M. $n=3$ for all compounds tested in both transformations, mean and individual points \pm standard deviation plotted. Used non-parametric Mann-Whitney t-test for statistical analysis. * p value ≤ 0.050 vs control.

Above in **Figure 70** the chemical structures of all the compounds investigated in the initial screen are shown and where a mixture of structural isomers was used for testing this is clearly indicated. All brominated compounds (**9-15**) were not investigated as these were not identified as potential inhibitors from computational screening. Compounds **9-12** were tested to demonstrate the lack of PTP activity these brominated compounds exert.

From the results shown in **Figure 71** and the appendix (section 2.1) compounds **6-12** and **16-23** had no significant effect on the T_d of PTP1B only or PTP1B + v-Src transformed cells.

However, compound **16** was taken forward for further investigation as it demonstrated a consistent and greatest average increase in the % change in T_d in PTP1B + v-Src transformed cells of 13.68 ± 2.22 %. The average fold change in T_d for compound **16** was 1.14 when compared to the corresponding base growth. T_d data can be found in the appendix (section 2.1).

4.3.4.2 Investigation of potential inhibitor compound 16

4.3.4.2.1 PTP1B activity

To investigate compound **16** as a PTP inhibitor a dose response investigation was conducted. The concentration range used was based upon work with known inhibitors shown in Chapter 3 (section 3.3.2) and the appendix (section 1.7). The concentration range utilised for all identified hit compounds in both PTP1B and TCPTP based cells was 0 – 500 μ M.

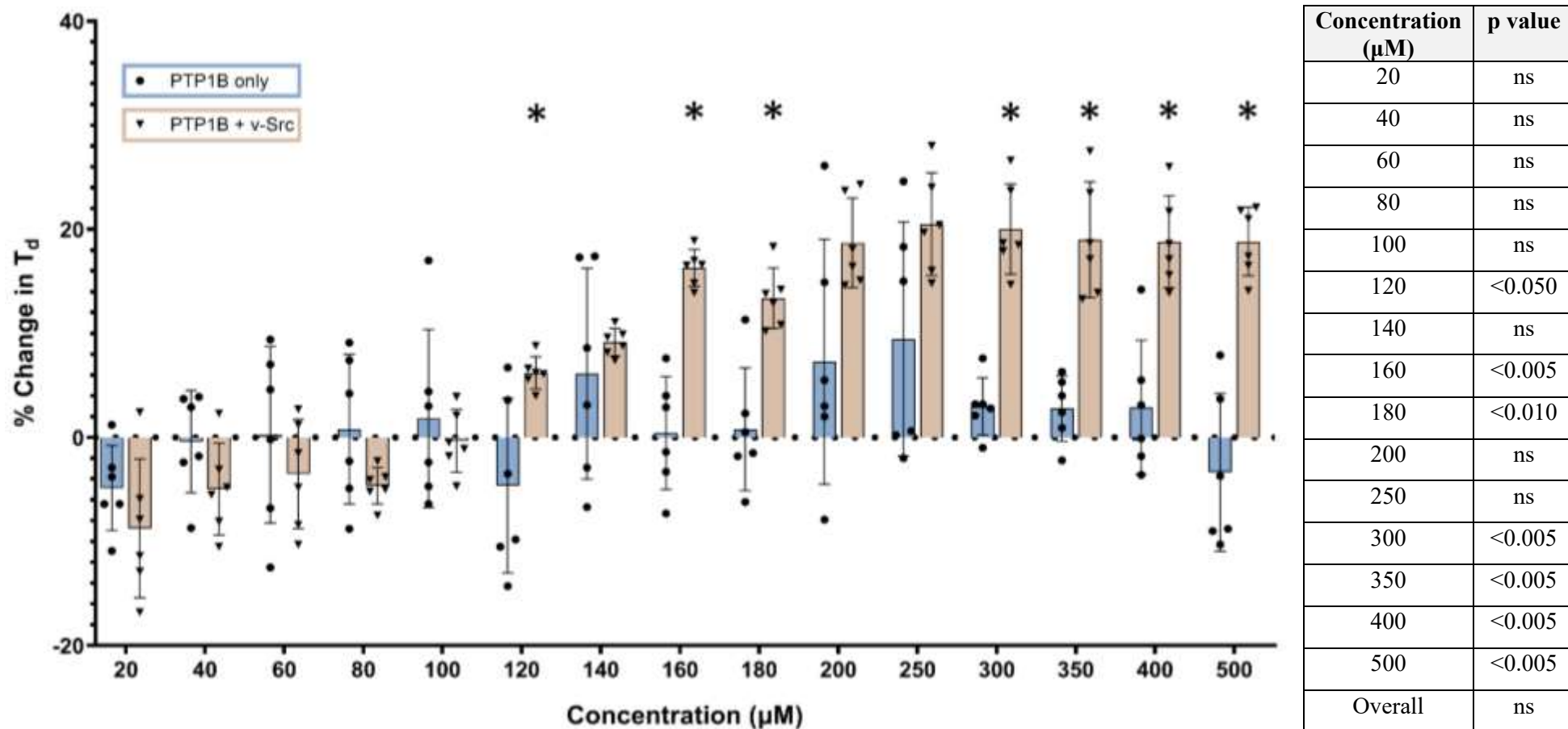


Figure 72: Comparison of % change in doubling time (T_d) of PTP1B only and PTP1B + v-Src transformed yeast cells in the presence of compound **16** at 20-500 μM . $n=6$ for all concentrations tested in both transformations, mean and individual points \pm standard deviation plotted. Used non-parametric Mann-Whitney t-test for statistical analysis. * p value ≤ 0.050 vs control.

As demonstrated in **Figure 72** the lowest concentration which saw a significantly greater increase in T_d in PTP1B + v-Src over PTP1B only was at 120 μM . When the dose of compound **16** was increased to 160 μM a significant increase in the % change in T_d of PTP1B + v-Src cells was observed and demonstrated further improvement of PTP1B inhibition (p value <0.005). However, when the concentration was increased above 160 μM no significant change in T_d occurred, in comparison of 160 μM to 500 μM . Hence 160 μM was found to be the optimum concentration of compound **16** for PTP1B inhibition.

In order to assess the PTP selectivity of compound **16** the same dose response experiment was conducted in TCPTP based transformed yeast cells.

4.3.4.2.2 TCPTP activity

The results for TCPTP inhibition by compound **16** are shown below in **Figure 73**.

The lowest concentration where a significant increase in % change in T_d in TCPTP + v-Src cells compared to TCPTP cells alone was 250 μM . When the dose was increased to 400 μM a significant two-fold uptick in TCPTP inhibitory activity occurred (p value <0.005). Hence for TCPTP inhibition the optimum concentration of compound **16** is 400 μM , as no significant difference between 400 μM and 500 μM in TCPTP + v-Src cells was present. When comparing **Figure 73** (TCPTP activity) to **Figure 72** (PTP1B) one clear difference was the concentration threshold required to enable activity, as over a two-fold increase in concentration was required for initial PTP inhibition for TCPTP when compared to PTP1B.

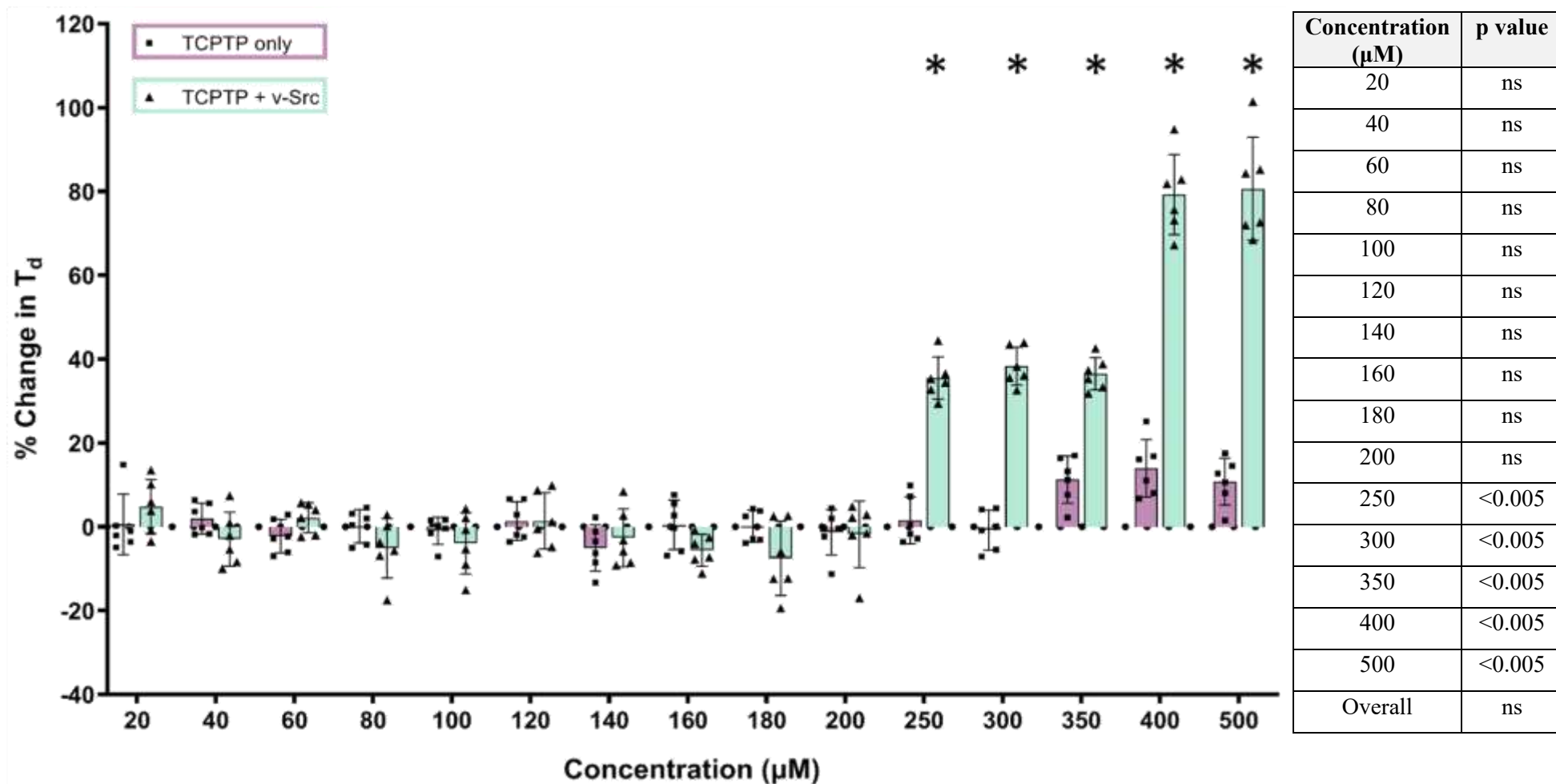


Figure 73: Comparison of % change in doubling time (T_d) of TCPTP only and TCPTP + v-Src transformed yeast cells in the presence of compound **16** at 20-500 μM . $n=6$ for all concentrations tested in both transformations, mean and individual points \pm standard deviation plotted. Used non-parametric Mann-Whitney t-test for statistical analysis. * p value ≤ 0.050 vs control.

4.3.4.2.3 PTP activity comparison

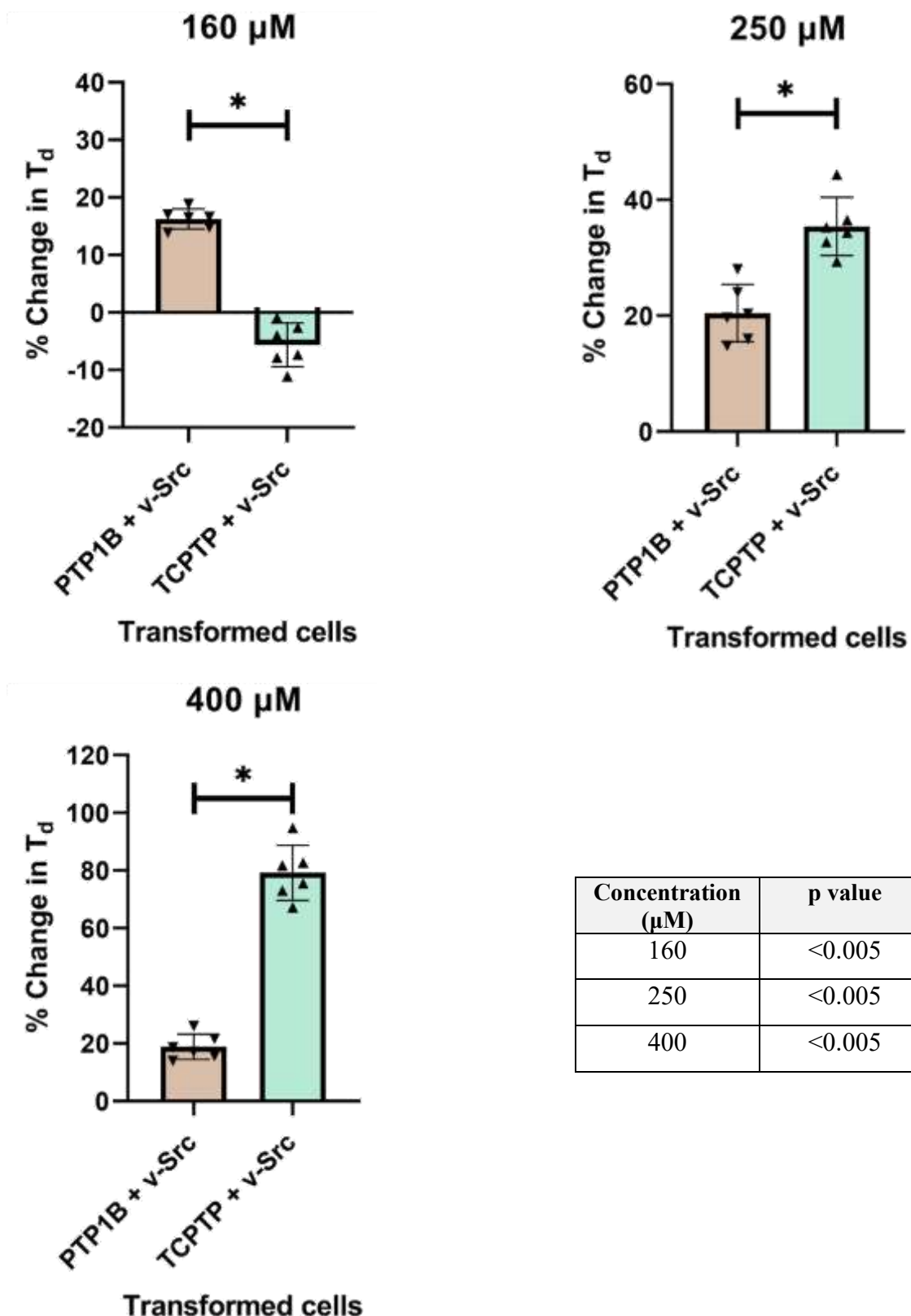


Figure 74: Comparison of % change in doubling time (T_d) of PTP1B + v-Src and TCPTP + v-Src transformed yeast cells in the presence of compound **16** at 160, 250 and 400 μM . $n=6$ for all concentrations tested in both transformations, mean and individual points \pm standard deviation plotted. Used non-parametric Mann-Whitney t-test for statistical analysis. * p value ≤ 0.050 PTP1B + v-Src vs TCPTP + v-Src.

As shown above in **Figure 74** at 160 μM (the optimum concentration for inhibition of PTP1B by compound **16**), not only did a significantly greater inhibitory effect occur in PTP1B based cells than in TCPTP based cells (p value <0.005). but additionally at this concentration, compound **16** enhanced the growth rate of the TCPTP + v-Src cells. This was the case for all six of the biological replicates up to a reduction of 11%, when compared to base TCPTP + v-Src growth. Therefore at 160 μM compound **16** is not only specific towards PTP1B but also is inactive as a TCPTP inhibitor which demonstrates PTP1B is the sole therapeutic protein target.

However, **Figure 74** also demonstrates that over a fourfold greater effect of an average 79% increase in T_d on at 400 μM in TCPTP + v-Src cells to PTP1B + v-Src cells which only on average resulted in 19% increase in the T_d . Meaning the maximum inhibitory response compound **16** exerts in TCPTP cells is significantly greater than that towards PTP1B (p value <0.005). In addition to being TCPTP specific at concentrations at and above 250 μM .

Once possible reason for the concentration dependency of compound **16** PTP selectivity and the maximum observed inhibitory effect towards PTP1B and TCPTP could be contributed the accessibility to the active site and the strength of the resultant binding interactions of compound **16** to each of the PTP active sites.

It can be theorised that the results shown in **Figure 74**, could be due to compound **16** potentially being able to bind more readily to PTP1B hence why significance is observed at a lower concentration (120 μM), but the strength of the interactions may be weaker than in the TCPTP active, potentially explaining the higher maximum inhibitory effect towards TCPTP.

This possibility was investigated computationally with docking studies. The optimum binding position proposed by Pyrx¹¹⁶ for each are shown below in **Figure 75** and **Figure 76**.

4.3.4.2.4 Computational modelling

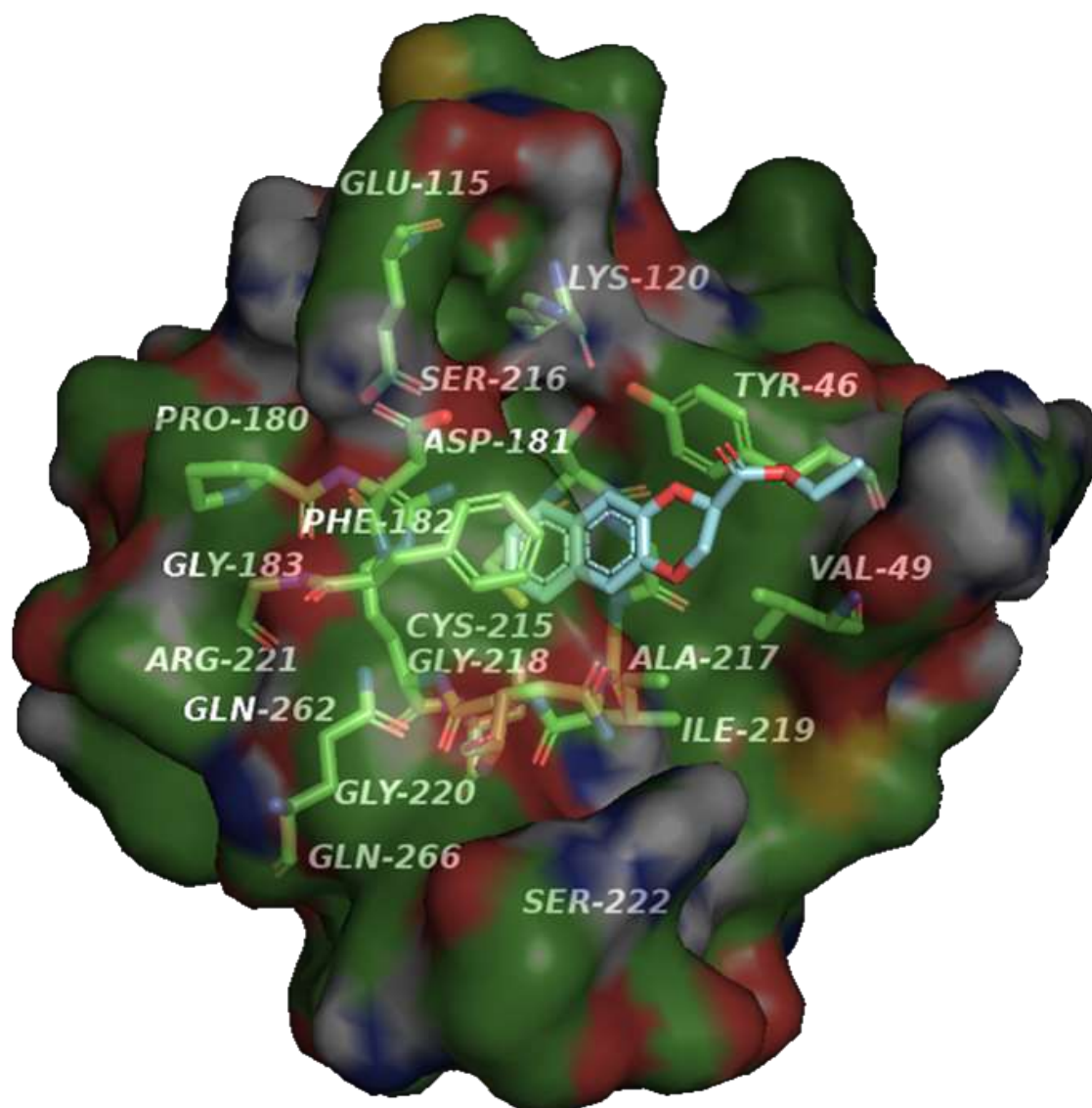


Figure 75: Computational most favoured proposed binding mode of compound **16** in the closed conformation of the PTP1B active site.

Figure 75 shows the computationally most probable binding position of compound **16** in the active site of PTP1B where the residues 12 Å around the Cys-215 residue are shown. From the above proposed positioning of compound **16** the probable binding interactions with the active site are as follows: π -stacking with residues Phe-182 and Tyr-46, and potential hydrogen bonding between the ester of compound **16** and the amide of Tyr-46.

However as shown below in **Figure 76** the proposed interactions between the active site of TCPTP and compound **16** are more extensive and therefore in theory stronger.

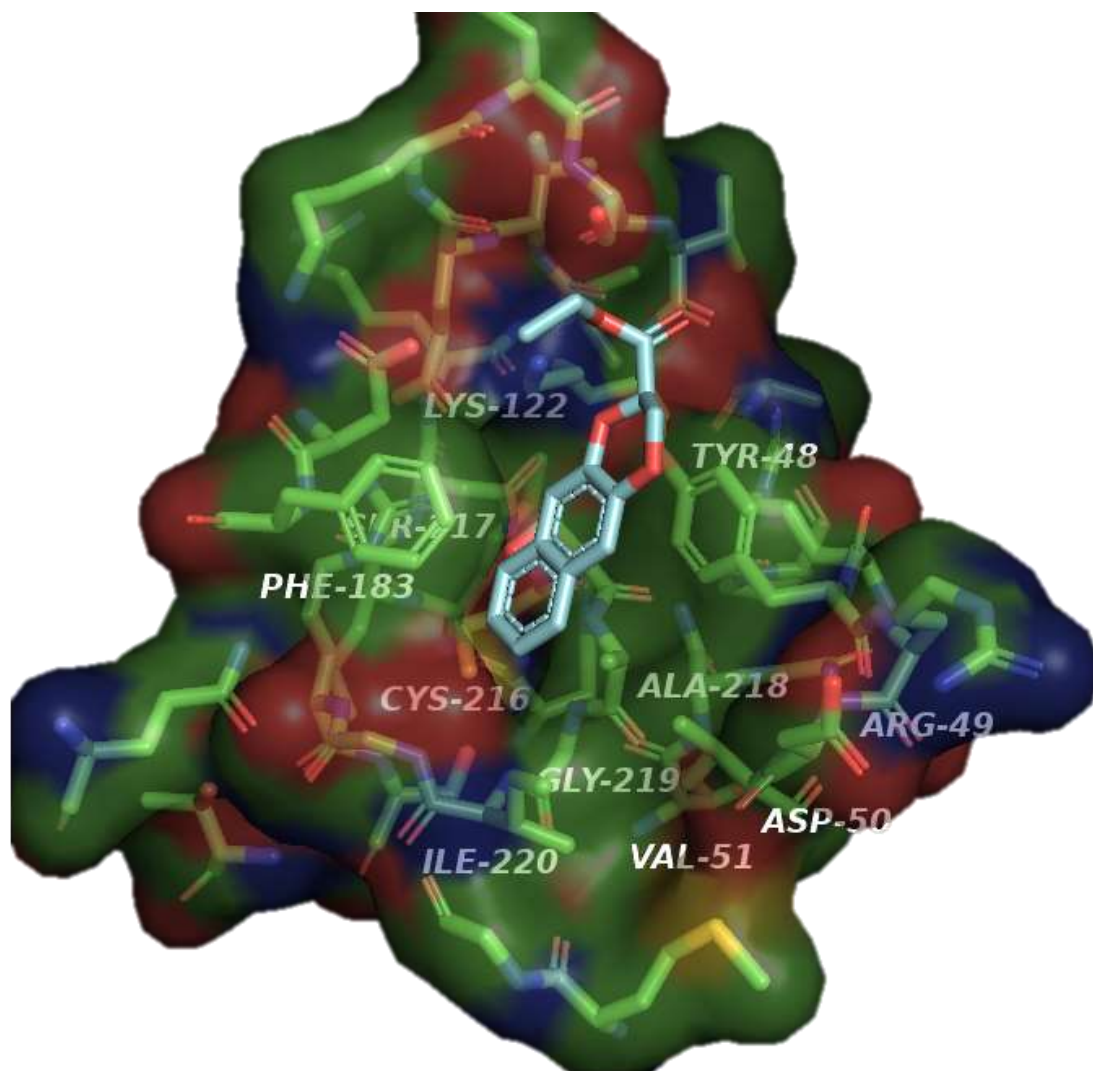


Figure 76: Computational most favoured proposed binding mode of compound **16** in the closed conformation of the TCPTP active site.

As with **Figure 75**, **Figure 76** also demonstrates the most probable binding position based upon computational docking studies of compound **16** in the active site of TCPTP, and again the residues 12 Å around the Cys-216 residue are shown. The probable binding interactions of compound **16** with the active site of TCPTP are as follows: π -stacking with residues Phe-183 and Arg-49, potential hydrogen bonding between the ester of compound **16** with the amide of Val-121, and the phenol of Tyr-48 in addition to a potential interaction between one of the benzodioxane oxygen and Tyr-48.

The increased proposed interactions of TCPTP with compound **16** would explain the increased inhibitory activity of TCPTP inhibition over PTP1B inhibition. However, from these docking studies the ease of compound **16** binding to either active site cannot be assessed easily so the proposal of TCPTP having a less assessable active site for compound **16** remains speculative.

4.3.4.2.5 Calculated EC₅₀ values

Another parameter of interest when investigating potential PTP inhibitor hits is the respective potency towards both PTP1B and TCPTP, this was assessed by calculating the EC₅₀ values. The calculated EC₅₀ values and maximum % change in T_d exerted in both PTP1B + v-Src and TCPTP + v-Src cells are shown and compared below in **Table 4**.

Table 4: Comparison of activity of compound **16** in PTP1B and TCPTP

	PTP1B inhibition	TCPTP inhibition
Maximum effect (%)	21	81
EC ₅₀ value (μM)	149	309
Ratio (max effect: potency)	1:7	1:4

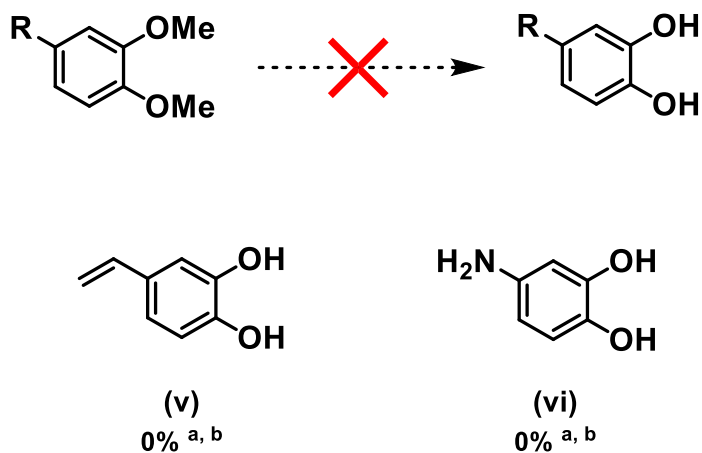
Maximum effect (%) denotes the percentage increase in doubling time of the PTP + v-Src cells with compound **16** compared against base growth / growth without compound **16** and does not refer to the percentage of PTP inhibited. All values are round to the nearest integral. Started EC₅₀ value is the calculated average from six biological replicates.

As shown in **Table 4** compound **16** is more potent towards PTP1B than TCPTP due to having an appropriately two-fold lesser calculated EC₅₀ value, meaning that to gain half the maximum effect a lesser concentration is needed for PTP1B inhibition than TCPTP. However, the maximum effect observed on TCPTP is approximately four times greater than that is observed for PTP1B. Therefore, it has been concluded that compound **16** overall operates better as a TCPTP inhibitor. However, at lower concentration compound **16** has been shown to be PTP1B specific, but as will be demonstrated below with subsequent PTP1B inhibitor hit compounds, a maximum increased in T_d of 20% can be considered a relatively low response.

However, when attempting to form the compounds presented in **Figure 70** not all reactions attempted were successful. These unsuccessful reactions are explored below in the subsequent section.

4.3.5 Attempted alternative synthesis pathways to benzodioxane precursors.

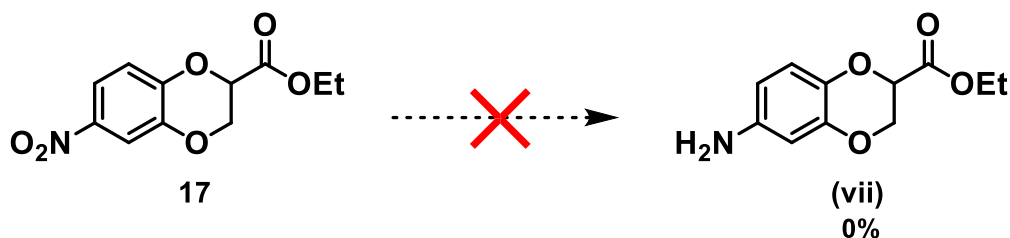
With the scope in **Scheme 18** forming numerous dibrominated precursors, and utilising commercially available aromatic diols, the next step was to attempt the synthesis of additional non-commercially available catechol derivatives. ^{132,154,155}



Scheme 22: Attempted hydrolysis of ethers to primary alcohols.

^a Aromatic diether (1.0 equiv.), HCl_{conc} (2.0 equiv.), H₂O, 120°C. ¹⁴⁷ ^b Aromatic diether (1.0 equiv.), BBr₃ (4.0 equiv.), DCM, N₂ (atm), 0°C. ^{145,148}

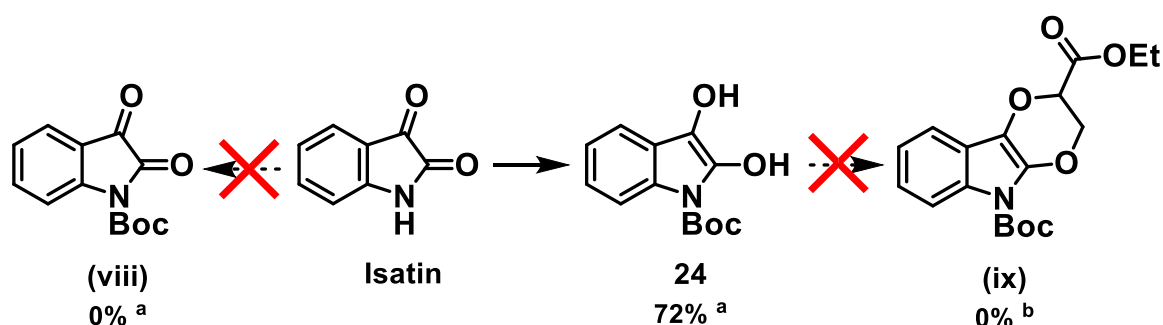
As shown above in **Scheme 22**, two different methodologies for the simultaneous hydrolysis of two OMe groups and subsequent benzodioxane formation were attempted on an alkene and an amine containing diether substrate. The point of this was to add motifs for easy subsequent specific functionalisation, for building off the benzodioxane core to create potential inhibitors that can bind to a greater number of PTP1B residues surrounding the active site. However, despite the employed harsh conditions, the desired reaction did not occur, and the respective starting material was largely recovered. The apparent stability of these aromatic diether resulted in the decision to return to this methodology at a later date and instead investigate alternative synthesis pathways to gain additional 1,4-benzodioxanes for PTP activity biological testing.



Scheme 24: Attempted reduction of a nitro to an amino group on compound **17**.

Compound **17** (1.0 equiv.), EtOAc, SnCl₂ (4.0 equiv.), HCl (cat), reflux, overnight.^{149, 156}

The failed reaction shown in **Scheme 24**¹⁵⁶ was attempted to form a compound (**vii**) that possess easy specific downstream reactivity for the benzodioxanes *via* the aniline motif to build out of PTP1B's active site and potentially bind more effectively to the active site. Despite the full conversion of the starting material (compound **17**), the desired product (**vii**) did not form in sufficient amount to be isolated separately, as a mixture of structurally similar compounds with comparable *R_f* values were formed.



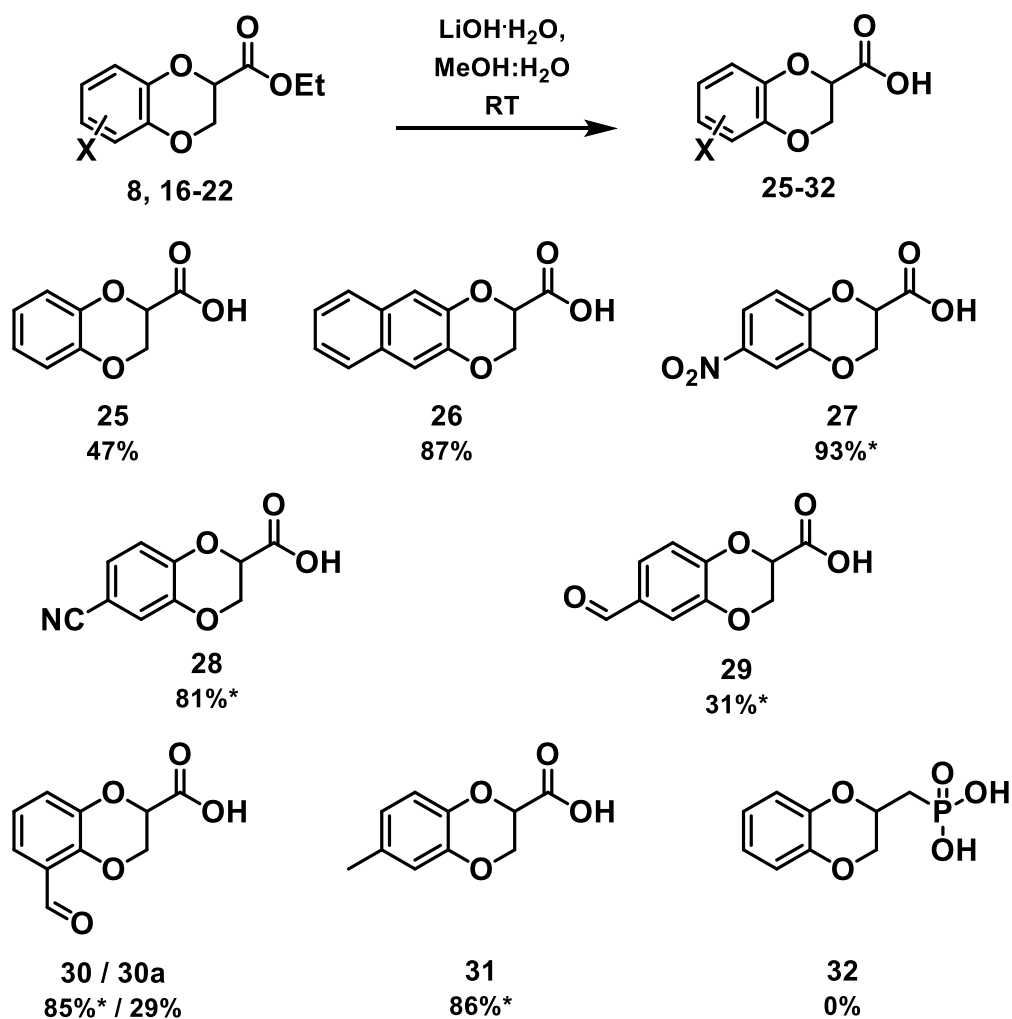
Scheme 23: Attempted cyclisation with isatin derivative.

^a Isatin (1.0 equiv.), NEt₃ (2.0 equiv.), DCM, DMAP (cat), Boc₂O (1.0 equiv.), RT.¹⁵¹ ^b Compound **24** (1.0 equiv.), K₂CO₃ (2.0 equiv.), acetone, after 10 mins compound **9** (1.0 equiv.) added, reflux until completion.¹⁴⁷

As shown above in **Scheme 23**, a different aromatic system was attempted to be incorporated with a dioxane motif, *via* the starting material isatin.^{133,145,153} If successful the unprotected amine would provide means for subsequent functionalisation with the aim of gaining a PTP1B active site inhibitor. Yet when the same Boc protection method was used to form the spirocycle product, compound **92** (see Chapter 5 section 5.3.5), the expected Boc protected isatin product (**viii**) did not form. Instead, under the conditions stated in **Scheme 23**, in addition to the Boc protection of the NH both the carbonyl motifs were also reacted with the triethylamine and an apparent double bond between the resultant diol of obtained product, compound **24**. This was formed in a good, isolated yield of 72% post purification. Compound **24** subsequently was reacted with the dibromoalkane compound **9**, in an attempt of forming compound (**ix**), using the original

literature method of K_2CO_3 in acetone. But with these conditions the reaction failed resulted in the acquirement of predominantly starting materials. If this reaction was conducted with one of the different aforementioned reaction conditions the product compound (**ix**) may have formed. As when two different isatin derivatives compounds were biologically tested, both resulted in yeast cell death hence further investigation with isatin derivative compounds was halted and alternative methods to form compound (**ix**) were not conducted.

4.3.6 Formation of potential benzodioxane active site inhibitors

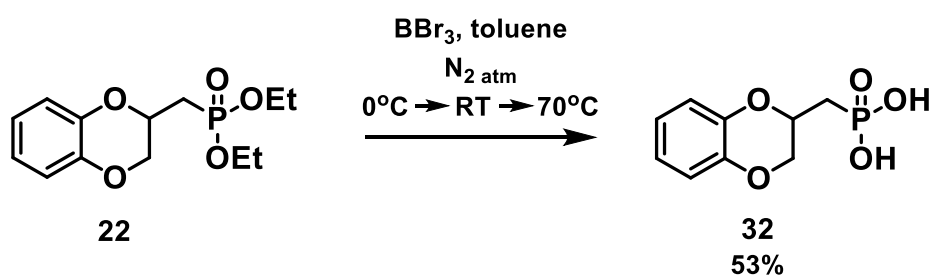


Scheme 25: Hydrolysed 1,4-benzodioxane compound library.

Benzodioxane ester (1.0 equiv.), $MeOH:H_2O$ (1:1), $LiOH \cdot H_2O$ (1.0 equiv.), RT. ¹⁵¹

* Mix of two structural isomers isolated major illustrated. Structural isomer product ratios: compound **27** - 3:2, compound **28** - 2:1, compound **29** - 2:1, compound **30** - 1:1, compound **31** - 1:1.

To achieve the target core, hit structure derived from the PTP1B computational active site studies, the previously synthesised ester containing 1,4-benzodioxanes had to be hydrolysed to their respective acid. The methodology shown in **Scheme 25**¹⁴⁵ above worked for all attempted substrates apart from for compound **22**, as for this substrate with these conditions only starting material was recovered. An observation from this methodology was that when a mixture of structural isomers (**17-21**) was reacted the ratio of the two subsequent hydrolysed structural isomers changed. The difference between the two isomers from ¹H NMR spectra was found to be smaller were possible. Suggesting a greater proportion of the minor structural isomer was present in (**17-20**) must have reacted in preference. This could be due to the 'R' groups being on the same side as the ester motif potentially resulting in reaction promotion by enabling better chelation with the Li⁺. This could also be contributing factor as to why when the single pure major structural isomer of **20** (**20a**) was reduced an isolated yield of only 29% was observed but when a 2.5:1 mixture of structural isomers (**20**) underwent the same hydrolysis reaction conditions a far greater isolated yield of 85% was acquired. If the reaction time with **20a** was extended than a more comparable yield of product is expected to be isolatable.

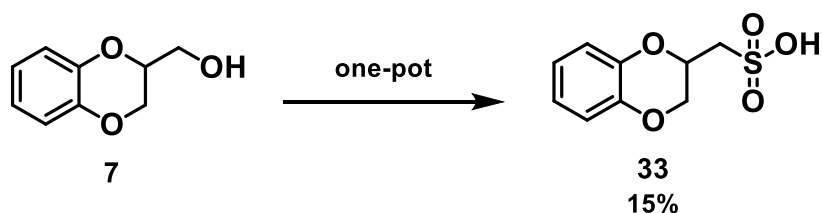


Scheme 26: Successful hydrolysis of compound **22**.

Compound **22** (1.0 equiv.), BBr₃ (1.0 equiv.), toluene, N₂ (atm), 0°C → RT → 70°C^{145,153}

Since the ester removal of compound **22** failed with the literature procedure using lithium hydroxide monohydrate, an alternative literature procedure involving harsher reaction conditions was deployed. This successfully formed the expected compound **32** in moderate yield as shown above in **Scheme 26**.¹³²

Based upon the computational results from the “shard” and ‘drug-like’ database screens of PTP1B’s active site, another motif of interest was sulfonic acid which was successfully synthesised from compound **7** to form compound **33**, as shown below in **Scheme 27**.¹⁵⁷



Scheme 27: Conversion of primary alcohol to sulfonic acid *via* thiol intermediate.

Pt 1, compound **7** (1.0 equiv.), thiourea (1.0 equiv.), 4M HBr in acetic acid (2.0 equiv.), IMS, RT. Resuspend salt in H₂O, 50°C, 33% NaOH_(aq) (excess). Formed thiol intermediate. Pt 2, Thiol (1.0 equiv.), glacial acetic acid, H₂O₂ (2.0 equiv.), RT.¹⁵²

This relatively poor isolated yield of 15%, and for this specific substrate can be explained as a twostep linear one-pot synthesis was utilised *via* a thiol intermediate which in this case was not isolated.

After compound **32** and **33** were acquired the first wave of target benzodioxanes (**25-33**) were tested, where the major structural isomer was tested solely where possible and applicable.

4.3.7 Identification of computationally designed hit compounds.

4.3.7.1 Initial screen of targeted benzodioxanes

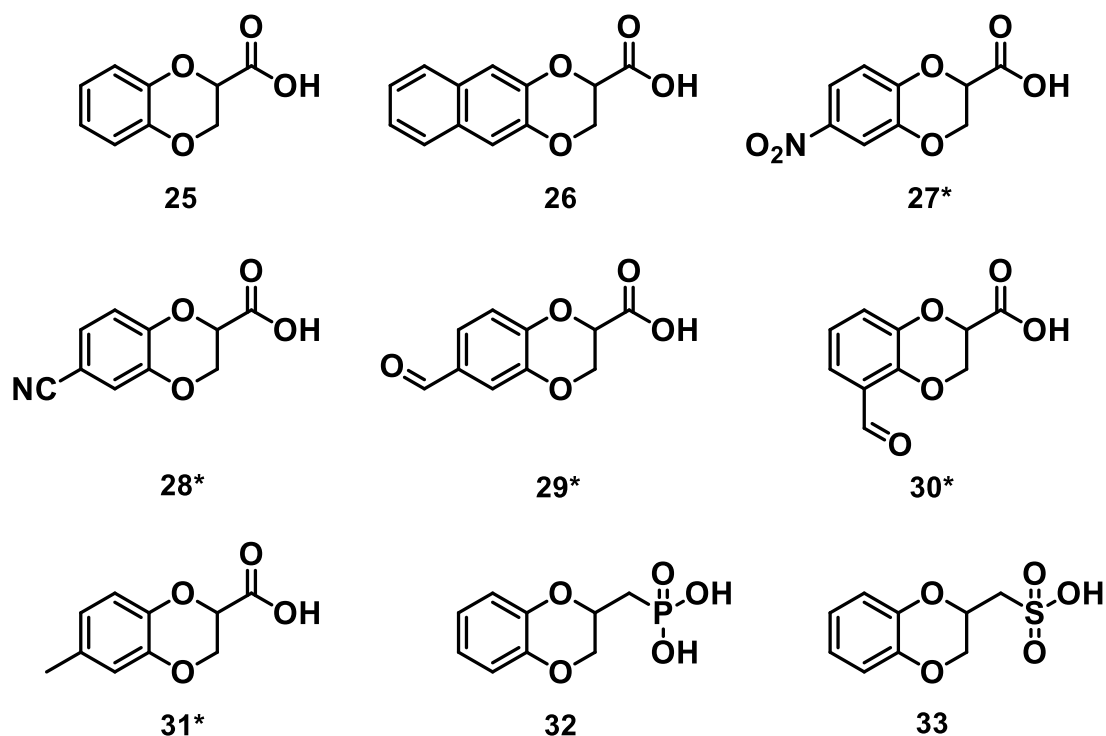
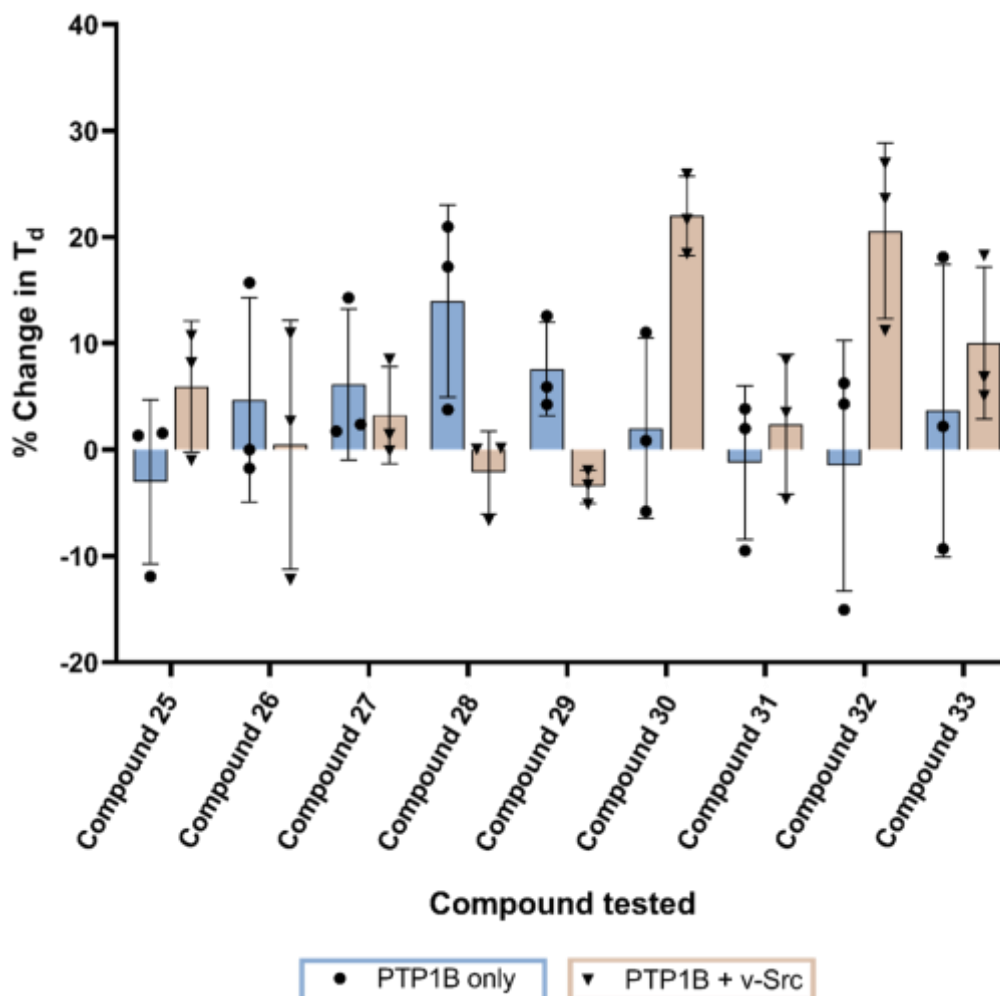


Figure 77: First wave of computationally targeted benzodioxanes tested for PTP1B inhibitory activity.

* Mix of two structural isomers utilised major illustrated. For ratios see Methodology chapter, or **Scheme 25**.

From **Figure 77** compound **25** is the closest structurally to the initial computationally found tetrahydronaphthalene hit outlined above in section 4.2.1. Any compounds tested

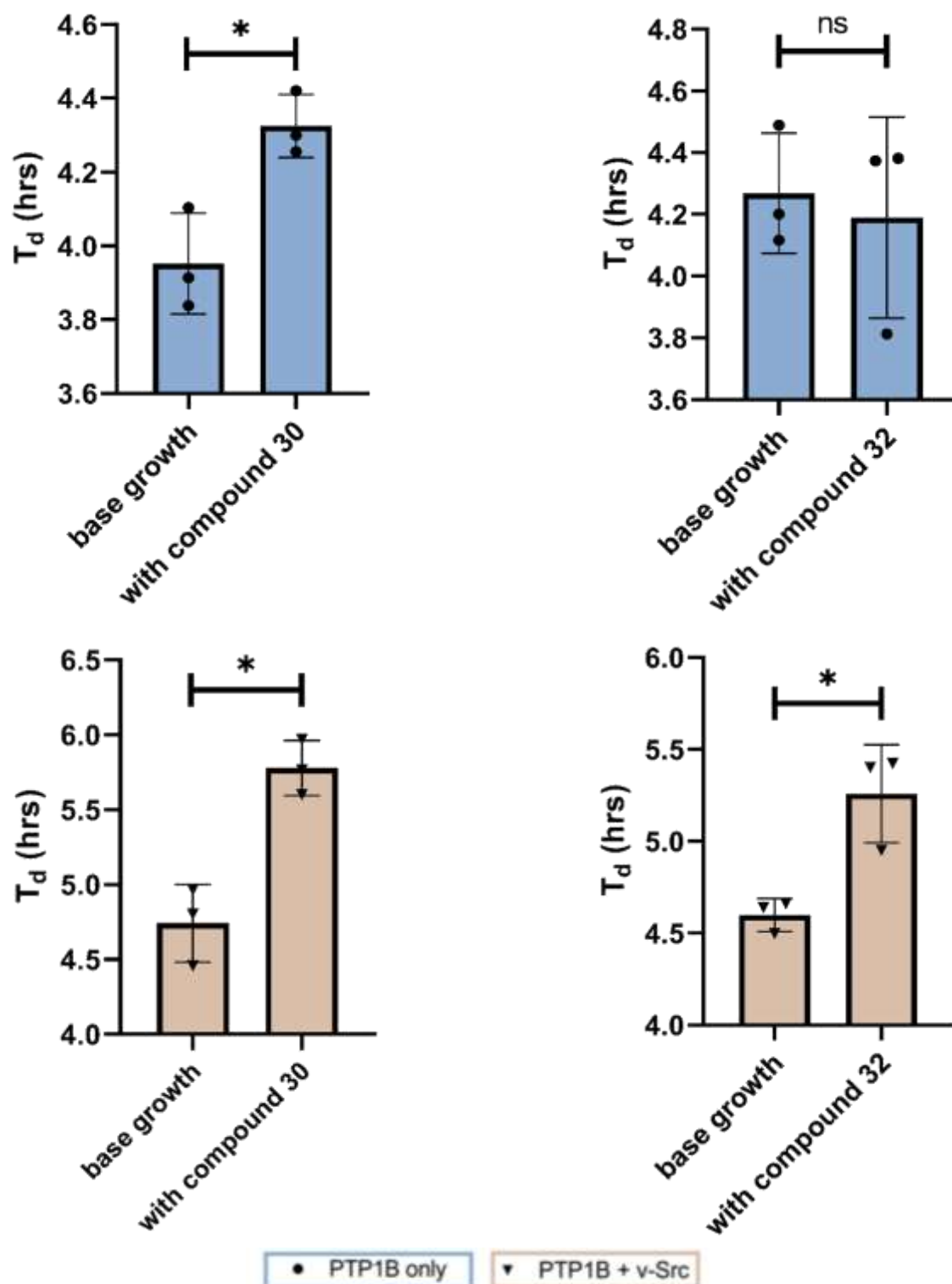
as a structural mixture have been clearly identified, in **Figure 77** above. The biological results from testing at 100 μM are shown below in **Figure 78**.



Compound	25	26	27	28	29	30	31	32	33
p value	ns	ns	ns	ns	ns	ns	ns	ns	ns

Figure 78: Comparison of % change in doubling time (T_d) of PTP1B only and PTP1B + v-Src transformed yeast cells in the presence of synthesised compounds **25-33** at 100 μM . $n=3$ for all compounds tested in both transformations, mean and individual points \pm standard deviation plotted. Used non-parametric Mann-Whitney t-test for statistical analysis. * p value $0.050 \leq$ vs control.

From **Figure 78**, three of the nine benzodioxanes showed consistent PTP1B inhibitory activity. These were compounds **30**, **32** and **33**, where **30** and **32** are of further interest due to both exhibiting the greatest average increase in the % change of T_d in the PTP1B + v-Src of approximately 20%. To further investigate significance the T_d values of PTP1B + v-Src cells with compounds **30** or **32** were compared against their corresponding base growth (**Figure 79** below).



	Compound 30		Compound 32	
Transformed cell	PTP1B only	PTP1B + v-Src	PTP1B only	PTP1B + v-Src
p value	<0.050	<0.010	ns	<0.050

Figure 79: Comparison of doubling time (T_d) of PTP1B only and PTP1B + v-Src transformed yeast cells in the presence of synthesised compounds **30** and **32** at 100 μ M. $n=3$ for all compounds tested in both transformations, mean and individual points \pm standard deviation plotted. Used parametric Welch's t-test for statistical analysis. * p value ≤ 0.050 vs control. (base growth).

As **Figure 79** illustrates, both compound **30** and **32** caused a significant increase in the doubling time of PTP1B + v-Src cells at 100 μM (p values = 0.0066 and 0.0394 respectively), demonstrating PTP1B inhibition. The significance observed in PTP1B only cells with addition of compound **30** is thought to be due to an off-target effect, but the fold change of the increase caused compared to base growth was only 0.1, and less significant than the result in PTP1B + v-Src.

Of compounds **30** and **32**, **30** was selected to undergo further investigation due primarily to two reasons: Firstly, this mixture of structural isomers had a more consistent effect and greater average increase in T_d implying a greater inhibitory effect at 100 μM than compound **32**. From the computational studies which are discussed further later (section 4.3.7.2.3), it was found that one structural isomer may be able to bind better than the other and therefore result in a greater inhibitory effect. Thus, further testing of ultimately the single structural isomer may result in higher response in terms of PTP inhibition.

Secondly numerous previous PTP1B active site inhibitors which contained a phosphoric acid to mimic the biological target failed to progress far in clinical trials^{42,86,93,94,115} in part due to the limited permeability through the phospholipid-bilayer of cells as discussed in the Chapter 1 (section 1.4.3.1).

It is important to highlight that for the results shown in **Figure 78** and **Figure 79** a 1:1 mixture of structural isomers (**30**) was utilised for this batch of testing.

4.3.7.2 Investigation of potential inhibitor compound **30**

Initially a dose response of 20-500 μM was conducted with the same 1:1 mixture of structural isomers (compound **30**) to investigate the maximum inhibitory effect on PTP1B. This was conducted as a means of assessing the activity of both structural isomers separately as latterly one structural isomer of compound **30** was able to be isolated from the mixture and tested. This isomer was identified and denoted as compound **30a**. Unfortunately, the other structural isomer was unable to be isolated from the mixture however as shown latter the testing of the compound mixture (**30**) this isomer (**30b**) may not be of interest. The results for the mixture of structural isomers in PTP1B based cells is illustrated below in **Figure 80**.

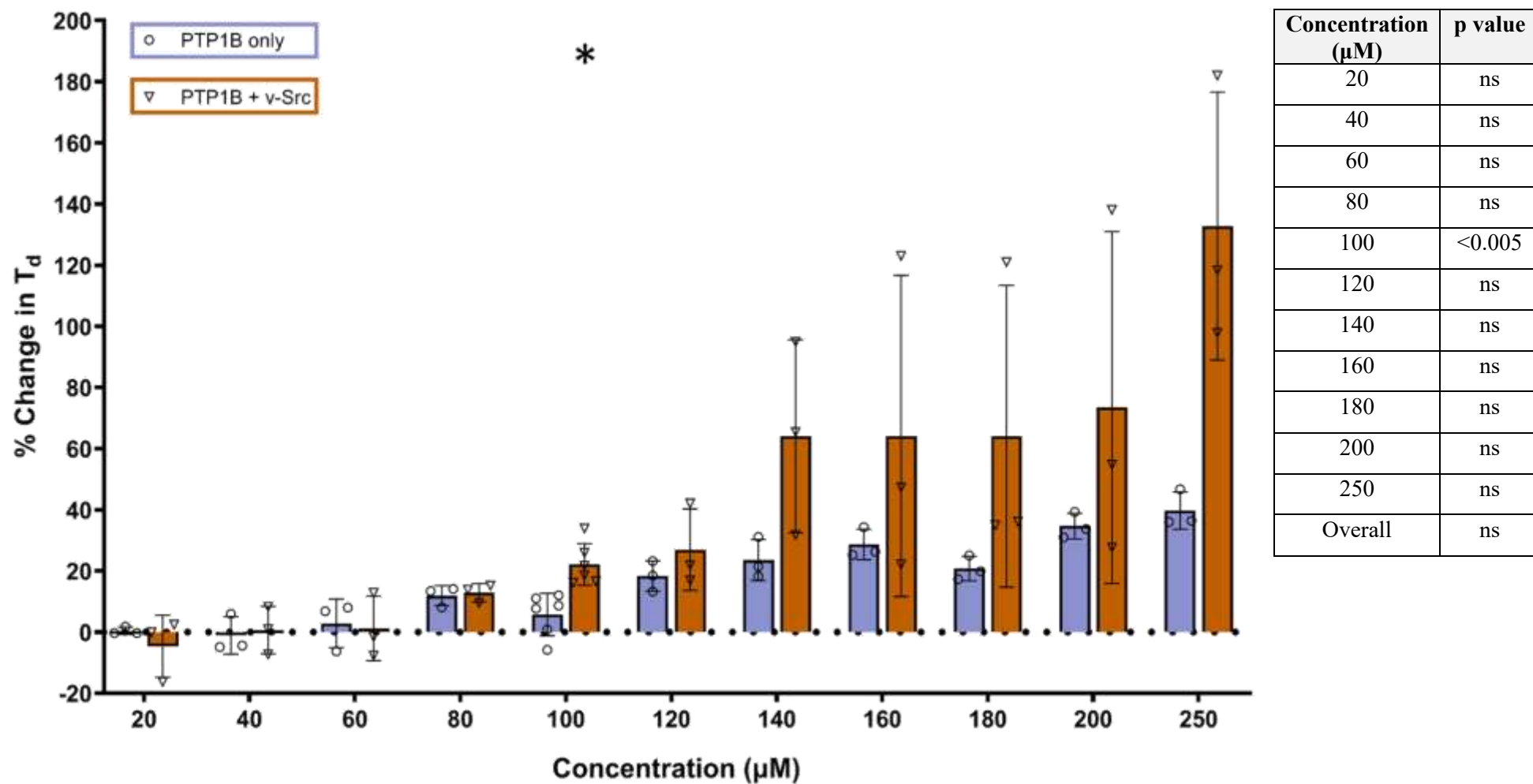


Figure 80: Comparison of % change in doubling time (T_d) of PTP1B only and PTP1B + v-Src transformed yeast cells in the presence of compound **30** at 20-250 μM . $n=3$ for all concentrations tested in both transformations apart from 100 μM where $n=6$. Mean and individual points \pm standard deviation plotted. Used non-parametric Mann-Whitney t-test for statistical analysis. * p value ≤ 0.050 vs control.

Experiments with compound **30** at 300-500 μM , were conducted but doubling time values were unable to be calculated. For compound **30** growth curves at each concentration tested can be found in the appendix (section 2.1.5).

From **Figure 80** only 100 μM resulted in a significantly greater response when compared to control (p value <0.005), this is due to the greater number of biological replicates conducted at this concentration. If further repeats were conducted at 120-250 μM it is also thought that these would also demonstrate significance.

The maximum inhibitory effect is approximately a 125 % increase in T_d at 250 μM additional biological replicates would again be beneficial to reduce the standard deviation and potential demonstrate significance. As these results were due to a 1:1 mixture of structural isomers it was deemed more worthwhile gathering biological data for the pure single structural isomer of compound **30**, compound **30a**, rather than additional repeats of the mixture.

4.3.7.2.1 Comparison of mixture of structural isomers and pure single major structural isomer of compound 30

The comparison of results between the inhibitory effect of the 1:1 mixture and single structural isomer is shown below in **Figure 81**.

An important key observation from the data presented in **Figure 81** and **Table 5** is that for the initial concentrations that showed significant activity (80-200 μM), the % increase in T_d for the single structural isomer of compound **30a**, is approximately a twofold increase over that of the biological response witnessed from the 1:1 structural isomer mixture, compound **30**, suggesting that at least in this concentration range the other structural isomer (**30b**) does not possess the ability to significantly inhibit PTP1B.

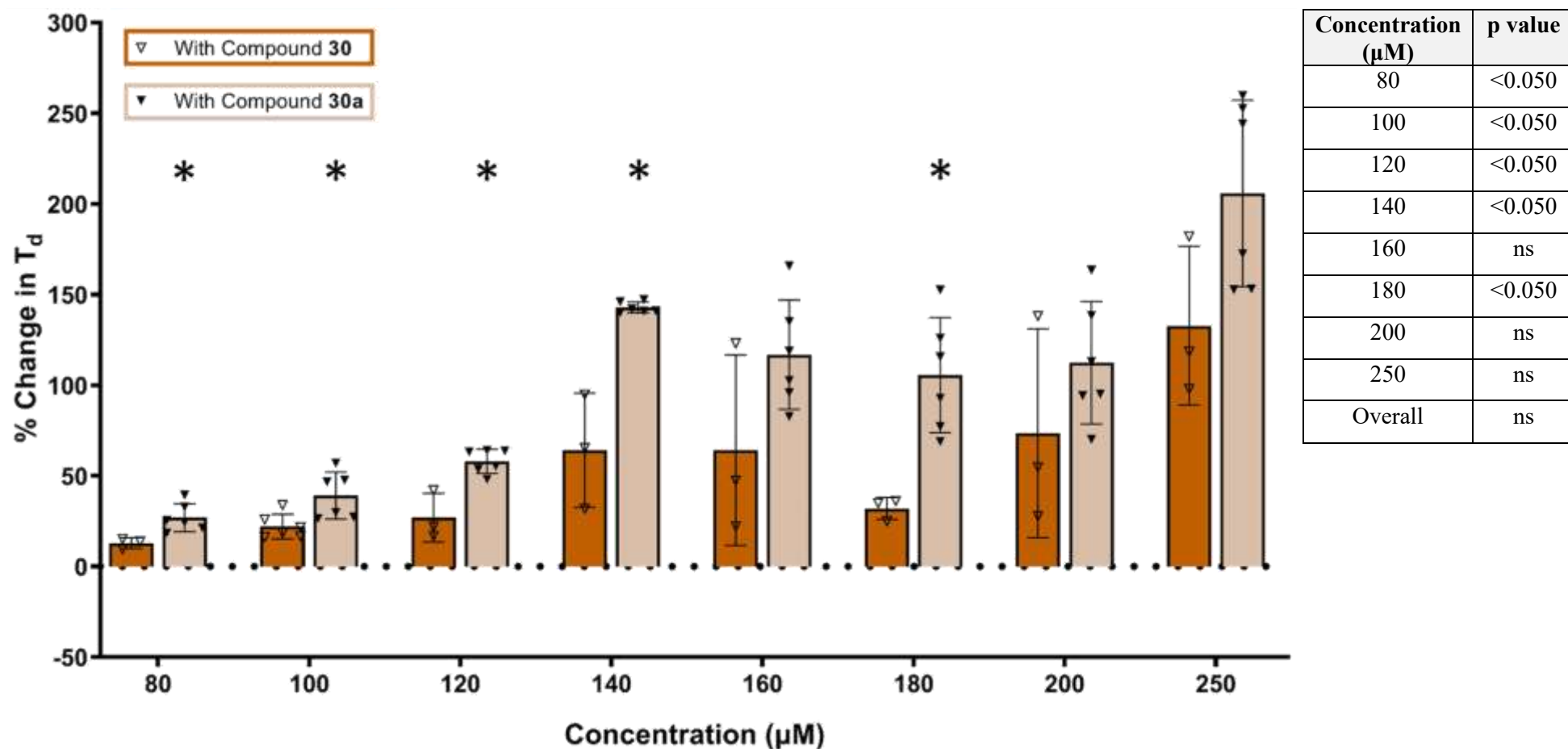


Figure 81: Comparison of % change in doubling time (T_d) of PTP1B + v-Src transformed yeast cells in the presence of compound **30** and **30a** at 80-250 μM . $n=3$ for compound **30** concentrations 60, 80 and 120-250 μM tested. $n=6$ for compound **30** at 100 μM and all concentrations of compound **30a** tested. Mean and individual points \pm standard deviation plotted. Used non-parametric Mann-Whitney t-test for statistical analysis. * p value ≤ 0.050 vs control.

Table 5: Averaged % change in T_d of PTP1B + v-Src cells with compound **30** or **30a**

Concentration (μM)	Compound 30 (mixture)	Compound 30a (single)
80	13%	27%
100	22%	39%
120	27%	58%
140	64%	143%
160	64%	117%
180	32%	106%
200	74%	112%
250	133%	206%

Percentage change in T_d denotes the average percentage increase in doubling time of the PTP + v-Src cells with compound **30** or **30a** compared against the corresponding base growth of each respective biological replicate. It does not refer to the percentage of PTP inhibited. All values are round to the nearest integral.

Figure 81 and **Table 5** demonstrate that from 80 μM an approximate two-fold increase in inhibitory activity of the single structural isomer (**30a**) over the mixture (**30**) in PTP1B + v-Src suggests that at concentrations, 80-180 μM , the other structural isomer (**30b**) has negligible PTP1B inhibitory activity.

However, at higher concentrations in particular 250 μM a greater response is observed (fold increase of 0.55) when testing the mixture of structural isomers (**30**) than expected if **30b** was completely inactive. This could mean that like compound **16** with TCPTP, compound **30b** is only sufficiently active at higher concentrations, but this can only be determined if isolated and tested separately. However, as the inhibitory response of **30a** was inherently higher, **30b** was not isolated or investigated further. The structure of both isomers which comprises compound **30** are shown below in **Figure 82**. The structure of the sole isolated isomer found as **30a** was determined with two-dimensional NMR.

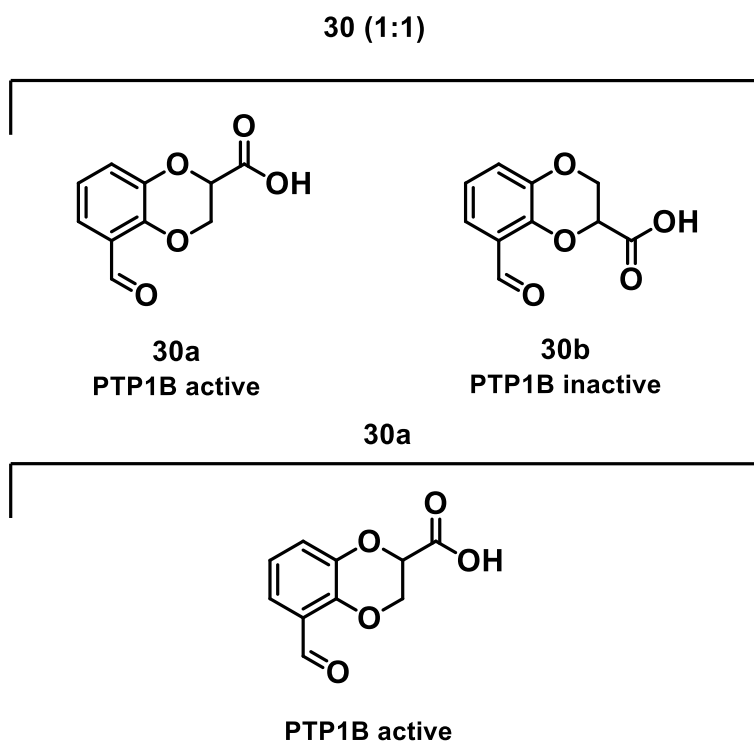


Figure 82: Structures of both structural isomers of compound **30** with compositions of **30** and **30a** identified with proposed activity included. Activity relates to 80-180 μM .

4.3.7.3 Investigation of potential inhibitor compound **30a**

As demonstrated below in **Figure 83** the % change of T_d in PTP1B + v-Src cells is significantly greater than the control group at 60-250 μM . Demonstrating significant (p value ≤ 0.05) PTP1B inhibition by compound **30a**. A significant increase in response was observed from 60 to 80 μM , 80 to 120 μM and 120 to 140 μM (p values = 0.0043, 0.0022 and 0.0022, respectively). Initially further increase in dose beyond 140 μM did not result in a significant inhibitory change until 250 μM , where a significantly greater % change in T_d occurred (p value < 0.005).

However, the concentration which produced the most consistent response of 140% was at 140 μM , therefore selected as the optimum concentration of compound **30a** for PTP1B inhibition.

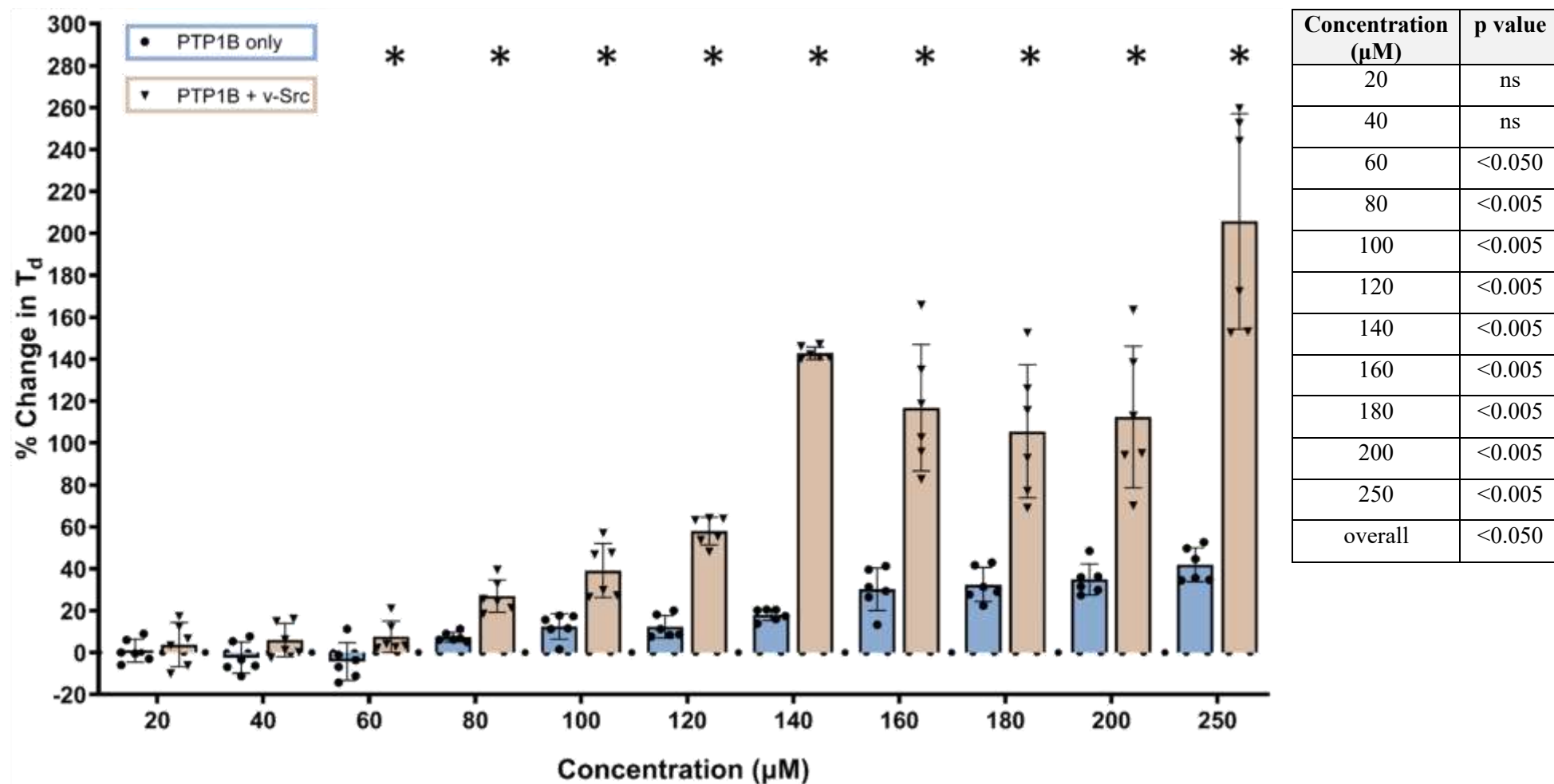


Figure 83: Comparison of % change in doubling time (T_d) of PTP1B only and PTP1B + v-Src transformed yeast cells in the presence of compound 30a at 20-250 μM . $n=6$ for all concentrations tested in both transformations, mean and individual points \pm standard deviation plotted. Used non-parametric Mann-Whitney t-test for statistical analysis. * p value ≤ 0.050 vs control.

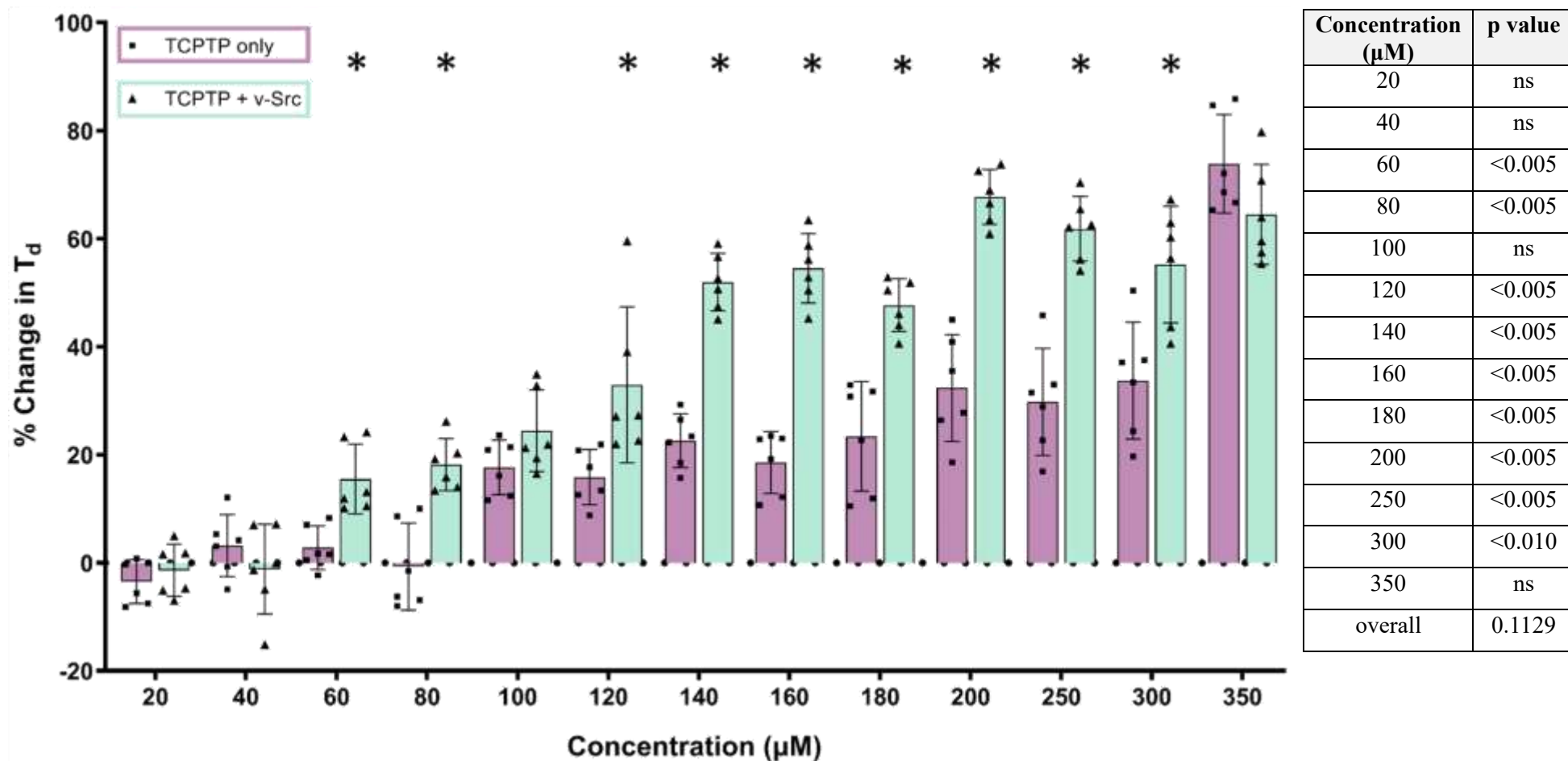


Figure 84: Comparison of % change in doubling time (T_d) of TCPTP only and TCPTP + v-Src transformed yeast cells in the presence of compound **30a** at 20-350 μM . $n=6$ for all concentrations tested in both transformations, mean and individual points \pm standard deviation plotted. Used non-parametric Mann-Whitney t-test for statistical analysis. * p value ≤ 0.050 vs control.

As demonstrated in **Figure 84**, 60 μM was the lowest concentration that caused a significant inhibitory TCPTP effect. However, unlike PTP1B (**Figure 83**) increasing the dose beyond 140 μM resulted in significantly greater response at 200 μM (p value <0.005). But further increasing the concentration of compound **30a** did not result in an increase in average response. Therefore, the optimum concentration of **30a** for TCPTP inhibition was 200 μM .

4.3.7.3.1 PTP selectivity

Figure 85 below shows that there is no statistical significance between PTP1B + v-Src and TCPTP + v-Src when 60 μM of compound **30a** was added. However, when the concentration of **30a** was increased a significantly greater inhibitory response occurred towards PTP1B at both 140 μM (PTP1B optimum concentration) and 200 μM (TCPTP optimum concentration) with p values <0.005 and <0.010 respectively.

Additionally, the maximum response of compound **30a** in PTP1B was on average a 206% increase in T_d that occurred at 250 μM and is more than double than was observed in TCPTP at the same concentration where the response was significantly less (p value <0.005).

Hence suggesting that compound **30a** is more selective towards PTP1B and thus potentially has a stronger binding mode with the active site PTP1B.

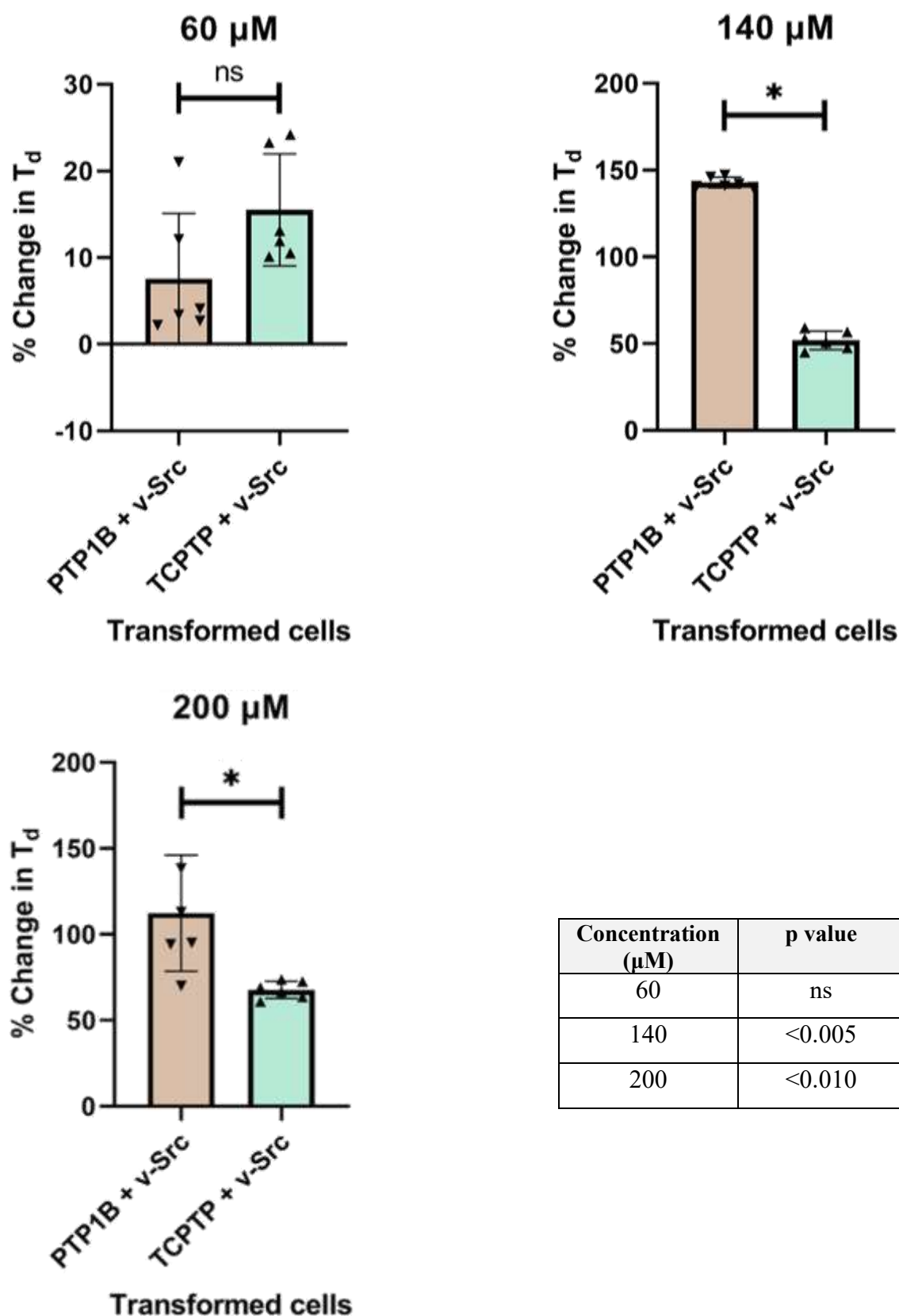


Figure 85: Comparison of % change in doubling time (T_d) of PTP1B + v-Src and TCPTP + v-Src transformed yeast cells in the presence of compound **30a** at 60, 140 and 200 μM . $n=6$ for all concentrations tested in both transformations, mean and individual points \pm standard deviation plotted. Used non-parametric Mann-Whitney t-test for statistical analysis. * p value ≤ 0.050 PTP1B + v-Src vs TCPTP + v-Src.

However as discussed previously the maximum activity is not one only factor to consider when looking at PTP inhibition, as potency which is calculated *via* EC₅₀ is also relevant. The calculated EC₅₀ values for compound **30a** in both PTP1B and TCPTP for the concentration range of 0-250 μ M are shown below in **Table 6**.

Table 6: Comparison of the EC₅₀ values for compound **30a** in PTP1B and TCPTP

	PTP1B inhibition	TCPTP inhibition
Maximum effect (%)	206	68
EC ₅₀ value (μ M)	158 \pm 21	132 \pm 10
Ratio (max effect: potency)	1:0.8	1:2

Maximum effect (%) denotes the percentage increase in doubling time of the PTP + v-Src cells with compound **30a** compared against base growth / growth without compound **30a** and does not refer to the percentage of PTP inhibited. All values are round to the nearest integral.

p value for EC₅₀: 0.0931 (ns)

As outlined in **Table 6** there is no statistically significant difference between the potency (EC₅₀) of compound **30a** towards PTP1B or TCPTP. Therefore, **30a** is equally potent towards both PTPs investigated.

Additionally compound **30a** can be described as selective for PTP1B but is not specific as it does as possess significant activity for TCPTP inhibition. To investigate this difference in inhibitory activity computational docking studies were conducted as it would be presumed that compound **30a** has a stronger binding affinity for the active site of PTP1B.

4.3.7.3.2 Computational modelling

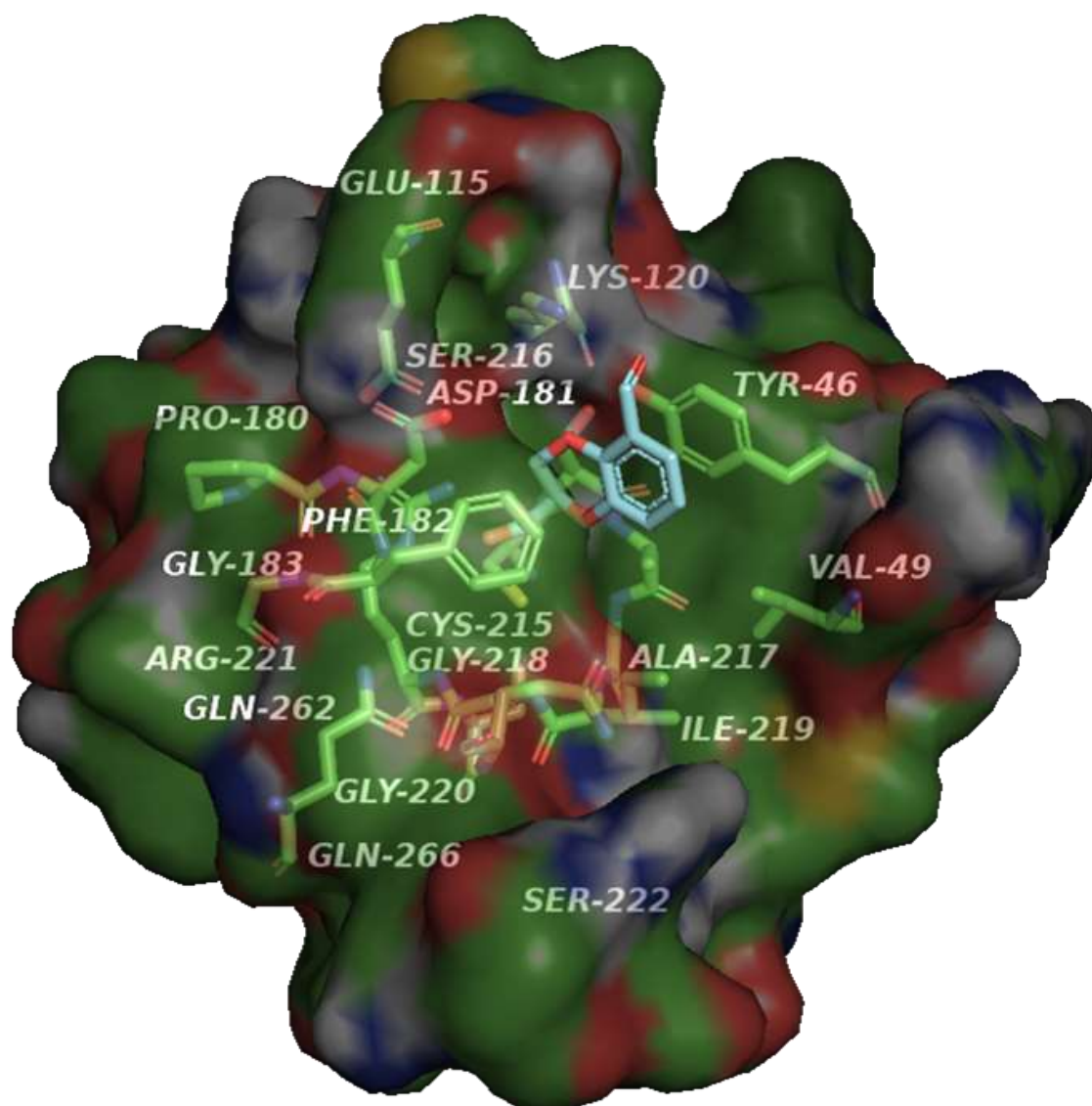


Figure 86: Computational most favoured proposed binding mode of compound **30a** in the closed conformation of the PTP1B active site.

From the computational docking study, the most computational favoured docking position of compound **30a** is presented in **Figure 86**. Protein-substrate interactions include the carboxylic acid residing in the base of the active site and interacting *via* hydrogen bonding with the Cys-215 and surrounding residues, Ser-216, Ala-217, Gly-220 and Arg-221. All of which are contained within the PTP1B active site loop as mentioned in Chapter 1 (section 1.4.3). Additional proposed interactions include the benzodioxane oxygens interacting with the amine of Ala-217 and phenol of Arg-46.

The benzene ring of compound **30a** is also thought to π -stack with Phe-182 and Tyr-46. But what is thought to be a significant contributor to the strength of the binding mode of compound **30a** to the PTP1B active site, thus the inhibitory activity is the proposed

covalent bond which forms between the aromatic carbonyl of compound **30a** and the anime of the Lys-120 residue.

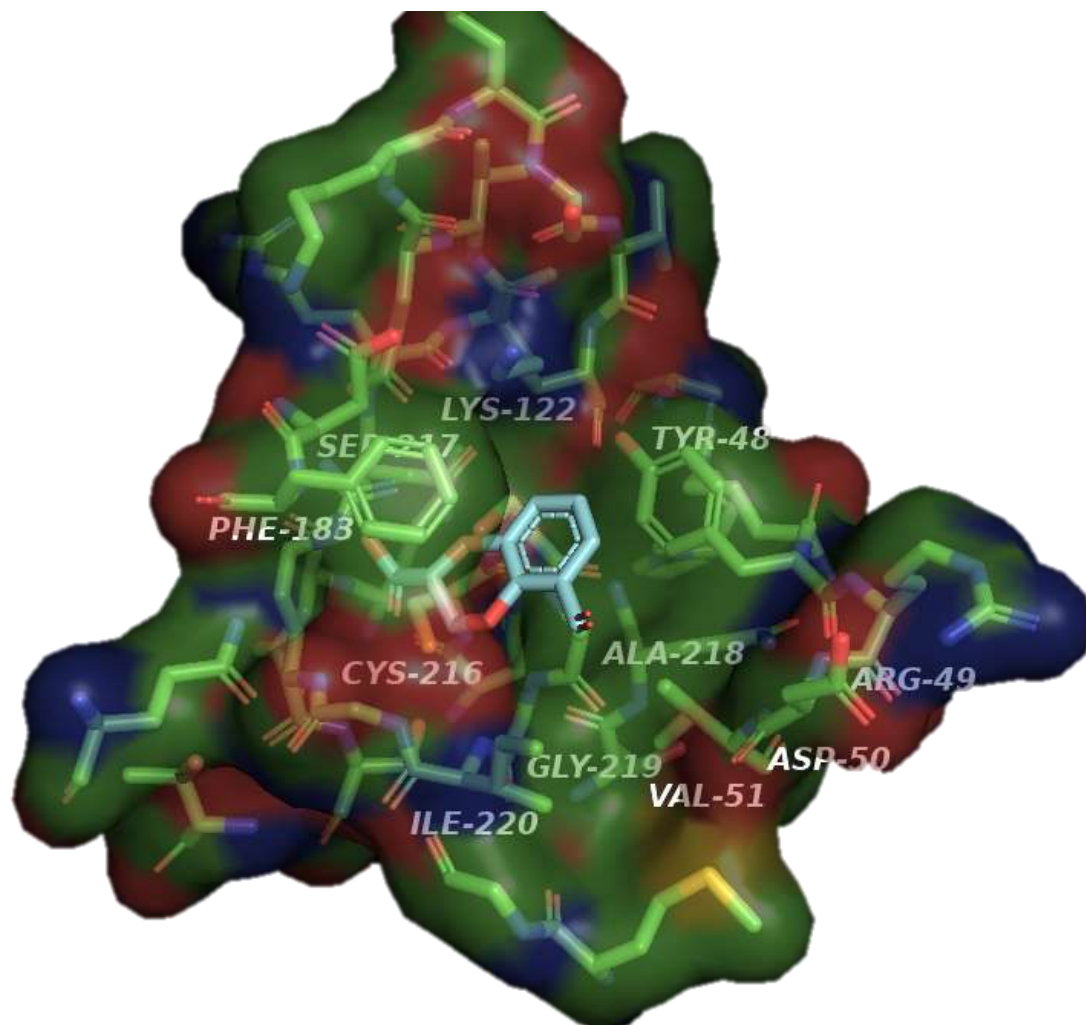


Figure 87: Computational most favoured proposed binding mode of compound **30a** in the closed conformation of the TCPTP active site.

Figure 87, illustrates the proposed binding mode of compound **30a** in the active site of TCPTP. This in part explains the reduced activity towards TCPTP as overall the probable binding mode in TCPTP is weaker, as from the computational data the orientation of compound **30a** with respect to the lysine residue (Lys-122), is inverted. As with PTP1B, the carboxylic acid motif of compound **30a** is located at the base of the TCPTP active site and interacting with the Cys-216 and surrounding residues, Ser-217, Ala-218, Gly-221 and Arg-222, again all of which are part of the active site loop and are essential for biological activity. However, unlike with PTP1B, in TCPTP it is computationally proposed that the favourable orientation of compound **30a** results in a relative 180° flip when compared to the PTP1B binding position. Therefore, the aromatic carbonyl is located away from Lys-122. Hence a covalent bond cannot be formed, meaning the

overall strength of the TCPTP bind mode is diminished thus resulting in a reduction inhibitory response in TCPTP. The orientation change may result in an interaction with the amide of Gln-260 however if such an interaction does occur it would be sufficiently weaker than the covalent bond formed with a lysine residue.

Despite this overall weaker TCPTP binding position, the interactions of compound **30a** with the carboxylic acid functional group, π -stacking with the benzene ring and a hydrogen bond between one of the benzodioxane oxygens, and the OH of the Ser-217 appear to still be sufficient for a significant biological response of TCPTP inhibition.

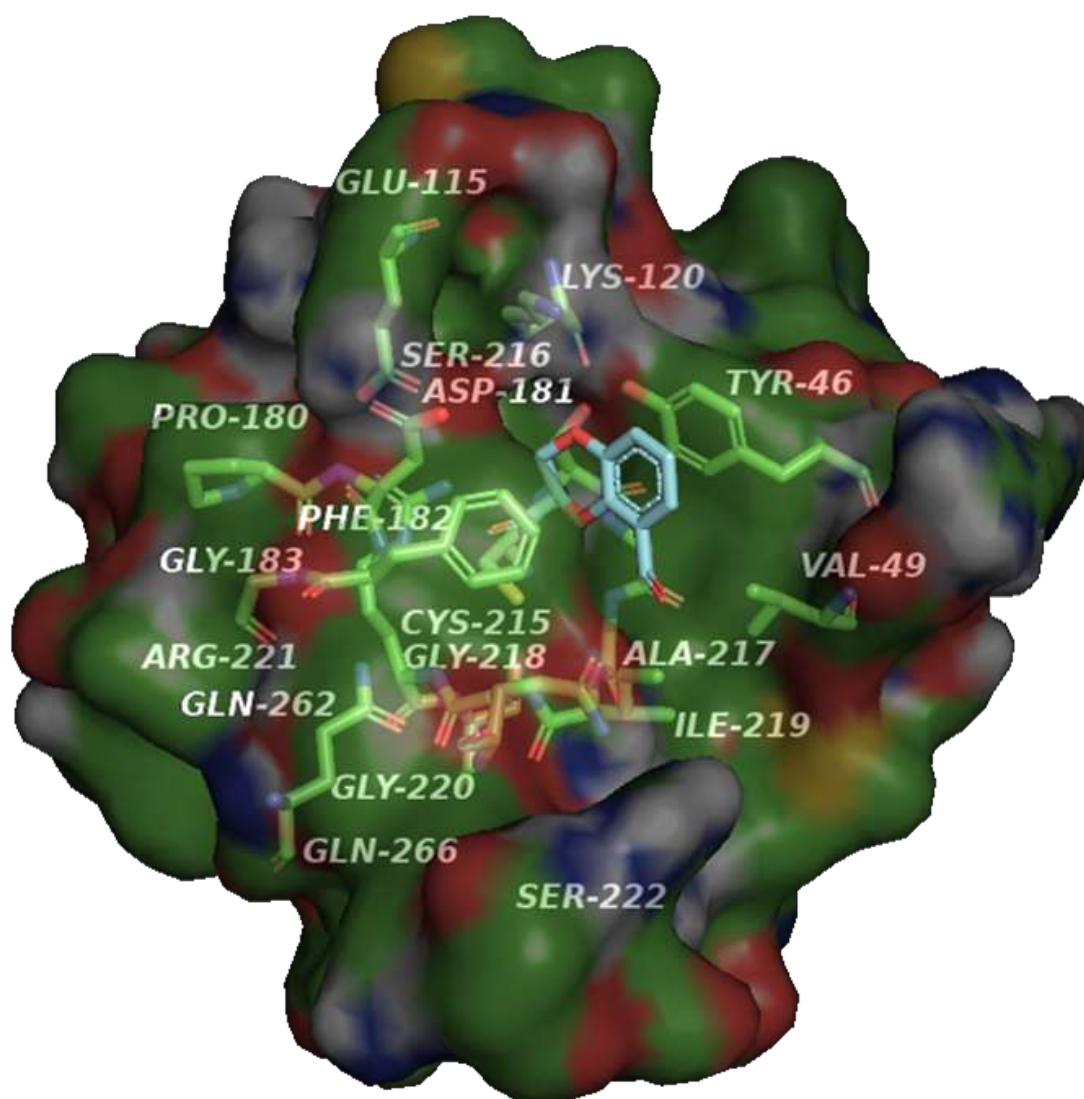


Figure 88: Computational most favoured proposed binding mode of the other structural isomer component of **30**, **30b** in the closed conformation of the PTP1B active site.

As discussed above when comparing the inhibitory activity of the 1:1 mixture of structural isomers to the single structural isomer of compound **30** it appears that the structural isomer compound **30b** (**Figure 82**) is mostly inactive as a PTP1B active site inhibitor. As shown in **Figure 88** the favoured computational docking position supports this isomers

inactivity as here the aldehyde away from the lysine residue preventing it from forming the covalent bond. Which as stated above is a key aspect of the binding mode of compound **30a** and the subsequent significant inhibitory activity. Hence the binding mode of compound **30b** in the PTP1B active site computationally is comparable to that of compound **25**, and as shown above also exhibited no significant inhibitory activity towards PTP1B.

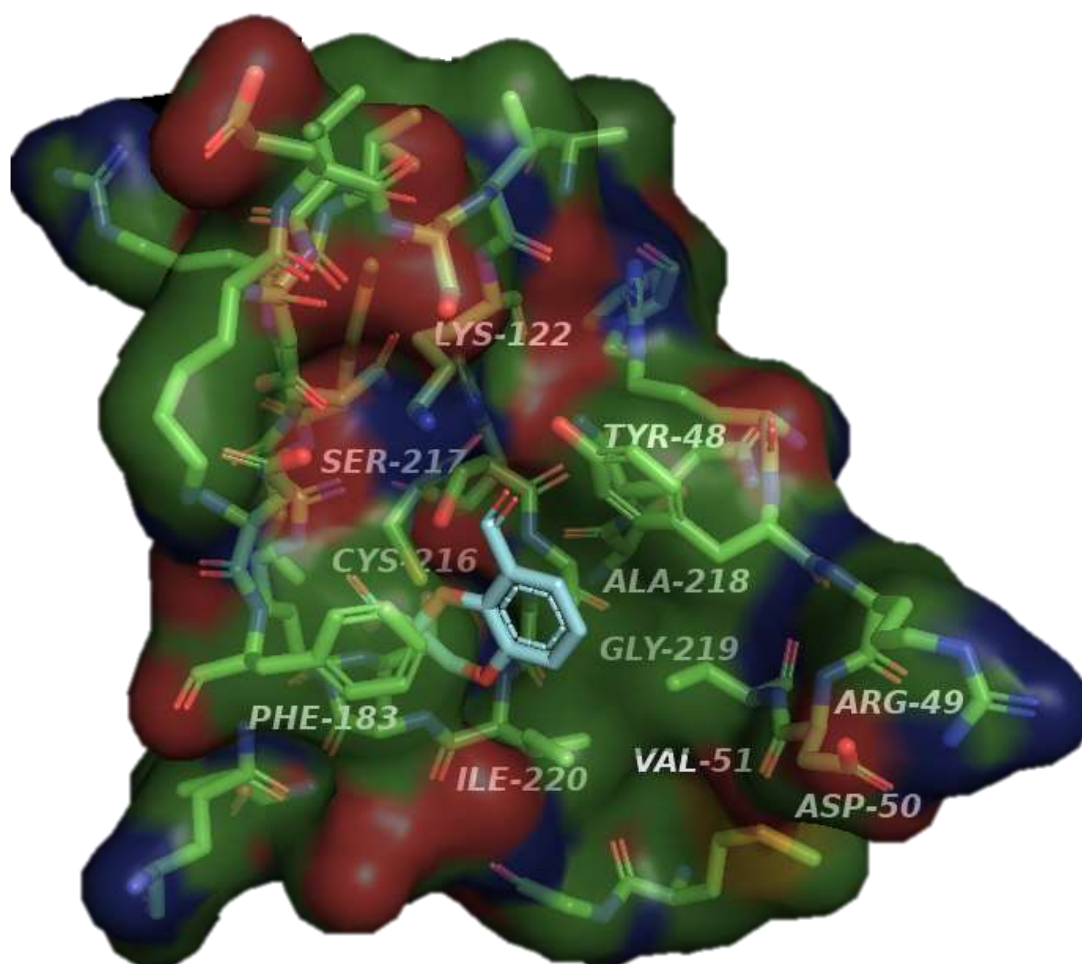


Figure 89: Computational most favoured proposed binding mode of the other structural isomer component of **30**, **30b** in the closed conformation of the TCPTP active site.

Because of this, it is proposed that the other structural isomer **30b** would not only be a significant TCPTP inhibitor but also selective towards TCPTP if the aldehyde is able to form a covalent with the Lys-122 residue present in the TCPTP active site. From the computational docking studies shown in **Figure 89** this is proposed to be plausible, but future work would need to be done to isolate and test this structural isomer.

When thinking about isomers another important consideration is that due to a chiral centre being present at the carbon adjacent to the carboxylic acid, for each structural isomer of compound **30** there are two enantiomers. Potentially only one of these is active or exerts a greater effect than the other. Hence the maximum inhibitory effect observed when testing compound **30a** in PTP1B + v-Src may in fact be greater if a single enantiomer of compound **30a** was acquired and tested. One possible way to achieve this other than with the use of a chiral column is by reacting the single structural isomer of compound **30a** with an enantiomerically pure amine as potentially one of the subsequent stereoisomer products could precipitate out of the solution enabling a single stereoisomer of compound **30a** to be acquired and tested.

When looking at the yeast-based T_d results of the single structural isomer (compound **30a**) a significant change in both the overall growth profile of PTP1B only cells and with the statistically higher than base T_d values at higher concentrations, it was determined that the toxicity of compound **30a** towards yeast cells would be investigated. This was done with the use of spot plates; the methodology and setup are explained in Chapter 7 (section 7.4.5).

4.3.7.3.3 Compound 30a yeast cell toxicity investigation

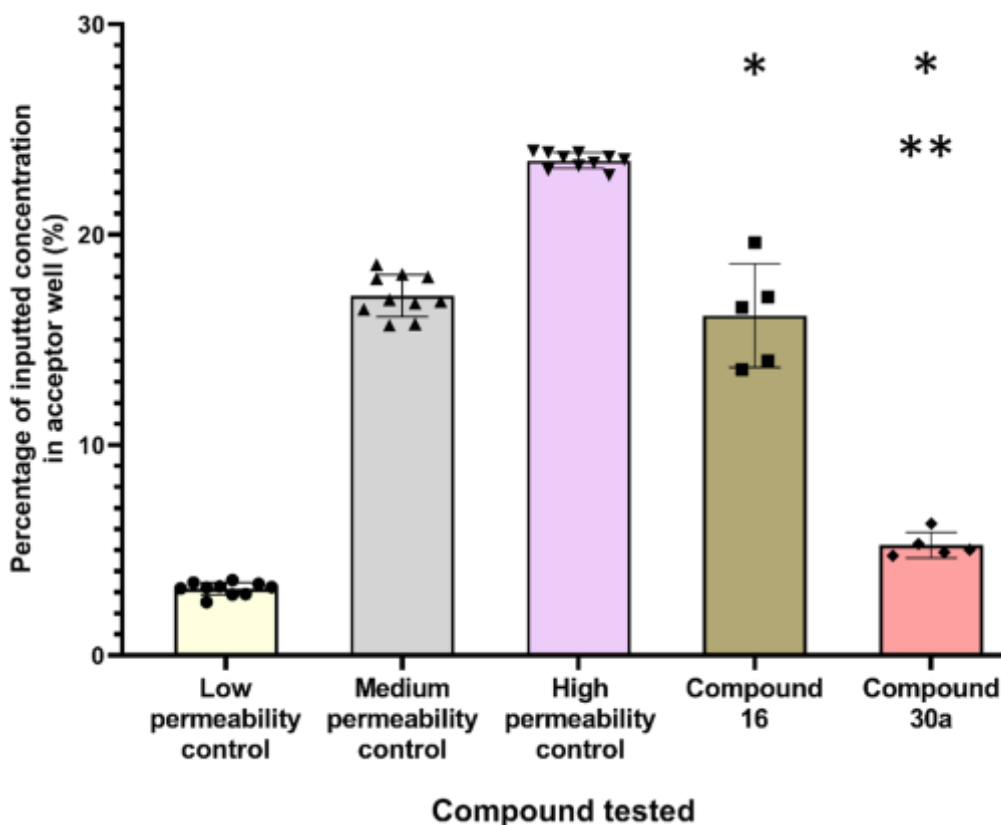
The toxicity of compound **30a** was investigated in both sets of PTP only and PTP + v-Src transcribed cells, in addition to the untransformed original YMK23 yeast cells. This was done to verify that the experimental data indeed was due to PTP inhibition and not off target effects.

The results for each transformation after 48 hours are presented in the appendix (section 2.3), as photographs, and demonstrate that compound **30a** is not toxic to any YMK23 transformation at or below a concentration of 250 μ M. Affirming that the significant increase in % change of T_d in PTP + v-Src transformed cells is predominately due to PTP inhibition.

4.3.7.3.4 Blood Brain Barrier comparison of initial hits

The final parameter considered before compound **16** or **30a** was taken forward as the bases of the subsequent compound library of potential inhibitors was blood brain barrier permeability. The BBB permeability of compound **16** and **30a** were assessed at RT and 37 °C. The results of which are stated in the appendix (section 2.2) and below in **Figure 90** at 37°C.

As shown below in **Figure 90**, at 37°C both compounds **16** and **30a**, were statistically more permeable to the synthetic BBB than the low permeability control (p value <0.001 for both). Despite this compound **16** is also significantly more BBB permeable than **30a** (p value <0.010) where the average acceptor well concentration of **16** was found to be over 2.5 times greater than for **30a**. compound **16** permeability was also found to be not significant when compared to the medium permeability control at 37°C however the permeability of compound **30a** was significantly less (p value <0.001).



Compound	16	30a
p value vs low control	<0.001	<0.001
p value vs medium control	ns	<0.001

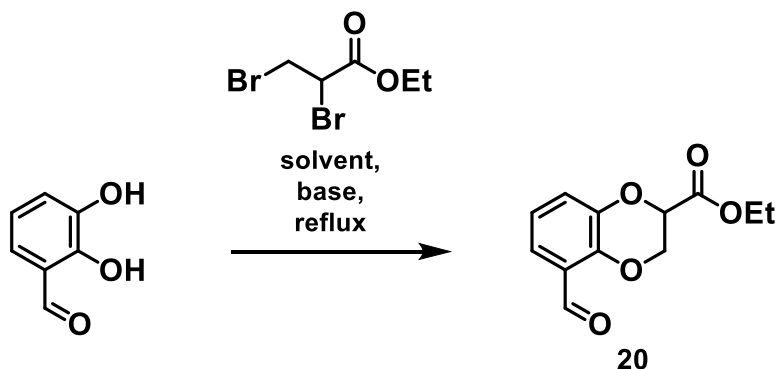
Figure 90: The percentage of the inputted concentration in the BBB assay acceptor well after 24 hrs at 37 °C. n=5 for all compounds tested, n=10 for permeability controls, mean and individual points \pm standard deviation plotted. Used non-parametric Mann-Whitney t-test for statistical analysis. * p value \leq 0.050 vs low control. ** p value \leq 0.050 vs medium control.

Therefore, in terms of predicted *in vivo* BBB permeability, compound **30a** is more promising than **16** as from acquired data **30a** is less permeable, and therefore more desirable for further investigation and functionalisation. In addition to exerting a greater biological effect.

4.3.7.3.5 Selection and justification of key hit for subsequent development.

Of all the identified PTP inhibitor hit compounds identified above, the single structural isomer of compound **30**, **30a** exerted the statistically best biological effect in PTP1B, demonstrated selectivity towards PTP1B over TCPTP and exhibiting low BBB permeability. Therefore, the contents of the subsequent compound library were based upon compound **30a** and the benzodioxane formation step of compound **20** was optimised to better enable compound **30a** and related compound synthesis.

4.3.8 Optimisation of compound 20 synthesis

Table 7: Optimisation of the formation of benzodioxane 20. ^a

entry	temp (°C)	base	solvent	% yield
1	60	K ₂ CO ₃	acetone	10
2	60	Cs ₂ CO ₃	acetone	38
3	60	Cs ₂ CO ₃	DMF	18
4	60	Cs ₂ CO ₃	THF	23
5	60	Cs ₂ CO ₃	DCM	32
6	60	Cs ₂ CO ₃	DMSO	- ^b
7	60	Cs ₂ CO ₃	toluene	- ^b
8	60	Cs ₂ CO ₃	chloroform	48
9	60	Cs ₂ CO ₃	EtOAc	73
10	80	K ₂ CO ₃	EtOAc	35
11	60	NEt ₃	acetone	- ^b
12	60	BaCO ₃	acetone	56
13	60	Li ₂ CO ₃	acetone	56
14	60	BaCO ₃	EtOAc	46
15	60	Li ₂ CO ₃	EtOAc	38
16	60	CsF	acetone	0 ^b
17	60	CsF	DMSO	0 ^c
18	60	NaOH	acetone	- ^b
19	60	KOtBu	acetone	85
20	60	Cs(OAc) ₂	acetone	27
21	70	Cs ₂ CO ₃	EtOAc	74
22	80	Cs₂CO₃	EtOAc	98

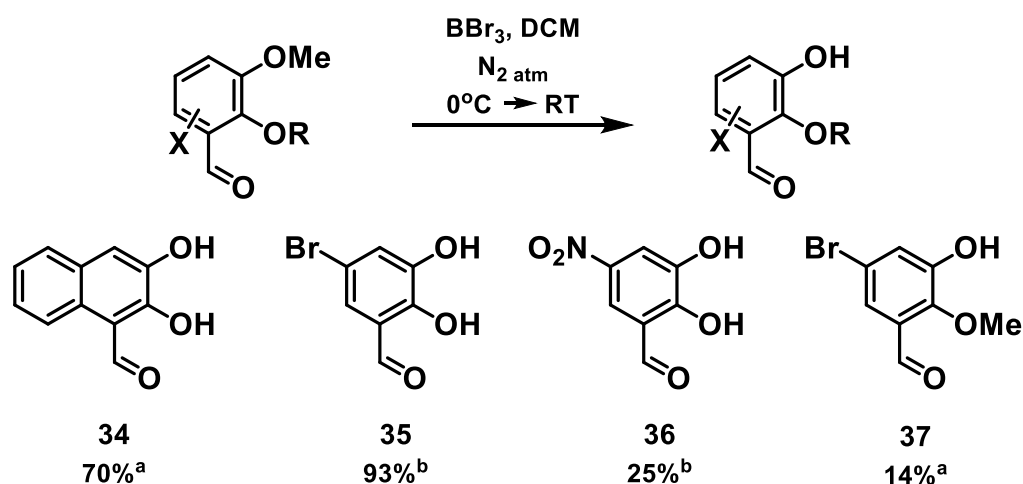
^a Reaction conditions: 0.5mmol scale, 1:1:2 Stoichiometry (2,3-dihydroxybenzaldehyde: compound 9: base), solvent = 3 ml, 24 hr reaction time. All stated yields are calculated with ¹H NMR using the internal standard 1,4-dinitrobenzene (0.025 equiv.). ^b Different product formed, or proportion of desired prod could not be identified. ^c Just starting material identified. Note NMR yields denotes both structural isomers.

As shown above in **Table 7**, the optimum conditions for forming compound **20** was **Table 7** entry 2: (caesium carbonate with acetone at 80 °C (reflux)), it was observed that of all the bases tested in both acetone and ethyl acetate only caesium carbonate performed better in ethyl acetate at 60 °C. Furthermore, generally stronger bases such as NaOH and triethylamine resulted in a mixture of compound including hydrolysis product. Therefore, such conditions are presumed to be too harsh for this substrate. Another result from this optimisation data is that different than was seen with spirocycle dihydropyrazole formation (Chapter 5, section 5.3.1) is that there is no correlation between the size of the group 1 counter ion and identified yield as Li_2CO_3 (**Table 7**, entry 13) and Cs_2CO_3 (**Table 7**, entry 2) both resulted in a higher yield than K_2CO_3 (**Table 7**, entry 1), despite having smaller and larger counterions than potassium respectively. The reason for this is unknown but regardless the optimisation for the formation of compound **20** resulted in an optimum isolated yield of 92% (structural isomer mixture (**20**)), or 60% (pure structural isomer (**20a**)).

With the formation of the precursor to compound **30a** optimised, the aim of the second compound library was to include derivatives of compound **30a** either by subsequent functionalisation of **30a** or with cyclisation with different but structurally related starting materials. As mentioned above it was identified computationally that having an H-bond acceptor *ortho* to the dioxane ring was beneficial for PTP1B active site binding.

4.3.9 Modification of compound 30a

4.3.9.1 Altering aromatic diol precursor of 30a



Scheme 28: Precursor formation of compound **30a** (hit) derivatives.

Aromatic diether ^a or ether ^b (1.0 equiv.), BBr_3 (2.0 equiv. per ether), DCM , N_2 (atm), 0°C .^{145,153}

$\text{R} = \text{H}$ or Me

Scheme 28 above shows a successful conversion from the diether or ether to diol when a benzaldehyde was present. None of these compounds (**34-37**) are commercially available.

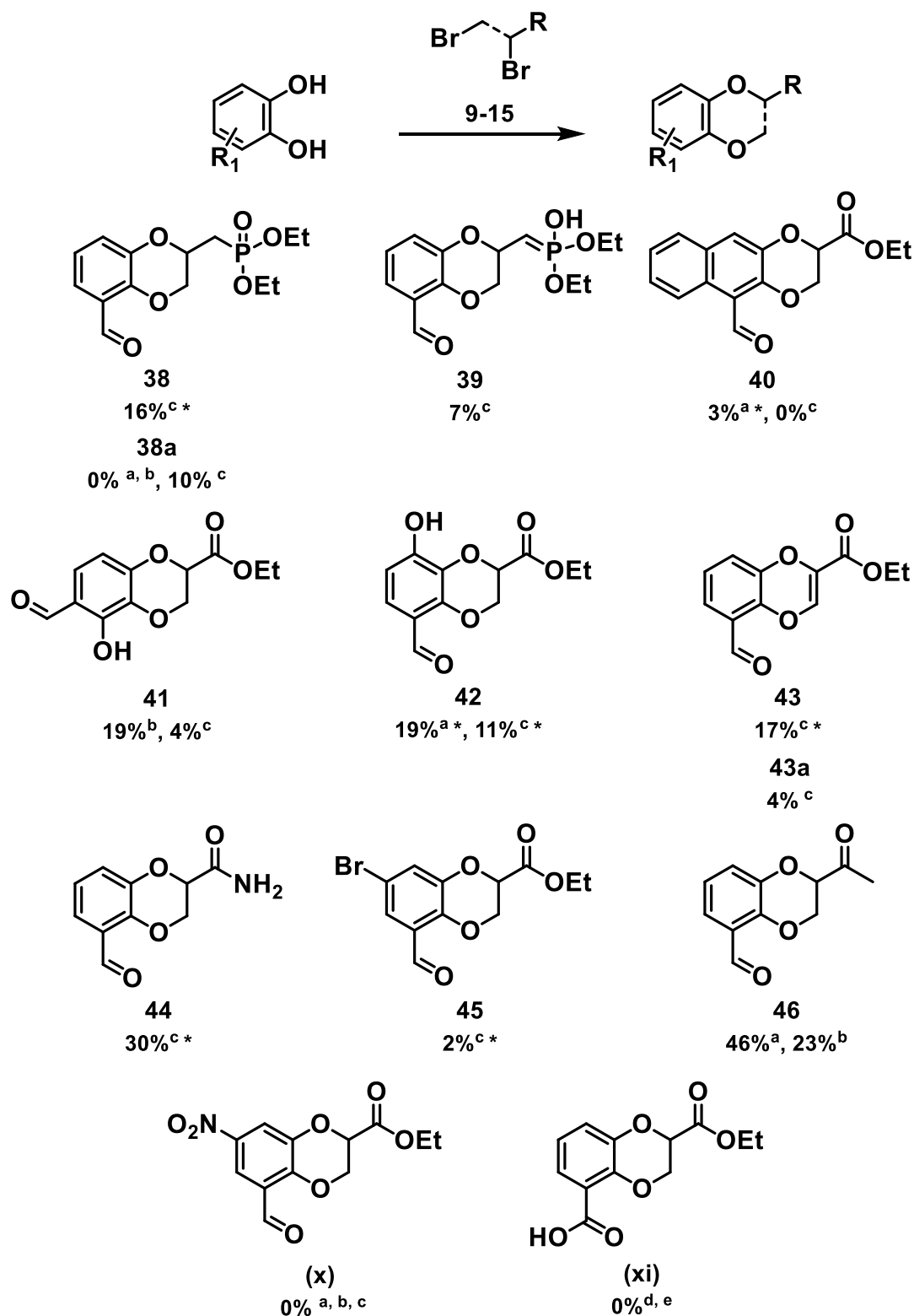
It is important to note that for the complete formation of compounds **34** a total of 4.0 equiv. of BBr_3 was needed, as two OMe groups were present to be hydrolysed and for compounds **35** and **36** 2.0 equiv. of BBr_3 was needed as only one ester (OMe group) was present in the starting material.

However, when the precursor to compound **37** was reacted with only 2.0 equiv. of BBr_3 , the resultant reaction mixture was of just compound **37**, meaning that for the 1,2-hydroxy-5-bromobenzaldehyde substrate the OMe *meta* to both the bromo and aldehyde functional groups exclusively reacted before the OMe *para* to the bromo 'R' group. Therefore, based on the known literature BBr_3 mechanism^{145,153} the oxygen of the favoured OMe is most likely more electron rich than the other. The evidence for the *meta* OMe being exclusively hydrolysed is demonstrated in the two-dimensional NMR spectroscopic data, as the aldehyde hydrogen signal can couple to the carbon signal of the aromatic carbon of the remaining OMe, but not for the formed OH. When 1,2-hydroxy-5-bromobenzaldehyde was reacted with 4.0 equiv. of BBr_3 complete conversion to compound **35** occurred in comparable yield (89%), when conducted on the same molar scale.

4.3.9.2 Utilising alternative dibrominated precursor compounds

With the 1,2-hydroxybenzaldehydes shown in **Scheme 28**, and the dibrominated compounds previously illustrated in **Scheme 18**, the following substrate scope of 1,4-benzodioxanes were formed with the previously shown with the cyclisation step. Isolated yields shown below in **Scheme 29**.

Despite all the compounds synthesised in **Scheme 29**, being based on compound **20** only one of the derivatives (compound **38**) resulted in the highest isolated yield when using the optimised methodology for compound **20**, for the rest (**39-46**) the literature reaction conditions¹³³ worked better.



Scheme 29: Formation of 1,4-benzodioxanes based on hit precursor compound **20**.

A 2,3-dihydroxybenzaldehyde (1.0 equiv.), base, solvent, after 10 mins compound **9-15** (1.0 equiv.) added, reflux until completion. ^a Acetone and K_2CO_3 (2.0 equiv.). ^b Acetone and Cs_2CO_3 (2.0 equiv.). ^c EtOAc and Cs_2CO_3 (2.0 equiv.). ^d EtOAc and Cs_2CO_3 (3.0 equiv.). ^e Acetone and K_2CO_3 (3.0 equiv.). ¹⁴⁵, 133

Structural isomer product ratios: compound **38** – 3:1, compound **40** – 1:1, compound **42** – 2:1, compound **43** – 5:1, compound **44** – 2:1 and compound **45** – 2:1.

* Mixture of two structural isomers, major illustrated.

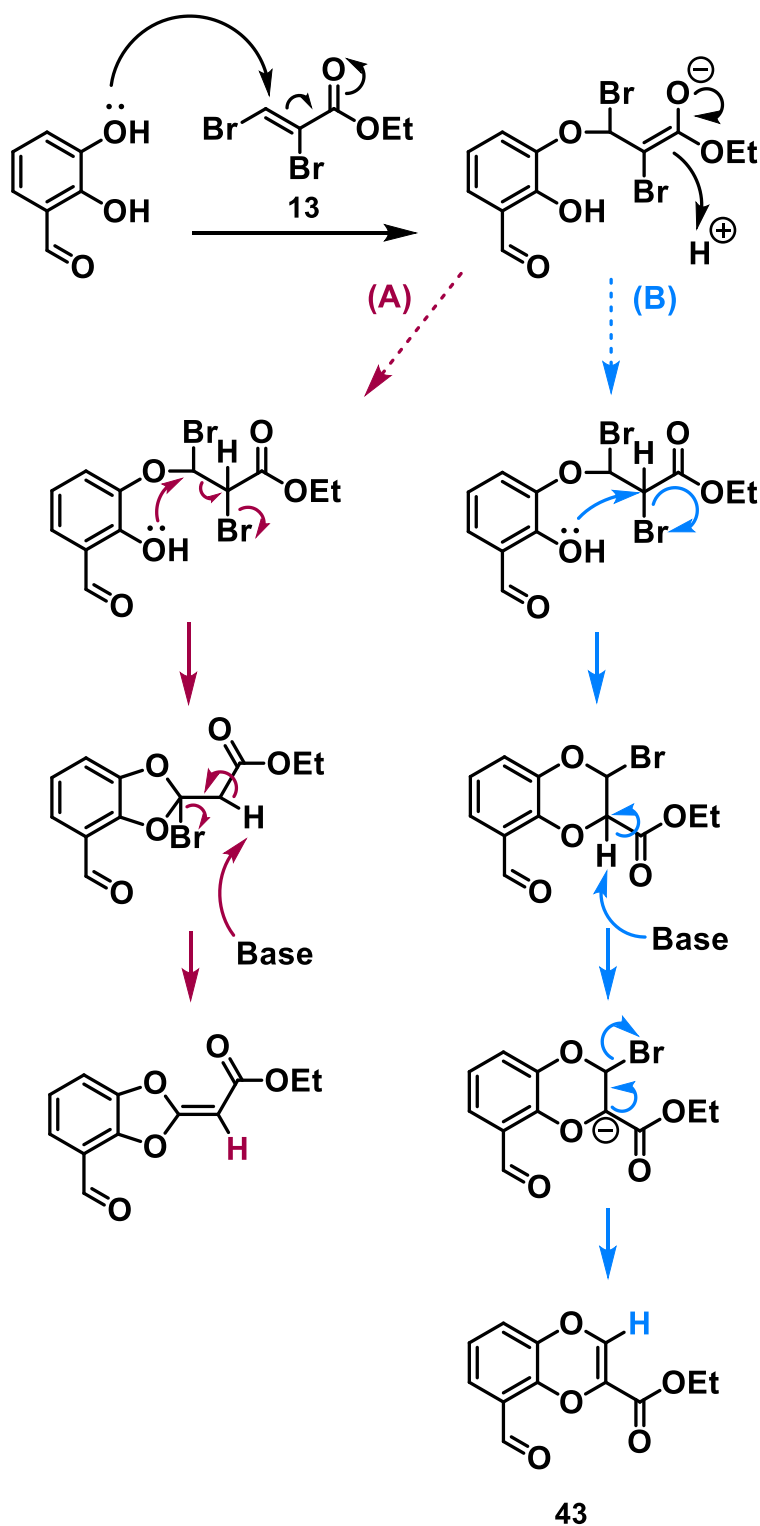
As **Scheme 29** shows, the attempted formation of compound **38** completely failed when K_2CO_3 was utilised with either acetone or EtOAc, as only starting materials were recovered. However, when the optimised conditions for the formation of compound **20** were deployed (Cs_2CO_3 with EtOAc at 80 °C), a moderate mixed yield of structural isomers (16%) was acquired. As with compound **20**, the major isomer of compound **38** could also be exclusively isolated *via* traditional column chromatography, as the major isomer would elute first, resulting in an isolated yield for the single isomer of 10%.

The increase in temperature with EtOAc over acetone maybe a primary reason why synthesis of compound **38** was unsuccessful when conducted in acetone. Additionally, a by-product (compound **39**) was also isolated simultaneously in the reaction between compound **10** and 2,3-dihydroxybenzaldehyde. Despite having only, a poor isolated yield of 7%, this is comparable to that of the expected major structural isomer product (compound **38**) whose yield was only 10%, and compound **39** formed exclusively the structural isomer shown in **Scheme 29**, however the mechanism for this compound's formation is not known and was not further investigated.

Compound **40** had a low isolated yield of 3% when the literature procedure was used, and no reaction occurred when the optimum methodology for compound **20** was used. The increased aromatic system may reduce likelihood of attack potentially due to the change in electronics and / or steric factors. This could be why a poor isolated yield occurs, as the reaction is less favourable.

Again, referring to **Scheme 29** when 2,3,4-trihydroxybenzaldehyde was reacted with compound **9**, as expected two different compounds, formed (**41** and **42**) due to three adjacent phenol motifs. When the literature procedure¹³³ was used, both compounds **41** and **42** were isolated in identical yields of 19%. However, when the alternative method was used a drop in yield for both products was observed, where the formation of compound **42** became favoured. Compound **41** was formed solely as a single structural isomer meaning that the top OH (*para* to aldehyde) also selectively attacks the same C-Br as shown above in **Scheme 21**, and if the middle OH initially attacks compound **9** it presumably cyclises with the OH *ortho* to the aldehyde. The reason is presumably due to the electronics of 2,3,4-trihydroxybenzaldehyde.

4.3.9.2.1 Proposed mechanism for compound 43 formation



Scheme 30: Two different proposed product forms of compound 43 and the potential corresponding mechanism of formation for each.

When an unsaturated debromination compound was used (**13**) the superior reaction conditions were Cs_2CO_3 with EtOAc at 80 °C, and the literature procedure yielded no product. But the maximum isolated yield of compound **43** was 17% as a mixture of structural isomers as a 5:1 ratio.

Due to the presence of the additional electron density from the alkene it was thought that the aforementioned mechanism of benzodioxane formation shown in **Scheme 21** may not be favoured. As shown in **Scheme 30**, a proposed alternative mechanism involving compound **13** resulted in the second oxygen anion attack occurring at the near unsaturated carbon instead resulting in a 5,6 fused ring system as seen in **Scheme 30** (A) rather than the previously exhibited 6,6 benzodioxane core (B). Due to both products from **Scheme 30** (A) and (B) having the same molecular mass and comparable IR profiles, ^1H NMR was the primary way of supporting which product had formed. This was done by looking at specifically the shift of the highlighted unsaturated H, as the expected shift at 400MHz for (A) product was ~4-5ppm and for (B) to be ~6-7ppm due to closer proximity to the benzodioxane ring making unsaturated (B) hydrogen more deshielded, thus more downfield. From the ^1H NMR spectra of the product for compound **43**, the unsaturated H was present at 6.94 ppm, so the product from **Scheme 30** (B) is the currently expected product.

The lower isolated yield of **43** when compared to **30** can be explained by the increased electron density of the dibrominated compound due to the unsaturated carbon-carbon bond. As it would make the attack of the oxygen lone pair from 2,3-dihydroxybenzaldehyde less favourable. Unfortunately, only a 4% yield for the major isomer of compound **43** was obtained *via* conventional column means as there was a greater degree of co-elution of the two structural isomers.

Compound **44** was the only compound **30a** derivative, where the major structural isomer was unable to be separated by conventional column techniques due to complete co-elution.

However, compound **44** as a structural isomer mixture, did show extensive biological activity against PTPs (see section 4.3.12 below), subsequent isomer separation and testing *via* more conventional means such as a chiral column would be justified for future work. This also could be achieved by utilising a Schmidt reaction¹⁵⁸ of the isometrically pure compound **30a** with an azide to convert the carboxylic acid to an amide (compound **44**).

From the biological results of testing just this structural isomer the relative activity of both structural isomers of compound **44** could be assessed.

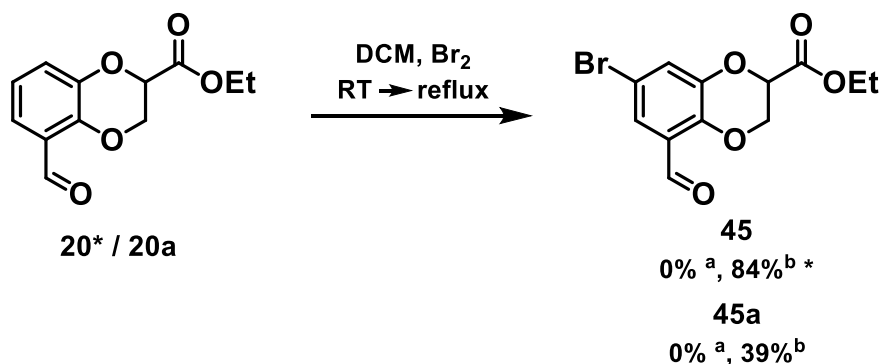
The formation of compound **46** (**Scheme 29**) was the only benzodioxane formation reaction which yielded a single structural isomer. It could be speculated that the reason why the OH *ortho* to the aldehyde of 2,3-dihydroxybenzaldehyde, is unable to attack compound **15** at the favoured position. Meaning that only the more electron rich OH of 2,3-dihydroxybenzaldehyde solely performs the initial attack yielding a single structural isomer.

Compound (**x**) was unable to be formed using any of the three deployed synthesis methods (**Scheme 29**). The reason for this is most likely comparable to why only a poor yield of 2% was acquired for compound **45**, as the presence of the nitro group most likely effects the electron density of the aromatic diol present in compound **36** resulting in the subsequent attack being unfavoured, hence why only starting material was recovered.

With regards to the attempted formation of compound (**xi**) (**Scheme 29**), an additional 1.0 equiv. of base was added to account for the presence of the carboxylic acid. This increase in base may be the primary reason as to why the formation of the desired product was identified let alone isolated. However as shown below in **Scheme 35**, the target compound for testing the hydrolysed version of compound (**xi**), compound **56** was successfully synthesised *via* a different synthetic route.

4.3.9.2.2 Alternative synthesis route for compound **45** formation

When compound **35** was reacted with compound **9** only a 2% yield was obtained (**Scheme 29**), however as shown below in **Scheme 31**, a superior isolated yield was obtained with an alternative synthesis route.



Scheme 31: Alternative synthesis route for the formation of compound **45**.

^a Compound **20** / **20a** (1.0 equiv.), NaAc (1.5 equiv.), acetic acid _{conc}, N₂ (atm), Br₂ (l) in acetic acid _{conc} (1.0 equiv.), RT. ^b Compound **20** / **20a** (1.0 equiv.), DCM, cooled to 0°C, Br₂ (l) (1.0 equiv.), acetic acid _{conc} (0.2 equiv.), RT to reflux. ^{145,153}

* Mixture of two structural isomers isolated major illustrated.

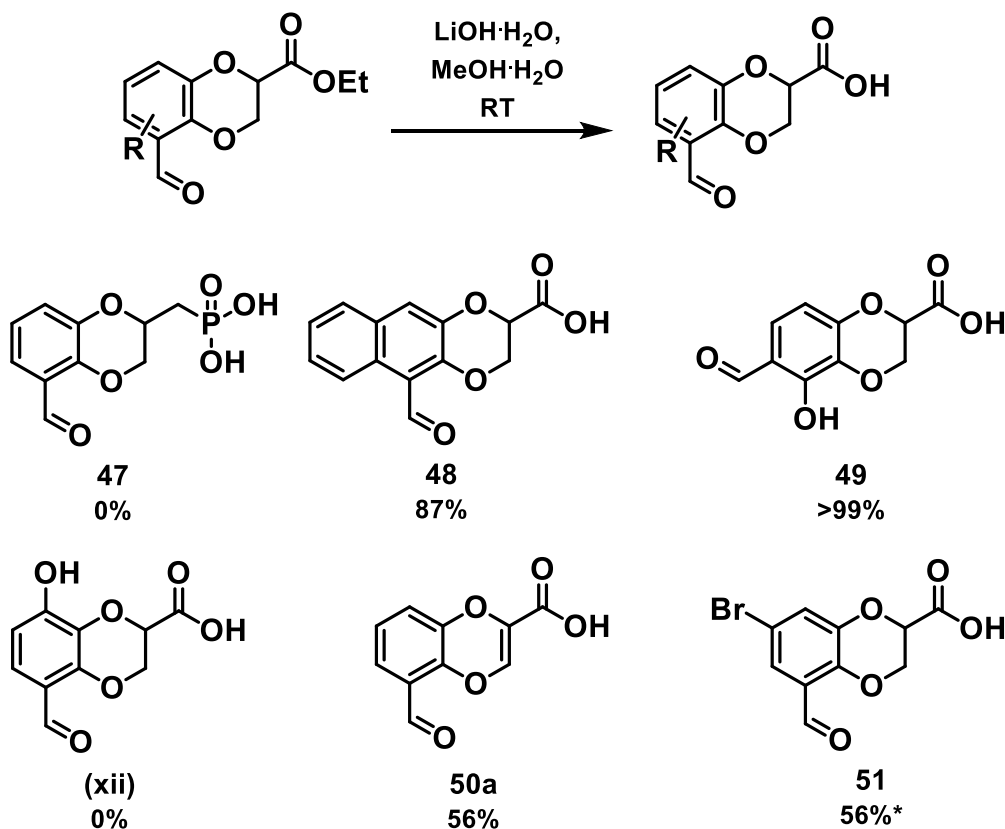
The initial investigation into the bromination of compound **20** was conducted using the structural isomer mixture as this was more prevalent and easier to acquire. The subsequent optimum methodology was latterly deployed on the isometrically pure version of compound **20**, compound **20a** to form compound **45a**. As shown in **Scheme 31**. ^{159,160}

The initial attempted reaction conditions utilising sodium acetate ¹⁶⁰ failed to occur as only starting material was recovered after an extensive reaction time. A synthetically simpler literature procedure ¹⁵⁹ was then deployed (procedure ^b from **Scheme 31**) at RT, as stated in this literature procedure. Again, only the starting materials were isolable but the presence of an additional compound forming by TLC was thought to be the product. This led the reaction to be repeated but after complete addition of all components the reaction mixture was refluxed at 50 °C overnight to selectively yield the bromination product compound **45**. This procedure was then repeated with compound **20a** to yield compound **45a** (single structural isomer).

The bromination of **45a** was shown to be selective at the position *meta* to the aldehyde by ¹H NMR as the splitting pattern of the remaining two aromatic hydrogens denotes w-coupling due the small frequency which is too small for the hydrogen environments to be adjacent.

4.3.9.3 Reactions to yield compound 30a derivatives.

With the derivatives of the precursor hit (compound 20) synthesised the next step in synthesising the next wave of benzodioxanes for biological testing was the ester removal of compounds 38, 40-43 and 45, as shown below in Scheme 32.



Scheme 32: Hydrolysis reaction to form compound 30a derivatives.

Compound 38a, 40-43 or 45 (1.0 equiv.), $\text{MeOH}\cdot\text{H}_2\text{O}$ (1:1), $\text{LiOH}\cdot\text{H}_2\text{O}$ (1.0 equiv.), RT.¹³³

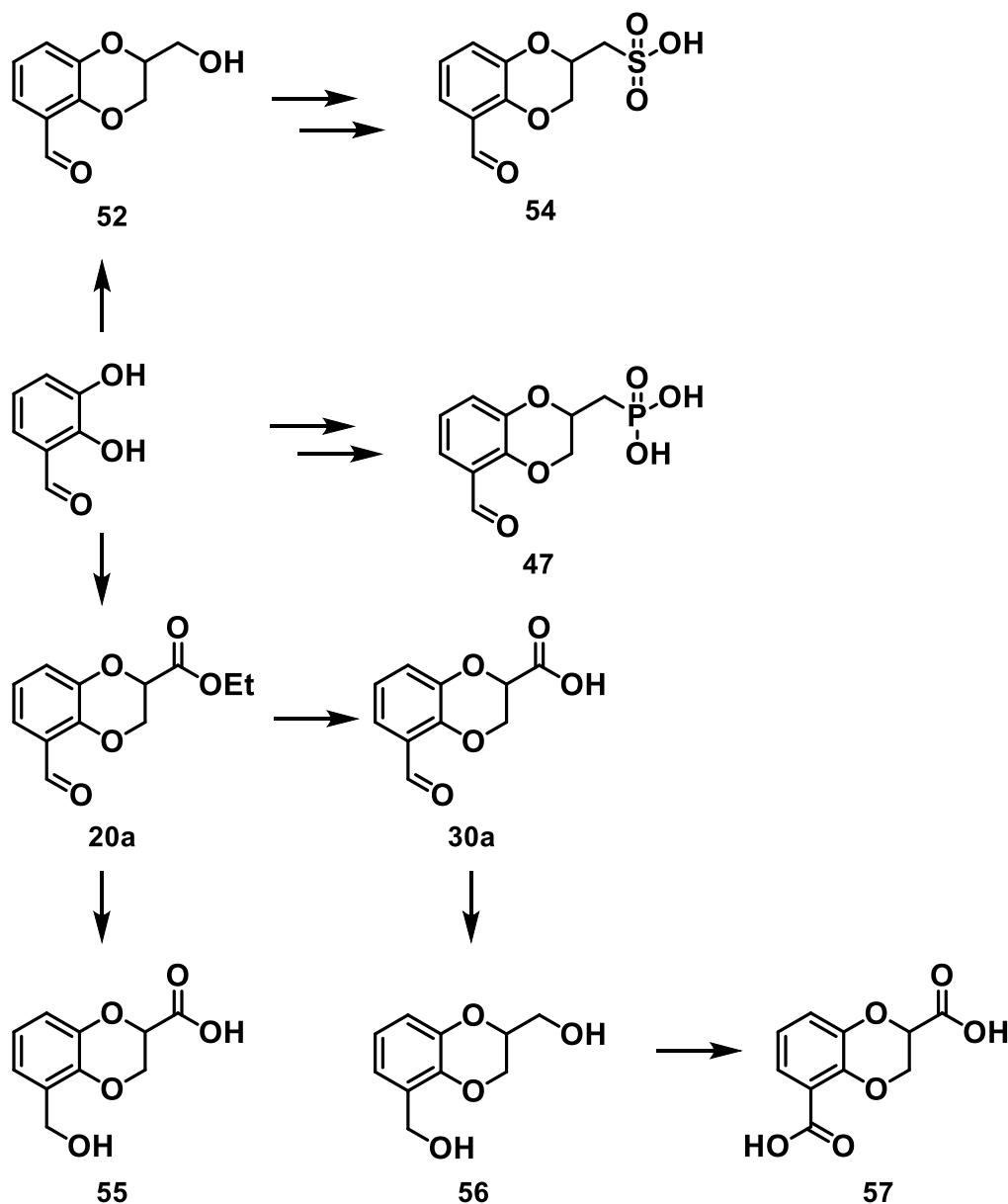
* Mix of two structural isomers isolated major illustrated, for ratio see Chapter 7.

As with the formation of compound 22, the methodology shown in Scheme 32 failed to hydrolyse the phosphodiester of compound 38 to form compound 47. However as shown in Scheme 33 and Scheme 34 below, the same synthesis method to form compound 32 also successfully formed compound 47 in a good, isolated yield of 70%.

In Scheme 32, an exceptional yield for the formation of compound 49 is reported, but the other benzodioxane formed from the prior synthesis step (compound 42) not only failed to form the desired product but also the starting material (compound 42) was unable to be recovered. It is thought that another unknown synthesis pathways occurred resulting in an inseparable reaction mixture. Due to the low isolated yield for compound 42 the removal of the ester was not attempted again with an alternative method. But if more time

was available the synthesis and biological testing of compound (xii) would be of interest as computationally the OH in the *para* position may be able to form additional hydrogen bond interactions.

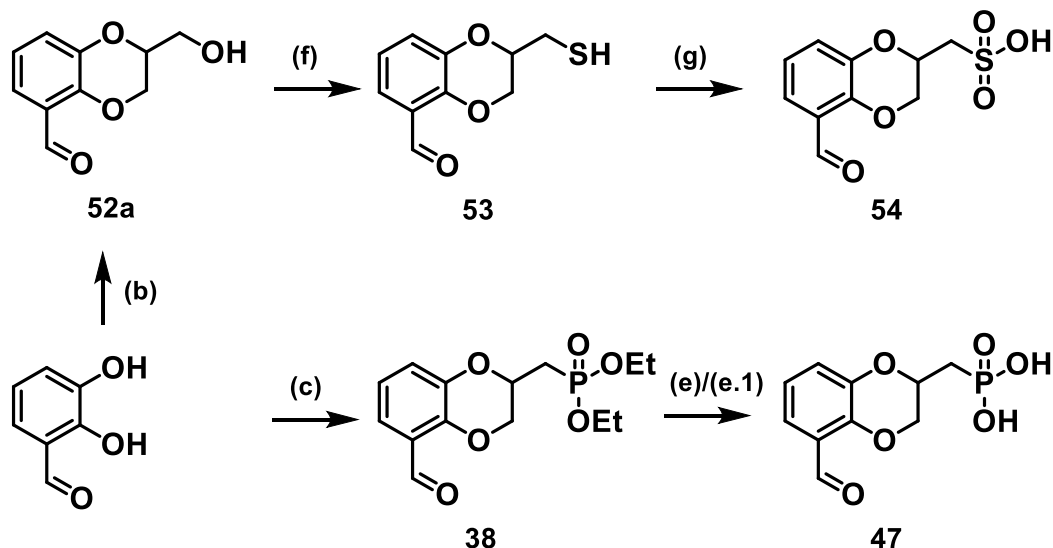
4.3.10 Synthesis of second wave of compound 30a derivatives.



Scheme 33: Overview of the final wave of compound 30a derivatives compounds synthesised.

An overview of final wave of benzodioxane based upon compound 30a, is summarised in **Scheme 33**^{132,145,148,153,161-165} where the key aim of this compound library was with improving potency and selectivity towards PTP1B.

This wave of benzodioxanes initially focused on combining prior hits with the aim of enhanced potency. These compounds, **47** and **54** were created in a moderate to good yield, as shown below in **Scheme 34**.



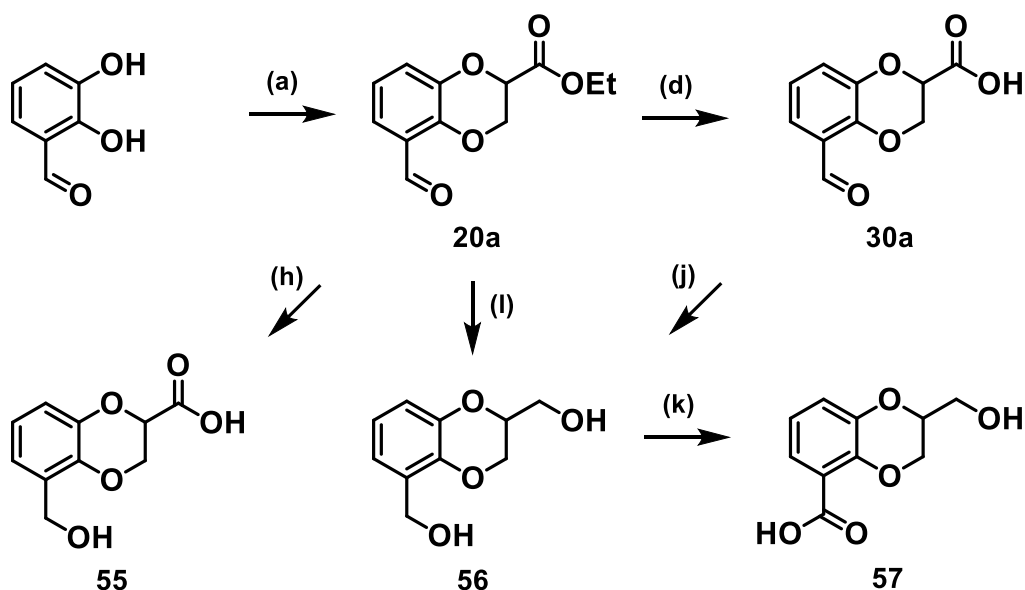
Scheme 34: Final wave of compound **30a** derivatives: part 1 combining hits.

(b): 2,3-dihydroxybenzaldehyde (1.0 equiv.), K_2CO_3 (2.0 equiv.), acetone, after 5 minutes compound **6** (1.0 equiv.) added, reflux until completion, 14% (**52a**), 40% (**50**)*. (c): 2,3-dihydroxybenzaldehyde (1.0 equiv.), Cs_2CO_3 (2.0 equiv.), EtOAc, after 10 mins compound **10** (1.0 equiv.) added, reflux until completion. 10%. (e): compound **38a** (1.0 equiv.), BBr_3 (1.0 equiv.), toluene, N_2 (atm), 0 °C to RT to 70 °C, 70%. (e.1): compound **38a** (1.0 equiv.), HCl_{conc} (2.0 equiv.), H_2O , 120 °C, 0%. (f): compound **52a** (1.0 equiv.), thiourea (1.0 equiv.), 4M HBr in acetic acid (2.0 equiv.), IMS, RT. Resuspend salt in H_2O , 50 °C, 33% NaOH (aq) (excess), 40%. (g) compound **53** (1.0 equiv.), glacial acetic acid, H_2O_2 (2.0 equiv.), RT, 31%.¹⁴⁵

* Mixture of two structural isomers isolated major illustrated.

The aim of the procedures outlined in **Scheme 34** was to combine the aspects from hit compounds **32** and **33** that bind to the Cys-215 residue of PTP1B better than a carboxylic acid motif, with the benzodioxane core structure of compound **30a**. In order enhance inhibitory activity while aiming to maintain low BBB permeability. The same methodologies were deployed as used to form compound **32** and **33**, however in the instance the intermediate thiol of **54**, compound **53** was also isolated and therefore tested.

The oxidation state of the carbon positioned in the carboxylic acid and the aldehyde of compound **30a** were also altered and the effects investigated to not only try and improve binding potential towards PTP active sites in general, but also provide selectivity towards the active site of PTP1B over TCPTP. In addition to better understand how and with which protein residues the interactions occur. This was conducted *via* the synthesis of compounds **56** – **58**, using the methodologies outlined in **Scheme 35** below.

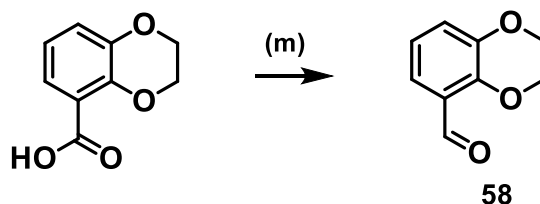


Scheme 35: Final wave of compound **30a** derivatives: part 2 altering oxidation states.

(a): 2,3-dihydroxybenzaldehyde (1.0 equiv.), Cs_2CO_3 (2.0 equiv.), EtOAc, after 10 mins compound **9** (1.0 equiv.) added, reflux until complexation, 34%. (d): compound **20a** (1.0 equiv.), MeOH:H₂O (1:1), LiOH.H₂O (1.0 equiv.), RT, 29%. (h): compound **20a** (1.0 equiv.), MeOH, NaBH₄ (1.0 equiv.), N₂ (atm), 0 °C to RT, 55%. (j): compound **30a** (1.0 equiv.), diethyl ether, LiAlH₄ (2.0 equiv.), N₂ (atm), 0 °C to RT 45%. (k): compound **56** (1.0 equiv.), MeOH:H₂O (1:2), 5 mol % Pd/C (0.05 equiv.), NaBH₄ (0.2 equiv.), KOH (6.0 equiv.), RT, 30%. (l): One-Pot synthesis. Pt 1, compound **20a** (1.0 equiv.), MeOH, NaBH₄ (1.0 equiv.), N₂ (atm), 0 °C to RT. Pt 2, MeOH, NaBH₄ (1.0 equiv.), N₂ (atm), 0 °C to RT 83%.

* Mixture of two structural isomers isolated major illustrated. ^{145,153}

The aim of the modifications on compound **30a** shown in **Scheme 35**, were again to improve the PTP1B inhibitor as a whole, with regards to potency, selectivity, and BBB impermeability, by altering the functional groups of compound **30a** which had been identified to be essential for binding from the computational docking data, and experimental work.



Scheme 36: Synthesis of compound **58**

(m): Step 1, 1,4-benzodioxan-5-carboxylic acid (1.0 equiv.), THF, LiAlH₄ (2.0 equiv.), N₂ (atm), 0 °C to RT. Step 2, PCC (2.0 equiv.), DCM, N₂ (atm), 0 °C to RT, 57%. ¹³²

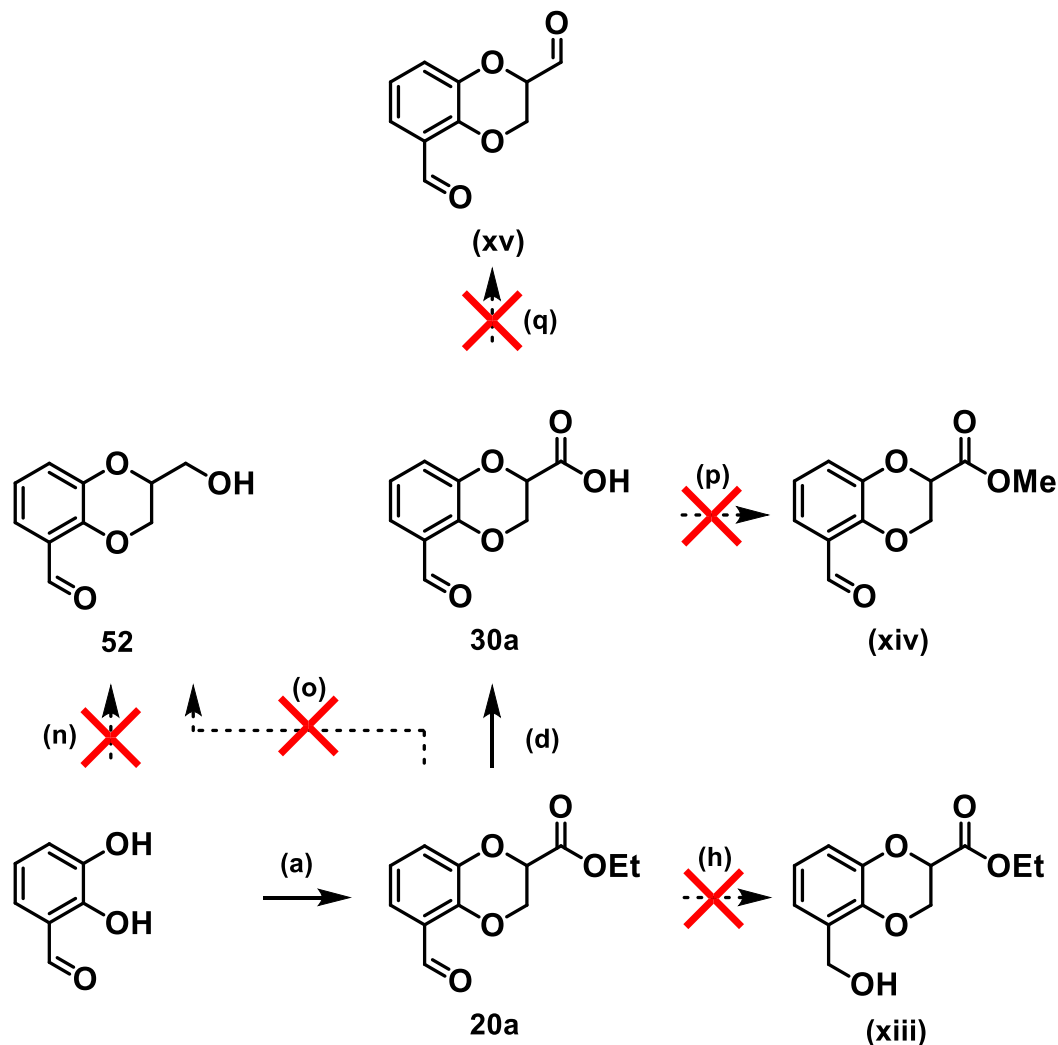
The aim of **Scheme 36** and the synthesis of compound **58**, ¹⁶⁶ was to investigate the binding mode of compound **30a** experimentally, by investigating the importance of different functional motifs in terms of binding. As demonstrated below in section 4.3.12, compound **58** does show greater PTP inhibitory activity (double the % change in T_d) than compound **20**, implying the aromatic aldehyde is a more important motif for the activity

of compound **30a** than the carboxylic acid. But the presence of both is drastically better than both individually.

4.3.11 Attempted unsuccessful procedures for other compound **30a** derivatives.

4.3.11.1 Further modification of compound **30a**.

Not every synthesis procedure utilised to form related compound to **30a** were successful. A number of these are shown below in **Scheme 37**.



Scheme 37: Failed functionalised reactions of hit compound **30a**.

(a): 2,3-dihydroxybenzaldehyde (1.0 equiv.), Cs_2CO_3 (2.0 equiv.), EtOAc, after 10 mins compound **9** (1.0 equiv.) added, reflux until completion, 34%. (d): compound **20a** (1.0 equiv.), MeOH:H₂O (1:1), LiOH.H₂O (1.0 equiv.), RT, 29%. compound **20a** (1.0 equiv.), MeOH, NaBH₄ (1.0 equiv.), N₂ (atm), 0 °C to RT, 0%. (n): 2,3-dihydroxybenzaldehyde (1.0 equiv.), Cs_2CO_3 (2.0 equiv.), acetone, after 5 minutes epichlorohydrin (1.0 equiv.) added, reflux until completion, 0%. (o): compound **20a** (1.0 equiv.), LiBH₄ (1.1 equiv.), ethyl ether, toluene, N₂ (atm), 40 °C, 0%. (p): compound **30a** (1.0 equiv.), KOH (1.2 equiv.), anhydrous DMSO, MeI (1.2 equiv.), RT, 0%. (q): Step 1, compound **30a** (1.0 equiv.), THF, LiAlH₄ (2.0 equiv.), N₂ (atm), 0 °C to RT. Step 2, PCC (4.0 equiv.), DCM, N₂ (atm), 0 °C to RT, 57%, 0%.¹³²

Scheme 37^{145,148,149,159,161,167,168} shows two-alternative attempted methods for the synthesis of compound **52a**. In both cases only starting material was recovered, implying conditions were insufficient for reactivity. For the hydrolysis of the corresponding ester (**Scheme 37**, procedure (o)), as this method provided the highest isolated yield for compound **7** (**Scheme 17**). But as the major structural isomer of compound **52a** was successfully formed with compound **6** (**Scheme 33**, procedure (b)), no further investigation into this method was conducted.

Another failed reaction was of compound **20a**, to form the respective ketone (compound **(xv)**, **Scheme 37**), an alternative method to obtain compound **(xv)** could be the selective partial oxidation of compound **52a**, but as this compound was not expected to have better biological activity than compound **30a** other synthetic reactions were prioritised.

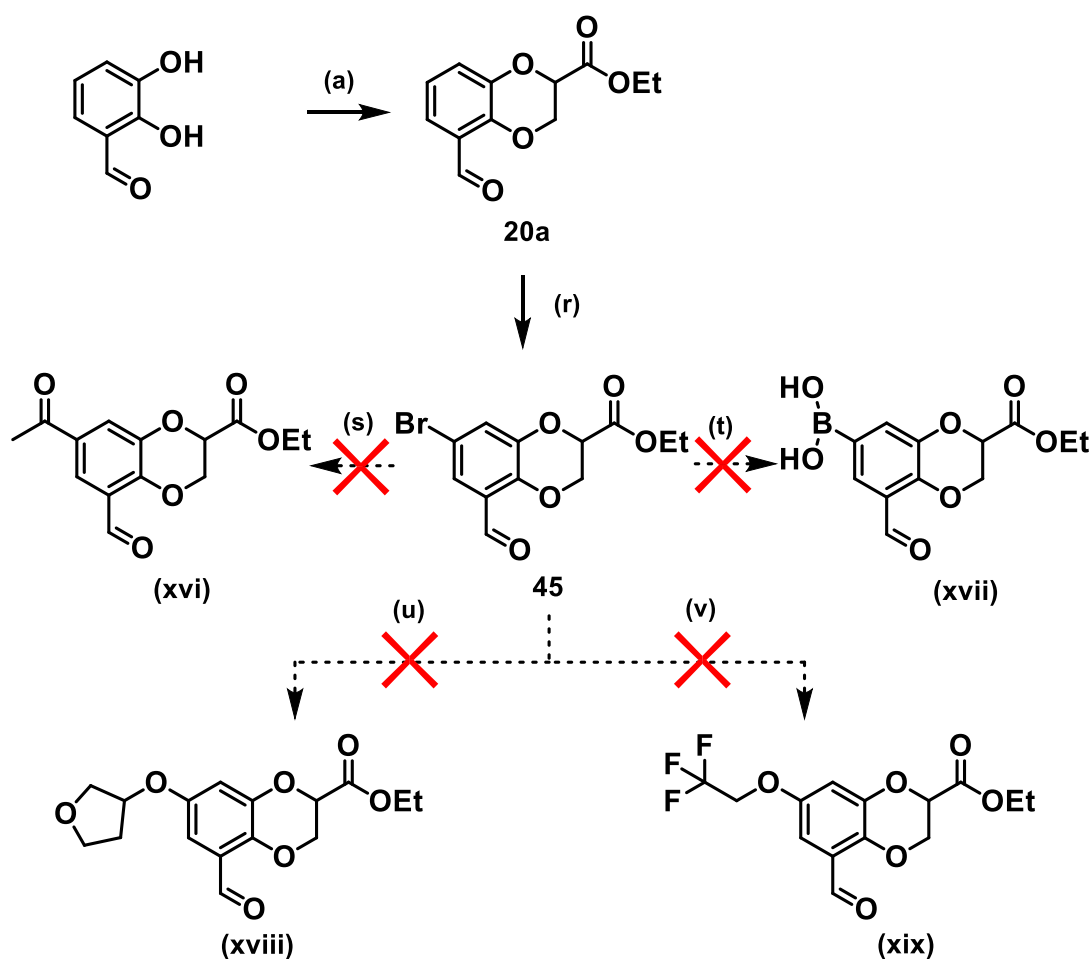
Procedure (p) in **Scheme 37**, was another reaction involving the carboxylic acid group of compound **30a**, and again the expected product of compound **(xiv)**, did not form and instead starting material was again mostly recovered.

The fact that these well-established literature procedures were unsuccessful, demonstrates the apparent stability of compound **30a**, which is a desirable trait for potential pharmaceutical compounds. Another synthetic route to obtain compound **(xiv)** could be the cyclisation method of 2,3-dihydroxybenzaldehyde with the required dibromo compound (methyl 2,3-dibromopropanoate).

Procedure (h) shown in **Scheme 33** and **Scheme 37** formed compound **56** instead of the expected product compound **(xiii)**, in a moderate yield of 55%. The ultimate target compound (the hydrolysed product of compound **(xiii)**) from this procedure was successfully formed *via* a different one-pot, two step synthesis method (procedure (l), **Scheme 33**), to form compound **55** in a good yield of 83%, so was not further investigated.

The hydrolysis of compound **45** to **51** seen in **Scheme 32** above was only conducted with the mixture of structural isomers as the formation of compound **45** was only for subsequent substitution reactions. To explore additional compound **30a** derivatives for testing, however as shown below in **Scheme 38** below such reactions with **45** all failed.

4.3.11.2 Attempted substitution reactions with compound 45



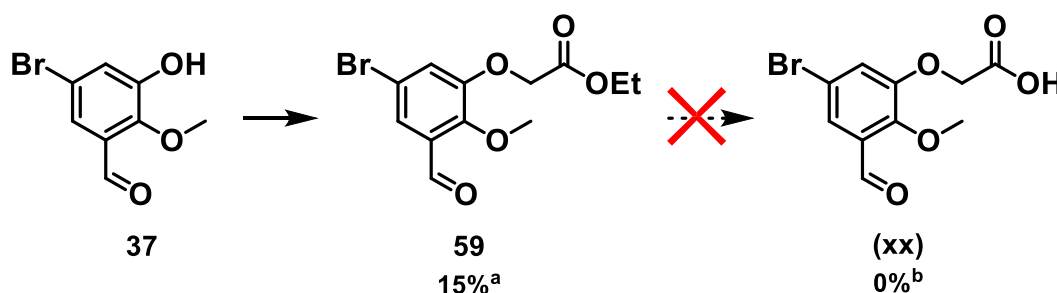
Scheme 38: Unsuccessful functionalised reactions of compound 45.

(a): 2,3-dihydroxybenzaldehyde (1.0 equiv.), Cs_2CO_3 (2.0 equiv.), EtOAc, after 10 mins compound 9 (1.0 equiv.) added, reflux until completion, 34%. (r): compound 20a (1.0 equiv.), DCM, cooled to 0 °C, Br_2 (l) (1.0 equiv.), RT to reflux, 39%. (s): compound 45 (1.0 equiv.), K_2CO_3 (2.0 equiv.), MeCN:H₂O (2:3), butyl vinyl ether (1.5 equiv.), $\text{Pd}(\text{OAc})_2$ (0.005 equiv.), 1,3-bis(diphenylphosphino)propane (0.01 equiv.), refluxed, 8 hrs, 0%. (t): compound 45 (1.0 equiv.), THF, 0 °C, n-BuLi (1.1 equiv.), after 30 minutes added $\text{B}(\text{OMe})_3$ (1.1 equiv.), 0%. (u): compound 45 (1.0 equiv.), NEt_3 (2.0 equiv.), DCM, primary alcohol (1.0 equiv.), RT, 0% (xvi), 0% (xvii). (v): compound 45 (1.0 equiv.), anhydrous DMF, Na metal (2.5 equiv.), CuI (0.02 equiv.), 3-hydroxytetrahydrofuran (1.0 equiv.), 110 °C, 0%.^{149,159,161,167}

As mentioned previously the main purpose for the synthesis of compound 45, was not for itself to be tested but rather be an intermediate compound enabling functionalisation to be built off the *meta* aromatic position (from the aldehyde). However as shown above in both Scheme 24 and Scheme 38 the functional groups bound to the 1,4-benzodioxane core appear to be unreactive. As when a literature procedure¹⁴⁹ to reduce aromatic nitro group of compound 17 to an anime group for subsequent reactivity was unsuccessful (Scheme 24). Furthermore, as shown in Scheme 38 four different literature procedures with a total of four different substrates all failed to react with the bromide of compound

45, resulting in partial starting material recovery after an extensive reaction time (72 hours plus). Potentially procedures (s) and (t) could be conducted on 5-bromo-2,3-dimethoxybenzaldehyde which is commercially available and then providing the subsequent acidic cleavage of the OMe groups and latter cyclisation and hydrolysis reactions were successful then this could be an alternative synthesis route to compounds (**xiv**) – (**xvii**) or similar.

4.3.11.3 Hydrolysis of compound **59**



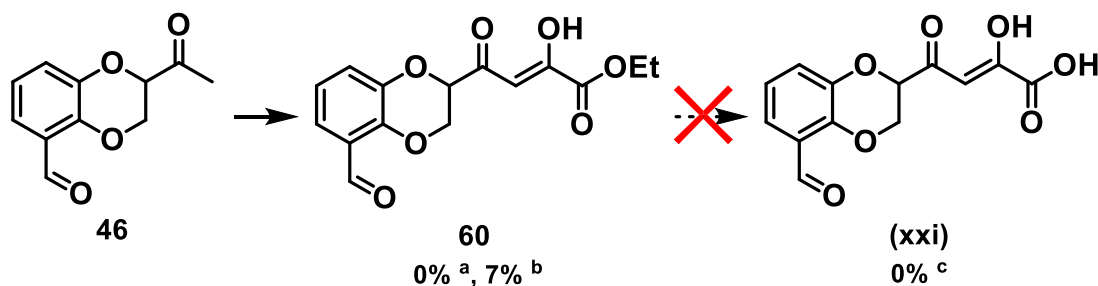
Scheme 39: Reactivity of compound **37**.

^a Compound **37** (1.0 equiv.), DCM, RT, NEt₃ (2.0 equiv.), after 5 minutes added ethyl 2-bromoacetate (1.1 equiv.), RT. ^b Compound **59** (1.0 equiv.), MeOH:H₂O (1:1), LiOH.H₂O (1.0 equiv.), RT. ¹⁴⁵

As demonstrated above in **Scheme 39**, procedure (u) from **Scheme 38** did successfully form compound **59** from **37** in a relatively poor yield of 15%. The subsequent ester removal method used failed to form compound (**xx**). Potentially the harsher method used to synthesise compounds **32** and **47**, could have been tried if a greater quantity of compound **59** was obtained.

If compound (**xx**) was acquired the same procedure would have been conducted on 3-hydroxy-2-methoxybenzaldehyde to form the non-brominated version of compound (**xx**). This would have been biologically tested for PTP active site inhibition and compared against **30a**. It is predicted that by altering the cyclic system the effectiveness would be reduced, as that is the normal observed trend in drug-discovery as molecular shape plays a key role in target binding.

4.3.11.4 Attempted incorporation of the binding motif of LZP25 with benzodioxane core of hit compound 30a.



Scheme 40: Attempted inclusion of LZP25 binding motif with 2,3-dihydroxybenzaldehyde.

^a Compound **46** (1.0 equiv.), toluene, KOtBu (2.0 equiv.), diethyl oxylate (2.0 equiv.), N₂ (atm), RT.

^b Compound **46** (1.0 equiv.), diethyl oxylate (2.0 equiv.), THF, NaOMe (2.0 equiv.), N₂ (atm), RT.

^c Compound **46** (1.0 equiv.), MeOH:H₂O (1:1), or MeOH:DCM (1:1), LiOH.H₂O (1.0 equiv.), RT. ^{135,145}

Another designed potential PTP1B inhibitor was compound **(xxi)** shown above in **Scheme 40**. ^{135,145} **(xxi)** was based upon the motif from the known inhibitor LZP25 which interacts with Cys-215 and surrounding residues of the active site and the discovered biological hit, **30a**. The intermediate, compound **60**, which was successfully synthesised from **46** *via* the same methodology used to form LZP25, as shown in Chapter 3 (section 3.3.2).

However only a poor yield of 7% was isolated for compound **60**, and the subsequent hydrolysis failed, resulting in limited recovery of starting material. Potentially the method used to form compounds **32** and **47**, may be successful but due to the poor yield of compound **60** this was not attempted.

During future work, the synthesis and investigation into compound **(xxi)** may be of interest but due to the increased size of the LZP25 motif the benzaldehyde motif which is thought to be key for compound **30a** binding would be in a different position and thus potential unable to interact as effectively with active site residues which could overall result in a less potent inhibitor, but this cannot be said with any certainty without experimental data.

4.3.12 Biological testing of compound 30a derivatives.

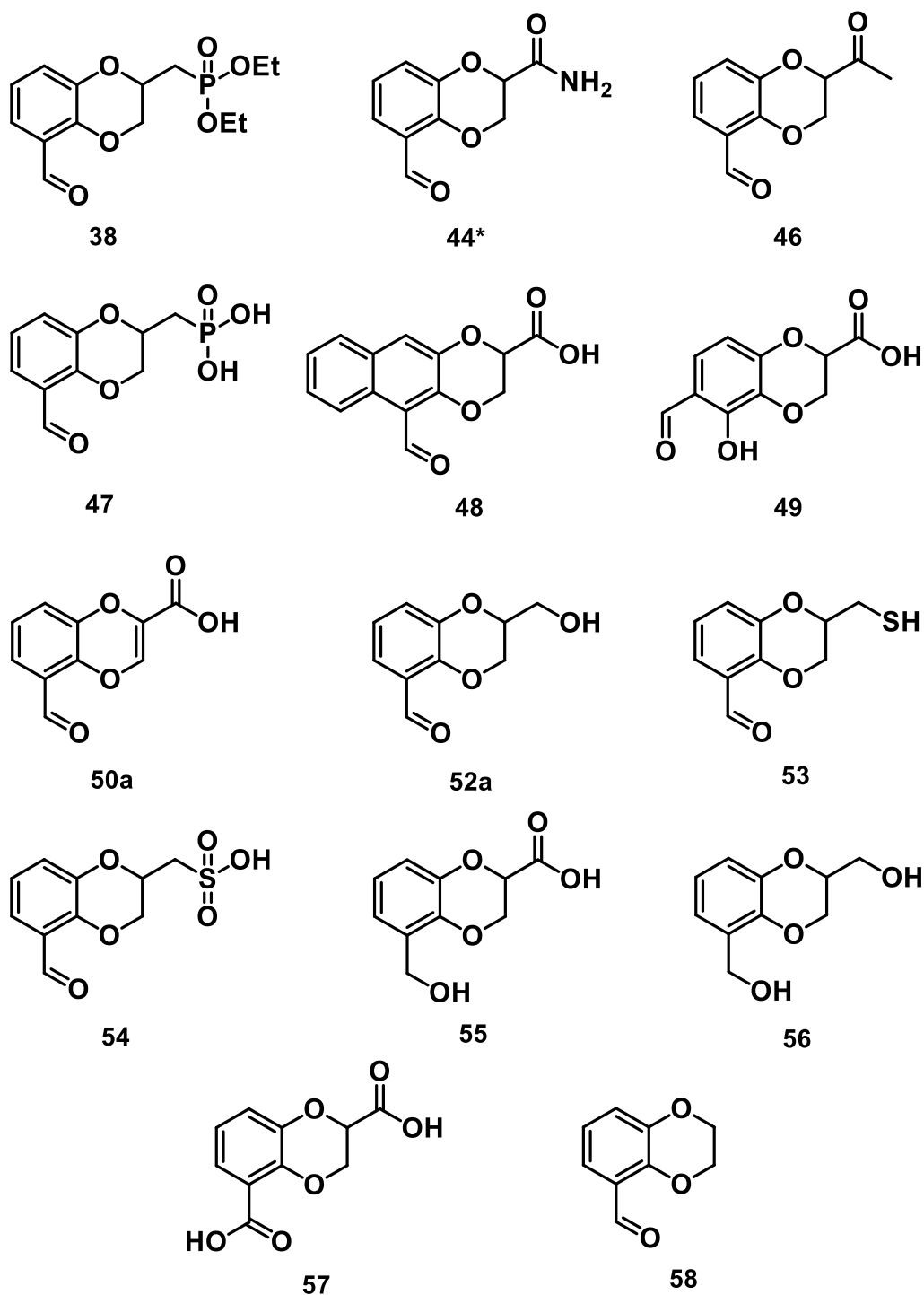


Figure 91: Compound library of compound 30a derivatives tested for PTP inhibitory activity.

* Mix of two structural isomers identified with major isomer illustrated, for the ratio see Chapter 7.

The structures of the compound **30a** derivatives tested are shown above in **Figure 91** the synthesis of which are predominantly found above in **Scheme 32**, **Scheme 34** and **Scheme 35**. With the exception of compound **38** where the synthesis is found in **Scheme 29**, none of the precursor benzodioxane compounds (**Scheme 32**) were tested. This was due to time constraints and from the computational data the final target derivatives were prioritised.

4.3.12.1 PTP activity compound **30a** derivatives

Due to the potential for all the derivatives of compound **30a** to possess activity towards both PTP1B and TCPTP it was decided that both would be tested, from the start.

Initial investigation of the compound library of compound **30a** derivatives displayed in **Figure 91** was conducted at 100 μM in both PTPs of interest, the results of which can be found in the appendix (section 2.1.7).

The only derivative to exert a significantly greater effect than compound **30a** was **44** (p value <0.050). As shown in **Figure 91**, the alteration of compound **30a** to **44** was the substitution of the carboxylic acid with an amide functional group. However as previously stated the biological results from **44** are from a mixture of structural isomers which unlike with compound **30** could not be separated by attempted methods. But due to time constraints, investigation of another more promising compounds was prioritised due to the high TCPTP inhibitory activity (average % increase of 83% at 100 μM) of compound **44**, but regardless future work on the separation and testing of both structural isomers of **44** is justified.

Of the fourteen derivative compounds tested, six of them exerted a statistically comparable inhibitory effect on PTP1B than compound **30a** at 100 μM (appendix, section 2.1.7). These were compounds **48**, **49**, **50a**, **55**, **56** and **57**. As the biological results of these six compounds was due to a single structural isomer, these were of particular interest TCPTP inhibition was investigated. As PTP selectivity is a key aspect of determining best identified hit compound.

As shown in the appendix (section 2.1.7) two of these six compounds (**48**, **49**, **50a**, **55**, **56** and **57**) was of particular interest, due to not demonstrating significant TCPTP inhibition at 100 μM . These two compounds were **49** and **55**, this apparent selectivity made them of interest particularly during the dose response experiment at 140 μM .

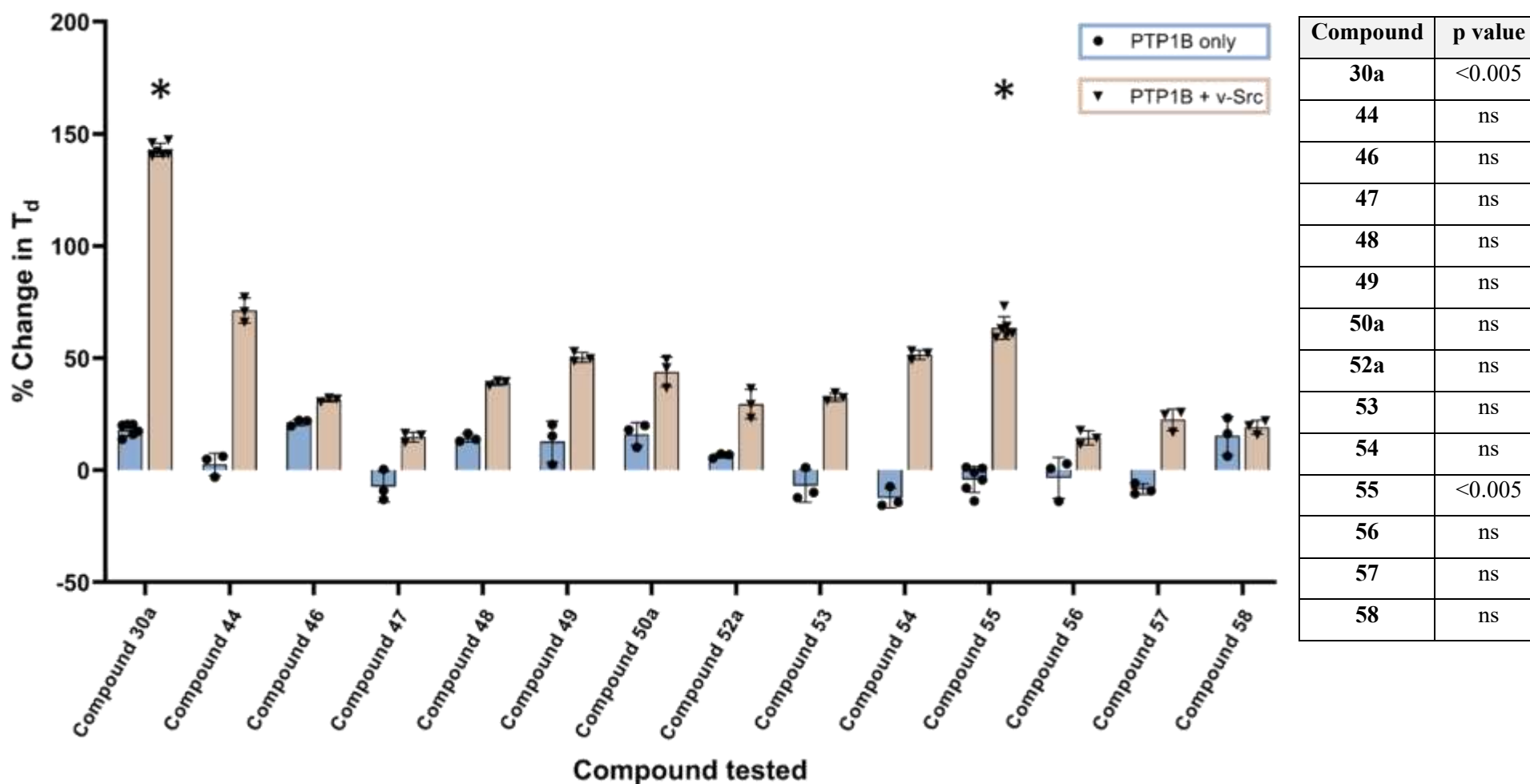


Figure 92: Comparison of % change in doubling time (T_d) of PTP1B only and PTP1B + v-Src transformed yeast cells in the presence of synthesised compounds **30a**, **44**, **46-50a**, **52a-58** at 140 μ M. $n=3$ for all compounds tested in both transformations, apart from **30a** and **55** where $n=6$. Mean and individual points \pm standard deviation plotted. Used non-parametric Mann-Whitney t-test for statistical analysis. * p value ≤ 0.050 vs control.

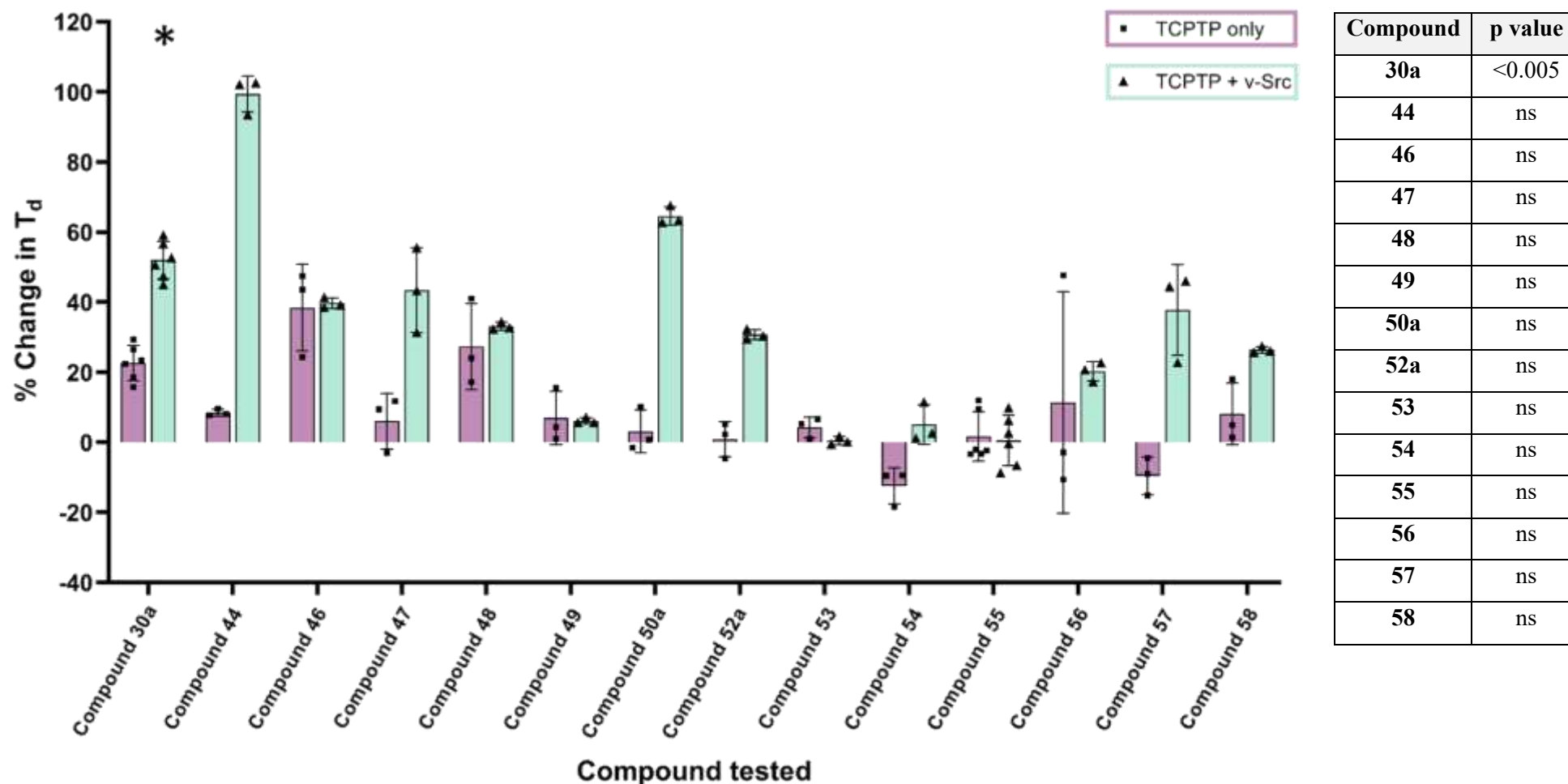


Figure 93: Comparison of % change in doubling time (T_d) of TCPTP only and TCPTP + v-Src transformed yeast cells in the presence of synthesised compounds **30a**, **44**, **46-50a**, **52a-58** at 140 μM . $n=3$ for all compounds tested in both transformations, apart from **30a** and **55** where $n=6$. Mean and individual points \pm standard deviation plotted. Used non-parametric Mann-Whitney t-test for statistical analysis. * p value ≤ 0.050 vs control.

As demonstrated in **Figure 92**, at 140 μM the biological effect in terms of percentage change in T_d of all the derivatives were significantly less than that of compound **30a** (statistical values shown in appendix 4.1). The two derivatives which exerted the greatest effect with regards to PTP1B inhibition were compounds **44** and **55**. As discussed previously, compound **44** was a mixture of structural isomers and demonstrated a greater effect on TCPTP than PTP1B. Whereas compound **55** at both 100 and 140 μM was found to be specific towards PTP1B as no TCPTP inhibition (average % increase at 140 μM was 0.5%). From **Figure 93** compound **44** has the greatest average response towards TCPTP (~100% increase) but only compound **30a** exerted a significant response (p value <0.005).

Ideally further biological repeats of all derivative compounds would have been conducted if time permitted, as with exception of compound **58**, all derivatives would most likely exhibit significant PTP inhibition with additional repeats. Instead, only the most promising derivative where a single structural isomer was deployed was investigated further. This was compound **55**; however, compound **49** can also be justified for further investigation which could be done as part of future work. This choice is further justified below with the presented BBB permeability data (**Figure 94**).

4.3.12.2 BBB permeability comparison

As illustrated in **Figure 94** the most specific PTP1B inhibitor derivative of compound **30a**, **55** also possesses a low BBB permeability at 37 °C where there is no significant difference in the concentration of compound **55** in the acceptor well after 24 hours when compared against both the low permeability control and compound **30a**. This further justified the selection of **55** to undergo further investigation in terms of a dose response screen with regards to both PTP1B and TCPTP inhibition.

It is also worth noting that despite compound **48** being the only derivative to be significantly less BBB permeable than the low permeability control (p value <0.001) other compounds namely **55** exhibited superior and more specific PTP1B inhibition.

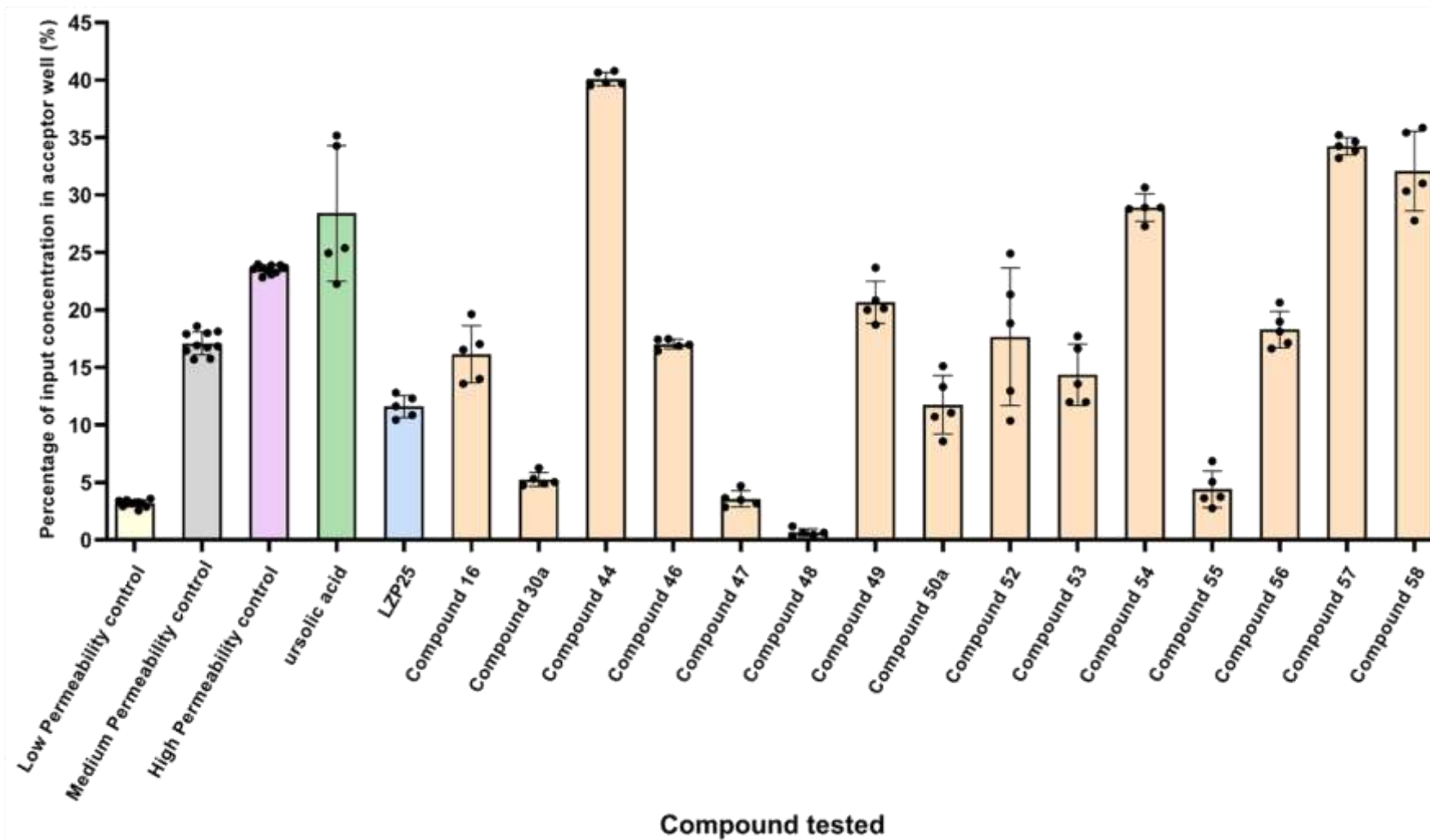


Figure 94: The percentage of the inputted concentration in the BBB assay acceptor well after 24 hrs at 37 °C. n=5 for all compounds tested, n=10 for permeability controls, mean and individual points \pm standard deviation plotted. For statistical analysis see appendix section 4.

Compound **44** possessing substantial inhibitory activity towards both PTP1B and TCPTP as shown above in **Figure 92** and **Figure 93**. However, in addition to being a mixture of structural isomers, and exhibiting TCPTP specificity, compound **44** is also significantly more permeable to the synthetic BBB than the high permeability control at 37 °C (p value <0.001). Hence further justifying why this derivative was not taken forwards for subsequent study.

The full statistical comparison of BBB permeability of the permeability controls, known inhibitors and compound **30a** derivatives for both RT and 37 °C can be found in the appendix (section 4.2).

4.3.13 Compound **55** activity investigation

4.3.13.1 PTP1B activity

As demonstrated in **Figure 95** and in the appendix (section 2.1.8) the addition of compound **55** at all concentrations tested resulted in a significantly greater % increase in doubling time in the PTP1B + v-Src cells when compared to control. Therefore, demonstrating that the increase exponential growth rate in PTP1B + v-Src is due exclusively to PTP1B inhibition by compound **55**, especially up to and including 140 µM where addition of **55** to PTP1B only cells did not cause an increase in doubling time of the cells when compared to base growth. Results and statistical analysis for T_d found in the appendix (section 2.1.8).

One important comment is that compound **55** is the only hit compound where every concentration tested exerted a significantly greater % increase in T_d in PTP1B + v-Src then PTP1B only transformed, meaning that during future work the testing of compound **55** at lower concentrations could be conducted to determine the minimum concentration that exerts a significant PTP1B inhibitory response. When comparing to compound **30a** the lowest concentration which exerted the same significance as **55** at 20 µM was at 80 µM which is a substantially higher concentration, and inhibitory response on **30a** and **55** at 80 and 20 µM are not significantly different.

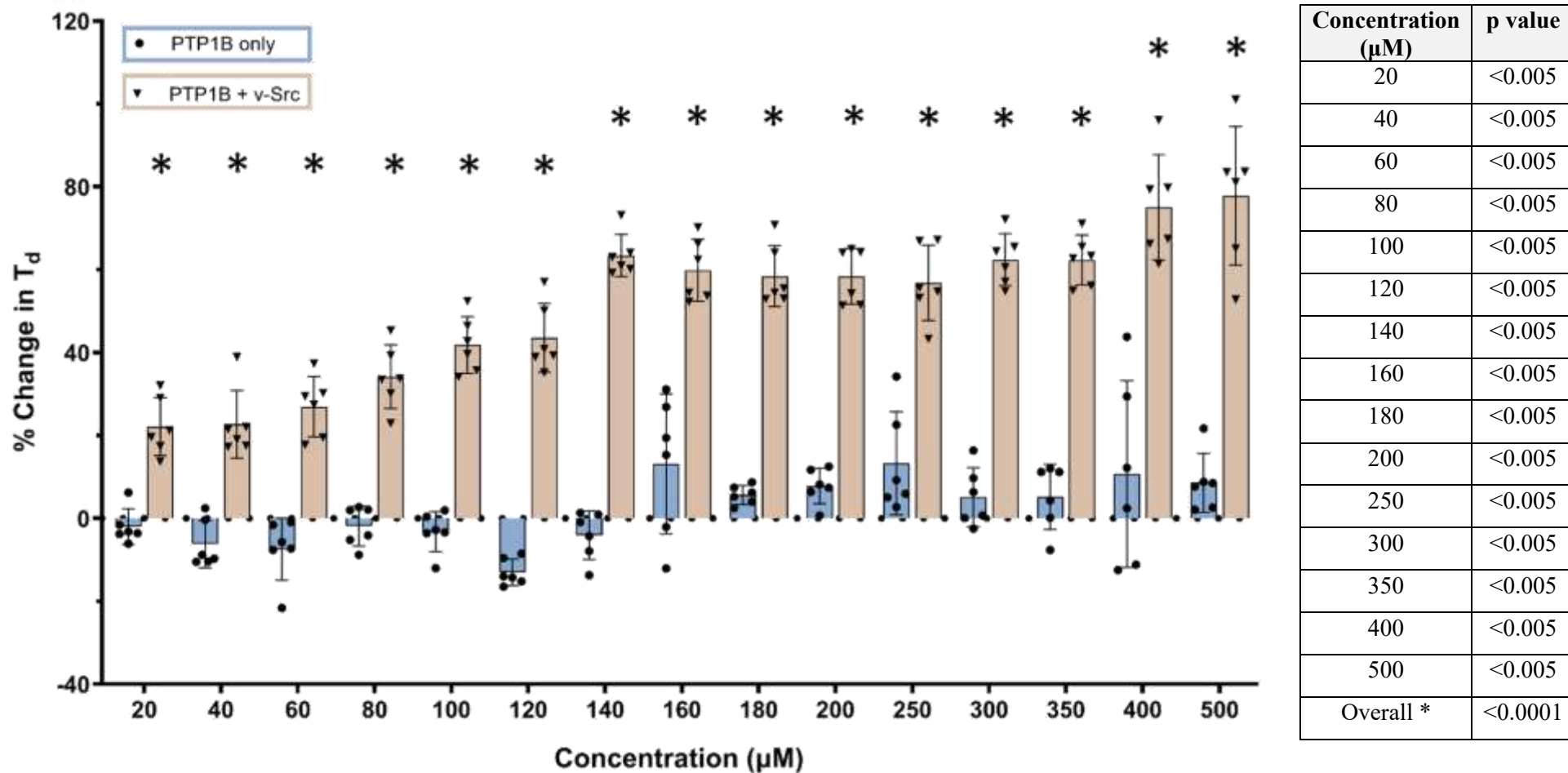


Figure 95: Comparison of % change in doubling time (T_d) of PTP1B only and PTP1B + v-Src transformed yeast cells in the presence of compound **55** at 20-500 μM . $n=6$ for all concentrations tested in both transformations, mean and individual points \pm standard deviation plotted. Used non-parametric Mann-Whitney t-test for statistical analysis. * p value ≤ 0.050 vs control.

As mentioned above and shown in **Figure 95** the lowest concentration of **55** which exerted a significant PTP1B inhibitory effect was at 20 μM , the response then significantly increased at 80 μM (p value <0.050). At 140 μM inhibitory effect of **55** significantly increased again (p value <0.005) where no significant change occurred again until a final significant increase at 400 μM (p value <0.050). However, 140 μM is again considered the optimum concentration for PTP1B inhibition as a substantial increase in dose is required to cause a slight significant increase in PTP1B inhibition.

4.3.13.2 TCPTP activity

As seen in **Figure 96** and the appendix (section 2.1.8.2), compound **55** does not inhibit TCPTP at any concentration investigated apart from at 500 μM . This is in addition to the fact that at every concentration at and below 160 μM , the average percentage increase in T_d is below a 10% increase, demonstrating negligible inhibition.

Hence this supports what was postulated earlier in that compound **55** is specific towards PTP1B, especially when looking at concentrations of 160 μM and below.

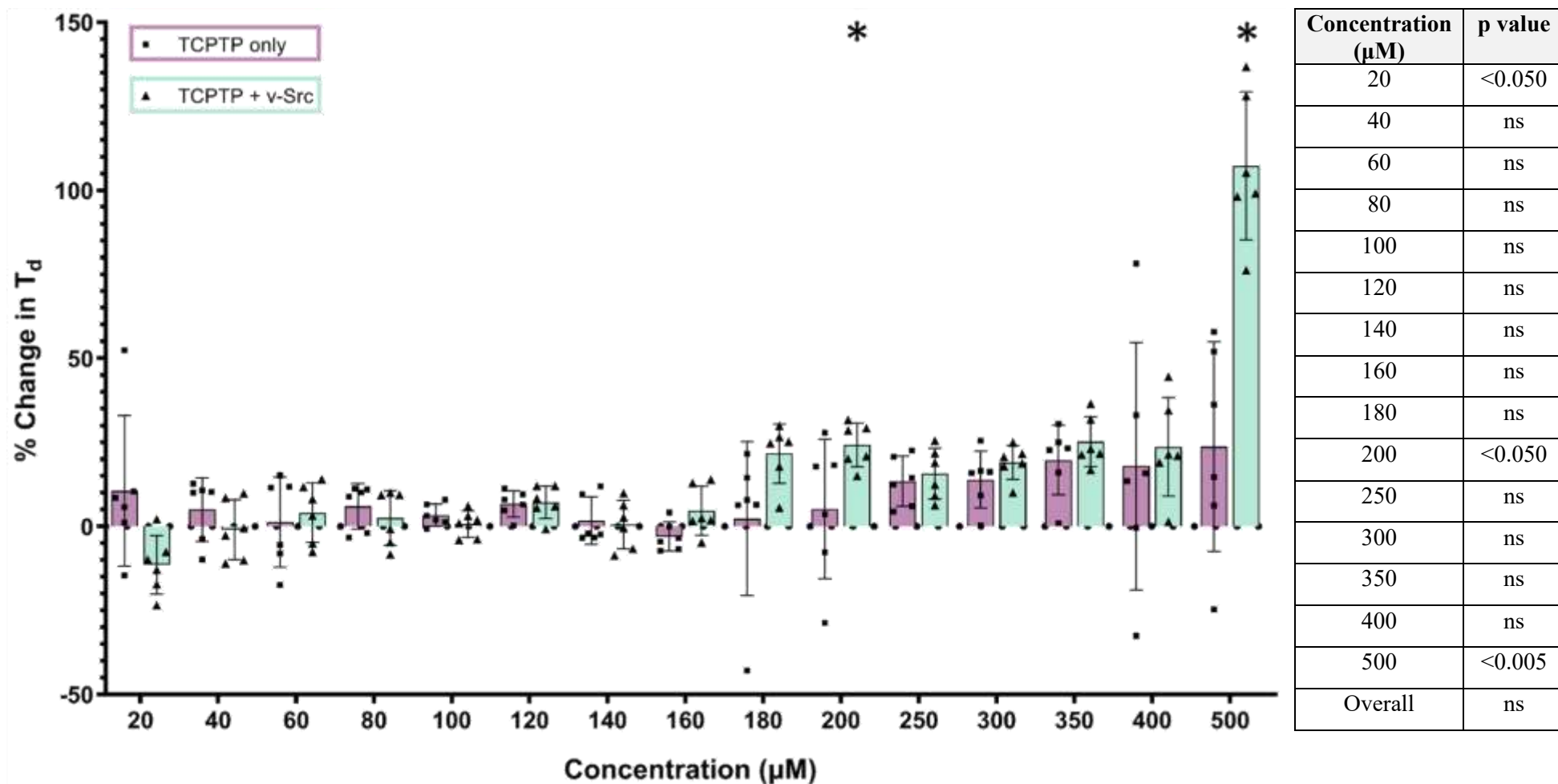


Figure 96: Comparison of % change in doubling time (T_d) of TCPTP only and TCPTP + v-Src transformed yeast cells in the presence of compound **55** at 20-500 μM . $n=6$ for all concentrations tested in both transformations, mean and individual points \pm standard deviation plotted. Used non-parametric Mann-Whitney t-test for statistical analysis. * p value ≤ 0.050 vs control.

4.3.13.3 PTP activity comparison

To further illustrate the overall superior inhibition of PTP1B by compound **55**, **Figure 97** and the appendix (section 2.8.1) demonstrate there is a significantly greater response in PTP1B + v-Src cells than TCPTP + v-Src overall for all concentrations of compound **55** tested and each concentrations individually with the exception of 500 μM where there is no significant difference between the percentage change in T_d values.

However, at 500 μM the average percentage increase is greater in TCPTP + v-Src cells than PTP1B + v-Src cells, this increase suggests that at 500 μM the inhibitory effect of compound **55** is slightly higher for TCPTP, on average but as not significantly different it may be due to natural variation of results. As at all other concentrations compound **55** is not only significantly more active but also solely inhibits PTP1B. The results directly comparing the effect on both PTPs are displayed below in **Figure 98**.

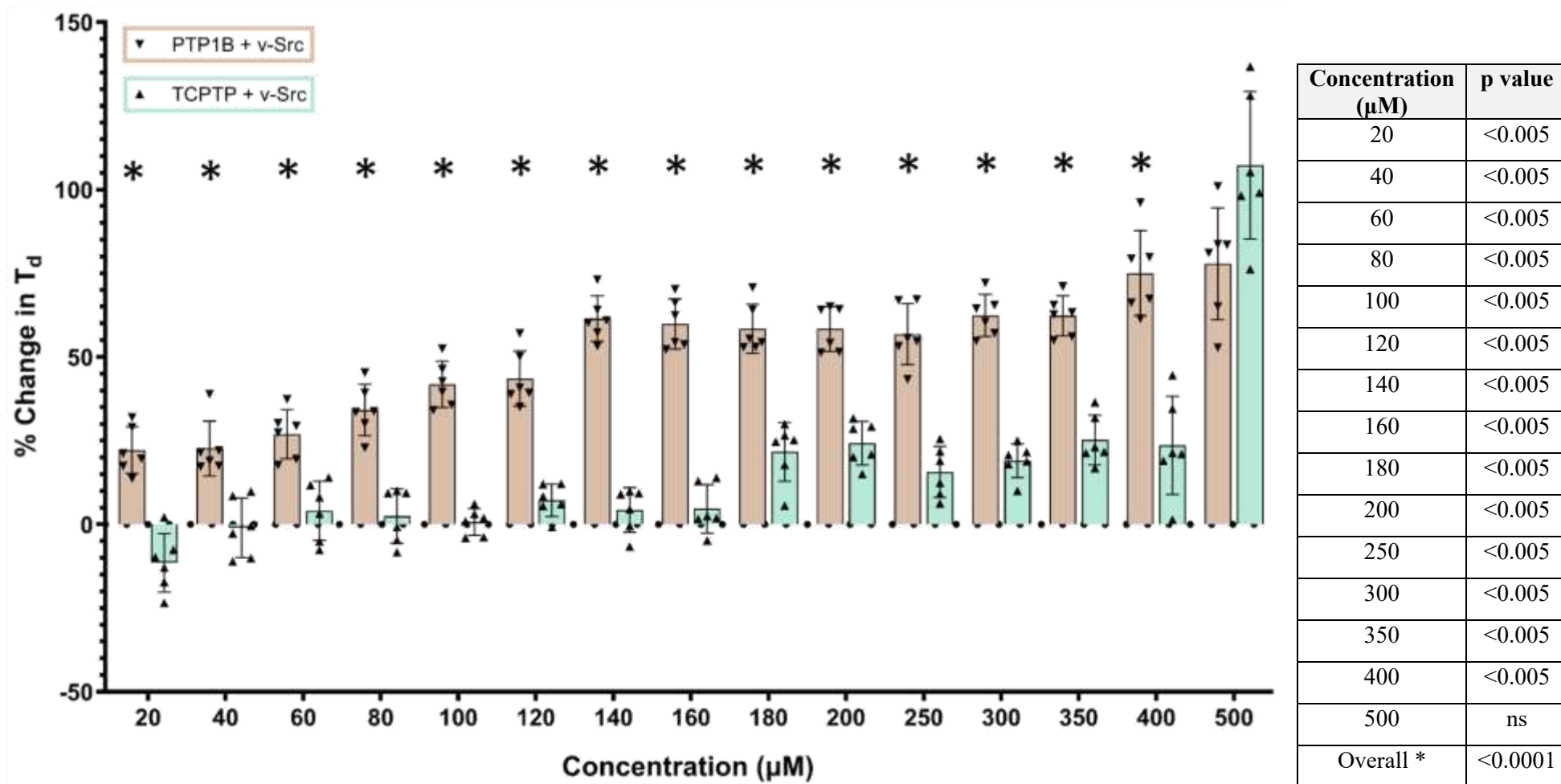
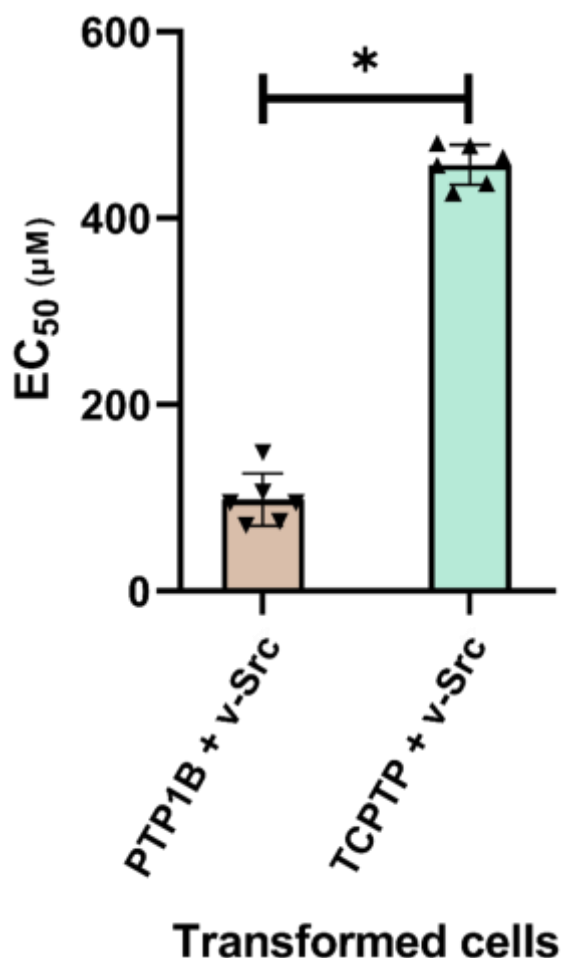


Figure 97: Comparison of % change in doubling time (T_d) of PTP1B + v-Src and TCPTP + v-Src transformed yeast cells in the presence of compound **55** at 20-500 μM . $n=6$ for all concentrations tested in both transformations, mean and individual points \pm standard deviation plotted. Used non-parametric Mann-Whitney t-test for statistical analysis. * p value ≤ 0.050 for PTP1B + v-Src vs TCPTP + v-Src.

From the data illustrated in **Figure 97** and **Figure 98** compound **55** is indeed more potent when inhibiting PTP1B over TCPTP, due to having a significantly high EC_{50} value with TCPTP (p value <0.005). This result was expected as the lowest concentration tested where the % increase in T_d was significantly higher in TCPTP + v-Src than TCPTP only transformed cells was at 500 μ M.



p value	<0.005
---------	--------

Figure 98: Comparison of EC_{50} values of compound **55** for PTP1B and TCPTP active site inhibition. $n=6$ for all both types of transformed cells. Mean and individual points \pm standard deviation plotted. Used non-parametric Mann-Whitney t-test for statistical analysis. * p value ≤ 0.05 for PTP1B + v-Src vs TCPTP + v-Src.

To investigate the disparity of activity compound **55** exerts in PTP1B and TCPTP, computational docking studies were again conducted to investigate the computationally favoured docking position and thus binding potential of compound **55** to each of the PTP active sites.

4.3.13.4 Computational binding mode

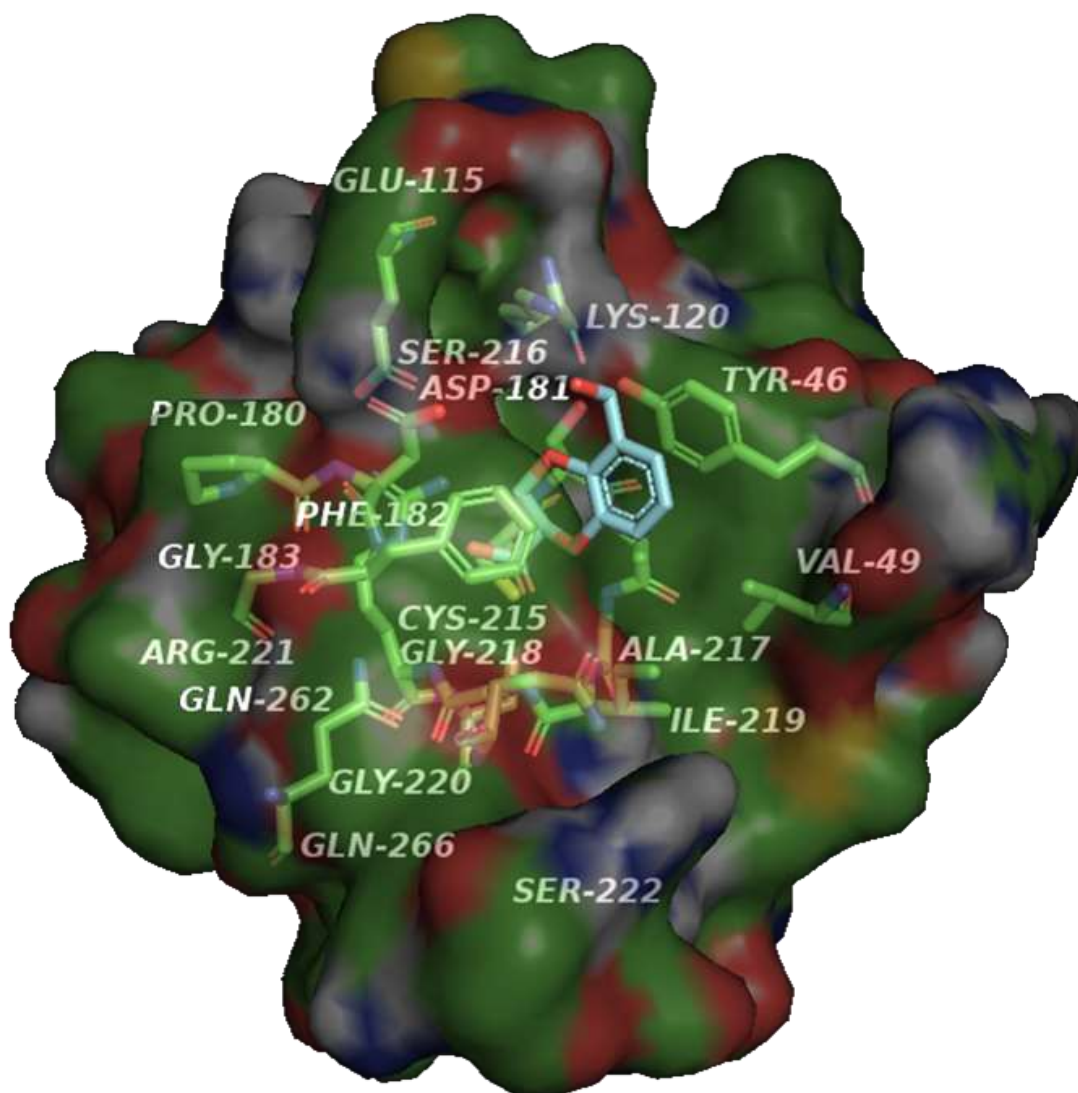


Figure 99: Computational most favoured proposed binding mode of compound **55** in the closed conformation of the PTP1B active site.

From the computational docking study results shown in **Figure 99**, the most favoured position of compound **55** is very comparable to that of compound **30a** as shown above in **Figure 86**. As interactions of compound **55** in the closed conformation of the active site for PTP1B include the carboxylic acid of **55** being located in the base of the active site and interacting *via* hydrogen bonding with the Cys-215 and surrounding residues, Ser-216, Ala-217, Gly-220 and Arg-221, as with compound **30a**. Additional proposed interactions include each of the benzodioxane oxygens interacting separately with the amine of Ala-217 or phenol of Arg-46. The benzene ring of is also again thought to π -stack with both Phe-182 and Tyr-46 of the active site.

But what is thought to be a significant contributor to the strength of the binding mode of these benzodioxanes to the PTP1B active site and thus the inhibitory activity is the interaction with the Lys residue (Lys-120) which is different for compound **55** due to the differing oxidation state of the aromatic oxygen containing 'R' group (primary alcohol in compound **55**). Instead of a covalent bond which forms between the carbonyl of compound **30a** and the amide of Lys, instead a hydrogen bond is thought to form between the primary OH of **55** and Lys-120. This weaker hydrogen bond interaction could explain in part the reduced maximum effect observed in PTP1B + v-Src cells when comparing the inhibitory effect of compound **30a** to **55** particularly at 140 μM . The effect of the composition and oxidation state of the oxygen of the functional group at this particular aromatic position is explored after the investigation of binding position of **55** to the TCPTP active site.

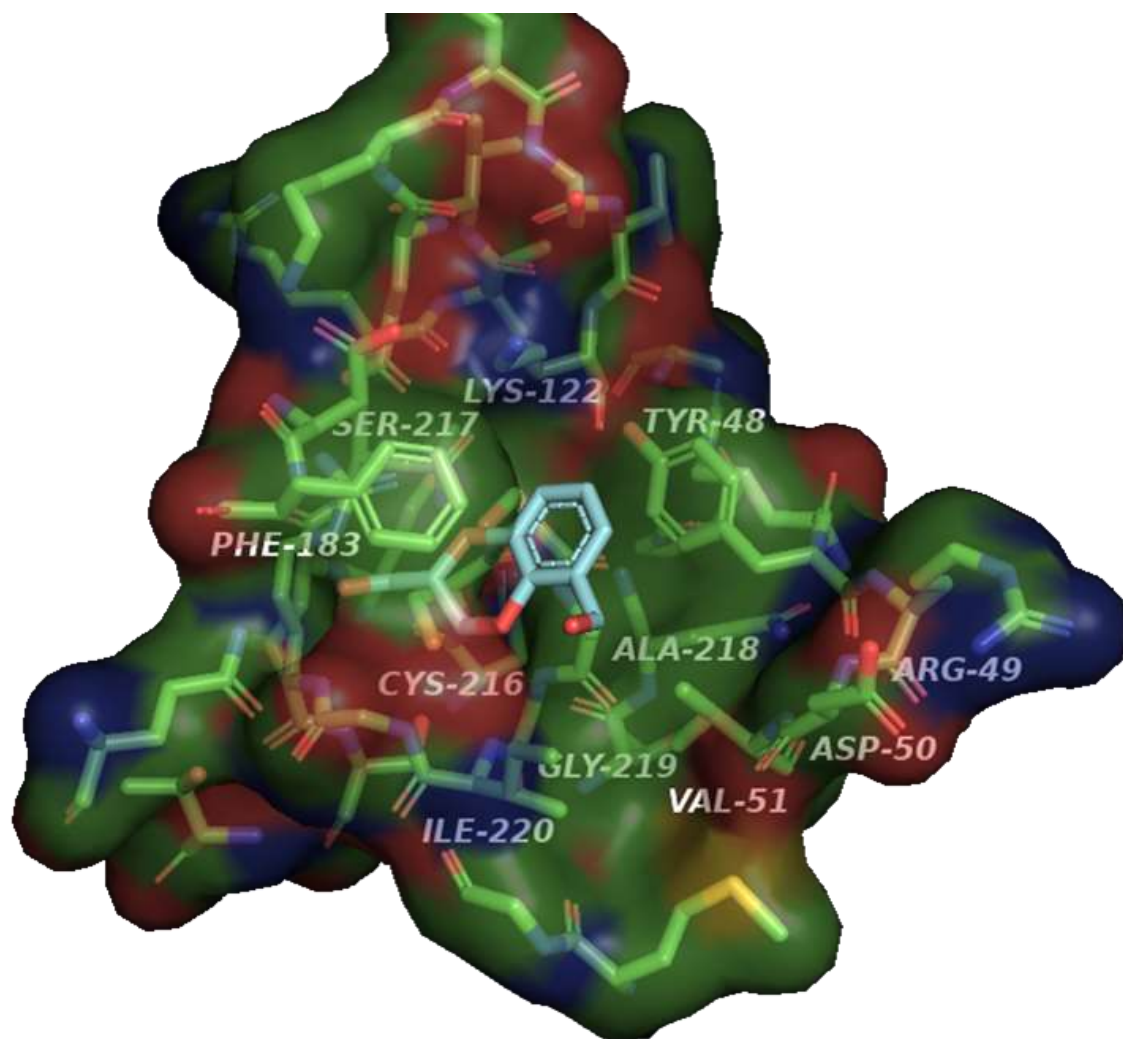


Figure 100: Computational most favoured proposed binding mode of compound **55** in the closed conformation of the TCPTP active site.

The computational favoured proposed binding position of compound **55** (shown in **Figure 100**) is comparable to that of compound **30a** (**Figure 87**), where once again when comparing to PTP1B the orientation of compound **55** is rotated about 180° with the point of axis through the plane of the molecule. This again results in the inability to interact with the Lys residue hence lowering the overall binding strength, thus contributing to the witnessed apparent PTP1B selectivity. However unlike with compound **30a**, **55** exerts no significant effect in terms of TCPTP inhibition at all concentrations below 500 μM, this is thought to be due to the primary alcohol being either unable to have a reduced strength interaction with Gln-260 thus resulting in the binding position of compound **55** in TCPTP being in essence comparable to that of compound **25**, which again did not exhibit a significant inhibitory effect.

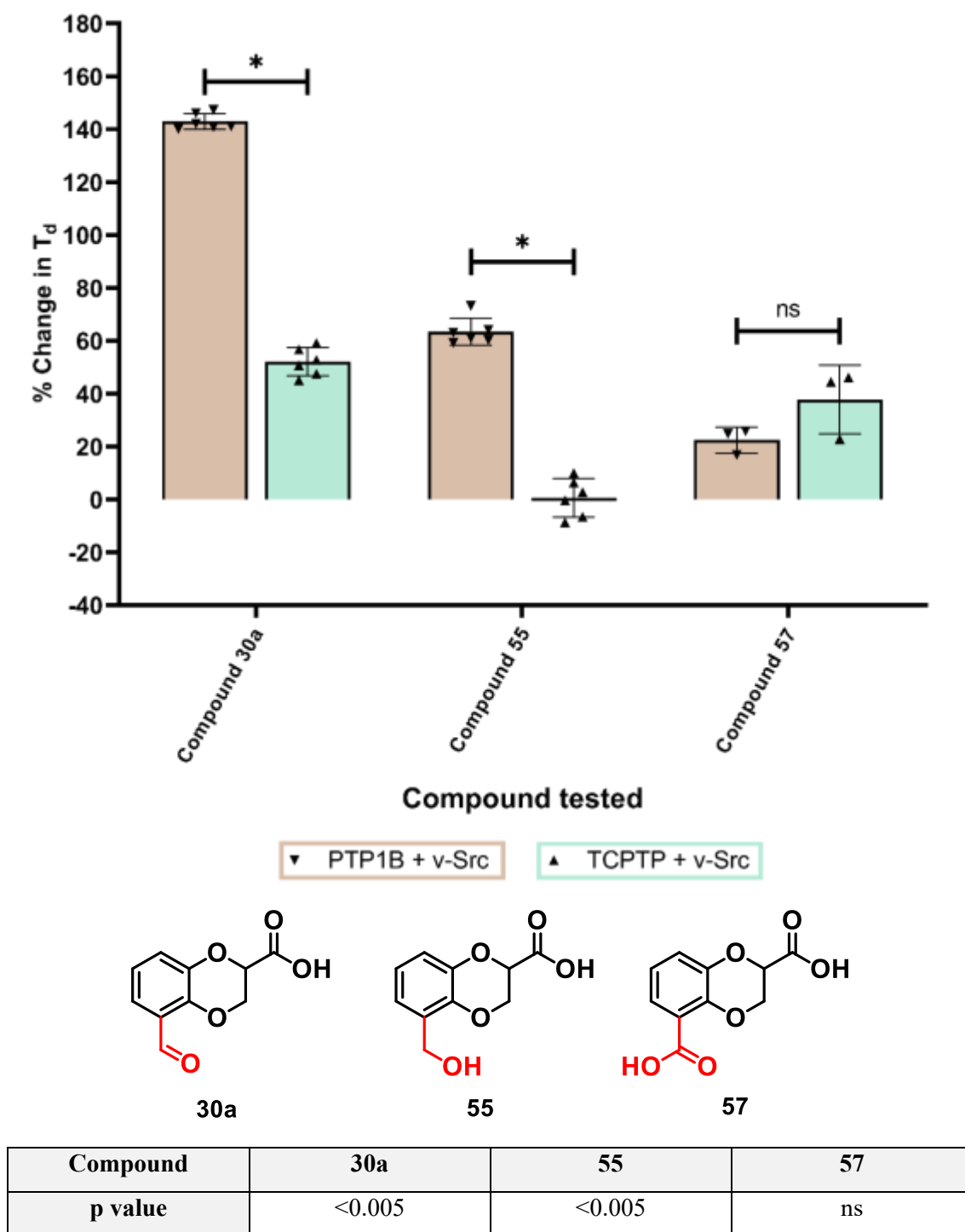


Figure 101: Comparison of % change in doubling time (T_d) of PTP1B + v-Src and TCPTP + v-Src transformed yeast cells in the presence of compound **30a**, **55** or **57** at 140 μ M. $n=6$ for all concentrations tested in both transformations, mean and individual points \pm standard deviation plotted. Used non-parametric Mann-Whitney t-test for statistical analysis. * p value ≤ 0.050 for PTP1B + v-Src vs TCPTP + v-Src.

Returning to the above discussion where the type of interaction between the potential PTP1B inhibitor and the Lys-122 residue appears to have a direct effect on the maximum inhibitory effect of that compound on PTP1B, where the composition and oxidation state of the carbon within the aromatic R group dictates the interaction type.

The inhibitory data is displayed above in **Figure 101** and the proposed type of interaction with the PTP1B lysine residue is illustrate below in **Figure 102**. In addition to compound **30a**, and **55**, compound **57** is also discussed as in this benzodioxane the aforementioned R group is a carboxylic acid where it is an aldehyde and primary alcohol in **30a** and **55** respectively. The percentage change in both PTP + v-Src cells at 140 μ M is shown again in **Figure 101** for compound **30a**, **55** and **57** in addition to the proposed interaction with the PTP1B Lys-122 residue. The computational favoured binding mode of compound **57** is comparable to that of compounds **30a** and **55**. This is shown for both PTP active sites in the appendix (section 2.4).

As shown in **Figure 102**, the strongest interaction which is a covalent bond occurs between the aldehyde of compound **30a** and the amine of the lysine PTP1B active site residue. Due to the rest of the compound structure of compound **30a** being identical to that of compounds **55** and **57**, the fact that compound **30a** had the highest maximum inhibitory effect on PTP1B as shown above in **Figure 101** is as expected due to the overall stronger proposed binding mode.

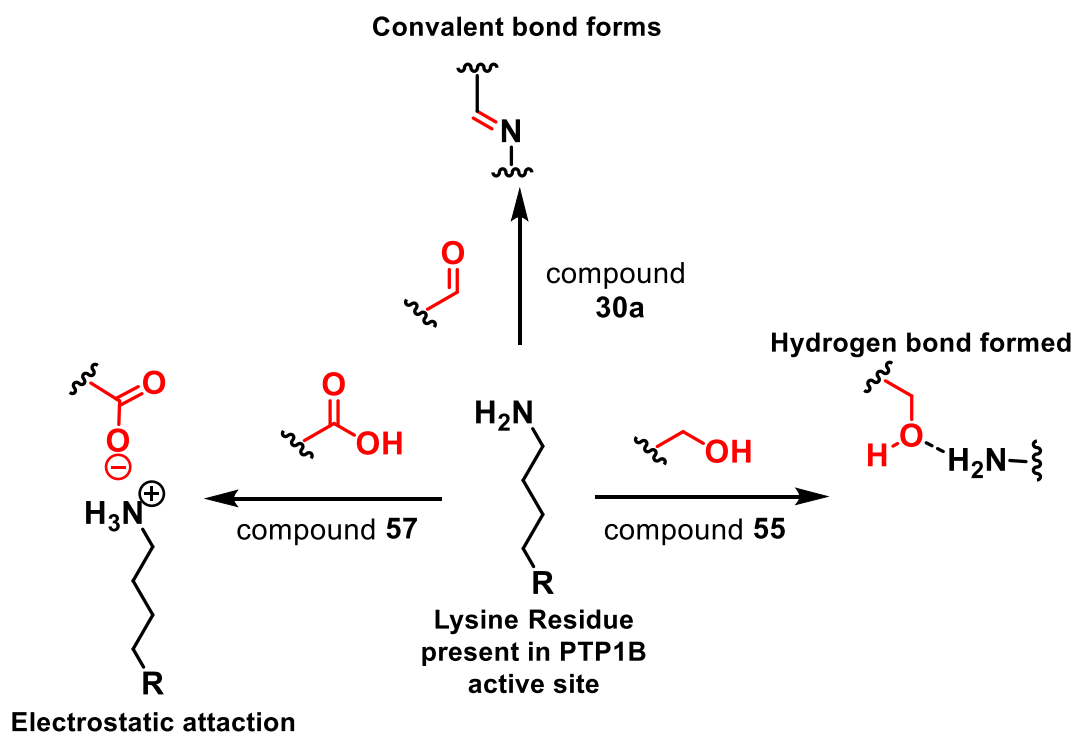


Figure 102: Proposed interactions that occur between Lys-122 of the PTP1B active site and the identified functional group of compounds **30a**, **55** and **57**.

However, the trend of stronger interactions with Lys-122 resulting in greater % increase in T_d and thus PTP1B inhibitory activity may not be maintained when looking at compounds **55** and **57**. Because compound **55** which exhibits hydrogen bonding has a greater biological effect than compound **57** where the carboxylic acid in this position can form electrostatic interactions with the lysine. Often such interactions between formal charges are considered stronger than hydrogen bonds and require more energy to break. But as demonstrated in **Figure 101** above compound **55** exhibits a stronger and more significant inhibitory effect on PTP1B than compound **57**, implying that other factors other than the type of interaction with Lys-122 contribute to the resultant activity of these benzodioxane inhibitions.

From all the data presented above, the determination of which of the benzodioxane hit compounds would in theory function the best as a PTP1B inhibitor for the purpose of obesity, TIID and related co-morbidities *in vivo*, and hence which should be the primary focus of future work, is investigated and justified below.

4.3.14 Overall benzodioxane hit compound comparison.

4.3.14.1 Yeast assay-based inhibition.

As demonstrated in **Figure 103** the highest average maximum biological effect in terms of percentage increase in T_d in PTP1B + v-Src is compound **30a**, which also is the only benzodioxane hit which exhibited a superior result to LZP25 but this difference at 140 μM is not significant. Compound **30a** also demonstrated selectivity towards PTP1B over TCPTP unlike LZP25 where no significant difference in response between PTP1B and TCPTP was noted. All statistical analysis involving cross-comparison of all hits compounds with known inhibitors is shown in the appendix (section 4.1).

However, a significant result in terms of TCPTP inhibition was also identified with the addition of compound **30a** which despite its greater result for PTP1B inhibition, ideally for a potential drug-like molecule no cross-target activity would be present. Hence compound **55** is of particular interest due to exhibiting the greatest significant percentage increase in T_d of any hit compound in PTP1B + v-Src while simultaneously having no statistical effect on TCPTP + v-Src cell, furthermore this was found to be true for all concentrations below 500 μM tested. Therefore, despite having a lower maximum effect compound **55** may be more justified for future work than compound **30a** due to exhibited superior PTP selectivity. But additionally, BBB permeability is also a key aspect in identifying the overall best benzodioxane PTP1B inhibitor for this project's ultimate future aim.

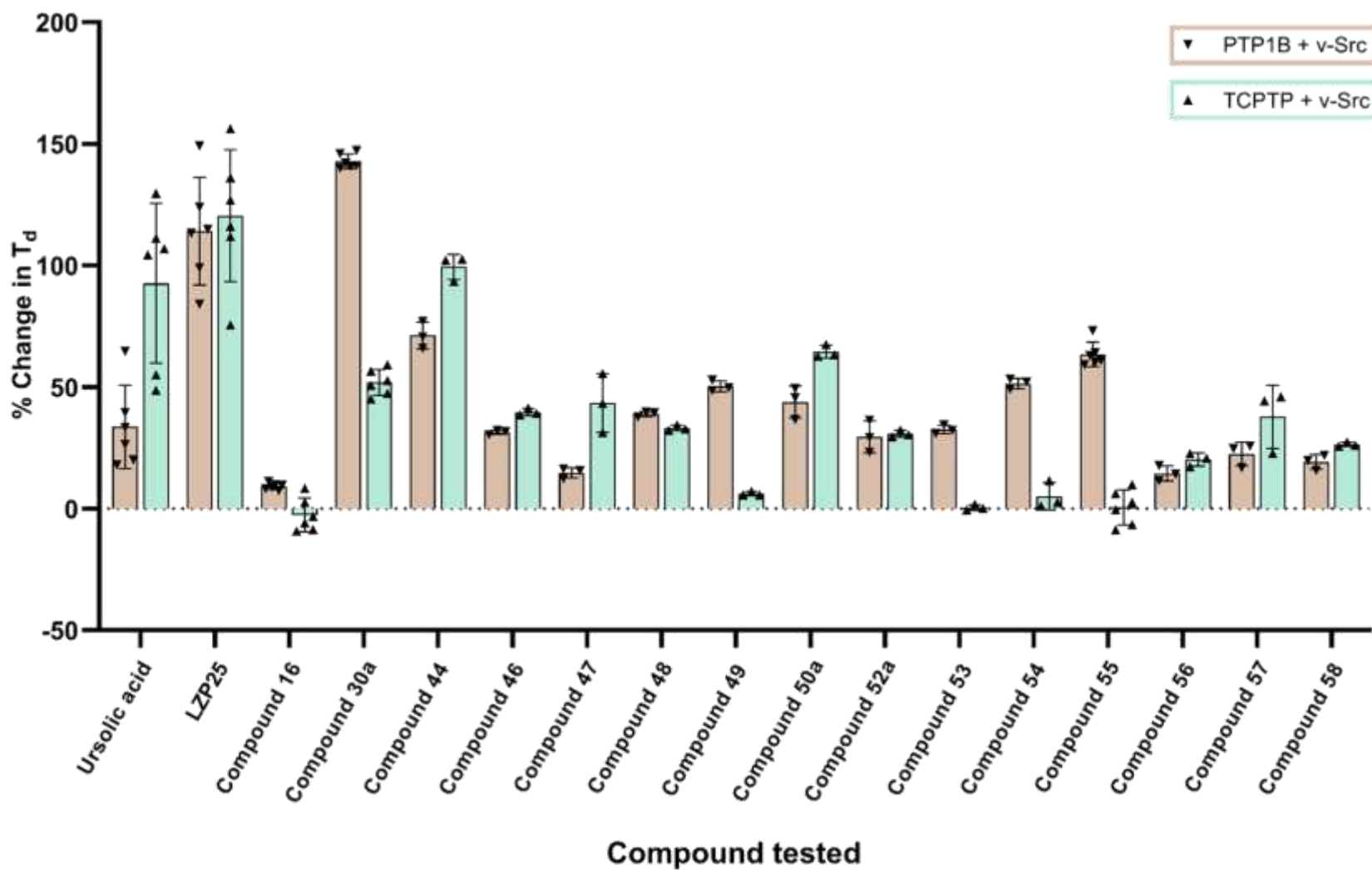
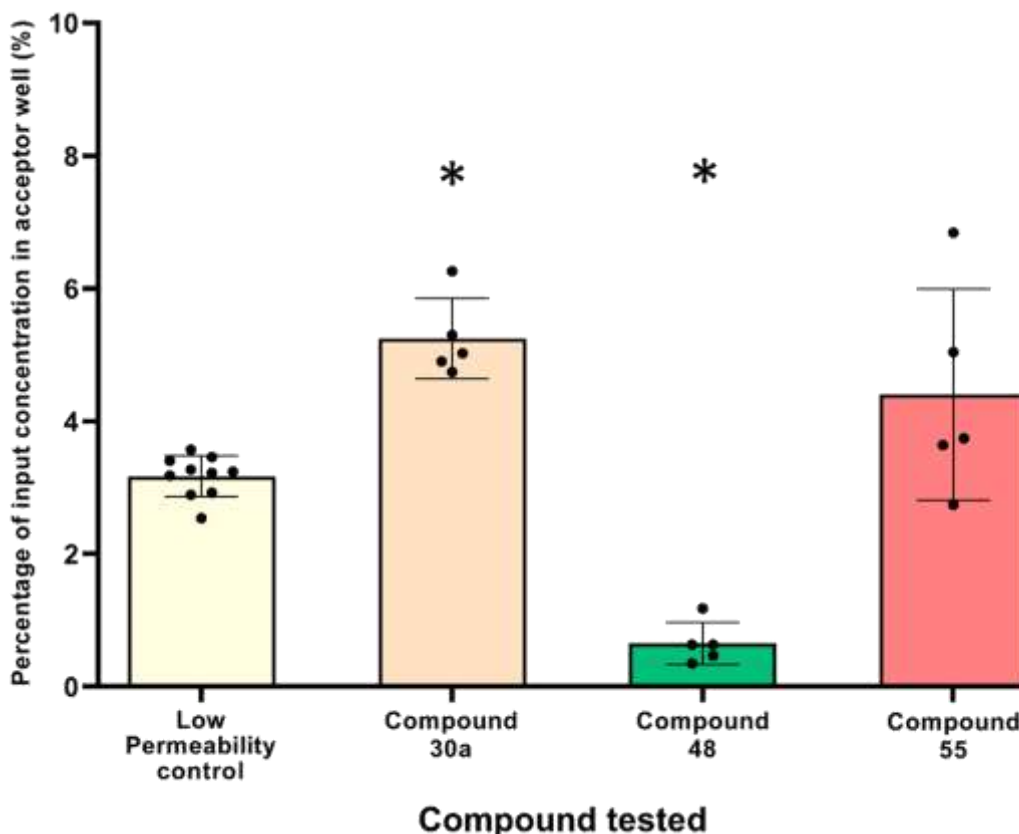


Figure 103: Comparison of all benzodioxane PTP hit compounds against two known inhibitors, at 140 μM. For statistical analysis of the inhibitory effect at 100 and 140 μM towards both PTP1B and TCPTP see appendix section 4.

4.3.14.2 Blood brain barrier permeability



Compound	30a	48	55
p value	<0.001	<0.001	ns

Figure 104: The percentage of the inputted concentration in the BBB assay acceptor well after 24 hrs at 37 °C. n=6 for all compounds tested. Mean and individual points \pm standard deviation plotted. Used non-parametric Mann-Whitney t-test for statistical analysis. * p value \leq 0.050 vs low permeability control.

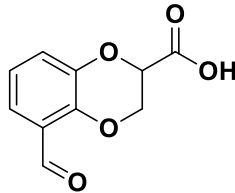
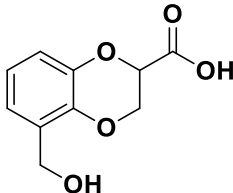
When looking at compound **55** specifically at 37 °C in **Figure 104**, the permeability was not statistically different than from the low permeability control provided with the assay. However, despite the synthetic BBB permeability of compound **30a** and **55** not being significantly different to each other at 37 °C, the concentration of **30a** in the acceptor well was significantly greater than that of the low permeability control. From the results of this assay both **30a** and **55** can be considered to have a low BBB permeability which is desirable for the aim of this work.

Compound **48** appeared to be statistically less permeable to the synthetic BBB than **30a**, **55** and the low permeability control with a negligible amount being identified in the acceptor well post assay run. However, due to **48** having poor PTP selectivity and lower activity it was not investigated further as previously mentioned.

A summary comparing properties of interest of compound **30a** and **55** and the subsequent justification on the identification of the overall superior PTP1B benzodioxane active site inhibitor which fulfilled the aim of this project is outlined below.

4.3.14.3 Identified best benzodioxane hit compound.

Table 8: Comparison of key results obtained from investigating compounds **30a** and **55** as PTP1B inhibitors.

	compound 30a ¹	compound 55 ¹
structure		
maximum % increase in T _d in PTP1B + v-Src cells	206 ± 47%	78 ± 15%
% increase in T _d in PTP1B + v-Src cells at 140 μM	143 ± 3%	63 ± 5%
EC ₅₀ for PTP1B (μM)	158 ± 21 μM	98 ± 26 μM
measure of PTP selectivity ²	60 μM	200 μM
BBB permeability at 37°C ³	5 ± 1%	4 ± 1%

¹All numerical values rounded to the nearest integral, colour code: green denotes superior compound in that category, yellow means results comparable.

² Measure of PTP specificity means the lowest concentration tested were a significant effect in TCPTP + v-Src cells than TCPTP only cells was measured.

³ Values denote the percentage of the inputted concentration present in the acceptor well after a 24-hour BBB permeability assay run.

From the comparison of compound **30a** and **55**, highlighted in **Table 8** it was determined that overall compound **55** was the best identified benzodioxane hit compound due primary to it being both highly specific towards PTP1B where no statistical effect in TCPTP was observed until at 500 μM dose was used. Additionally, when looking at PTP1B only cells only at a dose of 500 μM was a significant increase in the T_d values observed when compared to the corresponding base growth, further verifying the effect observed in PTP1B + v-Src to be solely due to PTP1B inhibition by compound **55**. However, in tandem to the testing of these computationally designed benzodioxane compounds, an investigation into spirocycle dihydropyrazoles was also

being conducted with the same aim of identifying a BBB impermeable PTP1B specific inhibitor. The results from which are illustrated and explored in Chapter 5.

4.4 Conclusion:

Herein this Chapter the target core structure of 1,4-benzodioxanes for active site PTP inhibition was justified and prior applications of and synthesis routes have been investigated. The utilisation of this core structure as potential PTP1B active site inhibitors has not to date been investigated in the literature. The potential application of 1,4-benzodioxanes is based on computational dockings studies reported in Chapter 2 (section 2.3.2). But as shown throughout this Chapter, the subsequent reactivity of the 2,3-dihydroxybenzaldehyde based compounds in particular presented numerous challenges many of which were overcome, but for the ones that were not achieved during this work a viable alternative was proposed. Once the main benzodioxane hit compound had been identified, all subsequent 1,4-benzodioxane compound library was based upon this compound, **30a**. Where the synthesis cyclisation step for this particular 1,4-benzodioxane was selectively optimised by altering reaction condition screen and utilizing NMR yields to determine the optimum reaction conditions. The majority of the successfully synthesised compounds were latterly biologically assessed as potential PTP inhibitors, where from the culmination of all relevant factors resulted in the identification that the overall superior benzodioxane based PTP1B inhibitor to be a derivative of compound **30a**, compound **55**.

Chapter 5

*Spirocyclic dihydropyrazole
synthesis and
PTP1B active site
inhibitor development*

5.1. Overview:

Compounds with inherent three dimensionality that also demonstrate an extensive range of biological activities are spirocycles. This class of compounds encompass a broad class of naturally occurring and synthetic molecules that have and still are receiving significant interest by the pharmaceutical industry. Herein, the preparation of a range of spirocyclic dihydropyrazoles is demonstrated *via* a procedurally simple two-step method. Initially cyclic ketones are converted to the respective bench stable cyclic tosylhydrazones, without need for purification. These tosylhydrazones are subsequently reacted with commercially available electron deficient alkenes to form the spirocyclic dihydropyrazoles. The synthetic utility of the core scaffold is also demonstrated to highlight potential utility for applications in future medicinal chemistry and drug development.¹⁶⁷

5.2. Background:

5.2.1. Justification for synthesis and biological testing

5.2.1.1. Computational studies

As shown in Chapter 2 (sections 2.3.2 and 2.3.3), spirocycle core structure hits were computationally identified separately as having the potential to act either active or allosteric site PTP1B inhibitions. This was reason why the prior optimised synthesis of spirocyclic dihydropyrazoles was used for the formation of a compound library for PTP1B inhibition testing, the synthesis of which was originally conducted for an unrelated publication cited here.¹⁶⁷

The predominant reason for the interest in investigating 5,6-spirocyclic dihydropyrazoles as potential PTP inhibitors was the active site example hit 3 from Chapter 2 (section 2.3.2) which closely resembles that of a 5,6 – spirocycle dihydropyrazoles. Specifically, because the two-step linear synthesis of which was mostly investigated and optimised during prior work conducted during a master’s level research project. Initial PhD synthesis work conducted was on the investigation of this spirocycle dihydropyrazole formation and the subsequent downstream selective functionalisation that could be conducted on the spirocycle core. The aim functionalisation being for improving pharmaceutical relevance. So the compound library of spirocycle dihydropyrazoles which were synthesised for publication during the PhD project were additionally tested for PTP activity regardless

due to the spirocycles inherited three-dimensionality and ‘drug-likenesses’. The latter discovery of the computational hit compounds, (active site example 3, and allosteric site example hits 2 and 4) was a coincidence, but it does inform the potential binding mode of spirocycle dihydropyrazoles and provide additional relevance for the testing as PTP inhibitors.

5.2.1.2. Molecular three-dimensionality

As previously stated in the literature the mean fraction of sp^3 -hybridised atoms in drug candidates tend to increase through the clinical trials process, due to attrition of less selective “flat” compounds.¹¹¹ As a response, in the previous decade, there has been an increased focus on incorporating a higher degree of molecular three dimensionality in screening library and discovery molecules for use in drug discovery and pharmaceutical industry. However, unlike for planar or linear molecules where transition metal catalysed cross coupling methodologies can be utilised in multiple cases,¹⁶⁹ bond formation to sp^3 -hybridised atoms (particularly carbon) represents a greater synthetic challenge. Such that, novel synthetic methodologies for the preparation of highly three-dimensional core scaffolds are of significant interest to medicinal chemists.^{111,170-175}

5.2.1.3. Known spirocyclic pharmaceuticals.

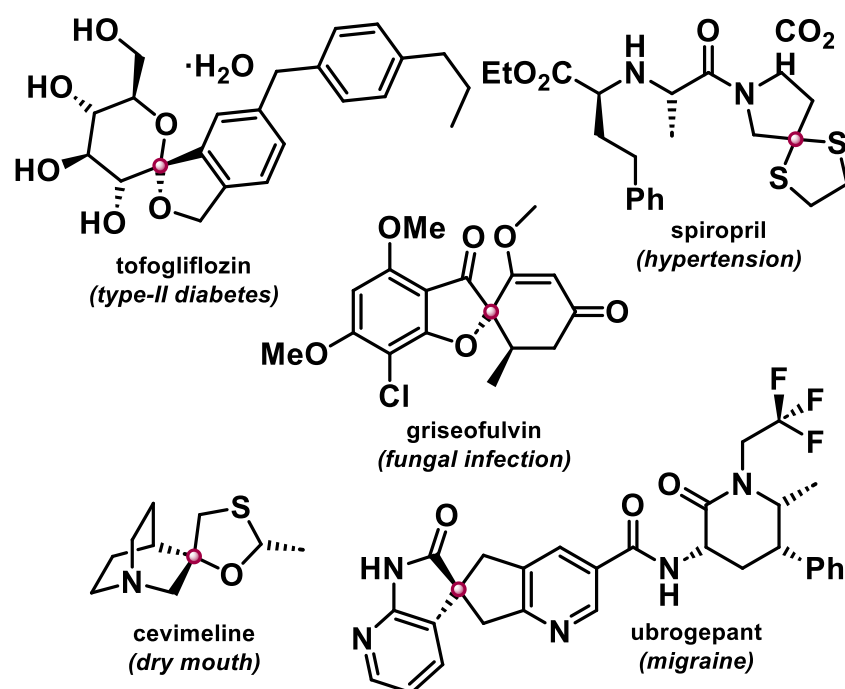


Figure 105: Example approved drug molecules featuring a spirocyclic ring junction.

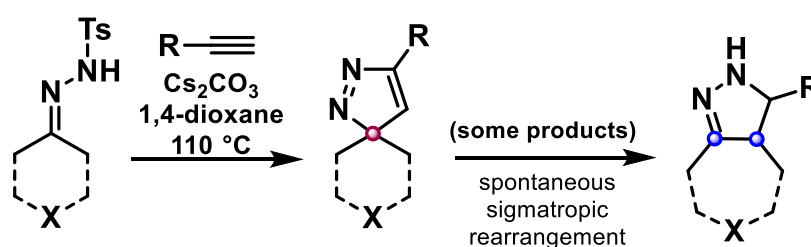
173,176-180

The incorporation of spirocyclic motifs into the core scaffold of a potential drug molecule, provides a means of increasing molecular three dimensionality, effectively providing the ability to engage all three dimensions *via* functionalisation, as the rings joined by the spirocyclic junction are mutually orthogonal. Hence spirocycles are an inviting synthetic target for medicinal chemists due to possessing inherent three dimensionality imparted by the spiro configuration and exhibit a known broad range of biological activities, examples of which are demonstrated in **Figure 105** above.^{173,176-180}

Of particular interest of the examples shown in **Figure 105** is tofogliflozin which is an orally active small molecule drug for the treatment of type II diabetes, which operates as a sodium-glucose co-transporter type 2 (SGLT2) inhibitor. SGLT2 is primarily located in the proximal tubules and functions as a key mediator of glucose reabsorption in the kidneys.^{173,181}

5.2.2. Literature procedures for 5,6-spirocyclic dihydropyrazole synthesis

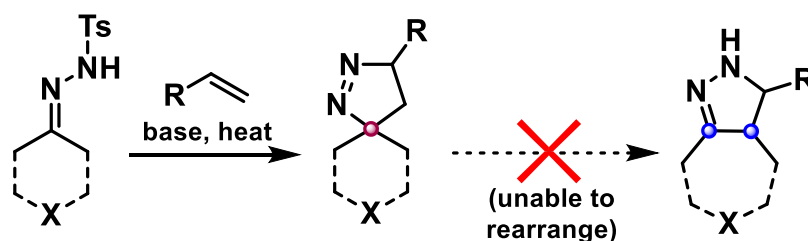
A relatively synthetically simple class of spirocycles are cyclic acetals which may be easily prepared by traditional acid-catalysed routes¹⁸²⁻¹⁸⁴ or by using gold-mediated spirocyclisations.^{185,186} However acetals are considered a poor choice for the potential medicinal compounds due to the often hydrolytically labile functionalities. So, to avoid this issue, more stable spirocyclic moieties are preferable for inclusion in drug candidates. As such there is significant interest in the preparation of this type of robust core scaffolds.



Scheme 41: Prior work on the synthesis of spirocyclic pyrazole compounds from alkyne. Some spirocycle (purple) examples were observed to spontaneously rearrange to the corresponding fused bicyclics (blue).¹⁷¹

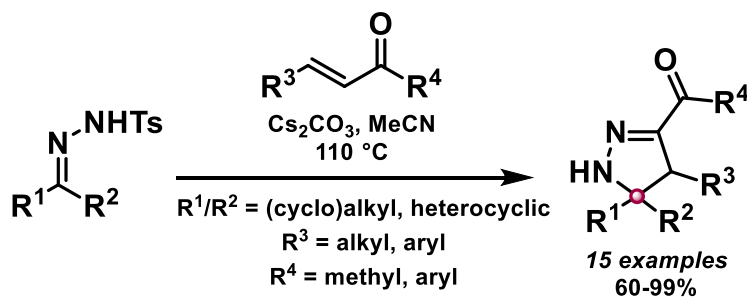
As shown above in **Scheme 41**, prior work by R. Merchant *et al.*, demonstrated a procedurally simple reaction of tosylhydrazones with alkyne to yield a broad range of spirocyclic pyrazoles.¹⁷¹ These molecules represent a highly three-dimensional heterocyclic core scaffold. Although it was observed that, in some cases, spirocyclic

pyrazoles underwent spontaneous sigmatropic rearrangement to the corresponding fused bicyclic scaffolds. Contributing factors for this rearrangement included being composed of more strained ring systems, or when more electronically activated by adjacent π systems.¹⁷¹



Scheme 42: Proposed synthesis of a more robust dihydropyrazole core scaffold. This is unable to undergo sigmatropic rearrangement to a fused bicyclic system, due to the removal of a π -bond.¹⁶⁷

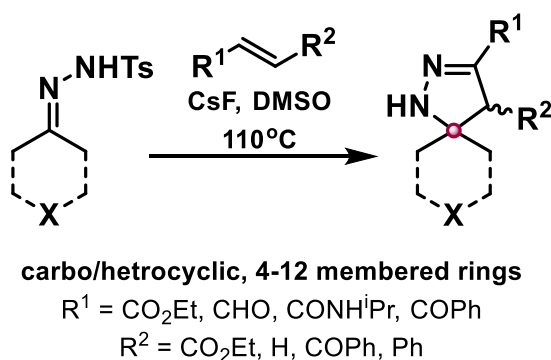
Therefore, it was theorised that by utilising alkenes instead of an alkyne and thus removing a π -bond from the pyrazole moiety would negate the ability of the spirocyclic scaffold to undergo sigmatropic rearrangement and therefore result in a more robust 3-dimensional core structure. Shown above in **Scheme 42**.



Scheme 43: A previous literature method for the synthesis of dihydropyrazoles.¹⁸⁸

Synthetic routes to spirocyclic dihydropyrazoles are sparsely represented in the current literature.¹⁸⁷⁻¹⁹⁰ A prominent example from Wu *et al.* (**Scheme 43**)¹⁸⁸ utilises tosylhydrazones with α,β -unsaturated ketones to provide dihydropyrazoles in good to excellent yields. Although, the substrate scope of this reaction is restricted to phenyl and methyl ketones, limiting the potential for further synthetic development of the core around the new dihydropyrazole moiety.

5.2.3. Utilised synthesis route

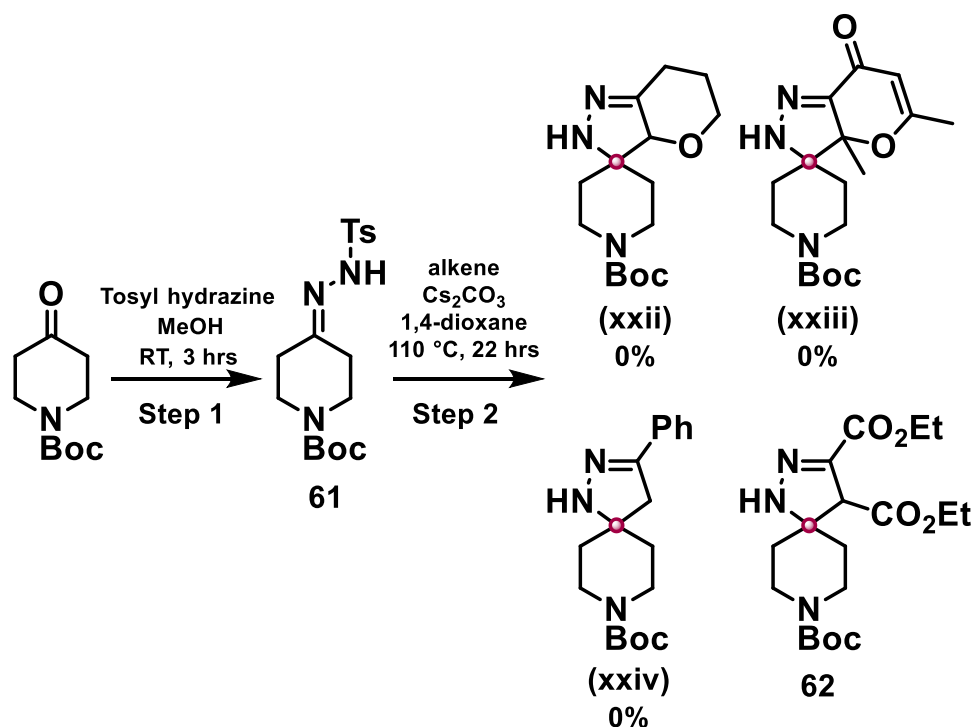


Scheme 44: Synthesis of spirocyclic dihydropyrazoles containing core scaffold. ¹⁶⁷

Shown above (**Scheme 44**) is the complementary, procedurally simple, method for the synthesis of spirocyclic dihydropyrazole scaffolds developed, which exhibit more synthetically tractable functional groups allowing a broader range of subsequent synthetic modifications for application in medicinal chemistry and drug discovery. ¹⁶⁷

5.2.4. Investigation into alkene incorporation into for spirocycle synthesis

The investigation was started by focusing on the chemical and structural properties of the alkene R groups that the reaction can tolerate and the effect on isolated yield. The initial reaction conditions used were previously developed for the synthesis of spirocyclic pyrazoles, from reacting sulfonyl hydrazones with alkynes. ^{191,192}

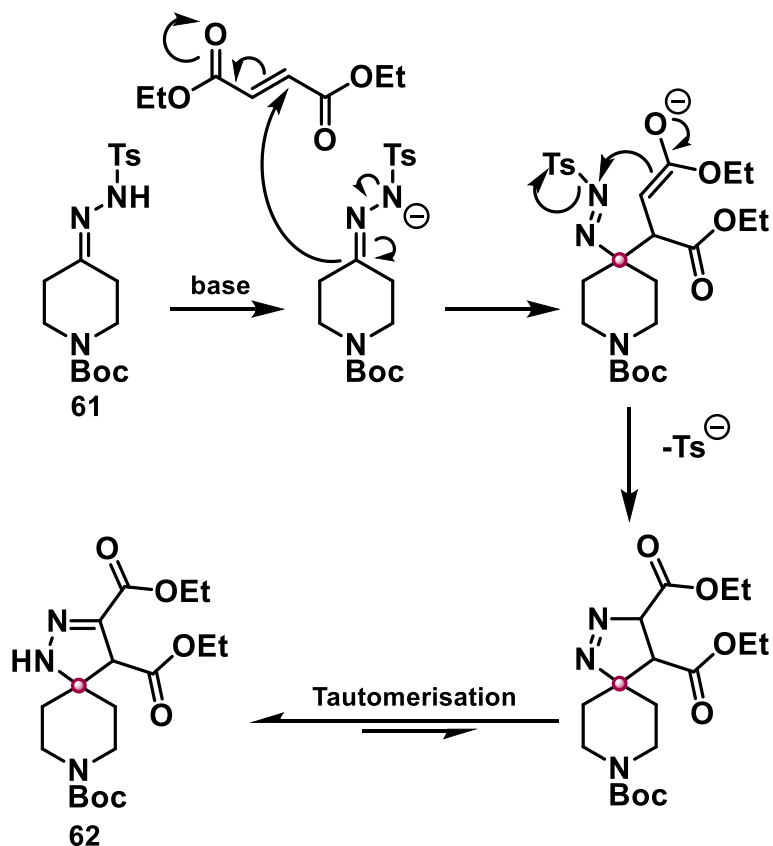


Scheme 45: Initial investigations into alkene electronics. Four separate reactions were run with alkenes: 3,4 dihydro 2H pyran, (**xxii**), 0%. 2,6-dimethyl-4H pyran-4 one, (**xxiii**), 0%. Styrene, (**xxiv**), 0%. Diethyl fumarate, **62**, 57%. Conditions: Step 1: 5.0 mmol tosyl hydrazine, 5.0 mmol ketone, 15 mL MeOH, RT, 3 hrs.^{167,171} Step 2: 0.1 mmol **61**, 0.15 mmol alkene, 0.15 mmol Cs₂CO₃, 0.5 mL 1,4-dioxane, 110°C, 22 hrs.^{167,171,191,192}

As shown in **Scheme 45** for the reactions which aimed to yield (**xxii**), (**xxiii**) and (**xxiv**) no spirocyclic product was observed. These reactions involved either the highly electron rich alkene (3,4-dihydro-2H-pyran, product (**xxii**)), a donor-acceptor “push-pull” alkene (2,6-dimethyl-4H-pyran-4-one, product (**xxiii**)) or a moderately electron deficient alkene (styrene, product (**xxiv**)). However, when a strongly electron deficient alkene was used (diethyl fumarate), a 57% isolated yield of the desired spirocyclic dihydropyrazole, **62** was obtained.

5.2.5. Proposed mechanism of formation

Because of the observation that conjugative electron withdrawn alkenes worked better, the following mechanism of action for the spirocycle formation step was proposed. Shown below in **Scheme 46**.



Scheme 46: Proposed mechanism for spirocycle formation.

After the sulfonamide has been deprotonated by a base, a conjugate addition of the tosyl group with a δ^+ (electron withdrawn) unsaturated carbon of diethyl fumarate is thought to occur. The resultant enolate intermediate displaces the tosylate, thus cyclizing to form the 5,6-spirocyclic dihydropyrazole.

With the optimum class of alkene for spirocycle synthesis determined and a probable mechanism proposed, the reaction between compound **61** and diethyl fumarate, was subsequently optimised using an internal standard and ^1H NMR yields for ranking of conditions.

5.3. Results and Discussion:

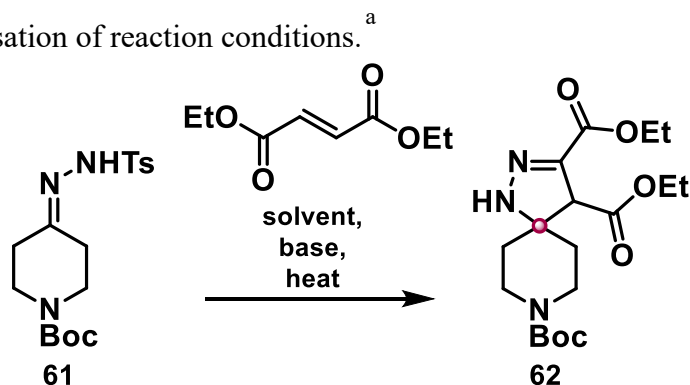
5.3.1. Spirocycle formation optimisation with model substrate

Initially optimisation of the reaction conditions focuses with a solvent screen (**Table 9**, entries 2-13) where polar aprotic solvents generally performed the best, with DMSO providing the highest yield at 74%. Polar aprotic solvents generally promote S_N2 reactions resulting in S_N1 reactions being comparatively slower thus rate-determining. Despite the reaction between the sulfonyl hydrazone and alkene not being a nucleophilic substitution, the intermolecular reaction step (**Scheme 46**) between the deprotonated sulfonamide and the alkene may be promoted by the polar aprotic solvent. Therefore, potentially enhancing overall rate, as the intramolecular cyclisation step would be considered faster relatively due to the tosyl being an excellent leaving group.

Since the yields of the optimisation reactions were being calculated using ^1H NMR, it was decided that for the remaining optimisation reactions d_6 -DMSO would be used as the reaction solvent to expedite the analysis process. It is important to note that the solvent screen and the initial base screen (**Table 9** entries 1-26) were conducted during prior work from a master's level project, with **Table 9** entries 27-40 done during this PhD project, by the titled PhD candidate.

The full optimisation for the spirocycle formation step is shown below in **Table 9**. *

* Denotes an important comment please refer to section 5.5 of this Chapter.

Table 9: Optimisation of reaction conditions.^a

entry	base	equiv. base	equiv. alkene	temp (°C)	solvent	yield (%) ^b
1*	Cs ₂ CO ₃	1.5	1.5	110	1,4-dioxane	57 ^c
2*	Cs ₂ CO ₃	1.5	1.5	110	toluene	29
3*	Cs ₂ CO ₃	1.5	1.5	110	DMF	52
4*	Cs ₂ CO ₃	1.5	1.5	100	acetone	22
5*	Cs ₂ CO ₃	1.5	1.5	100	MeCN	41
6*	Cs ₂ CO ₃	1.5	1.5	110	H ₂ O	0 ^d
7*	Cs ₂ CO ₃	1.5	1.5	100	1,2-DCE	27
8*	Cs ₂ CO ₃	1.5	1.5	110	DMSO	74
9*	Cs ₂ CO ₃	1.5	1.5	100	EtOH	41
10*	Cs ₂ CO ₃	1.5	1.5	80	THF	0 ^{d,e}
11*	Cs ₂ CO ₃	1.5	1.5	75	MTBE	47
12*	Cs ₂ CO ₃	1.5	1.5	50	Et ₂ O	0 ^d
13*	Cs ₂ CO ₃	1.5	1.5	110	PhCF ₃	33
14*	Cs ₂ CO ₃	1.5	1.5	110	<i>d</i> ₆ -DMSO	84
15*	Cs ₂ CO ₃	1.5	1.5	110	DMSO ^f	85
16*	Li ₂ CO ₃	1.5	1.5	110	<i>d</i> ₆ -DMSO	43
17*	Na ₂ CO ₃	1.5	1.5	110	<i>d</i> ₆ -DMSO	20
18*	K ₂ CO ₃	1.5	1.5	110	<i>d</i> ₆ -DMSO	58
19*	Rb ₂ CO ₃	1.5	1.5	110	<i>d</i> ₆ -DMSO	85
20*	LiOH·H ₂ O	1.5	1.5	110	<i>d</i> ₆ -DMSO	79
21*	NaOH	1.5	1.5	110	<i>d</i> ₆ -DMSO	71
22*	KOH	1.5	1.5	110	<i>d</i> ₆ -DMSO	75
23*	CsOH·H ₂ O	1.5	1.5	110	<i>d</i> ₆ -DMSO	85
24*	MgCO ₃	1.5	1.5	110	<i>d</i> ₆ -DMSO	58
25*	SrCO ₃	1.5	1.5	110	<i>d</i> ₆ -DMSO	10
26*	BaCO ₃	1.5	1.5	110	<i>d</i> ₆ -DMSO	0 ^e
27	DIPA	1.5	1.5	110	<i>d</i> ₆ -DMSO	82
28	NEt ₃	1.5	1.5	110	<i>d</i> ₆ -DMSO	13
29	KO ^t Bu	1.5	1.5	110	<i>d</i> ₆ -DMSO	0 ^d
30	TBAF	1.5	1.5	110	<i>d</i> ₆ -DMSO	55
31	CsF	1.5	1.5	110	<i>d</i>₆-DMSO	93
32	CsF	1.5	1.5	130	<i>d</i> ₆ -DMSO	39
33	CsF	1.5	1.5	90	<i>d</i> ₆ -DMSO	70
34	CsF	1.5	1.5	70	<i>d</i> ₆ -DMSO	20
35	CsF	1.5	1.5	50	<i>d</i> ₆ -DMSO	trace
36	CsF	0.5	1.5	110	<i>d</i> ₆ -DMSO	20
37	CsF	1.0	1.5	110	<i>d</i> ₆ -DMSO	32
38	CsF	2.0	1.5	110	<i>d</i> ₆ -DMSO	78
39	CsF	1.5	2.0	110	<i>d</i> ₆ -DMSO	90
40	CsF	1.5	1.0	110	<i>d</i> ₆ -DMSO	13

^a Reaction conditions: 0.25 mmol **61**, base, 0.375 mmol (1.5 equiv.) diethyl fumarate, 1 mL solvent, sealed tube, N₂ atmosphere, 22 hrs. ^b Yield determined by ¹H NMR using 1,4-dinitrobenzene as internal standard. ^c Isolated yield. ^d Complete conversion, no product formed. ^e Reaction ran for 48 h. ^f Solvent degassed, dried over 4Å molecular sieves and stored under N₂.

* Denotes an important comment please refer to section 5.5 of this Chapter.

However, when d_6 -DMSO was used instead of h_6 -DMSO an increase in yield to 84% was observed (**Table 9**, entries 8 and 14). This was concluded to be the result of the suspected reduced water content in the sealed vial of d_6 -DMSO compared with the pre-opened bottle of h_6 -DMSO. The reaction was subsequently run in h_6 -DMSO which had been degassed, dried over 4Å molecular sieves, and stored under a N₂ atmosphere prior to use, which provided an equivalent increased yield (**Table 9**, entry 15), thus confirming the cause for the initial difference in yields.

After the solvent was optimised the next aspect of the reaction that was investigated was the base, see **Table 9**, entries 16-31). Poorer yields were observed with small alkali metal carbonates (**Table 9**, entries 16-17), with the yield increasing with ionic radius (**Table 9**, entries 16-19). This is consistent with previous findings that large ionic radius carbonate bases provide better yields in reactions involving unstabilised tosylhydrazones.^{191,192} It is postulated that the lack of a tight ion pair between the hydrazone anion and the larger metal cations after deprotonation makes the former more reactive. However, in this case, the trend in yield is less pronounced than in previous studies,^{191,192} presumably due to the cation-coordinating nature of the solvent in this reaction having a sequestering effect, even on the smaller cations.

Stronger hydroxide bases provided similar high yields (**Table 9**, entries 20-23), but Cs₂CO₃ was preferred to avoid cross-reactivity with base sensitive functional groups when latterly exploring reaction scope.

Consistently poorer yields were observed with alkali earth metal carbonates (**Table 9**, entries 24-26). Whereas the secondary amine base diisopropylamine (DIPA) provided an equivalent yield to that of Cs₂CO₃ (**Table 9**, entry 27) but when, the tertiary amine base triethylamine performed very poorly (**Table 9**, entry 28).

Using a stronger base (KO^{*t*}Bu) provided complete conversion of the starting material but did not produce the desired spirocyclic product (**Table 9**, entry 29), this could be due to Bamford-Stevens type processes being favourable at utilised conditions. So further strong bases were discounted, as same or similar results to potassium *tert*-butoxide were expected. The Bamford-Stevens reaction is a chemical reaction whereby alkenes can be formed *via* treatment of tosylhydrazones with a strong base.¹⁹³ TBAF provided a moderate yield (**Table 9**, entry 30) before CsF provided a further improvement on the resultant ¹H NMR yield of 93% (**Table 9**, entry 31). Hence, CsF was selected as the

optimal base and taken forward into the final phase of reaction optimisation, assessing temperature and stoichiometry.

A short screen of reaction temperature revealed 110 °C to be optimal, with yields dropping off sharply above this and below 90 °C (**Table 9**, entries 31-35). A screen of base stoichiometry revealed 1.5 equivalents to provide the highest yield, with a small loss in yield from additional equivalents and fewer equivalents severely reducing the observed yield (**Table 9**, entries 31, 36-38). Finally, the reaction was found to be insensitive to increases in alkene stoichiometry, with further equivalents providing a similar yield (**Table 9**, entry 39), however the yield dropped sharply when the stoichiometry was reduced to 1.0 equivalent (**Table 9**, entry 40).

Further investigations found that the reaction was insensitive to being performed under open reflux conditions (rather than in a sealed tube) and that a N₂ atmosphere was not particularly beneficial. All yields in these examples were found to be within ± 3% of the optimised conditions (**Table 9**, entry 31). However, the optimised conditions were retained for exploration of the substrate scope as a precaution.

With regards to the formation of the sulfonyl hydrazone from the respective parent ketone (**Scheme 45** step 1) it was decided that no optimisation was required as the yields with the reported conditions being isolated were good to excellent in the majority of cases (30-82%).

5.3.2. Sulfonyl hydrazone

Therefore, with the overall optimised conditions (**Table 9**, entry 31) for the spirocycle formation step, a substrate scope of the reaction was conducted to determine the range of substrates the reaction could tolerate.

5.3.2.1. Synthesis

The initial branch of the spirocycle substrate scope was of a range of cyclic tosylhydrazones, the majority of which were made exclusively prior to the PhD project, the structures of the sulfonyl hydrazones synthesised additionally during the PhD project compound **61** or solely during the PhD project compounds **63**, **64**, **65**, **66** and **68**, hence all reported yields shown in **Figure 106** corresponds to this work.**

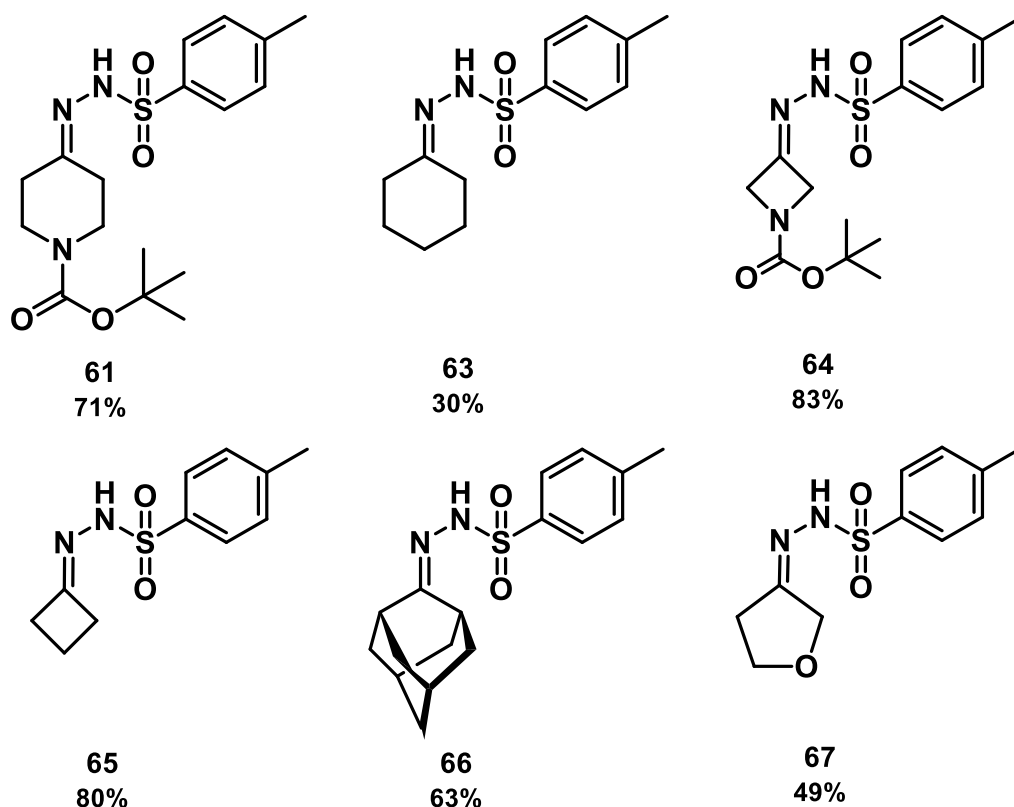


Figure 106: Structures of the sulfonyl hydrazone precursor compounds formed during the PhD project.

Reaction conditions for compounds **61**, **63-66** and step 2 for **67**: Cyclic ketone (1.0 equiv.), methanol, tosyl hydrazide (1.0 equiv.), RT, overnight. Reaction conditions for compound **67** (step 1) – One pot: 3-hydroxytetrahydrofuran (1.0 equiv.), DCM, PCC (2.0 equiv.), RT, upon completion, carefully concentrate then follow above step with this product as cyclic ketone.

For the majority of the sulfonyl hydrazones shown in **Figure 106**, a good to excellent yield was obtained, the two exceptions are **63** and **67**. The lower yield of 49% for **67** can be explained by the inclusion of an additional linear step in its synthesis, this contributing to the attrition of yield. However, the lowest yield of 30% obtained when forming **63** is perhaps an anomalous result and could be greater if repeated.

5.3.2.2. Biological testing

The initial compound library related to 5,6-spirocyclic dihydropyrazoles tested consisted of the sulfonyl hydrazone procurers which were synthesised for this work or from prior work conducted by Dr Allwood. The structures of all sulfonyl hydrazones tested for PTP1B activity in the aforementioned yeast based inhibitory assay are shown below in **Figure 107**.

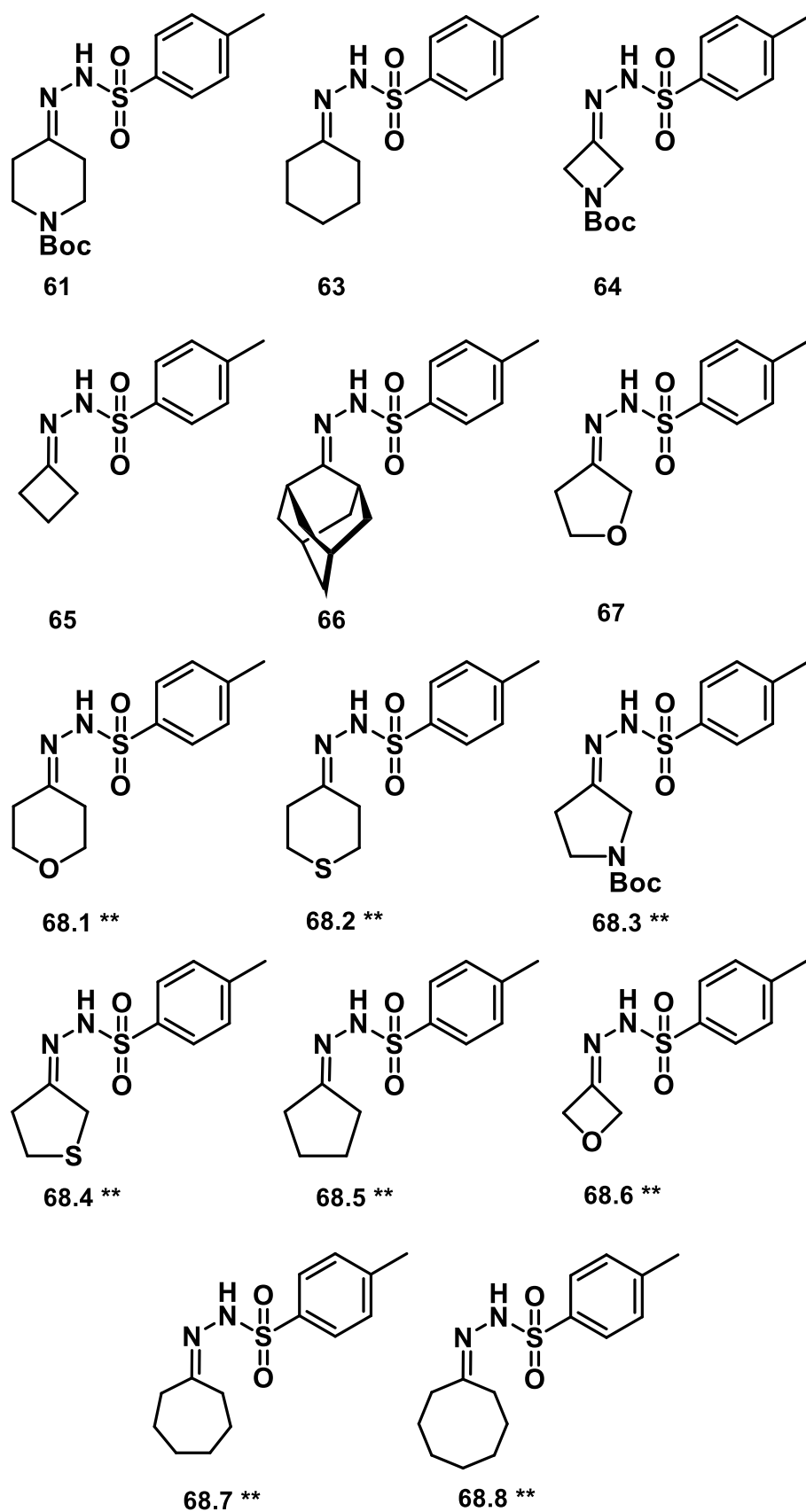


Figure 107: Composition of sulfonyl hydrazone compound library tested at 100 μ M.
****** Denotes important comment, see section 5.5 of this Chapter.

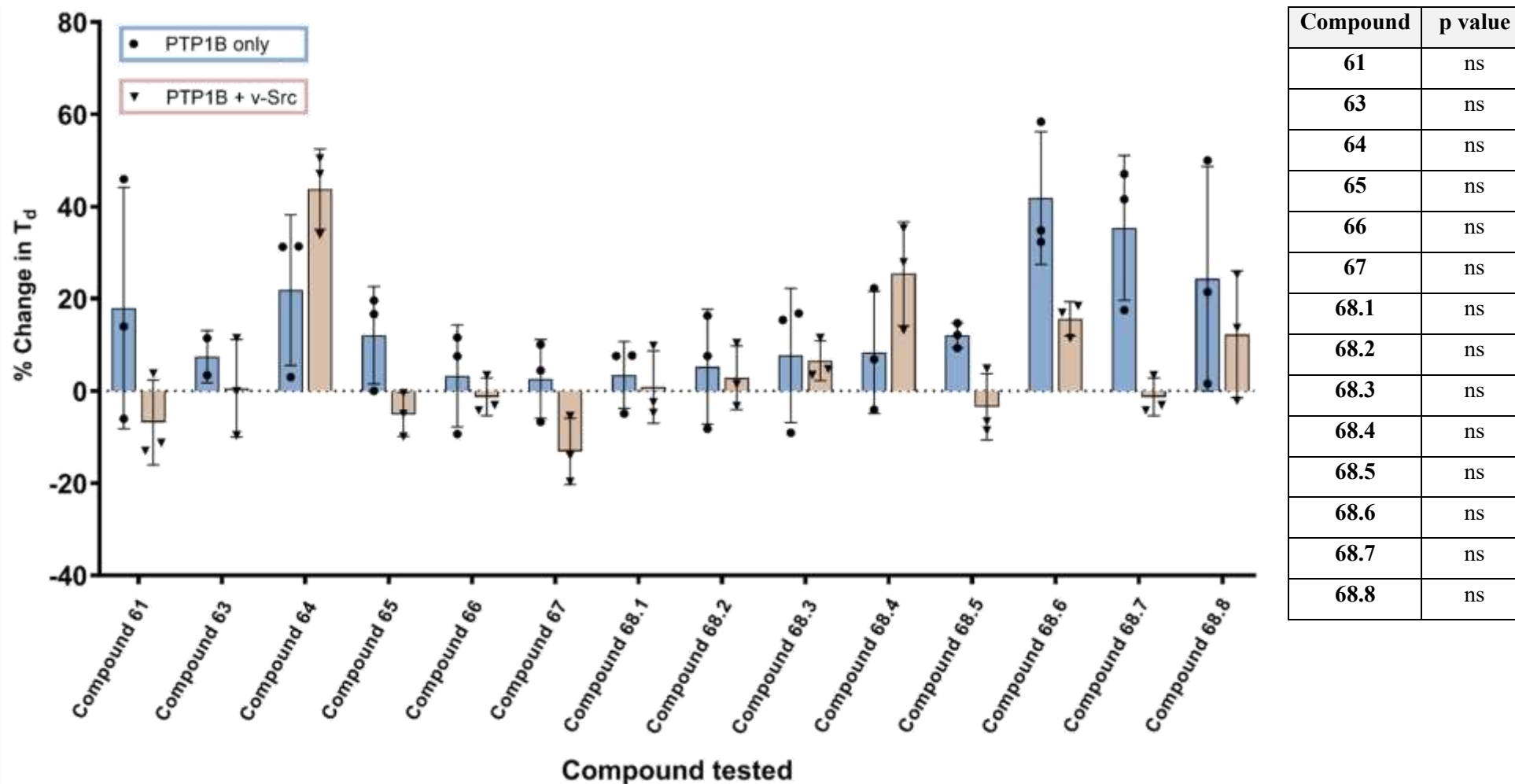


Figure 108: Comparison of % change in doubling time (T_d) of PTP1B only and PTP1B + v-Src transformed yeast cells in the presence of synthesised compounds **61**, **63-68** at 100 μ M. $n=3$ for all compounds tested in both transformations, mean and individual points \pm standard deviation plotted. Used non-parametric Mann-Whitney t-test for statistical analysis. * p value ≤ 0.050 vs control.

As illustrated above in **Figure 108**, and the appendix (section 3.1.2) only two of the sulfonyl hydrazones investigated compound **64** and **68.4**, demonstrated a significant increase in doubling time in PTP1B + v-Src cells than the observed effect in PTP1B only YMK23 yeast cells. However, the difference in the percentage increase in T_d values for PTP1B only and PTP1B + v-Src transformed cells was not significant for the addition of both compound **64** and **68.4**.

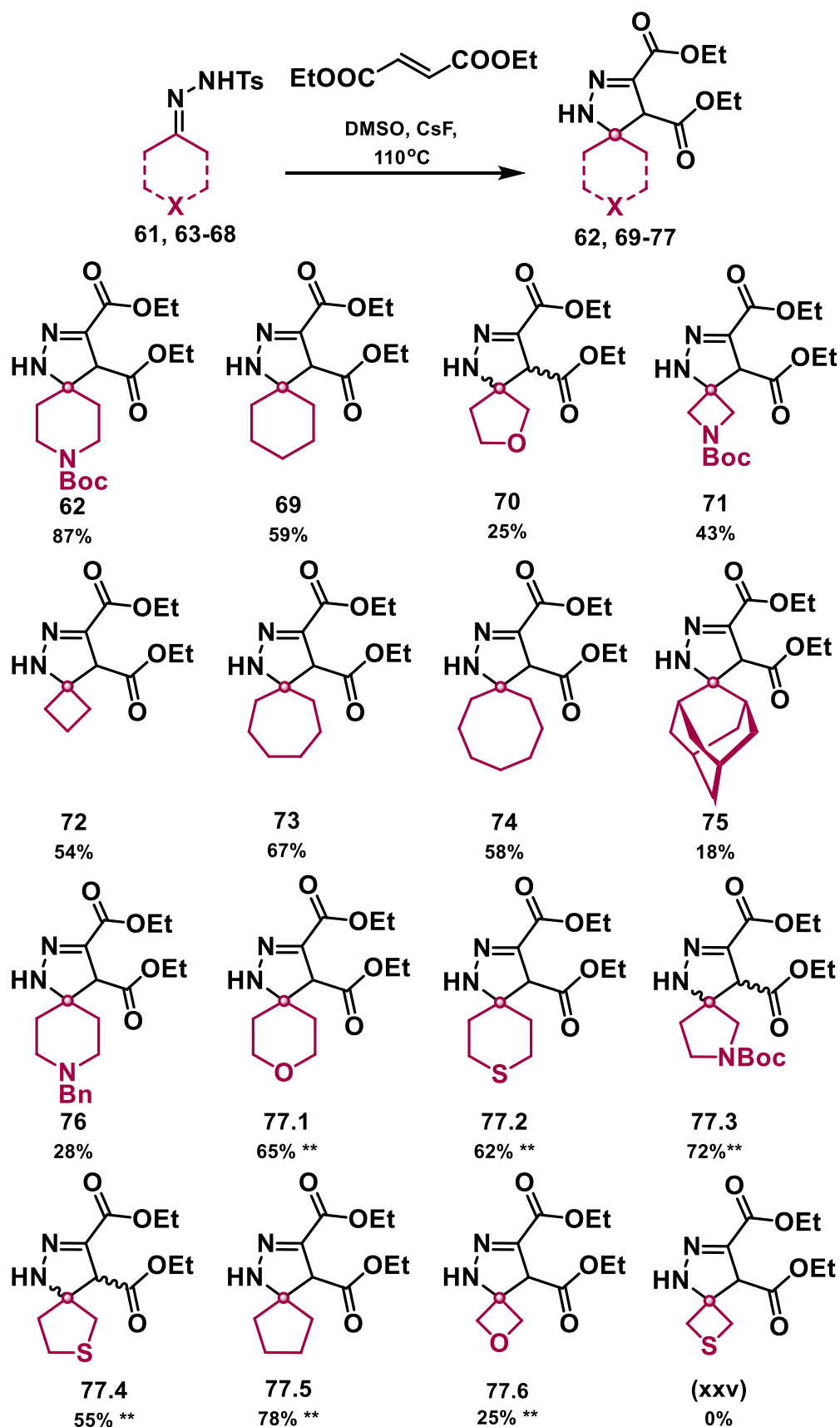
The lack of significance suggests that these compounds do not act as PTP1B inhibitors as the significant increase in PTP1B only transformed cells is not due to inhibition and instead other factors which may also translate to the PTP1B + v-Src transformed cells.

In order to gain additional information on whether compound **64** or **68.4**, can act as PTP1B inhibitors a dose response screen of 20-500 μ M was conducted in both **64** and **68.4**. Full % change in T_d results shown in the appendix (section 3.1.2). Again, no significant difference between the percentage increase in doubling times observed in PTP1B only cells with PTP1B + v-Src cells with the addition of either compound at any of the investigated concentrations, hence no sulfonyl hydrazone demonstrated significant PTP1B inhibitory properties and therefore were not investigated further.

5.3.3. Spirocycle substrate scope

5.3.3.1. Sulfonyl hydrazone altered spirocycle synthesis.

All the corresponding sulfonyl hydrazones utilised in the below spirocycle substrate scope (**Scheme 47**) were synthesised from the respective parent ketone with the previously published method shown above in **Scheme 45** step 1.^{167,171,191,192} The only exception is **70** as its corresponding sulfonyl hydrazone was formed in a one-pot process from the equivalent primary alcohol.



Scheme 47: Isolated yields from reaction of tosylhydrazones **61**, **63-68** with diethyl fumarate.

Reaction conditions: Sulfonyl hydrazone (1.0 mmol), diethyl fumarate (1.5 equiv.), CsF (1.5 equiv.), dried DMSO (4 mL), 110 °C, 22 hrs, sealed vial, N₂ atmosphere.¹⁶⁷

** Denotes important comment, see section 5.5 of this Chapter.

The isolated yield results and trends shown in **Scheme 47**, is discussed in previously published work, referenced here.¹⁶⁷

For the reaction on the thietane ring system, compound (**xxv**) no desired product was recovered, this may be due to the same ring-opening process on the thietane ring as mentioned previously published work.¹⁶⁷

Larger medium-sized carbocyclic rings provided spirocyclic products in moderate to good yields (**73** and **74**). However, when a sterically bulky adamantanone substrate (**75**) was utilised a poor yield of 18% was observed. This could be due to the bulky substrate blocking planes of attack of the diethyl fumarate thus causing the initial step to occur at a potentially slower rate.

However, with regards to **76** a poor yield of 28% was acquired, despite the only difference with the original substrate (**62**) being the amine protecting group. The electronic properties of the protecting group at this position (Boc or Bn) may contribute to the isolated yield, but such a vast difference of near 50% was not expected.

5.3.3.2. Biological testing of initial wave of spirocycles

The initial wave of spirocycles investigated as potential PTP1B inhibitors are shown in **Figure 109** and are the result of sulfonyl hydrazone precursor screen where the same electron deficient alkene, diethyl fumarate was utilised. The results presented as a percentage change in doubling time for these compounds in PTP1B based YMK23 yeast cells is shown below in **Figure 110**.

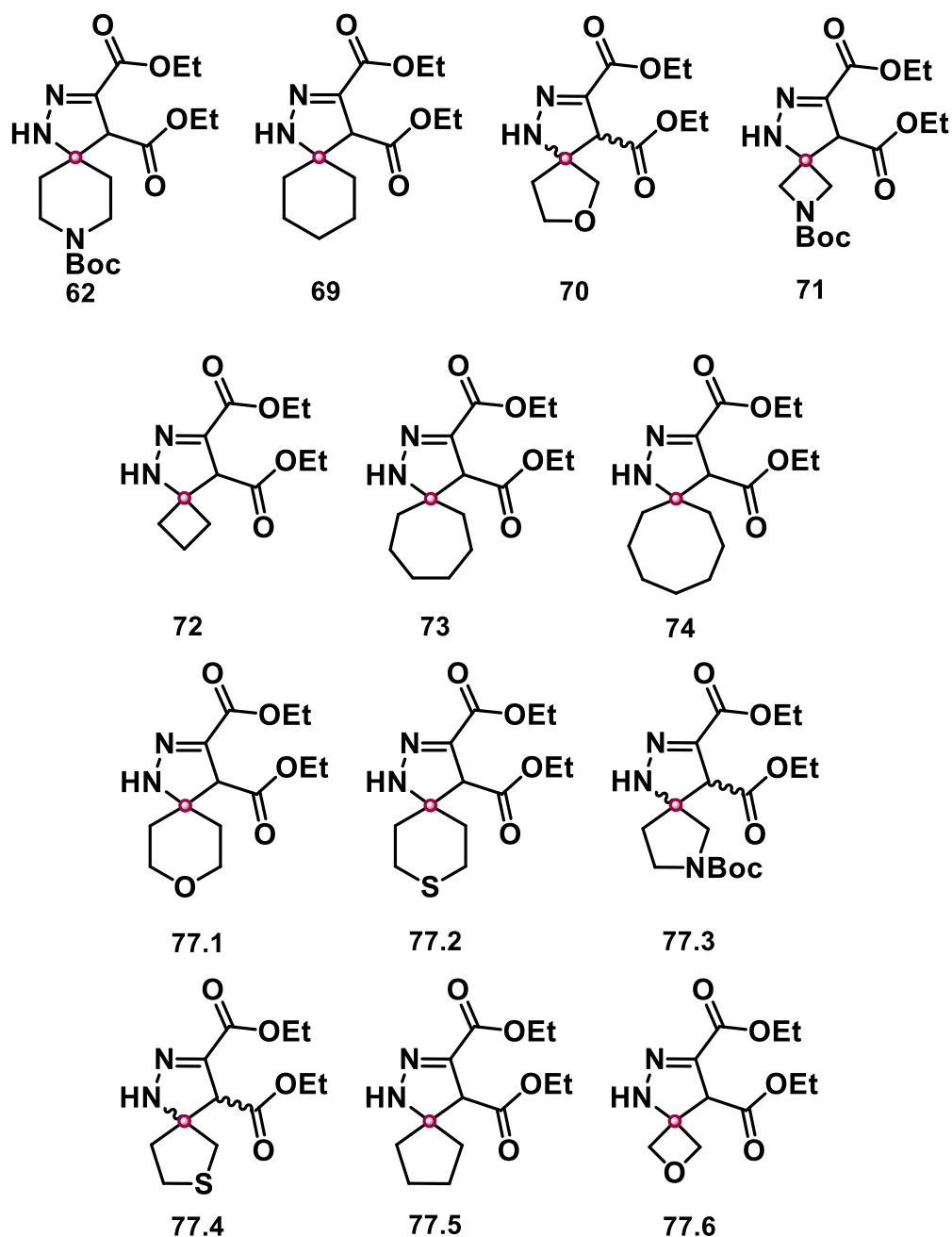


Figure 109: First compound library of spirocycle dihydropyrazoles tested at 100 μM .

From the initial spirocycle dihydropyrazoles investigated as potential PTP1B inhibitors as shown in **Figure 110** and the appendix (section 3.1.3) compounds **62** and **69-77.6** demonstrated significant PTP1B inhibition. Computational results highlighted in Chapter 2 (sections 2.3.2), support this as 5,6-spirocycles were identified as potential PTP1B active site inhibitors, and the majority of the compounds shown in **Figure 109** are comprised of different spirocyclic core structure.

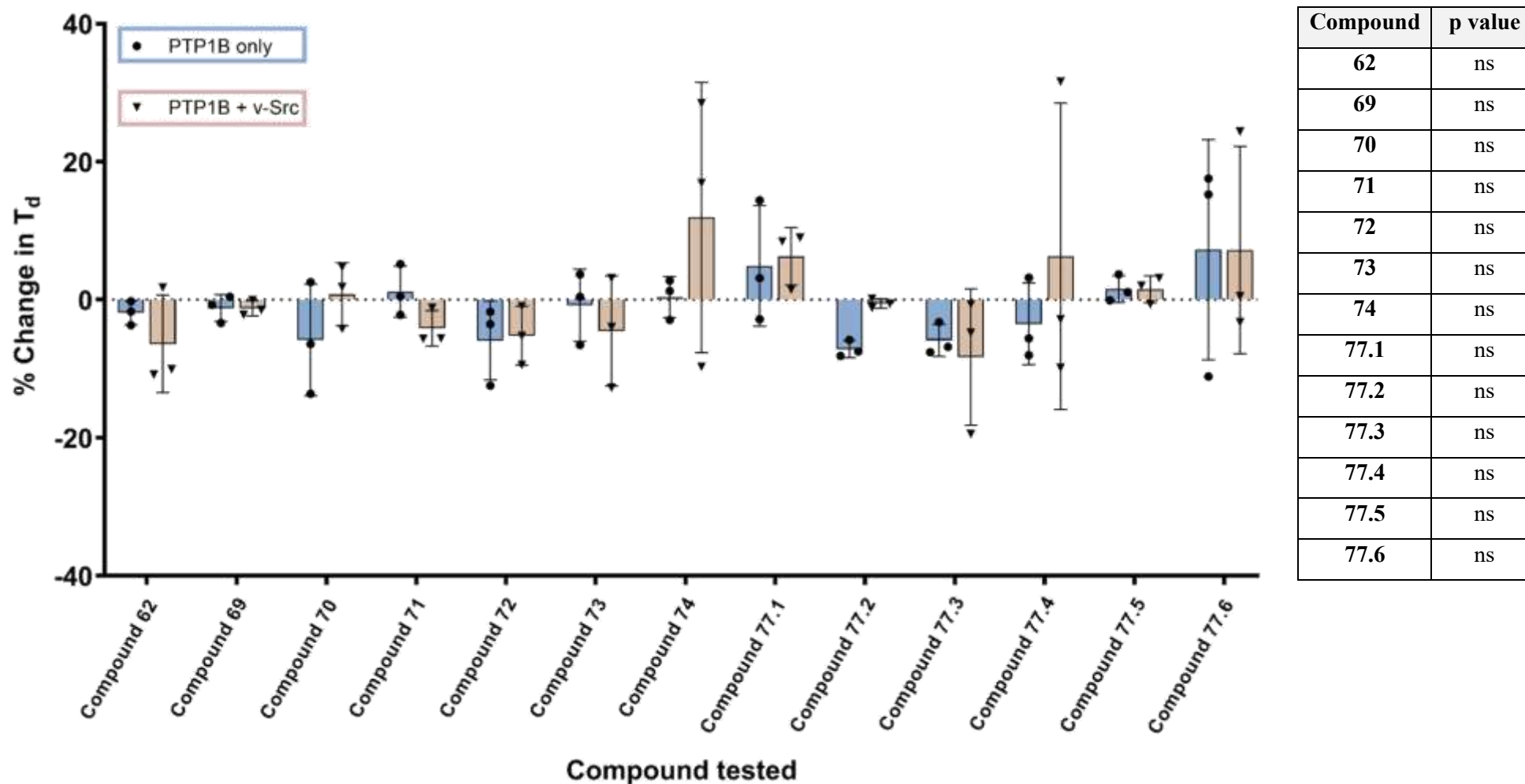
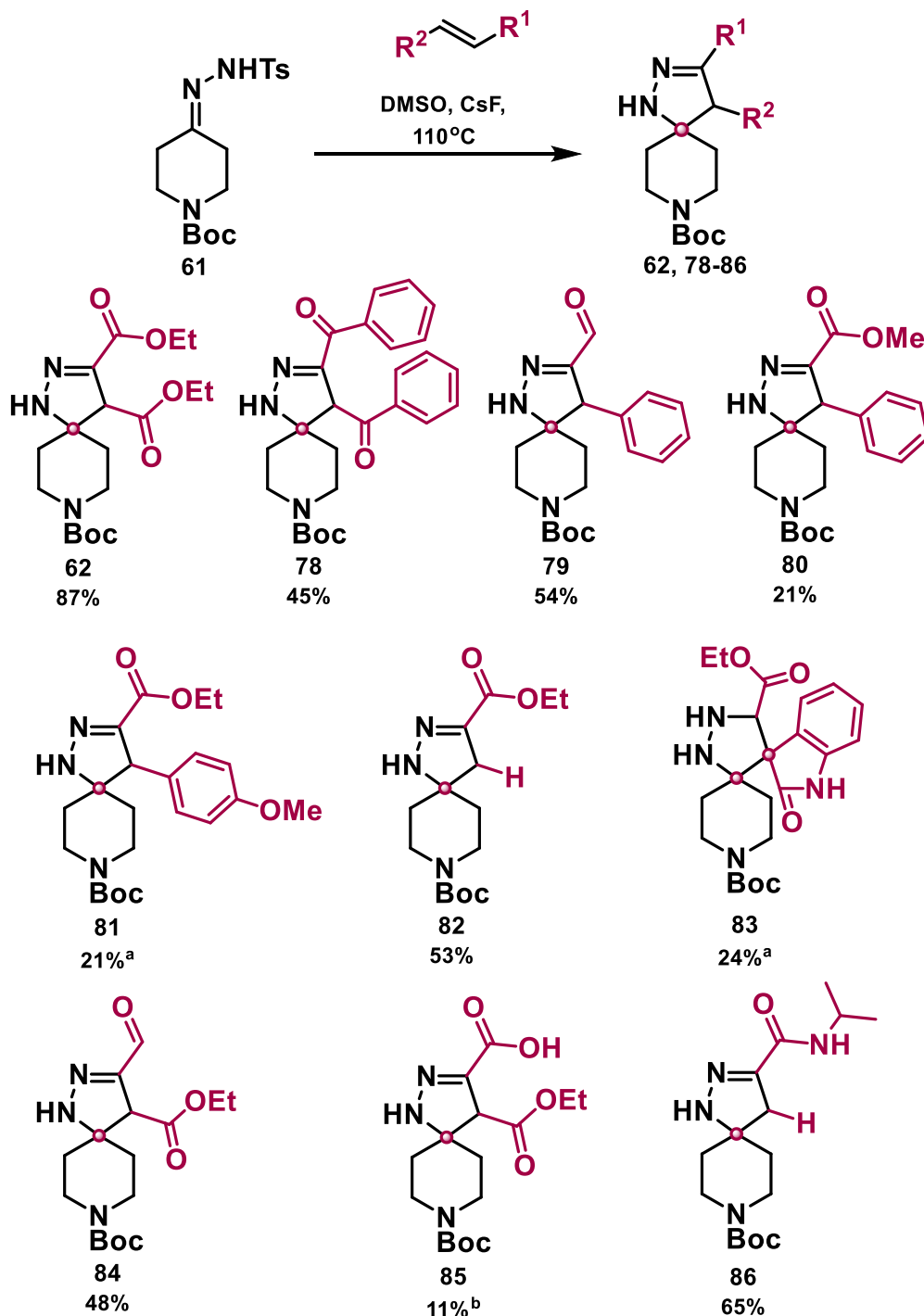


Figure 110: Comparison of % change in doubling time (T_d) of PTP1B only and PTP1B + v-Src transformed yeast cells in the presence of synthesised compounds **62**, **66-74** and **77** at 100 μM . $n=3$ for all compounds tested in both transformations, mean and individual points \pm standard deviation plotted. Used non-parametric Mann-Whitney t-test for statistical analysis. * p value ≤ 0.050 vs control.

The next compound library of spirocycles consisted of a core 5,6 bicyclic structure and were the result of a screen of different electron deficient alkenes which were reacted with the sulfonyl hydrazone **60**. The synthesis and subsequent testing are outlined below.

5.3.3.3. Alkene altered spirocycle synthesis.



Scheme 48: Isolated yields from reaction of **61** with a range of different alkenes.

Reaction conditions: **61** (1.0 mmol), alkene (1.5 equiv.), CsF (1.5 equiv.), dried DMSO (4 mL), 110 °C, 22 hrs, sealed vial, N₂ atmosphere.

^aAlkene used was synthesised *via* Wittig reaction (compounds **87** and **88**), all others are commercially available. ^b 2.5 equiv. of CsF used.

The alkene scope of successfully synthesised compounds is shown above in **Scheme 48**. The initial focus for the alkene scope was on the electronics and size of the 'R' groups that could be incorporated into the synthesis and the resultant effect they had on the isolated yields. As is shown in **Scheme 48**, a wide variety of alkenes, both symmetrical and non-symmetrical can be incorporated in the optimised synthesis method. However, the initial alkene used for the reaction optimisation (diethyl fumarate) resulted in the highest isolated yield of 87% (**62**).

The first alkene investigated was diethyl acrylate which as expected produced a lower percentage yield of 53% (**82**). This alkene is less electron deficient due to possessing one ethyl ester group, resulting in electron density only being pulled from the unsaturated carbons in one direction. Unlike with alkenes comprised of two electron withdrawing groups where electron density is pulled out of the unsaturated carbons in opposite directions.

One key trend that is maintained in all examples is that when unsymmetrical alkenes are deployed, regioselective for the more electron-withdrawing R group functionality being more distant from the spirocyclic ring junction (R¹ position). This is consistent with the previously proposed mechanism where the electron withdrawing group is required to be at that position for the initial conjugate attack of the tosylhydrazonyl anion to occur.⁹⁹

This is observed in compound **83** where the sterically bulky isatin derived group exclusively is adjacent to the spiroatom resulting in a more sterically strained product than if the reverse occurred, with the ester bound a spirocyclic ring junction. The resultant steric strain observed in the ring system of compound **83** could explain the relatively poor isolated yield of 24%, along with the saturation of the double bond normally present in the five-membered ring. Hence the alkenes R group's electronics takes precedence over the steric factors when assigning R group positions, thus supporting the above proposed mechanism (**Scheme 46**).

An alkene bearing both an aldehyde and ester functional group provided the corresponding product **84** in moderate yield and was regioselective for the aldehyde functionality being more distant from the spirocyclic ring junction. compound **84** represents a compound bearing mutually orthogonal reactivity on the dihydropyrazole ring, allowing selective further functionalisation. An alkene bearing two ketone functional groups provided product **82** in moderate yield, while cinnamaldehyde selectively formed the regioisomer of compound **79** shown, with the aromatic ring closest to the spirocyclic

junction. But, when a similar substrate to those used by Wu *et al.*¹⁸⁸ was assessed, the yield was relatively poor (compound **80**), demonstrating the complementarity of these protocols. However, this poor yield of 21% was maintained after the addition of OMe to the *para* position of the aromatic ring (compound **81**), thus enabling a means of subsequent functionalisation, at that position.

When N-isopropylacrylamide was utilised as the alkene a good yield of 65% was observed (compound **86**), despite only containing one electron withdrawing group. Again, the stated regioisomer was exclusively formed.

Finally, with regards to compound **85** the regioisomer shown in **Scheme 48** was again solely produced despite the two R groups present in 4-ethoxy-4-oxobut-2-enoic acid having comparable electronic properties, meaning that the unsaturated carbon in the β position to the carboxylic acid is preferential for attack by the tosylhydrazonyl anion. A potential reason for this could be the formal negative charge on the carboxylic acid (due to deprotonation by the excess base), as that would repel the tosylhydrazonyl anion attack thus making the cyclisation less favourable. Additionally, the low isolated yield of only 11% for compound **85** could also be partly due to the increased excess of base (CsF) utilised for this specific substrate, to account for the acidity of the carboxylic acid motif.

As shown above in **Table 9**, entry 38, when the equivalence of CsF was increased to 2.0 equiv. a drop in yield of ~15% was observed in the formation of compound **62**, compared against the optimal amount of CsF (1.5 equiv., **Table 9**, entry 31). This could also contribute to why the desired spirocyclic product for maleic acid could not be obtained as 3.5 equiv. of CsF were added to this reaction to account for presence of two acidic carboxylic acid functional groups.

5.3.3.4. Biological testing of selected examples from the alkene substrate scope

Of the ten compounds synthesised from electron deficient alkene substrate scope, five with different 'R' groups were selected and tested as potential PTP1B inhibitions. The chosen compounds are shown below in **Figure 111**.

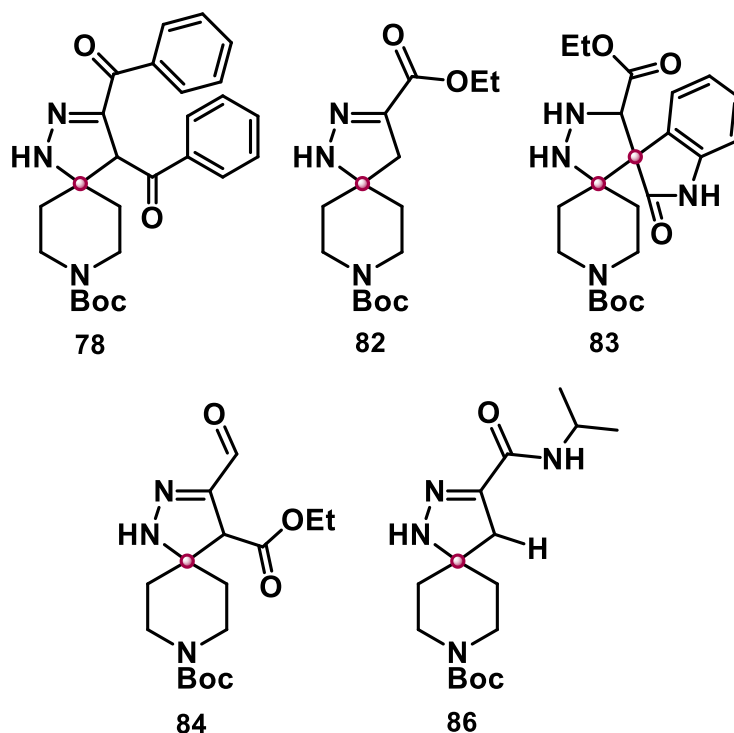
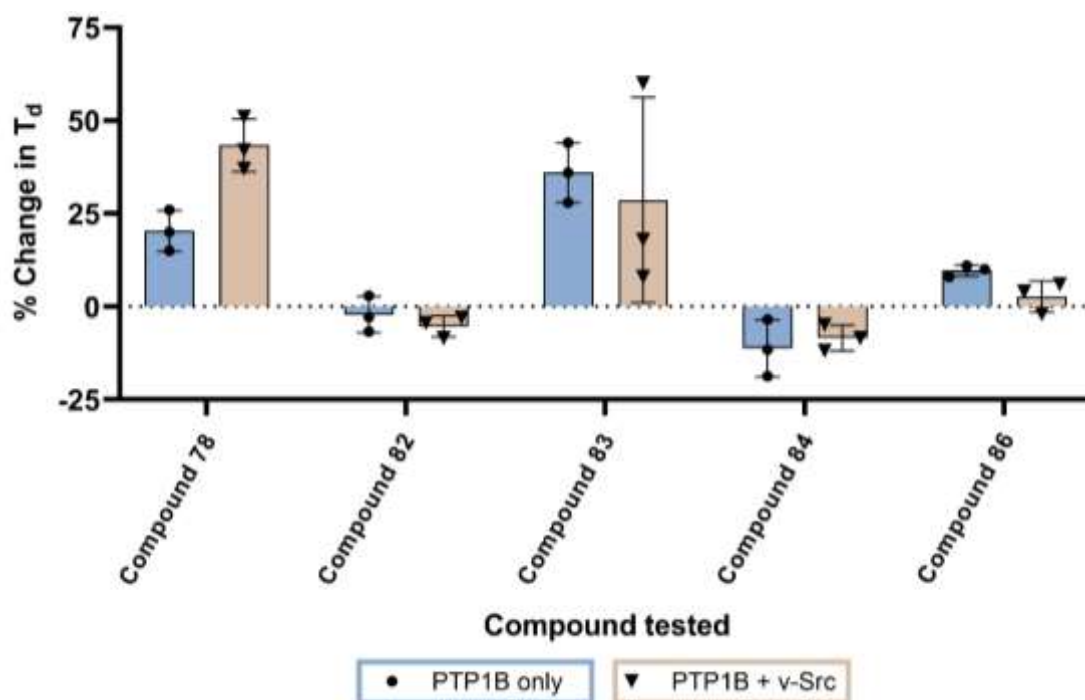


Figure 111: Second compound library of spirocycle dihydropyrazoles tested at 100 μM .

The biological inhibitory results from the compounds outlined in **Figure 111** are illustrated below in terms of a percentage change in the doubling time from that of the base growth for each specific biological replicate.

From the five-alkene substrate scope 5,6-spirocyclic dihydropyrazole compounds tested, one did demonstrate a consistently greater response in PTP1B + v-Src cells than PTP1B only transcribed cells. As shown in **Figure 112** this was compound **78**, and despite showing a significant increase in the doubling time of PTP1B only cells at 100 μM , where PTP1B inhibition is not tied to growth rate this compound **78** still underwent subsequent further study due to the increase in T_d value in PTP1B + v-Src being more significant when compared against the corresponding base growth than in PTP1B only cells. This is shown in the appendix (section 3.1.4).



Compound	78	82	83	84	86
p value	ns	ns	ns	ns	ns

Figure 112: Comparison of % change in doubling time (T_d) of PTP1B only and PTP1B + v-Src transformed yeast cells in the presence of synthesised compounds **78**, **82-84** and **86** at 100 μM . $n=3$ for all compounds tested in both transformations, mean and individual points \pm standard deviation plotted. Used non-parametric Mann-Whitney t-test for statistical analysis. * p value ≤ 0.050 vs control.

5.3.3.5. Hit compound 78 PTP inhibitor investigation.

As with the identified hit compounds and known inhibitors shown in the prior two chapters this potential PTP inhibitor **78** was investigated initially by undergoing a dose response screen of 20-500 μM in both PTP1B and TCPTP based transcribed yeast cells, results demonstrated below.

5.3.3.5.1. PTP1B based dose response screen.

Initially compound **78** was tested for PTP1B inhibition over a range of 20-500 μM the results for which are shown in **Figure 113**.

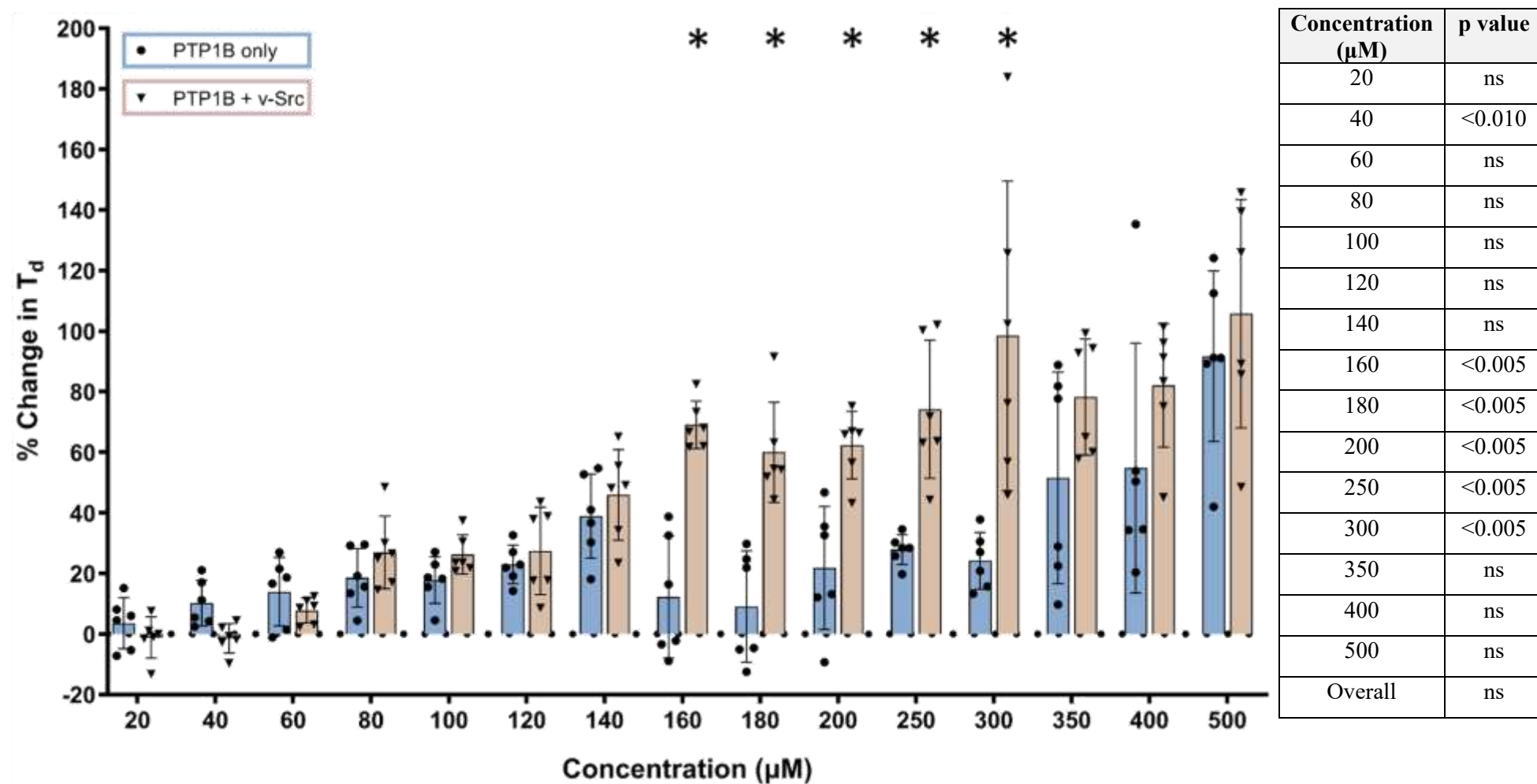


Figure 113: Comparison of % change in doubling time (T_d) of PTP1B only and PTP1B + v-Src transformed yeast cells in the presence of compound **78** at 20-500 μM . $n=6$ for all concentrations tested in both transformations, mean and individual points \pm standard deviation plotted. Used non-parametric Mann-Whitney t-test for statistical analysis. * p value ≤ 0.050 vs control.

As shown above in **Figure 113**, overall, in terms of percentage change in T_d there is no statistically significant difference between compound **78** addition in PTP1B only and PTP1B + v-Src transformed yeast cells. However, when compound **78** was added at 160, 180, 200, 250 and 300 μM the % change in T_d for PTP1B + v-Src was significantly greater than the response in PTP1B only for the corresponding concentration. This denotes inhibitory action of compound **78** towards PTP1B. The lowest concentration to exert a significant inhibitory response was 160 μM (p value <0.005), and the highest mean significant inhibitory response of 100% occurred at 300 μM (p value <0.005) The same concentration range was investigated in the corresponding TCPTP based YMK23 transformed yeast cells in order to investigate PTP selectivity.

5.3.3.5.2. TCPTP based dose response screen.

The results shown in **Figure 114** below indicate that compound **78** may be specific towards TCPTP over PTP1B. This is due to a couple of reasons. Firstly overall (20-500 μM) the % change in T_d of TCPTP + v-Src cells was significantly greater than controls (p value <0.050). Secondly a higher maximum average inhibitory response was present in TCPTP (135%) than PTP1B (100%), at 400 μM in TCPTP + v-Src. Thirdly the lowest concentration where a significant % increase in T_d for TCPTP was at 60 μM , which is 100 μM lower than the minimum concentration needed for PTP1B. This lower concentration where a statistically relevant TCPTP inhibition occurs again supports the notion that compound **78** exerts a greater inhibitory response towards TCPTP active site inhibition over PTP1B active site inhibition.

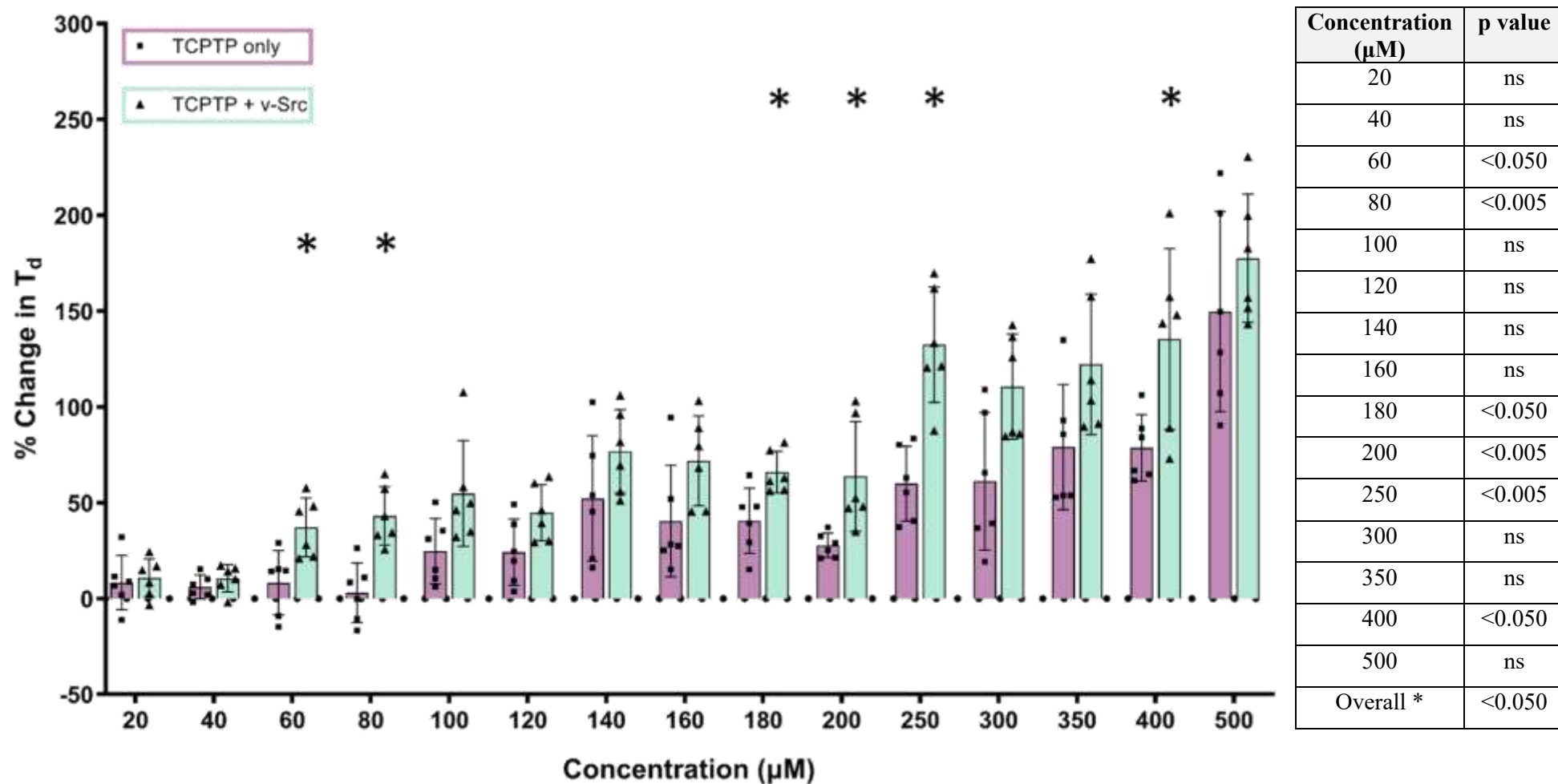
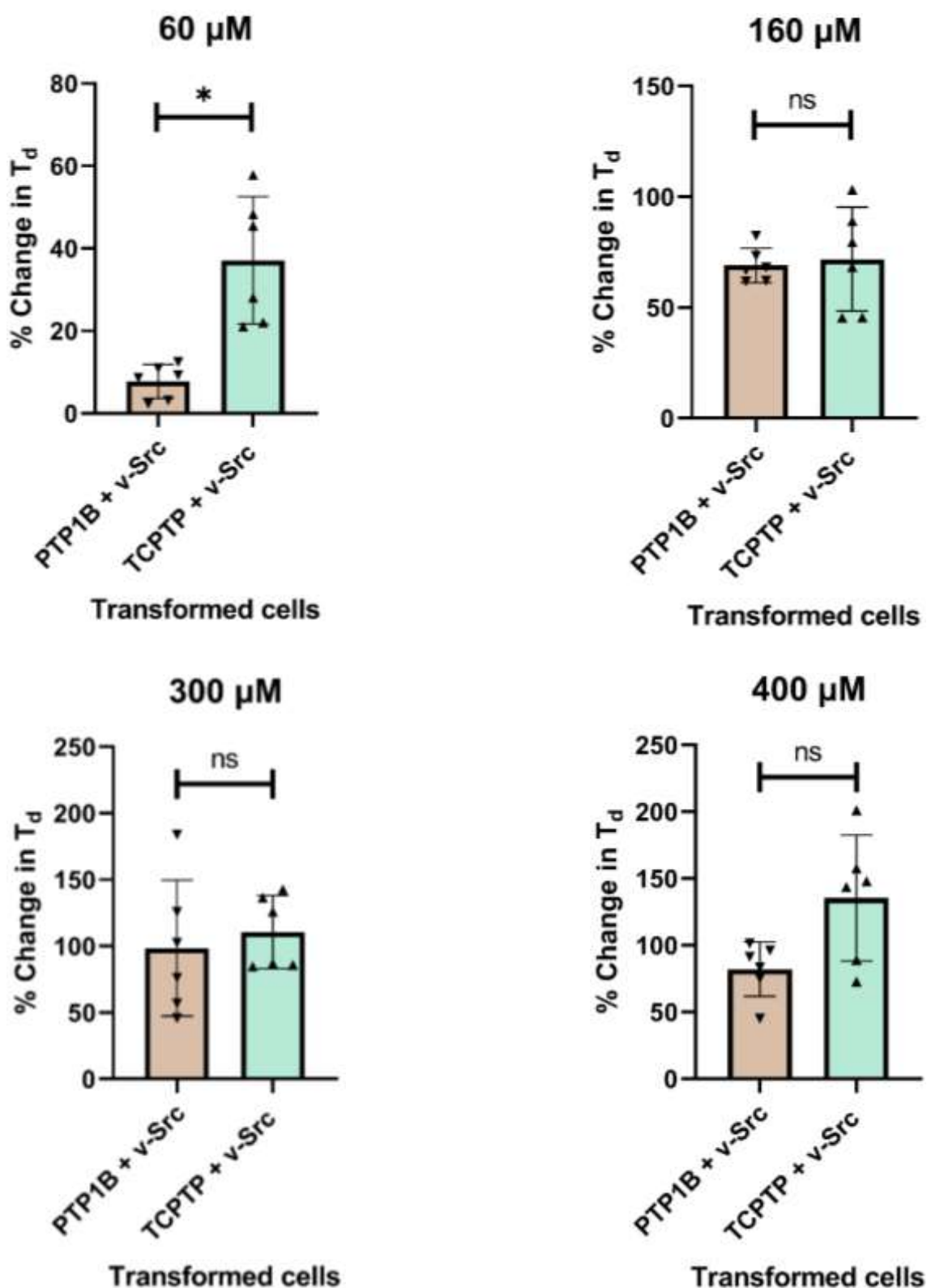


Figure 114: Comparison of % change in doubling time (T_d) of TCPTP only and TCPTP + v-Src transformed yeast cells in the presence of compound 78 at 20-500 μM . $n=6$ for all concentrations tested in both transformations, mean and individual points \pm standard deviation plotted. Used non-parametric Mann-Whitney t-test for statistical analysis. * p value ≤ 0.050 vs control.

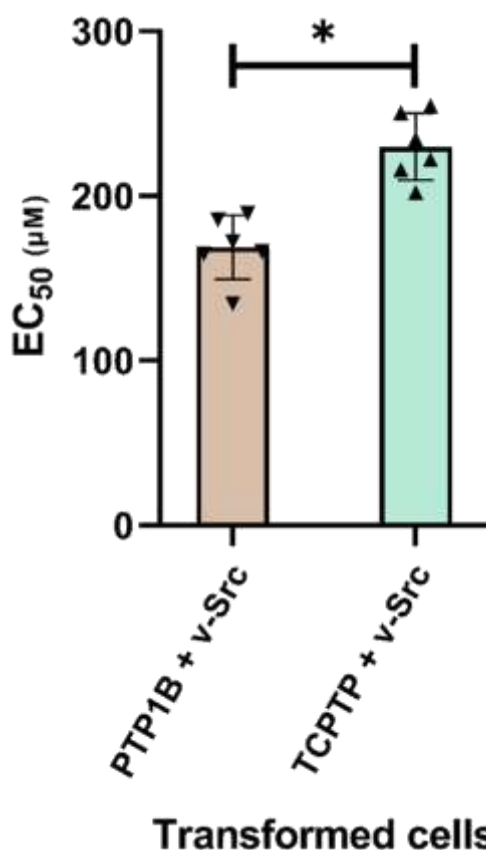


Concentration (μM)	60	160	300	400
p value	<0.005	ns	ns	ns

Figure 115: Comparison of % change in doubling time (T_d) of PTP1B + v-Src and TCPTP + v-Src transformed yeast cells in the presence of compound **78** at 60, 160, 300 and 400 μM . $n=6$ for all concentrations tested in both transformations, mean and individual points \pm standard deviation plotted. Used non-parametric Mann-Whitney t -test for statistical analysis. * p value ≤ 0.050 PTP1B + v-Src vs TCPTP + v-Src.

As demonstrated in **Figure 115**, despite the average inhibitory response being greater in TCPTP than the PTP1B for all concentrations tested (20-500 μM), overall, there is no significant difference in the inhibitory response caused by compound **78** towards PTP1B or TCPTP. Amongst the noteworthy concentrations investigated, only 60 μM (the minimum concentration for TCPTP inhibition) was significantly higher in TCPTP + v-Src than PTP1B + v-Src (p value <0.005). At 160 μM , the minimum concentration for PTP1B inhibition, the inhibitory response between both PTPs was not significantly different. This is also the case at both 300 and 400 μM , demonstrating that compound **78** is only significantly specific towards TCPTP at lower concentrations (40 and 60 μM). Another measure of this is potency which is investigated here and compared *via* the calculation of EC_{50} values, as shown below in **Figure 116**.

5.3.3.5.3. EC_{50} comparison



p value	<0.005
---------	----------

Figure 116: Comparison of EC_{50} values of compound **55** for PTP1B and TCPTP active site inhibition. $n=6$ for all both types of transformed cells. Mean and individual points \pm standard deviation plotted. Used non-parametric Mann-Whitney t-test for statistical analysis. * p value ≤ 0.05 for PTP1B + v-Src vs TCPTP + v-Src.

As **Figure 116** demonstrates, compound **78** appears to be more potent towards PTP1B than TCPTP due to having a significantly lower EC_{50} value. This was expected as the concentration needed to reach half the maximum % increase in T_d in PTP1B would be lower as the average maximum effect was an increase of 106%, whereas for TCPTP it is 180% (500 μ M).

However, despite the lower EC_{50} value of compound **78** in PTP1B, due in part to the lower initial concentration (60 μ M) where a significant inhibitory response occurred. In addition to the significantly greater maximum response in TCPTP (p value <0.050). Compound **78** is considered specific towards TCPTP at lower concentrations. This increased activity may in part be due to a stronger binding mode between **78** and the TCPTP active site. This was investigated computationally in both of the PTP active sites.

5.3.3.5.4. Computational binding mode investigation

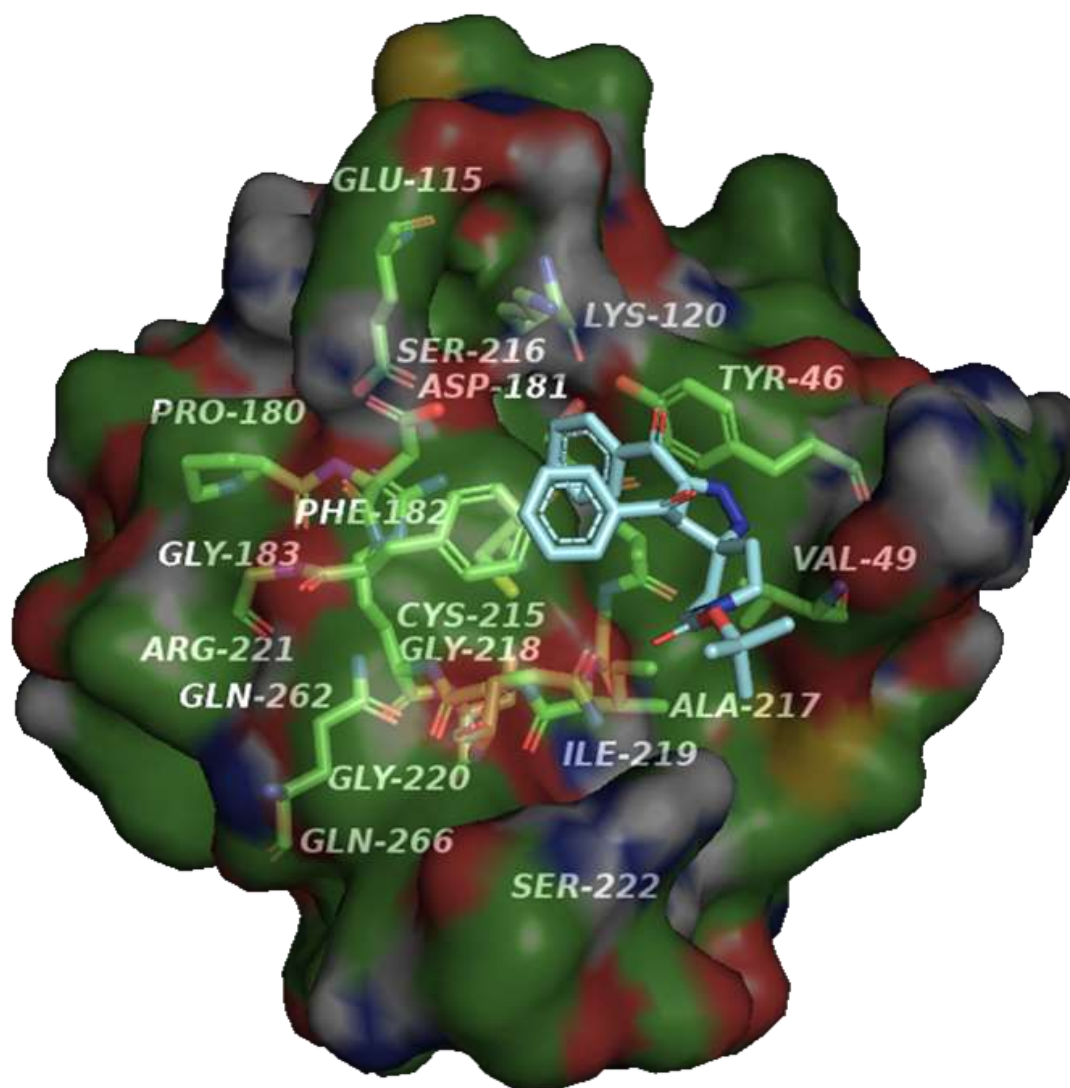


Figure 117: Computational most favoured proposed binding mode of compound **78** in the closed conformation of the PTP1B active site.

When looking at **Figure 117** from the computational docking data, as expected the main means of compound **78** binding is not with interactions involving Cys-215 and surrounding residues as with benzodioxane hit compounds such as **30a** (Chapter 4 section 4.3.7.3.2), but instead π -stacking of both aromatic 'R' groups of compound **78**, with both Tyr-46 and Phe-182. Additional interactions include hydrogen bonding with the residues Val-49 and with Gln-262, however from this proposed binding position numerous potential functional handles of compound **78** are unable to interact with the PTP1B active site, these include both the carbonyls adjacent to the benzene rings and the tri-methyl motif which could be a source of hydrophobic interactions, which as stated in Chapter 2 (section 2.3.1) has been shown beneficial for PTP active site binding.

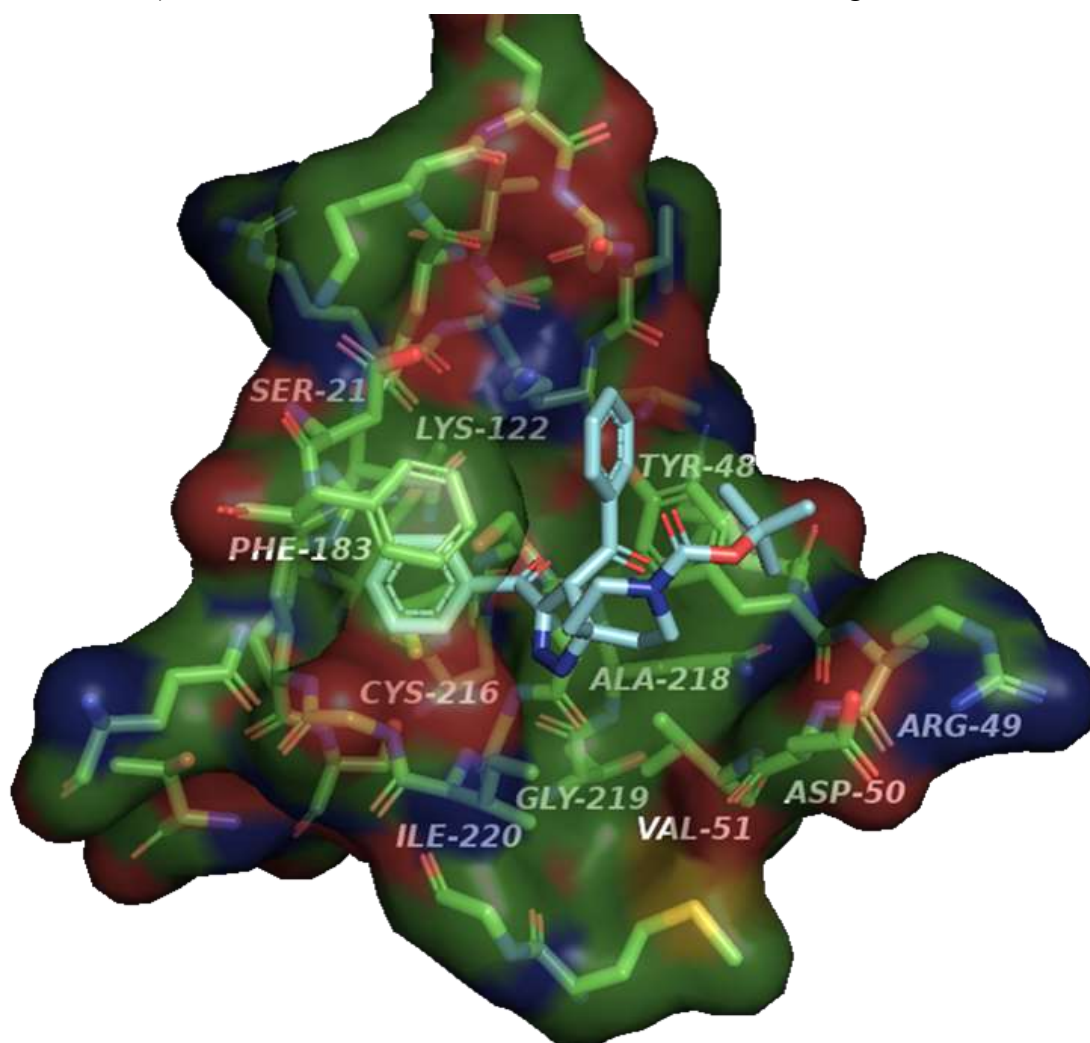


Figure 118: Computational most favoured proposed binding mode of compound **78** in the closed conformation of the TCPTP active site.

When comparing the proposed favoured binding mode of compound **78** in the TCPTP active site as shown in **Figure 118** it is apparent that in addition to the binding interaction predicted to occur between **78** and PTP1B, additional interactions are proposed to occur.

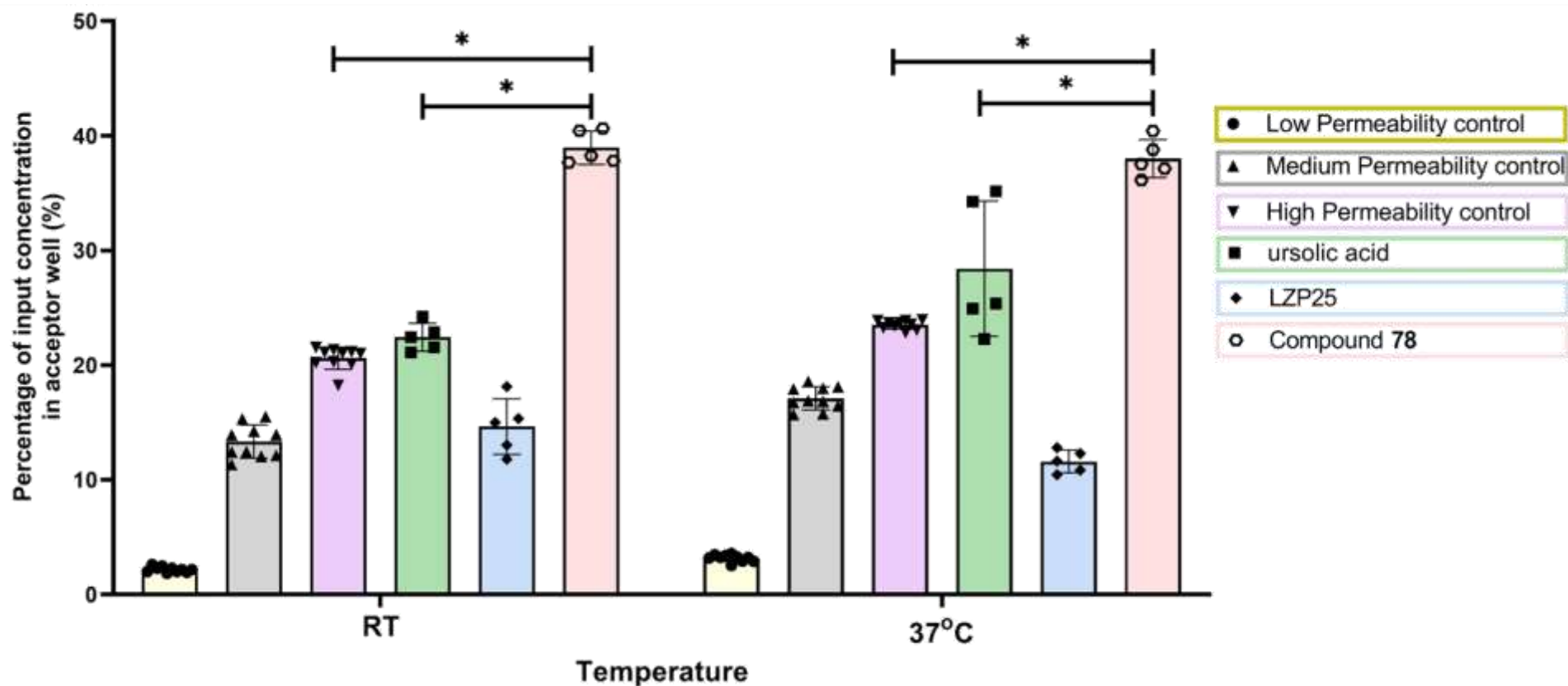
Specifically, the carbonyls adjacent to the benzene rings are in the correct orientation to hydrogen bond with Ser-217 and Ala-218, and the tri-methyl Boc motif can form hydrophobic interactions with Tyr-48 in TCPTP active site. This in addition to the Boc ester potentially being able to also hydrogen bond with aspects of the Asp-50 and the Val-51 residues. Hence the precited TCPTP binding position of **78** is in theory substantially stronger than that of **78** in PTP1B. This theoretical superior binding position of **78** in TCPTP explains both the lower concentration for significant inhibitory action and the substantially greater average maximum inhibitory effect observed in TCPTP.

As before the permeability of compound **78** through a synthetic BBB barrier was assessed. However, based upon the functional groups present and the cLogP of compound **78** it was predicted that this hit would be more BBB permeable. The BBB assay results are shown below support this.

5.3.3.5.5. BBB permeability

As predicted due to compound **78** having a high cLogP (4.6157) and therefore hydrophobic, compound **78** was found to be highly permeable to the synthetic BBB at both RT and the more biologically relevant temperature of 37 °C.

Of the 500 µM inputted concentration over 190 µM representing 38% on average, was recovered from the acceptor well at 37°C. Demonstrated below in **Figure 119** and the appendix (section 3.2). The permeability of **78** at these temperatures was also not significantly different to each other. Additionally, as shown below in **Figure 119**, the permeability of **78** was significantly higher than both the known inhibitors, ursolic acid (p value <0.010), LZP25 (p value <0.010), and the provided high permeability control (p value <0.001). Stated p values correct for results from both temperatures.

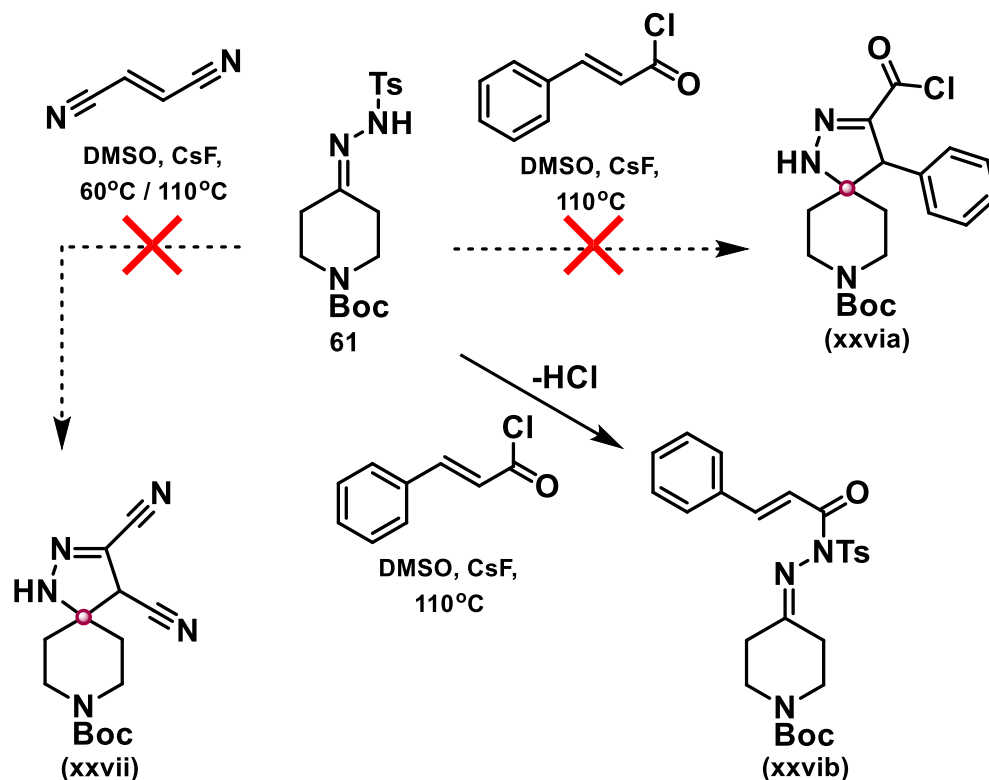


Compound (temperature of comparison)	78 (RT)	78 (37 °C)
p values vs ursolic acid	<0.010	<0.010
p values vs high permeability control	<0.001	<0.001

Figure 119: The percentage of the inputted concentration in the BBB assay acceptor well after 24 hrs at RT or 37 °C. of permeability controls (n=10) and compound 78 (n=5). Mean and individual points \pm standard deviation plotted. Used non-parametric Mann-Whitney t-test for statistical analysis. * p value \leq 0.050.

5.3.3.6. Unsuccessful spirocycle formations

The optimised synthesis was also attempted with fumaronitrile as the alkene, however at 110 °C the result was a mixture of numerous undesired compounds which could not be separated. Due to the increased reactivity of fumaronitrile, the reaction was also repeated at a lower temperature of 60 °C to try and promote the desired spirocycle formation. In this case a trace amount of the spirocycle (**xxvii**) was suspected to form but again as a part of an inseparable mixture, as illustrated below in **Scheme 49**.



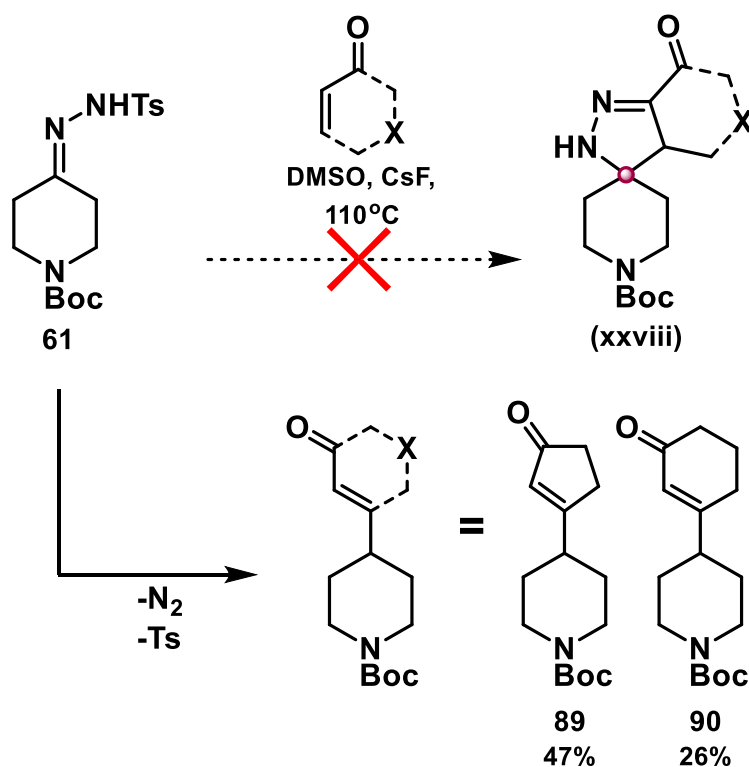
Scheme 49: Presumed and target synthetic product, from reaction of **61** with Cinnamoyl chloride.

Reaction conditions: **61** (1.0 mmol), alkene (1.5 equiv.), CsF (1.5 equiv.), dried DMSO (4 mL), 110 °C, 22 hrs, sealed vial, N₂ atmosphere.

Therefore, this two-step linear synthesis of spirocycle dihydropyrazoles does have its limitations. Moreover, when attempted with the alkene cinnamoyl chloride, instead of the desired spirocycle being formed (**xxvii**), the addition product (**xxvib**) where the amine attacks the carbonyl is suspected to form instead, as shown in **Scheme 49**. However, this result is not unexpected as the addition pathway was thought to be favourable but some spirocycle was hoped to form in tandem.

5.3.4. Metal free carbon-carbon bond formation

5.3.4.1. Synthesis



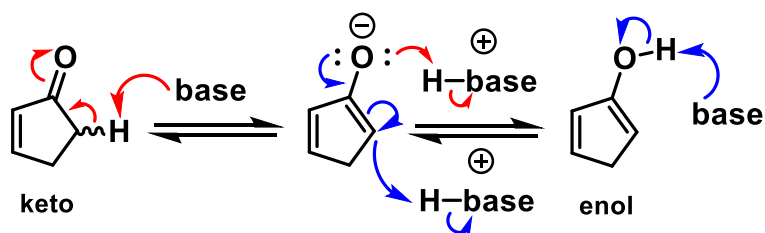
Scheme 50: Reaction of sulfonyl hydrazone **61** with cyclic enols.

Reaction conditions: **61** (1.0 mmol), cyclic enol (1.5 equiv.), CsF (1.5 equiv.), dried DMSO (4 mL), 110 °C, 22 hrs, sealed vial, N₂ atmosphere.

As shown above in **Scheme 50**, both utilised cyclic enones (5 and 6-member carbon rings) resulted in a carbon-carbon bond formation product without any formation of the expected spirocyclic tricyclic system. One possible contributing reason for this could be steric strain of the resultant tricyclic system.

Exhibited in **Scheme 47** above is the effect of steric strain on isolated yield particularly with the 4-membered sulfonyl hydrazones. Furthermore, if steric strain was the primary driver for reduced favourability of spirocycle formation it could be expected that the 6-membered cyclic enol could form a mixture of both products. But despite the reduced isolated yield of the 6-membered C-C bond formation product (**90**), no evidence of the corresponding spirocycle was present, hence the drop in C-C bond formation yield is most likely attributed to another factor.

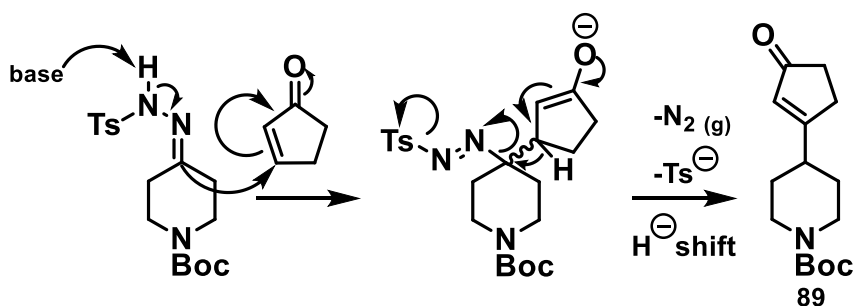
5.3.4.2. Proposed mechanism



Scheme 51: Keto-enol tautomerisation of cyclopent-2-en-1-one. Red arrows: keto to enol conjugation. Blue arrows: enol to keto conjugation.

Other than being cyclic the main difference between cyclopent-2-en-1-one and cyclohex-2-en-1-one when compared with all other alkenes utilised, is their ability to undergo keto-enol tautomerization. As electron density can be transferred resulting in the conversion between a ketone and secondary alcohol functionality (see **Scheme 51**). Potentially this increased conjugation may promote the C-C bond formation product pathway, as the electronics particularly involving the adjoining nitrogen atoms of the spirocycle play a key role in formation and subsequent reactivity, as mentioned in greater detail below. But further investigation is needed.

Two alkenes that would be worth investigating, are a linear alkene that can undergo keto-enol tautomerization such as pent-3-en-2-one, and furan-2-one (5-membered cyclic ester), which cannot. The resultant product(s) formed from these alkene substrates would provide additional information of what alkene parameters are required to enhance the spirocycle or C-C bond formation product, and whether both versions could be formed and isolated from a single alkene substrate.



Scheme 52: Proposed mechanisms for C-C bond formation, *via* keto form.

However, with the experimental observation of gas bubble formation (presumably $N_2(g)$), the above mechanisms for C-C bond formation are proposed with the reaction occurring *via* the keto form as demonstrated in **Scheme 52** above. It is not known whether the reaction progresses *via* the keto and / or enol form of the alkene, but the keto form appears more likely as with the enol form electron density would just be shunted around the C5 ring. But nevertheless, the key difference between the C-C bond formation mechanism and the spirocycle formation mechanism is the position of the intermediate's attack and whether just the tosylate is ejected and the cyclisation product is formed or if the electron density is shunted around the ring resulting in the release of nitrogen gas in addition to the tosylate anion, forming the C-C bond formation product. Regardless of how the reaction between cyclic enones and sulfonyl hydrazones occurs further investigation is warranted due to these reaction's ability to form C-C bonds without the use of metal catalysis.

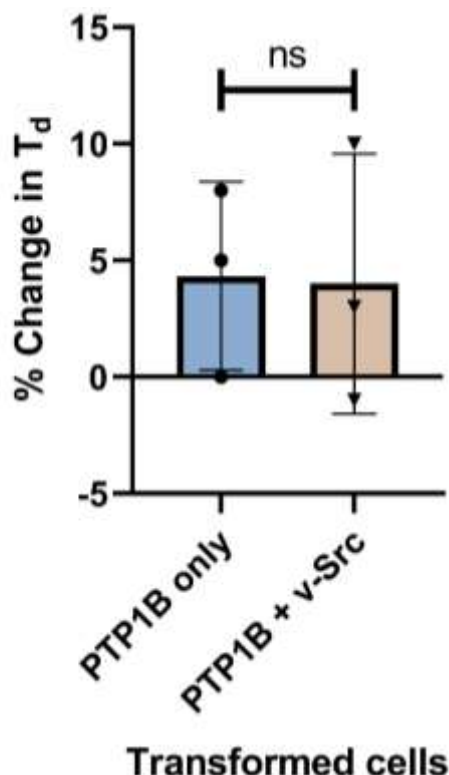
5.3.4.3. Prior literature on alternative synthesis methods

One of the most common methodologies found in the literature for the C-C bond formation with alkenes is palladium cross-coupling reactions such as Mizoroki-Heck coupling reaction. These have numerous positive benefits of being a procedurally simple and diverse reaction which utilises a chemoselective low toxicity palladium catalyst.^{194,195} However, such reactions occur with an alkene and aromatic halides, thus creating halogenated waste which is both difficult and expensive to dispose of. Additionally, the resultant products are intrinsically 2-dimensional compounds, making them less desirable for use in pharmaceutical research, as discussed above.

However, the C-C bond formation reaction presented in this work can operate with bench stable aliphatic sulfonyl hydrazones, thus enabling easier incorporation of three-dimensionality. But optimisation to improve the isolated yield and investigation into a substrate scope of this single step reaction, is needed to improve its appeal for use in drug-discovery synthesis.

5.3.4.4. Biological testing of compound **89**.

Despite these carbon bond formation products not being the desired targets, one of these compounds, compound **89** was tested for PTP1B inhibitory activity and the results of which are shown below. From the composition of compound **89** no significant activity was expected due to the limited compatible functional groups to interact sufficiently with the key active site residues of PTP1B.



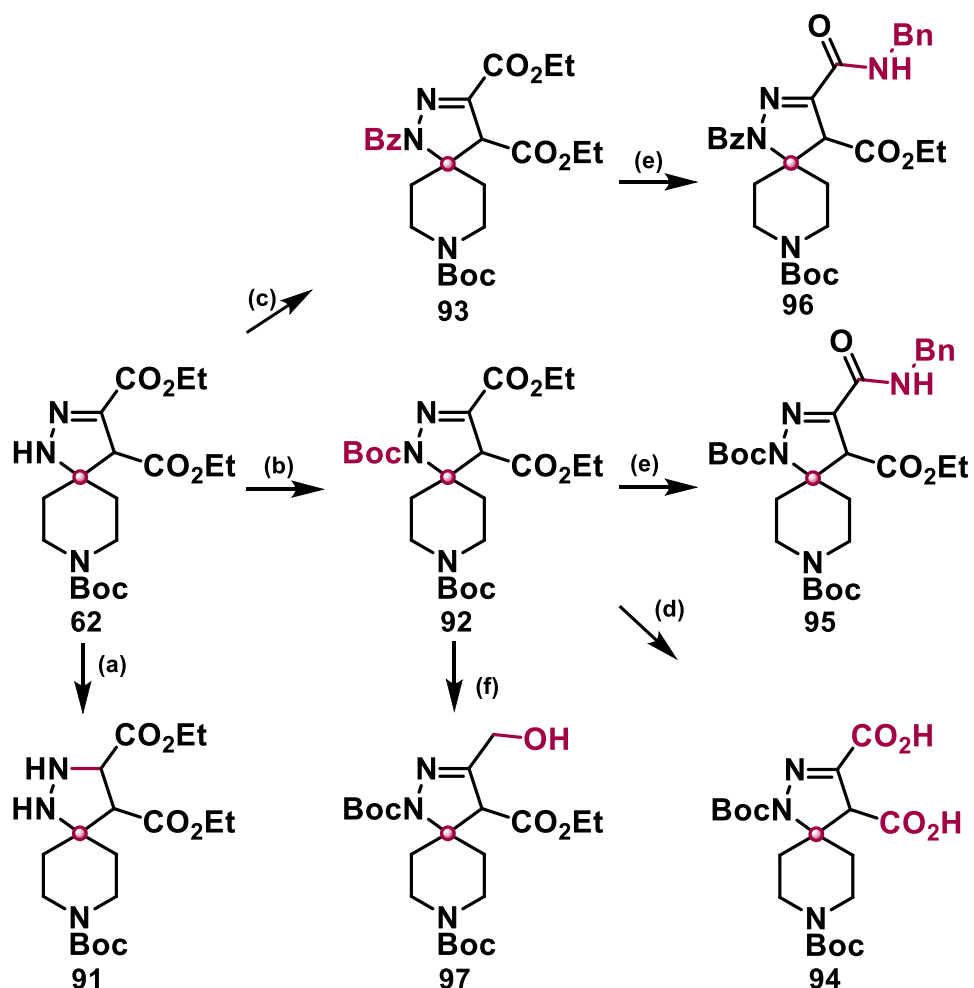
p value	ns
---------	----

Figure 120: Comparison of % change in doubling time (T_d) of PTP1B only and PTP1B + v-Src transformed yeast cells in the presence of compound **89** at 100 μ M. $n=3$ for all concentrations tested in both transformations, mean and individual points \pm standard deviation plotted. Used non-parametric Mann-Whitney t-test for statistical analysis. * p value ≤ 0.050 vs control.

As predicted, the results shown in **Figure 120** demonstrate that compound **89** does not cause a significant change in the exponential growth rate of the PTP1B + v-Src transcribed yeast cells and therefore does not inhibit PTP1B *via* the active site. Furthermore, the average percentage change of 4% is mirrored in both PTP1B and PTP1B + v-Src cells meaning that even this minimal effect is not due to the down regulation or inhibition of the PTP1B plasmid.

5.3.5. Spirocyclic dihydropyrazole synthetic utility

5.3.5.1. Successful functionalisation reactions



Scheme 53: Exploration of the synthetic utility of spirocyclic dihydropyrazole **62**.

Reaction conditions: (a) **62** (1.0 equiv.), NaBH_3CN (1.5 equiv.), diethyl ether, 0 °C to RT, 12 hrs, 33%. (b) **62** (1.0 equiv.), NEt_3 (2.0 equiv.), DMAP (0.1 equiv.), Boc_2O (1.1 equiv.), DCM RT, 12 hrs, 52%. (c) **62** (1.0 equiv.), DCM, 10% KOH aq. (3.6 equiv.), cooled to 0°C, BzCl (1.2 equiv.), RT, 12 hrs, 28%. (d) **92** (1.0 equiv.), 5% KOH in MeOH (18.0 equiv.), reflux, 72%. (e) **92** or **93** (1.0 equiv.), BnNH_2 (2.0 equiv.), MeOH, 60 °C, 75% (**95**), 22% (**96**). (f) **92** (1.0 equiv.), NaBH_4 (2.0 equiv.), MeOH, RT, 12 hrs, 30%. ^{151,191,198,199}

Once both the sulfonyl hydrazones and alkene substrate utilisation had been investigated a further set of studies aimed to assess the downstream synthetic utility of the spirocyclic dihydropyrazole core, was conducted, particularly with compound **62**, shown above in **Scheme 53**.

Initial synthetic studies on compound **62** found the core to be surprisingly stable, and the only observed reaction was the selective reduction of the iminyl π -bond ($\text{C}=\text{N}$) using cyanoborohydride to give compound **91**.

Fortunately, Boc-protection of compound **62** to give compound **92**, enhanced the reactivity of the ester groups. Presumably due to the reduction in conjugation from the nitrogen lone pair, enabling the hydrolysis of both ester groups in compound **92** under standard conditions to yield the diacid compound **94**. Treatment of compound **92** with a representative amine provided the corresponding monoamide **95** in excellent yield where reaction occurred selectively at the ester group more distant from the spirocyclic junction. Finally, treatment of compound **92** with a complex metal hydride led to the surprising observation of the selective total reduction of the distal ester to the primary alcohol, with both the proximal ester and the iminyl π -bond remaining intact, the expected product from this reaction was the di-Boc protected version of compound **97**. Therefore, it appears that the ester group more distant from the spirocyclic junction provides a selective point of chemical attack, potentially due to electron density being pulled out of that carbon position by the Boc protecting group *via* the hydrazine motif. This would support why the unprotected dihydropyrazole core of compound **62** is so stable, and that when this nitrogen position was protected with a benzyl group, (which is less electron withdrawing than Boc) a significantly lower yield for **96** is obtained than for compound **95**.

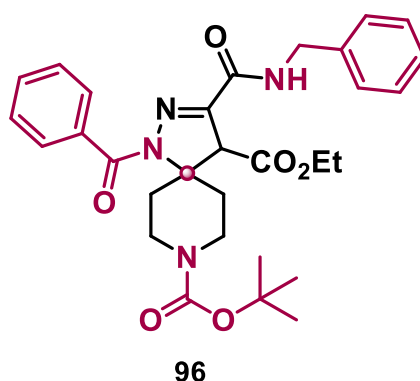
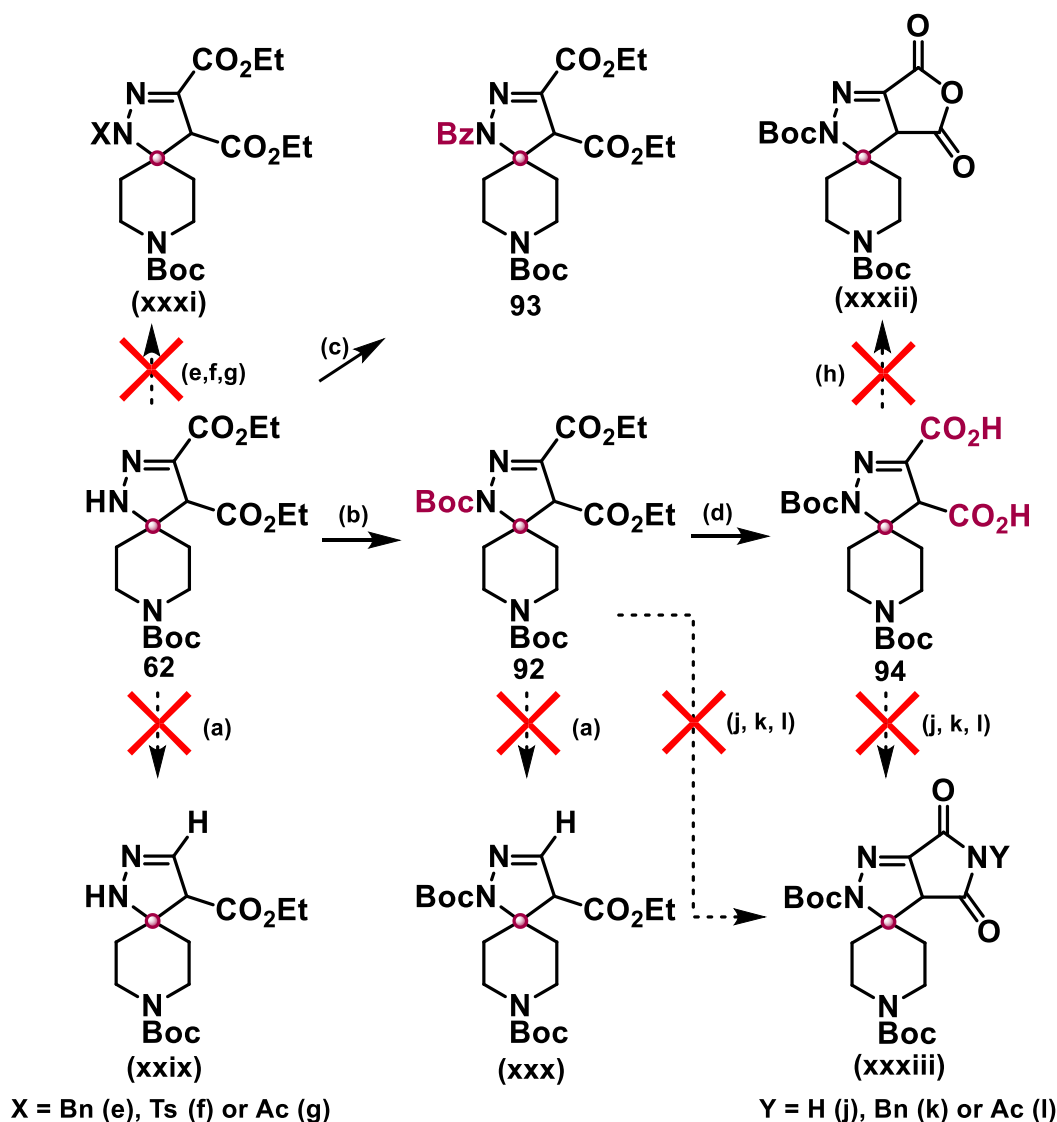


Figure 121: Orthogonal protected highly functionalisable spirocycle dihydropyrazole core.

Means to selectively remove the following protecting group: Bz, by treatment with a base such as NH₃. Boc, *via* treatment with a strong acid in DCM. Bn, removed with hydrolysis.

But despite the poor yields of both synthetic steps to from **96** from **62** (28% and 22% respectively), and with overall yield from **62** of only 6%, with some reaction condition optimisation highly functionalisable tri-orthogonally protected spirocycle structure of **96** (**Figure 121**) is of synthetic interest for controlled selective downstream reactivity.

5.3.5.2. Unsuccessful functionalisation reactions

**Scheme 54:** Unsuccessful synthetic utility reactions of spirocyclic dihydropyrazole **62**.

(a) **62** or **92** (1.0 equiv.), KOAc (2.0 equiv.), DMSO: H₂O (2.5:1 ratio), reflux, 0%. (a) Compound **62** or **92** (1.0 equiv.), LiOH (2.0 equiv.), DMSO, reflux, 0%. (b) Compound **62** (1.0 equiv.), NEt₃ (2.0 equiv.), DMAP (0.1 equiv.), Boc₂O (1.1 equiv.), CH₂Cl₂, RT, 12 hrs, 52%. (c) Compound **62** (1.0 equiv.), CH₂Cl₂, 10% KOH aq. (3.6 equiv.), cooled to 0°C, BzCl (1.2 equiv.), RT, 12 hrs, 28%. (c) Compound **62** (1.0 equiv.), pyridine, cooled to 0°C, BzCl (1.2 equiv.), RT, 12 hrs, 0%. (c) Compound **62** (1.0 equiv.), DMF or Et₂O, (C₂H₅)₃N (2.0 equiv.), cooled to 0°C, BzCl (1.2 equiv.), RT, 12 hrs, 0%. (d) Compound **92** (1.0 equiv.), 5% KOH in MeOH (18.0 equiv.), reflux, 72%. (e) **62** (1.0 equiv.), MeCN, K₂CO₃ (1.0 equiv.), NaI (cat.), BnBr (1.1 equiv.), reflux, 0%. (e) Compound **62** (1.0 equiv.), DMF 0°C, NaH (1.0 equiv.), BnBr (1.1 equiv.), RT, trace (*). (f) Compound **62** (1.0 equiv.), N₂ atm, NaH or (C₂H₅)₃N (1.2 equiv.), anhydrous THF, 0°C, TsCl (1.2 equiv.), RT, 0%. (g) Compound **62** (1.0 equiv.), anhydrous NiCl (0.1 mol%), Ac₂O (1.5 equiv.), RT, 0%. (g) Compound **62** (1.0 equiv.), MeCN, Ac₂O (1.5 equiv.), reflux, 0%. (h) Compound **92** or **94** (1.0 equiv.), N₂ atm, DCM, TFAA (1.2 equiv.), 0°C to RT, 0%. (j) Compound **92** or **94** (1.0 equiv.), DMSO, urea (4.0 equiv.), reflux, 0%. (k) Compound **92** or **94** (1.0 equiv.), MeOH or xylene, BnNH₂ (1.0 equiv.), reflux, 0%. (l) Compound **94** (1.0 equiv.), MeOH, AcNH₂ (1.0 equiv.), reflux, 0%.^{199,209-216}

(*). Benzyl protection for this method appeared to form product in trace amounts but unable to fully isolate from reaction mixture, to obtain pure product.

In addition to the analogues presented previously in **Scheme 47** and **Scheme 48**, these transformations on the model diester compound **62** demonstrated in **Scheme 53** illustrate the potential for further modification of the spirocyclic dihydropyrazole core and its potential utility in medicinal chemistry projects.

However, as shown in **Scheme 54** above due to the surprising stability of the unprotected dihydropyrazole core of the spirocycle and the adjoining diester of compound **62**, selective reactivity to alter one of the identical esters or just reactivity in general was challenging to achieve a significant isolated yield. This was overcome by the addition of a second Boc protecting group to the dihydropyrazole amine, as the removal of the nitrogen lone pair enables selective reactivity of the distal ester position. But having numerous copies of the same protecting group present in a compound can severely limit the options of selective downstream reactivity.

Hence, ideally orthogonal protecting groups would be incorporated into the compound. For compound **62** and the spirocyclic dihydropyrazole core in general, incorporation of any functional group other than Boc results in a significant drop in isolated yield, if successful at all. As shown above in **Scheme 54**, all attempts to protect the dihydropyrazole amine with any protecting group apart from Boc failed to yield any isolable product, with the exemption of a benzoyl protecting group (compound **93**), but this resulted in a significant drop in yield (down 24%) when compared to Boc protection (compound **92**). All attempts to increase the yield of compound **93** by altering the synthesis failed and resulted in no notable product for any alteration in methodology.

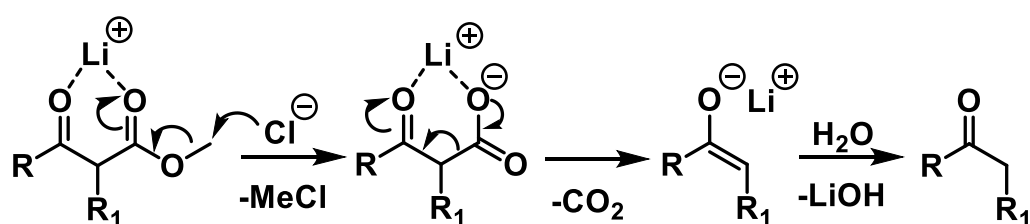
It is theorised that the protection with acyl or benzyl failed due to not being electron withdrawing enough. As has been mentioned demonstrated in **Scheme 53**, Boc protected nitrogen motifs are strongly correlated to yield, as when the benzyl protected sulfonyl hydrazone was reacted with diethyl fumarate the isolated yield for compound **76** was only 28% when compared to 87% isolated yield for compound **62** (Boc protected). Despite the exact same reaction conditions being deployed this nitrogen and its' protecting group decreased yield despite not being directly involved in the spirocycle formation. Thus, Boc protecting groups play a key role in spirocycle formation and subsequent synthesis.

Whereas with the tosyl protecting group it may be too electron withdrawing resulting in it being too liable for this substrate, and thus was a good leaving group in mild experimental conditions and / or conditions present in the protection reaction. But despite

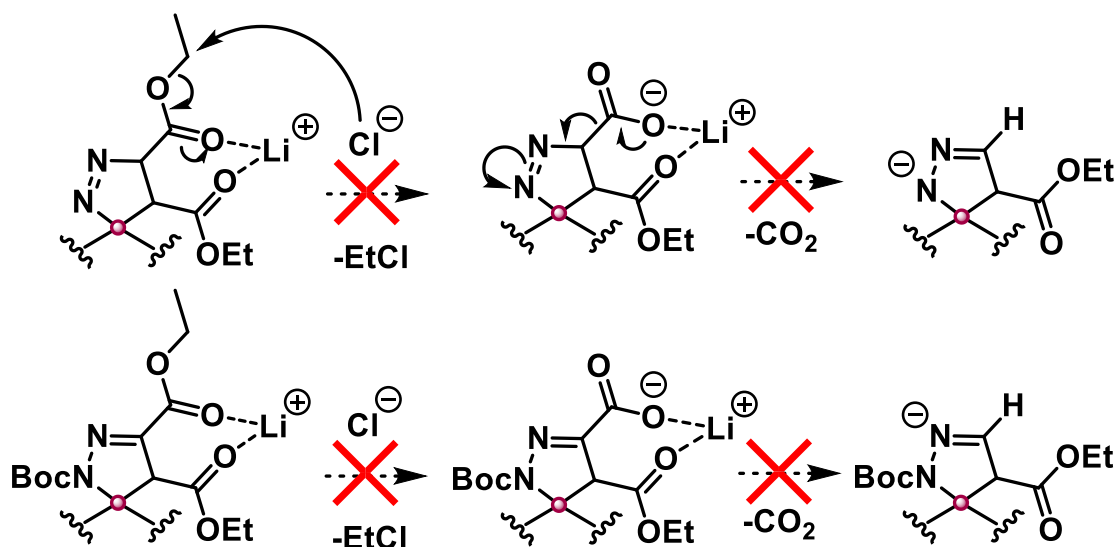
the numerous setbacks in terms of protection group experiments, the orthogonal protected highly functionalable spirocycle dihydropyrazole core compound **96** was still successfully synthesised as mentioned above.

Another means of increasing the downstream synthetic selectivity of compound **62** is to alter any symmetrical functional groups such as the diester motif to enable complementary synthetic pathways. As any alternative alkenes to diethyl fumarate resulted in a reduction in yield it was decided to selectively alter one of the ester groups post spirocycle formation, to enhance compound **62**'s subsequent synthesis potential.

Model substrate



Diester on spirocycle dihydropyrazole



Scheme 55: Mechanism of Krapcho decarboxylation on a model substrate, and proposed mechanism on the diester of the spirocycle if reaction occurred.^{211,217}

Initially a Krapcho style decarboxylation was attempted on compound **62** and subsequently on the di-Boc protected compound **92**. As mentioned previously, with the dihydropyrazole nitrogen being unprotected and the resultant resonance caused by the free lone pair of electrons the diester motif was found to be unreactive in all experimental conditions attempted. Hence the same Krapcho decarboxylation procedure stated in **Scheme 54**, was attempted on compound **92** due to the protection of the dihydropyrazole nitrogen and thus tying up the lone pair of electrons to enable reactivity of the ester

groups. However, this decarboxylation also failed to work with compound **92**, and it is thought to be due to the presence of the second Boc group. As with a protecting group on this nitrogen, a double bond cannot form thus preventing the Krapcho decarboxylation mechanism from occurring, as shown above in **Scheme 55**.

Despite the Krapcho decarboxylation reactions remaining unsuccessful, the aim of breaking the symmetry of the diester by selectively reacting one to form complementary functional handles was achieved with compounds **95**, **96** and **97** (see **Scheme 53**).

Cyclisation reactions with the diester and dicarboxylic acid spirocycle dihydropyrazoles, compound **92** and **94** respectively, were also attempted under numerous reactions conditions (**Scheme 54**), to synthesis compounds akin to the desired spirocycle products from the cyclic enols, which would contain a tri-cyclic spirocycle containing system. However, this was not accomplished. It is postulated that the resultant steric strain of the fused 5,5 ring system being attached to the spiro junction is too great, thus preventing formation altogether, or not being stable for a sufficient period to be visualised by spectroscopic techniques. This could contribute to the failed formation of compounds (**xxxii**) and (**xxxiii**) in **Scheme 54**. Additionally, when compound **92** underwent procedure (e) from **Scheme 53**, instead of the initial desired product (**xxxiii**), with procedure (k) from **Scheme 54** being formed, the expected intermediate product of compound **95**, was formed as the final isolated product *via* the selective attack of the distal ester. Meaning the required subsequent attack on the proximal ester to form the fused ring system was unable to occur presumably due to previously stated steric reasons of the resultant tri-cyclic system.

5.3.5.3. Biological testing of compounds 91-97

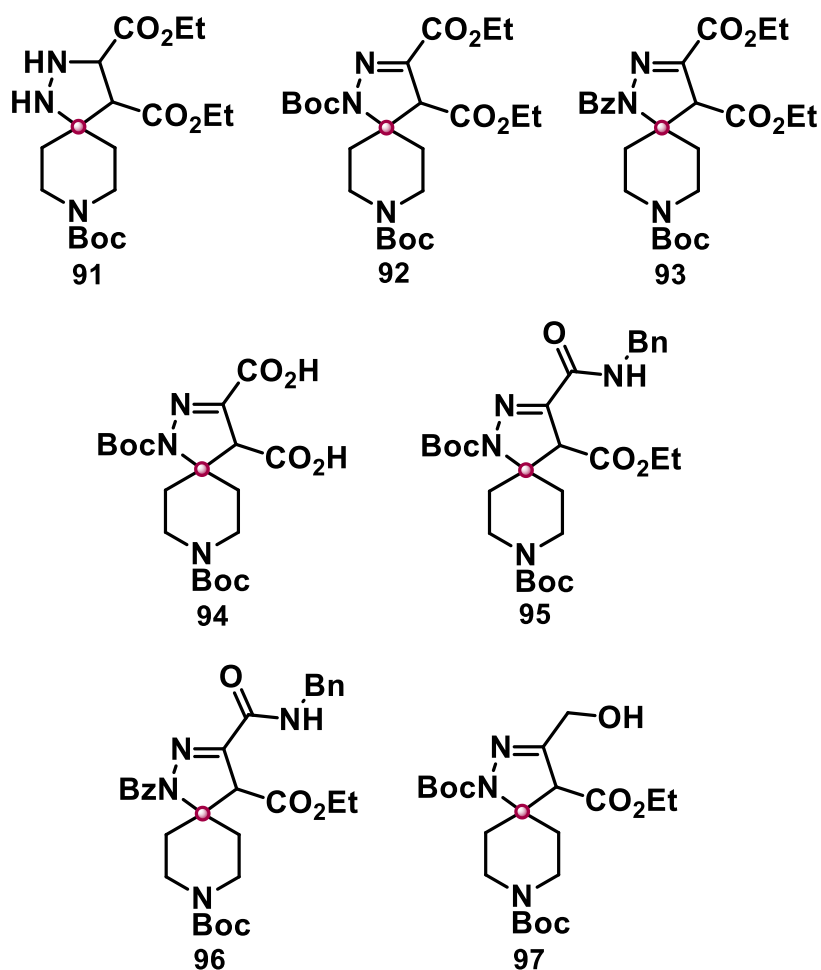
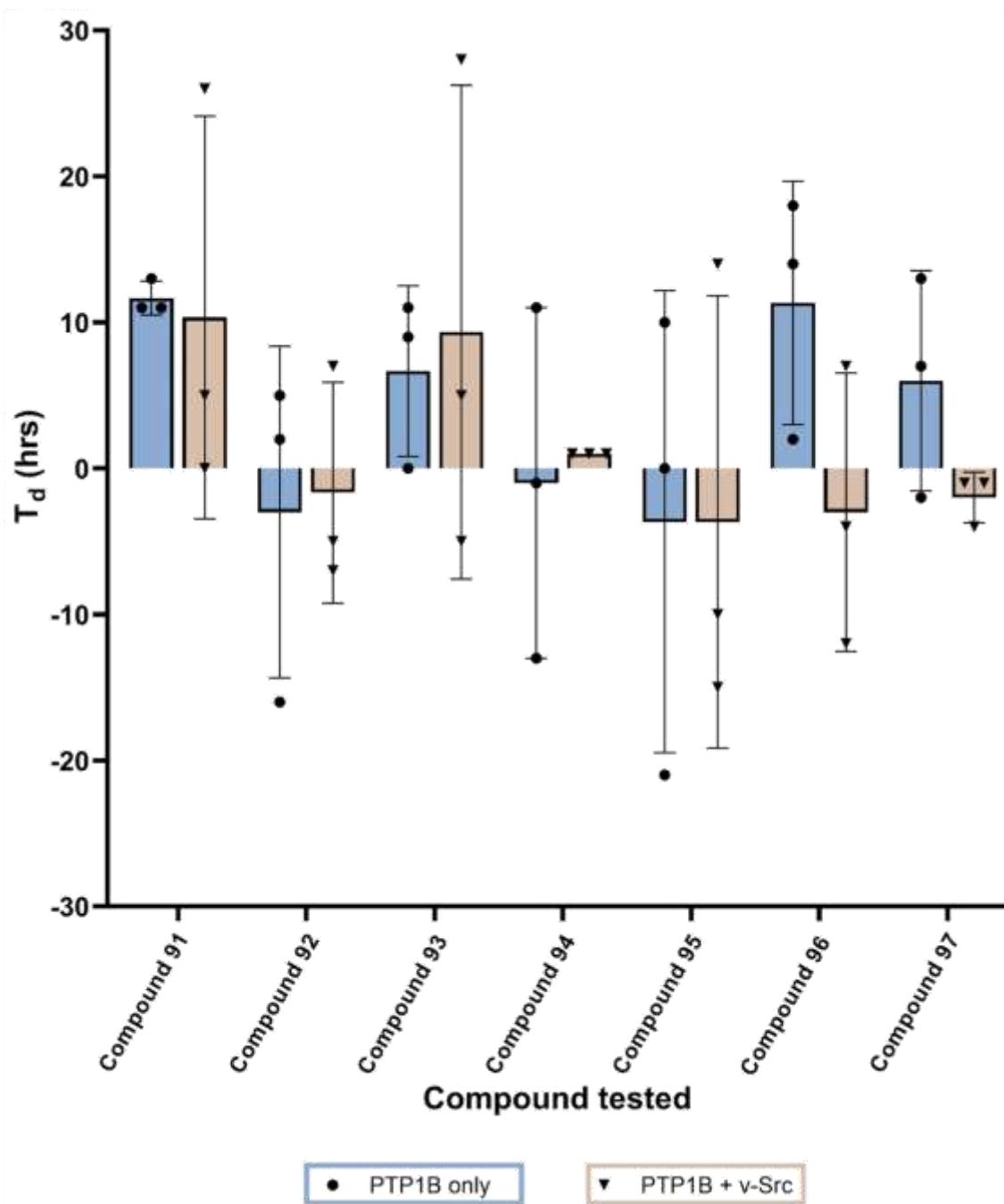


Figure 122: Final wave 5,6-spirocyclic dihydropyrazoles tested at 100 μ M.

Every successfully synthesised product from the synthetic utility reactions was investigated as potential PTP1B active site inhibitors, the structures of which are shown above in **Figure 122**. The reason for this primarily was due to the presence of the 5,6-spirocyclic core motif being present, which as stated previously was contained within the computationally found potential PTP1B active and allosteric site inhibitors. However, due to the nature of the yeast-based inhibition assay only the active site of PTP1B could be investigated and the results are shown below in terms of a percentage change in the doubling time of the yeast cells, when compared against the corresponding base growth rate which is specific for each biological repeat.

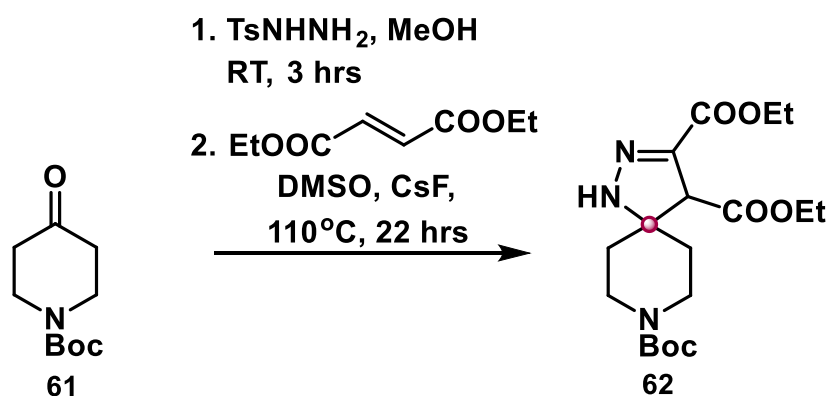


Compound	91	92	93	94	95	96	97
p value	ns	ns	ns	ns	ns	ns	ns

Figure 123: Comparison of % change in doubling time (T_d) of PTP1B only and PTP1B + v-Src transformed yeast cells in the presence of synthesised compounds **91-97** at 100 μM . $n=3$ for all compounds tested in both transformations, mean and individual points \pm standard deviation plotted. Used non-parametric Mann-Whitney t-test for statistical analysis. * p value $0.050 \leq$ vs control.

As demonstrated above in **Figure 123** none of the synthetic utility spirocyclic products showed any PTP1B inhibitory activity. Due to the precursor compound for all of these was compound **62** which itself did not possess any significant activity; this result was expected. The primary reason for the synthesis of compounds **91 – 97** was not for their potential as PTP inhibitors but instead to round off a separate publication. The activity exhibited by compound **78** and the latter computational data suggesting some 5,6-spirocycles may exhibit PTP inhibitory activity was a coincidence.

5.3.6. One-pot synthesis of **62**



Scheme 56: One-pot transformation of the parent ketone into compound **62** on a gram scale.

Finally, the reported procedure can be effectively performed as a one-pot process beginning from the parent ketone (**Scheme 56**). The scalability of the reaction was also demonstrated by performing this process on a gram scale resulting in a 65% yield.

5.3.7. Spirocycle hit biological data comparison.

The synthesis work illustrated in this Chapter was for the most part conducted in parallel to the benzodioxane synthesis work presented Chapter 4. Therefore, comparisons between the initial benzodioxane hit and spirocycle hit compounds were conducted to inform what should be the focus of the later stages of PTP1B inhibitory compound development. As has been discussed in Chapter 4 (section 4.3.7.3.5), compound **30a** was chosen to be further investigated and motivated to enhance the PTP selectivity of this hit resulting in compound **55**. The justification for the decision to take forward compound **30a** over **78** is presented below. The structures of the known inhibitors and identified hit compounds are shown below in **Figure 124**.

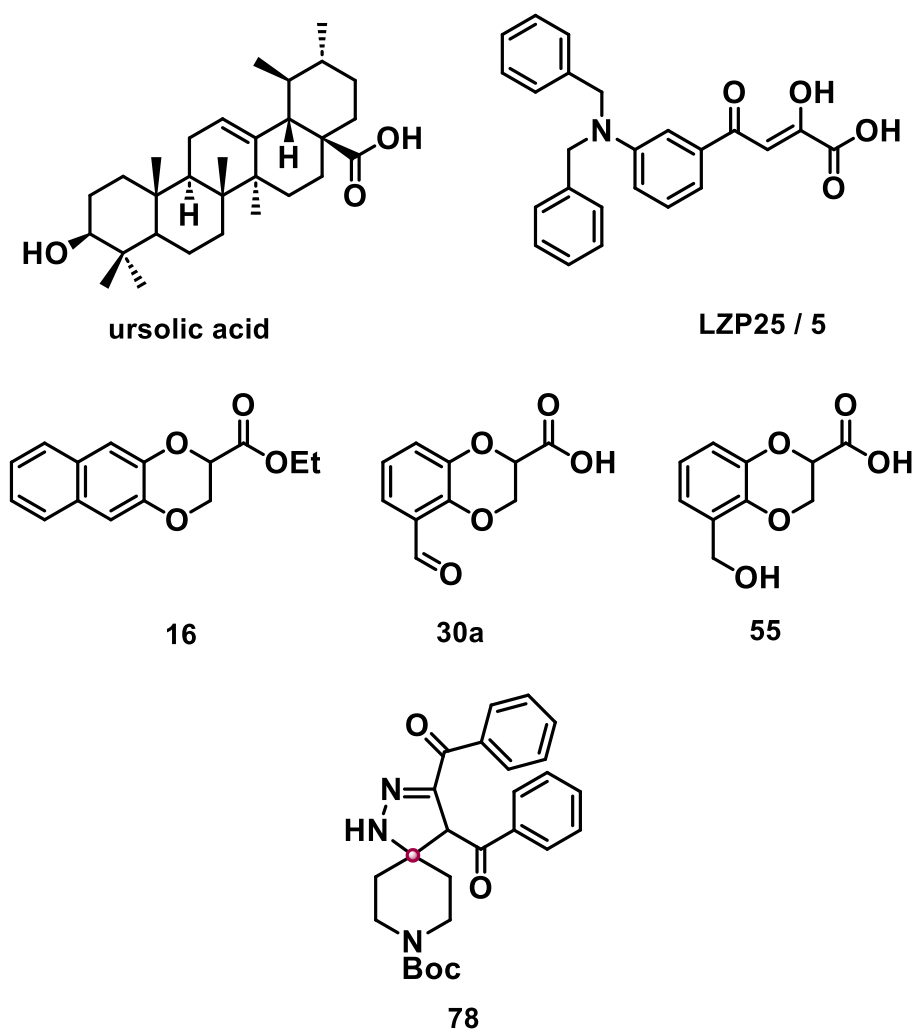


Figure 124: Structures of known and PTP1B inhibitors identified from this work.

5.3.7.1. Yeast-based PTP activity

5.3.7.1.1. PTP1B inhibitory activity

As shown in **Figure 125** below at 100 μM , the known inhibitor LZP25 exerts a significantly greater inhibitory response on PTP1B than all hit compounds, however at 140 μM , the hit benzodioxane compound **30a** exerted comparable inhibitory effect. When looking at the spirocycle hit, compound **78** at 100 μM the exerted response is significantly greater than for compound **16**, and comparable to that of ursolic acid and compound **30a** but significantly less than the subsequent derivative compound **55**. Whereas at 140 μM , again the observed effect due to compound **78** and ursolic acid addition is comparable but significantly less than witnessed due to the addition of the benzodioxane hits compound **30a** and **55**. The statistical analysis results for this are shown in the appendix (section 3.1.7). Therefore, providing evidence as to why the hit compound **30a** was taken forward for further study rather than the spirocycle **78**.

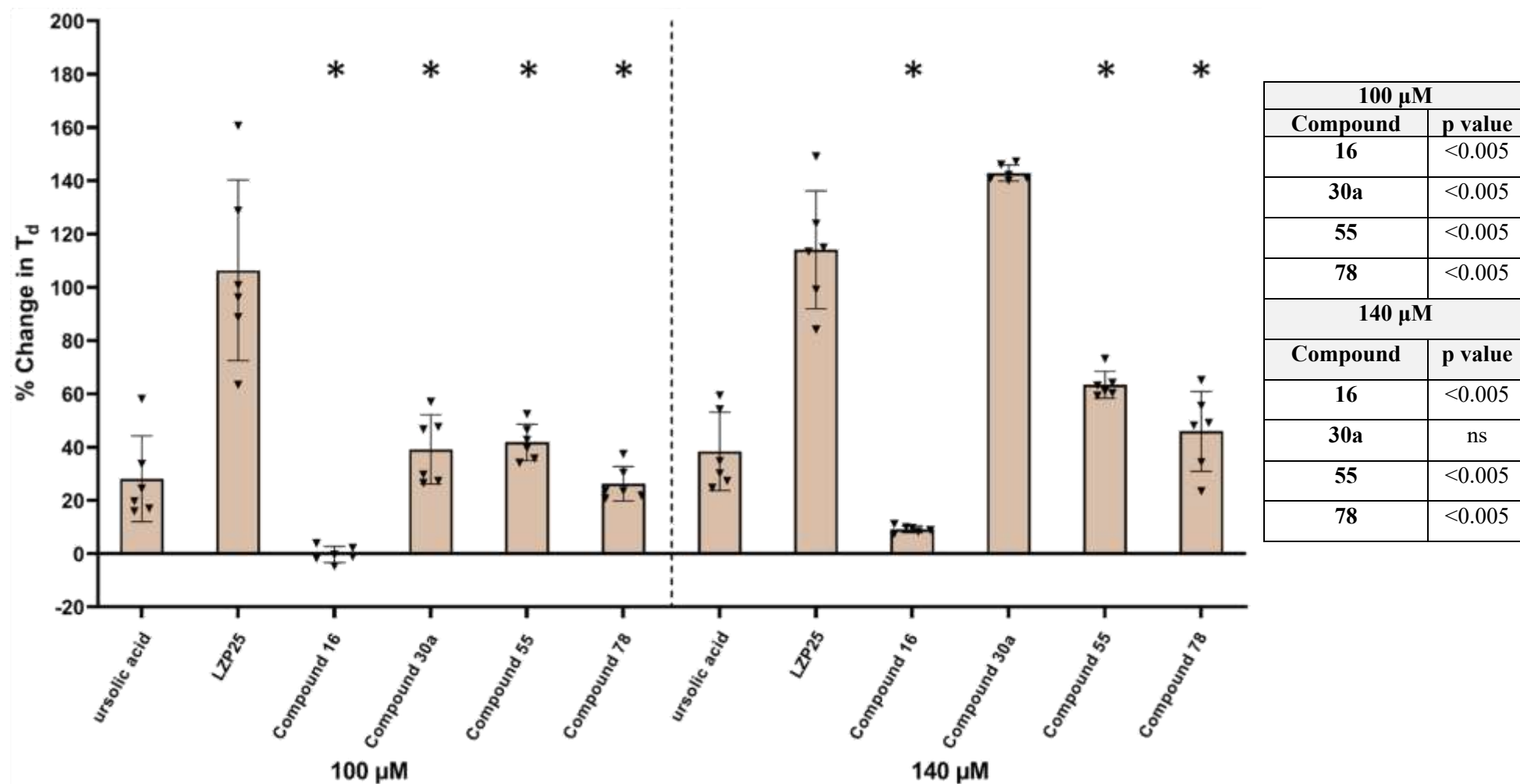


Figure 125: Comparison of % change in doubling time (T_d) of PTP1B + v-Src transformed yeast cells in the presence of synthesised hit compounds and known inhibitors at 100 and 140 μM . $n=6$ for all compounds tested in both transformations, mean and individual points \pm standard deviation plotted. Used non-parametric Mann-Whitney t-test for statistical analysis. * p value $0.050 \leq$ vs LZP25.

5.3.7.1.2. TCPTP inhibitory activity

When interpreting the data presented in **Figure 126**, it is important to note that for this work a lesser response in terms of TCPTP active site inhibition is desirable as PTP1B selectivity is one of the main attributes for the identified PTP inhibitors. Therefore, the result that compound **78** exerts a significantly greater inhibitory response in TCPTP cells at 100 and 140 μM than all of the three benzodioxane inhibitors, compounds **16**, **30a** and **55** further justified the reasoning for why compound **30a** was taken forward and developed into the derivative hit compound **55**. As the spirocycle hit **78** exhibited TCPTP selectivity over PTP1B which for other work may be a desirable outcome as for any pharmaceutical product, the ability to predominantly bind to a specific target is key in order to reduce off-target side effects. It is important to note that as previously stated the active site of PTP1B and TCPTP is 74% identical to each other⁶⁷ and hence selectivity over one than the other is of interest but for this work the protein tyrosine phosphatase of interest is PTP1B and not TCPTP.

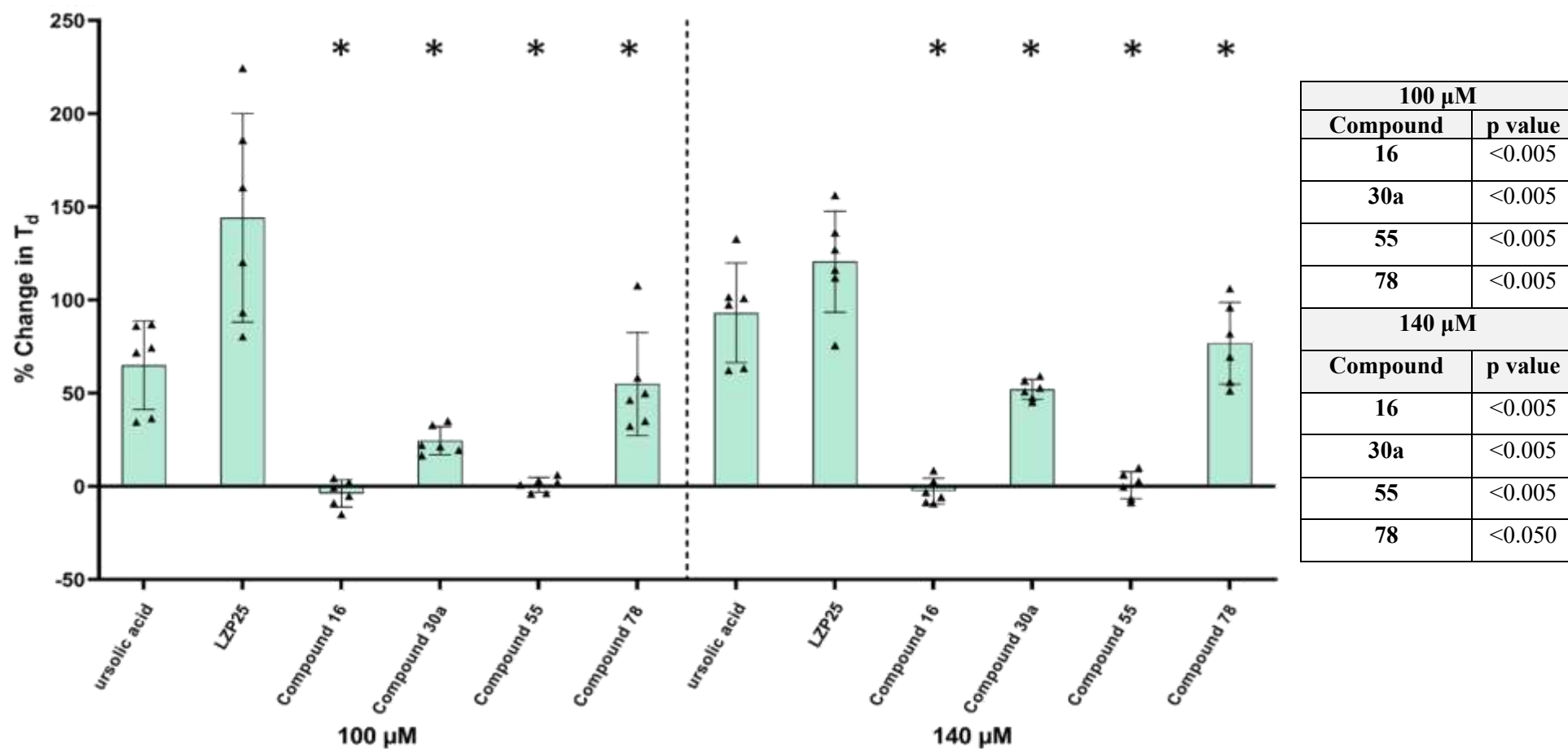


Figure 126: Comparison of % change in doubling time (T_d) of TCPTP + v-Src transformed yeast cells in the presence of synthesised hit compounds and known inhibitors at 100 and 140 μM . $n=6$ for all compounds tested in both transformations, mean and individual points \pm standard deviation plotted. Used non-parametric Mann-Whitney t-test for statistical analysis. * p value $0.050 \leq$ vs LZIP25.

5.3.7.2. BBB permeability

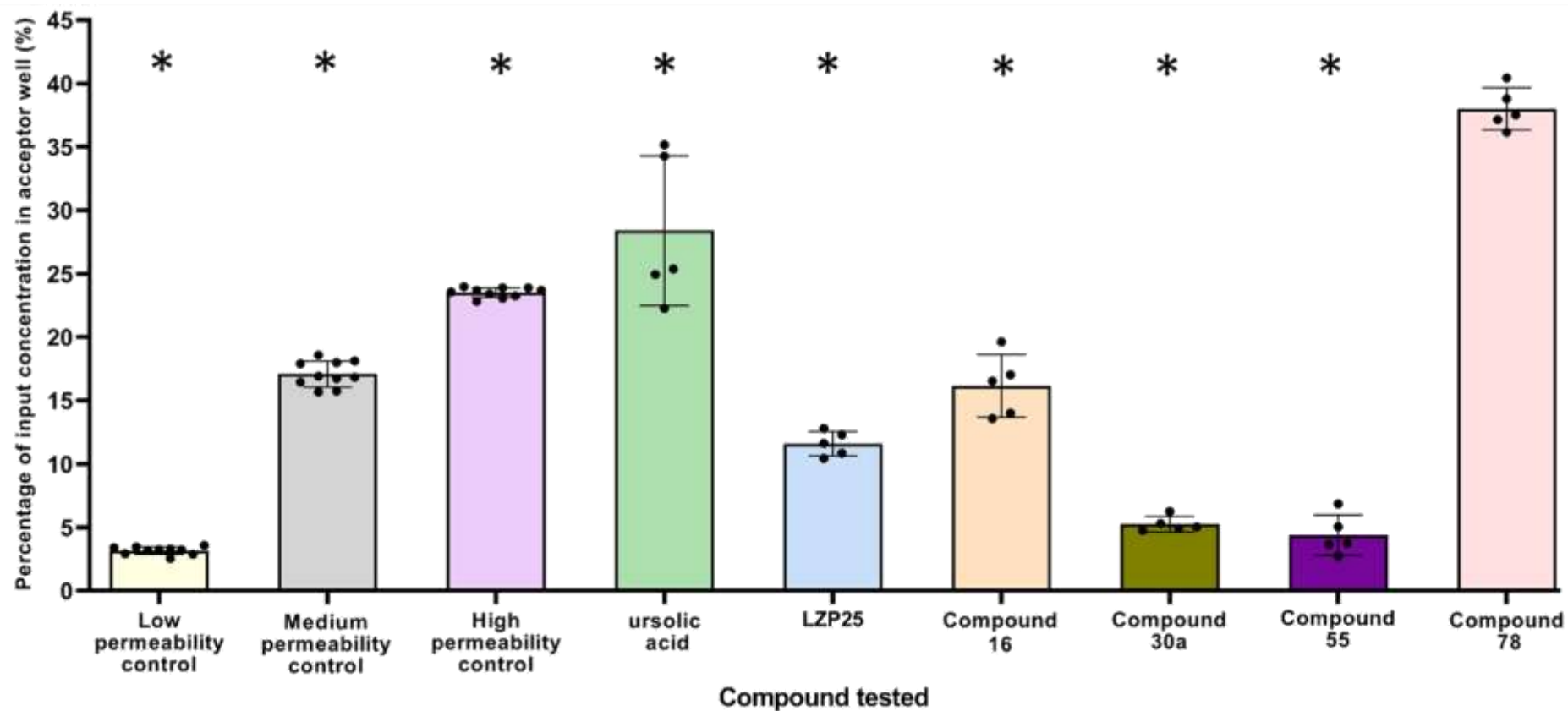
The other key property which is desirable for identified PTP1B inhibitors for this work is blood brain barrier (BBB) impermeability, as discussed previously the inhibition of neuronal PTP1B results in off-target negative cardiovascular effects. These can be avoided by developing an inhibitor that is impermeable to the BBB and hence only inhibit PTP1B peripheral tissues. The results comparing the ability of the key hit compounds to cross a synthetic BBB membrane are shown below.

Table 10: Comparison of known inhibitors and hit compounds properties that relate to BBB permeability.

Compound	cLogP	Total surface area
Ursolic acid	6.0021	337.87
LZP25	2.8429	303.96
16	2.7154	194.39
30a	0.6201	149.66
55	0.0895	150.23
78	3.4983	339.14

All values calculated with the software DataWarrior.¹²¹

Based on the correlation between lipophilicity (cLogP) in addition to the total surface area of a compound and the potential it has to cross the BBB, the data shown in **Table 10**, correlates to the acquired permeability results when compounds were left to diffuse through a synthetic BBB membrane at 37 °C. Results demonstrated below in **Figure 127**. This is due to the most permeability hit compound, **78** exhibiting both the highest cLogP (lipophilic) and total surface area, meaning the significantly greatest diffusion into the accepted well was expected. The reverse was also found for compound **30a** and **55** which from the data presented in **Table 10** were both expected to be relatively impermeable to the synthetic BBB and that was shown to be the case.



Compound	Low control	Medium control	High control	Ursolic acid	LZP25	16	30a	55
p value	<0.001	<0.010	<0.010	<0.010	<0.010	<0.010	<0.010	<0.010

Figure 127: The percentage of the inputted concentration in the BBB assay acceptor well after 24 hrs at 37 °C. n=5 for all compounds tested, n=10 for permeability controls, mean and individual points \pm standard deviation plotted. Used non-parametric Mann-Whitney t-test for statistical analysis. * p value \leq 0.050 vs compound 78.

The final justification for the selection of the benzodioxane hit compound **30a** to be the key focus for PTP1B inhibitor development is discussed above, as the only spirocycle compound to exhibit a significant inhibitory response in PTP1B, compound **78** was significantly more permeable to the synthetic BBB mimic membrane, than both initial benzodioxane hit compounds **16** (p value <0.010) and **30a** (p value <0.010) in addition to the high permeability control (p value <0.010). The significant BBB permeability of compound **78** in addition to the aforementioned TCPTP selectivity were the primary reasons to why this spirocyclic hit was not investigated further. Instead, the PTP1B specific and less BBB permeable benzodioxane hit **30a** was further developed into compound **55**.

5.4. Conclusion:

In summary, two procedurally simple methods for highly three-dimensional core structures are presented. One for the formation of spirocyclic dihydropyrazole building blocks bearing functionality for further synthetic elaboration and the other for metallic catalyst free carbon-carbon bond formation products are reported. The spirocycle dihydropyrazoles are particularly pharmaceutically relevant compounds that are formed from commercial electron deficient alkenes and bench stable tosylhydrazones, which are trivial to synthesise from their respective parent ketones in high yields without purification. Specifically in terms of relevance for this project as shown in Chapter 2 (sections 2.3.2 and 2.3.3) from computational database screening studies, found the potential for spirocycle dihydropyrazoles to operate as PTP1B inhibitors in both the active and or allosteric site. A versatile substrate scope is reported, including stable 4 and 5 membered rings at the spirocyclic junction. The further synthetic utility of this class of spirocycle is demonstrated *via* orthogonally reactive analogues and example synthetic transformations on the core structure. These building blocks represent a valuable addition to the arsenal of core structures for medicinal chemistry applications. Finally, numerous examples were screened for PTP activity utilising the procedures outlined in Chapter 3 (section 3.3.2), and the single found hit compound had its BBB permeability assessed which along with its activity compared against the benzodioxane hit compounds and known inhibitors. From these results the aforementioned benzodioxane based hit compounds were overall better and therefore investigated further as discussed in Chapter 4 (section 4.3.14.3).

5.5. Important comments:

* Work conducted during T. Wootton's Master level project, at Sheffield Hallam University (2018-2019).

** Compound synthesised by Dr Daniel Allwood, prior to PhD start.

Notes apply to this Chapter only.

Chapter 6

Conclusions and future direction

6.1. Conclusions

The aims of this work were to identify a new core structure not yet investigated as PTP inhibitors for obesity, TIID and related co-morbidities treatment. In addition to effectiveness and potency of any potential inhibitors two other factors were intensively investigated to order to increase pharmaceutical relevance by means of reducing off-target side effects. These other factors were PTP1B selectivity over TCPTP in particular and minimal blood brain barrier permeability.

Evidence of PTP1B being a valid target for obesity, TIID and related co-morbidities treatment is extensive as PTP1B is involved in both leptin and insulin signalling pathways by dephosphorylating key Tyrosine residues of both hormone's target sites, limiting biological activity. Upregulation of PTP1B occurs in obese and / or individuals with sustained elevated blood glucose levels resulting in the body becoming resistant to insulin and leptin reducing the biological response of appetite and blood glucose control.

As discussed above and illustrated below in **Figure 128**, a means of restoring insulin and leptin sensitivity and therefore treating TIID's, obesity and related co-morbidities is by restoring a more normal physiological level of PTP1B expression. This can be achieved through small molecule inhibition.

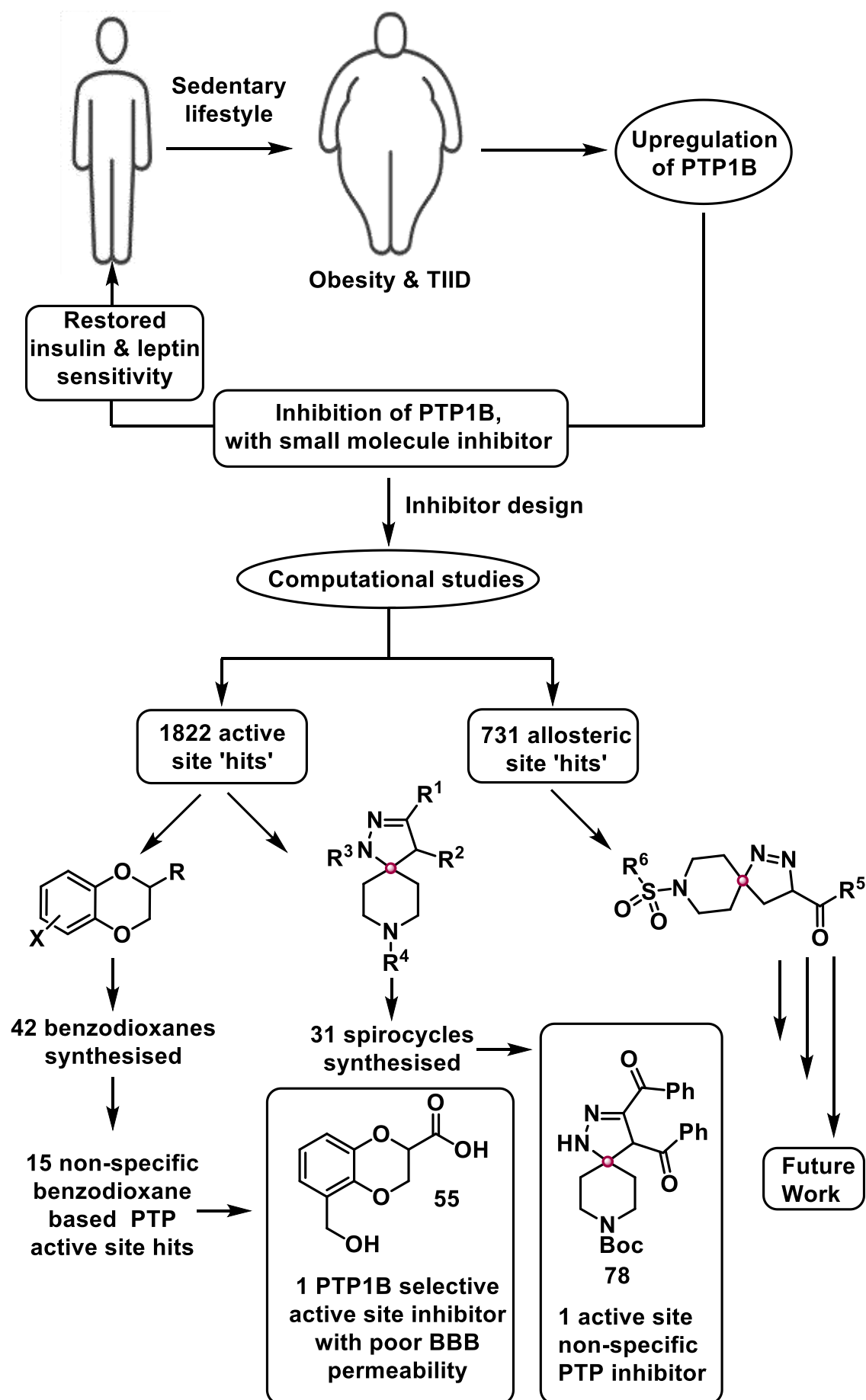


Figure 128: Summative figure illustrating overarching results of this work.

As shown above in **Figure 128**, herein both druggable well-defined regions of PTP1B were investigated *in silico*, by means of database screening, docking studies and modelling with known literature PTP1B inhibitors for both target sites. In order to compile key residues essential or preferable to be interacted with for binding of potential inhibitors. From this *in-silico* work the highlighted core structure for potential new active site PTP inhibitors were tetrahydronaphthalenes, which were redesigned to benzodioxanes due to synthesis constraints and from computational data showed no loss of binding potential by doing so.

Another class of compounds which showed potential computationally in both the active and the allosteric site of PTP1B were spirocycles, due to at the time the ongoing optimisation for the formation of 5,6-spirocycle dihydropyrazoles the library of compounds tested of the resultant publication were also tested along with the benzodioxanes for PTP active site activity.

Two biological assays were used to assess the potential of compounds being potent, effective, selective PTP1B inhibitors with low BBB permeability. These were a yeast based PTP inhibition assay which investigated the former three properties of interest and a commercially available BBB synthetic permeability assay which investigated the latter property of interest.

The initial screens of the target benzodioxane and spirocycle compound library yielded a total of five hits in terms of PTP1B inhibition. Four of these were benzodioxanes, two of these were confirmed with concentration screen, being compound **26** and **30a**, the fifth being the only spirocyclic dihydropyrazoles hit, compound **78**. From comparison of the subsequent comparison of PTP1B and TCPTP activity in addition to BBB permeability compound **30a** was identified as the most promising hit compound by being the most potent, being more effective towards PTP1B over TCPTP and being relatively impermeable to the synthetic BBB membrane.

Derivatives of compound **30a** were hence synthesised forming another compound library for testing, the main aim of which was to improve the selectivity of PTP1B while maintaining low BBB permeability and potency. This was partly achieved with compound **55**, as at 37 °C both compounds **30a** and **55** had comparable BBB permeabilities and compound **55** had a significant inhibitory effect on PTP1B, but not on TCPTP. However, the conversion of the aldehyde to the alcohol did result in a significant loss of effectiveness in PTP1B inhibition at 140 µM the optimum concentration for both hit

compounds, however compound **55** is still considered the current lead compound from this work as additionally aldehyde functional groups are less favourable for pharmaceutical compounds.

A secondary aim of the compound **30a** derivative compound library was the investigation of binding mode of the benzodioxane hit and determine what aspects of compound **30a** are essential, beneficial, or not required for binding to the PTP1B active site. When looking at the yeast assay data for compound **25** and **55** it is suggestive that the carboxylic acid or equivalent motif is not essential for binding as compound **25** itself showed no significant activity, whereas compound **55** did show significant activity implying that the aldehyde or equivalent electron acceptor in the *ortho* / *meta* position to the dioxane oxygen is essential for binding.

From computational modelling, the proposed reason for the selectivity of compound **55** towards PTP1B over its closest PTP family member in terms of active site structure TCPTP is the orientation of which the compound binds to the PTP active site relative to the Cys residue at the base of the active site. With PTP1B, from computational docking studies the favoured binding mode has the relative orientation of the primary alcohol of compound **55** directed up and hydrogen bonding with Lys-120, Ser-216 and Tyr-46. However, when investigating TCPTP, due to the difference residues surrounding the Cys residue among other structural differences of the active site, it is thought that the binding position in TCPTP is flipped over by 180 °C resulting in the case of compound **55** the primary alcohol facing down if comparing the proposed orientation to that of PTP1B. This proposed change in orientation in TCPTP results in the primary alcohol being unable to bind to the comparable residues to that of PTP1B and instead the neighbouring TCPTP residues are less favourable for binding, so TCPTP is a less favourable target due to a lesser binding potential resulting in compound **55** not having a significant effect on TCPTP + v-Src growth rate. However, when looking at the parent compound of **55**, **30a** which does exert a significant influence on TCPTP as well as PTP1B. The same relative change in orientation is also proposed based upon the found lowest energy position in both PTP active sites. A contributing reason for compound **30a** exerting a significant inhibitory effect in TCPTP is thought to be the aldehyde's ability to interact with Gln-262 of TCPTP better than the primary alcohol of **55** resulting in a superior binding and thus TCPTP inhibition with **30a** *via* the active site. If this is the case of the flip in relative orientation of benzodioxane binding modes of the two PTPs, then this enables further

future compound design for the selectivity towards the desired PTP target. The binding modes of compound **30a** in PTP1B and TCPTP could be confirmed by co-crystallising this hit compound with each protein.

In conclusion, the aims of this project have been met and thus a contribution to the current literature has been achieved with this work, as a selective PTP1B active site inhibitor with a proposed low BBB permeability has been successfully identified, compound **55**.

6.2.Future direction

The results obtained from the work have yielded multiple areas for further studies beyond the scope of this project.

Continuing with the development and implementation of benzodioxane based hit compounds as PTP1B inhibitors with use of the yeast-based inhibition assay, with the aim of further increasing potency, effectiveness, selectivity, and BBB impermeability is the most linear future work to be conducted from this project.

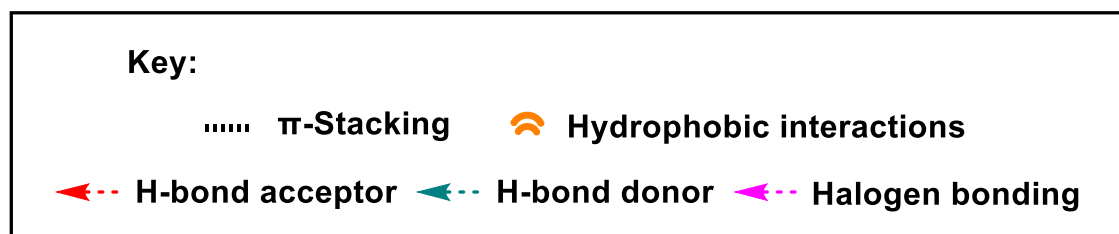
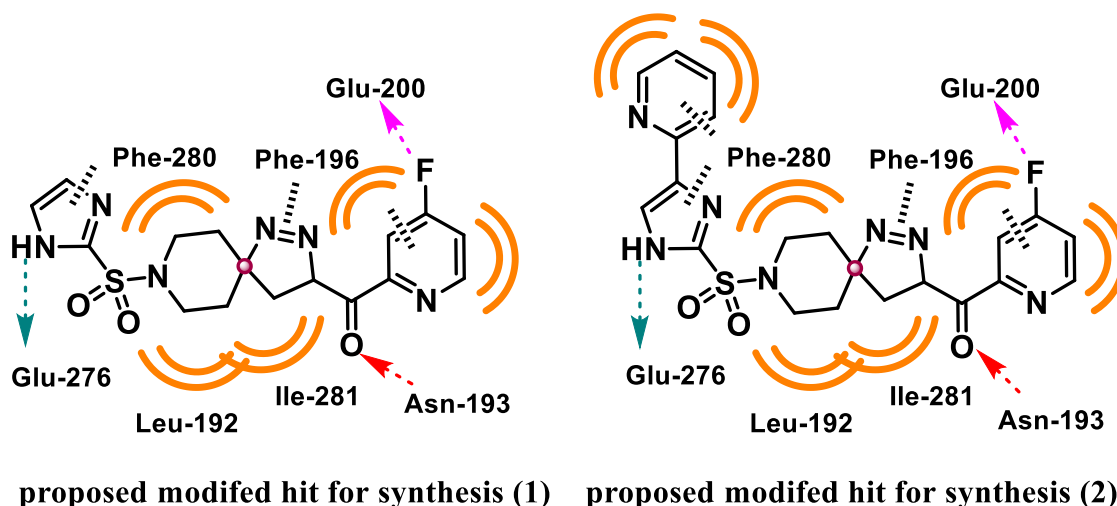


Figure 129: Chemical structures and computationally predicted interactions of proposed two iterations of a proposed modified hit for synthesis for PTP1B's allosteric site.

Another way in which the selectivity of PTP inhibitors towards PTP1B can be assessed is with the use of other PTP plasmids in addition to TCPTP, are evaluating the % change in T_d compound **55** has on HePTP or SHP1 + v-Src for example. TCPTP may be the closest member to PTP1B in terms of active site structural features, but numerous common features are shared with many members of the PTP family, so any PTP inhibitor that claims to be PTP1B specific with regards to all PTPs needs to be confirmed with additional testing.

Further investigation of the other well-defined druggable target the allosteric site as means of PTP1B inhibition would also be justified with the initial compound library being based upon the identified potential hit compounds identified. The structures of two potential allosteric site 5,6-spirocyclic dihydropyrazole based PTP1B inhibitors are shown above in **Figure 129**

Shown in **Figure 129** and **Table 11** are the chemical structures, predicted binding modes in the allosteric site and selected physicochemical properties of two iterations of a potential PTP1B allosteric site inhibitor, which was designed from all acquired database screening results.

Table 11: Physicochemical values of proposed PTP1B allosteric site hits.

Compound	cLogP	MW	Aromatic rings	H - acceptors	H - donors	Total molecular surface area	sp ³ -atoms
(1)	-1.6348	394.430	2	9	3	270.72	10
(2)	1.1766	471.528	3	10	3	331.44	10

The 5,6-spirocyclic core present in both (1) and (2) could be synthesised *via* the synthesis method explored in Chapter 5 (section 5.3.1). (2) is a theoretical evolution of (1) which processes additional means of interactions with the key allosteric residue Phe-280, and has potentially superior physicochemical properties for BBB impermeability, with the cLogP range within one of the afore mentioned ideal ranges and a larger total surface area, both of which impair BBB permeability. The computationally predicted binding mode of proposed modified hit for synthesis (2) docked into PTP1B allosteric site is shown below in **Figure 130**.

Currently, no known allosteric site inhibitor containing a spirocycle motif could be found in the literature, meaning synthesis and investigation of these proposed modified hit compounds is warranted for future work as they may result in improved PTP1B selectivity over other PTPs than previous PTP1B inhibitors.

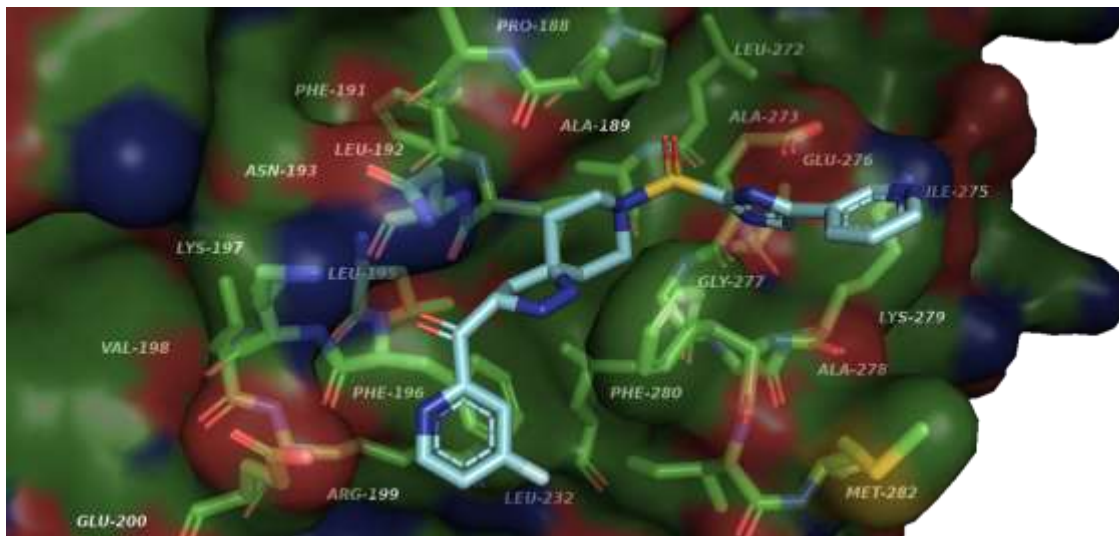


Figure 130: Theoretical binding position of proposed modified hit 2 in PTP1B's allosteric site.

Predicted interactions with PTP1B's allosteric site: Hydrophobic interactions with Phe-196, Ile-281, Leu-192 and Phe-280. π -stacking with Phe-196 and Phe-280. Halogen bond with Glu-200, and limited hydrogen bonding between the carbonyl motif of the substrate and Asn-193 (residue acts as the donor), and the substrates NH acting as a hydrogen bond donor with Glu-276.

In order to test for allosteric site inhibition with the utilised assay from this work a protein fragment denoting the allosteric site, which is three α -helices, and the surrounding residues of the C-terminus would need to be incorporated into the yeast cells as a plasmid, as was done for the region corresponding to the active site in this work. Potentially due to the overall size of the protein (PTP1B) itself not being significantly large, the whole unaltered PTP1B may be able to be transcribed and expressed in yeast cells. If this was the case, the location of binding of any subsequent hits could not be confirmed without comparing the % change in T_d in active site only containing transcribed yeast. However, unless the allosteric site was also transcribed and tested separately the disordered binding region could not be ruled out, unless the inhibitor protein binding complex could be co-crystallised out.

Further investigation into the permeability of hit PTP small molecule inhibitors with respect to the blood brain barrier could also be conducted. Since the assay utilised in this work was a commercially available kit which deployed a synthetic membrane which

mimics the properties of the BBB, conducting the same BBB permeability assessment with the most promising hit small molecules, compound **30a** and **55**, but instead using actual BBB mammalian cells which can be grown into a more biologically relevant barrier for testing. The results of this could then be subsequently compared to those obtained from the synthetic membrane kit to see if result or trends are consistent. Furthermore, with regards to BBB permeability, animal testing could also be conducted by injecting a fluorescence tagged version of the small molecule inhibitor into mice and after 24 hours terminate the mice and measure the amount of compound located within the brain. From this the *in vivo* permeability and the half-life of the PTP1B small molecule inhibitor can be determined.

Metal free carbon-carbon bond formation from the reaction between sulfonyl hydrazones and cyclic enones was a surprising result and investigation of further substrates which can be utilised in this reaction in addition to the reported results using cyclopentanone cyclohexanone would be of interest. In addition to a substrate, the reaction conditions could also be optimised as the used reaction conditions were optimum for the spirocycle formation with the electron deficient alkene diethyl fumarate. Hence since the yields obtained with cyclic enones were mediocre, alternative conditions may enhance the C-C bond formation and therefore isolated yield, if so, this would certainly be of synthetic interest.

As discussed, the results obtained from the PhD project work have potentially opened up numerous new avenues of scientific research, and therefore future projects.

Chapter 7

Methodology

7.1. General Experimental Details

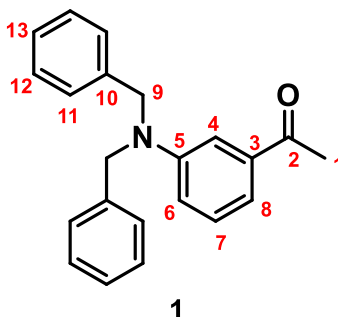
All reactions were conducted using standard Schlenk techniques. Analytical thin layer chromatography (TLC) was performed using silica gel 60 F₂₅₄ pre-coated glass-backed plates and visualised by ultraviolet radiation (254 nm), potassium permanganate, ceric ammonium molybdate or iodine dispersed on silica, as appropriate. Flash column chromatography was performed using silica gel (particle size 40-63 nm) under air pressure. ¹H NMR spectra were recorded on a Bruker 400 MHz spectrometer. Chemical shifts are reported in ppm with the resonance resulting from incomplete deuteration of the solvent as the internal standard (CDCl₃: 7.26 ppm, singlet. *d*₆-DMSO: 2.50 ppm, singlet. MeOD: 3.31 ppm, quintet and 4.8 ppm, singlet). ¹³C NMR spectra were recorded on a 100 MHz spectrometer with complete proton decoupling. Chemical shifts are reported in ppm with the solvent resonance as the internal standard (¹³CDCl₃: 77.0 ppm, t or ¹³C-*d*₆-DMSO: 39.5 ppm, septet or ¹³MeOD: 49.1 ppm, septet). HRMS was on a Xevo G2-XS-ToF, in either ESI positive mode or ASAP positive mode. HRMS signals are reported to 4 decimal places and are within ± 5 ppm of theoretical values. Infrared spectra were recorded neat as thin films on a Bruker Alpha Platinum-ATR and only selected peaks are reported.

All ¹H and ¹³C NMR spectra for all synthesised compounds is located in the appendix section 5.

7.2. Chemical Synthesis

7.2.1. Synthesis of LZP25 and precursors: 1-5

1-(3-(dibenzylamino)phenyl)ethan-1-one (1).



Procedure A: for synthesis of **1**

Adapted from a known procedure.¹³⁴

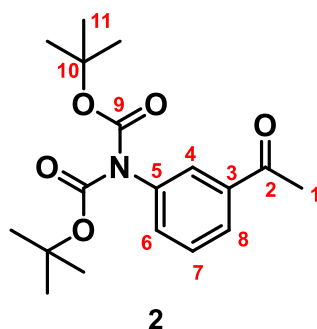
In a 100 mL RB flask the following was added sequentially: 1-(3-aminophenyl)ethan-1-one (2700 mg, 20.0 mmol, 1.0 equiv.) 20 mL of DMF, Cs₂CO₃, (13.0 g, 40.0 mmol, 2.0 equiv.) and (bromomethyl)benzene (4.75 mL, 40.0 mmol, 2.0 equiv.) The resultant reaction mixture was heated to 60 °C and stirred until completion, confirmed by TLC. Upon completion the solution was concentrated *in vacuo* and partitioned between 20 mL EtOAc and 20 mL water. The resultant organic layer was washed with a second 20 mL of water and dried over 50 mL of brine and subsequently MgSO₄. Filtered and concentrated *in vacuo* to yield impure title product. This crude residue was purified by flash column chromatography (30% EtOAc/hexanes) to yield title compound **1**. Isolated as a pale-yellow powder (3.90 g, 12.36 mmol, 77%).

¹H NMR (CDCl₃); δ 2.47 (3H, s, H1), 4.69 (4H, s, H9), 6.90 (1H, ddd, *J* 1.0, 2.5, 7.8 Hz, H7), 7.25 (8H, *app* t, H11 & H12), 7.32 (3H, d, H4, H6 & H8), 7.35 (2H, dt, *J* 1.1, 9.0 Hz, H13). ¹³C NMR (CDCl₃); δ 26.8 (C1), 54.3 (C9), 111.6 (C8), 117.09 (C7), 117.13 (C4), 126.7 (C11), 127.7 (C6 & C13), 128.8 (C12), 129.4 (C10), 138.1 (C3), 149.2 (C5), 198.7 (C2). *R*_f 0.683 (30% EtOAc/hexanes). FTIR (ν_{max} cm⁻¹), 2927, (w, CH_x), 2863, (w, CH_x), 1881 (s, C=O). 1250 (s, C-N). HRMS (XEVO G2-XS QToF) calculated for C₂₂H₂₂NO [M+H]⁺, 316.1701 found: 316.1711.

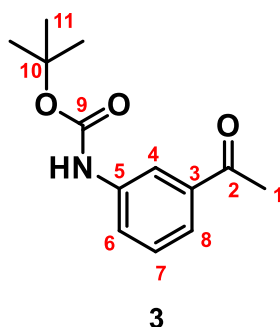
General procedure B: for synthesis of **2** and **3**.

Adapted from a known procedure.¹³³

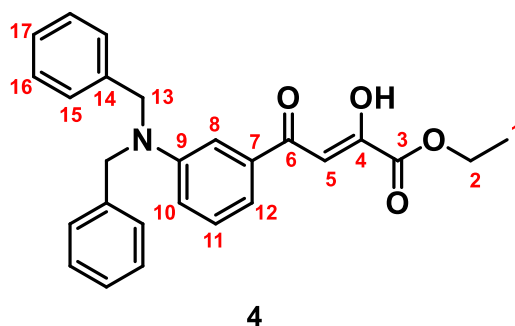
3-aminoacetophenone (5.0 mmol, 1.0 equiv.) was dissolved in DCM (50 mL), after which triethylamine (10.0 mmol, 2.0 equiv.) and a catalytic amount of DMAP was added and the reaction mixture was allowed to stir at RT for 10 minutes. Next Boc₂O (11.0 mmol, 2.2 equiv.) was added, and the reaction mixture was continued to be stirred at RT overnight. After reaction had concluded the following workup was conducted. Reaction mixture was added to a separating funnel containing 25 mL of water. Organic layer washed with a second 25 mL of water, aqueous layers combined and extracted with a fresh 15 mL of DCM. Organic layers combined and dried with 25 mL of brine and MgSO₄. Solvents removed *in vacuo* to provide a crude residue which was purified by flash column chromatography (30% EtOAc/hexanes) to yield the title compounds, in parallel.



tert-butyl (3-acetylphenyl)(tert-butoxycarbonyl)carbamate (2). Isolated as a viscous yellow oil (78.0 mg, 0.24 mmol, 5%), according to general procedure B. ^1H NMR (CDCl_3); δ 1.44 (18H, s, H11), 2.60 (3H, s, H1), 7.36 (1H, dq, J 1.1, 7.9 Hz, H8), 7.47 (1H, t, J 7.8 Hz, H7), 7.75 (1H, t, J 1.8 Hz, H6), 7.90 (1H, dt, J 1.2, 7.8 Hz, H4). ^{13}C NMR (CDCl_3); δ 26.7 (C1), 28.0 (C11), 83.1 (C10), 122.8 (C4), 127.4 (C6), 129.0 (C7), 132.7 (C8), 137.8 (C3), 139.9 (C5), 151.6 (C9), 197.1 (C2). R_f 0.442 (30% EtOAc/hexanes). FTIR (ν_{max} cm^{-1}), 2978, (w, CH_x), 2933, (w, CH_x), 1789 (s, C=O), 1707 (s, C=O), 1245 (s, C-N). HRMS (XEVO G2-XS QToF) calculated for $\text{C}_{18}\text{H}_{26}\text{NO}_5$ $[\text{M}+\text{H}]^+$, 336.1833 found: 336.1831.



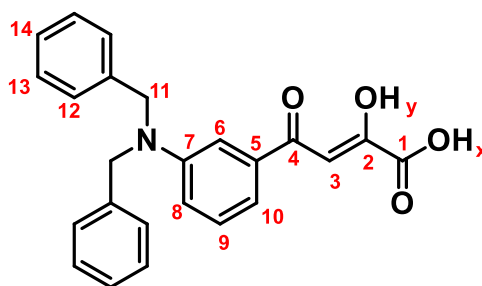
tert-butyl (3-acetylphenyl)carbamate (3). Isolated as an amorphous yellow solid (898 mg, 3.82 mmol, 76%), according to general procedure B. ^1H NMR (CDCl_3); δ 1.45 (9H, s, H11), 2.61 (3H, s, H1), 7.48 (1H, d, J 3.8 Hz, H8), 7.50 (1H, br. s, H7), 7.87 (1H, app q, 1.5 Hz, H6), 7.92 (1H, dt, J 1.9, 6.6 Hz, H4). ^{13}C NMR (CDCl_3); δ 27.0 (C1), 27.9 (C11), 84.0 (C10), 127.7 (C4), 129.1 (C6), 133.0 (C8), 138.0 (C7), 139.3 (C3), 151.7 (C5), 154.3 (C9), 197.0 (C2). R_f 0.209 (30% EtOAc/hexanes). FTIR (ν_{max} cm^{-1}), 2982, (w, CH_x), 2937, (w, CH_x), 1737 (s, C=O), 1703 (s, C=O), 1245 (s, C-N). HRMS (XEVO G2-XS QToF) calculated for $\text{C}_{13}\text{H}_{18}\text{NO}_3$ $[\text{M}+\text{H}]^+$, 236.1228 found: 236.1322.

ethyl-4-(3-(dibenzylamino)phenyl)-2-hydroxy-4-oxobut-2-enoate (4).**Procedure C:** for synthesis of **4**.

Adapted from a known procedure.¹³⁵

To a solution of compound **1** (1.10 g, 3.5 mmol, 1.0 equiv.) and diethyl oxalate (0.95 mL, 7.0 mmol, 2.0 equiv.) in anhydrous THF (14 mL) NaOMe (378 mg, 7.0 mmol, 2.0 equiv.) was added under N₂ gas protection. After 1.5 hrs at RT the mixture was poured into hexane (80 mL). The resultant precipitate was removed by filtration and then was vigorously stirred for 30 minutes in 1M HCl (20 mL). The formed yellow solid was filtered, washed with water, and dried to yield title compound **4**. Isolated as bright orange amorphous solid. (842 mg, 2.03 mmol, 58%).

¹H NMR (CDCl₃); δ 1.70 (3H, t, *J* 7.1 Hz, H1), 4.20 (1H, s, H5), 4.68 (2H, q, *J* 7.1 Hz, H2), 5.01 (4H, s, H13), 7.25 (1H, dd, *J* 2.1, 8.0 Hz, H12), 7.57 (8H, t, H15 & H16), 7.64 (3H, *app* d, H8, H9 & H10), 7.67 (1H, br. s, H17_α), 7.73 (1H, br. s, H17_β). 15.3 (1H, br. s, OH). ¹³C NMR (CDCl₃); δ 14.2 (C1), 54.1 (C2), 62.6 (C13), 98.5 (C5), 111.1 (C8), 116.1 (C12), 118.1 (C11), 126.8 (C15), 127.4 (C17), 129.0 (C16), 129.8 (C7), 136.0 (C10), 137.8 (C14), 149.5 (C9), 169.0 (C6), 191.9 (C4). *R*_f 0.738 (30% EtOAc/hexanes). FTIR (ν_{max} cm⁻¹), 3396 (s br., O-H), 3027, (w, CH_x), 2982, (w, CH_x), 1730 (s, C=O), 1247 (s, C-N). HRMS (XEVO G2-XS QToF) calculated for C₂₆H₂₆NO₄ [M+H]⁺, 416.1862 found: 416.1863.

LZP25 / 4-(3-(dibenzylamino)phenyl)-2-hydroxy-4-oxobut-2-enoic acid (5).**LZP25 / 5****Procedure D:** for synthesis of **5**.

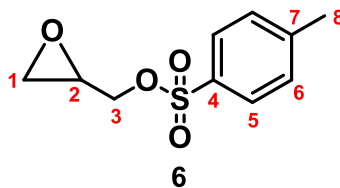
Adapted from a known procedure.¹⁴⁵

Compound **4** formed in procedure C (652 mg, 1.5 mmol, 1.0 equiv.) was dissolved in 12 mL of a 1:1 mixture of MeOH / DCM, to this the lithium hydroxide monohydrate (94 mg, 2.25 mmol, 1.5 equiv.) was added to the stirred reaction mixture at RT. Upon completion (approx. 3hrs), the reaction mixture was concentrated *in vacuo* and partitioned between water (acidized with 1M HCl) and DCM (20 mL of each). The resultant aqueous layer was extracted with a second 20 mL of DCM and the combined organic layers were dried with MgSO₄. MgSO₄ filtered off, and the resultant solution was dried *in vacuo* to yield pure title product compound **5** (LZP25). Isolated as a bright orange powder (532 mg, 1.37 mmol, 91%).

¹H NMR (CDCl₃); δ 1.58 (1H, br. s, OH_x), 3.94 (1H, s, H₃), 4.74 (4H, s, H₁₁), 6.98 (1H, d, *J* 7.1 Hz, H₁₀), 7.04 (1H, s, H₆), 7.26 (2H, *app* br. s, H₁₄), 7.3 (2H, dd, H₈ & H₉), 7.37 (8H, dt, H₁₂ & H₁₃), 15.27 (1H, br. s, OH_y). ¹³C NMR (CDCl₃); δ 54.6 (C₁₁), 97.5 (C₃), 98.6 (C₅), 111.2 (C₆), 116.8 (C₁₀), 118.2 (C₈), 126.7 (C₁₃), 127.3 (C₁₅), 128.9 (C₁₄), 129.8 (C₉), 137.8 (C₁₂), 149.3 (C₇), 162.9 (C₁), 168.4 (C₄), 191.9 (C₂). *R*_f 0.703 (30% EtOAc/hexanes). FTIR (*v*_{max} cm⁻¹), 3407 (s br., O-H), 3027, (w, CH_x), 2915, (w, CH_x), 1710 (s, C=O), 1684 (m, C=C), 1252 (s, C-N). HRMS (XEVO G2-XS QTof) calculated for C₂₆H₂₆NO₄ [M+H]⁺, 416.1862 found: 416.1863.

7.2.2. Synthesis of Benzodioxane precursors: 6, 9-15, 24, 34-37

Oxiran-2-ylmethyl 4-methylbenzenesulfonate (6).



General procedure E: for synthesis of **6**.

Adapted from a known procedure.¹⁵¹

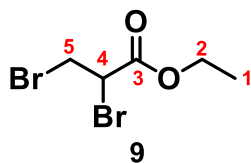
A solution of glycidol (2.23 g, 30.0 mmol, 1.0 equiv.) in DCM (60 mL) was stirred and cooled in an ice-bath for 10 mins. The following were hence subsequently added to the reaction vessel: Et₃N (8.4 mL, 60.0 mmol, 2.0 equiv.) DMAP (180 mg, 1.50 mmol, 0.15 equiv.) and TsCl (5740 mg, 30.0 mmol, 1.0 equiv.). Upon all additions the reaction mixture was removed from the ice-bath and stirred at RT overnight until completion had been reached (confirmed by TLC). Filtered off a white solid by-product. Workup: Reaction quenched with 2M HCl and the resultant layers separated. The aqueous layer was extracted with a fresh 40 mL of DCM. Combined organic layers washed with 50 mL of water, and subsequently dried with 40 mL of brine and MgSO₄. DCM removed under vacuum to yield compound **6** as a viscous yellow oil. (5920 mg, 25.9 mmol, 86%).

¹H NMR (CDCl₃); δ 2.74 (3H, s, H₈), 2.61 (1H, dd, *J* 2.0, 4.8 Hz, H_{1α}), 2.83 (1H, t, *J* 4.8 Hz, H_{1β}), 3.21 (1H, dq, *J* 0.5, 4.0 Hz, H₂), 3.97 (1H, dd, *J* 5.2, 11.2 Hz, H_{3α}), 4.27 (1H, dd, *J* 3.6, 11.2 Hz, H_{3β}), 7.37 (2H, d, *J* 7.4 Hz, H₆), 7.82 (2H, d, *J* 9.4 Hz, H₅). ¹³C NMR (CDCl₃); δ 21.7 (C₈), 44.7 (C₁), 48.9 (C₂), 70.5 (C₃), 128.0 (C₅), 130.0 (C₆), 132.7 (C₇), 145.2 (C₄). *R*_f 0.400 (30% EtOAc/hexanes). FTIR (*v*_{max} cm⁻¹), 3064 (w, CH_x), 3001 (w, CH_x), 1357 (s, S=O), 1174 (m, C-O). HRMS (XEVO G2-XS QToF) calculated for C₁₀H₁₃O₄S [M+H]⁺ 228.0716, found: 228.0718.

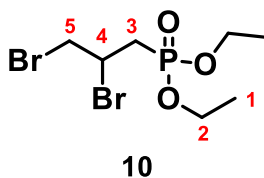
General procedure F: for synthesis of **9-15**.

Adapted from a known procedure.¹⁵²

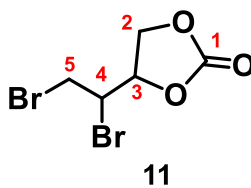
A stirred solution of alkene (10.0 mmol, 1.0 equiv.) in DCM (30.0 mL) was cooled in ice-bath for 10 minutes prior to the drop wise addition of bromine (0.51 mL, 10.0 mmol, 1.0 equiv.). Once added reaction vessel was removed from ice-bath and stirred at room temp until completion observed by TLC. Sodium thiosulphate was added to quench the reaction. Extracted with 3 x 30 mL of DCM. Organic layers combined and dried with brine and MgSO₄. Removal of solvent *in vacuo* to yield title prod (67 – 91%)



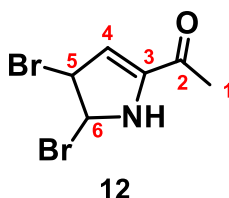
ethyl 2,3-dibromopropanoate (9). Isolated as a viscous yellow oil (2.29 g, 8.82 mmol, 86%), according to general procedure F. ^1H NMR (CDCl_3); δ 1.33 (3H, t, J 7.2 Hz, H1), 3.69 (1H, dd, J 5.6, 10.0 Hz, H5 $_{\alpha}$), 3.93 (1H, *app* t, J 10.8 Hz, H5 $_{\beta}$), 4.30 (2H, q, J 4.30 Hz, H2), 4.44 (1H, dd, J 7.2, 11.6 Hz, H4). ^{13}C NMR (CDCl_3); δ 13.9 (C1), 29.7 (C5), 41.1 (C4), 62.6 (C2), 167.5 (C3). R_f 0.783 (30% EtOAc/hexanes). FTIR (ν_{max} cm^{-1}), 3064 (w, CH_x), 2982, (w, CH_x), 1737 (s, C=O), 1144 (m, C-O). HRMS (XEVO G2-XS QTof) calculated for $\text{C}_5\text{H}_9\text{Br}_2\text{O}_2$ $[\text{M}+\text{H}]^+$, 260.8949 found: 260.8954.



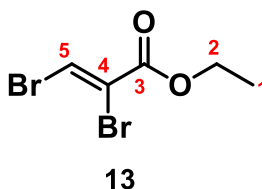
diethyl (2,3-dibromopropyl)phosphonate (10). Isolated as a viscous yellow oil (3.12 g, 9.27 mmol, 91%), according to general procedure F. ^1H NMR (CDCl_3); δ 1.37 (6H, t, J 7.0 Hz, H1), 2.41 (1H, td, J 7.4, 16.2 Hz, H3 $_{\alpha}$), 2.81 (1H, td, J 6.1, 15.9 Hz, H3 $_{\beta}$), 3.80 (1H, dd, J 5.2, 12.6 Hz, H5 $_{\alpha}$), 3.96 (1H, d, J 10.0 Hz, H5 $_{\beta}$), 4.16 (2H, q, J 8.0 Hz, H2), 4.44 (1H, quint, J 6.4 Hz, H4). ^{13}C NMR (CDCl_3); δ 16.4 (C1), 33.2 (C3), 38.0 (C5), 43.4 (C4), 62.2 (C2). R_f 0.256 (30% EtOAc/hexanes). FTIR (ν_{max} cm^{-1}), 2982 (w, CH_x), 2907, (w, CH_x), 1238 (s, P=O), 1018 (s, P-O). HRMS (XEVO G2-XS QTof) calculated for $\text{C}_7\text{H}_{16}\text{Br}_2\text{O}_3\text{P}$ $[\text{M}+\text{H}]^+$, 338.9204 found: 338.9208.



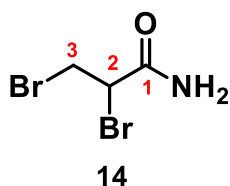
4-(1,2-dibromoethyl)-1,3-dioxolan-2-one (11). Isolated as a viscous yellow oil (2.19 g, 8.07 mmol, 83%), according to general procedure F. ^1H NMR (CDCl_3); δ 3.75 and 3.94 (1H, dd, J 7.2, 12.9 Hz, $\text{H}_{2\alpha}$), 3.98 (1H, d, J 8.3 Hz, $\text{H}_{2\beta}$), 4.23 (1H, dt, J 1.6, 7.9 Hz, H_3), 4.43 (1H, m, $\text{H}_{5\alpha}$), 4.67 (1H, *app* t, J 8.7 Hz, $\text{H}_{5\beta}$), 5.07 and 5.30 (1H, *app* q J 6.6 Hz, H_4). ^{13}C NMR (CDCl_3); δ 30.5 (C2), 51.5 (C3), 73.0 (C4), 153.8 (C1). R_f 0.967 (30% EtOAc/hexanes). FTIR (ν_{max} cm^{-1}), 2945 (w, CH_x), 2878, (w, CH_x), 1774 (s, C=O), 1144 (m, C-O). HRMS (XEVO G2-XS QToF) calculated for $\text{C}_5\text{H}_8\text{Br}_2\text{O}_3$ $[\text{M}+\text{H}]^+$, 274.8742 found: 274.8743.



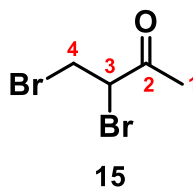
1-(4,5-dibromo-4,5-dihydro-1H-pyrrol-2-yl)ethan-1-one (12). Isolated as a viscous yellow oil (1.78 g, 6.66 mmol, 67%), according to general procedure F. ^1H NMR (CDCl_3); δ 2.42 (1H, s, H_4), 2.44 (3H, s, H_1), 6.91 (1H, *app* q, J 1.1 Hz, H_5), 7.05 (1H, *app* dd, J 1.4, 2.9 Hz, H_6), 9.75 (1H, s, NH). ^{13}C NMR (CDCl_3); δ 25.5 (C1), 98.0 (C4), 118.1 (C5), 124.4 (C6), 132.0 (C3), 187.6 (C2). R_f 0.576 (30% EtOAc/hexanes). FTIR (ν_{max} cm^{-1}), 3243 (w, N-H), 3116 (w, CH_x), 2967, (w, CH_x), 1637 (s, C=O). HRMS (XEVO G2-XS QToF) calculated for $\text{C}_6\text{H}_8\text{Br}_2\text{NO}$ $[\text{M}+\text{H}]^+$, 268.8874 found: 269.8815.



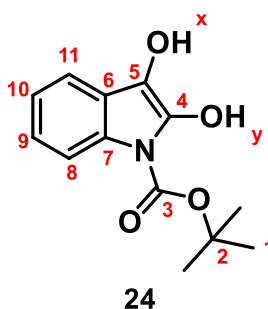
ethyl (Z)-2,3-dibromoacrylate (13). Isolated as a viscous colourless oil (2.48 g, 9.62 mmol, 96%), according to general procedure F. ^1H NMR (CDCl_3); δ 1.35 (3H, t, J 7.1 Hz, H_1), 4.30 (2H, q, J 7.1 Hz, H_2), 8.23 (1H, s, H_5). ^{13}C NMR (CDCl_3); δ 14.1 (C1), 63.2 (C2), 122.7 (C4), 126.5 (C5), 160.8 (C3). R_f 0.937 (30% EtOAc/hexanes). FTIR (ν_{max} cm^{-1}), 3071 (w, CH_x), 2982, (w, CH_x), 1730 (s, C=O), 1245 (s, C-O). HRMS (XEVO G2-XS QToF) calculated for $\text{C}_5\text{H}_7\text{Br}_2\text{O}_2$ $[\text{M}+\text{H}]^+$, 258.8794 found: 258.8796.



2,3-dibromopropanamide (14). Isolated as a white powder (1.85 g, 8.00 mmol, 80%), according to general procedure F. ^1H NMR (CDCl_3); δ 3.82 (1H, dd, J 4.6, 10.3 Hz, $\text{H}_{3\alpha}$), 3.96 (1H, dd, J 8.4, 10.4 Hz, $\text{H}_{3\beta}$), 4.50 (1H, dd, J 4.6, 8.4 Hz, H_2), 5.90 (1H, s, NH), 6.11 (1H, s, NH). ^{13}C NMR (CDCl_3); δ 31.6 (C3), 44.9 (C2), 168.2 (C1). R_f 0.131 (30% EtOAc/hexanes). FTIR (ν_{max} cm^{-1}), 3329 (m, N-H), 3187 (w, CH_x), 2889, (w, CH_x), 1662 (s, C=O). HRMS (XEVO G2-XS QToF) calculated for $\text{C}_3\text{H}_7\text{Br}_2\text{NO}$ $[\text{M}+\text{H}]^+$, 231.8796 found: 231.8802.



3,4-dibromobutan-2-one (15). Isolated as a viscous yellow oil (1.75 g, 7.61 mmol, 76%), according to general procedure F. ^1H NMR (CDCl_3); δ 2.40 (3H, s, H_1), 3.66 (1H, dd, J 4.4, 10.1 Hz, $\text{H}_{4\alpha}$), 3.92 (1H, *app* t, J 10.6 Hz, $\text{H}_{4\beta}$), 4.53 (1H, dd, J 4.4, 10.9 Hz, H_3). ^{13}C NMR (CDCl_3); δ 26.9 (C1), 28.5 (C4), 47.3 (C3), 198.5 (C2). R_f 0.764 (30% EtOAc/hexanes). FTIR (ν_{max} cm^{-1}), 3042 (w, CH_x), 2974, (w, CH_x), 1718 (s, C=O), HRMS (XEVO G2-XS QToF) calculated for $\text{C}_4\text{H}_7\text{Br}_2\text{O}$ $[\text{M}+\text{H}]^+$, 230.8843 found: 230.8843.

***tert*-butyl 2,3-dihydroxy-1H-indole-1-carboxylate (24).****General procedure B.1:** for synthesis of **24**

Adapted from a known procedure.¹³³

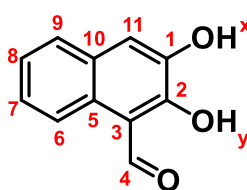
Isatin (1.47 g, 10.0 mmol, 1.0 equiv.) was dissolved in DCM (100 mL), after which triethylamine (2.79 mL, 20.0 mmol, 2.0 equiv.) and a catalytic amount of DMAP was added and the reaction mixture was allowed to stir at RT. Next BOC₂O (2400 mg, 11.0 mmol, 1.1 equiv.) was added, and the reaction mixture was continued to be stirred at RT overnight. After reaction had concluded (conformed by TLC) the following workup was conducted. Reaction mixture was added to a separating funnel containing 50 mL of water and organic layer washed with a second 50 mL of water, aqueous layers combined and extracted with 25 mL of DCM. Organic layers combined and dried with 50 mL of brine and MgSO₄. Solvents removed *in vacuo* to provide a crude residue which was purified by flash column chromatography (30% EtOAc/hexanes) to yield the title compound **24**. Isolated as a viscous yellow oil (1.70 g, 7.20 mmol, 72%),

¹H NMR (CDCl₃); note peaks at 1.39 and 3.18 are due to EtOAc which was unable to be fully removed post column. δ 1.53 (9H, s, H1), 7.01 (1H, t, *J* 7.2 Hz, H10), 7.50 (1H, t, *J* 7.2 Hz, H9), 7.90 (1H, *app* dd, *J* 1.4, 7.9 Hz, H11), 8.44 (1H, d, *J* 8.2 Hz, H8), 10.79 (1H, s, OH_x), 12.88 (1H, s, OH_y). ¹³C NMR (CDCl₃); δ 28.3 (C1), 80.4 (C2), 117.8 (C8), 121.0 (C10), 134.1 (C11), 135.0 (C9), 140.2 (C6), 142.9 (C7), 153.7 (C3), 170.9 (C4), 198.2 (C5). *R*_f 0.002 (30% EtOAc/hexanes). FTIR (ν_{max} cm⁻¹), 3273 (w, O-H), 2978, (w, CH_x), 1725 (s, C=O). HRMS (XEVO G2-XS QToF) calculated for C₁₃H₁₆NO₃ [M+H]⁺, 250.1186 found: 250.1191.

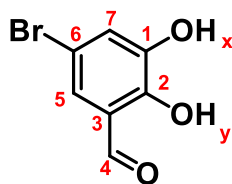
General procedure G: for synthesis of **34** and **35**.

Adapted from a known procedure.¹³²

BBR_3 (42.4 mL, 40 mmol, 1 M in heptane, 4.0 equiv.) was added dropwise to a stirred solution of diether (10 mmol, 1.0 equiv) in DCM (40 mL) under nitrogen at 0 °C and the mixture was stirred until completion observed *via* TLC at RT Saturated Ammonium chloride (aq) was added at RT. to quench the reaction. Organic layer collected and the solvent was removed *in vacuo* affording the crude phosphonic acid. Purified by being dissolved in a minimum amount of EtOAc and flushed through a silica pad with 100% EtOAc. Solvents removed *in vacuo* to yield the title compound (70 – 93%).

**34**

2,3-dihydroxy-1-naphthaldehyde (34). Isolated as a fine green powder (1.28 g, 6.99 mmol, 70%), according to general procedure G. ^1H NMR (CDCl_3); δ 4.01 (1H, s, OH_y), 7.42 (1H, *app* dt, J 1.2, 7.2 Hz, H8), 7.49 (1H, *app* dt, J 1.2, 7.2 Hz, H7), 7.52 (1H, s, H11), 7.71 (1H, d, J 8.4 Hz, H9), 8.27 (1H, d, J 8.4 Hz, H6), 13.50 (1H, s, OH_x). ^{13}C NMR (CDCl_3); δ 111.4 (C3), 114.8 (C5), 118.49 (C11), 118.54 (C6), 125.1 (C8), 126.6 (C7), 128.1 (C10), 144.1 (C1), 154.6 (C2), 193.8 (C4). R_f 0.615 (30% EtOAc/hexanes). FTIR (ν_{max} cm^{-1}), 3351 (br., m O-H), 3071, (w, CH_x), 2892, (w, CH_x), 1638 (s, C=O). HRMS (XEVO G2-XS QTof) calculated for $\text{C}_{11}\text{H}_9\text{O}_3$ $[\text{M}+\text{H}]^+$, 189.0553 found: 189.0552.

**35**

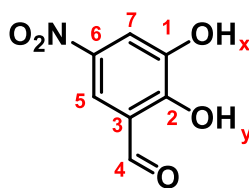
5-bromo-2,3-dihydroxybenzaldehyde (35). Isolated as a pale brown powder (2.03 g, 9.34 mmol, 93%), according to general procedure G. ^1H NMR (CDCl_3); δ 5.75 (1H, s, OH_x), 7.30 (1H, s, H7), 9.85 (1H, s, H4), 11.06 (1H, s, OH_y). ^{13}C NMR (CDCl_3); δ 111.7 (C6), 121.1 (C3), 124.4 (C5), 126.2 (C7), 146.0 (C2), 147.6 (C1), 195.7 (C4). R_f 0.688 (30% EtOAc/hexanes). FTIR (ν_{max} cm^{-1}), 3302 (br., m O-H), 3082, (w, CH_x), 2919, (w, CH_x), 1648 (s, C=O). HRMS (XEVO G2-XS QToF) calculated for $\text{C}_7\text{H}_6\text{BrO}_3$ $[\text{M}+\text{H}]^+$, 216.9502 found: 216.9455.

General procedure G.1: for synthesis of **36** and **37**.

Adapted from a known procedure.¹³²

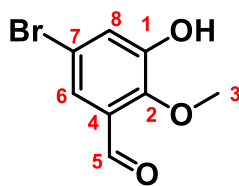
BBr_3 (21.2 mL, 20 mmol, 1 M in heptane, 2.0 equiv.) was added dropwise to a stirred solution of ether (10 mmol) in DCM (50 mL) under nitrogen at 0 °C and the mixture was stirred until completion observed *via* TLC at RT MeOH was added at RT, reaction was quenched*. The organic layer collected, and the solvent was removed in vacuo affording the crude phosphonic acid. Purified by being dissolved in a minimum amount of EtOAc and flushed through a silica pad with 100% EtOAc. Solvents removed *in vacuo* to yield the title compound (14 – 25%).

* Used MeOH for **36** and sat. Ammonium chloride (aq) for **37**.



36

2,3-dihydroxy-5-nitrobenzaldehyde (36). Isolated as a dark orange powder (460 mg, 2.50 mmol, 25%), according to general procedure G.1. ^1H NMR (d_6 -DMSO); δ 3.17 (1H, s, OH_x), 7.78 (1H, d, J 2.8 Hz, H7), 8.00 (1H, d, J 2.8 Hz, H5), 10.31 (1H, s, H4), 11.08 (1H, s, OH_y). ^{13}C NMR (d_6 -DMSO); δ 113.6 (C7), 115.0 (C5), 122.3 (C3), 139.7 (C6), 147.6 (C1), 156.4 (C2), 190.2 (C4). R_f 0.048 (30% EtOAc/hexanes). FTIR (ν_{max} cm^{-1}), 3280 (br., m O-H), 3086, (w, CH_x), 2978, (m, CH_x), 2889, (w, CH_x), 1666 (s, C=O), 1520 (s, N-O). HRMS (XEVO G2-XS QToF) calculated for $\text{C}_7\text{H}_6\text{NO}_5$ $[\text{M}+\text{H}]^+$, 184.0246 found: 184.0256.



37

5-bromo-3-hydroxy-2-methoxybenzaldehyde (37). Isolated as a fluffy white solid (314 mg, 1.37 mmol, 14%), according to general procedure G.1. ^1H NMR (CDCl_3); δ 3.93 (3H, s, H3), 7.18 (1H, d, J 2.1 Hz, H8), 7.32 (1H, d, J 2.1 Hz, H6), 9.86 (1H, s, H5), 11.03 (1H, s, OH). ^{13}C NMR (CDCl_3); δ 56.6 (C3), 111.1 (C7), 120.8 (C8), 121.3 (C4), 126.2 (C6), 149.3 (C2), 150.9 (C1), 195.4 (C5). R_f 0.562 (30% EtOAc/hexanes). FTIR (ν_{max} cm^{-1}), 3288 (br., m O-H), 3090, (w, CH_x), 2941, (w, CH_x), 2878, (w, CH_x), 1645 (s, C=O). HRMS (XEVO G2-XS QToF) calculated for $\text{C}_8\text{H}_8\text{BrO}_3$ $[\text{M}+\text{H}]^+$, 230.9657 found: 230.9661.

7.2.3. Synthesis of Benzodioxanes: 7, 8, 16-23, 38-46 and 52

General procedure H: for synthesis of 7 and 52.

Adapted from a known procedure.¹⁴⁸

To a solution of aromatic diol (10.0 mmol, 1.0 equiv.) in acetone* or ethyl acetate** (50 mL), Cs₂CO₃ (20.0 mmol, 2.0 equiv.) was added (while stirred). After 5 minutes the epichlorohydrin (10.0 mmol, 1.0 equiv.) was added, and the reaction mixture heated under reflux over night until completion (confirmed by TLC). Quenched with 40 mL of water. Liquid - liquid extraction conducted using 3 x 40 mL of DCM, dried with MgSO₄. The organic solvent removed *in vacuo* to yield pure title prod.

General procedure H.1: for synthesis of 7.

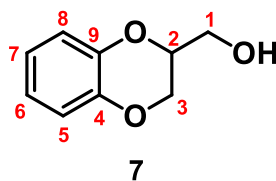
Adapted from a known procedure.¹⁴⁹

To a solution of catechol (5.0 mmol, 1.0 equiv.) in acetone (30 mL), K₂CO₃ (10 mmol, 2.0 equiv.) was added (while stirred). After 5 mins oxiran-2-ylmethyl 4-methylbenzenesulfonate (compound 6) (5 mmol, 1.0 equiv.) was added, and the reaction mixture heated under reflux over night until completion (confirmed by TLC). Quenched with 30 mL of water. Liquid - liquid extraction conducted using 3 x 30 mL of DCM, dried with MgSO₄. The organic solvent removed *in vacuo* to yield pure title product, compound 7.

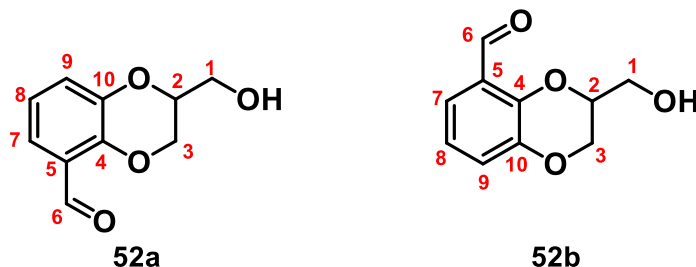
General procedure H.2: for synthesis of 7.

Adapted from a known procedure.^{148,149}

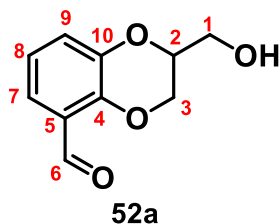
To a reaction flask ethyl 2,3-dihydrobenzo[1,4]dioxine-2-carboxylate (8) (10.0 mmol, 1.0 equiv.), lithium borohydride (11.0 mmol, 1.1 equiv.), ethyl ether (12 mL), and toluene (6 mL) was added. (Toluene was added to avoid caking of the residue and to serve as a heat-transfer medium.) The flask was connected to a reflux setup under nitrogen and heated to 40 °C. The ethyl ether was distilled off. Reaction monitored by TLC. Once reaction has reached completion, any remaining lithium borohydride was quenched with the dropwise addition of *sat* aqueous sodium sulphate sol. (until no further production of gas). Workup: EtOAc 2x 10 mL used for extraction (change pH of aq phase as needed). Dry combined org layers with MgSO₄. The organic solvent removed *in vacuo* to yield pure title product, compound 7.



(2,3-dihydrobenzo[1,4]dioxin-2-yl)methanol (7). Isolated as off-white powder (365 mg, 4.23 mmol, 22%), according to general procedure H* (10.0 mmol). Isolated as a pale-yellow powder (881 mg, 2.20 mmol, 67%), according to general procedure H.1 (5.0 mmol). Isolated as off-white powder (743 mg, 3.35 mmol, 89%), according to general procedure H.2 (5.0 mmol). ^1H NMR (CDCl_3); δ 1.90 (1H, s, OH), 3.87 (1H, dd, J 3.2, 6.8 Hz, H1 $_{\alpha}$), 3.94 (1H, dd, J 3.2, 6.8 Hz, H1 $_{\beta}$), 4.14 (1H, dd, J 3.4, 7.1 Hz, H3 $_{\alpha}$), 4.28 (1H, m, H2), 4.32 (1H, dd, J 3.4, 7.1 Hz, H3 $_{\beta}$), 6.91 (4H, m, H5 - H8). ^{13}C NMR (CDCl_3); δ 61.8 (C3), 65.1 (C1), 73.4 (C2), 117.2 (C6), 117.3 (C7), 121.6 (C5), 121.7 (C8), 140.0 (C9), 143.1 (C4). R_f 0.757 (30% EtOAc/hexanes). FTIR (ν_{max} cm^{-1}), 3347 (s, O-H), 2974, (w, CH_x), 2833, (w, CH_x), 1491 (s, C-O). HRMS (XEVO G2-XS QToF) calculated for $\text{C}_9\text{H}_{11}\text{O}_3$ $[\text{M}+\text{H}]^+$, 167.0704 found: 167.0704.



2-(hydroxymethyl)-2,3-dihydrobenzo[1,4]dioxine-5-carbaldehyde (52). Isolated as a bright yellow viscous oil (765 mg, 3.95 mmol, 40%), according to general procedure H** (10.0 mmol). The compound is an apparent 1:1 mixture of structural isomers by ^1H NMR. ^1H NMR (CDCl_3); δ 2.52 (1H, s, OH $_{\alpha}$), 3.12 (1H, s, OH $_{\beta}$), 3.93 (2H, *app* dd J 3.7, 8.6 Hz, H1 $_{\alpha}$), 4.00 (2H, *app* dd J 3.7, 8.6 Hz, H1 $_{\beta}$), 4.21 (1H, d J 3.8 Hz, H3 $_{\alpha, \alpha}$), 4.25 (1H, d J 7.4 Hz, H3 $_{\beta, \alpha}$), 4.34 (2H, m, H2), 4.39 (1H, dd, J 2.5, 8.8 Hz, H3 $_{\alpha, \beta}$), 4.47 (1H, dd, J 2.5, 8.8 Hz, H3 $_{\beta, \beta}$), 6.94 (2H, *app* dt, J 3.5, 8.0 Hz, H9), 7.13 (1H, t, J 1.8 Hz, H8 $_{\alpha}$), 7.15 (1H, t, J 1.8 Hz, H8 $_{\beta}$), 7.40 (2H, *app* tt, J 1.6, 5.4 Hz, H7), 10.32 (1H, s, H6 $_{\alpha}$), 10.37 (1H, s, H6 $_{\beta}$). ^{13}C NMR (CDCl_3); δ 61.4 (C1 $_{\alpha}$), 61.5 (C1 $_{\beta}$), 64.9 (C3 $_{\beta}$), 65.4 (C3 $_{\alpha}$), 73.2 (C2 $_{\alpha}$), 74.3 (C2 $_{\beta}$), 121.1 (C9 $_{\alpha}$), 121.2 (C9 $_{\beta}$), 122.2 (C7), 123.2 (C8), 125.0 (C10), 143.6 (C4), 145.8 (C5 $_{\alpha}$), 146.0 (C5 $_{\beta}$), 189.2 (C6 $_{\beta}$), 189.5 (C6 $_{\alpha}$). R_f 0.176 (30% EtOAc/hexanes).



2-(hydroxymethyl)-2,3-dihydrobenzo[1,4]dioxine-5-carbaldehyde (52a). Isolated as a bright yellow viscous oil (271 mg, 1.40 mmol, 14%), according to general procedure H**. Single stated structural isomer isolated. ^1H NMR (CDCl_3); δ 2.47 (1H, s, OH), 3.93 (1H, *app* dt, J 4.8, 12.0 Hz, H1 $_{\alpha}$), 4.00 (1H, *app* dt, J 4.8, 12.0 Hz, H1 $_{\beta}$), 4.25 (1H, dd, J 2.2, 11.0 Hz, H3 $_{\alpha}$), 4.34 (1H, m, H2), 4.48 1H, dd, J 2.2, 11.0 Hz, H3 $_{\beta}$), 6.96 (1H, t, J 3.8 Hz, H8), 7.15 (1H, dd, J 1.6, 8.0 Hz, H9), 7.43 (1H, dd, J 1.6, 8.0 Hz, H7), 10.4 (1H, s, H6). ^{13}C NMR (CDCl_3); δ 61.4 (C1), 64.9 (C3), 73.1 (C2), 121.2 (C9), 123.0 (C7), 125.1 (C8), 128.0 (C10), 143.6 (C4), 145.9 (C5), 189.0 (C6). R_f 0.176 (30% EtOAc/hexanes). FTIR (ν_{max} cm^{-1}), 3407 (s, O-H), 2930, (w, CH_x), 2878, (w, CH_x), 1677 (s, C=O), 1476 (s, C-O). HRMS (XEVO G2-XS QTof) calculated for $\text{C}_{10}\text{H}_{11}\text{O}_4$ $[\text{M}+\text{H}]^+$, 195.0657 found: 195.0663.

General procedure I: for synthesis of **8**, **16-19**, **21**, **40-42** and **46**.

Adapted from a known procedure. ^{145,153}

To a solution of a dihydroxybenzene (5 or 10 mmol, 1.0 equiv.) in acetone (15 or 30 mL), K_2CO_3 (5 or 10 mmol, 1.0 equiv.) was added (while stirred). After 15 minutes bromoalkane (5 or 10 mmol, 1.0 equiv.), and additional K_2CO_3 (5 or 10 mmol, 1.0 equiv.) in acetone (15 or 30 mL) was added, reaction mixture was heated under reflux (60 °C) overnight until reaction reached completion (confirmed by TLC).

General procedure I.1: for synthesis of **20**, **22**, **23** and **46**.

Adapted from a known procedure. ^{145,153}

To a solution of a dihydroxybenzene (5 or 10 mmol, 1.0 equiv.) in acetone (15 or 30 mL), Cs_2CO_3 (5 or 10 mmol, 1.0 equiv.) was added (while stirred). After 15 minutes bromoalkane (5 or 10 mmol, 1.0 equiv.), and additional Cs_2CO_3 (5 or 10 mmol, 1.0 equiv.) in acetone (15 or 30 mL) was added, reaction mixture was heated under reflux (60 °C) overnight until reaction reached completion (confirmed by TLC).

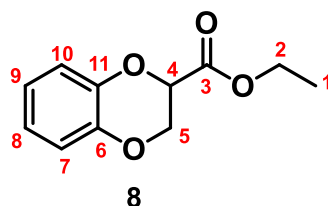
General procedure I.2: for synthesis of **38**, **39** and **41-45**.

Adapted from a known procedure.^{145,153}

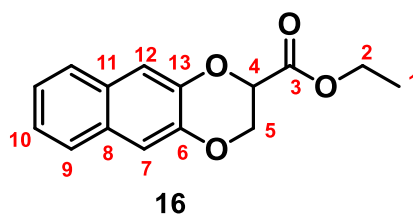
To a solution of a dihydroxybenzene (5 or 10 mmol, 1.0 equiv.) in EtOAc (15 or 30 mL), Cs₂CO₃ (5 or 10 mmol, 1.0 equiv.) was added (while stirred). After 15 minutes bromoalkane (5 or 10 mmol, 1.0 equiv.), and additional Cs₂CO₃ (5 or 10 mmol, 1.0 equiv.) in EtOAc (15 or 30 mL) was added, reaction mixture was heated under reflux (60 °C) overnight until reaction reached completion (confirmed by TLC).

General procedure I – I.2 workup and purification:^{145,153}

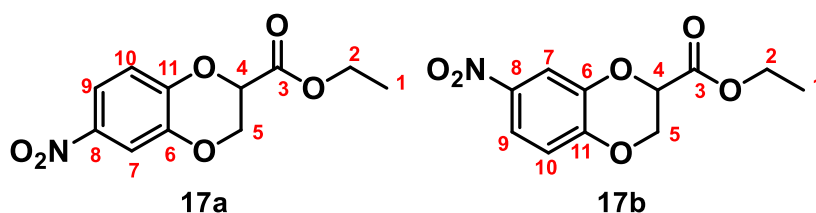
The reaction mixture was concentrated under vacuum. This residue was taken up with a minimum amount of 15% MeOH / 85% EtOAc and flushed through a pad of silica using the same solvent system. Pad flushed until no further prod comes off. The organic solvent removed *in vacuo* to yield pure title prod. If impurities remained; the crude residue was purified by flash column chromatography (30% EtOAc/hexanes) to yield the title compound.



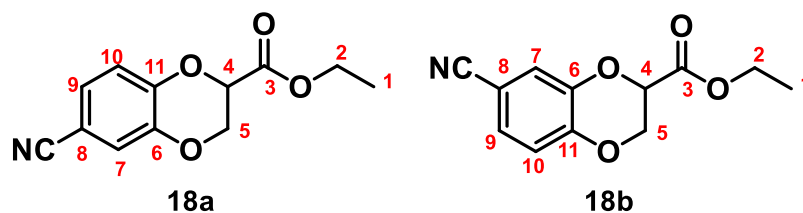
ethyl 2,3-dihydrobenzo[1,4]dioxine-2-carboxylate (8). Isolated as a viscous yellow oil (881 mg, 4.23 mmol, 85%), according to general procedure I (5.0 mmol). ¹H NMR (CDCl₃); δ 1.22 (3H, t, *J* 7.2 Hz, H1), 4.20 (2H, q, *J* 3.8 Hz, H2), 4.31 (2H, d, *J* 3.9 Hz, H5), 4.75 (1H, t, *J* 3.9 Hz, H4), 6.81 (3H, m, H7, H9 & H10), 6.94 (1H, *app* dt, *J* 1.2, 6.8 Hz, H8). ¹³C NMR (CDCl₃); δ 14.1 (C1), 62.0 (C2), 65.0 (C5), 72.0 (C4), 117.3 (C7), 117.4 (C10), 121.8 (C8), 122.1 (C9), 142.3 (C11), 143.0 (C6), 168.0 (C3). *R*_f 0.610 (30% EtOAc/hexanes). FTIR (*v*_{max} cm⁻¹), 2982, (w, CH_x), 2837, (w, CH_x), 1756 (s, C=O), 1491 (s, C-O). HRMS (XEVO G2-XS QTof) calculated for C₁₁H₁₃O₄ [M+H]⁺, 208.0814 found: 208.0855.



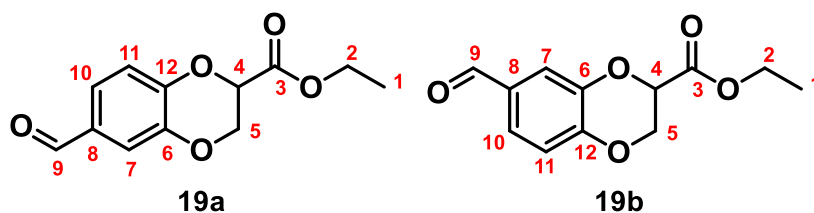
ethyl 2,3-dihydro-2,3-dioxo[2,3][1,4]dioxine-2-carboxylate (16). Isolated as a viscous orange oil (732 mg, 2.83 mmol, 57%), according to general procedure I (5.0 mmol). ^1H NMR (CDCl_3); δ 1.31 (3H, t, J 6.7 Hz, H1), 4.31 (2H, *app* dq, J 1.8, 7.1 Hz, H2), 4.50 (2H, *app* dq, 4.5, 9.9 Hz, H5), 4.94 (1H, dd, 1.5, 4.5, Hz, H4), 7.30 (1H, s, H12), 7.34 (2H, *app* m, H10), 7.43 (1H, s, H7), 7.69 (2H, *app*, m H9). ^{13}C NMR (CDCl_3); δ 14.1 (C1), 62.1 (C2), 65.1 (C5), 72.1 (C4), 112.8 (C12), 124.5 (C10), 126.6 (C9), 129.6 (C11), 129.9 (C8), 142.5 (C13), 143.2 (C6), 168.0 (C3). R_f 0.889 (30% EtOAc/hexanes). FTIR (ν_{max} cm^{-1}), 3056, (w, CH_x), 2982, (w, CH_x), 2937, (w, CH_x), 1751 (s, C=O), 1469 (s, C-O). HRMS (XEVO G2-XS QTof) calculated for $\text{C}_{15}\text{H}_{15}\text{O}_4$ $[\text{M}+\text{H}]^+$, 259.0970 found: 259.0975.



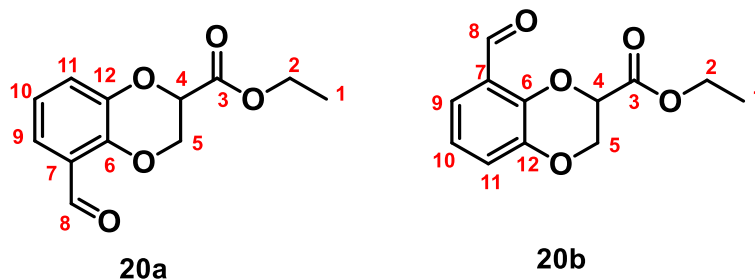
ethyl 6-nitro-2,3-dihydrobenzo[1,4]dioxine-2-carboxylate (17). Isolated as a viscous yellow oil (131 mg, 0.52 mmol, 10%), according to general procedure I (5.0 mmol). The compound is an apparent 3:1 mixture of structural isomers by ^1H NMR. ^1H NMR (CDCl_3); δ 1.31 (1H, t J 4.7 Hz, H1_b), 1.32 (3H, t, J 4.7 Hz, H1_a), 4.31 (2.63H, *app* dq, 1.6, 10.7 Hz, H2_{both}), 4.42 (1.3H, *app* dd, J 2.9, 11.7 Hz, H5 _{α} , both), 4.53 (1.3H, *app* dd, J 2.9, 11.7 Hz, H5 _{β} , both), 4.93 (0.36H, dd, J 1.2, 2.9 Hz, H4_b), 4.96 (1H, dd, J 1.2, 2.9 Hz, H4 _{α}), 6.99 (0.37H, d, J 9.0, H10_b), 7.12 (1H, d, J 9.0, H10_a), 7.83 (1H, *app* d, J 2.6 Hz, H7_a), 7.85 (1H, *app* d, J 2.6 Hz, H7_b), 7.87 (1H, *app* dd, J 2.6, 8.9 Hz, H9_a), 7.87 (0.36H, d, J 8.9 Hz, H9_b). ^{13}C NMR (CDCl_3); δ 14.1 (C1), 62.5 (C2), 64.5 (C5), 72.1 (C4), 113.5 (C7), 117.4 (C9), 118.3 (C8), 143.8 (C11) 148.1 (C6), 167.0 (C3). R_f 0.446 (30% EtOAc/hexanes). FTIR (ν_{max} cm^{-1}), 2982, (w, CH_x), 2937, (w, CH_x), 1726 (s, C=O), 1520 (s, C-O). HRMS (XEVO G2-XS QTof) calculated for $\text{C}_{11}\text{H}_{12}\text{NO}_6$ $[\text{M}+\text{H}]^+$, 254.0985 found: 254.0982.



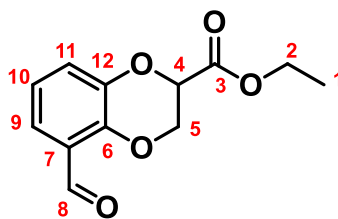
ethyl 6-cyano-2,3-dihydrobenzo[1,4]dioxine-2-carboxylate (18). Isolated as an off white solid (705 mg, 3.02 mmol, 60%), according to general procedure I (5.0 mmol). The compound is an apparent 2:1 mixture of structural isomers by ^1H NMR. ^1H NMR (CDCl_3); δ 1.210 (1.5H, t, J 7.1 Hz, H1_b), 1.212 (3H, t, J 7.1 Hz, H1_a), 4.20 (3H, *app* dq, 2.2, 7.1 Hz, H2), 4.31 (1.5H, m, H5 _{α} , both), 4.41 (1.5H, m, H5 _{β} , both), 4.80 (0.5H, dd, J 1.3, 2.9 Hz, H4_b), 4.84 (1H, dd, J 1.3, 2.9 Hz, H4_a), 6.86 (0.5H, d, J 8.4 Hz, H11_b), 6.98 (1H, d, J 8.4 Hz, H11_a), 7.09 (1H, d, J 1.9, H10_a), 7.11 (0.5H, d, J 8.4 Hz, H11_b), 7.13 (1H, *app* dd, J 1.9, 8.4 Hz, H11_a), 7.21 (0.5H, d, J 1.9, H10_b). ^{13}C NMR (CDCl_3); δ 14.0 (C1), 62.3 (C2), 64.8 (C5_a), 65.2 (C5_b), 71.6 (C4_b), 72.1 (C4_a), 105.0 (C9_a), 105.3 (C9_b), 118.28 (C11_b), 118.34 (C11_a), 121.4 (C10_a), 121.3 (C10_b), 126.4 (C7_b), 126.6 (C7_a), 142.6 (C6_b), 143.2 (C6_a), 146.4 (C12_a), 146.9 (C12_b), 167.1 (C3_b), 167.2 (C3_a). R_f 0.336 (30% EtOAc/hexanes). FTIR (ν_{max} cm^{-1}), 2989, (w, CH_x), 2222 (m, CN) 1744 (s, C=O), 1502 (s, C-O). HRMS (XEVO G2-XS QToF) calculated for $\text{C}_{12}\text{H}_{12}\text{NO}_4$ $[\text{M}+\text{H}]^+$, 237.0766 found: 237.0786.



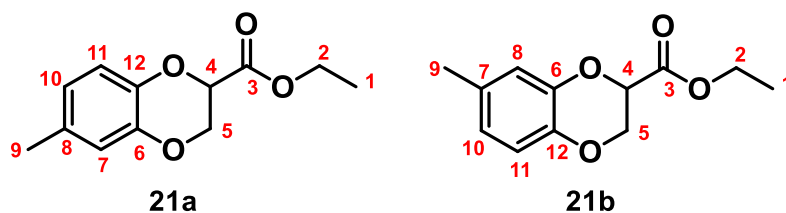
ethyl 6-formyl-2,3-dihydrobenzo[1,4]dioxine-2-carboxylate (19). Isolated as a very viscous pale-yellow oil (712 mg, 3.02 mmol, 60%), according to general procedure I (5.0 mmol). The compound is an apparent 2:1 mixture of structural isomers by ^1H NMR. ^1H NMR (CDCl_3); δ 1.30 (1.5H, t, J 7.1 Hz, $\text{H}_{1\text{b}}$), 1.31 (3H, t, J 7.1 Hz, $\text{H}_{1\text{a}}$), 4.30 (3H, *app* dq, 2.6, 7.1 Hz, H_2), 4.40 (0.5H, d, J 2.9 Hz, $\text{H}_{5\text{b}, \alpha}$), 4.43 (1H, d, J 2.9 Hz, $\text{H}_{5\text{a}, \alpha}$), 4.49 (1.0H, d, J 2.9 Hz, $\text{H}_{5\text{a}, \beta}$), 4.51 (0.5H, dd, J 1.0, 4.2 Hz, $\text{H}_{5\text{b}, \beta}$), 4.90 (0.5H, dd, J 1.4, 3.0 Hz, $\text{H}_{4\text{b}}$), 4.93 (1H, dd, J 1.4, 3.0 Hz, $\text{H}_{4\text{a}}$), 7.02 (0.5H, d, J 8.3 Hz, $\text{H}_{7\text{b}}$), 7.16 (1H, d, J 8.3 Hz, $\text{H}_{7\text{a}}$), 7.44 (1H, d, J 1.9, $\text{H}_{11\text{a}}$), 7.48 (1H, d, J 2.0 Hz, $\text{H}_{10\text{a}}$), 7.50 (0.5H, d, J 2.0 Hz, $\text{H}_{10\text{b}}$), 7.56 (0.5H, d, J 1.9, $\text{H}_{11\text{b}}$), 9.86 (1H, s, $\text{H}_{9\text{a}}$), 9.87 (0.5H, s, $\text{H}_{9\text{b}}$). ^{13}C NMR (CDCl_3); δ 14.1 (C_1), 62.4 (C_2), 64.8 ($\text{C}_{5\text{a}}$), 65.2 ($\text{C}_{5\text{b}}$), 71.7 ($\text{C}_{4\text{b}}$), 72.1 ($\text{C}_{4\text{a}}$), 117.9 ($\text{C}_{7\text{a}}$), 119.9 (C_8), 118.3 ($\text{C}_{7\text{b}}$), 124.2 (C_{10}), 124.9 (C_{11}), 131.0 ($\text{C}_{12\text{a}}$), 131.3 ($\text{C}_{12\text{b}}$), 142.7 ($\text{C}_{6\text{b}}$), 143.4 ($\text{C}_{6\text{a}}$), 147.8 ($\text{C}_{12\text{a}}$), 148.4 ($\text{C}_{12\text{b}}$), 167.3 ($\text{C}_{3\text{a}}$), 167.4 ($\text{C}_{3\text{b}}$), 190.6 ($\text{C}_{9\text{b}}$), 190.7 ($\text{C}_{9\text{a}}$). R_f 0.385 (30% EtOAc/hexanes). FTIR (ν_{max} cm^{-1}), 2986, (w, CH_x), 2833, (w, CH_x), 1744 (s, C=O), 1685 (s, C=O), 1498 (s, C-O). HRMS (XEVO G2-XS QTof) calculated for $\text{C}_{12}\text{H}_{13}\text{O}_5$ $[\text{M}+\text{H}]^+$, 237.0763 found: 237.0766.



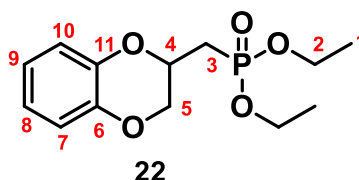
ethyl 5-formyl-2,3-dihydrobenzo[1,4]dioxine-2-carboxylate (20). Isolated as a pale-yellow solid (2.13 g, 9.20 mmol, 92%), according to general procedure I.2 (10.0 mmol). Isolated as an off-white solid (618 mg, 2.61 mmol, 52%), according to general procedure I.1 (5.0 mmol). Isolated as a very viscous pale-yellow oil (142 mg, 0.60 mmol, 12%), according to general procedure N (5.0 mmol). The compound is an apparent 2.5:1 mixture of structural isomers by ^1H NMR. ^1H NMR (CDCl_3); δ 1.22 (3H, t, J 7.2 Hz, H1_a), 1.24 (1.5H, t, J 7.2 Hz, H1_b), 4.22 (3H, *app non*, 3.7 Hz, H2), 4.33 (1H, d, J 2.8 Hz, H5_{a, α}), 4.36 (1H, d, J 2.8 Hz, H5_{a, β}), 4.49 (1.6H, m, H5_{b, both}), 4.86 (0.5H, dd, J 1.5, 2.9 Hz, H4_b), 4.95 (1H, dd, J , J 0.7, 2.9 Hz, H4_a), 6.90 (1.6H, m, H11), 7.04 (1H, dd, J 1.6, 8.0 Hz, H10_a), 7.18 (0.5H, dd, J 1.6, 8.0 Hz, H10_b), 7.36 (0.5H, dd, J 1.6, 7.8 Hz, H9_b), 7.50 (1.0H, dd, J 1.6, 7.8 Hz, H9_a), 10.3 (0.4H, s, J 0.7 Hz, H8 _{β}), 10.4 (1H, s, J 1.0 Hz, H8 _{α}). ^{13}C NMR (CDCl_3); δ 14.0 (C1), 62.1 (C2_a), 62.3 (C2_b), 64.6 (C5_a), 65.1 (C5_b), 71.5 (C4_b), 71.9 (C4_a), 121.1 (C11_a), 121.4 (C11_b), 121.6 (C9), 123.0 (C10_a), 123.2 (C10_b), 125.0 (C9), 142.8 (C12_b), 143.5 (C12_a), 145.2 (C6_a), 145.7 (C6_b), 167.3 (C3_a), 167.4 (C3_b), 188.5 (C9_b), 188.6 (C9_a). R_f 0.450 (30% EtOAc/hexanes).

**20a**

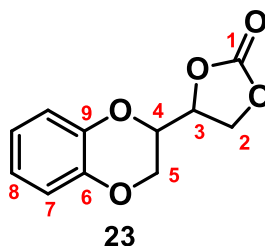
ethyl 5-formyl-2,3-dihydrobenzo[1,4]dioxine-2-carboxylate (20a). Isolated as a pale-yellow solid (1417 mg, 6.00 mmol, 60%), according to general procedure I.2 (10.0 mmol). Isolated as a white solid (402 mg, 1.70 mmol, 34%), according to general procedure F.1 (5.0 mmol). Single stated structural isomer isolated. ^1H NMR (CDCl_3); δ 1.30 (3H, t, J 7.1 Hz, H1), (2H, *app* non, 3.4 Hz, H2), 4.43 (1H, dd, J 2.8, 11.6 Hz, H5 $_{\alpha}$), 4.55 (1H, dd, J 2.8, 11.6 Hz, H5 $_{\beta}$), 4.70 (1H, dd, J 1.0, 2.9 Hz, H4), 6.97 (1H, dt, J 0.7, 7.9 Hz, H11), 7.12 (1H, dd, J 1.6, 8.0 Hz, H10), 7.48 (1H, dd, J 1.6, 8.0 Hz, H9), 10.48 (1H, *app* d, J 0.7 Hz, H8). ^{13}C NMR (CDCl_3); δ 14.1 (C1), 62.2 (C2), 64.7 (C5), 72.0 (C4), 121.35 (C11), 121.39 (C9), 123.1 (C10), 125.1 (C7), 143.5 (C6), 143.2 (C12), 167.4 (C3), 188.7 (C8). R_f 0.450 (30% EtOAc/hexanes). FTIR (ν_{max} cm^{-1}), 2982, (w, CH_x), 2878, (w, CH_x), 1752 (s, C=O), 1681 (s, C=O), 1476 (s, C-O). HRMS (XEVO G2-XS QTof) calculated for $\text{C}_{12}\text{H}_{13}\text{O}_5$ $[\text{M}+\text{H}]^+$, 237.0763 found: 237.0767.



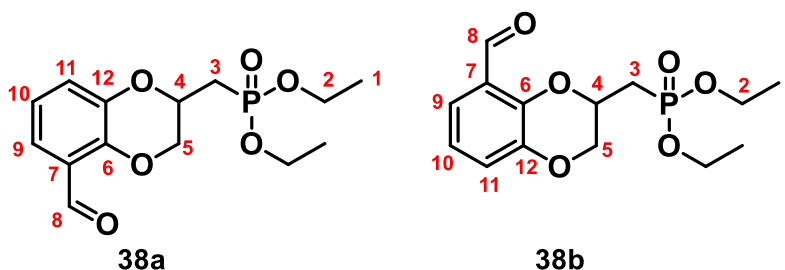
ethyl 6-methyl-2,3-dihydrobenzo[1,4]dioxine-2-carboxylate (21). Isolated as a viscous yellow oil (682 mg, 3.07 mmol, 61%), according to general procedure I (5.0 mmol). The compound is an apparent 1:1 mixture of structural isomers by ^1H NMR. ^1H NMR (CDCl_3); δ 1.31 (6H, t, J 7.1 Hz, H1), 2.27 (3H, s, H9_b), 2.28 (3H, s, H9_a), 4.29 (4H, dq, J 2.4, 7.2 Hz, H2), 4.38 (4H, d, J 4.3 Hz, H5_{both}), 4.81 (1.9H, m, H4), 6.68 (1H, *app* dd, J 1.5, 8.2 Hz, H10_a), 6.71 (1H, *app* d, J 1.8 Hz, H7_b), 6.72 (1H, d, J 1.5 Hz, H10_b), 6.78 (1H, d, J 8.2 Hz, H11_a), 6.85 (1H, *app* d, J 1.8 Hz, H7_a), 78 (1H, d, J 8.2 Hz, H11_b). ^{13}C NMR (CDCl_3); δ 14.1 (C1), 20.7 (C9), 61.9 (C2), 65.0 (C5), 72.1 (C4), 116.8 (C10_a), 117.0 (C10_b), 117.6 (C11_b), 117.7 (C11_a), 122.4 (C7_a), 122.7 (C7_b), 131.5 (C8_a), 131.9 (C8_b), 140.0 (C12_b), 140.6 (C12_a), 141.9 (C6_a), 142.5 (C6_b), 168.06 (C3_a), 168.08 (C3_b). R_f 0.625 (30% EtOAc/hexanes). FTIR (ν_{max} cm^{-1}), 2982, (w, CH_x), 2926, (w, CH_x), 1759 (s, C=O), 1505 (s, C-O). HRMS (XEVO G2-XS QToF) calculated for $\text{C}_{12}\text{H}_{15}\text{O}_4$ $[\text{M}+\text{H}]^+$, 223.0970 found: 223.0970.



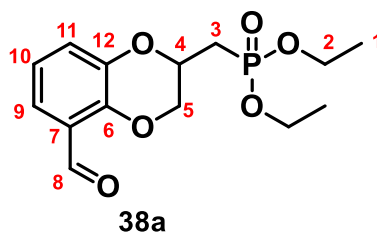
diethyl ((2,3-dihydrobenzo[*b*][1,4]dioxin-2-yl)methyl)phosphonate (22). Isolated as a viscous pale orange oil (910 mg, 3.18 mmol, 64%), according to general procedure I.1 (5.0 mmol). ^1H NMR (CDCl_3); δ 1.36 (6H, dt, J 3.6, 7.2 Hz, H1), 2.20 (2H, m, H3), 4.01 (1H, dd, J 6.8, 11.4 Hz, H5 _{α}), 4.16 (4H, m, H2), 4.39 (1H, dd, J 2.2, 11.4 Hz, H5 _{β}), 4.60 (1H, t, J 6.8 Hz, H4), 6.80 (4H, m, H7 - H10). ^{13}C NMR (CDCl_3); δ 16.4 (C1), 27.7 (C3), 29.1 (C3), 62.0 (C2), 67.7 (C5), 68.6 (C4), 117.2 (C8), 117.4 (C9), 121.6 (C7), 121.7 (C10), 142.6 (C11), 142.9 (C6). R_f 0.625 (30% EtOAc/hexanes). FTIR (ν_{max} cm^{-1}), 2982, (w, CH_x), 2907, (w, CH_x), 1595 (m, P=O), 1495 (s, P-O). HRMS (XEVO G2-XS QToF) calculated for $\text{C}_{13}\text{H}_{20}\text{PO}_5$ $[\text{M}+\text{H}]^+$, 287.1048 found: 287.1054.



4-(2,3-dihydrobenzo[1,4]dioxin-2-yl)-1,3-dioxolan-2-one (23). Isolated as a viscous pale orange oil (368 mg, 1.66 mmol, 33%), according to general procedure I.1 (5.0 mmol). ^1H NMR (CDCl_3); δ 4.40 (1H, dd, J 6.0, 8.8 Hz, H5_α), 4.64 (1H, *app t* J 8.6 Hz, H5_β), 5.21 (2H, dd, H3 & H4), 5.82 (1H, dd, J 0.4, 2.8 Hz, H2_α), 6.18 (1H, dd, J 1.1, 2.7 Hz, H5_β), 6.83 (2H, dt, J 3.8, 5.9 Hz, H8), 6.90 (2H, dt, J 3.6, 6.0 Hz, H7). ^{13}C NMR (CDCl_3); δ 68.5 (C5), 77.9 (C3 & C4), 115.5 (C7), 121.0 (C8), 121.5 (C2), 126.8 (C9), 143.8 (C6), 154.5 (C1). R_f 0.402 (30% EtOAc/hexanes). FTIR (ν_{max} cm^{-1}), 2982, (w, CH_x), 1782 (s, $\text{C}=\text{O}$), 1514 (m, $\text{C}-\text{O}$). HRMS (XEVO G2-XS QTof) calculated for $\text{C}_{11}\text{H}_{11}\text{O}_5$ $[\text{M}+\text{H}]^+$, 223.0606 found: 223.0603.

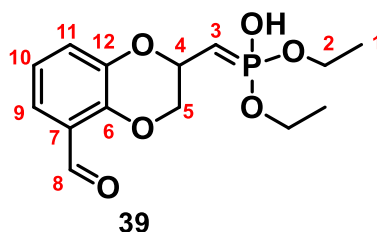


diethyl ((5-formyl-2,3-dihydrobenzo[1,4]dioxin-2-yl)methyl)phosphonate (38). Isolated as a pale-yellow solid (468 mg, 1.64 mmol, 16%), according to general procedure I.2 (10.0 mmol). The compound is an apparent 3:1 mixture of structural isomers by ^1H NMR. ^1H NMR (CDCl_3); δ 1.39 (8H, dt, J 3.1, 7.1 Hz, H1), 1.66 (3.7H, br. s, H5), 2.18 (1.4H, m, H3_α , both), 2.34 (1.4H, m, H3_β , both), 4.18 (5.4H, *app qd*, J 2.5, 9.6 Hz, H2), 4.49 (0.3H, dd, J 2.2, 11.6 Hz, H4_b), 4.57 (1H, dd, J 2.2, 11.6 Hz, H4_a), 6.95 (1.3H, t, J 8.0 Hz, H10), 7.11 (1H, dd J 1.6, 8.0, Hz, H11_a), 7.14 (0.3H, dd J 1.6, 8.0, Hz, H11_b), 7.44 (1.3H, dd, J 1.6, 7.7 Hz, H9), 10.39 (1H, s, H8_α), 10.41 (0.3H, s, H8_β). ^{13}C NMR (CDCl_3); δ 16.5 (C1), 27.8 (C3), 29.3 (C3), 62.2 (C2), 67.8 (C4_b), 68.4 (C4_a), 69.2 (C5), 121.2 (C9), 121.3 (C10), 123.0 (C11_b), 123.3 (C11_a), 125.0 (C7), 143.2 (C12), 145.7 (C6), 188.8 (C8_b), 188.9 (C8_a). R_f 0.673 (30% EtOAc/hexanes).



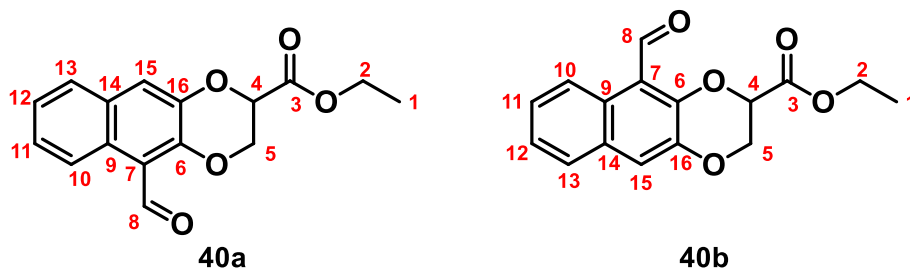
diethyl ((5-formyl-2,3-dihydrobenzo[1,4]dioxin-2-yl)methyl)phosphonate (38a).

Isolated as a pale-yellow solid (278 mg, 0.97 mmol, 10%), according to general procedure I.2 (10.0 mmol). Single stated structural isomer isolated. ^1H NMR (CDCl_3); δ 1.37 (6H, dt, J 2.8, 7.1 Hz, H1), 2.16 (2H, m, H3), 2.32 (1H, m, H4), 4.17 (4H, *app* qd, J 2.6, 7.3 Hz, H2), 4.56 (2H, dd, J 2.2, 11.4 Hz, H5), 6.93 (1H, t, J 7.9 Hz, H10), 7.09 (1H, dd J 1.6, 8.0, Hz, H11), 7.41 (1H, dd, J 1.6, 8.0 Hz, H9), 10.39 (1H, s, H8). ^{13}C NMR (CDCl_3); δ 16.4 (C1), 27.8 (C3), 29.3 (C4), 62.2 (C2), 67.8 (C2), 67.9 (C5), 121.15 (C9), 121.24 (C11), 123.2 (C10), 125.0 (C7), 143.2 (C12), 145.7 (C6), 188.9 (C8). R_f 0.673 (30% EtOAc/hexanes). FTIR (ν_{max} cm^{-1}), 2974, (w, CH_x), 2930, (w, CH_x), 1685 (s, C=O), 1595 (m, P=O), 1476 (s, P-O). HRMS (XEVO G2-XS QTof) calculated for $\text{C}_{14}\text{H}_{20}\text{PO}_6$ $[\text{M}+\text{H}]^+$, 315.0997 found: 315.1007.

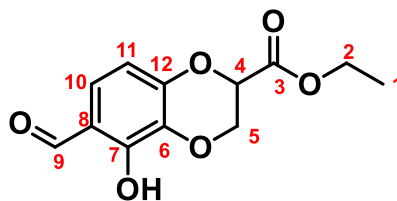


2-((diethoxy(hydroxy)phosphaneylidene)methyl)-2,3-dihydrobenzo[1,4]dioxine-5-

carbaldehyde (39). Isolated as a bright yellow oil (199 mg, 0.70 mmol, 7%), according to general procedure I.2 (10.0 mmol). Single stated structural isomer isolated. ^1H NMR (CDCl_3); δ 1.37 (6H, t, J 7.0 Hz, H1), 2.81 (1H, d, J 8.2 Hz, H5 $_{\alpha}$), 2.87 (1H, d, J 8.2 Hz, H5 $_{\beta}$), 4.19 (4H, *app* dec, J 3.6 Hz, H2), 4.78 (1H, *app* qui, 6.0 Hz, H4), 6.40 (1H, t, J 6.8 Hz, H3), 7.21 (1H, *app* d, J 7.7 Hz, H10), 7.27 (1H, d, J 7.7 Hz, H11), 7.36 (1H, d, J 7.7 Hz, H9), 9.71 (1H, s, OH), 10.2 (1H, s, H8). ^{13}C NMR (CDCl_3); δ 16.4 (C1), 21.5 (C5), 22.9 (C5), 62.7 (C2), 97.0 (C4), 119.9 (C9), 124.3 (C11), 126.3 (C10), 128.7 (C12), 146.6 (C6), 149.3 (C3), 150.9 (C7), 189.3 (C8). R_f 0.169 (30% EtOAc/hexanes).

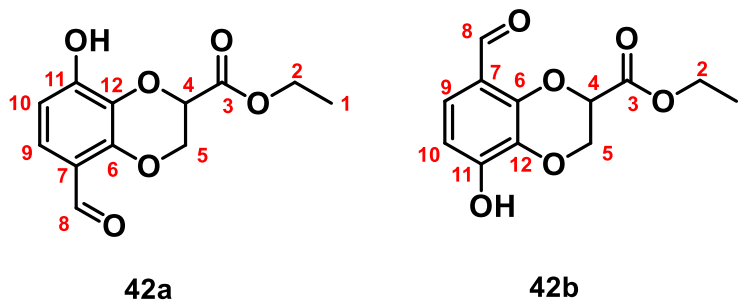


ethyl 5-formyl-2,3-dihydro[2,3][1,4]dioxine-2-carboxylate (40). Isolated as a light-yellow oil (85.0 mg, 0.30 mmol, 3%), according to general procedure I (10.0 mmol). The compound is an apparent 1:1 mixture of structural isomers by ^1H NMR. ^1H NMR (CDCl_3); δ 1.30 (6H, t, J 7.1 Hz, H1), 4.29 (4H, m, H2), 4.53 (2H, dd, J 2.8, 11.3 Hz, H5 $_{\alpha}$, both), 4.61 (2H, dd, J 2.8, 11.3 Hz, H5 $_{\beta}$, both), 5.02 (2H, dd, J 1.6, 4.5 Hz, H4), 6.82 (2H, s, H15), 7.38 (2H, *app* td, J 0.9, 4.8 Hz, H12), 7.51 (2H, t, J 1.8 Hz, H11), 7.66 (2H, *app* dd, J 2.3, 7.7 Hz, H13), 8.07 (2H, *app* dd, J 2.3, 7.7 Hz, H10), 9.17 (1H, s, H8 $_{\alpha}$), 9.19 (1H, s, H8 $_{\beta}$). ^{13}C NMR (CDCl_3); δ 14.1 (C1), 62.1 (C2 $_{\alpha}$), 62.4 (C2 $_{\beta}$), 64.6 (C5 $_{\beta}$), 65.3 (C5 $_{\alpha}$), 72.0 (C4 $_{\alpha}$), 72.4 (C4 $_{\beta}$), 99.6 (C15), 120.4 (C7), 123.8 (C11), 124.9 (C13), 125.4 (C12), 126.4 (C10), 130.9 (C9), 136.5 (C14), 141.0 (C16), 148.7 (C6), 167.7 (C3), 190.5 (C8 $_{\alpha}$), 190.7 (C8 $_{\beta}$). R_f 0.416 (30% EtOAc/hexanes). FTIR (ν_{max} cm^{-1}), 2992, (w, CH_x), 2933, (w, CH_x), 1752 (s, C=O), 1480 (m, C-O). HRMS (XEVO G2-XS QTof) calculated for $\text{C}_{16}\text{H}_{15}\text{O}_5$ $[\text{M}+\text{H}]^+$, 287.0919, found: 287.0938.

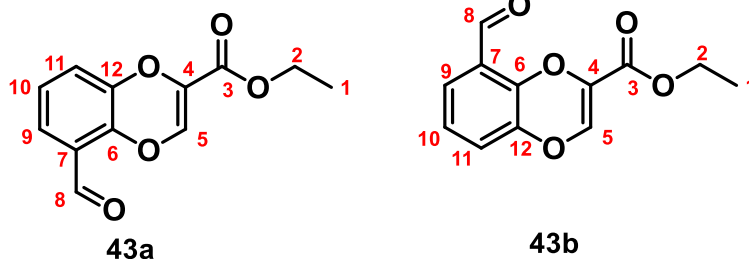


41

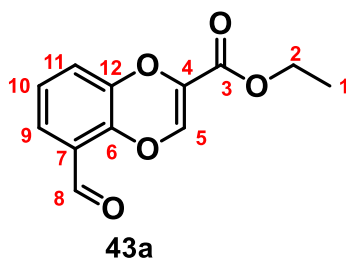
ethyl 6-formyl-5-hydroxy-2,3-dihydrobenzo[1,4]dioxine-2-carboxylate (41). Isolated as a very viscous orange oil (490 mg, 1.94 mmol, 19%), according to general procedure I (10.0 mmol). Isolated as a very viscous orange oil (97 mg, 0.38 mmol, 4%), according to general procedure I.2 (10.0 mmol). Single stated structural isomer isolated. ^1H NMR (CDCl_3); δ 1.30 (3H, t, J 7.2 Hz, H1), 4.28 (2H, *app* qd, J 2.0, 7.1 Hz, H2), 4.41 (1H, dd, J 2.8, 11.6 Hz, H5 $_{\alpha}$), 4.54 (1H, dd, J 2.8, 11.6 Hz, H5 $_{\beta}$), 4.94 (1H, dd, J 1.2, 2.9 Hz, H4), 6.69 (1H, d, J 8.7 Hz, H11), 7.14 (1H, d, J 8.7 Hz, H12), 9.74 (1H, s, H9), 11.49 (1H, s, OH). ^{13}C NMR (CDCl_3); δ 14.1 (C1), 62.4 (C2), 64.7 (C5), 72.3 (C4), 109.5 (C11), 115.8 (C6), 126.6 (C10), 131.2 (C8), 149.1 (C12), 152.0 (C7), 167.0 (C1), 195.3 (C9). R_f 0.292 (30% EtOAc/hexanes). FTIR (ν_{max} cm^{-1}), 3049 (m, OH), 2978, (w, CH_x), 1744 (s, C=O), 1744 (s, C=O), 1640 (m, C-O). HRMS (XEVO G2-XS QToF) calculated for $\text{C}_{16}\text{H}_{15}\text{O}_5$ $[\text{M}+\text{H}]^+$, 253.0742, found: 253.0743.



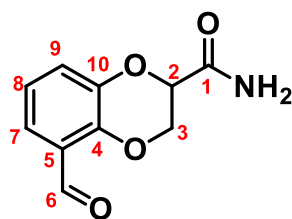
ethyl 5-formyl-8-hydroxy-2,3-dihydrobenzo[1,4]dioxine-2-carboxylate (42). Isolated as a fine yellow powder (502 mg, 1.99 mmol, 19%), according to general procedure I (10.0 mmol). Isolated as a very viscous orange oil (280 mg, 1.11 mmol, 11%), according to general procedure I.2 (10.0 mmol). The compound is an apparent 2:1 mixture of structural isomers by ^1H NMR. ^1H NMR (CDCl_3); δ 1.32 (4.5H, t, J 7.1 Hz, H1), 4.30 (3H, dq, J 2.2, 7.2 Hz, H2), 4.42 (0.5H, d, J 2.7 Hz, H5_{b, \alpha}), 4.45 (1H, d, J 2.7 Hz, H5_{a, \alpha}), 4.54 (1H, d, J 4.2 Hz, H5_{a, \beta}), 4.57 (0.5H, d, J 4.2 Hz, H5_{b, \beta}), 4.97 (1.5H, dt, J 2.9, 11.1 Hz, H4), 6.64 (0.5H, d, J 8.6 Hz, H10_b), 6.71 (1H, d, J 8.6 Hz, H10_a), 7.12 (0.5H, d, J 8.6 Hz, H9_b), 7.16 (1H, *app* dd, J 1.8, 8.7 Hz, H9_a), 9.73 (0.5H, s, H8_b), 9.77 (1H, s, H8_a), 11.4 (1H, s, OH_b), 11.5 (1H, s, OH_a). ^{13}C NMR (CDCl_3); δ 14.1 (C1), 62.1 (C2_b), 62.2 (C2_a), 64.7 (C5_b), 64.8 (C5_a), 107.6 (C10_b), 108.9 (C10_a), 123.1 (C9_a), 126.5 (C9_b), 131.5 (C12_b), 132.6 (C12_a), 135.6 (C6_b), 138.4 (C6_a), 149.1 (C11_b), 149.9 (C11_a), 151.1 (C7_b), 152.0 (C7_a), 167.4 (C3_b), 168.2 (C3_a), 188.3 (C8_b), 195.5 (C8_a). R_f 0.292 (30% EtOAc/hexanes). FTIR (ν_{max} cm^{-1}), 3317 (s, OH), 3116, (w, CH_x), 1744 (s, C=O), 1737 (m, C=O), 1614 (s, C-O). HRMS (XEVO G2-XS QTof) calculated for $\text{C}_{16}\text{H}_{15}\text{O}_5$ $[\text{M}+\text{H}]^+$, 253.0742, found: 253.0727.



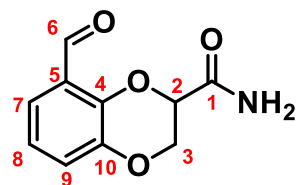
ethyl 5-formylbenzo[1,4]dioxine-2-carboxylate (43). Isolated as a yellow oil (387 mg, 1.66 mmol, 17%), according to general procedure I.2 (10.0 mmol). The compound is an apparent 5:1 mixture of structural isomers by ^1H NMR. ^1H NMR (CDCl_3); δ 1.58 (3.6H, t, J 4.8 Hz, H1), 4.53 (2.4H, q, J 7.2 Hz, H2), 7.17 (2.4H, *app* t, H9 & H11), 7.25 (1H, s, H5_a), 7.28 (0.2H, s, H5_b), 7.65 (1.2H, dd, J 3.1, 6.4 Hz, H10), 10.4 (0.2H, s, H8_b), 10.56 (1H, s, H8_a). ^{13}C NMR (CDCl_3); δ 14.1 (C1), 61.4 (C2), 121.7 (C11), 124.13 (C10), 124.15 (C9), 128.9 (C4), 134.7 (C7), 136.1 (C5), 140.9 (C12), 145.1 (C6), 160.4 (C3), 187.0 (C8). R_f 0.426 (30% EtOAc/hexanes).



ethyl 5-formylbenzo[1,4]dioxine-2-carboxylate (43a). Isolated as a yellow oil (82 mg, 0.35 mmol, 4%), according to general procedure I.2 (10.0 mmol). ^1H NMR (CDCl_3); δ 1.26 (3H, t, J 7.1 Hz, H1) 4.18 (2H, q, J 7.1 Hz, H2), 6.86 (2H, *app* t, H9 & H11), 6.94 (1H, s, H5), 7.35 (1H, dd, J 3.3, 6.2 Hz, H10), 10.26 (1H, s, H8). ^{13}C NMR (CDCl_3); δ 14.3 (C1), 61.6 (C2), 121.9 (C11), 123.8 (C10), 124.5 (C9), 129.0 (C4), 136.3 (C5), 141.0 (C12), 145.2 (C6), 159.3 (C7), 160.5 (C3), 187.6 (C8). R_f 0.426 (30% EtOAc/hexanes). FTIR (ν_{max} cm^{-1}), 2982, (w, CH_x), 2874, (w, CH_x), 1730 (s, C=O), 1606 (s, C-O). HRMS (XEVO G2-XS QToF) calculated for $\text{C}_{12}\text{H}_{11}\text{O}_5$ $[\text{M}+\text{H}]^+$, 235.0613, found: 235.0613.

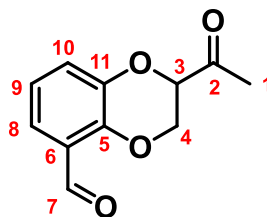


44a



44b

5-formyl-2,3-dihydrobenzo[1,4]dioxine-2-carboxamide (44). Isolated as a pale orange solid (308 mg, 1.49 mmol, 30%), according to general procedure I.2 (5.0 mmol). The compound is an apparent 2:1 mixture of structural isomers by ^1H NMR. ^1H NMR (CDCl_3); δ 4.25 (1H, dd, J 7.7, 11.6 Hz, $\text{H}_{3\text{a}, \alpha}$), 4.37 (0.5H, dd, J 7.7, 11.6 Hz, $\text{H}_{3\text{a}, \beta 1}$), 4.69 (1.5H, *app* td, $\text{H}_{3\text{b}, \text{both}}$ & $\text{H}_{3\text{a}, \beta 2}$), 4.80 (0.5H, dd, J 2.8, 7.28 Hz, $\text{H}_{2\text{b}}$), 4.85 (1H, dd, J 2.8, 7.3 Hz, $\text{H}_{2\text{a}}$), 5.85 (1.5H, s, 2 x $\text{NH}_{\text{a both}}$), 6.57 (0.5H, s, $\text{NH}_{\text{b}, \alpha}$), 6.84 (1H, s, $\text{NH}_{\text{b}, \beta}$), 7.03 (0.5H, d, J 3.4, Hz, $\text{H}_{9\text{b}}$), 7.07 (1H, d, J 7.9, Hz, $\text{H}_{9\text{a}}$), 7.21 (1.5H, *app* td, J 1.7, 8.1 Hz, H_8), 7.44 (1H, dd, J 1.6, 7.7 Hz, $\text{H}_{7\text{a}}$), 7.05 (0.5H, dd, J 1.6, 7.7 Hz, $\text{H}_{7\text{b}}$), 10.29 (1H, s, $\text{H}_{6\text{a}}$), 10.41 (0.5H, s, $\text{H}_{6\text{b}}$). ^{13}C NMR (CDCl_3); δ 64.8 ($\text{C}_{3\text{a}}$), 65.3 ($\text{C}_{3\text{b}}$), 72.8 ($\text{C}_{2\text{b}}$), 73.2 ($\text{C}_{2\text{a}}$), 122.0 (C_8), 123.6 (C_7), 124.5 (C_9), 125.4 (C_5), 168.9 (C_1), 188.5 ($\text{C}_{6\text{b}}$), 189.0 ($\text{C}_{6\text{a}}$). R_f 0.305 (30% EtOAc/hexanes). FTIR (ν_{max} cm^{-1}), 3429 (s, N-H), 2945, (w, CH_x), 2889, (w, CH_x), 1662 (s, C=O), 1592 (s, C-O). HRMS (XEVO G2-XS QTof) calculated for $\text{C}_{10}\text{H}_{10}\text{NO}_4$ [$\text{M}+\text{H}$] $^+$, 208.0610, found: 208.0614.



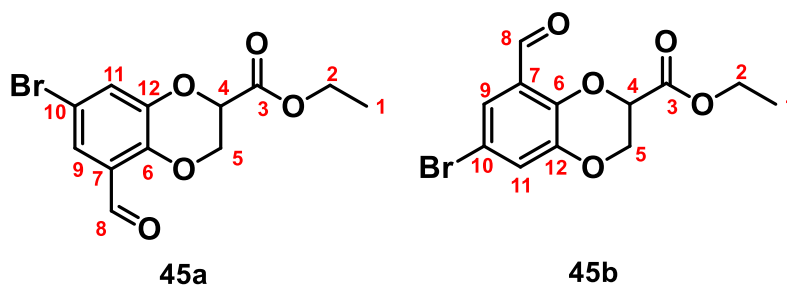
46

2-acetyl-2,3-dihydrobenzo[1,4]dioxine-5-carbaldehyde (46). Isolated as a light brown viscous oil (479 mg, 2.32 mmol, 46%), according to general procedure I (5.0 mmol). Isolated as a dark yellow powder (241 mg, 1.16 mmol, 23%), according to general procedure I.1 (5.0 mmol). Single stated structural isomer isolated. ^1H NMR (CDCl_3); δ 2.35 (3H, s, H1), 4.36 (1H, dd, J 2.9, 11.6 Hz, H4 $_{\alpha}$), 4.43 (1H, dd, J 2.9, 11.6 Hz, H4 $_{\beta}$), 4.77 1H, dd, J 3.0, 5.5 Hz, H3), 6.97 (2H, *app* dt, J 0.4, 7.8 Hz, H10), 7.13 (1H, *app* dd, J 1.6, 8.0 Hz, H9), 7.45 (1H, *app* dd, J 1.6, 8.0 Hz, H8), 10.45 (1H, *app* d, 0.5 Hz, H7). ^{13}C NMR (CDCl_3); δ 26.7 (C1), 64.0 (C4), 78.2 (C3), 121.7 (C10), 121.8 (C8), 123.4 (C9), 125.0 (C6), 143.6 (C11). 144.7 (C5), 188.4 (C2), 204.5 (C7). R_f 0.543 (30% EtOAc/hexanes). FTIR (ν_{max} cm^{-1}), 2922, (w, CH_x), 1715 (m, C=O), 1595 (m, C-O). HRMS (XEVO G2-XS QToF) calculated for $\text{C}_{11}\text{H}_{11}\text{O}_4$ $[\text{M}+\text{H}]^+$, 207.0657, found: 207.0666.

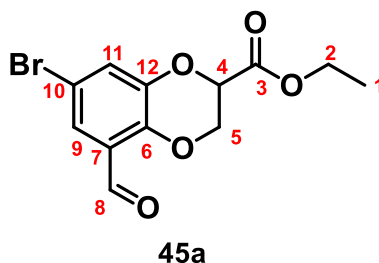
Procedure J: for synthesis of **45** and **45a**

Adapted from a known procedure.¹⁵⁹

Dissolved compound **8** (2.36 g, 10.0 mmol, 1.0 equiv.), in 25 mL of DCM under N_2 gas positive flow. Liquid bromine (1.02 mL, 20.0 mmol, 2.0 equiv.) was added dropwise to the reaction mixture over 30 minutes at RT, followed by glacial acetic acid (0.12 mL, 2.0 mmol, 0.2 equiv.), Refluxed the reaction mixture overnight or until completion (confirmed by TLC). The reaction mixture was neutralized with sat sodium carbonate aqueous sol. Extracted the crude product three times from the aqueous mixture with DCM (3x 10 mL). Washed combined organic layers with sat. sodium thiosulfate aqueous sol. Combined organic layers dried over MgSO_4 The organic solvent removed *in vacuo*. Recrystallized the crude product from a mixture of 40% water in ethanol (heated to 70°C). The resulting pale-yellow crystal were washed with water to obtain title product.



ethyl 7-bromo-5-formyl-2,3-dihydrobenzo[1,4]dioxine-2-carboxylate (45). Isolated as a pale-yellow powder (200 mg, 0.63 mmol, 2%), according to general procedure N.2 (10.0 mmol). Isolated as a viscous orange oil (265 mg, 8.40 mmol, 84%), according to general procedure J. The compound is an apparent 2:1 mixture of structural isomers by ^1H NMR. ^1H NMR (CDCl_3); δ 1.30 (4.5H, *app* q, J 7.3 Hz, H1), 1.60 (H_2O), 4.30 (3.2H, *app* qd J 1.8, 7.1 Hz, H2), 4.41 (1.5H, dd, J 2.4, 11.6 Hz, H5_α , both), 4.56 (1.5H, dd, J 2.4, 11.6 Hz, H5_β , both), 4.93 (0.5H, t, J 3.32, H4_b), 4.99 (1H, t, J 3.3, H4_a), 7.25 (1H, d, J 2.4 Hz, H11_a), 7.39 (0.5H, d, J 2.4 Hz, H11_b), 7.56 (0.5H, d, J 2.4 Hz, H9_b), 7.59 (1H, d, J 2.4 Hz, H9_a), 10.30 (0.5H, s, H8_b), 10.40 (1H, s, H8_a). ^{13}C NMR (CDCl_3); δ 14.1 (C1), 62.4 (C5), 64.8 (C2_a), 65.1 (C2_b), 71.6 (C4_b), 71.9 (C4_a), 113.6 (C10_a), 114.0 (C10_b), 123.7 (C11_b), 123.8 (C11_a), 125.6 (C9_a), 125.7 (C9_b), 144.4 (C12), 167.0 (C6), 187.2 (C8). R_f 0.513 (30% EtOAc/hexanes).



ethyl 7-bromo-5-formyl-2,3-dihydrobenzo[1,4]dioxine-2-carboxylate (45a). Isolated as a viscous dark yellow oil (1.23 mg, 3.90 mmol, 39%). Single stated structural isomer isolated, according to procedure J. ^1H NMR (CDCl_3); δ 1.22 (3H, t J 7.0 Hz, H1), 3.62 (2H, dq J 0.9, 7.0 Hz, H2), 3.80 (1H, dd, J 5.6, 10.4 Hz, H5_α), 3.97 (1H, dd, J 8.6, 10.4 Hz, H5_β), 4.37 (1H, dd, J 5.6, 8.5 Hz, H4), 6.41 (1H, d, J 1.7 Hz, H11), 7.11 (1H, d, J 1.7 Hz, H9), 10.01 (1H, s, H8). ^{13}C NMR (CDCl_3); δ 14.1 (C1), 62.4 (C5), 64.8 (C2), 71.9 (C4), 113.6 (C10), 123.7 (C11), 125.6 (C9), 144.4 (C12), 167.0 (C6), 174.1 (C8). R_f 0.513 (30% EtOAc/hexanes). FTIR (ν_{max} cm^{-1}), 2989, (w, CH_x), 2878, (w, CH_x), 1748 (s, C=O), 1674 (s, C=O), 1595 (s, C-O). HRMS (XEVO G2-XS QToF) calculated for $\text{C}_{12}\text{H}_{12}\text{O}_5\text{Br}$ $[\text{M}+\text{H}]^+$, 314.8964, found: 314.8964.

7.2.4. Hydrolysis of benzodioxane esters: 25-32, 47-51.

General procedure K: for synthesis of 25 – 31 and 48-51.

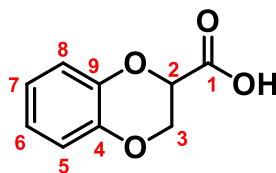
Adapted from a known procedure.¹⁴⁵

Corresponding benzodioxane ester from procedure I (2.0 mmol, 1.0 equiv.) was dissolved in 20 mL of a 1:1 mixture of MeOH / H₂O to this the lithium hydroxide monohydrate (3.0 mmol, 1.5 equiv.) was added to the stirred reaction mixture at RT. Upon completion (approx. 3hrs), the reaction mixture was concentrated *in vacuo* and partitioned between water (acidized with 1M HCl) and DCM (20 mL of each). The resultant aqueous layer was extracted with a second 20mL of DCM and the combined org layers were dried with MgSO₄. MgSO₄ filtered off, and the resultant solution was dried *in vacuo* to yield pure desired title carboxylic acid product.

General procedure K.1: for synthesis of 32 and 47.

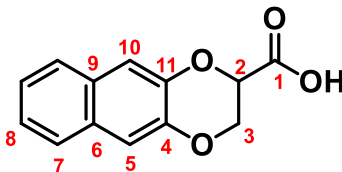
Adapted from a known procedure.¹³²

BBr₃ (2.0 mL, 2.0 mmol, 1 M in DCM, 1.0 equiv.) was added dropwise to a stirred solution of diethyl decylphosphonate (2.0 mmol, 1.0 equiv.) in toluene (15 mL) under nitrogen at 0 °C. The mixture was stirred overnight at RT (If completion not observed heat to 70 °C for 6 hrs). An excess of MeOH (10 mL) was added carefully at RT., to quench any unreacted BBr₃. The reaction mixture was concentrated *in vacuo* and partitioned between water (acidized with 1M HCl) and DCM (20 mL of each). The resultant aqueous layer was extracted with a second 20mL of DCM and the combined organic layers were dried with MgSO₄. MgSO₄ filtered off, and the resultant solution was dried *in vacuo* to yield the pure title product.



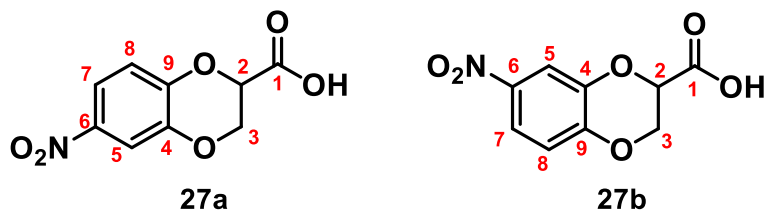
25

2,3-dihydrobenzo[1,4]dioxine-2-carboxylic acid (25). Isolated as a fine white powder (168 mg, 0.93 mmol, 47%), according to general procedure K. ^1H NMR (CDCl_3); δ 4.44 (2H, *app* dq, J 4.4, 10.7 Hz, H3), 4.92 (1H, t, J 3.8 Hz, H2), 6.91 (3H, *app* s, H6-8), 7.02 (1H, d, J 6.4 Hz, H5), 7.97 (1H, br. s, OH). ^{13}C NMR (CDCl_3); δ 64.6 (C3), 71.6 (C2), 117.3 (C8), 117.5 (C5), 122.1 (C7), 122.4 (C6), 141.9 (C9), 142.8 (C4), 173.4 (C1). R_f 0.070 (30% EtOAc/hexanes). FTIR (ν_{max} cm^{-1}), 3012 (1H, s, O-H), 2960, (w, CH_x), 1718 (m, C=O), 1491 (m, C-O). HRMS (XEVO G2-XS QTof) calculated for $\text{C}_9\text{H}_9\text{O}_4$ $[\text{M}+\text{H}]^+$, 181.0501, found: 181.0473.

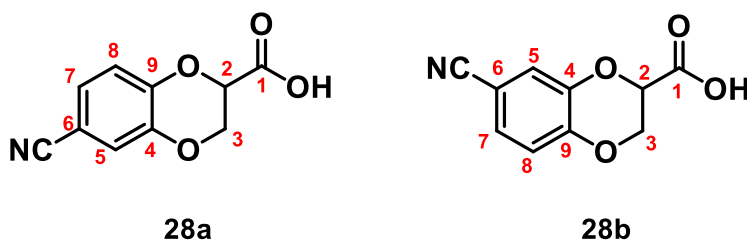


26

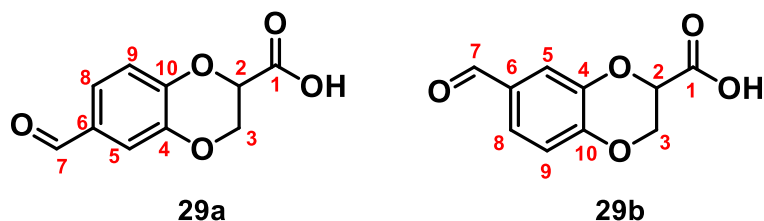
2,3-dihydronaphtho[2,3][1,4]dioxine-2-carboxylic acid (26). Isolated as an off-white powder (400 mg, 1.74 mmol, 87%), according to general procedure K. ^1H NMR (d_6 -DMSO); δ 3.44 (1H, s, OH), 4.39 (1H, dd, J 2.9, 11.7 Hz, H3_a), 4.55 (1H, dd, J 2.9, 11.7 Hz, H3_b), 5.17 (1H, t, J 3.3 Hz, H2), 7.31 (2H, dd, J 3.1, 6.2, Hz, H8), 7.34 (1H, s, H5), 7.42 (1H, s, H10), 7.72 (2H, dtd, J 2.5, 6.1, 9.9 Hz, H7). ^{13}C NMR (d_6 -DMSO); δ 65.5 (C3), 71.8 (C2), 112.5 (C7), 124.7 (C8), 126.8 (C6), 129.3 (C9), 143.3 (C11), 143.9 (C4), 170.2 (C1). R_f 0.020 (30% EtOAc/hexanes). FTIR (ν_{max} cm^{-1}), 3045 (s br., O-H), 2821, (w, CH_x), 1690 (m, C=O), 1472 (m, C-O). HRMS (XEVO G2-XS QTof) calculated for $\text{C}_{13}\text{H}_{11}\text{O}_4$ $[\text{M}+\text{H}]^+$, 231.0680, found: 231.0680.



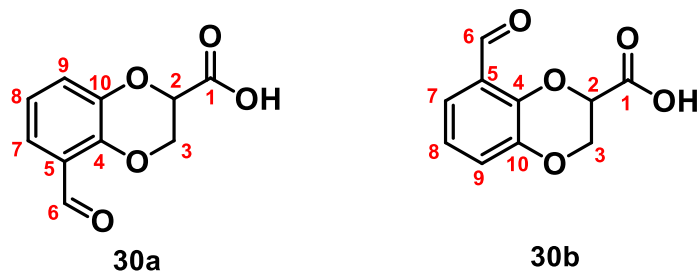
6-nitro-2,3-dihydrobenzo[1,4]dioxine-2-carboxylic acid (27). Isolated as a brown powder (412 mg, 1.83 mmol, 93%), according to general procedure K. The compound is an apparent 3:2 mixture of structural isomers by ^1H NMR. ^1H NMR (CDCl_3); δ 4.42 (1H, dd, J 2.9, 11.8 Hz, $\text{H}_{3\text{a},\alpha}$), 4.47 (1H, dd, J 2.9, 11.8 Hz, $\text{H}_{3\text{a},\beta}$), 4.59 (1.67H, m, $\text{H}_{3\text{b}}$, both), 5.00 (0.67H, t, J 3.6 Hz, $\text{H}_{2\text{b}}$), 5.03 (1H, t, J 3.6 Hz, $\text{H}_{2\text{a}}$), 7.00 (0.67H, d, J 9.0 Hz, $\text{H}_{8\text{b}}$), 7.09 (1H, d, J 9.0 Hz, $\text{H}_{8\text{a}}$), 7.73 (1.67H, s, OH both), 7.81 (1H, t, J 2.5 Hz, $\text{H}_{5\text{a}}$), 7.84 (0.67H, t, J 2.5 Hz, $\text{H}_{5\text{b}}$), 7.86 (0.67H, d, J 2.6 Hz, $\text{H}_{7\text{b}}$), 7.92 (1H, d, J 2.6 Hz, $\text{H}_{7\text{a}}$). ^{13}C NMR (CDCl_3); δ 64.6 ($\text{C}_{3\text{a}}$), 64.9 ($\text{C}_{3\text{b}}$), 71.2 ($\text{C}_{2\text{b}}$), 71.7 ($\text{C}_{2\text{a}}$), 113.59 ($\text{C}_{7\text{a}}$), 113.64 ($\text{C}_{7\text{b}}$), 117.5 ($\text{C}_{8\text{a}}$), 117.6 ($\text{C}_{8\text{b}}$), 118.1 ($\text{C}_{5\text{b}}$), 118.4 ($\text{C}_{5\text{a}}$), 141.7 ($\text{C}_{9\text{b}}$), 142.6 ($\text{C}_{9\text{a}}$), 147.7 (C_4), 148.4 (C_6), 171.9 ($\text{C}_{1\text{a}}$), 172.0 ($\text{C}_{1\text{b}}$). R_f 0.015 (30% EtOAc/hexanes). FTIR (ν_{max} cm^{-1}), 3086 (s br., O-H), 2837, (w, CH_x), 1733 (m, C=O), 1517 (s, C-O). HRMS (XEVO G2-XS QToF) calculated for $\text{C}_9\text{H}_8\text{NO}_6$ [$\text{M}+\text{H}$] $^+$, 226.0352, found: 226.0352.



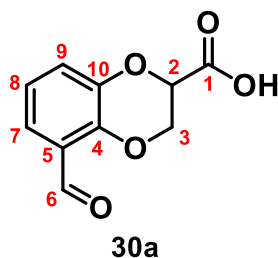
6-methyl-2,3-dihydrobenzo[1,4]dioxine-2-carboxylic acid (28). Isolated as a white powder (331 mg, 1.62 mmol, 81%), according to general procedure K. The compound is an apparent 2:1 mixture of structural isomers by ^1H NMR. ^1H NMR (CDCl_3); δ 2.90 (1.5H, s, OH both), 4.42 (1H, dd, J 2.9, 8.8 Hz, H3_{a, α}), 4.46 (0.5H, dd, J 2.9, 8.8 Hz, H3_{b, α}), 4.55 (1.5H, m, H3 _{β both}), 4.97 (0.5H, dd, J 3.0, 4.2 Hz, H2_b), (1H, dd, J 3.0, 4.2 Hz, H2_a), 6.98 (0.5H, d, J 8.4 Hz, H9_b), 7.09 (1H, d, J 8.4 Hz, H9_a), 7.22 (1H, t, J 2.0 Hz, H8_a), 7.24 (1H, t, J 2.0 Hz, H8_b), 7.26 (0.5H, d, J 2.0 Hz, H5_b), 7.33 (1H, d, J H5_a). ^{13}C NMR (CDCl_3); δ 64.6 (C3_a), 64.9 (C3_b), 71.2 (C2_b), 71.6 (C2_a), 118.4 (C9_a), 118.45 (C9_b), 118.5 (C7), 121.4 (C5_a), 121.5 (C5_b), 126.5 (C8_b), 126.8 (C8_a), 142.3 (C10), 143.3 (C4), 170.1 (C1). R_f 0.00 (30% EtOAc/hexanes). FTIR (ν_{max} cm^{-1}), 3097 (s br., O-H), 2837, (w, CH_x), 1771 (m, C=O), 1502 (s, C-O). HRMS (XEVO G2-XS QTof) calculated for $\text{C}_{10}\text{H}_8\text{O}_4\text{N}$ $[\text{M}+\text{H}]^+$, 206.0453, found: 206.0457.



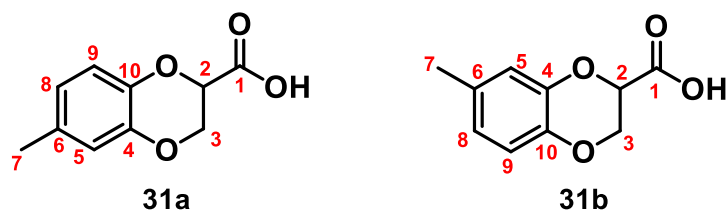
6-formyl-2,3-dihydrobenzo[1,4]dioxine-2-carboxylic acid (29). Isolated as a pale-yellow powder (130 mg, 0.63 mmol, 31%), according to general procedure K. The compound is an apparent 2:1 mixture of structural isomers by ^1H NMR. ^1H NMR (d_6 -DMSO); δ 3.38 (1.5H, s, OH both), 4.33 (1H, dd, J 2.8, 11.8 Hz, H3_{a, \alpha}), 4.39 (1H, dd, J 2.8, 11.8 Hz, H3_{a, \beta}), 4.55 (1H, *app* td, J 2.8, 11.8 Hz, H3_{b, both}), 5.17 (0.5H, t, J 2.9 Hz, H2_b), 5.17 (1H, t, J 2.9 Hz, H2_a), 7.08 (0.5H, d, J 8.1 Hz, H9_b), 7.16 (1H, d, J 8.1 Hz, H9_a), 7.39 (1H, d, J 1.9 Hz, H5_a), 7.44 (0.5H, d, J 1.9 Hz, H5_b), 7.47 (0.5H, t, J 1.7 Hz, H8_b), 7.49 (1H, dd, J 1.9, 8.3 Hz, H8_a), 9.81 (1H, s, H7_a), 9.84 (1H, s, H7_b). ^{13}C NMR (d_6 -DMSO); δ 65.3 (C3_a), 65.7 (C3_b), 71.6 (C2_b), 72.2 (C2_a), 118.1 (C9), 118.2 (C5), 124.0 (C8_b), 124.7 (C8_a), 130.7 (C6_a), 131.2 (C6_b), 143.3 (C10_b), 143.9 (C10_a), 148.6 (C4_a), 148.9 (C4_b), 169.6 (C1_a), 169.7 (C1_b), 191.77 (C7_b), 191.84 (C7_a). R_f 0.080 (30% EtOAc/hexanes). FTIR (ν_{max} cm^{-1}), 2859 (s br., O-H), 2755, (w, CH_x), 1744 (s, C=O), 1502 (s, C-O). HRMS (XEVO G2-XS QToF) calculated for C₁₀H₉O₅ [$\text{M}+\text{H}$]⁺, 209.0450, found: 209.0452.



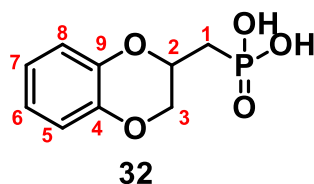
5-formyl-2,3-dihydrobenzo[1,4]dioxine-2-carboxylic acid (30). Isolated as a brown powder (355 mg, 1.70 mmol, 85%), according to general procedure K. The compound is an apparent 1:1 mixture of structural isomers by ^1H NMR. ^1H NMR (CDCl_3); δ 4.44 (1H, dd, J 2.8, 11.6 Hz, $\text{H}_{3\text{a},\alpha}$), 4.52 (1H, dd, J 2.8, 11.6 Hz, $\text{H}_{3\text{a},\beta}$), 4.60 (2H, dt, J 4.3, 11.8 Hz, $\text{H}_{3\text{b}}$), 4.99 (1H, t, J 3.2 Hz, $\text{H}_{2\text{a}}$), 5.06 (1H, t, J 3.2 Hz, $\text{H}_{2\text{b}}$), 5.97 (2H, s, OH_{both}), 6.98 (1H, t, J 4.2 Hz, $\text{H}_{9\text{a}}$), 7.01 (1H, t, J 4.2 Hz, $\text{H}_{9\text{b}}$), 7.14 (1H, d, J 8.0 Hz, $\text{H}_{8\text{a}}$), 7.26 (1H, d, J 8.0 Hz, $\text{H}_{8\text{b}}$), 7.47 (2H, t, J 7.6 Hz, H_7), 10.35 (1H, s, $\text{H}_{6\text{a}}$), 10.42 (1H, s, $\text{H}_{6\text{b}}$). ^{13}C NMR (CDCl_3); δ 64.4 ($\text{C}_{3\text{a}}$), 64.8 ($\text{C}_{3\text{b}}$), 71.2 ($\text{C}_{2\text{a}}$), 71.6 ($\text{C}_{2\text{b}}$), 121.6 ($\text{C}_{9\text{a}}$), 121.8 ($\text{C}_{9\text{b}}$), 121.9 ($\text{C}_{8\text{b}}$), 122.1 ($\text{C}_{8\text{a}}$), 123.36 ($\text{C}_{7\text{a}}$), 123.44 ($\text{C}_{7\text{b}}$), 125.0 ($\text{C}_{5\text{b}}$), 125.1 ($\text{C}_{5\text{a}}$), 142.3 ($\text{C}_{10\text{a}}$), 143.4 ($\text{C}_{10\text{b}}$), 144.7 ($\text{C}_{4\text{b}}$), 145.6 ($\text{C}_{4\text{a}}$), 171.5 (C_1), 189.0 ($\text{C}_{6\text{b}}$), 189.1 ($\text{C}_{6\text{a}}$). R_f 0.081 (30% EtOAc/hexanes).



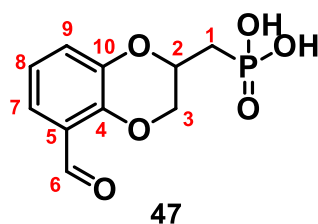
5-formyl-2,3-dihydrobenzo[1,4]dioxine-2-carboxylic acid (30a). Isolated as a pale-yellow powder (121 mg, 0.58 mmol, 29%), according to general procedure K. Single stated structural isomer isolated. ^1H NMR (CDCl_3); δ 4.42 (2H, dd, J 3.1, 11.5 Hz, H_3), 4.93 (1H, *app* dt, J 3.6, 11.8 Hz, H_2), 6.83 (1H, dt, J 4.0, 13.3 Hz, H_9), 6.95 (1H, d, J 8.0 Hz, H_8), 7.33 (2H, t, J 7.6 Hz, H_7), 8.15 (1H, s, OH), 10.30 (1H, s, H_6). ^{13}C NMR (CDCl_3); δ 65.5 (C_3), 71.3 (C_2), 117.6 (C_9), 121.8 (C_8), 123.6 (C_7), 128.7 (C_5), 142.5 (C_{10}), 145.8 (C_4), 171.6 (C_1), 189.4 (C_6). R_f 0.081 (30% EtOAc/hexanes). FTIR (ν_{max} cm^{-1}), 2922 (s br., O-H), 2878, (w, CH_x), 1733 (s, C=O), 1476 (s, C-O). HRMS (XEVO G2-XS QToF) calculated for $\text{C}_{10}\text{H}_9\text{O}_5$ [$\text{M}+\text{H}$] $^+$, 209.0450, found: 209.0450.



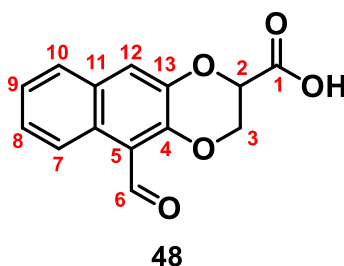
6-methyl-2,3-dihydrobenzo[1,4]dioxine-2-carboxylic acid (31). Isolated as a pale-yellow powder (333 mg, 1.72 mmol, 86%), according to general procedure K. The compound is an apparent 1:1 mixture of structural isomers by ^1H NMR. ^1H NMR (CDCl_3); δ 2.17 (1.5H, s, H7_b), 2.18 (3H, s, H7_a), 4.28 (1H, *app* td, J 2.9, 9.2 Hz, H3 _{α} , both), 4.34 (1H, *app* dt, J 4.1, 11.4 Hz, H3 _{β} , both), 4.79 (1H, m, H2), 6.21 (1H, *app* d, J 3.0 Hz, H5), 6.69 (1H, d, J 8.2 Hz, H8), 6.8 (1H, d, J 8.2 Hz, H9), 8.18 (1H, s, OH). ^{13}C NMR (CDCl_3); δ 20.7 (C7), 64.6 (C3), 71.6 (C2), 116.9 (C5_b), 117.1 (C5_a), 117.6 (C9_a), 117.7 (C9_b), 122.7 (C8_a), 122.9 (C8_b), 131.9 (C6_b), 132.2 (C6_a), 139.6 (C10_a), 140.6 (C10_b), 141.5 (C4_a), 142.4 (C4_b), 173.5 (C1_b), 173.6 (C1_a). R_f 0.016 (30% EtOAc/hexanes). FTIR (ν_{max} cm^{-1}), 2941 (s br., O-H), 2859, (w, CH_x), 1711 (s, C=O), 1506 (s, C-O). HRMS (XEVO G2-XS QToF) calculated for $\text{C}_{10}\text{H}_{11}\text{O}_4$ $[\text{M}+\text{H}]^+$, 195.0656, found: 195.0656.



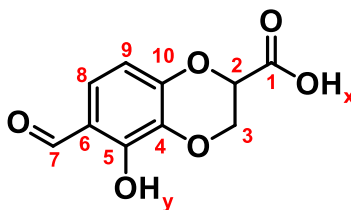
((2,3-dihydrobenzo[1,4]dioxin-2-yl)methyl)phosphonic acid (32). Isolated as a viscous colourless oil (243 mg, 1.06 mmol, 53%), according to general procedure K.1. ^1H NMR (CDCl_3); δ 1.35 (1H, t, J 7.1 Hz, H2), 2.18 (1H, *app* td, J 5.8, 9.5 Hz, H1 _{α}), 2.34 (1H, *app* td, J 5.8, 9.5 Hz, H1 _{β}), 4.09 (1H, *app* dt, J 7.3 Hz, H3 _{α}), 4.46 (1H, *app* dt, J 7.3 Hz, H3 _{β}), 6.86 (4H, *app* p, J 5.5 Hz, H5-8), 7.22 (2H, s, OH). ^{13}C NMR (CDCl_3); δ 16.2 (C2), 29.2 (C1), 67.5 (C3), 117.1 (C8), 117.6 (C5), 121.7 (C7), 121.8 (C8), 142.4 (C9), 142.8 (C4). R_f 0.017 (30% EtOAc/hexanes). FTIR (ν_{max} cm^{-1}), 2982 (s br., O-H), 2911, (w, CH_x), 1591 (m, P-O), 1491 (s, P=O), HRMS (XEVO G2-XS QToF) calculated for $\text{C}_9\text{H}_{12}\text{O}_5\text{P}$ $[\text{M}+\text{H}]^+$, 231.0422, found: 231.0429.



(5-formyl-2,3-dihydrobenzo[1,4]dioxin-2-yl)methylphosphonic acid (47). Isolated as a dark red powder (363 mg, 1.41 mmol, 70%), according to general procedure K.1. Single stated structural isomer isolated. ^1H NMR (d_6 -DMSO); δ 4.15 (2H, dd, J 7.4, 11.5 Hz, H3), 4.48 (2H, d, J 9.0 Hz, H1), 4.60 (1H, dd, J 2.1, 11.5 Hz, H2), 6.97 (1H, t, J 7.7 Hz, H8), 7.18 (1H, dd, J 1.5, 8.0 Hz, H9), 7.28 (1H, dd, J 1.5, 8.0 Hz, H7), 10.29 (1H, s, H6). ^{13}C NMR (d_6 -DMSO); δ 67.6 (C2), 68.2 (C1), 69.7 (C1), 120.3 (C7), 121.6 (C8), 123.6 (C9), 125.1 (C5), 143.9 (C10), 146.3 (C4), 189.0 (C6). R_f 0.000 (30% EtOAc/hexanes). FTIR (ν_{max} cm^{-1}), 3321 (s br., O-H), 2911, (w, CH_x), 1595 (m, P-O), 1472 (s, P=O), HRMS (XEVO G2-XS QToF) calculated for $\text{C}_{10}\text{H}_{12}\text{O}_6\text{P}$ $[\text{M}+\text{H}]^+$, 259.0371, found: 259.0371.

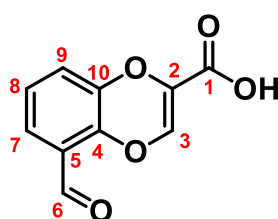


5-formyl-2,3-dihydronaphtho[2,3][1,4]dioxine-2-carboxylic acid (48). Isolated as a dark red powder (451 mg, 1.75 mmol, 87%), according to general procedure K. Single stated structural isomer isolated. ^1H NMR (CDCl_3); δ 4.52 (1H, dd, J 2.9, 8.4 Hz, $\text{H}3_\alpha$), 4.53 (1H, dd, J 2.9, 8.4 Hz, $\text{H}3_\beta$), 5.09 (1H, dd J 1.2, 2.9 Hz, H2). 6.71 (1H, s, OH), 6.83 (1H, s, H12), 7.38 (2H, dt, H8 & H9). 7.53 (1H, dd, J 1.7, 6.0, H10), 7.66 (1H, dd, J 1.7, 6.0, H7), 8.00 (1H, s, H6). ^{13}C NMR (CDCl_3); δ 64.6 (C3), 71.7 (C2), 100.0 (C12), 120.1 (C10), 123.2 (C9), 125.1 (C8), 127.7 (C7), 128.9 (C5), 130.9 (C11), 137.2 (C13), 145.8 (C4), 172.6 (C1), 191.0 (C6). R_f 0.000 (30% EtOAc/hexanes). FTIR (ν_{max} cm^{-1}), 2926 (s br., O-H), 2635, (w, CH_x), 2550 (w, CH_x), 1733 (s, C=O), 1480 (s, C-O), HRMS (XEVO G2-XS QToF) calculated for $\text{C}_{14}\text{H}_{11}\text{O}_5$ $[\text{M}+\text{H}]^+$, 259.0606, found: 259.0609.

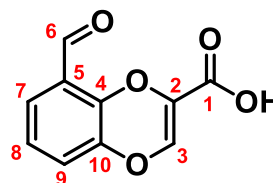


49

6-formyl-5-hydroxy-2,3-dihydrobenzo[b][1,4]dioxine-2-carboxylic acid (49). Isolated as a dark brown powder (449 mg, 2.00 mmol, >99%), according to general procedure K. Single stated structural isomer isolated. ^1H NMR (CDCl_3); δ 4.43 (1H, dd, J 4.2, 11.6 Hz, $\text{H}_{3\alpha}$), 4.54 (1H, dd, J 4.2, 11.6 Hz, $\text{H}_{3\beta}$), 4.97 (1H, dd, J 2.8, 4.2 Hz, H_2), 5.30 (1H, s, OH_x), 6.69 (1H, dd, J 2.1, 8.7 Hz, H_9), 7.15 (1H, dd, J 2.1, 8.7 Hz, H_8), 9.74 (1H, s, H_7), 11.47 (1H, s, OH_y). ^{13}C NMR (CDCl_3); δ 64.6 (C3), 72.5 (C2), 109.6 (C9), 115.8 (C6), 126.8 (C8), 131.2 (C4), 148.9 (C10), 152.0 (C5), 167.6 (C1), 195.4 (C7). R_f 0.313 (30% EtOAc/hexanes). FTIR (ν_{max} cm^{-1}), 3008 (s br., O-H), 2956, (w, CH_x), 1737 (m, C=O), 1491 (s, C-O), HRMS (XEVO G2-XS QTof) calculated for $\text{C}_{10}\text{H}_9\text{O}_6$ $[\text{M}+\text{H}]^+$, 225.0399, found: 225.0404.

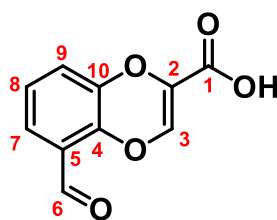


50a



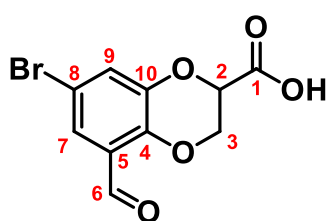
50b

5-formylbenzo[1,4]dioxine-2-carboxylic acid (50). Isolated as a pale-yellow powder (11.0 mg, 0.05 mmol, 25%), according to general procedure K (on 0.2 mmol scale). The compound is an apparent 2:1 mixture of structural isomers by ^1H NMR. ^1H NMR (d_6 -DMSO); δ 4.52 (1H, s, OH_a), 5.49 (0.5H, s, OH_b), 6.83 (1H, s, H_{3a}), 6.86 (0.5H, s, H_{3b}), 6.97 (1.5H, d, J 7.8 Hz, H_9), 7.03 (1H, dd, J 1.9, 7.8 Hz, H_{8a}), 7.09 (0.5H, dd, J 1.9, 7.8 Hz, H_{8b}), 7.26 (1.5H, dt, J 1.4, 7.7 Hz, H_7), 10.28 (1H, s, H_{6a}), 10.34 (1H, s, H_{6b}). ^{13}C NMR (d_6 -DMSO); δ 55.5 (C3), 119.9 (C_{8a}), 120.2 (C_{8b}), 122.0 (C_{9a}), 122.7 (C_{9b}), 123.3 (C7), 124.0 (C_{5a}), 124.2 (C_{5b}), 131.6 (C2), 141.7 (C10), 142.3 (C4), 146.5 (C4), 188.3 (C1), 189.2 (C6). R_f 0.676 (30% MeOH/DCM).

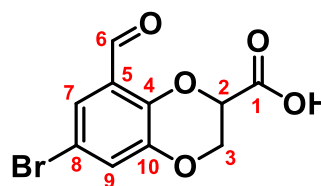


50a

5-formylbenzo[1,4]dioxine-2-carboxylic acid (50a). Isolated as a pale-yellow powder (149 mg, 0.723 mmol, 56%), according to general procedure K (on 1.3 mmol scale). Contains EtOAc containment. ^1H NMR (CDCl_3); δ 1.25 (t, 7.12 Hz, EtOAc), 4.12 (q, 7.12 Hz, EtOAc), 7.04 (1H, s, H3), 7.12 (2H, dd, H8 & H9), 7.48 (1H, dd, J 1.6, 7.8 Hz, H7), 9.46 (1H, s, OH), 10.43 (1H, s, H6). ^{13}C NMR (CDCl_3); δ 14.4 (EtOAc), 56.4 (C3), 60.9 (EtOAc), 90.3 (C2), 121.8 (C8), 122.0 (C9), 124.0 (C7), 124.4 (C5), 140.0 (C10), 142.3 (C4), 145.0 (C4), 170.7 (C1), 189.2 (C6). R_f 0.676 (30% MeOH/DCM). FTIR (ν_{max} cm^{-1}), 3325 (s br., O-H), 1640 (s, C=O), 1461 (m, C-O), HRMS (XEVO G2-XS QTof) calculated for $\text{C}_{10}\text{H}_7\text{O}_5$ $[\text{M}+\text{H}]^+$, 207.0293, found: 207.0295.



51a



51b

7-bromo-5-formyl-2,3-dihydrobenzo[1,4]dioxine-2-carboxylic acid (51). Isolated as a pale-yellow powder (161 mg, 0.56 mmol, 56%), according to general procedure K (on 1.0 mmol scale). The compound is an apparent 1:1 mixture of structural isomers by ^1H NMR. ^1H NMR (CDCl_3); δ 3.50 (2H, s, OH_{both}), 4.44 (1H, t, J 3.44 Hz, H3_{a, \alpha}), 4.46 (1H, d, J 3.0 Hz, H3_{a, \beta}), 4.54 (1H, d, J 4.0 Hz, H3_{b, \alpha}), 4.57 (1H, d, J 4.0 Hz, H3_{b, \beta}), 5.05 (2H, t, J 3.2 Hz, H2), 6.98 (1H, t, J 7.9 Hz, H9_a), 7.14 (1H, dd, J 1.6, 8.0 Hz, H9_b), 7.47 (1H, dd, J 1.6, 7.7 Hz, H7_a), 7.58 (1H, d, J 2.4 Hz, H7_b), 10.35 (1H, s, H6_a), 10.41 (1H, s, H6_b). ^{13}C NMR (CDCl_3); δ 64.2 (C3_a), 64.6 (C3_b), 71.2 (C2_b), 71.8 (C2_a), 113.8 (C8), 121.5 (C9_a), 122.1 (C9_b), 123.5 (C7), 125.6 (C5_b), 125.9 (C5_a), 143.4 (C10_a), 144.2 (C10_b), 145.0 (C4_a), 145.7 (C4_b), 170.9 (C1_b), 171.4 (C1_a), 187.0 (C6_b), 189.7 (C6_a). R_f 0.002 (30% EtOAc/hexanes). FTIR (ν_{max} cm^{-1}), 3078 (s br., O-H), 2926, (w, CH_x), 1718 (s, C=O), 1685 (s, C=O), 1591 (s, C=O), 1469 (s, C-O). HRMS (XEVO G2-XS QTof) calculated for $\text{C}_{10}\text{H}_{18}\text{O}_5\text{Br}$ $[\text{M}+\text{H}]^+$, 286.9555 found: 286.9556.

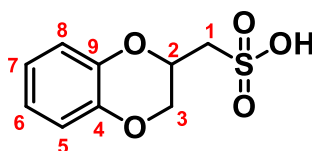
7.2.5. Continued synthesis of benzodioxanes: 33, 53-60

General procedure L: for synthesis of 33 and 53

Adapted from a known procedure.¹⁵⁷

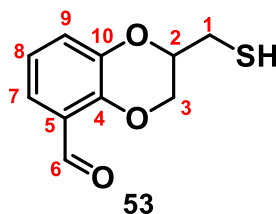
Formation of thiourea salts: Mixture of the alcohol formed in general procedure M (6.0 mmol, 1.0 equiv.), thiourea (6.0 mmol, 1.0 equiv.), 4M HBr in acetic acid (3 mL, 12.0 mmol, 2.0 equiv.), and IMS (3 mL) was refluxed overnight until reaction reached completion (confirmed by TLC). After cooling to RT, the reaction mixture was concentrated *in vacuo*, yielding a white solid or a syrup, depending on the substituent. This crude salt was used without further purification.

Hydrolysis of the thiourea salt to the thiol: The thiourea salt (6.0 mmol, 1.0 equiv.), was dissolved or suspended in water (3 mL) and heated to 50 °C. To this mixture 33% NaOH aqueous sol. was added drop wise, until no more cloudiness developed upon addition and the pH had risen to 10. Reaction mixture stirred overnight at 50 °C. After cooling to RT, 30% HCl was added until pH 6, then thiol product was extracted with DCM (3 × 5 mL). The combined organic layers were washed with brine, dried over Na₂SO₄ and concentrated *in vacuo* to yield title prod. This could be taken forward to General procedure N or purified and isolated by flash column chromatography (30% EtOAc/hexanes) to yield the title compound.



33

(2,3-dihydrobenzo[*b*][1,4]dioxin-2-yl)methanesulfonic acid (33). Isolated as off-white powder (209 mg, 0.908 mmol, 15%), according to general procedure L then M conducted as a one-pot reaction. ¹H NMR (CDCl₃); δ 1.57 (1H, s, OH), 3.88 (1H, *app* q, *J* 5.8 Hz, H1_α), 3.93 (1H, *app* q, *J* 5.8 Hz, H1_β), 4.14 (1H, dd, *J* 3.6, 7.6 Hz, H3_α), 4.29 (1H, m, H2), 4.30 (1H, dd, *J* 1.9, 11.0 Hz, H3_β), 6.90 (4H, *app* dt, *J* 4.7, 11.3 Hz, H5-H8). ¹³C NMR (CDCl₃); δ 61.8 (C3), 65.1 (C1), 73.4 (C2), 117.2 (C6), 117.3 (C7), 121.58 (C5), 121.64 (C8), 143.0 (C9), 143.1 (C4). *R*_f 0.294 (30% EtOAc/hexanes). FTIR (*v*_{max} cm⁻¹), 3198 (s, O-H), 2937, (w, CH_x), 2874, (w, CH_x), 1588 (m, S=O), 1491 (s, C-O). HRMS (XEVO G2-XS QTof) calculated for C₉H₁₁SO₅ [M+H]⁺, 231.0327 found: 231.0327.

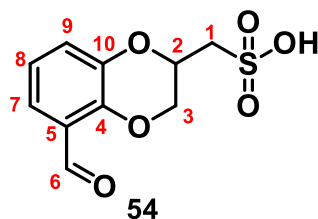


2-(mercaptomethyl)-2,3-dihydrobenzo[1,4]dioxine-5-carbaldehyde (53). Isolated as a pale yellow amorphous solid (510 mg, 2.43 mmol, 40%), according to general procedure L. Single stated structural isomer isolated. ^1H NMR (CDCl_3); δ 3.49 (1H, s, SH), 3.94 (2H, *app* ddd, J 4.3, 8.7, 12.2 Hz, H3), 4.22 (1H, dt, J 1.6, 8.0 Hz, H2), 4.38 (1H, dd, J 2.2, 11.0 Hz, H1 $_{\alpha}$), 4.46 (1H, dd, J 2.2, 11.0 Hz, H1 $_{\beta}$), 6.93 (1H, t, J 7.9 Hz, H8), 7.13 (1H, *app* ddd, J 1.6, 2.2, 8.0 Hz, H9), 7.40 (1H, *app* ddd, J 1.6, 3.0, 7.8 Hz, H7), 10.37 (1H, s, H6). ^{13}C NMR (CDCl_3); δ 61.6 (C3), 64.9 (C2), 65.5 (C2), 73.1 (C1), 74.1 (C1), 121.1 (C8), 121.2 (C9), 123.2 (C7), 125.1 (C5), 143.6 (C10), 145.9 (C4), 189.1 (C6). R_f 0.060 (30% EtOAc/hexanes). FTIR (ν_{max} cm^{-1}), 3175 (br. s, S-H), 2110, (w, CH_x), 1599 (s, C=O), 1472 (s, C-O). HRMS (XEVO G2-XS QTof) calculated for $\text{C}_{10}\text{H}_{11}\text{O}_3\text{S}$ $[\text{M}+\text{H}]^+$, 211.0429 found: 211.0432.

General procedure M: for synthesis of **33** and **54**.

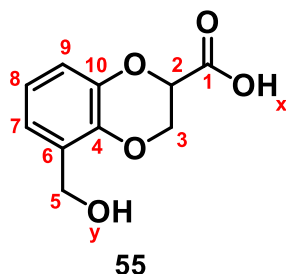
Adapted from a known procedure.¹⁵⁷

Oxidation of thiols: The thiol formed in general procedure S (6.0 mmol, 1.0 equiv.), was dissolved in glacial acetic acid (21 mL). Hydrogen peroxide (11.4 mL, 30%, 1.2 equiv.) was added dropwise, at such a rate that the temperature remained below 32 °C. After addition was complete and completion reached (according to TLC), sodium thiosulphate (sat aqueous sol.) was added at 0 °C until no more peroxides were present. The reaction mixture was concentrated *in vacuo* to yield an oil. This residue was suspended in water (48 mL) and 33% NaOH aqueous sol. was added until pH 7. The water layer was extracted with Et_2O (3×15 mL) and concentrated and dried *in vacuo* to yield the titled product, after undergoing purification by flash column chromatography (30% EtOAc/hexanes).



(5-formyl-2,3-dihydrobenzo[1,4]dioxin-2-yl)methanesulfonic acid (54). Isolated as a pale yellow amorphous solid (475 mg, 1.84 mmol, 31%), according to general procedure M. Single stated structural isomer isolated. ^1H NMR (d_6 -DMSO) ; δ 4.11 (2H, dd, J 4.2, 7.3 Hz, H1), 4.29 (2H, *app* br dd, J 2.5, 9.2 Hz, H3), 4.44 (1H, dt, 2.4, 9.2 Hz, H2), 6.85 (2H, m, H8 & H9), 7.03 (1H, d, J 3.3 Hz, H7), 10.22 (1H, s, H6), 11.97 (1H, s, OH). ^{13}C NMR (d_6 -DMSO); δ 60.0 (C3), 65.5 (C1), 74.2 (C2), 117.0 (C9), 120.4 (C8), 120.8 (C7), 142.2 (C10), 143.0 (C4), 160.1 (C5), 172.5 (C6). R_f 0.293 (30% EtOAc/hexanes). FTIR (ν_{max} cm^{-1}), 3340 (br. s, OH), 2830, (w, CH_x), 2251, (w, CH_x), 1700 (s, C=O), 1467 (s, C-O). HRMS (XEVO G2-XS QTof) calculated for $\text{C}_{10}\text{H}_{11}\text{O}_6\text{S}$ $[\text{M}+\text{H}]^+$, 259.0276 found: 259.0292.

5-(hydroxymethyl)-2,3-dihydrobenzo[1,4]dioxine-2-carboxylic acid (55).



Procedure N: for synthesis of **55**.

Adapted from known procedures. ^{145,163}

Formation of primary alcohol: A solution of compound **20a** (2362 mg, 10.0 mmol, 1.0 equiv.) in anhydrous MeOH (20 mL) was added dropwise to a stirred suspension of NaBH_4 (2156 mg, 10.0 mmol, 1.0 equiv.) in anhydrous MeOH (80 mL), at 0°C while under N_2 *atm*. Reaction stirred overnight at RT. Upon completion (confirmed by TLC), the reaction was quenched with the slow addition of acetone. Hence concentrated *in vacuo* and subsequently partitioned in separating funnel between EtOAc (20 mL), and water (10 mL), acidified with 1M HCl. Organic layer dried with MgSO_4 , and dried *in vacuo*, yielding ester containing precursor to compound **55**, which was used in subsequent step without further purification.

Ester hydrolysis: Intermediate compound (1190 mg, 5.0 mmol, 1.0 equiv.) was dissolved in 40 mL of a 1:1 mixture of MeOH / H₂O, to this the lithium hydroxide monohydrate (315 mg, 7.5 mmol, 1.5 equiv.) was added to the stirred reaction mixture at RT. Upon completion (approx. 3hrs), the reaction mixture was concentrated *in vacuo* and partitioned between water (acidized with 1M HCl) and DCM (40 mL of each). The resultant aqueous layer was extracted with a second 20 mL of DCM and the combined org layers were dried with MgSO₄. MgSO₄ filtered off, and the resultant solution was dried *in vacuo* to yield title compound **55**. Isolated as a very viscous dark orange oil (872 mg, 4.15 mmol, 83%).

¹H NMR (CDCl₃); δ 2.06 (1H, s, OH_y), 2.76 (1H, br. s, OH_x), 3.89 (1H, *app* t, *J* 5.0 Hz, H3_α), 4.13 (1H, dd, *J* 2.2, 4.8 Hz, H3_β), 4.33 (2H, *app* d, *J* 2.5 Hz, H6), 4.63 (1H, d, *J* 12.4 Hz, H2_α), 4.78 (1H, d, *J* 12.4 Hz, H2_β), 6.87 (3H, m, H7 - H9). ¹³C NMR (CDCl₃); δ 61.4 (C6), 65.0 (C3), 73.8 (C2), 117.4 (C9), 121.1 (C7), 122.0 (C8), 128.8 (C5), 141.5 (C10), 143.1 (C4), 170.6 (C1). *R*_f 0.00 (30% EtOAc/hexanes). FTIR (ν_{max} cm⁻¹), 3339 (br. s, OH), 2930, (w, CH_x), 2878, (w, CH_x), 1700 (m, C=O), 1472 (s, C-O). HRMS (XEVO G2-XS QToF) calculated for C₁₀H₁₁O₅ [M+H]⁺, 211.0606 found: 211.0608.

Procedure O: for synthesis of **56**.

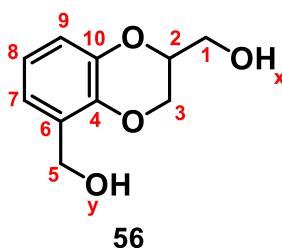
Adapted from a known procedure.¹⁶¹

A solution of compound **20a** (590 mg, 2.5 mmol, 1.0 equiv.) in anhydrous MeOH (25 mL) was cooled to 0 °C. NaBH₄ (539 mg, 2.5 mmol, 1.0 equiv.) was added to the reaction mixture at 0 °C while under N₂ atm. Reaction stirred overnight at RT Upon completion (confirmed by TLC), the reaction was quenched with the slow addition of water. Hence concentrated *in vacuo* and subsequently partitioned between EtOAc (10 mL), and water (5 mL), acidified with 1M HCl. Organic layer dried with MgSO₄, and dried *in vacuo*, yielding title compound **56** as a white amorphous solid (272 mg, 1.39 mmol, 55%).

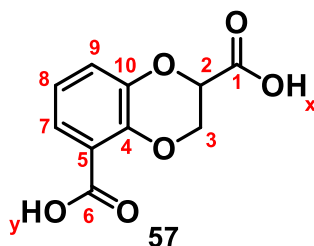
Procedure O.1: for synthesis of **56**.

Adapted from a known procedure.¹⁶²

A solution of compound **30a** (2.01 g, 8.5 mmol, 1.0 equiv.) in anhydrous diethyl ether (20 mL) was added dropwise to a stirred suspension of LiAlH₄ (759 mg, 20.0 mmol, 2.0 equiv.) in anhydrous diethyl ether (10 mL) at 0 °C while under N₂ atm. Reaction stirred overnight at RT Upon completion (confirmed by TLC), the reaction was quenched with the slow addition of water. This reaction mixture was hence filtered. Filtrate was acidified with 1M HCl. Then in separating funnel EtOAc (20ml) was added to filtrate. Organic layer dried with MgSO₄, and dried *in vacuo*, yielding title compound **56** as very viscous pale-orange oil (740 mg, 3.77 mmol, 45%).

(2,3-dihydrobenzo[1,4]dioxine-2,5-diyl)dimethanol (56).

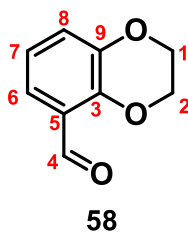
¹H NMR (CDCl₃); δ 2.96 (2H, br. s, OH_{both}), 3.81 (1H, d, *J* 6.7 Hz, H1_α), 3.89 (1H, d, *J* 6.7 Hz, H1_β), 4.11 (1H, m, H2), 4.27 (2H, s, H5), 4.56 (1H, d, *J* 12.1 Hz, H3_α), 4.75 (1H, d, *J* 12.1 Hz, H3_β), 6.83 (3H, m, H7 - H9). ¹³C NMR (CDCl₃); δ 61.1 (C1), 61.4 (C3), 64.9 (C6), 73.7 (C2), 117.2 (C9), 121.0 (C7), 121.7 (C8), 129.1 (C10), 141.2 (C4), 143.1 (C5). *R_f* 0.108 (30% EtOAc/hexanes). FTIR (ν_{max} cm⁻¹), 3329 (br. s, OH), 2930, (w, CH_x), 2878, (w, CH_x), 1472 (s, C-O). HRMS (XEVO G2-XS QToF) calculated for C₁₀H₁₃O₄ [M+H]⁺, 197.0804 found: 197.0798.

2,3-dihydrobenzo[1,4]dioxine-2,5-dicarboxylic acid (57).**Procedure P:** for synthesis of **57**.

Adapted from known procedures.¹⁶⁴

Compound **56** (1480 mg, 7.5 mmol, 1.0 equiv.) was dissolved in 40 mL of a 1:2 mixture of MeOH / H₂O, and to this the following was added sequentially: 5 mol % Pd/C (40.0 mg, 0.38 mmol, 0.05 equiv.), NaBH₄ (57 mg, 1.52 mmol, 0.2 equiv.) and KOH (2.53 g, 45.0 mmol, 6.0 equiv.). This was stirred at RT until completion observed by TLC. The catalyst was filtered off, with the resultant filtrate being concentrated *in vacuo* and partitioned between water (acidized with 1M HCl) and EtOAc (20 mL of each). The resultant aqueous layer was extracted with a second 20mL of DCM and the combined org layers were dried with MgSO₄. MgSO₄ filtered off, and the resultant solution was dried *in vacuo* to yield title compound **57**. Isolated as pale-yellow viscous oil (513 mg, 2.29 mmol, 30%).

¹H NMR (CDCl₃); δ 3.00 (2H, br. s, OH both), 3.89 (1H, dd, *J* 3.9, 10.0 Hz, H3_α), 4.16 (1H, dd, *J* 3.9, 10.0 Hz, H3_β), 4.70 (1H, m, H2), 6.86 (3H, *app t*, *J* 3.1 Hz, H7 – H9). ¹³C NMR (CDCl₃); δ 64.9 (C3), 73.7 (C2), 117.4 (C5), 121.1 (C9), 121.2 (C8), 121.8 (C7), 141.2 (C10), 143.0 (C4), 170.4 (C6), 170.5 (C1). *R_f* 0.065 (30% EtOAc/hexanes). FTIR (*v*_{max} cm⁻¹), 3321 (br. s, OH), 2930, (w, CH_x), 2878, (w, CH_x), 1707 (m. C=O), 1473 (s, C-O). HRMS (XEVO G2-XS QTof) calculated for C₁₀H₉O₆ [M+H]⁺, 225.0399 found: 225.0402.

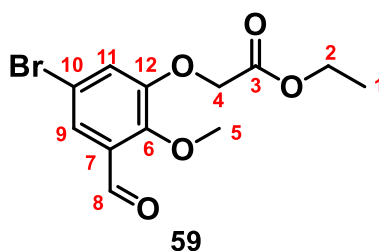
2,3-dihydrobenzo[1,4]dioxine-5-carbaldehyde (58).**Procedure Q:** for synthesis of **58**.

Adapted from a known procedure ¹⁶⁶

Formation of primary alcohol: A solution of 1,4-benzodioxan-5-carboxylic acid (1816 mg, 10.0 mmol, 1.0 equiv.) in anhydrous THF (10 mL) was added dropwise to a stirred suspension of LiAlH₄ (759 mg, 20.0 mmol, 2.0 equiv.) in anhydrous THF (10 mL), at 0 °C while under N₂ atm. Reaction stirred overnight at RT Upon completion (confirmed by TLC), the reaction was quenched with aqueous KOH (2.5%, 6 mL). Added anhydrous MgSO₄, subsequently filtered, and extracted with ether. The resulting filtrate and ether extracts were combined and concentrated *in vacuo*, resulting in primary alcohol precursor of the title compound **58**.

Oxidisation of alcohols: Added pyridinium chlorochromate (4.30 g, 20.0 mmol, 2.0 equiv.) to a stirred solution of above alcohol (10.0 mmol, 1.0 equiv.) in DCM (50 mL) at 0°C while under N₂ atm. Stirred the reaction overnight at RT The resultant solution was passed through a plug of silica gel. Hence extracted with DCM (250 mL). The combined solvent was dried *in vacuo* to yield the impure title compound **25**. This crude product was purified by flash column chromatography (30% EtOAc/hexanes) to yield the pure title compound **58**. Isolated as a viscous brown oil (935 mg, 5.70 mmol, 57%).

¹H NMR (CDCl₃); δ 4.35 (2H, br. s, H1), 4.42 2H, br. s, H2), 6.94 (1H, t, *J* 7.7 Hz, H8), 7.12 (1H, d, *J* 7.4 Hz, H7), 7.42 (1H, d, *J* 7.4 Hz, H6), 10.61 (H5). ¹³C NMR (CDCl₃); δ 63.9 (C1), 64.6 (C2), 120.9 (C8), 121.1 (C6), 123.2 (C7), 125.1 (C4), 144.1 (C9), 146.5 (C3), 189.1 (C5). *R*_f 0.344 (30% EtOAc/hexanes). FTIR (*v*_{max} cm⁻¹), 2937, (w, CH_x), 2881, (w, CH_x), 1685 (s, C=O), 1480 (s, C-O). HRMS (XEVO G2-XS QTof) calculated for C₉H₉O₃ [M+H]⁺, 165.0552 found: 165.0555.

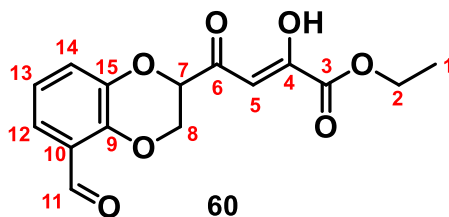
ethyl 2-(5-bromo-3-formyl-2-methoxyphenoxy)acetate (59).**Procedure R:** for synthesis of **59**.

Adapted from known procedures.¹⁶⁵

Compound **37** (231 mg, 1.0 mmol, 1.0 equiv.), was dissolved in 10 mL of DCM and stirred at RT. Triethylamine (0.28 mL, 2.0 mmol, 2.0 equiv.), was added while being stirred, after 5 minutes, ethyl 2-bromoacetate (0.11 mL, 1.0 mmol, 1.0 equiv.) was added. Stirred at RT until completion observed *via* TLC. Transferred to separating funnel and 5 mL of water was added. Resultant organic layer was separated and dried with brine and MgSO₄, sequentially, then filtered. The filtrate was dried *in vacuo* to yield the impure title compound **59**. This crude product was purified by flash column chromatography (30% EtOAc/hexanes) to yield the pure title compound **59**. Isolated as a pale-yellow powder (52.0 mg, 0.16 mmol, 15%).

¹H NMR (CDCl₃); δ 1.27 (3H, t, *J* 7.2 Hz, H1), 3.90 (3H, s, H5), 4.22 (2H, q, *J* 7.2 Hz, H2), 4.82 (2H, s, H4), 7.22 (1H, d, *J* 2.3 Hz, H11), 7.56 (1H, d, *J* 2.3 Hz, H9), 10.55 (1H, s, H8). ¹³C NMR (CDCl₃); δ 14.1 (C1), 56.4 (C5), 61.4 (C2), 69.3 (C4), 117.2 (C10), 120.7 (C11), 121.8 (C9), 130.7 (C7), 149.1 (C6), 152.7 (C12), 169.1 (C3), 189.3 (C8). *R*_f 0.395 (30% EtOAc/hexanes). FTIR (ν_{\max} cm⁻¹), 2948, (w, CH_x), 2911, (w, CH_x), 1752 (m, C=O), 1472 (s, C-O). HRMS (XEVO G2-XS QTof) calculated for C₁₂H₁₄BrO₅ [M+H]⁺, 315.9943 found: 315.9943.

ethyl-4-(5-formyl-2,3-dihydrobenzo[1,4]dioxin-2-yl)-2-hydroxy-4-oxobut-2-enoate (**60**).



Procedure C.1: for synthesis of **60**.

Adapted from a known procedure.¹³⁵

To a solution of compound **46** (1.00 g, 5.0 mmol, 1.0 equiv.) and diethyl oxalate (1.38 mL, 10.0 mmol, 2.0 equiv.) in anhydrous THF (20 mL) NaOMe (540 mg, 10.0 mmol, 2.0 equiv.) was added under N₂ gas protection and stirred at RT for approx. 1.5 hrs. Upon completion the mixture was poured into hexane (100 mL). The resultant precipitate was removed by filtration and then was vigorously stirred for 30 minutes in 1M HCl (30 mL). The formed yellow solid was filtered, washed with water, and dried *in vacuo* to yield the impure title compound **60**. This crude product was purified by flash column chromatography (30% EtOAc/hexanes) to yield compound **60**. Isolated as an orange powder (109 mg, 0.36 mmol, 7%).

¹H NMR (CDCl₃); δ 0.87 (3H, *app* dt *J* 2.4, 8.2 Hz, H1), 1.38 (2H, *app* dt, 0.7, 7.2 Hz, H2), 2.36 (1H, s, H5), 3.49 (1H, s, OH), 4.38 (1H, dd, *J* 3.0, 8.6 Hz, H8_α), 4.44 (1H, dd, *J* 3.0, 8.6 Hz, H8_β), 4.78 (1H, dd, *J* 3.0, 5.8 Hz, H7), 6.98 (1H, dt, *J* 0.5, 8.3 Hz, H13), 7.13 (1H, dd, *J* 1.6, 6.4 Hz, H14), 7.47 (1H, dd, *J* 1.6, 6.4 Hz, H12), 10.47 (1H, s, H11).
¹³C NMR (CDCl₃); δ 14.2 (C2), 26.3 (C1), 50.8 (C5), 66.2 (C8), 78.4 (C7), 121.7 (C13), 121.9 (C14), 123.5 (C12), 125.0 (C10), 143.6 (C15), 144.9 (C9), 188.5 (C11), 198.9 (C6), 204.6 (C3). *R*_f 0.211 (30% EtOAc/hexanes). FTIR (*v*_{max} cm⁻¹), 3440 (br. s, OH), 2922, (w, CH_x), 2873, (w, CH_x), 1722 (s, C=O), 1685 (s, C=O), 1465 (s, C-O). HRMS (XEVO G2-XS QTof) calculated for C₁₅H₁₅O₇ [M+H]⁺, 307.0622 found: 307.0619.

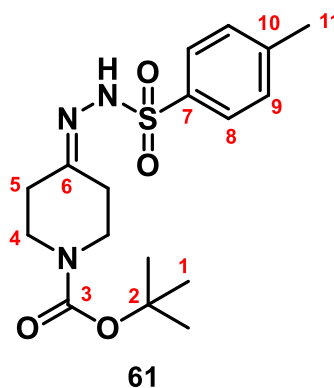
7.2.6. Synthesis of sulfonylhydrazones: 61, 63-67 and 68.1-68.8

Sulfonylhydrazones were prepared according to procedures described in prior work and full characterisation data for compounds **68.1-68.8** can be found in referenced published literature.^{167,171,191,192}

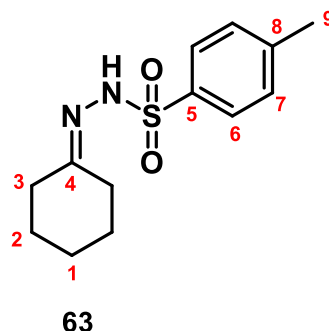
General Procedure S: for synthesis of **61, 63-66**.

Adapted from a known procedure.

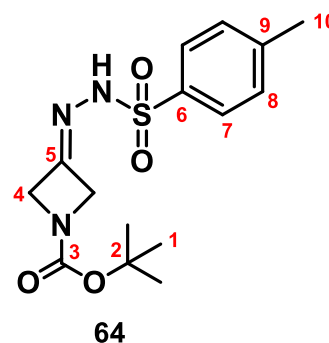
To a solution of cyclic ketone (5 or 10 mmol, 1.0 equiv.) in methanol (15 or 30 mL) was added tosyl hydrazide (1.0 equiv.) and the resulting solution was stirred at RT until completion of the reaction was indicated by TLC. In cases where the product precipitated out of solution during the reaction, it was vacuum filtered and dried *in vacuo* to give the title compound without need for further purification. In cases where the product remained in solution, the reaction mixture was evaporated to dryness *in vacuo* to yield the title compound without need for further purification (30 – 83%).



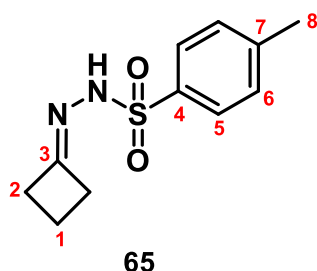
tert-Butyl 4-(2-tosylhydrazineylidene)piperidine-1-carboxylate (61). Isolated as a pure white powder (2.60 g, 7.08 mmol, 71%) according to general procedure S. ¹H NMR (CDCl₃); δ 1.46 (9H, s, H1), 1.50 (1H, s, H7), 2.37 (4H, dt, *J* 5.0, 6.0 Hz, H5), 2.45 (3H, s, H12), 3.51 (4H, q, *J* 5.8 Hz, H4), 7.33 (2H, d, *J* 8.0 Hz, H10), 7.85 (2H, d, *J* 8.3 Hz, H9). ¹³C NMR (CDCl₃); δ 21.6 (C12), 27.1 (C5), 28.4 (C1), 33.6 (C4), 41.2 (C6), 80.2 (C2), 128.1 (C9), 129.6 (C10), 135.2 (C11), 144.2 (C8), 154.5 (C3). FTIR (ν_{\max} cm⁻¹): 3116 (w, CH_x), 2974 (w, CH_x), 1666 (s, C=O), 1334 (s, S=O), 1156 (s, C-N). *R*_f 0.132 (30% EtOAc/hexanes). HRMS (XEVO G2-XS QToF) calculated for C₁₇H₂₆N₃O₄S [M+H]⁺ 368.1655, found: 368.1655.



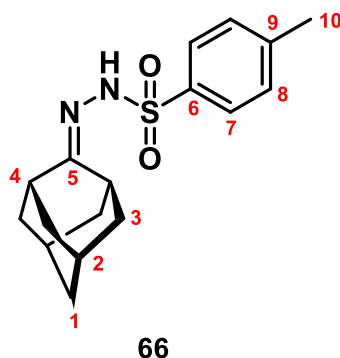
***N'*-cyclohexylidene-4-methylbenzenesulfonylhydrazide (63).** Isolated as a pure white powder (403 mg, 1.50 mmol, 30%) according to general procedure S. ^1H NMR (CDCl_3); δ 1.65 (6H, m, H1 and H1₂), 2.24 (4H, dt, J 5.8, 16.4 Hz, H3), 2.45 (3H, s, H9), 7.15 (1H, s, NH), 7.33 (2H, d, J 8.1 Hz, H7), 7.86 (2H, d, J 8.5 Hz, H6). ^{13}C NMR (CDCl_3); δ 21.6 (C9), 25.2 (C1), 26.9 (C2 _{α}), 27.0 (C2 _{β}), 35.1 (C3 _{α}), 42.0 (C3 _{β}), 125.9 (C5), 128.1 (C6), 129.6 (C7), 134.9 (C8), 144.3 (C4). FTIR (ν_{max} cm^{-1}): 2934 (w, CH_x), 2855 (w, CH_x), 1250 (s, S=O), 1157 (s, C-N), 1091 (s, C=N). R_f 0.483 (30% EtOAc/hexanes). HRMS (XEVO G2-XS QTof) calculated for $\text{C}_{13}\text{H}_{19}\text{N}_2\text{O}_2\text{S}$ $[\text{M}+\text{H}]^+$ 267.1239 found: 267.1239.



***tert*-butyl 3-(2-tosylhydrazineylidene)azetidine-1-carboxylate (64).** Isolated as a white powder (700 mg, 2.06 mmol, 83%) according to general procedure S. ^1H NMR (CDCl_3); δ 1.45 (9H, s, H1), 1.64 (1H, s, NH), 2.47 (3H, s, H10), 4.55 (4H, dd, J 2.9, 13.7 Hz, H4), 7.36 (2H, d, J 8.0 Hz, H8), 7.83 (2H, d, J 8.3 Hz, H7). ^{13}C NMR (CDCl_3); δ 21.67 (C10), 28.27 (C1), 58.71 (C4), 60.37 (C4), 80.93 (C2), 128.03 (C7), 129.85 (C8), 134.77 (C6), 144.69 (C9), 148.83 (C5), 155.93 (C3). FTIR (ν_{max} cm^{-1}): 2934 (w, CH_x), 2856 (w, CH_x), 1600 (s, C=O), 1368 (s, C-N), 1092 (s, C-O). R_f 0.038 (30% EtOAc/hexanes). HRMS (XEVO G2-XS QTof) calculated for $\text{C}_{15}\text{H}_{22}\text{N}_3\text{O}_4\text{S}$ $[\text{M}+\text{H}]^+$: 326.1300 found: 326.1300.



***N'*-Cyclobutylidene-4-methylbenzenesulfonohydrazide (65).** Isolated as a white powder (950 mg, 3.99 mmol, 80%) according to general procedure S. ^1H NMR (CDCl_3); δ 1.99 (1H, p, J 8.2 Hz, H1), 2.45 (3H, s, H9), 2.77-3.13 (4H *app* tt, H2), 4.94 (1H, s, NH), 7.34 (2H, d, J 8.0 Hz (H7), 7.85 (2H, dd, J 2.36, 13.5 Hz, H6). ^{13}C NMR (CDCl_3); δ 13.6 (C1), 21.5 (C9), 31.9 (C3), 33.9 (C3), 64.9 (C3), 126.6 (C6), 128.1 (C7), 129.9 (C8), 143.6 (C5). FTIR (ν_{max} cm^{-1}): 2965 (w, CH_x), 2863 (w, CH_x), 1340 (s, S=O), 1286 (s, C-N). R_f 0.400 (30% EtOAc/hexanes). HRMS (XEVO G2-XS QTof) calculated for $\text{C}_{11}\text{H}_{15}\text{N}_2\text{O}_2\text{S}$ $[\text{M}+\text{H}]^+$: 239.0854, found: 239.0854.



***N'*-((1*r*,3*r*,5*R*,7*S*)-adamantan-2-ylidene)-4-methylbenzenesulfonohydrazide (66).** Isolated as a white powder (1.99 mg, 6.036 mmol, 63%) according to general procedure S. ^1H NMR (CDCl_3); δ 1.79 (6H, m, H1 and H2), 1.95 (6H, d, J 13.0 Hz, H3), 2.06 (2H, m, H4), 2.43 (3H, s, H10), 2.66 (1H, s), 3.08 (1H, s, NH), 7.30 (2H, d, J 8.0 Hz, H8), 7.83 (2H, d, J 8.3 Hz, H7). ^{13}C NMR (CDCl_3); δ 21.6 (C10), 27.5 (C2), 31.8 ($\text{C}4_\alpha$), 36.3 (C1), 37.9 ($\text{C}4_\beta$), 39.1 (C3), 39.3 (C3), 39.4 (C3), 47.0 (C5), 128.0 (C7), 129.5 (C8), 135.2 (C9), 144.0 (C6). FTIR (ν_{max} cm^{-1}) FTIR (ν_{max} cm^{-1}) 2925 (w, CH_x), 2901 (w, CH_x) 2850, (w, CH_x), 1249 (s, S=O), 1157 (s, C-N), 1092 (s, C=N aliphatic). R_f 0.286 (30% EtOAc/hexanes). HRMS (XEVO G2-XS QTof) calculated for $\text{C}_{17}\text{H}_{23}\text{N}_2\text{O}_2\text{S}$ $[\text{M}+\text{H}]^+$ 319.1489, found: 319.1489.

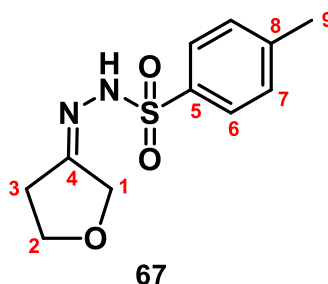
General Procedure S.1: for synthesis of **67**.

Adapted from a known procedure.

One-Pot synthesis:¹⁶⁷

Step 1: To solution of 3-hydroxytetrahydrofuran (880 mg, 10.0 mmol, 1.0 equiv.) in DCM (40 mL) pyridinium chlorochromate (4.31 g, 10.0 mmol, 2.0 equiv.) and sufficient celite was added concordantly. The resultant mixture was stirred at RT overnight. Once completion reached (indicated by TLC), the reaction mixture was flushed through a celite plug and then a silica plug. The obtained product solution was carefully concentrated under vacuum (not to dryness). This was carried through to step 2.

Step 2: To the above formed concentrated solution of cyclic ketone (*approx.* 10.0 mmol, 1.0 equiv.) had toluene (30 mL) and tosyl hydrazide (1.86 g, 10.0 mmol, 1.0 equiv.) added. The resulting solution was stirred at RT until completion of the reaction was indicated by TLC. In cases where the product precipitated out of solution during the reaction, it was vacuum filtered and dried *in vacuo* to give the title compound without need for further purification. In cases where the product remained in solution, the reaction mixture was evaporated to dryness *in vacuo* to yield the title compound **67** without need for further purification. Isolated as a pure white powder (1.25 g, 4.9 mmol, 49%).



(Z)-N'-(dihydrofuran-3(2H)-ylidene)-4-methylbenzenesulfonylhydrazide (67). Isolated as a pure white powder (1.25 g, 4.9 mmol, 49%) according to general procedure S.1. ¹H NMR (CDCl₃); δ 2.46 (3H, s, H9), 2.48 (2H, *app* s, H3), 4.07 (2H, t, *J* 6.9 Hz, H2), 4.24 (2H, *app* s, H1), 7.15 (1H, s, NH), 7.37 (2H, dd, *J* 4.2, 5.2 Hz, H7), 7.86 (2H, dd, *J* 4.2, 5.2 Hz, H6). ¹³C NMR (CDCl₃); δ 21.6 (C9), 28.3 (C2), 67.7 (C1), 69.6 (C3), 128.4 (C6), 129.8 (C7), 135.1 (C8), 144.4 (C5), 162.0 (C4). FTIR (ν_{\max} cm⁻¹): 3288 (m, CH_x), 3165 (m, CH_x), 1319 (s, S=O), 1148 (s, C-N), 1088 (s, C=N). *R*_f 0.570 (30% EtOAc/hexanes). HRMS (XEVO G2-XS QToF) calculated for C₁₁H₁₅N₂O₃S [M+H]⁺ 255.0803, found: 255.0803.

7.2.7. Synthesis of spirocyclic dihydropyrazoles: 62, 69-86

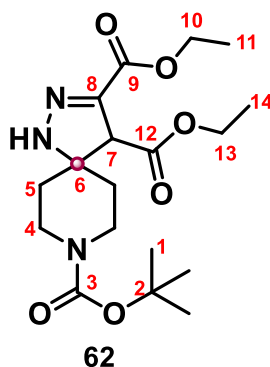
Compounds 77.1-77.6 were synthesised with general procedure T, but prior to this work, hence the full characterisation data can be found in this publication.¹⁶⁷

General procedure T: for synthesis of 62, 69-86.

Adapted from known procedure.^{167,191}

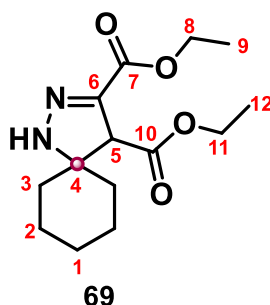
Sulfonylhydrazone (1.0 or 0.5 mmol, 1.0 equiv.), CsF (1.5 equiv.) and a magnetic stir bar were added to an oven-dried glass vial. The tube was evacuated and backfilled with nitrogen gas (x3 cycles) followed by addition of anhydrous DMSO (0.25 M with respect to sulfonylhydrazone) and the electron deficient alkene (1.5 equiv.). The vial was sealed with a PTFE-silicone cap and heated to 110 °C. Once the reaction was complete by TLC, the vial was allowed to cool to RT and the contents partitioned between EtOAc (50 or 25 mL) and water (50 or 25 mL), which was acidified with 1M HCl if needed. The organic phase was washed with water (50 or 25 mL) and the combined aqueous phases extracted with EtOAc (50 or 25 mL). The combined organic layers were washed with aqueous lithium chloride solution (5%, 4 x 20 or 10 mL), followed by brine (50 or 25 mL) before being dried over anhydrous MgSO₄ and solvents removed *in vacuo* to provide a crude residue which was purified by flash column chromatography (30% EtOAc/hexanes) to yield the title compound (18 – 78%).

* Note 2.5 equiv. of CsF was utilised for compound 85 synthesis.

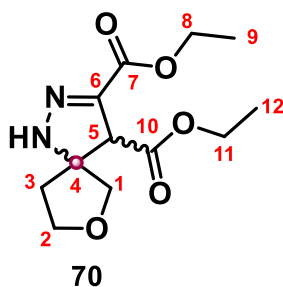


8-(tert-Butyl) 3,4-diethyl 1,2,8-triazaspiro[4.5]dec-2-ene-3,4,8-tricarboxylate (62).

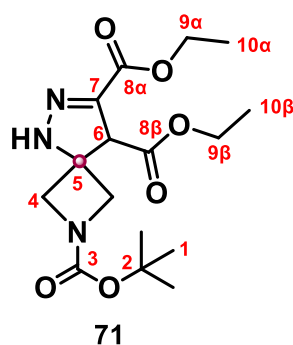
Isolated as a yellow oil (333 mg, 0.872 mmol, 87%) according to general procedure T. ^1H NMR (CDCl_3) δ 1.29 (3H, t, J 7.1 Hz, H14), 1.35 (3H, t, J 7.1 Hz, H11), 1.47 (9H, s, H1), 1.77 (4H, m, H5), 3.34 (2H, m, H4 $_{\alpha}$), 3.35 (2H, dt, J 5.2, 13.8 Hz, H4 $_{\beta}$), 3.78 (1H, s, H7), 4.23 (2H, dq, J 2.4, 6.8 Hz, H13), 4.32 (2H, dq, J 2.4, 6.8 Hz, H10), 6.33 (1H, s, NH). ^{13}C NMR (CDCl_3) δ 14.1 (C14), 14.2 (C11), 28.4 (C1), 31.7 (C5), 36.7 (C4) 57.9 (C7), 61.4 (C10), 61.5 (C13), 68.4 (C6), 80.1 (C2), 140.0 (C8), 154.5 (C3), 162.0 (C9), 168.2 (C12). R_f 0.440 (50% EtOAc/hexanes). FTIR (ν_{max} cm^{-1}) 2950 (w, CH_x), 1700 (s, C=O), 1300 (m, C-O), 1200 (m, C-N). HRMS (XEVO G2-XS QToF) calculated for $\text{C}_{18}\text{H}_{30}\text{N}_3\text{O}_6$ $[\text{M}+\text{H}]^+$ 384.2135, found: 384.2135.



Diethyl 1,2-diazaspiro[4.5]dec-2-ene-3,4-dicarboxylate (69). Isolated as a pale-yellow oil (168 mg, 0.595 mmol, 60%) according to general procedure T. ^1H NMR (CDCl_3) δ 1.29 (3H, t, J 7.1 Hz, H12), 1.35 (3H, t, J 7.1 Hz, H9), 1.47–1.72 (10H, m, H1 – H3), 3.72 (1H, s, H5), 4.22 (2H, m, H11), 4.31 (2H, m, H8), 6.32 (1H, s, NH). ^{13}C NMR (CDCl_3) δ 14.1 (C12), 14.2 (C9), 22.6 (C1), 32.1 (C2 $_{\alpha}$), 24.8 (C1/C2 $_{\beta}$), 37.6 (C3), 58.6 (C5), 61.1 (C8), 61.2 (C11), 70.2 (C4), 139.4 (C6), 162.4 (C7), 168.6 (C10). FTIR (ν_{max} cm^{-1}) 2978 (w, CH_x), 2866 (w, CH_x), 1732 (s, C=O), 1158 (m, C=N). R_f 0.500 (50% EtOAc/hexanes). HRMS (XEVO G2-XS QToF) calculated for $\text{C}_{14}\text{H}_{23}\text{N}_2\text{O}_4$ $[\text{M}+\text{H}]^+$ 283.1658, found: 283.1658.

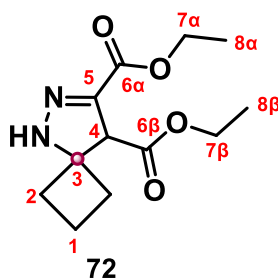


Diethyl 7-oxa-1,2-diazaspiro[4.4]non-2-ene-3,4-dicarboxylate (70). Isolated as a yellow oil (67.2 mg, 0.249 mmol, 25%) according to general procedure T. The compound is an approximate 5:4 mixture of diastereoisomers by ^1H NMR. ^1H NMR (CDCl_3) 1.268 (3H_{min}, t, J 7.1 Hz, H12_{min}), 1.270 (3H_{maj}, t, J 7.1 Hz, H12_{maj}), 1.325 (3H_{min}, t, J 7.1 Hz, H9_{min}), 1.327 (3H_{maj}, t, J 7.1 Hz, H9_{maj}), 2.09 (1H_{maj}, dddd, J 13.4, 7.8, 5.5, 0.9 Hz, H3 _{α ,maj}), 2.26 (1H_{maj} & 2H_{min}, m, H3 _{β ,maj} & H3 _{α & β ,min}), 3.56 (1H_{maj}, d, J 9.2 Hz, H1 _{α ,maj}), 3.64 (1H_{min}, d, J 9.7 Hz, H1 _{α ,min}), 3.79 (1H_{min}, d, J 9.7 Hz, H1 _{β ,min}), 3.85 (1H_{maj}, s, H5_{maj}), 3.86 (1H_{maj}, d, J 9.6 Hz, H1 _{β ,maj}), 3.88-4.04 (2H_{maj} & 2H_{min}, m, H2), 4.03 (1H_{min}, s, H5_{min}), 4.21 (2H_{maj} & 2H_{min}, app. quint., J 6.9 Hz, H11), 4.29 (2H_{maj} & 2H_{min}, m, H8), 6.67 (1H_{min}, br s, NH_{min}), 6.74 (1H_{maj}, br. s, NH_{maj}). ^{13}C NMR (CDCl_3) 14.09 (C12_{min}), 14.16 (C12_{maj}), 14.19 (C9), 33.3 (C3_{maj}), 39.9 (C3_{min}), 53.6 (C5_{maj}), 55.3 (C5_{min}), 61.33 (C8_{min}), 61.34 (C8_{maj}), 61.65 (C11_{maj}), 61.68 (C11_{min}), 66.5 (C2_{min}), 67.3 (C2_{maj}), 73.4 (C1_{min}), 75.8 (C4_{maj}), 75.9 (C4_{min}), 78.8 (C1_{maj}), 139.1 (C6_{min}), 139.3 (C6_{maj}), 161.7 (C7_{min}), 161.8 (C7_{maj}), 168.1 (C10_{min}), 168.3 (C10_{maj}). FTIR (ν_{max} cm^{-1}) 2981 (w, CH_x), 2937 (w, CH_x), 1703 (s, C=O), 1251 (m, C=N), 1169 (m, C-O). R_f 0.110 (30% EtOAc/hexanes). HRMS (XEVO G2-XS QToF) calculated for $\text{C}_{12}\text{H}_{19}\text{N}_2\text{O}_5$ $[\text{M}+\text{H}]^+$ 271.1294, found: 271.1294.



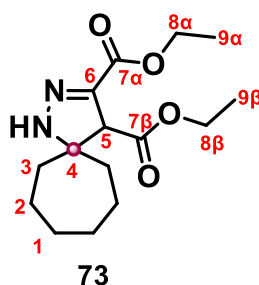
2-(tert-butyl) 7,8-diethyl (S)-2,5,6-triazaspiro[3.4]oct-6-ene-2,7,8-tricarboxylate (71).

Isolated as a viscous bright yellow oil (154 mg, 0.43 mmol, 43%) according to general procedure T. ^1H NMR (CDCl_3); δ 1.37 (6H, *app* q, J 10.8 Hz, H10), 1.46 (9H, s, H1), 2.93 (4H, s, H4), 4.16 (1H, s, H6) 4.33 (2H, q, J 7.1 Hz, H9 $_{\alpha}$), 4.41 (2H, q, J 7.1 Hz, H9 $_{\beta}$), 4.64 (1H, s, NH). ^{13}C NMR (CDCl_3); δ 14.0 (C10), 14.1 (C4), 28.2 (C1), 35.1 (C4), 42.0 (C6), 45.9 (C5), 60.8 (C10 $_{\alpha}$), 61.6 (C10 $_{\beta}$), 80.7 (C2), 144.8 (C7), 157.1 (C3), 162.3 (C8 $_{\beta}$), 162.7 (C8 $_{\alpha}$). FTIR (ν_{max} cm^{-1}) 2983 (w, CH $_x$), 1702 (s, C=O), 1216 (m, C=N), 1152 (m, C-O). R_f 0.028 (30% EtOAc/hexanes). HRMS (XEVO G2-XS QToF) calculated for $\text{C}_{17}\text{H}_{27}\text{N}_2\text{O}_6$ $[\text{M}+\text{H}]^+$ 356.1822, found: 356.1822.

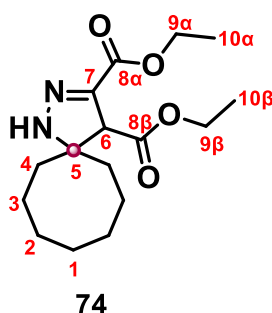


Diethyl 5,6-diazaspiro[3.4]oct-6-ene-7,8-dicarboxylate (72).

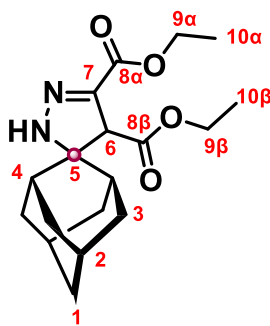
Isolated as a very viscous yellow oil (138 mg, 0.542 mmol, 54%) according to general procedure T. ^1H NMR (CDCl_3); δ 1.24 (3H, t, J 7.0 Hz, H8 $_{\alpha}$), 1.28 (3H, t, J 7.2 Hz, H8 $_{\beta}$), 1.76 (2H, q, J 8.4 Hz, H1), 2.24 (4H, m, H2), 3.93 (1H, s, H6), 4.18 (2H, q, J 6.9 Hz, H7 $_{\alpha}$), 4.24 (2H, q, J 5.4 Hz, H7 $_{\beta}$), 6.08 (1H, s, NH). ^{13}C NMR (CDCl_3); δ 13.8 (C1), 14.2 (C8 $_{\beta}$), 23.1 (C8 $_{\alpha}$), 31.9 (C2), 39.1 (C2), 58.1 (C6), 61.1 (C7 $_{\beta}$), 61.3 (C7 $_{\alpha}$), 70.7 (C3), 138.7 (C5), 162.3 (C6 $_{\beta}$), 168.7 (C6 $_{\alpha}$). FTIR (ν_{max} cm^{-1}) 2980 (w, CH $_x$), 2937 (w, CH $_x$), 1703 (s, C=O), 1285 (s, C-N), 1168 (m, C-O). R_f 0.474 (30% EtOAc/hexanes). HRMS (XEVO G2-XS QToF) calculated for $\text{C}_{12}\text{H}_{19}\text{N}_2\text{O}_4$ $[\text{M}+\text{H}]^+$ 255.1345, found: 255.1345.



Diethyl 1,2-diazaspiro[4.6]undec-2-ene-3,4-dicarboxylate (73). Isolated as a pale-yellow oil (198 mg, 0.668 mmol, 67%) according to general procedure T. ^1H NMR (CDCl_3); δ 1.52 (3H, t, J 7.1 Hz, $\text{H}_{9\alpha}$), 1.30 (3H, t, J 7.1 Hz, $\text{H}_{9\beta}$), 1.48-1.64 (8H, m, H_1 & H_2), 1.69-1.90 (4H, m, H_3), 3.88 (1H, s, H_5), 4.17 (2H, m, $\text{H}_{8\alpha}$), 4.26 (2H, m, $\text{H}_{8\beta}$). ^{13}C NMR (CDCl_3) δ 14.1 ($\text{C}_{9\alpha}$), 14.2 ($\text{C}_{9\beta}$), 26.2 ($\text{C}_{2\alpha}$), 26.5 ($\text{C}_{2\beta}$), 33.2 ($\text{C}_{1\alpha}$), 34.3 ($\text{C}_{1\beta}$), 34.65 ($\text{C}_{3\alpha}$), 37.3 ($\text{C}_{3\beta}$), 59.6 (C_5), 61.0 ($\text{C}_{8\beta}$), 61.1 ($\text{C}_{8\alpha}$), 79.9 (C_4), 139.0 (C_6), 162.4 ($\text{C}_{7\alpha}$), 169.0 ($\text{C}_{7\beta}$). FTIR main stretches (cm^{-1}): 3005 (w, CH_x), 2824 (w, CH_x), 1683 (s, $\text{C}=\text{O}$), 1024 (s, $\text{C}=\text{N}$). R_f 0.098 (30% EtOAc/hexanes). HRMS (XEVO G2-XS QToF) calculated for $\text{C}_{18}\text{H}_{27}\text{N}_2\text{O}_4$ $[\text{M}+\text{H}]^+$ 335.1971, found: 335.1971.

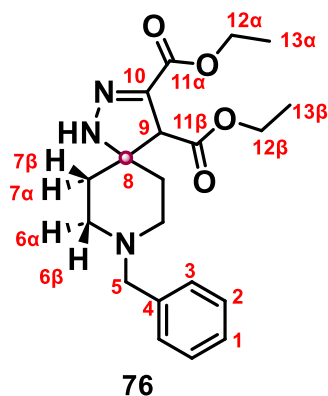


Diethyl 1,2-diazaspiro[4.7]dodec-2-ene-3,4-dicarboxylate (74). Isolated as a pale-yellow oil (180 mg, 0.58 mmol, 58%) according to general procedure T. ^1H NMR (CDCl_3) δ 1.25 (3H, t, J 7.1 Hz, $\text{H}_{10\beta}$), 1.30 (3H, t, J 7.1 Hz, $\text{H}_{10\alpha}$), 1.44-1.65 (8H, br m, H_2 & H_3), 1.68-1.98 (6H, br m, H_1 & H_4), 2.02 (1H, s, NH), 3.69 (1H, s, H_6), 4.17 (2H, m, $\text{H}_{9\beta}$), 4.25 (2H, m, $\text{H}_{9\alpha}$). ^{13}C NMR (CDCl_3) δ 14.1 ($\text{C}_{10\beta}$), 14.2 ($\text{C}_{10\alpha}$), 21.9 ($\text{C}_{3\alpha}$), 22.7 ($\text{C}_{3\beta}$), 29.1 ($\text{C}_{2\alpha}$), 29.4 ($\text{C}_{2\beta}$), 35.2 (C_1), 41.6 (C_4), 59.7 (C_6), 61.0 ($\text{C}_{9\alpha}$), 61.2 ($\text{C}_{9\beta}$), 74.0 (C_5), 138.8 (C_7), 162.4 ($\text{C}_{8\alpha}$), 168.8 ($\text{C}_{8\beta}$). R_f 0.590 (50% EtOAc/hexanes). FTIR (ν_{max} cm^{-1}) 2983 (w, CH_x), 2857 (w, CH_x), 1730 (s, $\text{C}=\text{O}$), 1021 (m, $\text{C}=\text{N}$). HRMS (XEVO G2-XS QToF) calculated for $\text{C}_{16}\text{H}_{27}\text{N}_2\text{O}_4$ $[\text{M}+\text{H}]^+$ 311.1698, found: 311.1698.

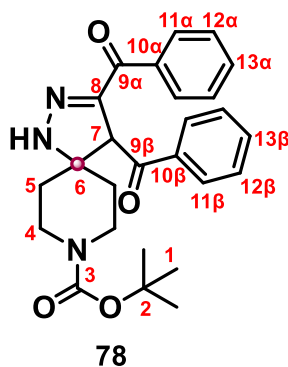


75

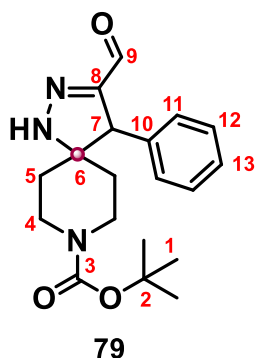
Diethyl (1*r*,3*r*,5*r*,7*r*)-2',4'-dihydrospiro[adamantane-2,3'-pyrazole]-4',5'-dicarboxylate (75). Isolated as a viscous yellow oil (60.0 mg, 0.180 mmol, 18%) according to general procedure T. ^1H NMR (CDCl_3) δ 1.20 (3H, t, J 7.1 Hz, $\text{H}_{10\alpha}$), 1.26 (3H, t, J 7.1 Hz, $\text{H}_{10\beta}$), 1.71 (7H, q, $\text{H}_{1\alpha}$ & $\text{H}_{3\alpha}$), 1.83 (4H, t, H_2 & H_4), 1.92 (2H, q, J 12.4 Hz, $\text{H}_{3\beta}$), 2.05 (1H, s, $\text{H}_{1\alpha}$), 3.87 (1H, s, H_6), 4.12 (2H, m, $\text{H}_{9\alpha}$), 4.21 (2H, m, $\text{H}_{9\beta}$). 9.13 (1H, s, NH). ^{13}C NMR (CDCl_3) δ 14.0 ($\text{C}_{10\alpha}$), 14.2 ($\text{C}_{10\beta}$), 26.2 (C_2), 26.5 (C_2), 32.9 (C_3), 33.2 (C_3), 33.3 (C_3), 34.3 (C_3), 34.7 (C_1), 37.3 (C_4), 56.6 (C_5), 61.0 ($\text{C}_{9\alpha}$), 61.1 ($\text{C}_{9\beta}$), 75.9 (C_6), 139.0 (C_7), 162.4 ($\text{C}_{8\alpha}$), 169.0 ($\text{C}_{8\beta}$). FTIR (ν_{max} cm^{-1}) 2981 (w, CH_x), 2933 (w, CH_x), 2859 (w, CH_x), 1722 (s, $\text{C}=\text{O}$), 1021 (m, $\text{C}=\text{N}$). R_f 0.500 (50% EtOAc/hexanes). HRMS (XEVO G2-XS QToF) calculated for $\text{C}_{15}\text{H}_{24}\text{N}_2\text{O}_4$ $[\text{M}+\text{H}]^+$ 297.1814, found: 297.1814.



Diethyl (*S*)-8-benzyl-1,2,8-triazaspiro[4.5]dec-2-ene-3,4-dicarboxylate (76). Isolated as a very viscous dark orange oil (210 mg, 0.561 mmol, 28%), according to general procedure T. ^1H NMR (CDCl_3); δ 1.25 (3H, t, J 7.1 Hz, $\text{H}_{13\alpha}$), 1.31 (3H, t, J 7.2 Hz, $\text{H}_{13\beta}$), 1.8 (4H, m, H_7), 2.4 (2H, *app* br. s, $\text{H}_{6\alpha}$), 2.7 (2H, *app* br. s, $\text{H}_{6\beta}$), 3.6 (2H, s, H_5), 3.7 (1H, s, H_9), 4.2 (2H, q, J 7.0 Hz, $\text{H}_{12\beta}$), 4.3 (2H, *app* t, J 6.2 Hz, $\text{H}_{12\alpha}$), 6.7 (1H, s, NH), 7.27 (1H, m, H_1), 7.32 (4H, *app* d, H_2 & H_3). ^{13}C NMR (CDCl_3); δ 14.18 ($\text{C}_{13\alpha}$), 14.23 ($\text{C}_{13\beta}$), 31.7 ($\text{C}_{7\text{x}}$), 36.9 ($\text{C}_{7\text{y}}$), 49.5 ($\text{C}_{6\text{x}}$), 50.2 ($\text{C}_{6\text{y}}$), 58.1 (C_{10}), 61.2 ($\text{C}_{12\alpha}$), 61.3 ($\text{C}_{12\beta}$), 62.7 (C_5), 68.2 (C_8), 127.4 (C_1), 128.4 (C_2), 129.2 (C_3), 137.3 (C_4), 139.4 (C_9), 162.2 ($\text{C}_{11\alpha}$), 168.4 ($\text{C}_{11\beta}$). R_f 0.176 (30% EtOAc/hexanes). FTIR (ν_{max} cm^{-1}) 2978 (w, CH_x), 2806 (w, CH_x (aromatic)), 1730 (s, C=O), 1350 (m, C-O), 1270 (m, C-N). HRMS (XEVO G2-XS QTof) calculated for $\text{C}_{20}\text{H}_{28}\text{N}_3\text{O}_4$ $[\text{M}+\text{H}]^+$ 374.2080, found: 374.2080.

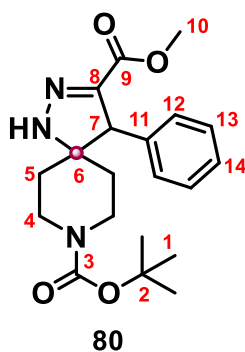


tert-Butyl 3,4-dibenzoyl-1,2,8-triazaspiro[4.5]dec-2-ene-8-carboxylate (78). Isolated as a dark red amorphous solid (53.2 mg, 0.119 mmol, 45%) according to general procedure T. ^1H NMR (CDCl_3) δ 1.44 (9H, s, H1), 1.65 (1H, br m, H5 $_{\alpha 1}$), 1.77 (1H, br m, H5 $_{\alpha 2}$), 1.90 (2H, br m, H5 $_{\beta}$), 3.09 (1H, br m, H4 $_{\alpha 1}$), 3.26 (1H, br m, H4 $_{\beta 1}$), 3.59 (1H, br d, H4 $_{\alpha 2}$), 3.86 (1H, br. H4 $_{\beta 2}$), 5.07 (1H, s, H7), 6.84 (1H, br s, NH), 7.44 (2H, t, J 7.6 Hz, H12 $_{\alpha}$), 7.54 (3H, t, H12 $_{\beta}$ & H13 $_{\alpha}$), 7.65 (1H, t, J 7.3 Hz, H13 $_{\beta}$), 8.06 (2H, d, J 7.5 Hz, H11 $_{\beta}$), 8.17 (2H, d, J 7.3 Hz, H11 $_{\alpha}$). ^{13}C NMR (CDCl_3) δ 28.3 (C1), 31.8 (C5 $_{\alpha}$), 37.2 (C5 $_{\beta}$), 40.0 (br. C4 $_{\beta}$), 41.5 (br. C4 $_{\alpha}$), 58.9 (C7), 67.9 (C6), 80.2 (C2), 128.1 (C12 $_{\alpha}$), 128.6 (C11), 129.0 (C12 $_{\beta}$), 130.0 (C13 $_{\beta}$), 132.6 (C13 $_{\alpha}$), 133.7 (C10 $_{\beta}$), 136.5 (C5), 137.3 (C10 $_{\alpha}$), 149.8 (C8), 154.5 (C3), 186.9 (C9 $_{\alpha}$), 196.0 (C9 $_{\beta}$). R_f 0.450 (30% EtOAc/hexanes). FTIR (ν_{max} cm^{-1}) 2974 (w, CH_x), 2867 (w, CH_x), 1673 (s, C=O), 1276 (m, C=N), 1156 (m, C-O). HRMS (XEVO G2-XS QTof) calculated for $\text{C}_{26}\text{H}_{30}\text{N}_3\text{O}_4$ $[\text{M}+\text{H}]^+$ 448.2236, found: 448.2236.

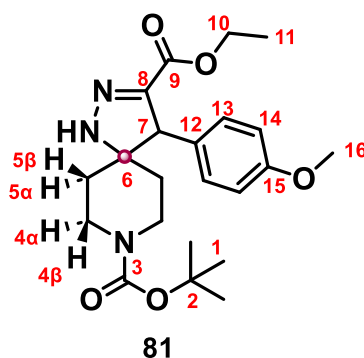


tert-Butyl 3-formyl-4-phenyl-1,2,8-triazaspiro[4.5]dec-2-ene-8-carboxylate (79).

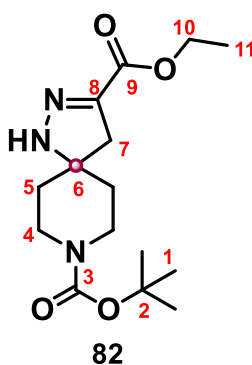
Isolated as an orange amorphous solid (183 mg, 0.534 mmol, 54%) according to general procedure T. ^1H NMR (CDCl_3) δ 1.28 (2H, app. q, J 6.7 Hz, H5_α), 1.35 (9H, s, H1), 1.64 (2H, t, J 5.4 Hz, H5_β), 3.16 (2H, m, H4_α), 3.41 (1H, m, $\text{H4}_{\beta 1}$), 3.54 (1H, m, $\text{H4}_{\beta 2}$), 3.98 (1H, s, H7), 6.87 (1H, s, NH), 6.96 (2H, br d, J 6.9 Hz, H13), 7.21 (4H, m, H11 & H12), 9.67 (1H, s, H9). ^{13}C NMR (CDCl_3) δ 28.4 (C1), 30.9 (C5_α), 36.3 (C5_β), 39.8 (br. C4_β), 41.2 (br. C4_α), 54.8 (C7), 69.0 (C6), 80.0 (C2), 127.7 (C13), 128.5 (br. C11), 128.8 (C12), 134.4 (C10), 153.4 (C8), 154.5 (C3), 186.4 (C9). R_f 0.590 (30% EtOAc/hexanes). FTIR (ν_{max} cm^{-1}) 2967 (w, CH_x), 2922 (w, CH_x), 2863 (w, CH_x (aromatic)), 1655 (s, C=O), 1244 (m, C-O), 1156 (m, C-N). HRMS (XEVO G2-XS QTof) calculated for $\text{C}_{19}\text{H}_{26}\text{N}_3\text{O}_3$ $[\text{M}+\text{H}]^+$ 344.1974, found: 344.1974.



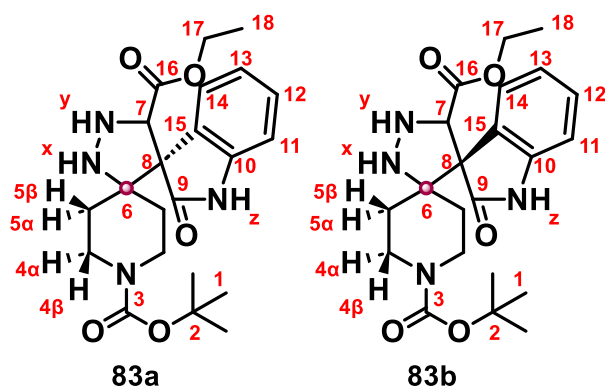
8-(tert-Butyl) 3-methyl 4-phenyl-1,2,8-triazaspiro[4.5]dec-2-ene-3,8-dicarboxylate (80). Isolated as an orange amorphous solid (77.5 mg, 0.208 mmol, 21%) according to general procedure T. ^1H NMR (CDCl_3) δ 1.34 (2H, m, $\text{H}_{5\alpha}$), 1.42 (9H, s, H1), 1.73 (2H, m, $\text{H}_{5\beta}$), 3.22 (2H, m, $\text{H}_{4\alpha}$), 3.55 (2H, m, $\text{H}_{4\beta}$) 3.74 (3H, s, H10), 4.03 (1H, s, H7), 6.25 (1H, br. NH), 7.10 (2H, br d, J 7.1 Hz, H12), 7.30 (3H, m, H13 & H14). ^{13}C NMR (CDCl_3) δ 28.4 (C1), 31.0 ($\text{C}_{5\alpha}$), 36.2 ($\text{C}_{5\beta}$), 40.0 ($\text{C}_{4\beta}$), 41.1 ($\text{C}_{4\alpha}$), 52.1 (C10), 57.5 (C7), 68.2 (C6), 79.9 (C2), 127.8 (C14), 128.6 (C12), 128.8 (C13), 134.8 (C11), 145.2 (C8), 154.5 (C3), 162.7 (C9). R_f 0.20 (30% EtOAc/hexanes). FTIR (ν_{max} cm^{-1}) 2974 (w, CH_x), 2930 (w, CH_x), 1685 (s, C=O), 1234 (m, C-N), 1163 (m, C-O). HRMS (XEVO G2-XS QTof) calculated for $\text{C}_{20}\text{H}_{28}\text{N}_3\text{O}_4$ $[\text{M}+\text{H}]^+$ 374.2080, found: 374.2080.



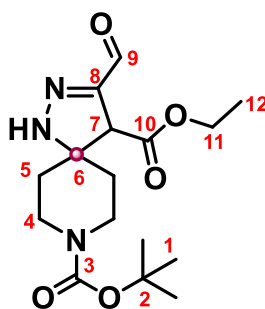
8-(tert-butyl) 3-ethyl 4-(4-methoxyphenyl)-1,2,8-triazaspiro[4.5]dec-2-ene-3,8-dicarboxylate (81). Isolated as pale-yellow solid (89.1 mg, 0.213 mmol, 21%), according to general procedure T. ^1H NMR (CDCl_3); δ 1.26 (3H, t, J 2.4 Hz, H11), 1.44 (9H, s, H1), 1.73 (4H, m, H5), 2.05 (1H, s, NH), 3.23 (2H, t, J 4.6 Hz, H4 $_{\alpha}$), 3.52 (1H, q, J 4.3 Hz, H4 $_{\beta 1}$), 3.60 (1H, q, J 4.3 Hz, H4 $_{\beta 2}$), 3.80 (3H, s, H16), 4.01 (1H, s, H7), 4.20 (2H, q, J 6.1 Hz, H10), 6.84 (2H, d, J 8.8 Hz, H14), 7.02 (2H, d, J 8.0 Hz, H13). ^{13}C NMR (CDCl_3); δ 14.1 (C11), 28.4 (C1), 36.1 (C5), 39.6 (C4), 41.3 (C4), 55.2 (C16), 56.8 (C7), 61.1 (C10), 67.8 (C6), 80.0 (C2), 114.12 (C14), 126.89 (C12), 146.29 (C8), 129.6 (C13), 154.6 (C9), 159.0 (C3), 159.2 (C15). R_f 0.070 (30% EtOAc/hexanes). FTIR (ν_{max} cm^{-1}): 2975 (w, CH_x), 2935 (w, CH_x), 1693 (s, C=O), 1246 (m, C-N), 1157 (m, C-O). HRMS (XEVO G2-XS QToF) calculated for $\text{C}_{22}\text{H}_{29}\text{N}_4\text{O}_5$ $[\text{M}+\text{H}]^+$ 416.2078, found: 416.2078.



8-(tert-Butyl) 3-ethyl 1,2,8-triazaspiro[4.5]dec-2-ene-3,8-dicarboxylate (82). Isolated as a viscous orange oil (163 mg, 0.530 mmol, 53%) according to general procedure T. ^1H NMR (CDCl_3) δ 1.27 (3H, t, J 7.1 Hz, H11), 1.39 (9H, s, H1), 1.61 (4H, m, H5), 2.74 (2H, s, H7), 3.12 (2H, qd, J 3.7, 9.1 Hz, H4 $_{\alpha}$), 3.64 (2H, m, H4 $_{\beta}$), 6.08 (1H, s, NH). ^{13}C NMR (CDCl_3); δ 14.3 (C11), 28.4 (C1), 35.9 (C5), 40.7 (C4), 40.9 (C7), 61.2 (C10), 66.3 (C2), 79.9 (C6), 141.5 (C8), 154.5 (C9), 162.8 (C3). R_f 0.579 (30% EtOAc/hexanes). FTIR (ν_{max} cm^{-1}) 2974 (w, CH_x), 2933 (w, CH_x), 1689 (s, C=O), 1241 (s, C=N), 1152 (s, C-O). HRMS (XEVO G2-XS QToF) calculated for $\text{C}_{15}\text{H}_{26}\text{N}_3\text{O}_4$ $[\text{M}+\text{H}]^+$ 340.1794, found: 340.1794.

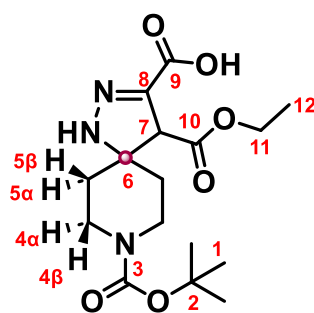


1''-(tert-butyl) 5'-ethyl 2-oxo-2'H-dispiro[indoline-3,4'-pyrazole-3',4''-piperidine]-1'',5'-dicarboxylate (83). Isolated as a viscous orange oil (52.0 mg, 0.121 mmol, 24%) according to general procedure T. The compound is an approximate 1:1 mixture of diastereoisomers by ^1H NMR. ^1H NMR (CDCl_3) δ 1.19 (3H, t, J 7.1 Hz, H16 $_{\beta}$, both), 1.27 (3H, t, J 7.1 Hz, H16 $_{\alpha}$, both), 1.32 (9H, s, H1 $_{\beta}$, both), 1.39 (9H, s, H1 $_{\alpha}$, both), 1.77 (2H, br. s, H5 $_{\alpha, a}$), 1.98 (2H, s, H7), 2.26 (2H, br. s, H5 $_{\alpha, b}$), 3.08 (2H, m, H4 $_{\alpha, a}$), 3.41 (2H, br. s, H4 $_{\alpha, b}$), 3.62 (2H, br. s, H4 $_{\beta, a}$), 3.85 (2H, t, J 3.2 Hz, H4 $_{\beta, b}$), 4.05 (2H, q, J 7.16 Hz, H17 $_{\beta}$, both), 4.25 (2H, m, H17 $_{\alpha}$, both), 4.29 (4H, dd, J 4.88, 11.7 Hz H5 $_{\beta}$, both), 5.38 (2H, s, NH $_x$), 5.60 (2H, s, NH $_y$), 6.70 (2H, d, J 7.7 Hz, H14), 6.90 (3H, dd, H12 $_{\alpha}$, both & H13), 7.09 (3H, t, H11 & H12 $_{\beta}$, both), 8.57 (2H, s, NH $_z$). ^{13}C NMR (CDCl_3); δ 13.9 (C18 $_b$), 14.2 (C18 $_a$), 21.1 (C7), 27.8 (C5), 28.4 (C1 $_b$), 28.5 (C1 $_a$), 47.2 (C4 $_a$), 50.1 (C4 $_b$), 61.4 (C17), 79.6 (C2), 108.3 (C13), 123.0 (C14), 124.5 (C11), 129.6 (C8), 130.6 (C12), 143.5 (C10), 170.8 (C9), 171.1 (C3), 177.0 (C16). R_f 0.145 (30% EtOAc/hexanes). FTIR (ν_{max} cm^{-1}) 2974 (w, CH $_x$), 2930 (w, CH $_x$), 1689 (s, C=O), 1156 (m, C-O). HRMS (XEVO G2-XS QTof) calculated for $\text{C}_{22}\text{H}_{31}\text{N}_4\text{O}_5$ $[\text{M}+\text{H}]^+$ 431.2294, found: 431.2294.



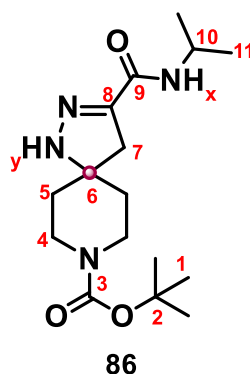
84

8-(tert-butyl) 3-ethyl (S)-4-formyl-1,2,8-triazaspiro[4.5]dec-2-ene-3,8-dicarboxylate (84). Isolated as a viscous orange oil (168 mg, 0.484 mmol, 48%) according to general procedure T. ^1H NMR (CDCl_3) δ 1.28 (3H, t, J 7.2 Hz, H12), 1.47 (9H, s, H1), 1.80 (4H, m, H5), 2.06 (1H, s, H9), 3.04 (2H, dt, J 2.9, 10.0 Hz, H5 $_{\alpha}$), 3.85 (2H, m, H5 $_{\beta}$), 4.20 (2H, q, J 3.2 Hz, H11), 7.00 (1H, s, NH), 9.71 (1H, s, H9). ^{13}C NMR (CDCl_3); δ 14.1 (C12), 21.1 (C7), 28.4 (C1), 34.2 (C5), 41.2 (C4), 61.7 (C11), 67.8 (C6), 79.6 (C2), 147.8 (C8), 154.8 (C10), 167.8 (C3), 185.9 (C8). R_f 0.056 (30% EtOAc/hexanes). FTIR (ν_{max} cm^{-1}) 2974 (w, CH_x), 2930 (w, CH_x), 1674 (s, C=O), 1238 (m, C=N), 1156 (m, C-O). HRMS (XEVO G2-XS QTof) calculated for $\text{C}_{16}\text{H}_{26}\text{N}_3\text{O}_5$ $[\text{M}+\text{H}]^+$ 340.1794, found: 340.1794.



85

(S)-8-(tert-butoxycarbonyl)-3-(ethoxycarbonyl)-1,2,8-triazaspiro[4.5]dec-2-ene-4-carboxylic acid (85). Isolated as a yellow gum (40.2 mg, 0.113 mmol, 11%) according to general procedure T. ^1H NMR (CDCl_3) δ 1.35 (3H, J 4.1 Hz, H12), 1.48 (9H, s, H1), 1.72 (4H, m, H5 $_{\text{both}}$), 2.07 (1H, s, NH), 2.83 (1H, s, H7), 3.31 (2H, td, J 3.4, 13.8 Hz, H4 $_{\alpha}$), 3.74 (2H, m, H4 $_{\beta}$), 4.30 (2H, q, J 7.1 Hz, H11), 6.91 (1H, *app* q, J 11.6 Hz, OH). ^{13}C NMR (CDCl_3) δ 14.3 (C12), 28.4 (C1), 35.9 (C5), 40.7 (C7), 40.8 (C4), 61.2 (C11), 66.3 (C6), 80.0 (C2), 141.6 (C8), 154.5 (C3), 162.8 (C9), 164.1 (C10). R_f 0.113 (30% EtOAc/hexanes). FTIR (ν_{max} cm^{-1}) 3321 (br. OH), 2974 (w, CH_x), 2930 (w, CH_x), 1684 (s, C=O), 1241 (C=N), 1156 (C-O). HRMS (XEVO G2-XS QTof) calculated for $\text{C}_{16}\text{H}_{26}\text{N}_3\text{O}_5$ $[\text{M}+\text{H}]^+$ 356.1822, found: 356.1822.



tert-butyl 3-(isopropylcarbamoyl)-1,2,8-triazaspiro[4.5]dec-1-ene-8-carboxylate (86).

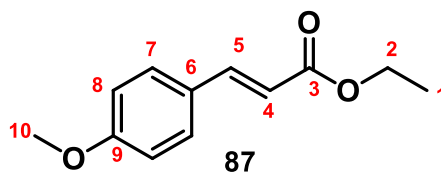
Isolated as an amorphous yellow powder (210 mg, 0.646 mmol, 65%) according to general procedure T. ^1H NMR (CDCl_3); δ 1.18 (6H, d, J 6.56 Hz, H11), 1.46 (9H, s, H1), 2.27 (1H, s, NH_x), 2.41 (4H, t, J 6.24 Hz, H5), 3.69 (4H, t, J 6.20 Hz, H4), 4.02 (1H, m, H10), 6.99 (1H, br. s, NH_y), 7.05 (1H, s, H7_a), 7.12 (1H, s, H7_b). ^{13}C NMR (CDCl_3); δ 22.4 (C10), 28.3 (C1), 37.0 (C5), 41.1 (C6), 41.6 (C10), 42.9 (C4), 80.4 (C2), 116.4 (C7), 154.4 (C8), 164.9 (C3), 186.3 (C9). R_f 0.704 (30% EtOAc/hexanes). FTIR (ν_{max} cm^{-1}) 2974 (w, CH_x), 1655 (s, C=O), 1148 (s, C-O). HRMS (XEVO G2-XS QTof) calculated for $\text{C}_{16}\text{H}_{29}\text{N}_4\text{O}_3$ $[\text{M}+\text{H}]^+$ 325.2263, found 325.2263.

7.2.8. Synthesis of alkenes for spirocycle synthesis: 87 and 88.

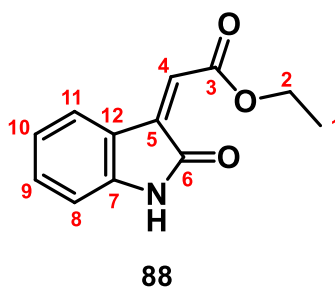
General procedure U: for synthesis of 87 and 88

Adapted from a known procedure.¹⁹⁶

To a soln. of Aldehyde (4.0 mmol, 1.0 equiv.) in toluene (10 mL) was added a soln. of (Carbethoxymethylene)triphenyl phosphorane (4.8 mmol, 1.2 equiv.) in toluene (20 mL), and the soln. was then refluxed overnight (at 115 °C), or until completion observed by TLC. After accomplishment of the reaction monitored by TLC, the soln. was allowed to reach RT, and concentrated *in vacuo*. The residue was treated with Et_2O (25 mL), and then the resultant white precipitate (Wittig salt by-product) was removed by filtration. Filtrate washed with 5x 20 mL of deionised water, combined aq layer extracted with 25mL of Et_2O . Organic layer dried with 2 x 25 mL brine, followed by over anhydrous MgSO_4 and solvents removed *in vacuo* to provide a crude residue which was purified by flash column chromatography (30% EtOAc/hexanes) to yield the title compound (38 - 39%).



Ethyl (E)-3-(4-methoxyphenyl)acrylate (87). Isolated as a dry yellow solid (320 mg, 1.55 mmol, 39%) according to general procedure U. ^1H NMR (CDCl_3); δ 1.35 (3H, t, J 7.1 Hz, H1), 3.85 (3H, s, H10), 4.27 (2H, q, J 7.1 Hz, H2), 6.32 (1H, d, J 15.9 Hz, H4), 6.92 (2H, d, J 12.8 Hz, H8), 7.49 (2H, d, J 8.7 Hz, H7), 7.66 (1H, d, J 16.0 Hz, H5). ^{13}C NMR (CDCl_3); δ 14.37 (C1), 55.39 (C10), 60.3461 (C2), 114.31 (C8), 115.76 (C4), 127.21 (C6), 129.70 (C7), 144.26 (C5), 161.33 (C9), 167.37 (C3). FTIR (ν_{max} cm^{-1}) 2934 (w, CH_x), 2978 (w, CH_x), 2840 (w, CH_x), 1700 (s, C=O), 1286 (s, C-O). R_f 0.208 (30% EtOAc/hexanes). HRMS (XEVO G2-XS QToF) calculated for $\text{C}_{12}\text{H}_{15}\text{O}_3$ $[\text{M}+\text{H}]^+$ 207.1021, found: 207.1021.



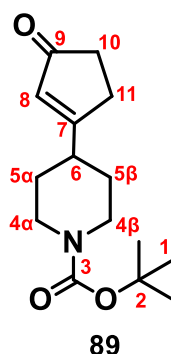
Ethyl (Z)-2-(2-oxoindolin-3-ylidene)acetate (88). Isolated as a light orange powder (334 mg, 1.54 mmol, 38%) according to general procedure U. ^1H NMR (CDCl_3); δ 1.41 (3H, t, J 7.1 Hz, H1), 1.68 (1H, s, NH), 4.43 (2H, q, J 7.1 Hz, H2), 6.79 (1H, dd, J 0.6, 7.8 Hz, H8), 7.02 (1H, dd, J 0.7, 8.2 Hz, H10), 7.23 (1H, t, J 8.0 Hz, H9), 7.53 (1H, s, H4), 8.31 (1H, *app* s, H11). ^{13}C NMR (CDCl_3); δ 14.2 (C1), 61.2 (C2), 109.9 (C8), 122.7 (C4), 123.0 (C10), 129.2 (C11), 132.5 (C9), 143.1 (C5), 143.5 (C7), 150.4 (C12), 165.3 (C3), 168.5 (C6). FTIR (ν_{max} cm^{-1}) 2981, (w, CH_x), 2929 (w, CH_x), 2856 (w, CH_x), 1707 (s, C=O), 1091 (s, C-O), 1025.54 (s, C-N). R_f 0.390 (30% EtOAc/hexanes). HRMS (XEVO G2-XS QToF) calculated for $\text{C}_{12}\text{H}_{12}\text{NO}_3$ $[\text{M}+\text{H}]^+$ 218.0835, found: 218.0835.

7.2.9. Synthesis of piperidinyls (C-C bond formation): 89 and 90

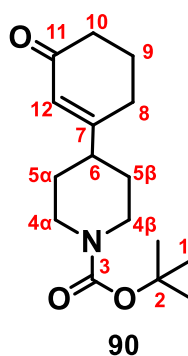
General procedure T.1: for synthesis of **89** and **90**.

Adapted from known procedure.^{167,191}

Sulfonylhydrazone (1.0 mmol, 1.0 equiv.), CsF (1.5 mmol, 1.5 equiv.) and a magnetic stir bar were added to an oven-dried glass vial. The tube was evacuated and backfilled with nitrogen gas (x3 cycles) followed by addition of anhydrous DMSO (0.25 M with respect to sulfonylhydrazone) and a cyclic enol (1.5 mmol, 1.5 equiv.). The vial was sealed with a PTFE-silicone cap and heated to 110 °C. Once the reaction was complete by TLC, the vial was allowed to cool to RT and the contents partitioned between EtOAc (50 mL) and water (50 mL). The organic phase was washed with water (50 or 25 mL) and the combined aqueous phases extracted with EtOAc (50 or). The combined organic layers were washed with aqueous 5% lithium chloride solution (4 x 20 mL), followed by brine (50 mL) before being dried over anhydrous MgSO₄ and solvents removed *in vacuo* to provide a crude residue which was purified by flash column chromatography (30% EtOAc/hexanes) to yield the title compound (26 – 47%).

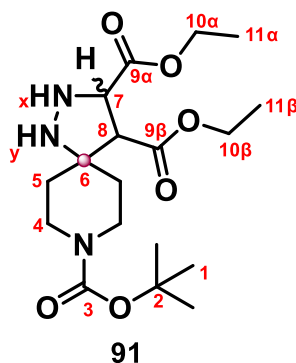


tert-Butyl 4-(3-oxocyclopent-1-en-1-yl)piperidine-1-carboxylate (89). Isolated as a viscous yellow/orange oil (125 mg, 0.47 mmol, 47%), according to general procedure T.1. ¹H NMR (CDCl₃); δ 1.42 (11H, *app* t, H1 & H5_β), 1.81 (2H, d, *J* 12.3 Hz, H5_α), 2.38 (2H, d, *J* 3.2 Hz, H10), 2.44 (1H, d, *J* 11.6 Hz, H6), 2.58 (2H, d, *J* 3.8 Hz, H11), 2.74 (2H, t, *J* 12.9 Hz, H4_β), 4.16 (2H, s, H4_α), 5.90 (1H, s, H8). ¹³C NMR (CDCl₃); δ 28.4 (C1), 29.4 (C11) 30.1 (C5), 35.0 (C10), 40.0 (C6), 43.6 (C4), 79.7 (C2), 128.5 (C8), 154.6 (C3), 184.7 (C7), 209.19 (C9). *R*_f 0.113 (30% EtOAc/hexanes. FTIR (*v*_{max} cm⁻¹) 2974 (w, CH_x), 2926 (w, CH_x), 2855 (w, CH_x), 1677 (s, C=O), 1230 (m, C-N), 1169 (s, C-O). HRMS (XEVO G2-XS QToF) calculated for C₁₅H₂₄NO₃ [M+H]⁺ 270.1461, found: 270.1461.



tert-Butyl 4-(3-oxocyclohex-1-en-1-yl)piperidine-1-carboxylate (90). Isolated as a yellow oil (73.1 mg, 0.262 mmol, 26%). according to general procedure T.1. ^1H NMR (CDCl_3); δ 1.42 (11H, *app* s, H1, H5 $_{\alpha}$), 1.69 (2H, d, J 12.9 Hz, H5 $_{\beta}$), 1.95 (2H, t, J 6.4 Hz, H8), 2.16 (1H, t, J 11.9 Hz, H6), 2.27 (2H, t, J 6.4 Hz, H7), 2.33 (2H, t, J 7.1 Hz, H9), 2.68 (2H, t, J 11.4 Hz, H4 $_{\alpha}$), 4.16 (2H, br. s, H4 $_{\beta}$), 5.82 (1H, s, H12). ^{13}C NMR (CDCl_3); δ 22.8 (C9), 28.1 (C8), 28.4 (C1), 29.9 (C5), 37.5 (C10), 43.8 (C4), 44.1 (C6), 79.6 (C2), 124.6 (C12), 154.7 (C3), 168.3 (C7), 206.5 (C11). R_f 0.169 (30% EtOAc/hexanes). FTIR (ν_{max} cm^{-1}) 2933 (w, CH_x), 2863 (w, CH_x), 1666 (s, C=O), 1230 (m, C-N), 1163 (s, C-O). HRMS (XEVO G2-XS QTof) calculated for $\text{C}_{16}\text{H}_{26}\text{NO}_3$ $[\text{M}+\text{H}]^+$ 281.1991 found: 281.1991.

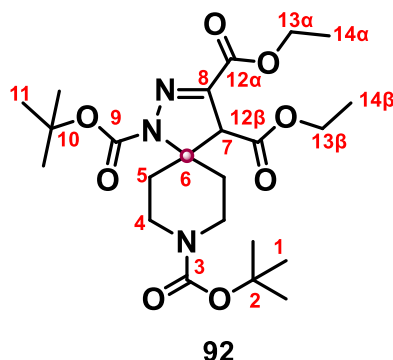
7.2.10. Spirocycle Functionalisation: 91-97

8-(*tert*-butyl) 3,4-diethyl (4*R*)-1,2,8-triazaspiro[4.5]decane-3,4,8-tricarboxylate (91).**Procedure V:** for synthesis of **91**.Adapted from a known procedure.¹⁹⁷

To a solution of compound **62** (191 mg, 0.50 mmol, 1.0 equiv.) in hexane (5.0 mL) at 0 °C was added sodium cyanoborohydride (19 mg, 1.0 mmol, 1.5 equiv.) over 10 minutes. Once addition was complete, the reaction mixture was allowed to warm to RT and stirred until completion was observed by TLC. The solvent was removed *in vacuo* and the residue dissolved in EtOAc (10 mL) and washed repeatedly with water (3 x 10 mL), and subsequently with sat NaHCO₃ (aq). The organic phase was dried over anhydrous MgSO₄, filtered and solvents removed *in vacuo* to give a residue which was purified by flash column chromatography to yield compound **91** as a viscous bright yellow oil (62.7 mg, 0.163 mmol, 33%).

¹H NMR (CDCl₃); δ 1.20, (3H, t, *J* 7.2 Hz, H11_β), 1.26 (2H, t, *J* 7.2 Hz, H11_α), 1.39 (9H, s, H1), 1.68 (4H, m, H5), 2.10 (1H, s, NH_y), 3.27 (2H, m, H4_α), 3.61 (2H, m, H4_β), 3.70 (1H, s, H7), 3.75 (1H, d, *J* 7.92 Hz, H8), 4.14 (2H, dq, *J* 1.96, 5.2 Hz, H10_β), 4.23 (2H, dq, *J* 2.2, 5.0 Hz, H10_α), 6.34 (1H, s, NH_x). ¹³C NMR (CDCl₃); δ 14.2 (C11), 28.4 (C1), 31.7 (C5), 40.3 (C4), 52.5 (C8), 57.9 (C7), 61.5 (C10), 68.4 (C6), 80.1 (C2), 154.5 (C9_α), 162.1 (C9_β), 168.1 (C3). *R*_f 0.246 (30% EtOAc/hexanes). FTIR (ν_{max} cm⁻¹) 2974 (w, CH_x), 2933 (w, CH_x), 1729 (s, C=O), 1689 (s, C=O), 1245 (m, C=N), 1148 (m, C-O). HRMS (XEVO G2-XS QToF) calculated for C₁₈H₃₂N₃O₆ [M+H]⁺ 386.2337, found: 386.2337.

1,8-Di-tert-butyl 3,4-diethyl 1,2,8-triazaspiro[4.5]dec-2-ene-1,3,4,8-tetracarboxylate (92).



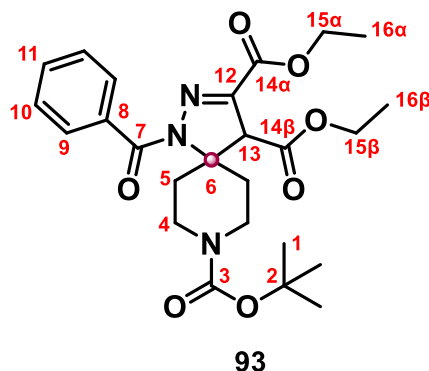
Procedure W: for synthesis of **92**.

Adapted from a known procedure.¹⁹⁸

To a solution of compound **62** (191 mg, 0.50 mmol, 1.0 equiv.) in CH₂Cl₂ (5 mL) was added NEt₃ (0.139 mL, 1.0 mmol, 2.0 equiv.) and DMAP (6.1 mg, 0.05 mmol, 0.1 equiv.) followed by Boc₂O (120 mg, 0.55 mmol, 1.1 equiv.) and the reaction mixture was allowed to stir at RT. After 12 h, the mixture was partitioned between CH₂Cl₂ (25 mL) and water (25 mL). The aqueous layer was extracted with CH₂Cl₂ (25 mL). The combined organic phases were washed with brine (25 mL) and dried over anhydrous MgSO₄ before being filtered and the solvents removed *in vacuo* to give a residue which was purified by flash column chromatography (30% EtOAc / hexanes) to provide compound **92** as an orange amorphous solid (125 mg, 0.258 mmol, 52%).

¹H NMR (CDCl₃) δ 1.24 (3H, t, *J* 7.1 Hz, H14_β), 1.31 (3H, t, *J* 7.1 Hz, H14_α), 1.42 (9H, s, H1), 1.45-1.55 (1H, br. s, H5_{α1}), 1.51 (1H, s, H11), 1.81 (1H, br. s, H5_{β1}), 2.43 (1H, br. s, H5_{α2}), 2.85 (3H, br. s, H4_{α1}, H4_{β1} & H5_{β2}), 3.93-4.24 (2H, br. s, H4_{α2} & H4_{β2}), 4.03 (1H, br. s, H7), 4.19 (2H, q, *J* 7.1 Hz, H13_β), 4.28 (2H, m, H13_α). ¹³C NMR (CDCl₃) δ 13.99 (C14_β), 14.04 (C14_α), 28.1 (C11), 28.3 (C1), 29.3 (br. C5_β), 32.9 (br. C5_α), 39.3 (br. C4_{α, rotamer 1}), 40.2 (br. C4_{α, rotamer 2}), 40.6 (br. C4_{β, rotamer 1}), 41.7 (br. C4_{β, rotamer 2}), 58.7 (C7), 61.9 (C13), 71.6 (C6), 79.8 (C2), 83.3 (C10), 141.0 (C8), 150.4 (C9), 154.2 (C3), 161.5 (C12_α), 167.6 (C12_β). *R*_f 0.573 (30% EtOAc/hexanes). FTIR (*ν*_{max} cm⁻¹) 2974 (w, CH_x), 2933 (w, CH_x), 1692 (s, C=O), 1241 (m, C=N), 1126 (s, C-O). HRMS (XEVO G2-XS QTof) calculated for C₂₃H₃₈N₃O₈ [M+H]⁺ 484.2659, found: 484.2659.

8-(tert-butyl) 3,4-diethyl (S)-1-benzoyl-1,2,8-triazaspiro[4.5]dec-2-ene-3,4,8-tricarboxylate (93).

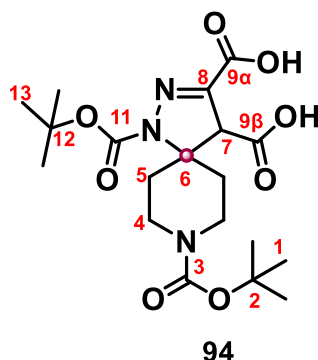


Procedure W.1: for synthesis of **93**.

Adapted from a known procedure ¹⁹⁹

To a solution of compound **62** (573 mg, 1.50 mmol, 1.0 equiv.) was dissolved in CH₂Cl₂ (3 mL) was added 10% aqueous KOH (3 mL, 5.35 mmol, 3.6 equiv). Subsequently stirred and immersed in an ice bath (0°C). Benzoyl chloride (253 mg, 1.80 mmol, 1.2 equiv.) was added dropwise. The reaction stirred at RT and monitored with TLC. After reaction had concluded the reaction mixture was concentrated and redissolved in 10 mL EtOAc. Workup: Added reaction mixture to 10 mL of deionised water in separating funnel (acidified with 1M HCl). Extracted aqueous layer with 10 mL of EtOAc. Combined organic layers and washed with 10ml of deionised water and hence dried resultant org layer with 20 mL of brine and then MgSO₄. Filtered and the solvents removed *in vacuo* to give a residue which was purified by flash column chromatography (10% EtOAc / hexanes) to provide compound **93** as a viscous orange oil (209 mg, 0.419 mmol, 28%).

¹H NMR (CDCl₃) δ 1.20 (3H, t, *J* 7.12 Hz, H16_α), 1.26 (3H, t, *J* 7.12 Hz, H16_β), 1.41 (9H, s, H1), 1.74 (2H, m, H5_α), 2.37 (2H, t, *J* 6.20 Hz, H4_α), 2.82 (2H, m, H5_β), 3.65 (2H, t, *J* 6.20 Hz, H4_β), 3.77 (1H, s, H13), 4.14 (2H, m, H15_β), 4.22 (2H, m, H15_α), 7.38 (2H, dd, 1.2, 6.4 Hz, H10), 7.67 (2H, m, H9), 8.03 (1H, dd, 1.2, 6.4 Hz, H11). ¹³C NMR (CDCl₃); δ 14.2 (C16), 28.4 (C1), 31.9 (C5), 41.2 (C4), 52.9 (C13), 58.2 (C15), 72.9 (C6), 80.2 (C2), 127.9 (C9), 130.1 (C10), 131.6 (C11), 134.5 (C8), 154.5 (C12), 161.2 (C14_α), 161.8 (C14_β), 167.7 (C3), 207.9 (C7). *R*_f 0.341 (30% EtOAc/hexanes). FTIR (ν_{max} cm⁻¹) 2974 (w, CH_x), 2930 (w, CH_x), 1689 (s, C=O), 1241 (m, C=N), 1152 (s, C-O). HRMS (XEVO G2-XS QToF) calculated for C₂₅H₃₄N₃O₇ [M+H]⁺ 488.2319, found 488.2318.

1,8-Bis(tert-butoxycarbonyl)-1,2,8-triazaspiro[4.5]dec-2-ene-3,4-dicarboxylic acid (94)**Procedure X:** for synthesis of **94**.

Adapted from a known procedure.¹⁹⁷

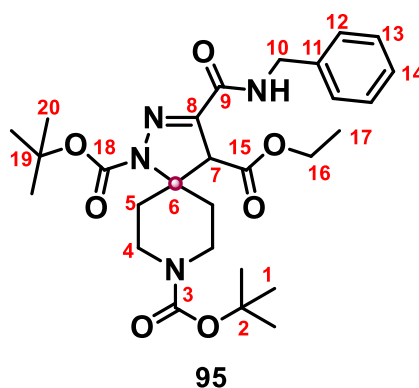
To compound **92** (121 mg, 0.25 mmol, 1.0 equiv.) in MeOH (5 mL) was added KOH (0.25 g, 4.46 mmol, 18 equiv.) and the solution heated to 80 °C. After 3 h, the reaction mixture was concentrated *in vacuo*. The residue was resuspended in water (10 mL) and extracted with Et₂O (10 mL). The aqueous layer was acidified with 3M aqueous HCl and reextracted with Et₂O (3 x 10 mL). The combined organic layers were dried with MgSO₄, and solvents removed *in vacuo* to afford compound **94** as a yellow powder (76.2 mg, 0.178 mmol, 72%) without further purification.

¹H NMR (*d*₆-DMSO); δ 1.41 (9H, s, H1), 1.47 (9H, s, H13), 1.65 (1H, br d, *J* 12.6 Hz, H5_{α1}), 1.75 (1H, br. d, *J* 12.6 Hz, H5_{β1}), 2.12 (2H, *app* td, *J* 12.6, 2.9 Hz, H5_{α2}), 2.67-2.75 (1H, br. s, H5_{β2}), 2.80-3.00 (2H, br. s, H4_α), 3.80-4.00 (2H, br. H4_β), 4.07 (1H, s, H7), 13.0-13.6 (2H, br. s, OH both). ¹³C NMR (CDCl₃); δ 28.3 (C1/C13), 28.5 (C1/C13), 29.4 (C5), 40.9 (C4), 58.8 (C7), 71.08 (C6), 79.4 (C2), 82.5 (C12), 144.0 (C8), 154.1 (C11), 163.0 (C3), 169.9 (C9). *R*_f 0.108 (30% EtOAc/hexanes). FTIR (*v*_{max} cm⁻¹) 3630 (b, OH), 2971 (w, CH_x), 2926 (w, CH_x), 1689 (s, C=O), 1241 (m, C=N), 1129 (m, C-O). HRMS (XEVO G2-XS QTof) calculated for C₁₉H₂₉N₃O₈ [M+H]⁺ 428.2062, found: 428.2062.

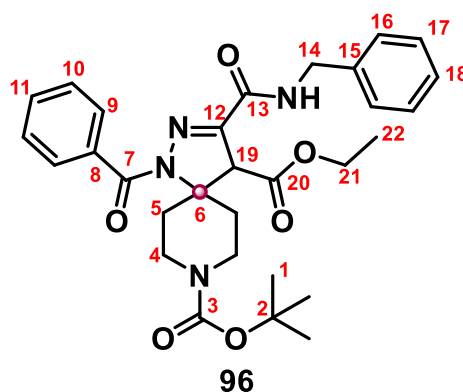
Procedure Y: for synthesis of **95** and **96**.

Adapted from a known procedure.¹⁹¹

To compound **92** or **93** (0.25 mmol, 1.0 equiv.) in methanol (1 mL) was added benzylamine (53.5 mg, 0.50 mmol, 2.0 equiv.) and the mixture was heated to 60 °C. After 12 hrs, the mixture was concentrated *in vacuo* and the residue partitioned between Et₂O (25 mL) and water (25 mL). The aqueous phase was extracted with Et₂O (2 x 25 mL) and the combined organic phases were washed with saturated aqueous Na₂CO₃ (25 mL) before being dried over MgSO₄. Solvents were removed *in vacuo* to provide a residue which was purified by flash column chromatography (30% EtOAc/hexanes) to provide title product as a viscous yellow oil (22 - 75%).

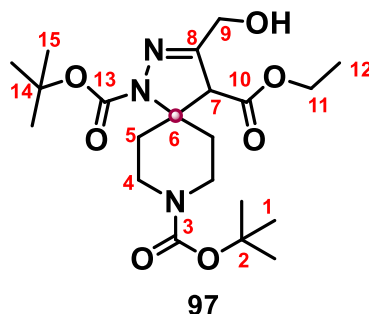


1,8-Di-tert-butyl 4-ethyl 3-(benzylcarbamoyl)-1,2,8-triazaspiro[4.5]dec-2-ene-1,4,8-tricarboxylate (95). Isolated as a viscous yellow oil (102 mg, 0.205 mmol, 75%), according to procedure Y. ¹H NMR (CDCl₃); δ 1.29 (3H, t, *J* 7.1 Hz, H17), 1.47 (9H, s, H1), 1.53 (10H, s, H20 & H5_{α1}), 1.87 (1H, br. s, H5_{β1}), 2.39 (1H, br. s, H5_{α2}), 2.70-3.05 (3H, br. s, H5_{β2}, H4_{α1} & H4_{β1}), 4.00-4.20 (1H, br. s, H4_{α2}), 4.20 (1H, s, H7), 4.25 (2H, q, *J* 7.1 Hz, H16), 4.48 (1H, dd, *J* 14.8, 5.9 Hz, H10_α), 4.57 (1H, dd, *J* 14.8, 6.3 Hz, H10_β), 7.14 (1H, br. t, *J* 5.4 Hz, NH), 7.30 (5H, m, H12 - H14). ¹³C NMR (CDCl₃); δ 14.0 (C17), 28.2 (C1), 28.4 (C20), 29.4 (br. C5_β rotamer 1), 29.7 (br. C5_β rotamer 2), 32.9 (br. C5_α rotamer 1), 33.2 (C5_α rotamer 2), 39.4 (br. C4_α rotamer 1), 40.4 (C4_α rotamer 2), 40.7 (C4_β rotamer 1), 41.8 (br. C4_β rotamer 2), 43.4 (C10), 58.4 (br. C7), 61.9 (C16), 71.5 (C6), 79.9 (C2), 83.2 (C19), 127.6 (C14), 127.9 (C12), 128.7 (C13), 137.5 (C11), 144.6 (C8), 150.7 (C18), 154.2 (C3), 160.5 (C9), 167.8 (C15). *R*_f 0.410 (30% EtOAc/hexanes). FTIR (ν_{max} cm⁻¹) 2974 (w, CH_x), 2930 (w, CH_x), 1666 (s, C=O), 1245 (m, C=N), 1133 (m, C-O). HRMS (XEVO G2-XS QTof) calculated for C₂₈H₄₁N₄O₇ [M+H]⁺ 545.1870, found: 545.1870.



8-(tert-butyl) 4-ethyl (S)-1-benzoyl-3-(benzylcarbamoyl)-1,2,8-triazaspiro[4.5]dec-2-ene-4,8-dicarboxylate (96). Isolated as a viscous yellow oil (30.1 mg, 0.06 mmol, 22%), according to procedure Y. ^1H NMR (CDCl_3); δ 1.26 (3H, t, J 7.12 Hz, H1), 1.41 (9H, s, H1), 1.76 (2H, m, H5), 2.35 (2H, s, H14), 2.78 (2H, m, H5), 4.18 (1H, s, H19), 4.21 (2H, dq, J 1.1, 7.1 Hz, H21), 4.39 (4H, m, H4), 6.68 (1H, s, NH), 7.16 (2H, d, J 6.6 Hz, H16), 7.23 (3H, dt, H17 & H18), 7.31 (2H, t, J 7.2 Hz, H10), 7.39 (1H, d, J 4.08 Hz, H11), 7.58 (2H, d, J 7.0 Hz, H9). ^{13}C NMR (CDCl_3); δ 14.0 (C22), 28.4 (C4), 29.7 (C5), 41.2 (C14), 43.8 (C4), 57.8 (C19), 62.2 (C6), 76.7 (C6), 80.0 (C2), 127.6 (C16), 127.8 (C10), 128.2 (C9), 128.6 (C17), 130.6 (C18), 131.3 (C11), 146.2 (C12), 167.7 (C3), 168.5 (C7), 207.9 (C13). R_f 0.291 (30% EtOAc/hexanes). FTIR (ν_{max} cm^{-1}) 2974 (w, CH_x), 2930 (w, CH_x), 1655 (s, C=O), 1241 (m, C=N), 1159 (m, C-O). HRMS (XEVO G2-XS QTof) calculated for $\text{C}_{30}\text{H}_{37}\text{N}_4\text{O}_6$ $[\text{M}+\text{H}]^+$ 529.2713, found 529.2713.

1,8-Di-tert-butyl 4-ethyl 3-(hydroxymethyl)-1,2,8-triazaspiro[4.5]dec-2-ene-1,4,8-tricarboxylate (97).



Procedure Z: for synthesis of **97**.

Adapted from a known procedure.¹⁹⁸

To compound **92** (221 mg, 0.5 mmol, 1.0 equiv.) in MeOH (5 mL) was added NaBH₄ (38.0 mg, 1.0 mmol, 2.0 equiv.) and the mixture was stirred at RT. After 12 hrs, the mixture was concentrated *in vacuo* and the residue partitioned between EtOAc (10 mL) and water (10 mL). The aqueous phase was extracted with EtOAc (10 mL) followed by 5:1 DCM:MeOH (2 x 30 mL). The combined organic phases were dried over anhydrous MgSO₄ and solvents removed *in vacuo* to give a residue which was purified by flash column chromatography to yield compound **97** as a viscous yellow oil (65.3 mg, 0.148 mmol, 30%).

¹H NMR (CDCl₃); δ 1.30 (3H, t, *J* 7.1 Hz, H₁₂), 1.47 (11H, s, H₁/H₁₅ & H_{5_α}), 1.54 (9H, s, H₁/H₁₅), 1.86 (2H, br. m, H_{5_β}), 3.03 (2H, br. ddd, *J* 13.3, 10.1, 3.1 Hz, H_{4_α}), 3.84 (2H, br m, H_{4_β}), 3.95 (1H, br. s, H₇), 4.23 (2H, q, *J* 7.1 Hz, H₁₁), 4.40 (1H, d, *J* 14.8 Hz, H_{9_α}), 4.42 (1H, d, *J* 15.0 Hz, H_{9_β}). ¹³C NMR (CDCl₃); δ 14.1 (C₁₂), 28.3 (C₁/C₁₃), 28.4 (C₁/C₁₃), 34.1 (C₅), 41.2 (br. C₄), 59.4 (br. C₇), 59.8 (C₉), 61.9 (C₁₁), 69.5 (C₆), 79.6 (C₂/C₁₄), 79.9 (C₂/C₁₄), 151.4 (C₈), 154.3 (C₃), 154.8 (C₁₃), 168.1 (C₁₀). *R*_f 0.040 (30% EtOAc/hexanes). FTIR (ν_{max} cm⁻¹) 3414 (br., O-H), (w, CH_x), 2974 (w, CH_x), 2930 (w, CH_x), 1733 (s, C=O), 1629 (s, C=O), 1244 (m, C=N), 1156 (m, C-O). HRMS (XEVO G2-XS QToF) calculated for C₂₁H₃₆N₃O₇ [M+H]⁺ 442.2553, found: 442.2553.

7.3. Computational studies

7.3.1. Database screening

According to Lipinski's rule of five (Ro5)¹¹⁰, a drug-like compound database comprised of 981,247,974 was downloaded from the ZINC database,¹²⁰ and screened for potential binding ability against the active / catalytic site and the allosteric site of PTP1B. The binding regions of interest, including key residues of the protein were identified from co-crystallized structures of known inhibitors to their respective binding site; obtained from the Protein data bank (PDB).¹¹⁴ Using the Cambridge Crystallographic Data Centre (CCDC) – Cross miner 2022 software a proposed pharmacophore of both binding regions of interest was constructed and the drug-like database was screened, to find potential hit compounds for synthesis, and subsequent testing.

7.3.2. Docking studies

Inputted the co-crystallized structures of known inhibitors PTP1B as separate entities (obtained from the PDB¹¹⁴) into the open-source software PyRx (0.8 version)¹¹⁶, the parameters for the defined binding area in which compounds of interest were docked was based upon the binding positions of the known inhibitors. Before any compounds of interest could be docked, they were drawn and set to lowest energy state. The software Avogadro²⁰⁰ was employed to achieve this. Once potential PTP1B inhibitors / compounds of interest had been docked the most likely binding position has exported (maintaining its chemical space information) to PyMol.¹¹⁷ In PyMol the binding mode of the potential PTP1B inhibitors were investigated by investigating the surrounding residues of the specific PTP protein's binding site, in addition to the functional groups possessed by the potential inhibitor and thus chemical interactions attributed to binding were proposed.

7.4. Biological methodologies

7.4.1. Yeast cell transformation

Two different yeast strains (YMK23 and YSC1) were transcribed with one or two plasmids to link yeast growth rate to inhibition of PTPs:

YMK23 (W303 strain background) and YSC1 (BY474 strain background)

Specific plasmids utilised:

P415 Gal (v-*Src*) *Leu2* *Cen/Ars* plasmids (low copy), P426Gal (catalytic domain of PTP1B), *Ura2* 2u plasmid (high copy) and pSMF043 (catalytic domain of TCPTP), This plasmid has a p426 backbone so has *URA3* selection for yeast and therefore also a 2u high copy.

YMK23 Genotype: *Mat a*, *ade2-1*, *his3-11,15*, *leu2-3,112*, *trp1-1*, *ura3-1*, *can1-100*, *GCD1-P180*

YSC1 Genotype: *MATa his3Δ1 leu2Δ0 met15Δ0 ura3Δ0*

Note: All microbiological work was conducted in sterile conditions.

Frozen-EZ Yeast Transformation II™ kit protocol: ²⁰¹

Preparation of Competent cells:

One colony of both the untransformed yeast strains (YMK23 and YSC1) were incubated overnight at 30°C separately in 10ml of 1x YPD broth. A third control tube (just 1x YPD broth from same bottle), was also incubated in the same manner.

After an 18-hr incubation each of the tubes were removed from the incubator and a 100 μL aliquot was moved from each and diluted with an additional 900 μL of growth media (1x YPD). The optical density (OD) of the 1:10 dilution was measured at 600 nm. Instrument blanked with 1x YPD.

The overnight cultures were diluted with 1x YPD media in a ratio to achieve an undiluted OD₆₀₀ of 0.8 - 1.0 after a further 3-4 hr incubation period at 30 °C. Note: the doubling time (Td) for both yeast strain cells are *approx.* 90 minutes. After the desired OD₆₀₀ value was acquired, these cells were taken forward for transcription preparation.

The cells were pelleted at 500 x g for 4 minutes. The supernatant removed and discarded. Washed, resuspend, and redissolved the pellet in 10ml of Frozen-EZ solution 1, re-pelleted at 500 x g for 4 minutes. The supernatant was discarded, and the pellet resuspended in 1 mL of Frozen-EZ solution 2, and then transferred to a 1.5 mL Eppendorf tube.

The transformation occurred based on instructions present with the utilised Zymo Research: Frozen-EZ Yeast Transformation II™.

Transformation:

Note: for both yeast strain 6x separate transformations were conducted; v-Src only, PTP1B only, TCPTP only, PTP1B with v-Src (multiple-plasmid transformation) and TCPTP with v-Src (multiple-plasmid transformation). The 6th was a control where the DNA was swapped with sterile deionised water.

For each transformation 500 µL of Frozen-EZ solution 3, 50 µL of one of the competent cell types in addition to 3 - 5 µL (0.2-1 µg) of DNA, were added and mixed thoroughly prior to incubation. This was repeated for each of the aforementioned transformation / plasmid combinations for both yeast strains (12 x tubes for incubation, includes 2x water controls).

Note: For the specific plasmids used in this work kindly supplied by Anthony C. Bishop, Amherst College, Department of Chemistry, Amherst, Massachusetts had the following concentrations: PTP1B (274 ng / 1 µL), TCPTP (227 ng / 1 µL), and v-Src (319 ng / 1 µL).

The tubes were incubated (12 x total) at 30 °C for 45 minutes. Each tube was flicked 3 times at 15-minute intervals. Post incubation, the newly transformed cells were plated on 3x of the corresponding knock-out plate. Used *approx.* 150 µL of each transformation yeast culture per plate.

Plates were incubated upside down at 30 °C for 2-4 days / until a suitable number of colonies had grown. Plates were wrapped in parafilm and stored at -20 °C prior to single colony purification.

Single Colony purification:

The following procedure was conducted on all transformations (5x), for both YMK23 and YSC1 based yeast cells.

A specific knock-out agar plate was divided into quarters and a single corresponding colony was picked and spread in a 'Christmas tree' pattern for each quarter. The resultant plate was incubated at 30 °C. for 2 – 4 days. To produce 1st phase purified cells.

From the above plates a single colony was picked from each quarter and replated on separate corresponding specific drop out agar plates. The single colony was spread in a single area on the edge, and from this the cells were spread *via* a 'kris cross' pattern. The resultant plate was incubated at 30 °C. for 2 – 4 days, this produces 2nd phase purified cells. Plates wrapped in parafilm and stored at -20 °C prior to use.

7.4.2. Yeast cell maintenance**Plate composition:**

PTP (-ura only) plates: 100 mL 4x SC Ura drop out (*aq*), 100 mL 4x YNB media (*aq*), 200 mL 4% micro agar (*aq*) and 20 mL 40% glucose (*aq*).

v-*Src* (-leu only) plates: 100 mL 4x SC Leu drop out (*aq*), 100 mL 4x YNB media (*aq*), 200 mL 4% micro agar (*aq*) and 20 mL 40% glucose (*aq*).

PTP + v-*Src* (-ura and -leu) plates: 100 mL 4x SC Ura + Leu double drop out (*aq*), 100 mL 4x YNB media (*aq*), 200 mL 4% micro agar (*aq*) and 20 mL 40% glucose (*aq*).

All components were sterilised prior to addition. Components were added to the sterile set 4 % agar, which was steamed after complete addition and mixed prior to the pouring of the plates, done in sterile conditions. Once the plates had set they were stored upside down at -20 °C.

Growth media composition:

PTP (-ura only) media:

2.5 mL 40% Raffinose (*aq*), 12.5 mL 4x SC Ura drop out (*aq*), 12.5 mL 4x YNB media (*aq*) and 22.5 mL sterile deionised water. (-Ura 2% Raffinose growth media)

5.0 mL 40% Galactose (*aq*), 12.5 mL 4x SC Ura drop out (*aq*), 12.5 mL 4x YNB media (*aq*) and 20.0 mL sterile deionised water. (-Ura 4% Galactose growth media)

v-*Src* (-*leu* only) media:

2.5 mL 40% Raffinose (*aq*), 12.5 mL 4x SC *Leu* drop out (*aq*), 12.5 mL 4x YNB media (*aq*) and 22.5 mL sterile deionised water. (-*Leu* 2% Raffinose growth media)

5.0 mL 40% Galactose (*aq*), 12.5 mL 4x SC *Leu* drop out (*aq*), 12.5 mL 4x YNB media (*aq*) and 20.0 mL sterile deionised water. (-*Leu* 4% Galactose growth media)

PTP + v-*Src* (-*ura* and -*leu*) media:

2.5 mL 40% Raffinose (*aq*), 12.5 mL 4x SC *Ura* + *Leu* double drop out (*aq*), 12.5 mL 4x YNB media (*aq*) and 22.5 mL sterile deionised water. (-*Ura* and -*Leu* 2% Raffinose growth media)

5.0 mL 40% Galactose (*aq*), 12.5 mL 4x SC *Ura* + *Leu* double drop out (*aq*), 12.5 mL 4x YNB media (*aq*) and 20.0 mL sterile deionised water. (-*Ura* and -*Leu* 4% Galactose growth media)

All components were sterilised prior to addition. Growth media made up in sterile conditions and stored at -20 °C.

Short-term yeast cell storage:

Yeast cells stored on corresponding drop out plates upside down at -20 °C and replated on fresh corresponding plates *via* a single picked colony every 3rd week and incubated at 30 °C for 2 - 3 days. Biannually the cells were replated from thawed frozen down aliquots of the yeast cells (30 µL per plate) and incubated at 30 °C for 3 - 4 days.

Long-term yeast cell storage:

Grew up an overnight culture from a single picked colony for each yeast strain / transformation in the corresponding 2 % Raffinose growth media. OD₆₀₀ was taken and cultures were either diluted or left to further incubate to achieve an OD₆₀₀ value of *approx.* 1.0. 880 µL of each ~OD₆₀₀ 1.0 overnight culture were added to 120 µL of sterile DMSO in cryo vials, which were wrapped in tissue paper prior insertion in -80°C to avoid snap freezing. Once fully frozen, tissue paper was removed, resulting in frozen down aliquots of each yeast cell transformation.

7.4.3. Yeast growth curves

Adapted from a known procedure.²⁰²

Growth curve setup:

Six overnight cultures of each transformation were incubated separately overnight (*approx.* 18 hrs) at 30 °C. in 4 - 5 mL of corresponding 2% raffinose growth media to produce six biological repeats, for each transformation. Recommended to conduct the PTP single drop out in parallel with the corresponding PTP + v-Src double drop out transformation in the same plate each run.

When testing a compound, a stock solution (in the range of 20–100 μ M) was created using sterile DMSO as the solvent. From this stock solution a range of concentrations were formed with sterile water as the diluent, to enable the desired concentration of the compound, when added as part total well volume of 180 μ L. 96 well plate were used when running growth curve experiments.

Growth curve experiment:

After an *approx.* 18 hr incubation at 30 °C, OD₆₀₀ of 1:10 dilutions of the overnight cultures were measured. Used corresponding raffinose growth media as the diluent. Volume required for initial OD₆₀₀ value of 0.05 for cells in the wells calculated.

The remaining composition of the well in addition to the yeast cells is 2 μ L of the respective DMSO stock solution of the compound of interest for testing and the corresponding galactose growth media as the diluent with the total volume of 180 μ L per well.

After the addition of the compound of interest to the applicable well, the corresponding 4% galactose growth media was added to each assigned well, the volume of which was the amount needed to acquire a total volume of 180 μ L per well after the addition of 2 μ L of compound solution (if applicable) and volume overnight yeast culture needed for initial OD₆₀₀ value of *approx.* 0.05 (volume previously calculated).

Subsequently the calculated volume of the overnight yeast cultures were added to the corresponding wells. After all components had been added the well contents were carefully mixed with a pipette.

Note: For every biological repeat run, solely the culture was ran in parallel to obtain the base growth for that specific culture, this was done for every transformation, as significant base growth variation can occur.

Once complete the 96 well plate was placed inside the plate reader CLARIOstar plate reader with the lid remaining on. Experiment ran at 96 cycles (47.5 hrs) where reading was taken at time point 0 and subsequently every 30 minutes, plates was shaken prior to each reading and specific 96 well plate and volume per well was included to gain accurate absorption reading for the yeast cells. The experiment was run at 30 °C and wavelength of 600 nm was utilised. All measurements were blank corrected against the corresponding 4% galactose growth media.

Once completed observed data was collected, and the doubling times calculated and compared to investigate the PTP inhibitory activity of the tested compound.

6.4.3.1. Doubling time calculations:

Equation 1a:

$$y = Ae^{Bx}$$

Equation 1b:

$$T_d = \frac{\ln(2)}{B}$$

Equation 1c:

$$\% \text{ change in } T_d = ((T_d a - T_d b) / T_d b) * 100$$

Equation 1: Equations used to investigation the effect of potential PTP inhibitors.

$T_d a$ = base growth of corresponding yeast culture, $T_d b$ = growth of corresponding yeast culture with the addition of small molecule. ^{125,126}

Plot growth curve with time against OD₆₀₀ convert the y-axis to a logarithmic base 10 scale, alter the time frame so that a straight linear line with a positive correlation remains, this is the exponential growth phase. Use the exponential line of best fit of this time frame to get the equation of the line as $y = Ae^{Bx}$. From this calculation the doubling time (T_d) by dividing the natural logarithm base 2 by B from the aforementioned exponential growth phase graph. % change in T_d is calculated by working out the change in T_d from that of the base growth (corresponding cell transformation without the addition of the potential inhibitor) for that biological replicate.

6.4.3.2. EC₅₀ calculation

Equation 2a: $EC_{50} = 10^a$

Equation 2b: $a = \frac{\ln\left(\frac{b}{c}\right)}{d}$

Equation 2c: $y = ce^{dx}$

Equation 2: Equations used to calculate the EC₅₀ values of known and potential PTP inhibitors based upon % change in T_d as the means of determining maximum effect.

a = Log(10) of EC₅₀, b = half of the maximum percentage change for the concentration range used as a decimal, c and d obtained from exponential line of best fit. (Equation 2c) ²⁰³

As shown above with the **Equation 2a-c** ²⁰³ EC₅₀ can be calculated by plotting a semi logometric graph of dose / concentration of inhibitor added as a Log(10) on the x-axis and % change in T_d (inhibitory response) on the y-axis. The equation of the resultant graph was calculated, and in conjunction with the half maximum response value the EC₅₀ was calculated for each biological repeat and averaged.

The base line response is 0% with the maximum being the highest recorded % change in T_d and varied for each biological repeat of each inhibitor investigated. Hence half the maximum effect is not necessarily 50%.

7.4.4. Blood Brain Barrier (BBB) Permeability assay

Kit utilised: - BioAssay Systems Parallel Artificial Membrane Permeability Assay-Blood Brain Barrier (BBB) Kit (PMBBB-096). ¹²⁹⁻¹³¹

The main reasons for the selection of this assay over other kits was throughput, cost, and length of storage. This assay due to its 96 well plate format is able to simultaneously test 32 compounds with an n number of three in 18 – 24 hours making its cost per compound sufficiently lower than that of alternative assays which utilise actual BBB membrane cells. This assay also provides each set up as at -20 °C the kit is able to be stored for 12 months if kept sealed and the components just bought up to RT prior to use. However, once the BBB lipid solution had been reconstituted in dodecane, the solution is only viable for 6 days if kept at -20 °C so it would be advisable to use the entire 96 wells in one experiment.

BBB assay setup:**Preparing BBB membrane:**

Resuspended the dried brain lipids with 600 μL dodecane. Pipette repeatedly, *approx.* 100 times to fully solubilize the dried brain lipids, if required vortexing could assist. Stored at -20°C and were used within 6 days.

Preparing test compound stock solutions:

Prepared 300 μL of 10 mmol stock solutions of all test compounds in sterile DMSO. Assay supplied 3x permeability controls as 10 mmol solutions in DMSO.

Determining optimum absorbance wavelength for test compounds:

Acquired optimum absorbance wavelength for each test compound by running an absorbance spectrum over a 200 nm to 500 nm range in 10nm intervals to determine peak absorbance of each test compound. Used the CLARIOstar plate reader with UV transparent plates. The blank control is equal to the DMSO concentration in the test compound solutions in 1x PBS. Peak absorbance for High Permeability, Medium Permeability, and Low Permeability Controls are 250 nm, 250 nm, and 270 nm respectively.

Calibration curve for BBB assay test compounds:

The CLARIOstar plate reader with a UV transparent plate was used at the above determined optimum wavelength for absorbance of each test compound over 50 - 500 μM range (50 μM intervals). Blank correct with DMSO / 1x PBS solution, per concentration DMSO concentration varies, hence a different blank solution for each concentration. Did 5x repeats per concentration for each test compound, used fresh 10 mmol stock solution for each repeat.

BBB assay protocol:

Note: all stated volume enables five replicates of each test compound.

For each compound being investigated, 1500 μL of a 500 μM solution was created *via* the dilution of a 10 mmol stock in DMSO (75 μL) with 1x PBS (1425 μL) as the diluent. Same was completed for the permeability controls provided with the kit.

1000 μL of 200 μM equilibrium standards were subsequently created for each test compound and permeability control, again with 1x PBS as the diluent. Blank Controls

created a separate tube, equilibrium standards were set aside for analysis the following day.

A 5% DMSO blank solution comprised of 50 μL of DMSO in 950 μL 1x PBS, was made up to be run in parallel with test compounds and permeability controls. This DMSO concentration is equal to that present initially in the donor wells.

Per acceptor plate well 300 μL of 1x PBS was added, followed with the addition of 5 μL of the resuspended BBB Lipid Solution directly to the well membranes of the donor plate. The membrane turned colourless from white.

For each test compound, permeability control and 5% DMSO blank control, 200 μL was added to five different donor plate wells, to give five replicates.

The donor plate was subsequently placed into the acceptor plate and incubated at RT or 37 $^{\circ}\text{C}$ for a predetermined time period (16 – 24 hours).

Once the assay had concluded the donor plate was removed from the acceptor plate and the liquid in both the acceptor and donor plate wells collect. These along with the pre-prepared equilibrium standards for each test compound and permeability controls, were transferred to different UV transparent plate where the optical density values were acquired using the optimum wavelengths found previously for each compound test.

BBB data analysis:

Permeability rate:

From the absorbance values taken at the respective optimum wavelengths the permeability rate of each compound was calculated from the be below equations. ¹²⁹⁻¹³¹

$$P_e = C x - \ln \left(1 - \frac{OD_A}{OD_E} \right) \text{ cm/s}$$

Equation 3: Permeability rate equation.

Where OD_A was the absorbance of acceptor well solution, OD_E equalled the absorbance of the equilibrium standard of each compound at the respective optimum wavelength.

$$C = \frac{V_D (cm^3) \times V_A (cm^3)}{(V_D (cm^3) + V_A (cm^3)) \times CSA (cm^2) \times t (hrs)} \text{ cm/s}$$

Equation 4: Calculation of ‘C’ dependent on volume present in wells, cross-sectional area of membrane and time.

V_D : initial volume of the donor well in cm^3 . V_A : initial volume in cm^3 of the acceptor well. Cross-sectional area (csa): cm^2 and t represents run time of experiment in hours.

Percentage distribution of test compounds post run:

From absorbance values obtained of the acceptor wells and donor wells post BBB assay inhibition the concentration (μM) of each test compound present both sides of the membrane were calculated *via* the use of the calibration curves.

The equilibrium standard is created prior to running the experiment and is set at 200 μL for each compound or control tested as this would be the final concentration in the acceptor well if the compound is able to permeate the membrane and fully reach equilibrium. In order to gain the most relevant information from this assay it was important to ensure that none of the compounds or controls tested reached the equilibrium concentration in the time frame of the reaction as if multiple compounds of interest had, there would be no way to determine which was most permeable after the fact. This is why the 24-hour assay experiment length was decided upon as from the model data provided¹²⁹⁻¹³¹ at RT the high permeability control does not reach its equilibrium concentration of 200 μL , and also from the results of this project the high permeability control, or any of the compounds tested also did not reach the equilibrium concentration at RT or 37°C after 24 hours.

7.4.5. Spot Plate assay

For each transformation investigated two cultures were set up the day before, incubated in the corresponding 2% raffinose media overnight.

Made up 2x 50 mL of each agar type: 2x 50 mL YPD (untransformed), 2x 50 mL -ura PTP, and 2x 50 mL -ura, -leu double knockout PTP + v-Src agar. The composition of each agar type is detailed above under yeast growth curves section.

These were then autoclaved. One of each agar version was poured in separate labelled square plates which had an 8 x 6 grid outlined prior to pouring. These plates were left to set at an angle using standard blue pipette tips. While setting the second corresponding set of 50 mL agar solutions had the compound of interest added to them and thoroughly mixed. In this work that was compound **30a** where 0.0026 g was added to each agar to gain a subsequent maximum concentration of 250 μ M of each final plate. After initial agar had set at an angle to corresponding compound infused agar was carefully poured on top of the initial layer of agar from the highest agar level and left to set. These final plates resulted in a concentration gradient of the compound of interest of 0 – 250 μ M. Use the plates straight away to avoid concentration normalisation *via* diffusion.

For the transformed cells one plate denoted PTP only transcription and the other PTP + v-Src co-expression. For these plates two biological repeats each with two mechanical repeats were conducted for each PTP variant, PTP1B based or TCPTP based. For this an initial optical density at 600 nm (OD_{600}) of 1.0 was used. For the untransformed YMK23 cells as only one version is present instead two biological repeats with two mechanical repeats each were conducted with initial OD_{600} of 1.0 and 0.1.

In each square of the drawn grid in each plate 3.0 μ L of the corresponding yeast cell overnight cultured which had been diluted to the desired concentration (0.1 or 1.0), was pipetted on all squares. The plates were subsequently left to incubate over 48hrs at 30°C. with visual qualitative data recorded over the following time points for each plate: 4, 20, 24, 28, 45 and 48 hours.

The results from this were used to investigate whether the compound of interest **30a** was causing off-target general yeast toxicity effects.

Thesis References

8. References

- 1 S. Samson and A. Garber, 2014, **43**, 1-23 (DOI:10.1016/j.ecl.2013.09.009).
- 2 P. L. Huang, *DMM*, 2009, **2**, 231-237 (DOI:10.1242/dmm.001180).
- 3 J. J. Martyn, M. Kaneki, S. Yasuhara, D. Warner and M. Warner, *Anesthesiology (Philadelphia)*, 2008, **109**, 137-148 (DOI:10.1097/ALN.0b013e3181799d45).
- 4 B. B. Kahn and J. S. Flier, *JCI*, 2000, **106**, 473-481 (DOI:10.1172/JCI10842).
- 5 T. D. Adams, R. E. Gress, S. C. Smith, R. C. Halverson, S. C. Simper, W. D. Rosamond, M. J. LaMonte, A. M. Stroup and S. C. Hunt, *NEJM*, 2007, **357**, 753-761 (DOI:10.1056/NEJMoA066603).
- 6 Z. Idrees, I. Cancarevic and L. Huang, *Cureus*, 2022, **14** (DOI:10.7759/cureus.29262).
- 7 E. A. Finkelstein, M. A. Khavjou, H. Thompson, J. G. Trogon, S. Bettylou and W. Dietz, *Am. J. Prev. Med*, 2012, **42**, 563-570 (DOI:10.1016/j.amepre.2011.10.026).
- 8 Gov.uk, <https://www.gov.uk/government/statistics/obesity-profile-update-july-2022/obesity-profile-short-statistical-commentary-july-2022>, (accessed 12/9/2023).
- 9 House of Commons Library, <https://commonslibrary.parliament.uk/research-briefings/sn03336/#:~:text=The%20Health%20Survey%20for%20England,is%20classified%20as%20%27overweight>, (accessed 12/9/2023).
- 10 Royal College of Physicians, <https://www.rcplondon.ac.uk/news/health-inequalities-and-obesity#:~:text=It%20is%20clear%20that%20socio,health%20inequalities%20and%20obesity%20rates.>, (accessed 12/9/2023).
- 11 X. Wen, B. Zhang, B. Wu, H. Xiao, Z. Li, R. Li, X. Xu and T. Li, *Signal Transduct. Target. Ther.*, 2022, **7**, 298 (DOI:10.1038/s41392-022-01149-x).
- 12 X. Lin and H. Li, *Front. Endocrinol. (Lausanne)*, 2021, **12**, 706978 (DOI:10.3389/fendo.2021.706978).
- 13 A. Pérez-Pérez, F. Sánchez-Jiménez, T. Vilariño-García and V. Sánchez-Margalet, *Int. J. Mol. Sci.*, 2020, **21**, 5887 (DOI:10.3390/ijms21165887).
- 14 V. V. Thaker, *Adolesc Med State Art Rev.*, 2017, **28**, 379-405.
- 15 D. M. Patrick, J. P. Van Beusecum and A. Kirabo, *Curr Opin Physiol*, 2021, **19**, 92-98 (DOI:10.1016/j.cophys.2020.09.016).
- 16 S. Julius, M. Valentini and P. Palatini, *Phenotypic Changes in the Transition from Prehypertension to Established Hypertension*, Springer International Publishing, 2017. (DOI:10.1007/978-3-319-59918-2_34).

- 17 R. Divella, A. Mazzocca, A. Daniele, C. Sabbà and A. Paradiso, *Int. J. Biol. Sci.*, 2019, **15**, 610-616 (DOI:10.7150/ijbs.29599).
- 18 M. Dharmalingam and P. Yamasandhi, *Indian J of Endocrinol Metab*, 2018, **22**, 421-428 (DOI:10.4103/ijem.IJEM_585_17).
- 19 E. Fabbrini, S. Sullivan and S. Klein, *Hepatology (Baltimore, Md.)*, 2010, **51**, 679-689 (DOI:10.1002/hep.23280).
- 20 A. S. Al-Goblan, M. A. Al-Alfi and M. Z. Khan, *Diabetes metab. syndr. obes*, 2014, **7**, 587-591 (DOI:10.2147/DMSO.S67400).
- 21 R. A. Nianogo and O. A. Arah, *Front Public Health.*, 2022, **10**, 1-13.
- 22 C. Daousi, I. F. Casson, G. V. Gill, I. A. MacFarlane, J. P. H. Wilding and J. H. Pinkney, *Postgrad. Med. J.*, 2006, **82**, 280-284 (DOI:10.1136/pmj.2005.039032).
- 23 N. Hex, C. Bartlett, D. Wright, M. Taylor and D. Varley, *Diabet. Med.*, 2012, **29**, 855-862 (DOI:10.1111/j.1464-5491.2012.03698.x).
- 24 C. Bommer, V. Sagalova, E. Heesemann, J. Manne-Goehler, R. Atun, T. Barnighausen, J. Davies and S. Vollmer, *Diabetes Care*, 2018, **41**, 963-970 (DOI:<https://doi.org/10.2337/dc17-1962>).
- 25 J. M. Khalid, M. Raluy-Callado, B. H. Curtis, K. S. Boye, A. Maguire and M. Reaney, *Int. J. Clin. Pract.*, 2014, **68**, 40-48 (DOI:10.1111/ijcp.12265).
- 26 K. K. Dhatariya, I. Nunney, K. Higgins, M. J. Sampson and G. Iceton, *Diabet. Med.*, 2016, **33**, 252-260 (DOI:10.1111/dme.12875).
- 27 Type 2 diabetes: prevention in people at high-risk public health guideline, 2012. <https://www.nice.org.uk/guidance/ph38> (accessed 28/11/2023).
- 28 M. C. Petersen, D. F. Vatner and G. I. Shulman, *Nat Rev Endocrinal*, 2017, **13**, 572-587 (DOI:10.1038.nendo.2017.80.)
- 29 H. Zhang, A. Qiao, D. Yang, L. Yang, A. Dai, C. de Graaf, S. Reedtz-Runge, V. Dharmarajan, H. Zhang, G. W. Han, T. D. Grant, R. G. Sierra, U. Weierstall, G. Nelson, W. Liu, Y. Wu, L. Ma, X. Cai, G. Lin, X. Wu, Z. Geng, Y. Dong, G. Song, P. R. Griffin, J. Lau, V. Cherezov, H. Yang, M. A. Hanson, R. C. Stevens, Q. Zhao, H. Jiang, M. W. Wang and B. Wu, *Nature*, 2017, **546**, 259-264 (DOI:10.1038/nature22363).
- 30 S. Azam, M. E. Haque, M. D. Jakaria, S. Jo, I. Kim and D. Choi, *Cells*, 2020, **9**, 1-28, (DOI:10.3390/cells9020506)
- 31 M. H. Baig, K. Ahmad, Q. Hasan, M. K. A. Khan, N. S. Rao, M. A. Kamal and I. Choi, *eCAM*, 2015, **6**, 1-6. (DOI:10.1155/2015/497253).

- 32 S. L. Aronoff, K. Berkowitz, B. Shreiner and L. Want, *Diabetes Spectr*, 2004, **17**, 183-190 (DOI:10.2337/diaspect.17.3.183).
- 33 A. M. D'Souza, U. H. Neumann, M. M. Glavas and T. J. Kieffer, *Mol Metab*, 2017, **6**, 1052-1065 (DOI:10.1016/j.molmet.2017.04.011).
- 34 S. Yip, S. Saha and J. Chernoff, *TIBS*, 2010, **35**, 442-449 (DOI:10.1016/j.tibs.2010.03.004).
- 35 L. V. Ravichandran, H. Chen, Y. Li and M. J. Quon, *Mol. Endo. (Baltimore, Md.)*, 2001, **15**, 1768-1780 (DOI:10.1210/mend.15.10.0711).
- 36 F. M. Moeslein, M. P. Myers and G. E. Landreth, *JBC*, 1999, **274**, 26697-26704 (DOI:10.1074/jbc.274.38.26697).
- 37 D. Bandyopadhyay, A. Kusari, K. A. Kenner, F. Liu, J. Chernoff, T. A. Gustafson and J. Kusari, *JBC*, 1997, **272**, 1639-1645 (DOI:10.1074/jbc.272.3.1639).
- 38 S. Li, R. S. Depetris, D. Barford, J. Chernoff and S. R. Hubbard, *Structure*, 2005, **13**, 1643-1651 (DOI:10.1016/j.str.2005.07.019).
- 39 A. J. Flint, T. Tiganis, D. Barford and N. K. Tonks, *PNAS*, 1997, **94**, 1680-1685 (DOI:10.1073/pnas.94.5.1680).
- 40 Panzhinskiy Evgeniy, Ren Jun and Nair Sreejayan, *PLOS one*, 2013, **8**, 1-12. (DOI: 10.1371/journal.pone.0077228).
- 41 E. J. Belin de Chantemele, K. Muta, J. Mintz, M. L. Tremblay, M. B. Marrero, D. J. Fulton and D. W. Stepp, *Circulation*, 2009, **120**, 753-763 (DOI:10.1161/CIRCULATIONAHA.109.853077).
- 42 R. N. Shinde and M. E. Sobhia, *J. Mol. Graph. Model.*, 2013, **45**, 98-110 (DOI:10.1016/j.jmgm.2013.08.001).
- 43 X. F. Tan, Z. Uddin, C. Park, Y. H. Song, M. Son, K. W. Lee and K. H. Park, *Bioorg. Med. Chem.*, 2017, **25**, 2498-2506 (DOI:10.1016/j.bmc.2017.03.010).
- 44 H. Knobler and A. Elson, *J. Biomed. Res*, 2014, **28**, 157-168 (DOI:10.7555/JBR.28.20140012).
- 45 R. C. Tsou and K. K. Bence, *Front Neuro*, 2013, **6**, 192 (DOI:10.3389/fnins.2012.00192).
- 46 Y. Cohen-Sharir, Y. Kuperman, D. Apelblat, J. den Hertog, I. Spiegel, H. Knobler and A. Elson, *FASEB*, 2019, **33**, 5101-5111 (DOI:10.1096/fj.201800860RR).
- 47 G. J. Song, M. Jung, J. Kim, H. Park, M. H. Rahman, S. Zhang, Z. Zhang, D. H. Park, H. Kook, I. Lee and K. Suk, *J. Neuroinflammation*, 2016, **13**, 86 (DOI:10.1186/s12974-016-0545-3).

- 48 S. S. Abdelsalam, H. M. Korashy, A. Zeidan and A. Agouni, *Biomolecules*, 2019, **9**, 286 (DOI:10.3390/biom9070286).
- 49 S. Jamwal and S. Sharma, *Inflamm. Res*, 2018, **67**, 391-405 (DOI:10.1007/s00011-018-1129-8).
- 50 E. Cersosimo and R. A. DeFronzo, *Diabetes Metab Res Rev*, 2006, **22**, 423-436 (DOI:10.1002/dmrr.634).
- 51 L. Gautron and J. K. Elmquist, *JCI*, 2011, **121**, 2087-2093 (DOI:10.1172/JCI45888).
- 52 C. D. Wrann, J. Eguchi, A. Bozec, Z. Xu, T. Mikkelsen, J. Gimble, H. Nave, E. F. Wagner, S. Ong and E. D. Rosen, *JCI*, 2012, **122**, 1010-1021 (DOI:10.1172/JCI58431).
- 53 Y. Zhou and L. Rui, *Front Med*, 2013, **7**, 207-222 (DOI:10.1007/s11684-013-0263-5).
- 54 Y. Minokoshi, C. Toda and S. Okamoto, *Indian J. Endocrinol Metab*, 2012, **16**, S562-S568 (DOI:10.4103/2230-8210.105573).
- 55 M. Amitani, A. Asakawa, H. Amitani and A. Inui, *Front. Neurosci*, 2013, **7**, 51 (DOI:10.3389/fnins.2013.00051).
- 56 L. Marroquí, A. Gonzalez, P. Neco, E. Caballero-Garrido, E. Vieira, C. Ripoll, A. Nadal and I. Quesada, *J. Mol. Endocrinol*, 2012, **49**, 9-17 (DOI:10.1530/JME-12-0025).
- 57 L. Jiang, Z. Li and L. Rui, *JBC*, 2008, **283**, 28066-28073 (DOI:10.1074/jbc.M805545200).
- 58 A. Bettaieb, S. Liu, Y. Xi, N. Nagata, K. Matsuo, I. Matsuo, S. Chahed, J. Bakke, H. Keilhack, T. Tiganis and F. G. Haj, *JBC*, 2011, **286**, 9225-9235 (DOI:10.1074/jbc.M110.186148).
- 59 R. Banno, D. Zimmer, B. C. De Jonghe, M. Atienza, K. Rak, W. Yang and K. K. Bence, *JCI*, 2010, **120**, 720-734 (DOI:10.1172/JCI39620).
- 60 T. Jin, H. Yu and X. Huang, *Sci. Rep.*, 2016, **6**, 20766 (DOI:10.1038/srep20766).
- 61 R. Liu, C. Mathieu, J. Berthelet, W. Zhang, J. Dupret and F. Rodrigues Lima, *Int. J. Mol. Sci*, 2022, **23**, 7027 (DOI:10.3390/ijms23137027).
- 62 J. M. Zabolotny, Y. Kim, L. A. Welsh, E. E. Kershaw, B. G. Neel and B. B. Kahn, *JBC*, 2008, **283**, 14230-14241 (DOI:10.1074/jbc.M800061200).
- 63 T. Tiganis and A. M. Bennett, *Biochem. J.*, 2007, **402**, 1-15 (DOI:10.1042/BJ20061548).
- 64 N. K. Tonks, *Nat. Rev. Mol. Cell Bio.*, 2006, **7**, 833-846 (DOI:10.1038/nrm2039).
- 65 J. E. Bleasdale, D. Ogg, B. J. Palazuk, C. S. Jacob, M. L. Swanson, X. Wang, D. P. Thompson, R. A. Conradi, W. R. Mathews, A. L. Laborde, C. W. Stuchly, A. Heijbel,

- K. Bergdahl, C. A. Bannow, C. W. Smith, C. Svensson, C. Liljebris, H. J. Schostarez, P. D. May, F. C. Stevens and S. D. Larsen, *Biochem. (Easton)*, 2001, **40**, 5642-5654 (DOI:10.1021/bi002865v).
- 66 K. R. Torgeson, M. W. Clarkson, G. S. Kumar, R. Page and W. Peti, *JBC*, 2020, **295**, 13829-13837 (DOI:10.1074/jbc.RA120.014652).
- 67 L. F. Iversen, K. B. Møller, A. K. Pedersen, G. H. Peters, A. S. Petersen, H. S. Andersen, S. Branner, S. B. Mortensen and N. P. H. Møller, *JBC*, 2002, **277**, 19982-19990 (DOI:10.1074/jbc.M200567200).
- 68 J. P. Singh, M. Lin, S. Hsu, W. Peti, C. Lee and T. Meng, *Biochemistry*, 2021, **60**, 3856-386. (DOI: <https://doi.org/10.1021/acs.biochem.1c00519>)
- 69 T. Mustelin, L. Tautz and R. Page, *J. Mol Biol.*, 2005, **354**, 150-163 (DOI:10.1016/j.jmb.2005.09.049).
- 70 E. V. Bobkova, W. H. Liu, S. Colayco, J. Rascon, S. Vasile, C. Gasior, D. A. Critton, X. Chan, R. Dahl, Y. Su, E. Sergienko, T. D. Y. Chung, T. Mustelin, R. Page and L. Tautz, *ACS Med. Chem. Lett.*, 2011, **2**, 113-118 (DOI:10.1021/ml100103p).
- 71 D. A. Critton, A. Tortajada, G. Stetson, W. Peti and R. Page, *Biochemistr*, 2008, **47**, 13336-13345 (DOI:10.1021/bi801724n).
- 72 S. Zhang, S. Liu, R. Tao, D. Wei, L. Chen, W. Shen, Z. Yu, L. Wang, D. R. Jones, X. C. Dong and Z. Zhang, *J. Am. Chem. Soc.*, 2012, **134**, 18116-18124 (DOI:10.1021/ja308212y).
- 73 N. L. Alicea-Velázquez, J. Jakoncic and T. J. Boggon, *J. Struct. Biol.*, 2013, **181**, 243-251 (DOI:10.1016/j.jsb.2012.12.009).
- 74 N. L. Alicea-Velazquez and T. J. Boggon, *Protein Peptide Lett*, 2013, **20**, 1039-1048 (DOI:10.2174/09298665113209990041).
- 75 M. Muppirala, V. Gupta and G. Swarup, *BBA – Mol. Cell. Res.*, 2013, **1833**, 1125-1132 (DOI:10.1016/j.bbamcr.2013.01.004).
- 76 K. Nika, H. Hyunh, S. Williams, S. Paul, N. Bottini, K. Taskén, P. J. Lombroso and T. Mustelin, *Biochem. J*, 2004, **378**, 335-342 (DOI:10.1042/bj20031244).
- 77 M. Desjarlais, P. Ruknudin, M. Wirth, I. Lahaie, R. Dabouz, J. C. Rivera, T. Habelrih, S. Omri, P. Hardy, A. Rivard and S. Chemtob, *Front. Cell dev. Biol.*, 2021, **9**, 1-16. (DOI:10.3389/fcell.2021.679906).
- 78 J. Yang, X. Liang, T. Niu, W. Meng, Z. Zhao and G. W. Zhou, *JBC*, 1998, **273**, 28199-28207 (DOI:10.1074/jbc.273.43.28199).
- 79 B. SarathKumar and B. S. Lakshmi, *J. Mol. Model*, 2019, **25**, 272-17 (DOI:10.1007/s00894-019-4172-7).

- 80 R. N. Shinde and M. E. Sobhia, *J. Mol. Graph. Model*, 2013, **45**, 98-110 (DOI:10.1016/j.jmgm.2013.08.001).
- 81 M. Delibegovic and N. Mody, *Acta Medica Saliniana*, 2009, **38**, 2-7 (DOI:10.5457/ams.v38i1.23).
- 82 S. Dadke and J. Chernoff, *Biochem J.*, 2002, **364**, 377-383 (DOI:10.1042/bj20011372).
- 83 J. M. Lipchock, H. P. Hendrickson, B. B. Douglas, K. E. Bird, P. S. Ginther, I. Rivalta, N. S. Ten, V. S. Batista and J. P. Loria, *Biochemistry (Easton)*, 2017, **56**, 96-106 (DOI:10.1021/acs.biochem.6b01025).
- 84 N. K. Tonks, *FEBS Letters*, 2003, **546**, 140-148. (DOI: 10.1016/S0014-5793(03)00603-3)
- 85 N. Krishnan, C. A. Bonham, I. A. Rus, O. K. Shrestha, C. M. Gauss, A. Haque, A. Tocilj, L. Joshua-Tor and N. K. Tonks, *Nat. Com.*, 2018, **9**, 283-300. (DOI:10.1038/s41467-017-02252-2)
- 86 S. Liu, L. Zeng, L. Wu, X. Yu, T. Xue, A. M. Gunawan, Y. Long and Z. Zhang, *J. Am. Chem. Soc.*, 2008, **130**, 17075-17084 (DOI:10.1021/ja8068177).
- 87 A. Panthong, P. Norkaew, D. Kanjanapothi, T. Taesotikul, N. Anantachoke and V. Reutrakul, *J. Ethnopharmacol.*, 2007, **111**, 335-340 (DOI:10.1016/j.jep.2006.11.038).
- 88 Y. Chen, S. He, C. Tang, J. Li and G. Yang, *Fitoterapia*, 2016, **109**, 106-112 (DOI:10.1016/j.fitote.2015.12.002).
- 89 M. R. Shah, Ishtiaq, S. M. Hizbullah, S. Habtemariam, A. Zarrelli, A. Muhammad, S. Collina and I. Khan, *J. Enzyme Inhib. Med. Chem*, 2016, **31**, 563-567 (DOI:10.3109/14756366.2015.1047358).
- 90 A. Saifudin, S. Lallo and Y. Tezuka, *RJP*, 2016, **8**, 38-41 (DOI:10.4103/0974-8490.178644).
- 91 J. Lee, K. Jung, E. Woo and Y. Kim, *Bull. Korean Chem. Soc.*, 2008, **8**, 1479-1484. (DOI: 10.5012/bkcs.2008.29.8.1479)
- 92 S. K. Hansen, C. Wiesmann, K. J. Barr, J. Kung, J. Zhu, D. A. Erlanson, W. Shen, B. J. Fahr, M. Zhong, L. Taylor, M. Randal and R. S. McDowell, *Nat. Struct. Mol. Biol.*, 2004, **11**, 730-737 (DOI:10.1038/nsmb803).
- 93 G. S. Kumar, R. Page, and W. Peti, *PLOS one*, 2020, **15**, e0240044 (DOI:10.1371/journal.pone.0240044).
- 94 S. Singh, A. Singh Grewal, R. Grover, N. Sharma, B. Chopra, A. Kumar Dhingra, S. Arora, S. Redhu and V. Lather, *Bioorg Chem*, 2022, **121**, 105626 (DOI:10.1016/j.bioorg.2022.105626).

- 95 M. Na, B. Y. Kim, H. Osada and J. S. Ahn, *J. Enzyme Inhib. Med. Chem.*, 2009, **24**, 1056-1059 (DOI:10.1080/14756360802693312).
- 96 R. Limbocker, S. Errico, D. Barbut, T. P. J. Knowles, M. Vendruscolo, F. Chiti and M. Zasloff, *Nat. Prod. Rep.*, 2022, **39**, 742-753. (DOI:10.1039/D1NP00042J)
- 97 Z. Qin, N. R. Pandey, X. Zhou, C. A. Stewart, A. Hari, H. Huang, A. F. R. Stewart, J. M. Brunel and H. Chen, *BBRC.*, 2015, **458**, 21-27 (DOI:10.1016/j.bbrc.2015.01.040).
- 98 N. Aberdein, R. J. Dambrino, J. M. Do Carmo, Z. Wang, L. E. Mitchell, H. A. Drummond and J. E. Hall, *Am J Physiol Regul Integr Comp Physiol*, 2018, **314**, R474-R488. (DOI:10.1152/ajpregu.00287.2017)
- 99 R. Huang, H. Tao and C. Wang, *Org. Lett.*, 2017, **19**, 1176 (DOI:10.1021/acs.orglett.7b00215).
- 100 J. Y. Choi, M. Na, I. Hyun Hwang, S. Ho Lee, E. Young Bae, B. Yeon Kim and J. Seog Ahn, *Molecules*, 2009, **14**, 266-272 (DOI:10.3390/molecules14010266).
- 101 S. Legeay, P. Fautrat, J. B. Norman, G. Antonova, S. Kennard, T. Bruder-Nascimento, V. S. Patel, S. Faure and E. J. Belin de Chantemèle, *Biomed. Pharmacother.*, 2020, **127**, 110200 (DOI:10.1016/j.biopha.2020.110200).
- 102 M. Delibegovic, D. Zimmer, C. Kauffman, K. Rak, E. Hong, Y. Cho, J. K. Kim, B. B. Kahn, B. G. Neel and K. K. Bence, *Diabetes*, 2009, **58**, 590-599 (DOI:10.2337/db08-0913).
- 103 K. Choi and Y. Kim, *KJIM*, 2010, **25**, 119-129 (DOI:10.3904/kjim.2010.25.2.119).
- 104 G. W. Millington, *Nutr. Metab.*, 2007, **4**, 18 (DOI:10.1186/1743-7075-4-18).
- 105 R. C. Frederich, A. Hamann, S. Anderson, B. Lollmann, B. B. Lowell and J. S. Flier, *Nat. Med.*, 1995, **12**, 1311-1314. (DOI: 10.1038/nm1295-1311).
- 106 C. Toda, A. Santoro, J. D. Kim and S. Diano, *Annu. Rev. Physiol.*, 2017, **79**, 209-236 (DOI:10.1146/annurev-physiol-022516-034110).
- 107 C. Owen, A. Czopek, A. Agouni, L. Grant, R. Judson, E. K. Lees, G. D. Mcilroy, O. Göransson, A. Welch, K. K. Bence, B. B. Kahn, B. G. Neel, N. Mody and M. Delibegović, *PLoS One*, 2012, **7**, e32700 (DOI:10.1371/journal.pone.0032700).
- 108 G. Gerebtzoff and A. Seelig, *JCIM*, 2006, **46**, 2638-2650 (DOI:10.1021/ci0600814).
- 109 H. Pajouhesh and G. R. Lenz, *NeuroRx*, 2005, **2**, 541-553 (DOI:10.1602/neurorx.2.4.541).
- 110 C. A. Lipinski, *Drug Discov. Today. Technol.*, 2004, **1**, 337-341 (DOI:10.1016/j.ddtec.2004.11.007).

- 111 F. Lovering, J. Bikker and C. Humblet, *J. Med. Chem.*, 2009, **52**, 6752-6756 (DOI:10.1021/jm901241e).
- 112 O. Korb, B. Kuhn, J. Hert, N. Taylor, J. Cole, C. Groom and M. Stahl, *J. Med. Chem.*, 2016, **59**, 4257-4266 (DOI:10.1021/acs.jmedchem.5b01756).
- 113 C. Coley, *Trends Chem.*, 2020, **3**, 133-145. (DOI: 10.1016/j.trechm.2020.11.004)
- 114 , <https://www.rcsb.org/>, (accessed May 8, 2023).
- 115 M. R. Groves, Z. Yao, P. P. Roller, T. R. Burke and D. Barford, *Biochemistry (Easton)*, 1998, **37**, 17773-17783 (DOI:10.1021/bi9816958).
- 116 O. Trott and A. J. Olson, *J. Comput. Chem.*, 2010, **31**, 455-461 (DOI:10.1002/jcc.21334).
- 117 <http://www.pymol.org/pymol>, (accessed 8/5/2023).
- 118 S. K. Hansen, C. Wiesmann, K. J. Barr, J. Kung, J. Zhu, D. A. Erlanson, W. Shen, B. J. Fahr, M. Zhong, L. Taylor, M. Randal and R. S. McDowell, *Nat. Struct. Mol. Biol.*, 2004, **11**, 730-737 (DOI:10.1038/nsmb803).
- 119 D. Motiejunas and R. C. Wade, *Comprehensive Medicinal Chemistry II*, Elsevier Science, 2007.
- 120 J. J. Irwin, K. G. Tang, J. Young, C. Dandarchuluun, B. R. Wong, M. Khurelbaatar, Y. S. Moroz, J. Mayfield and R. A. Sayle, *JCIM.*, 2023, **63**, 1166-1176.
- 121 T. Sander, J. Freyss, M. von Korff and C. Rufener, *JCIM*, 2015, **55**, 460-473 (DOI:10.1021/ci500588j).
- 122 Y. H. Song, Z. Uddin, Y. M. Jin, Z. Li, M. J. Curtis-Long, K. D. Kim, J. K. Cho and K. H. Park, *J. Enzyme Inhib. Med. Chem.*, 2017, **32**, 1195-1202 (DOI:10.1080/14756366.2017.1368502).
- 123 R. N. Shinde, G. S. Kumar, S. Eqbal and M. E. Sobhia, *PLOS ONE*, 2018, **13**, e0199020 (DOI:10.1371/journal.pone.0199020).
- 124 M. R. Baranowski, J. Wu, Y. N. Han, L. J. Lambert, N. D. P. Cosford and L. Tautz *Bio-Protocol*, 2022, **12**, 1-20. (DOI:10.21769/BioProtoc .4510).
- 125 L. K. Harris, S. M. Frumm and A. C. Bishop, *Anal. Biochem*, 2013, **435**, 99-105 (DOI:10.1016/j.ab.2012.12.025).
- 126 J. Montalibet and B. P. Kennedy, *Biochem. Pharmacol.*, 2004, **68**, 1807-1814 (DOI:10.1016/j.bcp.2004.06.024).
- 127 J. B. Trager and G. S. Martin, *Int. J. Biochem. Cell Biol.* 1997, **29**, 635-648. (DOI: 10.1016/s1357-2725(96)00162-8).

- 128 J. A. Kritzer, Y. Freyzon and S. Lindquist, *FEMS*, 2018, **18**, 1-9. (DOI:10.1093/femsyr/foy027).
- 129 F. Wohnsland and B. Faller, *J. Med. Chem.*, 2001, **44**, 923-930 (DOI:10.1021/jm001020e).
- 130 M. Kansy, F. Senner and K. Gubernator, *J. Med. Chem.*, 1998, **41**, 1007-1010 (DOI:10.1021/jm970530e).
- 131 L. Di, E. H. Kerns, K. Fan, O. J. McConnell and G. T. Carter, *EJMECH*, 2003, **38**, 223-232. (DOI: 10.1016/s0223-5234(03)00012-6)
- 132 N. Gauvry and J. Mortier, *Synthesis*, 2001, **4**, 553 (DOI:10.1055/s-2001-12354).
- 133 M. Giroud, J. Ivkovic, M. Martignoni, M. Fleuti, N. Trapp, W. Haap, A. Kuglstatter, J. Benz, B. Kuhn, T. Schirmeister and F. Diederich, *ChemMedChem*, 2017, **12**, 257-270 (DOI:10.1002/cmdc.201600563).
- 134 M. Chinmoy, L. Lin and N. Pohl, *Adv Synth Catal.*, 2014, **356**, 2247-2256.
- 135 R. Di Santo, Y. Pommier, C. Marchand, M. Artico, R. Costi, *J. Med. Chem.*, 2021, **64**, 8579-8598. (DOI: 10.1021/acs.jmedchem.1c00535).
- 136 R. Sreedharan, P. Rajeshwaran, P. K. R. Panyam, S. Yadav, C. M. Nagaraja and T. Gandhi, *Org. Biomol. Chem.*, 2020, **18**, 3843-3847 (DOI:10.1039/D0OB00789G).
- 137 K. Nobuaki, T. Takashi, M. Noritaka, M. Shinji and S. Noboru, *BCSJ*, 1986, **59**, 3013-3018.
- 138 Y. Nishiyama, H. Kawabata, A. Kobayashi, T. Nishino and N. Sonoda, *Tetrahedron Lett.*, 2005, **46**, 867-869 (DOI:10.1016/j.tetlet.2004.11.114).
- 139 Y. Nishiyama, H. Kawabata, T. Nishino, K. Hashimoto and N. Sonoda, *Dehalogenation of o-dihalogen substituted arenes and α,α' -dihalogen substituted o-xylenes with lanthanum metal*, Elsevier BV, 2003.
- 140 A. Burgess and S. Kundu, *CDSR*, 2006, **3**, CD003599 (DOI:10.1002/14651858.CD003599.pub2).
- 141 G. O. Nifontova, S. P. Krechetov, O. V. Dolotova, S. R. Buyukli, A. R. Akhmetzyanova and I. I. Krasnyuk, *Pharm Chem J*, 2018, **52**, 361-365 (DOI:10.1007/s11094-018-1822-5).
- 142 C. A. Halliday, B. J. Jones, M. Skingle, D. M. Walsh, H. Wise and M. B. Tyers, *Br. J. Pharmacol.*, 1991, **102**, 887-895 (DOI:10.1111/j.1476-5381.1991.tb12272.x).
- 143 P. Svenningsson, C. Rosenblad, K. Arvidsson, K. Victorin, C. Keywood, B. Shankar, D. Lowe, A. Bjorklund and H. Widner, *BRAIN*, 2015, **138**, 963-973.
- 144 J. Sun, W. He, H. Liu, J. Qin and C. Ye, *Bioorg. Chem.*, 2019, **88**, 102958 (DOI:10.1016/j.bioorg.2019.102958).

- 145 Q. K. Fang, P. Grover, Z. Han, F. X. Mcconville, R. F. Rossi, D. J. Olsson, D. W. Kessler, S. A. Wald and C. H. Senanayake, *Tetrahedron: Asymmetry*, 2001, **12**, 2169-2174. (DOI:10.1016/S0957-4166(01)00368-8).
- 146 T. Tabanelli, C. Giliberti, R. Mazzoni, R. Cucciniello and F. Cavani, *Green Chem*, 2019, **21**, 329-338 (DOI:10.1039/C8GC02811G).
- 147 G. Guillaumet and F. Suzenet, in *Comprehensive Heterocyclic Chemistry III*, ed. A. Katritzky, C. Ramsden, R. Taylor and E. Scriven, Elsevier Science, 2008, p. 857-905.
- 148 B. Ahmed, S. A. Khan and T. Alam, *Pharmazie*, 2003, **58**, 173-176.
- 149 A. Delgado, G. Leclerc, C. Lobato and D. Mauleon, *Tetrahedron Lett.*, 1988, **29**, 3671-3674.
- 150 H. C. Brown, S. Narasimhan, Y. M. Choi, *J. Org. Chem*, 1982, **47**, 4702-4708. (DOI:10.1021/jo00145a018).
- 151 E. Brun, V. Bellosta and J. Cossy, *J. Org. Chem.*, 2015, **80**, 8668-8676 (DOI:10.1021/acs.joc.5b01323).
- 152 H. Takemura, S. Goto, T. Hosoya and S. Yoshida, *ChemComm. (Cambridge, England)*, 2020, **56**, 15541-15544 (DOI:10.1039/d0cc07212e).
- 153 J. Staroń, D. Warszycki, R. Kurczab, G. Satała, R. Bugno, A. Hogendorf and A. J. Bojarski, *RSC Advances*, 2016, **6**, 54918-54925 (DOI:10.1039/C6RA08714K).
- 154 R. Burwell, *Chem. Rev.*, 1954, **54**, 615-685 (DOI:10.1021/cr60170a003).
- 155 M. Vivekananda Bhatt and S. Kulkarni, *Synthesis*, 1983, **4**, 249-282 (DOI:10.1055/s-1983-30301).
- 156 M. Orlandi, D. Brenna, R. Harms, S. Jost and M. Benaglia, *Org. Process Res. Dev.*, 2018, **22**, 430-445. (DOI:10.1021/acs.oprd.6b00205).
- 157 R. M. Kellogg, J. W. Nieuwenhuijzen, K. Pouwer, T. R. Vries, Q. B. Broxterman, R. F. P. Grimbergen, B. Kaptein, R. M. Crois, E. de Wever, K. Zwaagstra and A. C. van der Laan, *Synthesis*, 2003, **1**, 1626-1638 (DOI:10.1055/s-2003-40508).
- 158 S. Denmark and L. Overman, *Organic Reactions*, 2004, **96**, 400-417 (DOI: 10.1002/0471264180)
- 159 K. R. More and R. S. Mali, *Tetrahedron*, 2016, **72**, 7496-7504 (DOI:10.1016/j.tet.2016.09.068).
- 160 M. H. Barbee, T. Kouznetsova, S. L. Barrett, G. R. Gossweiler, Y. Lin, S. K. Rastogi, W. J. Brittain and S. L. Craig, *J. Am. Chem. Soc.*, 2018, **140**, 12746-12750 (DOI:10.1021/jacs.8b09263).
- 161 R. Johnson and B. Rickborn, *J. Org. Chem.*, 1970, **35**, 1041-1045. (DOI:10.1021/jo00829a039).

- 162 T. Yoshimura, H. Sakae, M. Yoshizawa, K. Hasegawa and E. Tsukurimichi, *Phosphorus, Sulfur, and Silicon*, 2010, **185**, 1162-1173. (DOI:10.1080/10426501003773563).
- 163 S. R. Kasibhatla, B. C. Bookser, G. Probst, J. R. Appleman and M. D. Erion, *J. Med. Chem.*, 2000, **43**, 1508-1518 (DOI:10.1021/jm990448e).
- 164 G. An, H. Ahn, K. A. De Castro and H. Rhee, *Synthesis (Stuttgart)*, 2010, **3**, 477-485 (DOI:10.1055/s-0029-1217115).
- 165 R. Ouellette and D. Rawn, *Organic Chemistry Structure, Mechanism, Synthesis*, Academic Press, 2019.
- 166 M. E. Blake, K. L. Bartlett and M. Jones, *JACS.*, 2003, **125**, 6485-6490 (DOI:10.1021/ja0213672).
- 167 T. L. Wootton and D. M. Allwood, *Org. Biomol. Chem*, 2022, **2**, 2255-2260 (DOI:10.1039/d2ob00093h).
- 168 A. Willard, R. Smith and E. Cragoe, *J. Org. Chem.*, 1981, **46**, 3846-3852.
- 169 N. Miyaura and A. Suzuki, *Chem. Rev.*, 1995, **95**, 2457-2483 (DOI:10.1021/cr00039a007).
- 170 M. Aldeghi, S. Malhotra, D. L. Selwood and A. W. E. Chan, *Chem. Biol Drug. Des.*, 2014, **83**, 450-461 (DOI:10.1111/cbdd.12260).
- 171 R. R. Merchant, D. M. Allwood, D. C. Blakemore and S. V. Ley, *J. Org. Chem.*, 2014, **79**, 8800-8811 (DOI:10.1021/jo501624t).
- 172 T. J. Ritchie and S. J. F. Macdonald, *Drug Discov. Today*, 2009, **14**, 1011-1020 (DOI:10.1016/j.drudis.2009.07.014).
- 173 Y. Zheng, C. M. Tice and S. B. Singh, *BMCL*, 2014, **24**, 3673-3682 (DOI:10.1016/j.bmcl.2014.06.081).
- 174 S. Lee, J. Song, C. M. Park, J. Kim, J. Jeong, W. Cho and D. Lim, *ACS Med. Chem. Lett.*, 2013, **4**, 1054-1058 (DOI:10.1021/ml400235c).
- 175 Y. Dong, T. Furuta, H. Sabit, T. Kitabayashi, S. Jiapaer, M. Kobayashi, Y. Ino, T. Todo, L. Teng, A. Hirao, S. G. Zhao, and M. Nakada, *Oncotarget*, 2017, **8**, 111728-111741. (DOI:10.18632/oncotarget.22904).
- 176 M. Develoux, *Ann Dermatol Venereol*, 2001, **12**, 1317-1325. (DOI: MDOI-AD-12-2001-128-12-0151-9638-101019-ART6).
- 177 J. Weber and G. M. Keating, *Drugs*, 2008, **68**, 1691-1698. (DOI: 10.2165/00003495-200868120-00006)
- 178 G. Reams, A. Lau, V. Knaus, and J. Bauer, *J. Clin. Pharmacol.*, 1993, **4**, 348-353. (DOI: 10.1002/j.1552-4604.1993.tb04668.x).

- 179 D. W. Dodick, R. B. Lipton, J. Ailani, K. Lu, M. Finnegan, J. M. Trugman and A. Szegedi, *NEJM*, 2019, **381**, 2230-2241 (DOI:10.1056/NEJMoa1813049).
- 180 L. J. Scott, *Drugs*, 2020, **80**, 323-328 (DOI:10.1007/s40265-020-01264-5).
- 181 Y. Zheng and C. M. Tice, *EXPERT OPIN DRUG DIS*, 2016, **11**, 831-834 (DOI:10.1080/17460441.2016.1195367).
- 182 A. Stephen, K. Hashmi, L. Schwarz and J. W. Bats, *J. Prakt Chem*, 2000, **1**, 40-51. (DOI: 1436-9966/99/3410X-40).
- 183 S. Yamada, S. Karasawa, Y. Takahashi, M. Aso and H. Suemune, *Asymmetric spirocyclization: A new type of acid-catalyzed intramolecular 1, 4-addition to form carba-spirocyclic compounds*, Elsevier BV, 1998.
- 184 Y. Zheng, C. M. Tice, S. B. Singh, *Bioorg. Med. Chem. Lett.*, 2014, **16**, 3673-3682 (DOI:10.1016/j.bmcl.2014.06.081).
- 185 D. Vachhani, M. Galli, J. Jacobs, L. Van Meervelt and E. V. Van der Eycken, *Chem. Comm.*, 2013, **49**, 7171-7173 (DOI:10.1039/c3cc43418d).
- 186 X. Chen, H. Chen, X. Ji, H. Jiang, Z. Yao and H. Liu, *Org. Lett.*, 2013, **15**, 1846-1849 (DOI:10.1021/ol4004542).
- 187 Y. Yang, L. Li, Y. He, J. Luo and Y. Liang, *Tetrahedron*, 2014, **70**, 702-707 (DOI:10.1016/j.tet.2013.11.084).
- 188 H. Li, Y. Wu, Q. Wu, H. Wang, Z. Zhang and C. Wang, *Synlett*, 2015, **26**, 243 (DOI:10.1055/s-0034-1379616).
- 189 R. Huang, H. Tao and C. Wang, *Org. Lett.*, 2017, **19**, 1176 (DOI:10.1021/acs.orglett.7b00215).
- 190 A. Molchanov, A. Stepanov and R. Kostikov, *Russ. J. Org. Chem.*, 2004, **40**, 1512-1517 (DOI:10.1007/s11178-005-0052-y).
- 191 D. M. Allwood, D. C. Blakemore and S. V. Ley, *Org. Lett.*, 2014, **16**, 3064-3067 (DOI:10.1021/ol5011714).
- 192 D. M. Allwood, D. C. Blakemore, A. D. Brown and S. V. Ley, *J. Org. Chem.*, 2014, **79**, 328-338 (DOI:10.1021/jo402526z).
- 193 W. R. Bamford and T. S. Stevens, *J. Chem. Soc.*, 1952, **18**, 4735-474 (DOI:10.1039/jr9520004735).
- 194 V. Farina, *ASC*, 2004, **346**, 1553-1582 (DOI:10.1002/adsc.200404178).
- 195 S. Jagtap, *Catalysts*, 2017, **7**, 267 (DOI:10.3390/catal7090267).

- 196 G. E. Magoulas, S. E. Bariamis, C. M. Athanassopoulos, A. Haskopoulos, P. G. Dedes, M. G. Krokidis, N. K. Karamanos, D. Kletsas, D. Papaioannou and G. Maroulis, *EJMECH*, 2011, **46**, 721-737 (DOI:10.1016/j.ejmech.2010.12.008).
- 197 E. G. Mamedov, *Russ. J. Org. Chem.*, 2007, **43**, 184-187 (DOI:10.1134/s1070428007020054).
- 198 J. Â Barluenga, F. Fernández-Marí, A. L. Viado, E. Aguilar, B. Olano, S. García-Granda and C. Moya-Rubiera, *Chem. Eur. J.*, 1999, **5**, 883-896. (DOI: 10.1002/(SICI)1521-3765(19990301))
- 199 K. W. Lam, C. L. Tham, C. Y. Liew, A. Syahida, M. B. Abdul Rahman, D. A. Israf and N. H. Lajis, *Med Chem Res*, 2012, **21**, 333-344 (DOI:10.1007/s00044-010-9521-0).
- 200 M. D. Hanwell, D. E. Curtis, D. C. Lonie, T. Vandermeersch, E. Zurek and G. R. Hutchison, *J Cheminform*, 2012, **4**, 17 (DOI:10.1186/1758-2946-4-17).
- 201 , https://files.zymoresearch.com/protocols/t2001_frozen_ez_yeast_transformation_ii.pdf, (accessed May 7, 2023).
- 202 J. Montalibet and B. P. Kennedy, *Biochem. Pharmacol.*, 2004, **68**, 1807-1814 (DOI:10.1016/j.bcp.2004.06.024).
- 203 E. Nyman, I. Lindgren, W. Lövfors, K. Lundengård, I. Cervin, T. A. Sjöström, J. Altimiras and G. Cedersund, *FEBS J.*, 2015, **282**, 951-962 (DOI:10.1111/febs.13194).
- 204 M. N. N. Vieira, N. M. Lyra E Silva, S. T. Ferreira and F. G. De Felice, *Front. Aging neurosci.*, 2017, **9**, 7 (DOI:10.3389/fnagi.2017.00007).
- 205 D. J. Bonda, J. G. Stone, S. L. Torres, S. L. Siedlak, G. Perry, R. Kryscio, G. Jicha, G. Casadesus, M. A. Smith, X. Zhu and H. Lee, *J. Neurochem.*, 2014, **1**, 162-172. (DOI: 10.1111/jnc.12380).
- 206 D. J. Koss, G. Riedel, K. Bence and B. Platt, *Cell calcium (Edinburgh)*, 2013, **53**, 125-138 (DOI:10.1016/j.ceca.2012.11.004).
- 207 A. Cheng, N. Uetani, P. D. Simoncic, V. P. Chaubey, A. Lee-Loy, C. J. Mcglade, B. P. Kennedy and M. L. Tremblay, *Dev Cell.*, 2002, **4**, 497-503. (DOI:10.1016/s1534-5807(02)00149-1).
- 208 D. A. Keedy, Z. B. Hill, J. T. Biel, E. Kang, T. J. Rettenmaier, J. Brandão-Neto, N. M. Pearce, F. Von Delft, J. A. Wells and J. S. Fraser, *MBSB*, 2018, **7**, 1-36. (DOI:10.7554/eLife.36307)
- 209 A. V. Stepanov, A. P. Molchanov and R. R. Kostikov, *Russ. J. Org. Chem*, 2005, **41**, 243-254 (DOI:10.1007/s11178-005-0151-9).
- 210 D. Marcoux, P. Bindschädler, A. W. H. Speed, A. Chiu, J. E. Pero, G. A. Borg and D. A. Evans, *Org. Lett.*, 2011, **13**, 3758-3761 (DOI:10.1021/ol201448h).

- 211 P. Poon, A. Banerjee and M. Laya, *J. Chem. Res.*, 2011, **35**, 67-73
(DOI:10.3184/174751911x12964930076403).
- 212 E. Beckmann, N. Bahr, O. Cullmann, F. Yang, M. Kegel, M. Vögtle, K. Exner, M. Keller, L. Knothe and H. Prinzbach, *EurJOC*, 2003, **1**, 4248-4264
(DOI:10.1002/ejoc.200300298).
- 213 N. P. Grigoryan, S. A. Pogosyan and R. S. Sukasyan, *Pharm. Chem. J.*, 2007, **41**, 59-61 (DOI:10.1007/s11094-007-0013-6).
- 214 R. Sri Vastava and N Venkatathri, *Indian J. Chem.*, 2004, **43**, 888-891.
(DOI:10.1002/chin.200433066).
- 215 G. Meshram and V. D. Patil, *Synth. Commun.*, 2009, **39**, 4384-4395
(DOI:10.1080/00397910902906529).
- 216 H. Mao, A. Lin, Y. Shi, Z. Mao, X. Zhu, W. Li, H. Hu, Y. Cheng and C. Zhu, *Angew. Chem. (International ed.)*, 2013, **52**, 6288-6292
(DOI:10.1002/anie.201301509).
- 217 A. P. Krapcho, J. F. Weimaster, J. M. Eldridge, E. G. E. Jahngen, A. J. Lovey and W. P. Stephens, *J. Org. Chem.*, 1978, **43**, 138-147 (DOI:10.1021/jo00395a032).

Appendix

For Thesis titled: 'Synthesis and drug development of small molecule inhibitors of PTP1B.'

Appendix: Table of Contents

1. Content relating to Chapter 3: Biological assay development.	394
1.1 YSC1 initial investigation	394
1.1.1 Doubling times (T_d) calculated values.	394
1.2 YMK23 initial investigation	395
1.2.1 Doubling time (T_d) calculated values.	395
1.3 Comparison of YMK23 and YSC1 yeast cell lines	396
1.3.1 Growth profiles	396
1.3.2 % change in T_d individual values for YSC1 based transformed cells	401
1.3.3 % change in T_d individual values for YMK23 based transformed cells	402
1.4 All biological repeats for YMK23 transformations	403
1.4.1 Growth curve	403
1.4.2 Doubling time values	404
1.5 DMSO cell toxicity investigation	405
1.5.1 Growth curve	406
1.5.2 Doubling time graph for DMSO toxicity investigation	408
1.5.3 Doubling time data	409
1.6 Known inhibitor yeast assay T_d data	410
1.6.1 Ursolic acid	410
1.6.1.1 PTP1B based	410
1.6.1.2 TCPTP based	412
1.6.2 LZP25	414
1.6.2.1 PTP1B based	414
1.6.2.2 TCPTP based	416
1.7 Reason for use of different concentration ranges of known inhibitors	418
1.8 Example image of cells crashing out of growth media due to addition of certain test compounds at higher concentrations.	419
1.9 Accompanying BBB results of controls and known inhibitors	420
1.9.1 Maximum absorption wavelength	420
1.9.2 Blank corrected absorbance values of known concentrations	420
1.9.2.1 Low permeability control	420
1.9.2.2 Medium permeability control	421
1.9.2.3 High permeability control	421
1.9.2.4 Ursolic acid	422
1.9.2.5 LZP25	422

1.9.3	Concentrations of permeability controls and known inhibitors in both acceptor and donor wells after 24-hours at RT or 37°C.	423
1.9.3.1	Low permeability control	423
1.9.3.2	Medium permeability control	423
1.9.3.3	High permeability control	424
1.9.3.4	Ursolic acid	425
1.9.3.5	LZP25.....	425
1.9.4	Permeability rate comparison.....	426
1.9.4.1	Comparing the two in-house data runs.....	426
1.9.4.2	Comparing in-house data runs to provided example data.	428
1.9.4.3	Equilibrium standard absorbance values.....	431
1.9.4.4	Permeability rate results of permeability controls and known inhibitors.	431
2.	Content relating to Chapter 4: Benzodioxane.....	433
2.1	Doubling time values and growth curves of all benzodioxanes tested.	433
2.1.1	Compounds 6-12, 16-23.	433
2.1.2	Compound 16 dose response screen.	450
2.1.2.1	PTP1B based.....	450
2.1.2.2	TCPTP based.....	454
2.1.3	Compounds 25-33.....	458
2.1.4	Compounds 32 and 33 TCPTP investigation	469
2.1.5	Compound 30 doubling time and growth curve data	473
2.1.6	Compound 30a	477
2.1.6.1	PTP1B based.....	477
2.1.6.2	TCPTP based.....	482
2.1.7	Compound 30a derivatives doubling time and growth curve data.....	486
2.1.8	Compound 55 T _d and growth curves for dose response screen.....	506
2.1.8.1	PTP1B based.....	506
2.1.8.2	TCPTP based.....	511
2.2	Accompanying BBB results of hit benzodioxane compounds.....	515
2.2.1	Maximum absorption wavelength	515
2.2.2	Blank corrected absorbance values of known concentrations.	515
2.2.2.1	Compound 16	515
2.2.2.2	Compound 30a	516
2.2.2.3	Compound 44	516
2.2.2.4	Compound 46	516
2.2.2.5	Compound 47	517

2.2.2.6	Compound 48	517
2.2.2.7	Compound 49	517
2.2.2.8	Compound 50a	518
2.2.2.9	Compound 52a	518
2.2.2.10	Compound 53	518
2.2.2.11	Compound 54	519
2.2.2.12	Compound 55	519
2.2.2.13	Compound 56	519
2.2.2.14	Compound 57	520
2.2.2.15	Compound 58	520
2.2.3	Concentrations of benzodioxane hit compounds in both acceptor and donor wells after 24-hours at RT or 37°C.	521
2.2.3.1	Compound 16	521
2.2.3.2	Compound 30a	521
2.2.3.3	Compound 44	522
2.2.3.4	Compound 46	522
2.2.3.5	Compound 47	522
2.2.3.6	Compound 48	523
2.2.3.7	Compound 49	523
2.2.3.8	Compound 50a	523
2.2.3.9	Compound 52a	524
2.2.3.10	Compound 53	524
2.2.3.11	Compound 54	524
2.2.3.12	Compound 55	525
2.2.3.13	Compound 56	525
2.2.3.14	Compound 57	525
2.2.3.15	Compound 58	526
2.2.4	Equilibrium standard absorbance values for benzodioxane hit compounds. 526	
2.2.5	Permeability rate results for benzodioxane hit compounds.	527
2.3	Compound 30a spot plate results.....	528
2.4	Computational binding modes of comp 57 in PTP active sites.....	529
3.	Content relating to Chapter 5: Spirocyclic dihydropyrazole.	531
3.1	Doubling time and growth curve data of all spirocyclic dihydropyrazoles and related precursor compounds tested.....	531
3.1.1	Sulfonyl hydrazones tested, compounds 61, 63-68	532
3.1.2	Further investigation into Compound 64 and 68.4	548

3.1.3	Doubling time and growth curve data for 62, 69-74 and 77	559
3.1.4	Doubling time and growth curve data for 78, 82-84, 86	574
3.1.5	Dose response screen of compound 78; doubling time and growth curve results. 581	
3.1.6	Doubling time and growth curve data of compound 89.	589
3.1.7	Doubling time and growth curve data for compounds 91-97.....	591
3.2	Accompanying BBB results of the hit spirocyclic dihydropyrazole	600
3.2.1	Maximum absorption wavelength	600
3.2.2	Blank corrected absorbance values of known concentrations.	600
3.2.2.1	Compound 78	600
3.2.3	Concentrations of spirocyclic hit compound in both acceptor and donor wells after 24-hours at RT or 37°C.	601
3.2.3.1	Compound 78	601
3.2.4	Permeability rate of spirocyclic hit compound through synthetic BBB after 24-hours at RT or 37°C.....	601
3.2.4.1	Equilibrium standard absorbance values for compound 78	601
3.2.4.2	Compound 78: permeability rate.....	602
4.	Full statistical comparison of all identified hits within thesis with each other and known inhibitors.....	602
5.	Content relating to Chapter 6: Methodology, ¹ H and ¹³ C NMR Spectra of synthesised compounds.	608
6.	Appendix references.....	823

1. Content relating to Chapter 3: Biological assay development.

1.1 YSC1 initial investigation

1.1.1 Doubling times (T_d) calculated values.

Table I: Calculated doubling times of each plasmid combination transcribed into YSC1 yeast cells.

	Transcribed plasmids incorporated into YSC1 yeast cells					
		PTP1B only	TCPTP only	PTP1B + v- Src	TCPTP + v- Src	untransformed
Biological repeat 1	Mechanical repeat 1	3.25727	3.15067	3.73463	4.10389	2.4571
	Mechanical repeat 2	2.9075	2.94205	3.90286	4.23684	2.44066
	Mechanical repeat 3	3.18542	3.08889	3.65391	4.10389	2.40342
	Mechanical repeat 4	2.8678	3.0616	3.47268	3.7186	2.60876
	Mechanical repeat 5	3.14924	2.9647	3.54551	4.00663	2.51231
	Average	3.18542	3.16795	3.9859	4.30526	2.99157
Biological repeat 2	Mechanical repeat 1	3.70469	3.16361	3.74068	4.09661	2.84777
	Mechanical repeat 2	3.0295	3.01762	4.43756	3.46574	2.72893
	Mechanical repeat 3	2.99028	3.26033	3.45537	3.53647	2.90141
	Average	3.18396	3.22544	4.13326	4.43189	3.1723
Biological repeat 3	Mechanical repeat 1	2.73647	3.77531	3.8637	3.64239	2.93334
	Mechanical repeat 2	3.31016	2.63956	4.36766	3.85725	2.94205
	Mechanical repeat 3	2.89414	3.89627	4.2577	5.11548	2.85481
	Average	3.17666	3.14781	4.18315	4.68659	3.19863
Overall Mean		3.1820	3.1804	4.1008	4.68659	3.1208
Std		0.0047	0.0403	0.1026	0.1942	0.1127

Note: Average T_d values calculated for each biological repeats done so from the averaged growth data. Overall mean is the calculated mean of each biological repeat average T_d value.

Data in the above table relates to Figure 5 in Chapter 3 of the Thesis.

1.2 YMK23 initial investigation

1.2.1 Doubling time (T_d) calculated values.

Table II: Calculated doubling times of each plasmid combination transcribed into YMK23 yeast cells.

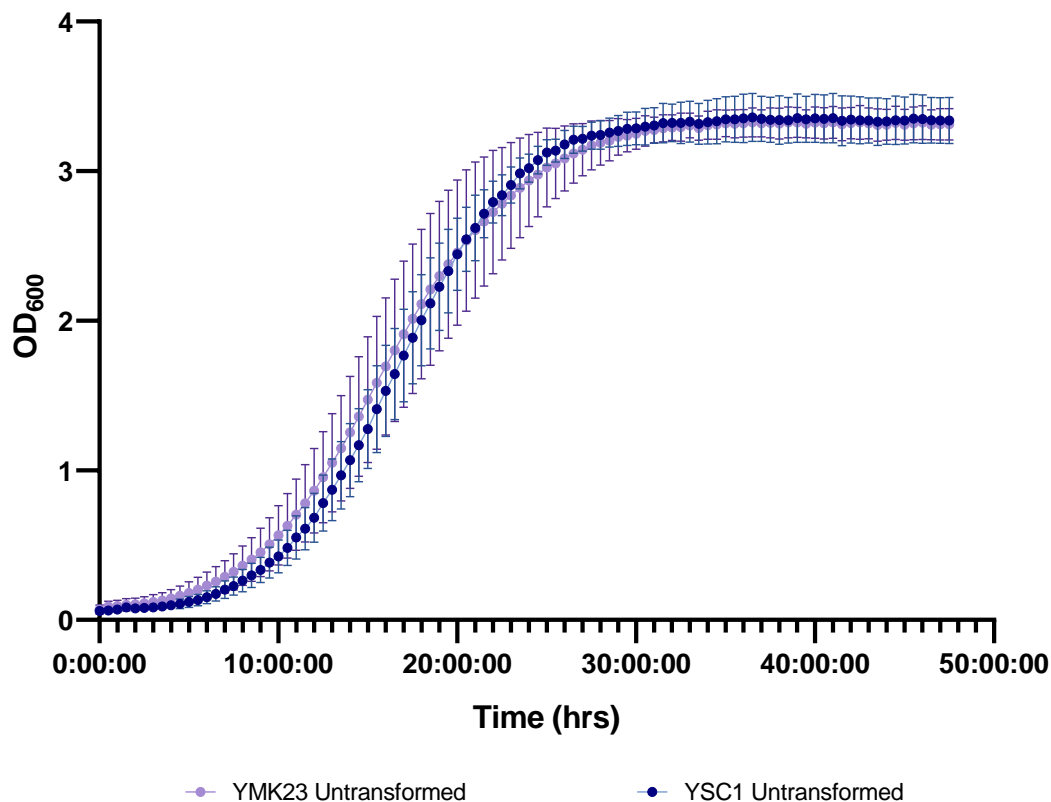
	Transcribed plasmids incorporated into YMK23 yeast cells					
		PTP1B only	TCPTP only	PTP1B + v- Src	TCPTP + v- Src	untransformed
Biological repeat 1	Mechanical repeat 1	3.88398	3.53647	3.48315	4.51268	3.12228
	Mechanical repeat 2	3.28974	3.66939	3.81059	4.04167	3.38947
	Mechanical repeat 3	3.81059	3.61391	3.70667	4.4037	3.32764
	Mechanical repeat 4	3.2913	3.31332	3.78355	4.13472	3.23901
	Mechanical repeat 5	3.42295	3.81689	3.56924	4.20599	3.15067
	Average	3.61391	3.54189	3.76915	4.74433	3.60076
Biological repeat 2	Mechanical repeat 1	3.36479	4.86419	3.86154	4.08454	3.20308
	Mechanical repeat 2	3.40613	4.29459	3.66939	4.23943	3.01631
	Mechanical repeat 3	3.09303	4.07974	4.10146	4.87103	3.30858
	Average	3.83802	3.88971	3.93387	4.62406	3.63094
Biological repeat 3	Mechanical repeat 1	3.84654	4.13819	3.7569	4.50096	2.8556
	Mechanical repeat 2	3.89627	3.90066	3.90726	4.65825	2.82226
	Mechanical repeat 3	3.92273	3.68892	3.78976	4.5363	2.72678
	Average	4.01359	4.01824	4.64887	5.2313	2.99416
Overall Mean		3.8218	3.8166	4.1173	4.8666	3.4086
Std		0.2003	0.2464	0.4677	0.3215	0.3592

Note: Average T_d values calculated for each biological repeats done so from the averaged growth data. Overall mean is the average of each biological repeat average.

Data in the above table relates to **Figure 4** in Chapter 3 of the Thesis

1.3 Comparison of YMK23 and YSC1 yeast cell lines

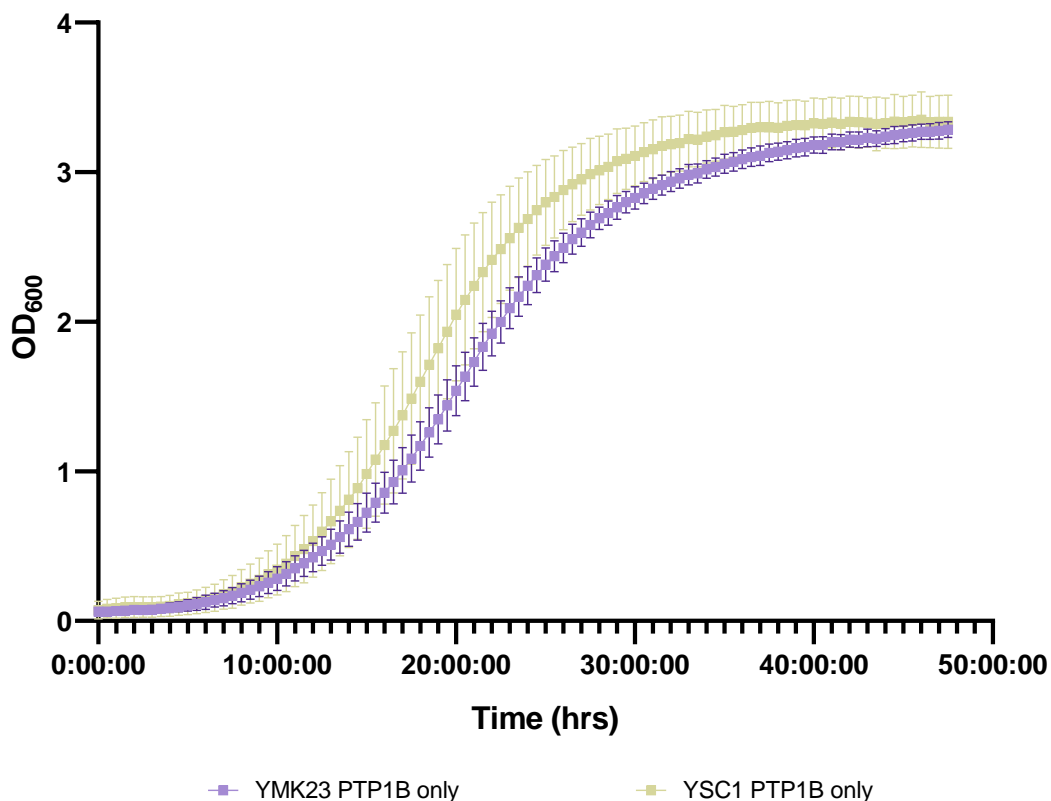
1.3.1 Growth profiles



p value	ns
----------------	----

Figure I: Untransformed yeast cell growth curves of a 47.5-hour period for both utilised strains. $n=3$ for both strains. Mean points \pm standard deviation plotted. Data is normally distributed according to a Shapiro-Wilk test. Used a 2-way ANOVA where column factor was source of variance. * p value ≤ 0.050 .

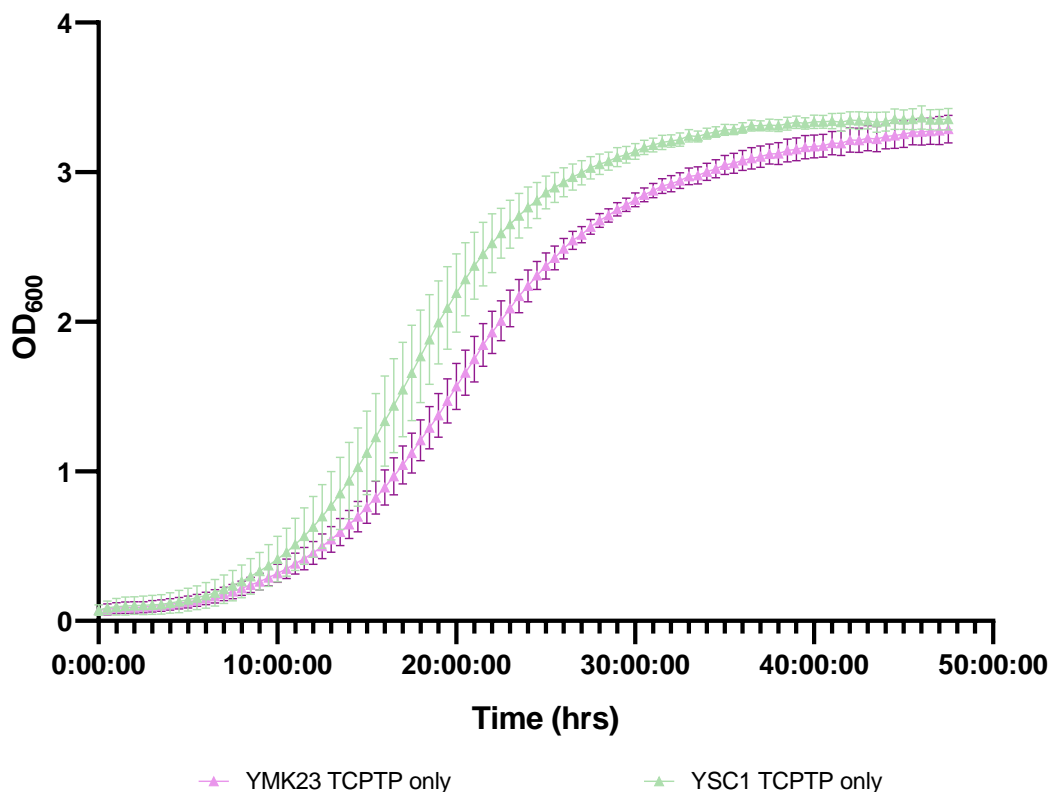
As demonstrated the untransformed growth profiles of both strains YSC1 and YMK23 are not only insignificantly different but also mirror each other very closely.



p value	<0.010 *
---------	----------

Figure II: PTP1B only transformed yeast cell growth curves of a 47.5-hour period for both utilised strains. n=3 for both strains. Mean points \pm standard deviation plotted. Data is normally distributed according to a Shapiro-Wilk test. Used a 2-way ANOVA where column factor was source of variance. * p value \leq 0.050.

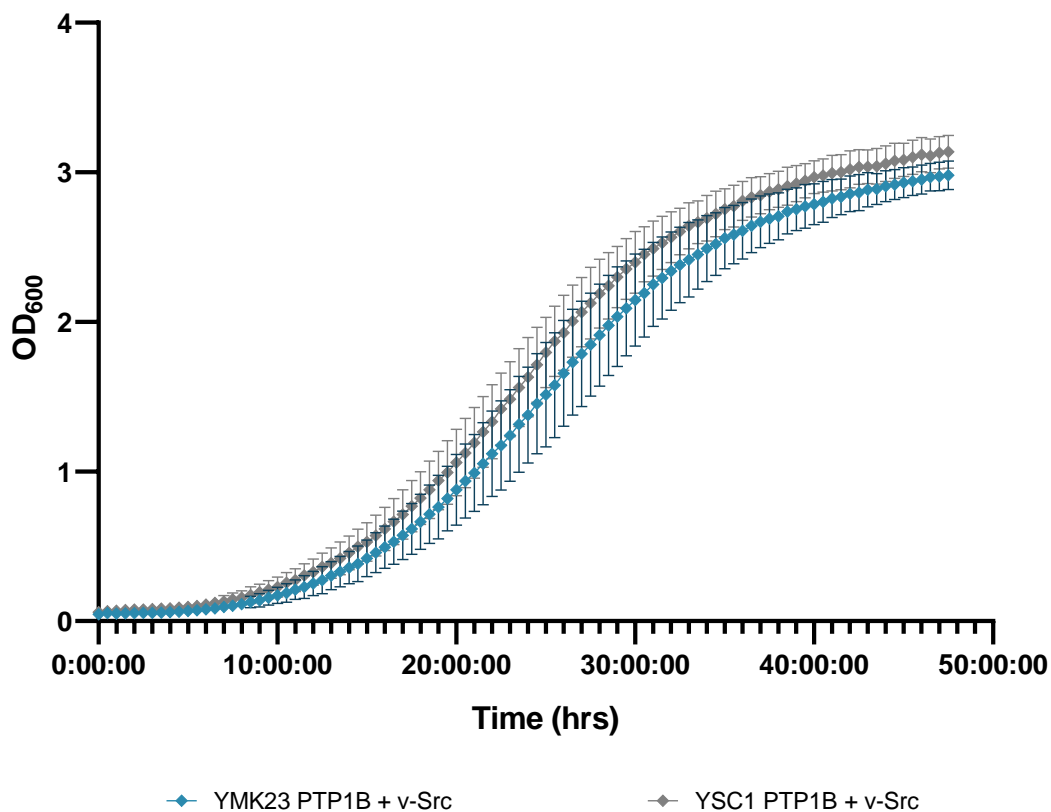
From the growth profiles the absorbance values for YSC1 PTP1B only are significantly higher than those of YMK23 PTP1B only, this is particularly apparent during the 15 to 35-hour period. However, the YMK23 cells ultimately end at the same final absorbance value at the YSC1 version, and the YMK23 biological repeats are more consistent with each other across the entire 47.5-hour time period. Consistently is not essential for the function of the assay but more reproducible base growth data can be considered a bonus.



p value	<0.0001 *
---------	-----------

Figure III: TCPTP only transformed yeast cell growth curves of a 47.5-hour period for both utilised strains. n=3 for each both strains. Mean points \pm standard deviation plotted. Data is normally distributed according to a Shapiro-Wilk test. Used a 2-way ANOVA where column factor was source of variance. * p value \leq 0.050.

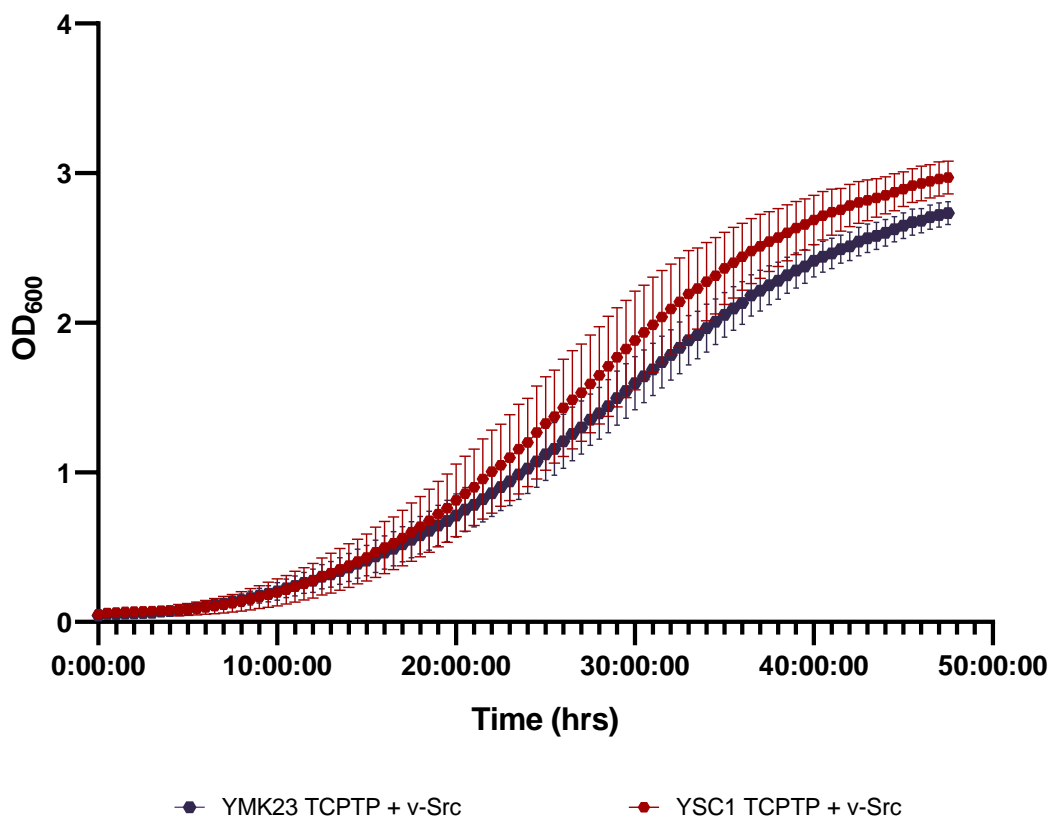
The most significant difference in the growth profiles of YMK23 and YSC1 transformed cells is with the PTP only versions, this is particularly apparent with TCPTP only where a p value of < 0.0001 (****) is calculated. This is predominantly due to the YSC1 based TCPTP only exhibiting significantly higher absorbance values consistently through the 47.5-hour period and thus the presumed greater cell count for the vast majority of the recorded time points. Contributing factors to this significant difference can be attributed to the same reasons as why the PTP only YMK23 cells were also significantly different to YMK23 untransformed cells, as explained above.



p value	<0.050 *
---------	----------

Figure IV: PTP1B + v-Src transformed yeast cell growth curves of a 47.5-hour period for both utilised strains. n=3 for both strains. Mean points \pm standard deviation plotted. Data is normally distributed according to a Shapiro-Wilk test. Used a 2-way ANOVA where column factor was source of variance. * p value \leq 0.050.

The cells lines of greater interest for the assays function are the PTP + v-Src double transcribed cells. The difference between the corresponding YMK23 and YSC1 versions in terms of overall growth profiles are significant with the same trend of the YSC1 absorbance generally being higher is also observed. However, the significance is substantially less than when comparing the PTP only versions of the YMK23 and YSC1 transformations.



p value	<0.050 *
---------	----------

Figure V: TCPTP + v-Src transformed yeast cell growth curves of a 47.5-hour period for both utilised strains. n=3 for both strains. Mean points \pm standard deviation plotted. Data is normally distributed according to a Shapiro-Wilk test. Used a 2-way ANOVA where column factor was source of variance. * p value \leq 0.050.

1.3.2 % change in T_d individual values for YSC1 based transformed cells

Table III: Calculated percentage change in doubling times of each plasmid combination transcribed into YSC1 yeast cells, compared against untransformed YSC1 growth.

	% change in T _d : Transcribed plasmids incorporated into YSC1 yeast cells				
		PTP1B only	TCPTP only	PTP1B + v-Src	TCPTP + v-Src
Biological repeat 1	Mechanical repeat 1	19%	15%	36%	50%
	Mechanical repeat 2	6%	7%	42%	55%
	Mechanical repeat 3	16%	13%	33%	50%
	Mechanical repeat 4	5%	12%	27%	36%
	Mechanical repeat 5	15%	8%	29%	46%
	Average	12%	11%	34%	47%
Biological repeat 2	Mechanical repeat 1	35%	15%	37%	50%
	Mechanical repeat 2	11%	10%	62%	26%
	Mechanical repeat 3	9%	19%	26%	29%
	Average	18%	15%	42%	35%
Biological repeat 3	Mechanical repeat 1	0%	38%	41%	33%
	Mechanical repeat 2	21%	-4%	59%	41%
	Mechanical repeat 3	6%	42%	55%	87%
	Average	9%	25%	52%	54%
Overall Mean		13%	17%	42%	45%
Std deviation		3%	5%	6%	7%

% change in T_d calculated with this equation:

$$((T_d \text{ of transformed} - T_d \text{ of untransformed}) / T_d \text{ of untransformed}) \times 100.$$

Overall Mean and standard deviation, calculated from the averaged value of each biological repeat.

1.3.3 % change in T_d individual values for YMK23 based transformed cells

Table IV: Calculated percentage change in doubling times of each plasmid combination transcribed into YMK23 yeast cells, compared against untransformed YMK23 growth.

	% change in T_d : Transcribed plasmids incorporated into YMK23 yeast cells				
		PTP1B only	TCPTP only	PTP1B + v-Src	TCPTP + v-Src
Biological repeat 1	Mechanical repeat 1	26%	15%	13%	47%
	Mechanical repeat 2	7%	19%	24%	31%
	Mechanical repeat 3	24%	18%	21%	43%
	Mechanical repeat 4	7%	8%	23%	34%
	Mechanical repeat 5	11%	24%	16%	37%
	Average	15%	17%	19%	39%
Biological repeat 2	Mechanical repeat 1	9%	58%	26%	33%
	Mechanical repeat 2	11%	40%	19%	38%
	Mechanical repeat 3	1%	33%	33%	58%
	Average	7%	44%	26%	43%
Biological repeat 3	Mechanical repeat 1	25%	35%	22%	46%
	Mechanical repeat 2	27%	27%	27%	52%
	Mechanical repeat 3	28%	20%	23%	48%
	Average	27%	27%	24%	49%
Overall Mean		16%	29%	23%	43%
Std deviation		7%	10%	2%	4%

% change in T_d calculated with this equation:

$$((T_d \text{ of transformed} - T_d \text{ of untransformed}) / T_d \text{ of untransformed}) \times 100.$$

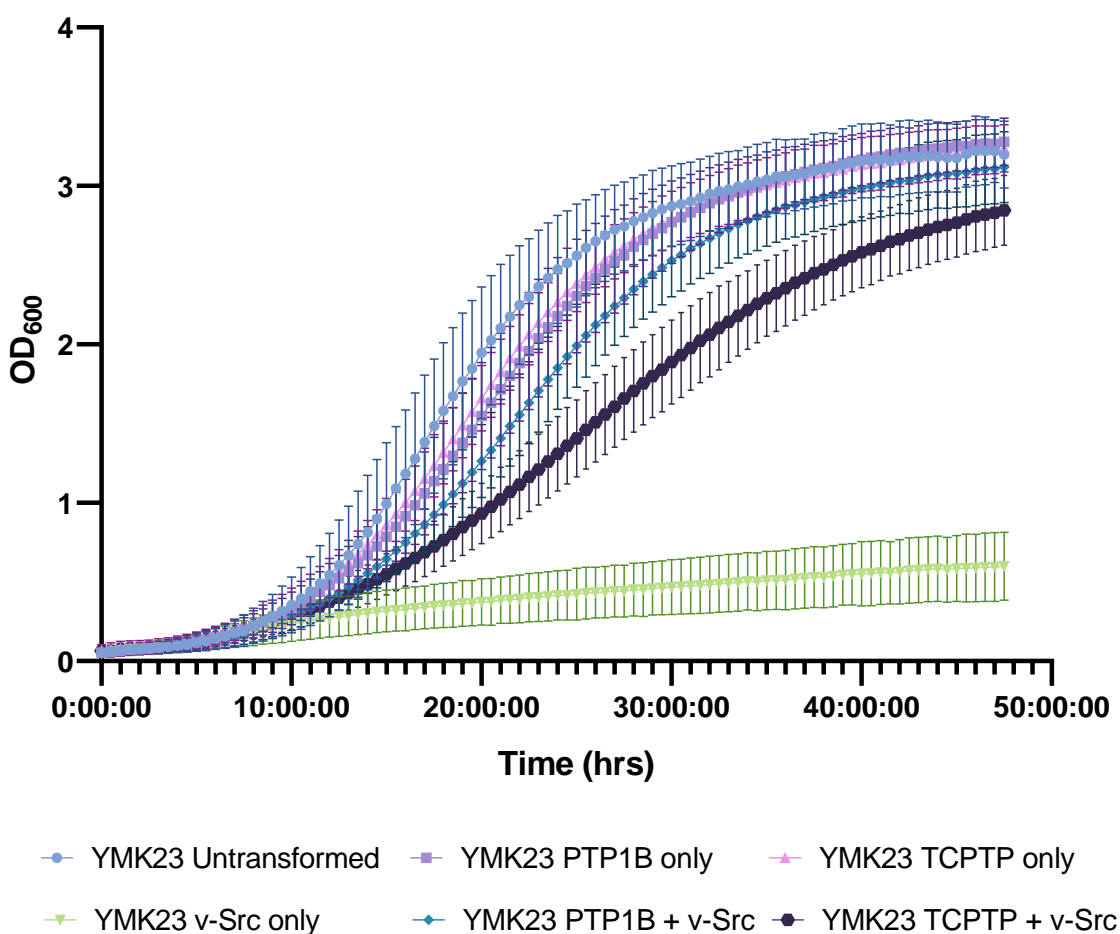
Overall Mean and standard deviation, calculated from the averaged value of each biological repeat.

The calculated % change in T_d data presented in **Table III** and **Table IV** denotes the values shown graphically in **Figure 10** of Chapter 3 of the Thesis.

1.4 All biological repeats for YMK23 transformations

With the yeast strain YMK23 selected for all subsequent yeast assay PTP inhibition testing a compilation of all biological repeats of the base growth curves and T_d values for all transformation is graphed below. The biological repeat n number for each YMK23 transformation is as follows: Untransformed n=13, v-Src only n=17, PTP1B only n=100, PTP1B + v-Src n=100, TCPTP only n=62, TCPTP + v-Src n=62.

1.4.1 Growth curve

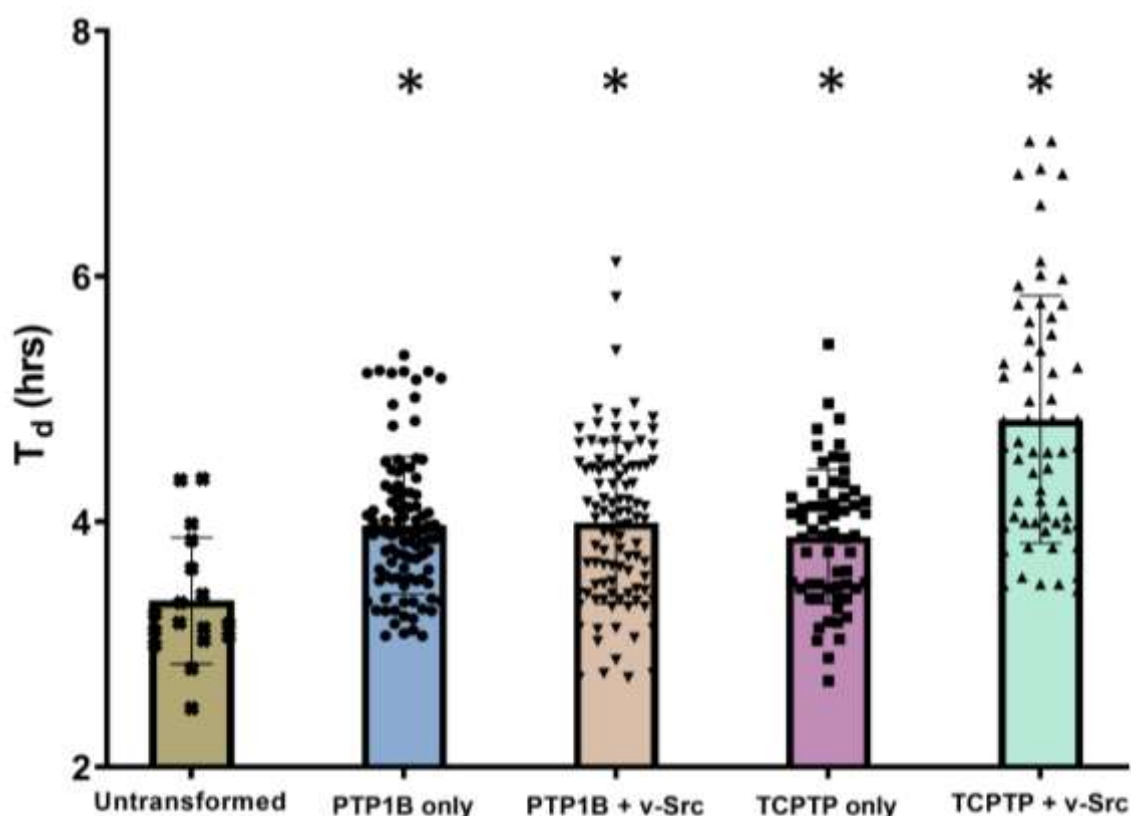


Transformed cell	PTP1B only	TCPTP only	v-Src only	PTP1B + v-Src	TCPTP + v-Src
p value	<0.050 *	ns	<0.0001 *	<0.0001 *	<0.0001 *

Figure VI: Complete compiled growth profiles of each YMK23 transformation. Untransformed cells n=16, PTP1B only and PTP1B + v-Src cells n=100, TCPTP only and TCPTP + v-Src cells n=62. Mean and individual biological points \pm standard deviation plotted. Data is normally distributed according to a Shapiro-Wilk test. Used a parametric t-test with Welch's corrections. * p value \leq 0.050 vs untransformed cells.

As shown above with a greater number of repeats the sole PTP transformation growth profiles are less significantly different from the untransformed original cells with the TCPTP only not being significantly different. However, the PTP + v-Src transformation remained very significantly different, but as mentioned previously this is as expected as the PTP plasmids does not completely rescue the growth downregulation caused by v-Src plasmid incorporation. As demonstrated in the main text the profile of v-Src only transformation also maintained the desired growth profile.

1.4.2 Doubling time values



Transformed cells	PTP1B only	TCPTP only	PTP1B + v-Src	TCPTP + v-Src
p value	<0.0050	<0.0500	<0.0005	<0.0001

Figure VII: Complete compiled T_d values of each YMK23 transformation.

Untransformed cells n=16, PTP1B only and PTP1B + v-Src cells n=100, TCPTP only and TCPTP + v-Src cells n=62. Mean and individual biological points \pm standard deviation plotted. Data is normally distributed according to a Shapiro-Wilk test. Used a parametric t-test with Welch's corrections. * p value \leq 0.050 vs untransformed cells.

Unlike with the initial investigation of yeast strains, the inclusion of any single or combination of plasmids does cause a significant difference in the doubling time (T_d) value when compared to untransformed yeast, but importantly there is no significant difference between the base growth of PTP1B only and PTP1B + v-Src (p value = 0.7820), meaning that in terms of the exponential growth phase the PTP1B plasmid is able to recover the growth effectively. However, this is not the case when comparing TCPTP only with TCPTP + v-Src as there is a significant difference (p value < 0.0001), in part due to the increased range of biological repeat values particularly the top six which skew the average. This implies that the TCPTP plasmid is less capable at restoring the exponential growth phase than PTP1B is. As mentioned previously, this does not lessen the relevance of the TCPTP based inhibition results as when the percentage change in T_d is calculated the inhibitory effect of potential inhibitors can still be verified against the TCPTP only line in which the potential inhibitor should have minimal effect, as in the case of the sole PTP transcribed cells PTP inhibition is not tied to growth rate.

1.5 DMSO cell toxicity investigation

Another aspect of verifying this yeast-based assay prior to starting testing compounds is to ensure that the resultant concentration of DMSO in the wells for the testing of potential inhibitors does not itself cause a significant effect on the growth rate (T_d value).

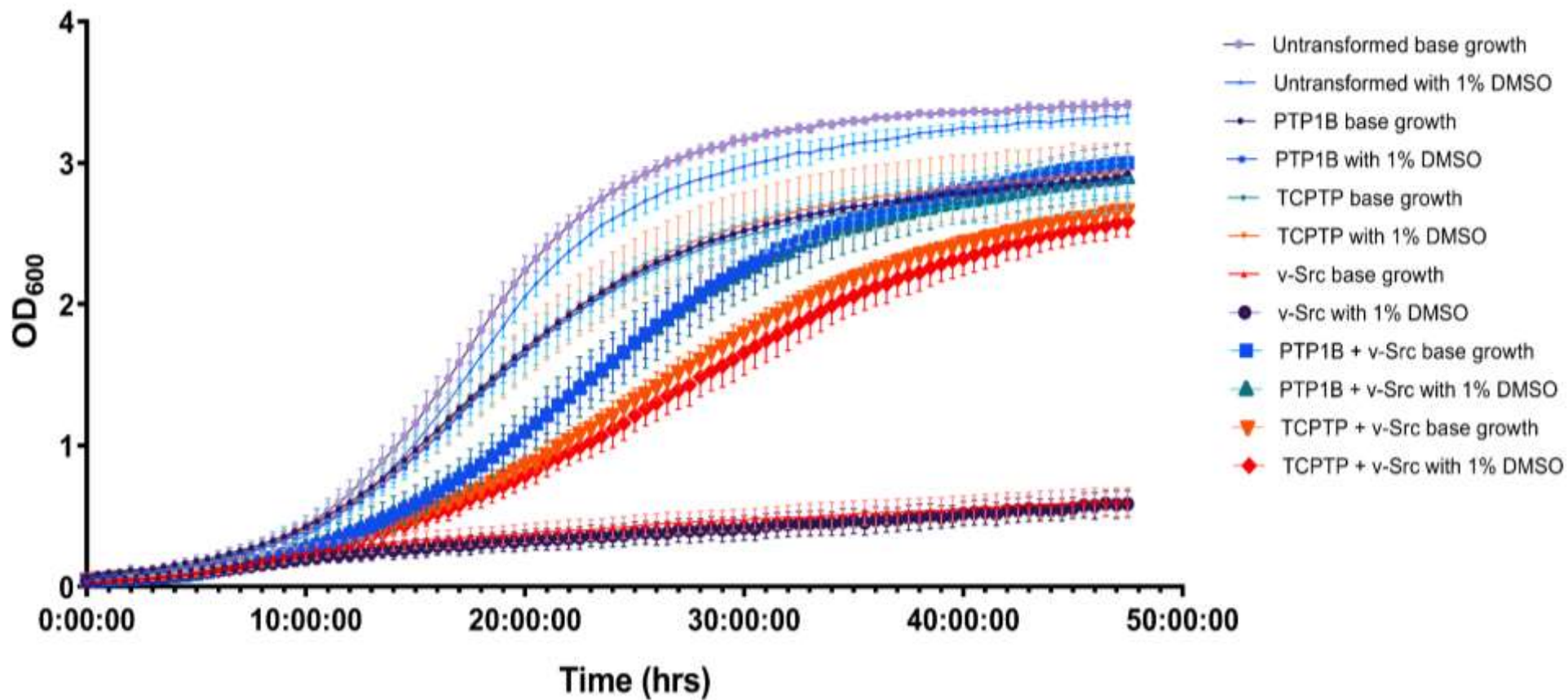
This is because all stock solutions for each compound tested were dissolved in 100% DMSO and subsequently diluted in the required amount of sterile water prior to the final addition to the wells for testing to ensure the desired compound concentration is present.

Previous literature has shown that DMSO can negatively impact yeast growth via inducing oxidative stress resulting in decreasing cell viability, however it has been previously stated to not cause cell lysis (protein leakage from the cells).^{3,4}

Since the function of the assay is identifying PTP inhibitors by measuring the % change in growth rate so it is important to reduce or remove any other factors which affect this if possible. Hence why the final percentage of DMSO in each well was limited to a maximum of 1% to prevent the DMSO negatively impacting growth. This is confirmed to be the case with only 1% DMSO being run in each version of transformed YMK23 cells.

1.5.1 Growth curve

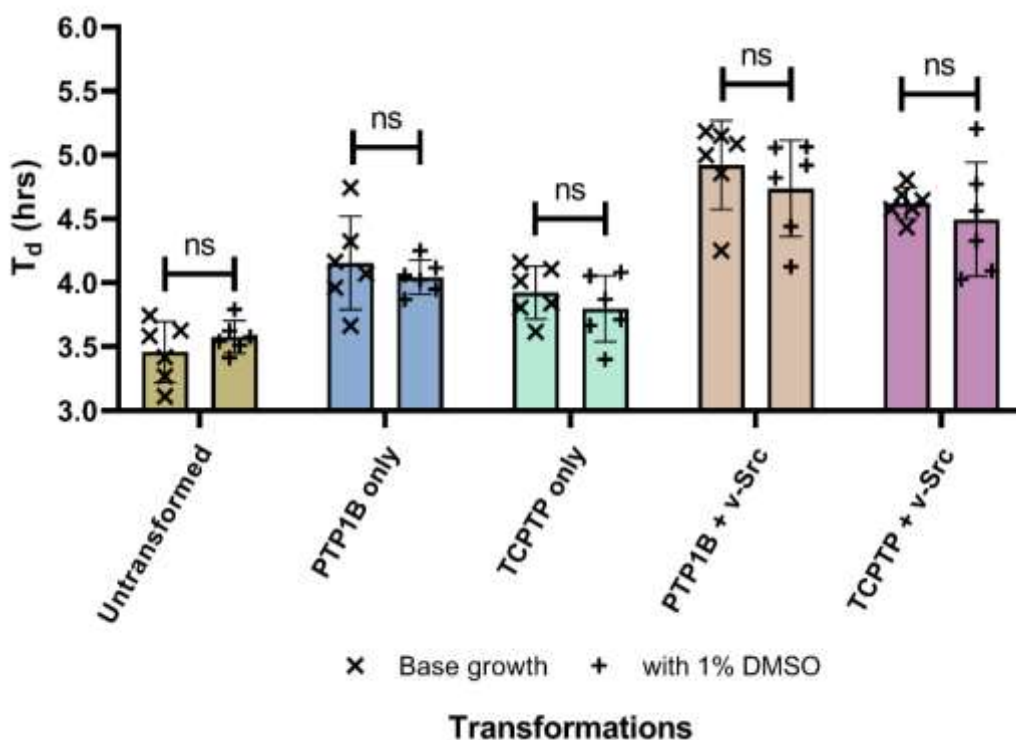
As shown in **Figure VIII** the addition of 1% DMSO had no significant effect on the overall growth profile the exponential growth phase in any of the YMK23 yeast cell transformations used. This is further demonstrated below in **Figure IX** with the corresponding T_d values also not being significantly different when comparing base growth to the addition of 1% DMSO.



Transformation	Untransformed	PTP1B only	TCPTP only	v-Src only	PTP1B + v-Src	TCPTP + v-Src
p value	<0.001 *	ns	ns	ns	ns	ns

Figure VIII: YMK23 growth curves of all YMK23 transformations with and without the addition of 1% DMSO. n=6 for each parameter. Mean points \pm standard deviation plotted. Data is normally distributed according to a Shapiro-Wilk test. Used a 2-way ANOVA where column factor was source of variance. * p value ≤ 0.050 corresponding base growth vs with 1% DMSO.

1.5.2 Doubling time graph for DMSO toxicity investigation



Cells	Untransformed	PTP1B only	TCPTP only	PTP1B + v-Src	TCPTP + v-Src
p value	ns	ns	ns	ns	ns

Figure IX: Doubling times for YMK23 transformations with and without the addition of 1% DMSO, n=6 for all cell transformations. Mean points \pm standard deviation plotted. Data is normally distributed according to a Shapiro-Wilk test. Used parametric Welch t-test for statistical analysis. * p value \leq 0.050 vs base growth.

Based on the results presented in **Figure VIII** and **Figure IX** it is apparent that at the maximum DMSO concentration used there is no significant impact on the growth of any of the transformed yeast cells, with regards to the overall growth profile and the exponential growth phase specifically. With regards to untransformed yeast cells the addition of 1% DMSO resulted in no significant change in the doubling time of the exponential growth phase of the yeast cells. Therefore, presumably any DMSO concentration less than 1% also would not exert a significant response.

1.5.3 Doubling time data

Table V: Calculated T_d values of each plasmid combination transcribed into YMK23 yeast cells with addition of DMSO, compared against corresponding base growth.

	T_d : Effect of DMSO addition on YMK23 transformed yeast cells			
		Base growth	DMSO at 1%	% change in T_d
Untransformed	1	3.41957	3.54008	3.5%
	2	3.26802	3.57846	9.5%
	3	3.11107	3.41284	9.7%
	4	3.7427	3.51138	-6.2%
	5	3.62525	3.79183	4.6%
	6	3.58401	3.62335	1.1%
	Mean	3.45844	3.57632	3.7%
	Std deviation	0.20101	0.10752	0.05
PTP1B only	1	4.744334	4.25244	-10.4%
	2	4.32406	4.11608	-4.8%
	3	4.16305	4.02058	-3.4%
	4	3.96084	4.05824	2.5%
	5	4.07015	3.86801	-5.0%
	6	3.66357	3.94956	7.8%
	Mean	4.154334	4.04415	-2.2%
	Std deviation	0.30761	0.11294	0.05405
TCPTP only	1	4.10632	3.87233	-5.7%
	2	4.15805	4.08214	-1.8%
	3	4.01359	4.05349	1.0%
	4	3.61579	3.40111	-5.9%
	5	3.80641	3.71064	-2.5%
	6	3.83802	3.66745	-4.4%
	Mean	3.92303	3.79786	-3.2%
	Std deviation	0.17413	0.21835	0.02243
PTP1B + v-Src	1	4.25244	4.4404	4.4%
	2	4.85737	5.06316	4.2%
	3	4.9997	4.91943	-1.6%
	4	5.18435	5.05578	-2.5%
	5	5.08545	4.82022	-5.2%
	6	5.14968	4.12588	-19.9%
	Mean	4.9215	4.73748	-3.4%
	Std deviation	0.294207	0.3184	0.07547
TCPTP + v-Src	1	4.58431	4.77046	4.1%
	2	4.57523	4.32946	-5.4%
	3	4.68659	4.09419	-12.6%
	4	4.80685	4.56018	-5.1%
	5	4.64723	5.20381	12.0%
	6	4.43472	4.02524	-9.2%
	Mean	4.62249	4.49722	-2.7%
	Std deviation	0.10533	0.37630	0.077058

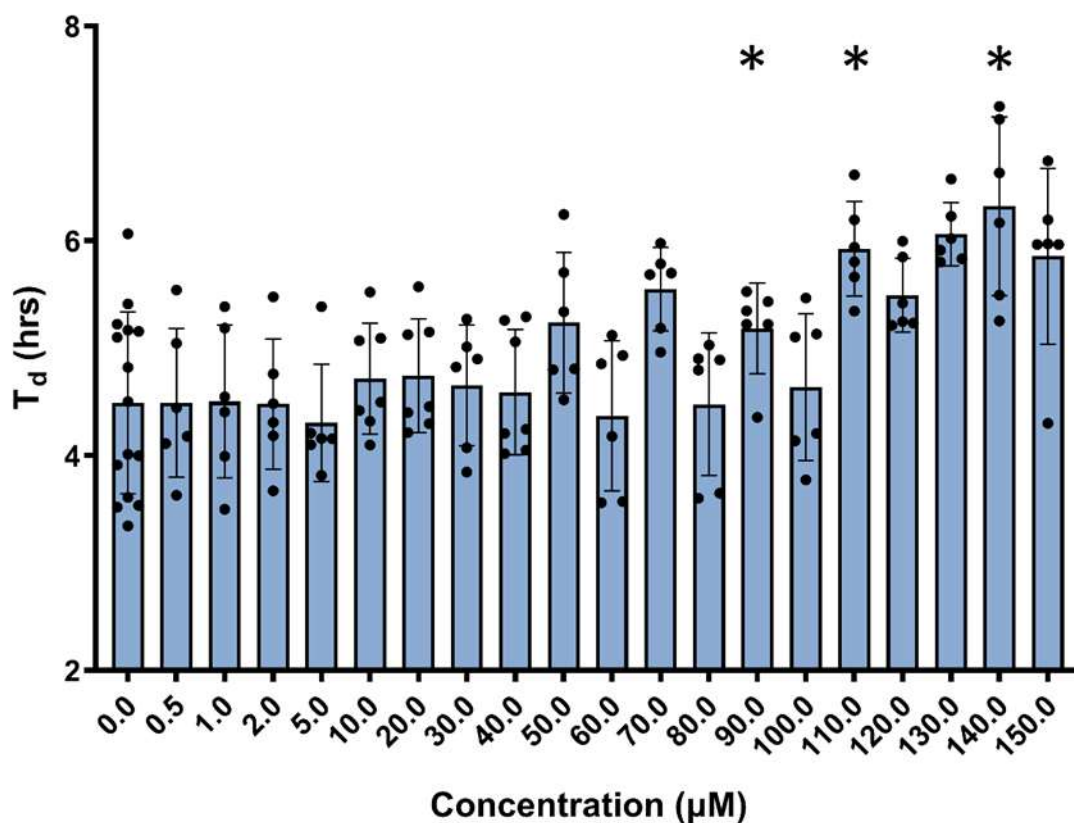
Data in **Table V** is the plotted above in **Figure IX**.

% change in T_d calculated with this equation:

1.6 Known inhibitor yeast assay T_d data.

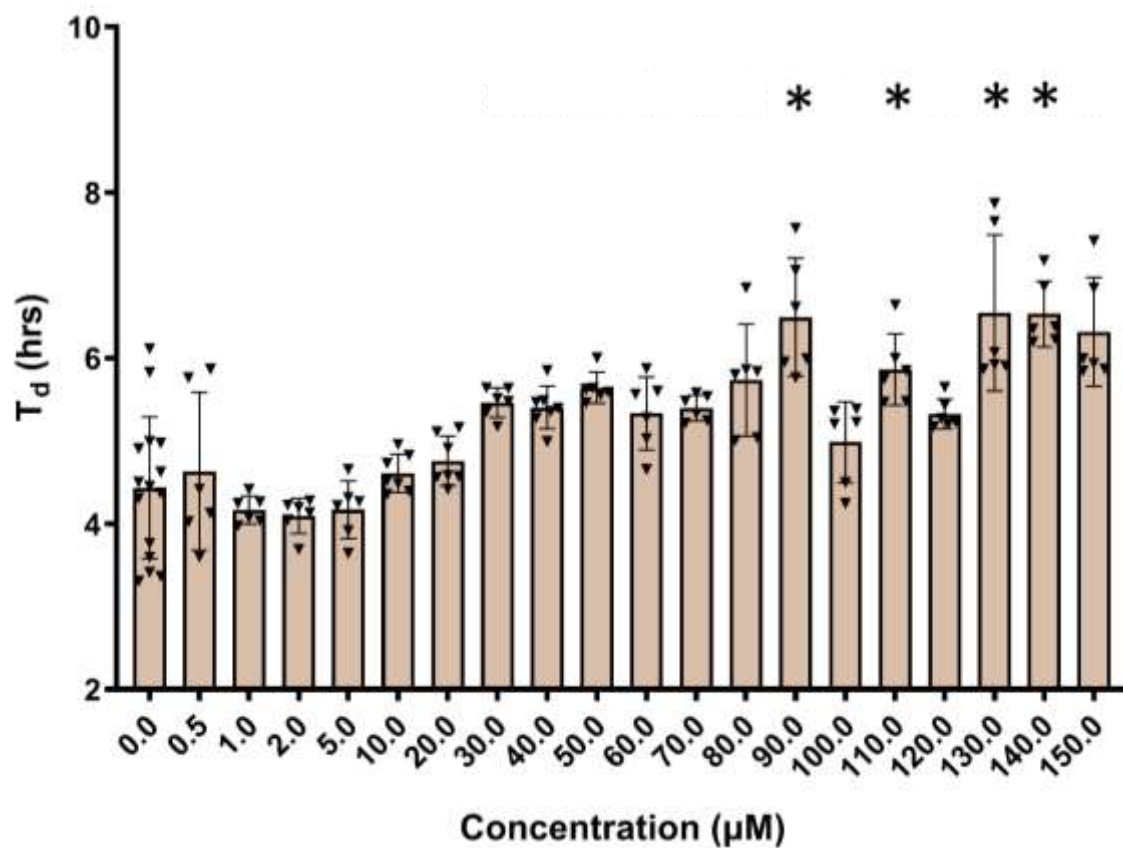
1.6.1 Ursolic acid

1.6.1.1 PTP1B based.



μM	μM
ns	0.5
ns	1.0
ns	2.0
ns	5.0
ns	10.0
ns	20.0
ns	30.0
ns	40.0
ns	50.0
ns	60.0
ns	70.0
ns	80.0
<0.050	90.0
ns	100.0
<0.050	110.0
ns	120.0
ns	130.0
<0.050	140.0
ns	150.0

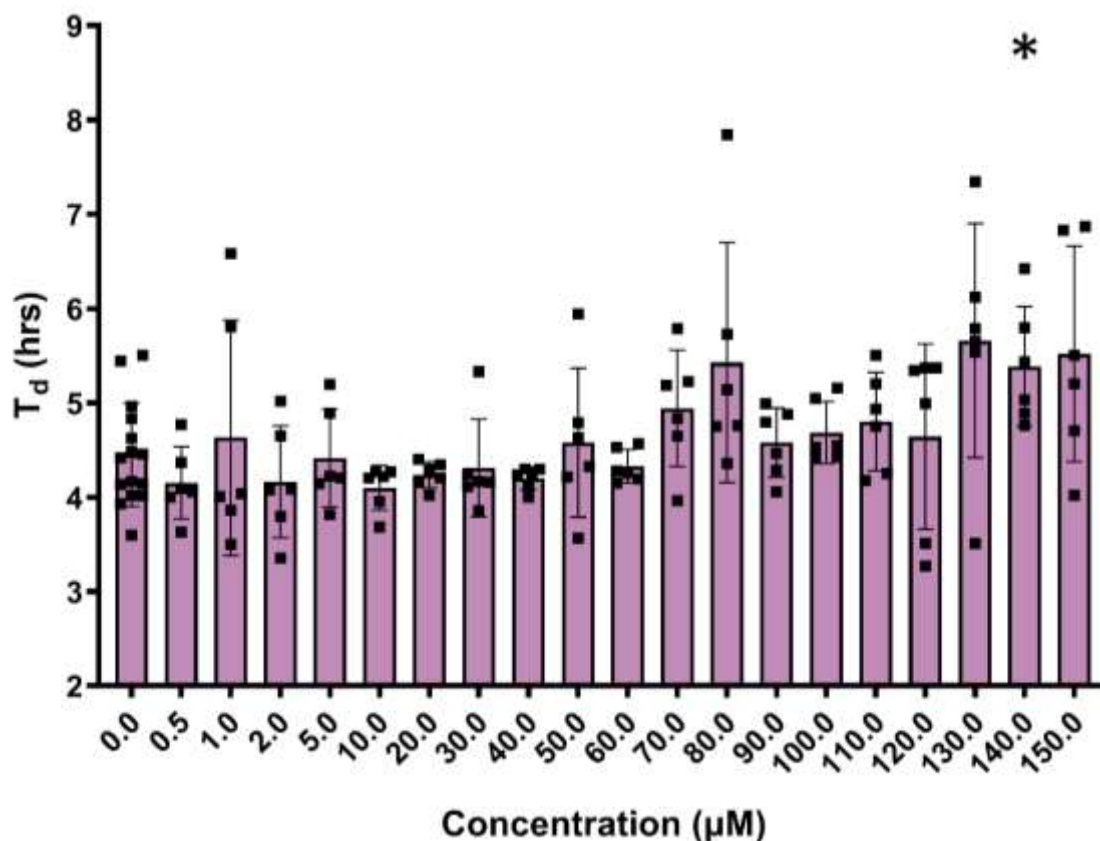
Figure X: Comparison in doubling time (T_d) of PTP1B only transformed yeast cells in the presence of ursolic acid at 0.5-150 μM . $n=7$ for 0.5-20 and 40 μM $n=6$ for rest of concentrations tested in both transformations, $n=15$ for base growth (0.0 μM). Mean and individual points \pm standard deviation plotted. Data is not normally distributed according to a Shapiro-Wilk test. Used non-parametric Mann-Whitney t-test for statistical analysis. * p value ≤ 0.050 vs base growth. Comparison occurred with corresponding base growth values, not all presented biological repeats.



μM	p values
0.5	ns
1.0	ns
2.0	ns
5.0	ns
10.0	ns
20.0	ns
30.0	ns
40.0	ns
50.0	ns
60.0	ns
70.0	ns
80.0	ns
90.0	<0.050
100.0	ns
110.0	<0.050
120.0	ns
130.0	<0.050
140.0	<0.050
150.0	ns

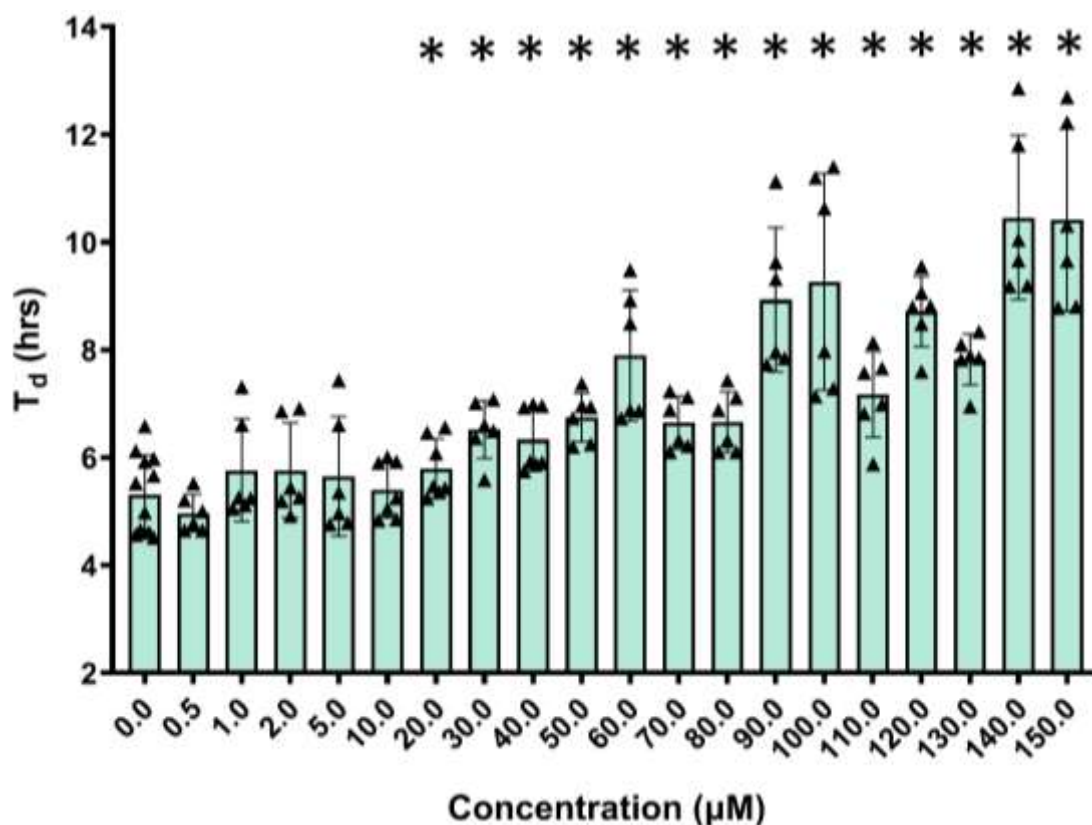
Figure XI: Comparison in doubling time (T_d) of PTP1B + v-Src transformed yeast cells in the presence of ursolic acid at 0.5-150 μM . $n=7$ for 0.5-20 and 40 μM $n=6$ for rest of concentrations tested in both transformations, $n=15$ for base growth (0.0 μM). Mean and individual points \pm standard deviation plotted. Data is normally distributed according to a Shapiro-Wilk test. Used parametric Welch's t-test for statistical analysis. * p value ≤ 0.050 vs base growth. Comparison occurred with corresponding base growth values, not all presented biological repeats.

1.6.1.2 TCPTP based.



μM	p values
0.5	ns
1.0	ns
2.0	ns
5.0	ns
10.0	ns
20.0	ns
30.0	ns
40.0	ns
50.0	ns
60.0	ns
70.0	ns
80.0	ns
90.0	ns
100.0	ns
110.0	ns
120.0	ns
130.0	ns
140.0	<0.050
150.0	ns

Figure XII: Comparison in doubling time (T_d) of TCPTP only transformed yeast cells $n=6$ for all concentrations tested in both transformations, $n=12$ for base growth (0.0 μM). Mean and individual points \pm standard deviation plotted. Data is not normally distributed according to a Shapiro-Wilk test. Used non-parametric Mann-Whitney t-test for statistical analysis. * p value ≤ 0.050 vs base growth. Comparison occurred with corresponding base growth values, not all presented biological repeats.

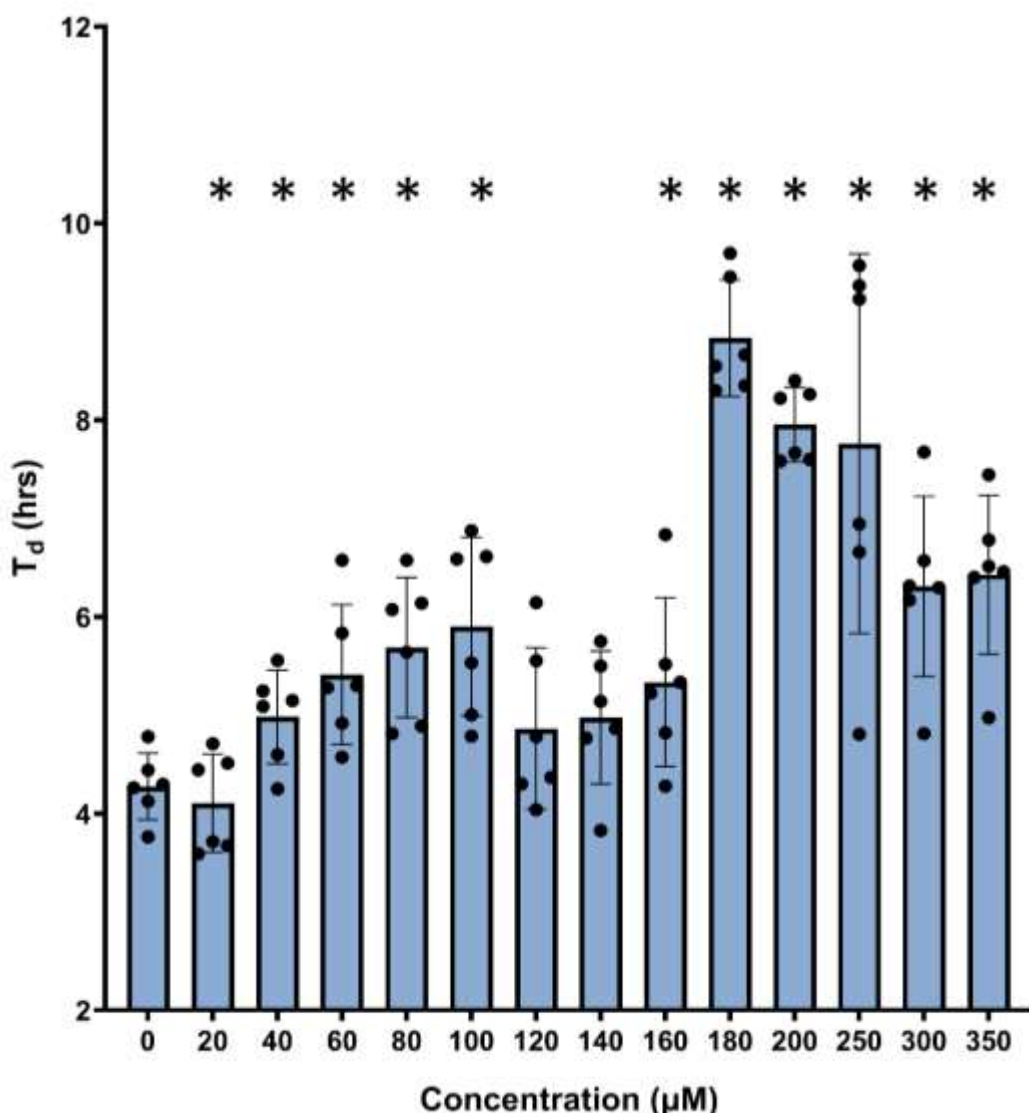


μM	p values
0.5	ns
1.0	ns
2.0	ns
5.0	ns
10.0	ns
20.0	<0.0500
30.0	<0.0010
40.0	<0.0010
50.0	<0.0050
60.0	<0.0050
70.0	<0.0050
80.0	<0.0050
90.0	<0.0010
100.0	<0.0050
110.0	<0.0050
120.0	<0.0001
130.0	<0.0001
140.0	<0.0005
150.0	<0.0010

Figure XIII: Comparison in doubling time (T_d) of TCPTP + v-Src transformed yeast cells in the presence of ursolic acid at 0.5-150 μM . $n=6$ for all concentrations tested in both transformations, $n=12$ for base growth (0.0 μM). Mean and individual points \pm standard deviation plotted. Data is normally distributed according to a Shapiro-Wilk test. Used parametric Welch's t-test for statistical analysis. * p value ≤ 0.050 vs base growth. Comparison occurred with corresponding base growth values, not all presented biological repeats.

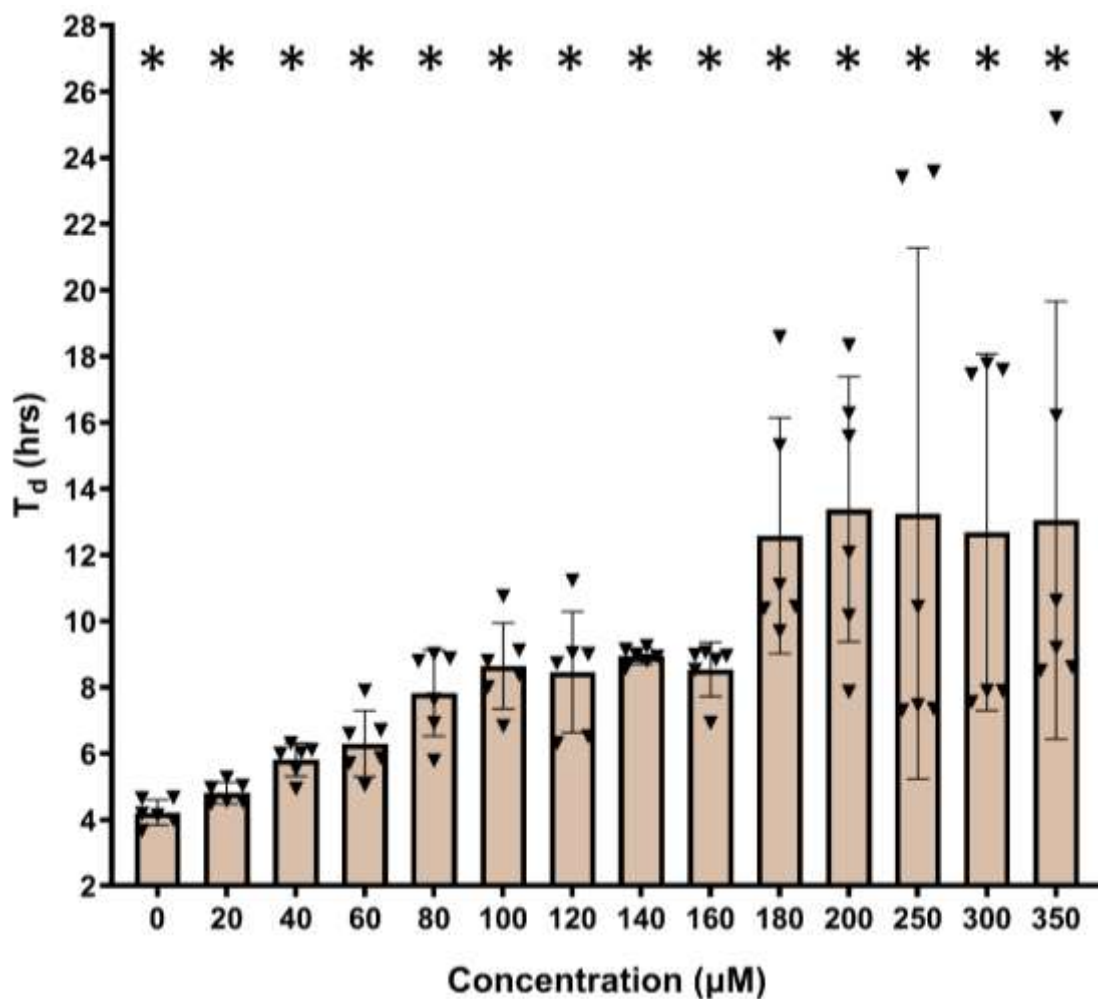
1.6.2 LZP25

1.6.2.1 PTP1B based.



μM	20	40	60	80	100	120	140	160	180	200	250	300	350
p values	ns	<0.0500	<0.0100	<0.0050	<0.0100	ns	ns	<0.0500	<0.0001	<0.0001	<0.0100	<0.0050	<0.0010

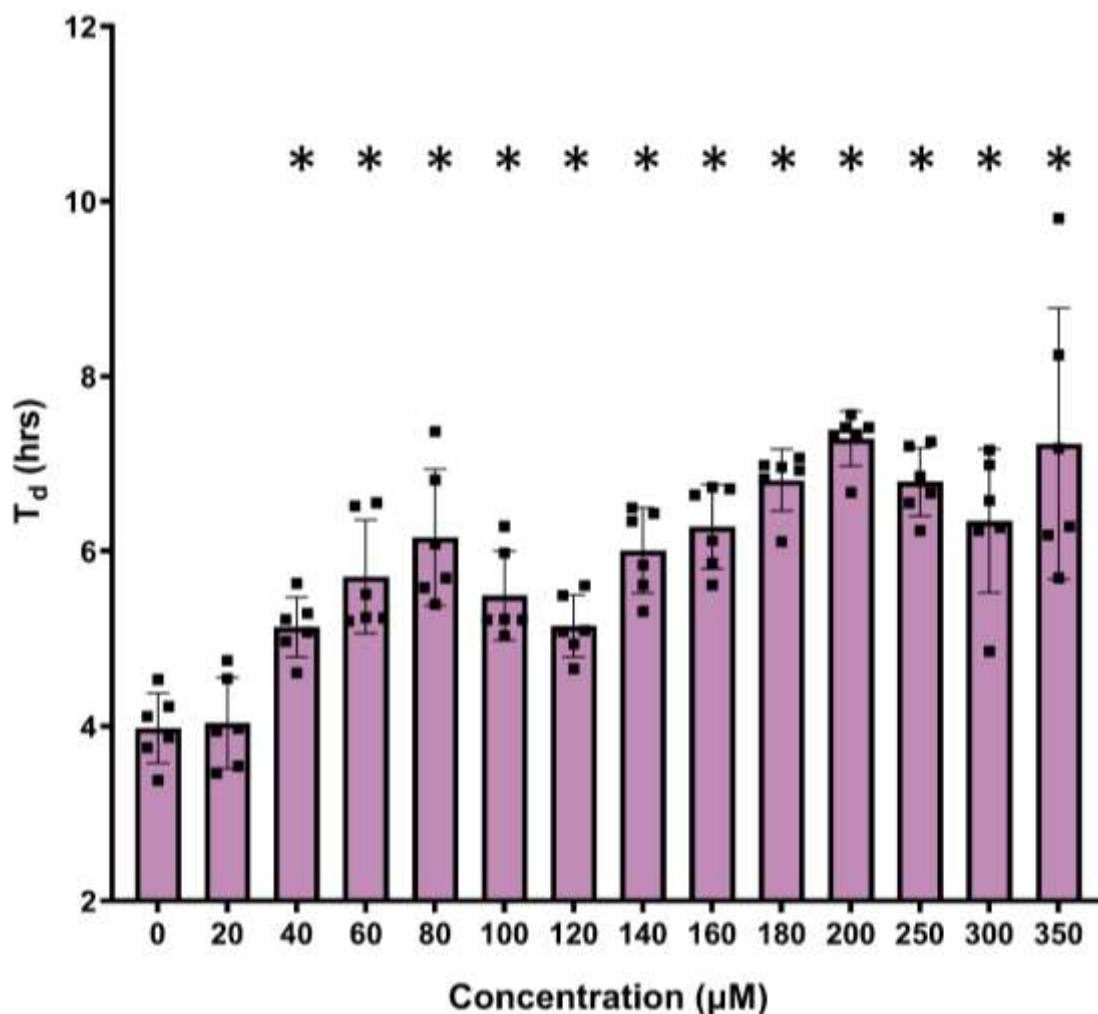
Figure XIV: Comparison in doubling time (T_d) of PTP1B only transformed yeast cells in the presence of LZP25 at 20-350 μM . $n=6$ base growth and all concentrations tested in both transformations. Mean and individual points \pm standard deviation plotted. Data is normally distributed according to a Shapiro-Wilk test. Used parametric Welch's t-test for statistical analysis. * p value ≤ 0.050 vs base growth.



μM	20	40	60	80	100	120	140	160	180	200	250	300	350
p values	<0.0500	<0.0005	<0.0050	<0.0010	<0.0002	<0.0050	<0.0001	<0.0001	<0.0050	<0.0050	<0.0500	<0.0500	<0.0500

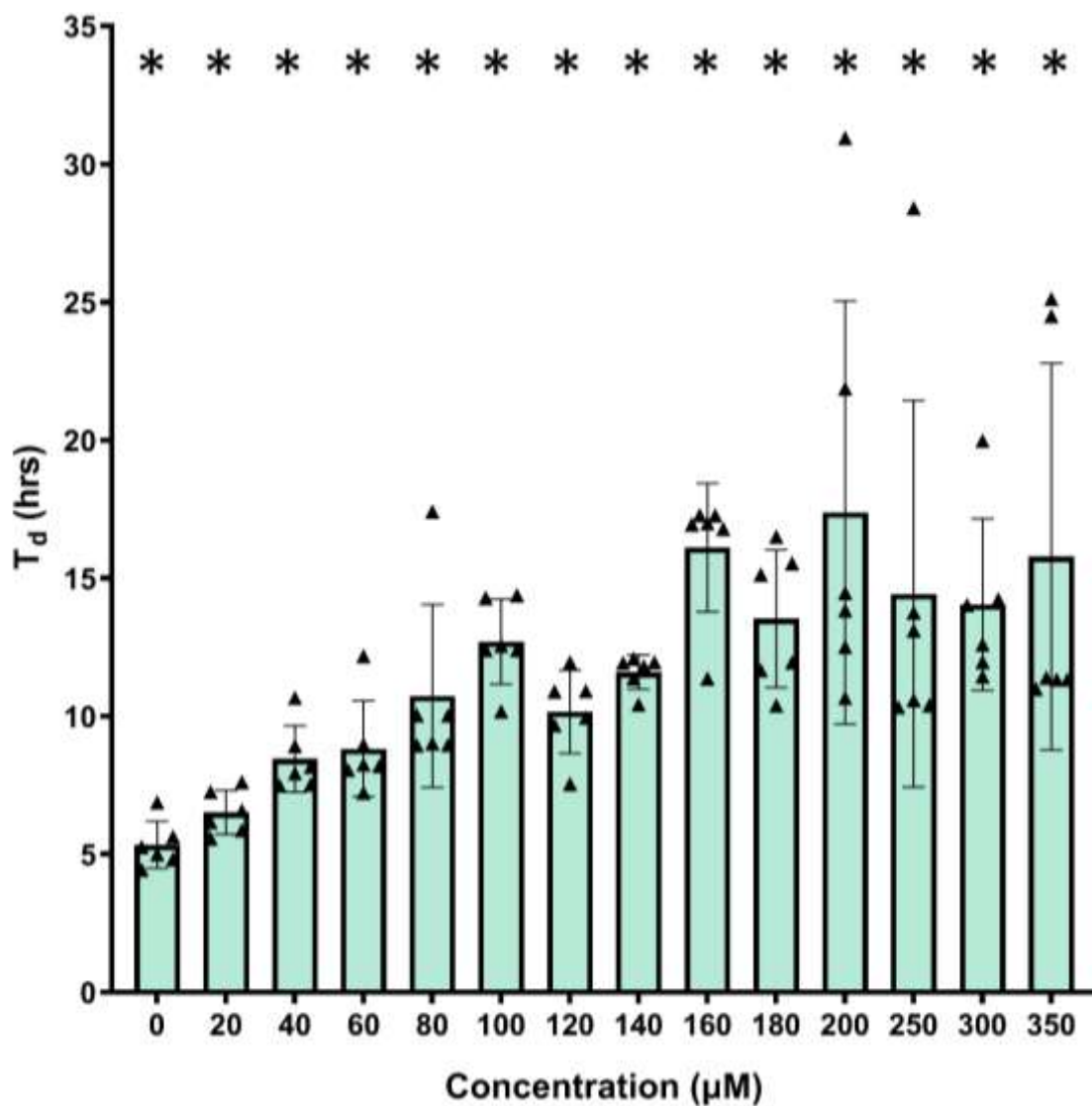
Figure XV: Comparison in doubling time (T_d) of PTP1B + v-Src transformed yeast cells in the presence of LZP25 at 20-350 μM . $n=6$ base growth and all concentrations tested in both transformations. Mean and individual points \pm standard deviation plotted. Data is normally distributed according to a Shapiro-Wilk test. Used parametric Welch's t-test for statistical analysis. * p value ≤ 0.050 vs base growth.

1.6.2.2 TCPTP based.



μM	20	40	60	80	100	120	140	160	180	200	250	300	350
p values	ns	<0.0005	<0.0010	<0.0005	<0.0005	<0.0005	<0.0001	<0.0001	<0.0001	<0.0001	<0.0001	<0.0005	<0.0001

Figure XVI: Comparison in doubling time (T_d) of TCPTP only transformed yeast cells in the presence of LZP25 at 20-350 μM . $n=6$ base growth and all concentrations tested in both transformations. Mean and individual points \pm standard deviation plotted. Data is not normally distributed according to a Shapiro-Wilk test. Used non-parametric Mann-Whitney t-test for statistical analysis. * p value ≤ 0.050 vs base growth.



μM	20	40	60	80	100	120	140	160	180	200	250	300	350
p values	<0.0500	<0.0010	<0.0050	<0.0100	<0.0001	<0.0005	<0.0001	<0.0001	<0.0005	<0.0500	<0.0500	<0.0010	<0.0500

Figure XVII: Comparison in doubling time (T_d) of TCPTP + v-Src transformed yeast cells in the presence of LZP25 at 20-350 μM . $n=6$ base growth and all concentrations tested in both transformations. Mean and individual points \pm standard deviation plotted. Data is normally distributed according to a Shapiro-Wilk test. Used parametric Welch's t-test for statistical analysis. * p value ≤ 0.050 vs base

1.7 Reason for use of different concentration ranges of known inhibitors.

It is important to mention and explain why different concentration ranges for the known inhibitors ursolic acid (0.5 – 150 μM) and LZP25 (20 – 500 μM), were deployed when assessing the validity of the yeast-based assay. As previously mentioned, due to the lipophilicity (high LogP) of ursolic acid no concentrations higher than 150 μM could be reliability tested due to this known inhibitor crashing out of solution. The concentration range of 20 – 500 μM was decided upon for LZP25 and all identified hit compounds post initial activity screen, this range was primarily selected for two reasons. Firstly, as this range provided the ability to test all synthesis compounds without the concern of the potential inhibitors crashing out of solution and thus provides a false negative, due to all synthesised compounds being designed to be less lipophilic. While secondly able to exert not only a significant effect on the growth rate via PTP inhibition when compared to the corresponding base growth but also to each other, to enable easy ranking and thus selection of the optimum hit for further functionalization and study. The initial order of magnitude of micromolar (μM) was based upon both previous yeast based PTP inhibition assays^{1,2} and accepted pharmaceutical dosage. In hindsight it would have been more beneficial to have assessed LZP25 activity at 5 and 10 μM , instead of 400 and 500 μM , as these concentrations did not provide any T_d values due to not having an exponential growth phase. Lower concentrations were not investigated as none of the latter discussed identified PTP inhibitors showed significant activity at 20 μM , hence would presumably also not at lower concentrations. Additionally, more concentrations within the range were not tested due to the constraints of the 96 well plate. It was decided that it was more imperative to obtain six biological repeats ($n=6$) for each concentration so that the required non-parametric t-tests utilised for the % change in T_d had sufficient power to accurately determine significance. Furthermore, overall testing of more different potential inhibitors is required to fulfil the aim of identifying more hit compounds rather than investigate fewer but at a greater number of concentrations.

1.8 Example image of cells crashing out of growth media due to addition of certain test compounds at higher concentrations.

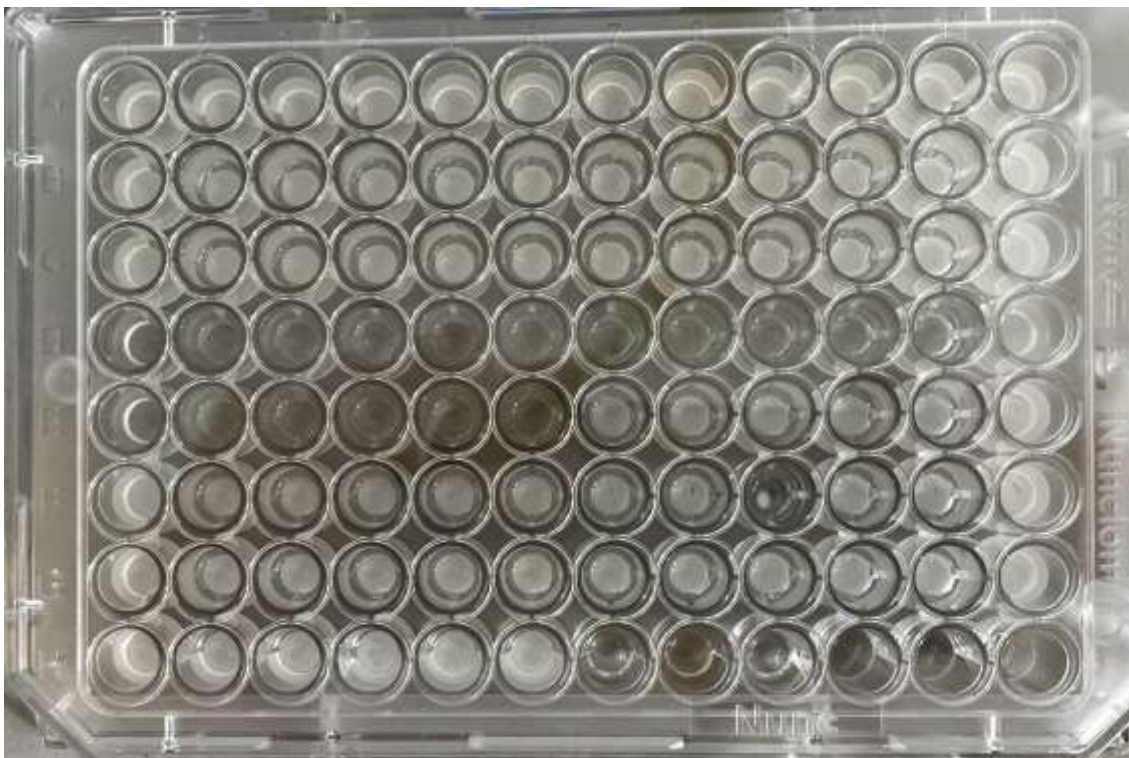


Figure XVIII: Example image of a 96-well plate where yeast cells have crashed out of solution after the 47.5-hour growth experiment.

For wells where this has occurred see, D1-D11, E1-6 and F9.

1.9 Accompanying BBB results of controls and known inhibitors.

1.9.1 Maximum absorption wavelength

Table VI: Maximum absorption wavelengths of BBB permeability controls and known inhibitors.

	Permeability controls			Known inhibitors	
	Low	Medium	High	Ursolic acid	LZP25
Wavelength (nm)	270	280	280	240	250

Above **Table VI** shows the wavelength of light in which the stated compounds absorb the maximum amount.

1.9.2 Blank corrected absorbance values of known concentrations.

Blanks used were comprised of 1x PBS and DMSO the proportion of which corresponds to the amount for each concentration of compound tested. These blanks were ran over the same wavelength range (220 – 500 nm) as the compounds were when determining maximum absorbance value.

1.9.2.1 Low permeability control

Table VII: Blank corrected absorbance data of the low permeability control used to construct calibration curve.

270nm		Concentration of low permeability BBB control used (μM)									
		50	100	150	200	250	300	350	400	450	500
Absorbance values	1	0.469	0.986	1.691	1.740	2.231	2.853	3.116	3.640	4.123	4.713
	2	0.442	0.893	1.382	1.660	2.388	2.928	3.562	3.566	4.118	4.608
	3	0.392	0.895	1.517	1.898	2.273	2.933	3.339	3.622	4.131	4.413
	4	0.421	0.930	1.579	1.900	2.347	2.894	2.810	3.607	4.096	4.612
	5	0.508	0.869	1.671	2.020	2.260	2.842	3.084	3.686	3.988	4.588
	Mean	0.446	0.915	1.569	1.844	2.3	2.89	3.183	3.625	4.092	4.587
	Std dev.	0.040	0.041	0.112	0.128	0.058	0.037	0.254	0.039	0.053	0.097

1.9.2.2 Medium permeability control

Table VIII: Blank corrected absorbance data of the medium permeability control used to construct calibration curve.

280nm		Concentration of medium permeability BBB control used (μM)									
		50	100	150	200	250	300	350	400	450	500
Absorbance values	1	0.544	0.872	1.660	1.913	2.269	2.898	3.265	3.725	3.977	4.631
	2	0.448	0.904	1.539	1.966	2.215	2.610	2.983	3.66	4.083	4.657
	3	0.512	0.848	1.561	1.918	2.173	2.582	3.132	3.826	3.904	4.566
	4	0.365	0.940	1.706	1.792	2.212	2.603	3.048	3.434	4.194	4.607
	5	0.435	0.916	1.612	1.721	2.162	2.937	3.347	3.747	4.191	4.400
	Mean	0.461	0.896	1.615	1.862	2.206	2.726	3.155	3.678	4.070	4.572
	Std dev.	0.063	0.032	0.062	0.091	0.038	0.157	0.135	0.133	0.115	0.091

1.9.2.3 High permeability control

Table IX: Blank corrected absorbance data of the high permeability control used to construct calibration curve.

280nm		Concentration of high permeability BBB control used (μM)									
		50	100	150	200	250	300	350	400	450	500
Absorbance values	1	0.600	1.144	1.662	2.233	2.525	3.153	3.780	3.817	4.679	5.219
	2	0.533	0.834	1.807	2.144	2.563	2.887	3.413	4.162	4.873	5.291
	3	0.673	1.219	1.843	2.146	2.532	3.512	3.807	4.134	4.535	5.222
	4	0.555	0.803	1.926	2.139	2.588	3.135	3.432	3.884	4.672	5.201
	5	0.545	1.055	1.739	2.012	2.659	3.098	3.740	4.396	4.637	5.171
	Mean	0.581	1.011	1.795	2.135	2.573	3.157	3.635	4.079	4.679	5.221
	Std dev.	0.051	0.166	0.090	0.071	0.048	0.201	0.174	0.208	0.110	0.040

1.9.2.4 Ursolic acid

Table X: Blank corrected absorbance data of ursolic acid used to construct calibration curve.

240nm		Concentration of ursolic acid used (μM)									
		50	100	150	200	250	300	350	400	450	500
Absorbance values	1	0.053	0.110	0.150	0.178	0.226	0.299	0.286	0.397	0.397	0.461
	2	0.054	0.099	0.127	0.174	0.234	0.233	0.316	0.320	0.429	0.433
	3	0.038	0.120	0.137	0.181	0.208	0.273	0.344	0.296	0.397	0.407
	4	0.037	0.105	0.121	0.200	0.209	0.236	0.342	0.336	0.373	0.469
	5	0.049	0.013	0.141	0.193	0.232	0.309	0.278	0.480	0.370	0.482
	Mean	0.046	0.090	0.135	0.185	0.222	0.270	0.313	0.365	0.393	0.451
	Std dev.	0.007	0.039	0.010	0.010	0.011	0.031	0.027	0.066	0.021	0.027

1.9.2.5 LZP25

Table XI: Blank corrected absorbance data of ursolic acid used to construct calibration curve.

250nm		Concentration of LZP25 used (μM)									
		50	100	150	200	250	300	350	400	450	500
Absorbance values	1	0.381	0.638	1.086	1.522	1.650	1.984	2.166	2.585	2.882	3.157
	2	0.360	0.674	1.008	1.181	1.528	2.116	2.423	2.875	2.698	3.325
	3	0.253	0.768	0.996	1.199	1.532	2.070	2.144	2.632	2.961	2.934
	4	0.318	0.678	1.116	1.106	1.638	2.043	2.034	2.651	2.721	3.033
	5	0.375	0.712	1.071	1.060	1.648	2.218	2.032	2.502	2.946	3.082
	Mean	0.338	0.694	1.056	1.214	1.600	2.086	2.160	2.649	2.842	3.107
	Std dev.	0.048	0.044	0.046	0.162	0.057	0.079	0.143	0.124	0.111	0.131

1.9.3 Concentrations of permeability controls and known inhibitors in both acceptor and donor wells after 24-hours at RT or 37°C.

1.9.3.1 Low permeability control

Table XII: Concentration of low permeability control recorded to be present in the acceptor and donor wells of the assay kit after 24-hours at RT and 37°C.

270nm Low control		Temperature of assay run							
		In-house run 1				In-house run 2			
		RT		37°C		RT		37°C	
		Acceptor	Donor	Acceptor	Donor	Acceptor	Donor	Acceptor	Donor
Concentration (µM)	1	10.00	459.57	15.89	500.13	9.26	494.15	12.72	496.63
	2	9.67	510.98	16.22	493.72	10.89	486.33	14.46	495.11
	3	13.04	512.61	16.98	494.48	11.43	483.07	17.28	498.48
	4	12.39	481.63	14.59	485.78	10.02	494.04	17.83	500.22
	5	11.52	462.61	16.33	478.72	10.89	490.89	16.09	497.61
	Mean	11.33	485.48	16.00	490.57	10.50	489.70	15.67	497.61
	Std dev.	1.31	22.78	0.79	7.48	0.77	4.37	1.88	1.72

1.9.3.2 Medium permeability control

Table XIII: Concentration of medium permeability control recorded to be present in the acceptor and donor wells of the assay kit after 24-hours at RT and 37°C.

280nm Medium control		Temperature of assay run							
		In-house run 1				In-house run 2			
		RT		37°C		RT		37°C	
		Acceptor	Donor	Acceptor	Donor	Acceptor	Donor	Acceptor	Donor
Concentration (µM)	1	76.55	468.35	83.71	409.87	71.25	450.00	89.96	391.63
	2	60.73	442.97	78.44	399.21	69.71	438.35	90.62	383.38
	3	56.66	433.08	89.54	395.14	62.24	427.36	82.26	402.29
	4	62.15	467.69	84.15	393.49	69.60	429.12	92.92	392.29
	5	77.54	441.43	78.77	387.12	60.26	439.67	84.57	395.36
	Mean	66.73	450.70	82.92	396.97	66.62	436.90	88.07	392.99
	Std dev.	8.62	14.54	4.08	7.53	4.46	8.16	3.99	6.11

As with the low permeability control the results for the final concentrations of the medium permeability control in the acceptor and donor wells were again as expected with a greater concentration in the acceptor wells on average for the run conducted at 37 °C.

1.9.3.3 High permeability control

Table XIV: Concentration of high permeability control recorded to be present in the acceptor and donor wells of the assay kit after 24-hours at RT and 37°C.

280nm High control		Temperature of assay run							
		In-house run 1				In-house run 2			
		RT		37°C		RT		37°C	
		Acceptor	Donor	Acceptor	Donor	Acceptor	Donor	Acceptor	Donor
Concentration (µM)	1	101.02	405.81	117.77	388.44	105.62	409.63	117.08	399.21
	2	100.44	401.77	119.40	386.90	105.23	407.71	118.42	397.96
	3	91.21	391.38	119.79	394.21	105.81	408.87	116.31	390.17
	4	107.65	417.44	119.40	389.50	106.67	410.40	118.33	391.71
	5	101.50	390.62	114.12	412.77	105.04	406.56	115.35	399.12
	Mean	100.37	401.40	118.10	394.37	105.67	408.63	117.10	395.63
	Std dev.	5.27	9.94	2.11	9.52	0.57	1.37	1.18	3.89

Finally, the expected results for the high permeability control in terms of acceptor well concentration were obtained. As only gain a greater permeability rate for the high permeability control was recorded at 37°C. It is important to note that the initial concentration of each permeability control was 500 µM, and the total required concentration was around this value, but in the majority of case slightly over, this could be due to a number of reasons including manual error in adding the compound solution or in the stock dilution itself, or with the calibration curves used to convert the measured absorbance values into concentration values. However, as none of these are significantly different to the actual inputted concentration it can be considered as inconsequence. Another observation is that the standard deviations of all the measurements for the 37°C assay results are smaller than the corresponding RT counterparts, potentially this could mean that the assay performs more consistently at the more psychologically relevant temperature, but further testing would be needed to confirm this.

1.9.3.4 Ursolic acid

Table XV: Concentration of ursolic acid recorded to be present in the acceptor and donor wells of the assay kit after 24-hours at RT and 37°C.

240nm Ursolic acid		Temperature of assay run			
		RT		37°C	
		Acceptor	Donor	Acceptor	Donor
Concentration (µM)	1	107.78	390.89	171.33	383.78
	2	121.11	407.56	175.78	341.56
	3	112.22	379.78	111.33	393.78
	4	105.56	384.22	124.67	338.22
	5	114.44	380.89	126.89	316.00
	Mean	112.22	388.67	142.00	354.67
	Std dev.	5.44	10.21	26.35	29.38

1.9.3.5 LZP25

Table XVI: Concentration of ursolic acid recorded to be present in the acceptor and donor wells of the assay kit after 24-hours at RT and 37°C.

250nm LZP25		Temperature of assay run			
		RT		37°C	
		Acceptor	Donor	Acceptor	Donor
Concentration (µM)	1	65.09	400.66	52.22	404.13
	2	74.94	418.31	58.16	414.91
	3	76.66	403.78	54.25	405.53
	4	90.72	400.66	63.94	400.53
	5	59.00	412.22	61.44	423.50
	Mean	73.28	407.13	58.00	409.72
	Std dev.	10.86	7.01	4.35	8.37

1.9.4 Permeability rate comparison

1.9.4.1 Comparing the two in-house data runs

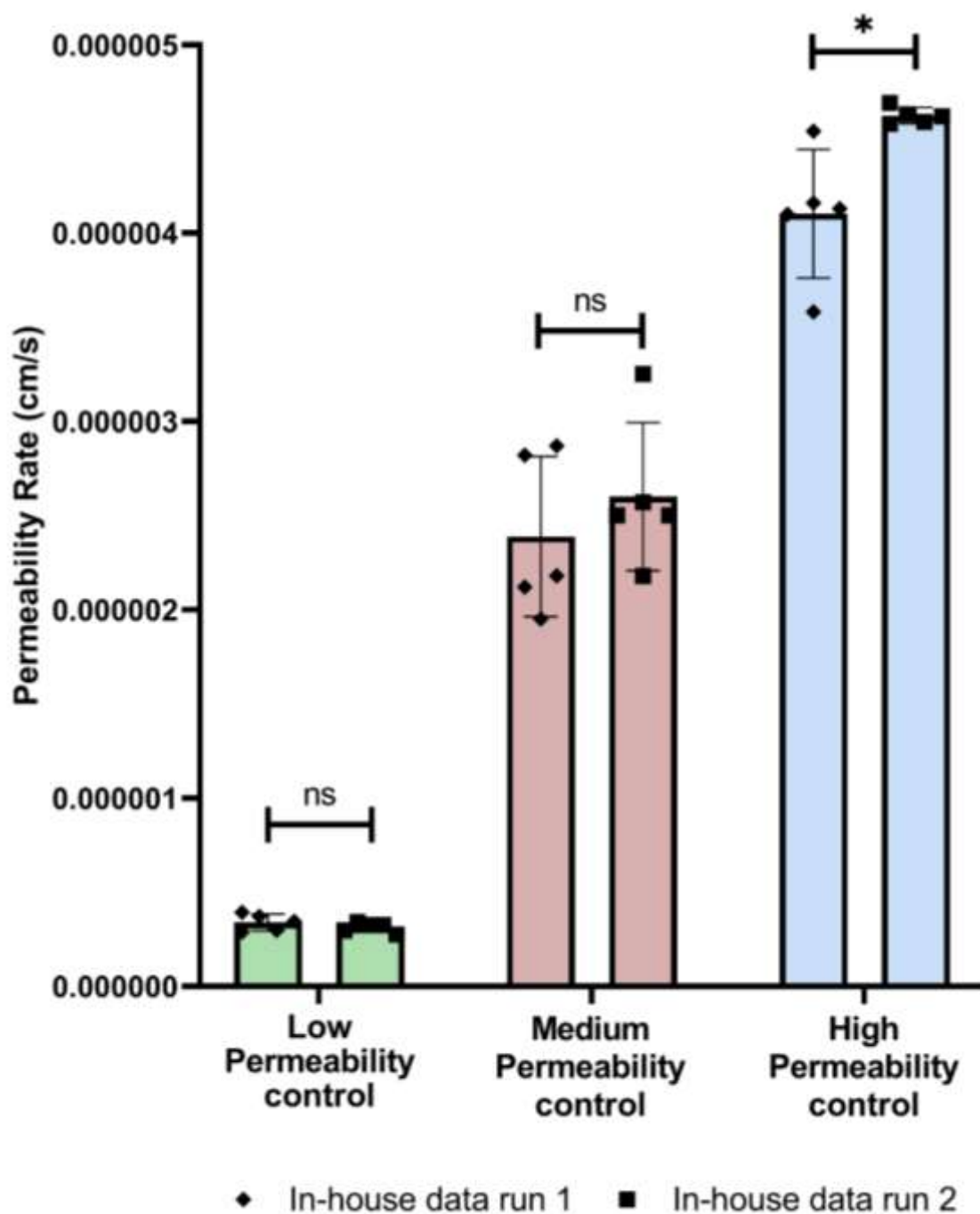
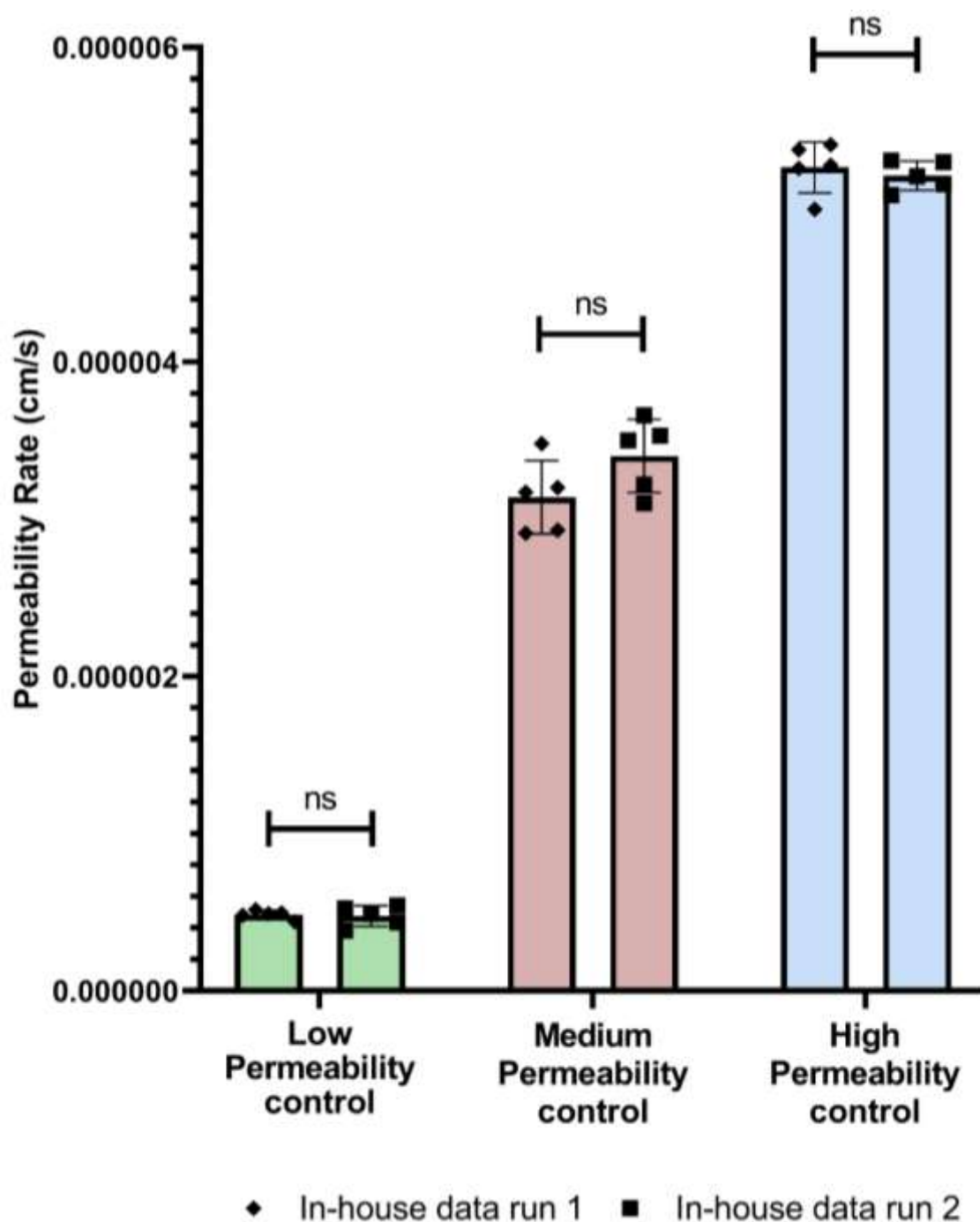


Figure XIX: Comparing the permeability results of two separate in-house results from separate kits at RT. n=5 for all permeability controls. Used non-parametric Mann-Whitney t-test for statistical analysis. * p value ≤ 0.050 .



Permeability control	Low	Medium	High
p value	ns	ns	ns

Figure XX: Comparing the permeability results of two separate in-house results from separate kits at 37°C. n=5 for all permeability controls. Used non-parametric Mann-Whitney t-test for statistical analysis. * p value ≤ 0.050 .

As illustrated in **Figure XIX** there was no significant difference between the corresponding low and medium permeability controls in each separate assay run, meaning the assay was providing consistent results. This in conjunction which the in-house data

being in the same order of magnitude as the provided manufacturer data, was sufficient for the assay to be taken forward and used to test both known inhibitor and hit compounds. Particularly because the permeability controls themselves main purpose is to provide points of reference in terms of how permeable a compound could be to the BBB, and the comparison between the hit compounds is more important in determining the optimum hit PTP1B inhibitor from this work.

As demonstrated in **Figure XX** at the more psychologically relevant temperature of 37°C there is no significant between the two separate data runs for any of the three provided permeability controls.

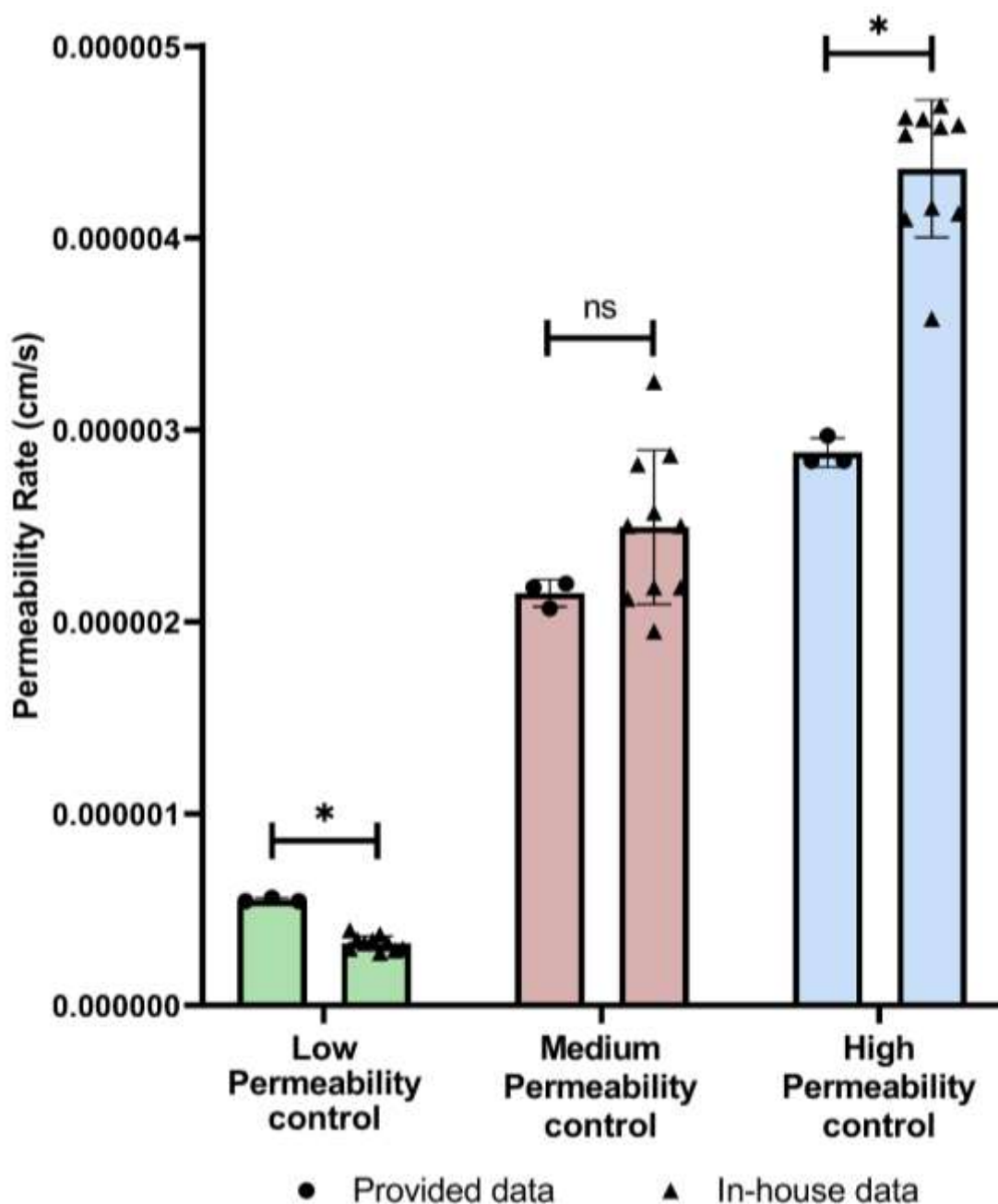
1.9.4.2 Comparing in-house data runs to provided example data.

The reliability and reproducibility of the BBB assay were assessed by comparing the permeability rate (cm/s) data provided by the kit's manufacturers (BioAssay) upon request for the permeability controls provided with the aforementioned kit with the results obtained in-house on two separate occasions with different purchased kit. Permeability rates are calculated using the equations located in the methodology chapter of the adjoining thesis.

The manufacturer of the assay provided three repeat values for each of the supplier permeability controls. When compared to the tabulated in-house results from two separate kits conducted on different days it was found that there was no significant difference the medium permeability control results. However, the results for the low and high permeability control were significantly different between the provided manufacturer results and the in-house data. As the in-house low permeability control data was significantly lower and the in-house high permeability control data being significantly higher than the respective manufacturer provided data. Potential contributing factors for this significance are time of experiment and temperature. The length of the assay run may affect the calculated permeability rate as the rate of diffusion of the compound through the synthetic membrane may not be uniform as when the equilibrium is close to being reached the rate may slow down, thus a longer experiment time up to when the equilibrium is reached may result in an overall slower permeability rate than a shorter experiment time, potentially. It is important to note that for the provided data the experiment run was 18 hrs, and the in-house data was collected after 24 hours. However, the utilised equation for calculating permeability rate does take into account time, so this

difference in experimental length is most likely not a contributing factor, additionally the assay procedure recommends an 18 to 24-hour experiment run.

Another possible contributing factor is the temperature. For the provided data set this was specified to be 25 °C, whereas the in-house runs were conducted at the room temperature of the laboratory, this was not recorded in either instance, but the laboratory should have been close to 25 °C hence again the temperature is unlikely to be a key contributor to the significant difference for the low and high permeability results.



Permeability control	Low	Medium	High
p value	<0.0050	ns	<0.0100

Figure XXI: Comparing the permeability results provided by the manufacture with the combined in-house result from two separate kits at RT. n=10 for in-house data and n=3 for manufacturer's data. Used non-parametric Mann-Whitney t-test for statistical analysis. * p value \leq 0.050.

1.9.4.3 Equilibrium standard absorbance values.

Table XVII: Absorbance values of the equilibrium standards at the corresponding wavelength for the BBB permeability controls and known inhibitors.

		Control or known inhibitor Equilibrium standard				
		Low (270nm)	Medium (280nm)	High (280nm)	Ursolic acid (240nm)	LZP25 (250nm)
Absorbance (Abs)	1	1.766	1.672	2.069	0.181	1.228
	2	1.858	1.903	2.004	0.159	1.235
	3	1.840	1.838	1.981	0.168	1.155
	4	1.831	1.815	1.961	0.198	1.291
	5	1.870	1.795	1.971	0.166	1.236
	Mean	1.833	1.805	1.997	0.174	1.229
	Std dev.	0.036	0.076	0.039	0.014	0.043

The above blank corrected absorbance values shown in **Table XVII** were utilised in the equation to calculate the permeability rate. These values are the same regardless of assay temperature.

1.9.4.4 Permeability rate results of permeability controls and known inhibitors.

Table XVIII: Permeability rate values in cm/s for BBB permeability controls and known inhibitors at RT.

		Permeability control or known inhibitor (RT)				
		Low	Medium	High	Ursolic acid	LZP25
Permeability rate (cm/s)	1	2.98E-07	2.82E-06	4.13E-06	4.72E-06	2.40E-06
	2	2.88E-07	2.12E-06	4.10E-06	5.70E-06	2.87E-06
	3	3.92E-07	1.95E-06	3.58E-06	5.03E-06	2.95E-06
	4	3.72E-07	2.18E-06	4.54E-06	4.57E-06	3.70E-06
	5	3.45E-07	2.87E-06	4.16E-06	5.19E-06	2.13E-06
	6	2.75E-07	3.25E-06	4.62E-06	-	-
	7	3.25E-07	2.57E-06	4.59E-06	-	-
	8	3.41E-07	2.50E-06	4.63E-06	-	-
	9	2.98E-07	2.18E-06	4.69E-06	-	-
	10	3.25E-07	2.50E-06	4.58E-06	-	-
	Mean	3.26E-07	2.49E-06	4.36E-06	5.04E-06	2.81E-06
	Std dev.	3.554E-08	3.826E-07	3.405E-07	3.950E-07	5.400E-07

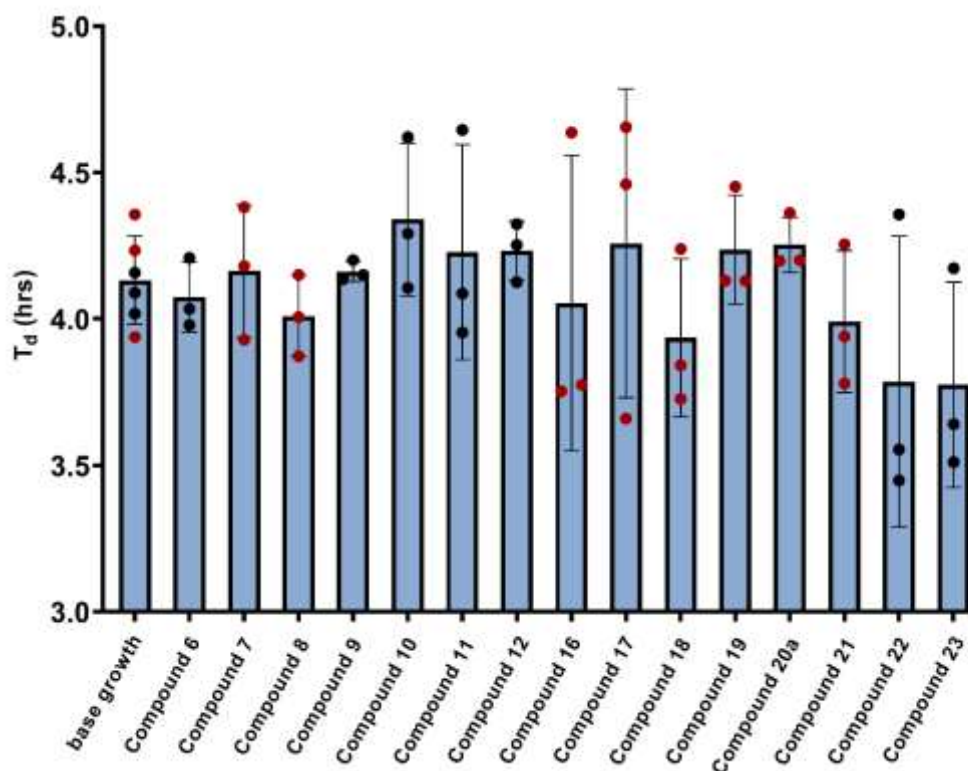
Table XIX: Permeability rate values in cm/s for BBB permeability controls and known inhibitors at 37°C.

		Permeability control or known inhibitor (37°C)				
		Low	Medium	High	Ursolic acid	LZP25
Permeability rate (cm/s)	1	4.80E-07	3.17E-06	5.23E-06	1.25E-05	1.84E-06
	2	4.91E-07	2.91E-06	5.25E-06	1.38E-05	2.09E-06
	3	5.15E-07	3.48E-06	5.38E-06	4.95E-06	1.92E-06
	4	4.39E-07	3.20E-06	5.35E-06	5.97E-06	2.34E-06
	5	4.94E-07	2.93E-06	4.97E-06	6.16E-06	2.23E-06
	6	3.82E-07	3.50E-06	5.18E-06	-	-
	7	4.36E-07	3.53E-06	5.28E-06	-	-
	8	5.25E-07	3.10E-06	5.13E-06	-	-
	9	5.42E-07	3.66E-06	5.27E-06	-	-
	10	4.87E-07	3.22E-06	5.06E-06	-	-
	Mean	4.79E-07	3.27E-06	5.21E-06	8.68E-06	2.08E-06
	Std dev.	4.555E-08	2.460E-07	1.205E-07	3.706E-06	1.879E-07

2. Content relating to Chapter 4: Benzodioxane.

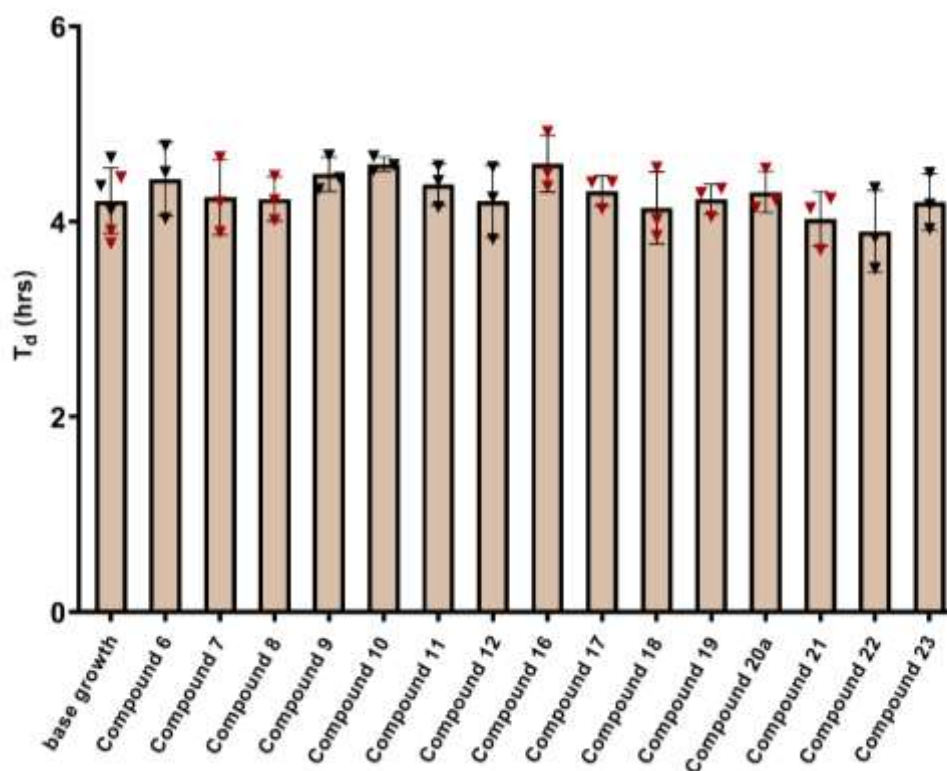
2.1 Doubling time values and growth curves of all benzodioxanes tested.

2.1.1 Compounds 6-12, 16-23.



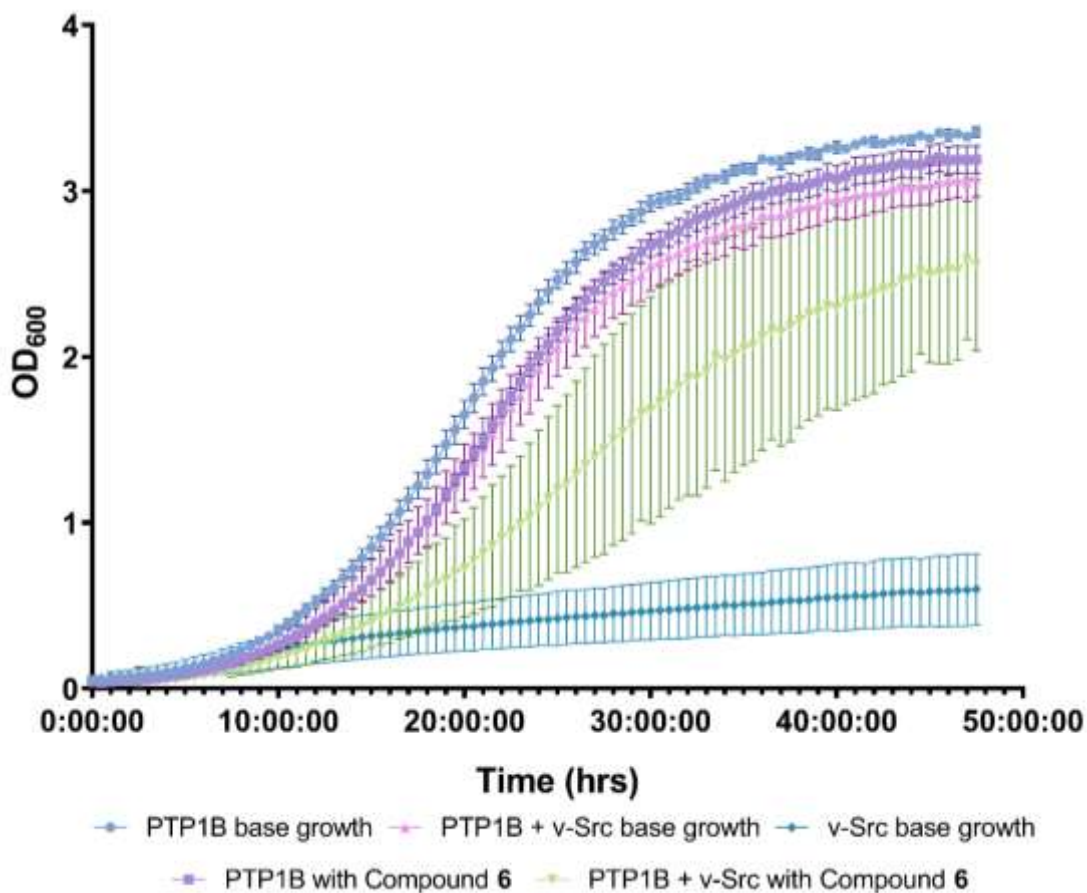
Compound	p value
6	ns
7	ns
8	ns
9	ns
10	ns
11	ns
12	ns
16	ns
17	ns
18	ns
19	ns
20a	ns
21	ns
22	ns
23	ns

Figure XXII: Effect of compounds 6-12, 16-23 on the T_d value of PTP1B only transformed yeast cells. $n=3$ for all compounds and $n=6$ for base growth. Colour coded denotes corresponding base growth values for each compound tested. Mean points \pm standard deviation plotted. Data is normally distributed according to a Shapiro-Wilk test. Used parametric Welch t-test for statistical analysis. * p value ≤ 0.050 vs base growth. Comparison occurred with corresponding base growth values, not all presented biological repeats.



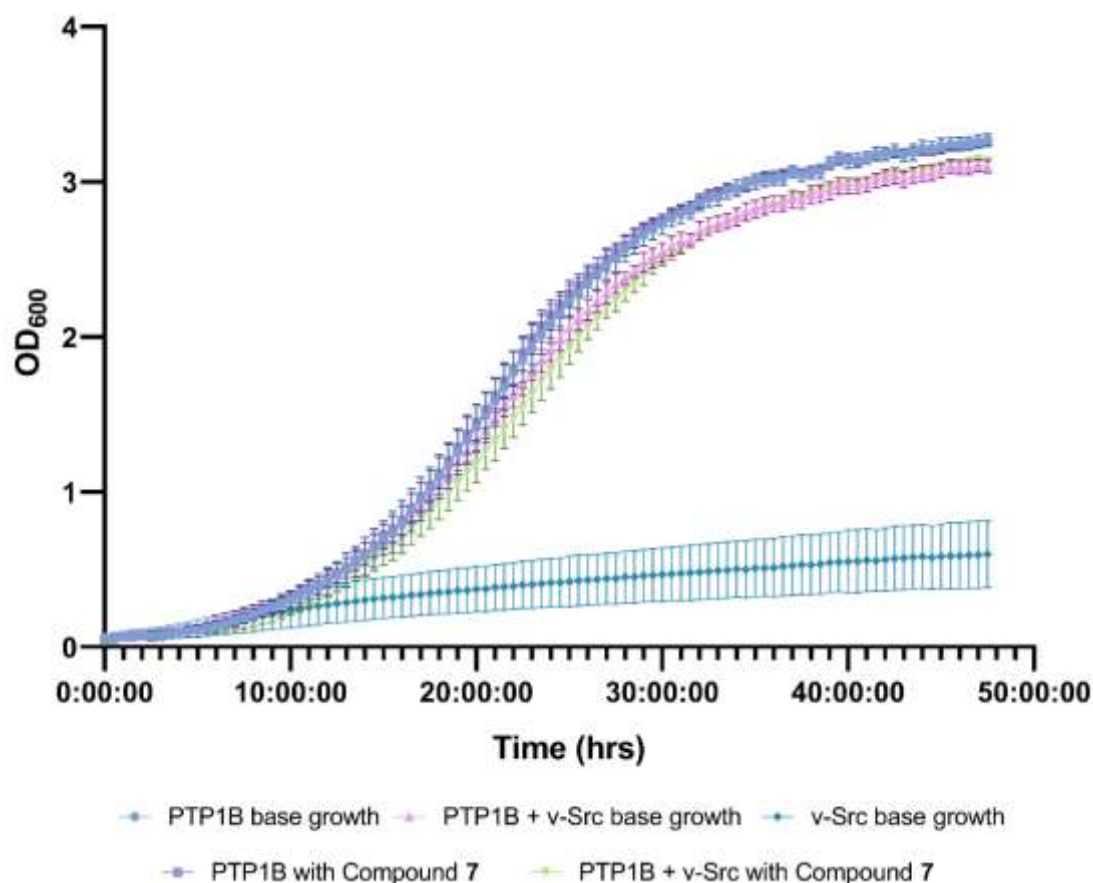
Compound	p value
6	ns
7	ns
8	ns
9	ns
10	ns
11	ns
12	ns
16	ns
17	ns
18	ns
19	ns
20a	ns
21	ns
22	ns
23	ns

Figure XXIII: Effect of compounds 6-12, 16-23 on the T_d value of PTP1B + v-Src transformed yeast cells. n=3 for all compounds and n=6 for base growth. Colour coded denotes corresponding base growth values for each compound tested. Mean points ± standard deviation plotted. Data is normally distributed according to a Shapiro-Wilk test. Used parametric Welch t-test for statistical analysis. * p value ≤ 0.050 vs base growth. Comparison occurred with corresponding base growth values, not all presented biological repeats.



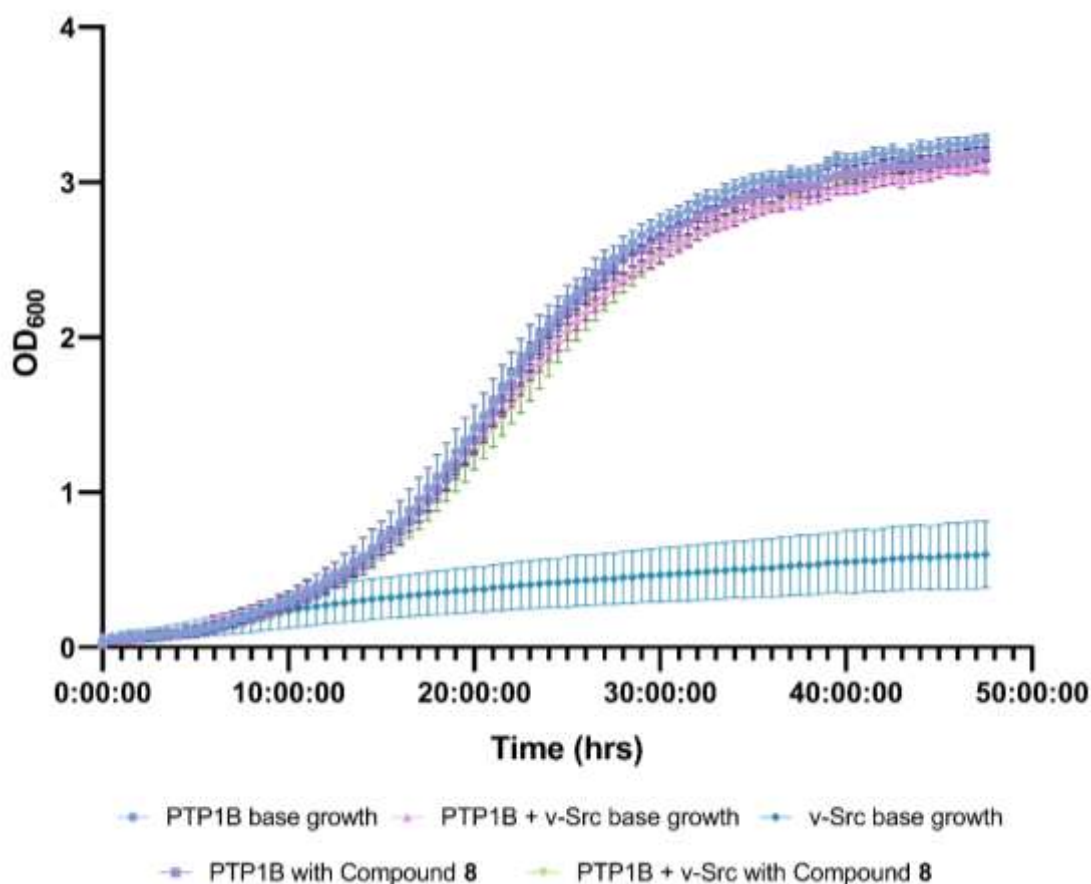
Transformed cells	PTP1B only	PTP1B + v-Src
p value	<0.010 *	ns

Figure XXIV: Growth curves of PTP1B only, PTP1B + v-Src and v-Src only YMK23 transformations with and without the addition of compound 6 at 100µM. n=3 for each PTP1B based parameter, n=13 for v-Src. Mean and individual biological points ± standard deviation plotted. Data is normally distributed according to a Shapiro-Wilk test. Used a 2-way ANOVA. * p value ≤ 0.050 vs corresponding base growth.



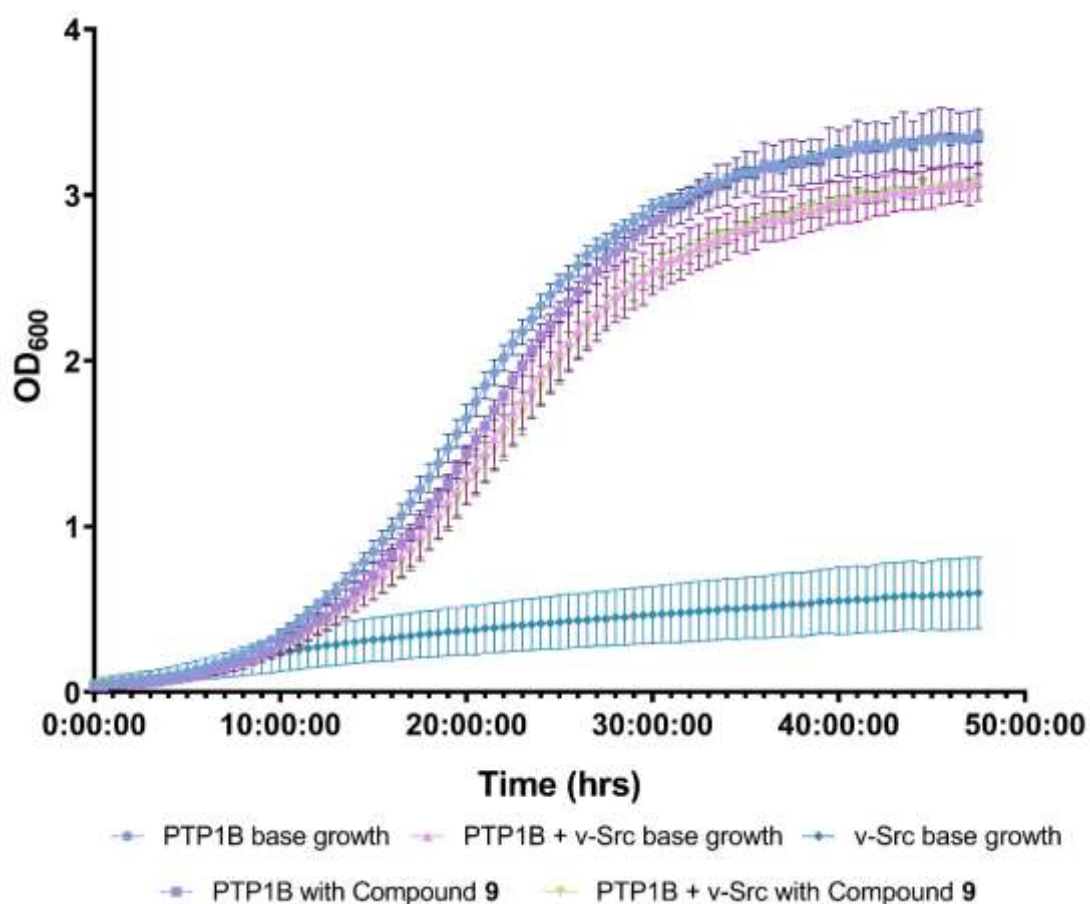
Transformed cells	PTP1B only	PTP1B + v-Src
p value	ns	ns

Figure XXV: Growth curves of PTP1B only, PTP1B + v-Src and v-Src only YMK23 transformations with and without the addition of compound 7 at 100 μ M. n=3 for each PTP1B based parameter, n=13 for v-Src. Mean and individual biological points \pm standard deviation plotted. Data is normally distributed according to a Shapiro-Wilk test. Used a 2-way ANOVA. * p value \leq 0.050 vs corresponding base growth.



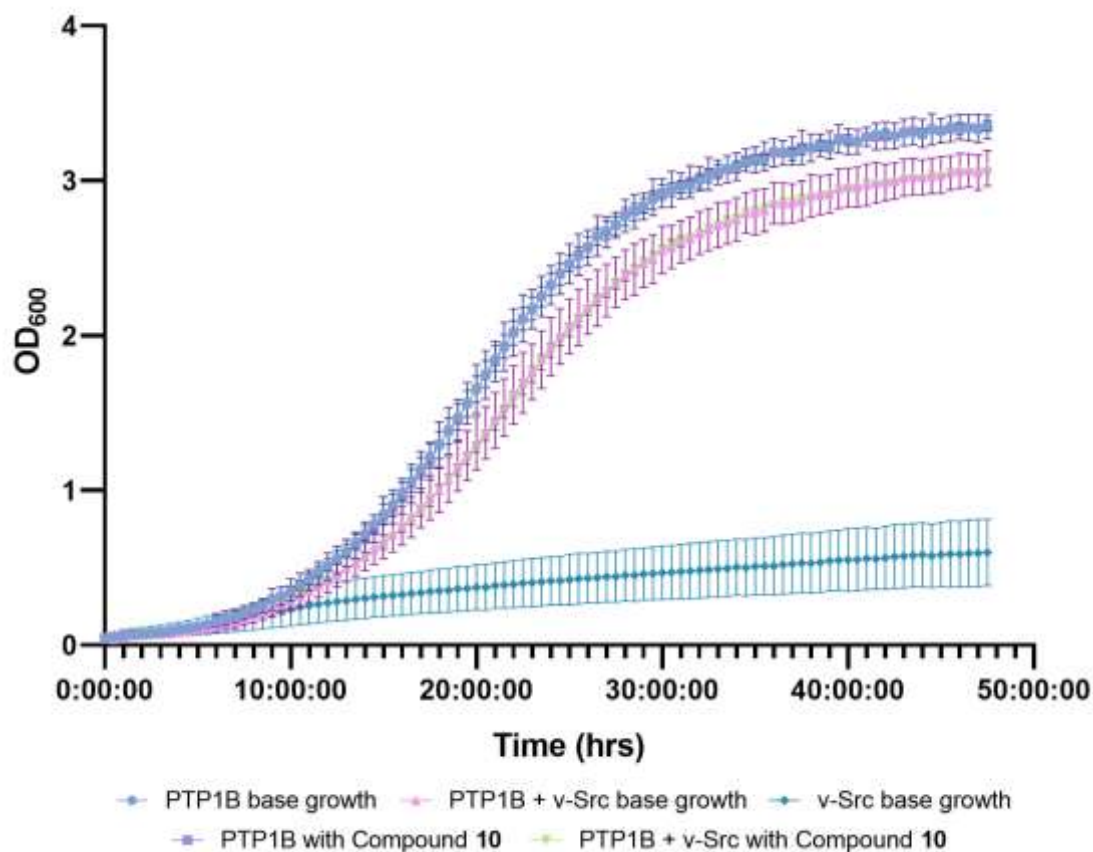
Transformed cells	PTP1B only	PTP1B + v-Src
p value	ns	ns

Figure XXVI: Growth curves of PTP1B only, PTP1B + v-Src and v-Src only YMK23 transformations with and without the addition of compound **8** at 100 μ M. n=3 for each PTP1B based parameter, n=13 for v-Src. Mean and individual biological points \pm standard deviation plotted. Data is normally distributed according to a Shapiro-Wilk test. Used a 2-way ANOVA. * p value \leq 0.050 vs corresponding base growth.



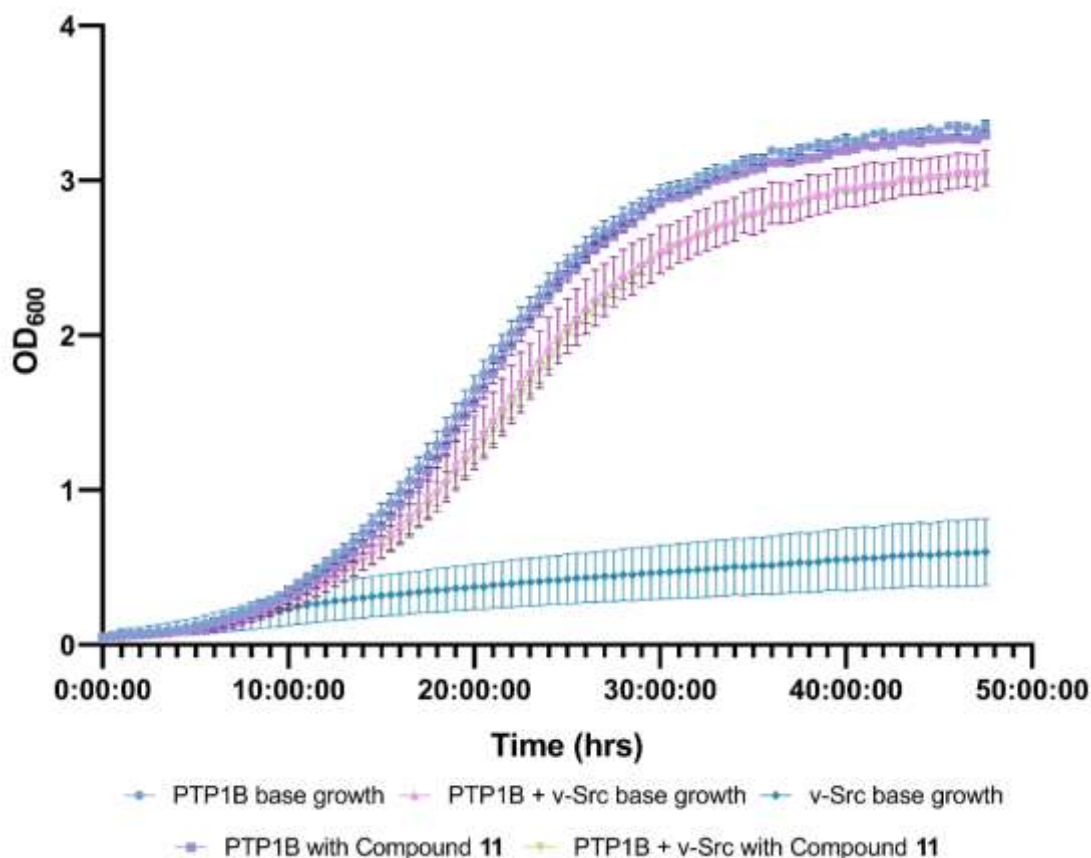
Transformed cells	PTP1B only	PTP1B + v-Src
p value	ns	ns

Figure XXVII: Growth curves of PTP1B only, PTP1B + v-Src and v-Src only YMK23 transformations with and without the addition of compound **9** at 100 μ M. n=3 for each PTP1B based parameter, n=13 for v-Src. Mean and individual biological points \pm standard deviation plotted. Data is normally distributed according to a Shapiro-Wilk test. Used a 2-way ANOVA. * p value \leq 0.050 vs corresponding base growth.



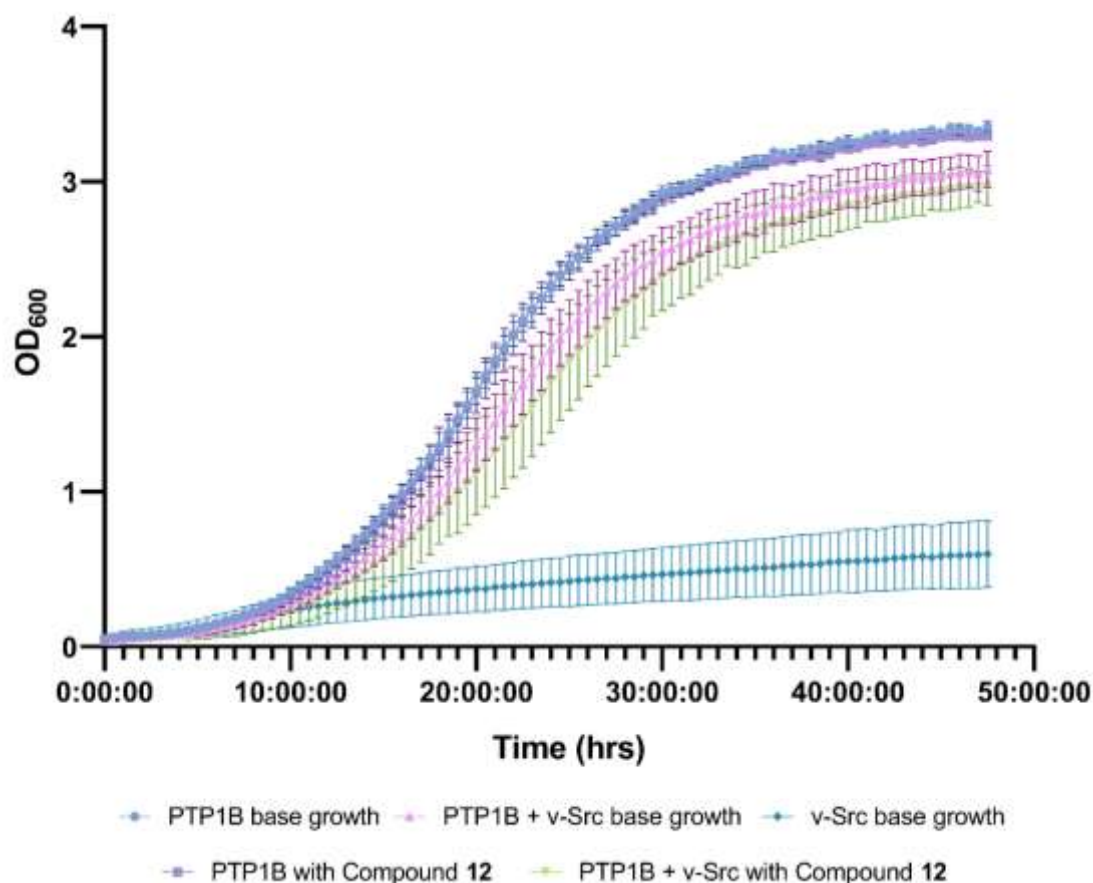
Transformed cells	PTP1B only	PTP1B + v-Src
p value	ns	ns

Figure XXVIII: Growth curves of PTP1B only, PTP1B + v-Src and v-Src only YMK23 transformations with and without the addition of compound **10** at 100 μ M. n=3 for each PTP1B based parameter, n=13 for v-Src. Mean and individual biological points \pm standard deviation plotted. Data is normally distributed according to a Shapiro-Wilk test. Used a 2-way ANOVA. * p value \leq 0.050 vs corresponding base growth.



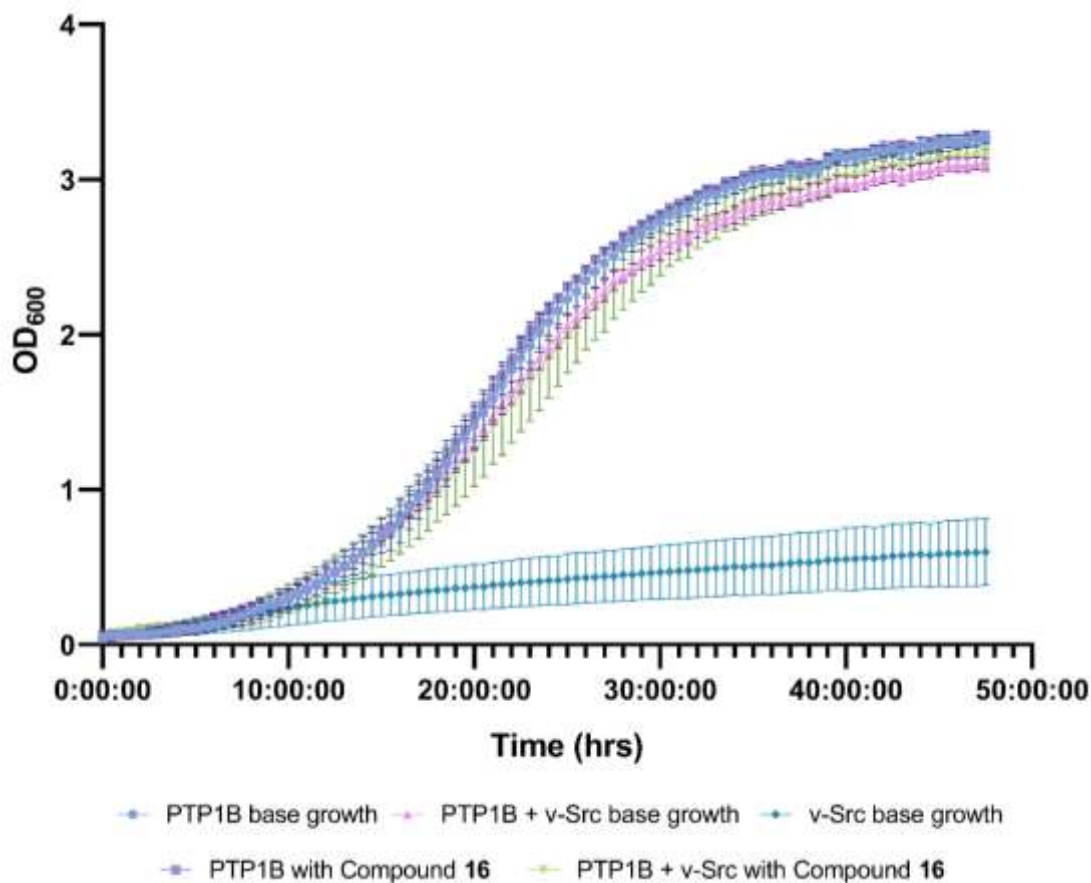
Transformed cells	PTP1B only	PTP1B + v-Src
p value	ns	ns

Figure XXIX: Growth curves of PTP1B only, PTP1B + v-Src and v-Src only YMK23 transformations with and without the addition of compound **11** at 100 μ M. n=3 for each PTP1B based parameter, n=13 for v-Src. Mean and individual biological points \pm standard deviation plotted. Data is normally distributed according to a Shapiro-Wilk test. Used a 2-way ANOVA. * p value \leq 0.050 vs corresponding base growth.



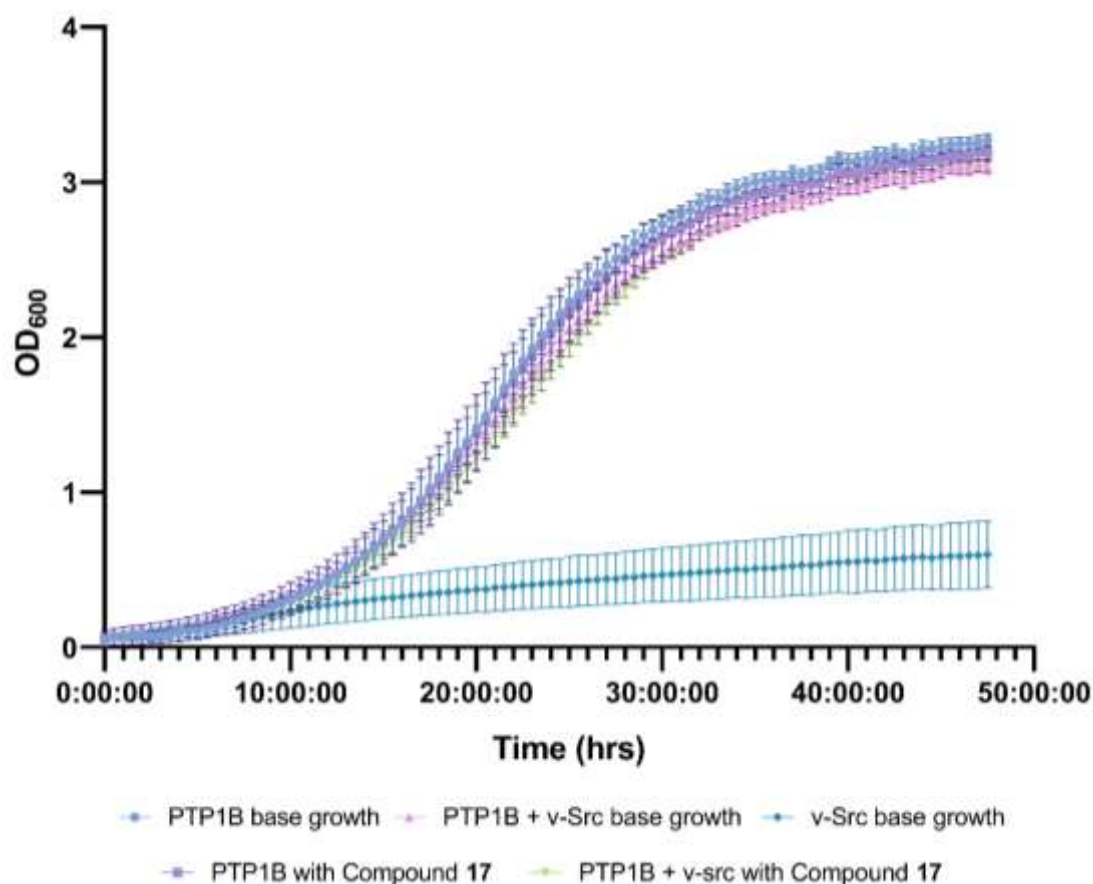
Transformed cells	PTP1B only	PTP1B + v-Src
p value	ns	ns

Figure XXX: Growth curves of PTP1B only, PTP1B + v-Src and v-Src only YMK23 transformations with and without the addition of compound **12** at 100 μ M. n=3 for each PTP1B based parameter, n=13 for v-Src. Mean and individual biological points \pm standard deviation plotted. Data is normally distributed according to a Shapiro-Wilk test. Used a 2-way ANOVA. * p value \leq 0.050 vs corresponding base growth.



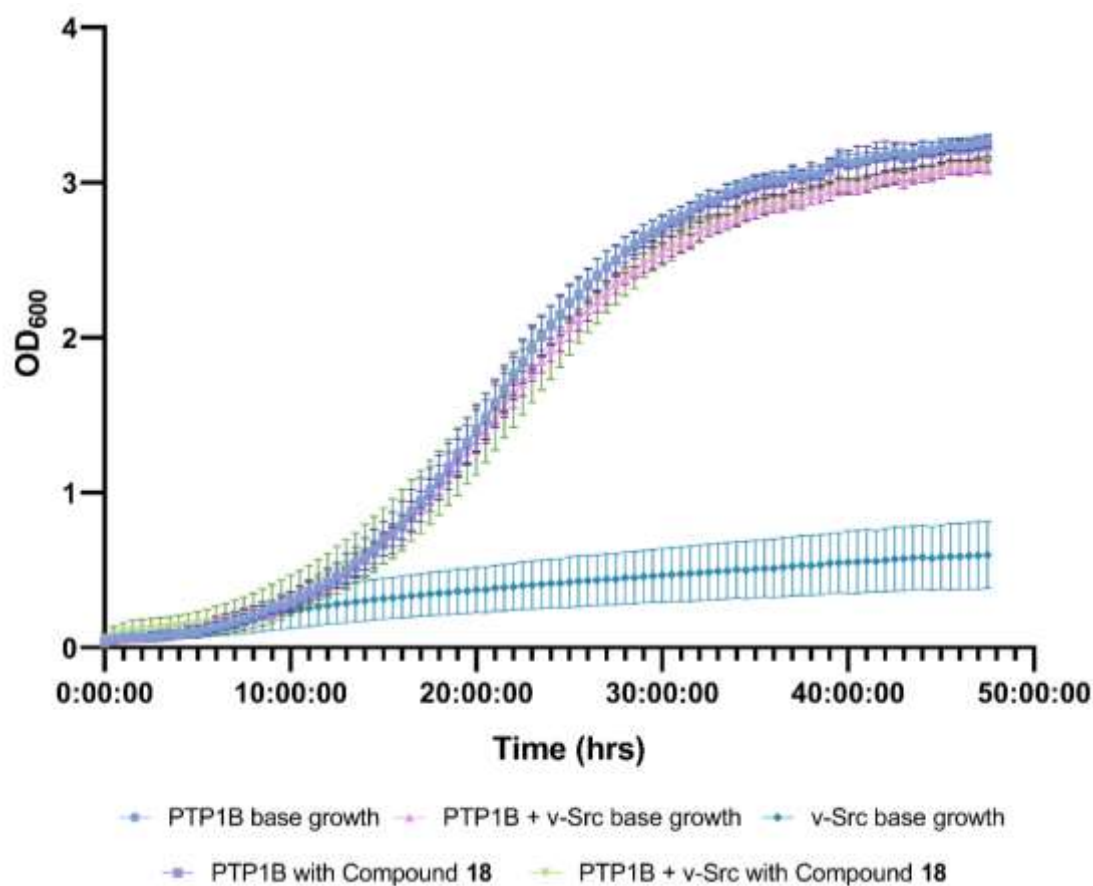
Transformed cells	PTP1B only	PTP1B + v-Src
p value	ns	ns

Figure XXXI: Growth curves of PTP1B only, PTP1B + v-Src and v-Src only YMK23 transformations with and without the addition of compound **16** at 100 μ M. n=3 for each PTP1B based parameter, n=13 for v-Src. Mean and individual biological points \pm standard deviation plotted. Data is normally distributed according to a Shapiro-Wilk test. Used a 2-way ANOVA. * p value \leq 0.050 vs corresponding base growth.



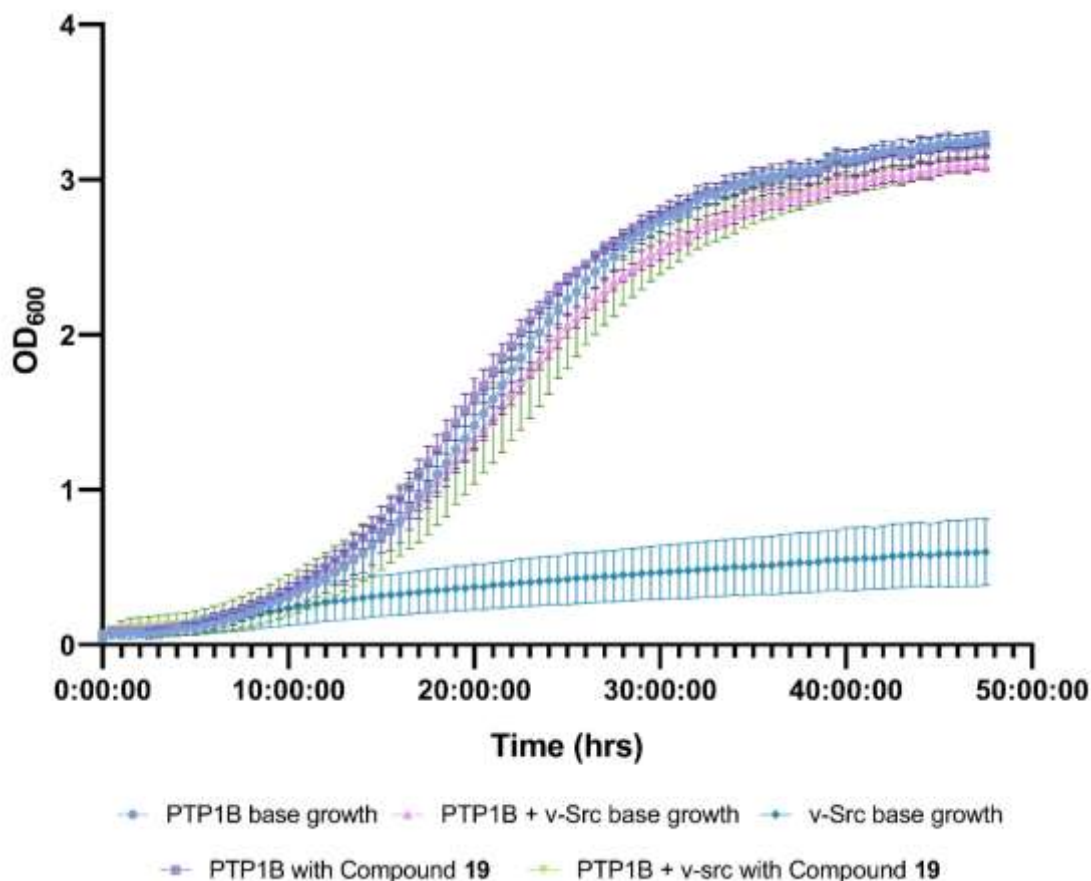
Transformed cells	PTP1B only	PTP1B + v-Src
p value	ns	ns

Figure XXXII: Growth curves of PTP1B only, PTP1B + v-Src and v-Src only YMK23 transformations with and without the addition of compound **17** at 100 μ M. n=3 for each PTP1B based parameter, n=13 for v-Src. Mean and individual biological points \pm standard deviation plotted. Data is normally distributed according to a Shapiro-Wilk test. Used a 2-way ANOVA. * p value \leq 0.050 vs corresponding base growth.



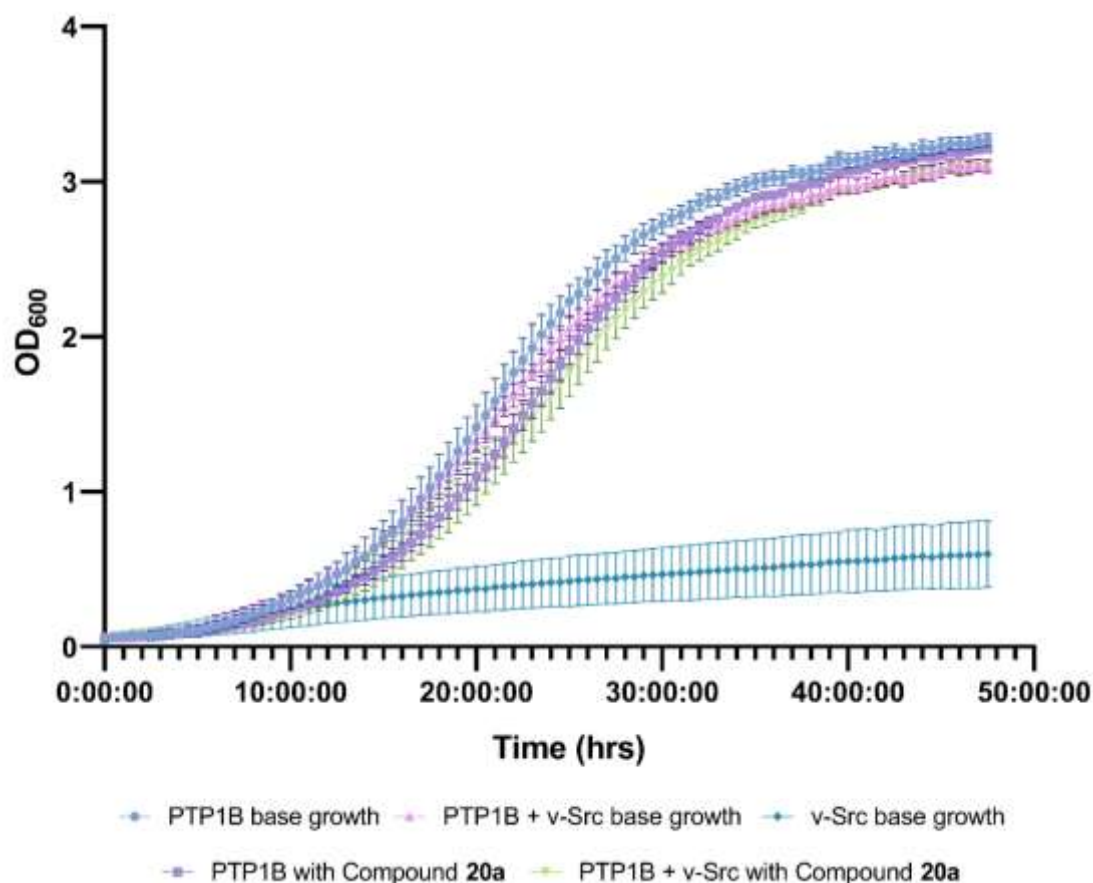
Transformed cells	PTP1B only	PTP1B + v-Src
p value	ns	ns

Figure XXXIII: Growth curves of PTP1B only, PTP1B + v-Src and v-Src only YMK23 transformations with and without the addition of compound **18** at 100 μ M. n=3 for each PTP1B based parameter, n=13 for v-Src. Mean and individual biological points \pm standard deviation plotted. Data is normally distributed according to a Shapiro-Wilk test. Used a 2-way ANOVA. * p value \leq 0.050 vs corresponding base growth.



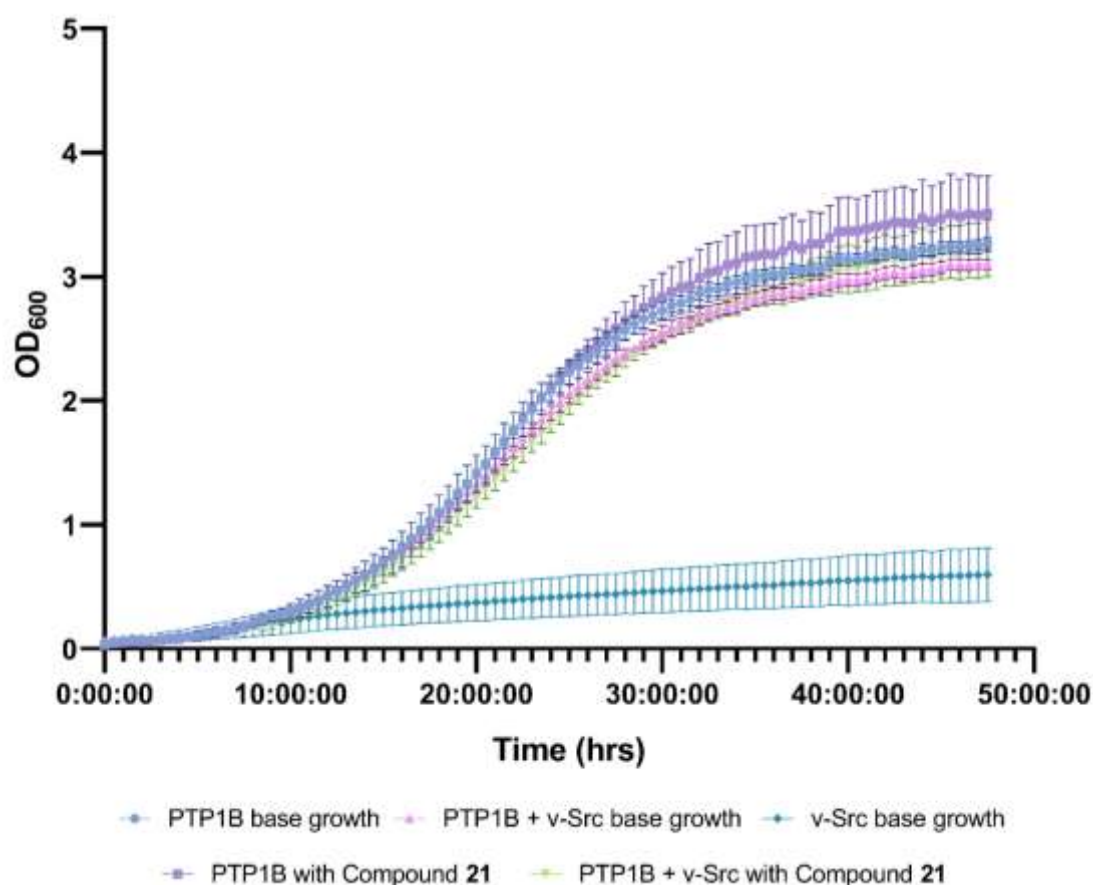
Transformed cells	PTP1B only	PTP1B + v-Src
p value	ns	ns

Figure XXXIV: Growth curves of PTP1B only, PTP1B + v-Src and v-Src only YMK23 transformations with and without the addition of compound **19** at 100µM. n=3 for each PTP1B based parameter, n=13 for v-Src. Mean and individual biological points ± standard deviation plotted. Data is normally distributed according to a Shapiro-Wilk test. Used a 2-way ANOVA. * p value ≤ 0.050 vs corresponding base growth.



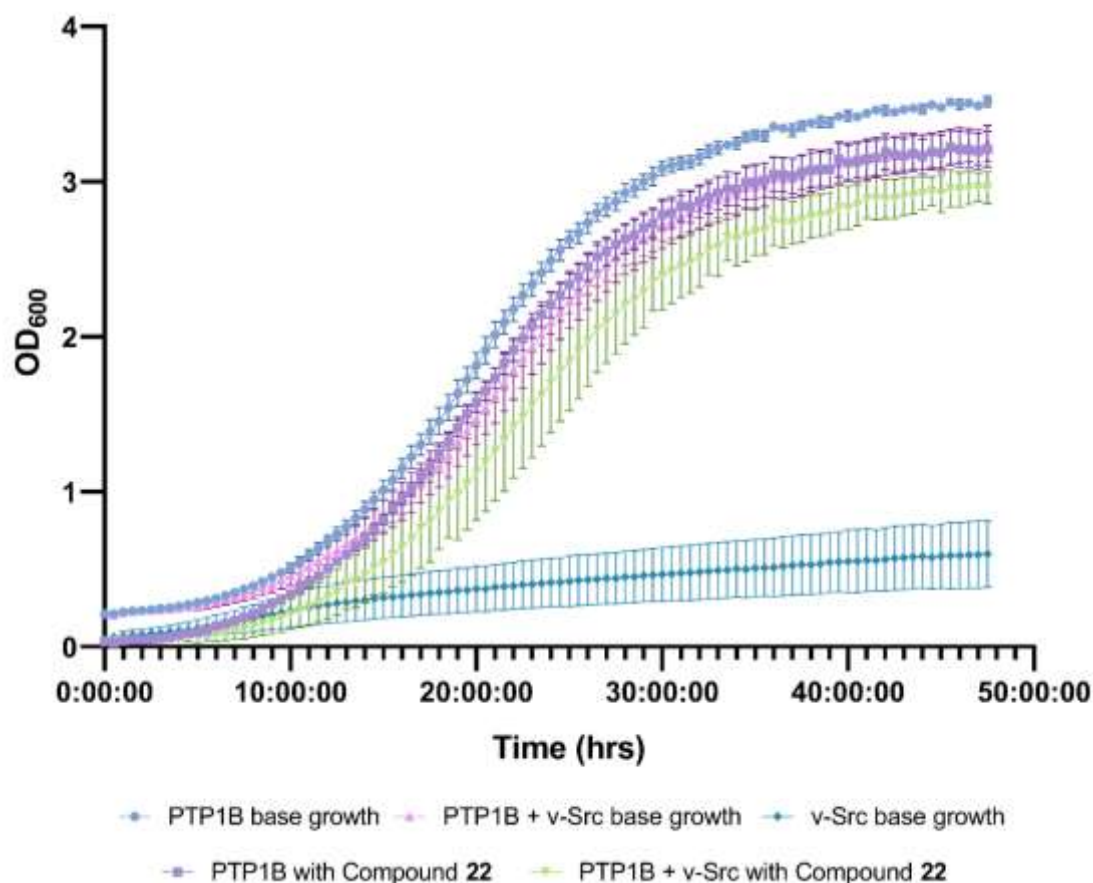
Transformed cells	PTP1B only	PTP1B + v-Src
p value	<0.0500 *	ns

Figure XXXV: Growth curves of PTP1B only, PTP1B + v-Src and v-Src only YMK23 transformations with and without the addition of compound **20a** at 100 μ M. n=3 for each PTP1B based parameter, n=13 for v-Src. Mean and individual biological points \pm standard deviation plotted. Data is normally distributed according to a Shapiro-Wilk test. Used a 2-way ANOVA. * p value \leq 0.050 vs corresponding base growth.



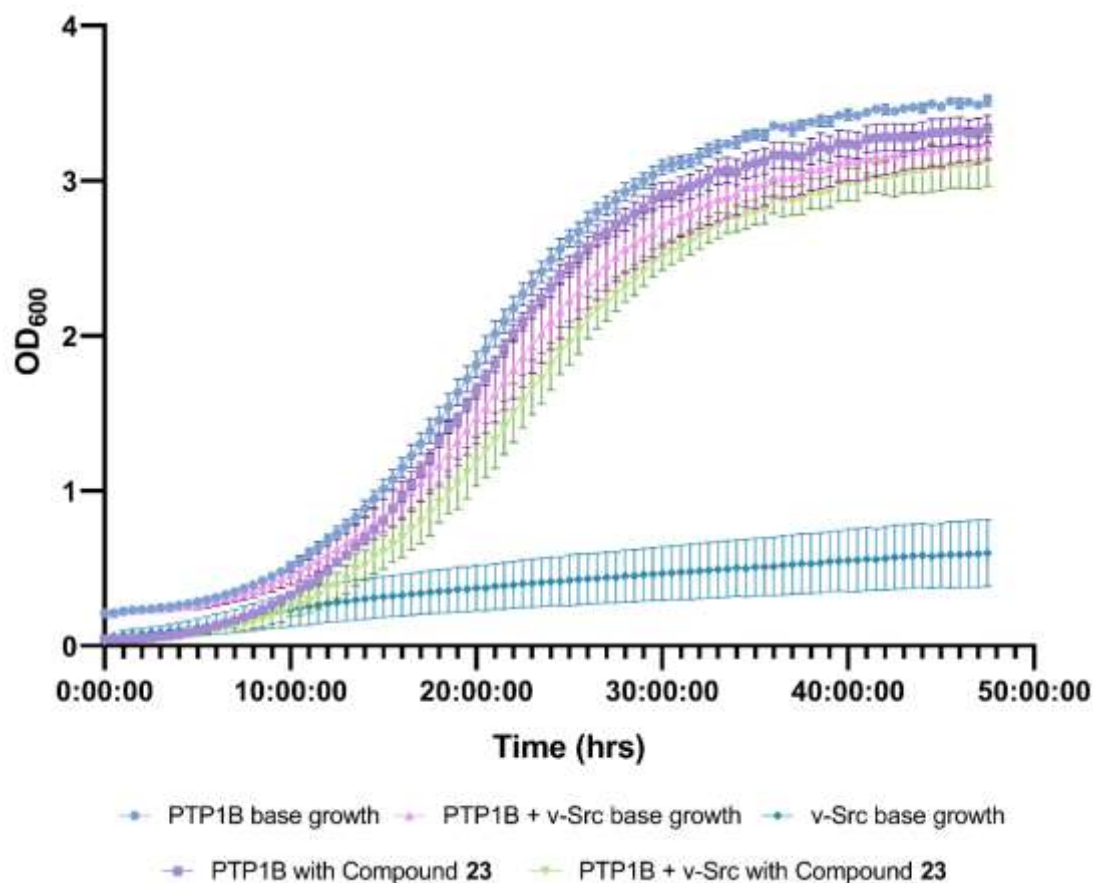
Transformed cells	PTP1B only	PTP1B + v-Src
p value	ns	ns

Figure XXXVI: Growth curves of PTP1B only, PTP1B + v-Src and v-Src only YMK23 transformations with and without the addition of compound **21** at 100µM. n=3 for each PTP1B based parameter, n=13 for v-Src. Mean and individual biological points ± standard deviation plotted. Data is normally distributed according to a Shapiro-Wilk test. Used a 2-way ANOVA. * p value ≤ 0.050 vs corresponding base growth.



Transformed cells	PTP1B only	PTP1B + v-Src
p value	<0.0100 *	ns

Figure XXXVII: Growth curves of PTP1B only, PTP1B + v-Src and v-Src only YMK23 transformations with and without the addition of compound **22** at 100 μ M. n=3 for each PTP1B based parameter, n=13 for v-Src. Mean and individual biological points \pm standard deviation plotted. Data is normally distributed according to a Shapiro-Wilk test. Used a 2-way ANOVA. * p value \leq 0.050 vs corresponding base growth.

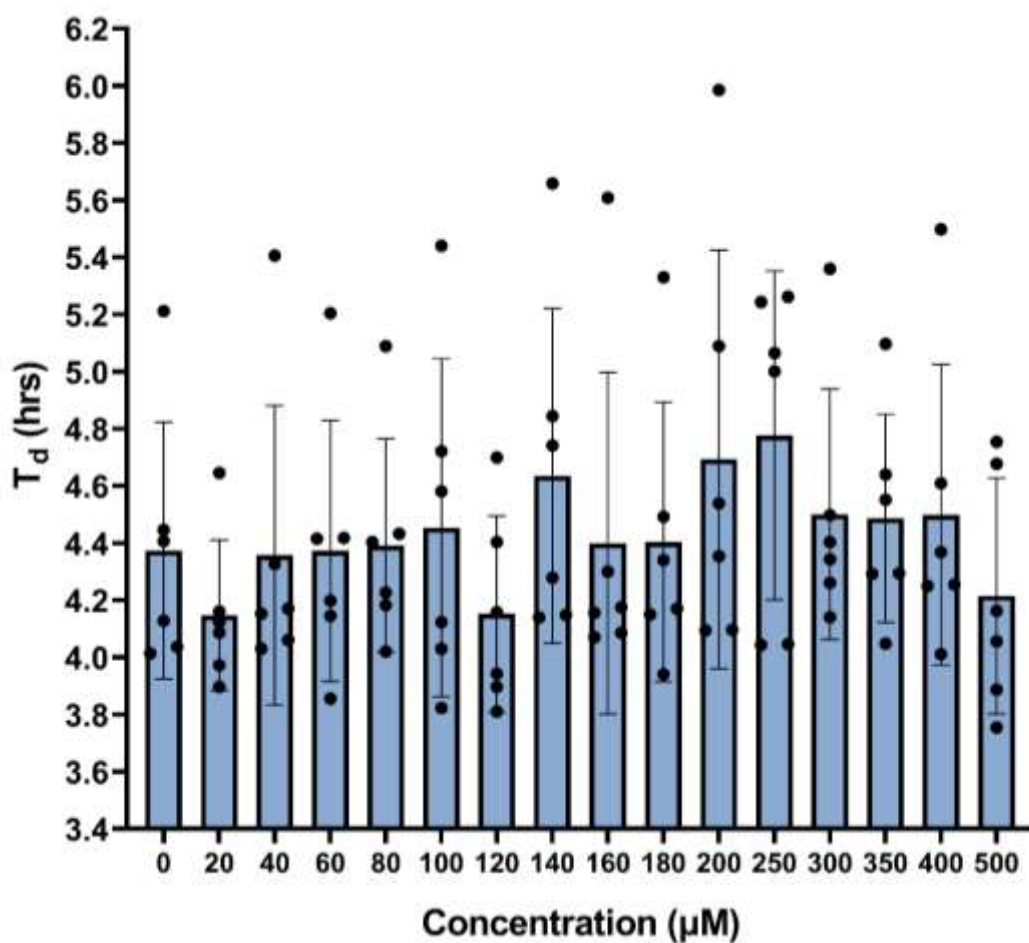


Transformed cells	PTP1B only	PTP1B + v-Src
p value	<0.010 *	ns

Figure XXXVIII: Growth curves of PTP1B only, PTP1B + v-Src and v-Src only YMK23 transformations with and without the addition of compound **23** at 100 μ M. n=3 for each PTP1B based parameter, n=13 for v-Src. Mean and individual biological points \pm standard deviation plotted. Data is normally distributed according to a Shapiro-Wilk test. Used a 2-way ANOVA. * p value \leq 0.050 vs corresponding base growth.

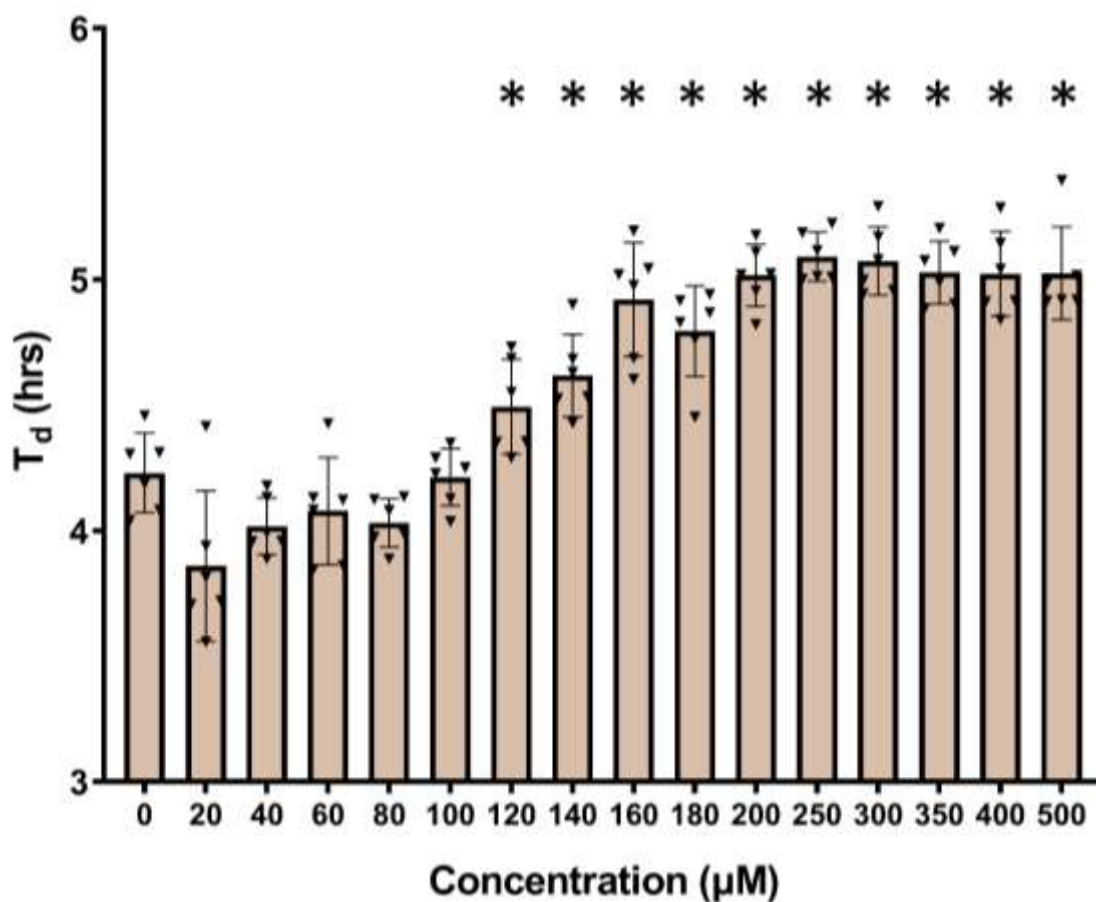
2.1.2 Compound 16 dose response screen.

2.1.2.1 PTP1B based.



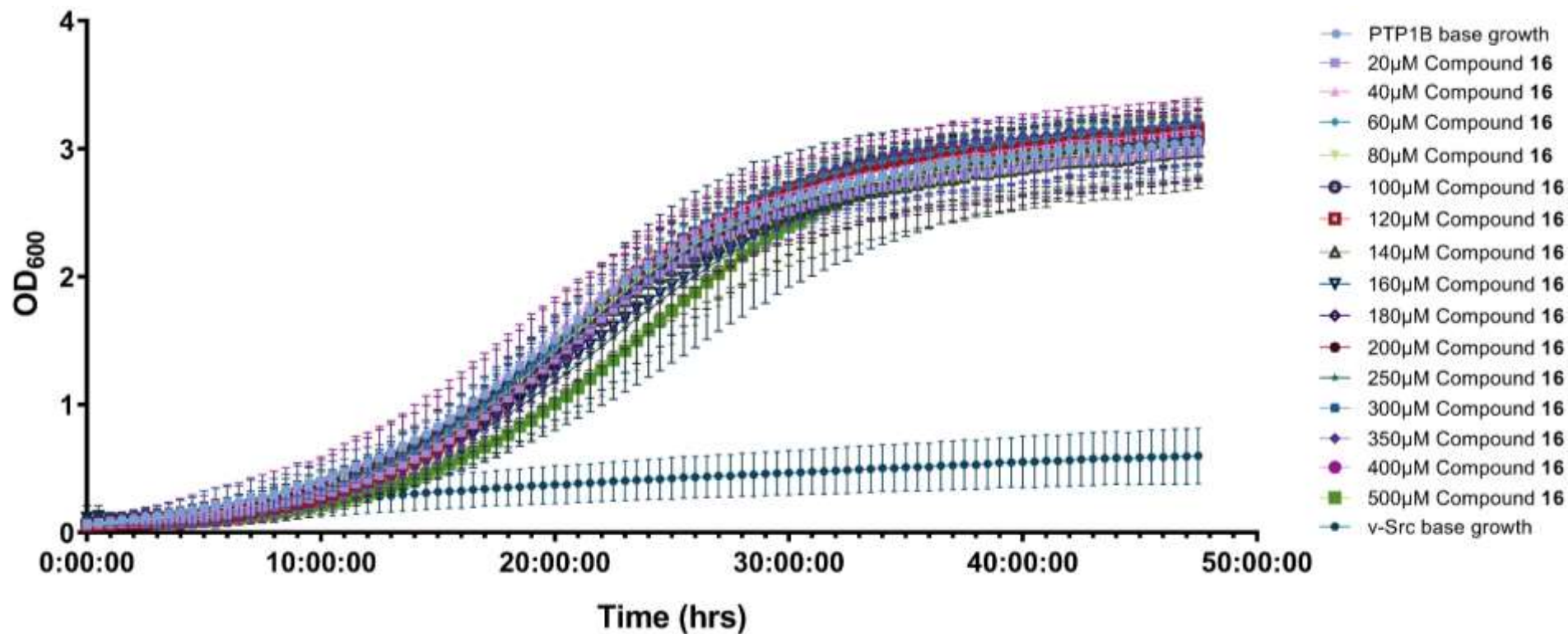
μM	20	40	60	80	100	120	140	160	180	200	250	300	350	400	500
p values	ns	ns	ns	ns	ns	ns	ns	ns	ns	ns	ns	ns	ns	ns	ns

Figure XXXIX: Comparison in doubling time (T_d) of PTP1B only transformed yeast cells in the presence of compound **16** at 20-500 μM . $n=6$ base growth and all concentrations tested in both transformations. Mean and individual points \pm standard deviation plotted. Data is normally distributed according to a Shapiro-Wilk test. Used parametric Welch's t-test for statistical analysis. * p value ≤ 0.050 vs base growth.



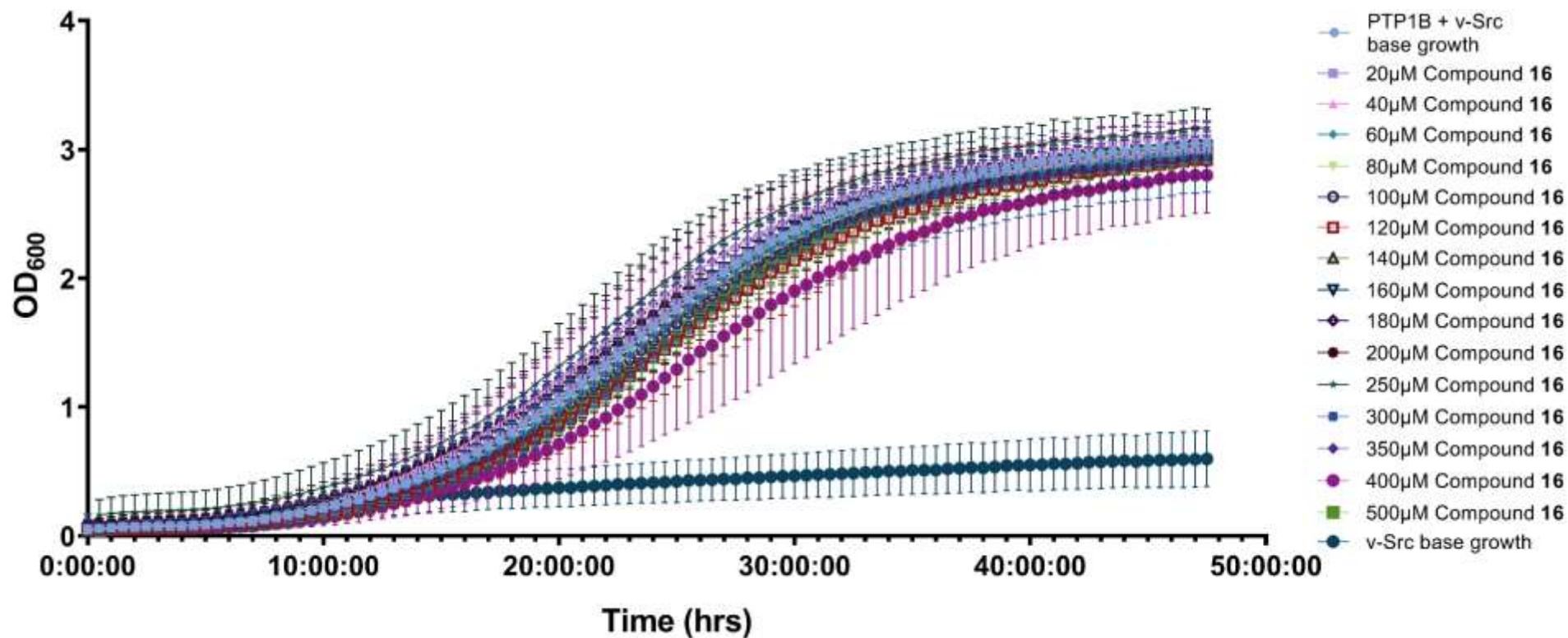
μM	p values
20	ns
40	ns
60	ns
80	ns
100	ns
120	<0.0500
140	<0.0050
160	<0.0050
180	<0.0050
200	<0.0050
250	<0.0050
300	<0.0050
350	<0.0050
400	<0.0050
500	<0.0050

Figure XL: Comparison in doubling time (T_d) of PTP1B + v-Src transformed yeast cells in the presence of compound 16 at 20-500 μM . $n=6$ base growth and all concentrations tested in both transformations. Mean and individual points \pm standard deviation plotted. Data is not normally distributed according to a Shapiro-Wilk test. Used non-parametric Mann Whitney t-test for statistical analysis. * p value ≤ 0.050 vs base growth.



μM	20	40	60	80	100	120	140	160	180	200	250	300	350	400	500 *
p value	ns	ns	ns	ns	ns	ns	ns	ns	ns	ns	ns	ns	ns	ns	<0.0500

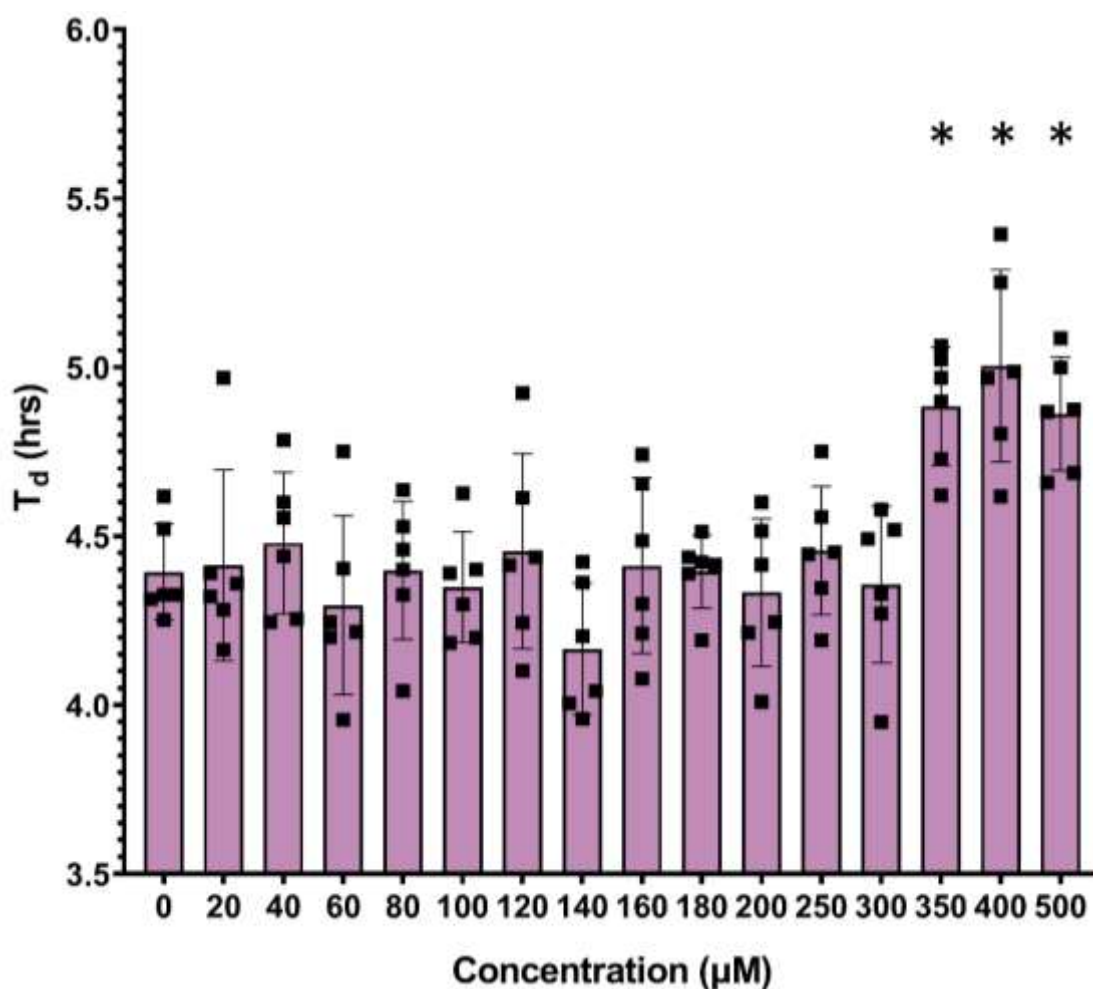
Figure XLI: Growth profile of PTP1B only yeast cells with the addition of compound 16 at 20-500 μM. n=6 for all concentrations in PTP1B only cells, n=13 for v-Src base growth. Mean points ± standard deviation plotted. Data is normally distributed according to a Shapiro-Wilk test. Used a 2-way ANOVA where column factor was source of variance. * p value ≤ 0.050 vs control.



μM	20	40	60	80	100	120	140	160	180	200	250	300	350	400	500
p value	ns	ns	ns	ns	ns	ns	ns	ns	ns	ns	ns	ns	ns	ns	ns

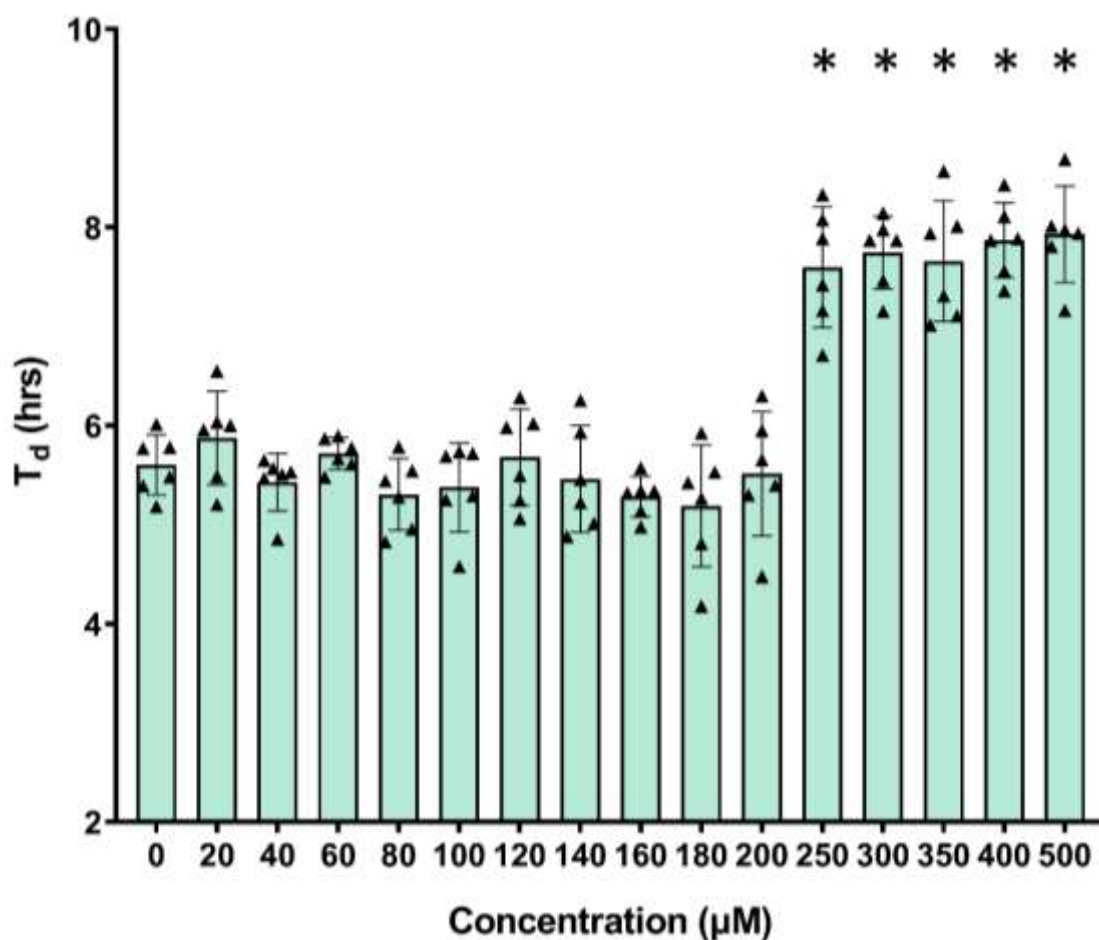
Figure XLII: Growth profile of PTP1B + v-Src yeast cells with the addition of compound 16 at 20-500 μM . $n=6$ for all concentrations in PTP1B + v-Src cells, $n=13$ for v-Src base growth. Mean points \pm standard deviation plotted. Data is normally distributed according to a Shapiro-Wilk test. Used a 2-way ANOVA where column factor was source of variance. * p value ≤ 0.050 vs control.

2.1.2.2 TCPTP based.



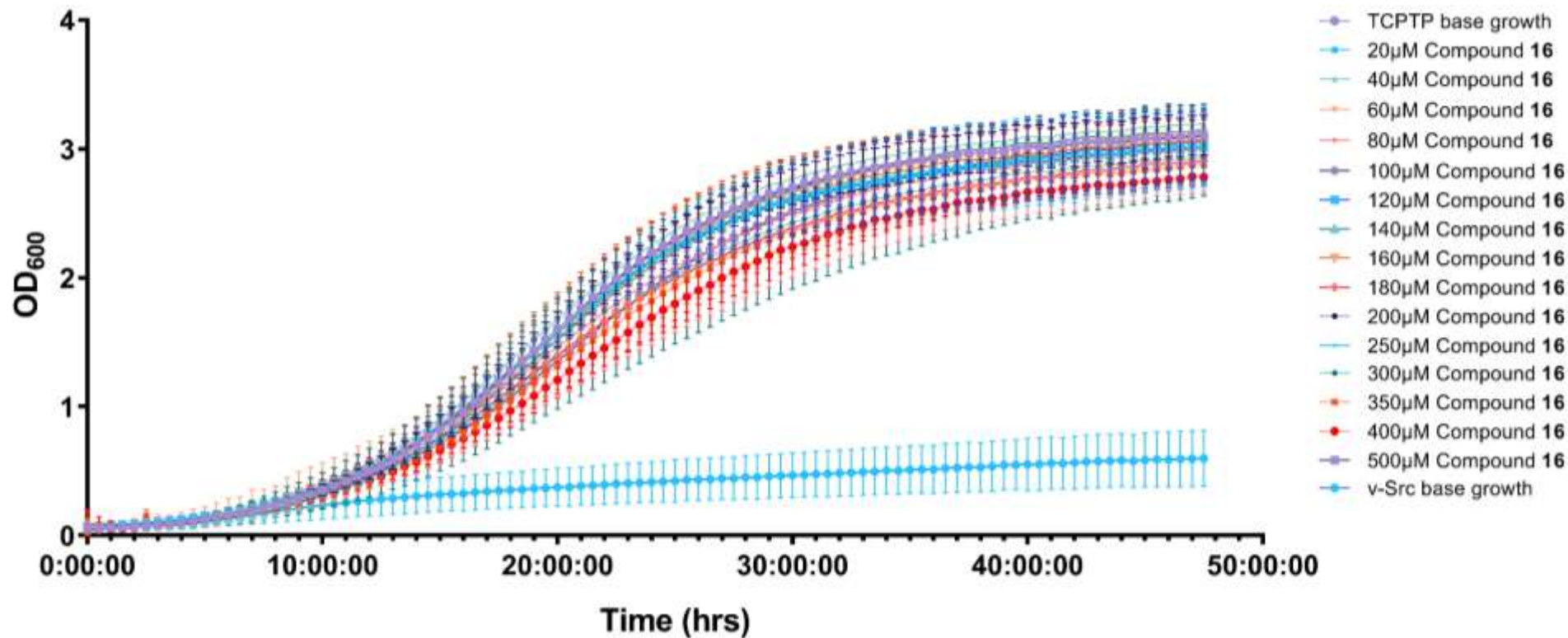
μM	p values
20	ns
40	ns
60	ns
80	ns
100	ns
120	ns
140	ns
160	ns
180	ns
200	ns
250	ns
300	ns
350	<0.0050
400	<0.0050
500	<0.0050

Figure XLIII: Comparison in doubling time (T_d) of TCPTP only transformed yeast cells in the presence of compound **16** at 20-500 μM . $n=6$ base growth and all concentrations tested in both transformations. Mean and individual points \pm standard deviation plotted. Data is normally distributed according to a Shapiro-Wilk test. Used parametric Welch's t-test for statistical analysis. * p value ≤ 0.050 vs base growth.



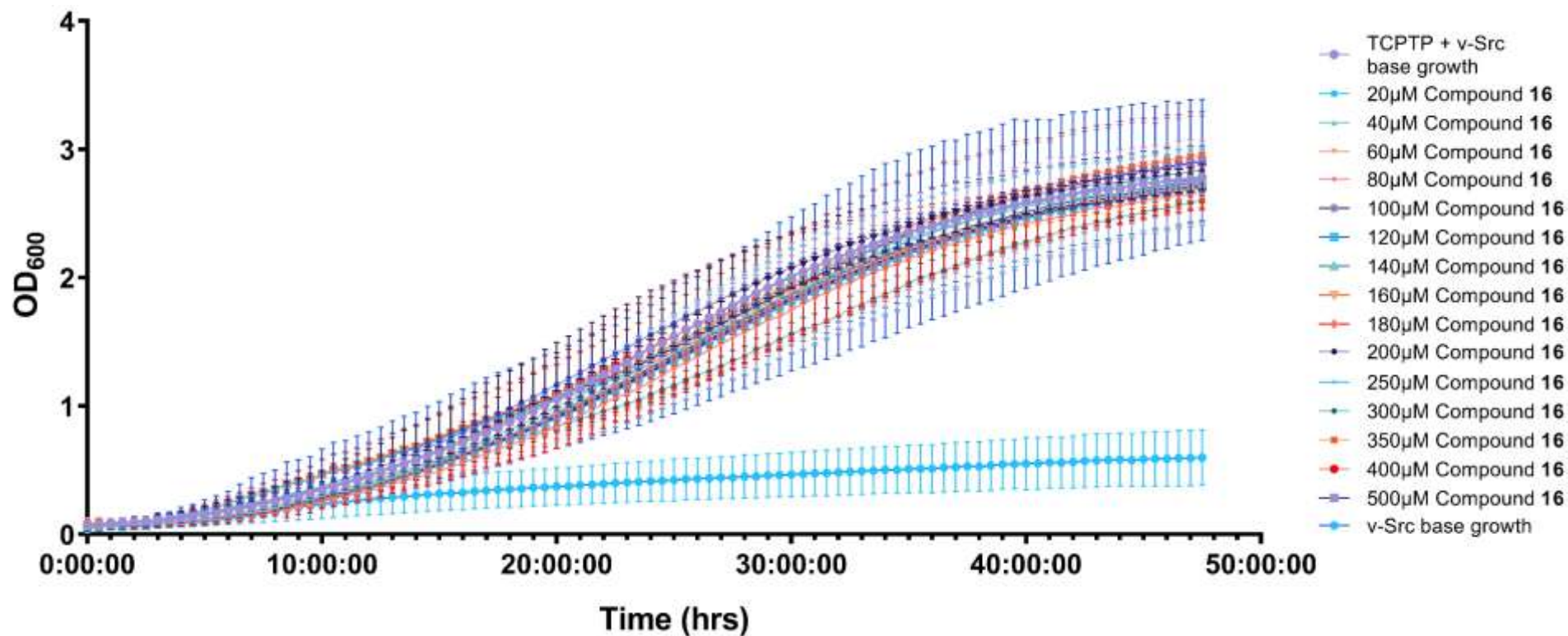
μM	20	40	60	80	100	120	140	160	180	200	250	300	350	400	500
p values	ns	ns	ns	ns	ns	ns	ns	ns	ns	ns	<0.0050	<0.0050	<0.0050	<0.0050	<0.0050

Figure XLIV: Comparison in doubling time (T_d) of TCPTP + v-Src transformed yeast cells in the presence of compound **16** at 20-500 μM . $n=6$ base growth and all concentrations tested in both transformations. Mean and individual points \pm standard deviation plotted. Data is not normally distributed according to a Shapiro-Wilk test. Used non-parametric Mann-Whitney t-test for statistical analysis. * p value ≤ 0.050 vs base growth.



μM	20	40	60	80	100	120	140	160	180	200	250	300	350 *	400 *	500
p value	ns	ns	ns	ns	ns	ns	ns	ns	ns	ns	ns	ns	<0.0100	<0.0005	ns

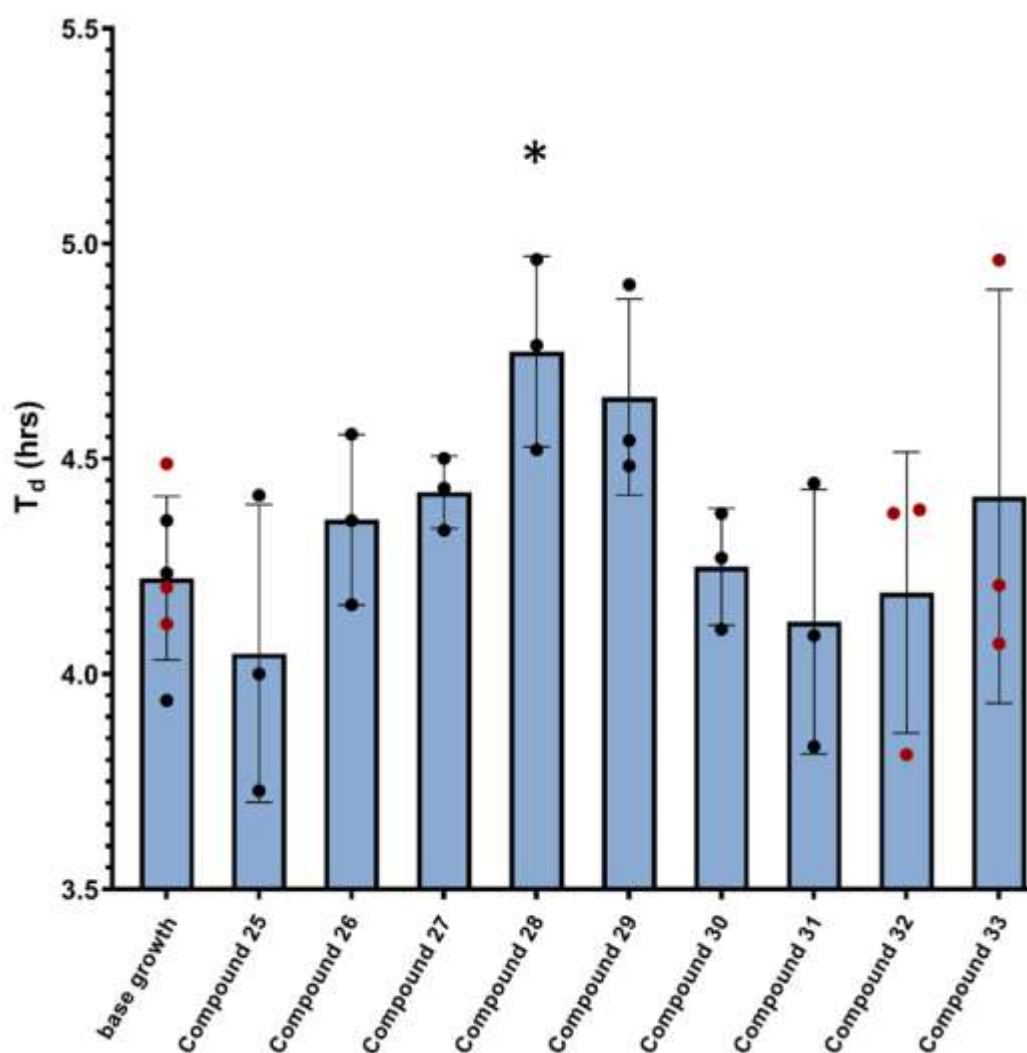
Figure XLV: Growth profile of TCPTP only yeast cells with the addition of compound **16** at 20-500 μM. n=6 for all concentrations in PTP1B only cells, n=13 for v-Src base growth. Mean points ± standard deviation plotted. Data is normally distributed according to a Shapiro-Wilk test. Used a 2-way ANOVA where column factor was source of variance. * p value ≤ 0.050 vs control.



μM	20	40	60	80 *	100	120	140	160	180	200	250	300 *	350	400	500
p value	ns	ns	ns	<0.0500	ns	ns	ns	ns	ns	ns	ns	<0.0005	ns	ns	ns

Figure XLVI: Growth profile of TCPTP + v-Src yeast cells with the addition of compound **16** at 20-500 μM . n=6 for all concentrations in PTP1B only cells, n=13 for v-Src base growth. Mean points \pm standard deviation plotted. Data is not normally distributed according to a Shapiro-Wilk test. Used a 2-way ANOVA where column factor was source of variance. * p value ≤ 0.050 vs control.

2.1.3 Compounds 25-33.



Compound	25	26	27	28	29	30	31	32	33
p values	ns	ns	ns	ns	ns	ns	ns	ns	ns

Figure XLVII: Effect of compounds 25-33 on the T_d value of PTP1B only transformed yeast cells. $n=3$ for all compounds and $n=6$ for base growth. Colour coded denotes corresponding base growth values for each compound tested. Mean points \pm standard deviation plotted. Data is normally distributed according to a Shapiro-Wilk test. Used parametric Welch t-test for statistical analysis. * p value ≤ 0.050 vs base growth. Comparison occurred with corresponding base growth values, not all presented biological repeats.

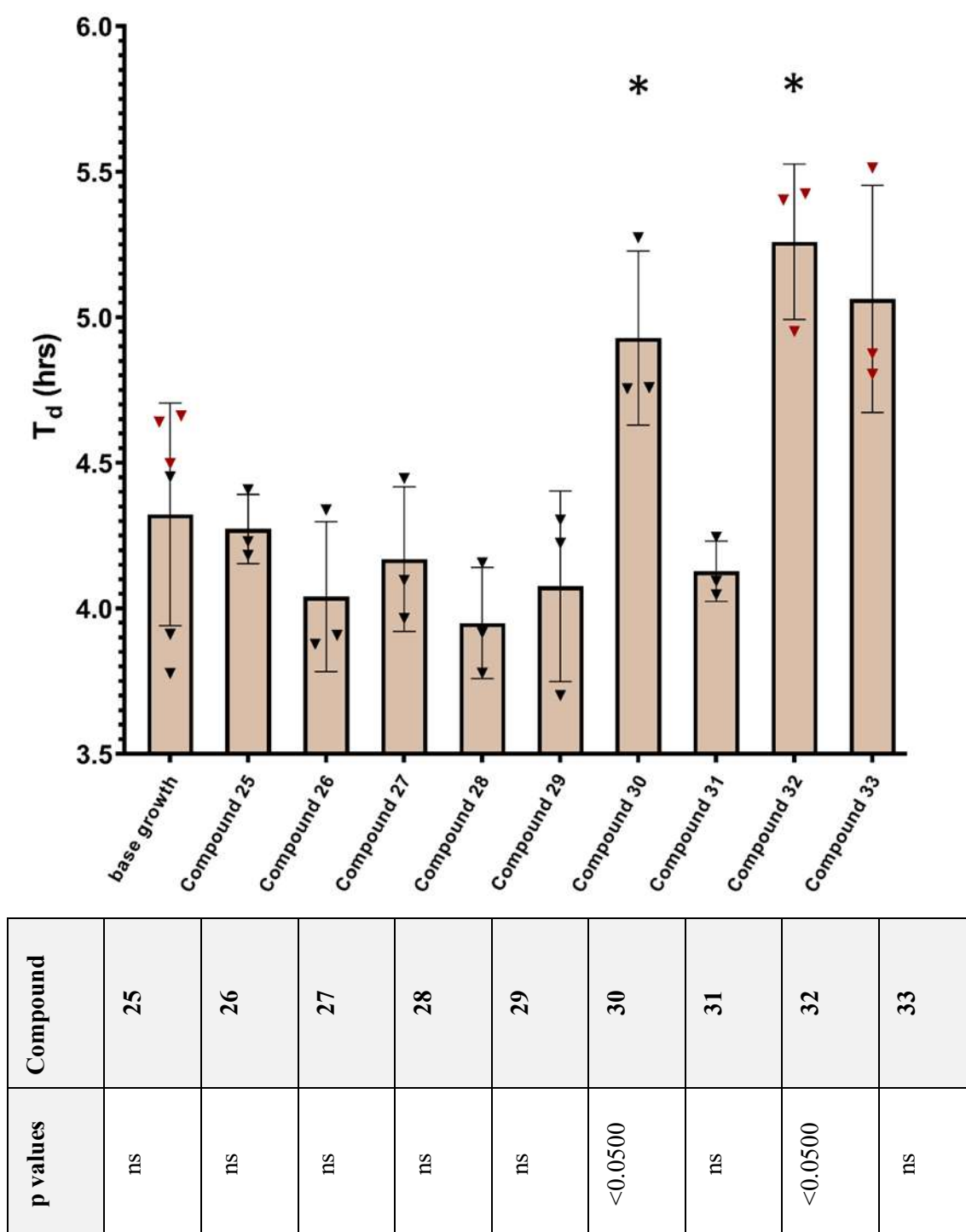
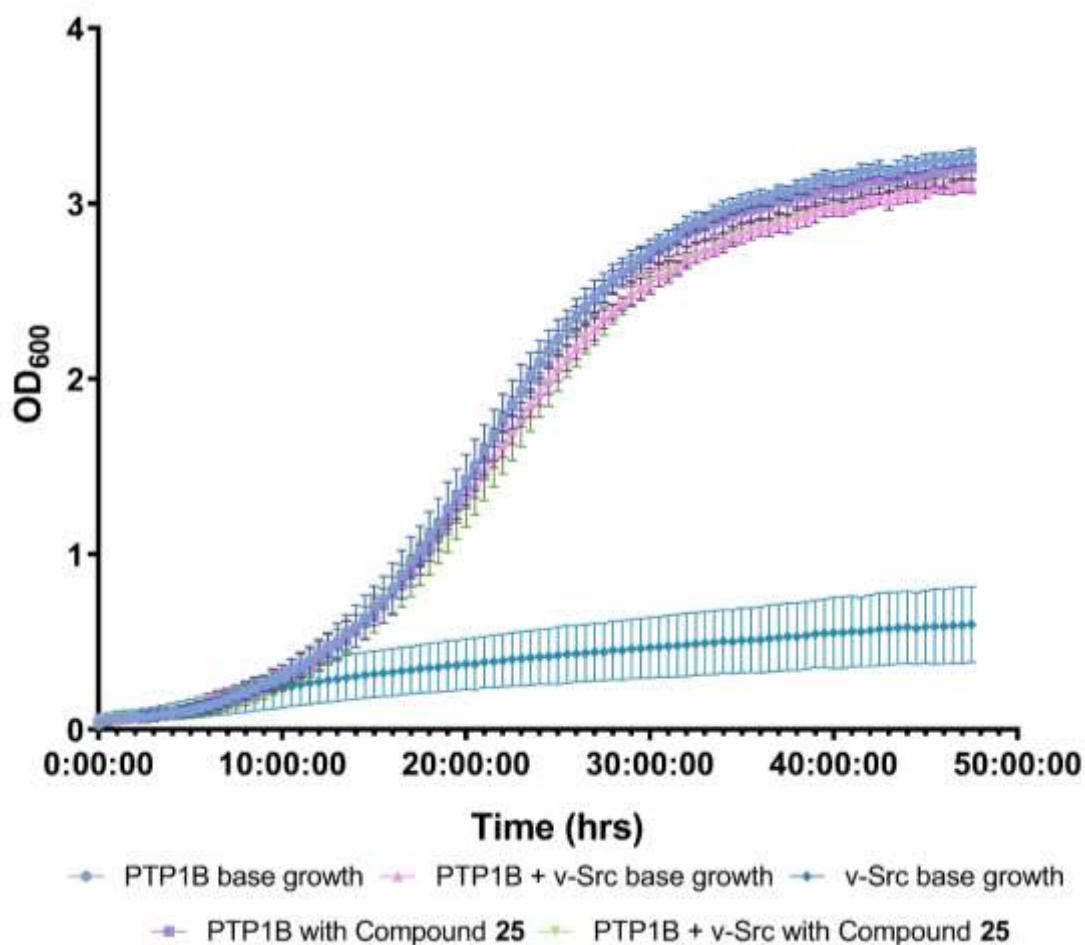
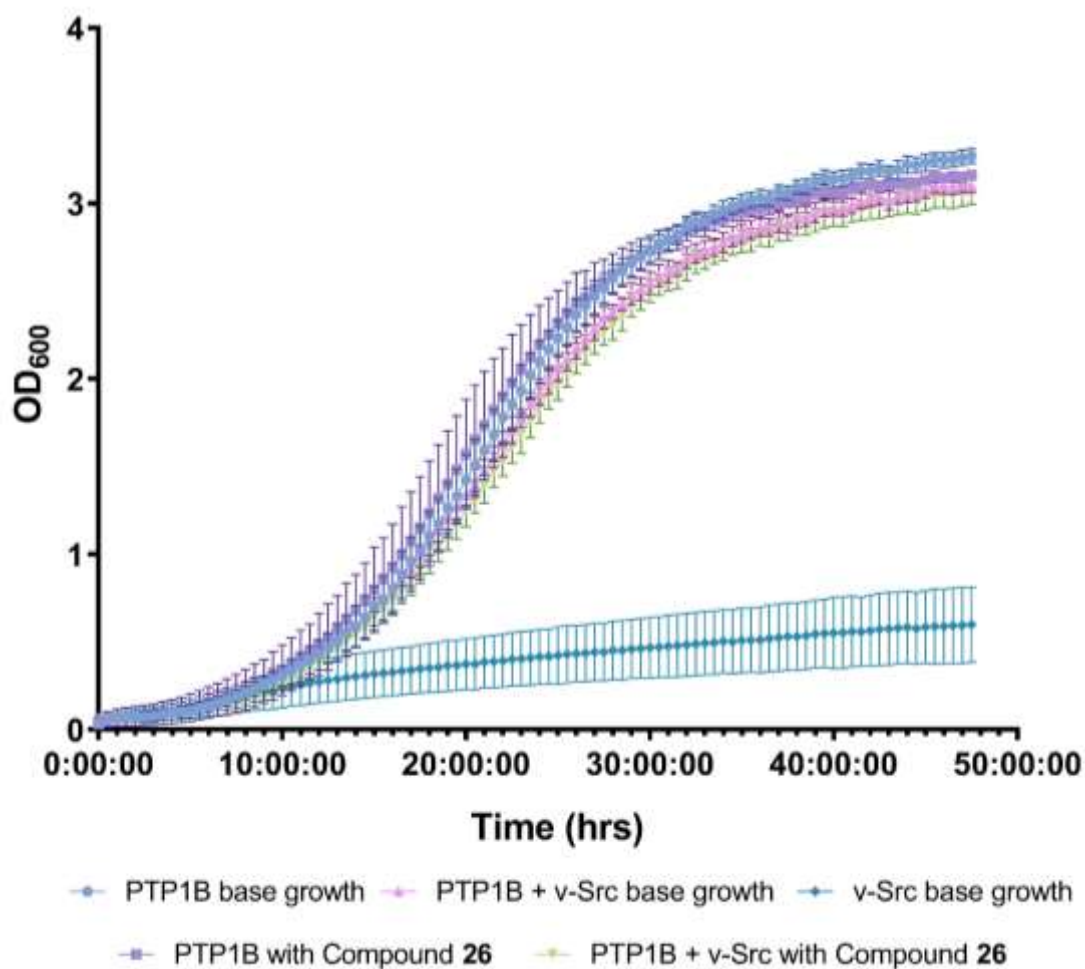


Figure XLVIII: Effect of compounds **25-33** on the T_d value of PTP1B + v-Src transformed yeast cells. $n=3$ for all compounds and $n=6$ for base growth. Colour coded denotes corresponding base growth values for each compound tested. Mean points \pm standard deviation plotted. Data is normally distributed according to a Shapiro-Wilk test. Used parametric Welch t-test for statistical analysis. * p value ≤ 0.050 vs base growth. Comparison occurred with corresponding base growth values, not all presented biological repeats.



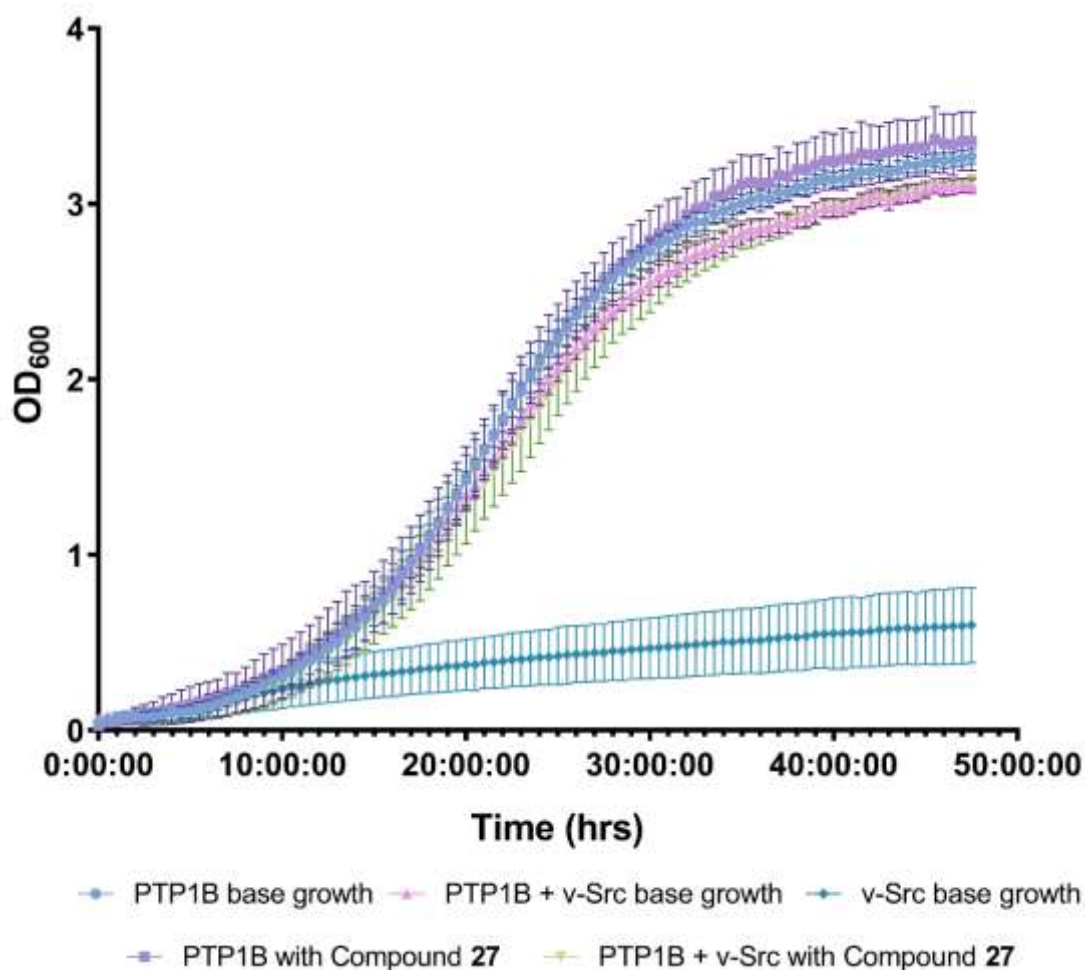
Transformed cells	PTP1B only	PTP1B + v-Src
p value	ns	ns

Figure XLIX: Growth curves of PTP1B only, PTP1B + v-Src and v-Src only YMK23 transformations with and without the addition of compound **25** at 100 μ M. n=3 for each PTP1B based parameter, n=13 for v-Src. Mean and individual biological points \pm standard deviation plotted. Data is normally distributed according to a Shapiro-Wilk test. Used a 2-way ANOVA. * p value \leq 0.050 vs corresponding base growth.



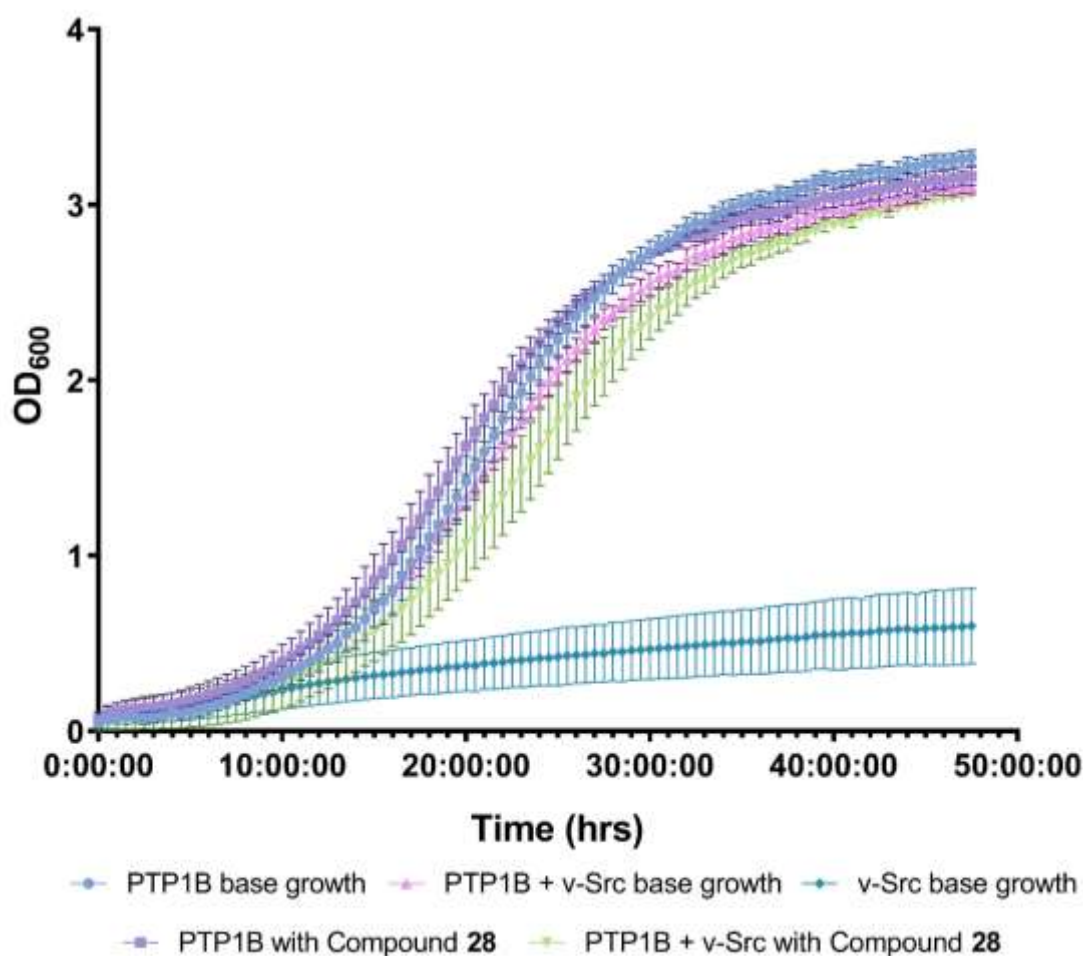
Transformed cells	PTP1B only	PTP1B + v-Src
p value	ns	ns

Figure L: Growth curves of PTP1B only, PTP1B + v-Src and v-Src only YMK23 transformations with and without the addition of compound **26** at 100 μ M. n=3 for each PTP1B based parameter, n=13 for v-Src. Mean and individual biological points \pm standard deviation plotted. Data is normally distributed according to a Shapiro-Wilk test. Used a 2-way ANOVA. * p value \leq 0.050 vs corresponding base growth.



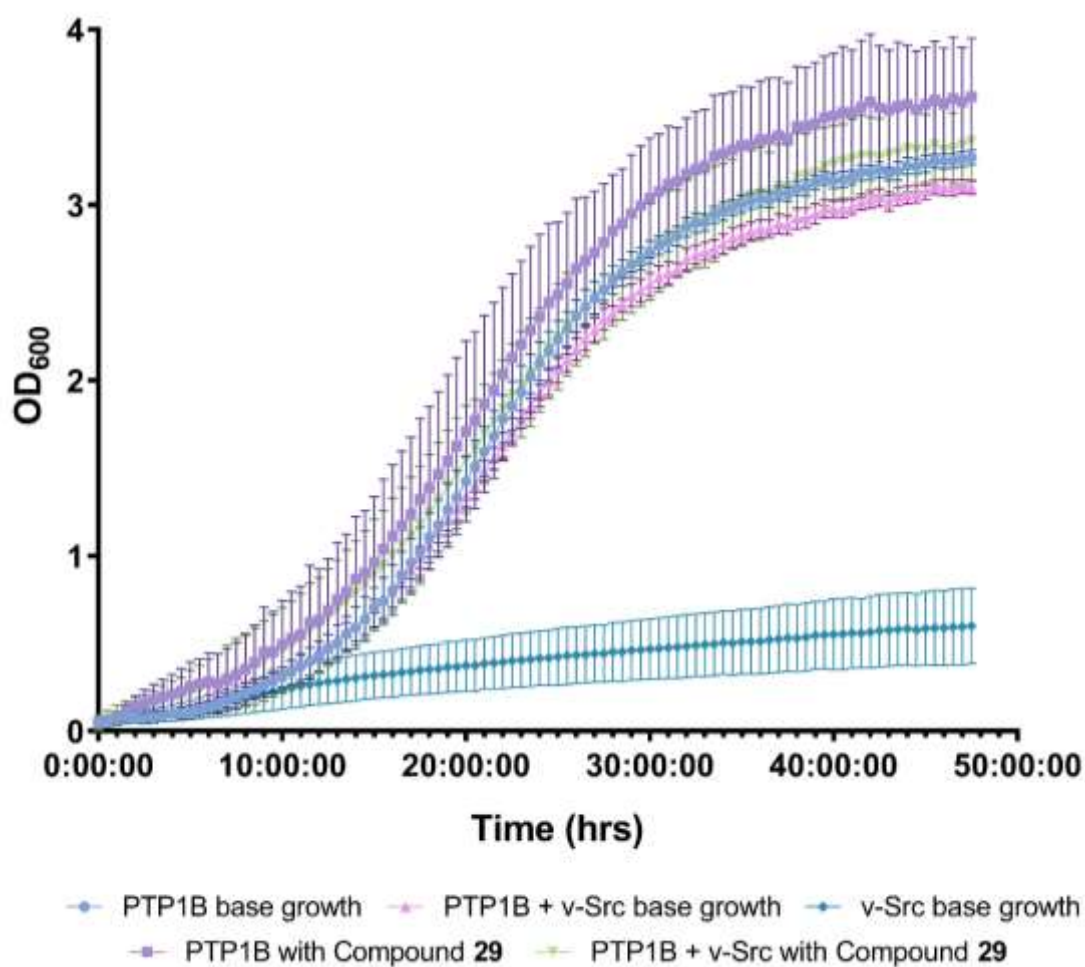
Transformed cells	PTP1B only	PTP1B + v-Src
p value	ns	ns

Figure LI: Growth curves of PTP1B only, PTP1B + v-Src and v-Src only YMK23 transformations with and without the addition of compound **27** at 100 μ M. $n=3$ for each PTP1B based parameter, $n=13$ for v-Src. Mean and individual biological points \pm standard deviation plotted. Data is normally distributed according to a Shapiro-Wilk test. Used a 2-way ANOVA. * p value ≤ 0.050 vs corresponding base growth.



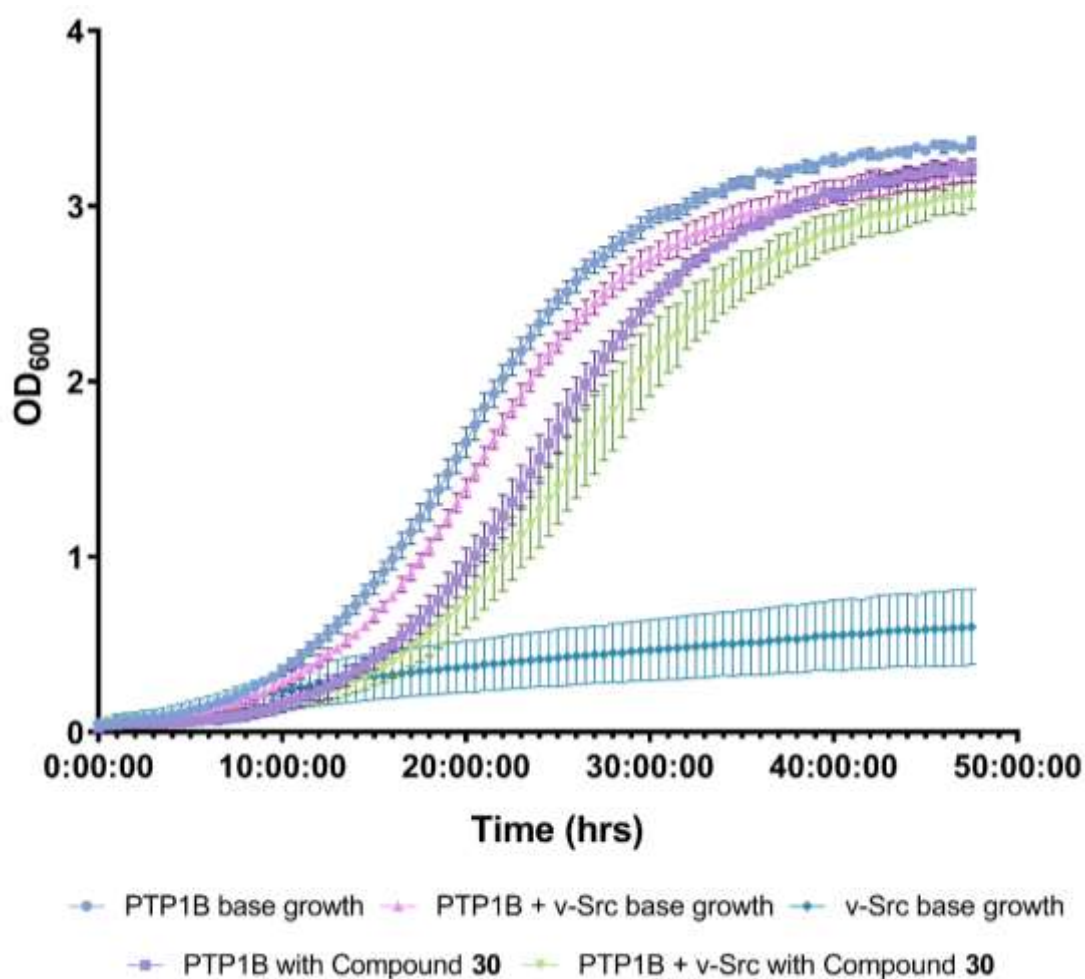
Transformed cells	PTP1B only	PTP1B + v-Src
p value	ns	ns

Figure LII: Growth curves of PTP1B only, PTP1B + v-Src and v-Src only YMK23 transformations with and without the addition of compound **28** at 100 μ M. n=3 for each PTP1B based parameter, n=13 for v-Src. Mean and individual biological points \pm standard deviation plotted. Data is normally distributed according to a Shapiro-Wilk test. Used a 2-way ANOVA. * p value \leq 0.050 vs corresponding base growth.



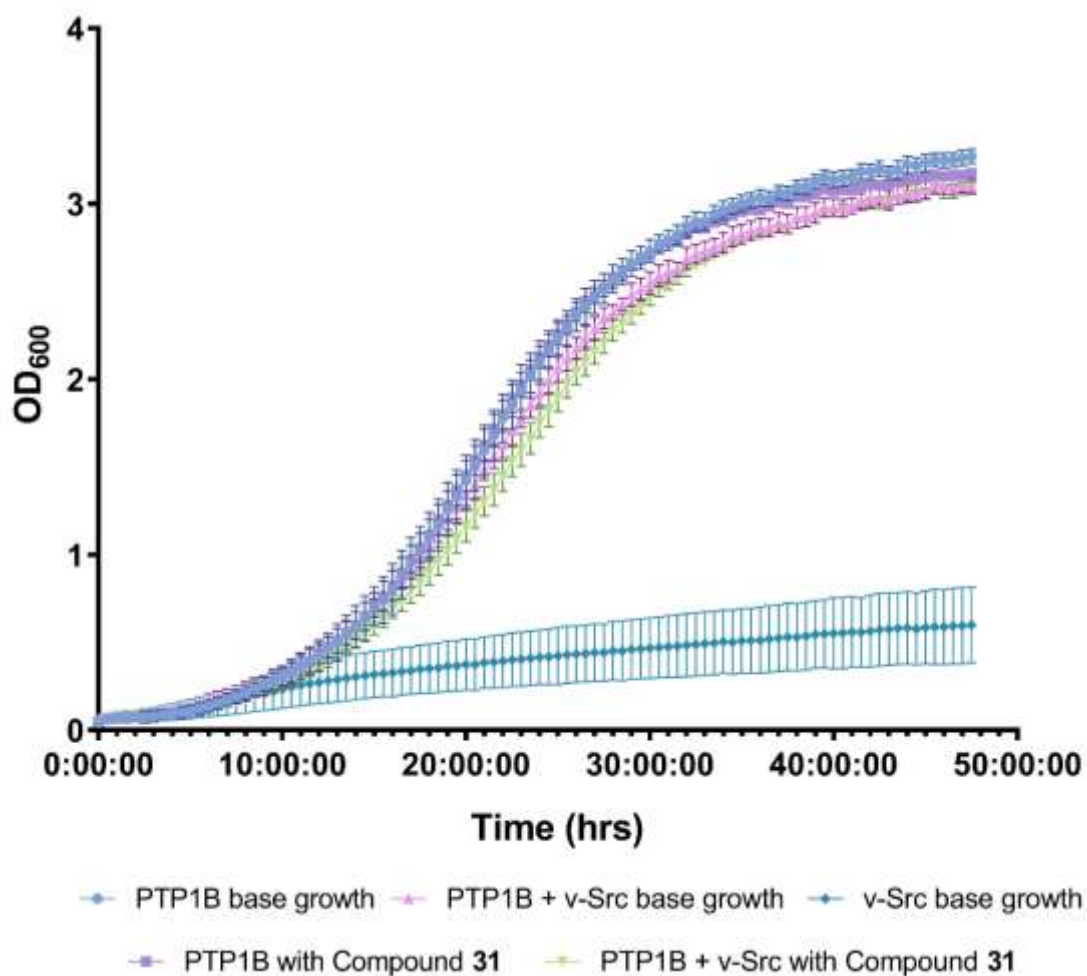
Transformed cells	PTP1B only	PTP1B + v-Src
p value	ns	ns

Figure LIII: Growth curves of PTP1B only, PTP1B + v-Src and v-Src only YMK23 transformations with and without the addition of compound **29** at 100 μ M. n=3 for each PTP1B based parameter, n=13 for v-Src. Mean and individual biological points \pm standard deviation plotted. Data is normally distributed according to a Shapiro-Wilk test. Used a 2-way ANOVA. * p value \leq 0.050 vs corresponding base growth.



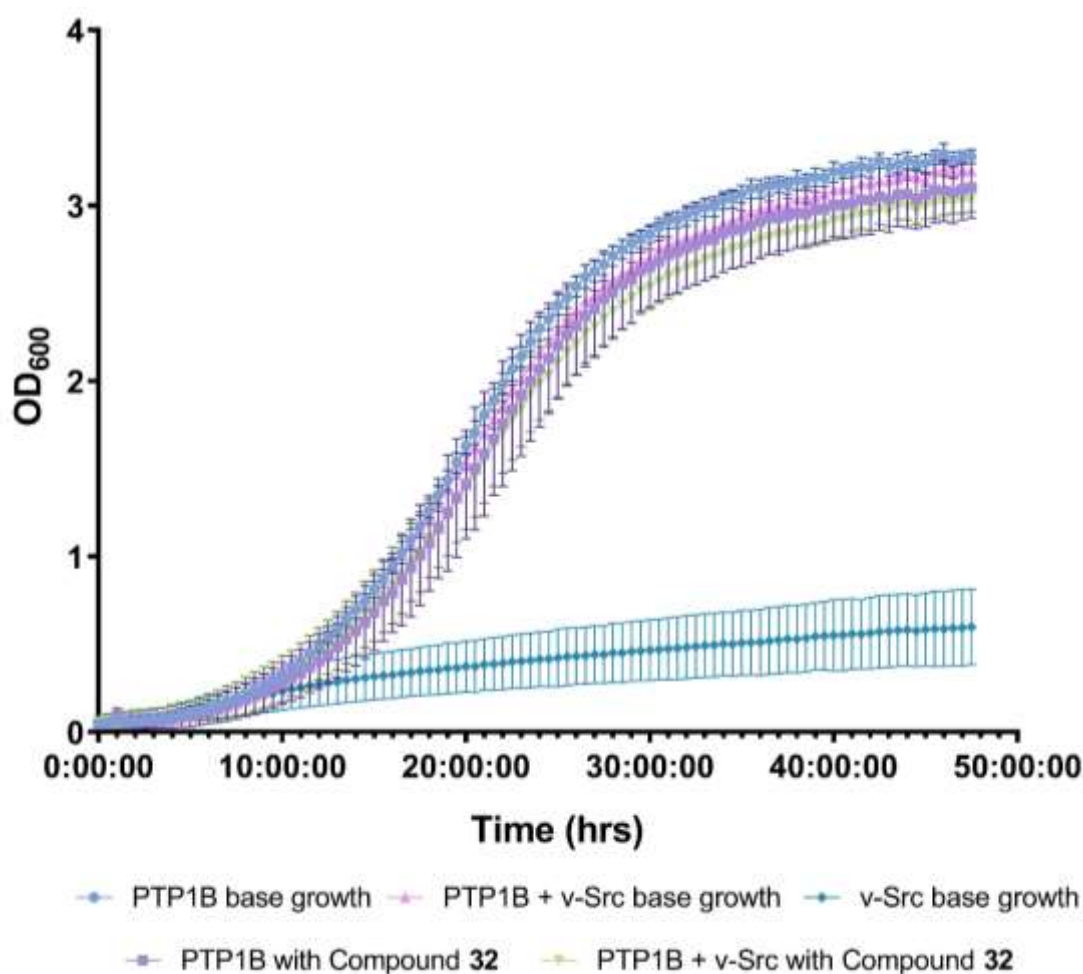
Transformed cells	PTP1B only	PTP1B + v-Src
p value	<0.0010 *	<0.0100 *

Figure LIV: Growth curves of PTP1B only, PTP1B + v-Src and v-Src only YMK23 transformations with and without the addition of compound **30** at 100 μ M. n=3 for each PTP1B based parameter, n=13 for v-Src. Mean and individual biological points \pm standard deviation plotted. Data is normally distributed according to a Shapiro-Wilk test. Used a 2-way ANOVA. * p value \leq 0.050 vs corresponding base growth.



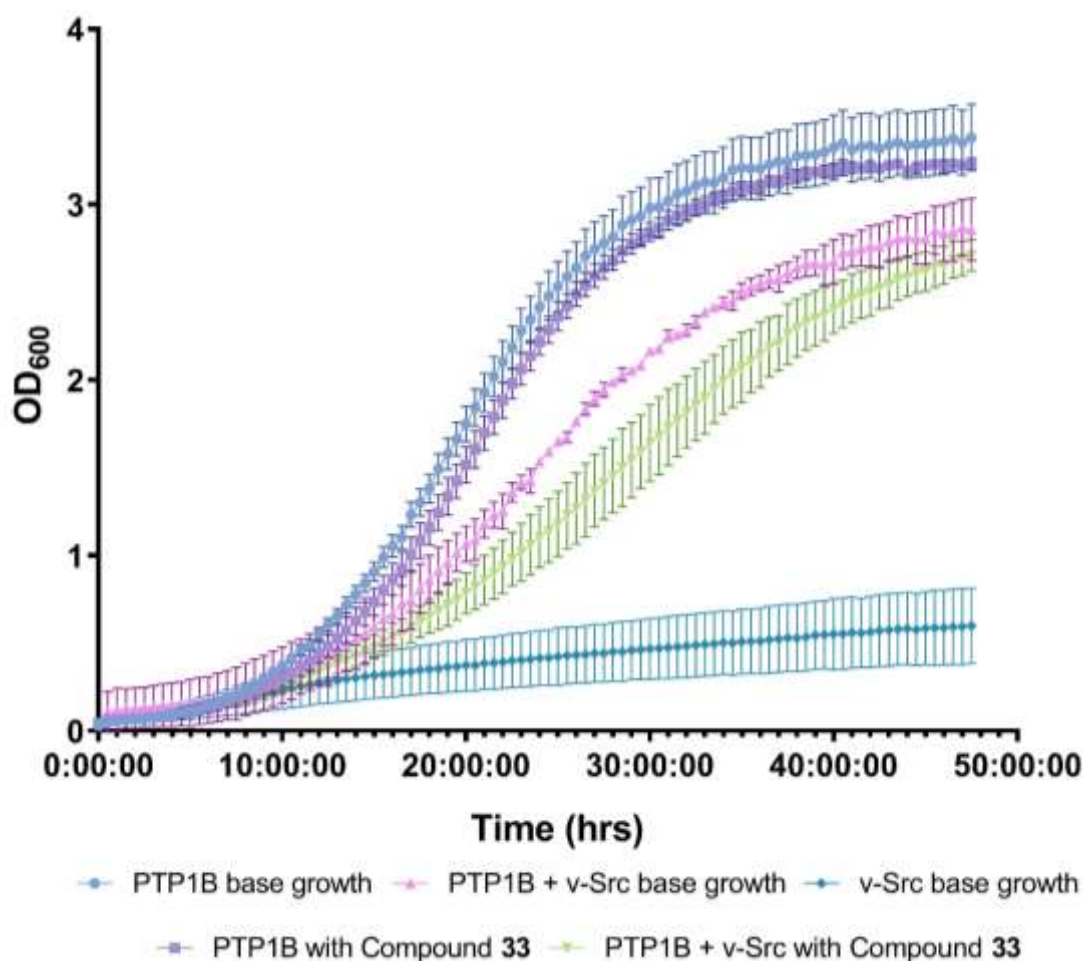
Transformed cells	PTP1B only	PTP1B + v-Src
p value	ns	ns

Figure LV: Growth curves of PTP1B only, PTP1B + v-Src and v-Src only YMK23 transformations with and without the addition of compound **31** at 100 μ M. n=3 for each PTP1B based parameter, n=13 for v-Src. Mean and individual biological points \pm standard deviation plotted. Data is normally distributed according to a Shapiro-Wilk test. Used a 2-way ANOVA. * p value \leq 0.050 vs corresponding base growth.



Transformed cells	PTP1B only	PTP1B + v-Src
p value	ns	ns

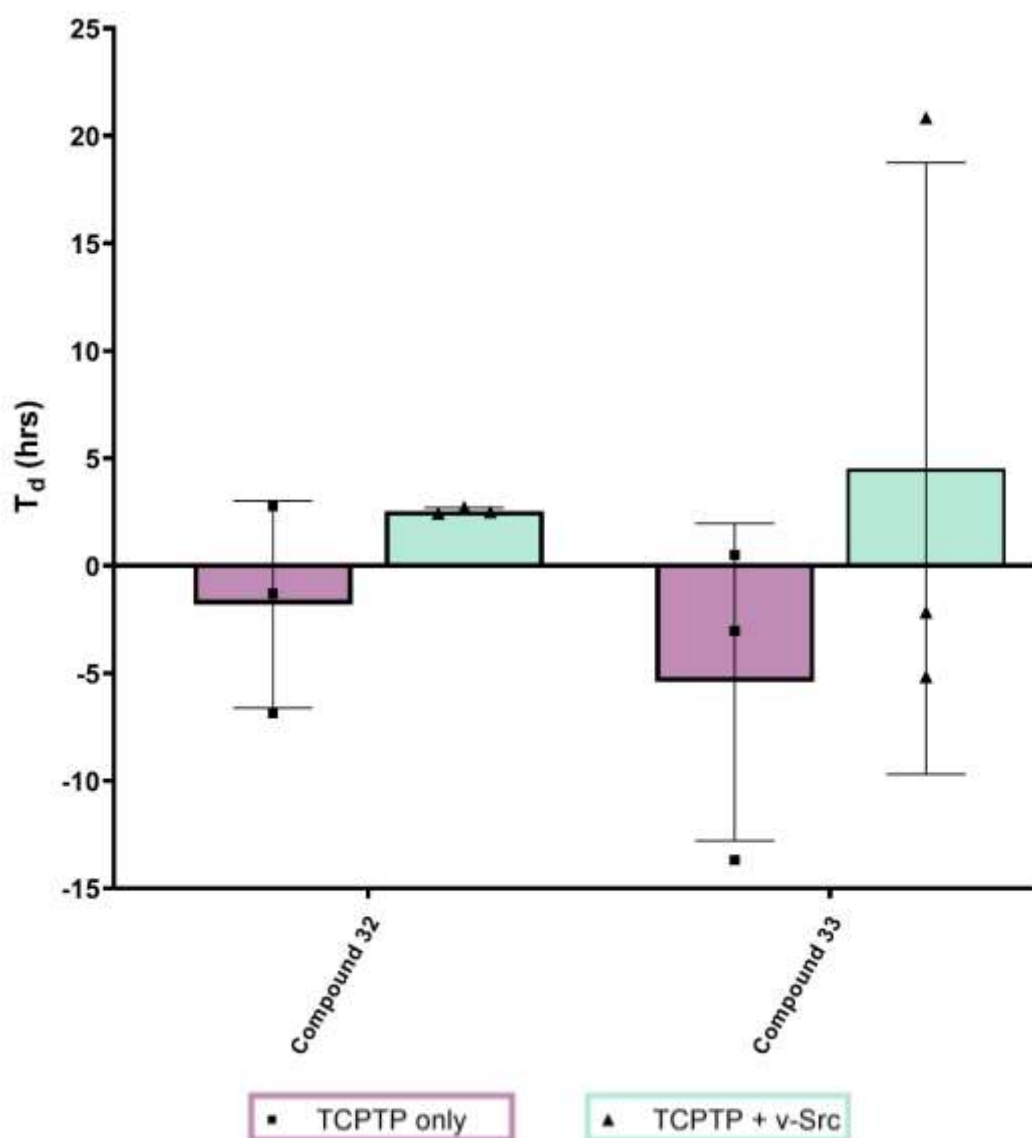
Figure LVI: Growth curves of PTP1B only, PTP1B + v-Src and v-Src only YMK23 transformations with and without the addition of compound **32** at 100 μ M. n=3 for each PTP1B based parameter, n=13 for v-Src. Mean and individual biological points \pm standard deviation plotted. Data is normally distributed according to a Shapiro-Wilk test. Used a 2-way ANOVA. * p value \leq 0.050 vs corresponding base growth.



Transformed cells	PTP1B only	PTP1B + v-Src
p value	ns	<0.0500 *

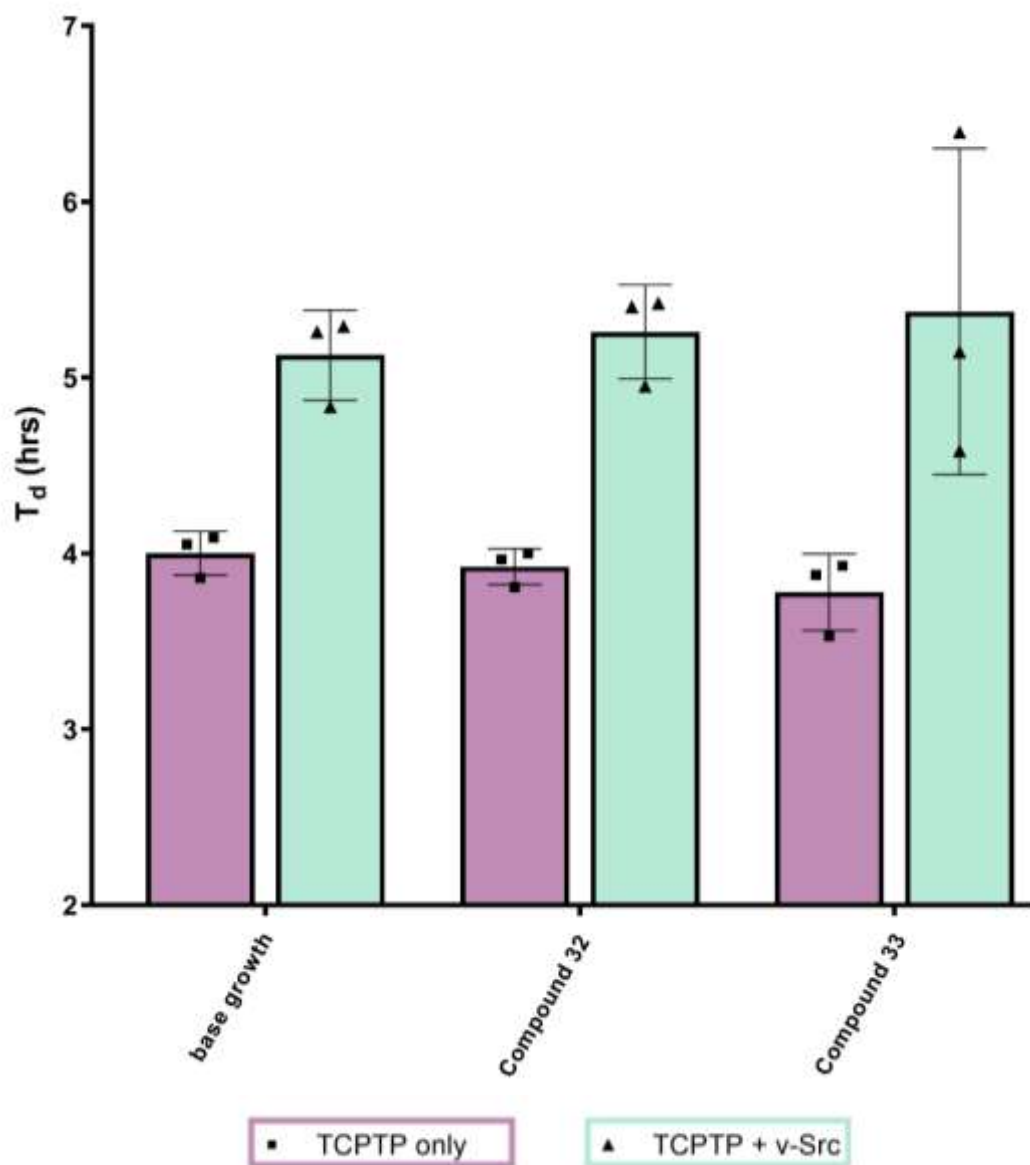
Figure LVII: Growth curves of PTP1B only, PTP1B + v-Src and v-Src only YMK23 transformations with and without the addition of compound **33** at 100 μ M. n=3 for each PTP1B based parameter, n=13 for v-Src. Mean and individual biological points \pm standard deviation plotted. Data is normally distributed according to a Shapiro-Wilk test. Used a 2-way ANOVA. * p value \leq 0.050 vs corresponding base growth.

2.1.4 Compounds 32 and 33 TCPTP investigation



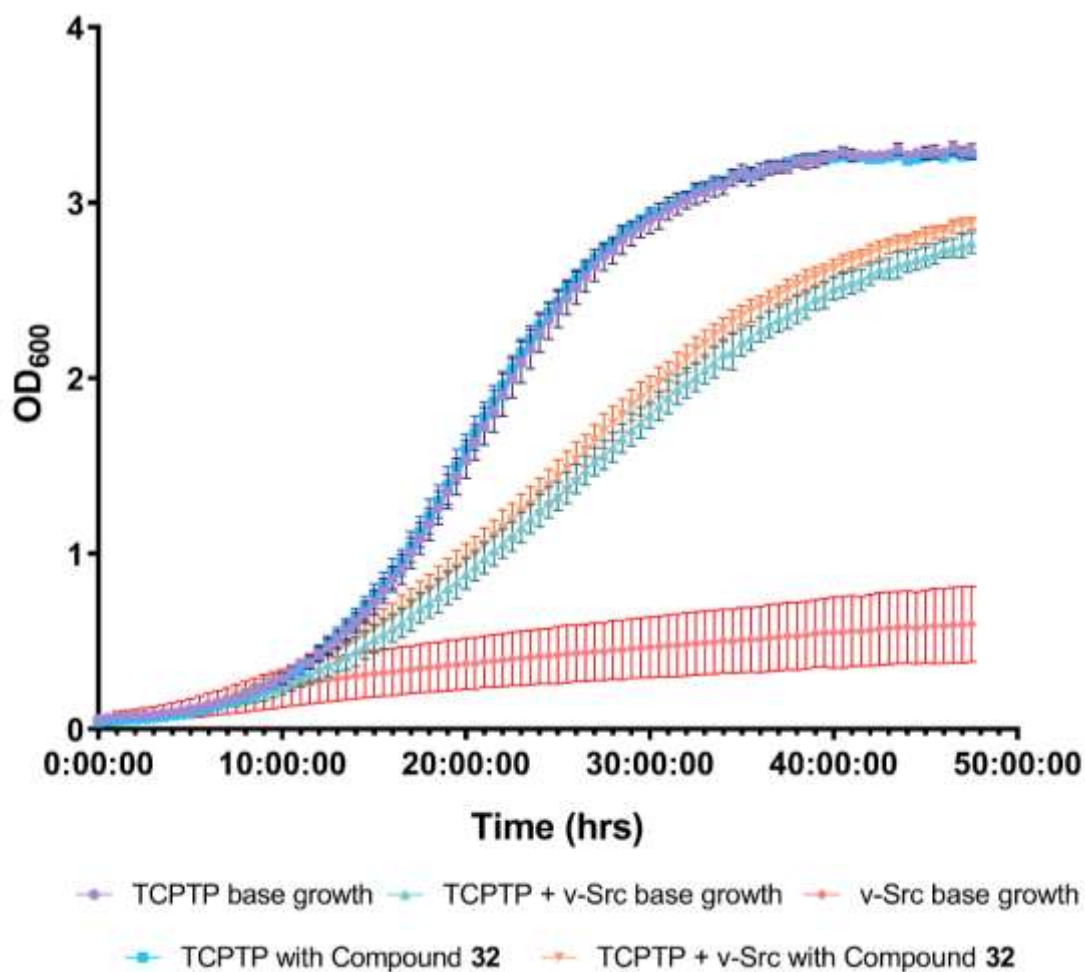
Compound	32	33
p value	ns	ns

Figure LVIII: Comparison of % change in doubling time (T_d) of TCPTP only and TCPTP + v-Src transformed yeast cells in the presence of synthesised compounds **32** and **33** at 100 μ M. $n=3$ for all compounds tested in both transformations, mean and individual points \pm standard deviation plotted. Used non-parametric Mann-Whitney t-test for statistical analysis. * p value ≤ 0.050 vs control.



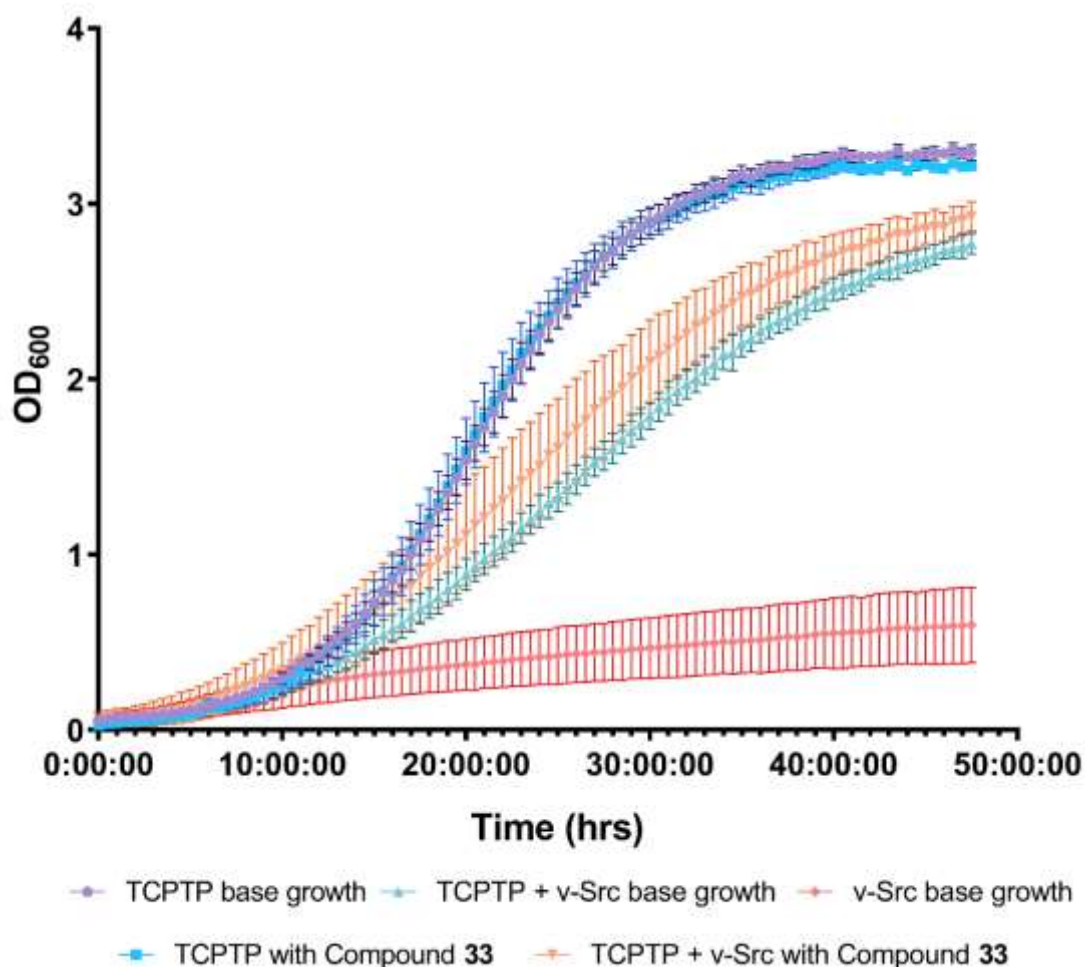
Transformed cells	TCPTP only		TCPTP + v-Src	
Compound	32	33	32	33
p value	ns	ns	ns	ns

Figure LIX: Effect of compounds **32-33** on the T_d value of PTP1B + v-Src transformed yeast cells. $n=3$ for all compounds and $n=6$ for base growth. Mean points \pm standard deviation plotted. Data is normally distributed according to a Shapiro-Wilk test. Used parametric Welch t-test for statistical analysis. * p value ≤ 0.050 vs base growth.



Transformed cells	TCPTP only	TCPTP + v-Src
p value	ns	ns

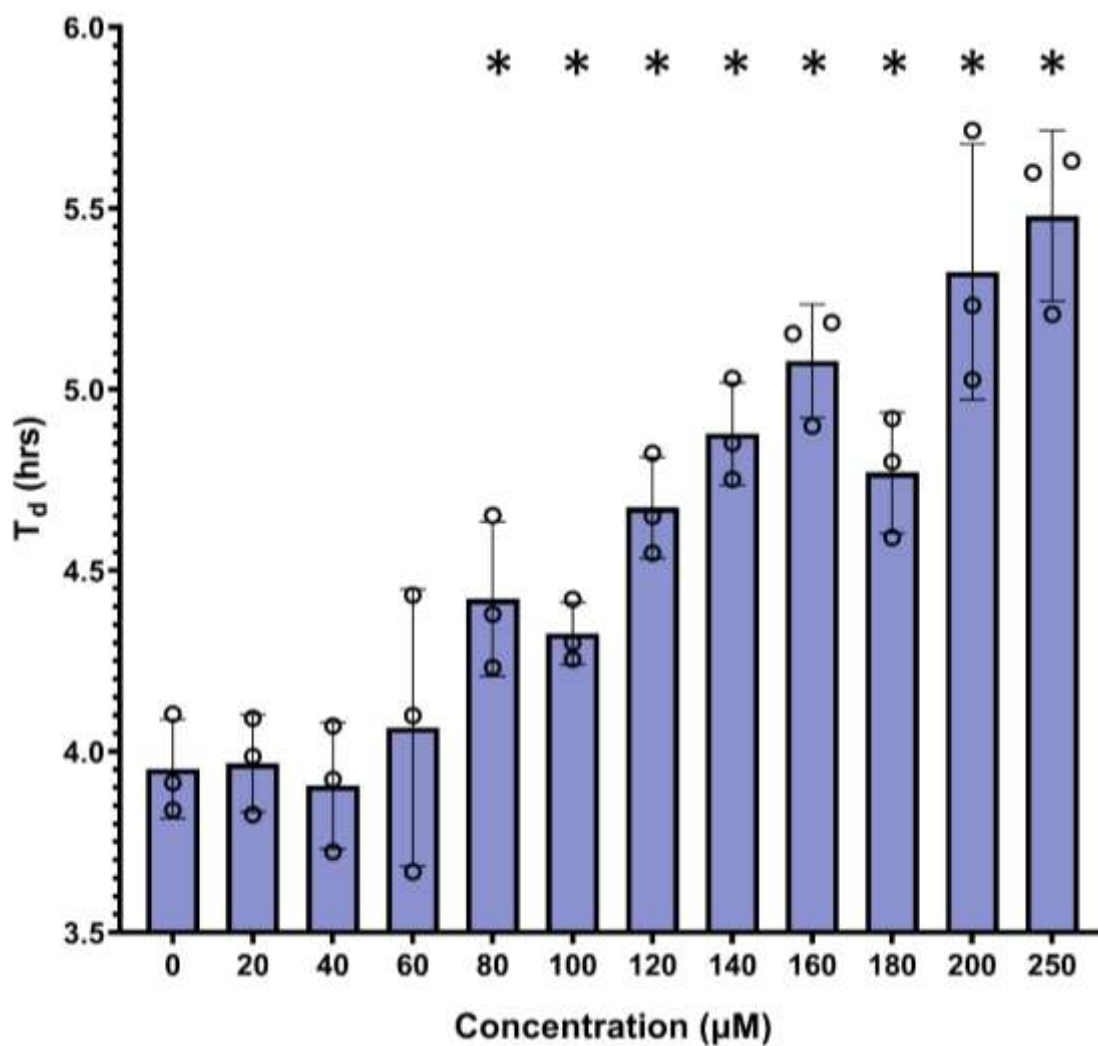
Figure LX: Growth curves of TCPTP only, TCPTP + v-Src and v-Src only YMK23 transformations with and without the addition of compound **32** at 100 μ M. n=3 for each PTP1B based parameter, n=13 for v-Src. Mean and individual biological points \pm standard deviation plotted. Data is normally distributed according to a Shapiro-Wilk test. Used a 2-way ANOVA. * p value \leq 0.050 vs corresponding base growth.



Transformed cells	TCPTP only	TCPTP + v-Src
p value	ns	ns

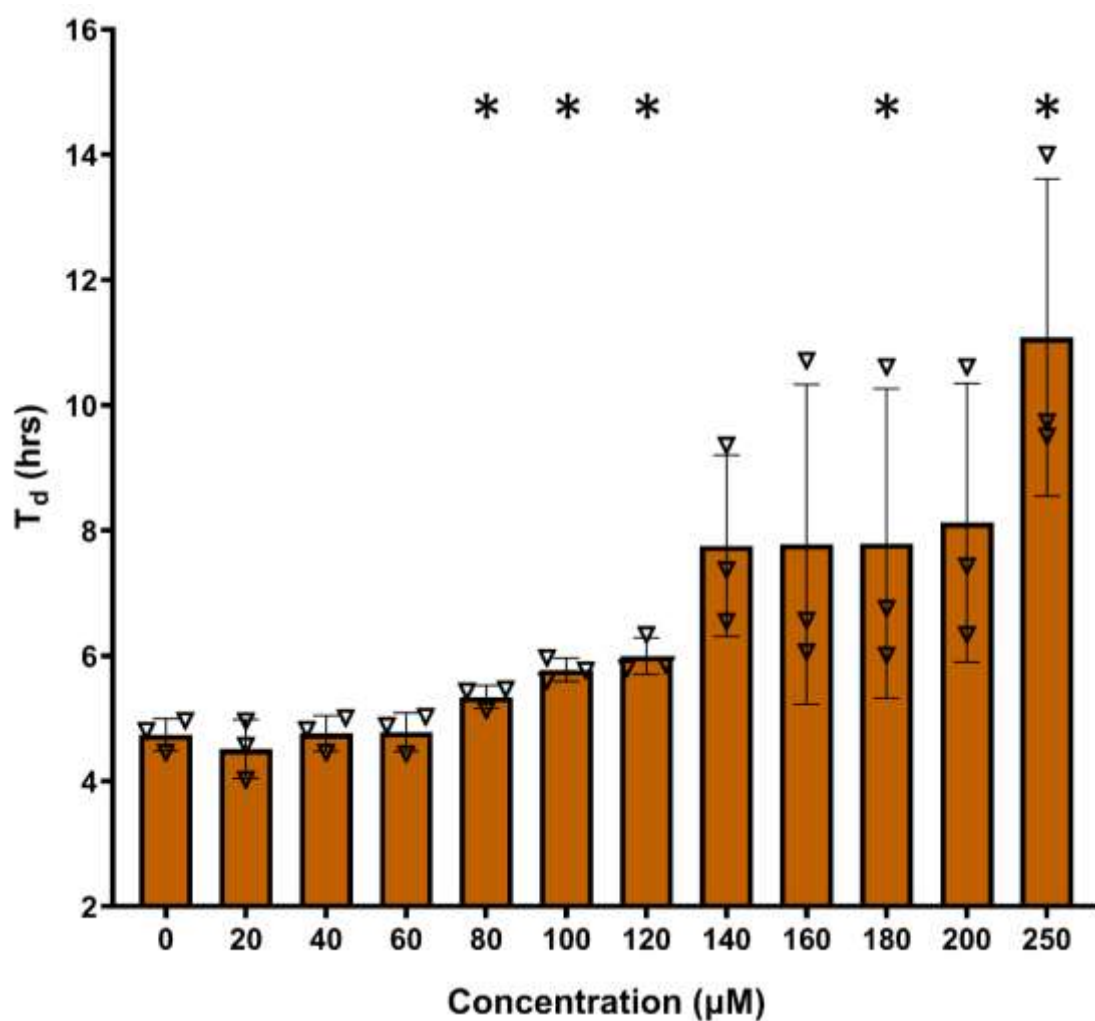
Figure LXI: Growth curves of TCPTP only, TCPTP + v-Src and v-Src only YMK23 transformations with and without the addition of compound **33** at 100 μ M. n=3 for each PTP1B based parameter, n=13 for v-Src. Mean and individual biological points \pm standard deviation plotted. Data is normally distributed according to a Shapiro-Wilk test. Used a 2-way ANOVA. * p value \leq 0.050 vs corresponding base growth.

2.1.5 Compound 30 doubling time and growth curve data



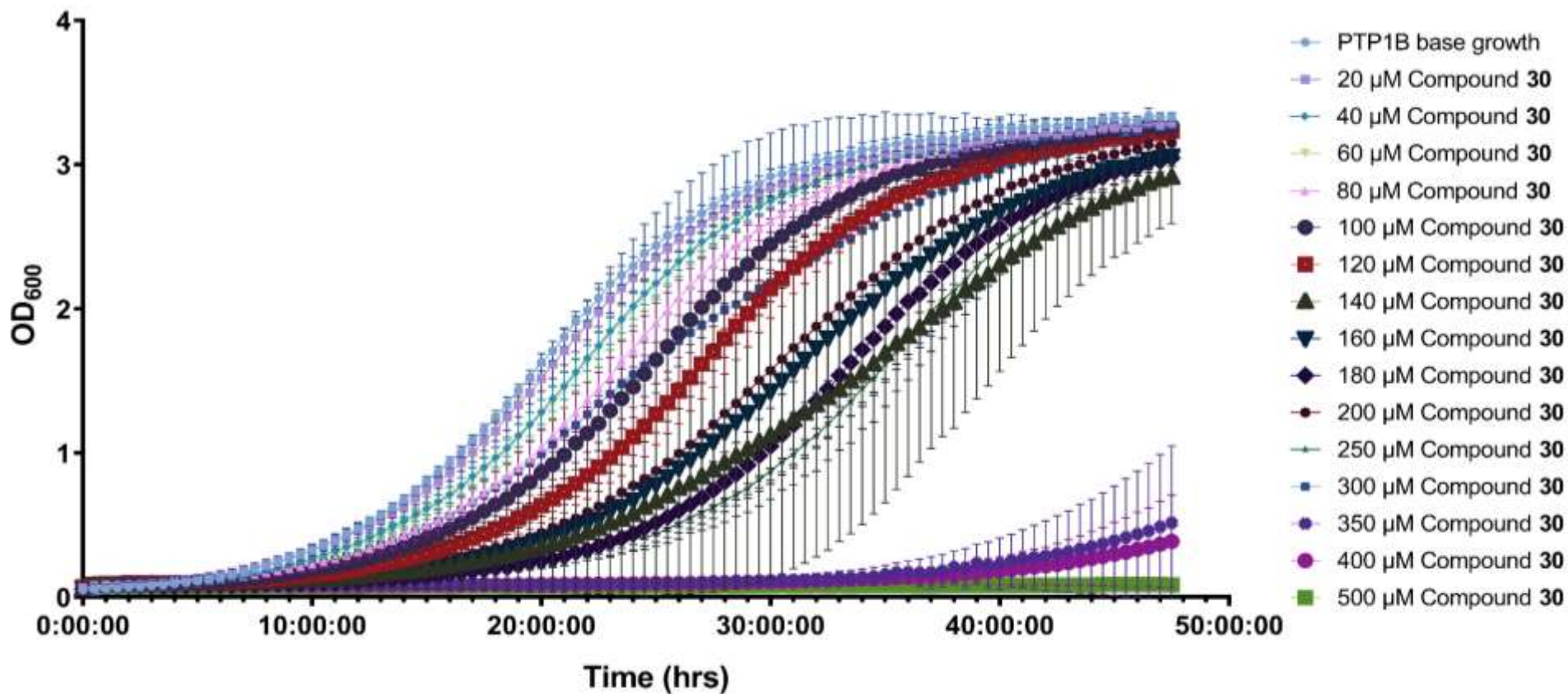
μM	20	40	60	80	100	120	140	160	180	200	250
p values	ns	ns	ns	<0.0500	<0.0500	<0.0050	<0.0050	<0.0010	<0.0050	<0.0500	<0.0050

Figure LXII: Effect of compound **30** addition at 20-250 μM on the T_d value of PTP1B only transformed yeast cells. n=3 for all concentrations. Mean points ± standard deviation plotted. Data is normally distributed according to a Shapiro-Wilk test. Used parametric Welch t-test for statistical analysis. * p value ≤ 0.050 vs base growth.



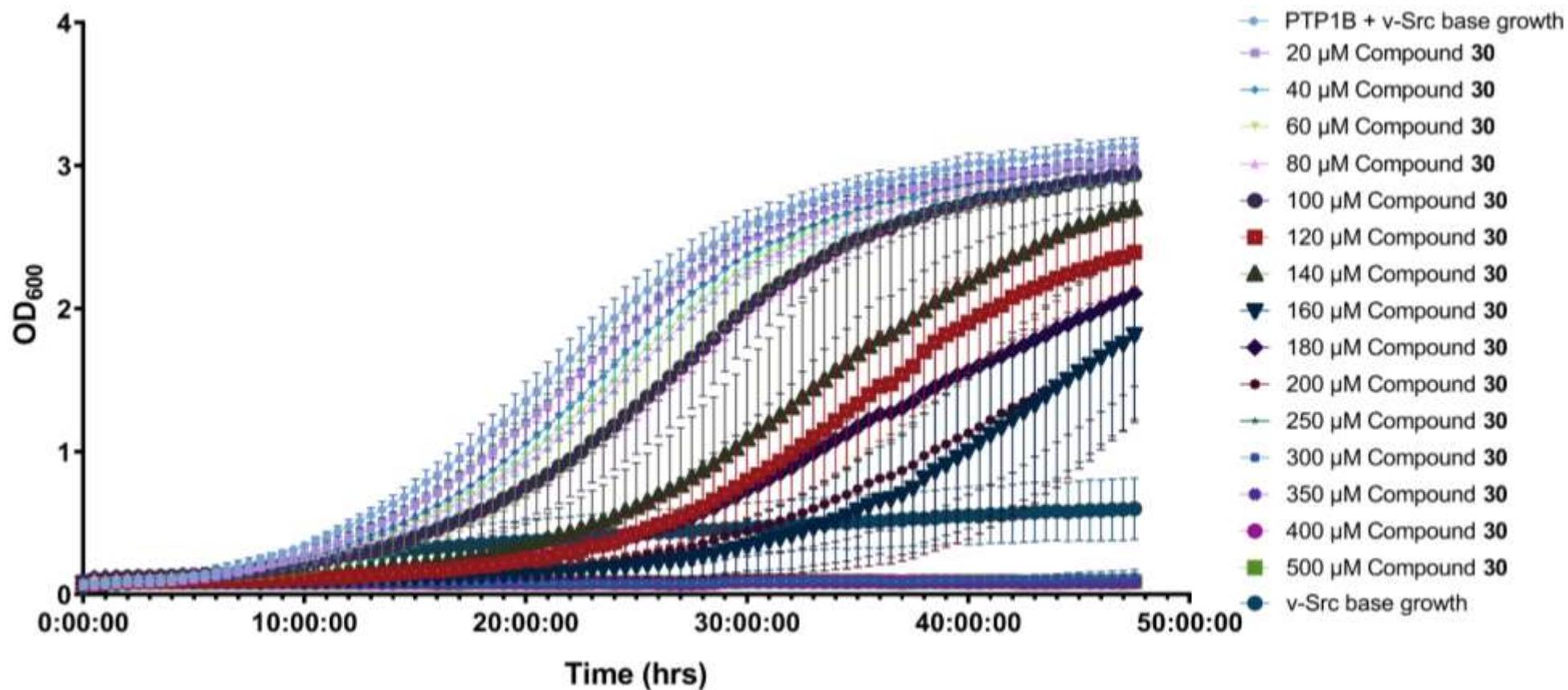
µM	20	40	60	80	100	120	140	160	180	200	250
p values	ns	ns	ns	<0.0500	<0.0100	<0.0100	ns	ns	<0.0500	ns	<0.0500

Figure LXIII: Effect of compound **30** addition at 20-250 µM on the T_d value of PTP1B + v-Src transformed yeast cells. n=3 for all concentrations. Mean points ± standard deviation plotted. Data is normally distributed according to a Shapiro-Wilk test. Used parametric Welch t-test for statistical analysis. * p value ≤ 0.050 vs base growth.



μM	20	40 *	60 *	80 *	100 *	120 *	140 *	160 *	180 *	200 *	250 *	300	350 *	400 *	500 *
p value	ns	<0.0500	<0.0500	<0.0100	<0.0100	<0.0050	<0.0500	<0.0100	<0.0005	<0.0500	<0.0001	ns	<0.0001	<0.0001	<0.0001

Figure LXIV: Growth profile of PTP1B only yeast cells with the addition of compound 30 at 20-500 μM. n=3 for all concentrations in PTP1B only cells. Mean points ± standard deviation plotted. Data is normally distributed according to a Shapiro-Wilk test. Used a 2-way ANOVA where column factor was source of variance. * p value ≤ 0.050 vs control.

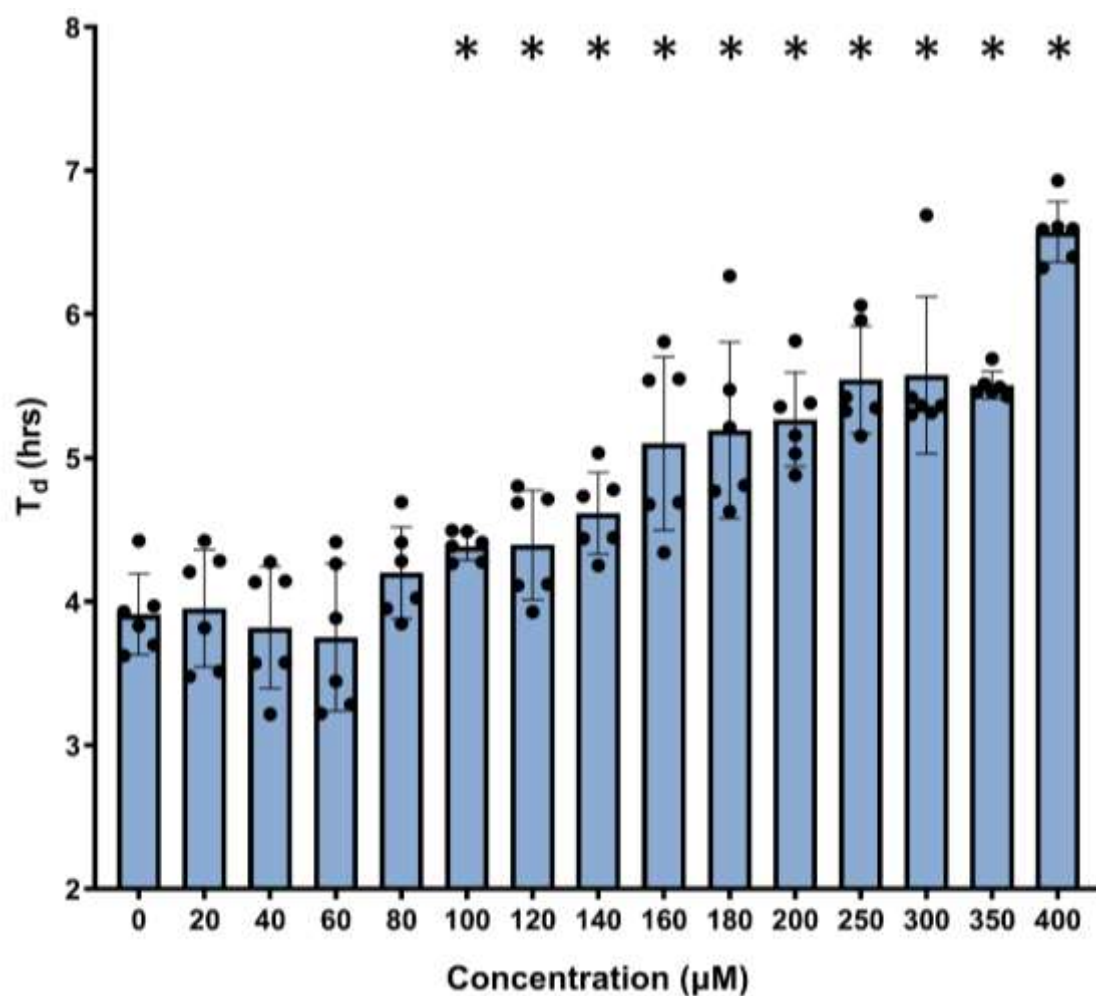


μM	20	40	60	80	100 *	120 *	140 *	160 *	180 *	200 *	250 *	300 *	350 *	400 *	500 *
p value	ns	ns	ns	ns	<0.0500	<0.0010	<0.0500	<0.0010	<0.010	<0.0050	<0.0050	<0.0001	<0.0001	<0.0001	<0.0001

Figure LXV: Growth profile of PTP1B + v-Src yeast cells with the addition of compound 30 at 20-500 μM . n=3 for all concentrations in PTP1B only cells, n=13 for v-Src base growth. Mean points \pm standard deviation plotted. Data is normally distributed according to a Shapiro-Wilk test. Used a 2-way ANOVA where column factor was source of variance. * p value \leq 0.050 vs control.

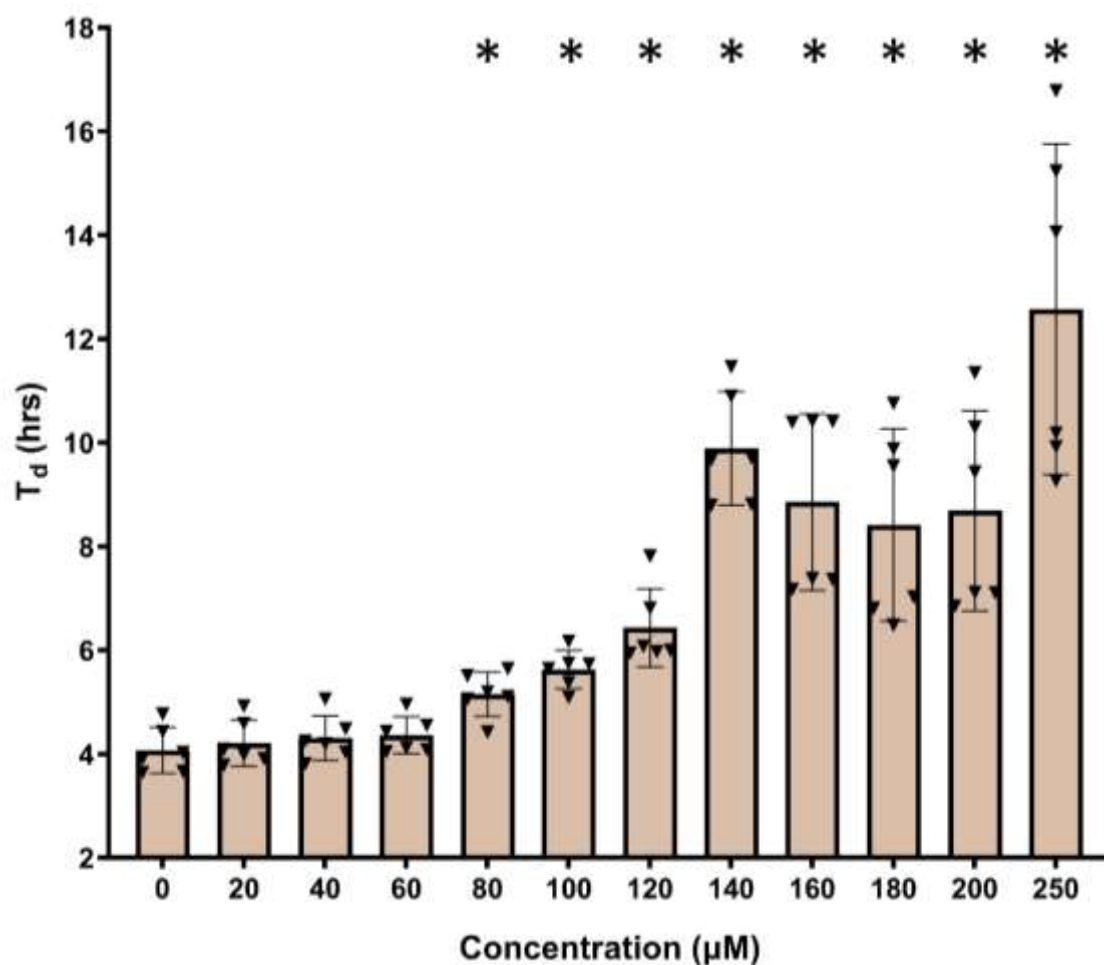
2.1.6 Compound 30a

2.1.6.1 PTP1B based.



μM	20	40	60	80	100	120	140	160	180	200	250	300	350	400
p values	ns	ns	ns	ns	<0.0100	<0.0500	<0.0050	<0.0050	<0.0050	<0.00001	<0.00001	<0.00050	<0.00001	<0.00001

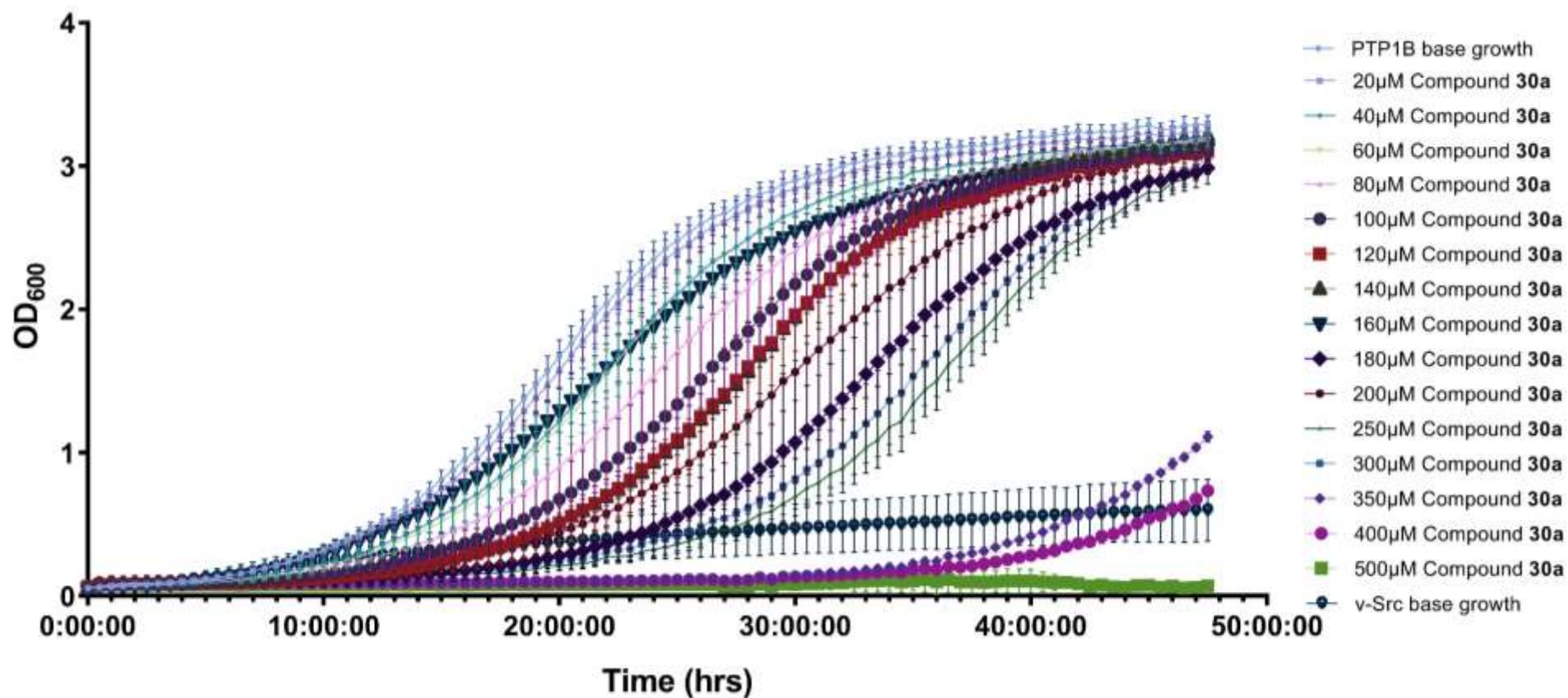
Figure LXVI: Effect of compound **30a** addition at 20-400 μM on the T_d value of PTP1B only transformed yeast cells. $n=6$ for all concentrations. Mean points \pm standard deviation plotted. Data is normally distributed according to a Shapiro-Wilk test. Used parametric Welch t-test for statistical analysis. * p value ≤ 0.050 vs base growth.



μM	20	40	60	80	100	120	140	160	180	200	250
p values	ns	ns	ns	<0.0050	<0.00001	<0.0005	<0.00001	<0.0010	<0.0005	<0.0050	<0.0050

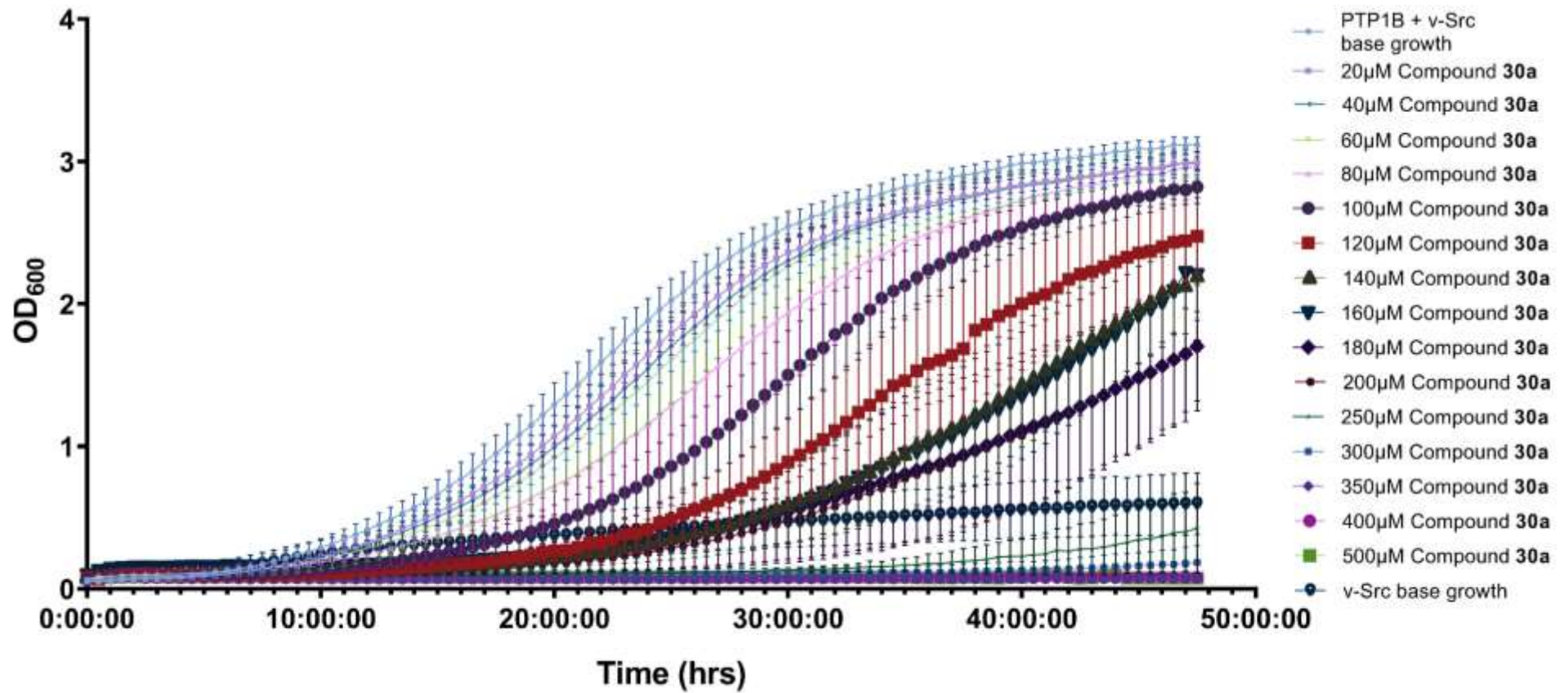
Figure LXVII: Effect of compound **30a** addition at 20-250 μM on the T_d value of PTP1B + v-Src transformed yeast cells. n=6 for all concentrations. Mean points ± standard deviation plotted. Data is normally distributed according to a Shapiro-Wilk test. Used parametric Welch t-test for statistical analysis. * p value ≤ 0.050 vs base growth.

As with compound **30** no exponential growth phase was present when PTP1B + v-Src cells were tested with compound **30a** at 300-500 μM. This is due to a progressively greater extension of the lag phase as also occurred with the known inhibitor LZP25. Hence why no T_d values for this concentration are presented.



μM	20	40*	60*	80*	100 *	120 *	140 *	160 *	180 *	200 *	250 *	300*	350 *	400 *	500 *
p value	ns	<0.0050	<0.0005	<0.0100	<0.0001	<0.0001	<0.0001	0.0002	<0.0001	<0.0001	<0.0001	<0.0001	<0.0001	<0.0001	<0.0001

Figure LXVIII: Growth profile of PTP1B only yeast cells with the addition of compound **30a** at 20-500 μM.. n=6 for all concentrations in PTP1B only cells, n=13 for v-Src base growth. Mean points ± standard deviation plotted. Data is normally distributed according to a Shapiro-Wilk test. Used a 2-way ANOVA where column factor was source of variance. * p value ≤ 0.050 vs control.



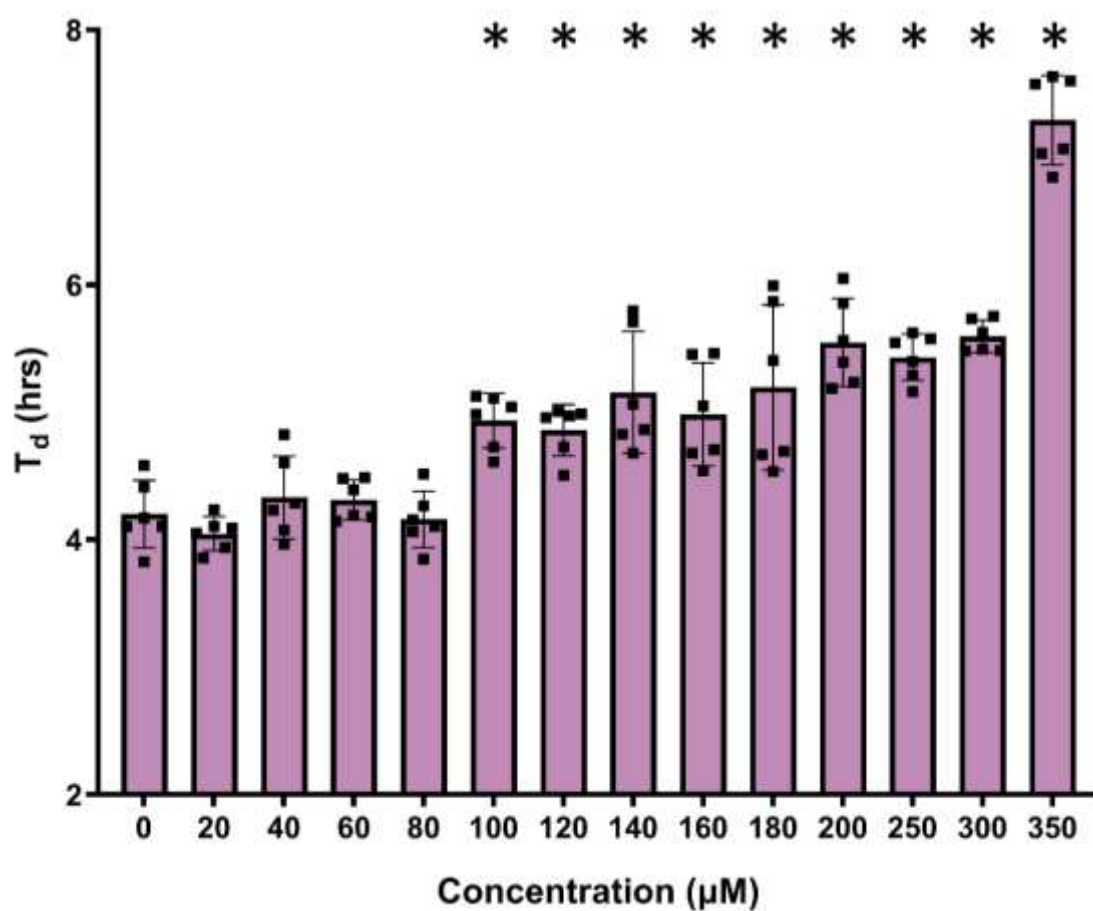
μM	20*	40*	60*	80*	100 *	120 *	140 *	160 *	180 *	200 *	250 *	300*	350 *	400 *	500 *
p value	<0.0500	<0.010	<0.0500	<0.0100	<0.0001	<0.0001	<0.0001	<0.0001	<0.0001	<0.0001	<0.0001	<0.0001	<0.0001	<0.0001	<0.0001

Figure LXIX: Growth profile of PTP1B + v-Src yeast cells with the addition of compound **30a** at 20-500 μM . $n=6$ for all concentrations in PTP1B only cells, $n=13$ for v-Src base growth. Mean points \pm standard deviation plotted. Data is normally distributed according to a Shapiro-Wilk test. Used a 2-way ANOVA where column factor was source of variance. * p value ≤ 0.050 vs control.

When looking at the overall growth profiles of PTP1B only and PTP1B + v-Src yeast cells with compound **30a** addition a progressively greater increase in the lag phase and subsequently a delayed exponential growth phase occurred when compared to the corresponding base growth. With PTP1B only cells it is apparent that the exponential growth phase itself remains comparable to the base growth.

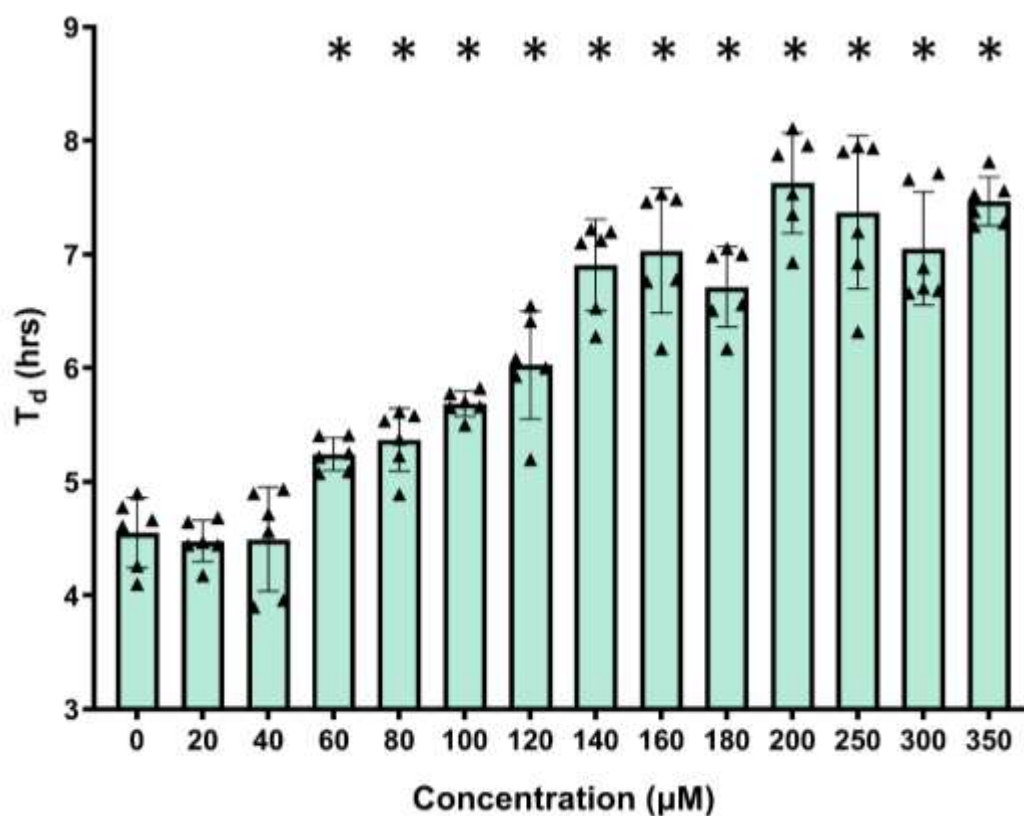
This delay in lag phase is more prevalent in the PTP1B + v-Src as the inhibitory effect of compound **30a** on the PTP1B lower the exponential growth phase doubling time resulting in this case lower final absorbance values. Later in this section the toxicity of compound **30a** is investigated in yeast cells of all transformations of interest to confirm that the increased lag phase and lower final absorbance values in the PTP1B + v-Src cells is not due to off-target toxicity effects.

2.1.6.2 TCPTP based.



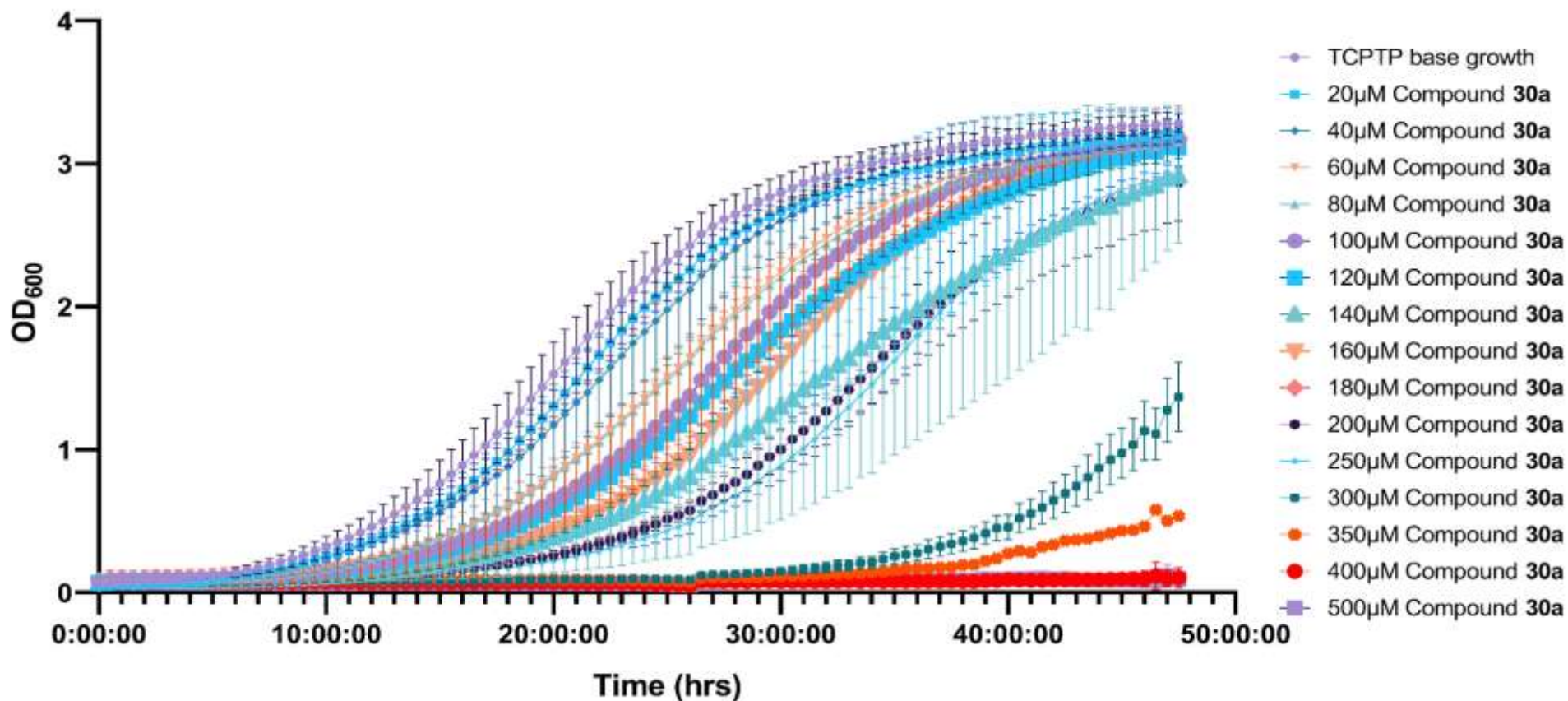
μM	20	40	60	80	100	120	140	160	180	200	250	300	350
p values	ns	ns	ns	ns	<0.0005	<0.0010	<0.0050	<0.0050	<0.0500	<0.0001	<0.0001	<0.0001	<0.0001

Figure LXX: Effect of compound **30a** addition at 20-400 μM on the T_d value of TCPTP only transformed yeast cells. $n=6$ for all concentrations. Mean points \pm standard deviation plotted. Data is normally distributed according to a Shapiro-Wilk test. Used parametric Welch t-test for statistical analysis. * p value ≤ 0.050 vs base growth.



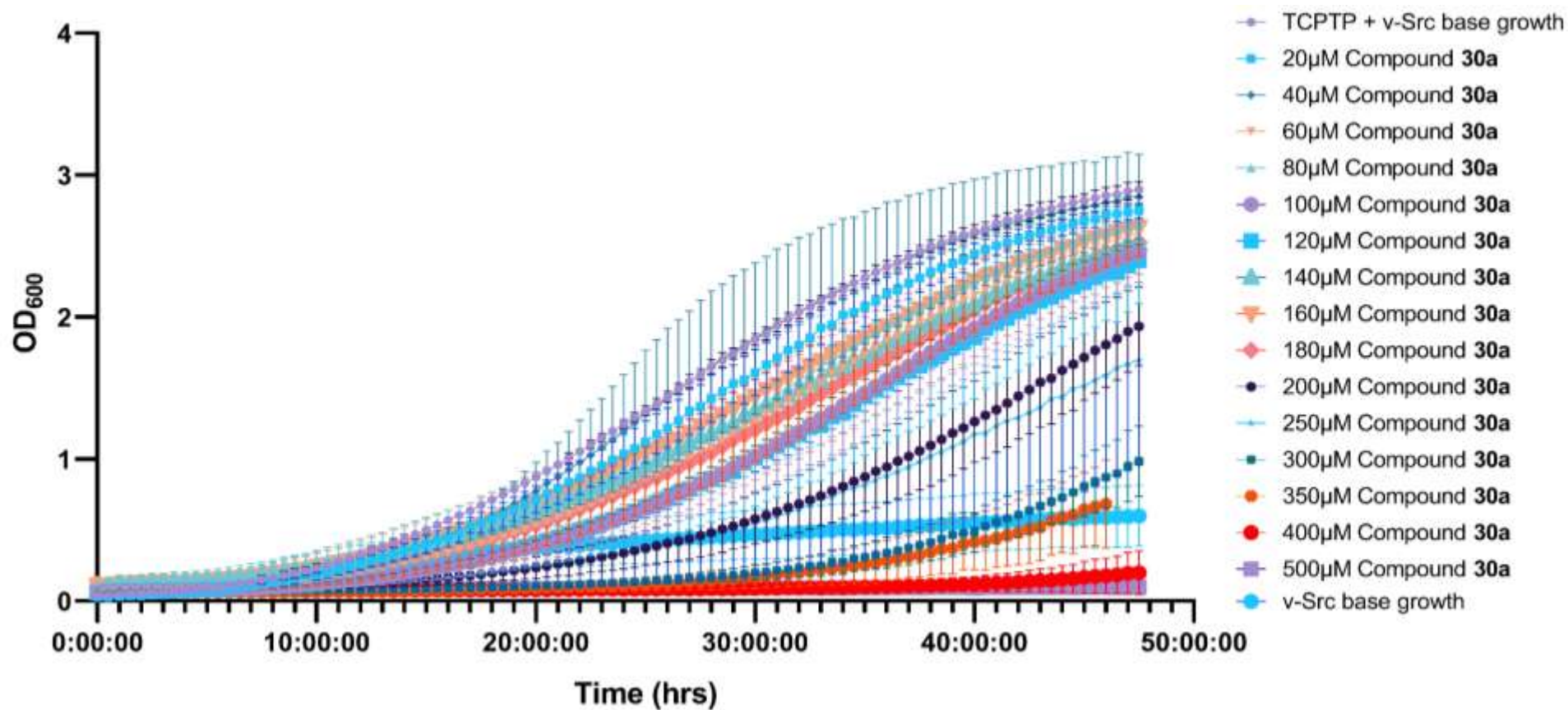
μM	20	40	60	80	100	120	140	160	180	200	250	300	350
p values	ns	ns	<0.0050	<0.0010	<0.0005	<0.0005	<0.000	<0.000	<0.000	<0.0001	<0.0001	<0.0001	<0.0001

Figure LXXI: Effect of compound **30a** addition at 20-400 μM on the T_d value of TCPTP + v-Src transformed yeast cells. $n=6$ for all concentrations. Mean points \pm standard deviation plotted. Data is normally distributed according to a Shapiro-Wilk test. Used parametric Welch t-test for statistical analysis. * p value ≤ 0.050 vs base growth.



μM	20*	40	60*	80 *	100 *	120 *	140 *	160 *	180 *	200 *	250 *	300 *	350 *	400 *	500 *
p value	<0.0500	ns	<0.0100	<0.0500	<0.0001	<0.0050	<0.0050	<0.0001	<0.0100	<0.0001	<0.0001	<0.0001	<0.0001	<0.0001	<0.0001

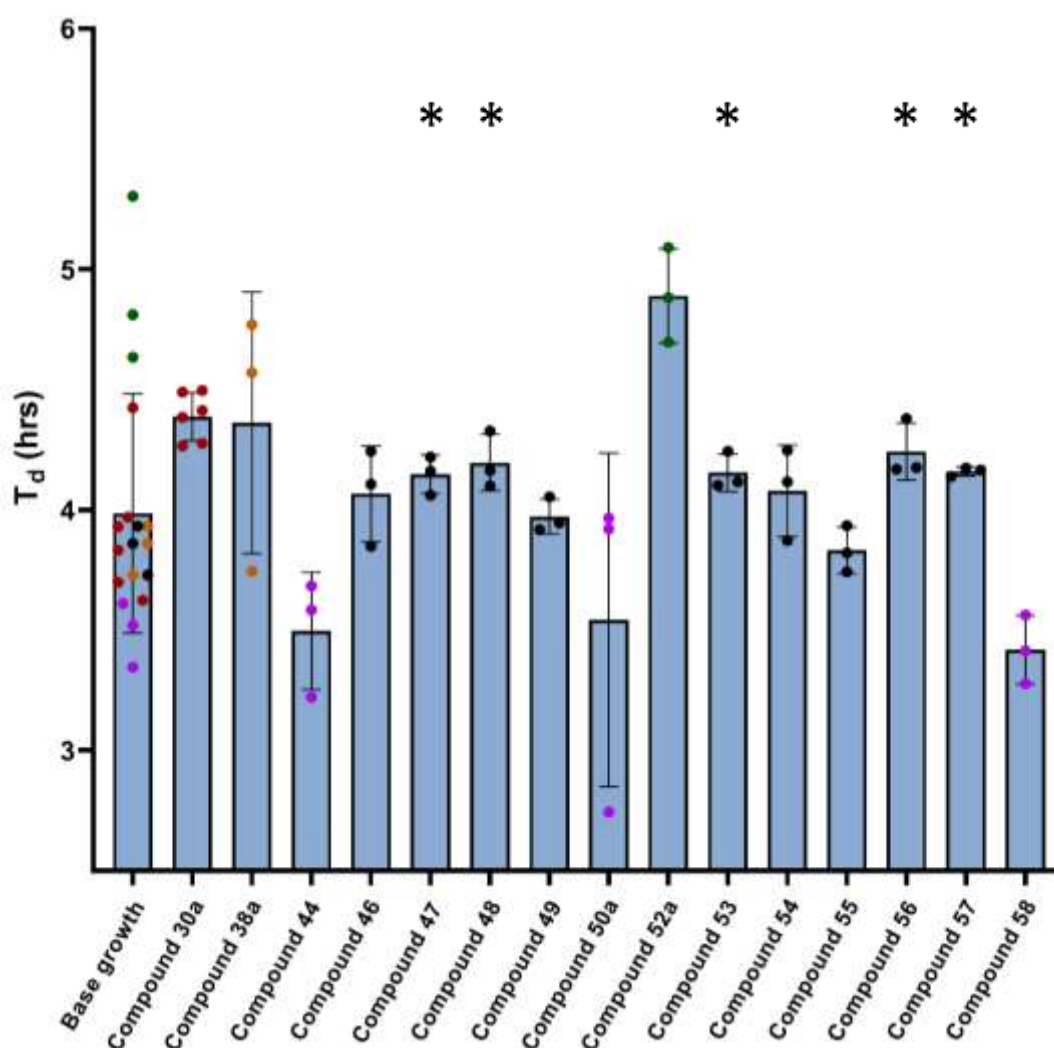
Figure LXXII: Growth profile of TCPTP only yeast cells with the addition of compound **30a** at 20-500 μM.. n=6 for all concentrations in PTP1B only cells, n=13 for v-Src base growth. Mean points ± standard deviation plotted. Data is normally distributed according to a Shapiro-Wilk test. Used a 2-way ANOVA where column factor was source of variance. * p value ≤ 0.050 vs control.



μM	20 *	40	60 *	80 *	100 *	120 *	140 *	160 *	180 *	200 *	250 *	300 *	350 *	400 *	500 *
p value	<0.0050	ns	<0.0050	<0.0050	<0.0001	<0.0005	<0.0500	<0.0500	<0.0050	<0.0001	<0.0001	<0.0001	<0.0001	<0.0001	<0.0001

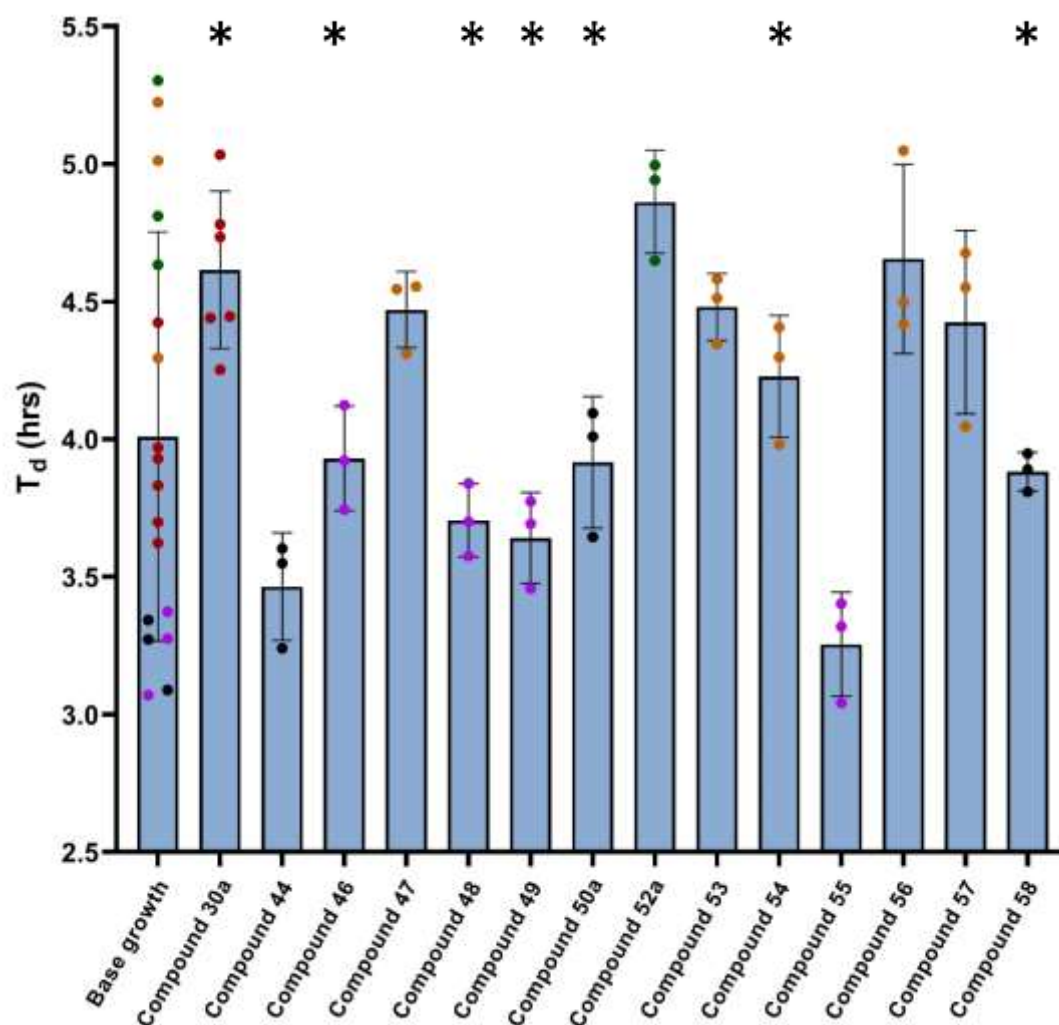
Figure LXXIII: Growth profile of TCPTP + v-Src yeast cells with the addition of compound **30a** at 20-500 μM . n=6 for all concentrations in PTP1B only cells, n=13 for v-Src base growth. Mean points \pm standard deviation plotted. Data is normally distributed according to a Shapiro-Wilk test. Used a 2-way ANOVA where column factor was source of variance. * p value \leq 0.050 vs control.

2.1.7 Compound 30a derivatives doubling time and growth curve data.



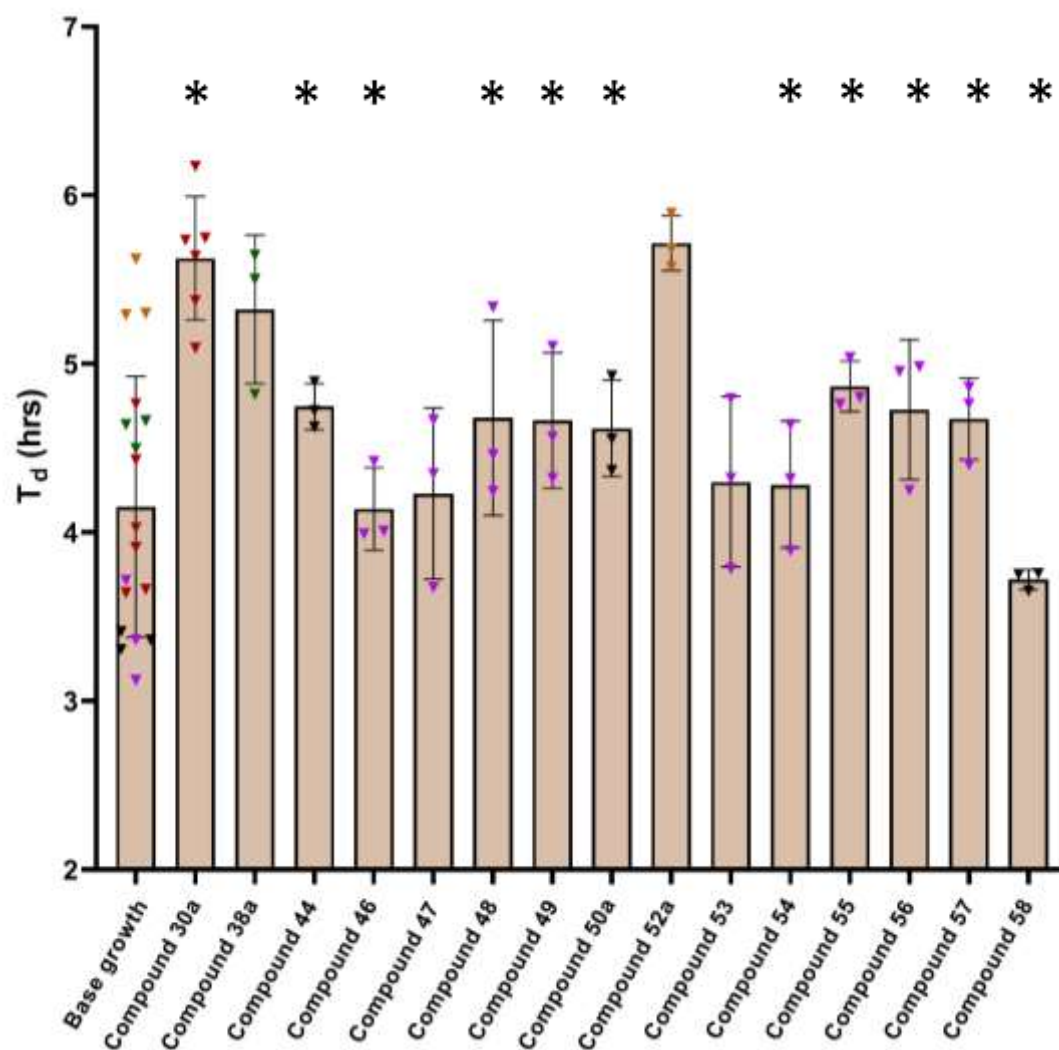
Compound	30a	38a	44	46	47	48	49	50a	52a	53	54	55	56	57	58
p value	ns	ns	ns	ns	<0.0500	<0.0500	ns	ns	ns	<0.0500	ns	ns	<0.0500	<0.0500	ns

Figure LXXIV: Effect of compound **30a** derivatives at 100 μ M on the T_d value of PTP1B only transformed yeast cells. $n=3$ for all compounds, apart from **30a** were $n=6$, and $n=18$ for base growth. Colour coded denotes corresponding base growth values for each compound tested. Mean points \pm standard deviation plotted. Data is normally distributed according to a Shapiro-Wilk test. Used parametric Welch t-test for statistical analysis. * p value ≤ 0.050 vs base growth. Comparison occurred with corresponding base growth values, not all presented biological repeats.



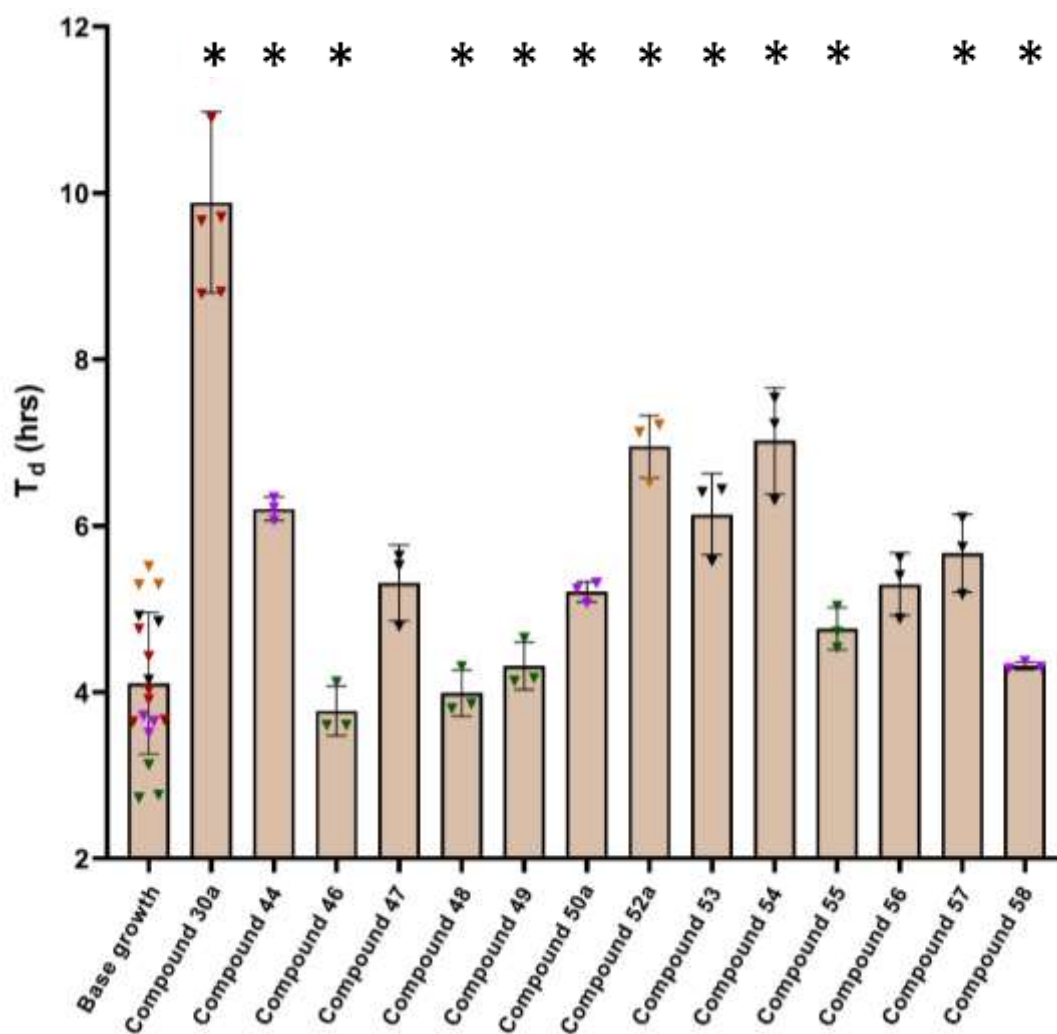
Compound	p value
30a	<0.0050
44	ns
46	<0.0100
47	ns
48	<0.0500
49	<0.0500
50a	<0.0050
52a	ns
53	ns
54	<0.0050
55	ns
56	ns
57	ns
58	<0.0010

Figure LXXV: Effect of compound **30a** derivatives at 140 μ M on the T_d value of PTP1B only transformed yeast cells. $n=3$ for all compounds, apart from **30a** were $n=6$, and $n=18$ for base growth. Colour coded denotes corresponding base growth values for each compound tested. Mean points \pm standard deviation plotted. Data is normally distributed according to a Shapiro-Wilk test. Used parametric Welch t-test for statistical analysis. * p value ≤ 0.050 vs base growth. Comparison occurred with corresponding base growth values, not all presented biological repeats.



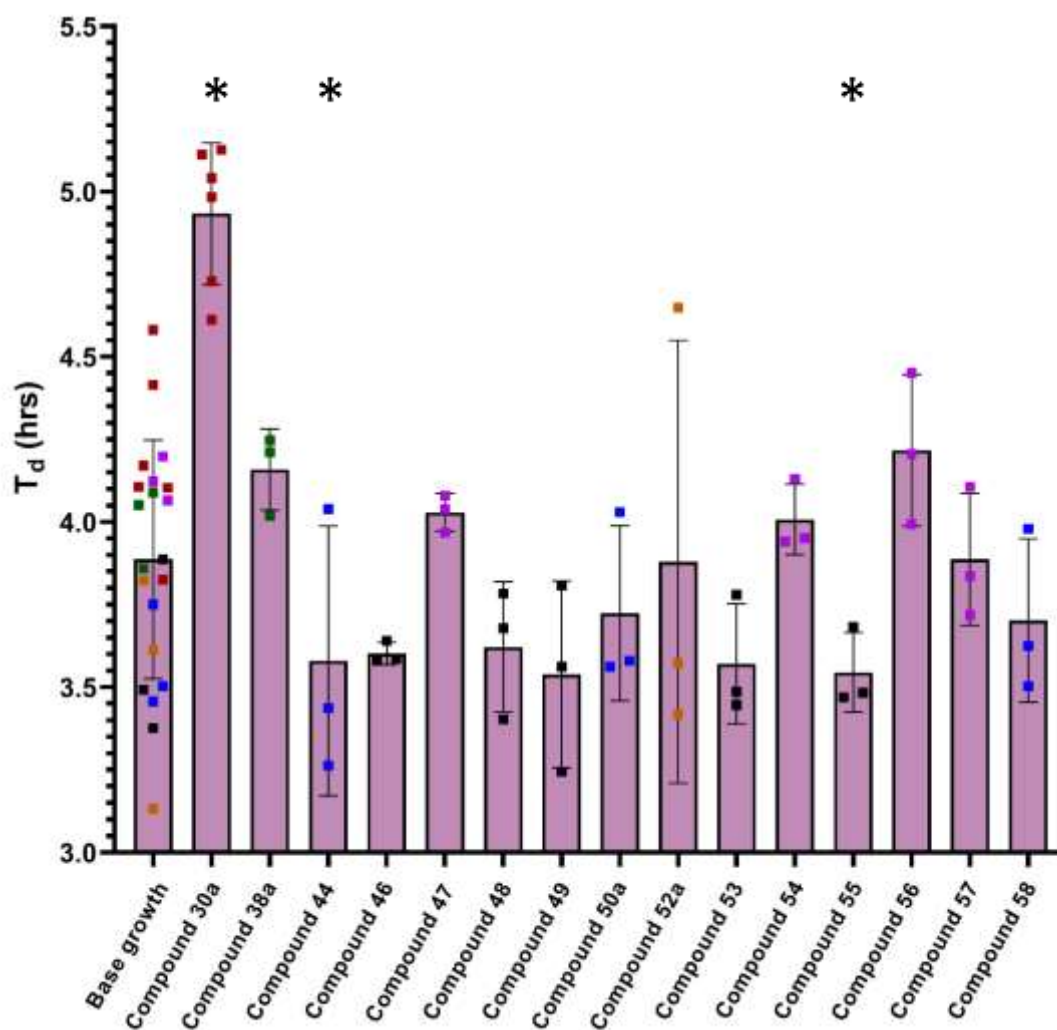
Compound	p value
30a	<0.0001
38a	ns
44	<0.0050
46	<0.0500
47	ns
48	<0.0500
49	<0.0500
50a	<0.0500
52a	ns
53	ns
54	<0.0500
55	<0.0001
56	<0.0500
57	<0.0050
58	<0.0500

Figure LXXVI: Effect of compound **30a** derivatives at 100 μ M on the T_d value of PTP1B + v-Src transformed yeast cells. $n=3$ for all compounds, apart from **30a** were $n=6$, and $n=18$ for base growth. Colour coded denotes corresponding base growth values for each compound tested. Mean points \pm standard deviation plotted. Data is normally distributed according to a Shapiro-Wilk test. Used parametric Welch t-test for statistical analysis. * p value ≤ 0.050 vs base growth. Comparison occurred with corresponding base growth values, not all presented biological repeats.



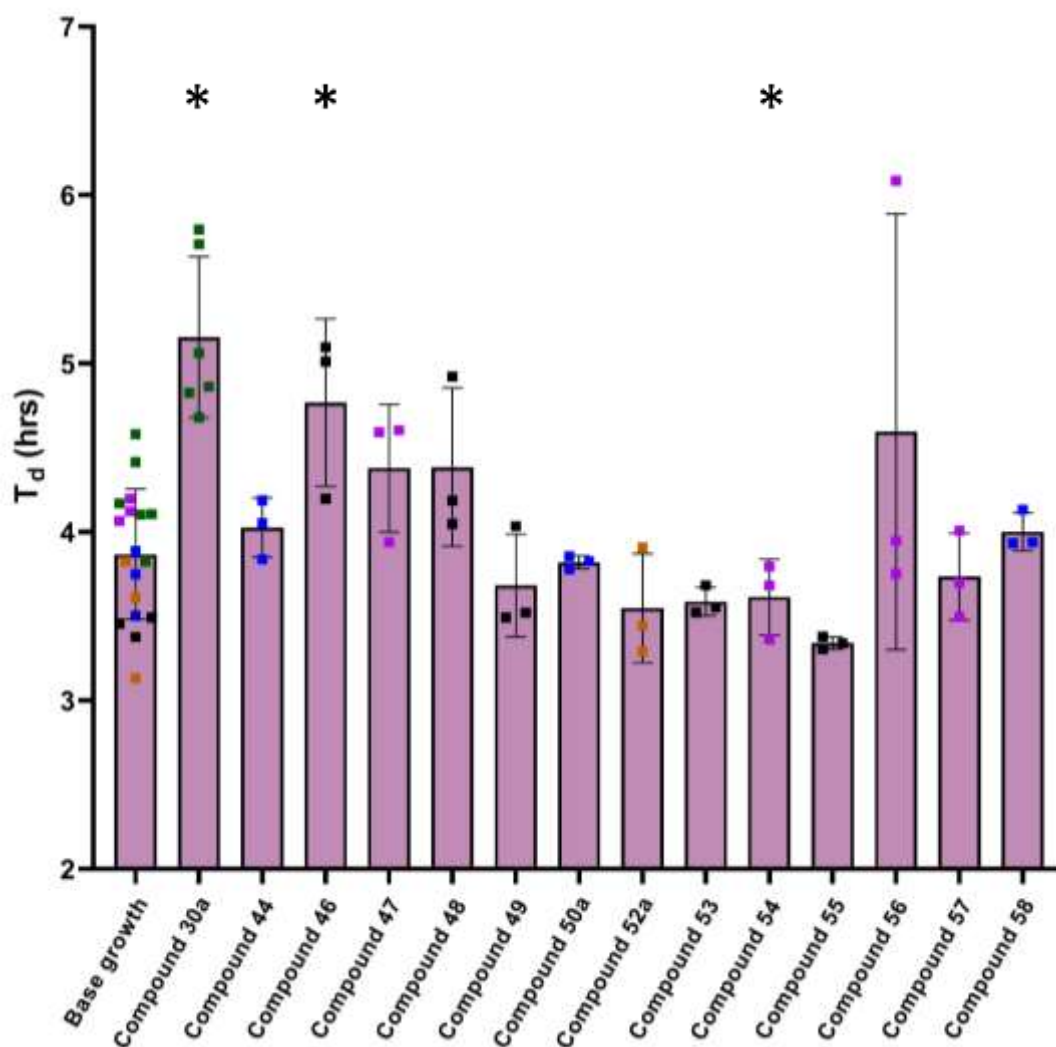
Compound	p value
30a	<0.0001
44	<0.0001
46	<0.0500
47	ns
48	<0.0100
49	<0.0050
50a	<0.0500
52a	<0.0500
53	<0.0500
54	<0.0100
55	<0.0005
56	ns
57	<0.0500
58	<0.0500

Figure LXXVII: Effect of compound **30a** derivatives at 140 μ M on the T_d value of PTP1B + v-Src transformed yeast cells. $n=3$ for all compounds, apart from **30a** were $n=6$, and $n=18$ for base growth. Colour coded denotes corresponding base growth values for each compound tested. Mean points \pm standard deviation plotted. Data is normally distributed according to a Shapiro-Wilk test. Used parametric Welch t-test for statistical analysis. * p value ≤ 0.050 vs base growth. Comparison occurred with corresponding base growth values, not all presented biological repeats.



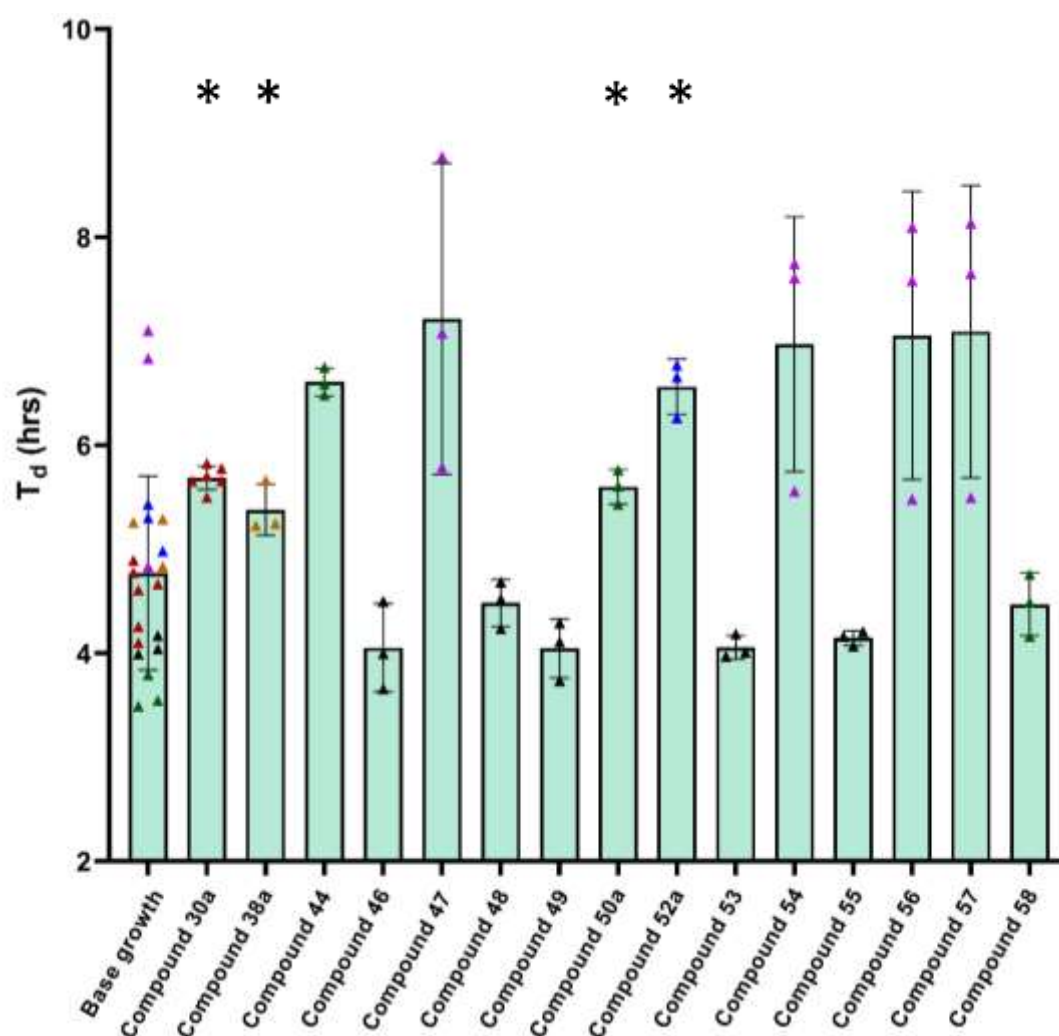
Compound	30a	44	46	47	48	49	50a	52a	53	54	55	56	57	58
p value	<0.0005	ns	<0.0500	ns	ns	ns	ns	ns	ns	ns	<0.0500	ns	ns	ns

Figure LXXVIII: Effect of compound **30a** derivatives at 100 μ M on the T_d value of TCPTP only transformed yeast cells. $n=3$ for all compounds, apart from **30a** were $n=6$, and $n=21$ for base growth. Colour coded denotes corresponding base growth values for each compound tested. Mean points \pm standard deviation plotted. Data is normally distributed according to a Shapiro-Wilk test. Used parametric Welch t-test for statistical analysis. * p value ≤ 0.050 vs base growth. Comparison occurred with corresponding base growth values, not all presented biological repeats.



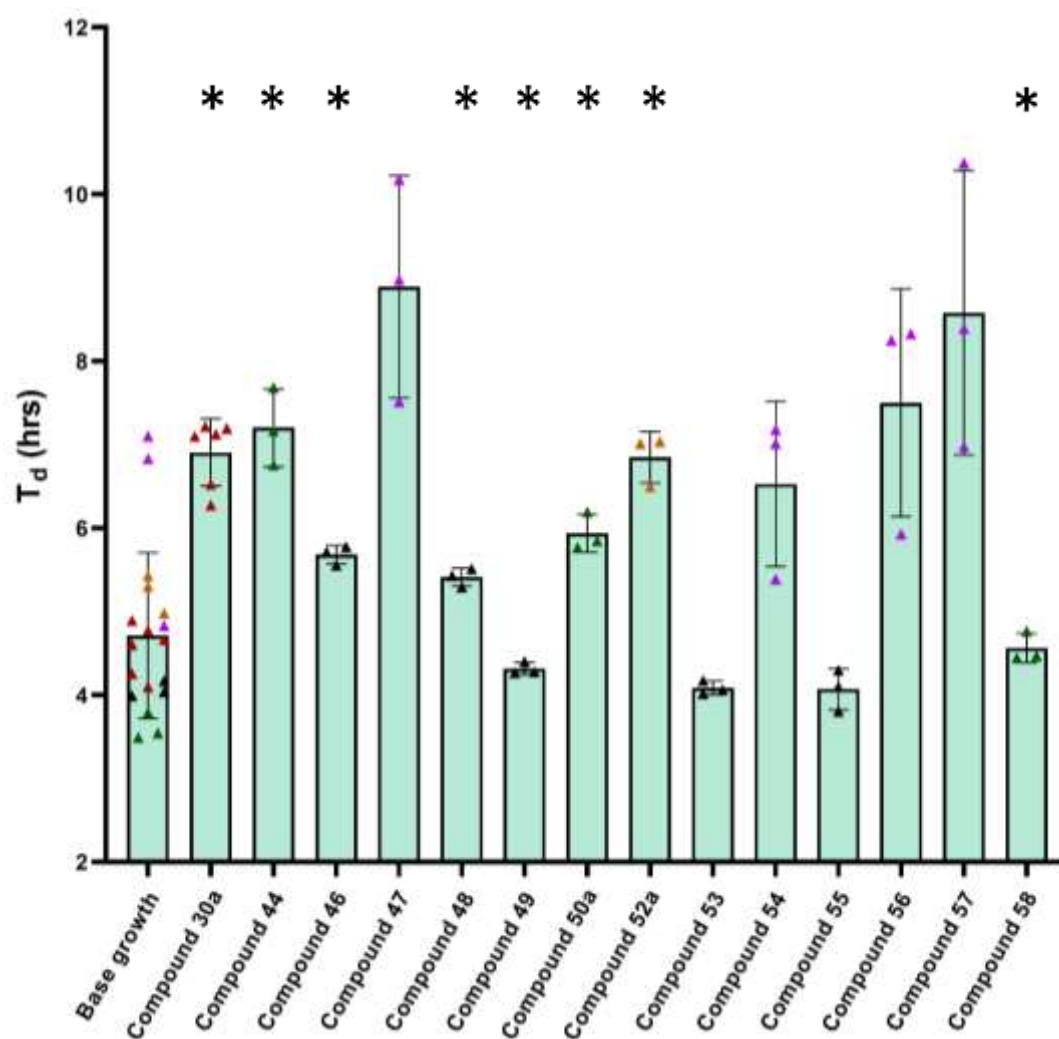
Compound	30a	44	46	47	48	49	50a	52a	53	54	55	56	57	58
p value	<0.0050	ns	<0.0500	ns	ns	ns	ns	ns	ns	<0.0500	ns	ns	ns	ns

Figure LXXIX: Effect of compound **30a** derivatives at 140 μ M on the T_d value of TCPTP only transformed yeast cells. $n=3$ for all compounds, apart from **30a** were $n=6$, and $n=21$ for base growth. Colour coded denotes corresponding base growth values for each compound tested. Mean points \pm standard deviation plotted. Data is normally distributed according to a Shapiro-Wilk test. Used parametric Welch t-test for statistical analysis. * p value ≤ 0.050 vs base growth. Comparison occurred with corresponding base growth values, not all presented biological repeats.



Compound	30a	44	46	47	48	49	50a	52a	53	54	55	56	57	58
p value	<0.0005	<0.0001	ns	ns	ns	ns	<0.0010	<0.0050	ns	ns	ns	ns	ns	ns

Figure LXXX: Effect of compound **30a** derivatives at 100 μ M on the T_d value of TCPTP + v-Src transformed yeast cells. $n=3$ for all compounds, apart from **30a** were $n=6$, and $n=21$ for base growth. Colour coded denotes corresponding base growth values for each compound tested. Mean points \pm standard deviation plotted. Data is normally distributed according to a Shapiro-Wilk test. Used parametric Welch t-test for statistical analysis. * p value ≤ 0.050 vs base growth. Comparison occurred with corresponding base growth values, not all presented biological repeats.



Compound	p value
30a	<0.0001
44	<0.0100
46	<0.0001
47	ns
48	<0.0001
49	<0.0001
50a	<0.0050
52a	<0.0050
53	ns
54	ns
55	ns
56	ns
57	ns
58	<0.0500

Figure LXXXI: Effect of compound **30a** derivatives at 140 μ M on the T_d value of TCPTP + v-Src transformed yeast cells. n=3 for all compounds, apart from **30a** were n=6, and n=21 for base growth. Colour coded denotes corresponding base growth values for each compound tested. Mean points \pm standard deviation plotted. Data is normally distributed according to a Shapiro-Wilk test. Used parametric Welch t-test for statistical analysis. * p value \leq 0.050 vs base growth. Comparison occurred with corresponding base growth values, not all presented biological repeats.

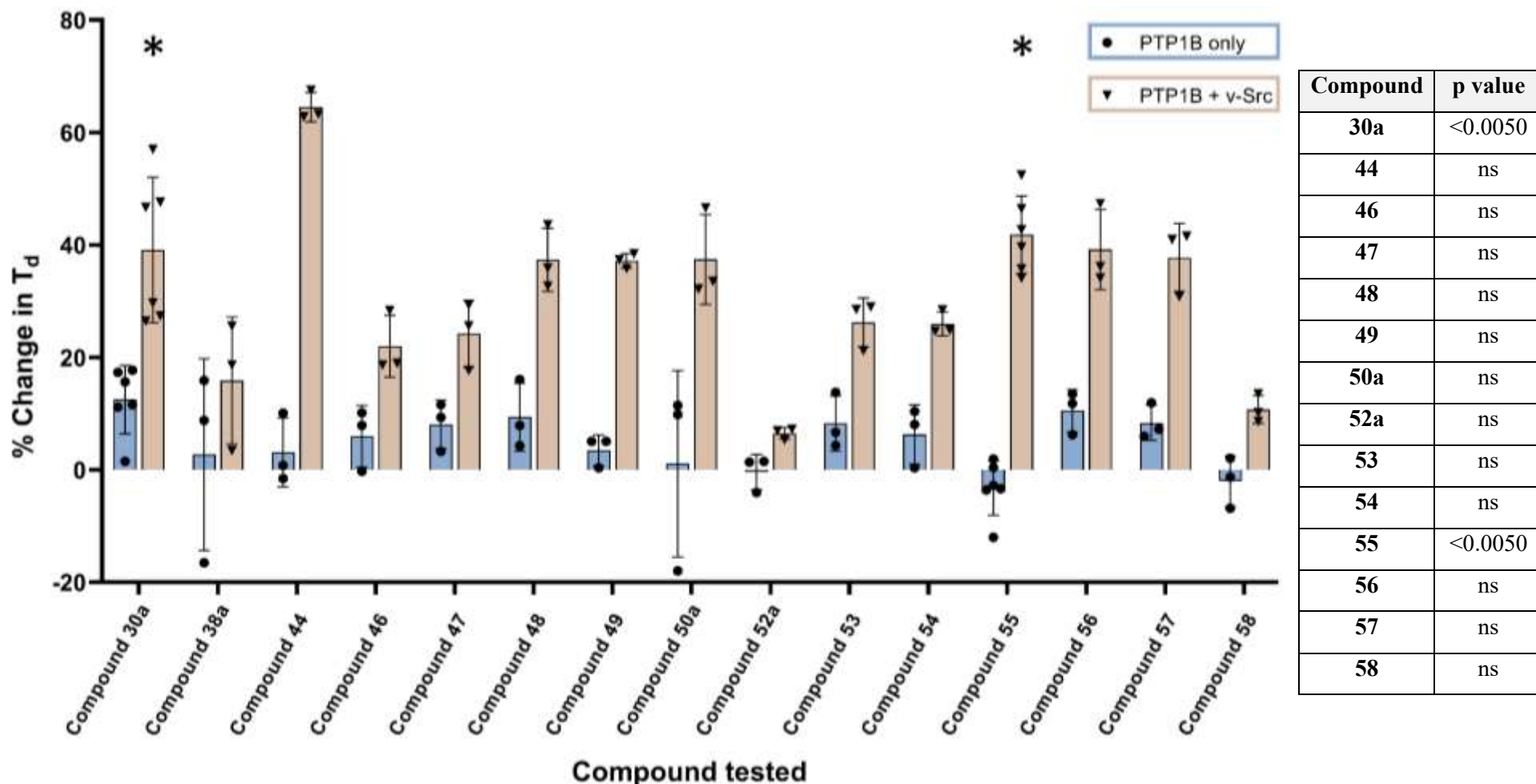
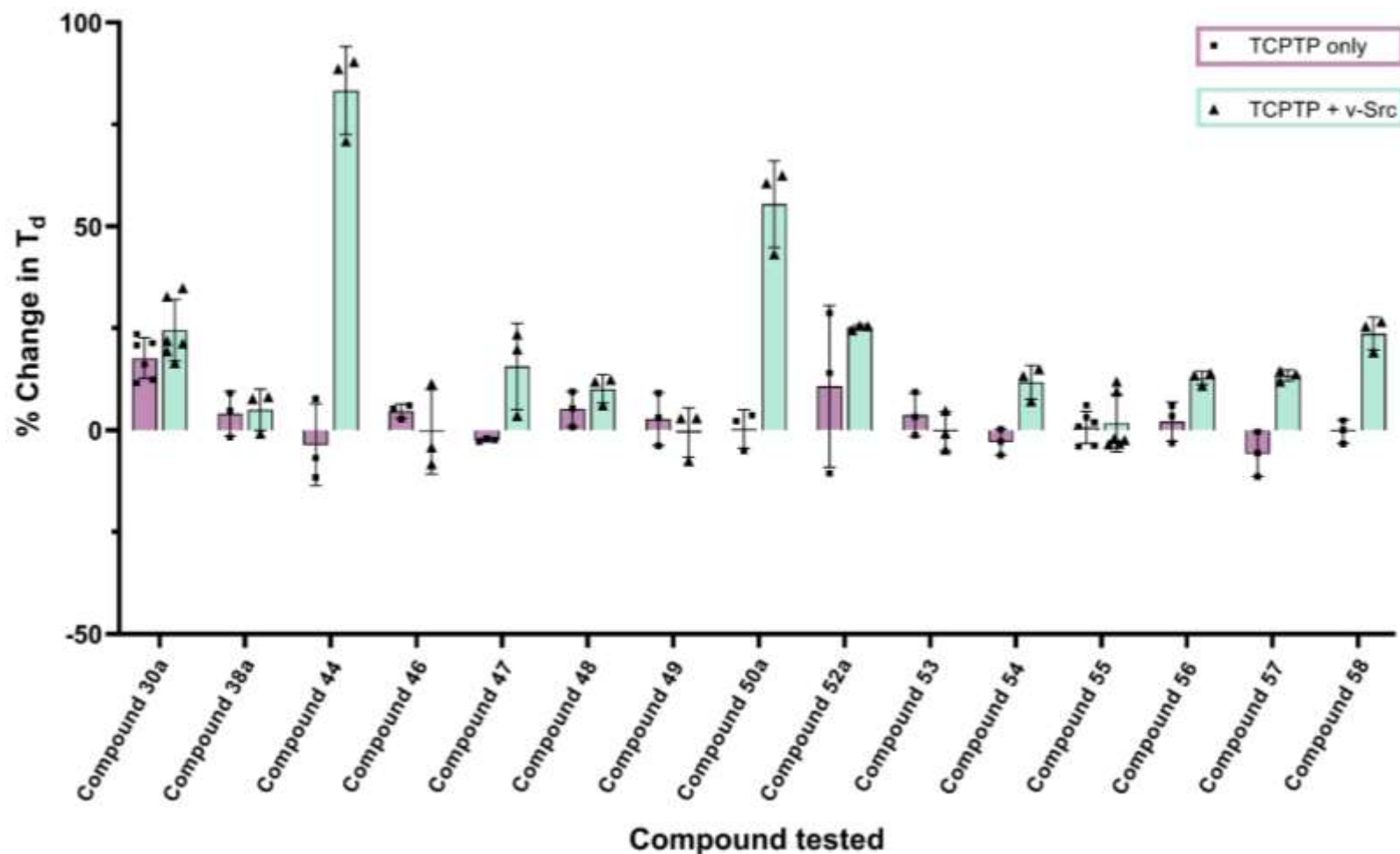
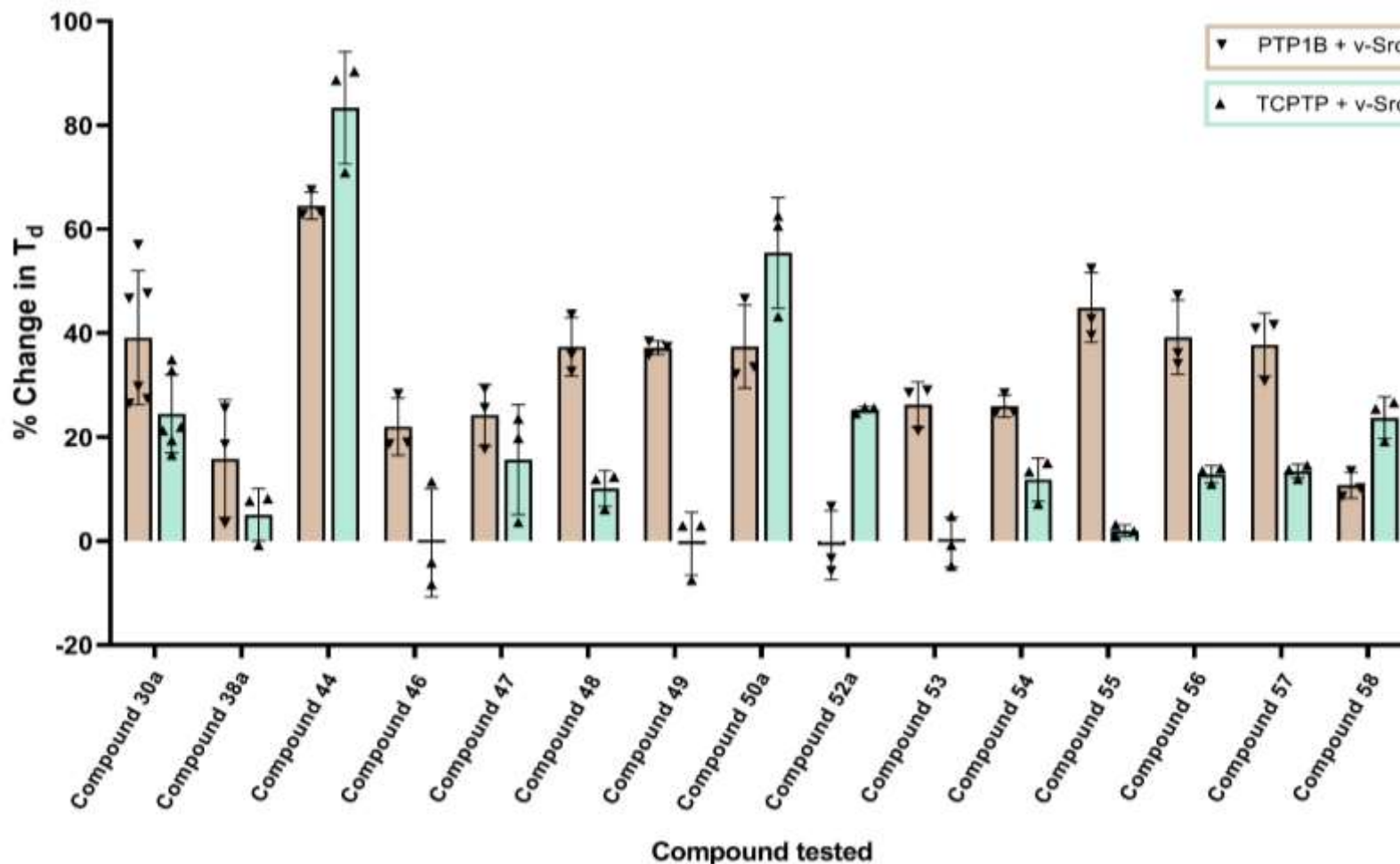


Figure LXXXII: Comparison of % change in doubling time (T_d) of PTP1B only and PTP1B + v-Src transformed yeast cells in the presence of synthesised compounds **30a**, **44**, **46-50a** and **52a-58** at 100 μM . $n=3$ for all compounds tested in both transformations, apart from **30a** and **55** where $n=6$. Mean and individual points \pm standard deviation plotted. Used non-parametric Mann-Whitney t-test for statistical analysis. * p value ≤ 0.050 vs control.



Compound	p value
30a	ns
44	ns
46	ns
47	ns
48	ns
49	ns
50a	ns
52a	ns
53	ns
54	ns
55	ns
56	ns
57	ns
58	ns

Figure LXXXIII: Comparison of % change in doubling time (T_d) of TCPTP only and TCPTP + v-Src transformed yeast cells in the presence of synthesised compounds **30a**, **44**, **46-50a** and **52a-58** at 100 μ M. $n=3$ for all compounds tested in both transformations, apart from **30a** and **55** where $n=6$. Mean and individual points \pm standard deviation plotted. Used non-parametric Mann-Whitney t-test for statistical analysis. * p value ≤ 0.050 vs control.



Compound	p value
30a	ns
38	ns
44	ns
46	ns
47	ns
48	ns
49	ns
50a	ns
52a	ns
53	ns
54	ns
55	ns
56	ns
57	ns
58	ns

Figure LXXXIV: Comparison of % change in doubling time (T_d) of PTP1B + v-Src and TCPTP + v-Src transformed yeast cells in the presence of synthesised compounds **30a**, **44**, **46-50a** and **52a-58** at 100 μ M. $n=3$ for all compounds tested in both transformations, apart from **30a** and **55** where $n=6$. Mean and individual points \pm standard deviation plotted. Used non-parametric Mann-Whitney t-test for statistical analysis. * p value ≤ 0.050 .

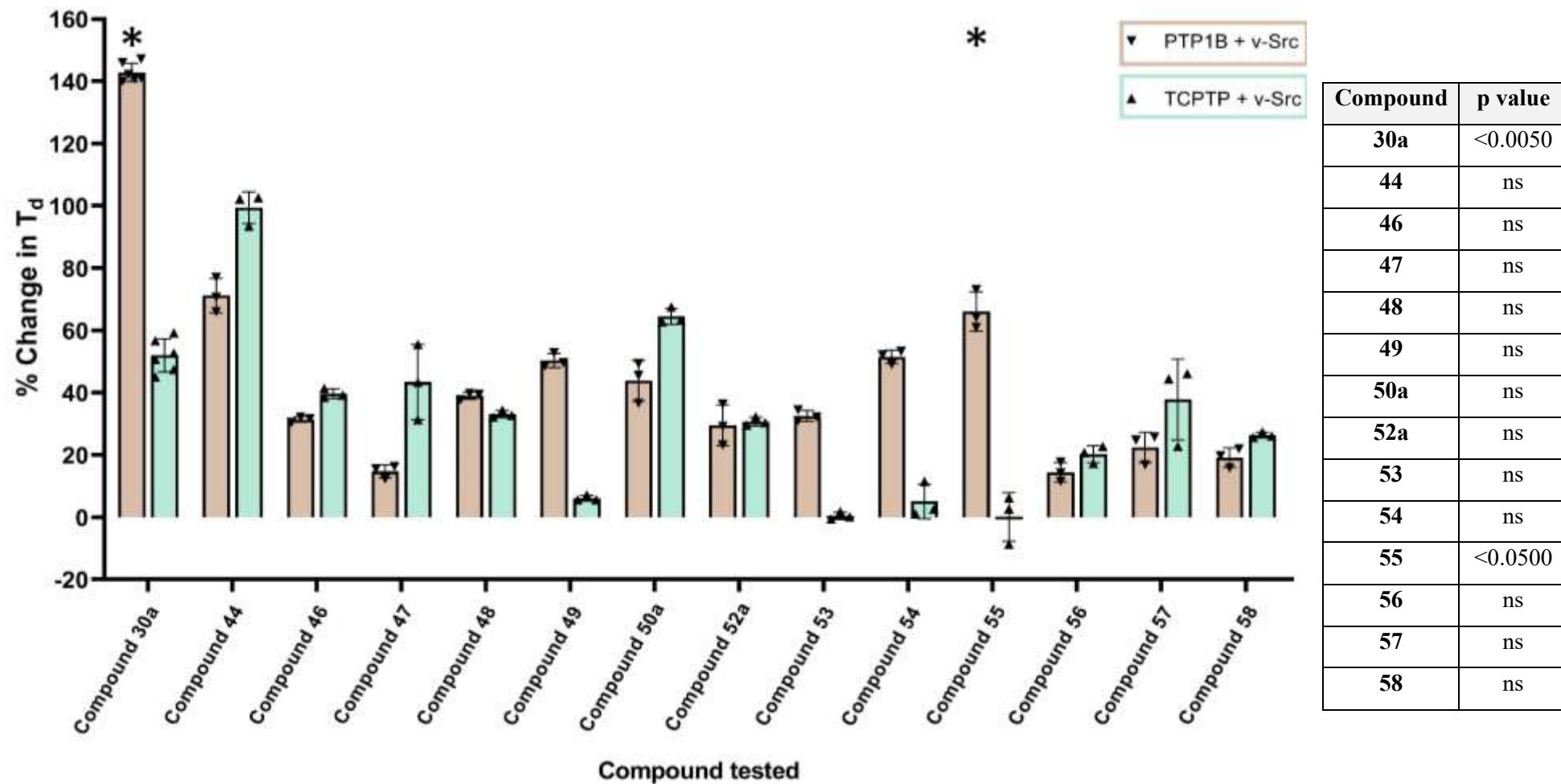
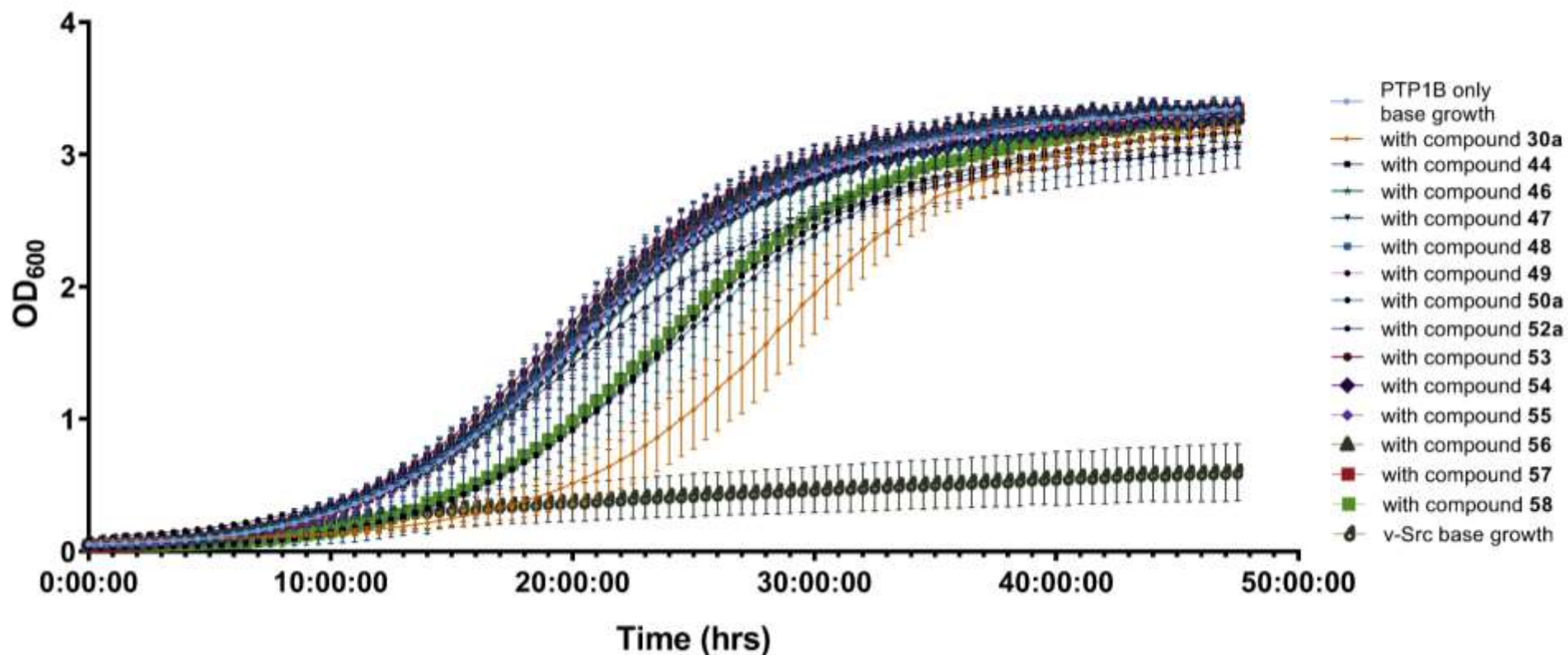
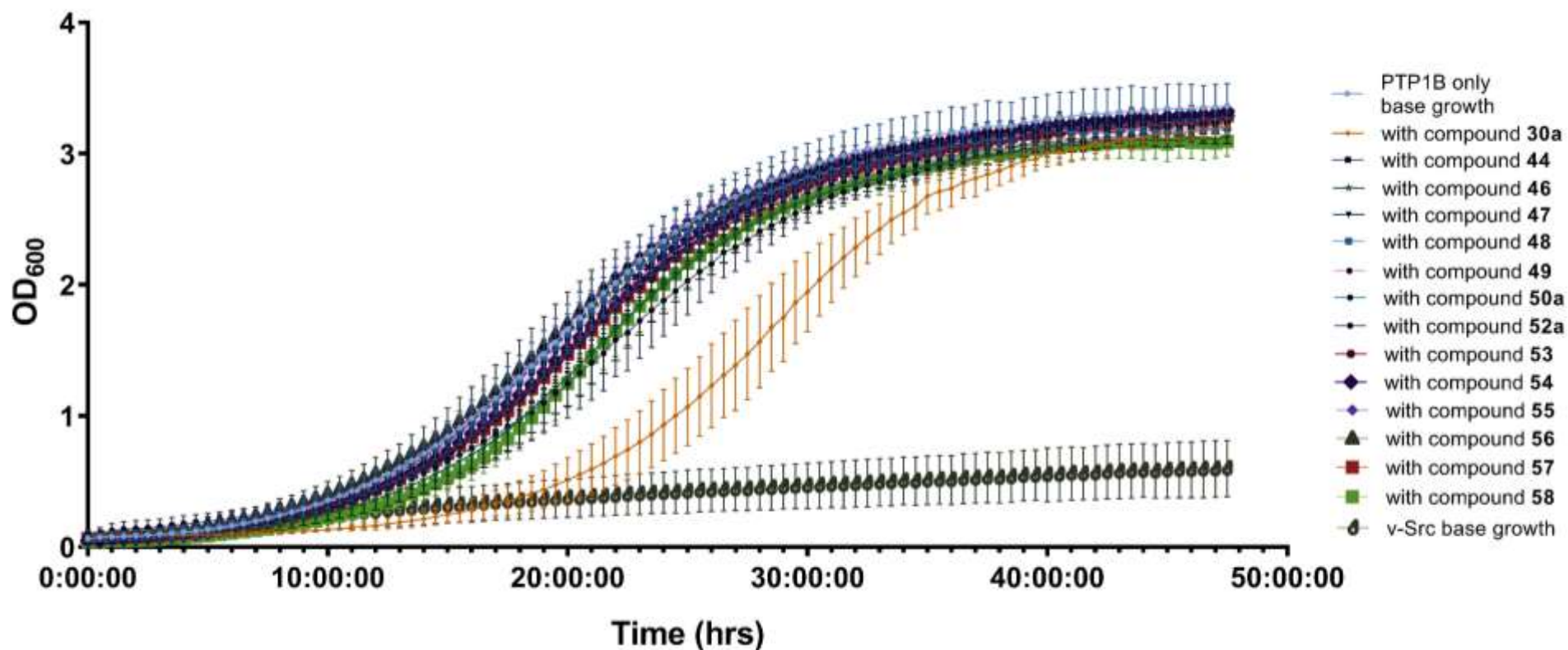


Figure LXXXV: Comparison of % change in doubling time (T_d) of PTP1B + v-Src and TCPTP + v-Src transformed yeast cells in the presence of synthesised compounds **30a**, **44**, **46-50a** and **52a-58** at 140 μ M. $n=3$ for all compounds tested in both transformations, apart from **30a** and **55** where $n=6$. Mean and individual points \pm standard deviation plotted. Used non-parametric Mann-Whitney t-test for statistical analysis. * p value ≤ 0.050 .



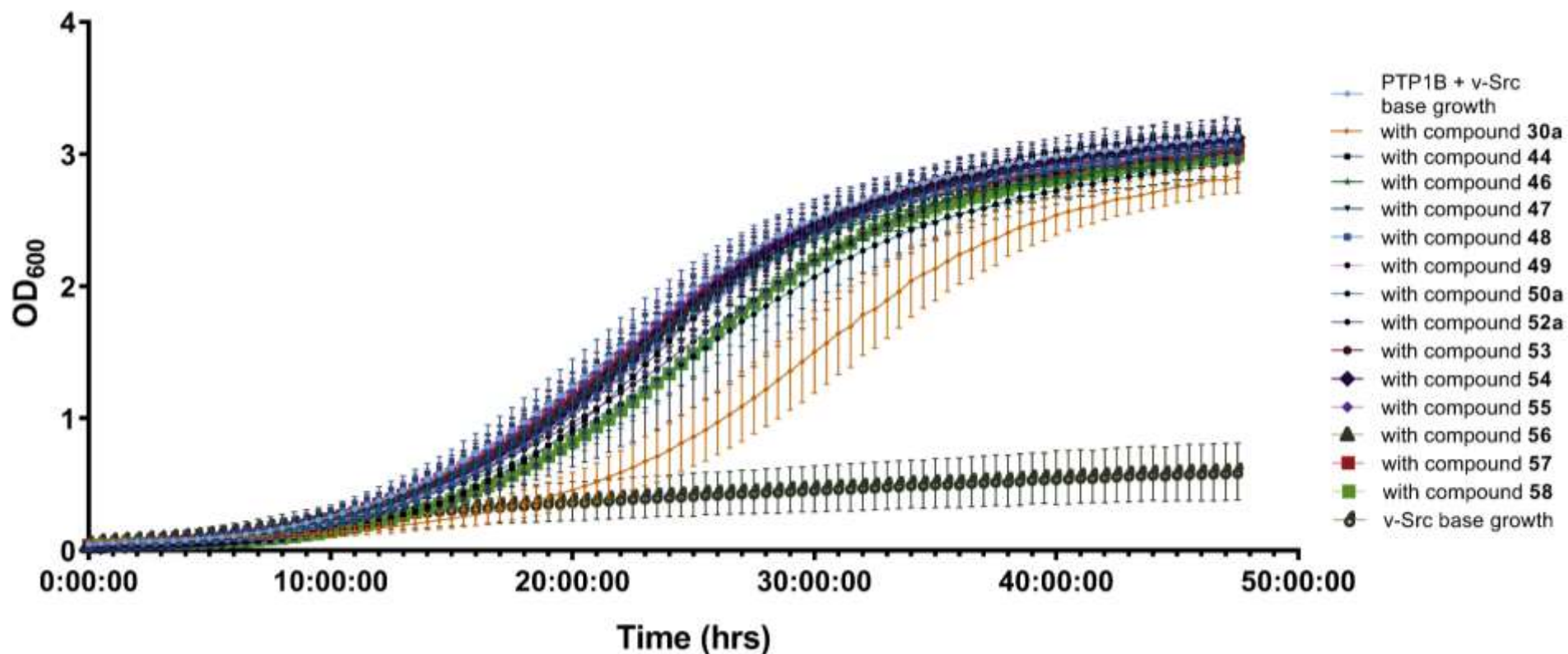
Compound	30a *	44	46	47	48	49	50a	52a *	53	54	55	56	57	58
p value	<0.0001	ns	ns	ns	ns	ns	ns	<0.0100	ns	ns	ns	ns	ns	ns

Figure LXXXVI: Growth profile of PTP1B only yeast cells with the addition of compounds **30a**, **44**, **46-50a** and **52a-58** at 100 μ M. n=3 for all compounds tested apart from **30a** and **55** where n=6 in PTP1B only cells, n=13 for v-Src base growth, n=18 for PTP1B only base growth. Mean points \pm standard deviation plotted. Data is normally distributed according to a Shapiro-Wilk test. Used a 2-way ANOVA where column factor was source of variance. * p value \leq 0.050 vs control.



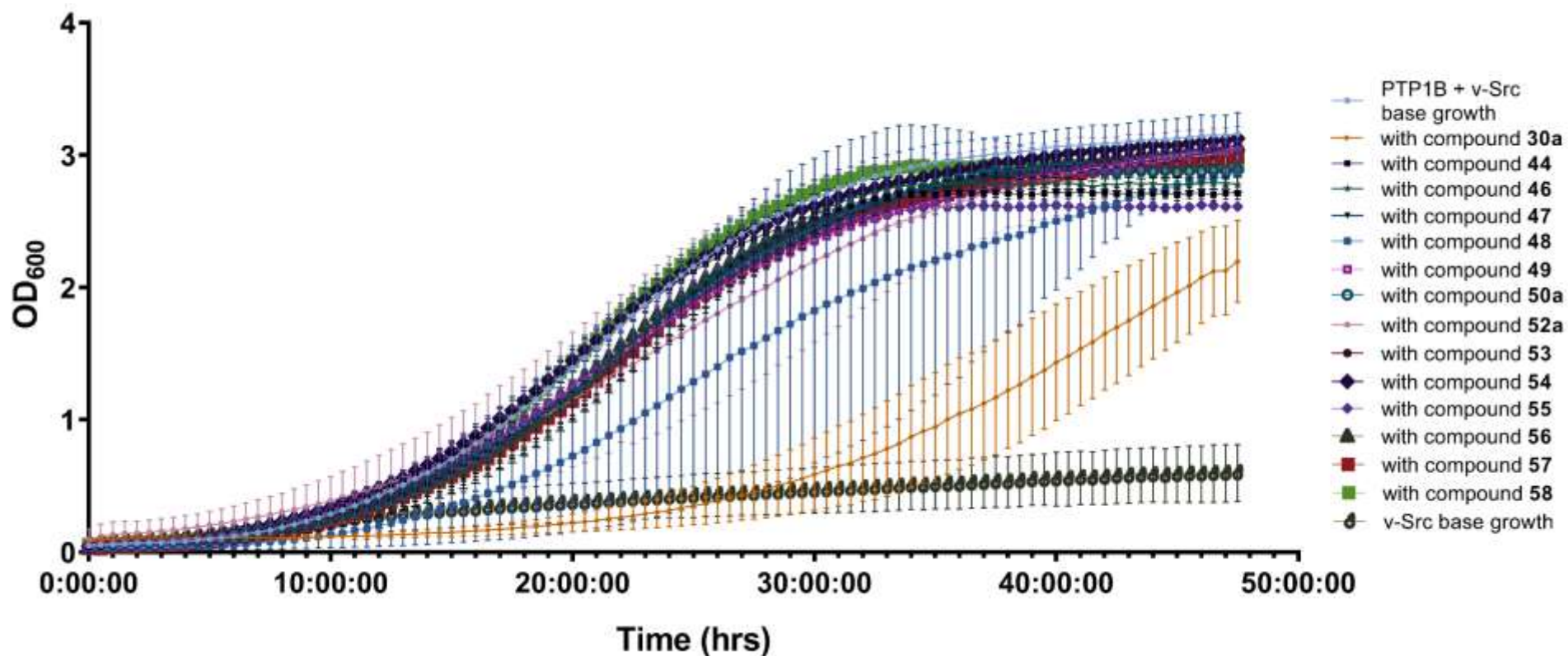
Compound	30a *	44 *	46	47	48	49 *	50a *	52a	53 *	54	55	56	57	58 *
p value	<0.0001	<0.0500	ns	ns	ns	<0.0050	<0.0100	ns	<0.0500	ns	ns	ns	ns	<0.0100

Figure LXXXVII: Growth profile of PTP1B only yeast cells with the addition of compounds **30a**, **44**, **46-50a** and **52a-58** at 140 μ M. n=3 for all compounds tested apart from **30a** and **55** where n=6 in PTP1B only cells, n=13 for v-Src base growth, n=18 for PTP1B only base growth. Mean points \pm standard deviation plotted. Data is normally distributed according to a Shapiro-Wilk test. Used a 2-way ANOVA where column factor was source of variance. * p value \leq 0.050 vs control.



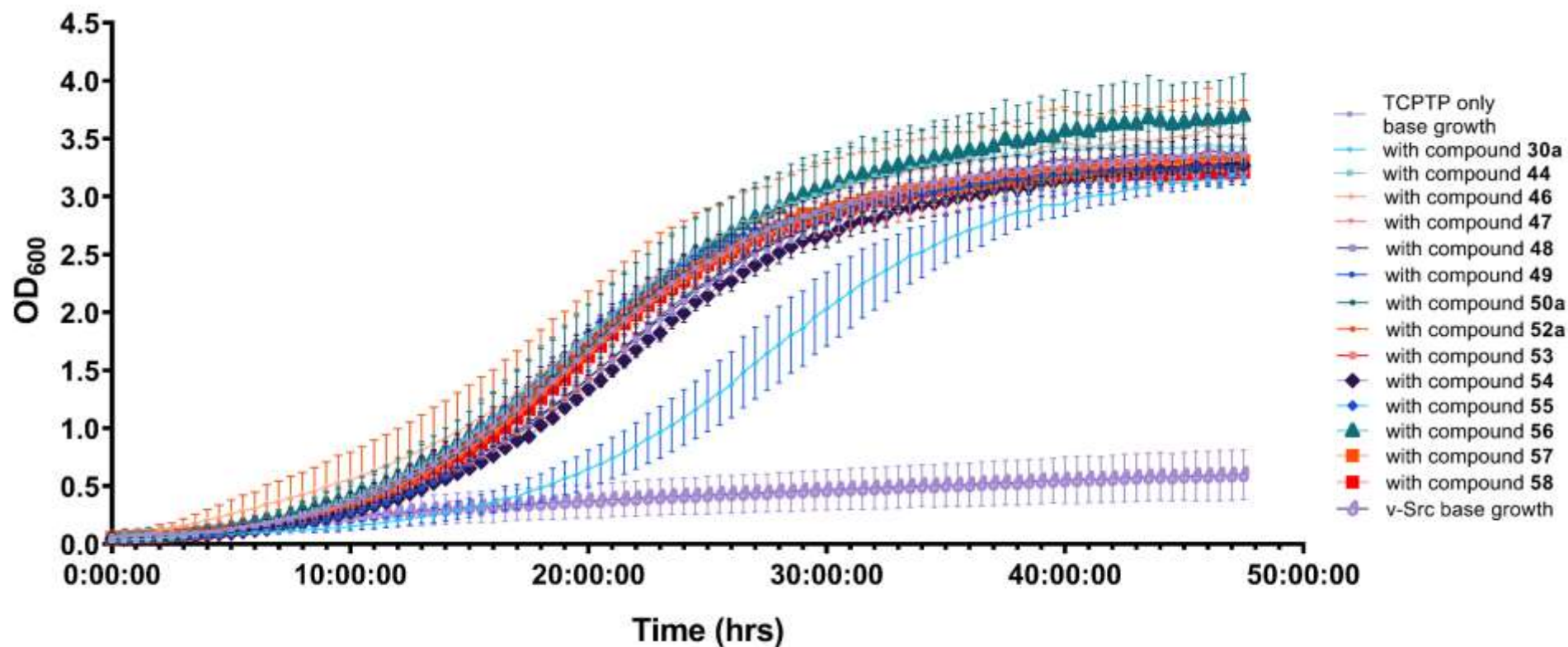
Compound	30a *	44 *	46	47	48	49	50a	52a	53	54	55	56	57	58 *
p value	<0.0001	<0.0005	ns	ns	ns	ns	ns	ns	ns	ns	ns	ns	ns	<0.0500

Figure LXXXVIII: Growth profile of PTP1B + v-Src yeast cells with the addition of compounds **30a**, **44**, **46-50a** and **52a-58** at 100 μ M. n=3 for all compounds tested apart from **30a** and **55** where n=6 in PTP1B + v-Src cells, n=13 for v-Src base growth, n=18 for PTP1B only base growth. Mean points \pm standard deviation plotted. Data is normally distributed according to a Shapiro-Wilk test. Used a 2-way ANOVA where column factor was source of variance. * p value \leq 0.050 vs control.



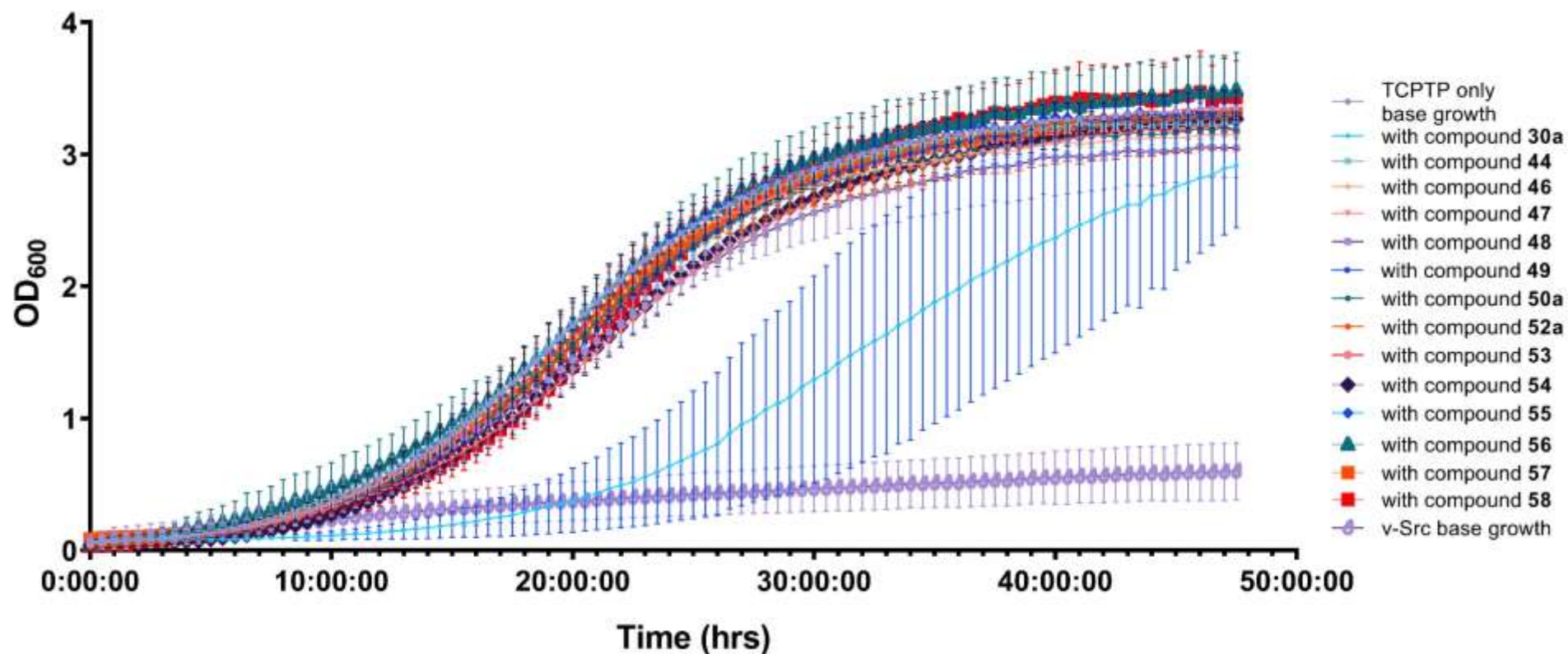
Compound	30a *	44 *	46	47	48	49	50a *	52a	53 *	54	55 *	56	57 *	58 *
p value	<0.0001	<0.0100	ns	ns	ns	ns	<0.0050	ns	<0.0500	ns	<0.0010	ns	<0.010	<0.0500

Figure LXXXIX: Growth profile of PTP1B + v-Src yeast cells with the addition of compounds **30a**, **44**, **46-50a** and **52a-58** at 140 μ M. n=3 for all compounds tested apart from **30a** and **55** where n=6 in PTP1B + v-Src cells, n=13 for v-Src base growth, n=18 for PTP1B only base growth. Mean points \pm standard deviation plotted. Data is normally distributed according to a Shapiro-Wilk test. Used a 2-way ANOVA where column factor was source of variance. * p value \leq 0.050 vs control.



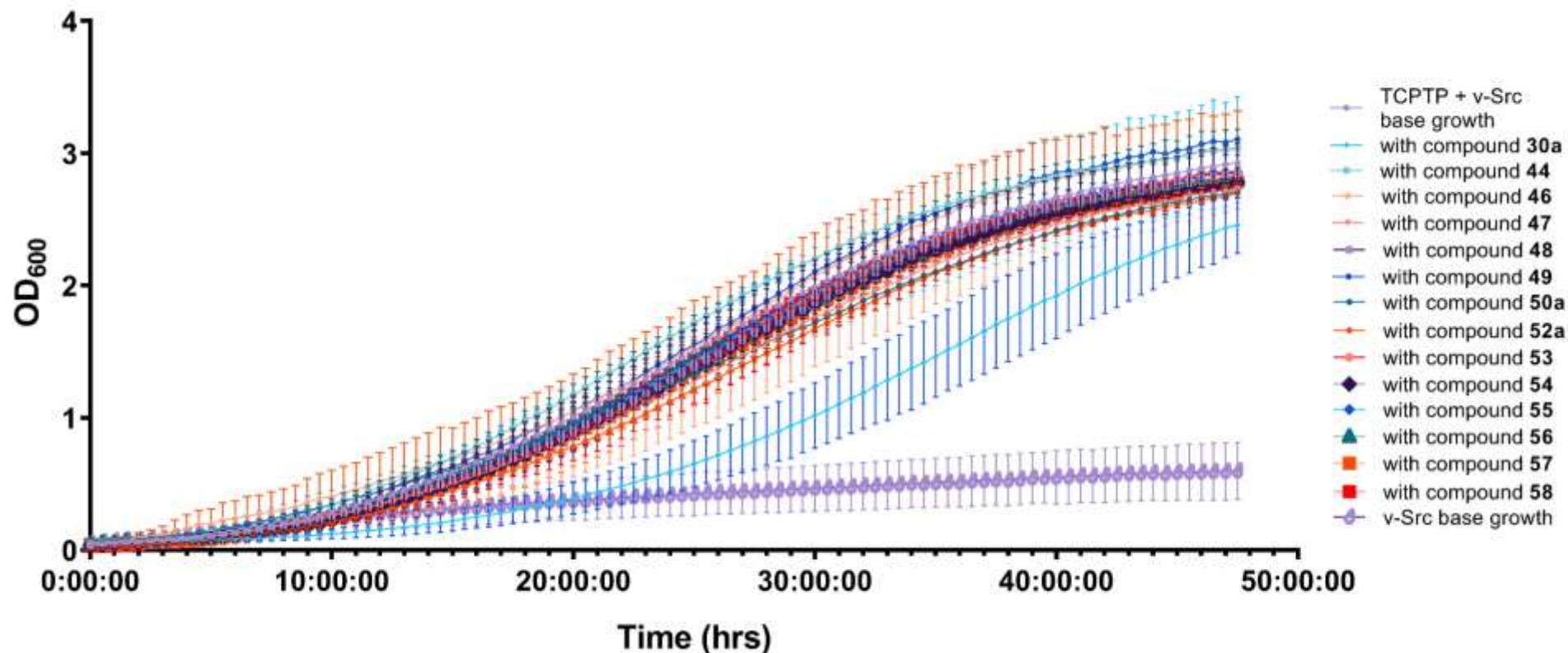
Compound	30a *	44	46	47	48	49 *	50a *	52a	53	54 *	55	56	57	58 *
p value	<0.0001	ns	ns	ns	ns	<0.0050	<0.0500	ns	ns	<0.0500	ns	ns	ns	<0.0500

Figure XC: Growth profile of TCPTP only yeast cells with the addition of compounds **30a**, **44**, **46-50a** and **52a-58** at 100 μ M. n=3 for all compounds tested apart from **30a** and **55** where n=6 in TCPTP only cells, n=13 for v-Src base growth, n=21 for PTP1B only base growth. Mean points \pm standard deviation plotted. Data is normally distributed according to a Shapiro-Wilk test. Used a 2-way ANOVA where column factor was source of variance. * p value \leq 0.050 vs control.



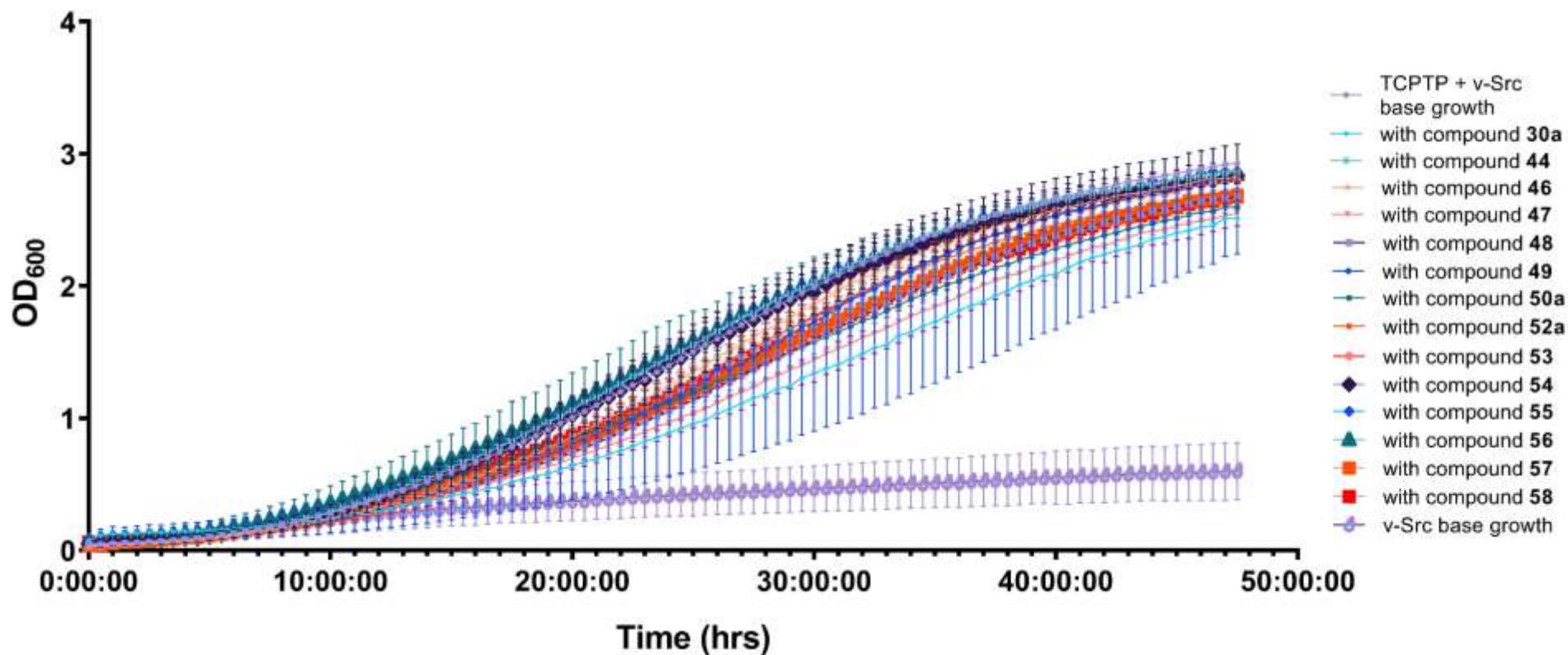
Compound	30a *	44 *	46	47 *	48 *	49 *	50a *	52a	53	54 *	55	56	57	58
p value	<0.0001	<0.0500	ns	<0.0050	<0.0500	<0.0100	<0.0500	ns	ns	<0.0500	ns	ns	ns	ns

Figure XCI: Growth profile of TCPTP only yeast cells with the addition of compounds **30a**, **44**, **46-50a** and **52a-58** at 140 μ M. n=3 for all compounds tested apart from **30a** and **55** where n=6 in TCPTP only cells, n=13 for v-Src base growth, n=21 for PTP1B only base growth. Mean points \pm standard deviation plotted. Data is normally distributed according to a Shapiro-Wilk test. Used a 2-way ANOVA where column factor was source of variance. * p value \leq 0.050 vs control.



Compound	30a *	44	46	47	48 *	49	50a *	52a	53 *	54	55	56	57	58 *
p value	<0.0001	ns	ns	ns	<0.0050	ns	<0.0500	ns	<0.0050	ns	ns	ns	ns	<0.0500

Figure XCII: Growth profile of TCPTP + v-Src yeast cells with the addition of compounds **30a**, **44**, **46-50a** and **52a-58** at 100 μ M. n=3 for all compounds tested apart from **30a** and **55** where n=6 in TCPTP + v-Src cells, n=13 for v-Src base growth, n=21 for PTP1B only base growth. Mean points \pm standard deviation plotted. Data is normally distributed according to a Shapiro-Wilk test. Used a 2-way ANOVA where column factor was source of variance. * p value \leq 0.050 vs control.



Compound	30a *	44	46 *	47	48 *	49 *	50a *	52a *	53 *	54	55	56	57	58 *
p value	<0.0001	ns	<0.0050	ns	<0.0050	<0.0500	<0.0100	<0.0500	<0.0100	ns	ns	ns	ns	<0.0100

Figure XCIII: Growth profile of TCPTP + v-Src yeast cells with the addition of compounds **30a**, **44**, **46-50a** and **52a-58** at 140 μ M. n=3 for all compounds tested apart from **30a** and **55** where n=6 in TCPTP + v-Src cells, n=13 for v-Src base growth, n=21 for PTP1B only base growth. Mean points \pm standard deviation plotted. Data is normally distributed according to a Shapiro-Wilk test. Used a 2-way ANOVA where column factor was source of variance. * p value \leq 0.050 vs control.

2.1.8 Compound 55 T_d and growth curves for dose response screen.

2.1.8.1 PTP1B based.

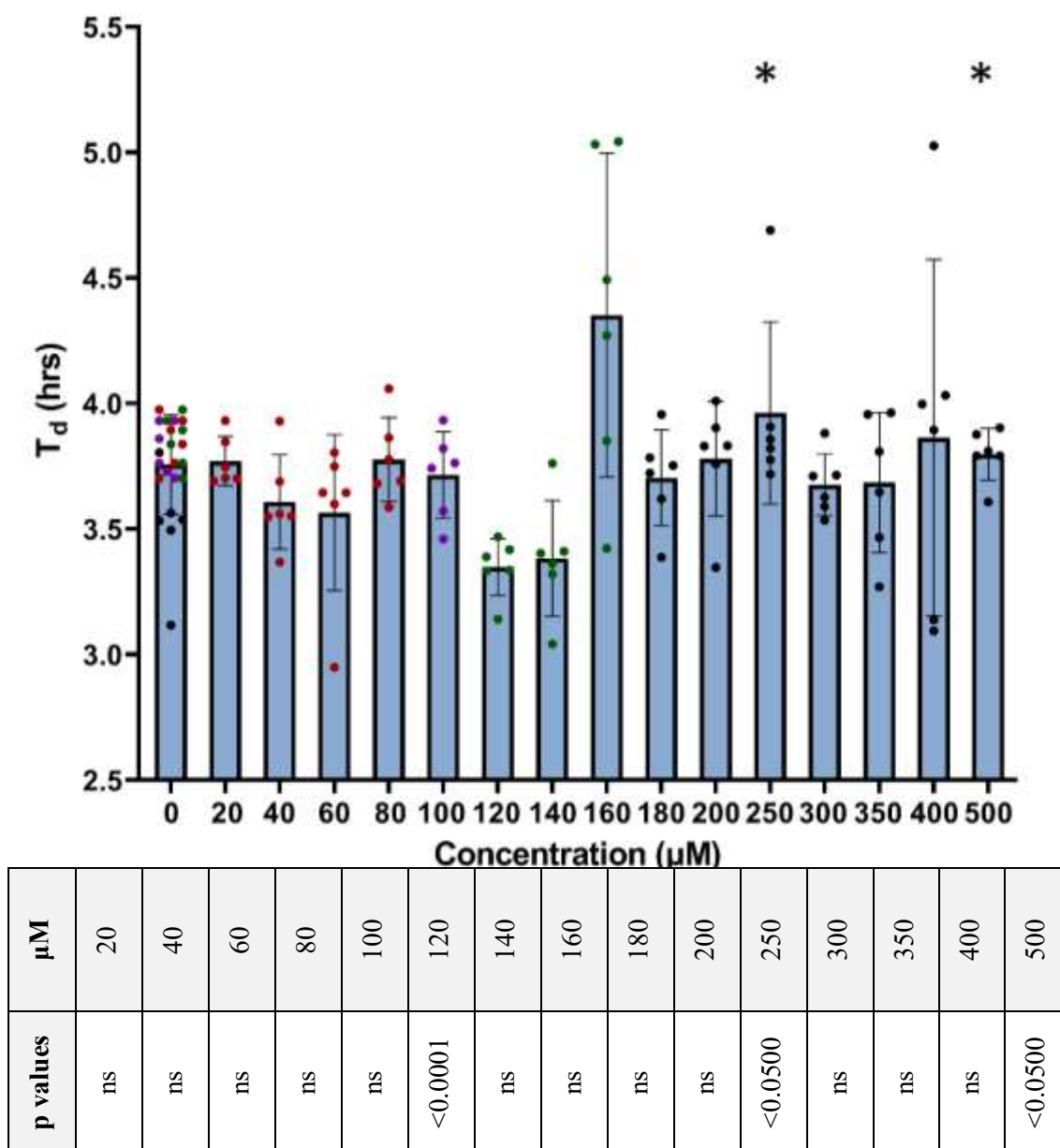


Figure XCIV: Effect of compound **55** addition at 20-500 μM on the T_d value of PTP1B only transformed yeast cells. $n=6$ for all concentrations, $n=24$ for base growth. Colour coded denotes corresponding base growth values for each concentration tested. Mean points \pm standard deviation plotted. Data is normally distributed according to a Shapiro-Wilk test. Used parametric Welch t-test for statistical analysis. * p value ≤ 0.050 vs base growth. All statistical analysis utilised corresponding base growth doubling time values. Note: the addition of **55** at 40 and 120 μM had the effect of significantly lowering the T_d rate.

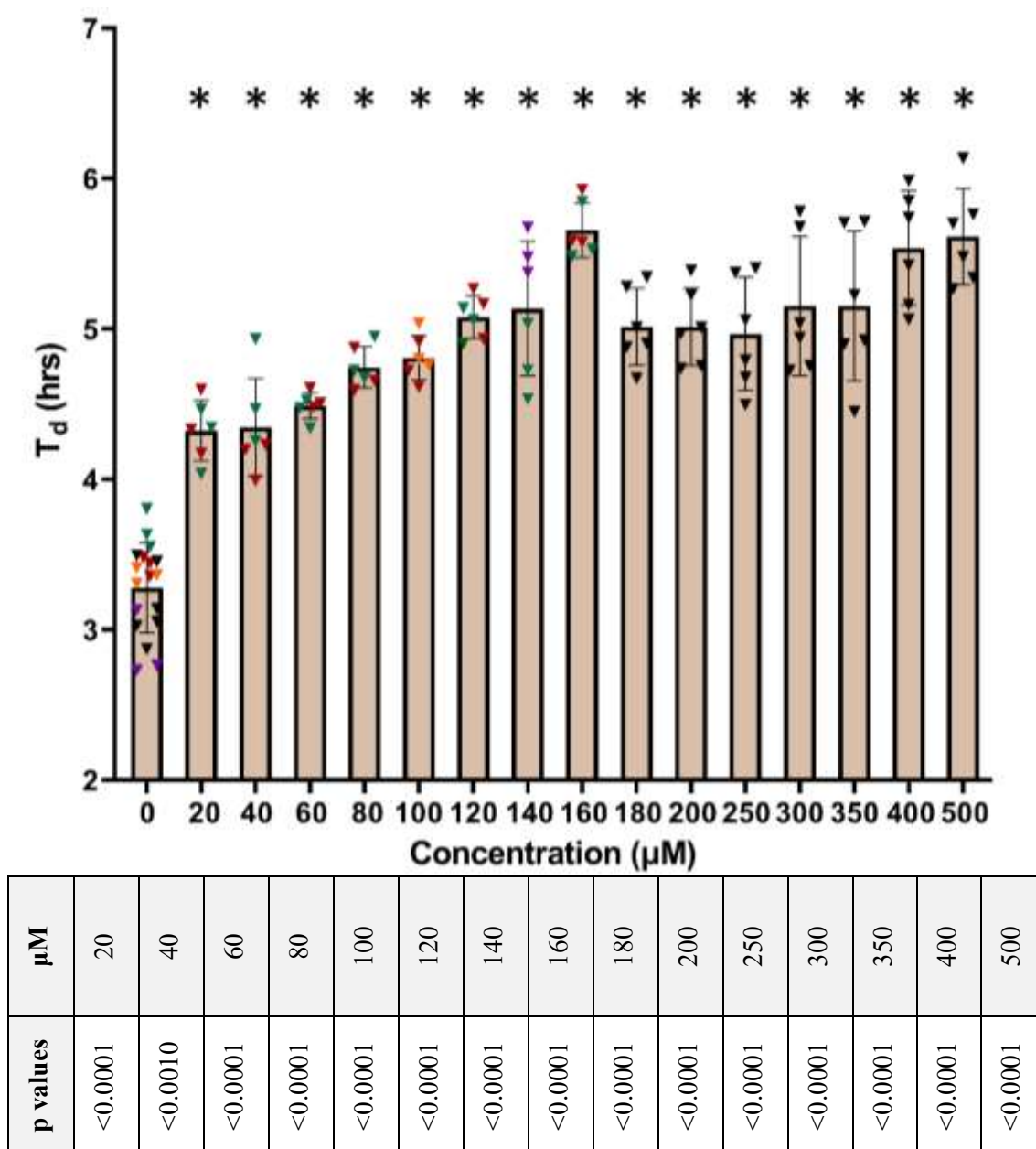
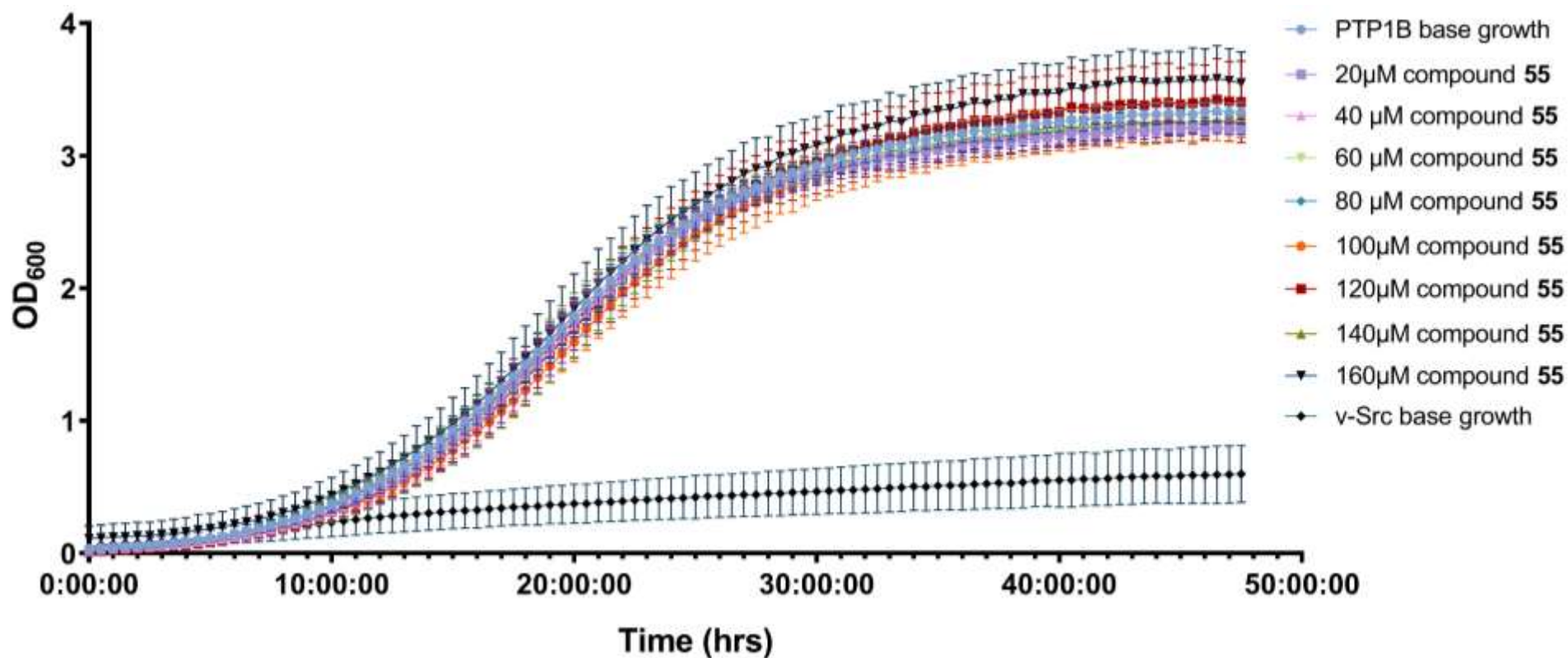
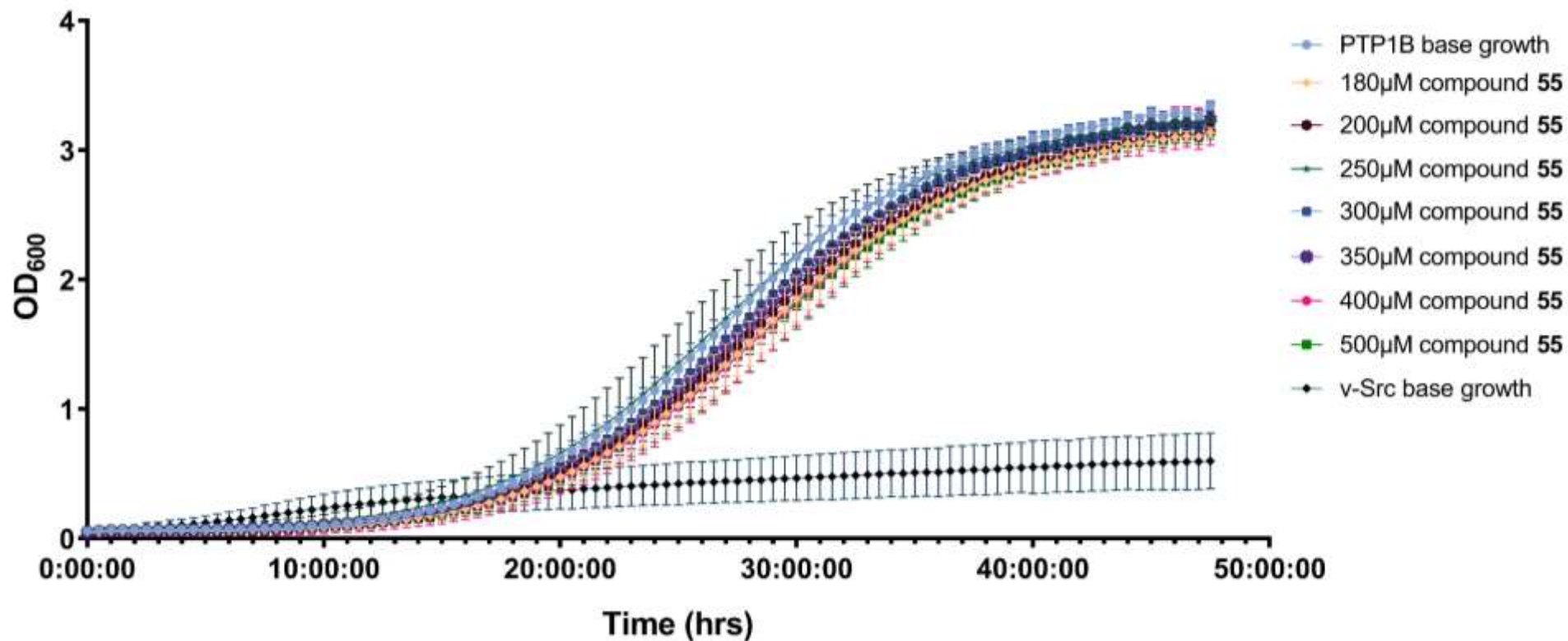


Figure XCV: Effect of compound **55** addition at 20-500 μM on the T_d value of PTP1B + v-Src transformed yeast cells. $n=6$ for all concentrations, $n=18$ for base growth. Colour coded denotes corresponding base growth values for each concentration tested. Mean points \pm standard deviation plotted. Data is normally distributed according to a Shapiro-Wilk test. Used parametric Welch t-test for statistical analysis. * p value ≤ 0.050 vs base growth. All statistical analysis utilised corresponding base growth doubling time values.



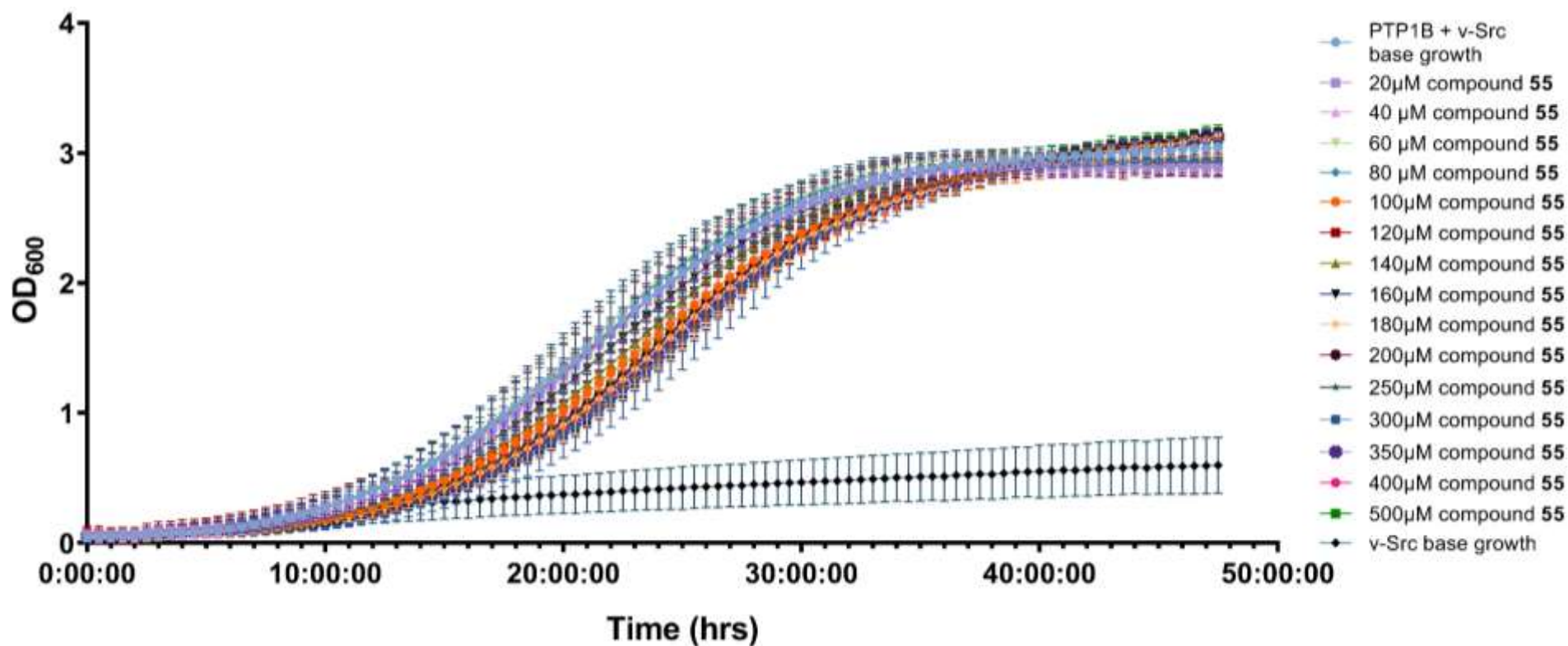
μM	20	40	60	80	100 *	120	140	160
p value	ns	ns	ns	ns	<0.0500	ns	ns	ns

Figure XCVI: Growth profile of PTP1B only yeast cells with the addition of compound **55** at 20-160 μM . $n=6$ for all concentrations in PTP1B only cells, $n=6$ for PTP1B only base growth, $n=13$ for v-Src base growth. Mean points \pm standard deviation plotted. Data is normally distributed according to a Shapiro-Wilk test. Used a 2-way ANOVA where column factor was source of variance. * p value ≤ 0.050 vs control.



μM	180 *	200 *	250	300 *	350	400 *	500 *
p value	<0.0050	<0.0050	ns	<0.0500	ns	<0.0500	<0.0050

Figure XCVII: Growth profile of PTP1B only yeast cells with the addition of compound **55** at 180-500 μM. n=6 for all concentrations in PTP1B only cells, n=6 for PTP1B only base growth, n=13 for v-Src base growth. Mean points ± standard deviation plotted. Data is normally distributed according to a Shapiro-Wilk test. Used a 2-way ANOVA where column factor was source of variance. * p value ≤ 0.050 vs control.



µM	20	40 *	60	80	100	120	140 *	160 *	180 *	200	250	300 *	350 *	400	500
p value	ns	<0.0500	ns	ns	ns	ns	<0.0050	<0.0500	<0.0500	ns	ns	<0.0500	<0.0500	ns	ns

Figure XCVIII: Growth profile of PTP1B + v-Src yeast cells with the addition of compound **55** at 20-500 µM. n=6 for all concentrations in PTP1B + v-Src cells, n=18 for PTP1B + v-Src base growth, n=13 for v-Src base growth. Mean points ± standard deviation plotted. Data is normally distributed according to a Shapiro-Wilk test. Used a 2-way ANOVA where column factor was source of variance. * p value ≤ 0.050 vs control.

2.1.8.2 TCPTP based.

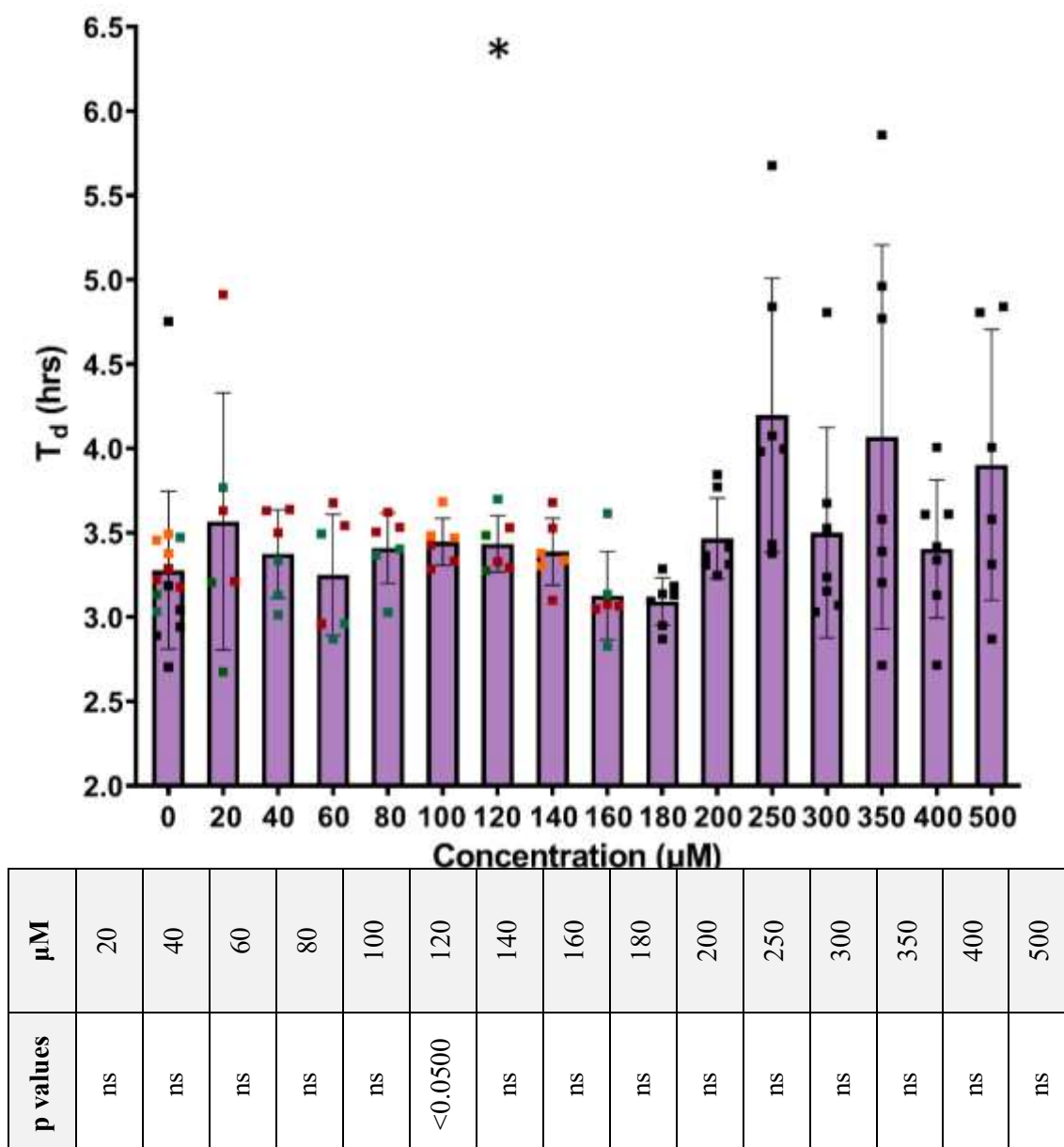


Figure XCIX: Effect of compound **55** addition at 20-500 μM on the T_d value of TCPTP only transformed yeast cells. $n=6$ for all concentrations, $n=15$ for base growth. Colour coded denotes corresponding base growth values for each compound tested. Mean points \pm standard deviation plotted. Data is normally distributed according to a Shapiro-Wilk test. Used parametric Welch t-test for statistical analysis. * p value ≤ 0.050 vs base growth. All statistical analysis utilised corresponding base growth doubling time values.

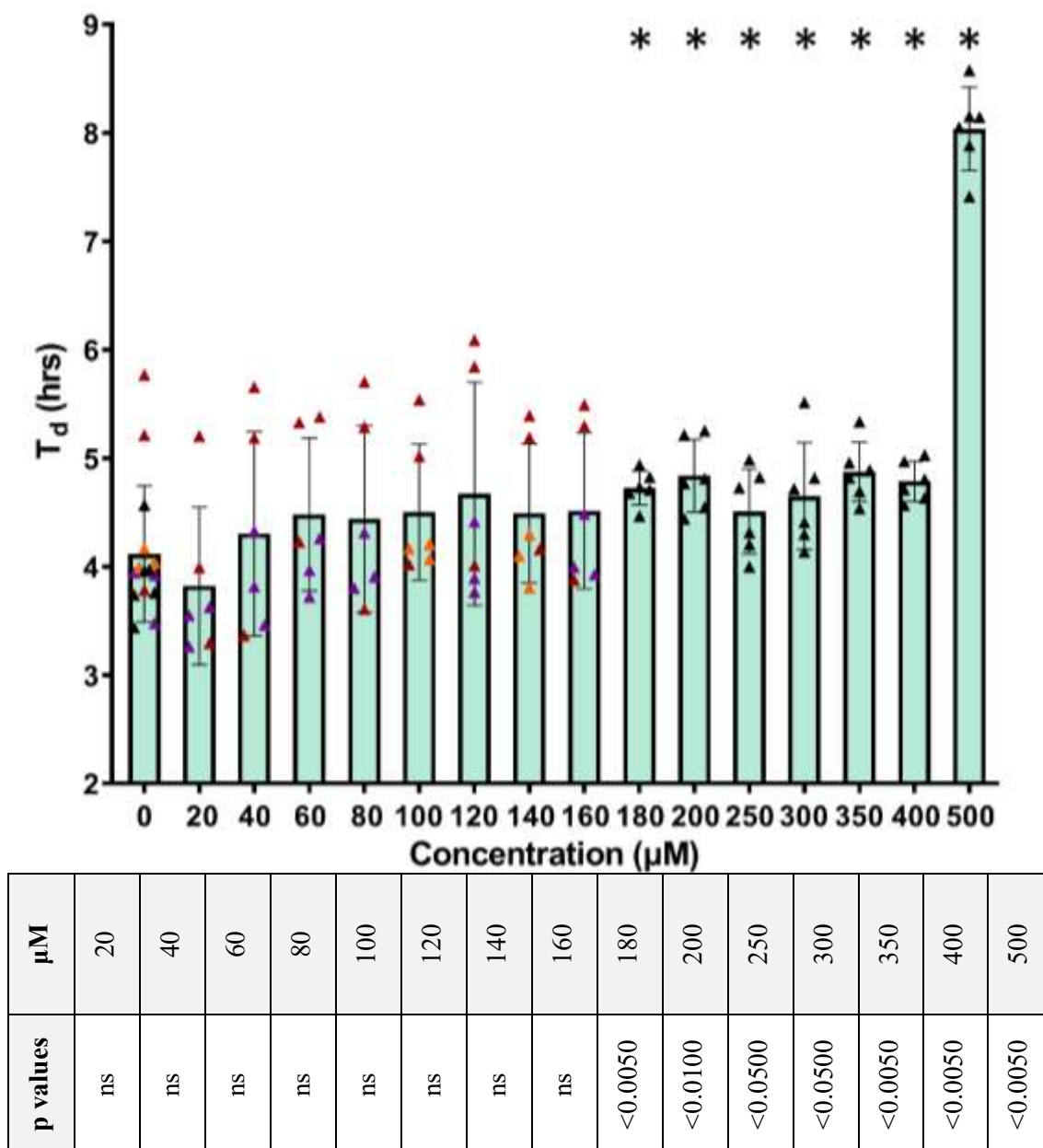
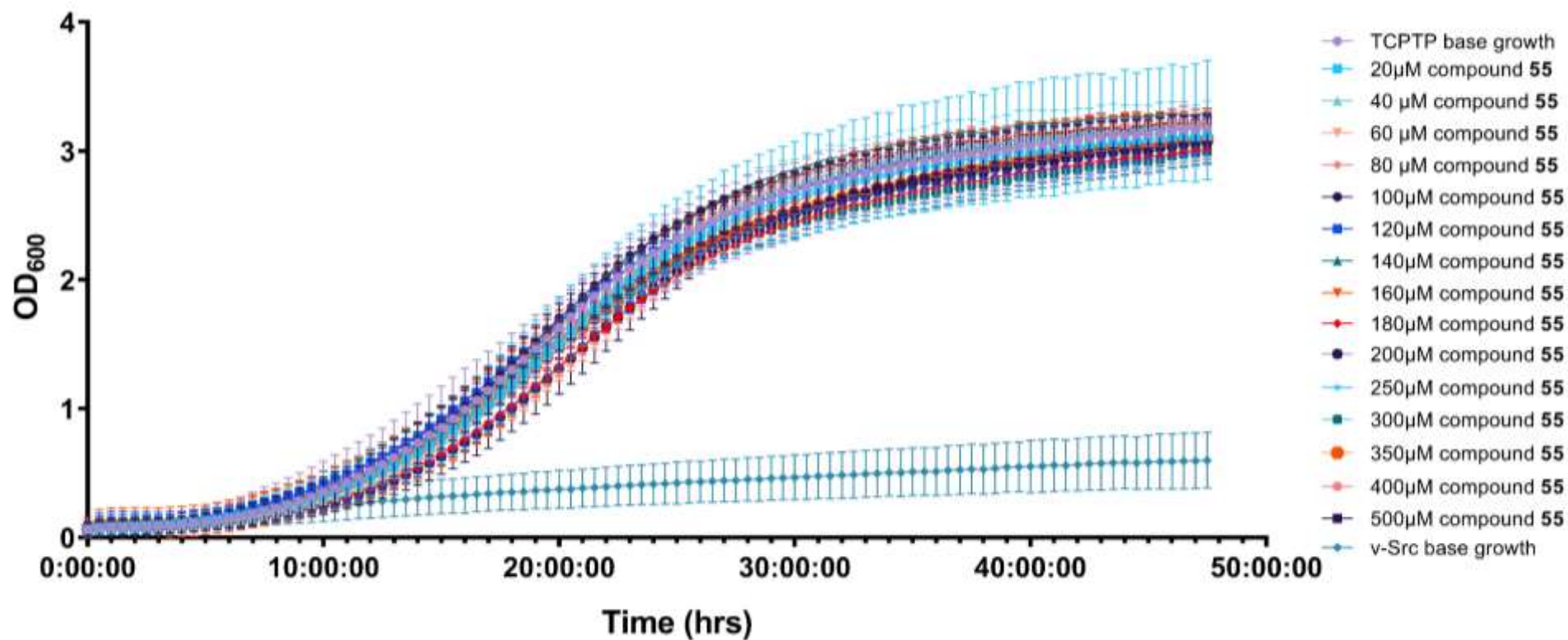
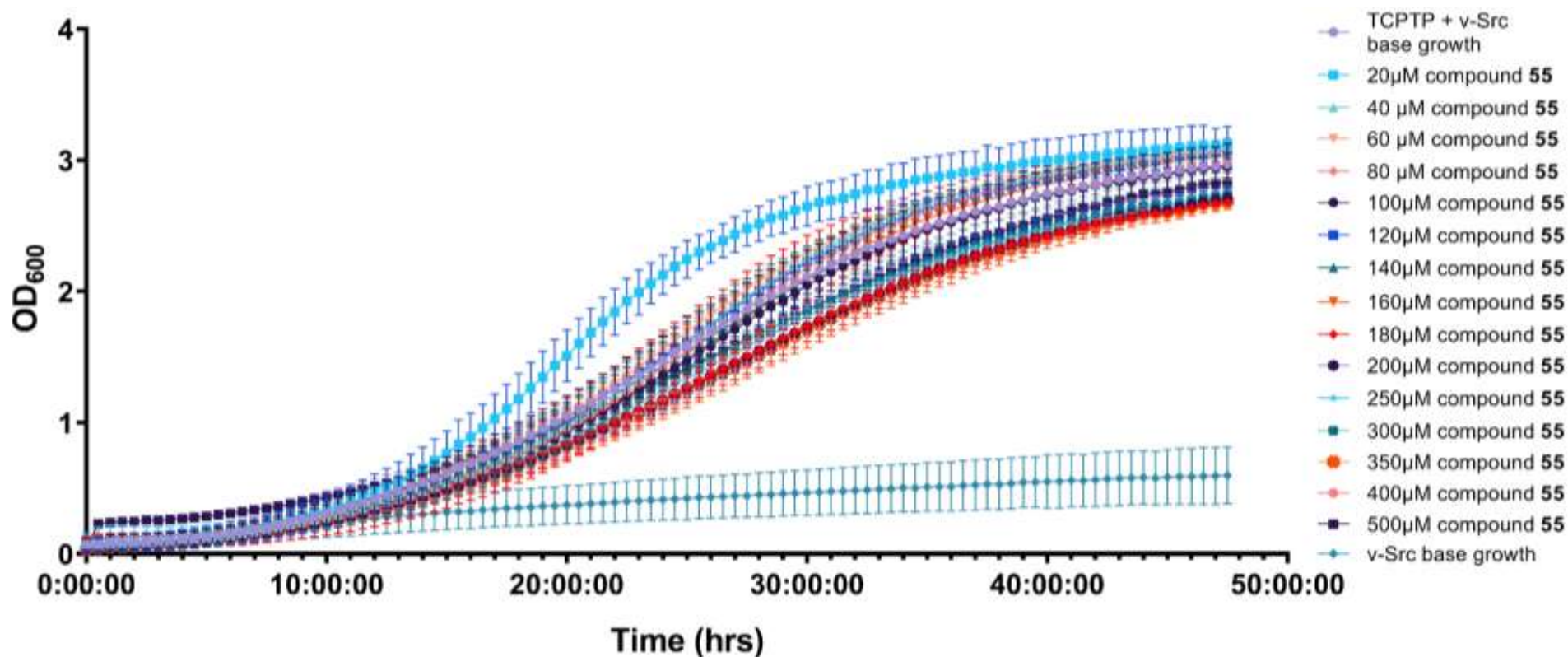


Figure C: Effect of compound **55** addition at 20-500 µM on the T_d value of TCPTP + v-Src transformed yeast cells. n=6 for all concentrations, n=15 for base growth. Colour coded denotes corresponding base growth values for each compound tested. Mean points ± standard deviation plotted. Data is normally distributed according to a Shapiro-Wilk test. Used parametric Welch t-test for statistical analysis. * p value ≤ 0.050 vs base growth. All statistical analysis utilised corresponding base growth doubling time values.



μM	20	40	60	80	100 *	120	140 *	160	180 *	200 *	250 *	300 *	350 *	400	500
p value	ns	ns	ns	ns	<0.0500	ns	<0.0500	ns	<0.0050	<0.0100	<0.0500	<0.0500	<0.0500	ns	ns

Figure CI: Growth profile of TCPTP only yeast cells with the addition of compound **55** at 20-500 μM . $n=6$ for all concentrations in TCPTP only cells, $n=15$ for TCPTP only base growth, $n=13$ for v-Src base growth. Mean points \pm standard deviation plotted. Data is normally distributed according to a Shapiro-Wilk test. Used a 2-way ANOVA where column factor was source of variance. * p value ≤ 0.050 vs control.



µM	20 *	40	60	80	100 *	120	140	160	180 *	200 *	250	300	350 *	400 *	500 *
p value	<0.0500	ns	ns	ns	<0.0500	ns	ns	ns	<0.0500	<0.0500	ns	ns	<0.0500	<0.0500	<0.0500

Figure CII: Growth profile of TCPTP + v-Src yeast cells with the addition of compound **55** at 20-500 µM. n=6 for all concentrations in TCPTP + v-Src cells, n=15 for TCPTP + v-Src base growth, n=13 for v-Src base growth. Mean points ± standard deviation plotted. Data is normally distributed according to a Shapiro-Wilk test. Used a 2-way ANOVA where column factor was source of variance. * p value ≤ 0.050 vs control.

2.2 Accompanying BBB results of hit benzodioxane compounds.

2.2.1 Maximum absorption wavelength

Table XX: Maximum absorption wavelengths of each hit benzodioxane compound.

	Compound														
	16	30a	44	46	47	48	49	50a	52a	53	54	55	56	57	58
Wavelength (nm)	230	220	270	270	270	240	230	240	220	270	230	230	280	230	260

Above **Table XX** shows the wavelength of light in which the stated compounds absorb the maximum amount.

2.2.2 Blank corrected absorbance values of known concentrations.

Blanks used were comprised of 1x PBS and DMSO the proportion of which corresponds to the amount for each concentration of compound tested. These blanks were ran over the same wavelength range (220 – 500 nm) as the compounds were, when determining maximum absorbance value.

2.2.2.1 Compound 16

Table XXI: Blank corrected absorbance data of compound **16** used to construct calibration curve.

230 nm		Concentration of compound used (μM)									
		50	100	150	200	250	300	350	400	450	500
Absorbance values	1	0.581	1.147	1.855	2.206	3.233	4.135	4.713	5.069	5.572	6.488
	2	0.415	1.088	1.810	2.769	2.990	4.036	4.602	4.910	5.598	6.464
	3	0.591	1.085	1.718	2.522	2.822	4.280	4.504	4.937	5.648	6.334
	4	0.592	1.055	1.663	2.476	3.399	3.655	4.448	5.067	5.624	6.440
	5	0.589	1.163	1.807	2.409	2.877	4.111	4.677	5.084	5.649	6.379
	Mean	0.553	1.107	1.771	2.477	3.064	4.043	4.588	5.013	5.618	6.421
	Std dev.	0.069	0.041	0.070	0.182	0.219	0.210	0.100	0.074	0.030	0.057

2.2.2.2 Compound 30a

Table XXII: Blank corrected absorbance data of compound **30a** used to construct calibration curve.

220 nm		Concentration of compound used (μM)									
		50	100	150	200	250	300	350	400	450	500
Absorbance values	1	0.187	0.615	0.639	0.973	1.202	1.719	1.928	1.848	2.191	2.520
	2	0.325	0.570	0.880	0.978	1.147	1.489	1.984	2.096	2.333	2.502
	3	0.255	0.521	0.729	1.024	1.180	1.352	2.019	2.070	2.211	2.643
	4	0.216	0.590	0.700	1.084	1.282	1.292	1.655	2.038	2.144	2.521
	5	0.182	0.518	0.864	0.934	1.357	1.412	1.415	1.778	2.135	2.329
	Mean	0.233	0.563	0.762	0.999	1.234	1.452	1.801	1.966	2.203	2.503
	Std dev.	0.053	0.038	0.094	0.051	0.076	0.148	0.231	0.128	0.071	0.100

2.2.2.3 Compound 44

Table XXIII: Blank corrected absorbance data of compound **44** used to construct calibration curve.

270 nm		Concentration of compound used (μM)									
		50	100	150	200	250	300	350	400	450	500
Absorbance values	1	0.317	0.494	0.711	1.009	1.216	1.410	1.783	1.981	2.167	2.434
	2	0.224	0.494	0.719	0.917	1.227	1.422	1.691	1.970	2.292	2.489
	3	0.212	0.517	0.702	0.994	1.181	1.394	1.655	1.964	2.260	2.461
	4	0.220	0.505	0.709	0.939	1.239	1.395	1.758	2.054	2.250	2.465
	5	0.221	0.476	0.717	0.989	1.210	1.394	1.738	1.923	2.134	2.453
	Mean	0.239	0.497	0.711	0.969	1.215	1.403	1.725	1.978	2.220	2.460
	Std dev.	0.039	0.014	0.006	0.035	0.019	0.011	0.046	0.043	0.060	0.018

2.2.2.4 Compound 46

Table XXIV: Blank corrected absorbance data of compound **46** used to construct calibration curve.

270 nm		Concentration of compound used (μM)									
		50	100	150	200	250	300	350	400	450	500
Absorbance values	1	0.163	0.295	0.632	0.774	0.939	1.252	1.238	1.478	1.654	1.934
	2	0.258	0.288	0.612	0.659	0.901	1.002	1.291	1.454	1.664	1.817
	3	0.215	0.363	0.505	0.773	0.969	0.899	1.237	1.516	1.719	1.815
	4	0.154	0.428	0.562	0.725	0.889	1.026	1.241	1.444	1.616	1.945
	5	0.128	0.418	0.449	0.766	0.893	1.133	1.248	1.500	1.547	1.905
	Mean	0.184	0.359	0.552	0.739	0.918	1.062	1.251	1.478	1.640	1.883
	Std dev.	0.047	0.059	0.068	0.044	0.031	0.121	0.020	0.027	0.057	0.056

2.2.2.5 Compound 47

Table XXV: Blank corrected absorbance data of compound **47** used to construct calibration curve.

270 nm		Concentration of compound used (μM)									
		50	100	150	200	250	300	350	400	450	500
Absorbance values	1	0.166	0.371	0.668	0.701	0.941	1.191	1.351	1.315	1.655	2.040
	2	0.176	0.337	0.535	0.678	1.028	1.094	1.346	1.799	1.659	1.884
	3	0.168	0.391	0.527	0.789	0.987	1.158	1.358	1.361	1.767	2.039
	4	0.183	0.352	0.602	0.800	0.913	1.149	1.317	1.505	1.750	1.947
	5	0.252	0.406	0.600	0.843	1.012	1.194	1.150	1.498	1.852	1.857
	Mean	0.189	0.372	0.586	0.762	0.976	1.157	1.305	1.495	1.736	1.953
	Std dev.	0.032	0.025	0.051	0.062	0.043	0.036	0.078	0.169	0.074	0.076

2.2.2.6 Compound 48

Table XXVI: Blank corrected absorbance data of compound **48** used to construct calibration curve.

240 nm		Concentration of compound used (μM)									
		50	100	150	200	250	300	350	400	450	500
Absorbance values	1	0.675	1.410	2.170	2.268	3.686	3.775	4.346	5.022	5.605	6.334
	2	0.693	1.196	2.103	2.955	2.904	3.789	4.584	5.016	5.627	6.354
	3	0.684	1.297	1.513	2.789	3.397	3.931	4.426	5.170	6.173	6.447
	4	0.688	1.186	2.290	2.243	3.079	3.722	4.405	5.150	5.635	6.483
	5	0.684	1.368	1.498	2.353	3.058	3.817	4.599	5.004	5.663	6.499
	Mean	0.684	1.292	1.915	2.522	3.225	3.807	4.472	5.072	5.740	6.424
	Std dev.	0.006	0.090	0.340	0.293	0.281	0.069	0.101	0.072	0.217	0.067

2.2.2.7 Compound 49

Table XXVII: Blank corrected absorbance data of compound **49** used to construct calibration curve.

230 nm		Concentration of compound used (μM)									
		50	100	150	200	250	300	350	400	450	500
Absorbance values	1	0.476	1.103	1.372	2.064	2.400	3.062	3.309	3.618	4.311	4.840
	2	0.441	0.877	1.483	1.894	2.409	3.095	3.364	3.929	4.305	4.762
	3	0.482	1.005	1.496	1.961	2.403	3.069	3.562	3.922	4.312	4.920
	4	0.463	0.916	1.378	1.867	2.415	2.983	3.344	3.904	4.302	4.706
	5	0.462	0.926	1.326	1.909	2.405	3.075	3.357	3.873	4.312	4.931
	Mean	0.465	0.965	1.411	1.939	2.406	3.056	3.387	3.849	4.308	4.832
	Std dev.	0.014	0.080	0.067	0.070	0.005	0.039	0.089	0.117	0.004	0.088

2.2.2.8 Compound 50a

Table XXVIII: Blank corrected absorbance data of compound **50a** used to construct calibration curve.

220 nm		Concentration of compound used (μM)									
		50	100	150	200	250	300	350	400	450	500
Absorbance values	1	0.156	0.314	0.418	0.723	0.800	0.866	1.079	1.200	1.314	1.489
	2	0.137	0.321	0.409	0.624	0.799	0.878	1.087	1.210	1.352	1.490
	3	0.125	0.299	0.470	0.605	0.732	0.885	1.065	1.178	1.422	1.499
	4	0.190	0.304	0.463	0.604	0.810	0.884	1.087	1.287	1.331	1.501
	5	0.130	0.303	0.471	0.605	0.810	0.876	1.090	1.217	1.366	1.525
	Mean	0.148	0.308	0.446	0.633	0.790	0.878	1.081	1.218	1.357	1.501
	Std dev.	0.024	0.008	0.027	0.046	0.029	0.007	0.009	0.037	0.037	0.013

2.2.2.9 Compound 52a

Table XXIX: Blank corrected absorbance data of compound **52a** used to construct calibration curve.

240 nm		Concentration of compound used (μM)									
		50	100	150	200	250	300	350	400	450	500
Absorbance values	1	0.400	0.537	0.757	1.020	1.680	1.637	1.972	2.192	2.443	2.985
	2	0.470	0.630	0.737	1.040	1.261	1.715	2.089	2.233	2.440	2.569
	3	0.370	0.532	1.007	0.962	1.382	1.686	1.647	2.190	2.538	2.612
	4	0.292	0.500	1.138	1.200	1.232	1.506	1.740	2.227	2.421	2.687
	5	-0.127	0.613	0.547	1.193	1.040	1.509	2.043	1.826	2.516	2.970
	Mean	0.281	0.563	0.837	1.083	1.319	1.610	1.899	2.134	2.472	2.765
	Std dev.	0.212	0.050	0.210	0.096	0.211	0.088	0.174	0.155	0.046	0.178

2.2.2.10 Compound 53

Table XXX: Blank corrected absorbance data of compound **53** used to construct calibration curve.

270 nm		Concentration of compound used (μM)									
		50	100	150	200	250	300	350	400	450	500
Absorbance values	1	0.068	0.163	0.227	0.327	0.376	0.452	0.515	0.564	0.632	0.737
	2	0.067	0.173	0.231	0.321	0.354	0.453	0.581	0.653	0.868	0.829
	3	0.080	0.150	0.214	0.327	0.389	0.446	0.586	0.607	0.621	0.758
	4	0.083	0.144	0.221	0.314	0.410	0.424	0.480	0.579	0.598	0.737
	5	0.082	0.144	0.221	0.307	0.343	0.435	0.497	0.609	0.670	0.738
	Mean	0.076	0.155	0.222	0.319	0.375	0.442	0.532	0.602	0.677	0.759
	Std dev.	0.007	0.011	0.006	0.008	0.024	0.011	0.044	0.030	0.098	0.036

2.2.2.11 Compound 54

Table XXXI: Blank corrected absorbance data of compound **54** used to construct calibration curve.

240 nm		Concentration of compound used (μM)									
		50	100	150	200	250	300	350	400	450	500
Absorbance values	1	0.047	0.155	0.228	0.346	0.389	0.491	0.570	0.581	0.756	0.857
	2	0.106	0.148	0.259	0.290	0.413	0.501	0.567	0.606	0.727	0.859
	3	0.048	0.172	0.214	0.291	0.404	0.457	0.582	0.630	0.743	0.846
	4	0.125	0.135	0.251	0.326	0.388	0.503	0.572	0.664	0.719	0.822
	5	0.065	0.165	0.257	0.305	0.381	0.492	0.566	0.658	0.740	0.868
	Mean	0.078	0.155	0.242	0.312	0.395	0.489	0.571	0.627	0.737	0.851
	Std dev.	0.032	0.013	0.018	0.022	0.012	0.017	0.006	0.031	0.013	0.016

2.2.2.12 Compound 55

Table XXXII: Blank corrected absorbance data of compound **55** used to construct calibration curve.

230 nm		Concentration of compound used (μM)									
		50	100	150	200	250	300	350	400	450	500
Absorbance values	1	0.106	0.174	0.277	0.407	0.512	0.482	0.740	0.790	0.862	0.984
	2	0.037	0.169	0.280	0.366	0.558	0.561	0.702	0.770	0.927	0.989
	3	0.125	0.187	0.288	0.344	0.466	0.616	0.735	0.870	0.832	1.094
	4	0.143	0.218	0.253	0.377	0.488	0.763	0.612	0.795	0.833	0.989
	5	0.076	0.239	0.256	0.415	0.525	0.520	0.665	0.699	0.937	0.949
	Mean	0.097	0.197	0.271	0.382	0.510	0.588	0.690	0.784	0.878	1.001
	Std dev.	0.037	0.027	0.014	0.026	0.031	0.098	0.048	0.055	0.045	0.049

2.2.2.13 Compound 56

Table XXXIII: Blank corrected absorbance data of compound **56** used to construct calibration curve.

280 nm		Concentration of compound used (μM)									
		50	100	150	200	250	300	350	400	450	500
Absorbance values	1	0.021	0.108	0.184	0.239	0.289	0.386	0.381	0.433	0.506	0.628
	2	0.013	0.109	0.180	0.247	0.343	0.392	0.387	0.481	0.531	0.533
	3	0.096	0.106	0.174	0.231	0.260	0.399	0.380	0.496	0.504	0.612
	4	0.098	0.095	0.191	0.250	0.262	0.340	0.416	0.409	0.530	0.608
	5	0.014	0.084	0.167	0.254	0.263	0.317	0.403	0.518	0.519	0.528
	Mean	0.048	0.101	0.179	0.244	0.283	0.366	0.394	0.467	0.518	0.582
	Std dev.	0.040	0.010	0.008	0.008	0.032	0.032	0.014	0.040	0.011	0.042

2.2.2.14 Compound 57

Table XXXIV: Blank corrected absorbance data of compound **57** used to construct calibration curve.

230 nm		Concentration of compound used (μM)									
		50	100	150	200	250	300	350	400	450	500
Absorbance values	1	0.189	0.251	0.384	0.267	0.664	0.803	0.963	1.128	1.018	1.236
	2	0.112	0.227	0.348	0.661	0.469	0.739	0.929	1.119	1.204	1.467
	3	0.133	0.213	0.375	0.555	0.604	0.958	1.034	0.996	1.154	1.238
	4	0.122	0.181	0.464	0.554	0.838	0.764	0.891	0.905	1.241	1.358
	5	0.131	0.512	0.470	0.677	0.832	0.908	0.969	0.943	1.505	1.479
	Mean	0.137	0.277	0.409	0.543	0.681	0.834	0.957	1.018	1.224	1.356
	Std dev.	0.027	0.120	0.049	0.147	0.140	0.085	0.047	0.091	0.159	0.106

2.2.2.15 Compound 58

Table XXXV: Blank corrected absorbance data of compound **58** used to construct calibration curve.

260 nm		Concentration of compound used (μM)									
		50	100	150	200	250	300	350	400	450	500
Absorbance values	1	0.181	0.317	0.449	0.586	0.798	0.891	1.003	1.153	1.240	1.413
	2	0.140	0.307	0.458	0.607	0.751	0.905	1.027	1.137	1.336	1.445
	3	0.115	0.269	0.446	0.596	0.727	0.970	1.072	1.152	1.321	1.429
	4	0.131	0.290	0.460	0.600	0.773	0.917	1.000	1.135	1.313	1.450
	5	0.162	0.292	0.431	0.601	0.793	0.918	1.024	1.139	1.355	1.451
	Mean	0.146	0.295	0.448	0.598	0.768	0.920	1.025	1.143	1.313	1.438
	Std dev.	0.023	0.016	0.010	0.007	0.027	0.027	0.026	0.008	0.039	0.015

2.2.3 Concentrations of benzodioxane hit compounds in both acceptor and donor wells after 24-hours at RT or 37°C.

2.2.3.1 Compound 16

Table XXXVI: Concentration of compound **16** recorded to be present in the acceptor and donor wells of the assay kit after 24-hours at RT and 37°C.

230nm compound 16		Temperature of assay run			
		RT		37°C	
		Acceptor	Donor	Acceptor	Donor
Concentration (µM)	1	38.724	465.386	85.150	430.598
	2	50.772	449.008	98.142	431.780
	3	48.646	469.165	67.906	436.898
	4	33.528	459.717	69.953	438.709
	5	48.882	445.701	82.630	445.559
	Mean	44.110	457.795	80.756	436.709
	Std dev.	6.763	9.100	11.017	5.366

2.2.3.2 Compound 30a

Table XXXVII: Concentration of compound **30a** recorded to be present in the acceptor and donor wells of the assay kit after 24-hours at RT and 37°C.

220nm compound 30a		Temperature of assay run			
		RT		37°C	
		Acceptor	Donor	Acceptor	Donor
Concentration (µM)	1	3.560	492.200	31.280	449.840
	2	3.160	493.400	23.680	457.840
	3	3.360	496.600	26.480	472.040
	4	4.560	530.200	24.480	453.840
	5	11.760	465.000	25.080	455.440
	Mean	5.280	495.480	26.200	457.800
	Std dev.	3.276	20.741	2.700	7.581

2.2.3.3 Compound 44

Table XXXVIII: Concentration of compound **44** recorded to be present in the acceptor and donor wells of the assay kit after 24-hours at RT and 37°C.

270nm compound 44		Temperature of assay run			
		RT		37°C	
		Acceptor	Donor	Acceptor	Donor
Concentration (µM)	1	203.306	293.714	198.367	284.694
	2	203.918	292.694	197.755	281.224
	3	204.122	293.102	203.878	285.510
	4	204.122	294.735	203.265	284.082
	5	202.286	289.837	198.776	284.694
	Mean	203.551	292.816	200.408	284.041
	Std dev.	0.700	1.641	2.610	1.480

2.2.3.4 Compound 46

Table XXXIX: Concentration of compound **46** recorded to be present in the acceptor and donor wells of the assay kit after 24-hours at RT and 37°C.

270nm compound 46		Temperature of assay run			
		RT		37°C	
		Acceptor	Donor	Acceptor	Donor
Concentration (µM)	1	70.000	443.243	87.351	430.324
	2	34.324	442.703	84.919	431.135
	3	41.351	437.838	84.378	421.676
	4	57.568	440.541	87.081	417.622
	5	41.081	440.270	82.216	431.946
	Mean	48.865	440.919	85.189	426.541
	Std dev.	13.045	1.931	1.888	5.794

2.2.3.5 Compound 47

Table XL: Concentration of compound **47** recorded to be present in the acceptor and donor wells of the assay kit after 24-hours at RT and 37°C.

270nm compound 47		Temperature of assay run			
		RT		37°C	
		Acceptor	Donor	Acceptor	Donor
Concentration (µM)	1	12.105	494.211	18.211	499.000
	2	16.316	486.579	23.474	461.632
	3	18.158	458.947	14.263	456.632
	4	16.579	490.000	15.842	490.579
	5	16.053	481.053	17.421	492.684
	Mean	15.842	482.158	17.842	480.105
	Std dev.	2.007	12.380	3.125	17.420

2.2.3.6 Compound 48

Table XLI: Concentration of compound **48** recorded to be present in the acceptor and donor wells of the assay kit after 24-hours at RT and 37°C.

240nm compound 48		Temperature of assay run			
		RT		37°C	
		Acceptor	Donor	Acceptor	Donor
Concentration (µM)	1	6.406	470.531	5.875	528.859
	2	2.891	525.219	2.359	450.734
	3	1.016	473.344	3.141	502.141
	4	3.359	476.781	1.734	500.656
	5	2.891	533.734	3.141	513.391
	Mean	3.313	495.922	3.250	499.156
	Std dev.	1.744	27.600	1.415	26.233

2.2.3.7 Compound 49

Table XLII: Concentration of compound **49** recorded to be present in the acceptor and donor wells of the assay kit after 24-hours at RT and 37°C.

230nm compound 49		Temperature of assay run			
		RT		37°C	
		Acceptor	Donor	Acceptor	Donor
Concentration (µM)	1	47.711	453.546	93.546	378.309
	2	44.825	450.247	100.041	371.093
	3	54.309	438.804	100.660	398.619
	4	64.412	397.670	118.289	442.124
	5	86.165	456.433	104.165	393.052
	Mean	59.485	439.340	103.340	396.639
	Std dev.	14.943	21.678	8.223	24.796

2.2.3.8 Compound 50a

Table XLIII: Concentration of compound **50a** recorded to be present in the acceptor and donor wells of the assay kit after 24-hours at RT and 37°C.

260nm compound 50a		Temperature of assay run			
		RT		37°C	
		Acceptor	Donor	Acceptor	Donor
Concentration (µM)	1	31.333	471.067	75.533	444.533
	2	26.333	470.067	42.867	442.200
	3	31.333	460.733	66.533	440.533
	4	30.667	471.067	55.200	442.867
	5	39.667	469.400	53.533	439.533
	Mean	31.867	468.467	58.733	441.933
	Std dev.	4.324	3.918	11.264	1.756

2.2.3.9 Compound 52a

Table XLIV: Concentration of compound **52a** recorded to be present in the acceptor and donor wells of the assay kit after 24-hours at RT and 37°C.

220nm compound 52a		Temperature of assay run			
		RT		37°C	
		Acceptor	Donor	Acceptor	Donor
Concentration (µM)	1	64.963	448.148	124.519	473.741
	2	82.370	425.926	51.741	362.815
	3	57.741	436.481	64.704	405.593
	4	57.370	438.704	94.148	411.889
	5	67.000	432.407	106.741	451.889
	Mean	65.889	436.333	88.370	421.185
	Std dev.	9.085	7.334	26.756	38.578

2.2.3.10 Compound 53

Table XLV: Concentration of compound **53** recorded to be present in the acceptor and donor wells of the assay kit after 24-hours at RT and 37°C.

280nm compound 53		Temperature of assay run			
		RT		37°C	
		Acceptor	Donor	Acceptor	Donor
Concentration (µM)	1	46.400	446.267	88.533	441.200
	2	63.733	438.933	83.200	451.200
	3	69.733	434.267	67.867	476.533
	4	94.400	430.933	59.867	406.533
	5	72.400	441.600	59.867	396.533
	Mean	69.333	438.400	71.867	434.400
	Std dev.	15.461	5.390	11.918	29.374

2.2.3.11 Compound 54

Table XLVI: Concentration of compound **54** recorded to be present in the acceptor and donor wells of the assay kit after 24-hours at RT and 37°C.

240nm compound 54		Temperature of assay run			
		RT		37°C	
		Acceptor	Donor	Acceptor	Donor
Concentration (µM)	1	173.750	333.625	153.250	379.625
	2	178.125	332.375	144.500	372.125
	3	163.125	330.500	136.375	349.625
	4	150.625	363.625	144.500	377.750
	5	120.000	348.000	143.875	345.250
	Mean	157.125	341.625	144.500	364.875
	Std dev.	20.851	12.633	5.347	14.516

2.2.3.12 Compound 55

Table XLVII: Concentration of compound **55** recorded to be present in the acceptor and donor wells of the assay kit after 24-hours at RT and 37°C.

230nm compound 55		Temperature of assay run			
		RT		37°C	
		Acceptor	Donor	Acceptor	Donor
Concentration (µM)	1	20.400	466.200	18.700	471.800
	2	8.900	450.700	25.200	494.300
	3	30.900	471.700	34.200	435.800
	4	22.400	467.200	18.200	518.800
	5	24.400	532.700	13.700	478.800
	Mean	21.400	477.700	22.000	479.900
	Std dev.	7.176	28.399	7.118	27.321

2.2.3.13 Compound 56

Table XLVIII: Concentration of compound **56** recorded to be present in the acceptor and donor wells of the assay kit after 24-hours at RT and 37°C.

280nm compound 56		Temperature of assay run			
		RT		37°C	
		Acceptor	Donor	Acceptor	Donor
Concentration (µM)	1	75.500	409.500	90.667	408.167
	2	94.667	357.833	94.833	399.000
	3	63.833	382.833	103.167	376.500
	4	64.667	434.500	83.167	405.667
	5	139.667	383.667	85.667	394.833
	Mean	87.667	393.667	91.500	396.833
	Std dev.	28.277	26.151	7.091	11.213

2.2.3.14 Compound 57

Table XLIX: Concentration of compound **57** recorded to be present in the acceptor and donor wells of the assay kit after 24-hours at RT and 37°C.

230nm compound 57		Temperature of assay run			
		RT		37°C	
		Acceptor	Donor	Acceptor	Donor
Concentration (µM)	1	186.593	322.370	173.111	272.444
	2	189.926	321.630	169.407	299.852
	3	191.778	288.296	171.259	295.778
	4	194.741	305.333	176.074	370.963
	5	179.556	340.148	166.074	347.630
	Mean	188.519	315.556	171.185	317.333
	Std dev.	5.203	17.525	3.373	36.275

2.2.3.15 Compound 58

Table L: Concentration of compound **58** recorded to be present in the acceptor and donor wells of the assay kit after 24-hours at RT and 37°C.

260 nm compound 58		Temperature of assay run			
		RT		37°C	
		Acceptor	Donor	Acceptor	Donor
Concentration (µM)	1	20.690	476.621	155.034	356.414
	2	17.586	493.517	177.103	340.897
	3	11.379	495.931	151.586	337.448
	4	16.207	485.586	138.828	360.897
	5	17.241	482.483	179.172	333.310
	Mean	16.621	486.828	160.345	345.793
	Std dev.	3.017	7.102	15.513	10.866

2.2.4 Equilibrium standard absorbance values for benzodioxane hit compounds.

Table LI: Absorbance values of the equilibrium standards at the corresponding wavelength for the benzodioxane hit compounds.

		Absorbance (Abs)						
		1	2	3	4	5	Mean	Std dev.
Compound	16	2.534	2.424	2.412	2.482	2.810	2.532	0.145
	30a	1.071	0.899	1.142	0.921	1.077	1.022	0.095
	44	0.924	1.009	0.924	1.109	1.039	1.001	0.071
	46	0.769	0.757	0.785	0.780	0.812	0.780	0.018
	47	0.761	0.765	0.758	0.767	0.778	0.766	0.007
	48	2.527	2.627	2.538	2.552	2.602	2.569	0.039
	49	1.849	1.958	2.010	1.879	2.089	1.957	0.087
	50a	0.538	0.554	0.540	0.525	0.553	0.542	0.011
	52a	1.214	1.037	0.934	0.950	0.740	0.975	0.154
	53	0.309	0.276	0.328	0.293	0.299	0.301	0.017
	54	0.310	0.313	0.259	0.269	0.311	0.292	0.023
	55	0.330	0.342	0.428	0.600	0.348	0.410	0.101
	56	0.792	0.792	0.715	0.823	0.797	0.784	0.036
	57	0.522	0.517	0.540	0.559	0.498	0.527	0.021
58	0.598	0.587	0.591	0.589	0.574	0.588	0.008	

The above blank corrected absorbance values shown in **Table LI** were utilised in the equation to calculate the permeability rate. These values are the same regardless of assay temperature.

2.2.5 Permeability rate results for benzodioxane hit compounds.

Table LII: Permeability rate values for benzodioxane hit compounds at RT.

		Permeability rate at RT (cm/s)						
		1	2	3	4	5	Mean	Std dev.
Compound	16	1.25E-06	1.70E-06	1.62E-06	1.07E-06	1.63E-06	1.45E-06	2.50E-07
	30a	1.03E-07	9.13E-08	9.71E-08	1.32E-07	3.44E-07	1.53E-07	9.636E-08
	44	1.88E-05	3.65E-05	4.06E-05	4.06E-05	2.71E-05	3.27E-05	8.55E-06
	46	2.34E-06	1.03E-06	1.26E-06	1.85E-06	1.25E-06	1.55E-06	4.788E-07
	47	9.92E-07	1.38E-06	1.56E-06	1.41E-06	1.36E-06	1.34E-06	1.875E-07
	48	1.88E-07	8.39E-08	2.94E-08	9.77E-08	8.40E-08	9.65E-08	5.127E-08
	49	1.56E-06	1.46E-06	1.82E-06	2.23E-06	3.22E-06	2.06E-06	6.412E-07
	50a	1.11E-06	9.19E-07	1.11E-06	1.09E-06	1.45E-06	1.13E-06	1.718E-07
	52a	2.58E-06	3.53E-06	2.13E-06	2.21E-06	2.69E-06	2.63E-06	4.965E-07
	53	1.17E-06	1.81E-06	2.06E-06	3.17E-06	2.17E-06	2.08E-06	6.488E-07
	54	1.76E-05	2.16E-05	1.30E-05	1.01E-05	6.20E-06	1.37E-05	5.423E-06
	55	6.41E-07	2.60E-07	9.49E-07	6.73E-07	7.37E-07	6.52E-07	2.234E-07
	56	2.09E-06	6.29E-06	2.74E-06	2.79E-06	1.00E-05	4.79E-06	3.010E-06
	57	1.81E-05	2.06E-05	2.36E-05	3.04E-05	1.46E-05	2.15E-05	5.344E-06
58	6.23E-07	5.25E-07	3.34E-07	4.82E-07	5.14E-07	4.96E-07	9.340E-08	

Table LIII: Permeability rate values for benzodioxane hit compounds at 37 °C.

		Permeability rate at 37 °C (cm/s)						
		1	2	3	4	5	Mean	Std dev.
Compound	16	1.44E-06	1.38E-06	1.48E-06	1.37E-06	1.38E-06	1.41E-06	4.308E-08
	30a	9.59E-07	7.10E-07	8.00E-07	7.36E-07	7.55E-07	7.92E-07	8.838E-08
	44	2.05E-05	1.99E-05	3.60E-05	3.07E-05	1.04E-05	2.35E-05	8.940E-06
	46	3.09E-06	2.98E-06	2.96E-06	3.08E-06	2.86E-06	2.99E-06	8.57E-08
	47	5.42E-07	7.15E-07	4.23E-07	4.72E-07	5.21E-07	5.35E-07	9.905E-08
	48	1.72E-07	6.80E-08	9.08E-08	4.98E-08	9.08E-08	9.42E-08	4.162E-08
	49	3.60E-06	3.96E-06	4.00E-06	5.11E-06	4.20E-06	4.17E-06	5.041E-07
	50a	3.14E-06	1.57E-06	2.67E-06	2.12E-06	2.04E-06	2.31E-06	5.423E-07
	52a	6.76E-06	1.95E-06	2.56E-06	4.26E-06	5.17E-06	4.14E-06	1.745E-06
	53	2.85E-06	2.60E-06	1.95E-06	1.63E-06	1.63E-06	2.13E-06	5.031E-07
	54	1.06E-05	9.06E-06	7.94E-06	9.06E-06	8.97E-06	9.12E-06	8.385E-07
	55	5.47E-07	7.53E-07	1.05E-06	5.32E-07	3.94E-07	6.55E-07	2.278E-07
	56	8.66E-07	9.09E-07	9.96E-07	7.90E-07	8.15E-07	8.75E-07	7.328E-08
	57	1.26E-05	1.17E-05	1.21E-05	1.34E-05	1.10E-05	1.21E-05	8.161E-07
58	8.39E-06	1.20E-05	7.99E-06	6.69E-06	1.25E-05	9.51E-06	2.302E-06	

2.3 Compound 30a spot plate results.

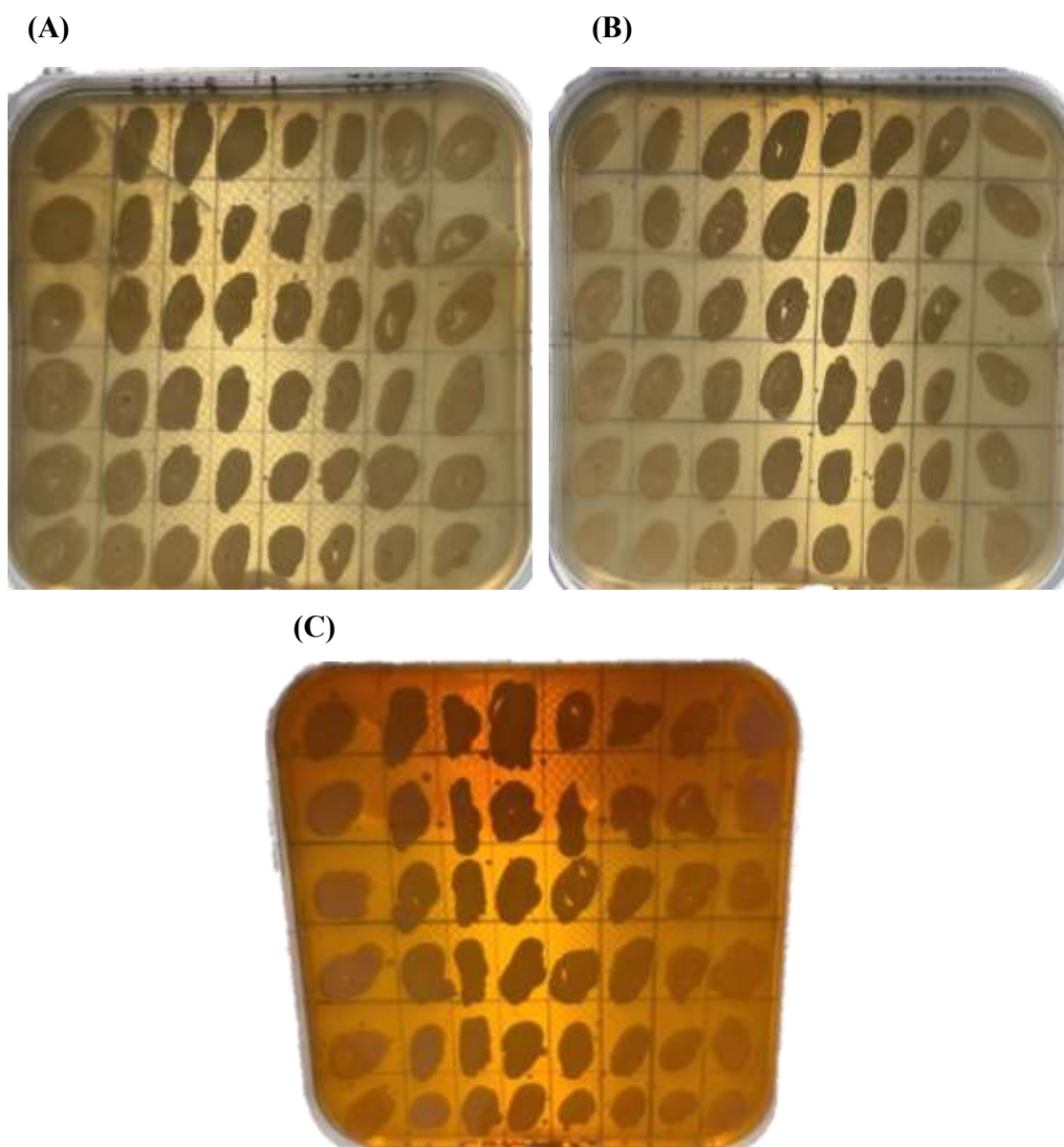


Figure CIII: Spot plate results of compound **30a** after a 48-hour incubation.

Maximum concentration of 250 μM is found at the bottom of each plate, with the top having no Compound **30a** (0 μM) present. For (A) and (B) the OD_{600} value of the yeast cells used was 1.0, where a few drops were added per outlined section.

(A): PTP only cells, where left is PTP1B only and right is TCPTP only transcribed cells. (B) PTP + v-Src cells, where left is PTP1B + v-Src and right is TCPTP + v-Src transcribed cells. (C) Untransformed YMK23 cells, left the OD_{600} value of the yeast cells used was 1.0, and for the right-hand side the OD_{600} value of the yeast cells used was 0.1.

From visualising the final results from the 48-hour incubation, it suggests that compound **30a** is not inherently toxic to any of the transformed cells at a concentration of 250 μM or below. From monitoring the visible growth progression in person both versions of PTP + v-Src cells had a general dose dependent relationship to the concentration of compound **30a**. This was not the case for the untransformed or PTP only cells as expected, however

the visible trend is less clear. Hence the upward trend of T_d times in just PTP cell lines is presumed to not be due to toxicity but instead, it is proposed to be due to the clumping and the subsequent crashing out of cells at higher concentrations, an example of this phenomenon of cells crashing out is demonstrated in section 1.8.

2.4 Computational binding modes of comp 57 in PTP active sites

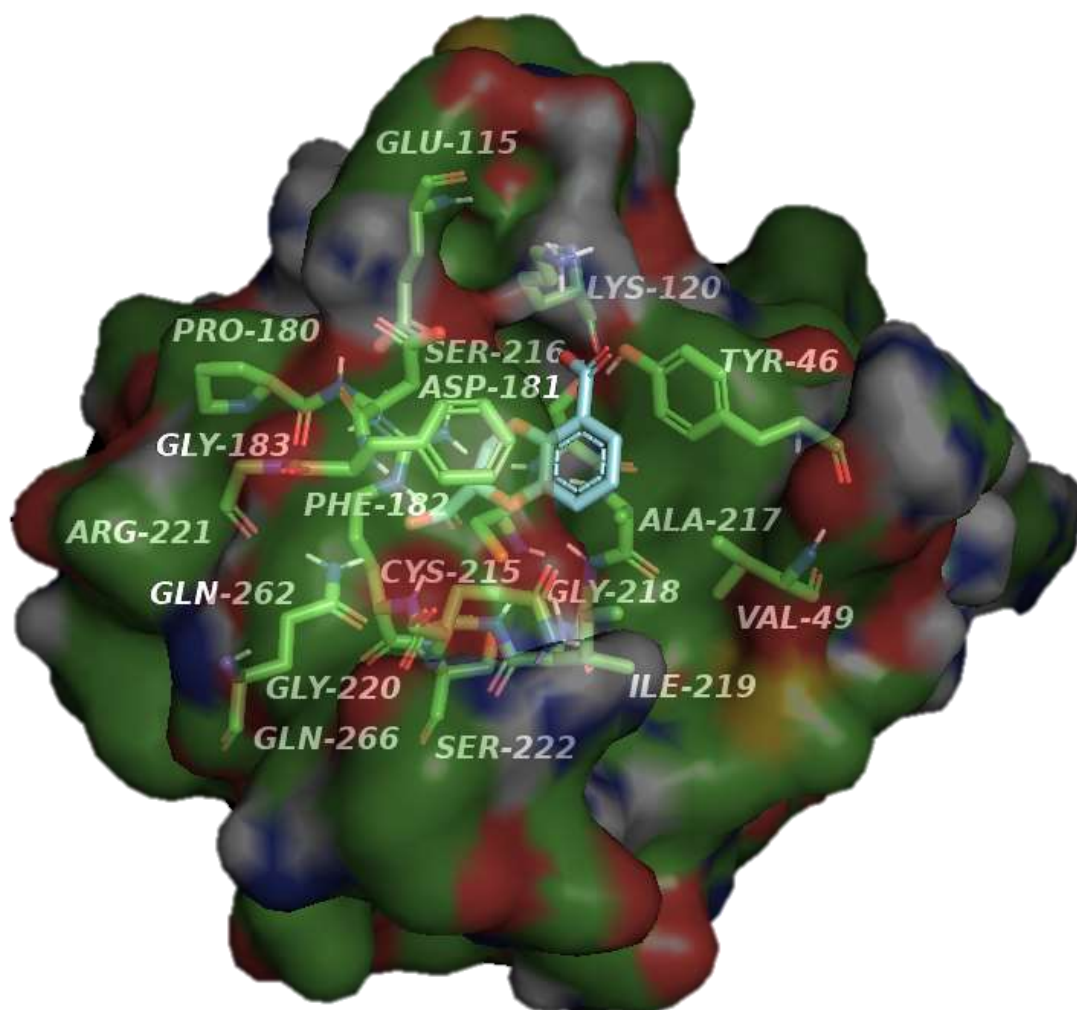


Figure CIV: Computational most favoured proposed binding mode of compound **57** in the closed conformation of the PTP1B active site.

The non-aromatic carboxylic acid can interact with Cys-215 and its surrounding residues of Ser-216, Ala-217, Gly-220 and Arg-221, in a manner comparable to compounds **30a** and **55**. The present aromatic system can π -stack with Phe-182 and Tyr-46. Further interactions include the benzodioxane oxygens, which may be able to hydrogen bond with amine of Ala-217 and the phenol of Tyr-46. The aromatic carboxylic acid is predicted to interact with the amine of the Lys-120 via the electrostatic interaction of a hydrogen bond.

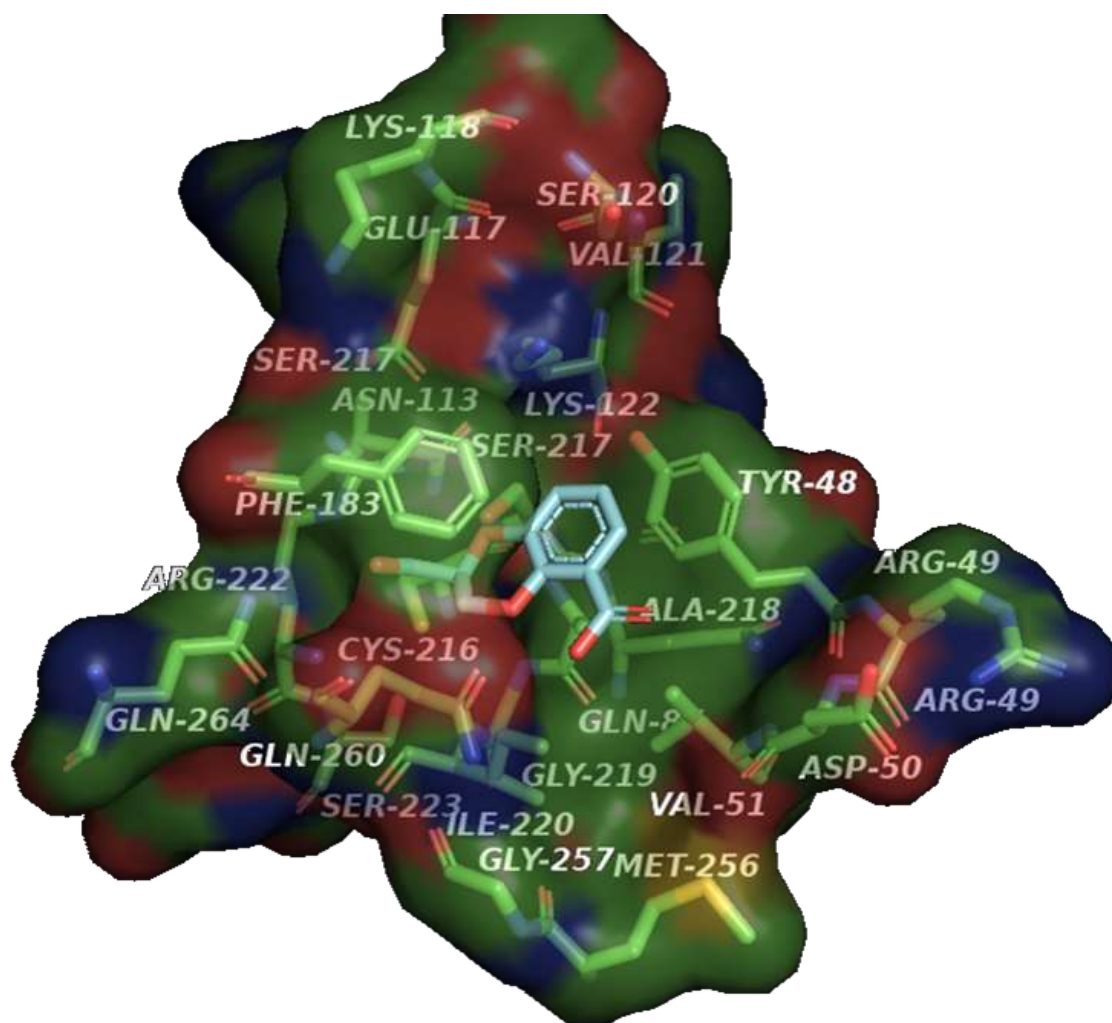


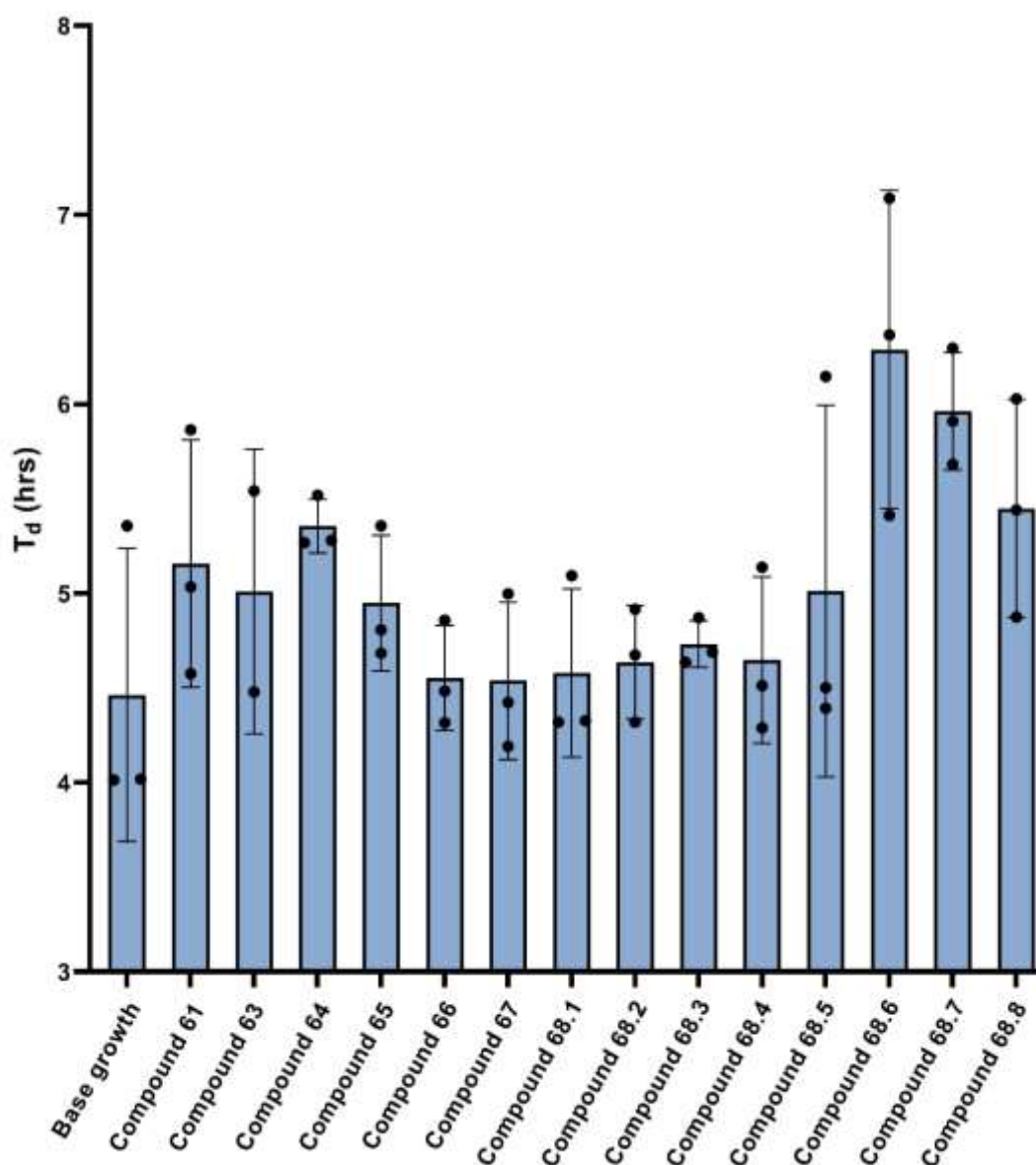
Figure CV: Computational most favoured proposed binding mode of compound **57** in the closed conformation of the TCPTP active site.

The non-aromatic carboxylic acid can interact with Cys-216 and its surrounding residues of Ser-217, Ala-218, Gly-221 and Arg-222, in a manner comparable to compounds **30a** and **55**. The present aromatic system can π -stack with Phe-183 and Tyr-48. Further interactions include the benzodioxane oxygens, which may be able to hydrogen bond with the amine of Ala-218 and the phenol of Tyr-48. The aromatic carboxylic acid is predicted to interact with the amide of the Gln-260.

3. Content relating to Chapter 5: Spirocyclic dihydropyrazole based.

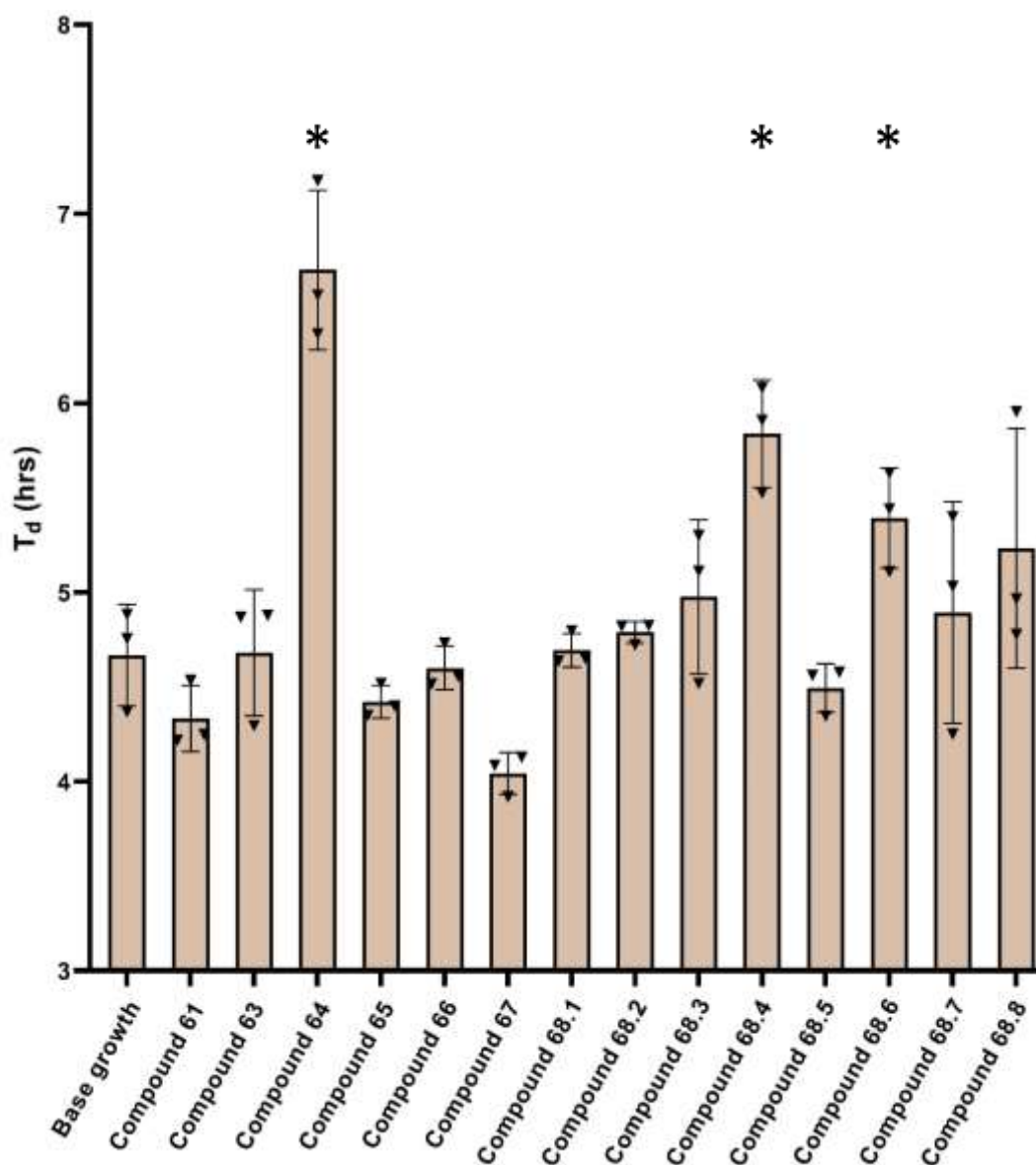
3.1 Doubling time and growth curve data of all spirocyclic dihydropyrazoles and related precursor compounds tested.

3.1.1 Sulfonyl hydrazones tested, compounds 61, 63-68.



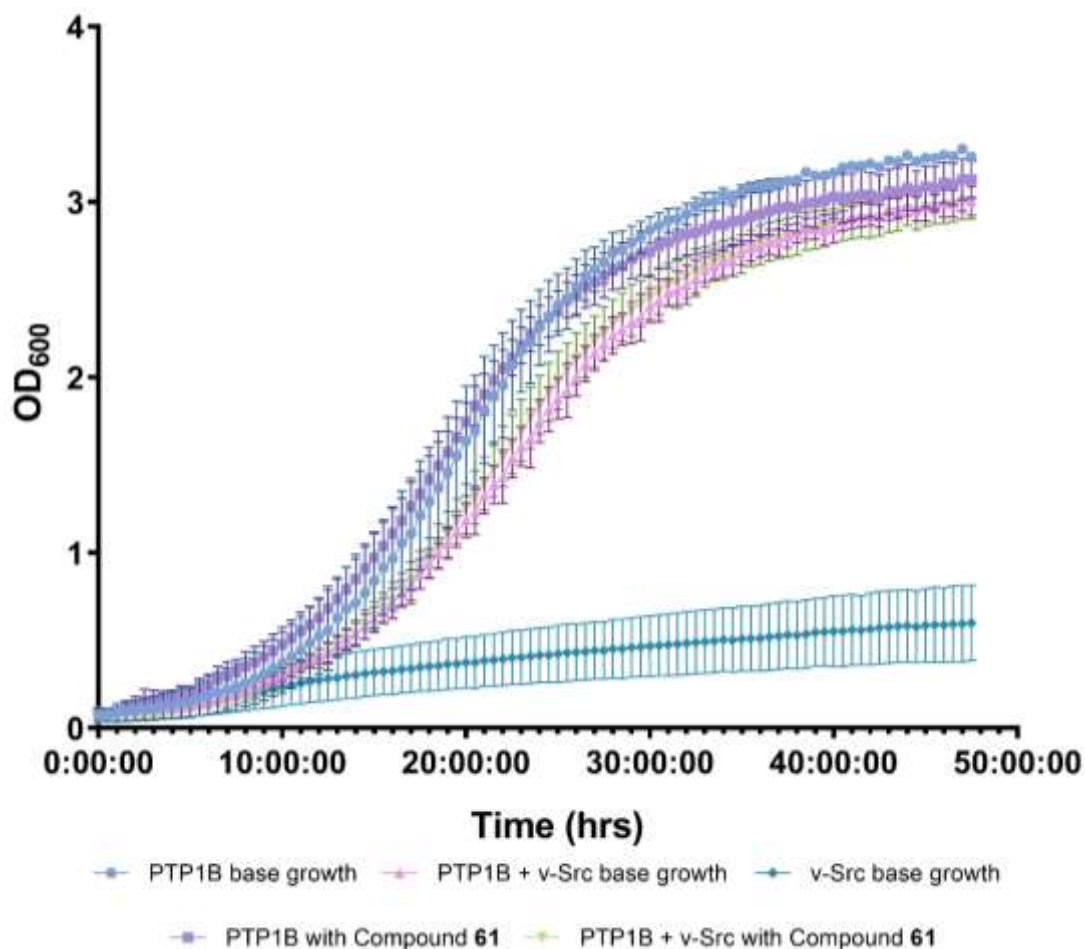
Compound	61	63	64	65	66	67	68.1	68.2	68.3	68.4	68.5	68.6	68.7	68.8
p value	ns	ns	ns	ns	ns	ns	ns	ns	ns	ns	ns	ns	ns	ns

Figure CVI: Effect of compound 61, 63-68 addition at 100 μ M on the T_d value of PTP1B only transformed yeast cells. n=3 for all compounds tested and n=3 for base growth. Mean points \pm standard deviation plotted. Data is normally distributed according to a Shapiro-Wilk test. Used parametric Welch t-test for statistical analysis. * p value \leq 0.050 vs base growth.



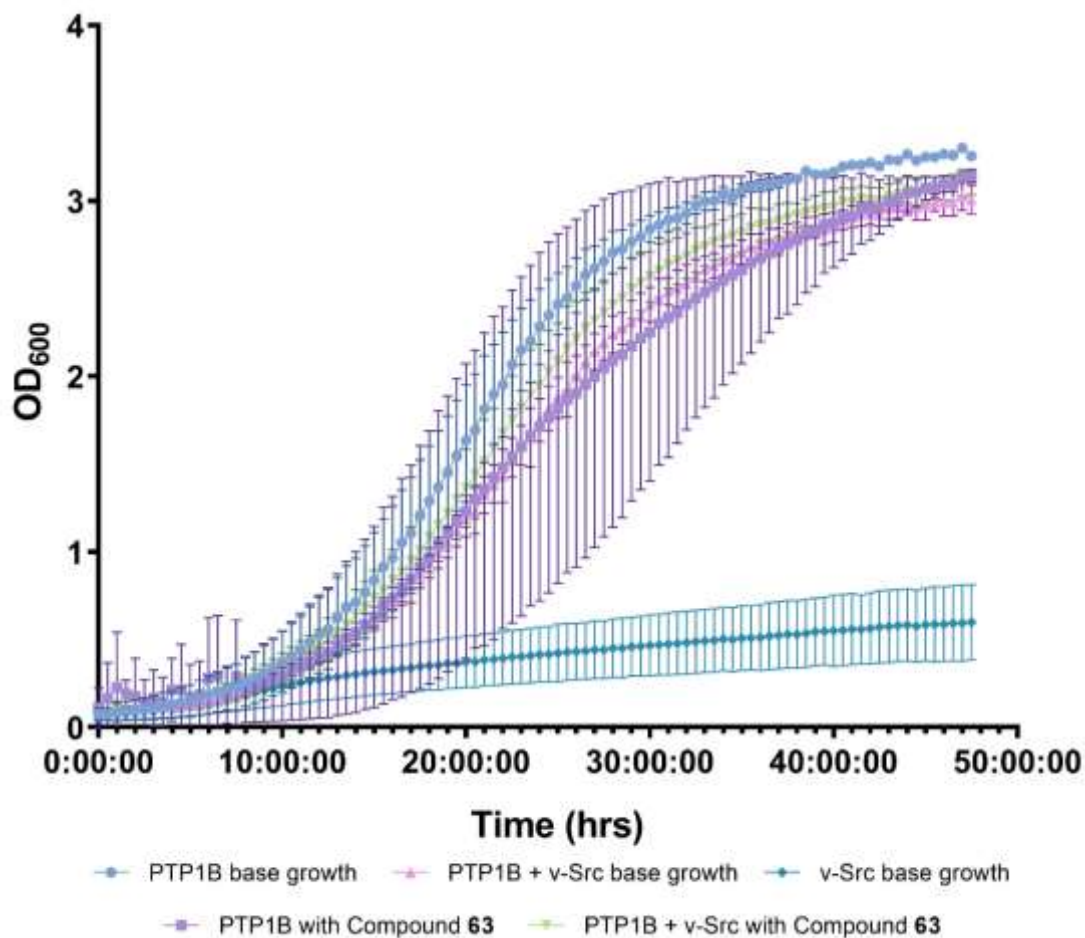
Compound	p value
61	ns
63	ns
64	<0.0050
65	ns
66	ns
67	<0.0500
68.1	ns
68.2	ns
68.3	ns
68.4	<0.0100
68.5	ns
68.6	<0.0500
68.7	ns
68.8	ns

Figure CVII: Effect of compound **61**, **63-68** addition at 100 μ M on the T_d value of PTP1B + v-Src transformed yeast cells. n=3 for all compounds tested and n=3 for base growth. Mean points \pm standard deviation plotted. Data is normally distributed according to a Shapiro-Wilk test. Used parametric Welch t-test for statistical analysis. * p value \leq 0.050 vs base growth. Note: Compound **67** addition resulted in a significant decrease in the T_d of the PTP1B + v-Src transformed cells



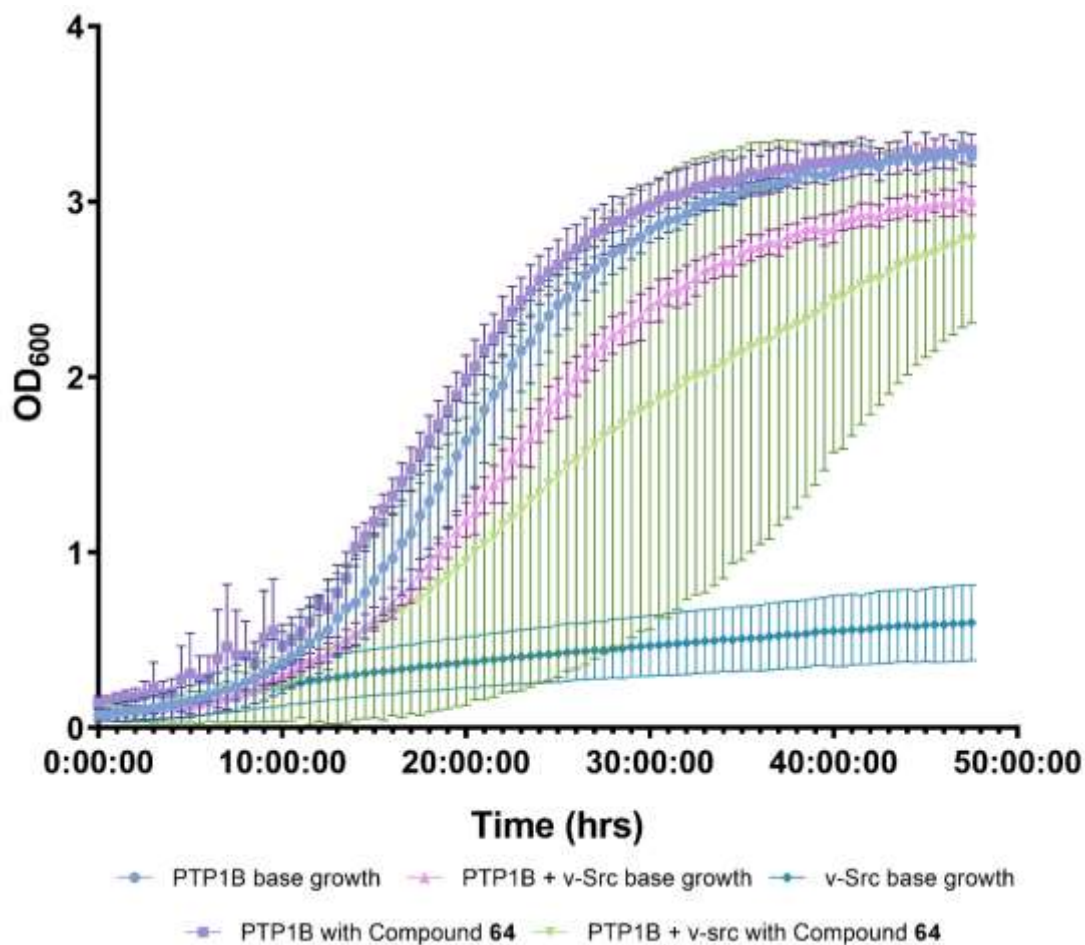
Transformed cells	PTP1B only	PTP1B + v-Src
p value	ns	ns

Figure CVIII: Growth curves of PTP1B only, PTP1B + v-Src and v-Src only YMK23 transformations with and without the addition of compound **61** at 100µM. n=3 for each PTP1B based parameter, n=13 for v-Src. Mean and individual biological points ± standard deviation plotted. Data is normally distributed according to a Shapiro-Wilk test. Used a 2-way ANOVA. * p value ≤ 0.050 vs corresponding base growth.



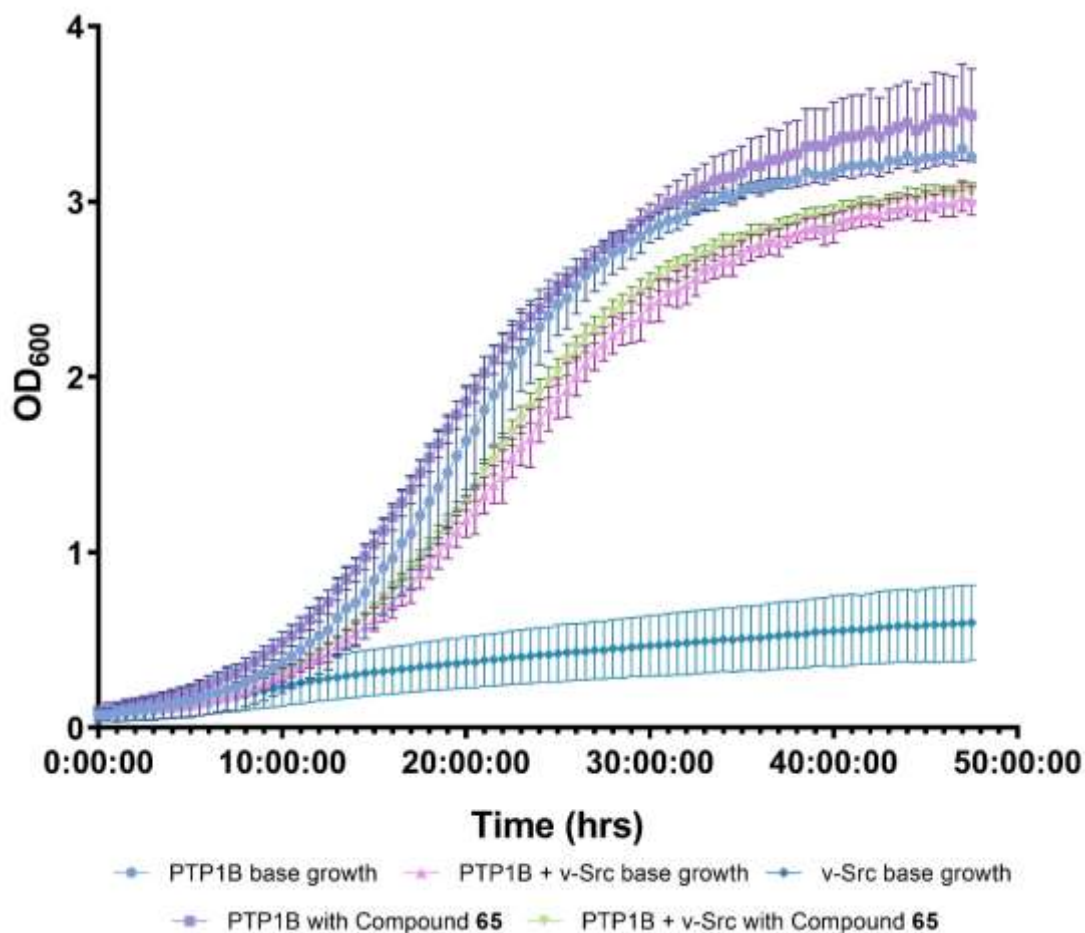
Transformed cells	PTP1B only	PTP1B + v-Src
p value	ns	ns

Figure CIX: Growth curves of PTP1B only, PTP1B + v-Src and v-Src only YMK23 transformations with and without the addition of compound **63** at 100 μ M. n=3 for each PTP1B based parameter, n=13 for v-Src. Mean and individual biological points \pm standard deviation plotted. Data is normally distributed according to a Shapiro-Wilk test. Used a 2-way ANOVA. * p value \leq 0.050 vs corresponding base growth.



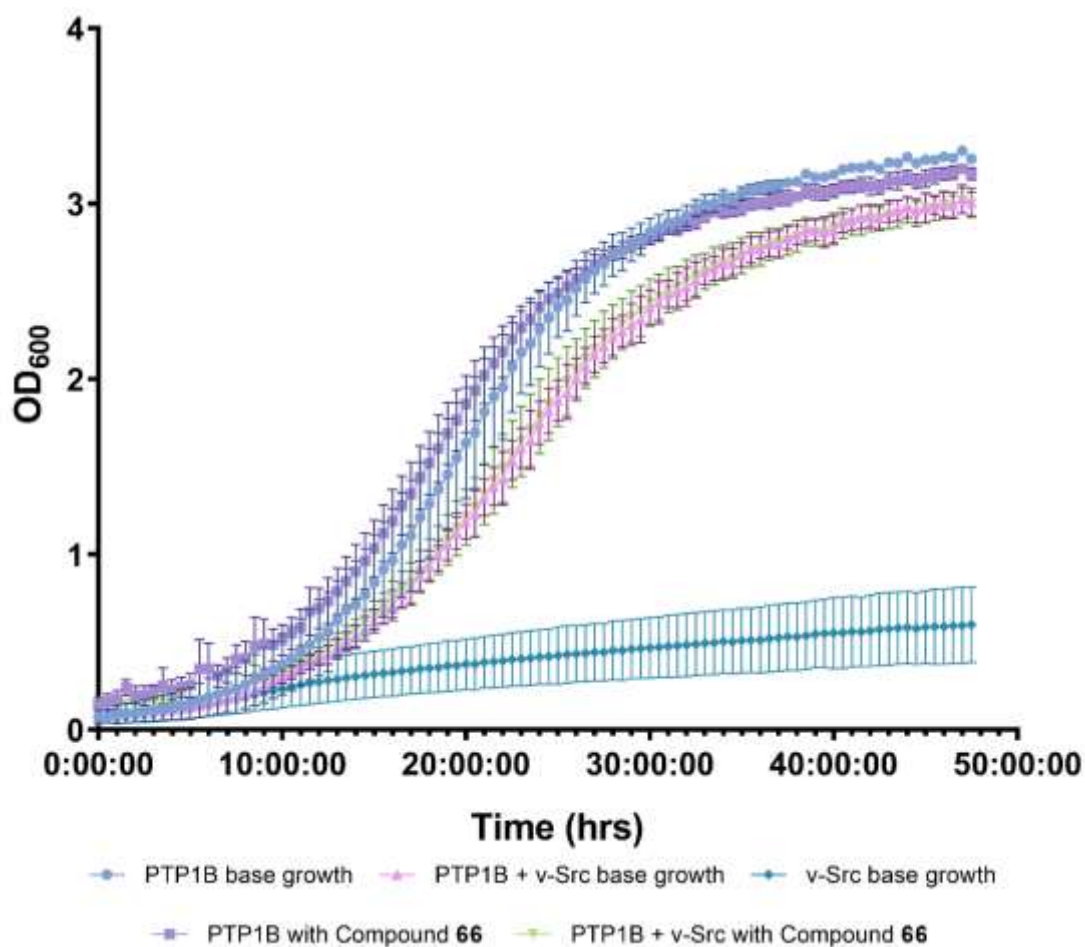
Transformed cells	PTP1B only	PTP1B + v-Src
p value	ns	ns

Figure CX: Growth curves of PTP1B only, PTP1B + v-Src and v-Src only YMK23 transformations with and without the addition of compound **64** at 100 μ M. n=3 for each PTP1B based parameter, n=13 for v-Src. Mean and individual biological points \pm standard deviation plotted. Data is normally distributed according to a Shapiro-Wilk test. Used a 2-way ANOVA. * p value \leq 0.050 vs corresponding base growth.



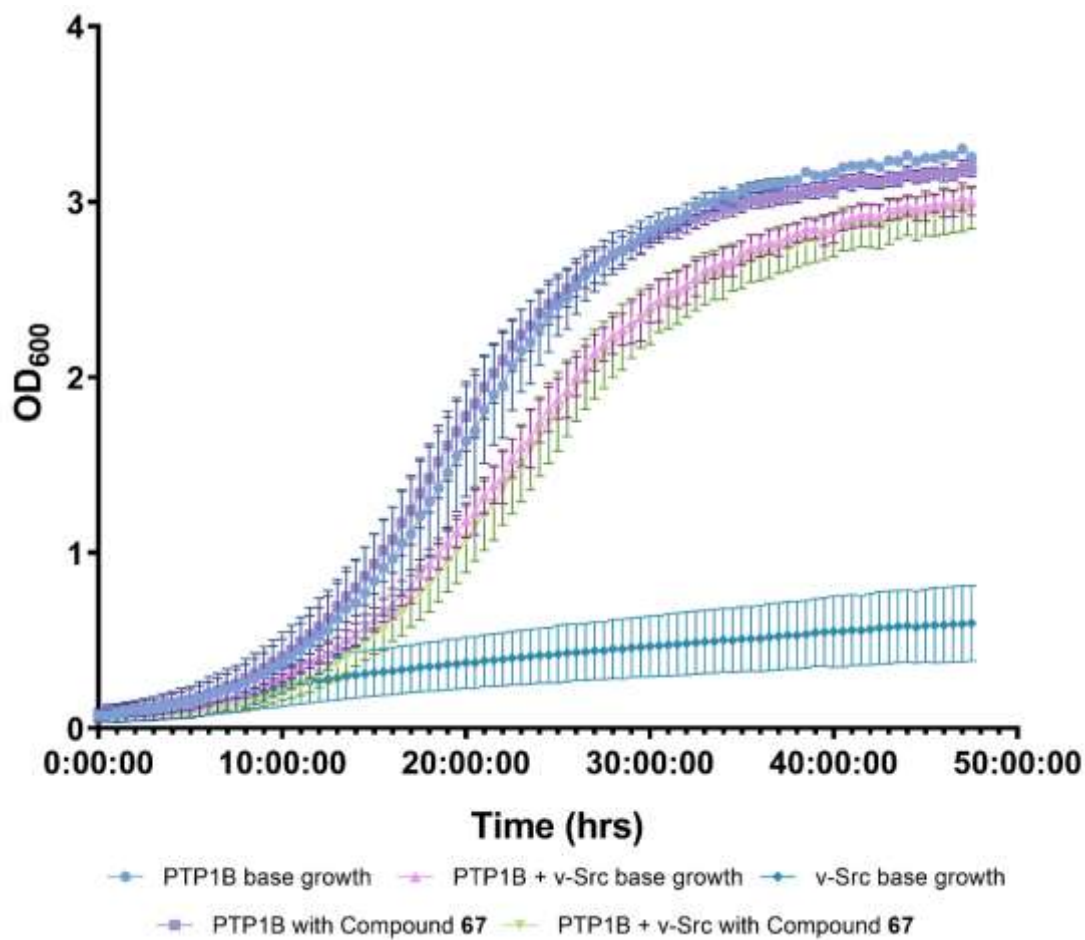
Transformed cells	PTP1B only	PTP1B + v-Src
p value	ns	ns

Figure CXI: Growth curves of PTP1B only, PTP1B + v-Src and v-Src only YMK23 transformations with and without the addition of compound **65** at 100 μ M. n=3 for each PTP1B based parameter, n=13 for v-Src. Mean and individual biological points \pm standard deviation plotted. Data is normally distributed according to a Shapiro-Wilk test. Used a 2-way ANOVA. * p value \leq 0.050 vs corresponding base growth.



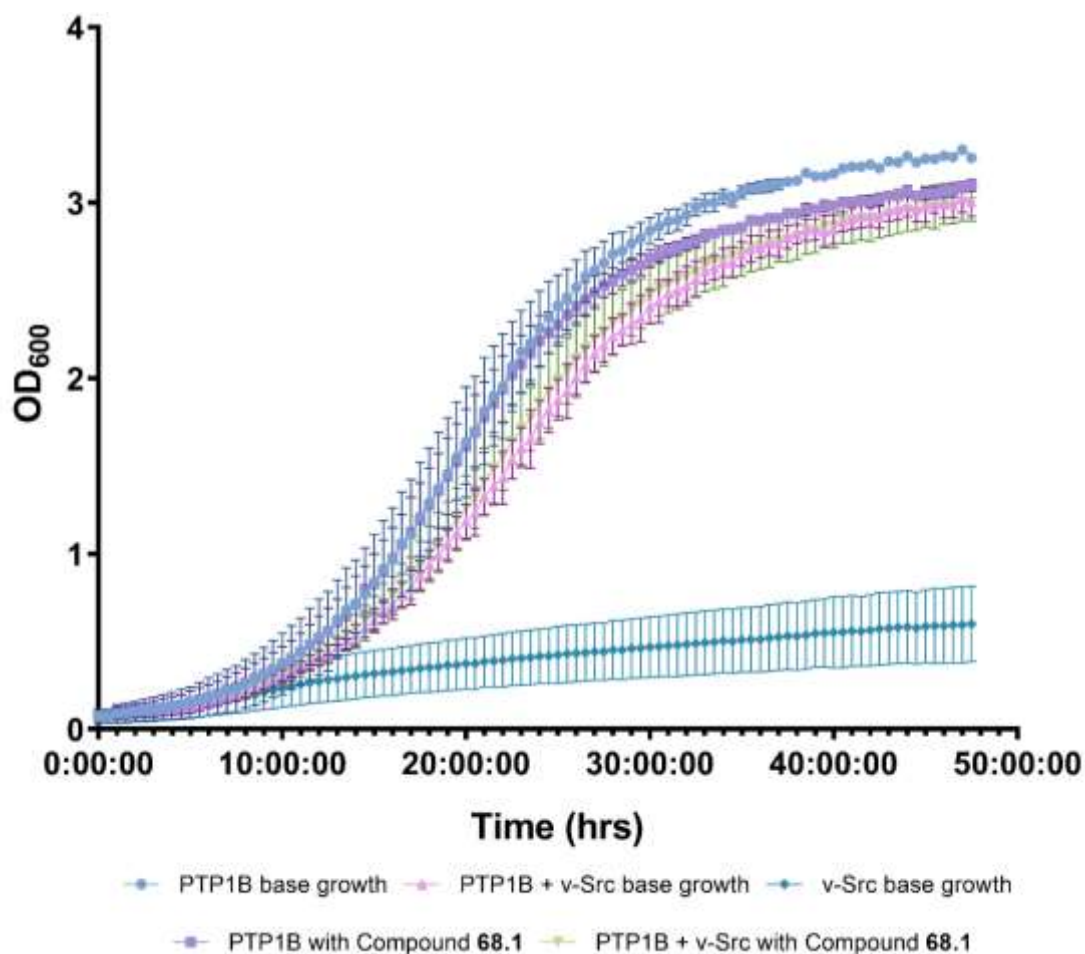
Transformed cells	PTP1B only	PTP1B + v-Src
p value	ns	ns

Figure CXII: Growth curves of PTP1B only, PTP1B + v-Src and v-Src only YMK23 transformations with and without the addition of compound **66** at 100µM. n=3 for each PTP1B based parameter, n=13 for v-Src. Mean and individual biological points ± standard deviation plotted. Data is normally distributed according to a Shapiro-Wilk test. Used a 2-way ANOVA. * p value ≤ 0.050 vs corresponding base growth.



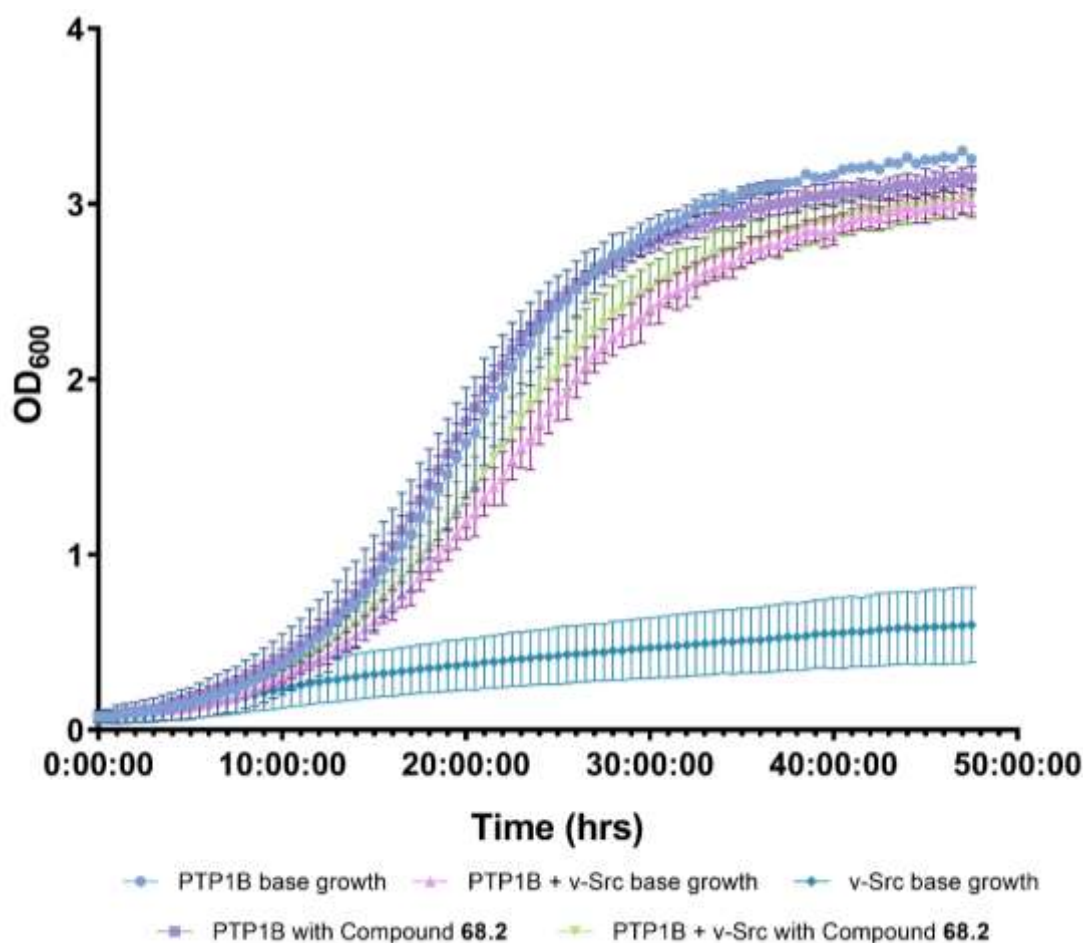
Transformed cells	PTP1B only	PTP1B + v-Src
p value	ns	ns

Figure CXIII: Growth curves of PTP1B only, PTP1B + v-Src and v-Src only YMK23 transformations with and without the addition of compound **67** at 100 μ M. n=3 for each PTP1B based parameter, n=13 for v-Src. Mean and individual biological points \pm standard deviation plotted. Data is normally distributed according to a Shapiro-Wilk test. Used a 2-way ANOVA. * p value \leq 0.050 vs corresponding base growth.



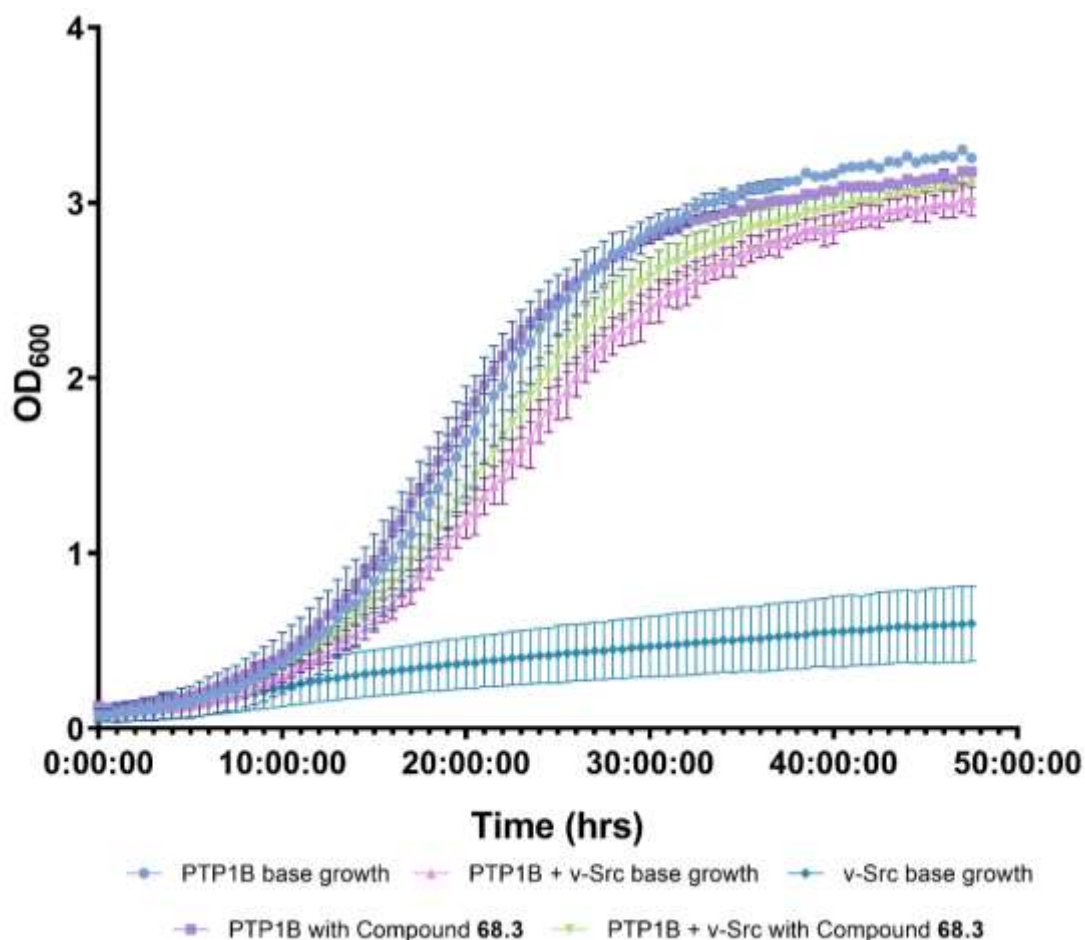
Transformed cells	PTP1B only	PTP1B + v-Src
p value	ns	ns

Figure CXIV: Growth curves of PTP1B only, PTP1B + v-Src and v-Src only YMK23 transformations with and without the addition of compound **68.1** at 100µM. n=3 for each PTP1B based parameter, n=13 for v-Src. Mean and individual biological points ± standard deviation plotted. Data is normally distributed according to a Shapiro-Wilk test. Used a 2-way ANOVA. * p value ≤ 0.050 vs corresponding base growth.



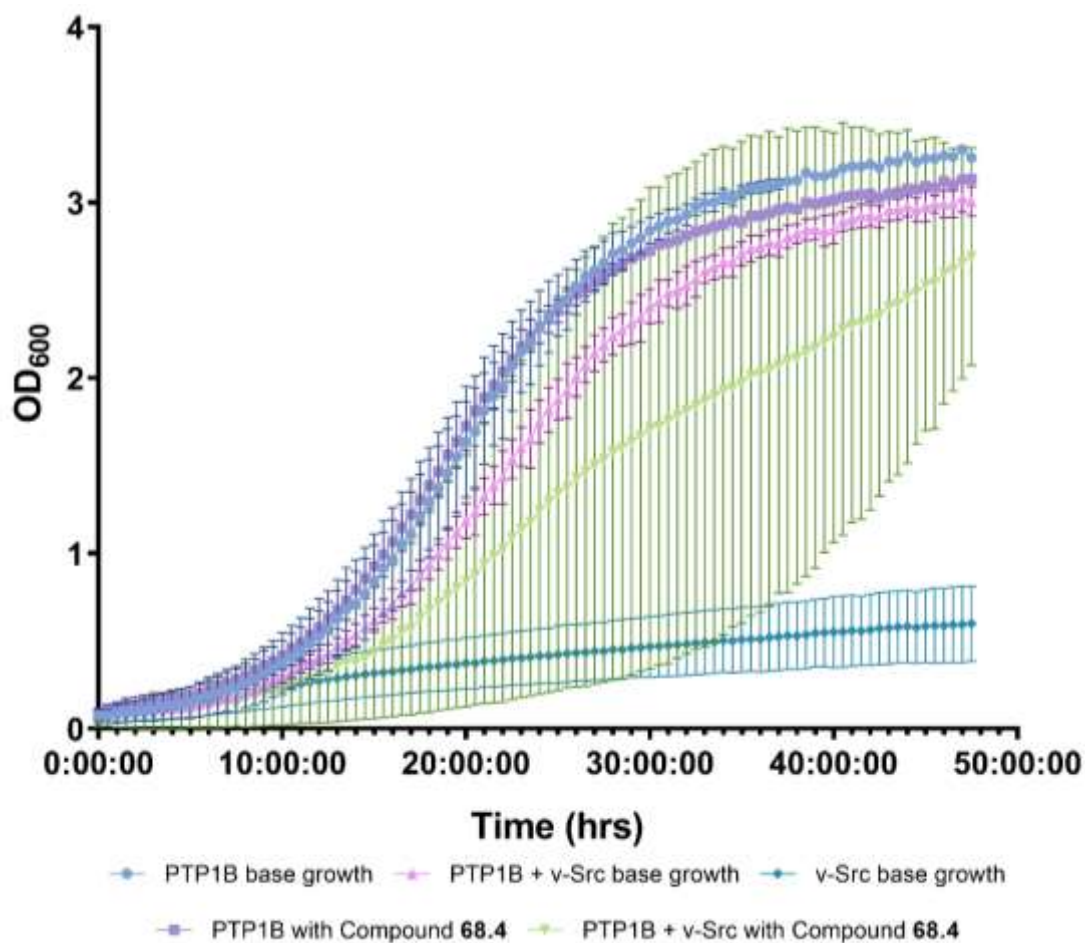
Transformed cells	PTP1B only	PTP1B + v-Src
p value	ns	ns

Figure CXV: Growth curves of PTP1B only, PTP1B + v-Src and v-Src only YMK23 transformations with and without the addition of compound **68.2** at 100 μ M. n=3 for each PTP1B based parameter, n=13 for v-Src. Mean and individual biological points \pm standard deviation plotted. Data is normally distributed according to a Shapiro-Wilk test. Used a 2-way ANOVA. * p value \leq 0.050 vs corresponding base growth.



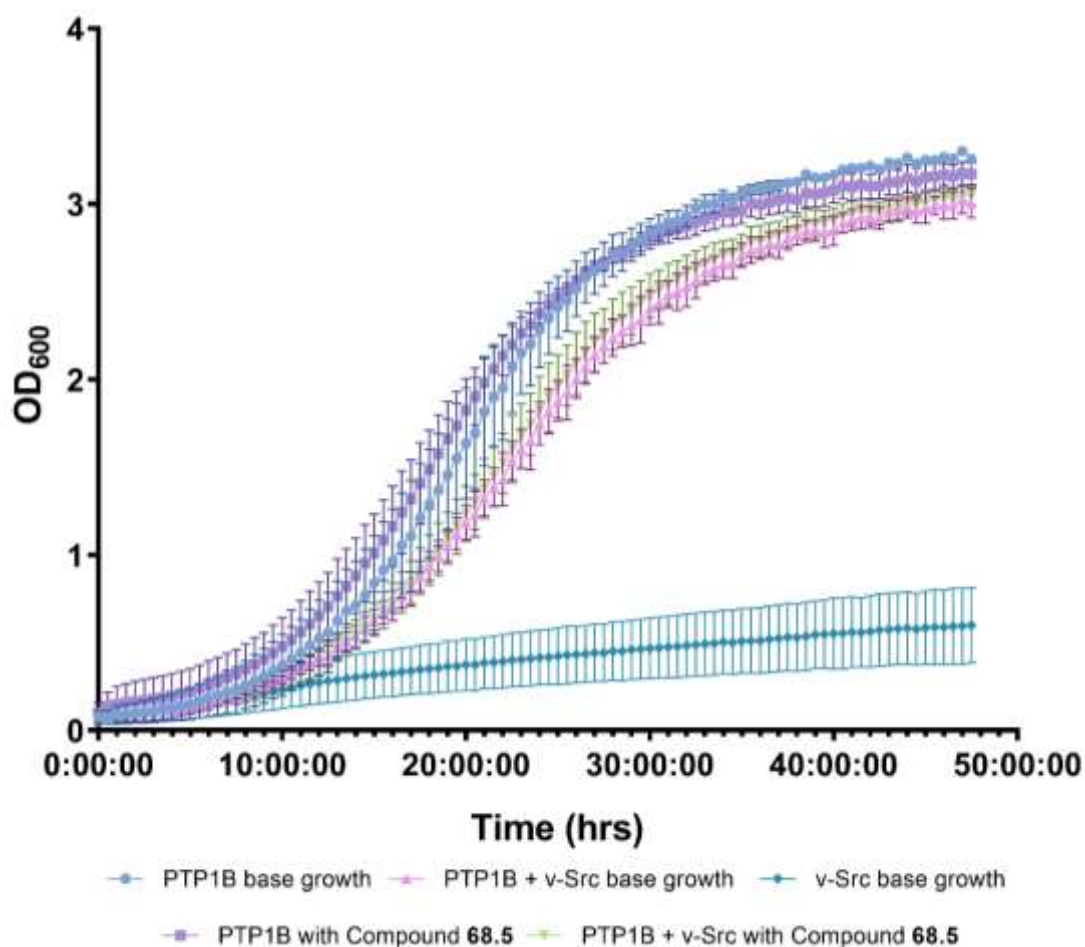
Transformed cells	PTP1B only	PTP1B + v-Src
p value	ns	ns

Figure CXVI: Growth curves of PTP1B only, PTP1B + v-Src and v-Src only YMK23 transformations with and without the addition of compound **68.3** at 100 μ M. n=3 for each PTP1B based parameter, n=13 for v-Src. Mean and individual biological points \pm standard deviation plotted. Data is normally distributed according to a Shapiro-Wilk test. Used a 2-way ANOVA. * p value \leq 0.050 vs corresponding base growth.



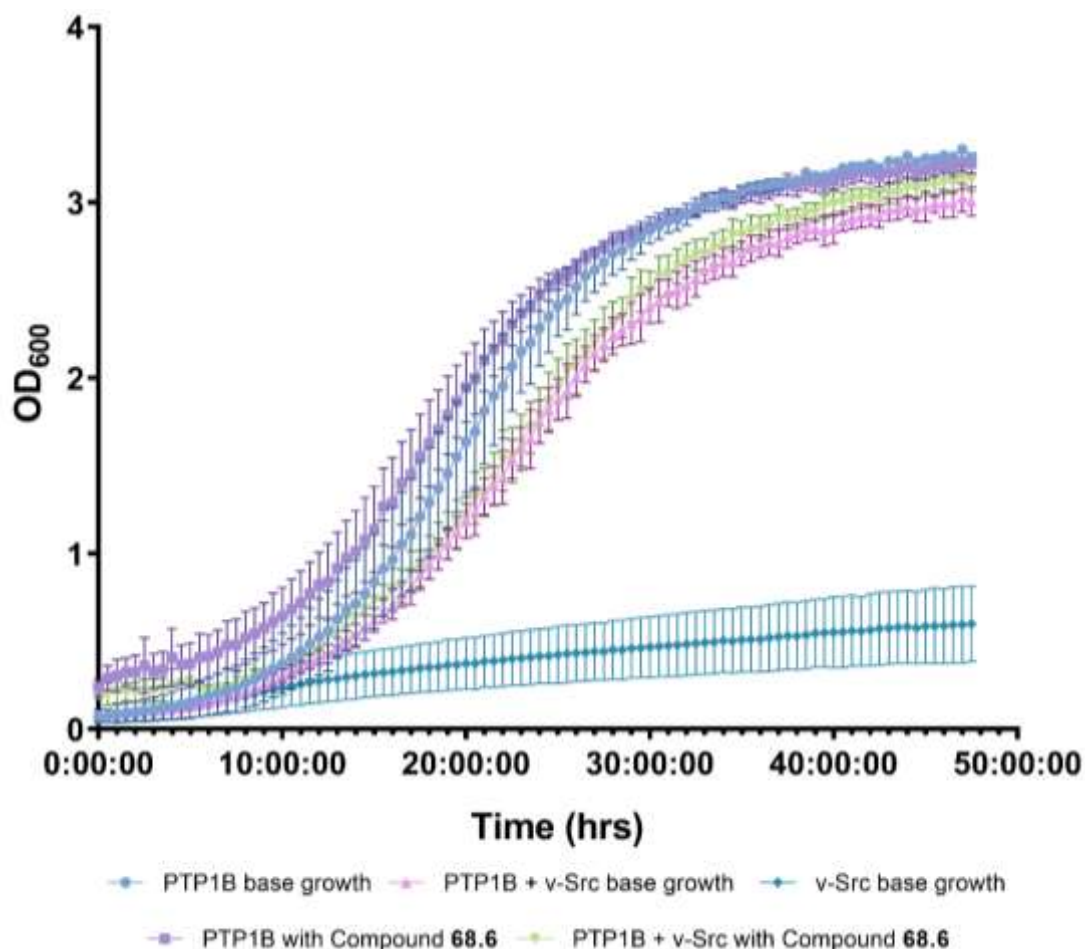
Transformed cells	PTP1B only	PTP1B + v-Src
p value	ns	ns

Figure CXVII: Growth curves of PTP1B only, PTP1B + v-Src and v-Src only YMK23 transformations with and without the addition of compound **68.4** at 100 μ M. $n=3$ for each PTP1B based parameter, $n=13$ for v-Src. Mean and individual biological points \pm standard deviation plotted. Data is normally distributed according to a Shapiro-Wilk test. Used a 2-way ANOVA. * p value ≤ 0.050 vs corresponding base growth.



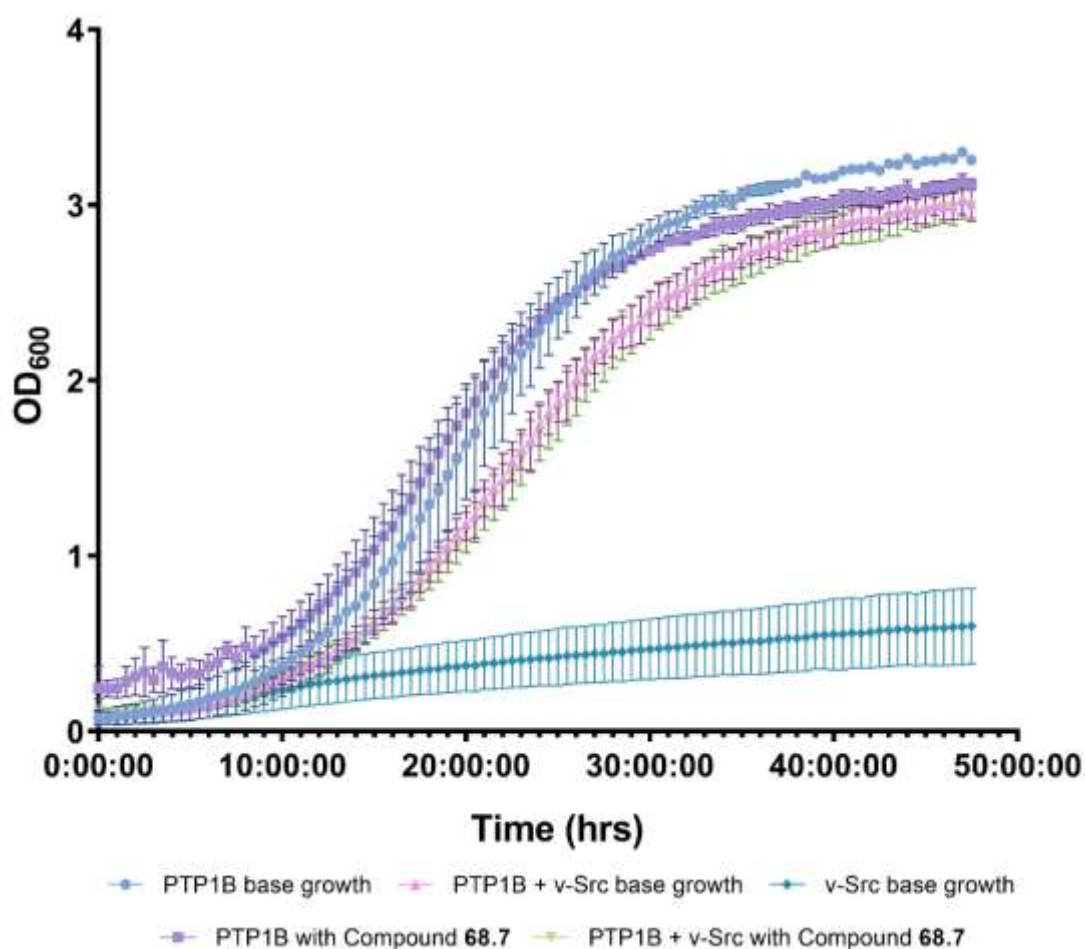
Transformed cells	PTP1B only	PTP1B + v-Src
p value	ns	ns

Figure CXVIII: Growth curves of PTP1B only, PTP1B + v-Src and v-Src only YMK23 transformations with and without the addition of compound **68.5** at 100 μ M. n=3 for each PTP1B based parameter, n=13 for v-Src. Mean and individual biological points \pm standard deviation plotted. Data is normally distributed according to a Shapiro-Wilk test. Used a 2-way ANOVA. * p value \leq 0.050 vs corresponding base growth.



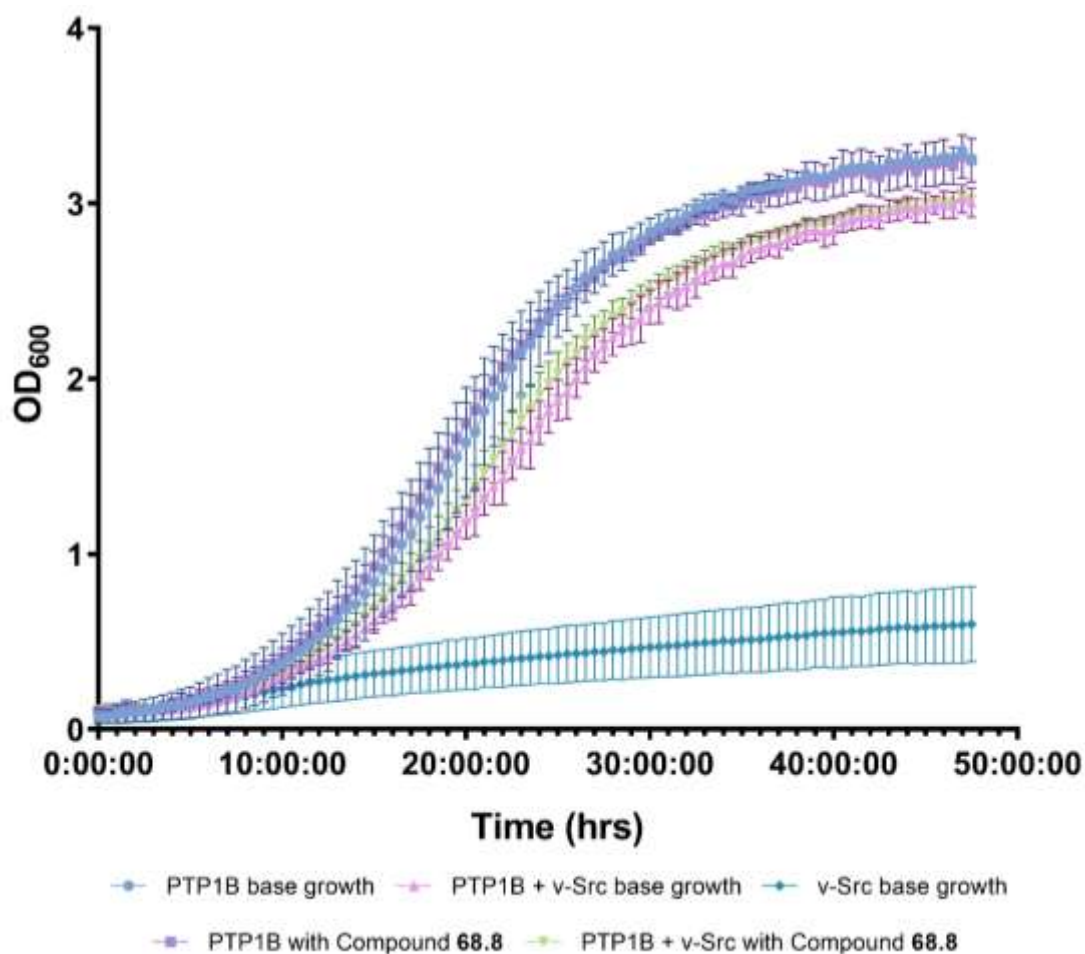
Transformed cells	PTP1B only	PTP1B + v-Src
p value	ns	ns

Figure CXIX: Growth curves of PTP1B only, PTP1B + v-Src and v-Src only YMK23 transformations with and without the addition of compound **68.6** at 100 μ M. n=3 for each PTP1B based parameter, n=13 for v-Src. Mean and individual biological points \pm standard deviation plotted. Data is normally distributed according to a Shapiro-Wilk test. Used a 2-way ANOVA. * p value \leq 0.050 vs corresponding base growth.



Transformed cells	PTP1B only	PTP1B + v-Src
p value	ns	ns

Figure CXX: Growth curves of PTP1B only, PTP1B + v-Src and v-Src only YMK23 transformations with and without the addition of compound **68.7** at 100µM. n=3 for each PTP1B based parameter, n=13 for v-Src. Mean and individual biological points ± standard deviation plotted. Data is normally distributed according to a Shapiro-Wilk test. Used a 2-way ANOVA. * p value ≤ 0.050 vs corresponding base growth.

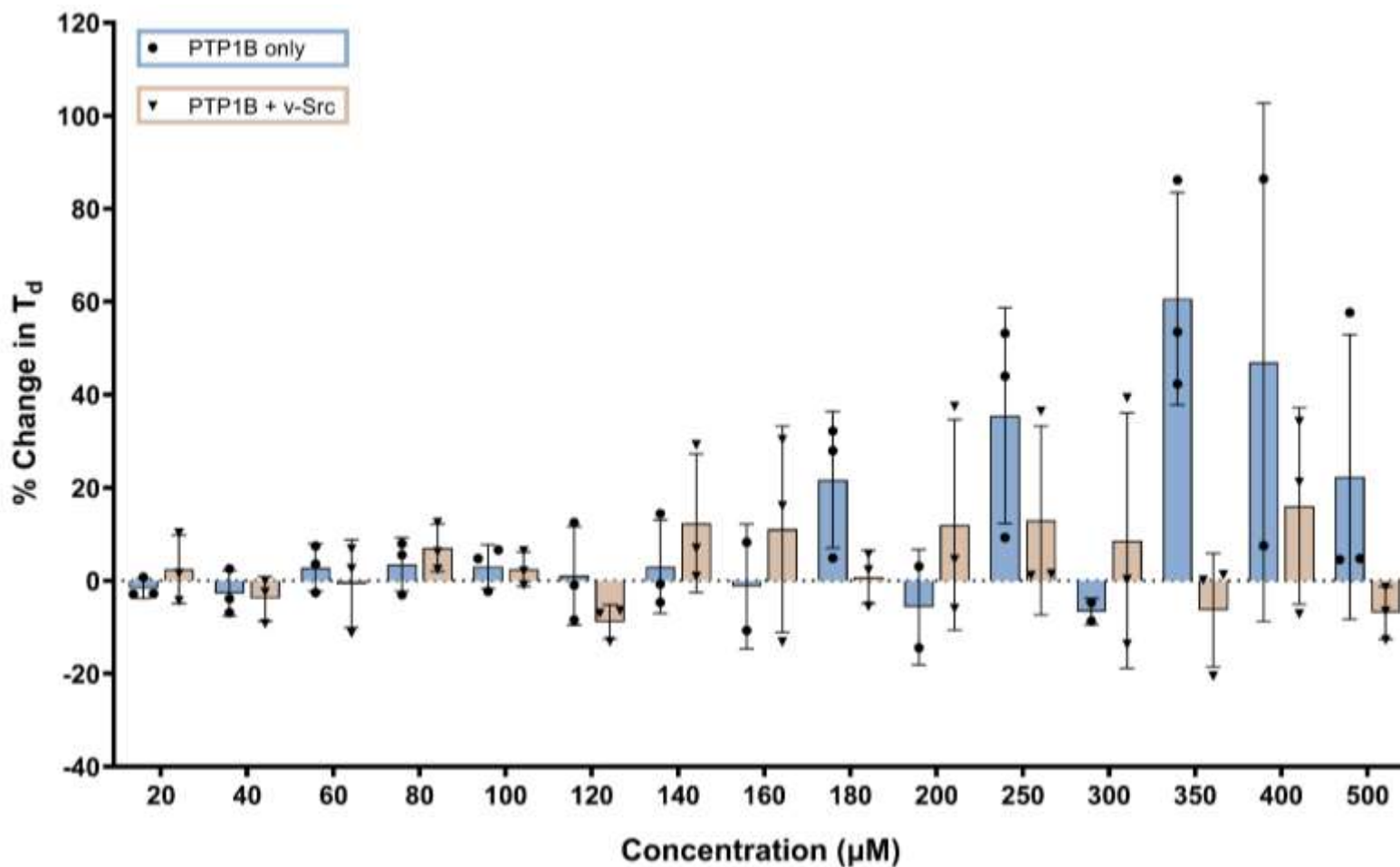


Transformed cells	PTP1B only	PTP1B + v-Src
p value	ns	ns

Figure CXXI: Growth curves of PTP1B only, PTP1B + v-Src and v-Src only YMK23 transformations with and without the addition of compound **68.8** at 100 μ M. n=3 for each PTP1B based parameter, n=13 for v-Src. Mean and individual biological points \pm standard deviation plotted. Data is normally distributed according to a Shapiro-Wilk test. Used a 2-way ANOVA. * p value \leq 0.050 vs corresponding base growth.

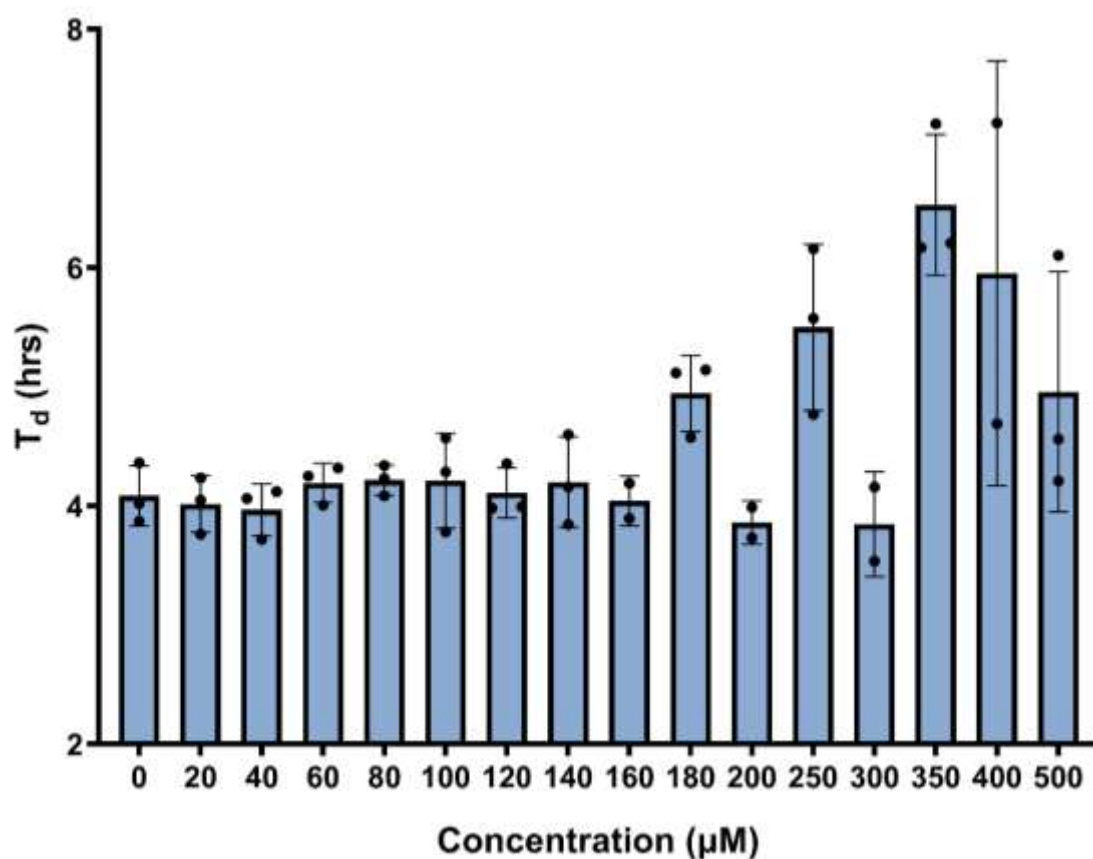
3.1.2 Further investigation into Compound 64 and 68.4

The dose response results of compounds **64** and **68.4** shown below. It was found that no concentration tested in either compound possessed significant PTP1B inhibitory activity.



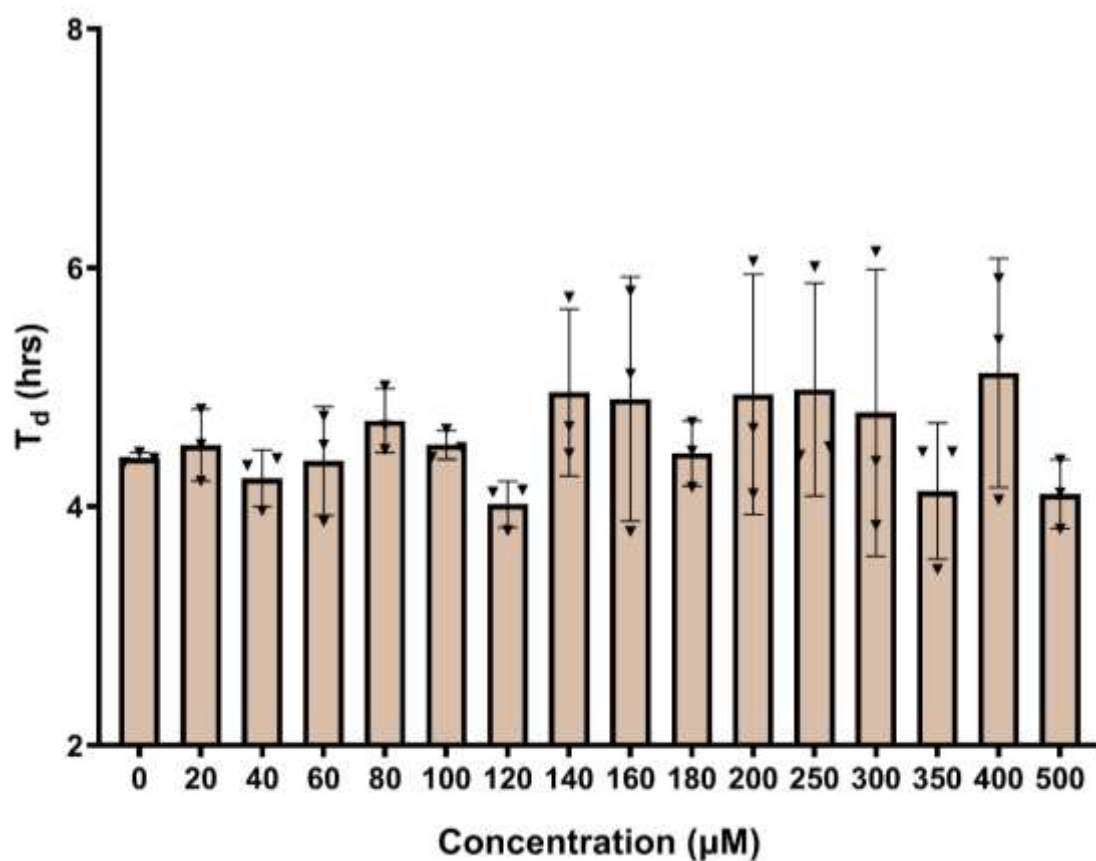
μM	p value
20	ns
40	ns
60	ns
80	ns
100	ns
120	ns
140	ns
160	ns
180	ns
200	ns
250	ns
300	ns
350	ns
400	ns
500	ns
Overall	ns

Figure CXXII: Comparison of % change in doubling time (T_d) of PTP1B only and PTP1B + v-Src transformed yeast cells in the presence of compound **64** at 20-500 μM . $n=3$ for all concentrations tested in both transformations, mean and individual points \pm standard deviation plotted. Used non-parametric Mann-Whitney t-test for statistical analysis. * p value ≤ 0.050 vs control.



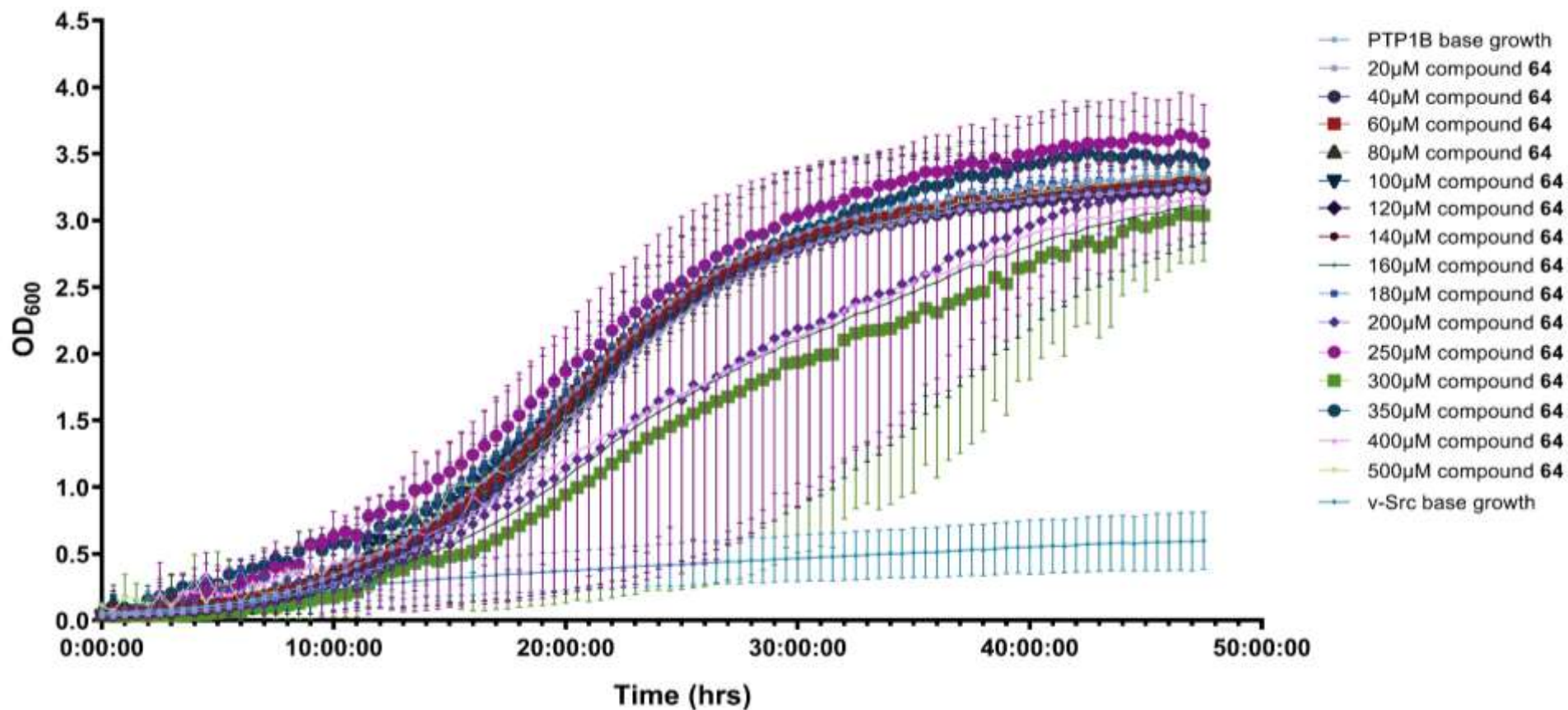
μM	20	40	60	80	100	120	140	160	180	200	250	300	350	400	500
p values	ns	ns	ns	ns	ns	ns	ns	ns	ns	ns	ns	ns	ns	ns	ns

Figure CXXIII: Effect of compound **64** addition at 20-500 μM on the T_d value of PTP1B only transformed yeast cells. n=3 for all concentrations, n=3 for base growth. Mean points ± standard deviation plotted. Data is not normally distributed according to a Shapiro-Wilk test. Used non-parametric Mann-Whitney t-test for statistical analysis. * p value ≤ 0.050 vs base growth.



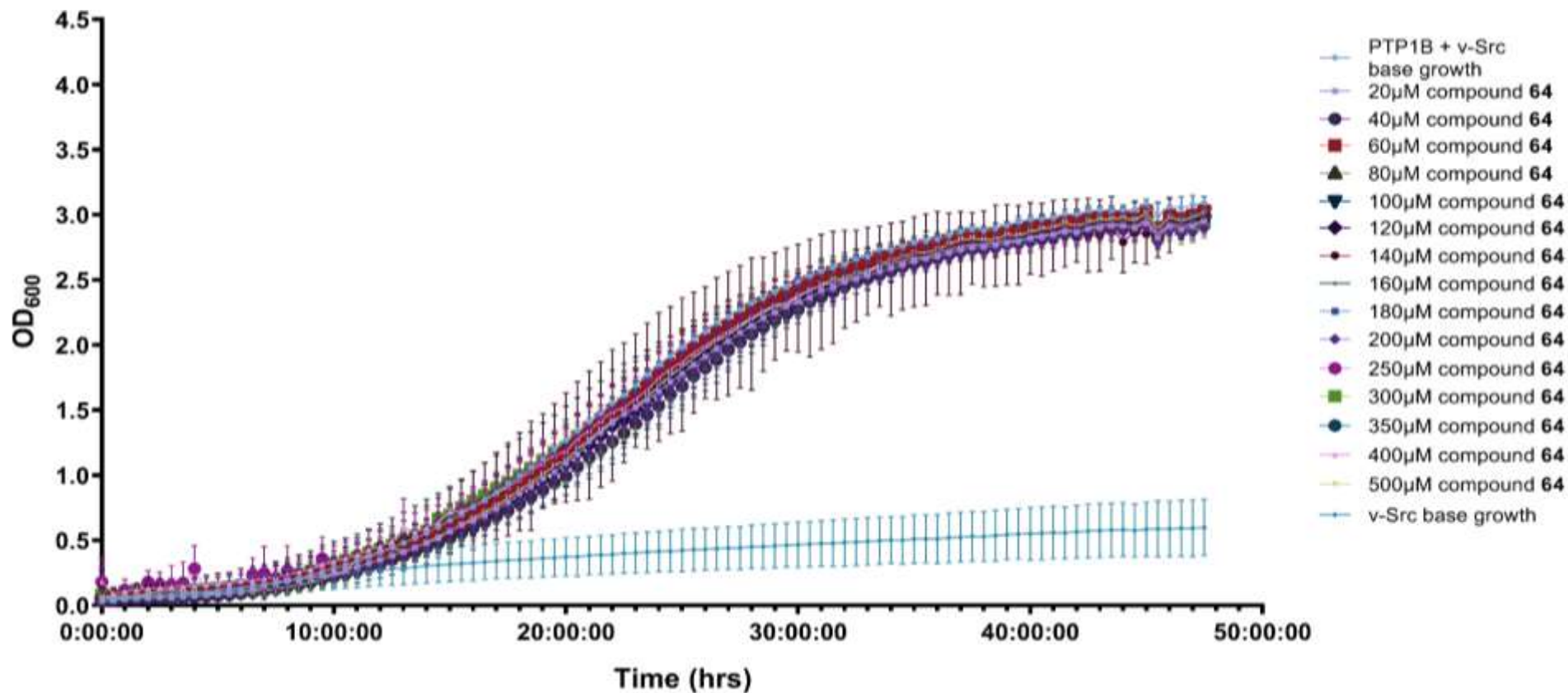
μM	20	40	60	80	100	120	140	160	180	200	250	300	350	400	500
p values	ns	ns	ns	ns	ns	ns	ns	ns	ns	ns	ns	ns	ns	ns	ns

Figure CXXIV: Effect of compound **64** addition at 20-500 μM on the T_d value of PTP1B + v-Src transformed yeast cells. n=3 for all concentrations, n=3 for base growth. Mean points ± standard deviation plotted. Data is normally distributed according to a Shapiro-Wilk test. Used parametric Welch's t-test for statistical analysis. * p value ≤ 0.050 vs base growth.



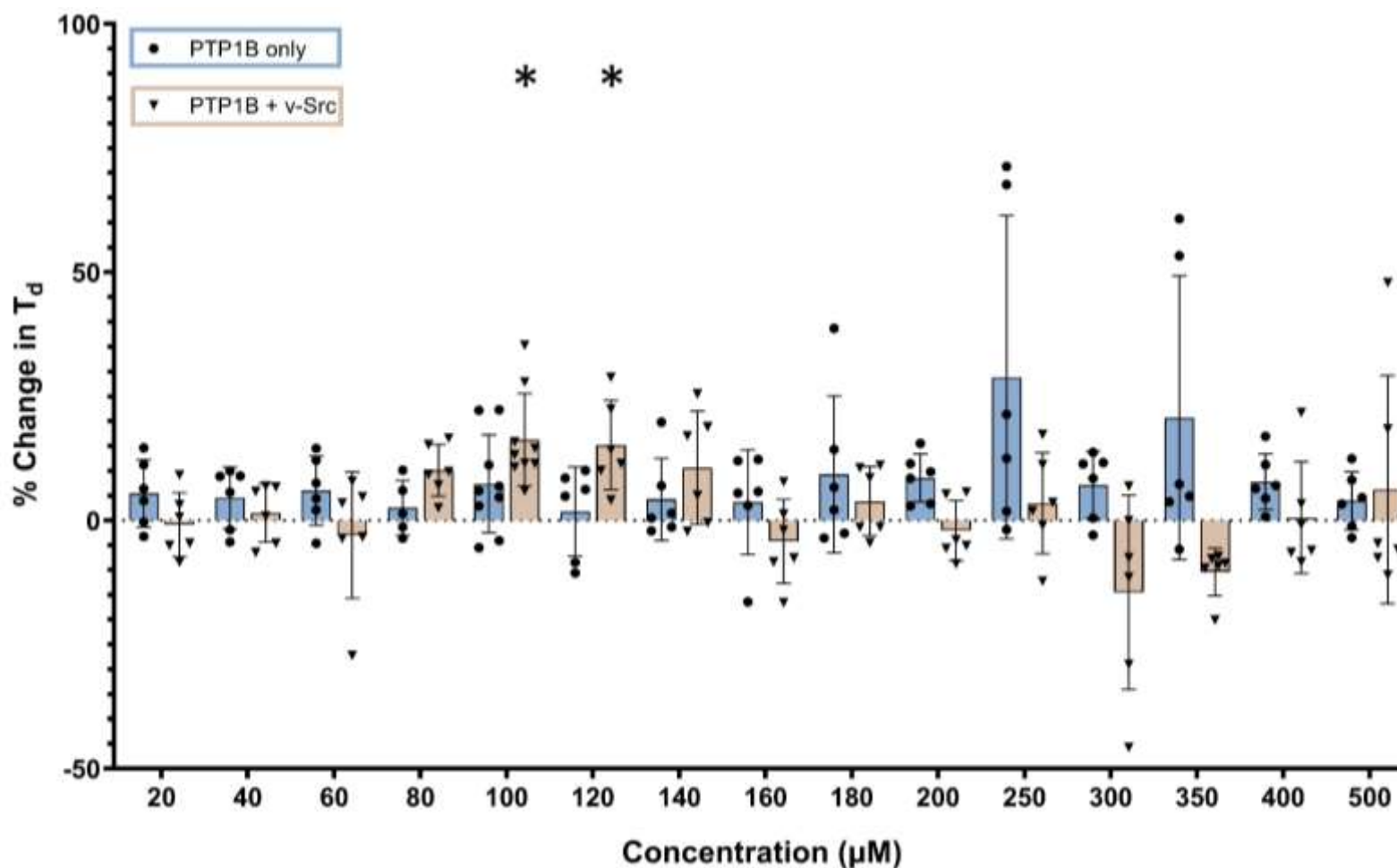
μM	20	40	60	80	100	120	140	160	180	200	250	300	350	400	500
p value	ns	ns	ns	ns	ns	ns	ns	ns	ns	ns	ns	ns	ns	ns	ns

Figure CXXV: Growth profile of PTP1B only yeast cells with the addition of compound **64** at 20-500 μM. n=3 for all concentrations in PTP1B only cells, n=3 for base growth, n=13 for v-Src base growth. Mean points ± standard deviation plotted. Data is normally distributed according to a Shapiro-Wilk test. Used a 2-way ANOVA where column factor was source of variance. * p value ≤ 0.050 vs control.



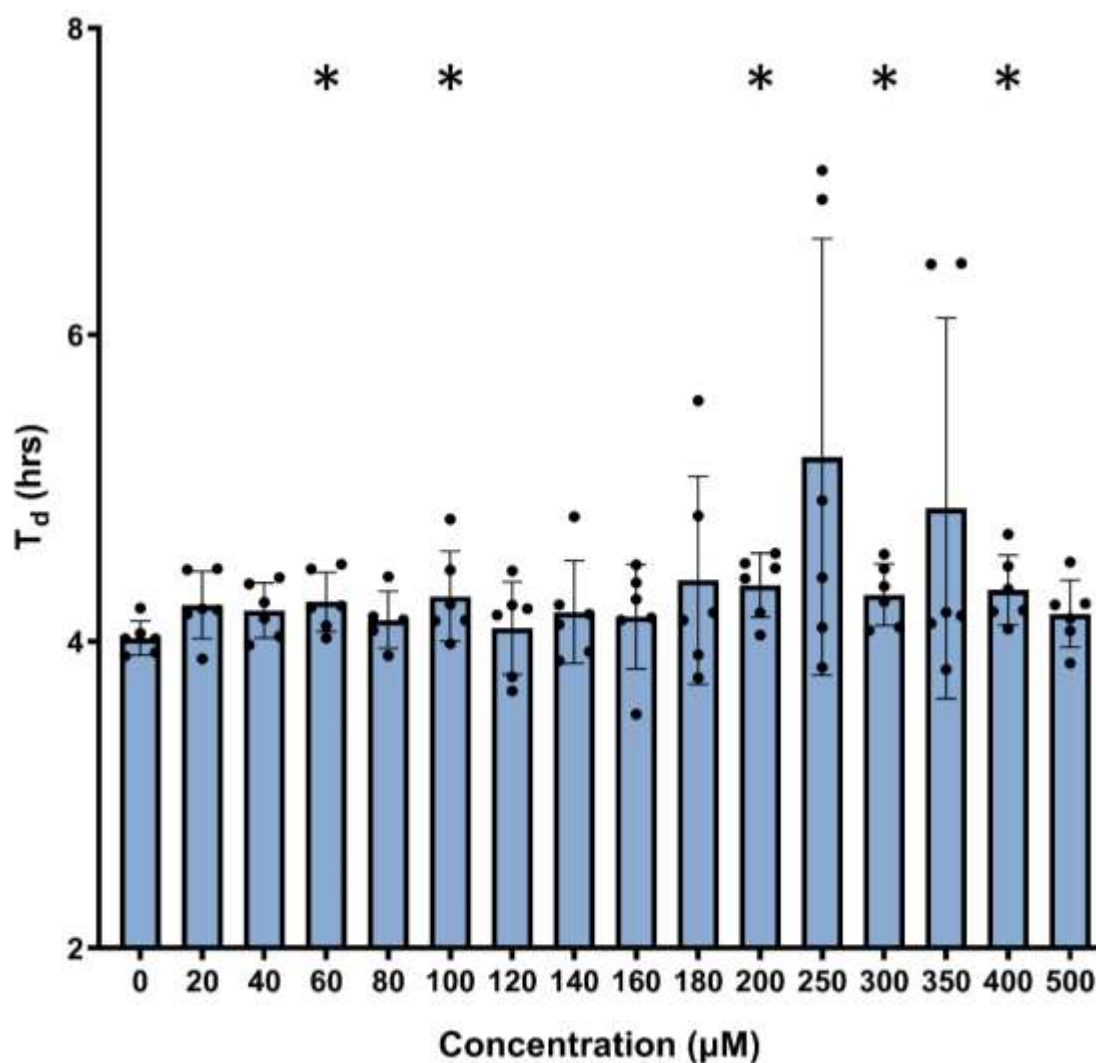
μM	20 *	40 *	60	80	100	120	140	160	180	200	250	300	350	400	500
p value	<0.0500	<0.0500	ns	ns	ns	ns	ns	ns	ns	ns	ns	ns	ns	ns	ns

Figure CXXVI: Growth profile of PTP1B + v-Src yeast cells with the addition of compound **64** at 20-500 μM . $n=3$ for all concentrations in PTP1B + v-Src cells, $n=3$ for base growth, $n=13$ for v-Src base growth. Mean points \pm standard deviation plotted. Data is normally distributed according to a Shapiro-Wilk test. Used a 2-way ANOVA where column factor was source of variance. * p value ≤ 0.050 vs control.



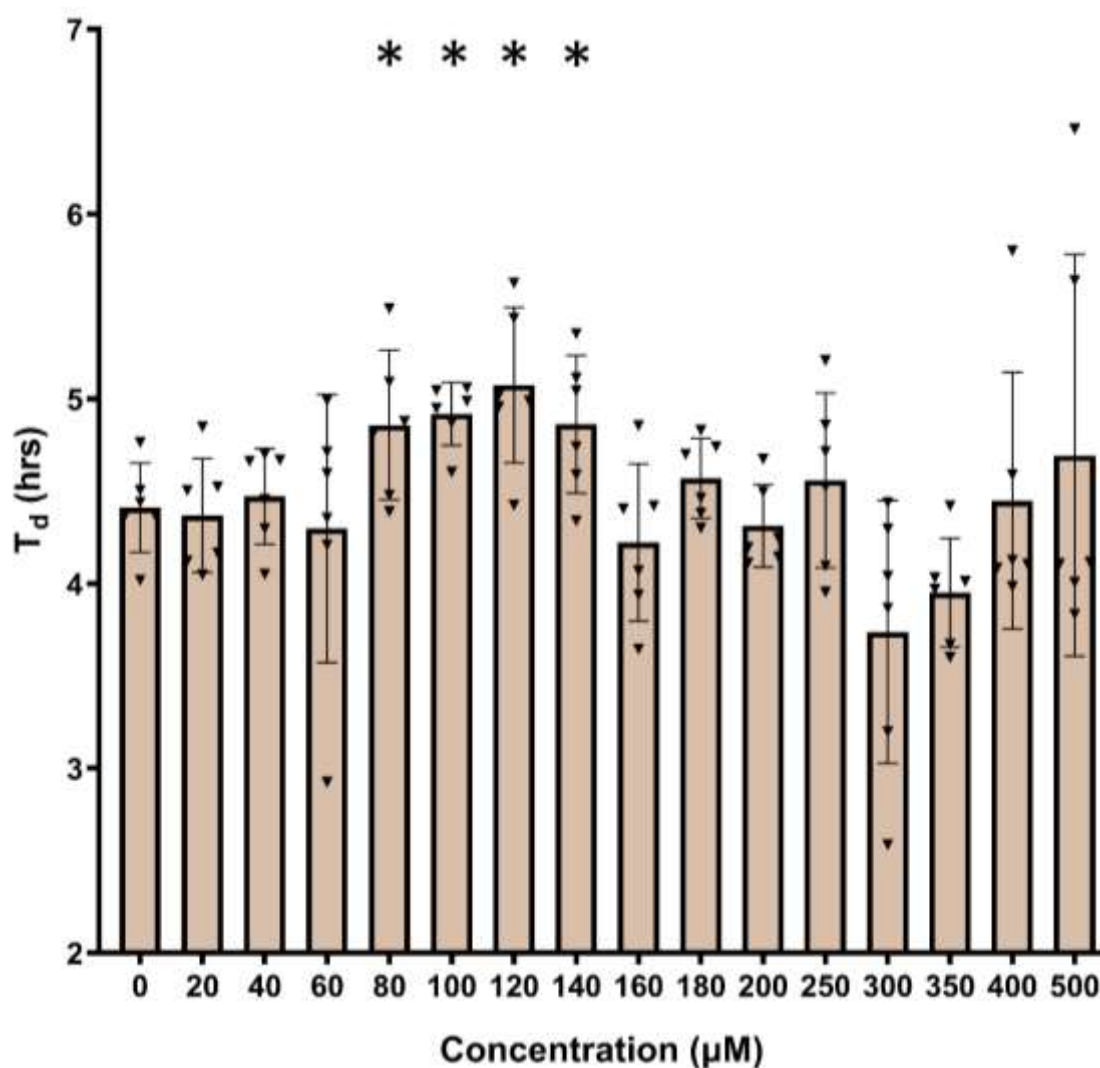
μM	p value
20	ns
40	ns
60	ns
80	ns
100	<0.0500
120	<0.0500
140	ns
160	ns
180	ns
200	<0.0500
250	<0.0500
300	ns
350	<0.0050
400	ns
500	ns
Overall	ns

Figure CXXVII: % Comparison of % change in doubling time (T_d) of PTP1B only and PTP1B + v-Src transformed yeast cells in the presence of compound **68.4** at 20-500 μM . $n=6$ for all concentrations tested in both transformations apart from 100 μM where $n=9$. Mean and individual points \pm standard deviation plotted. Used non-parametric Mann-Whitney t-test for statistical analysis. * p value ≤ 0.050 vs control. Note: 200, 300 and 350 μM % change in T_d values are significantly lower in PTP1B + v-Src than PTP1B only cells.



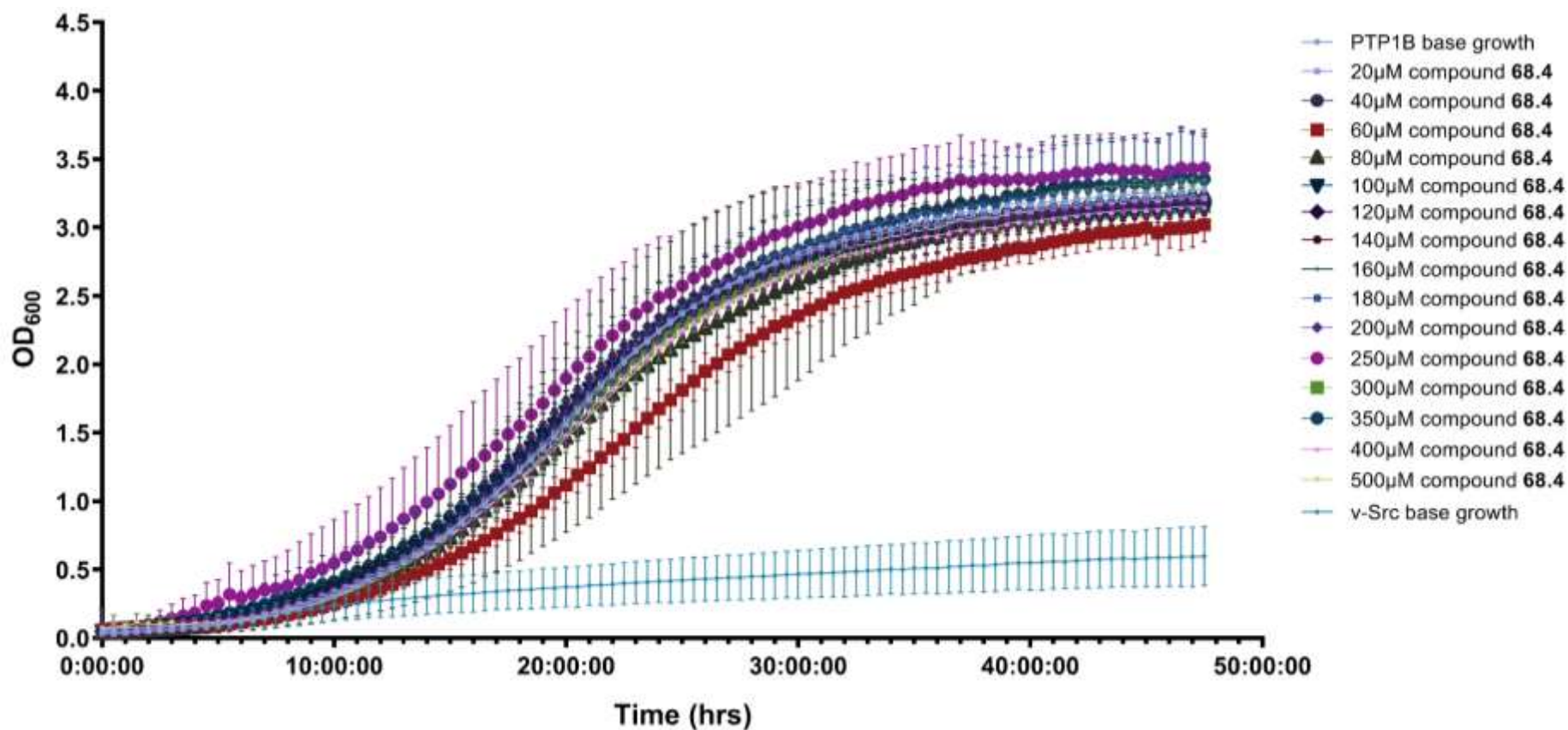
μM	20	40	60	80	100	120	140	160	180	200	250	300	350	400	500
p values	ns	ns	<0.0500	ns	ns	ns	ns	ns	ns	<0.0500	ns	<0.0100	ns	<0.0500	ns

Figure CXXVIII: Effect of compound **68.4** addition at 20-500 μM on the T_d value of PTP1B only transformed yeast cells. $n=6$ for all concentrations, $n=6$ for base growth. Mean points \pm standard deviation plotted. Data is not normally distributed according to a Shapiro-Wilk test. Used non-parametric Mann-Whitney t-test for statistical analysis. * p value ≤ 0.050 vs base growth.



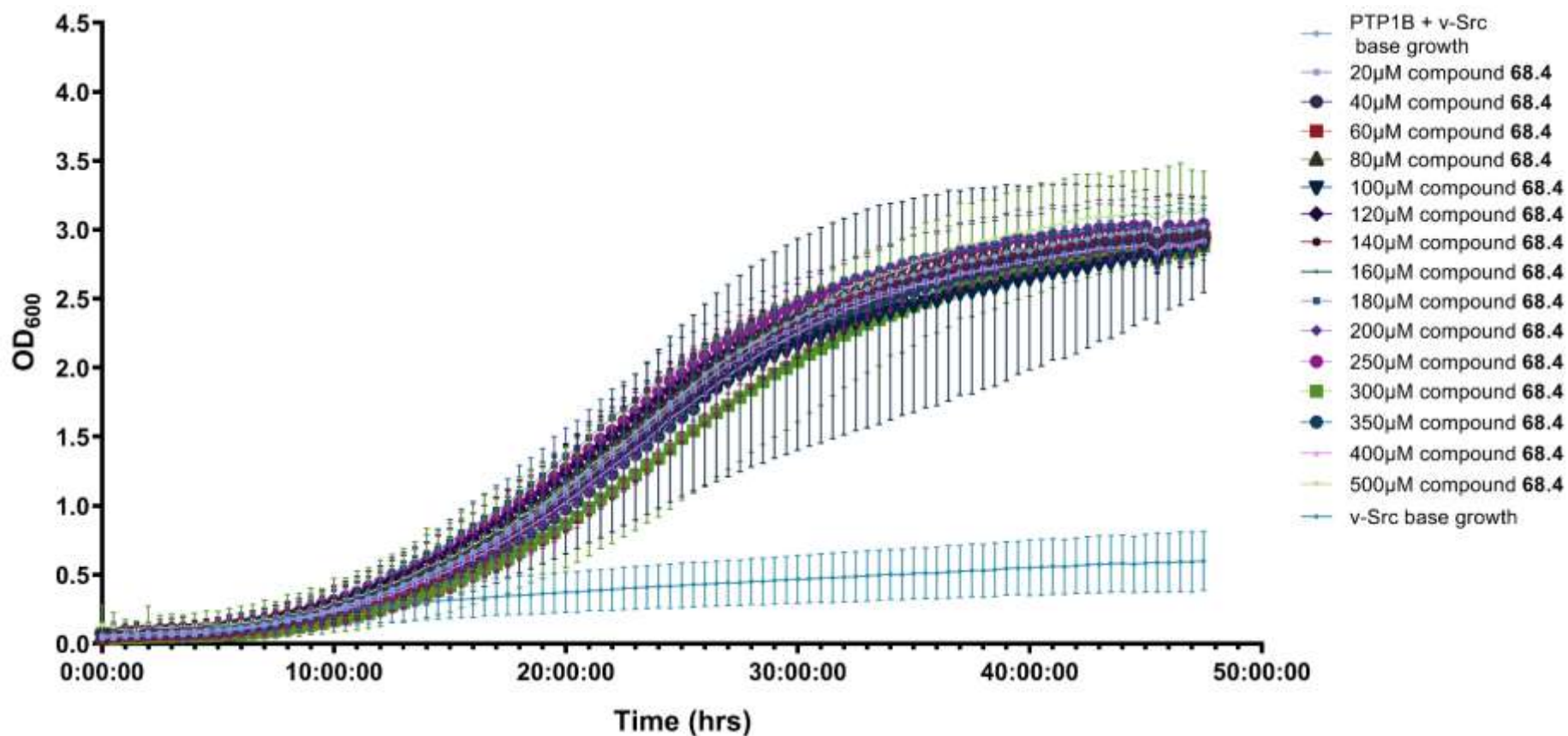
μM	20	40	60	80	100	120	140	160	180	200	250	300	350	400	500
p values	ns	ns	ns	<0.0500	<0.0050	<0.0100	<0.0500	ns	ns	ns	ns	ns	<0.0500	ns	ns

Figure CXXIX: Effect of compound **68.4** addition at 20-500 μM on the T_d value of PTP1B + v-Src transformed yeast cells. n=6 for all concentrations, n=6 for base growth. Mean points ± standard deviation plotted. Data is normally distributed according to a Shapiro-Wilk test. Used parametric Welch's t-test for statistical analysis. * p value ≤ 0.050 vs base growth. Note: at 300 and 350 μM the T_d values are significantly lower than the base growth of only PTP1B + v-Src cells.



μM	20	40	60	80	100	120	140	160	180	200	250	300 *	350	400 *	500
p value	ns	ns	ns	ns	ns	ns	ns	ns	ns	ns	ns	<0.0500	ns	<0.0050	ns

Figure CXXX: Growth profile of PTP1B only yeast cells with the addition of compound **68.4** at 20-500 μM. n=6 for all concentrations in PTP1B only cells, n=6 for base growth, n=13 for v-Src base growth. Mean points ± standard deviation plotted. Data is normally distributed according to a Shapiro-Wilk test. Used a 2-way ANOVA where column factor was source of variance. * p value ≤ 0.050 vs control.



μM	20	40	60	80	100	120	140	160 *	180	200 *	250	300 *	350 *	400	500
p value	ns	ns	ns	ns	ns	ns	ns	<0.0500	ns	<0.0100	ns	<0.0500	<0.0100	ns	ns

Figure CXXXI: Growth profile of PTP1B + v-Src yeast cells with the addition of compound **68.4** at 20-500 μM . n=6 for all concentrations in PTP1B only cells, n=6 for base growth, n=13 for v-Src base growth. Mean points \pm standard deviation plotted. Data is normally distributed according to a Shapiro-Wilk test. Used a 2-way ANOVA where column factor was source of variance. * p value \leq 0.050 vs control.

3.1.3 Doubling time and growth curve data for 62, 69-74 and 77

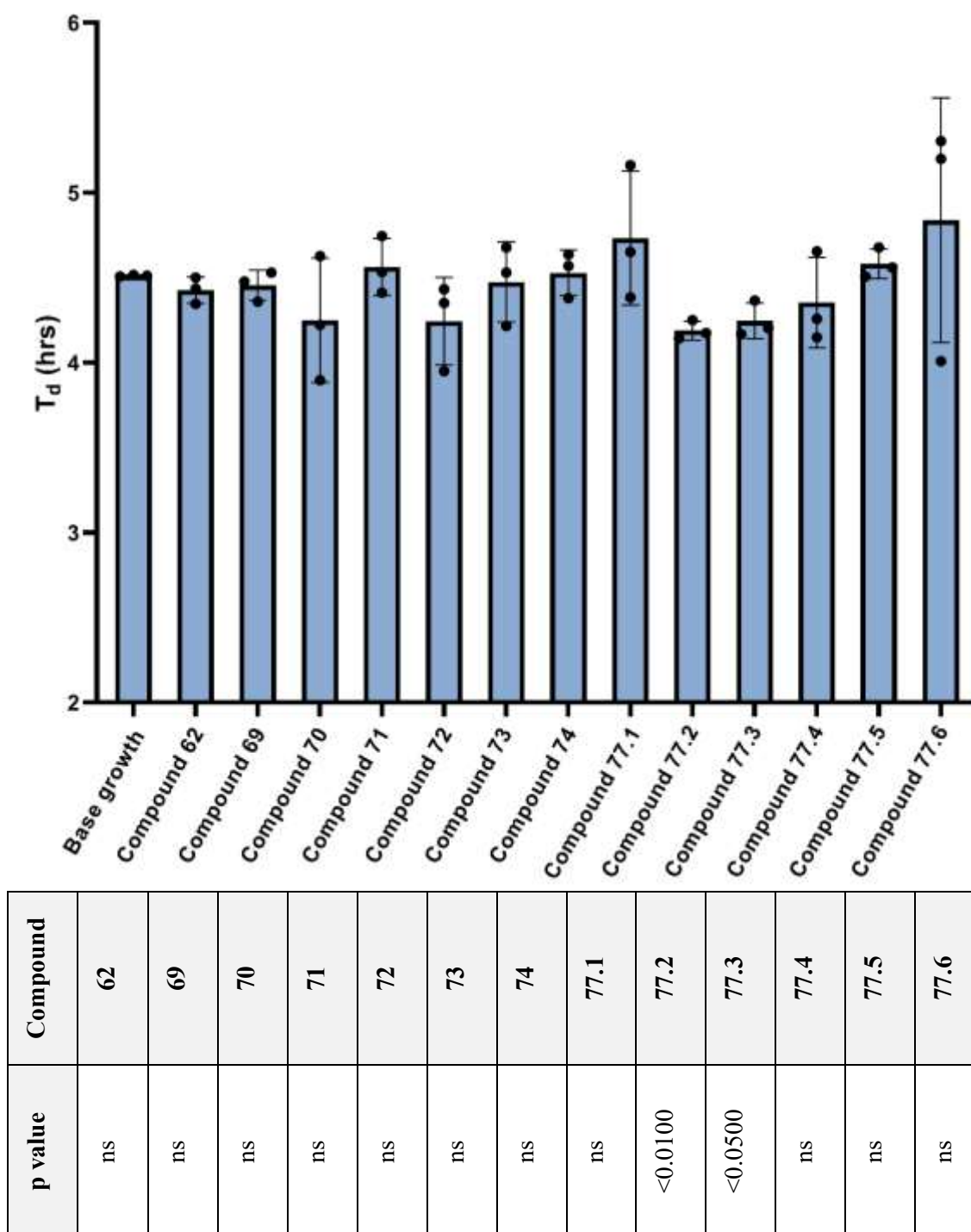
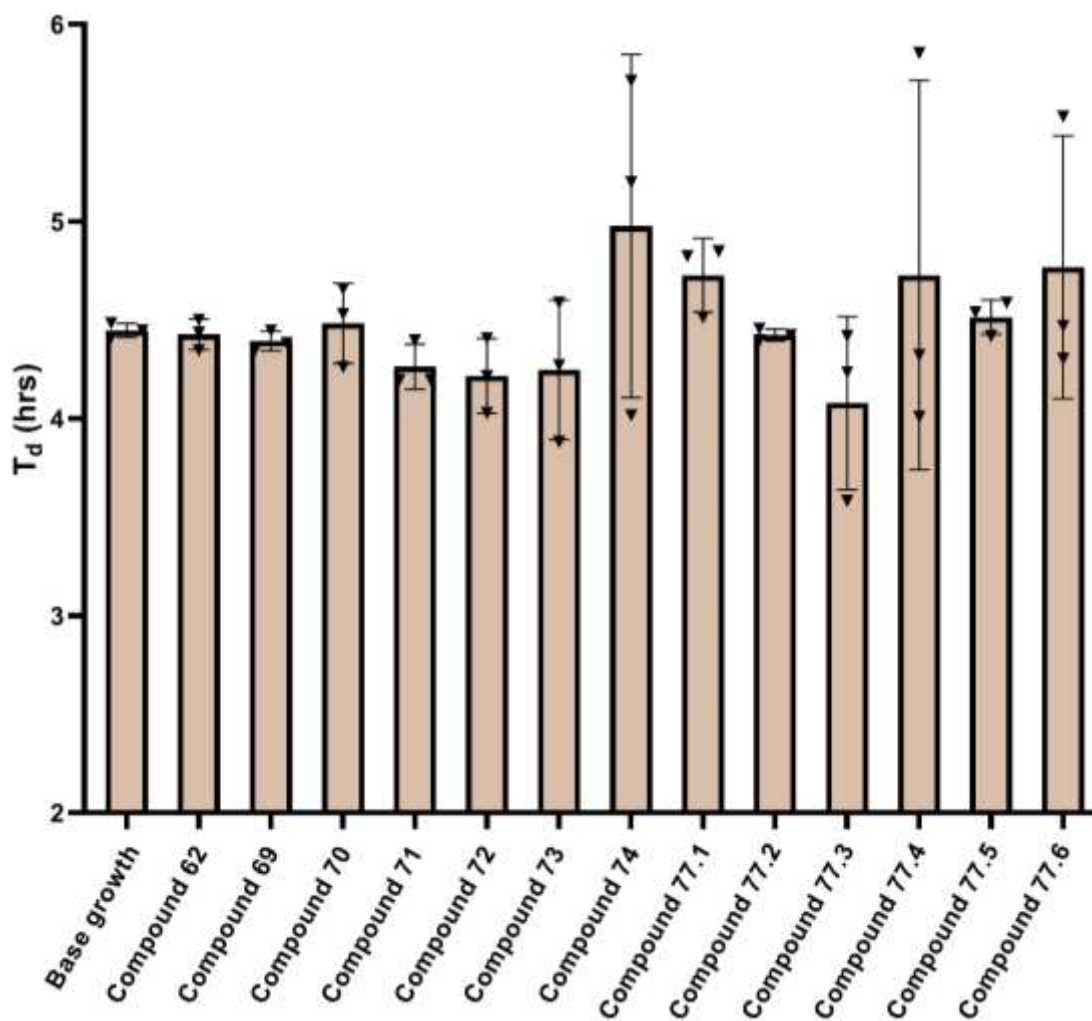
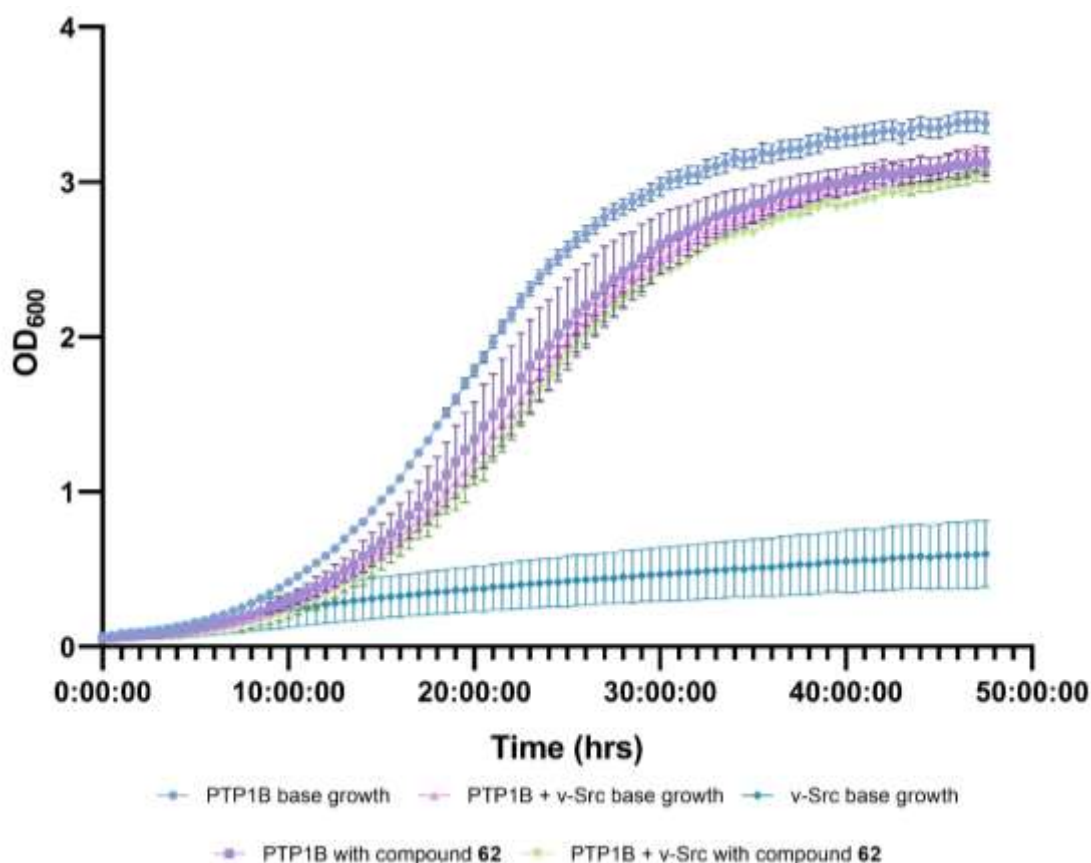


Figure CXXXII: Effect of compound 62, 69-74, 77 addition at 100 μM on the T_d value of PTP1B only transformed yeast cells. $n=3$ for all compounds tested and $n=3$ for base growth. Mean points \pm standard deviation plotted. Data is normally distributed according to a Shapiro-Wilk test. Used parametric Welch t-test for statistical analysis. * p value ≤ 0.050 vs base growth. Note: 77.2 and 77.3 both caused a significant decrease in T_d .



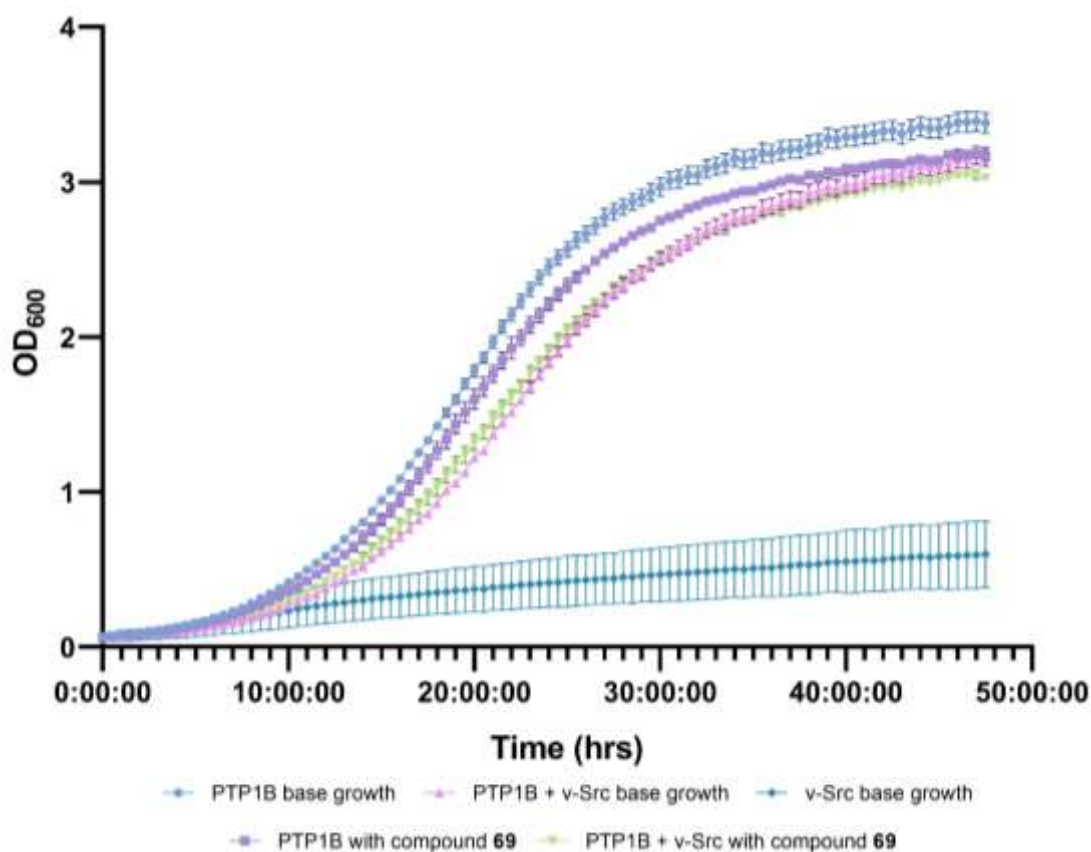
Compound	p value
62	ns
69	ns
70	ns
71	ns
72	ns
73	ns
74	ns
77.1	ns
77.2	ns
77.3	ns
77.4	ns
77.5	ns
77.6	ns

Figure CXXXIII: Effect of compound **62, 69-74, 77** addition at 100 μ M on the T_d value of PTP1B + v-Src transformed yeast cells. $n=3$ for all compounds tested and $n=3$ for base growth. Mean points \pm standard deviation plotted. Data is normally distributed according to a Shapiro-Wilk test. Used parametric Welch t-test for statistical analysis. * p value ≤ 0.050 vs base growth.



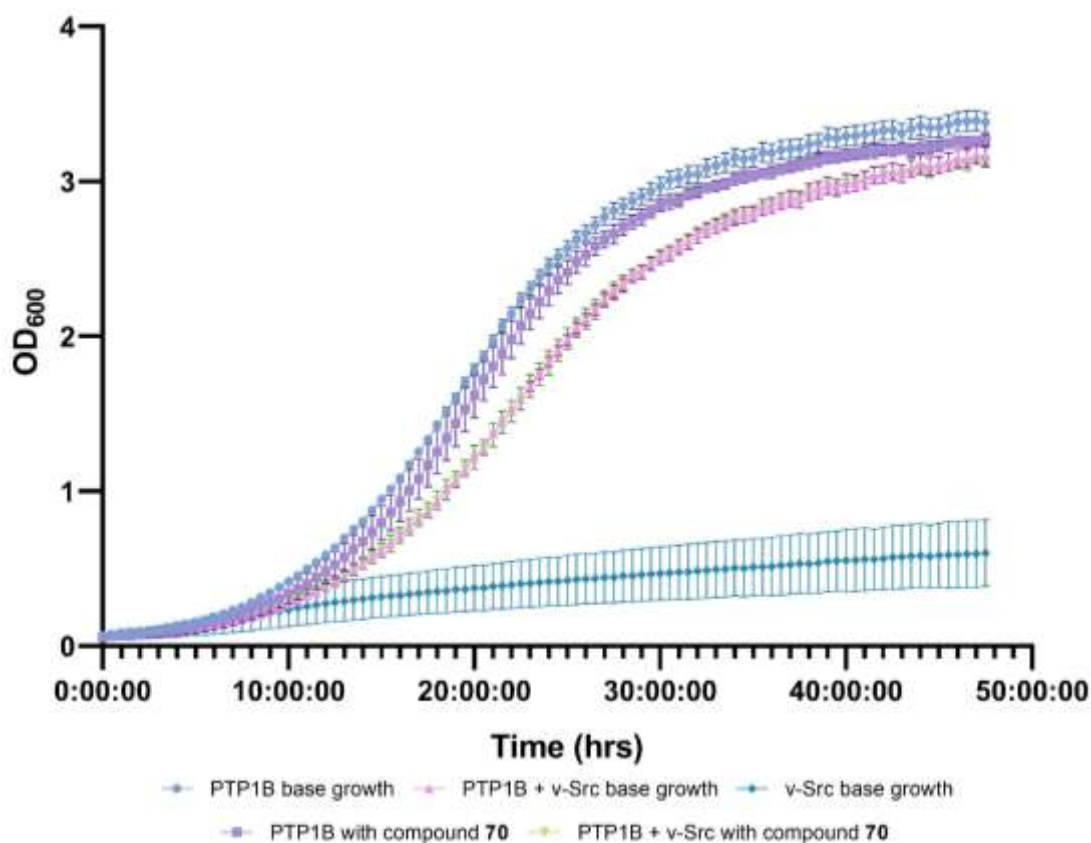
Transformed cells	PTP1B only *	PTP1B + v-Src *
p value	<0.0500	<0.0500

Figure CXXXIV: Growth curves of PTP1B only, PTP1B + v-Src and v-Src only YMK23 transformations with and without the addition of compound **62** at 100 μ M. n=3 for each PTP1B based parameter, n=13 for v-Src. Mean and individual biological points \pm standard deviation plotted. Data is normally distributed according to a Shapiro-Wilk test. Used a 2-way ANOVA. * p value \leq 0.050 vs corresponding base growth.



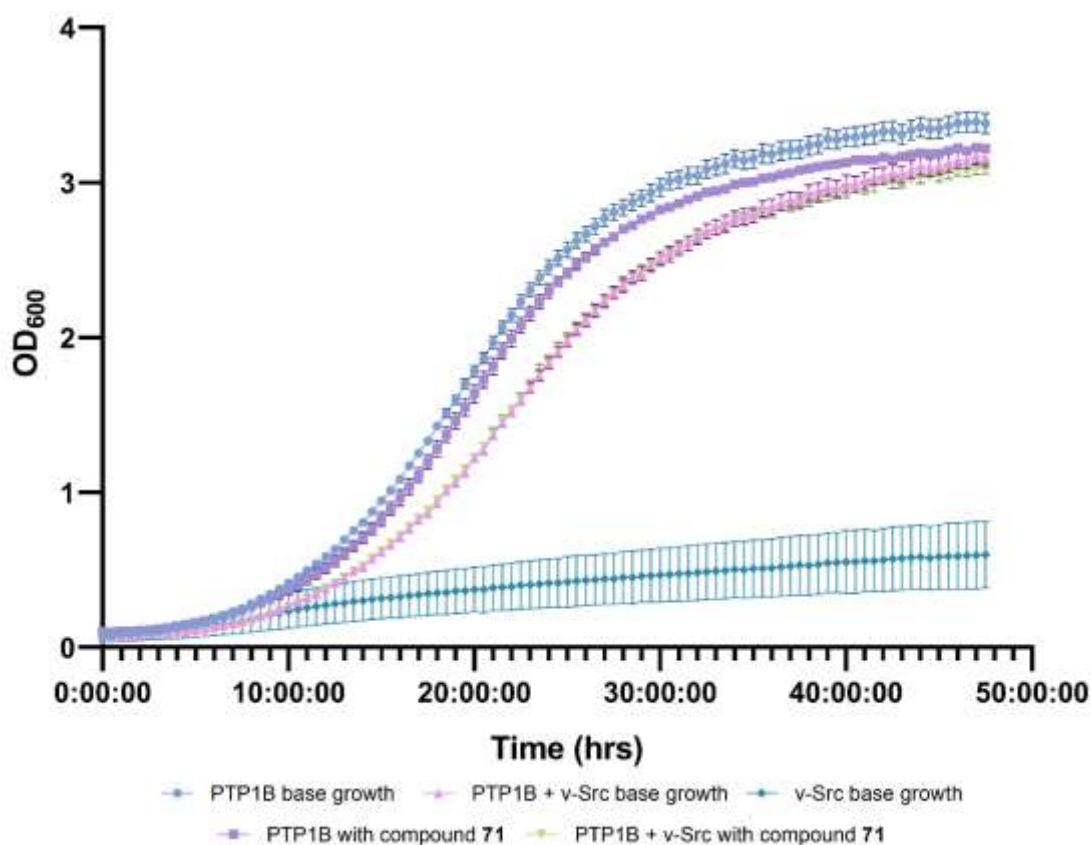
Transformed cells	PTP1B only *	PTP1B + v-Src
p value	<0.0050	ns

Figure CXXXV: Growth curves of PTP1B only, PTP1B + v-Src and v-Src only YMK23 transformations with and without the addition of compound **69** at 100 μ M. n=3 for each PTP1B based parameter, n=13 for v-Src. Mean and individual biological points \pm standard deviation plotted. Data is normally distributed according to a Shapiro-Wilk test. Used a 2-way ANOVA. * p value \leq 0.050 vs corresponding base growth.



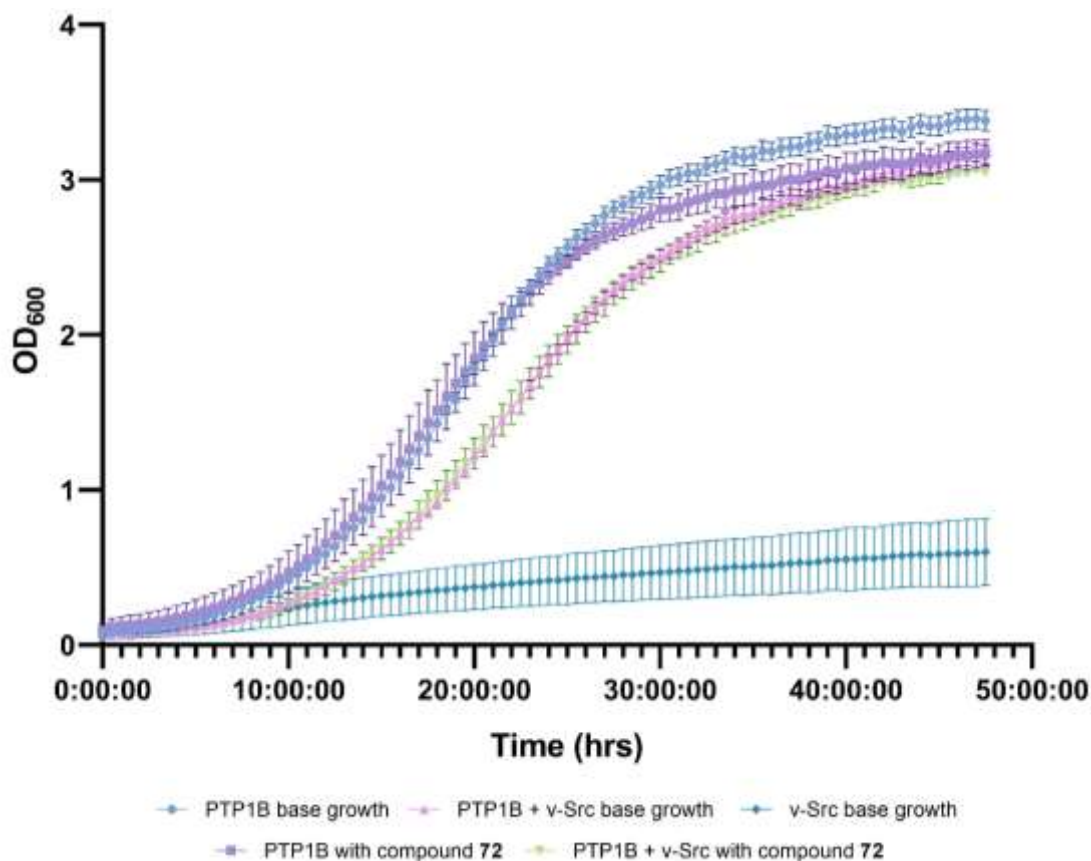
Transformed cells	PTP1B only *	PTP1B + v-Src
p value	<0.0500	ns

Figure CXXXVI: Growth curves of PTP1B only, PTP1B + v-Src and v-Src only YMK23 transformations with and without the addition of compound **70** at 100 μ M. n=3 for each PTP1B based parameter, n=13 for v-Src. Mean and individual biological points \pm standard deviation plotted. Data is normally distributed according to a Shapiro-Wilk test. Used a 2-way ANOVA. * p value \leq 0.050 vs corresponding base growth.



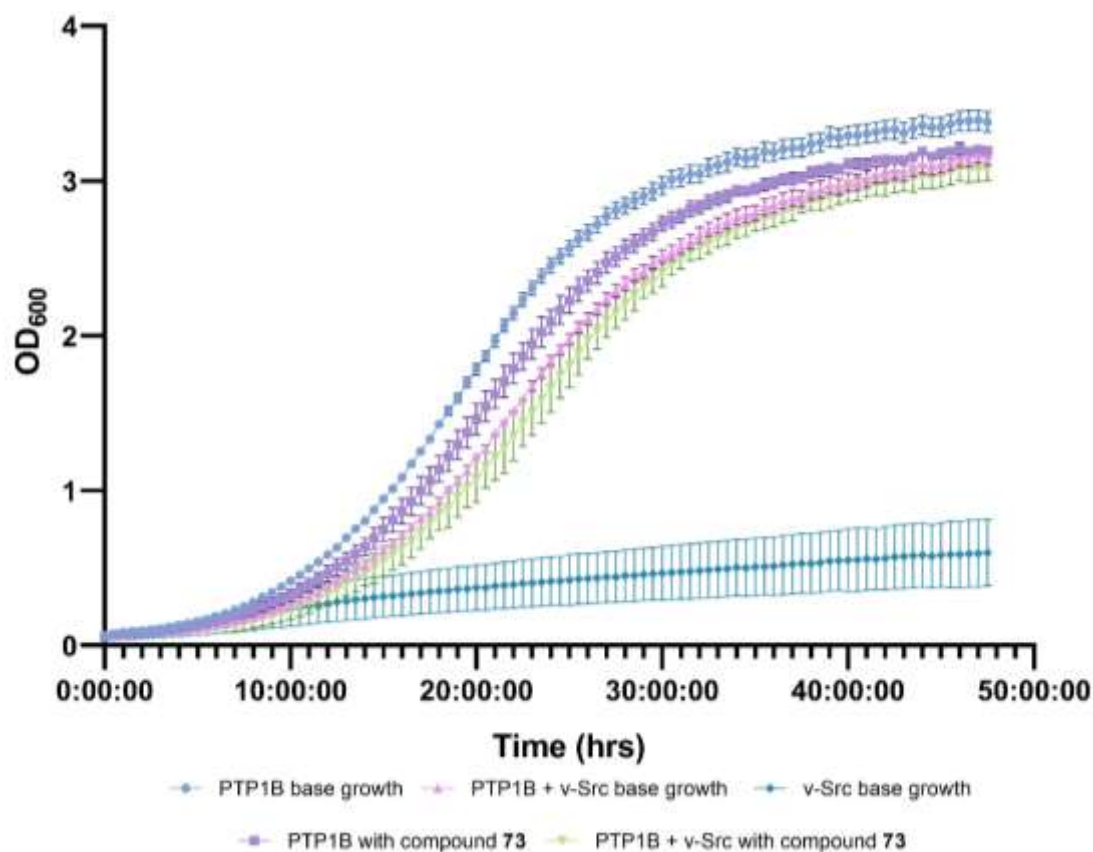
Transformed cells	PTP1B only *	PTP1B + v-Src
p value	<0.0500	ns

Figure CXXXVII: Growth curves of PTP1B only, PTP1B + v-Src and v-Src only YMK23 transformations with and without the addition of compound **71** at 100 μ M. n=3 for each PTP1B based parameter, n=13 for v-Src. Mean and individual biological points \pm standard deviation plotted. Data is normally distributed according to a Shapiro-Wilk test. Used a 2-way ANOVA. * p value \leq 0.050 vs corresponding base growth.



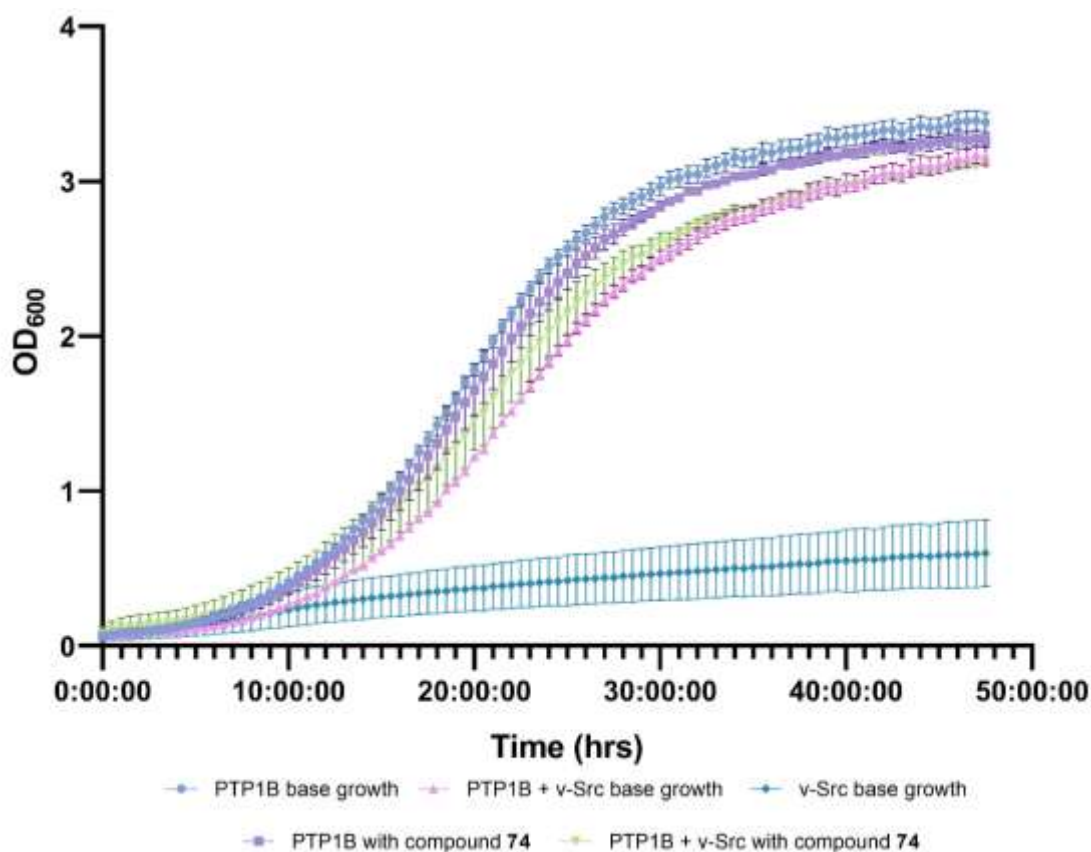
Transformed cells	PTP1B only	PTP1B + v-Src
p value	ns	ns

Figure CXXXVIII: Growth curves of PTP1B only, PTP1B + v-Src and v-Src only YMK23 transformations with and without the addition of compound **72** at 100 μ M. n=3 for each PTP1B based parameter, n=13 for v-Src. Mean and individual biological points \pm standard deviation plotted. Data is normally distributed according to a Shapiro-Wilk test. Used a 2-way ANOVA. * p value \leq 0.050 vs corresponding base growth.



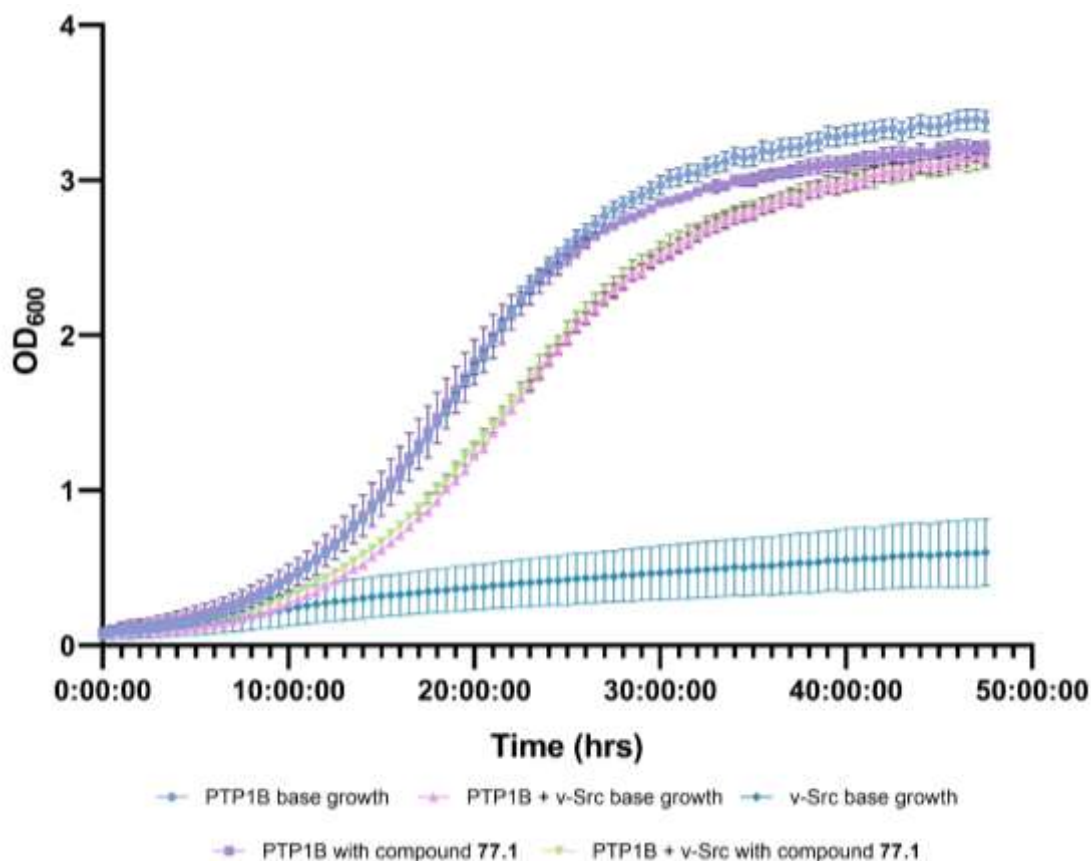
Transformed cells	PTP1B only *	PTP1B + v-Src
p value	<0.0050	ns

Figure CXXXIX: Growth curves of PTP1B only, PTP1B + v-Src and v-Src only YMK23 transformations with and without the addition of compound **73** at 100 μ M. n=3 for each PTP1B based parameter, n=13 for v-Src. Mean and individual biological points \pm standard deviation plotted. Data is normally distributed according to a Shapiro-Wilk test. Used a 2-way ANOVA. * p value \leq 0.050 vs corresponding base growth.



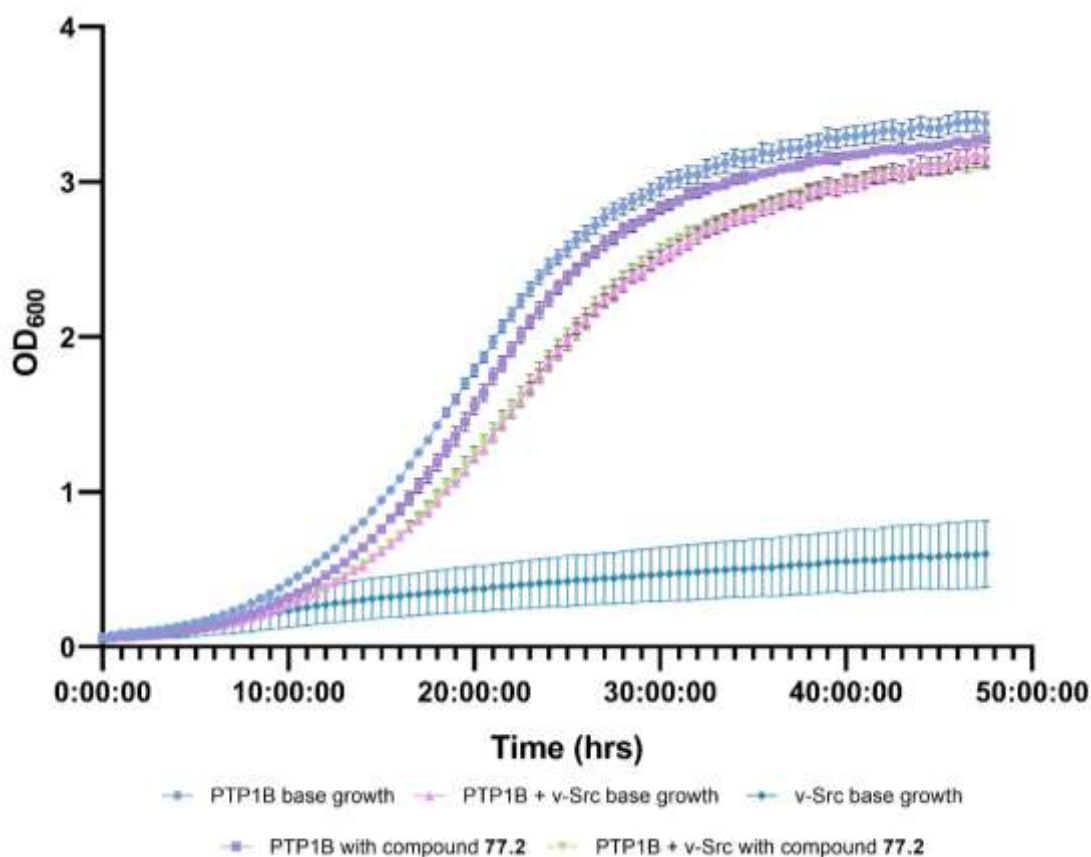
Transformed cells	PTP1B only *	PTP1B + v-Src
p value	<0.0500	ns

Figure CXL: Growth curves of PTP1B only, PTP1B + v-Src and v-Src only YMK23 transformations with and without the addition of compound 74 at 100 μ M. n=3 for each PTP1B based parameter, n=13 for v-Src. Mean and individual biological points \pm standard deviation plotted. Data is normally distributed according to a Shapiro-Wilk test. Used a 2-way ANOVA. * p value \leq 0.050 vs corresponding base growth.



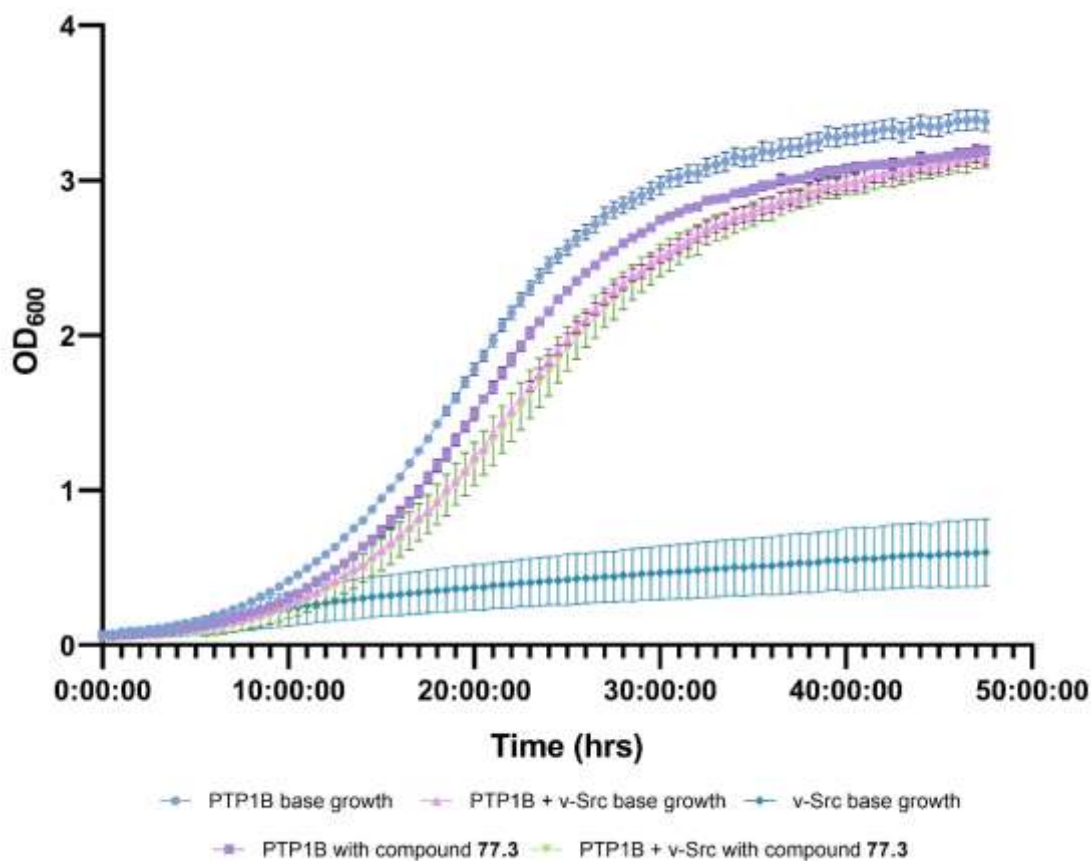
Transformed cells	PTP1B only	PTP1B + v-Src
p value	ns	ns

Figure CXLI: Growth curves of PTP1B only, PTP1B + v-Src and v-Src only YMK23 transformations with and without the addition of compound **77.1** at 100 μ M. n=3 for each PTP1B based parameter, n=13 for v-Src. Mean and individual biological points \pm standard deviation plotted. Data is normally distributed according to a Shapiro-Wilk test. Used a 2-way ANOVA. * p value \leq 0.050 vs corresponding base growth.



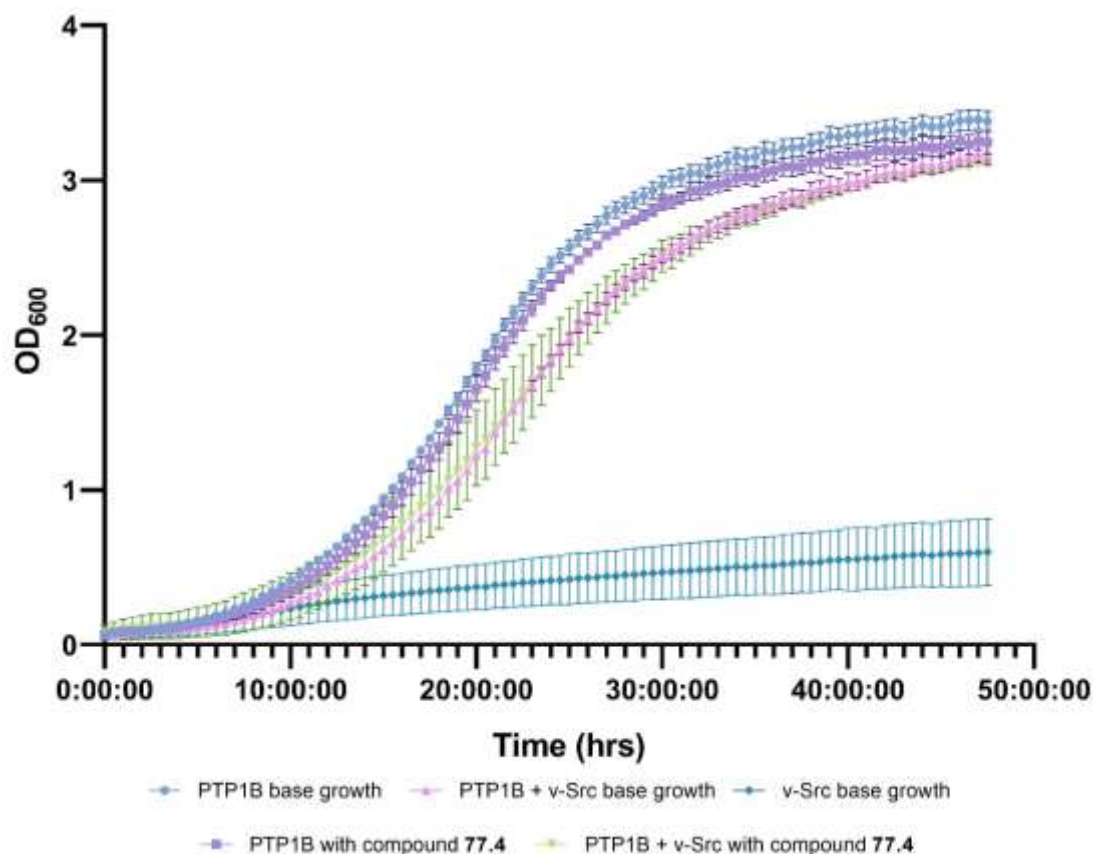
Transformed cells	PTP1B only *	PTP1B + v-Src
p value	<0.0100	ns

Figure CXLII: Growth curves of PTP1B only, PTP1B + v-Src and v-Src only YMK23 transformations with and without the addition of compound 77.2 at 100 μ M. n=3 for each PTP1B based parameter, n=13 for v-Src. Mean and individual biological points \pm standard deviation plotted. Data is normally distributed according to a Shapiro-Wilk test. Used a 2-way ANOVA. * p value \leq 0.050 vs corresponding base growth.



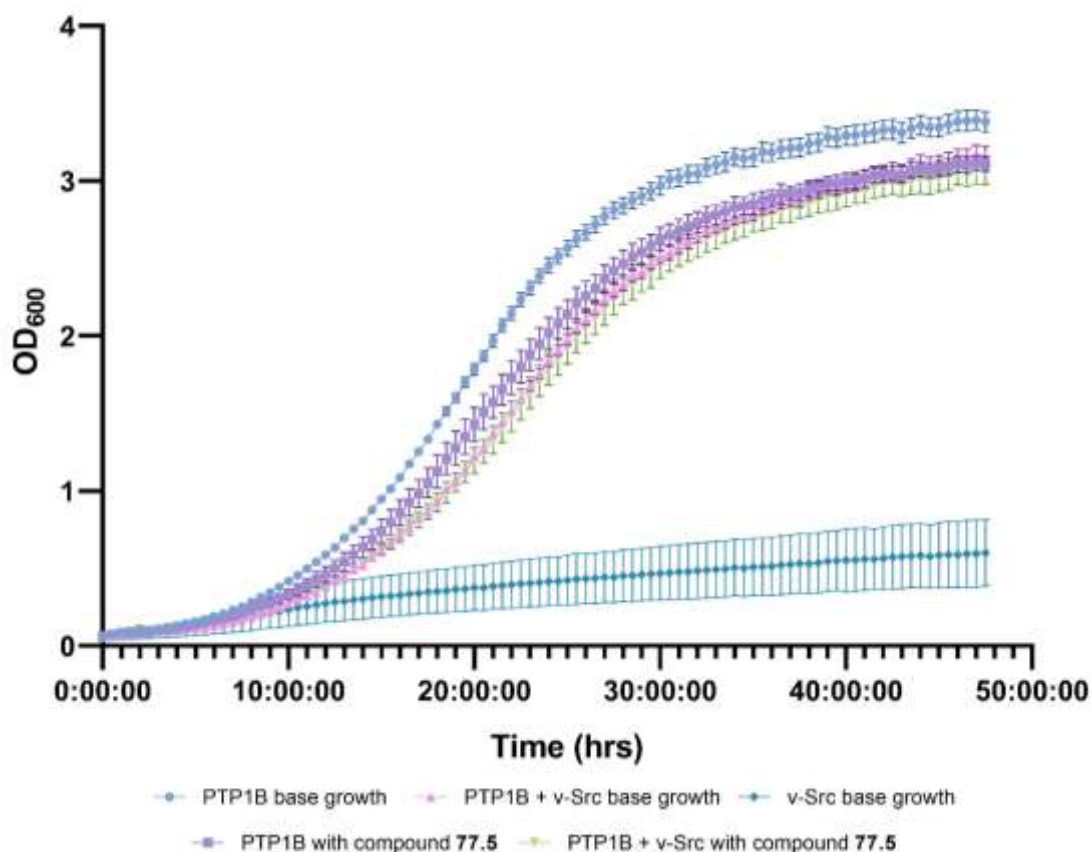
Transformed cells	PTP1B only *	PTP1B + v-Src
p value	<0.0010	ns

Figure CXLIII: Growth curves of PTP1B only, PTP1B + v-Src and v-Src only YMK23 transformations with and without the addition of compound **77.3** at 100 μ M. n=3 for each PTP1B based parameter, n=13 for v-Src. Mean and individual biological points \pm standard deviation plotted. Data is normally distributed according to a Shapiro-Wilk test. Used a 2-way ANOVA. * p value \leq 0.050 vs corresponding base growth.



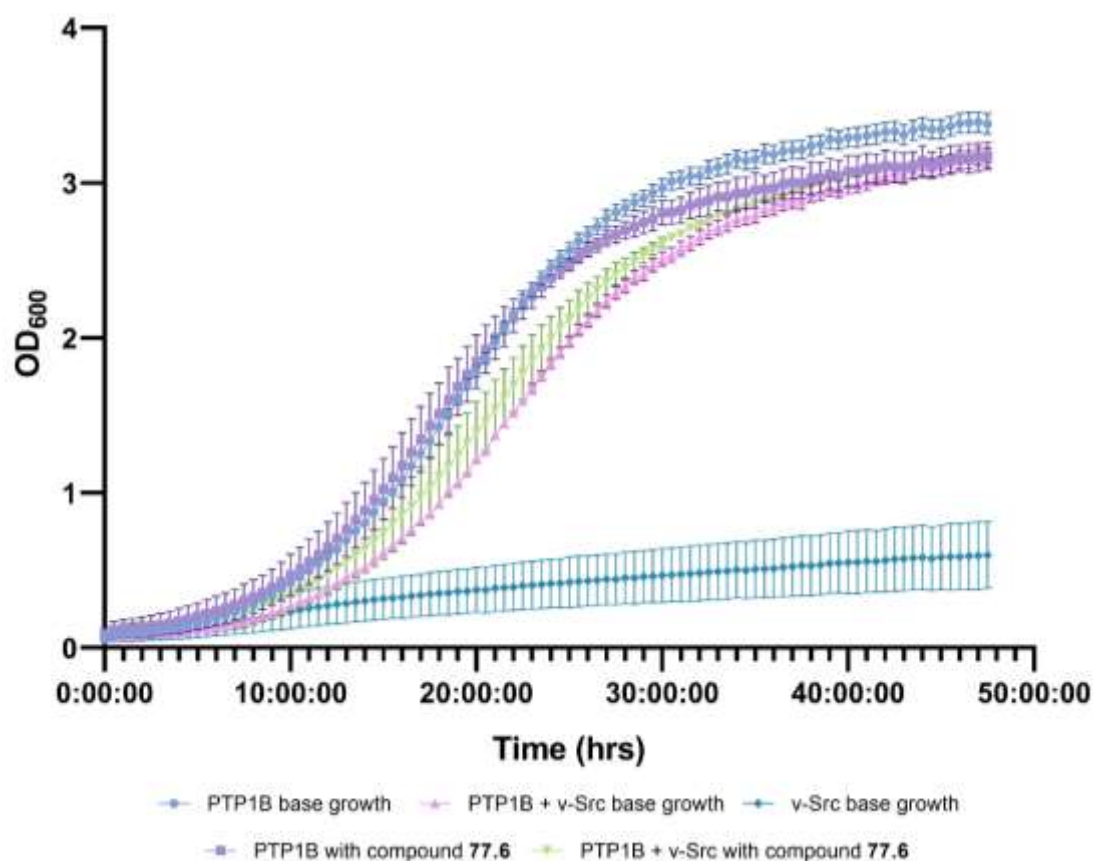
Transformed cells	PTP1B only *	PTP1B + v-Src
p value	<0.0100	ns

Figure CXLIV: Growth curves of PTP1B only, PTP1B + v-Src and v-Src only YMK23 transformations with and without the addition of compound **77.4** at 100 μ M. n=3 for each PTP1B based parameter, n=13 for v-Src. Mean and individual biological points \pm standard deviation plotted. Data is normally distributed according to a Shapiro-Wilk test. Used a 2-way ANOVA. * p value \leq 0.050 vs corresponding base growth.



Transformed cells	PTP1B only *	PTP1B + v-Src
p value	<0.0050	ns

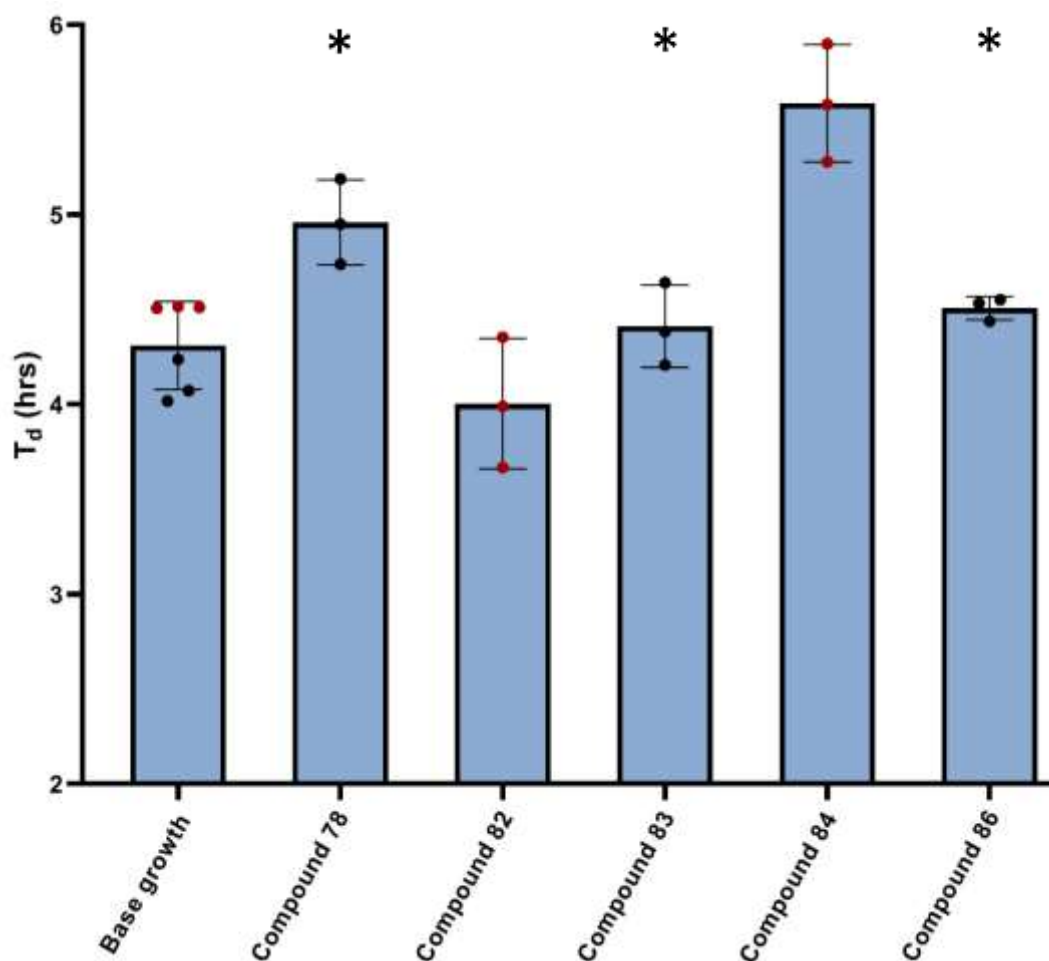
Figure CXLV: Growth curves of PTP1B only, PTP1B + v-Src and v-Src only YMK23 transformations with and without the addition of compound **77.5** at 100 μ M. n=3 for each PTP1B based parameter, n=13 for v-Src. Mean and individual biological points \pm standard deviation plotted. Data is normally distributed according to a Shapiro-Wilk test. Used a 2-way ANOVA. * p value \leq 0.050 vs corresponding base growth.



Transformed cells	PTP1B only	PTP1B + v-Src
p value	ns	ns

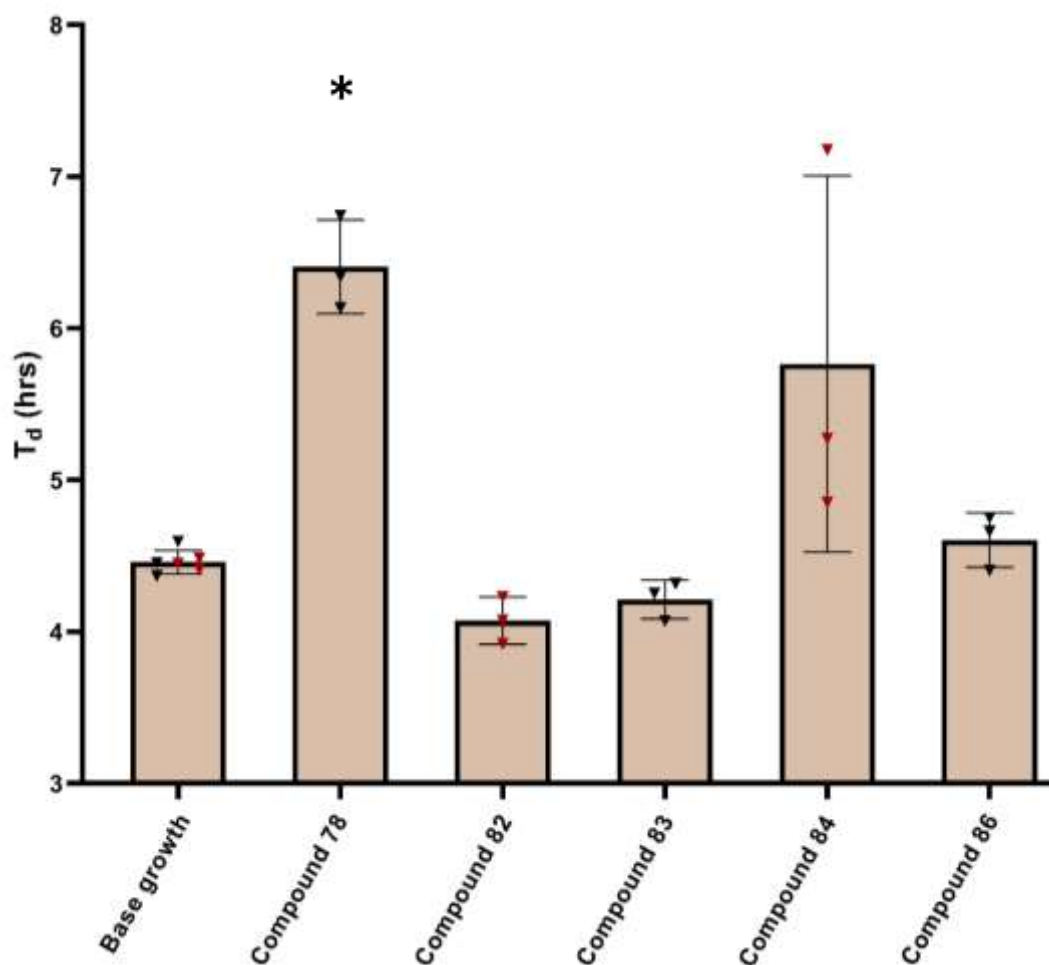
Figure CXLVI: Growth curves of PTP1B only, PTP1B + v-Src and v-Src only YMK23 transformations with and without the addition of compound 77.6 at 100 μ M. n=3 for each PTP1B based parameter, n=13 for v-Src. Mean and individual biological points \pm standard deviation plotted. Data is normally distributed according to a Shapiro-Wilk test. Used a 2-way ANOVA. * p value \leq 0.050 vs corresponding base growth.

3.1.4 Doubling time and growth curve data for 78, 82-84, 86



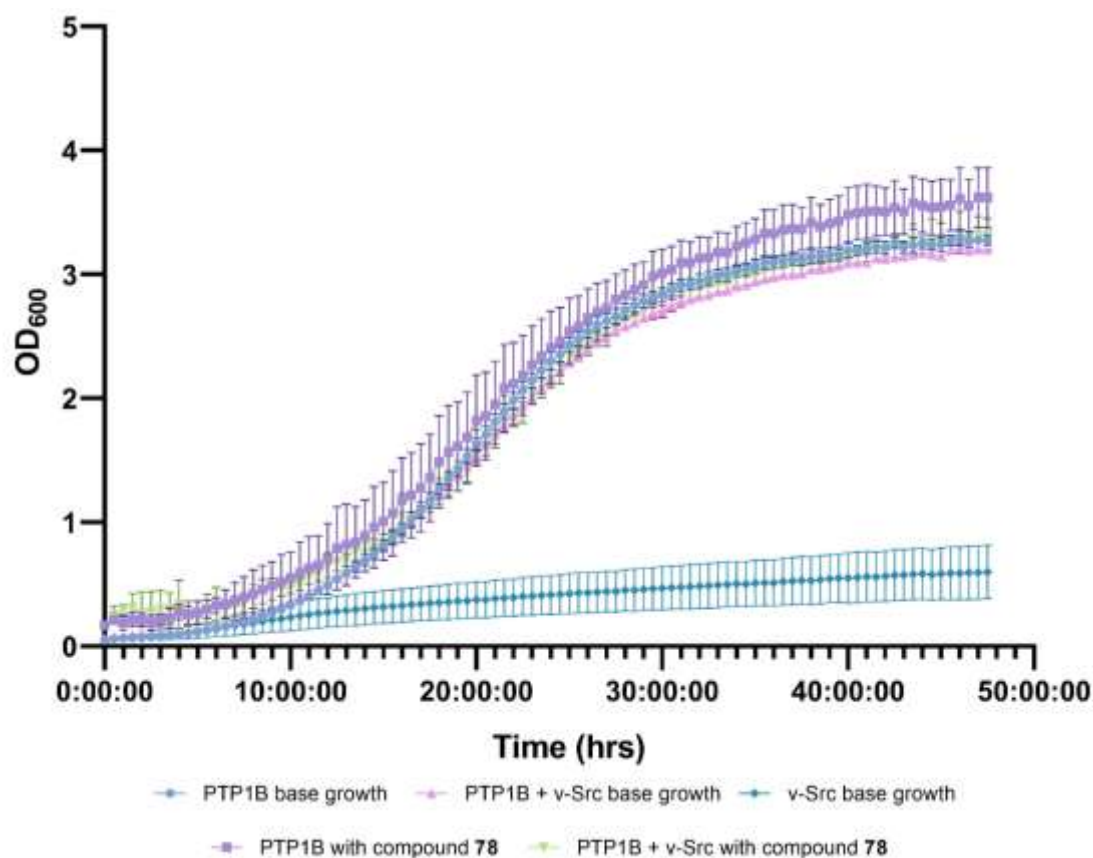
Compound	78	82	83	84	86
p value	<0.0500	ns	<0.0100	ns	<0.0500

Figure CXLVII: Effect of compound **78**, **82-84** and **86** addition at 100 μ M on the T_d value of PTP1B only transformed yeast cells. $n=3$ for all compounds tested $n=6$ for base growth. Colour coded denotes corresponding base growth values for each compound tested. Mean points \pm standard deviation plotted. Data is normally distributed according to a Shapiro-Wilk test. Used parametric Welch t-test for statistical analysis. * p value ≤ 0.050 vs base growth. All statistical analysis utilised corresponding base growth doubling time values.



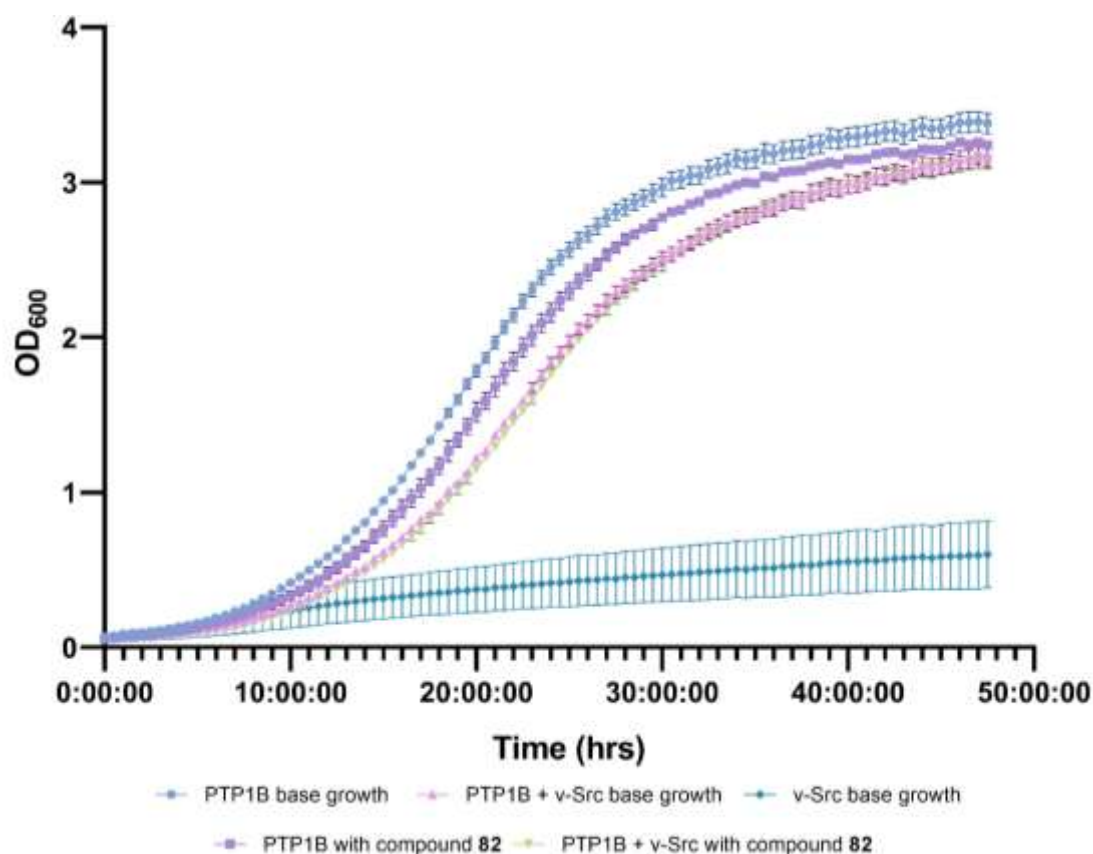
Compound	78	82	83	84	86
p value	<0.0050	ns	ns	<0.0500	ns

Figure CXLVIII: Effect of compound **78**, **82-84** and **86** addition at 100 μ M on the T_d value of PTP1B + v-Src transformed yeast cells. $n=3$ for all compounds tested $n=6$ for base growth. Colour coded denotes corresponding base growth values for each compound tested. Mean points \pm standard deviation plotted. Data is normally distributed according to a Shapiro-Wilk test. Used parametric Welch t-test for statistical analysis. * p value ≤ 0.050 vs base growth. All statistical analysis utilised corresponding base growth doubling time values. Note: **84** caused a significant decrease in the T_d value of PTP1B + v-Src cells.



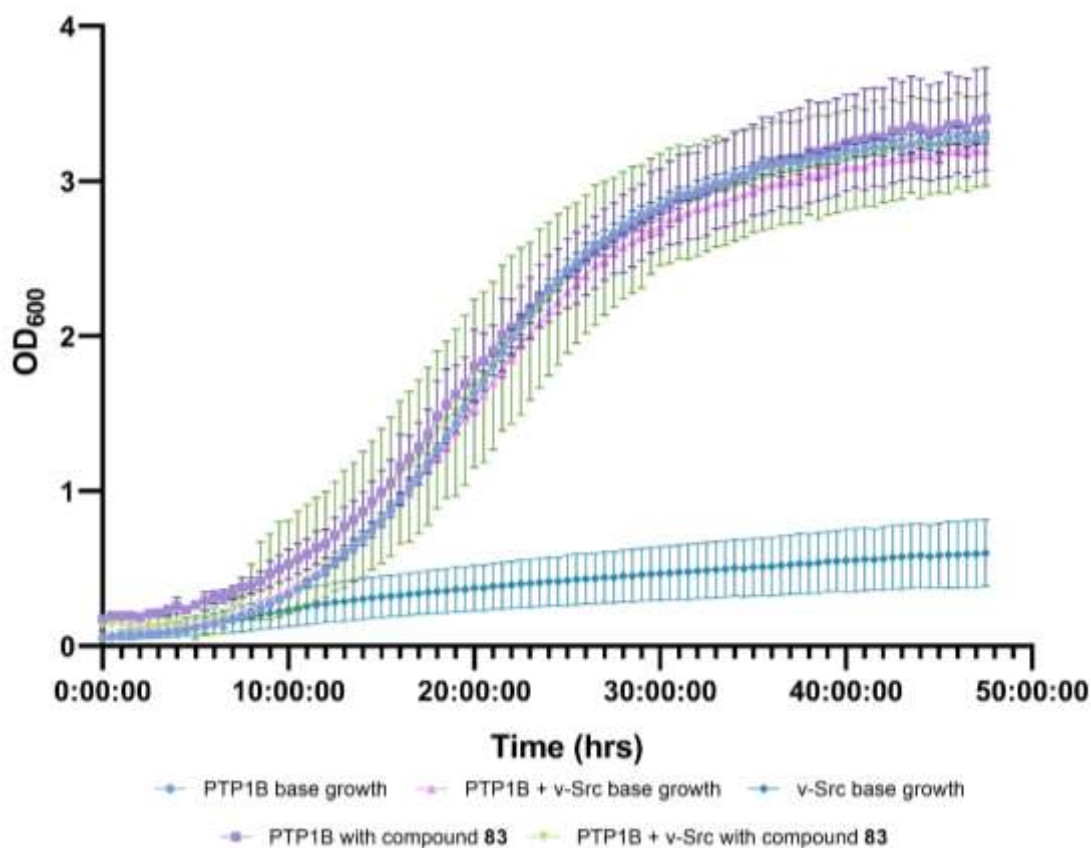
Transformed cells	PTP1B only	PTP1B + v-Src
p value	ns	ns

Figure CXLIX: Growth curves of PTP1B only, PTP1B + v-Src and v-Src only YMK23 transformations with and without the addition of compound **78** at 100 μ M. n=3 for each PTP1B based parameter, n=13 for v-Src. Mean and individual biological points \pm standard deviation plotted. Data is normally distributed according to a Shapiro-Wilk test. Used a 2-way ANOVA. * p value \leq 0.050 vs corresponding base growth.



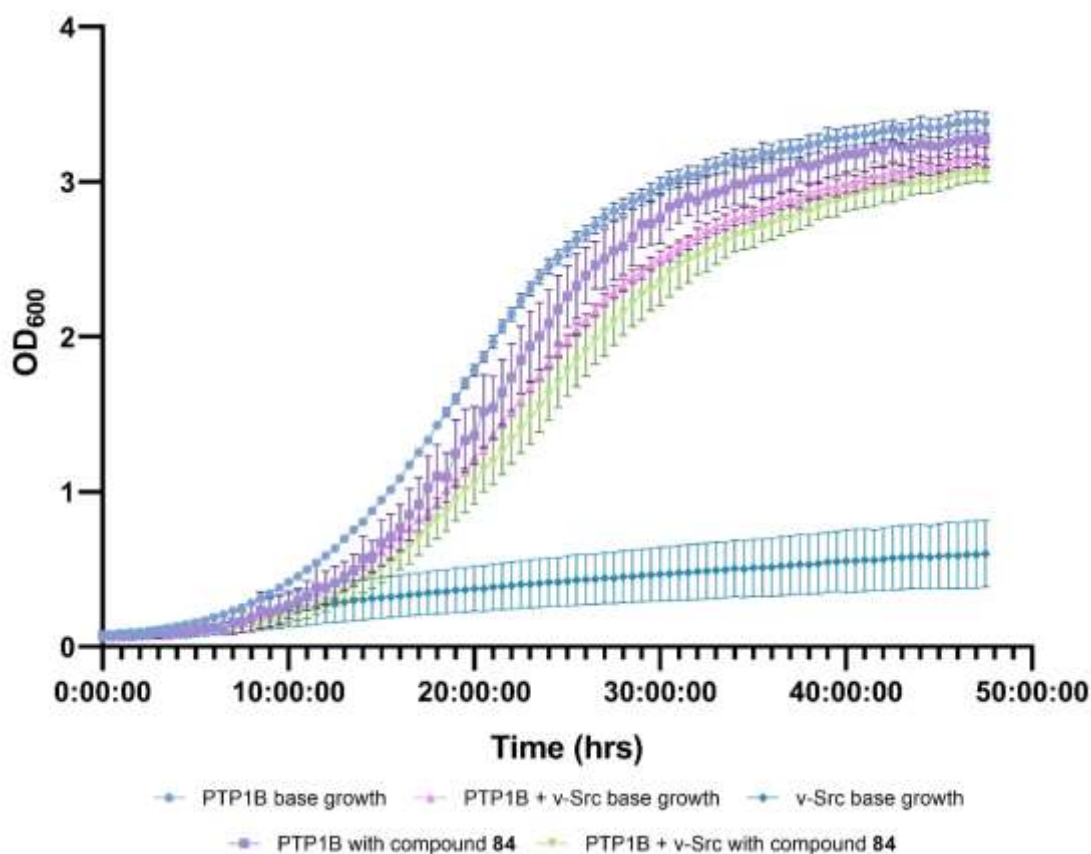
Transformed cells	PTP1B only *	PTP1B + v-Src
p value	<0.0050	ns

Figure CL: Growth curves of PTP1B only, PTP1B + v-Src and v-Src only YMK23 transformations with and without the addition of compound **82** at 100 μ M. n=3 for each PTP1B based parameter, n=13 for v-Src. Mean and individual biological points \pm standard deviation plotted. Data is normally distributed according to a Shapiro-Wilk test. Used a 2-way ANOVA. * p value \leq 0.050 vs corresponding base growth.



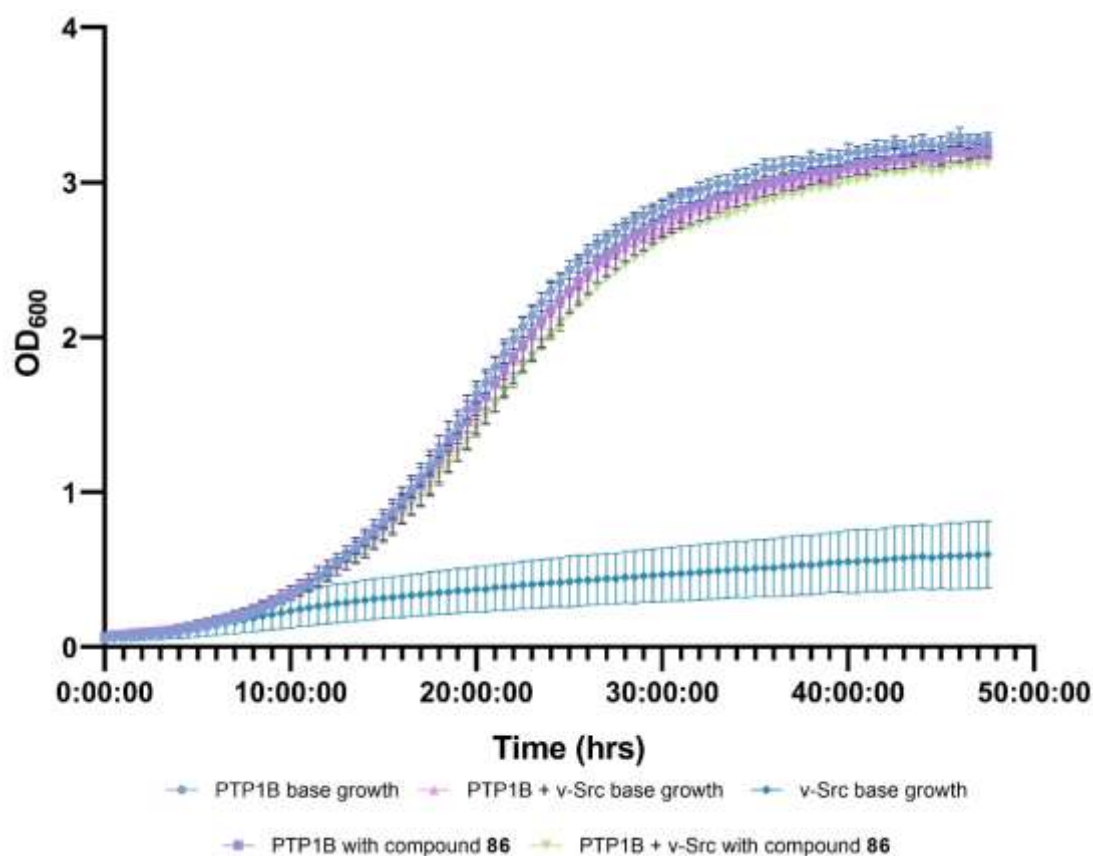
Transformed cells	PTP1B only	PTP1B + v-Src
p value	ns	ns

Figure CLI: Growth curves of PTP1B only, PTP1B + v-Src and v-Src only YMK23 transformations with and without the addition of compound **83** at 100 μ M. n=3 for each PTP1B based parameter, n=13 for v-Src. Mean and individual biological points \pm standard deviation plotted. Data is normally distributed according to a Shapiro-Wilk test. Used a 2-way ANOVA. * p value \leq 0.050 vs corresponding base growth.



Transformed cells	PTP1B only	PTP1B + v-Src
p value	ns	ns

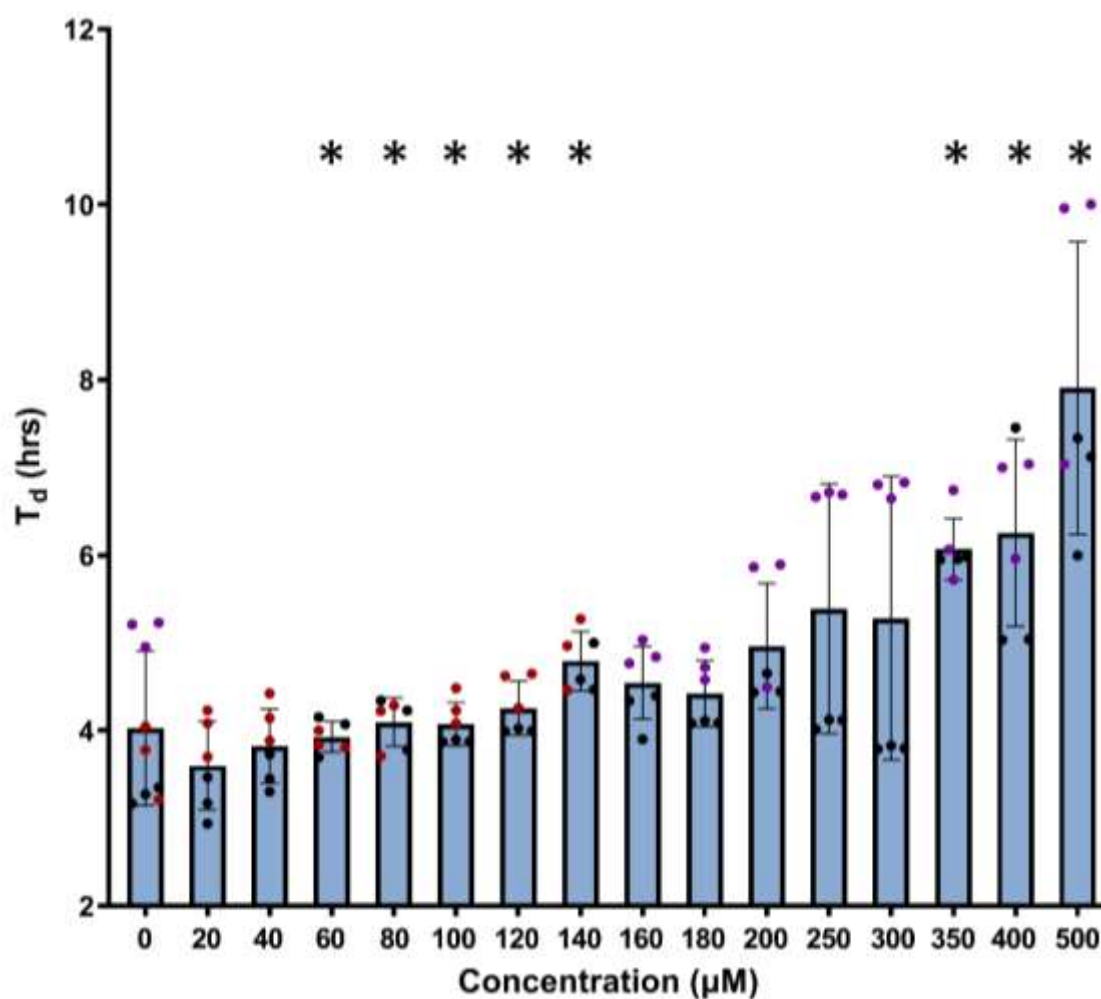
Figure CLII: Growth curves of PTP1B only, PTP1B + v-Src and v-Src only YMK23 transformations with and without the addition of compound **84** at 100 μ M. n=3 for each PTP1B based parameter, n=13 for v-Src. Mean and individual biological points \pm standard deviation plotted. Data is normally distributed according to a Shapiro-Wilk test. Used a 2-way ANOVA. * p value \leq 0.050 vs corresponding base growth.



Transformed cells	PTP1B only	PTP1B + v-Src *
p value	ns	<0.0500

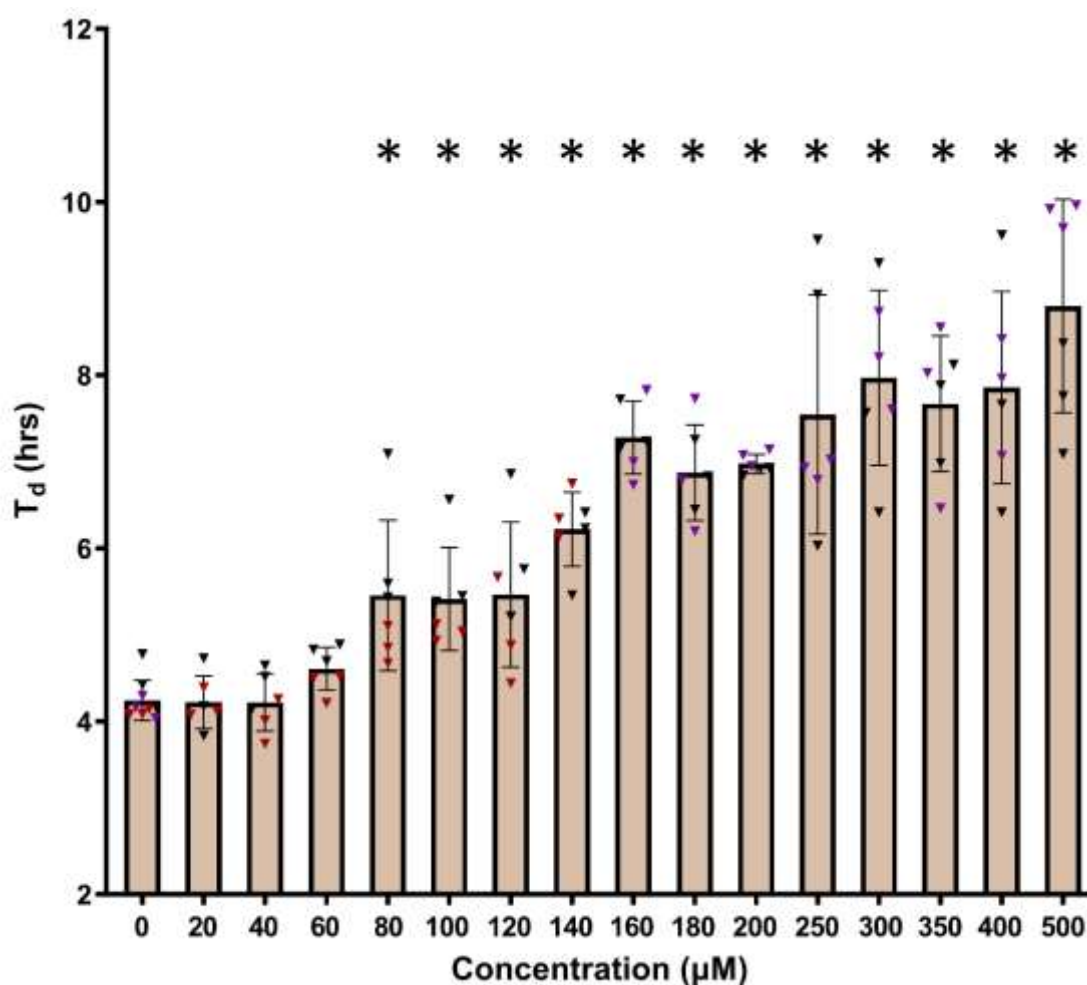
Figure CLIII: Growth curves of PTP1B only, PTP1B + v-Src and v-Src only YMK23 transformations with and without the addition of compound **86** at 100 μ M. n=3 for each PTP1B based parameter, n=13 for v-Src. Mean and individual biological points \pm standard deviation plotted. Data is normally distributed according to a Shapiro-Wilk test. Used a 2-way ANOVA. * p value \leq 0.050 vs corresponding base growth.

3.1.5 Dose response screen of compound 78; doubling time and growth curve results.



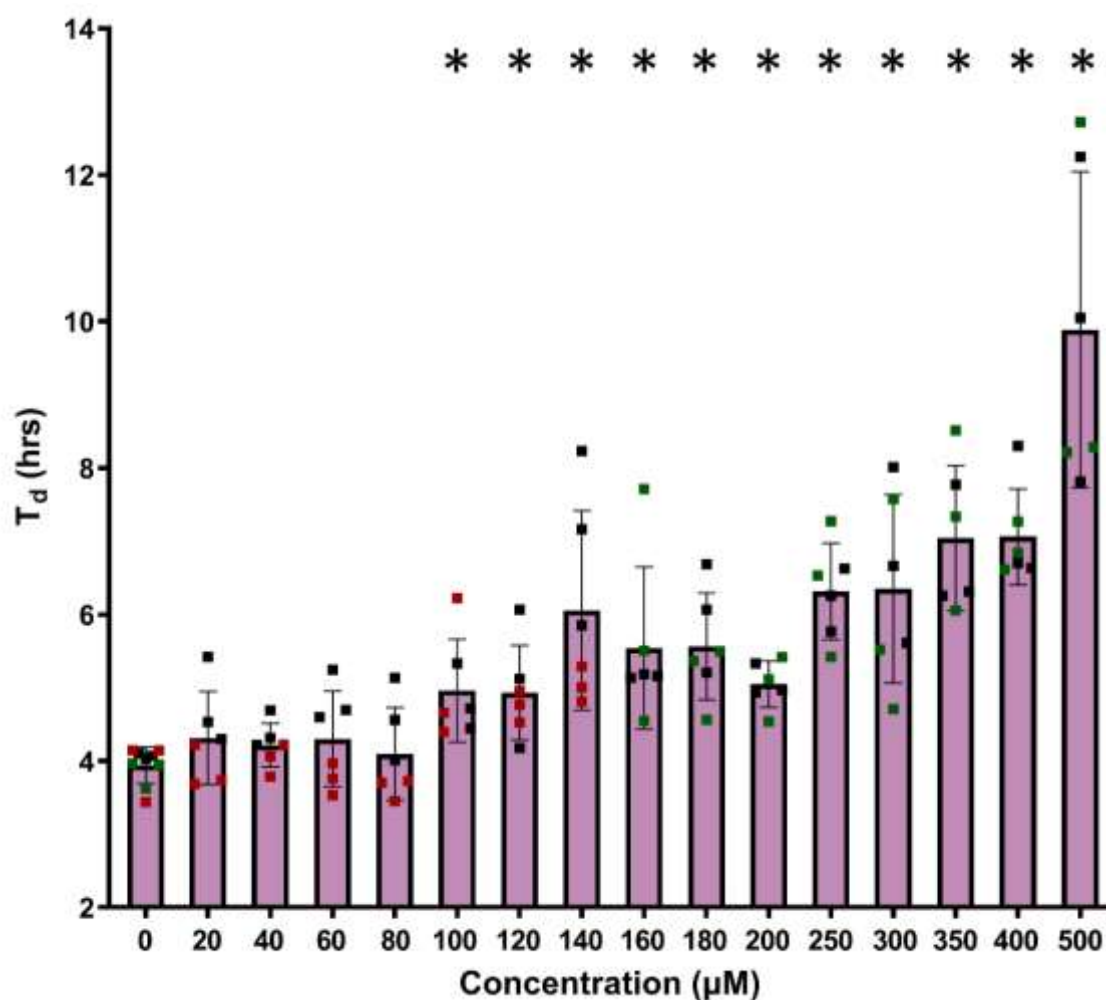
µM	20	40	60	80	100	120	140	160	180	200	250	300	350	400	500
p values	ns	ns	<0.0500	<0.0500	<0.0500	<0.0500	<0.0050	ns	ns	ns	ns	ns	<0.0050	<0.0500	<0.0050

Figure CLIV: Effect of compound 78 addition at 20-500 µM on the T_d value of PTP1B only transformed yeast cells. n=6 for all concentrations, n=9 for base growth. Colour coded denotes corresponding base growth values for each compound tested. Mean points ± standard deviation plotted. Data is not normally distributed according to a Shapiro-Wilk test. Used non-parametric Mann-Whitney t-test for statistical analysis. * p value ≤ 0.050 vs base growth. All statistical analysis utilised corresponding base growth doubling time values.



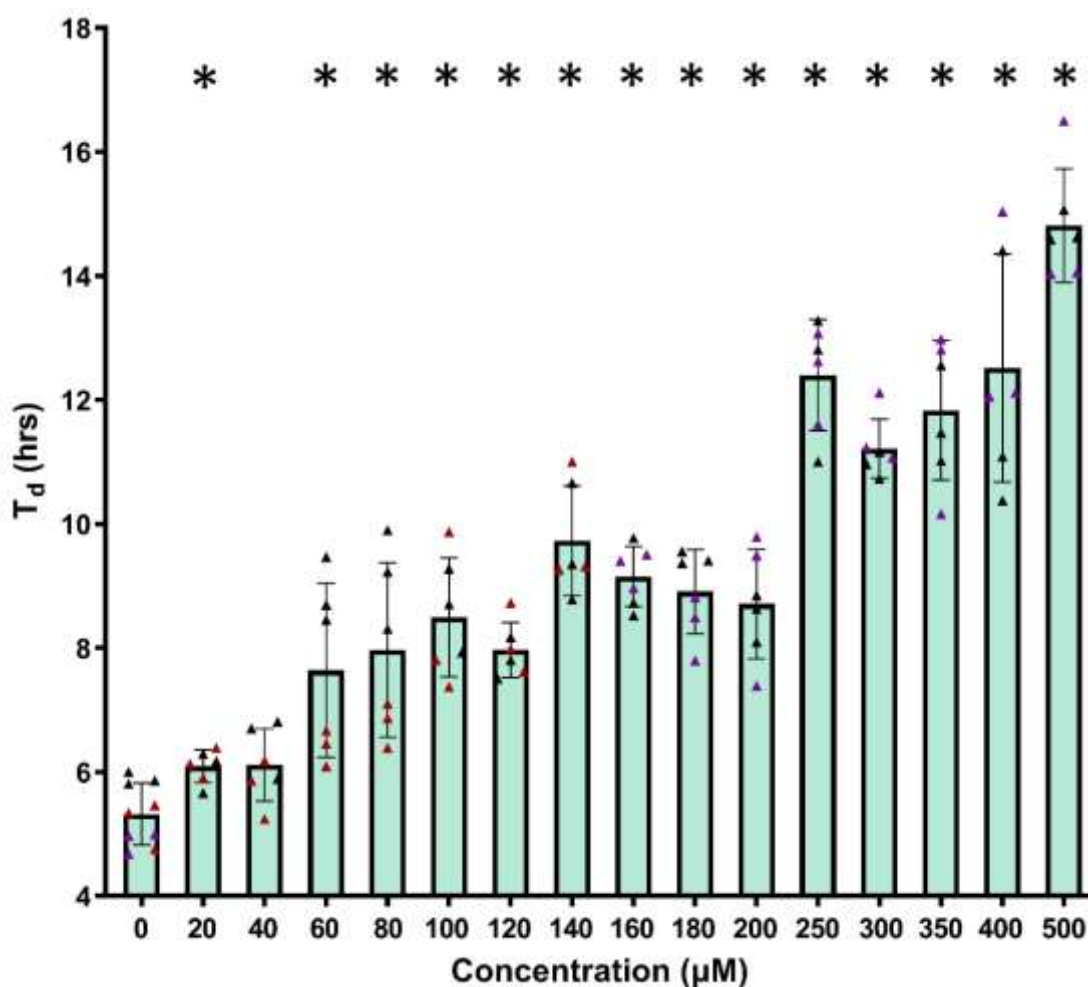
µM	p values
20	ns
40	ns
60	ns
80	<0.0500
100	<0.0050
120	<0.0500
140	<0.0001
160	<0.0001
180	<0.0001
200	<0.0001
250	0.0019
300	0.0002
350	<0.0001
400	<0.0005
500	<0.0005

Figure CLV: Effect of compound **78** addition at 20-500 µM on the T_d value of PTP1B + v-Src transformed yeast cells. n=6 for all concentrations, n=9 for base growth. Colour coded denotes corresponding base growth values for each compound tested Mean points ± standard deviation plotted. Data is normally distributed according to a Shapiro-Wilk test. Used parametric Welch's t-test for statistical analysis. * p value ≤ 0.050 vs base growth. All statistical analysis utilised corresponding base growth doubling time values.



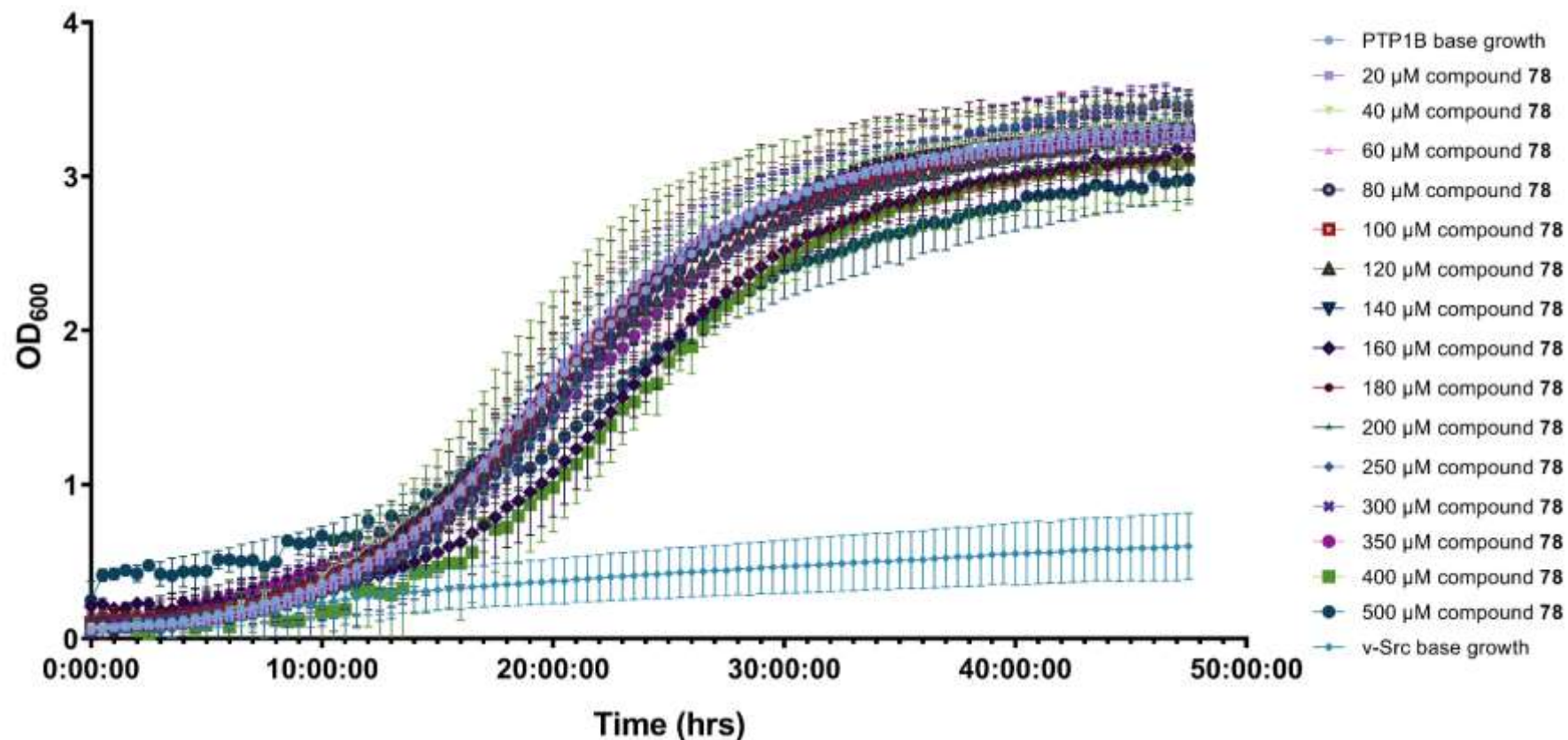
μM	20	40	60	80	100	120	140	160	180	200	250	300	350	400	500
p values	ns	ns	ns	ns	<0.0050	<0.0050	<0.0050	<0.0050	<0.0050	<0.0050	<0.0050	<0.0050	<0.0050	<0.0050	<0.0050

Figure CLVI: Effect of compound **78** addition at 20-500 μM on the T_d value of TCPTP only transformed yeast cells. $n=6$ for all concentrations, $n=9$ for base growth. Colour coded denotes corresponding base growth values for each compound tested. Mean points \pm standard deviation plotted. Data is not normally distributed according to a Shapiro-Wilk test. Used non-parametric Mann-Whitney t-test for statistical analysis. * p value ≤ 0.050 vs base growth. All statistical analysis utilised corresponding base growth doubling time values.



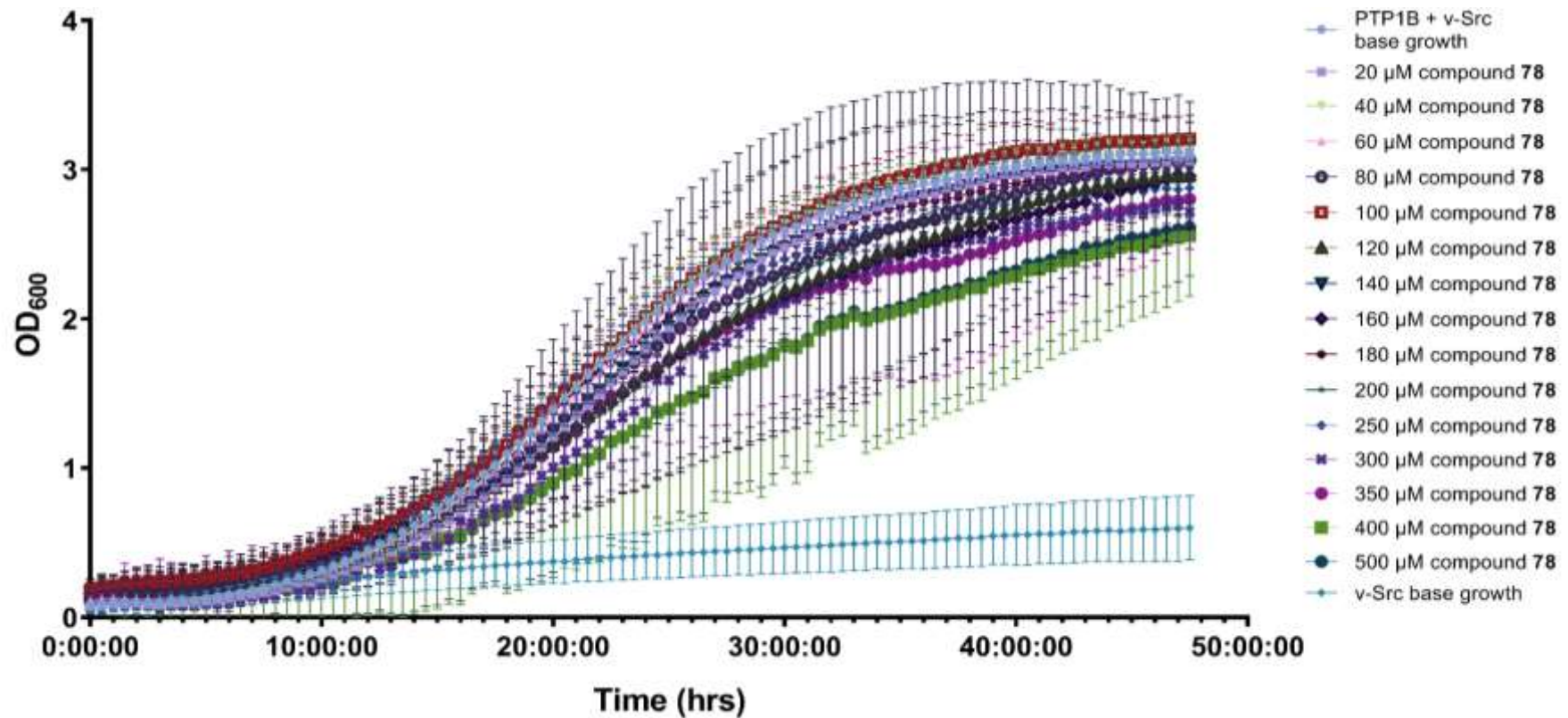
µM	p values
20	<0.0500
40	ns
60	<0.0500
80	<0.0100
100	<0.0005
120	<0.0001
140	<0.0001
160	<0.0001
180	<0.0001
200	<0.0001
250	<0.0001
300	<0.0001
350	<0.0001
400	<0.0001
500	<0.0001

Figure CLVII: Effect of compound **78** addition at 20-500 µM on the T_d value of TCPTP + v-Src transformed yeast cells. n=6 for all concentrations, n=9 for base growth. Colour coded denotes corresponding base growth values for each compound tested Mean points ± standard deviation plotted. Data is normally distributed according to a Shapiro-Wilk test. Used parametric Welch's t-test for statistical analysis. * p value ≤ 0.050 vs base growth. All statistical analysis utilised corresponding base growth doubling time values.



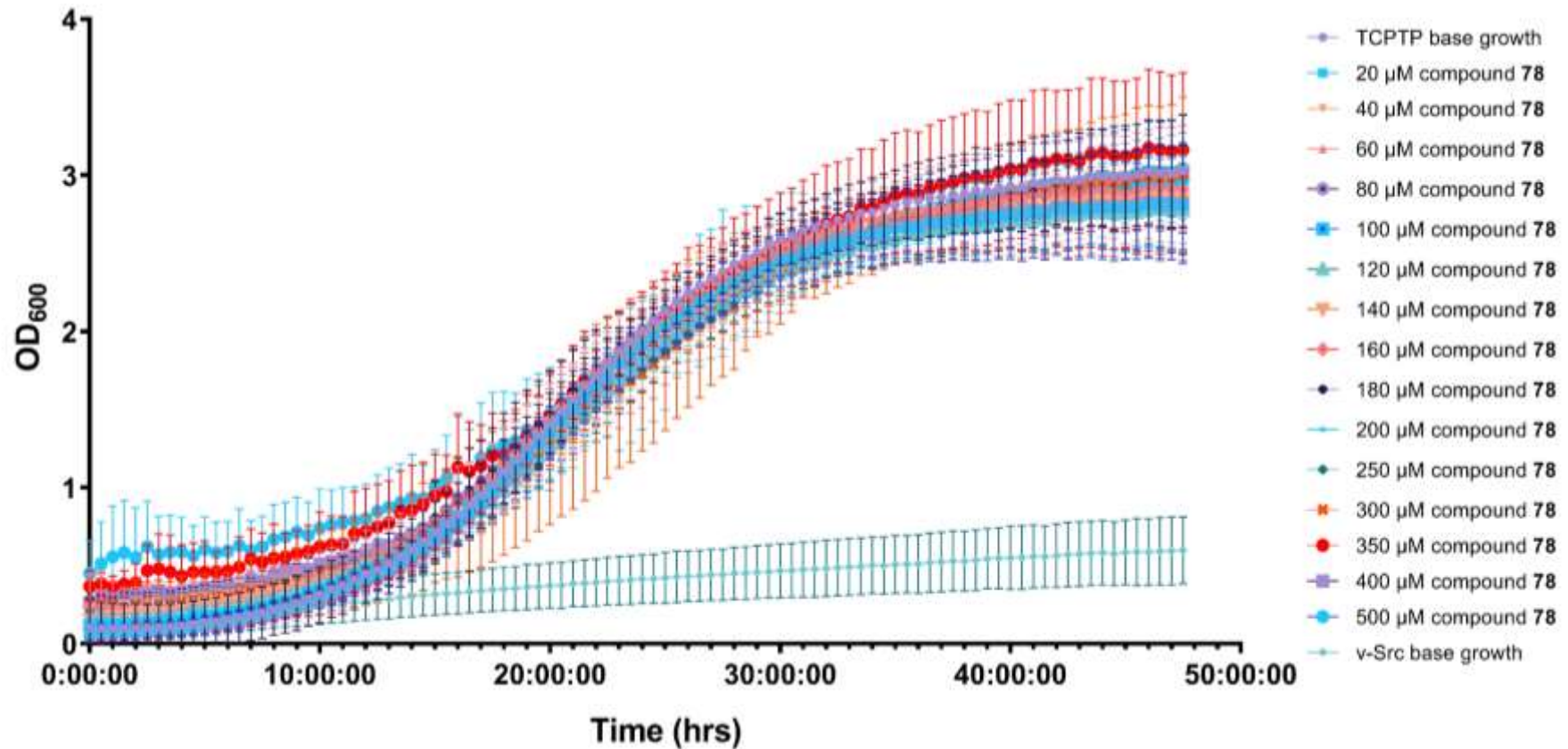
μM	20	40	60	80	100	120	140	160 *	180	200	250	300	350	400 *	500*
p value	ns	ns	ns	ns	ns	ns	ns	<0.0100	ns	ns	ns	ns	ns	<0.0100	<0.0010

Figure CLVIII: Growth profile of PTP1B only yeast cells with the addition of compound **78** at 20-500 μM . $n=6$ for all concentrations in PTP1B only cells, $n=9$ for base growth, $n=13$ for v-Src base growth. Mean points \pm standard deviation plotted. Data is not normally distributed according to a Shapiro-Wilk test. Used a 2-way ANOVA where column factor was source of variance. * p value ≤ 0.050 vs control. All statistical analysis utilised corresponding base growth doubling time values.



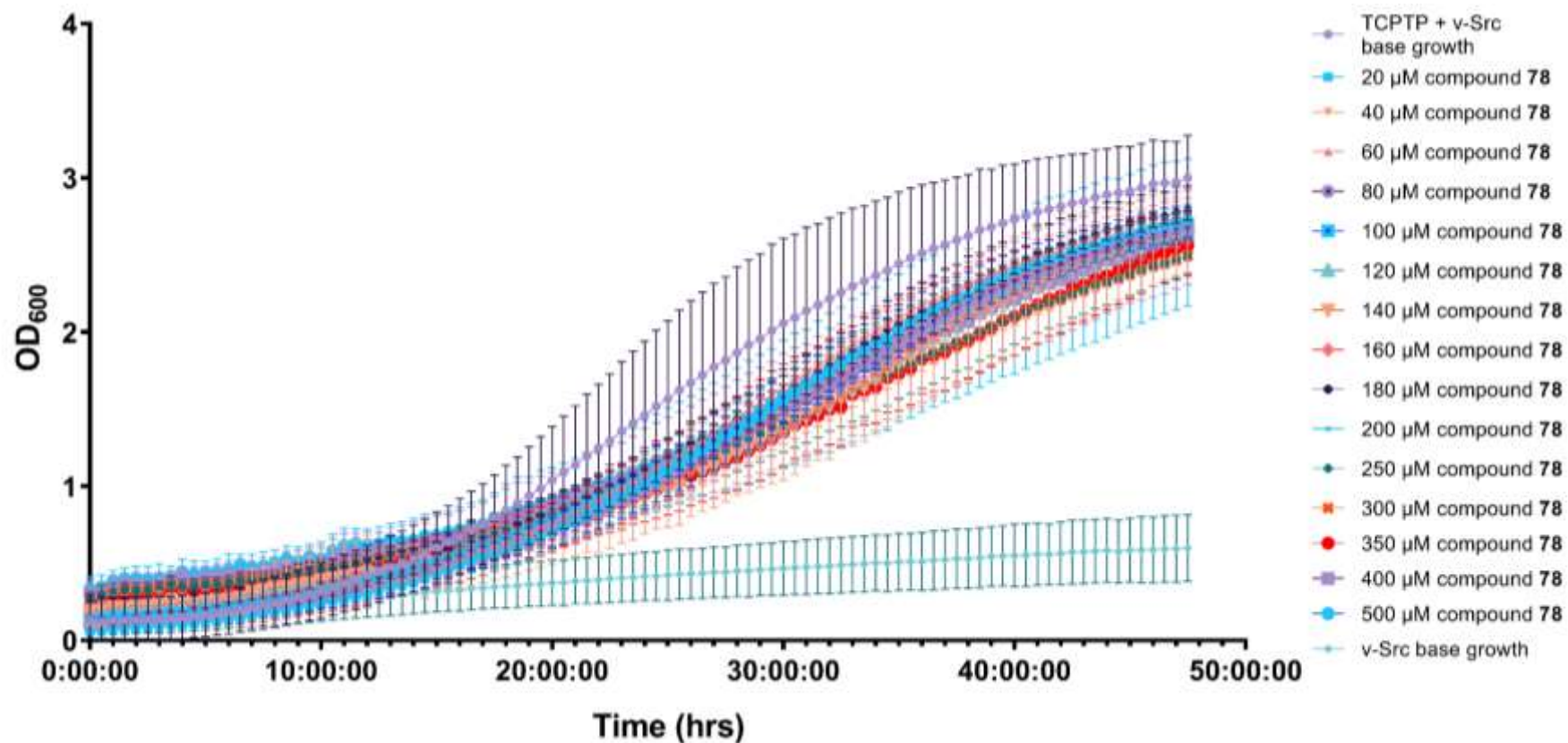
μM	20	40	60	80	100	120	140	160	180	200	250	300 *	350	400	500
p value	ns	ns	ns	ns	ns	ns	ns	ns	ns	ns	ns	<0.0005	ns	ns	ns

Figure CLIX: Growth profile of PTP1B + v-Src yeast cells with the addition of compound 78 at 20-500 μM. n=6 for all concentrations in PTP1B only cells, n=9 for base growth, n=13 for v-Src base growth. Mean points ± standard deviation plotted. Data is normally distributed according to a Shapiro-Wilk test. Used a 2-way ANOVA where column factor was source of variance. * p value ≤ 0.050 vs control. All statistical analysis utilised corresponding base growth doubling time values.



μM	20	40	60	80	100	120	140	160	180	200	250	300	350	400	500
p value	ns	ns	ns	ns	ns	ns	ns	ns	ns	ns	ns	ns	ns	ns	ns

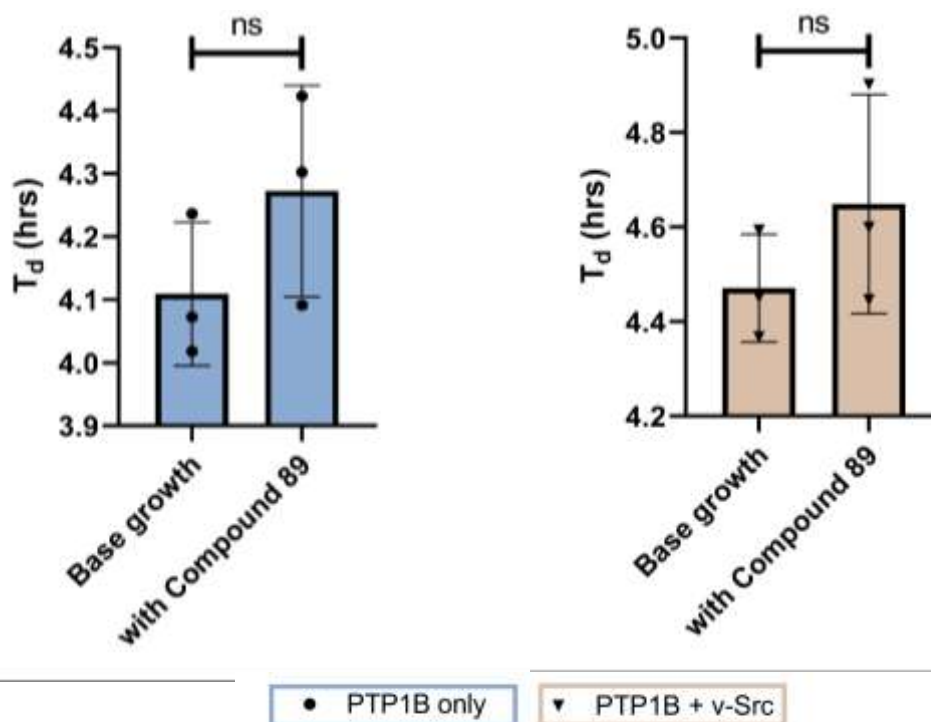
Figure CLX: Growth profile of TCPTP only yeast cells with the addition of compound **78** at 20-500 μM. n=6 for all concentrations in PTP1B only cells, n=9 for base growth, n=13 for v-Src base growth. Mean points ± standard deviation plotted. Data is not normally distributed according to a Shapiro-Wilk test. Used a 2-way ANOVA where column factor was source of variance. * p value ≤ 0.050 vs control. All statistical analysis utilised corresponding base growth doubling time values.



μM	20	40	60	80	100	120	140	160	180	200	250	300	350	400	500
p value	ns	ns	ns	ns	ns	ns	ns	ns	ns	ns	ns	ns	ns	ns	ns

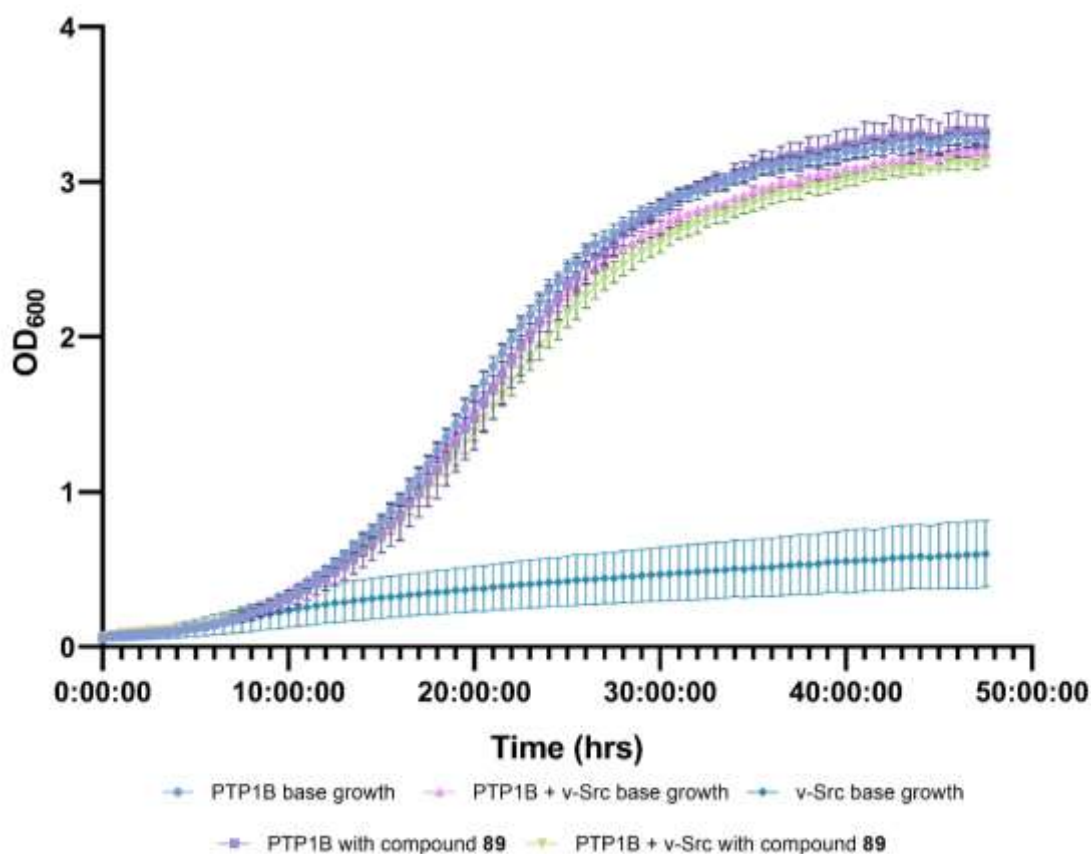
Figure CLXI: Growth profile of TCPTP + v-Src yeast cells with the addition of compound **78** at 20-500 μM. n=6 for all concentrations in PTP1B only cells, n=9 for base growth, n=13 for v-Src base growth. Mean points ± standard deviation plotted. Data is normally distributed according to a Shapiro-Wilk test. Used a 2-way ANOVA where column factor was source of variance. * p value ≤ 0.050 vs control. All statistical analysis utilised corresponding base growth doubling time values.

3.1.6 Doubling time and growth curve data of compound 89.



Transformed cells	PTP1B only	PTP1B + v-Src
p value	ns	ns

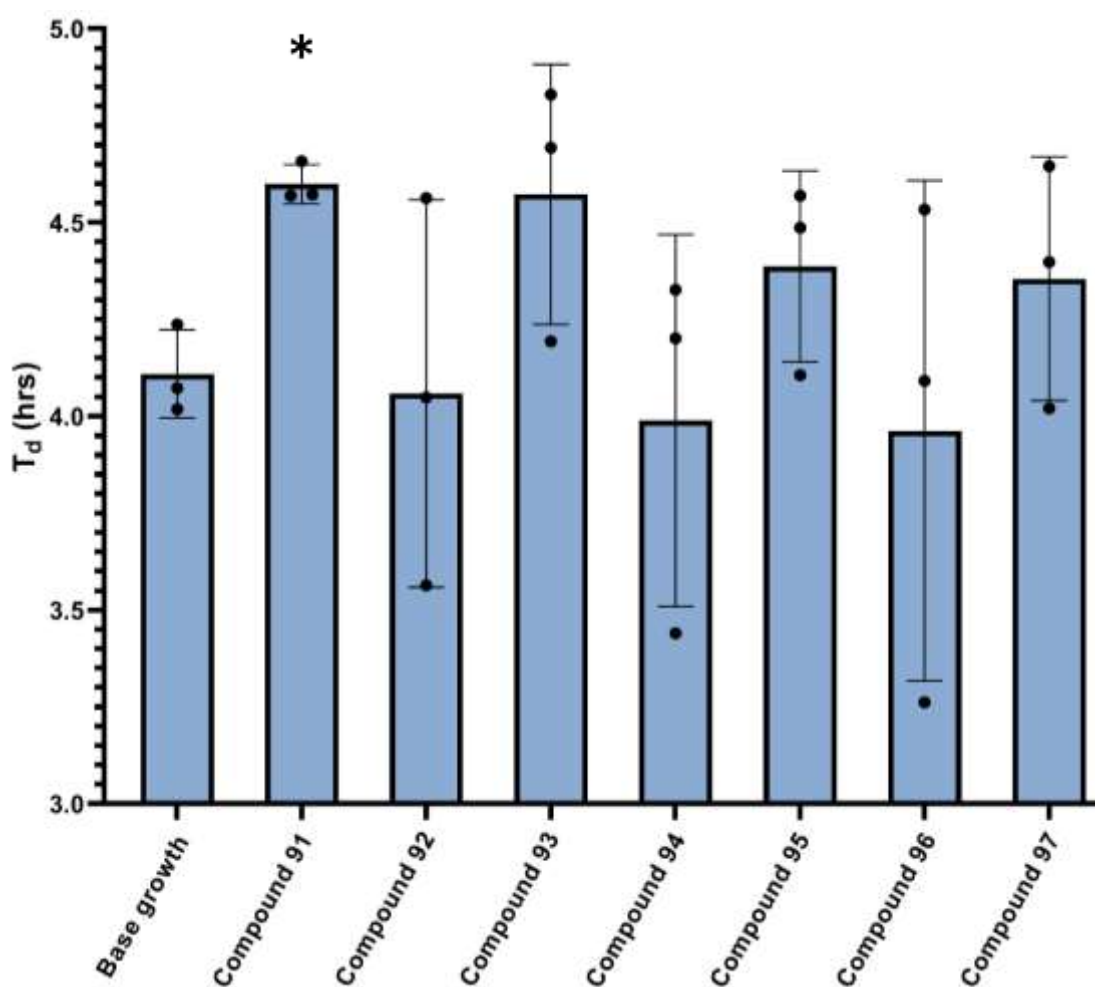
Figure CLXII: Effect of compound **89** addition at 100 μ M on the T_d value of PTP1B only and PTP1B + v-Src transformed yeast cells. $n=3$ for all parameters. Mean points \pm standard deviation plotted. Data is normally distributed according to a Shapiro-Wilk test. Used parametric Welch t-test for statistical analysis. * p value ≤ 0.050 vs base growth.



Transformed cells	PTP1B only	PTP1B + v-Src
p value	ns	ns

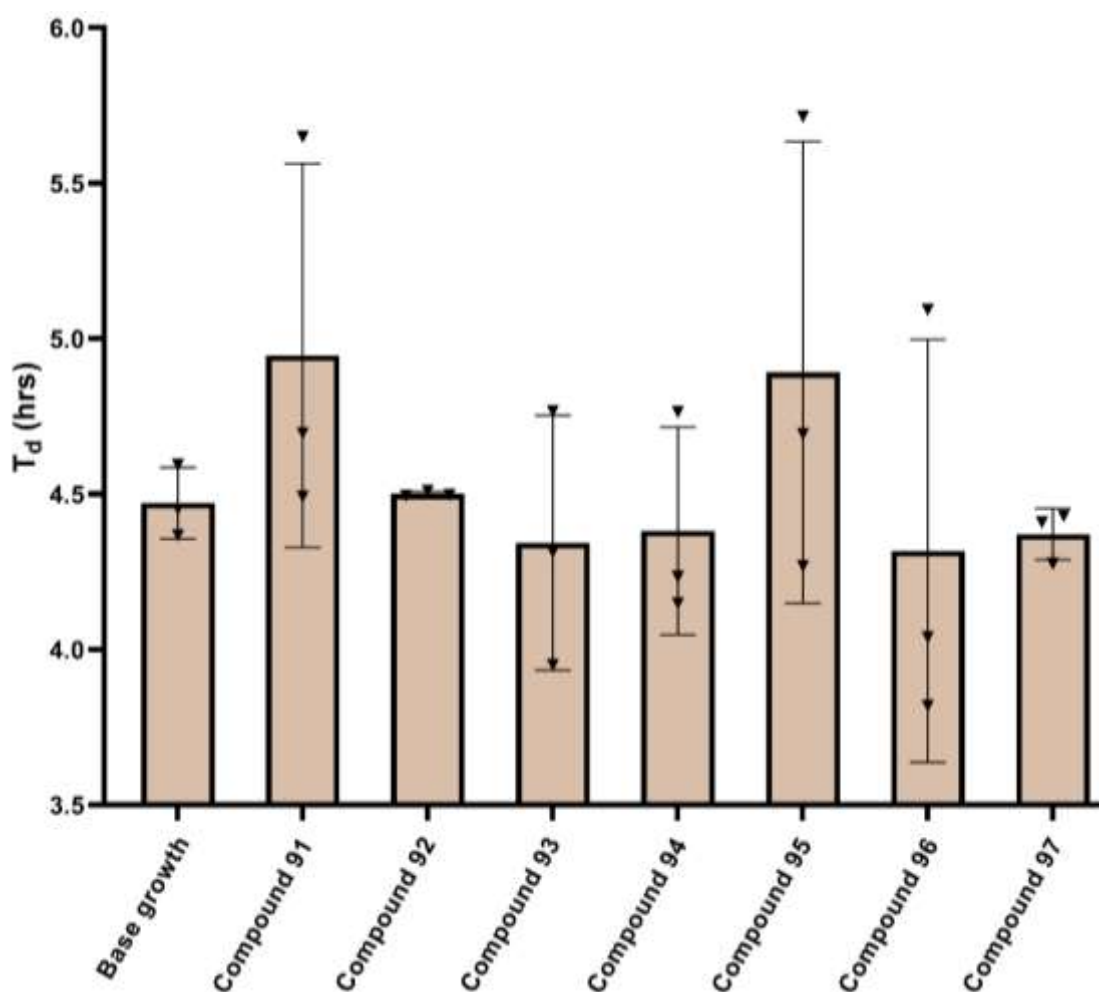
Figure CLXIII: Growth curves of PTP1B only, PTP1B + v-Src and v-Src only YMK23 transformations with and without the addition of compound **89** at 100 μ M. n=3 for each PTP1B based parameter, n=13 for v-Src. Mean and individual biological points \pm standard deviation plotted. Data is normally distributed according to a Shapiro-Wilk test. Used a 2-way ANOVA. * p value \leq 0.050 vs corresponding base growth.

3.1.7 Doubling time and growth curve data for compounds 91-97.



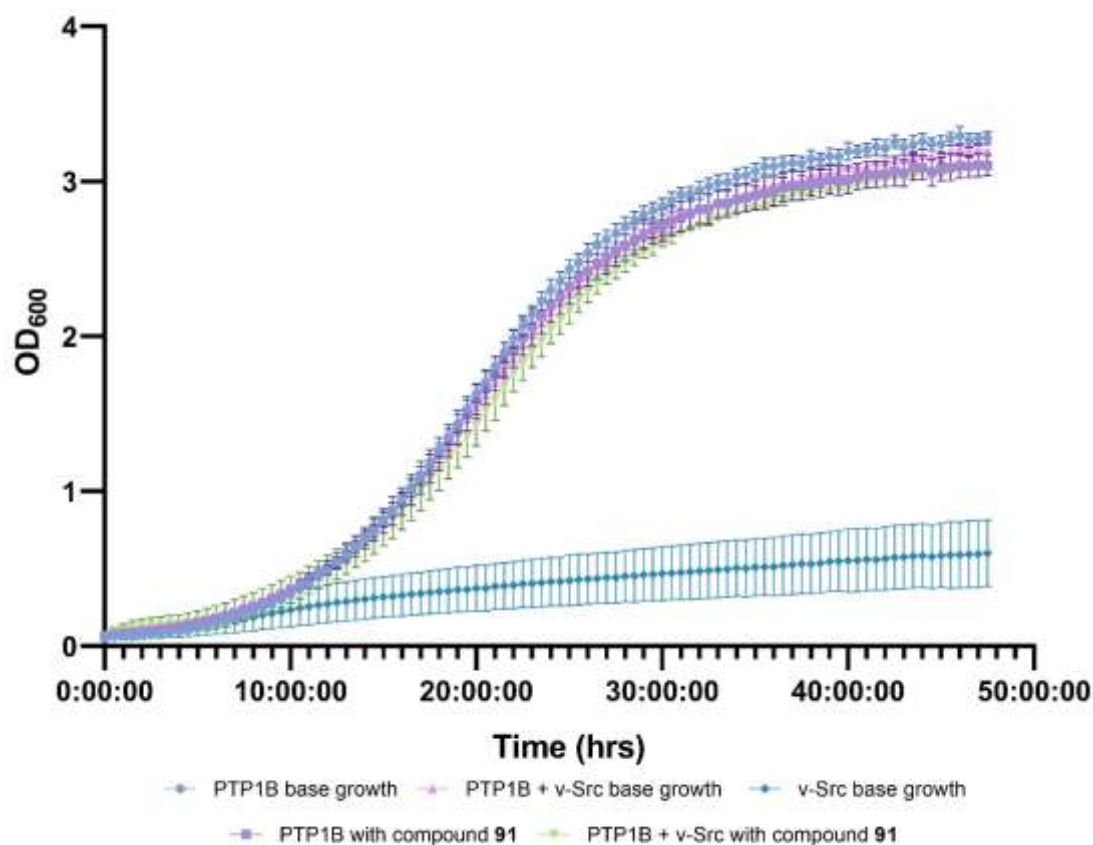
Compound	91	92	93	94	95	96	97
p value	<0.010	ns	ns	ns	ns	ns	ns

Figure CLXIV: Effect of compound 91-97 addition at 100 μ M on the T_d value of PTP1B only transformed yeast cells. $n=3$ for all compounds tested $n=3$ for base growth. Mean points \pm standard deviation plotted. Data is normally distributed according to a Shapiro-Wilk test. Used parametric Welch t-test for statistical analysis. * p value ≤ 0.050 vs base growth.



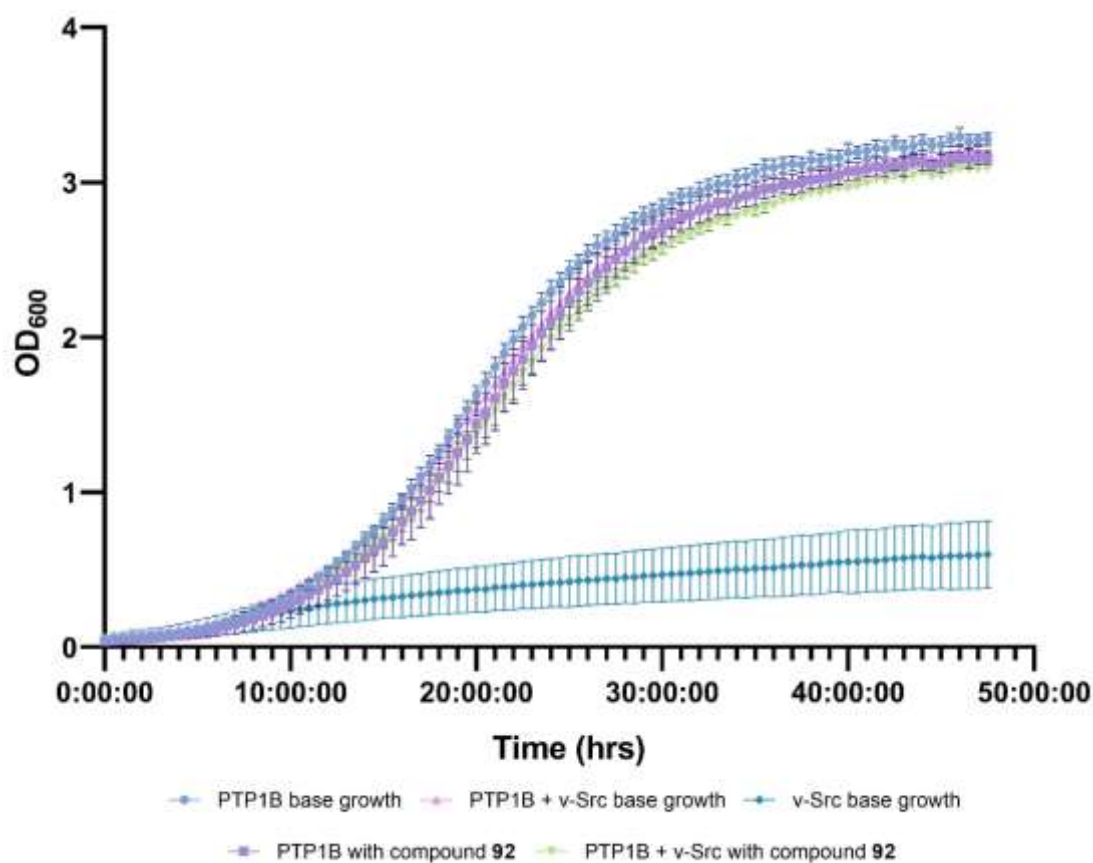
Compound	91	92	93	94	95	96	97
p value	ns	ns	ns	ns	ns	ns	ns

Figure CLXV: Effect of compound 91-97 addition at 100 μ M on the T_d value of PTP1B + v-Src transformed yeast cells. $n=3$ for all compounds tested $n=3$ for base growth. Mean points \pm standard deviation plotted. Data is normally distributed according to a Shapiro-Wilk test. Used parametric Welch t-test for statistical analysis. * p value ≤ 0.050 vs base growth.



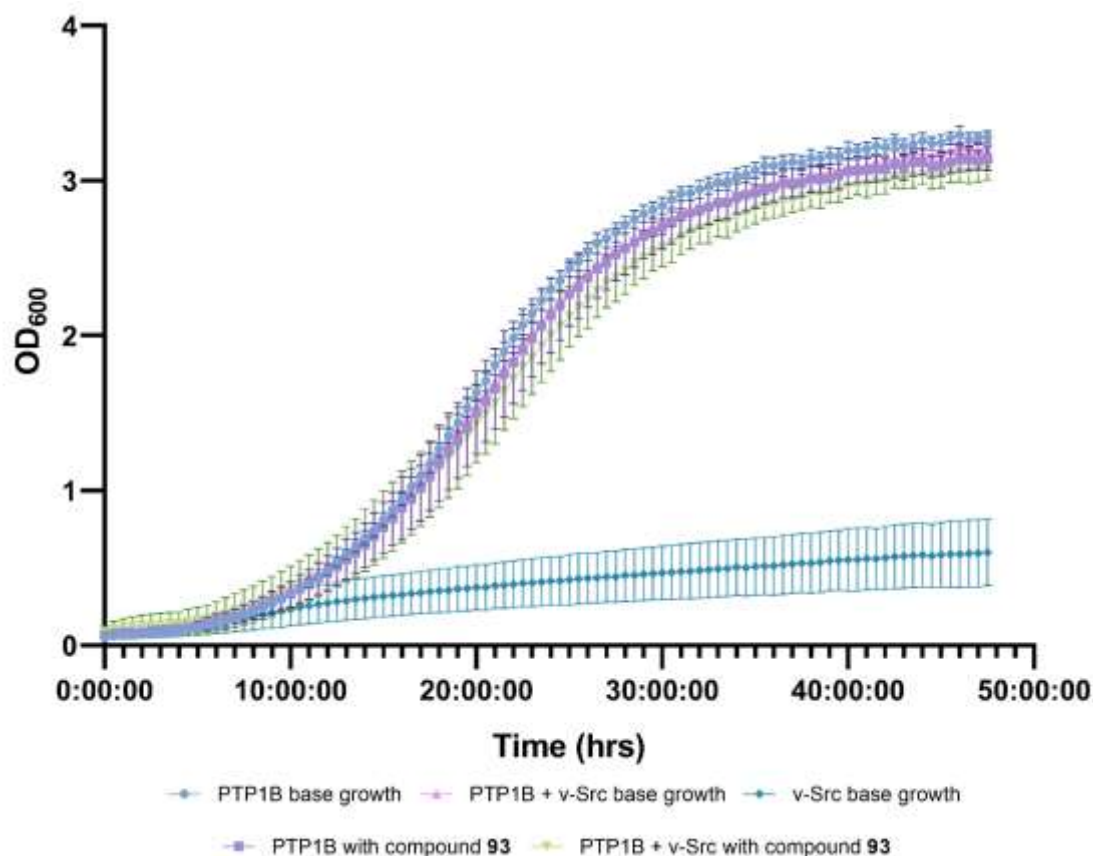
Transformed cells	PTP1B only	PTP1B + v-Src
p value	ns	ns

Figure CLXVI: Growth curves of PTP1B only, PTP1B + v-Src and v-Src only YMK23 transformations with and without the addition of compound **91** at 100 μ M. n=3 for each PTP1B based parameter, n=13 for v-Src. Mean and individual biological points \pm standard deviation plotted. Data is normally distributed according to a Shapiro-Wilk test. Used a 2-way ANOVA. * p value \leq 0.050 vs corresponding base growth.



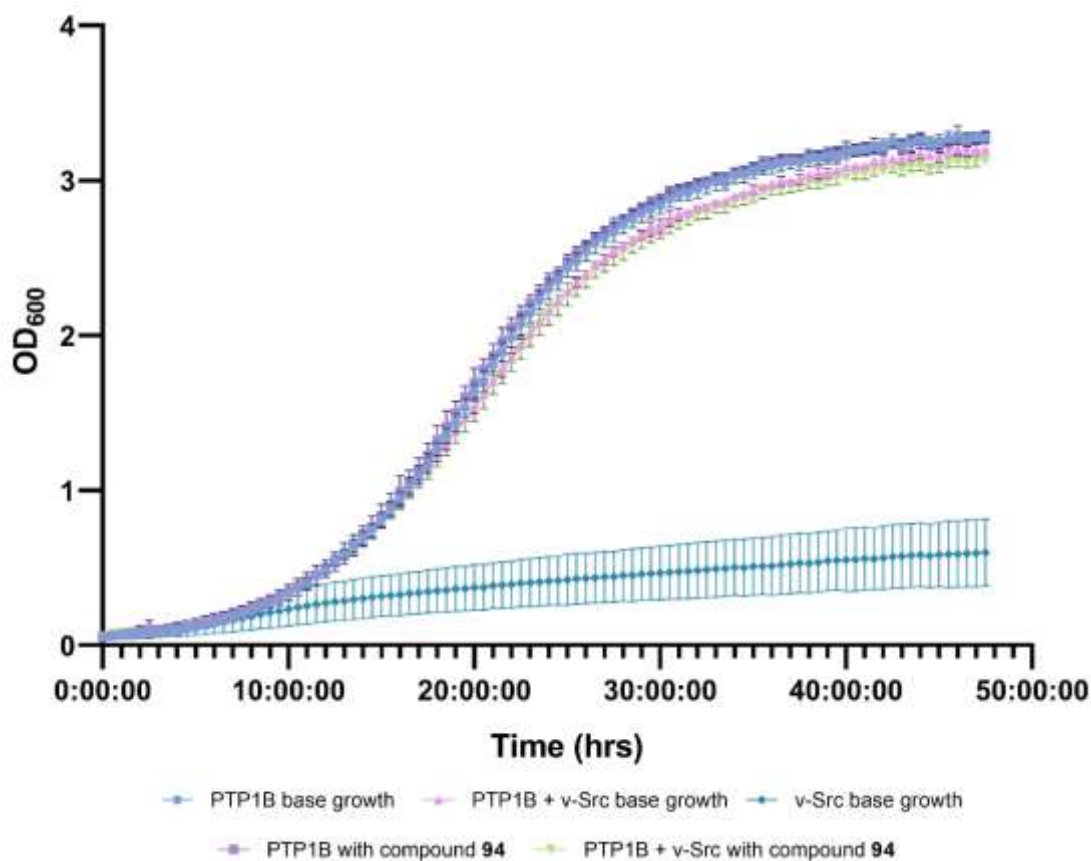
Transformed cells	PTP1B only	PTP1B + v-Src *
p value	ns	<0.0500

Figure CLXVII: Growth curves of PTP1B only, PTP1B + v-Src and v-Src only YMK23 transformations with and without the addition of compound **92** at 100 μ M. n=3 for each PTP1B based parameter, n=13 for v-Src. Mean and individual biological points \pm standard deviation plotted. Data is normally distributed according to a Shapiro-Wilk test. Used a 2-way ANOVA. * p value \leq 0.050 vs corresponding base growth.



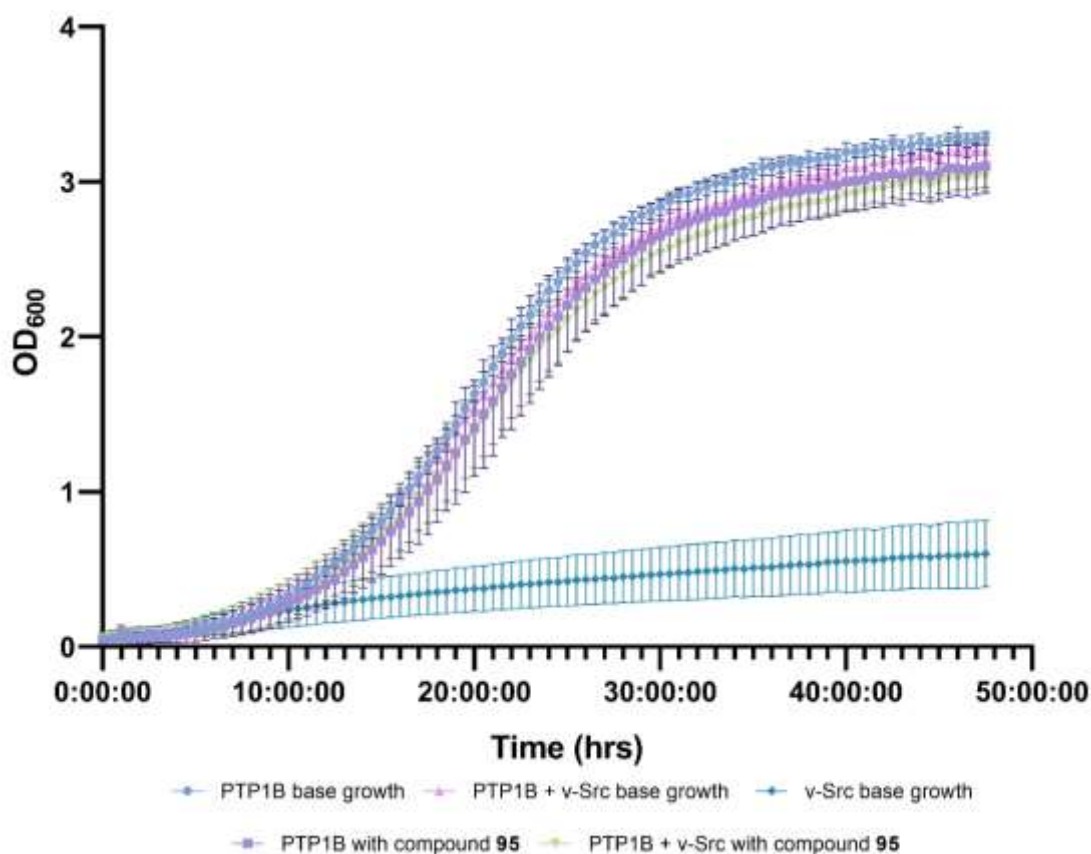
Transformed cells	PTP1B only	PTP1B + v-Src
p value	ns	ns

Figure CLXVIII: Growth curves of PTP1B only, PTP1B + v-Src and v-Src only YMK23 transformations with and without the addition of compound **93** at 100 μ M. n=3 for each PTP1B based parameter, n=13 for v-Src. Mean and individual biological points \pm standard deviation plotted. Data is normally distributed according to a Shapiro-Wilk test. Used a 2-way ANOVA. * p value \leq 0.050 vs corresponding base growth.



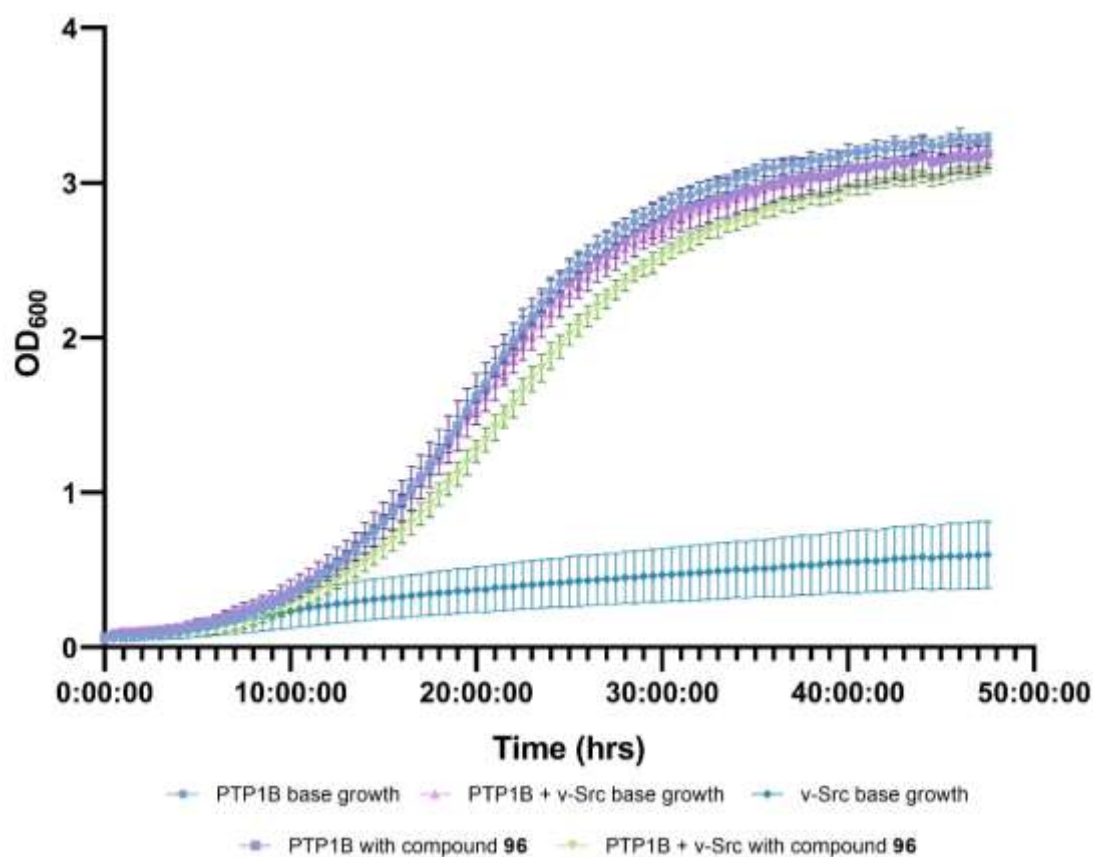
Transformed cells	PTP1B only	PTP1B + v-Src
p value	ns	ns

Figure CLXIX: Growth curves of PTP1B only, PTP1B + v-Src and v-Src only YMK23 transformations with and without the addition of compound **94** at 100 μ M. n=3 for each PTP1B based parameter, n=13 for v-Src. Mean and individual biological points \pm standard deviation plotted. Data is normally distributed according to a Shapiro-Wilk test. Used a 2-way ANOVA. * p value \leq 0.050 vs corresponding base growth.



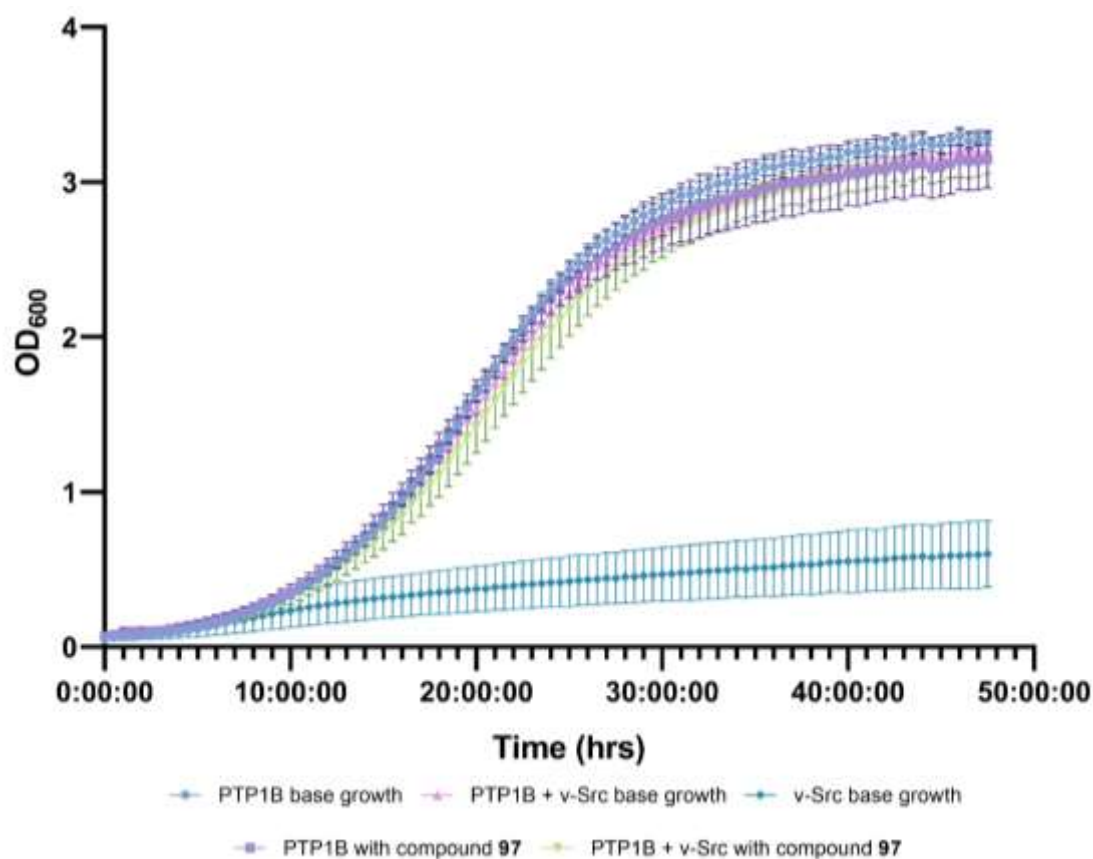
Transformed cells	PTP1B only	PTP1B + v-Src
p value	ns	ns

Figure CLXX: Growth curves of PTP1B only, PTP1B + v-Src and v-Src only YMK23 transformations with and without the addition of compound **95** at 100 μ M. n=3 for each PTP1B based parameter, n=13 for v-Src. Mean and individual biological points \pm standard deviation plotted. Data is normally distributed according to a Shapiro-Wilk test. Used a 2-way ANOVA. * p value \leq 0.050 vs corresponding base growth.



Transformed cells	PTP1B only	PTP1B + v-Src *
p value	ns	<0.0100

Figure CLXXI: Growth curves of PTP1B only, PTP1B + v-Src and v-Src only YMK23 transformations with and without the addition of compound **96** at 100 μ M. n=3 for each PTP1B based parameter, n=13 for v-Src. Mean and individual biological points \pm standard deviation plotted. Data is normally distributed according to a Shapiro-Wilk test. Used a 2-way ANOVA. * p value \leq 0.050 vs corresponding base growth.



Transformed cells	PTP1B only	PTP1B + v-Src
p value	ns	ns

Figure CLXXII: Growth curves of PTP1B only, PTP1B + v-Src and v-Src only YMK23 transformations with and without the addition of compound **97** at 100 μ M. n=3 for each PTP1B based parameter, n=13 for v-Src. Mean and individual biological points \pm standard deviation plotted. Data is normally distributed according to a Shapiro-Wilk test. Used a 2-way ANOVA. * p value \leq 0.050 vs corresponding base growth.

3.2 Accompanying BBB results of the hit spirocyclic dihydropyrazole

3.2.1 Maximum absorption wavelength

Table LIV: Maximum absorption wavelengths of each hit benzodioxane compound.

	Compound 78
Wavelength (nm)	220

Above **Table LIV** shows the wavelength of light in which the stated compounds absorb the maximum amount.

3.2.2 Blank corrected absorbance values of known concentrations.

Blanks used were comprised of 1x PBS and DMSO the proportion of which corresponds to the amount for each concentration of compound tested. These blanks were ran over the same wavelength range (220 – 500 nm) as the compounds were, when determining maximum absorbance value.

3.2.2.1 Compound 78

Table LV: Blank corrected absorbance data of compound **78** used to construct calibration curve.

220 nm		Concentration of compound used (μM)									
		50	100	150	200	250	300	350	400	450	500
Absorbance values	1	0.190	0.365	0.675	1.210	1.022	1.817	1.901	1.744	1.876	2.130
	2	0.174	0.369	0.747	0.873	1.233	1.357	1.899	1.928	1.961	1.901
	3	0.108	0.428	0.699	0.271	1.137	0.886	1.530	1.840	1.985	2.154
	4	0.301	0.440	0.717	0.943	1.012	1.394	1.470	1.467	1.955	2.299
	5	0.274	0.376	0.691	0.775	1.241	1.358	0.946	1.706	2.069	2.533
	Mean	0.210	0.396	0.706	0.815	1.129	1.362	1.550	1.737	1.969	2.204
	Std dev.	0.070	0.032	0.025	0.308	0.099	0.295	0.351	0.156	0.062	0.208

3.2.3 Concentrations of spirocyclic hit compound in both acceptor and donor wells after 24-hours at RT or 37°C.

3.2.3.1 Compound 78

Table LVI: Concentration of compound 78 recorded to be present in the acceptor and donor wells of the assay kit after 24-hours at RT and 37°C.

230nm compound 78		Temperature of assay run			
		RT		37°C	
		Acceptor	Donor	Acceptor	Donor
Concentration (µM)	1	203.136	322.500	185.773	270.500
	2	191.318	321.818	193.955	317.545
	3	188.364	285.455	187.591	324.818
	4	202.227	330.455	180.773	303.682
	5	189.045	263.636	202.136	311.182
	Mean	194.818	304.773	190.045	305.545
	Std dev.	6.501	25.806	7.372	18.862

3.2.4 Permeability rate of spirocyclic hit compound through synthetic BBB after 24-hours at RT or 37°C.

3.2.4.1 Equilibrium standard absorbance values for compound 78

Table LVII: Absorbance values of the equilibrium standards measured at the corresponding maximum wavelength for absorbance of compound 78.

230nm compound 78		Equilibrium standard
Concentration (µM)	1	0.897
	2	0.992
	3	0.818
	4	0.940
	5	0.872
	Mean	0.903
	Std dev.	0.059

Used same equilibrium standard mean value outlined in **Table LVII** for the calculation of permeability rate of compound 78 at both RT and 37°C.

3.2.4.2 Compound 78: permeability rate

Table LVIII: Permeability rate of spirocyclic hit compound through synthetic BBB after 24-hours at RT or 37°C.

230nm compound 78		Permeability rate (cm/s)	
		RT	37°C
Biological repeat	1	2.667E-05	1.361E-05
	2	1.560E-05	1.675E-05
	3	1.448E-05	1.417E-05
	4	2.454E-05	1.229E-05
	5	1.472E-05	1.505E-05
	Mean	1.920E-05	1.437E-05
	Std dev.	5.284E-06	1.488E-06

4. Full statistical comparison of all identified hits within thesis with each other and known inhibitors.

A full statistical comparison of all identified hits within thesis and the two aforementioned known PTP inhibitors has been conducted in terms of PTP1B and TCPTP activity at 100 and 140 μ M, and BBB permeability at 37°C. The results are shown below.

Table LIX to **Table LXII** illustrate the statistical analysis of the PTP inhibitory effect of known inhibitors and key identified hit compounds to each other at 100 and 140 μ M.

Table LXIII demonstrates the comparison of % of input in the acceptor well as a means of assessing BBB permeability.

Table LIX: The statistical analysis of the percentage change in doubling time (T_d) of PTP1B + v-Src transformed YMK23 yeast cells with addition of hit compounds and known inhibitors at 100 μ M.

% Change in T_d (100 μ M)	A																	
	Ursolic acid	LZP25	Comp 16	Comp 30a	Comp 44	Comp 46	Comp 47	Comp 48	Comp 49	Comp 50a	Comp 52a	Comp 53	Comp 54	Comp 55	Comp 56	Comp 57	Comp 58	Comp 78
B	Ursolic acid																	
	LZP25	**																
	Comp 16	**	**															
	Comp 30a	ns	**	**														
	Comp 44	*	*	*	ns													
	Comp 46	ns	*	*	ns	ns												
	Comp 47	ns	*	*	ns	ns	-											
	Comp 48	*	*	*	ns	ns	-	-										
	Comp 49	*	*	*	ns	ns	-	-	-									
	Comp 50a	*	*	*	ns	ns	-	-	-	-								
	Comp 52a	*	*	*	*	ns	-	-	-	-	-							
	Comp 53	ns	*	*	ns	ns	-	-	-	-	-	-						
	Comp 54	ns	*	*	ns	ns	-	-	-	-	-	-	-					
	Comp 55	**	**	**	ns	ns	*	*	ns	ns	ns	*	*	*				
	Comp 56	*	*	*	ns	ns	-	-	-	-	-	-	-	-	ns			
	Comp 57	*	*	*	ns	ns	-	-	-	-	-	-	-	-	ns	-		
	Comp 58	*	*	*	*	ns	-	-	-	-	-	-	-	*	-	-		
	Comp 78	ns	**	**	ns	*	ns	ns	ns	ns	ns	*	ns	ns	**	ns	*	*

Green highlighted cells indicate the compound in column B caused a significantly higher inhibitory effect than the compound in column A.

* p value <0.0500, ** p value <0.0050, *** p value <0.0100.

Used non-parametric Mann-Whitney t-test for statistical analysis. * p value \leq 0.050.

Table LX: The statistical analysis of the percentage change in doubling time (T_d) of PTP1B + v-Src transformed YMK23 yeast cells with addition of hit compounds and known inhibitors at 140 μ M.

% Change in T_d (140 μ M)	A																	
	Ursolic acid	LZP25	Comp 16	Comp 30a	Comp 44	Comp 46	Comp 47	Comp 48	Comp 49	Comp 50a	Comp 52a	Comp 53	Comp 54	Comp 55	Comp 56	Comp 57	Comp 58	Comp 78
B	Ursolic acid																	
	LZP25	**																
	Comp 16	**	**															
	Comp 30a	**	ns	**														
	Comp 44	*	*	*	*													
	Comp 46	ns	*	*	*	ns												
	Comp 47	*	*	*	*	ns	-											
	Comp 48	ns	*	*	*	ns	-	-										
	Comp 49	ns	*	*	*	ns	-	-	-									
	Comp 50a	ns	*	*	*	ns	-	-	-	-								
	Comp 52a	ns	*	*	*	ns	-	-	-	-	-							
	Comp 53	ns	*	*	*	ns	-	-	-	-	-	-						
	Comp 54	ns	*	*	*	ns	-	-	-	-	-	-	-					
	Comp 55	**	**	**	**	ns	*	*	*	*	*	*	*	*				
	Comp 56	*	*	*	*	ns	-	-	-	-	-	-	-	-	-			
	Comp 57	ns	*	*	*	ns	-	-	-	-	-	-	-	-	-	-		
	Comp 58	ns	*	*	*	ns	-	-	-	-	-	-	-	-	-	-	-	
	Comp 78	ns	**	**	*	*	ns	*	*	ns	ns	ns	ns	ns	*	*	ns	*

* p value <0.0500, ** p value <0.0050

Used non-parametric Mann-Whitney t-test for statistical analysis. * p value \leq 0.050.

Green highlighted cells indicate the compound in column B caused a significantly higher inhibitory effect than the compound in column A.

Table LXI: The statistical analysis of the percentage change in doubling time (T_d) of TCPTP + v-Src transformed YMK23 yeast cells with addition of hit compounds and known inhibitors at 100 μ M.

% Change in T_d (100 μ M)	A																	
	Ursolic acid	LZP25	Comp 16	Comp 30a	Comp 44	Comp 46	Comp 47	Comp 48	Comp 49	Comp 50a	Comp 52a	Comp 53	Comp 54	Comp 55	Comp 56	Comp 57	Comp 58	Comp 78
B	Ursolic acid																	
	LZP25	**																
	Comp 16	**	**															
	Comp 30a	ns	**	**														
	Comp 44	*	ns	*	*													
	Comp 46	*	*	ns	*	ns												
	Comp 47	ns	*	*	ns	ns	-											
	Comp 48	ns	*	*	*	ns	-	-										
	Comp 49	*	*	ns	*	ns	-	-	-									
	Comp 50a	ns	*	*	*	ns	-	-	-	-								
	Comp 52a	ns	*	*	ns	ns	-	-	-	-	-							
	Comp 53	*	*	ns	*	ns	-	-	-	-	-	-						
	Comp 54	ns	*	*	*	ns	-	-	-	-	-	-	-					
	Comp 55	**	**	ns	**	*	ns	*	*	ns	*	*	ns	*				
	Comp 56	ns	*	*	*	ns	-	-	-	-	-	-	-	*				
	Comp 57	ns	*	*	*	ns	-	-	-	-	-	-	-	*	-			
	Comp 58	ns	*	*	ns	ns	-	-	-	-	-	-	-	*	-	-		
	Comp 78	ns	**	**	*	ns	*	*	*	*	ns	*	*	*	**	*	*	*

Blue highlighted cells indicate the compound in column B caused a significantly higher inhibitory effect than the compound in column A.

* p value <0.0500, ** p value <0.0050, *** p value <0.0100,

Used non-parametric Mann-Whitney t-test for statistical analysis. * p value \leq 0.050.

Table LXII: The statistical analysis of the percentage change in doubling time (T_d) of TCPTP + v-Src transformed YMK23 yeast cells with addition of hit compounds and known inhibitors at 140 μ M.

% Change in T_d (140 μ M)	A																	
	Ursolic acid	LZP25	Comp 16	Comp 30a	Comp 44	Comp 46	Comp 47	Comp 48	Comp 49	Comp 50a	Comp 52a	Comp 53	Comp 54	Comp 55	Comp 56	Comp 57	Comp 58	Comp 78
B	Ursolic acid																	
	LZP25	*																
	Comp 16	**	**															
	Comp 30a	ns	**	**														
	Comp 44	ns	ns	*	*													
	Comp 46	*	*	*	*	ns												
	Comp 47	ns	*	*	ns	ns	-											
	Comp 48	*	*	*	*	ns	-	-										
	Comp 49	*	*	ns	*	ns	-	-	-									
	Comp 50a	ns	*	*	*	ns	-	-	-	-								
	Comp 52a	*	*	*	*	ns	-	-	-	-	-							
	Comp 53	*	*	ns	*	ns	-	-	-	-	-	-						
	Comp 54	*	*	ns	*	ns	-	-	-	-	-	-	-					
	Comp 55	*	**	ns	**	*	*	*	*	ns	*	*	ns	ns				
	Comp 56	*	*	*	*	ns	-	-	-	-	-	-	-	-	*			
	Comp 57	*	*	*	*	ns	-	-	-	-	-	-	-	-	*	-		
	Comp 58	*	*	*	*	ns	-	-	-	-	-	-	-	-	*	-	-	
	Comp 78	ns	*	**	*	ns	*	*	*	*	ns	*	*	*	**	*	*	*

Blue highlighted cells indicate the compound in column B caused a significantly higher inhibitory effect than the compound in column A.

* p value <0.0500, ** p value <0.0050.

Used non-parametric Mann-Whitney t-test for statistical analysis. * p value \leq 0.050

Table LXIII: The statistical analysis of the percentage of the 500 µM inputted compound in the acceptor well of the BBB assay after 24 hours at 37°C.

% in acceptor well (37°C)	A																					
	Low control	Medium control	High control	Ursolic acid	LZP25	Comp 16	Comp 30a	Comp 44	Comp 46	Comp 47	Comp 48	Comp 49	Comp 50a	Comp 52a	Comp 53	Comp 54	Comp 55	Comp 56	Comp 57	Comp 58	Comp 78	
B	Low control																					
	Medium control	****																				
	High control	****	****																			
	Ursolic acid	***	***	ns																		
	LZP25	***	***	***	**																	
	Comp 16	***	ns	***	**	**																
	Comp 30a	***	***	***	**	**	**															
	Comp 44	***	***	***	**	**	**	**														
	Comp 46	***	ns	***	**	*	ns	**	**													
	Comp 47	ns	***	***	**	**	**	**	**	-												
	Comp 48	***	***	***	**	**	**	**	**	-	-											
	Comp 49	***	***	*	**	**	*	**	**	-	-	-										
	Comp 50a	***	***	***	**	**	*	**	**	-	-	-	-									
	Comp 52a	***	ns	ns	**	ns	ns	**	**	-	-	-	-	-								
	Comp 53	***	ns	**	**	ns	**	**	**	-	-	-	-	-	-							
	Comp 54	***	***	***	*	**	**	**	**	-	-	-	-	-	-	-						
	Comp 55	ns	***	***	**	**	**	*	**	**	**	*	**	**	**	**						
	Comp 56	***	ns	***	**	**	**	**	**	-	-	-	-	-	-	-	**					
	Comp 57	***	***	***	**	**	**	**	**	-	-	-	-	-	-	-	**	-				
	Comp 58	**	***	***	**	**	**	*	**	-	-	-	-	-	-	-	**	-	-			
	Comp 78	***	***	***	**	**	**	**	*	**	**	**	**	**	**	**	**	**	**	**	**	

Green highlighted cells indicate the compound in column B is significantly less permeable than the compound in column A.

* p value <0.0500, ** p value <0.0100, *** p value <0.0010, **** p value <0.0005, ***** p value <0.0001.

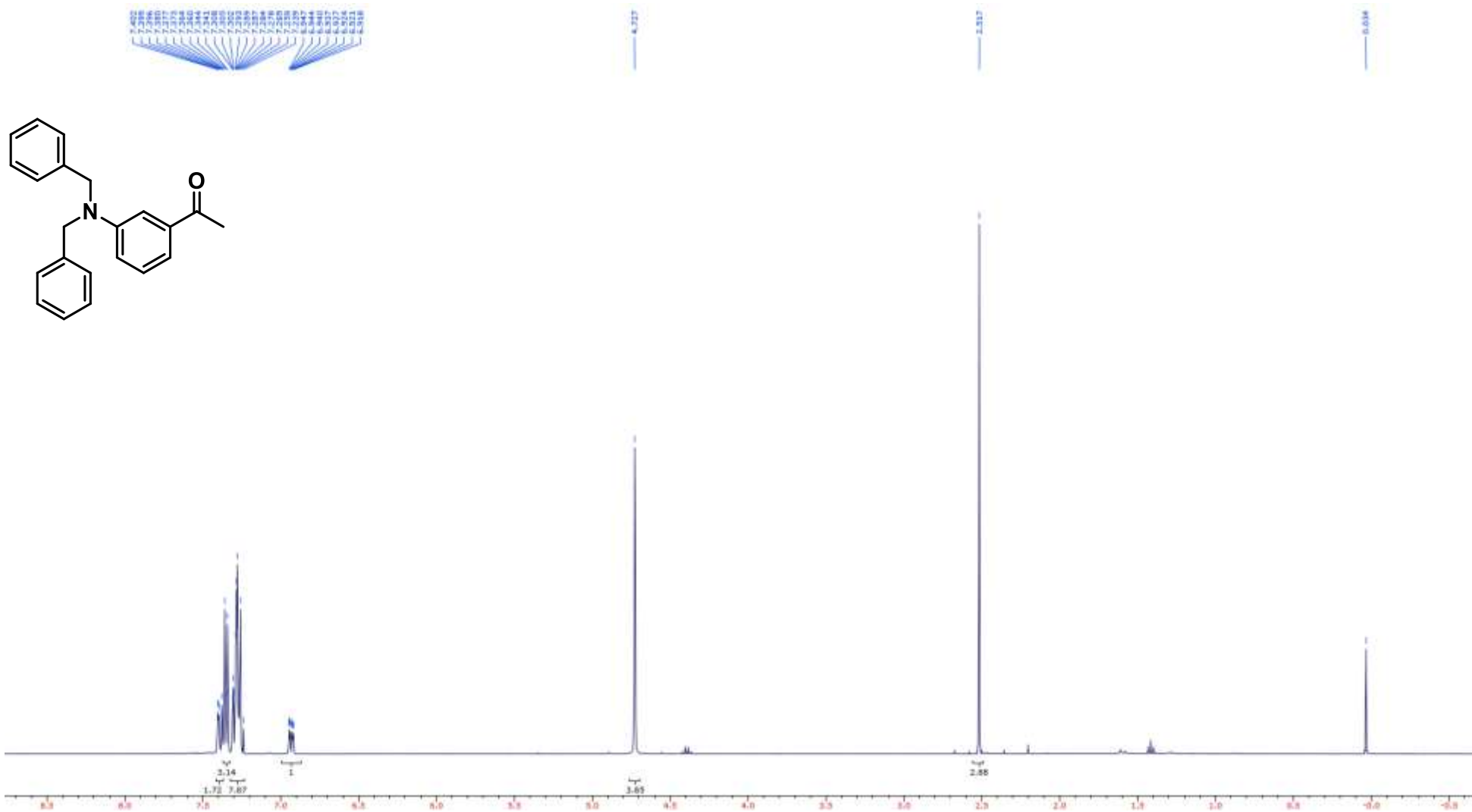
5. Content relating to Chapter 6: Methodology, ^1H and ^{13}C NMR Spectra of synthesised compounds.

Herin this section of the appendix is the produced ^1H and ^{13}C NMR and where beneficial two-dimensional NMR spectra are also included for all synthesised compounds produced and presented within the Thesis titled: ‘Synthesis and drug development of small molecule inhibitors of PTP1B’.

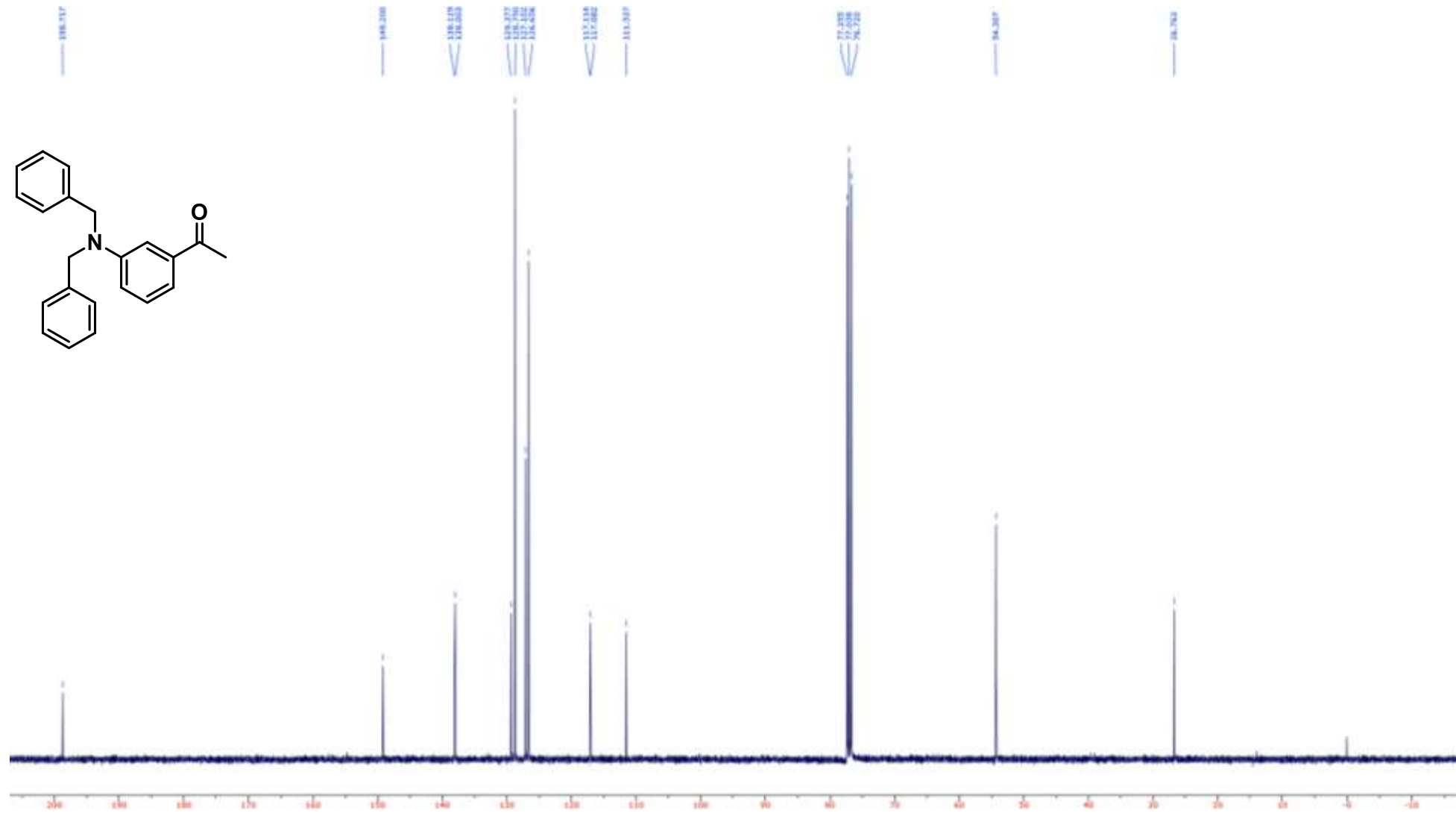
Sulfonylhydrazones were prepared according to procedures described in prior work and full characterisation data for compounds **68.1-68.8** can be found in referenced published literature.⁵⁻⁸

Compounds **77.1-77.6** were synthesised with general procedure T, but prior to this work, hence the full characterisation data can be found in this referenced publication.⁵

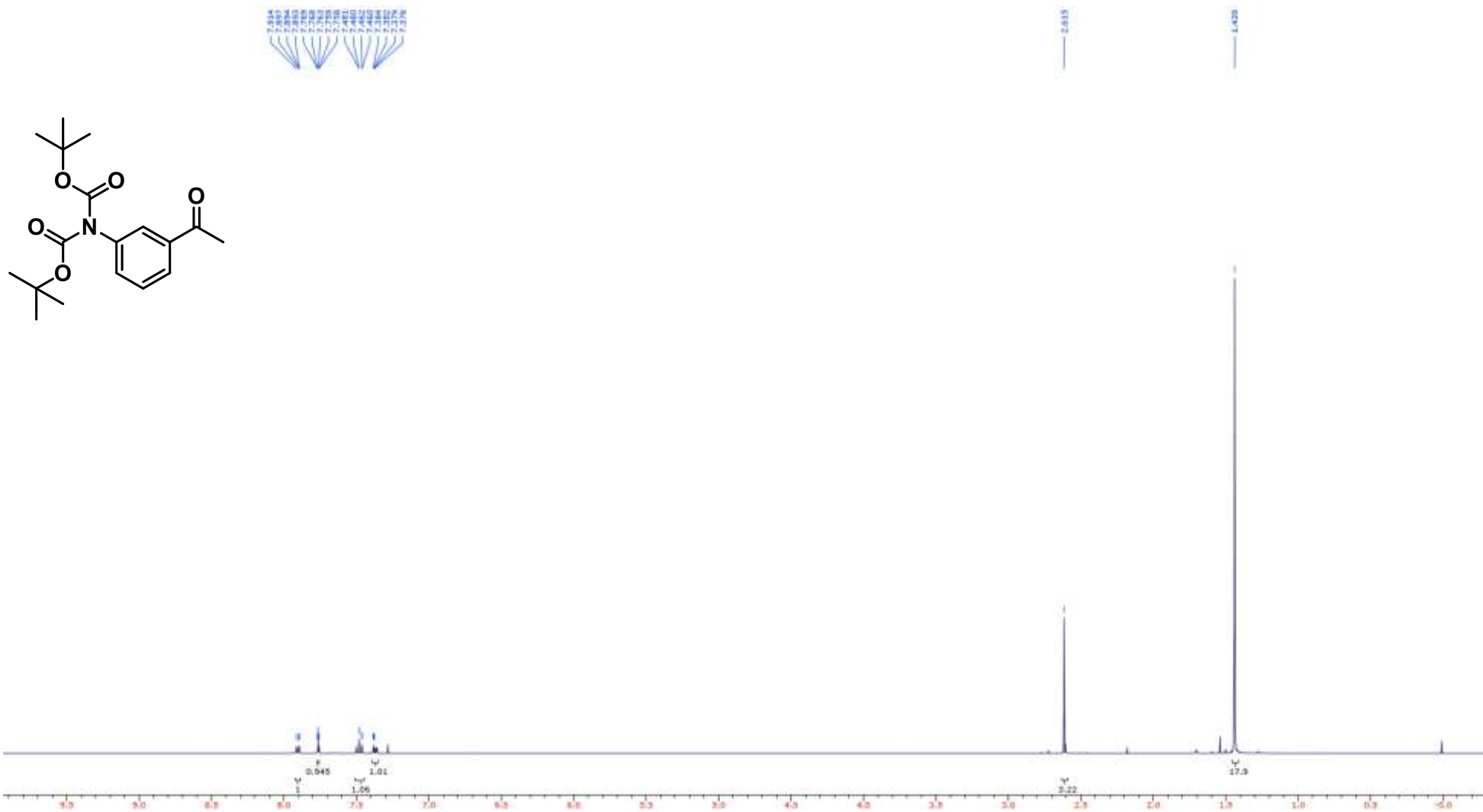
Compound 1 ^1H NMR (400 MHz, CDCl_3)



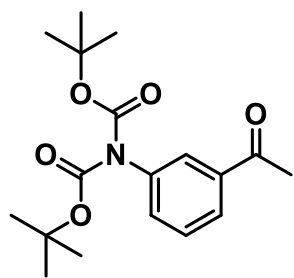
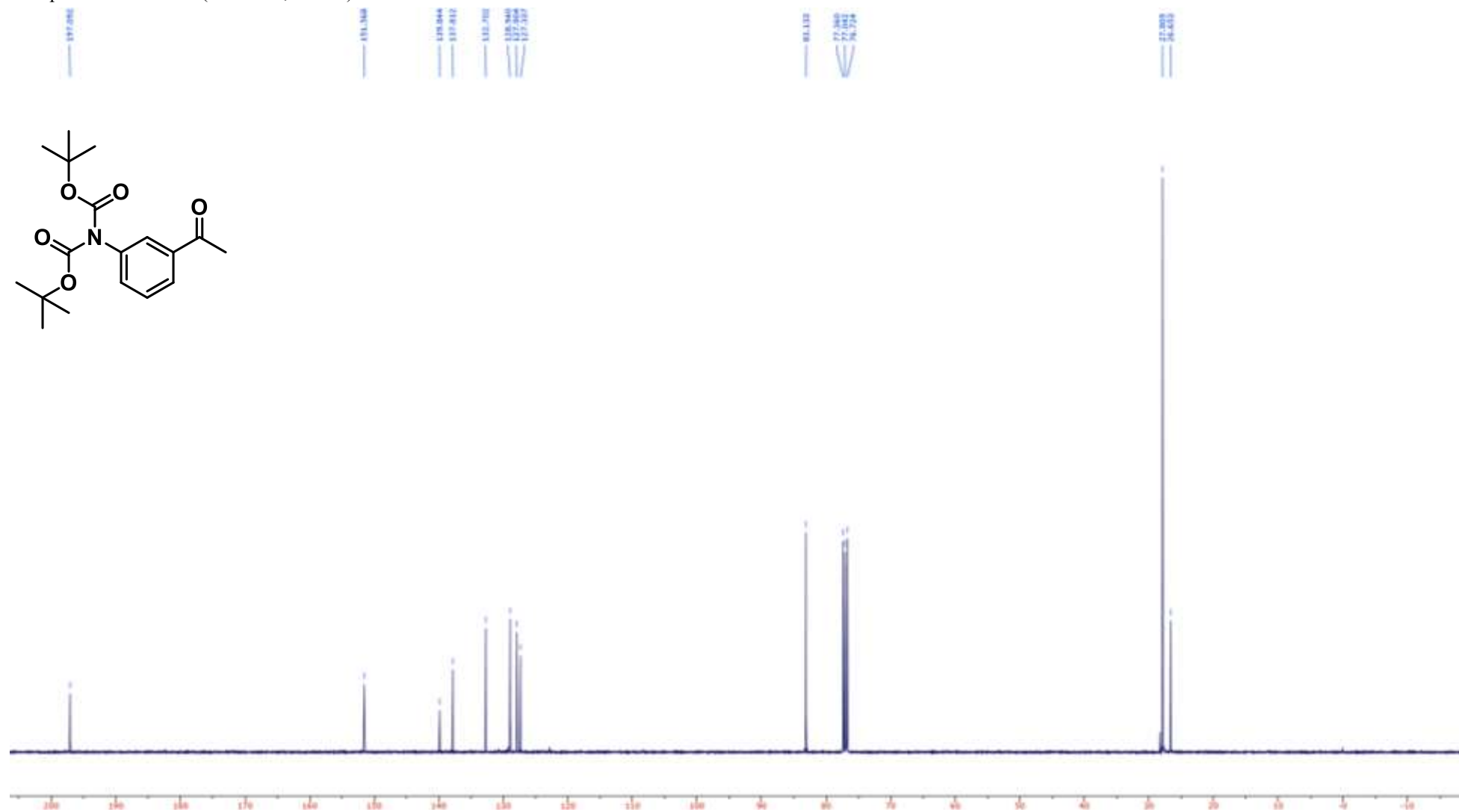
Compound 1 ¹³C NMR (100 MHz, CDCl₃)



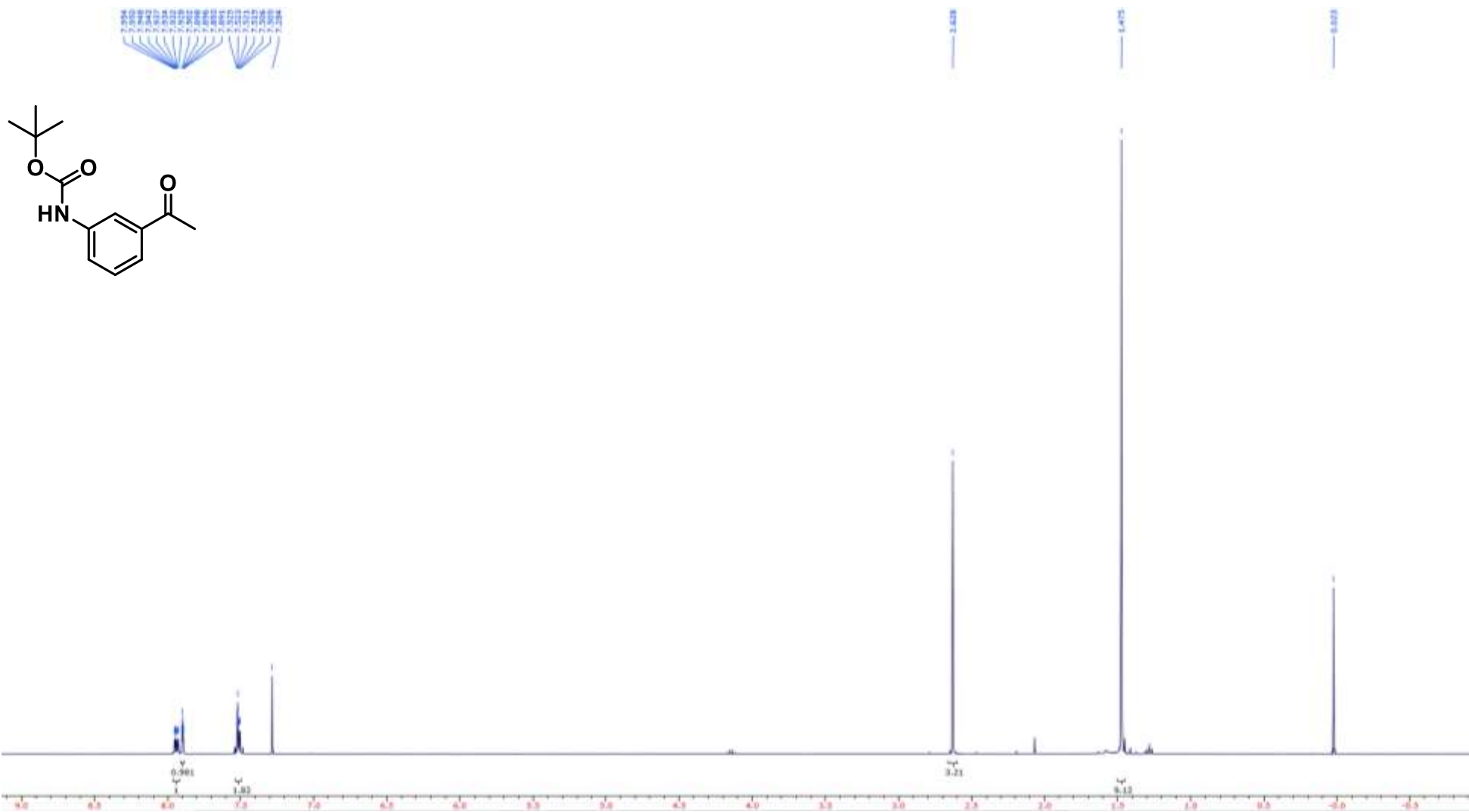
Compound **2** ^1H NMR (400 MHz, CDCl_3)



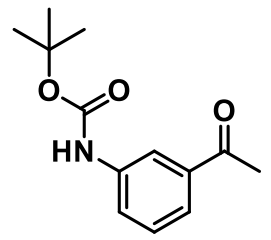
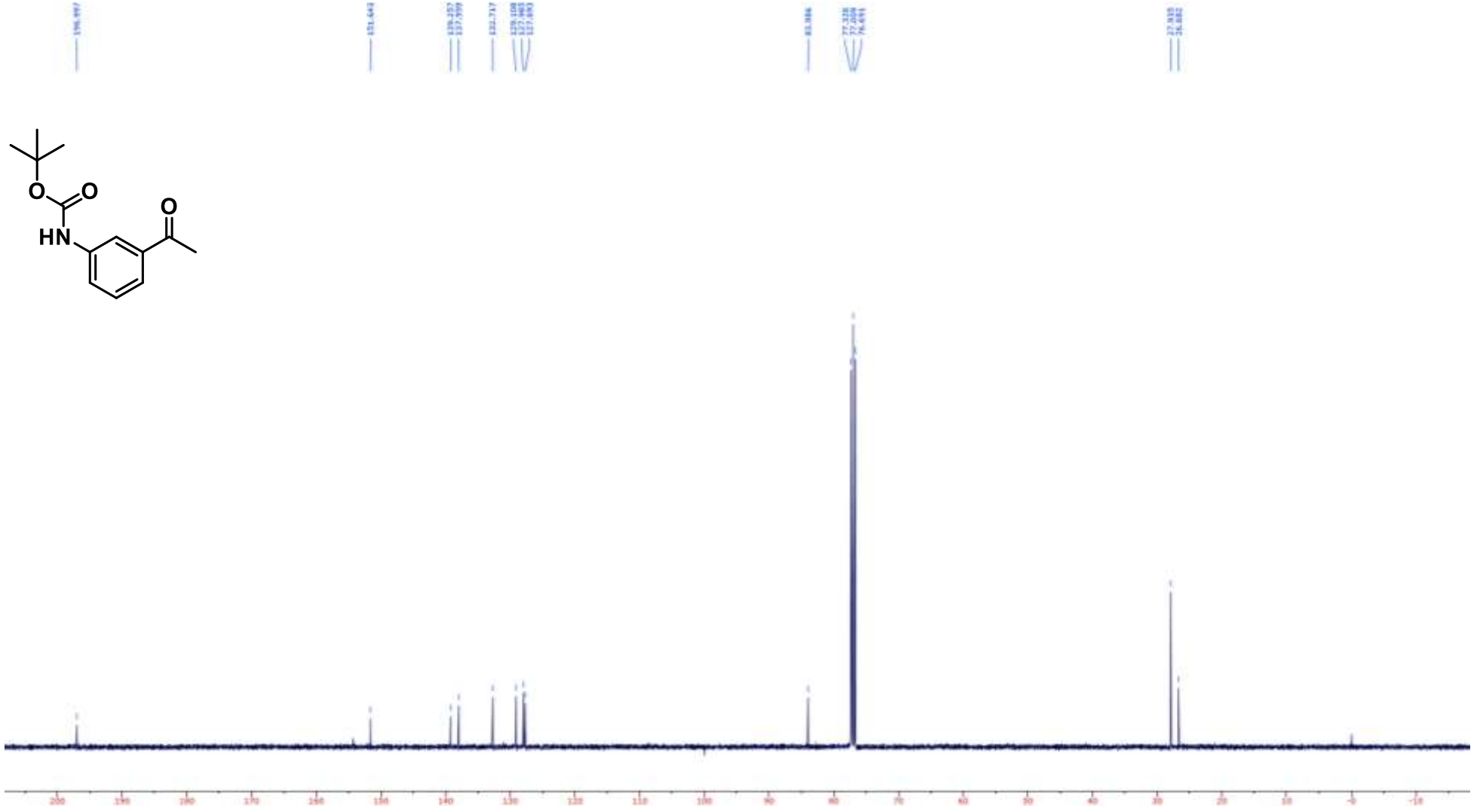
Compound 2 ¹³C NMR (100 MHz, CDCl₃)



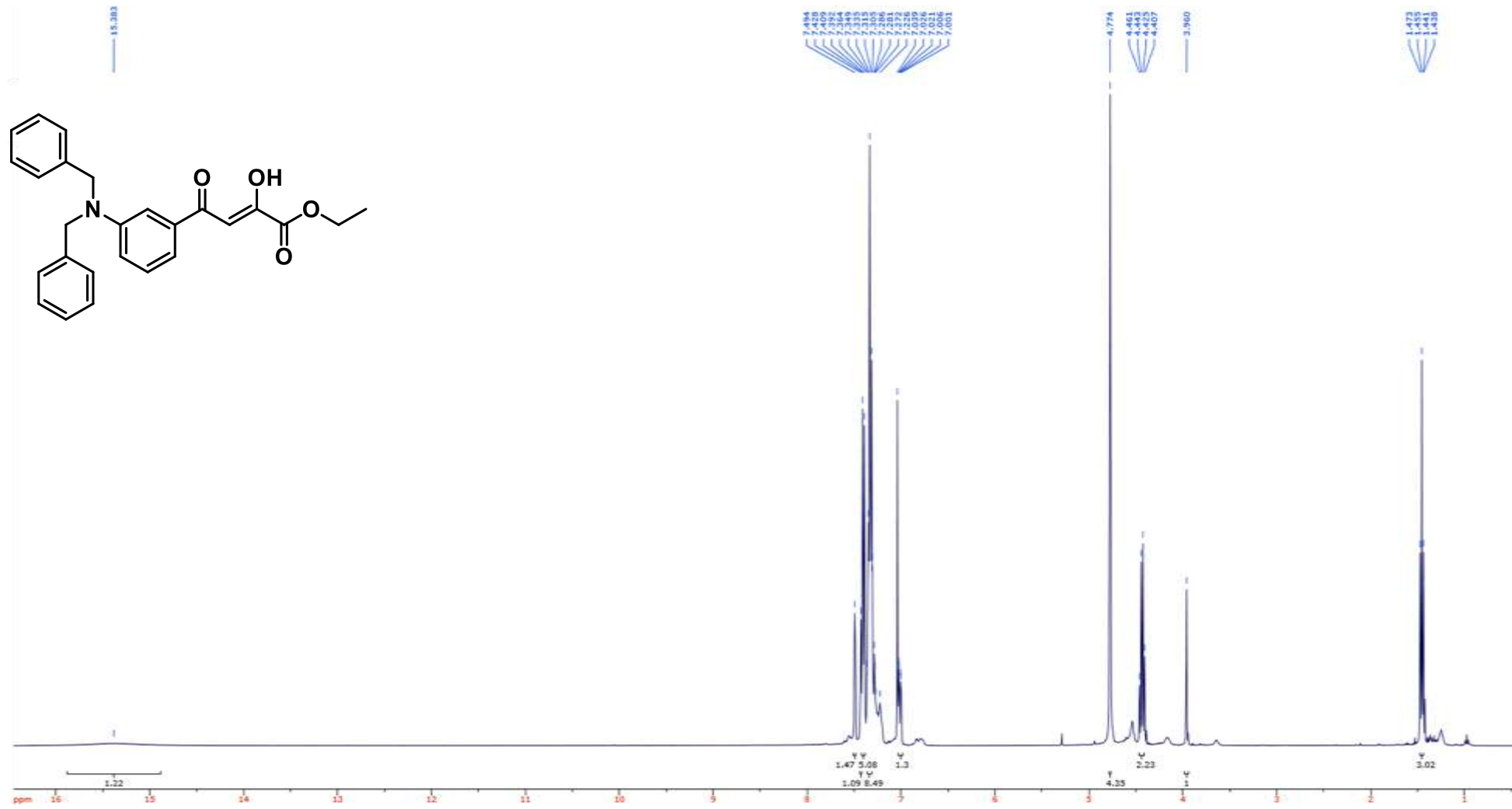
Compound **3** ^1H NMR (400 MHz, CDCl_3)



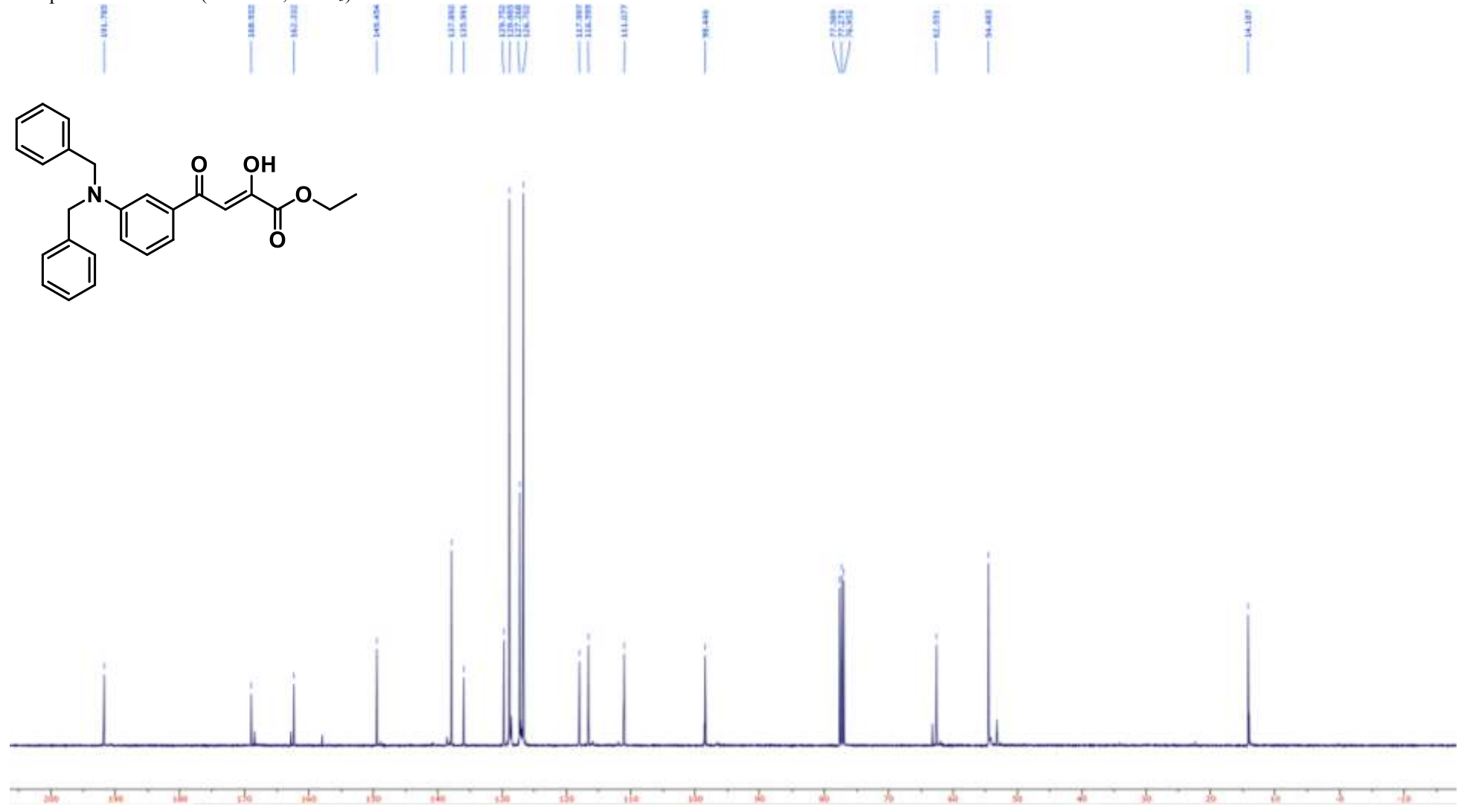
Compound **3** ^{13}C NMR (100 MHz, CDCl_3)



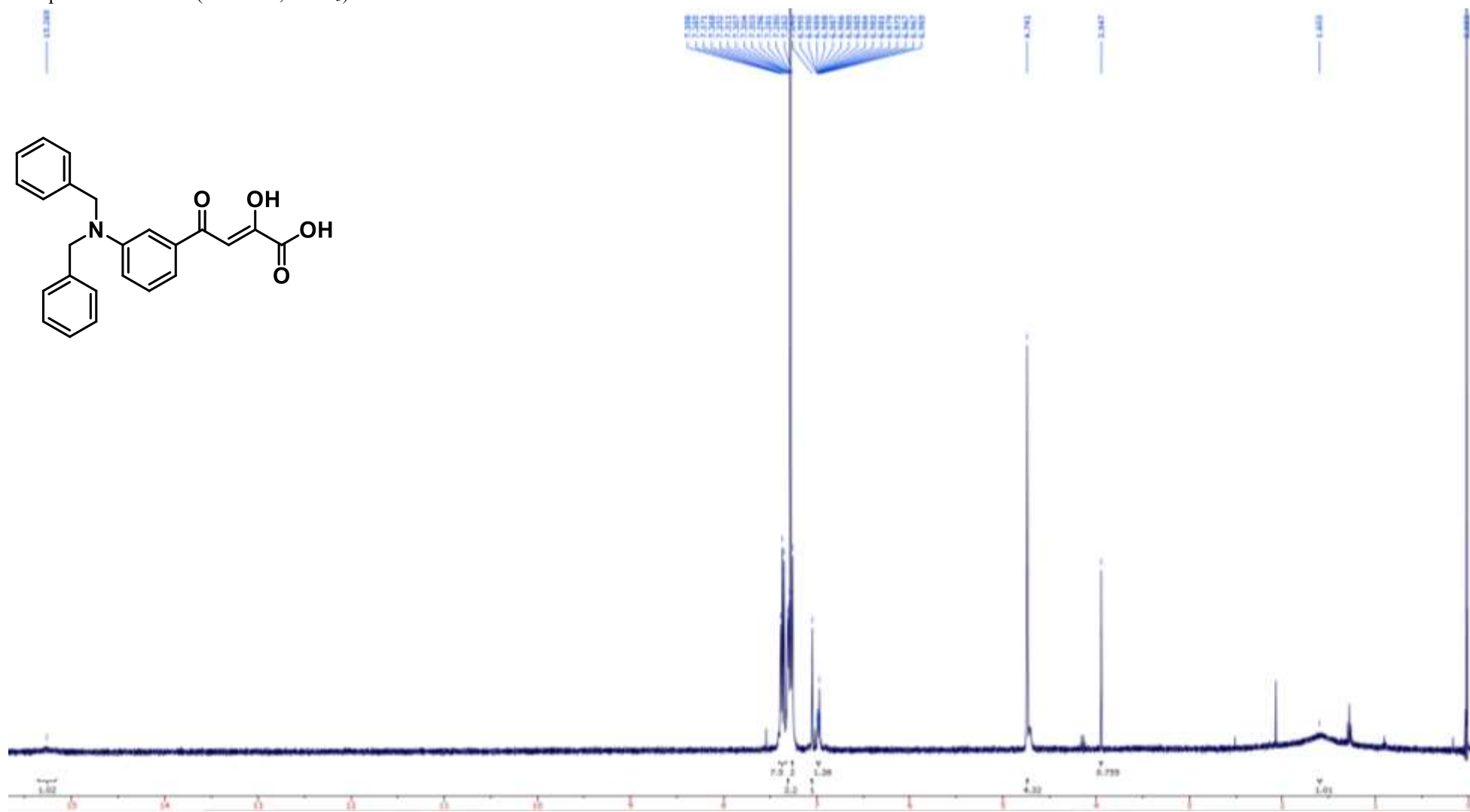
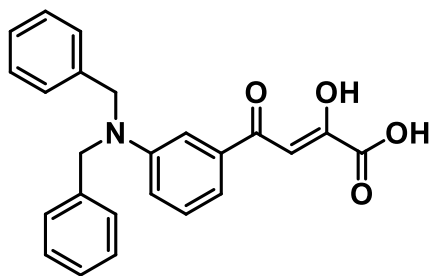
Compound 4 ¹H NMR (400 MHz, CDCl₃)



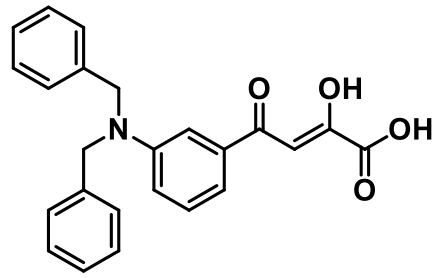
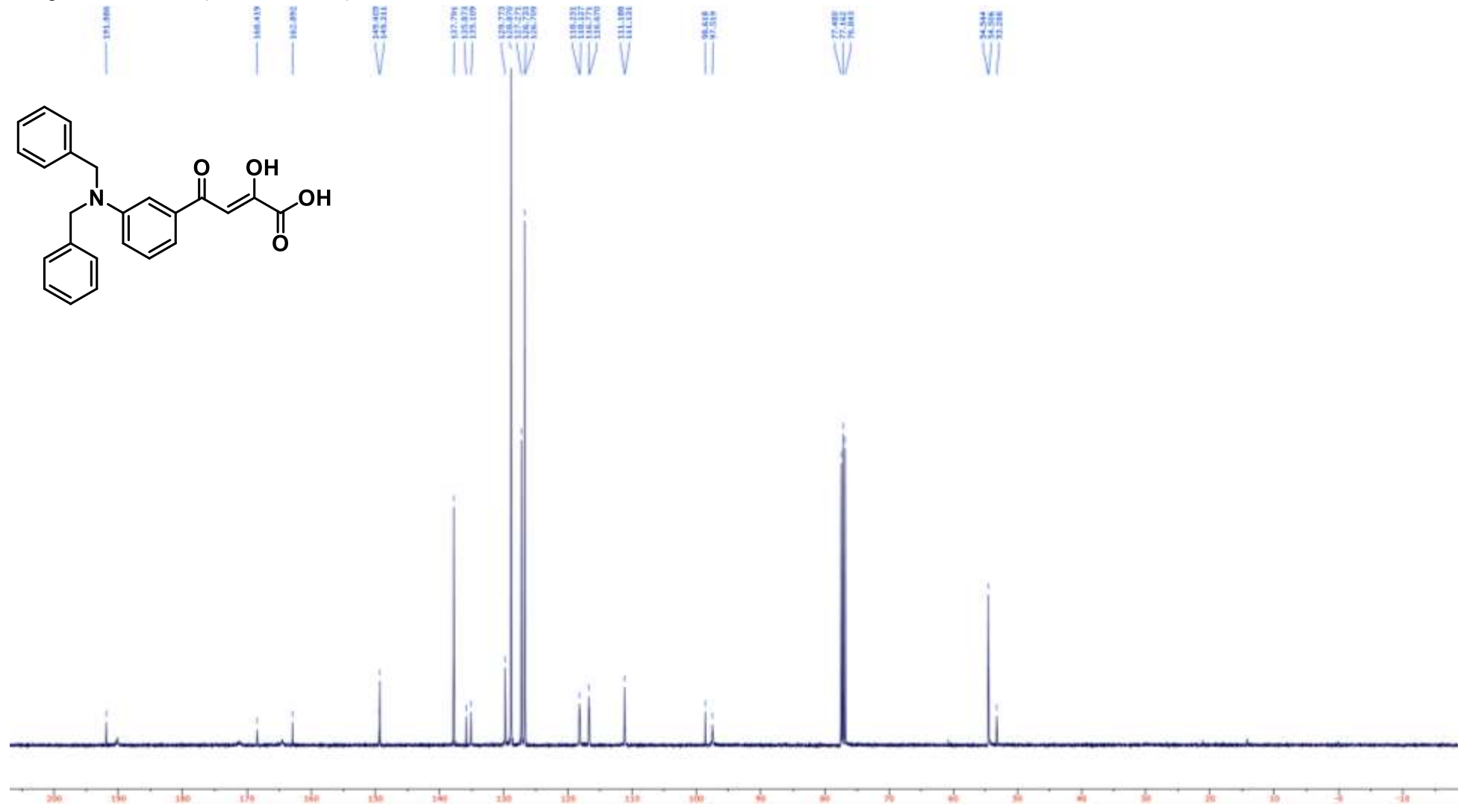
Compound 4 ¹³C NMR (100 MHz, CDCl₃)



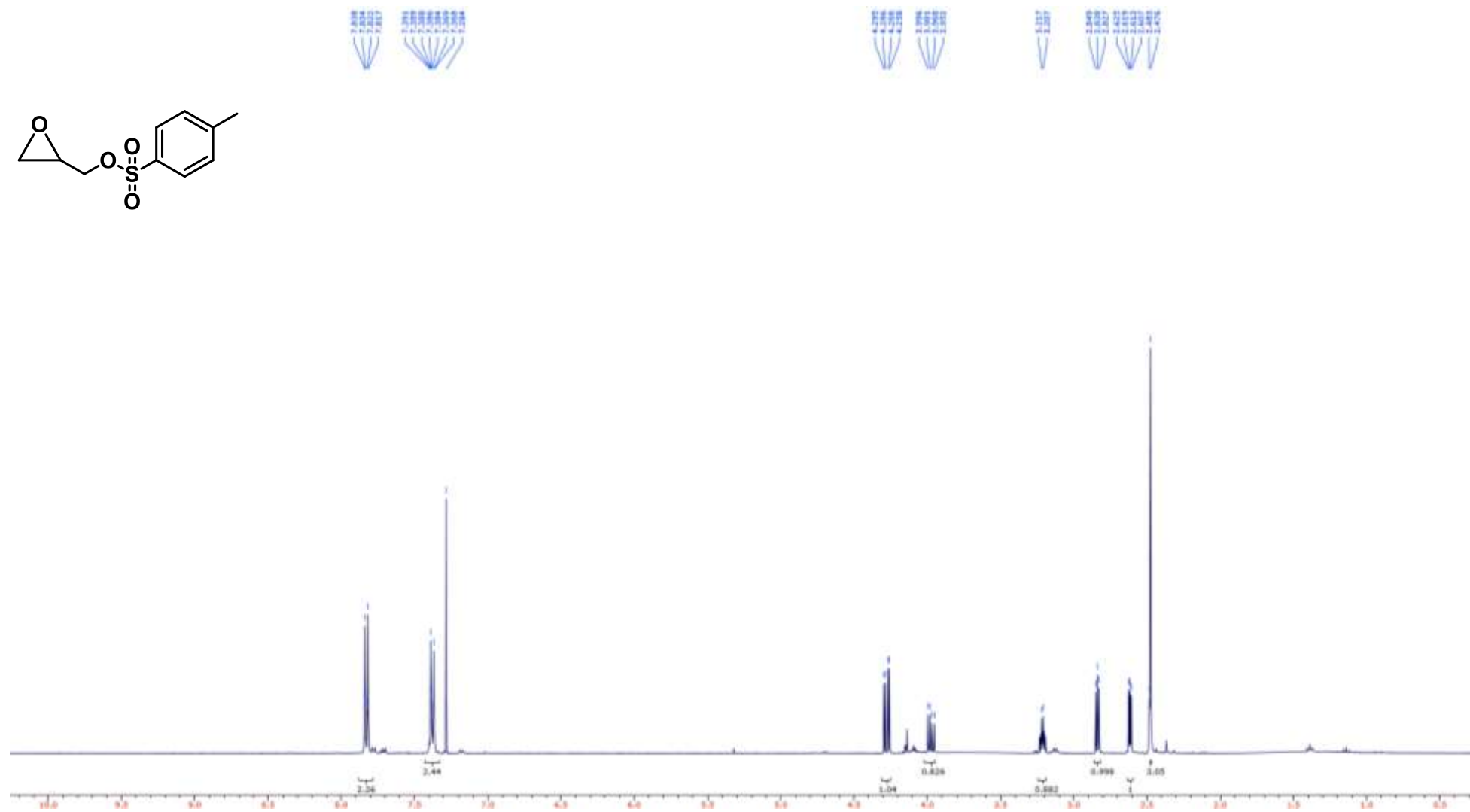
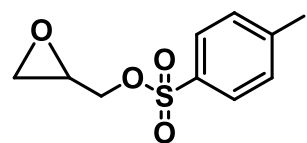
Compound 5 ¹H NMR (400 MHz, CDCl₃)



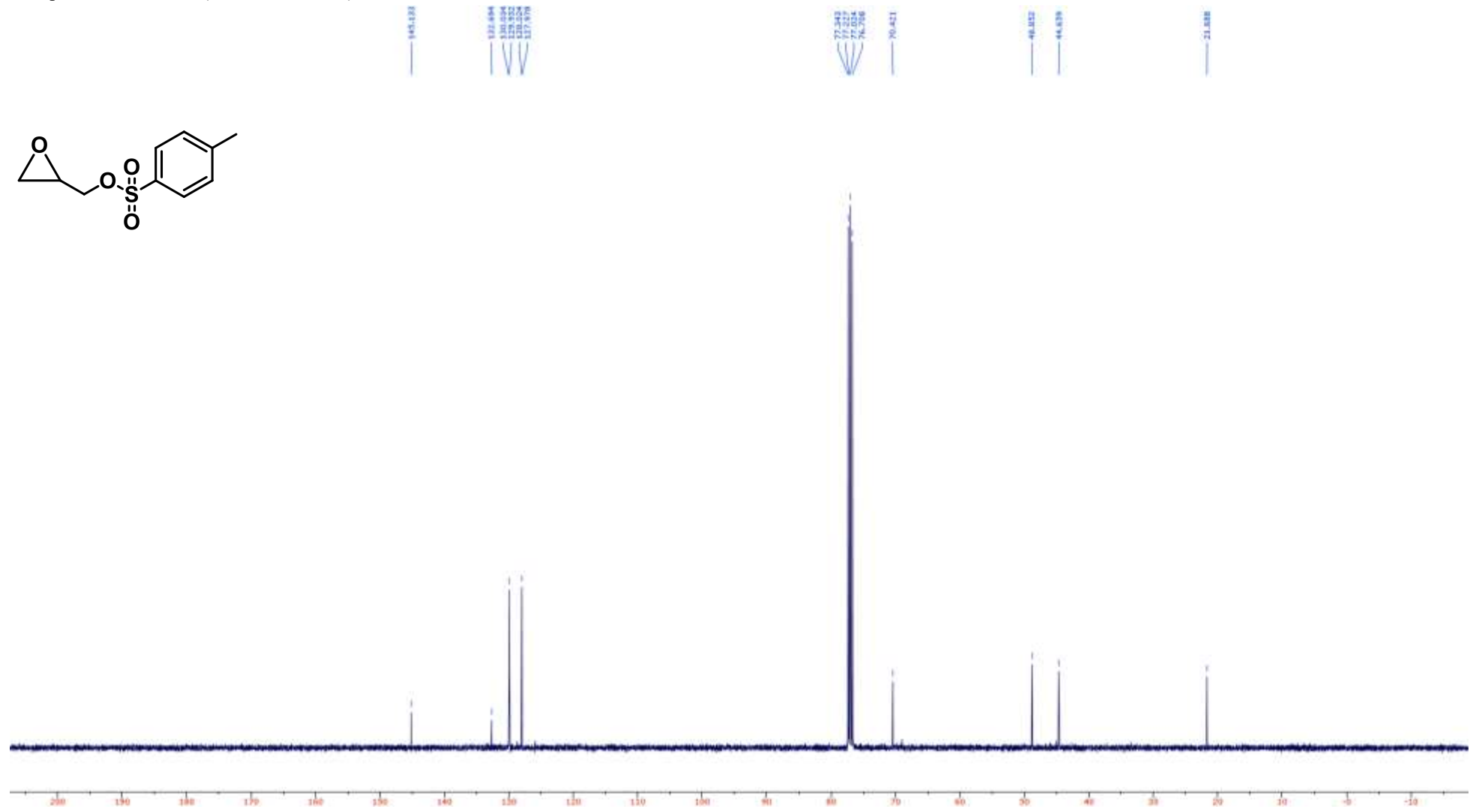
Compound **5** ^{13}C NMR (100 MHz, CDCl_3)



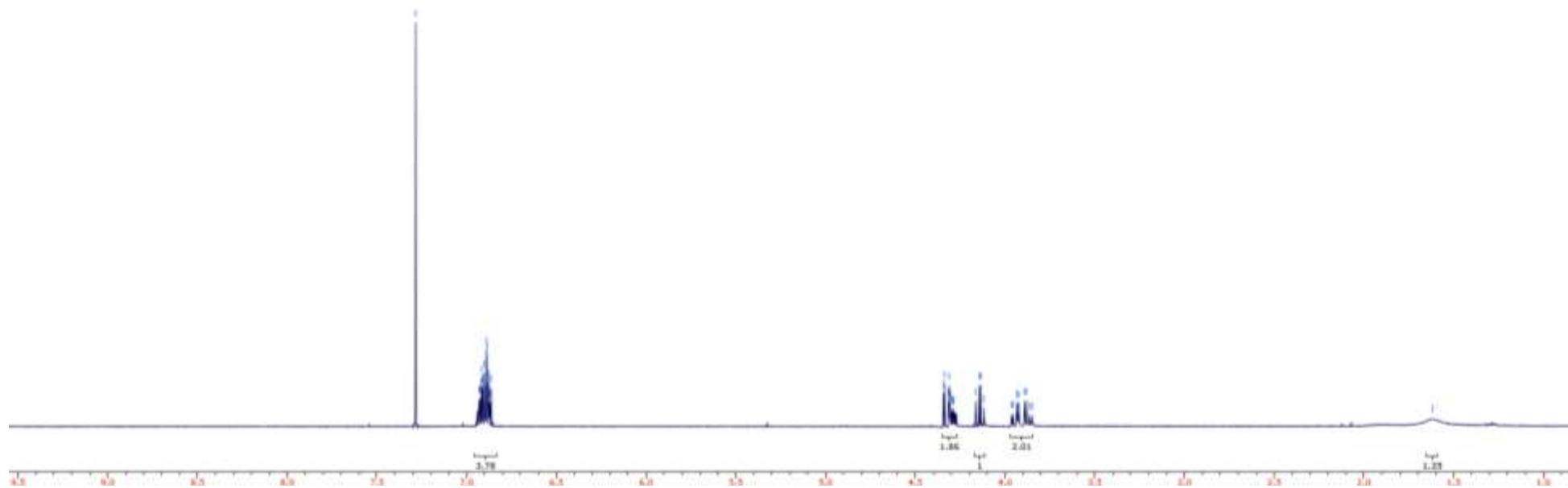
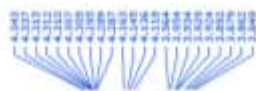
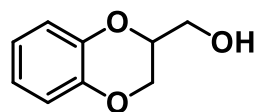
Compound **6** ^1H NMR (400 MHz, CDCl_3)



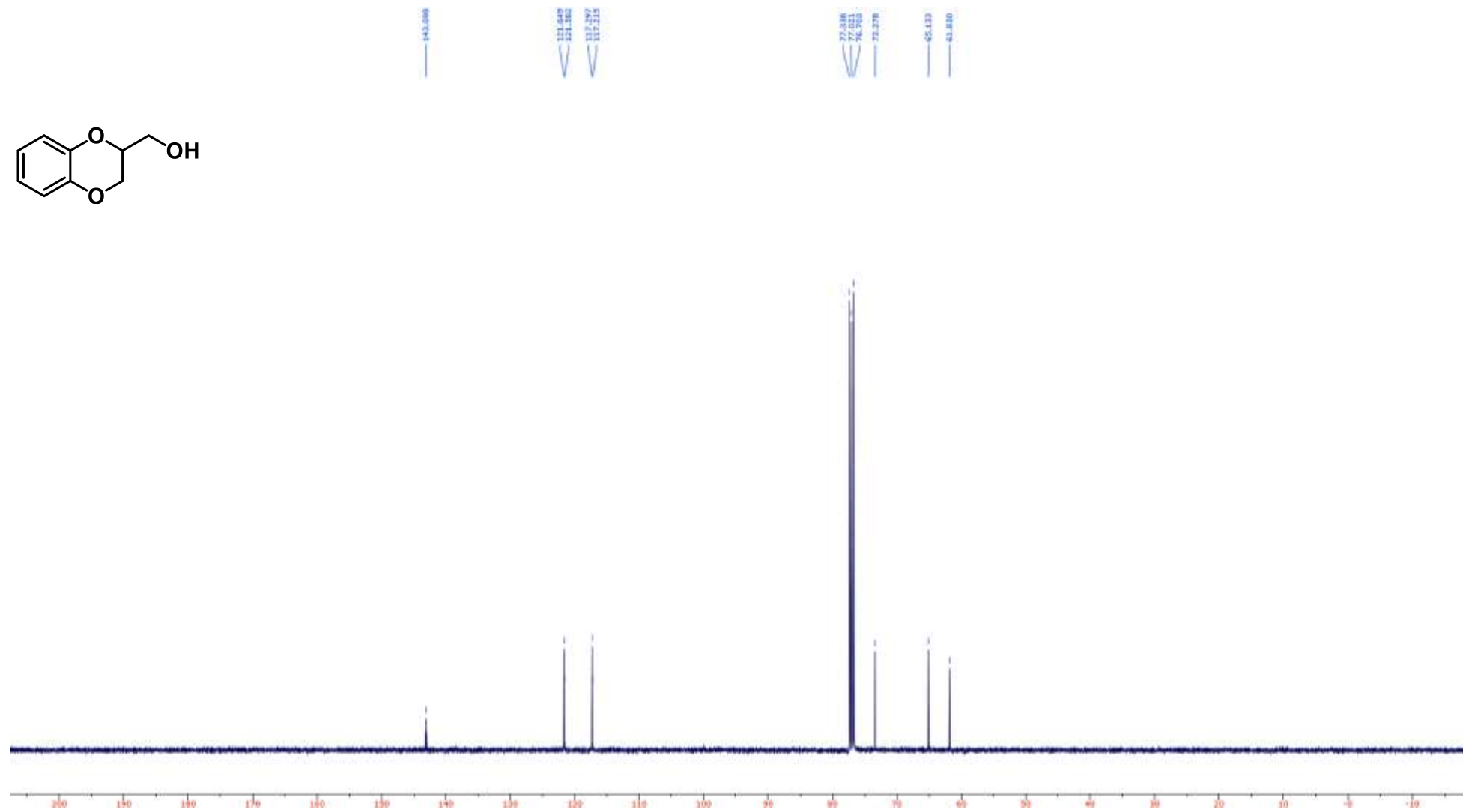
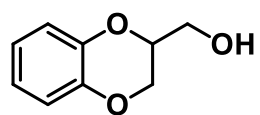
Compound **6** ^{13}C NMR (100 MHz, CDCl_3)



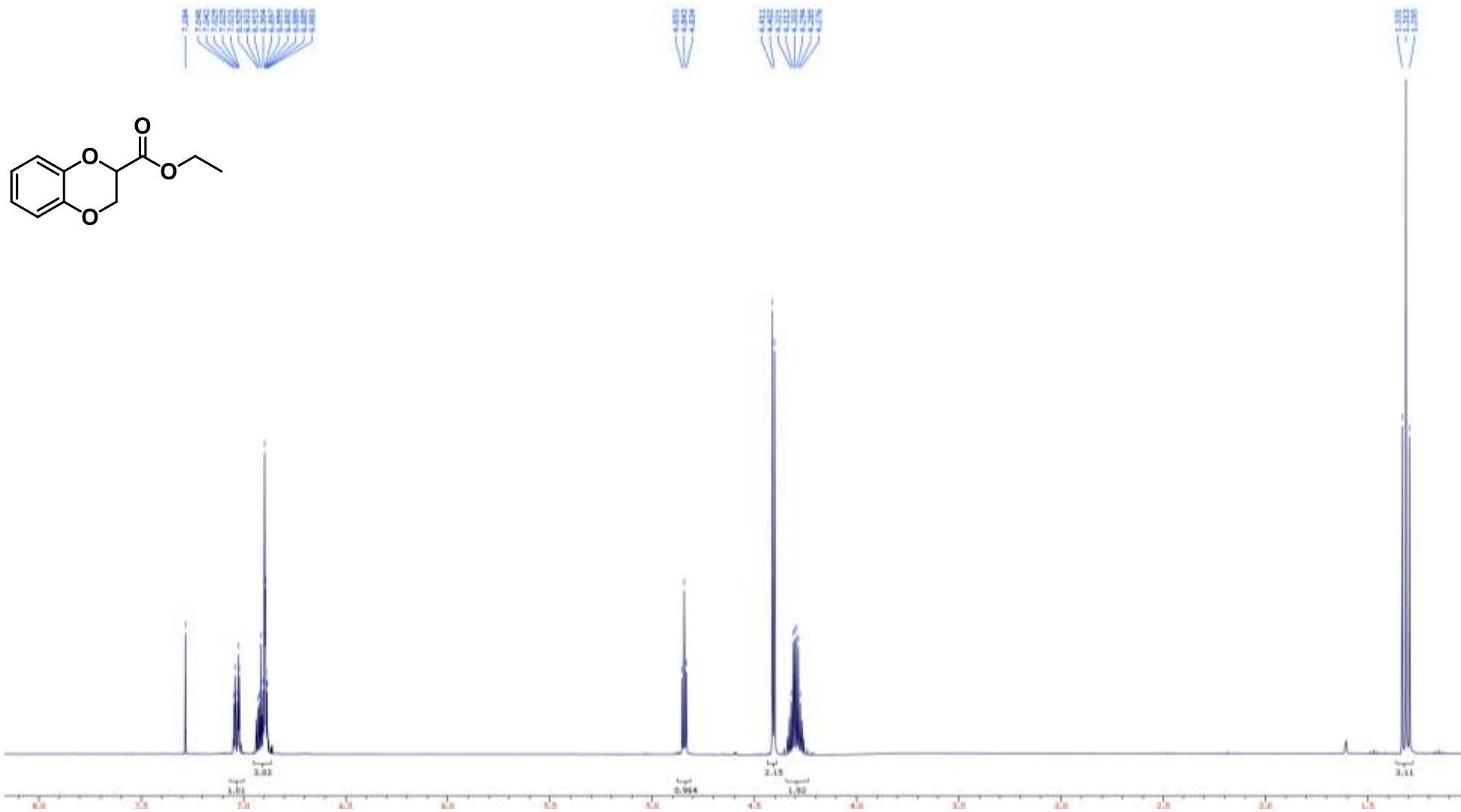
Compound 7 ^1H NMR (400 MHz, CDCl_3)



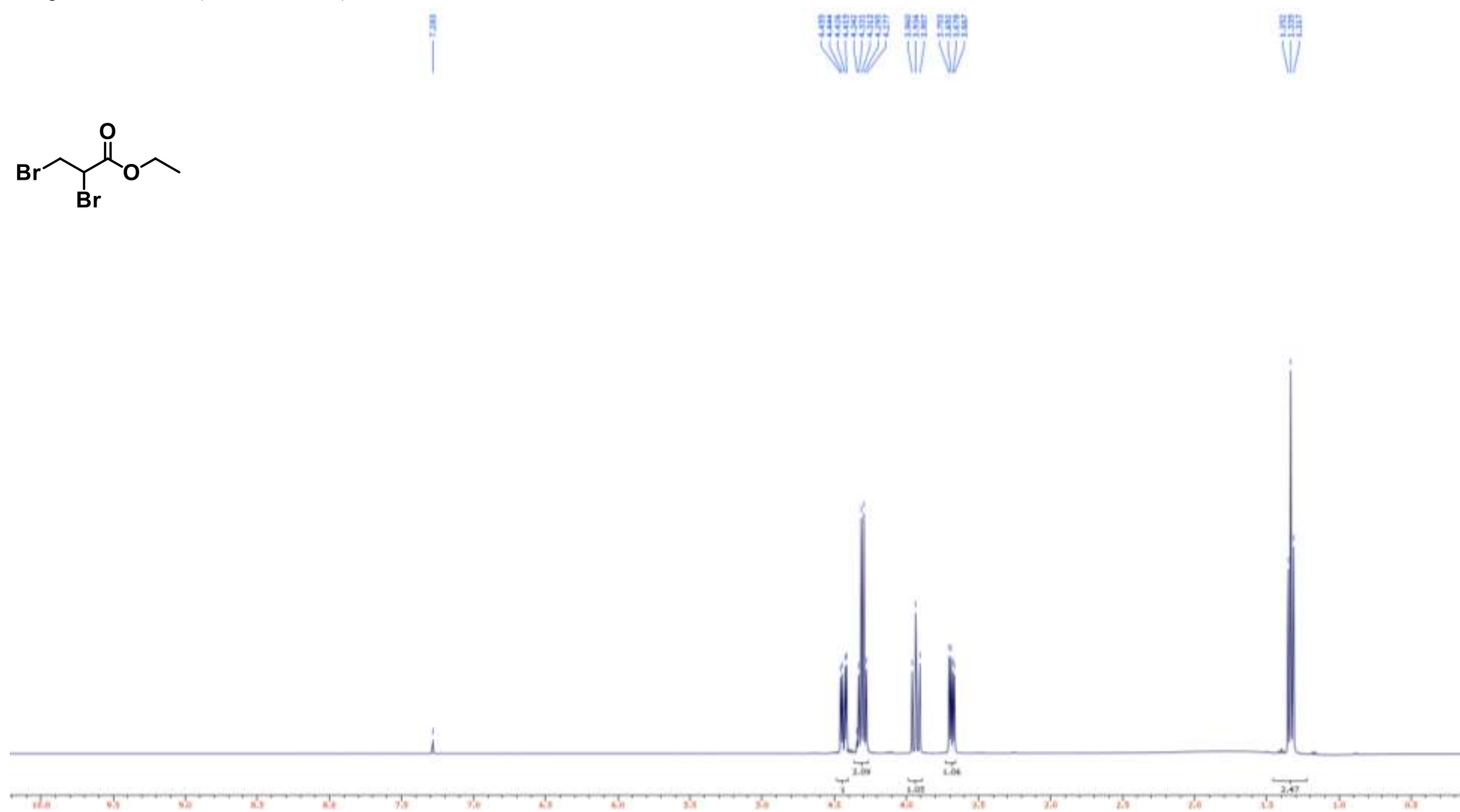
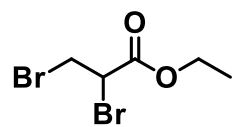
Compound 7 ¹³C NMR (100 MHz, CDCl₃)



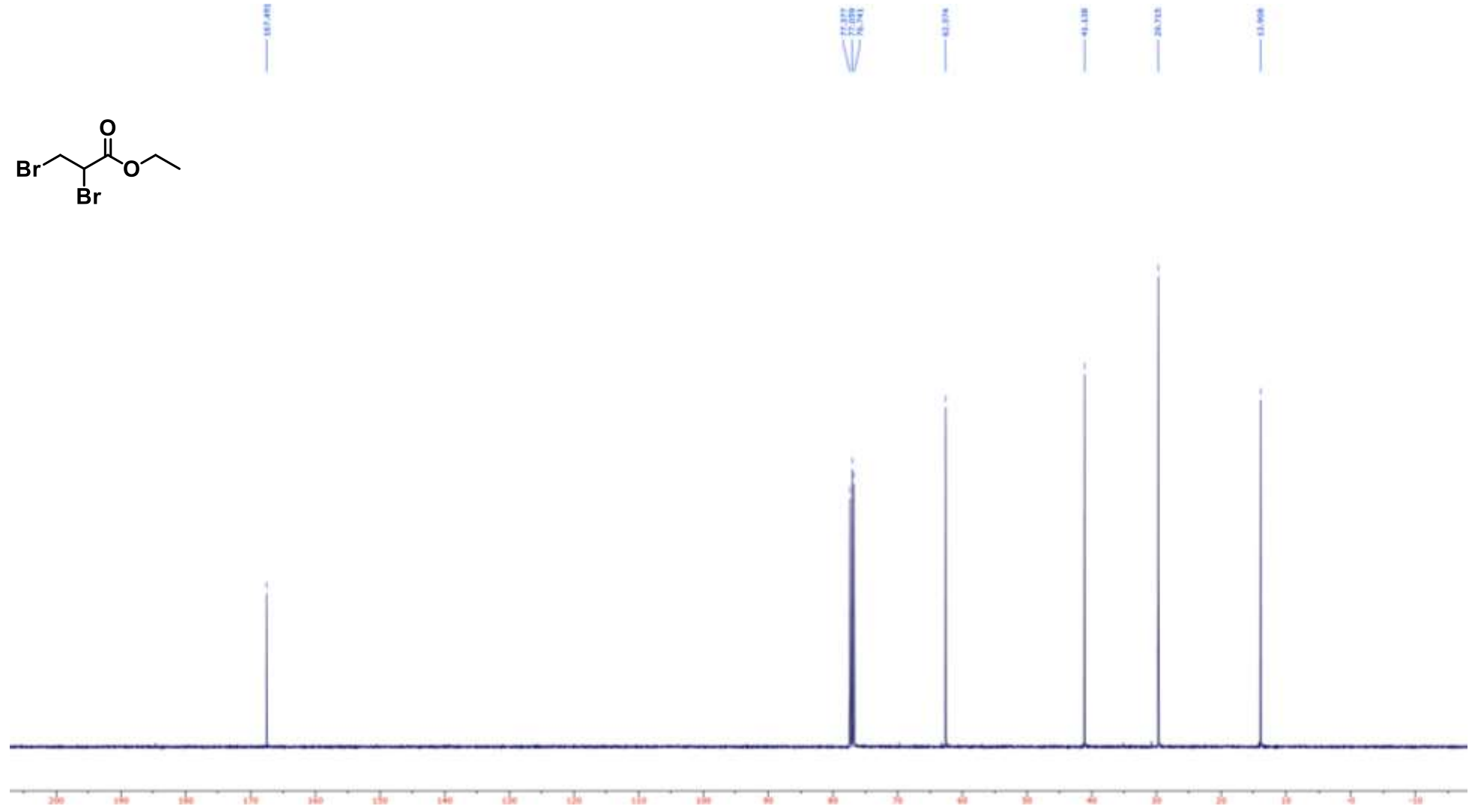
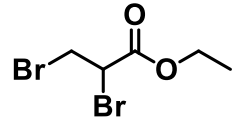
Compound **8** ^1H NMR (400 MHz, CDCl_3)



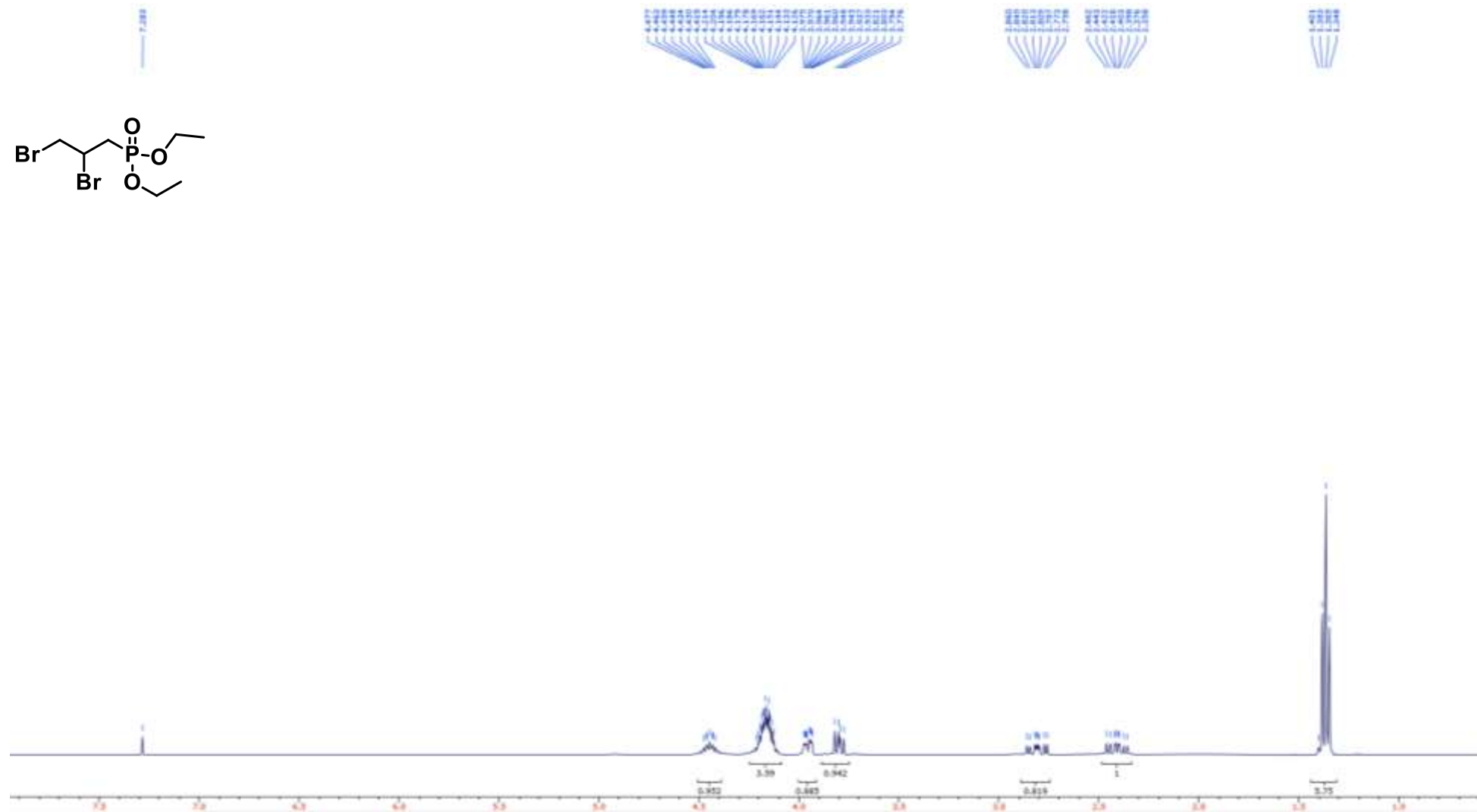
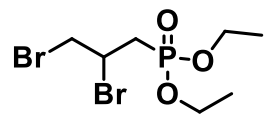
Compound **9** ^1H NMR (400 MHz, CDCl_3)



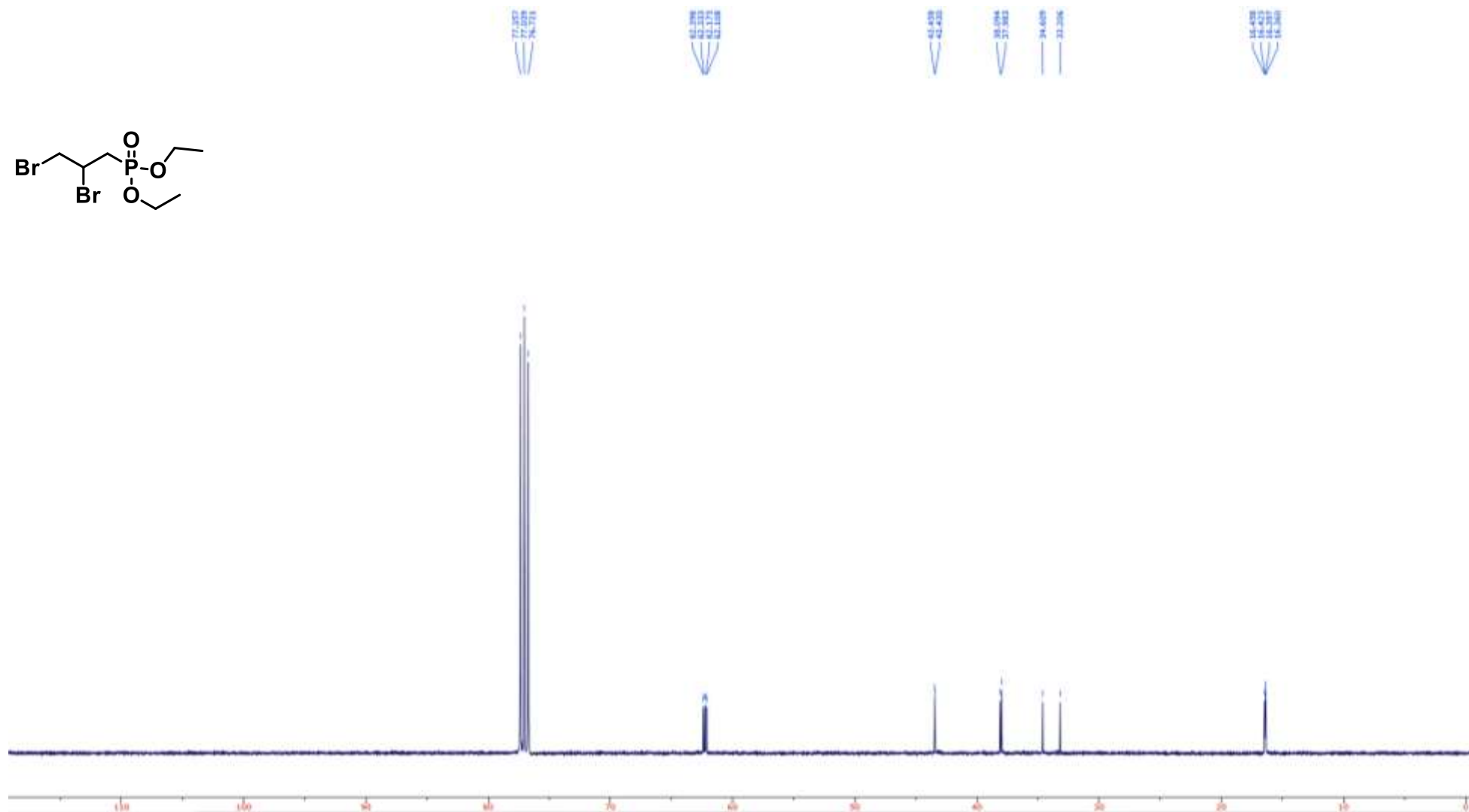
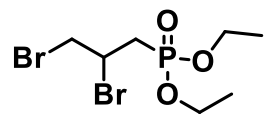
Compound **9** ^{13}C NMR (100 MHz, CDCl_3)



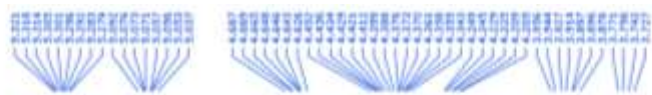
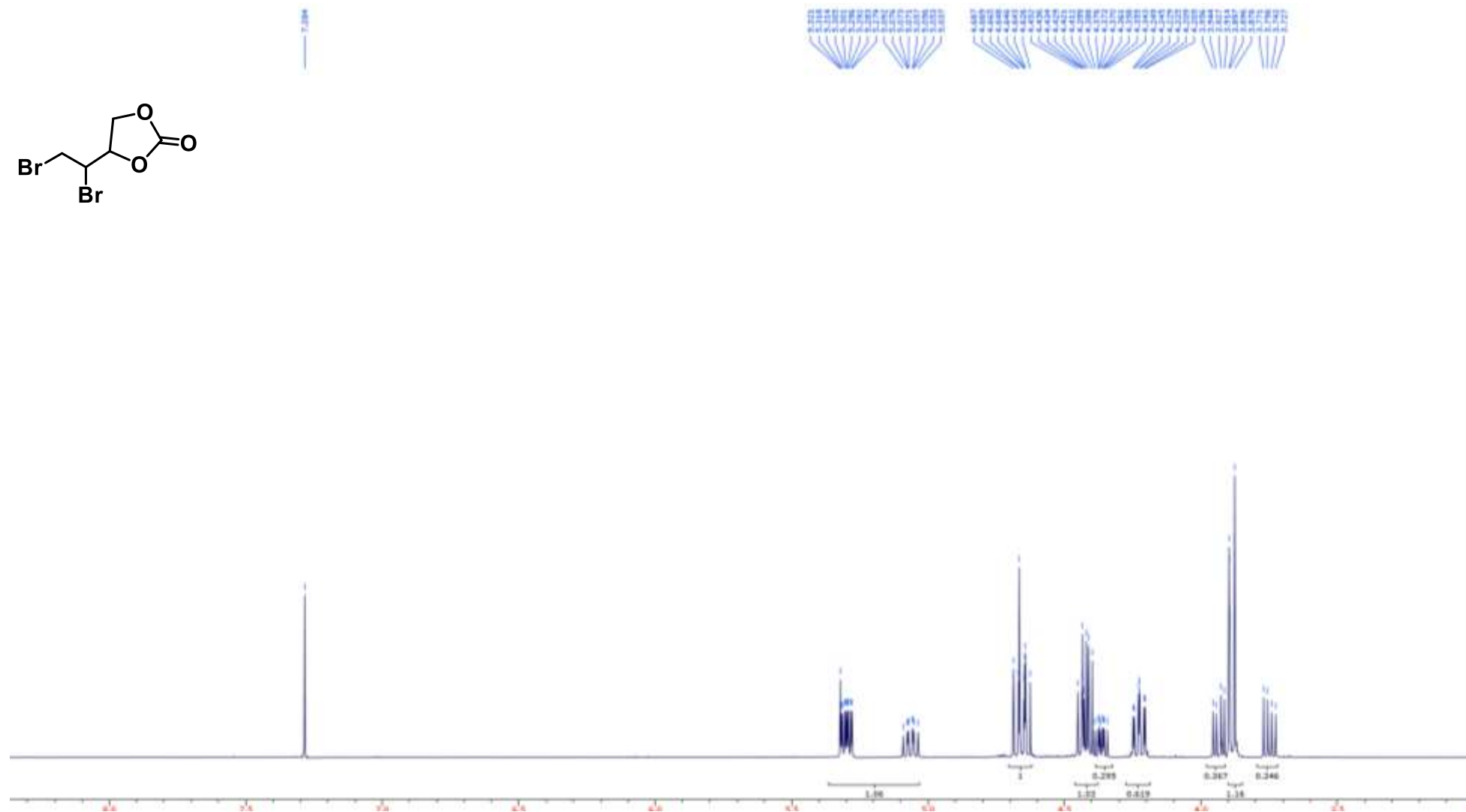
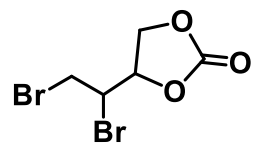
Compound **10** ^1H NMR (400 MHz, CDCl_3)



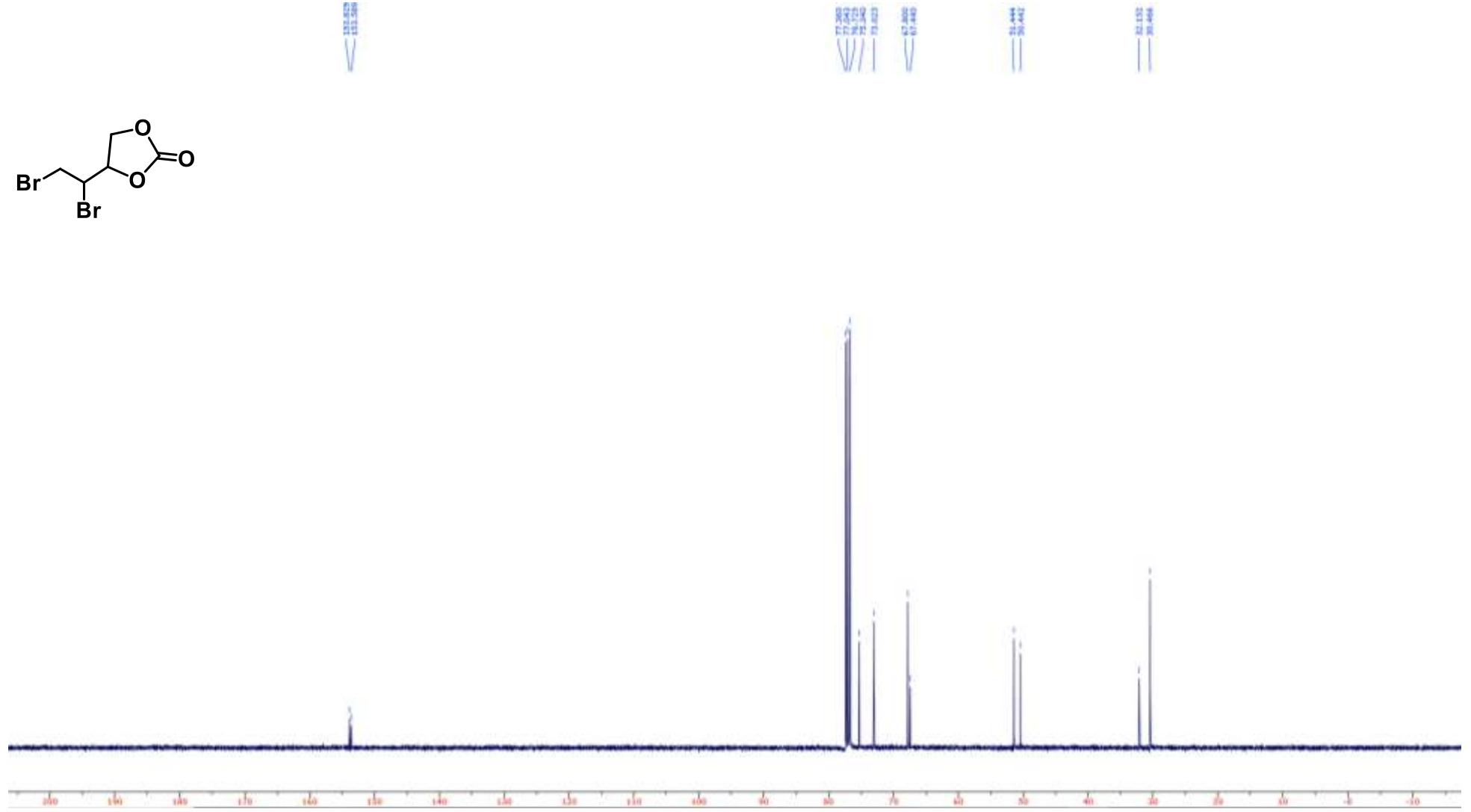
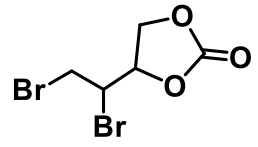
Compound **10** ^{13}C NMR (400 MHz, CDCl_3)



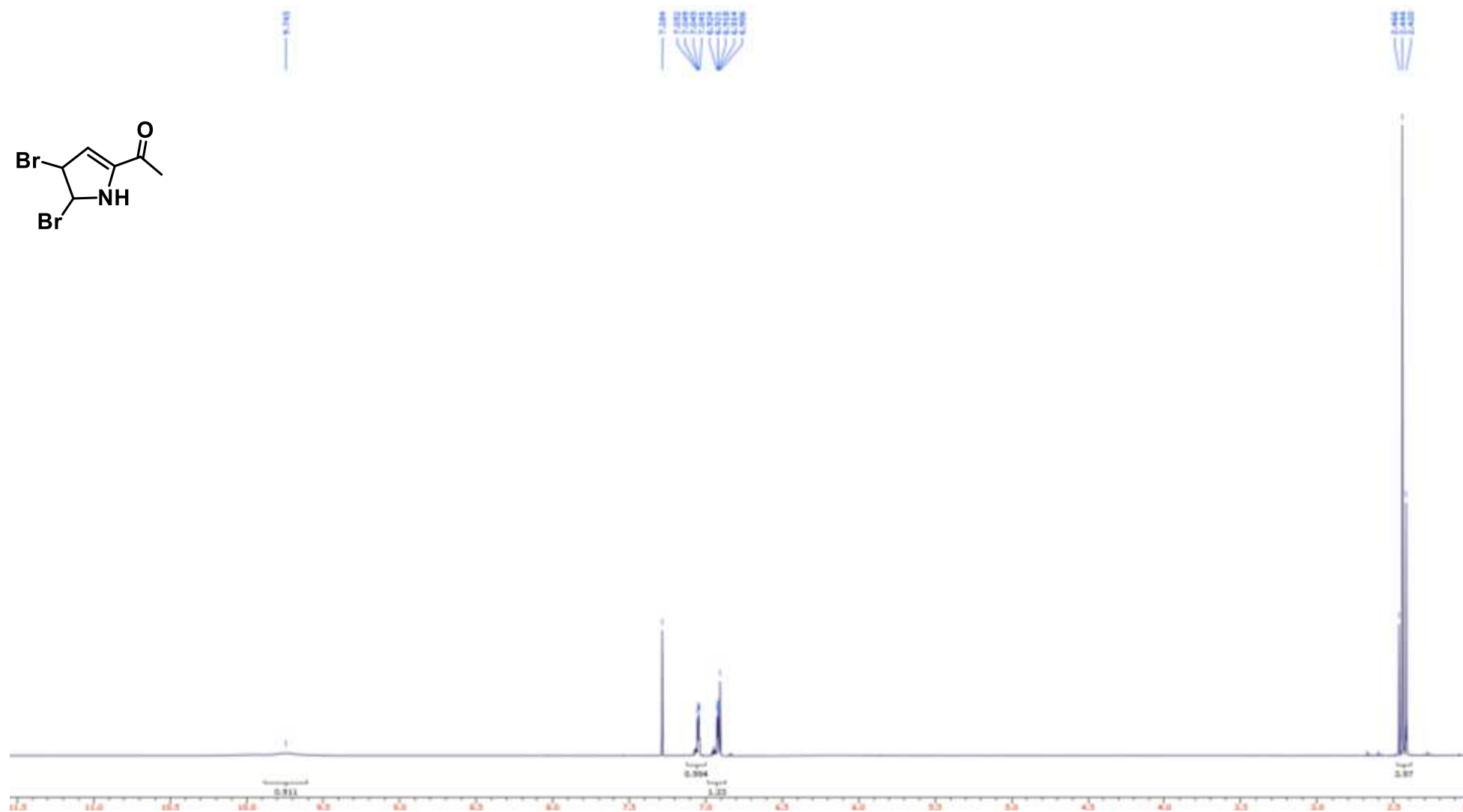
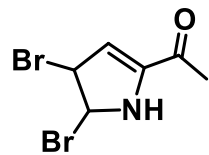
Compound **11** ^1H NMR (400 MHz, CDCl_3)



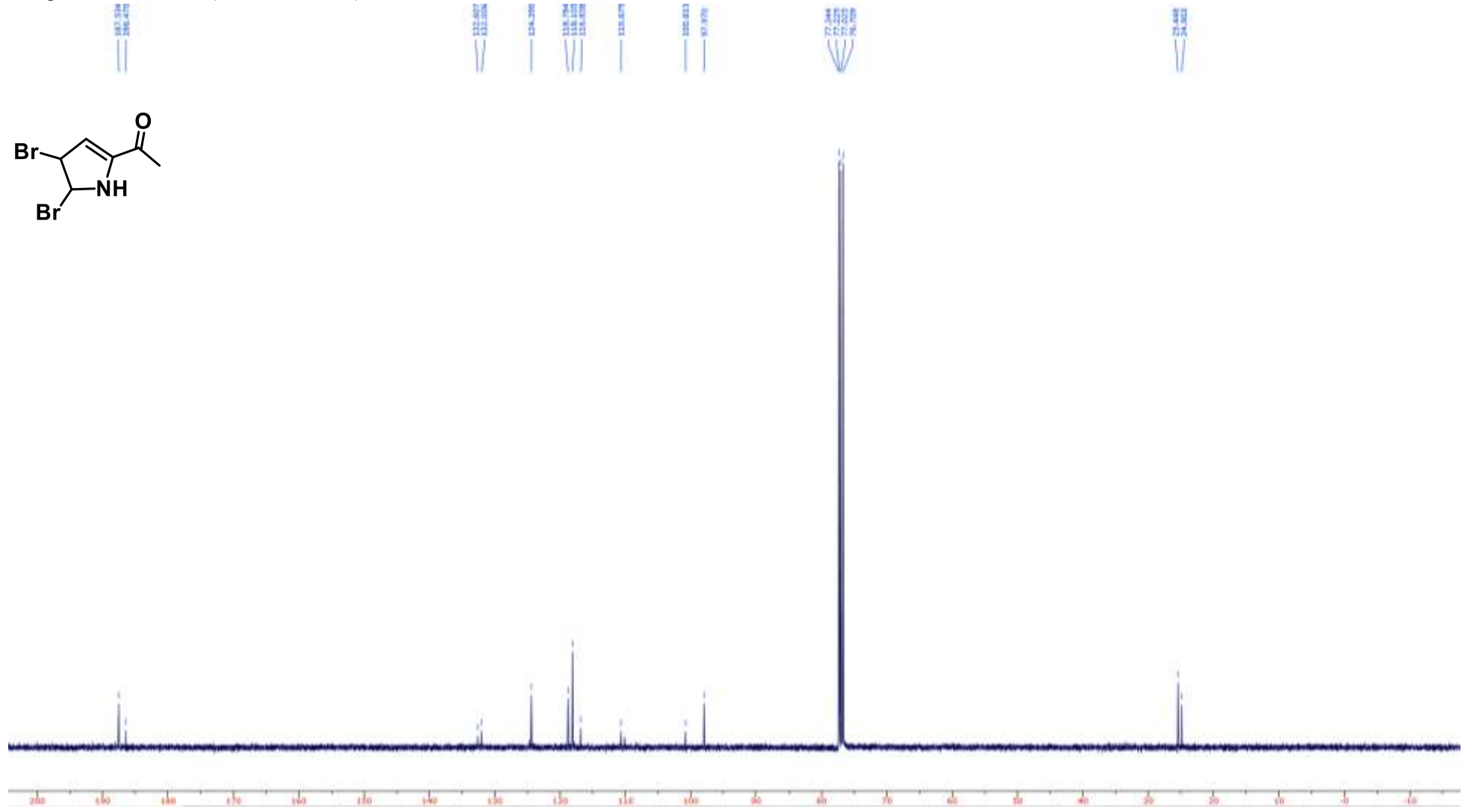
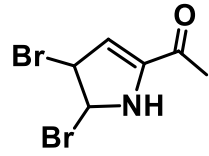
Compound **11** ^{13}C NMR (100 MHz, CDCl_3)



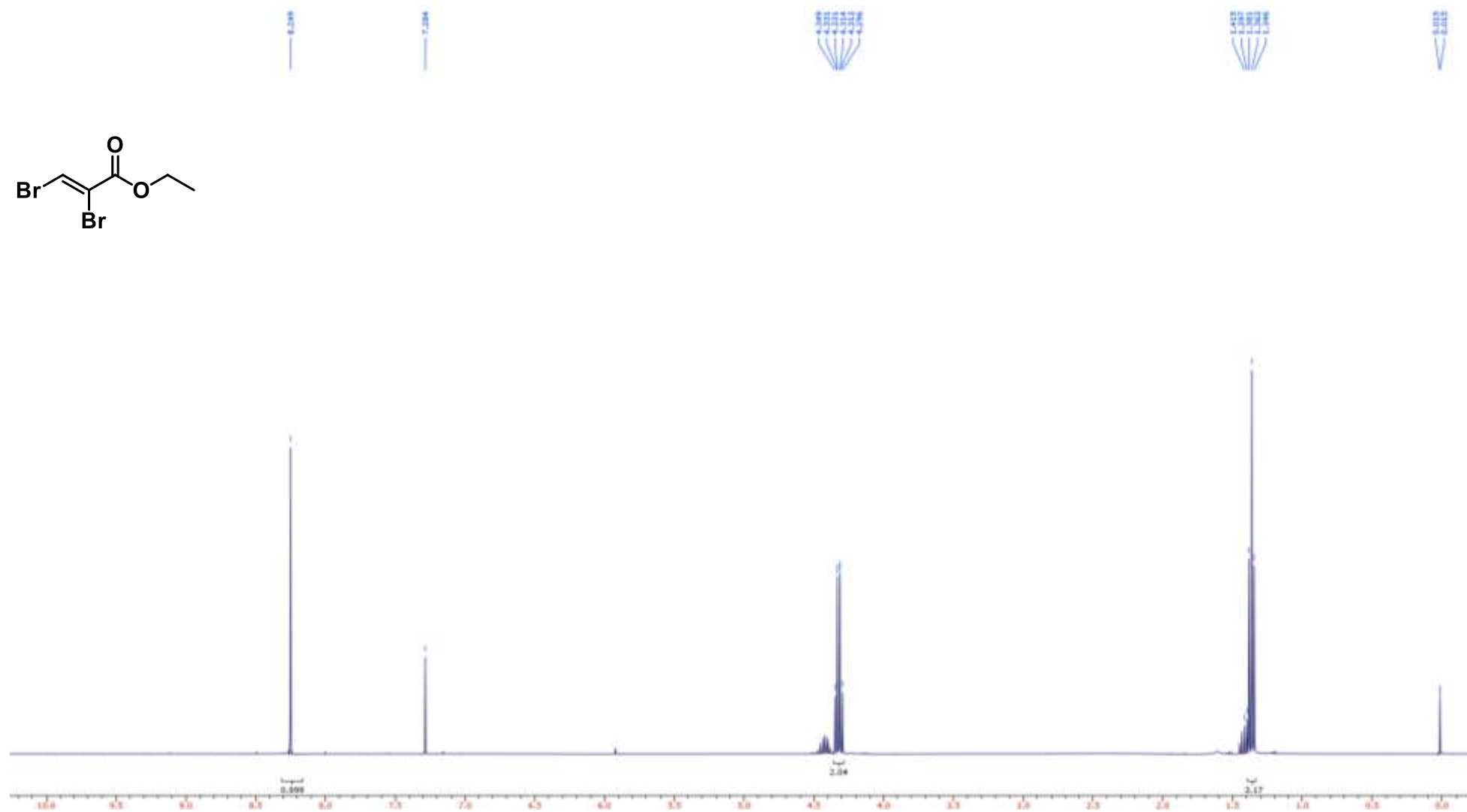
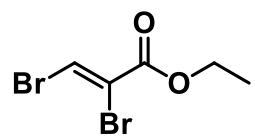
Compound **12** ^1H NMR (400 MHz, CDCl_3)



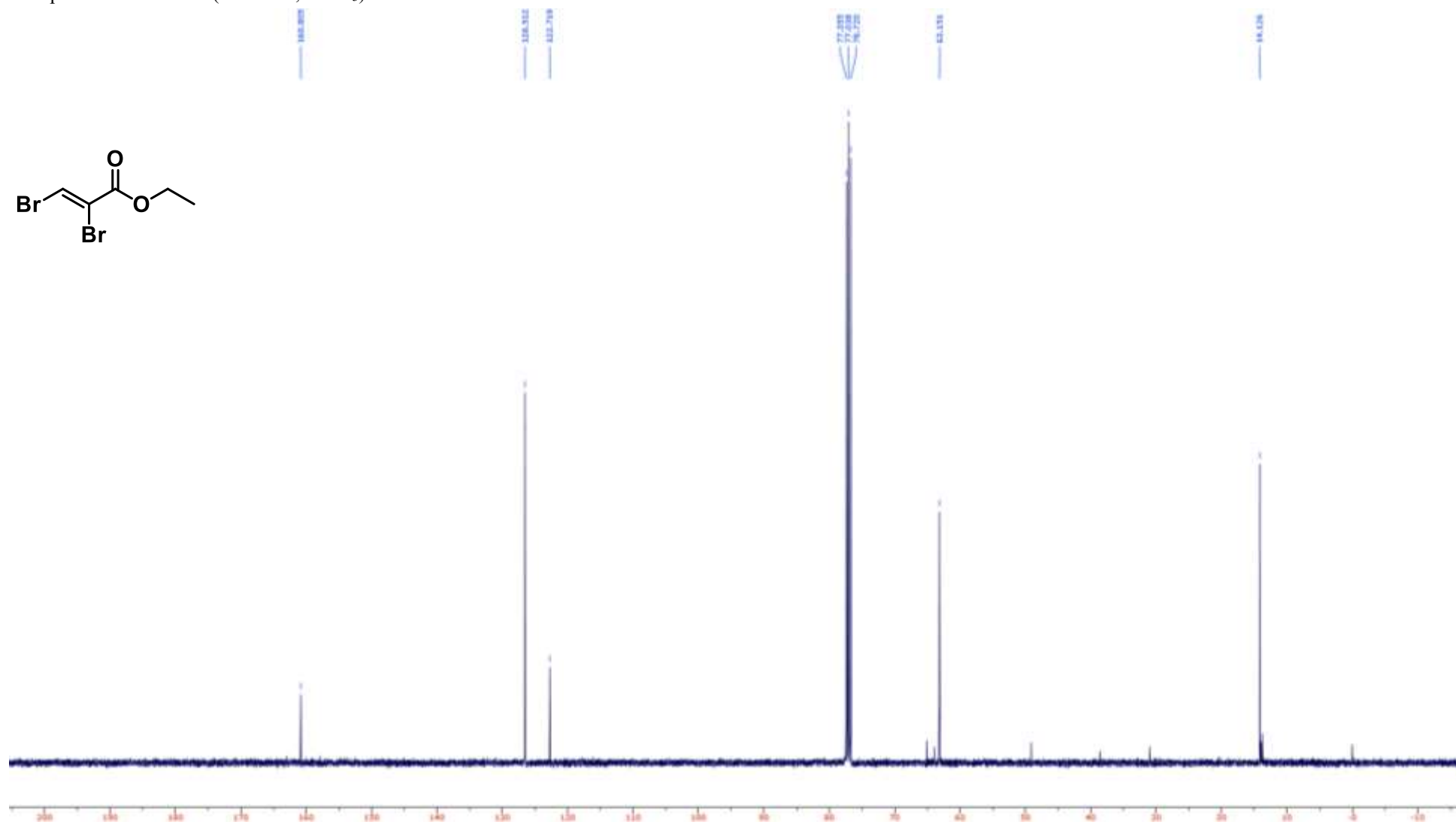
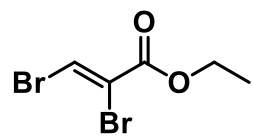
Compound **12** ^{13}C NMR (100 MHz, CDCl_3)



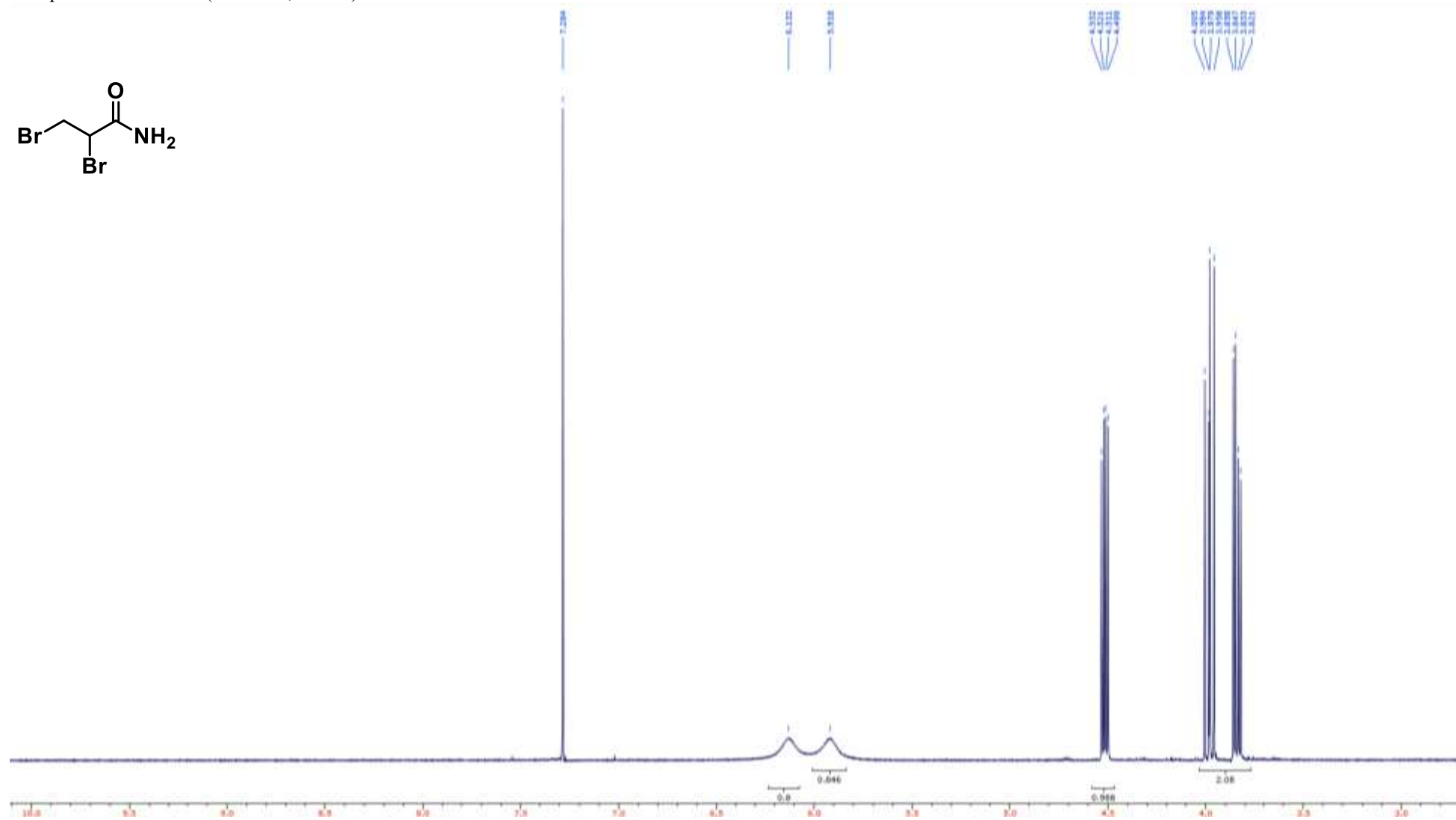
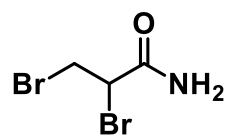
Compound **13** ^1H NMR (400 MHz, CDCl_3)



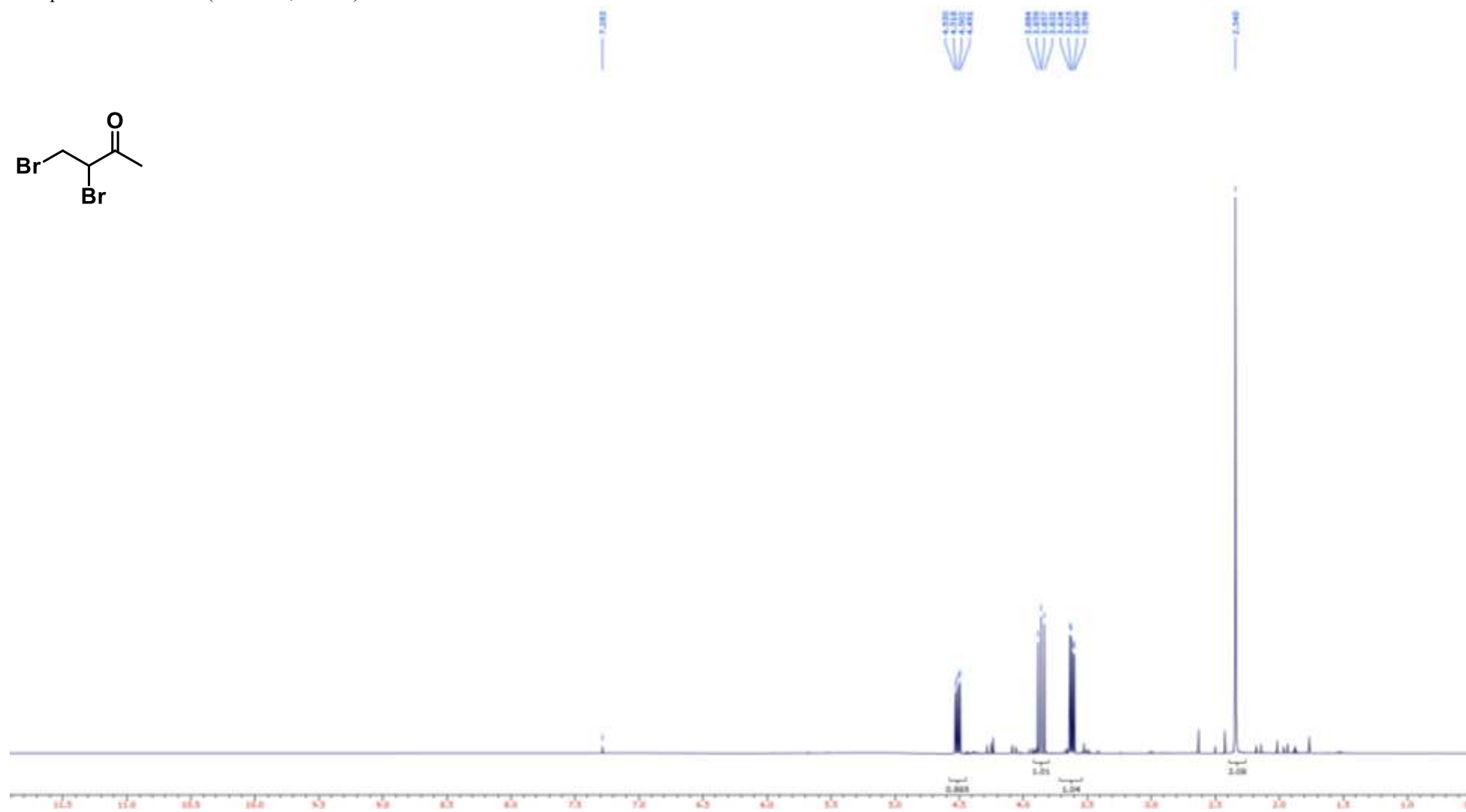
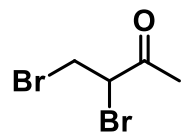
Compound **13** ^{13}C NMR (100 MHz, CDCl_3)



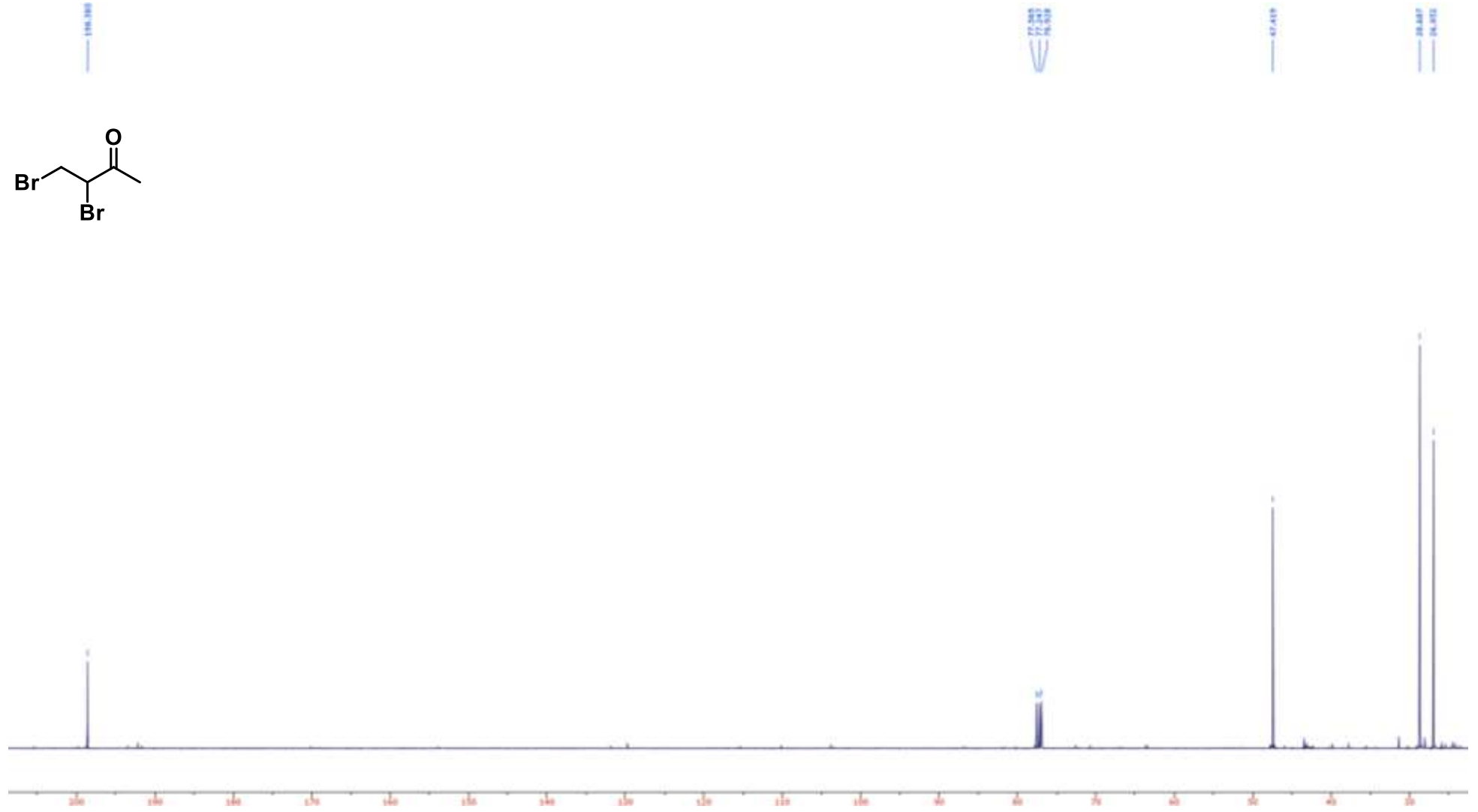
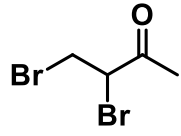
Compound 14 ^1H NMR (400 MHz, CDCl_3)



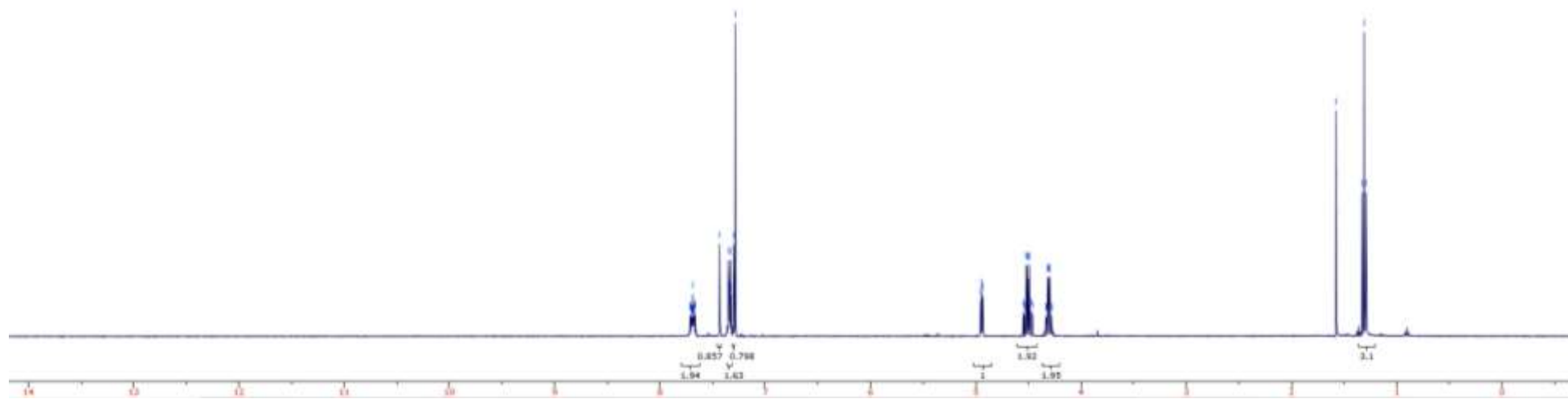
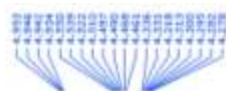
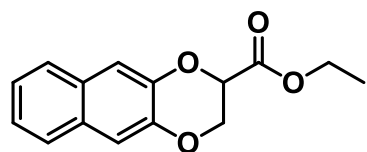
Compound **15** ^1H NMR (400 MHz, CDCl_3)



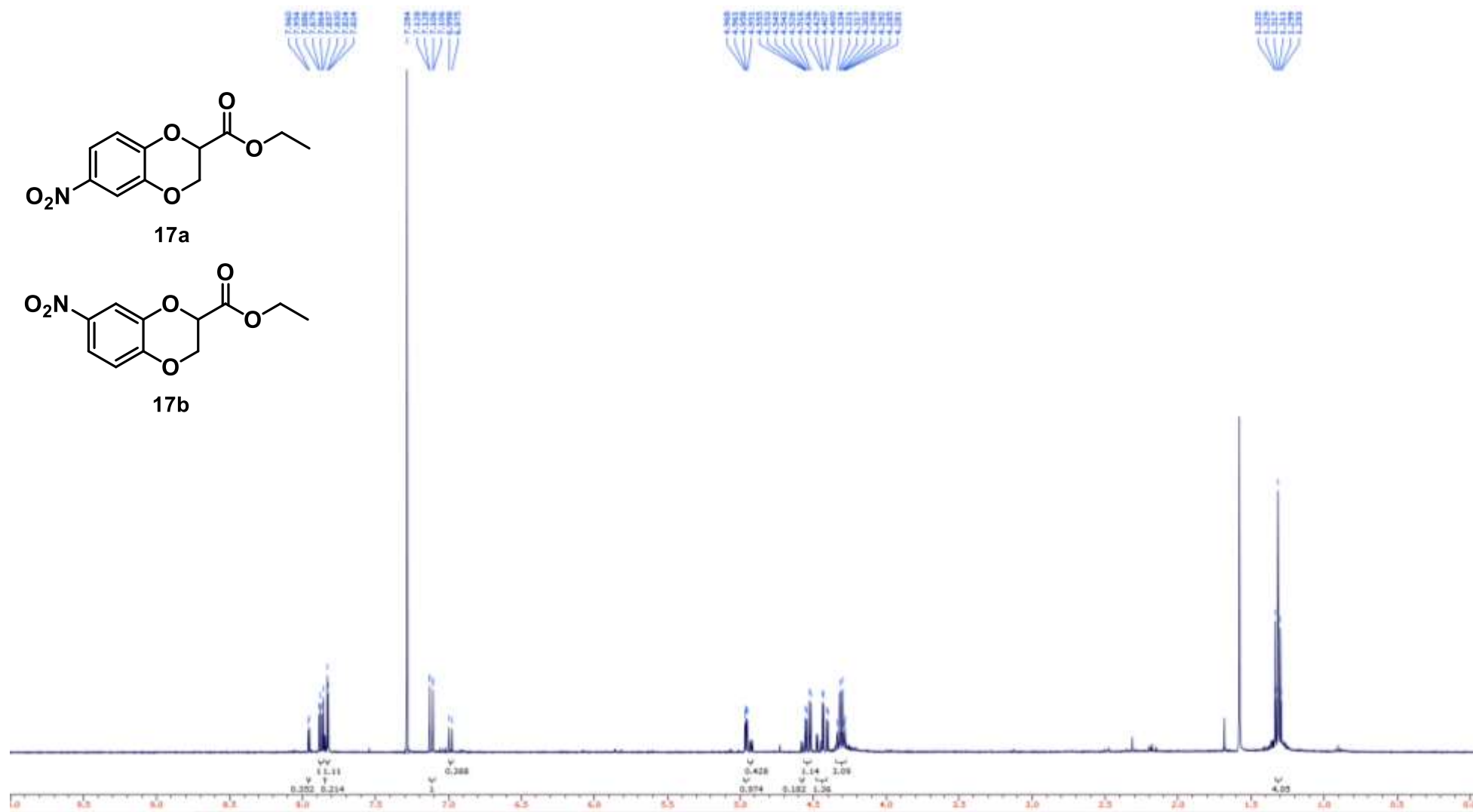
Compound **15** ^{13}C NMR (100 MHz, CDCl_3)



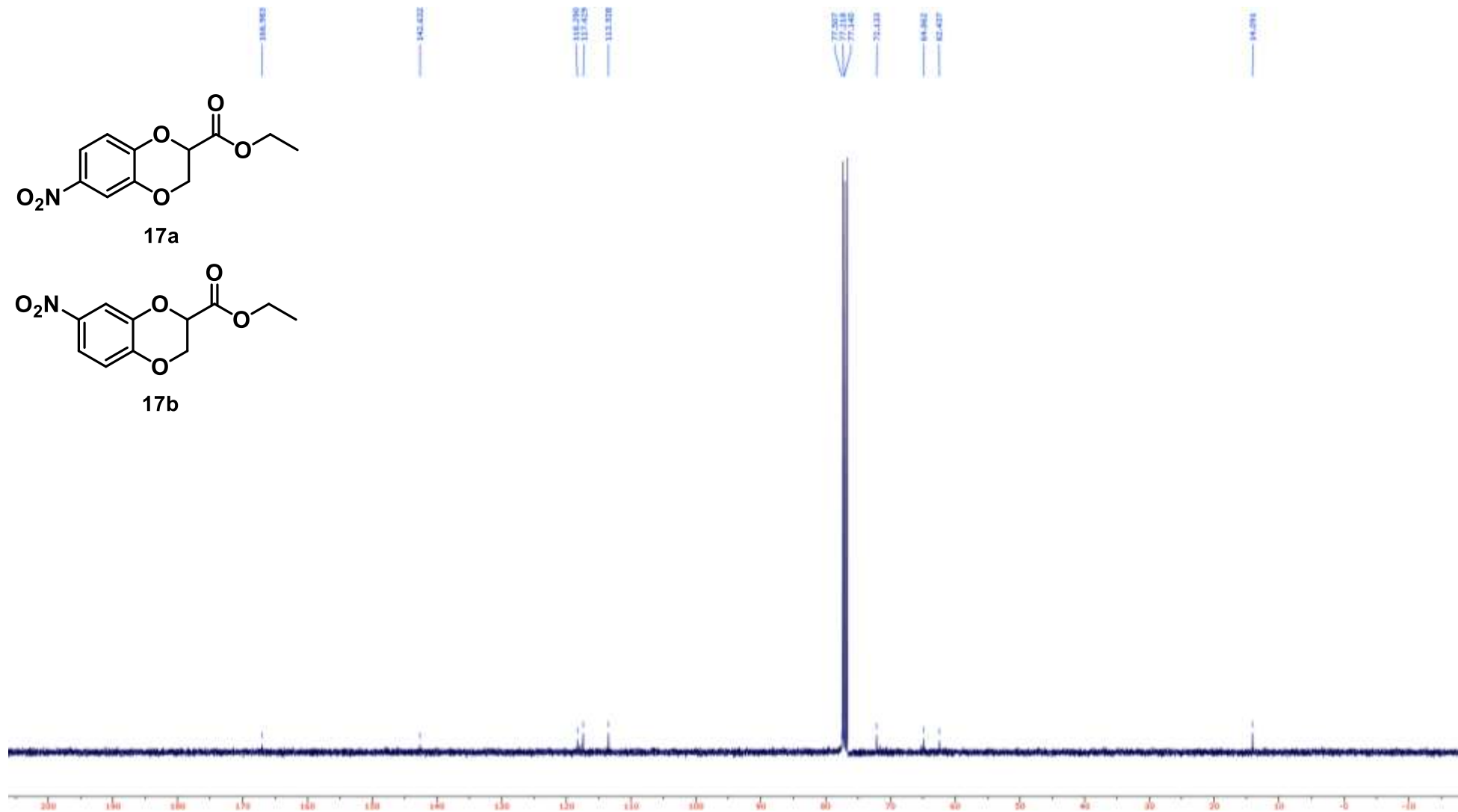
Compound **16** ^1H NMR (400 MHz, CDCl_3)



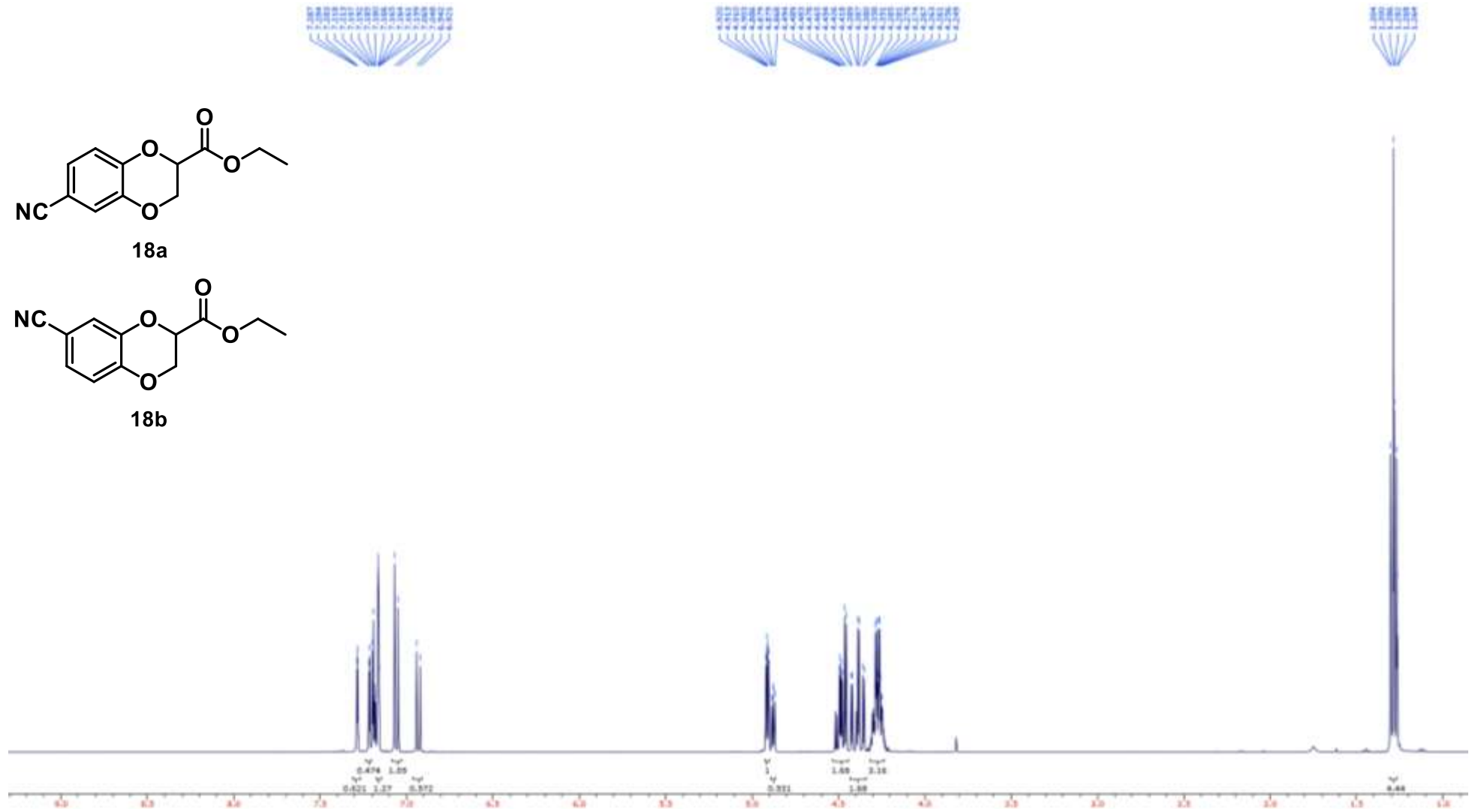
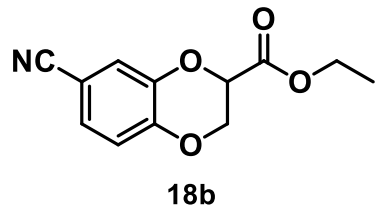
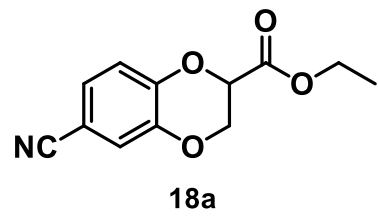
Compound 17 ¹H NMR (400 MHz, CDCl₃)



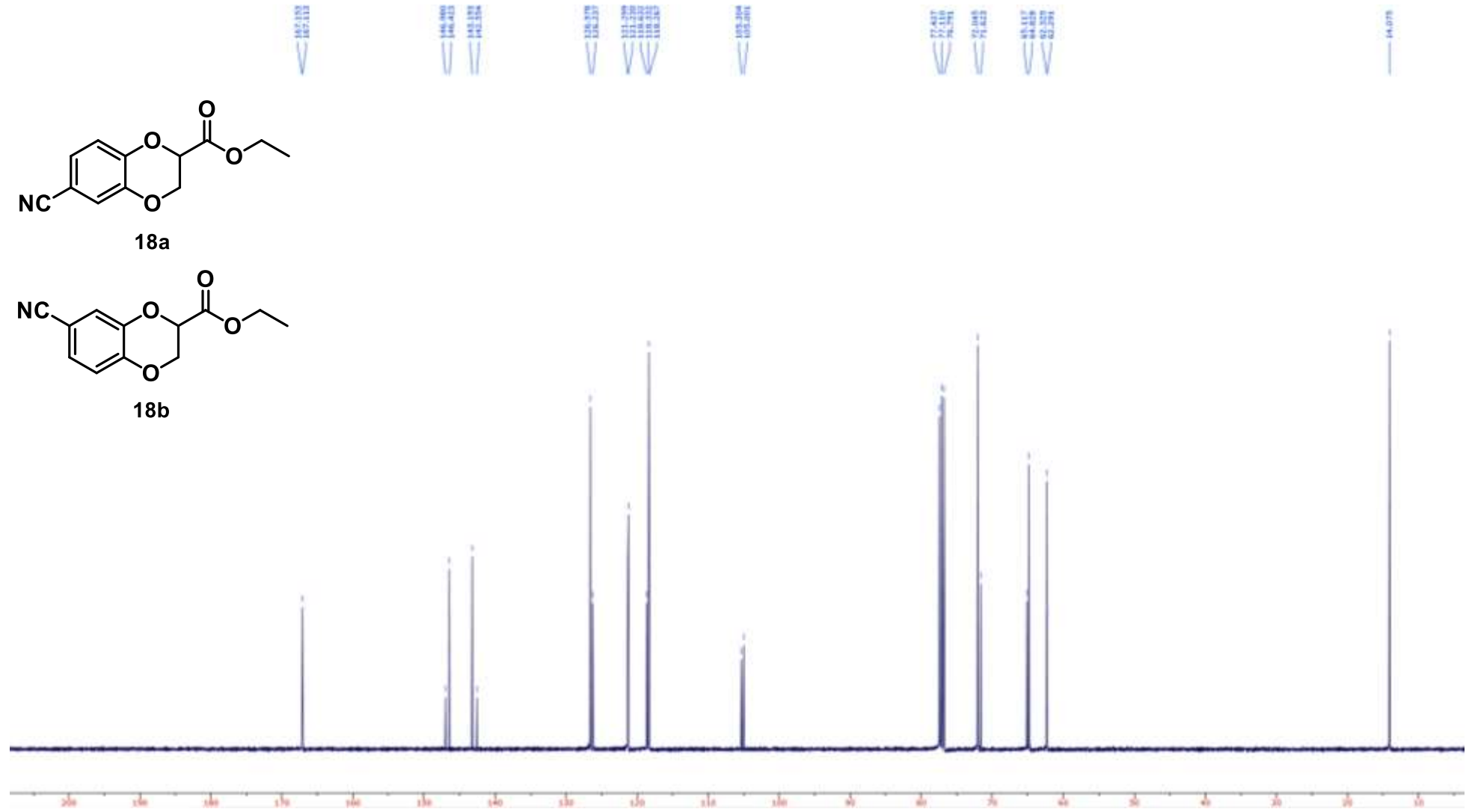
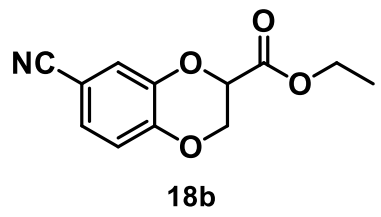
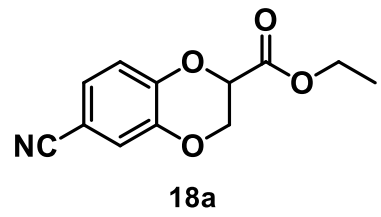
Compound 17 ¹³C NMR (100 MHz, CDCl₃)



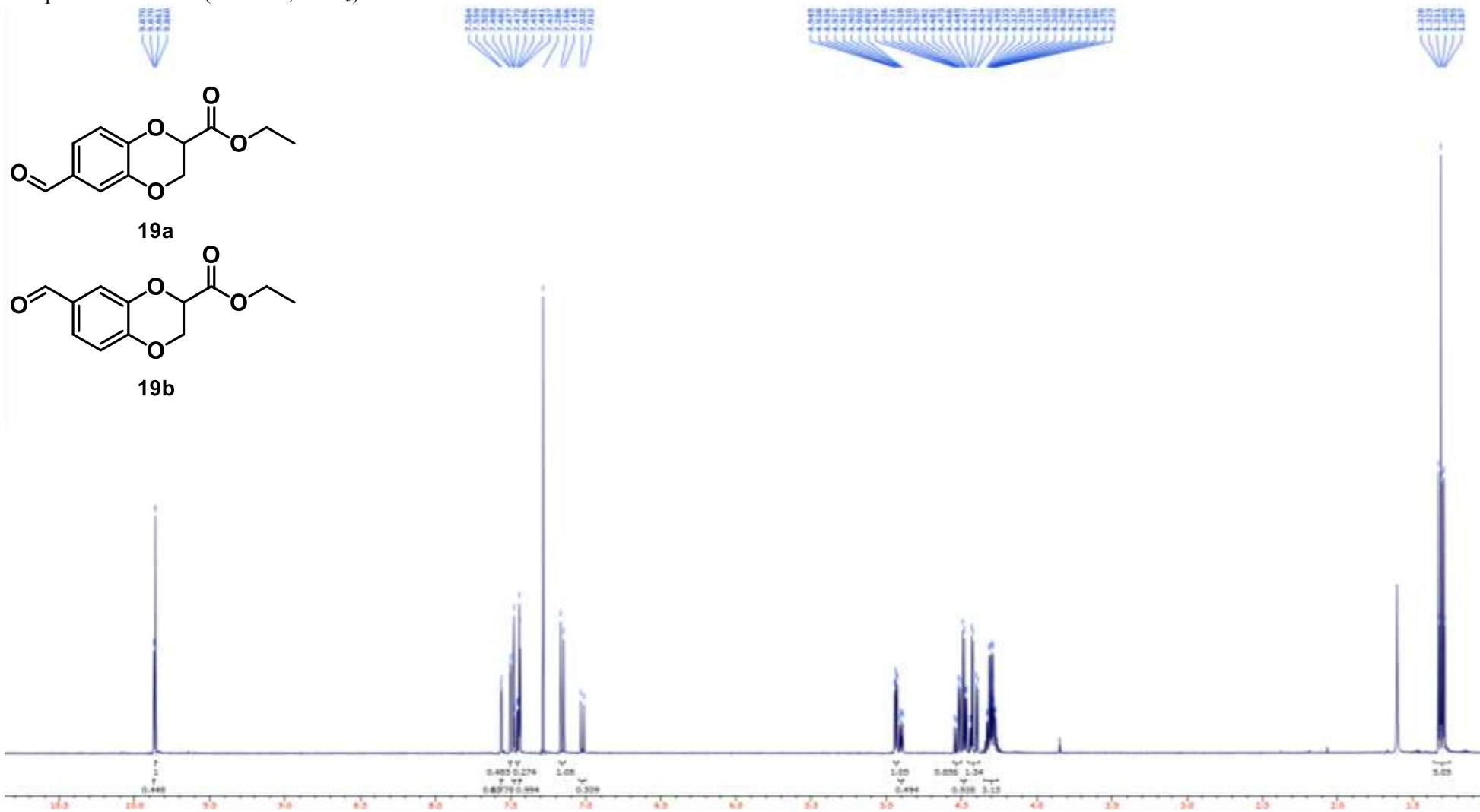
Compound **18** ^1H NMR (400 MHz, CDCl_3)



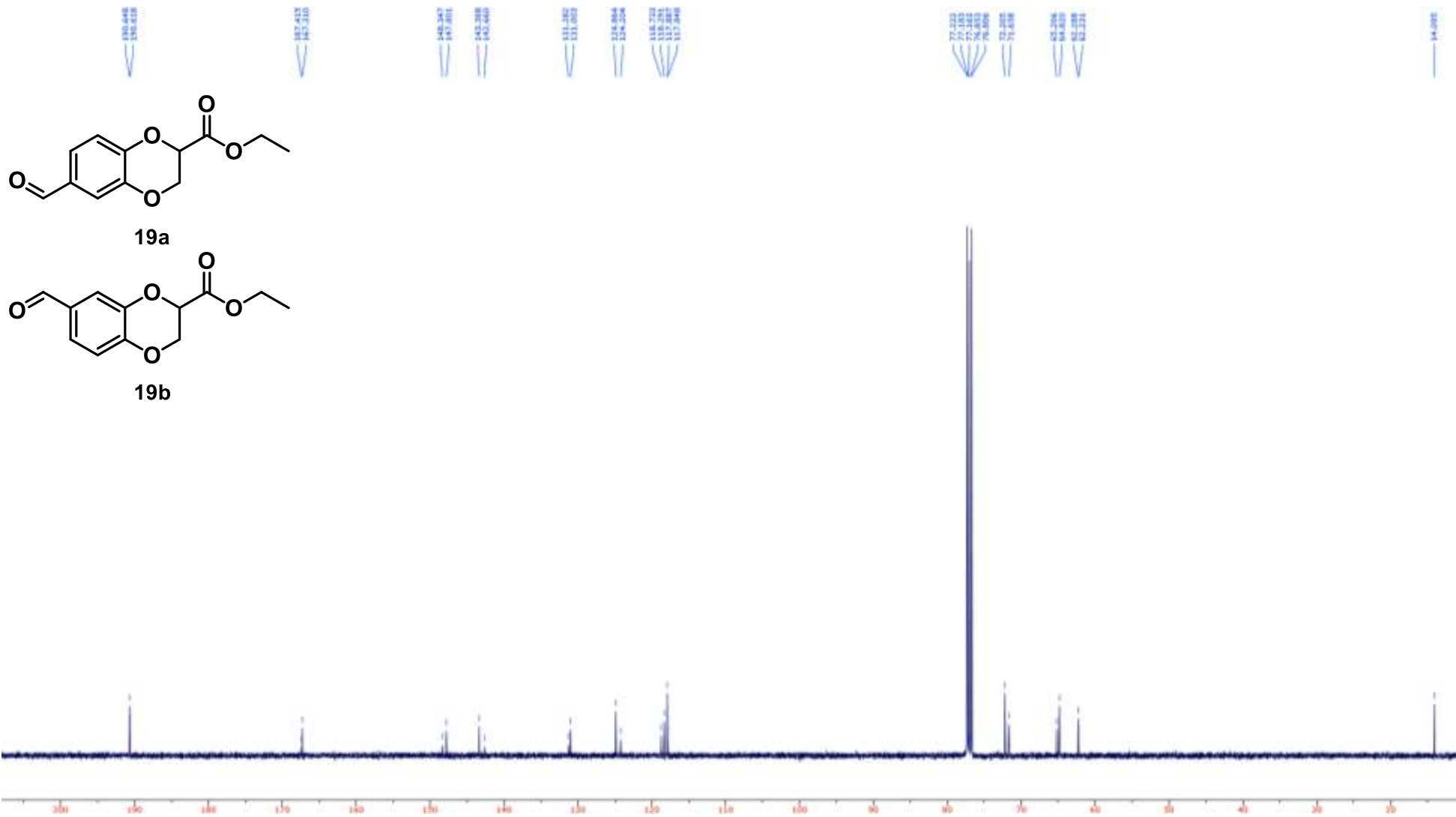
Compound **18** ¹³C NMR (100 MHz, CDCl₃)



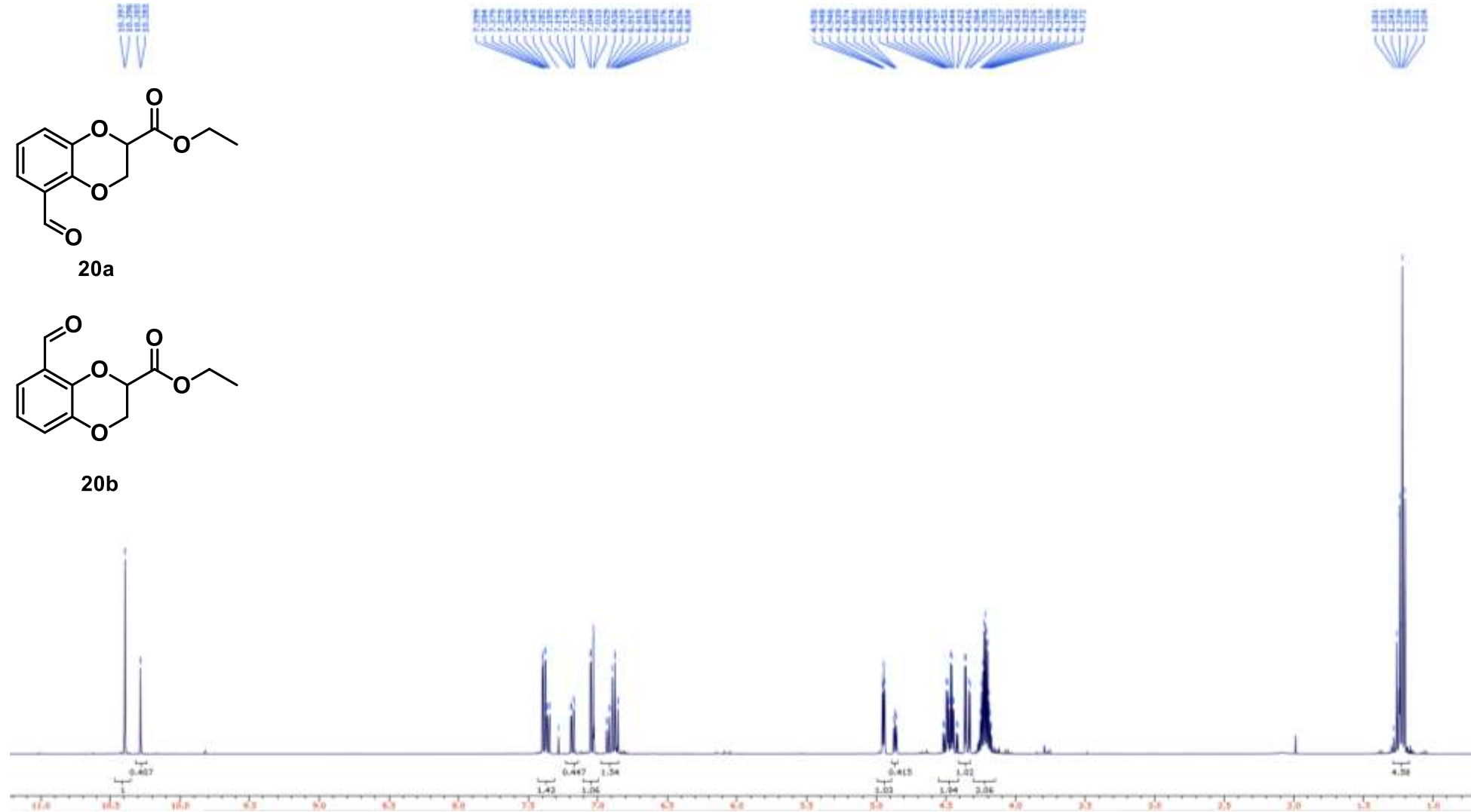
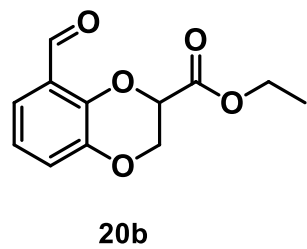
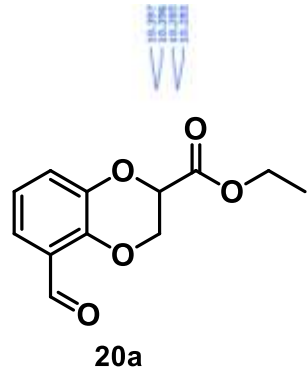
Compound **19** ^1H NMR (400 MHz, CDCl_3)



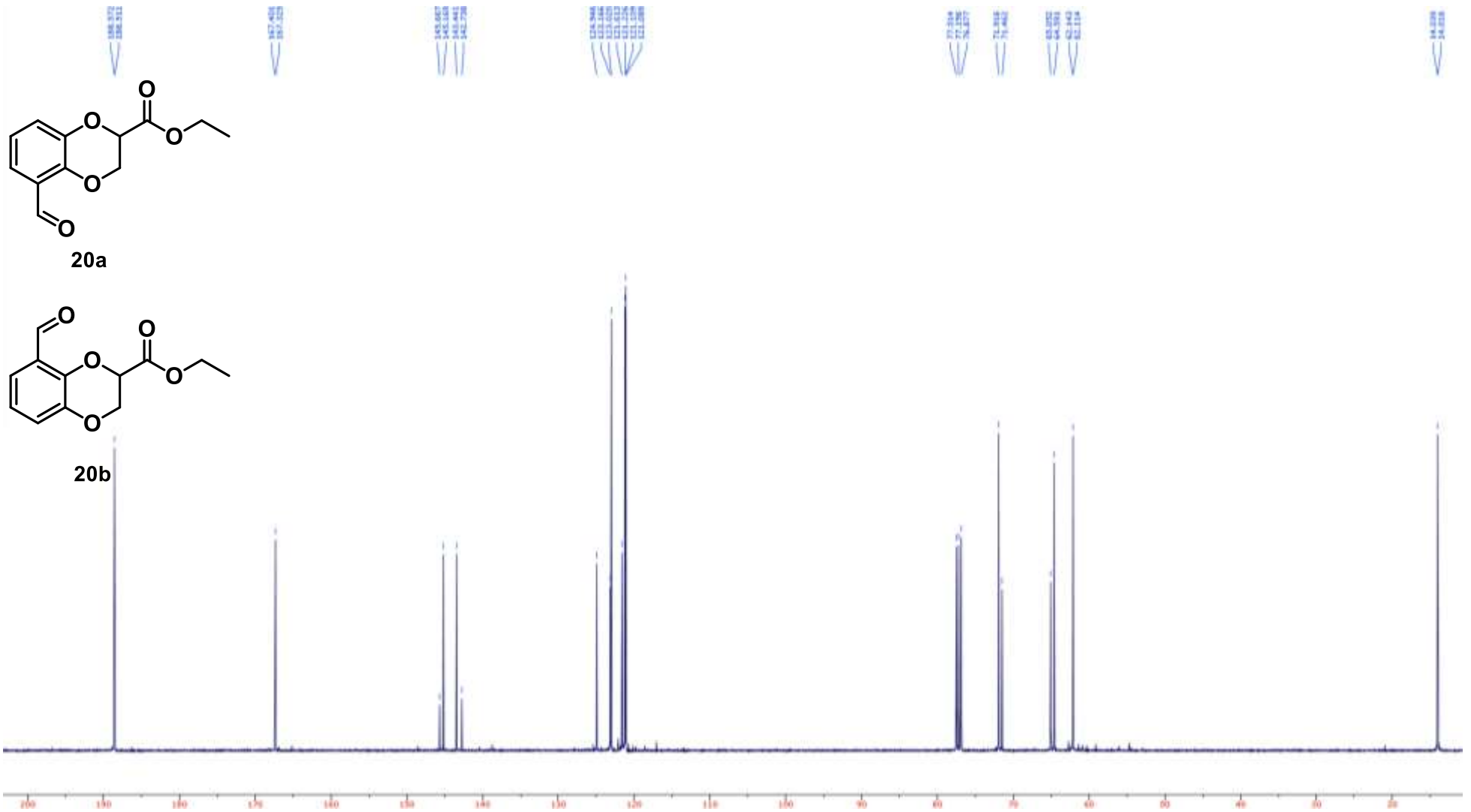
Compound **19** ¹³C NMR (100 MHz, CDCl₃)



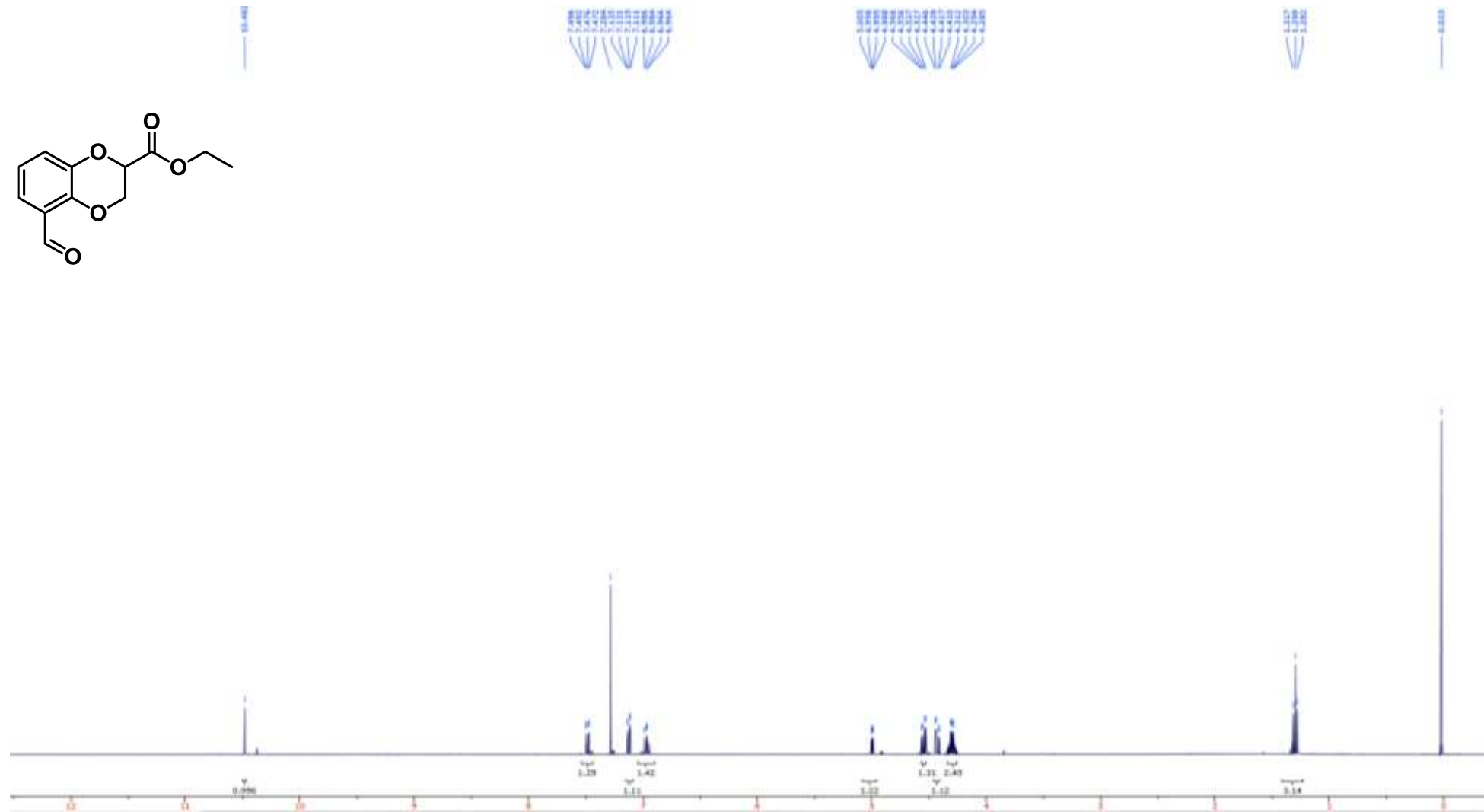
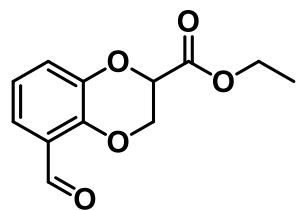
Compound **20** ^1H NMR (400 MHz, CDCl_3)



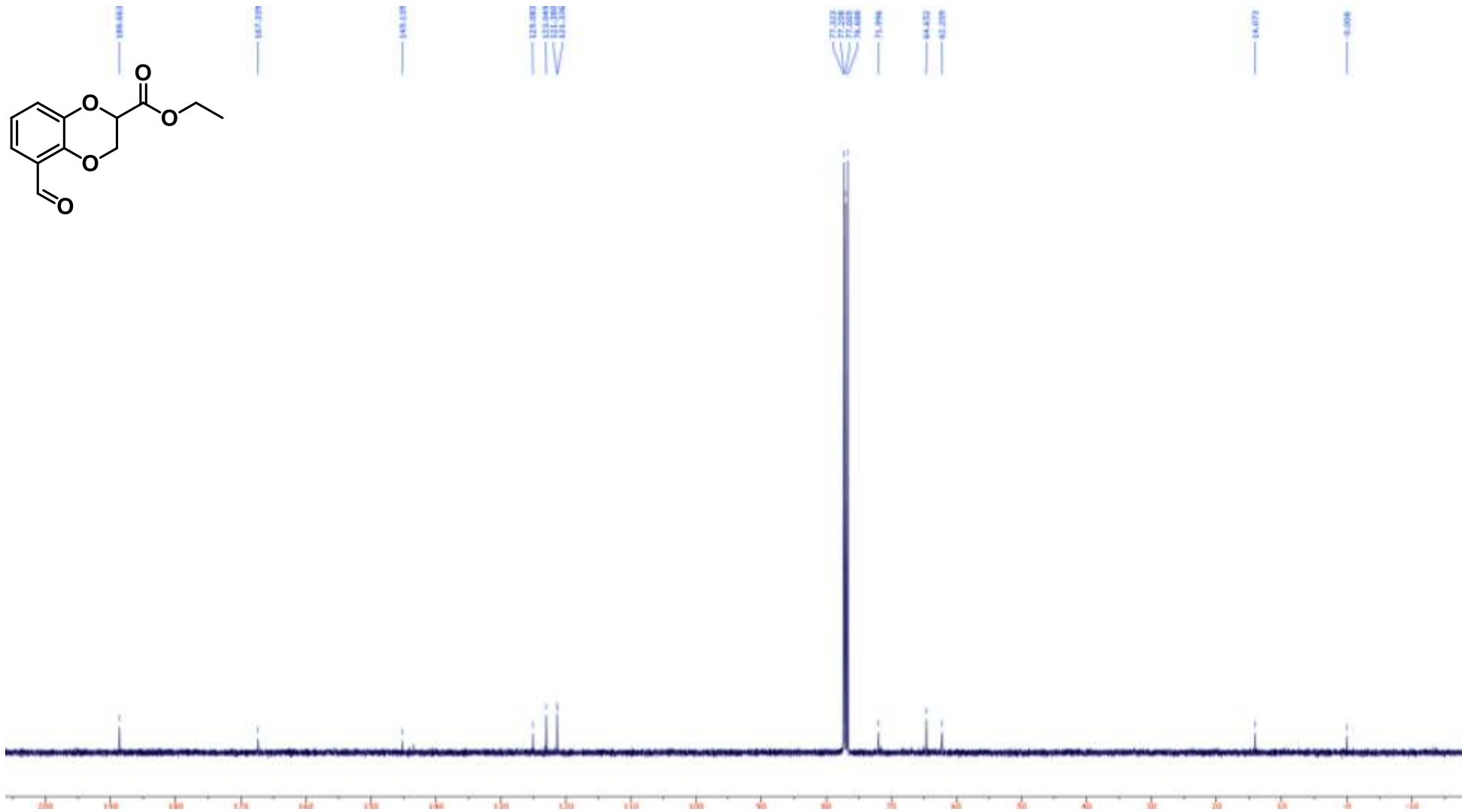
Compound **20** ^{13}C NMR (100 MHz, CDCl_3)



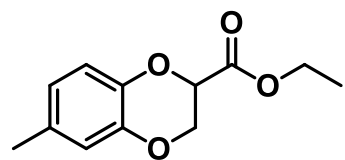
Compound **20a** ^1H NMR (400 MHz, CDCl_3)



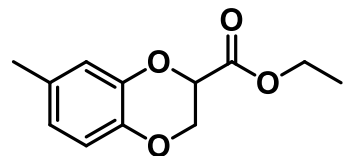
Compound **20a** ^{13}C NMR (100 MHz, CDCl_3)



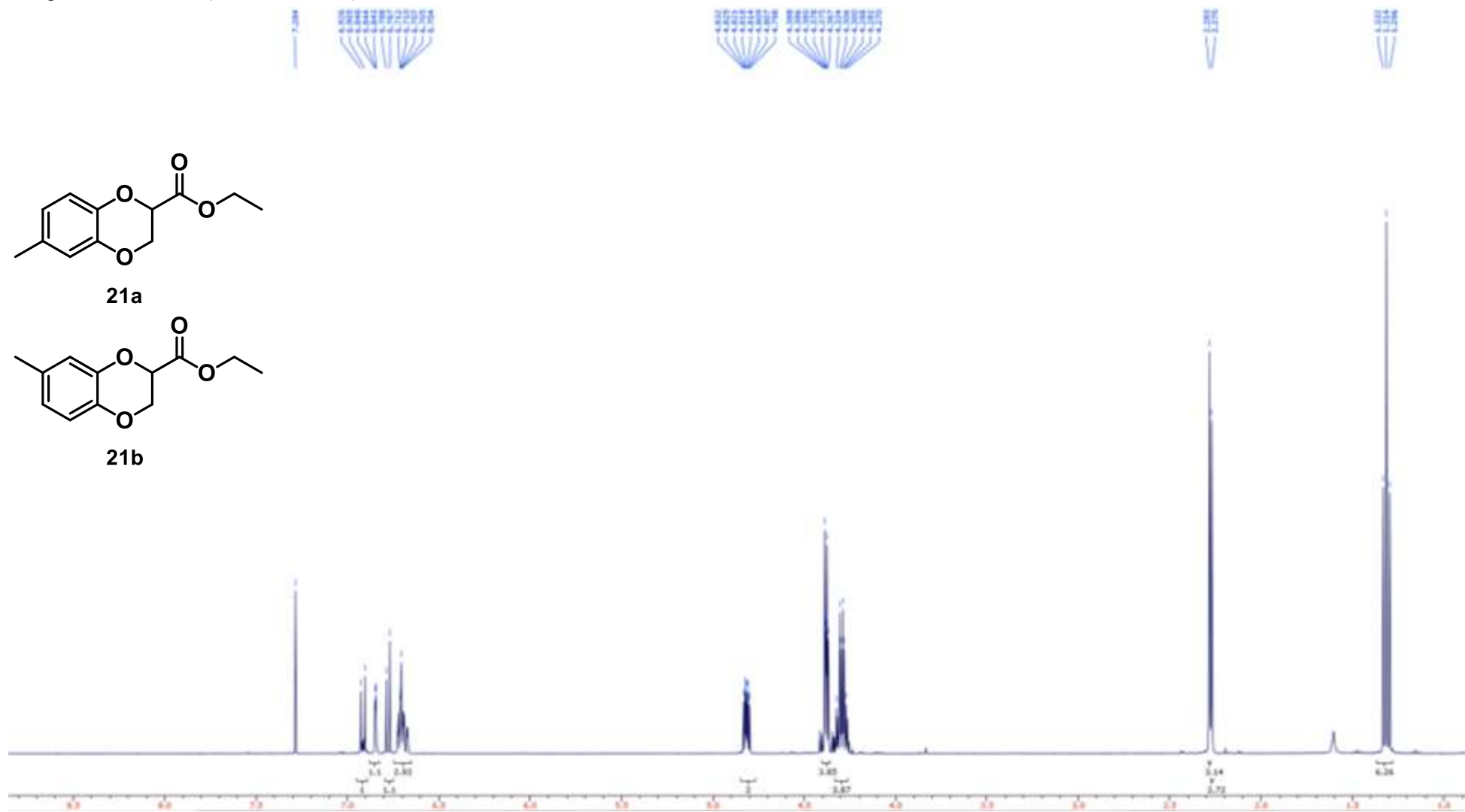
Compound **21** ^1H NMR (400 MHz, CDCl_3)



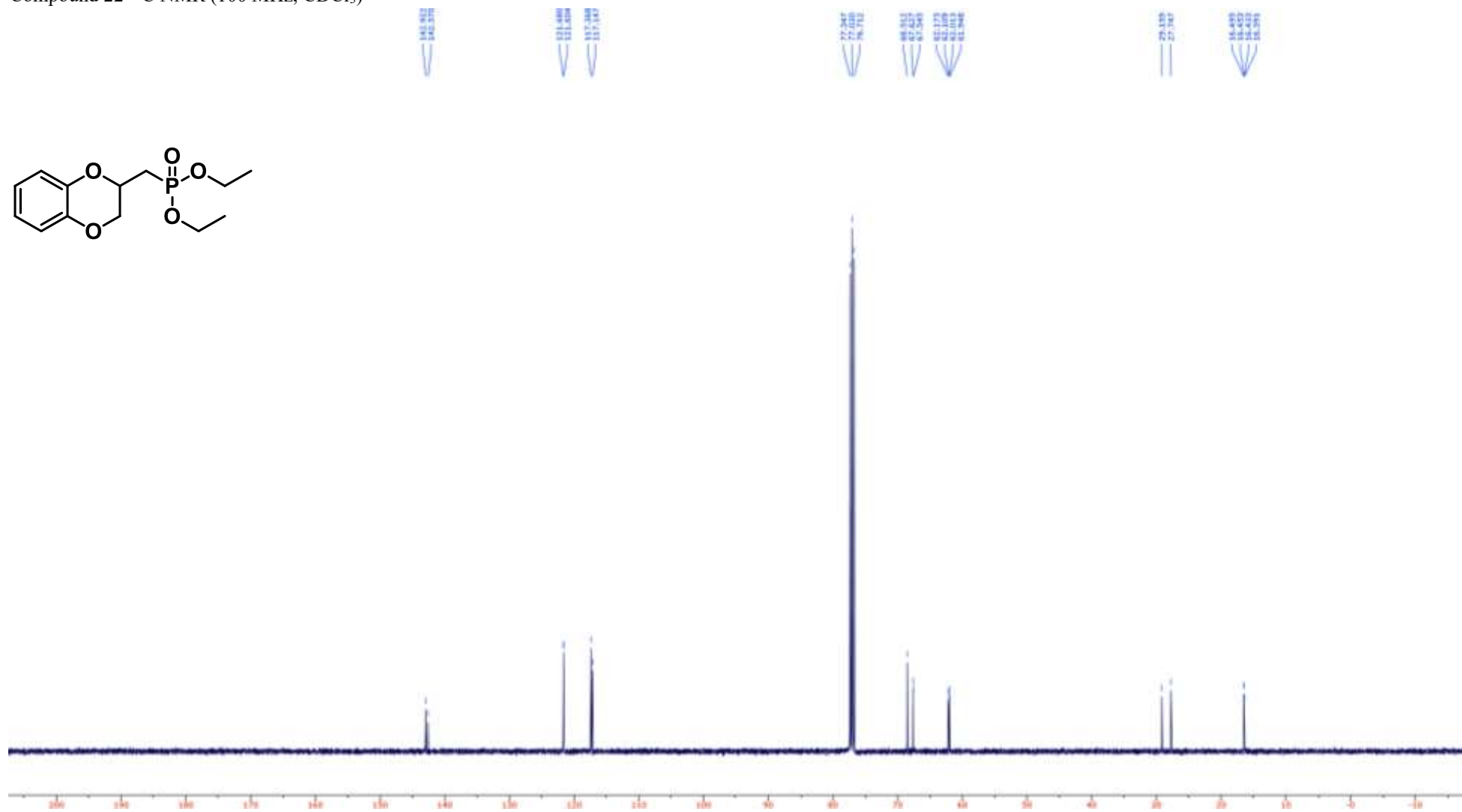
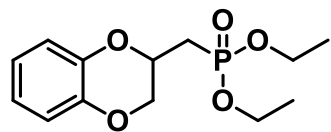
21a



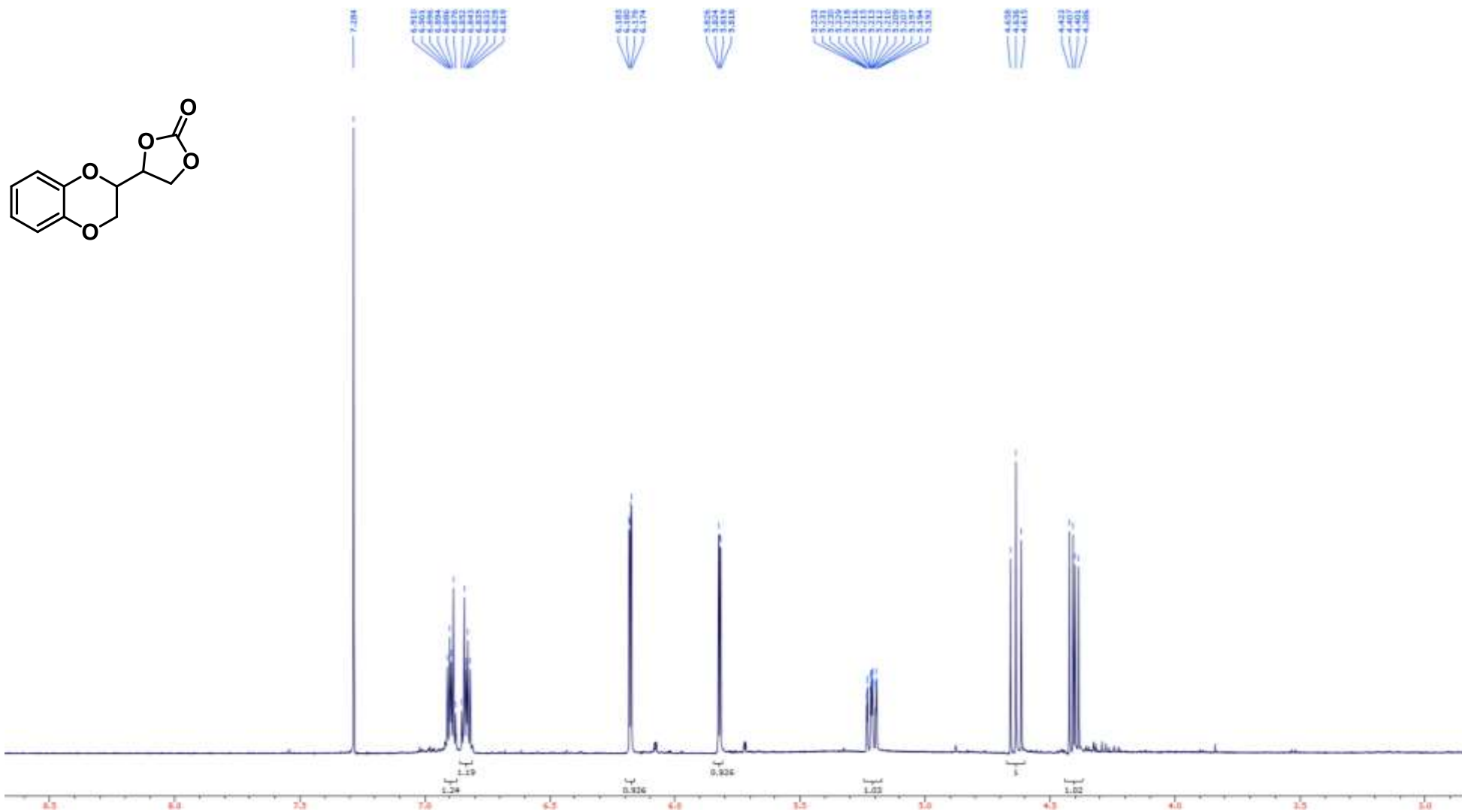
21b



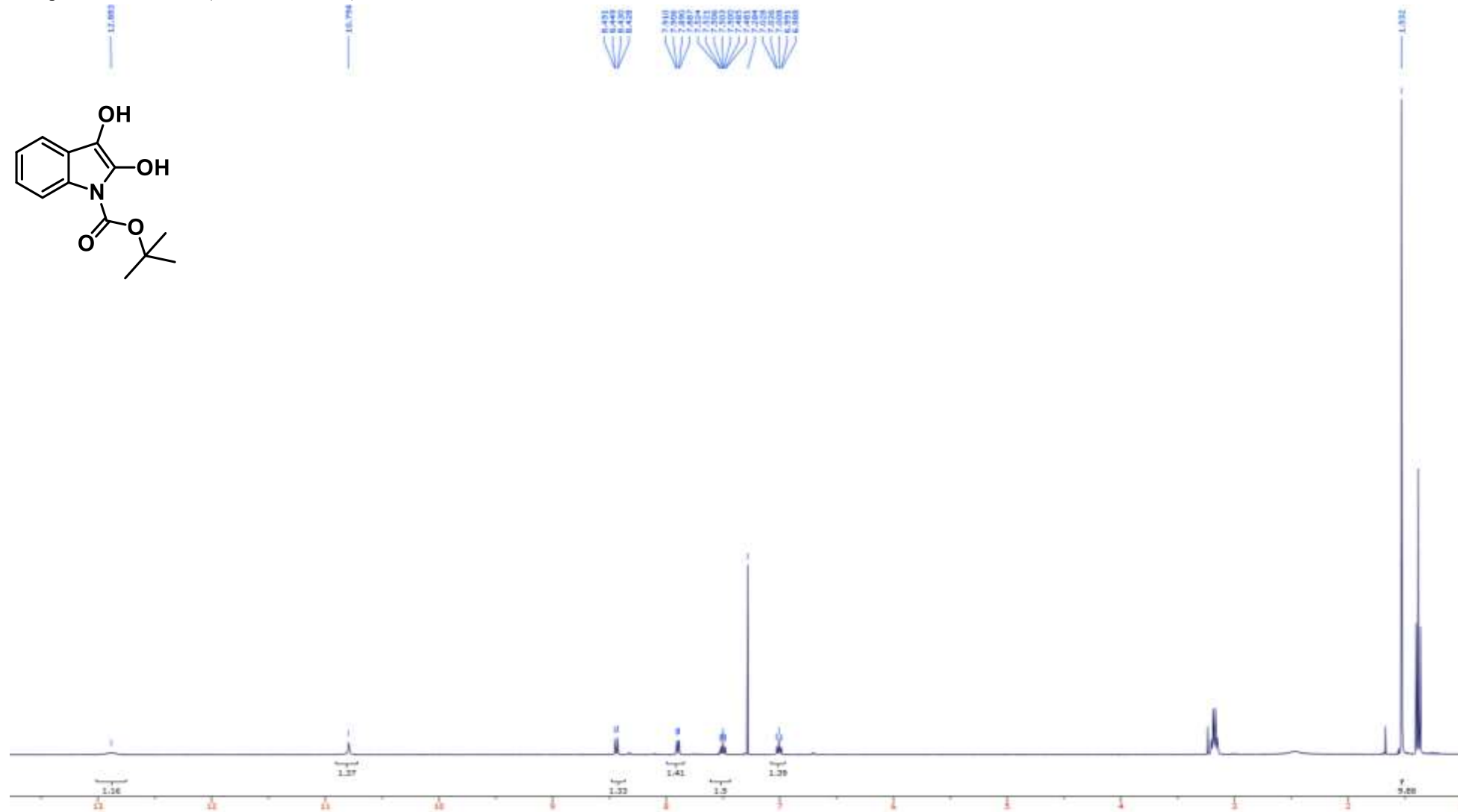
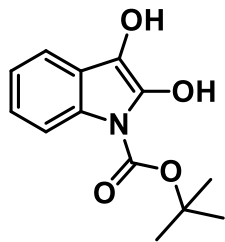
Compound **22** ^{13}C NMR (100 MHz, CDCl_3)



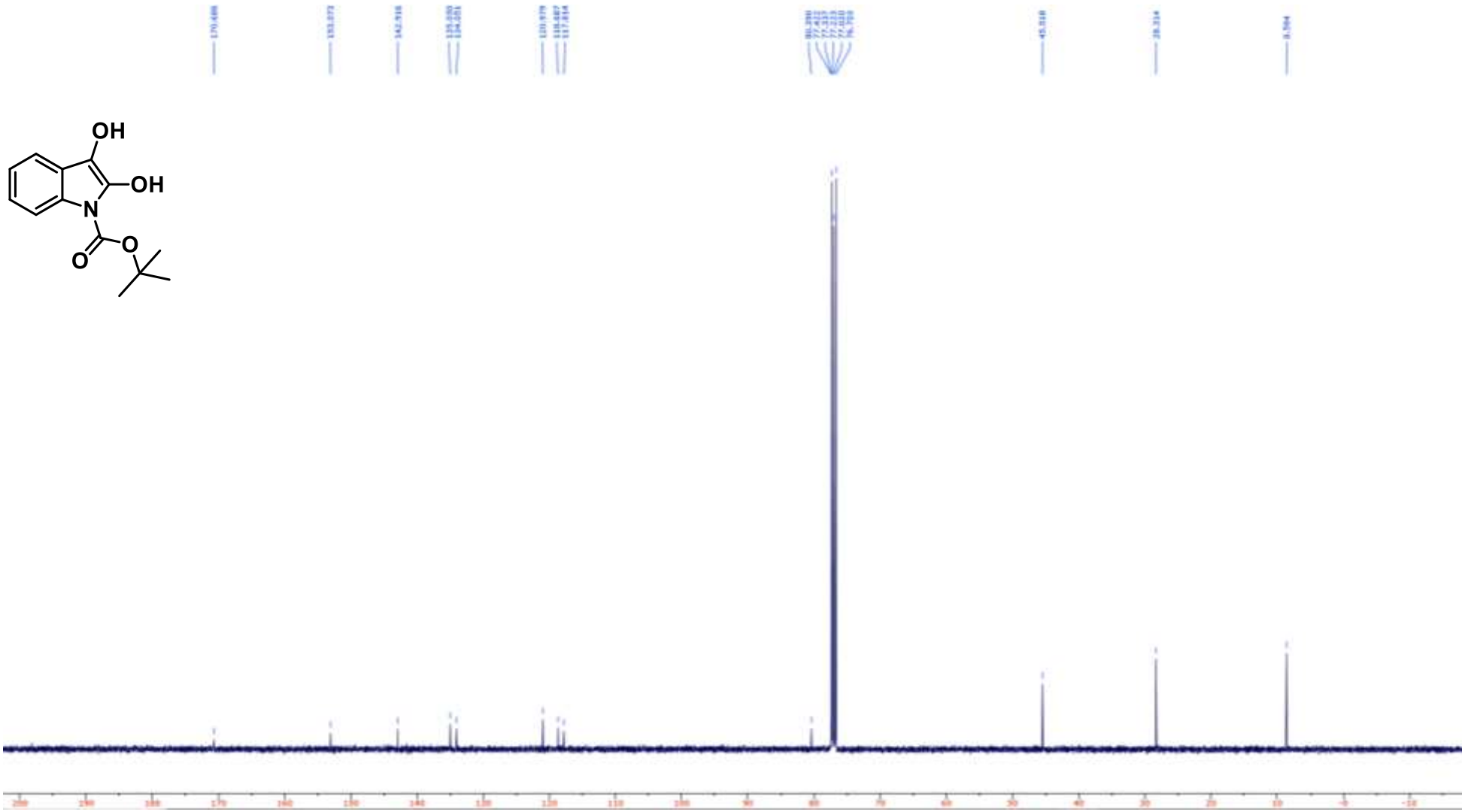
Compound **23** ^1H NMR (400 MHz, CDCl_3)



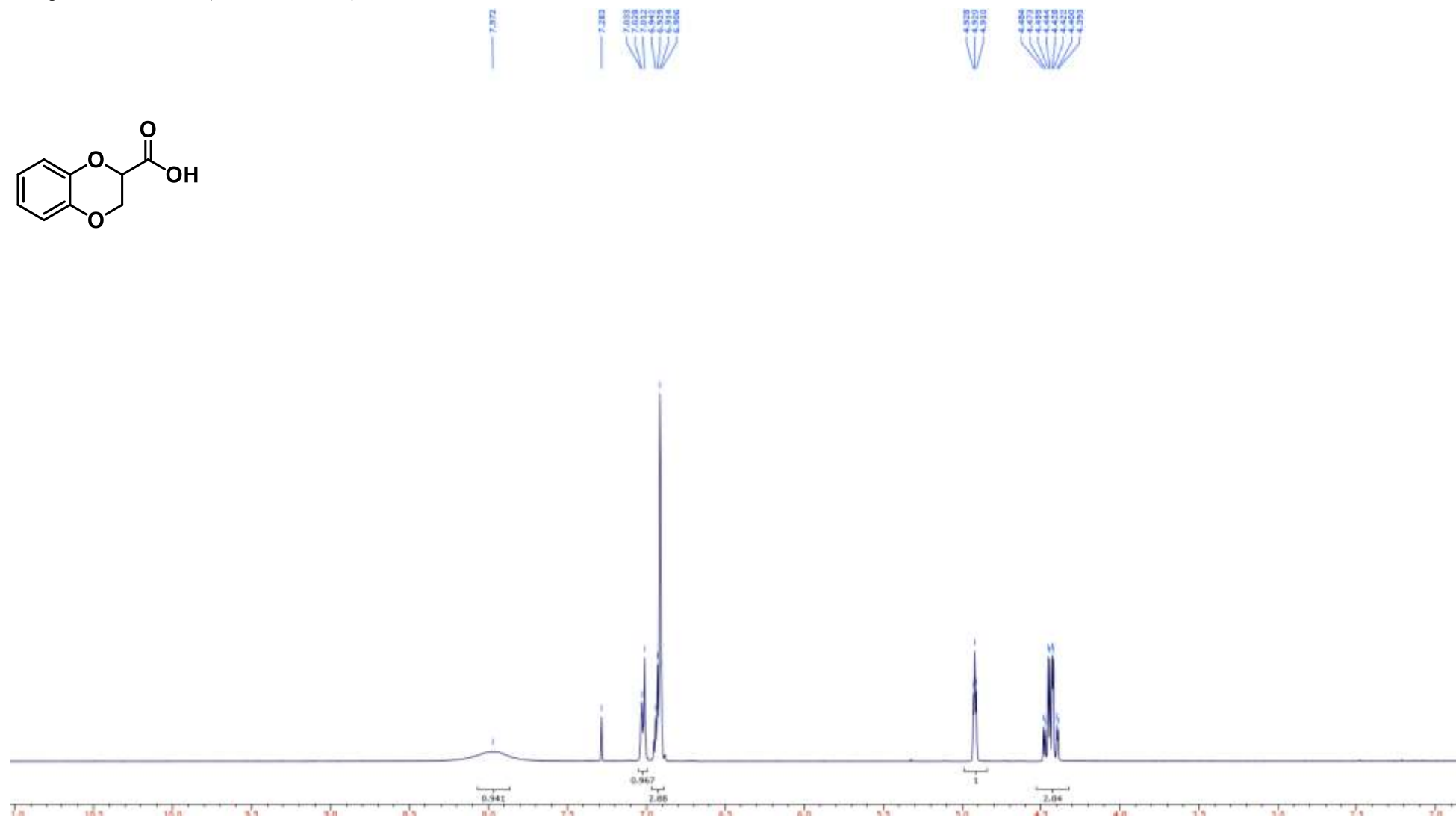
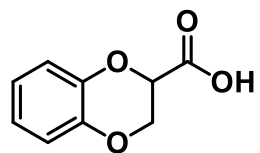
Compound **24** ^1H NMR (400 MHz, CDCl_3)



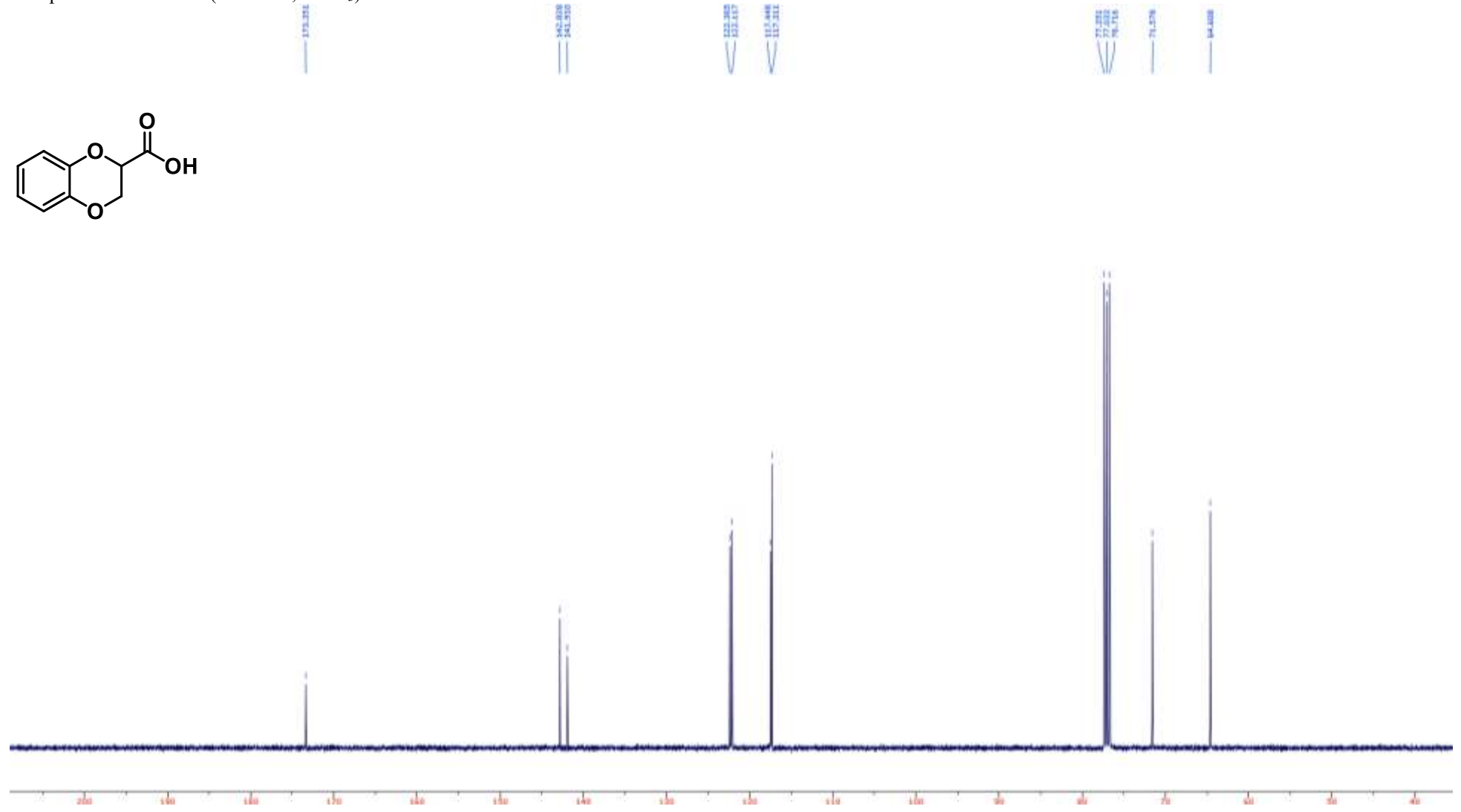
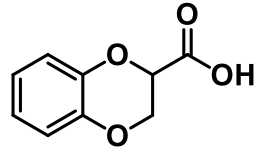
Compound **24** ^{13}C NMR (100 MHz, CDCl_3)



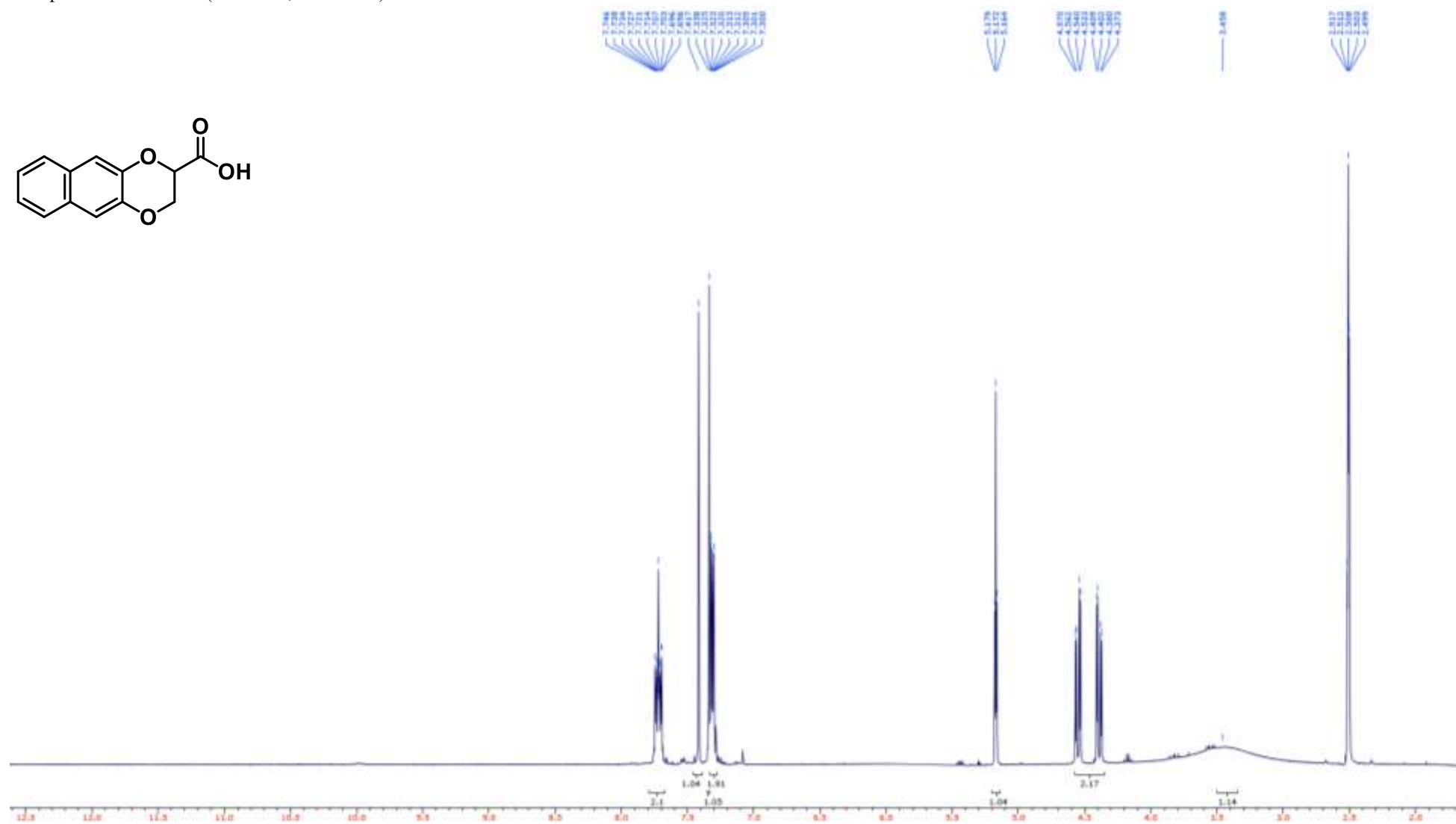
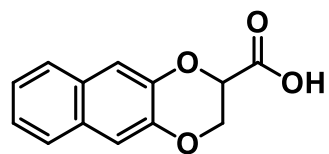
Compound **25** ^1H NMR (400 MHz, CDCl_3)



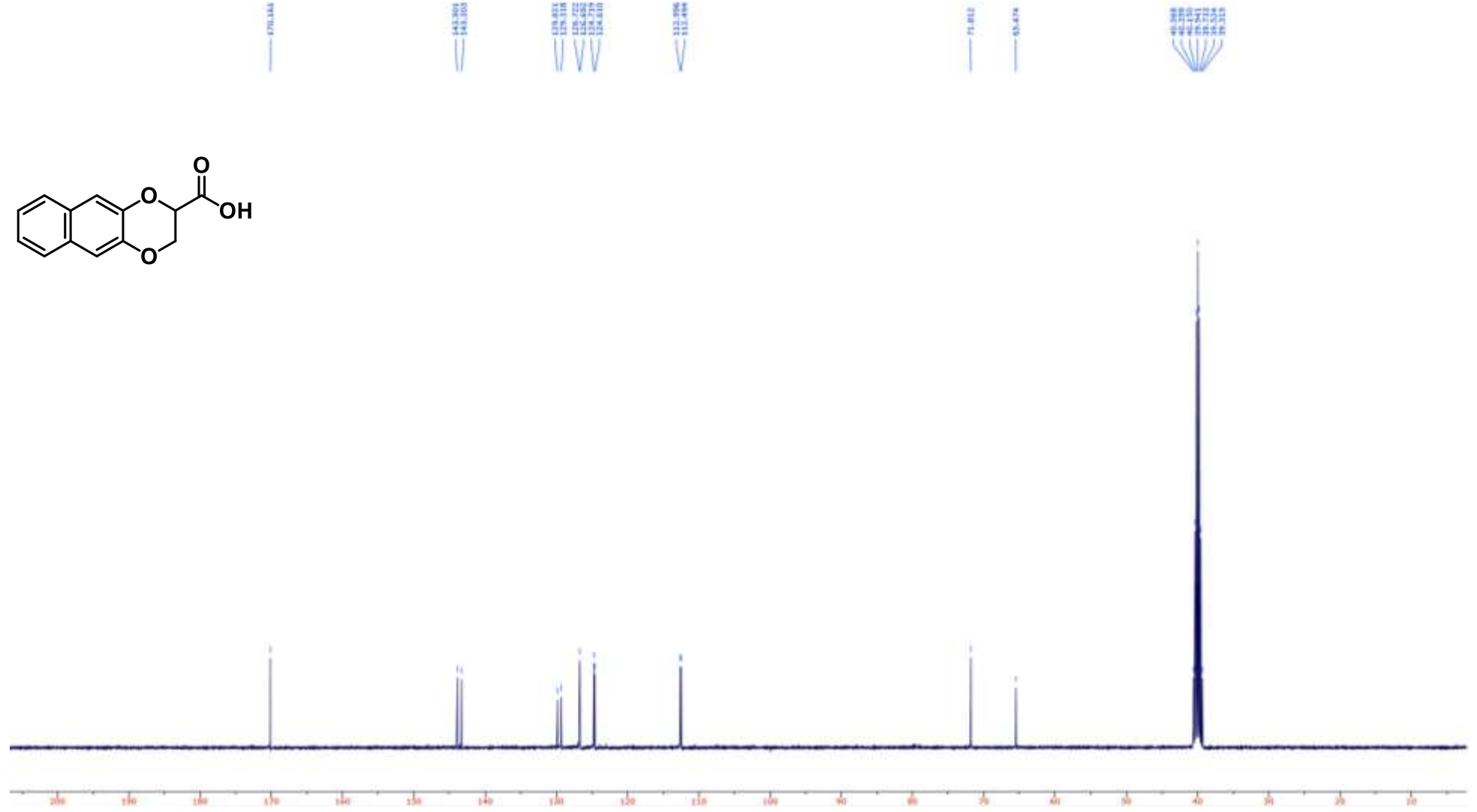
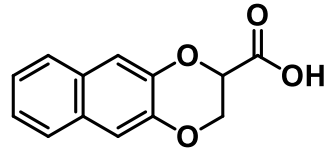
Compound **25** ^{13}C NMR (100 MHz, CDCl_3)



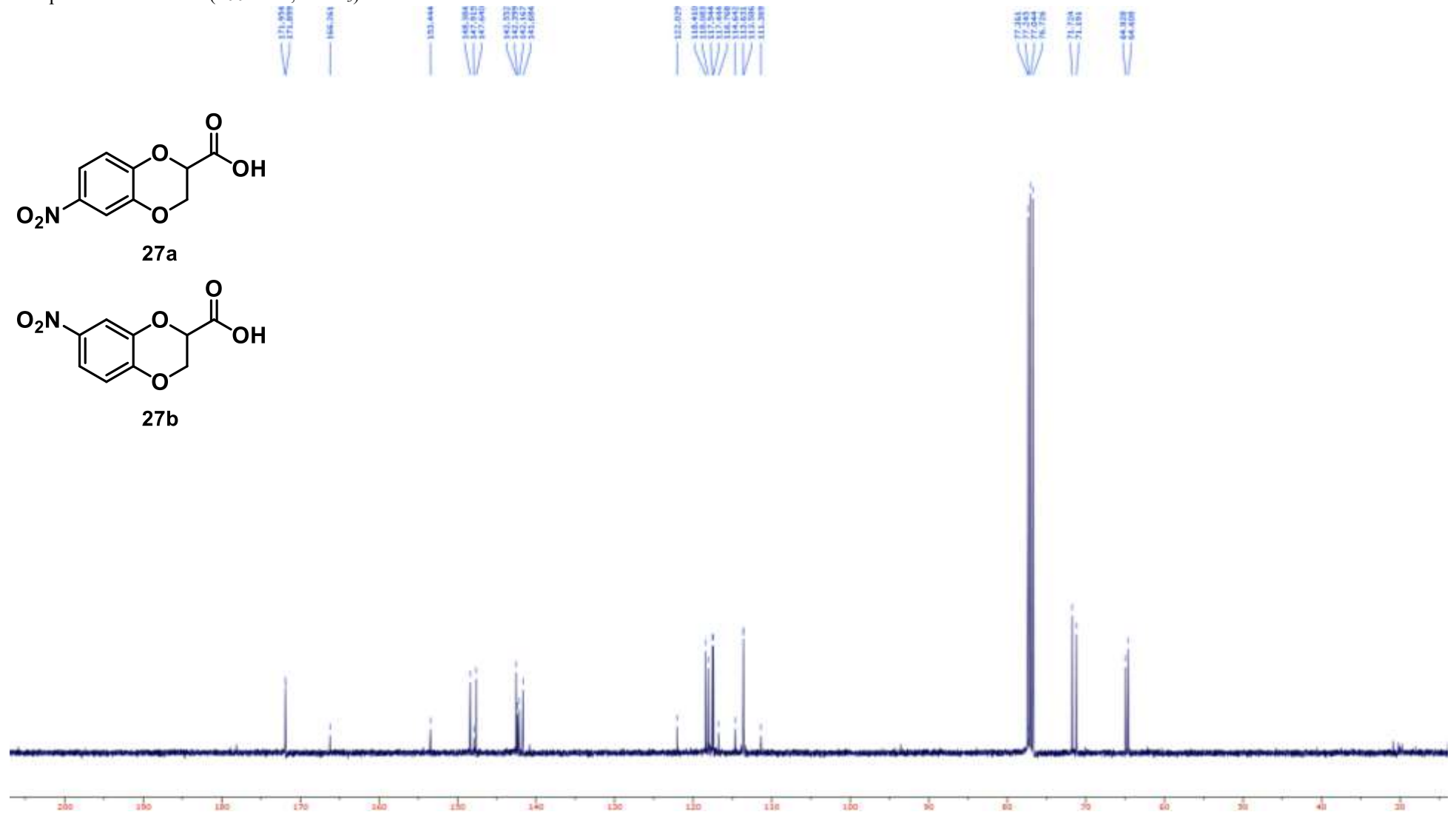
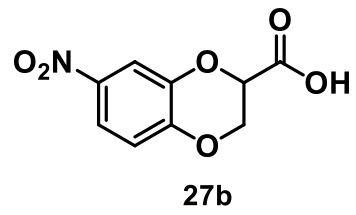
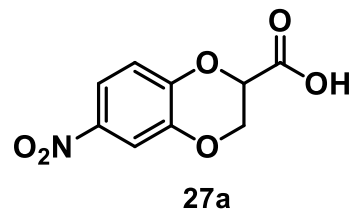
Compound **26** ^1H NMR (400 MHz, d_6 -DMSO)



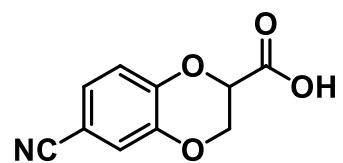
Compound **26** ^{13}C NMR (100 MHz, d_6 -DMSO)



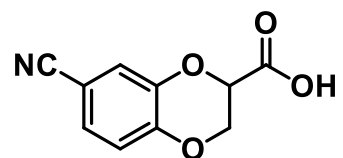
Compound 27 ¹³C NMR (100 MHz, CDCl₃)



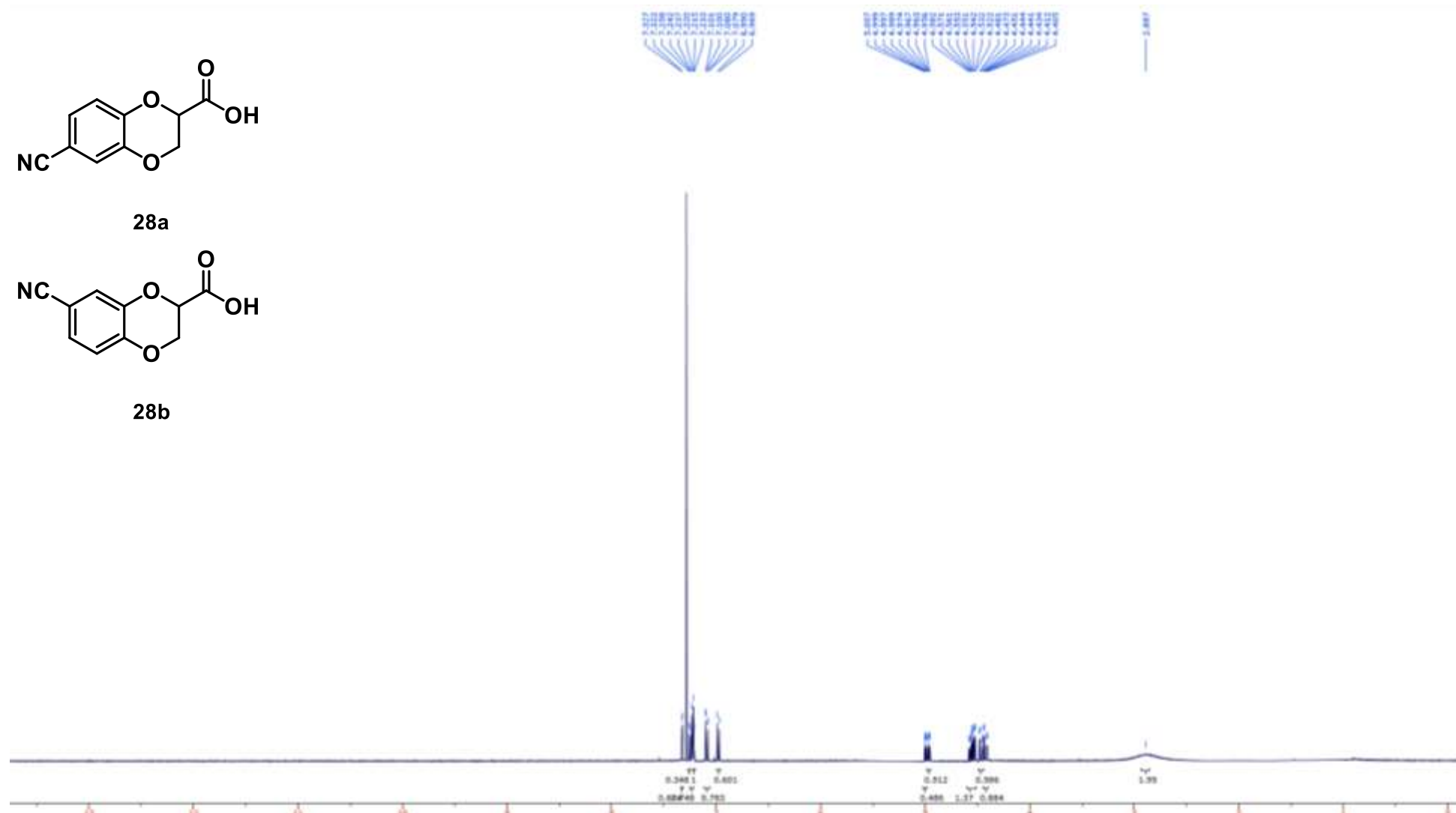
Compound **28** ^1H NMR (400 MHz, CDCl_3)



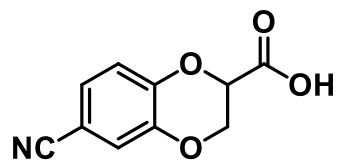
28a



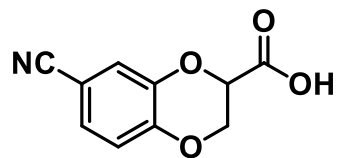
28b



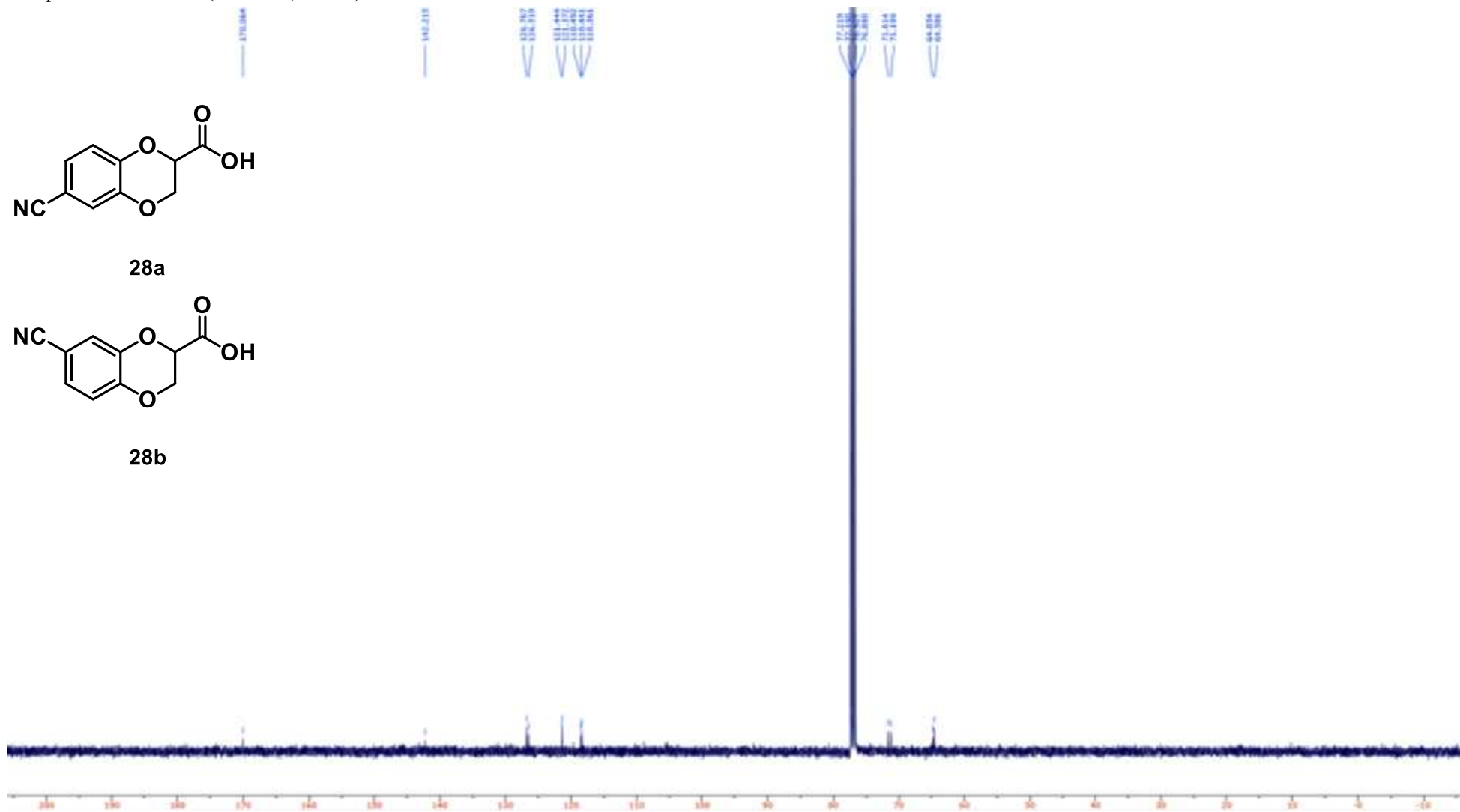
Compound **28** ^{13}C NMR (100 MHz, CDCl_3)



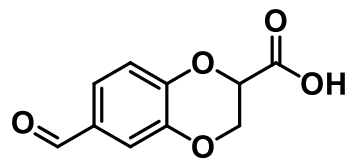
28a



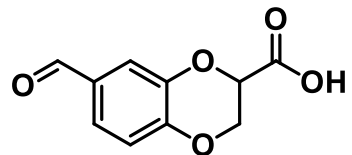
28b



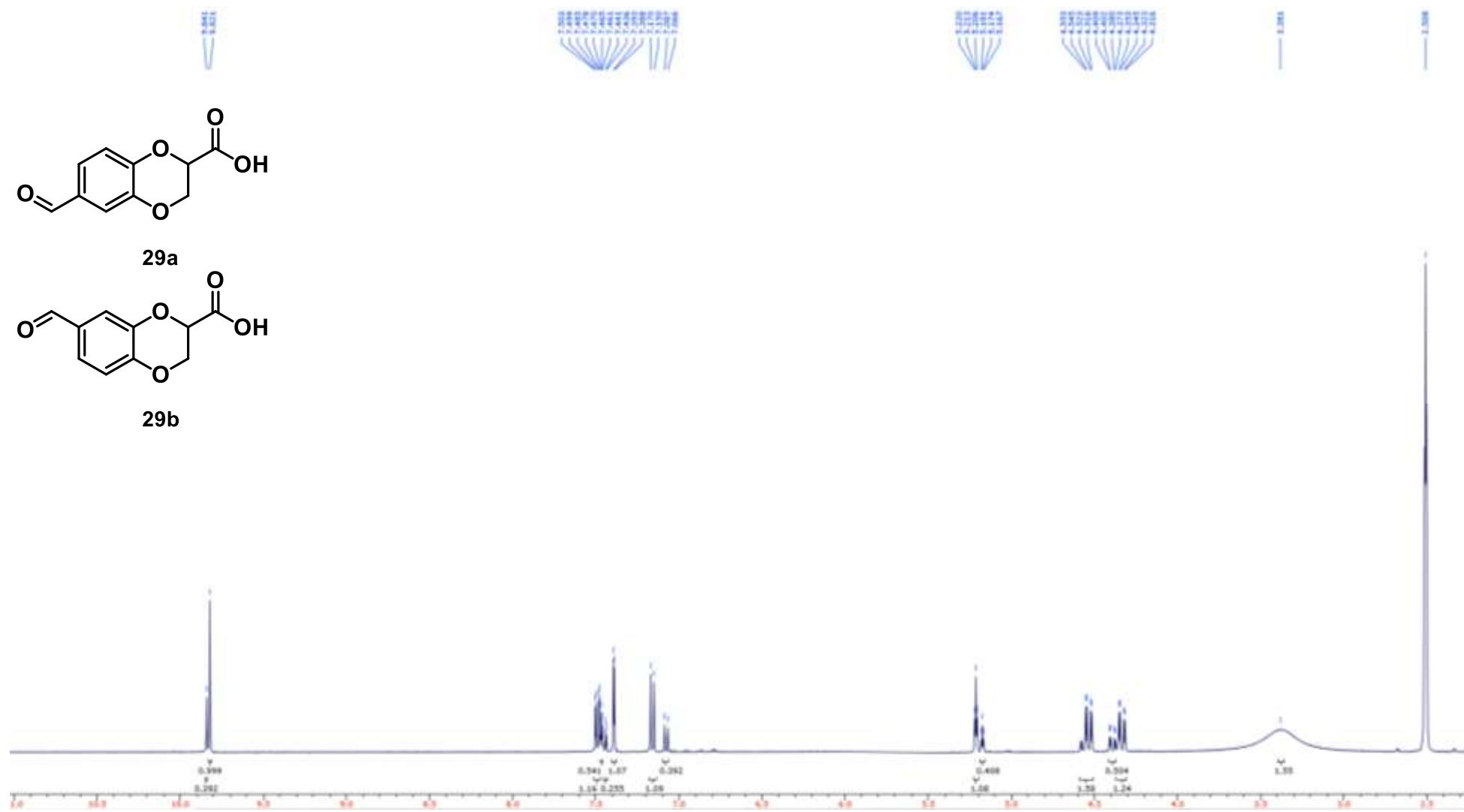
Compound **29** ^1H NMR (400 MHz, d_6 -DMSO)



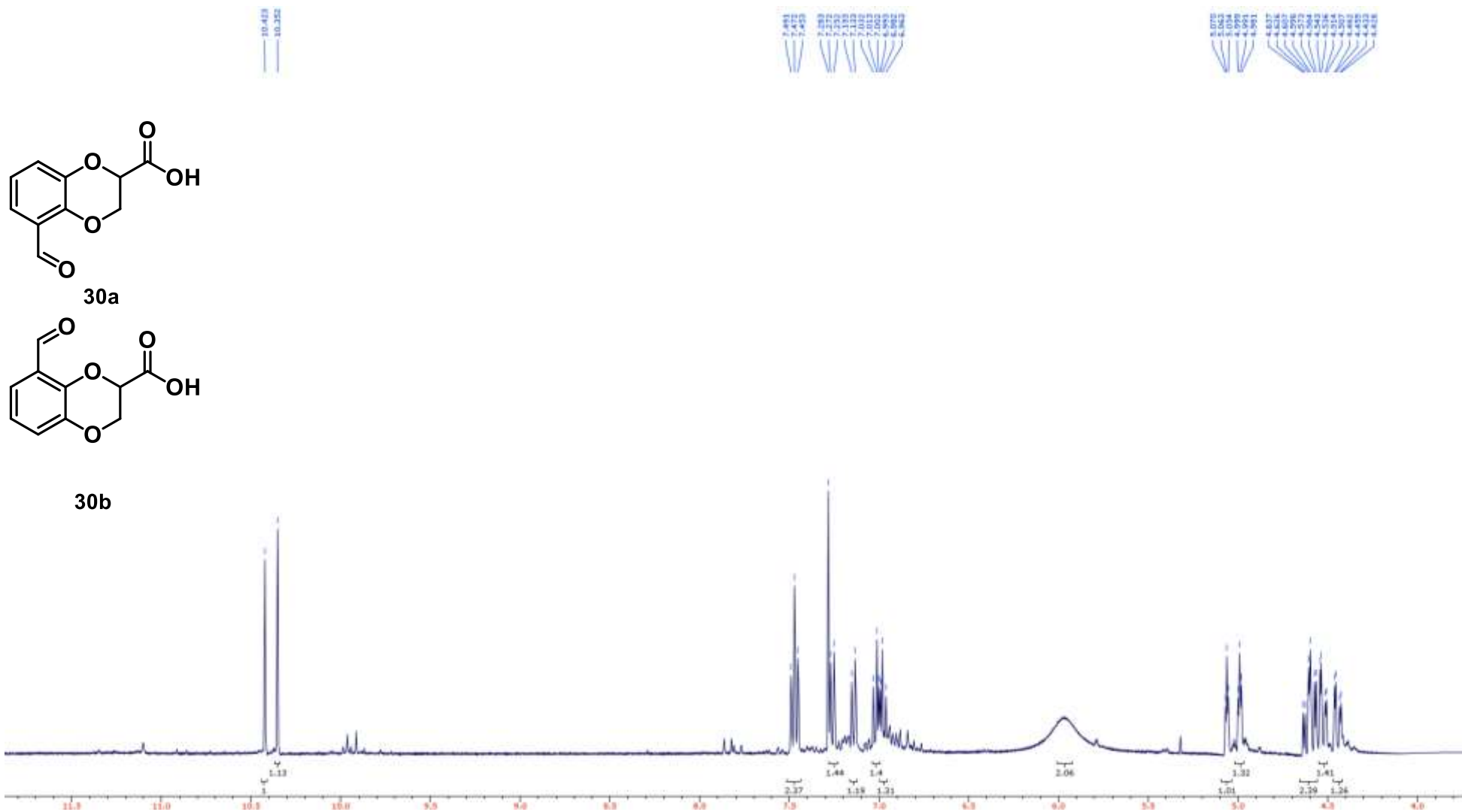
29a



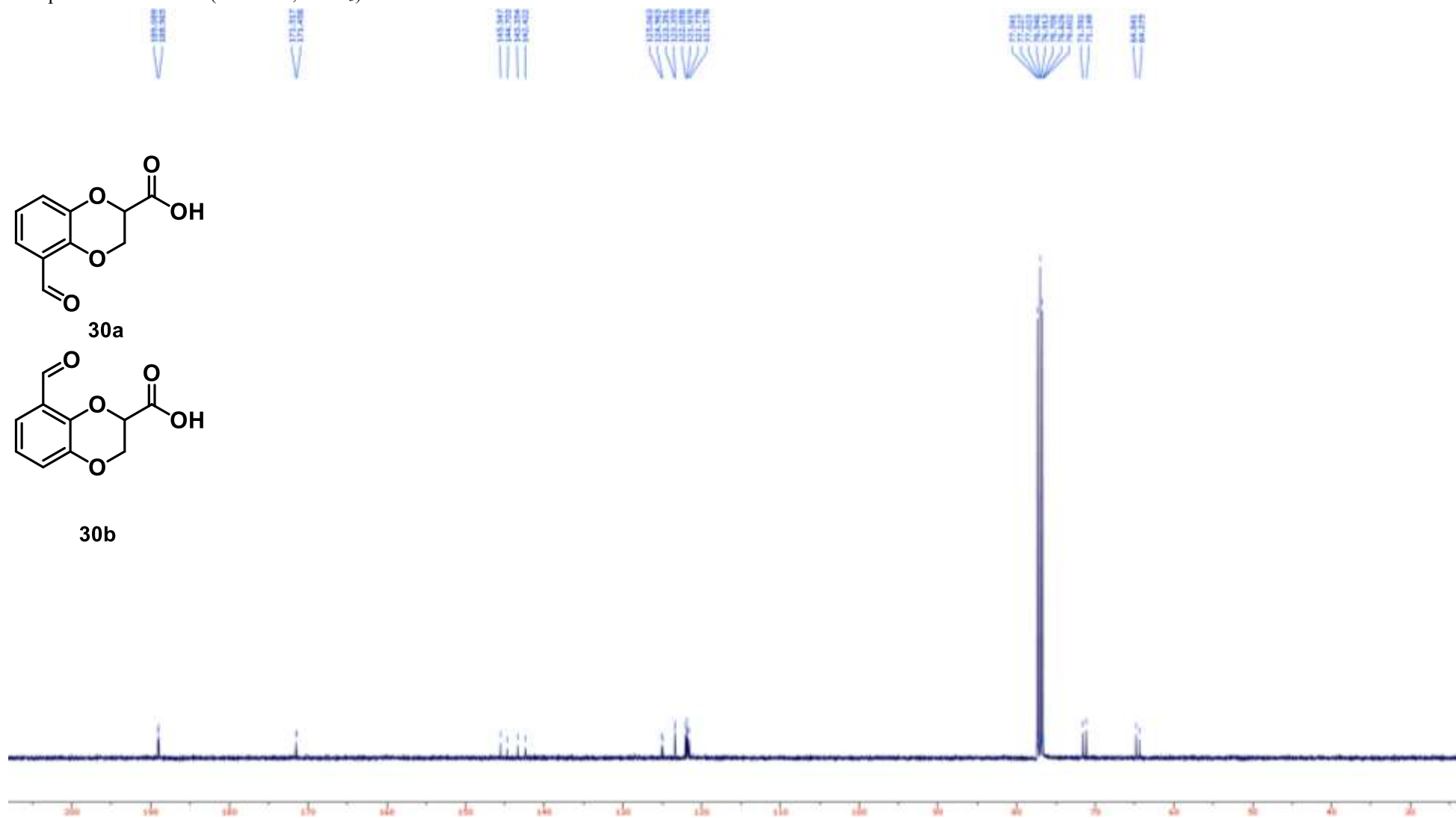
29b



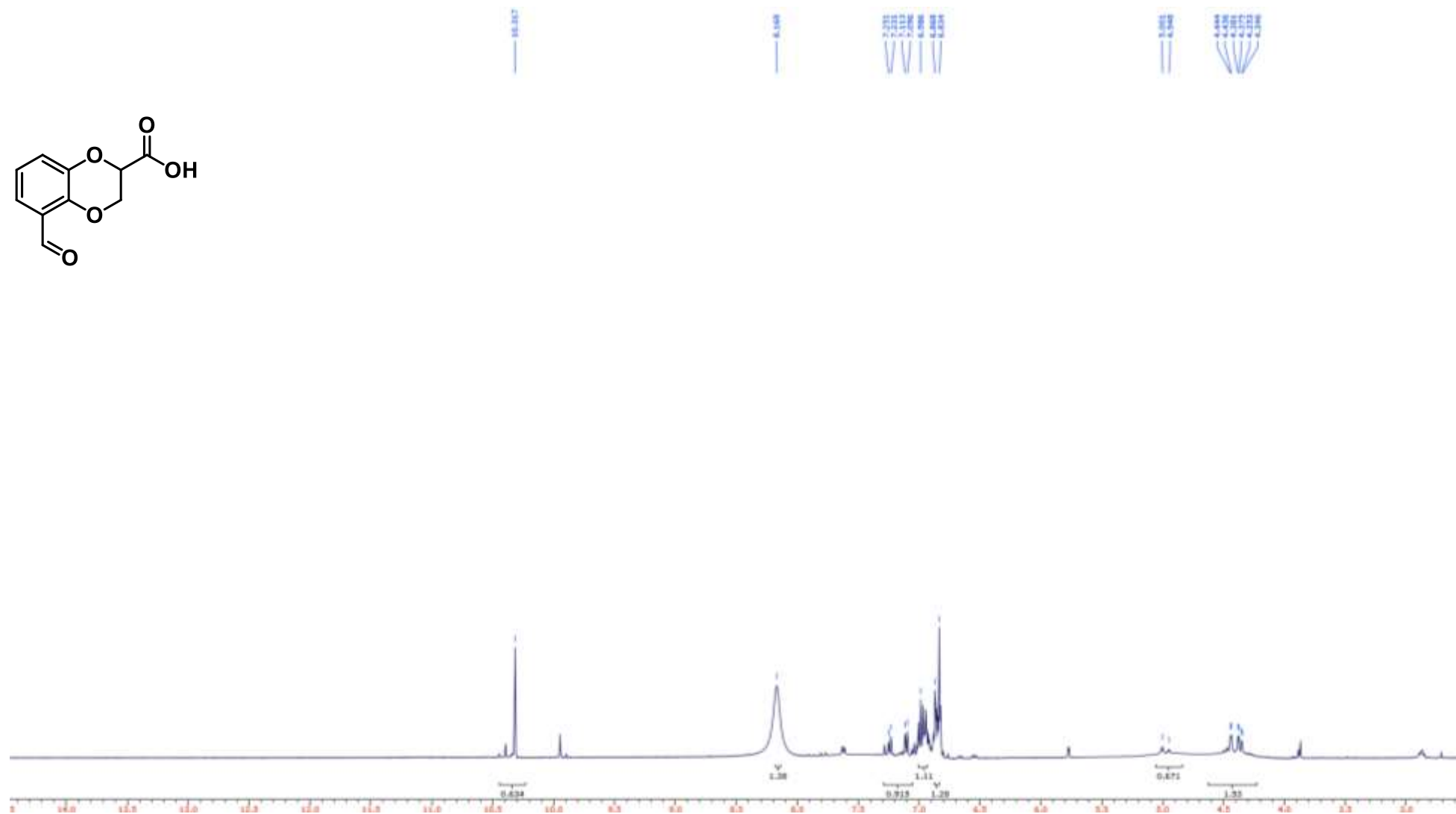
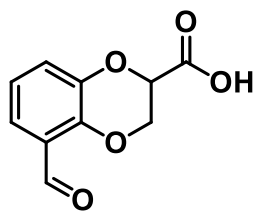
Compound **30** ^1H NMR (400 MHz, CDCl_3)



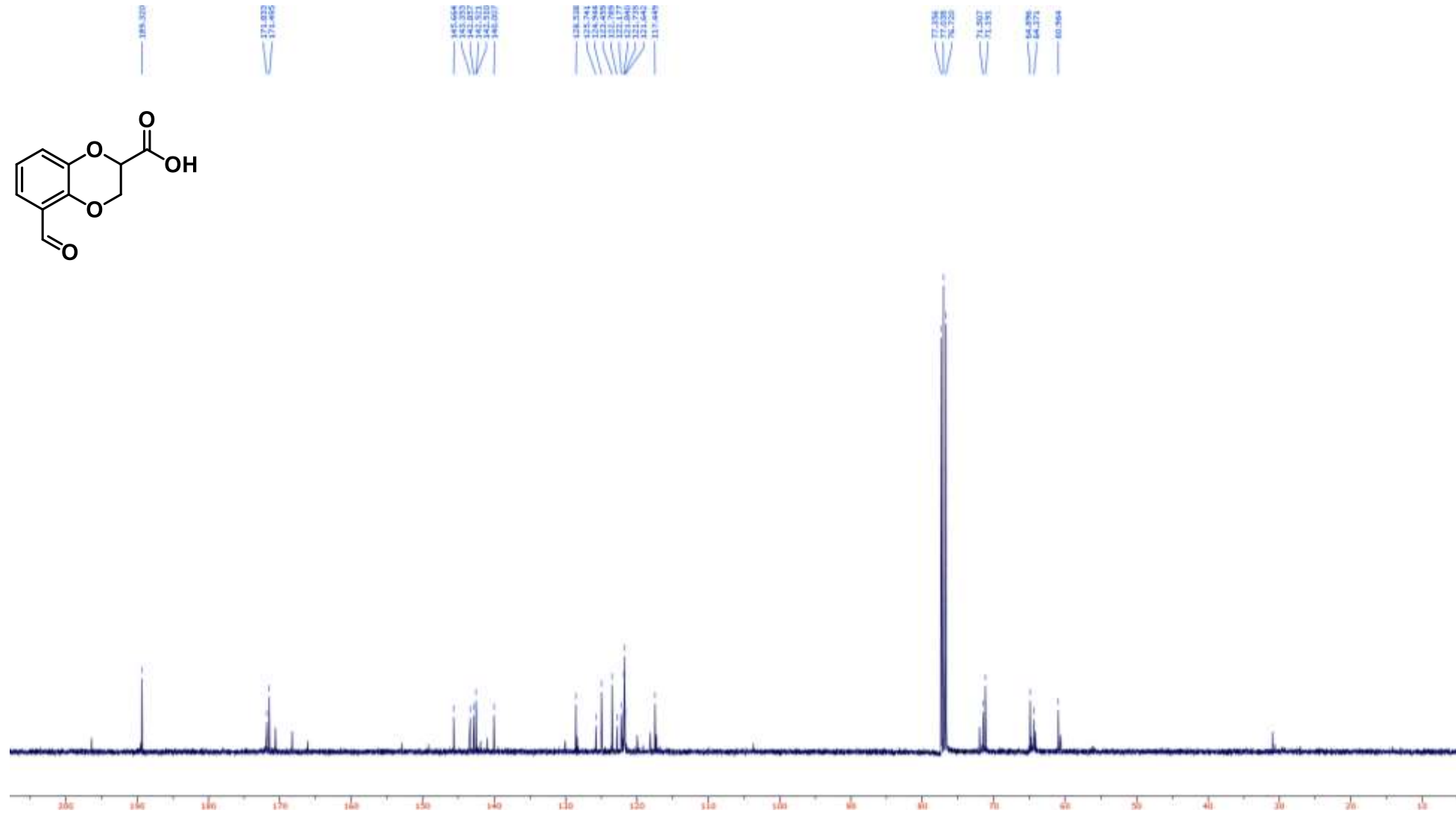
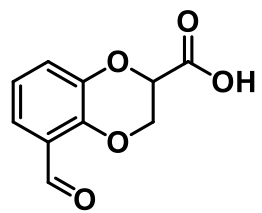
Compound **30** ^{13}C NMR (100 MHz, CDCl_3)



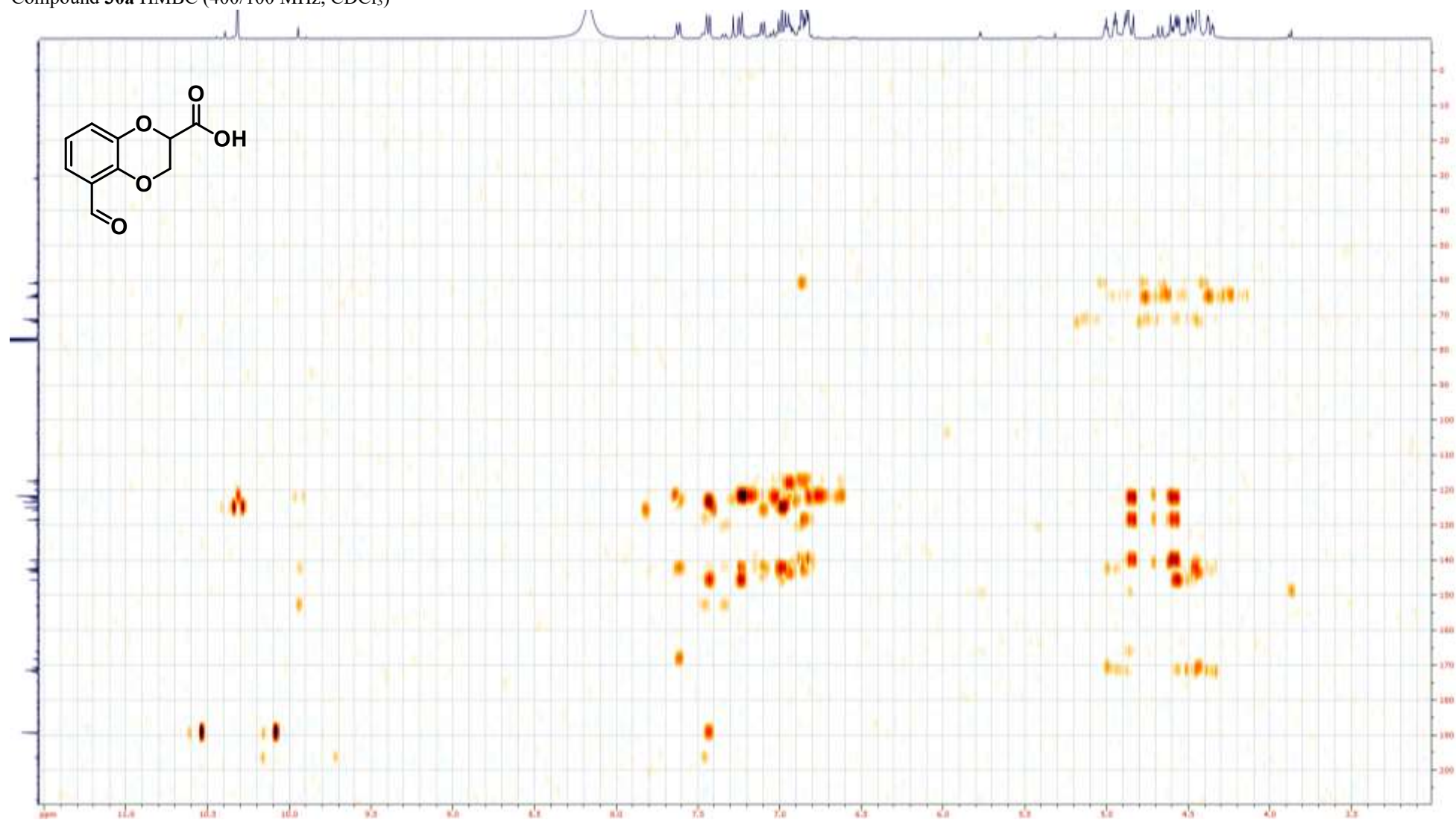
Compound **30a** ^1H NMR (400 MHz, CDCl_3)



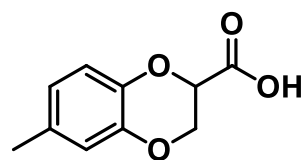
Compound **30a** ^{13}C NMR (100 MHz, CDCl_3)



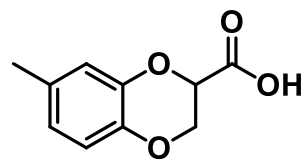
Compound **30a** HMBC (400/100 MHz, CDCl₃)



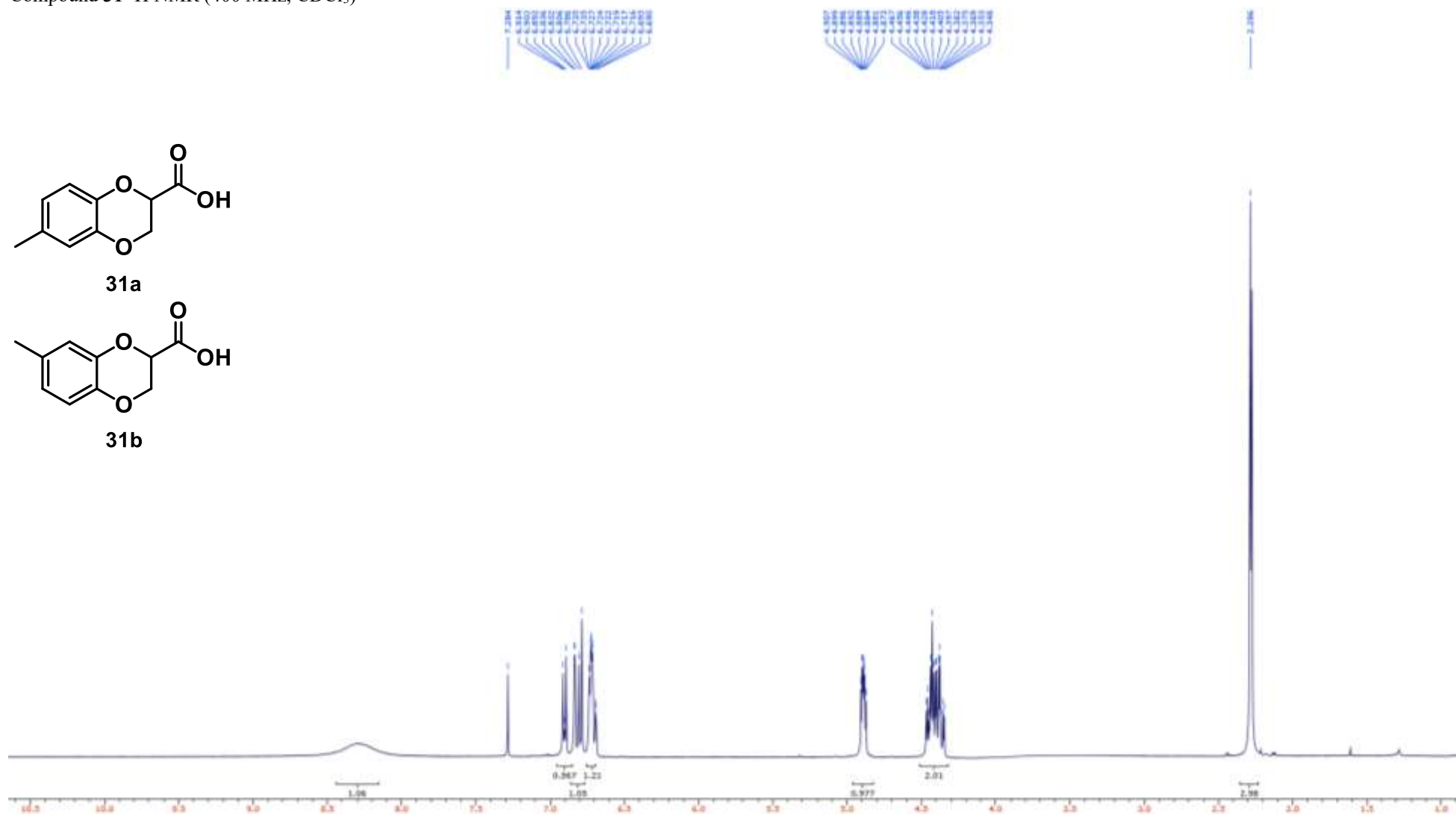
Compound **31** ^1H NMR (400 MHz, CDCl_3)



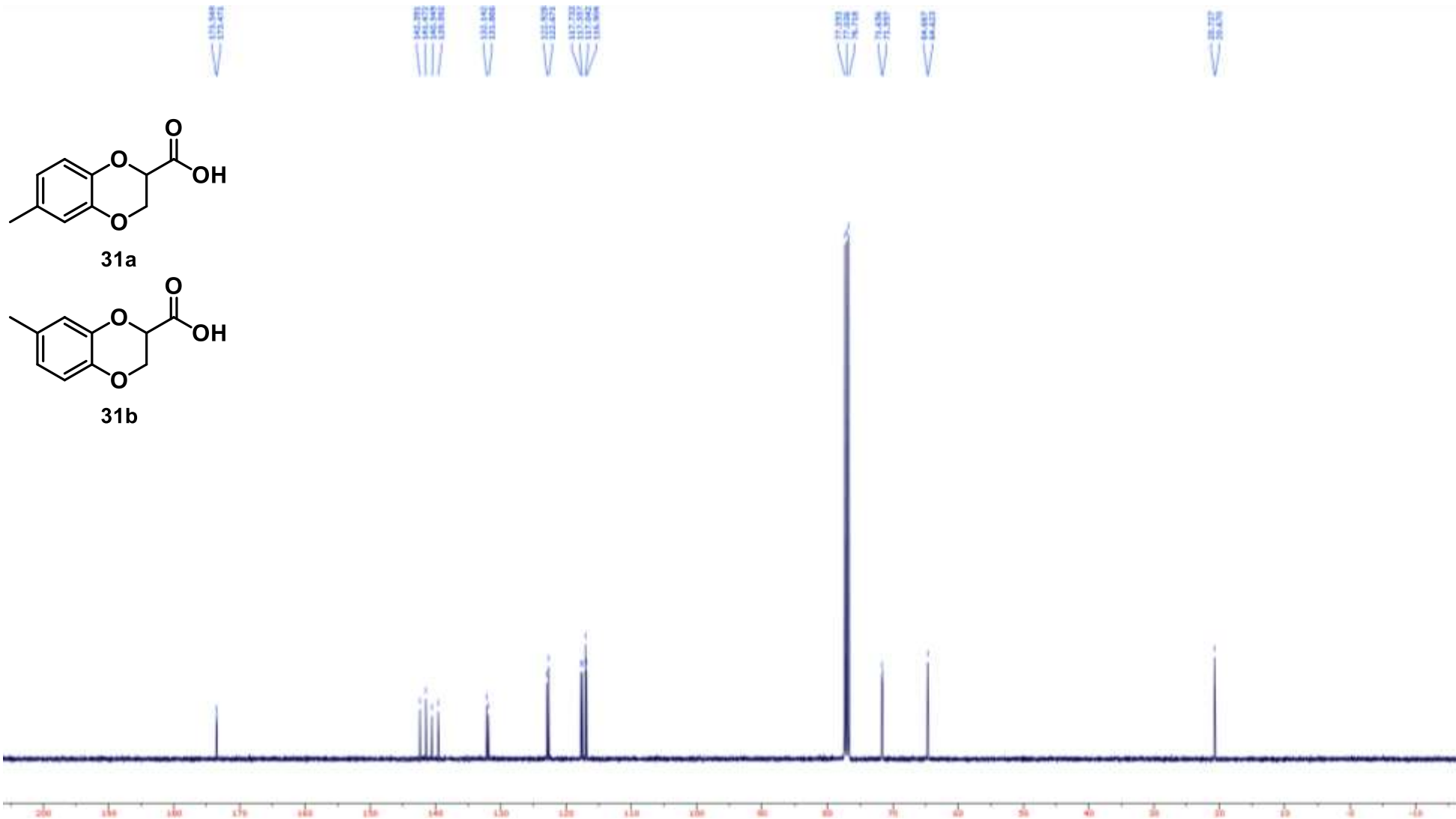
31a



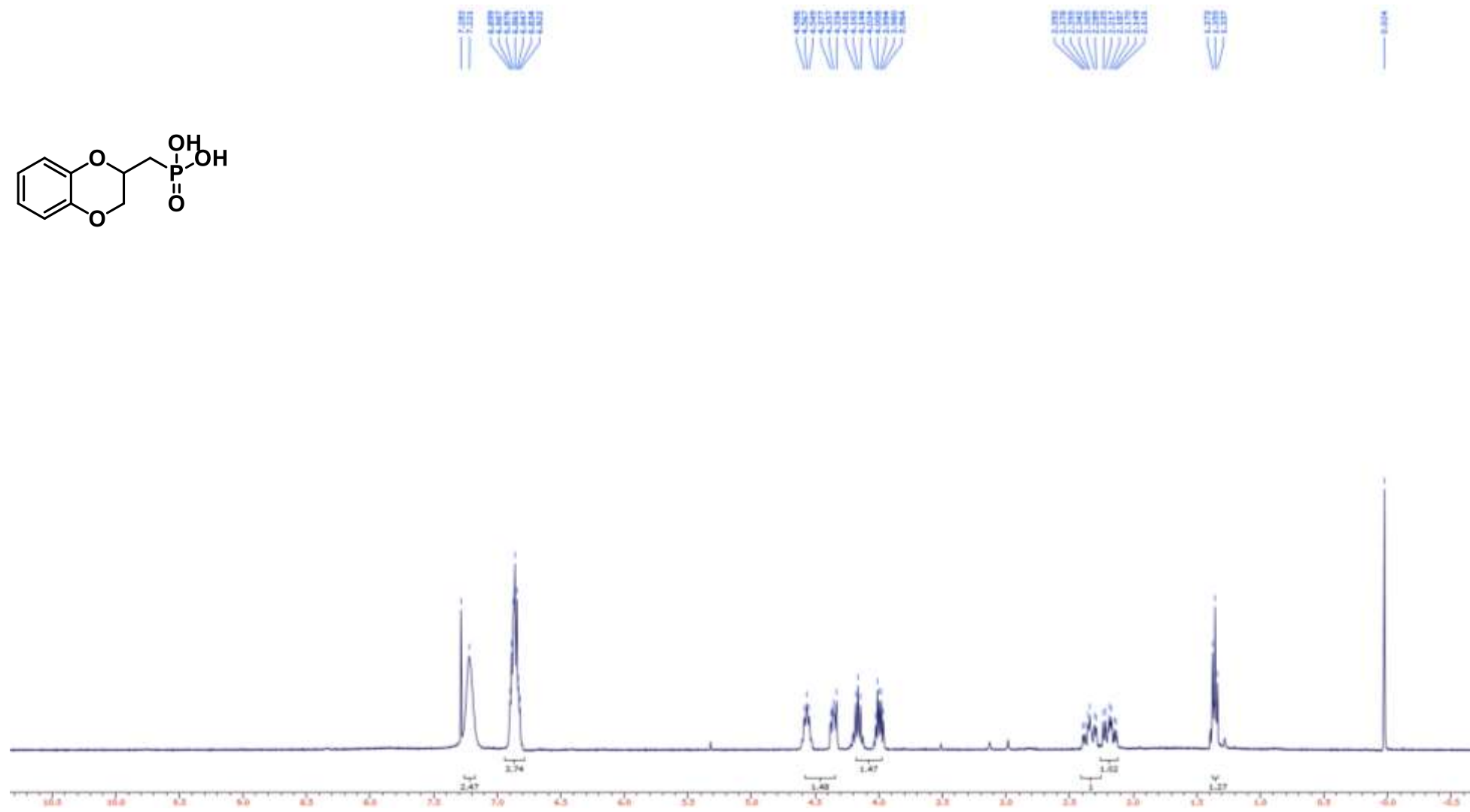
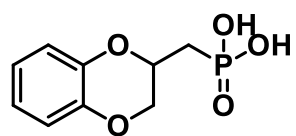
31b



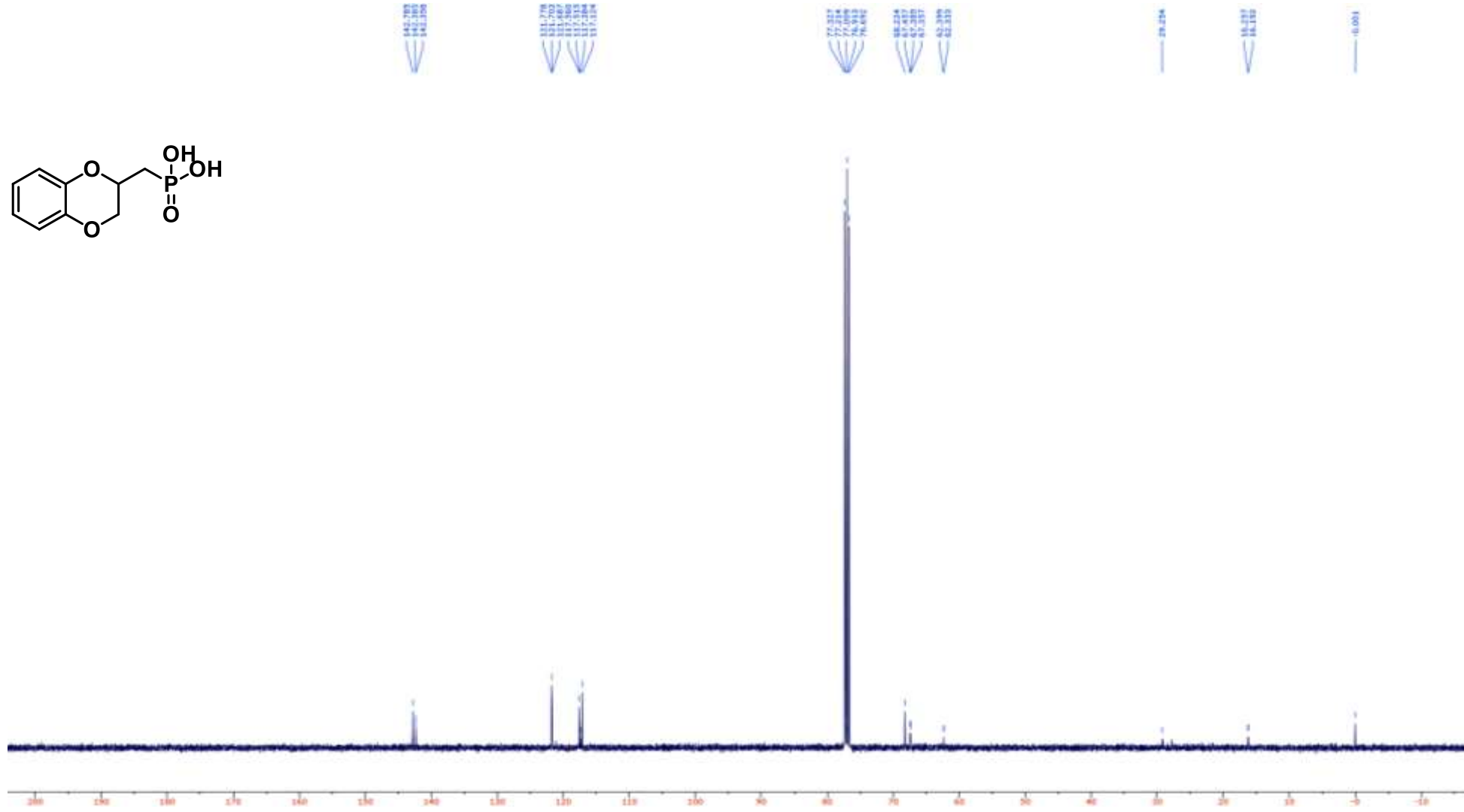
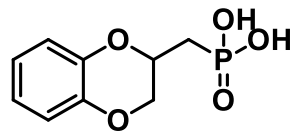
Compound **31** ^{13}C NMR (100 MHz, CDCl_3)



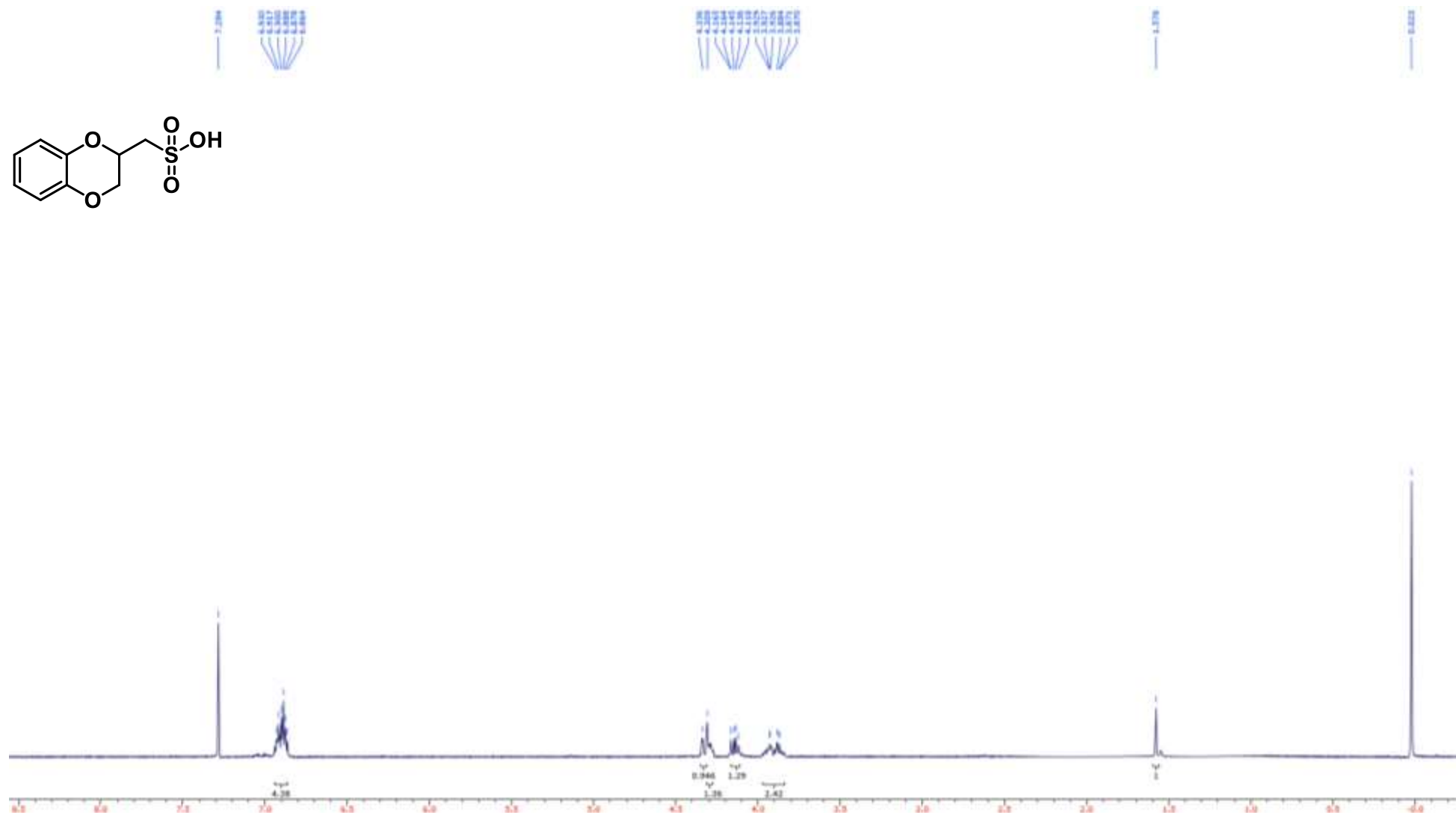
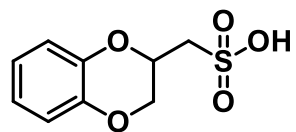
Compound **32** ^1H NMR (400 MHz, CDCl_3)



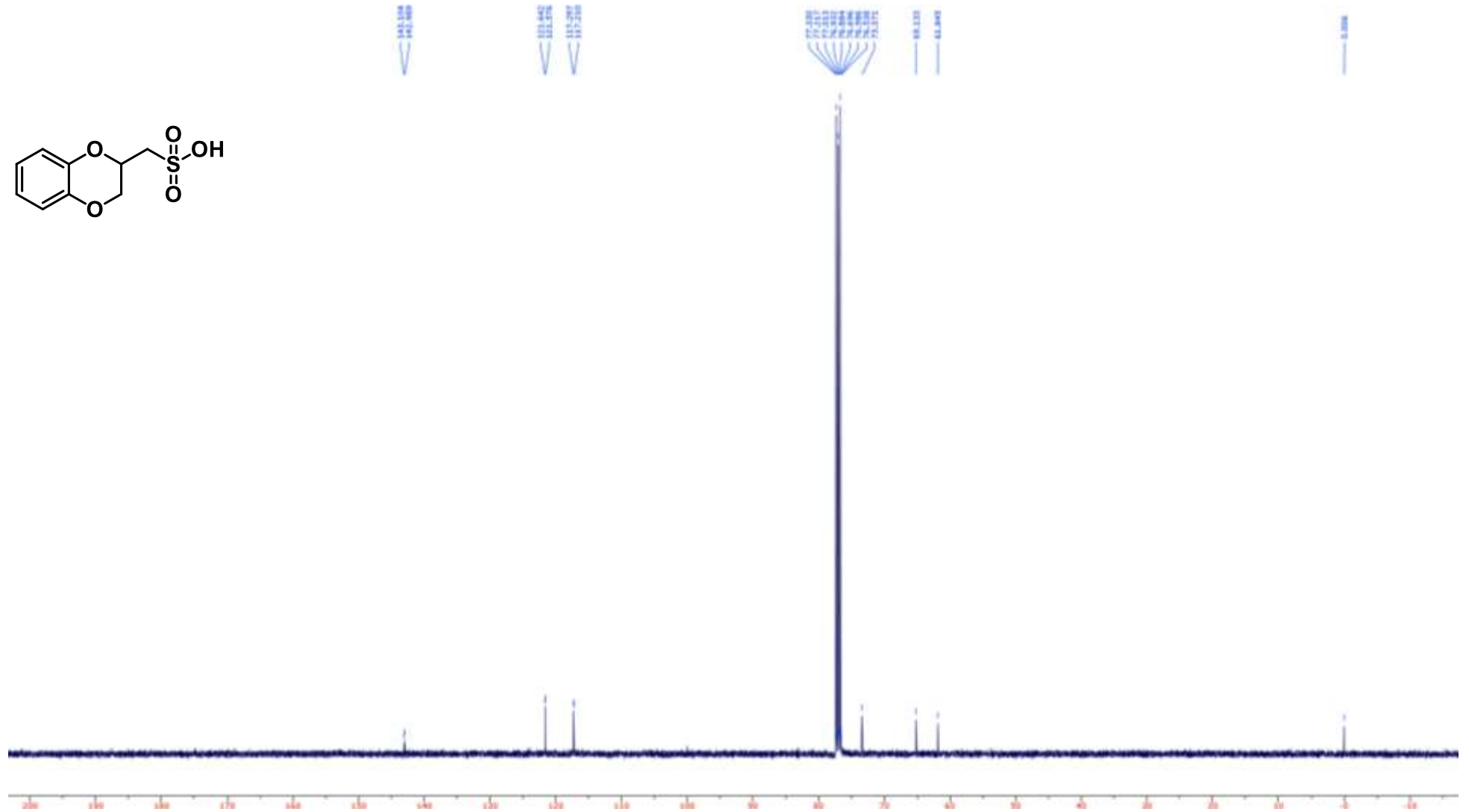
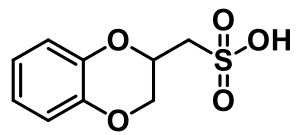
Compound **32** ^{13}C NMR (100 MHz, CDCl_3)



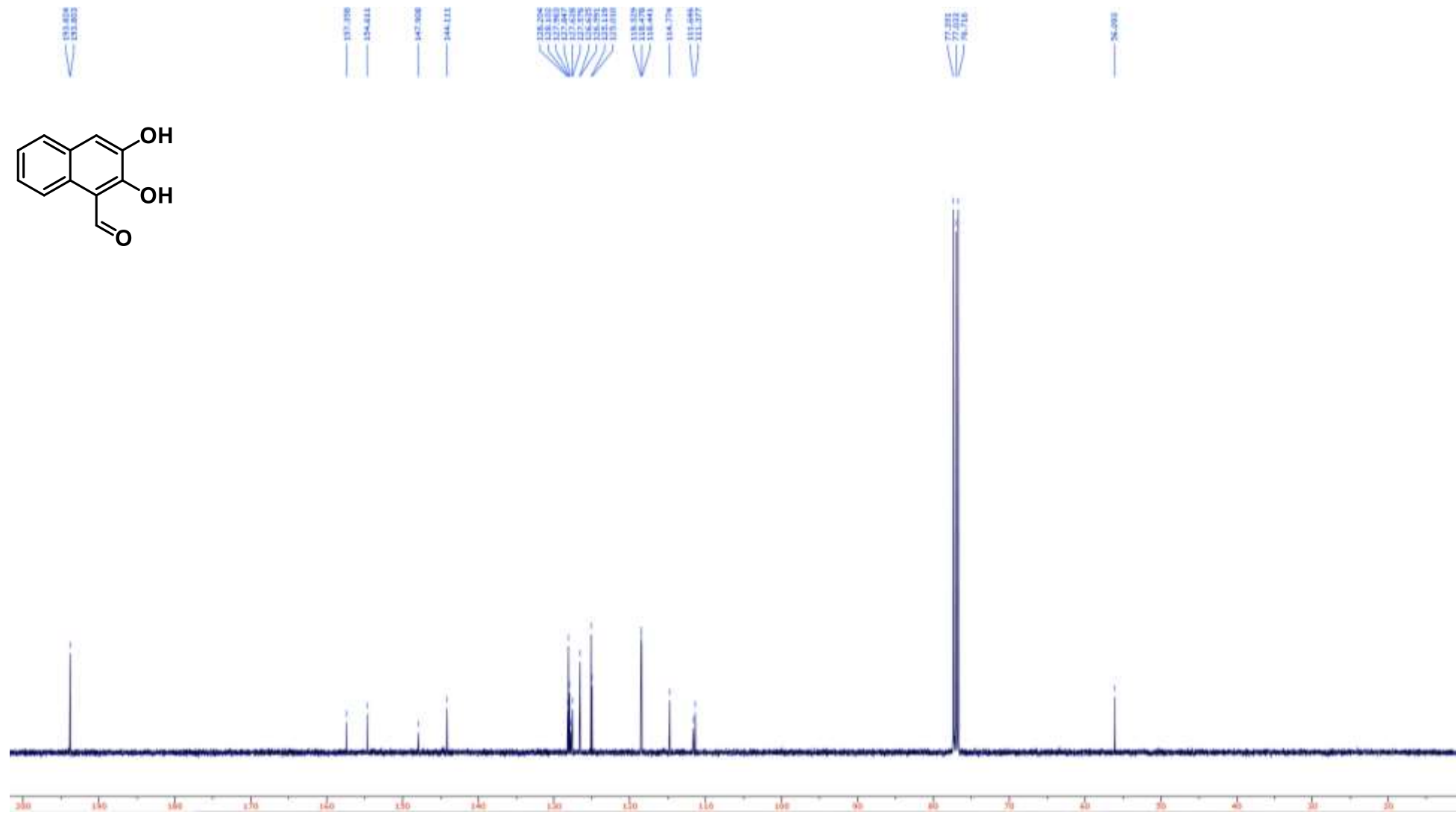
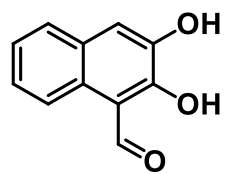
Compound **33** ^1H NMR (400 MHz, CDCl_3)



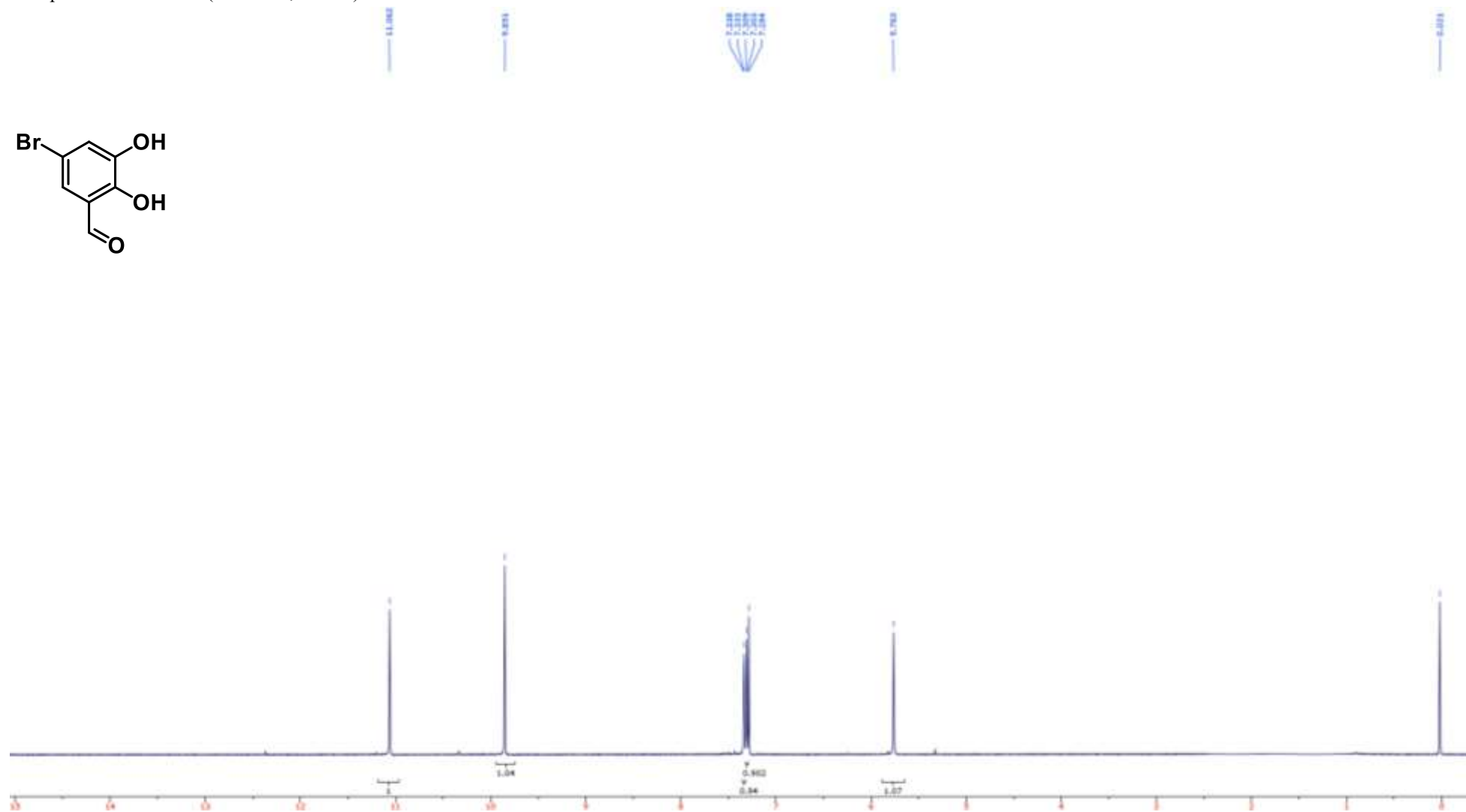
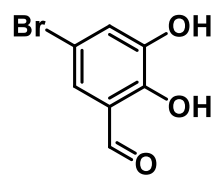
Compound **33** ^{13}C NMR (100 MHz, CDCl_3)



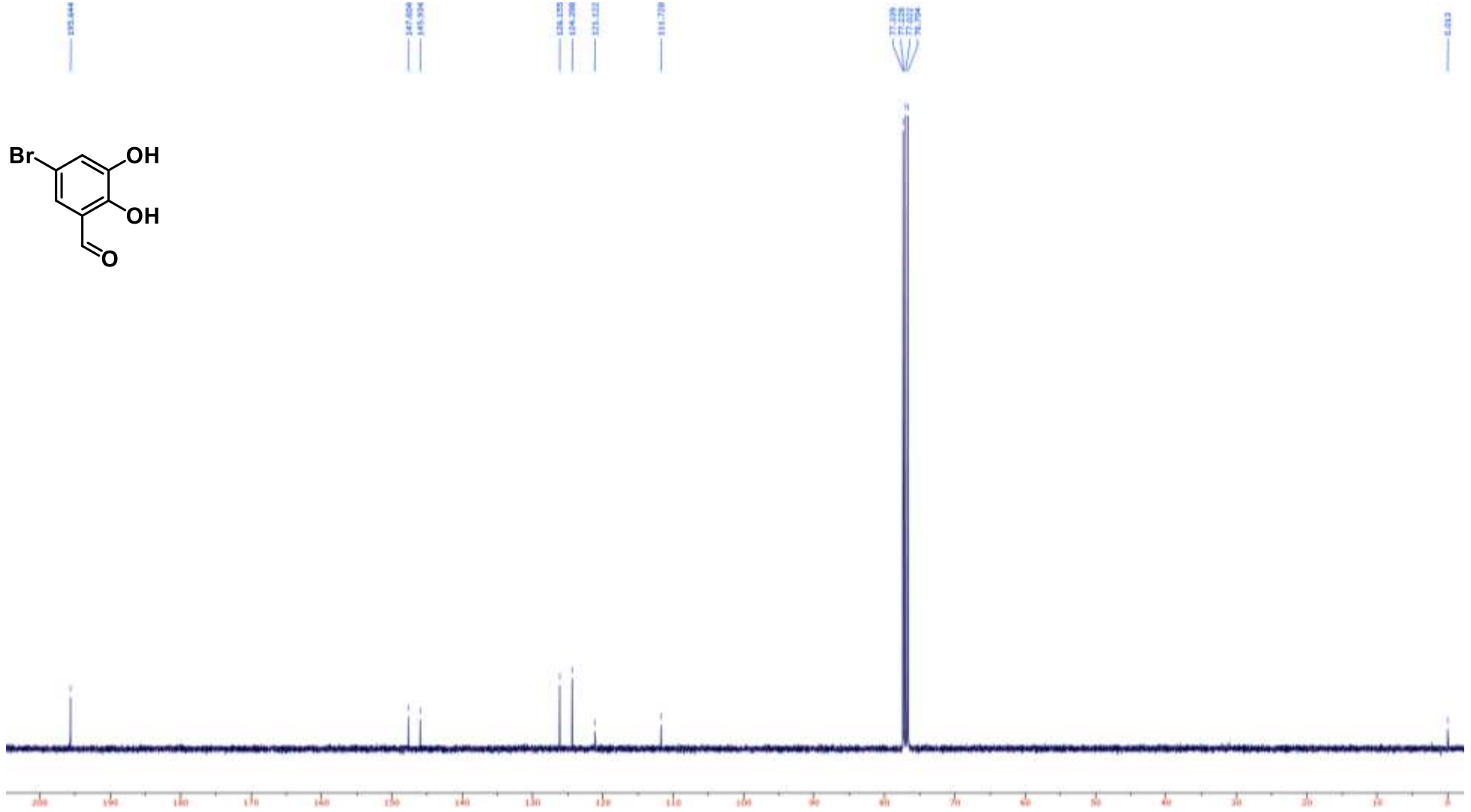
Compound **34** ^{13}C NMR (100 MHz, CDCl_3)



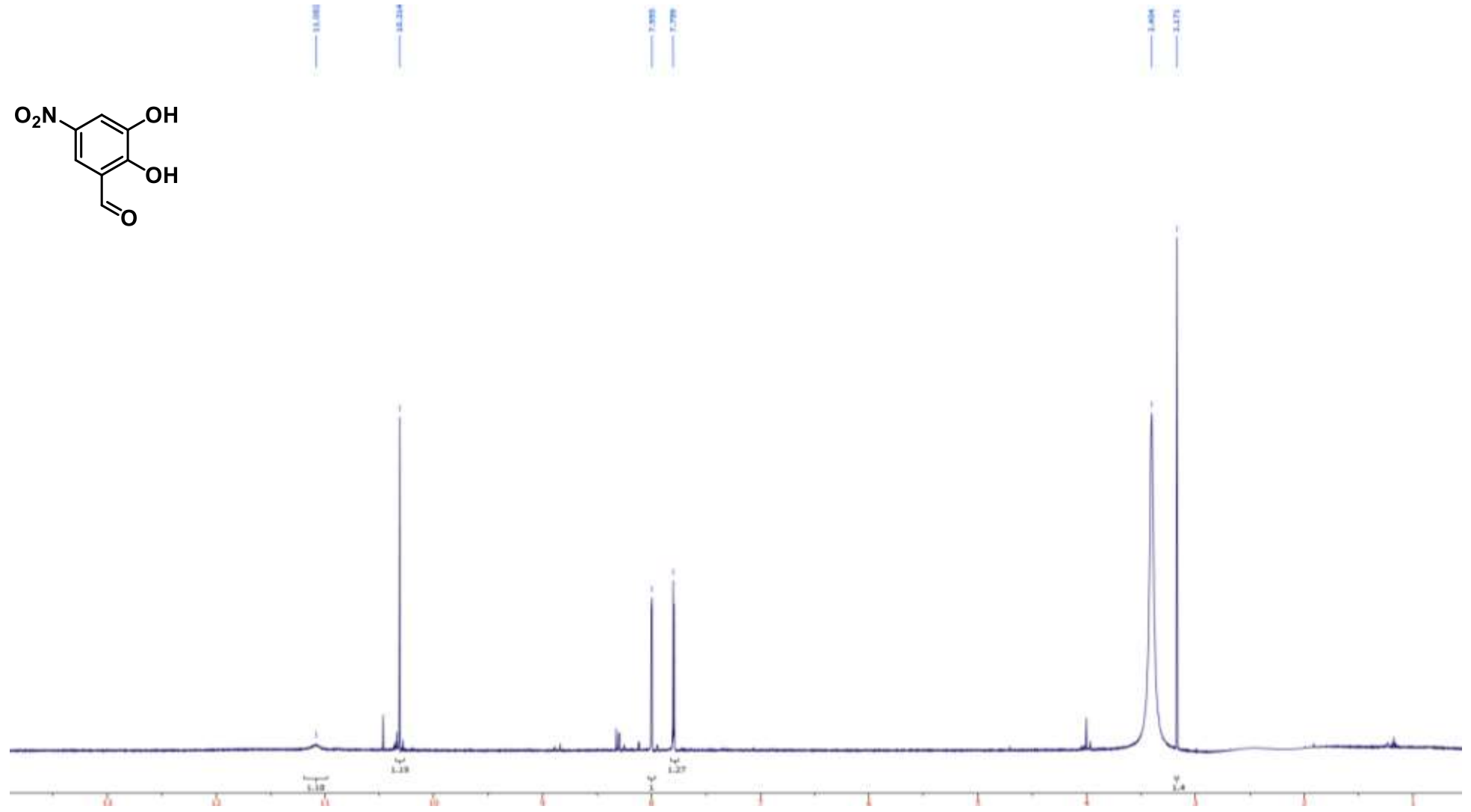
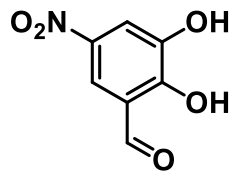
Compound **35** ^1H NMR (400 MHz, CDCl_3)



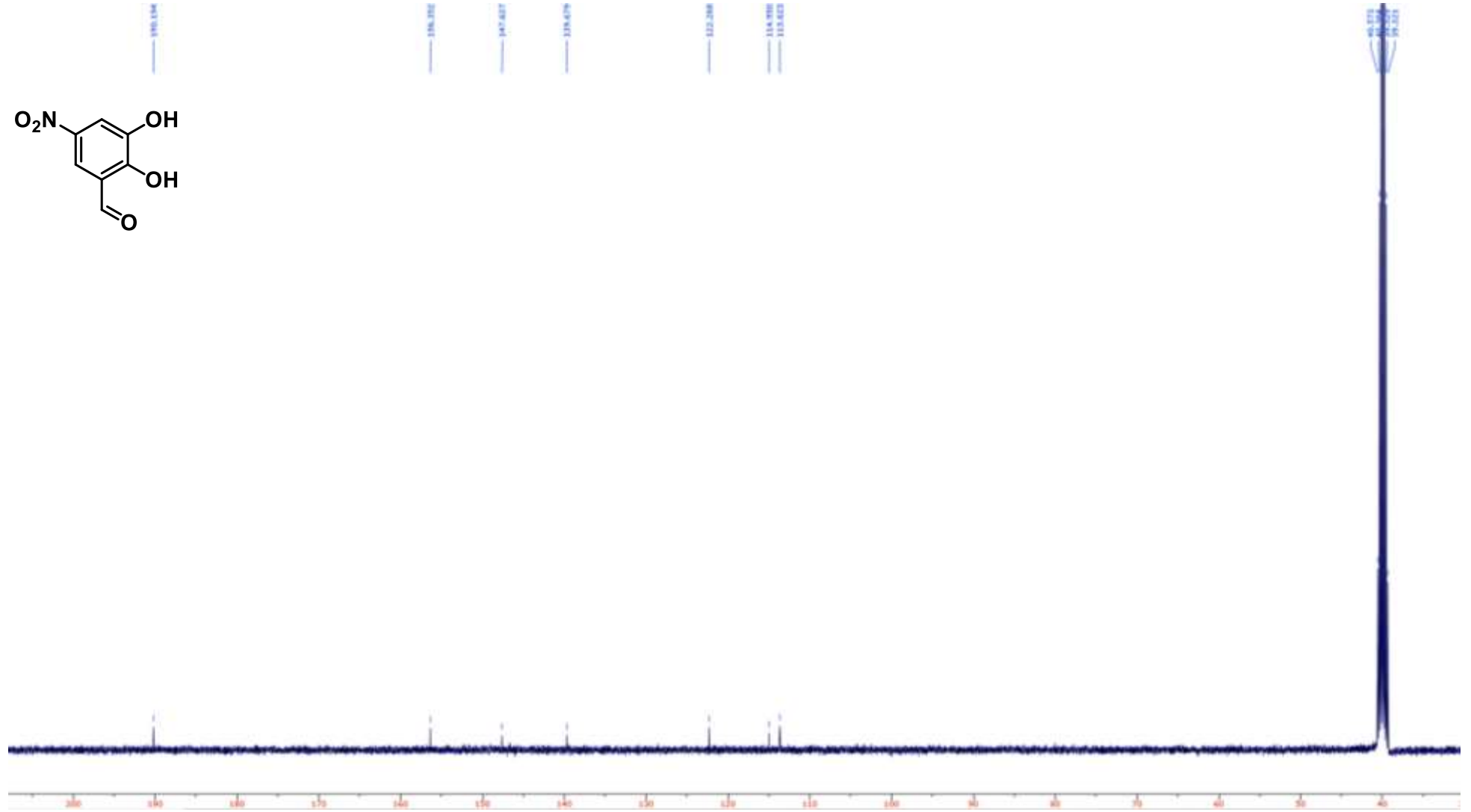
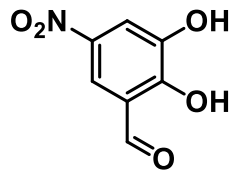
Compound **35** ^{13}C NMR (100 MHz, CDCl_3)



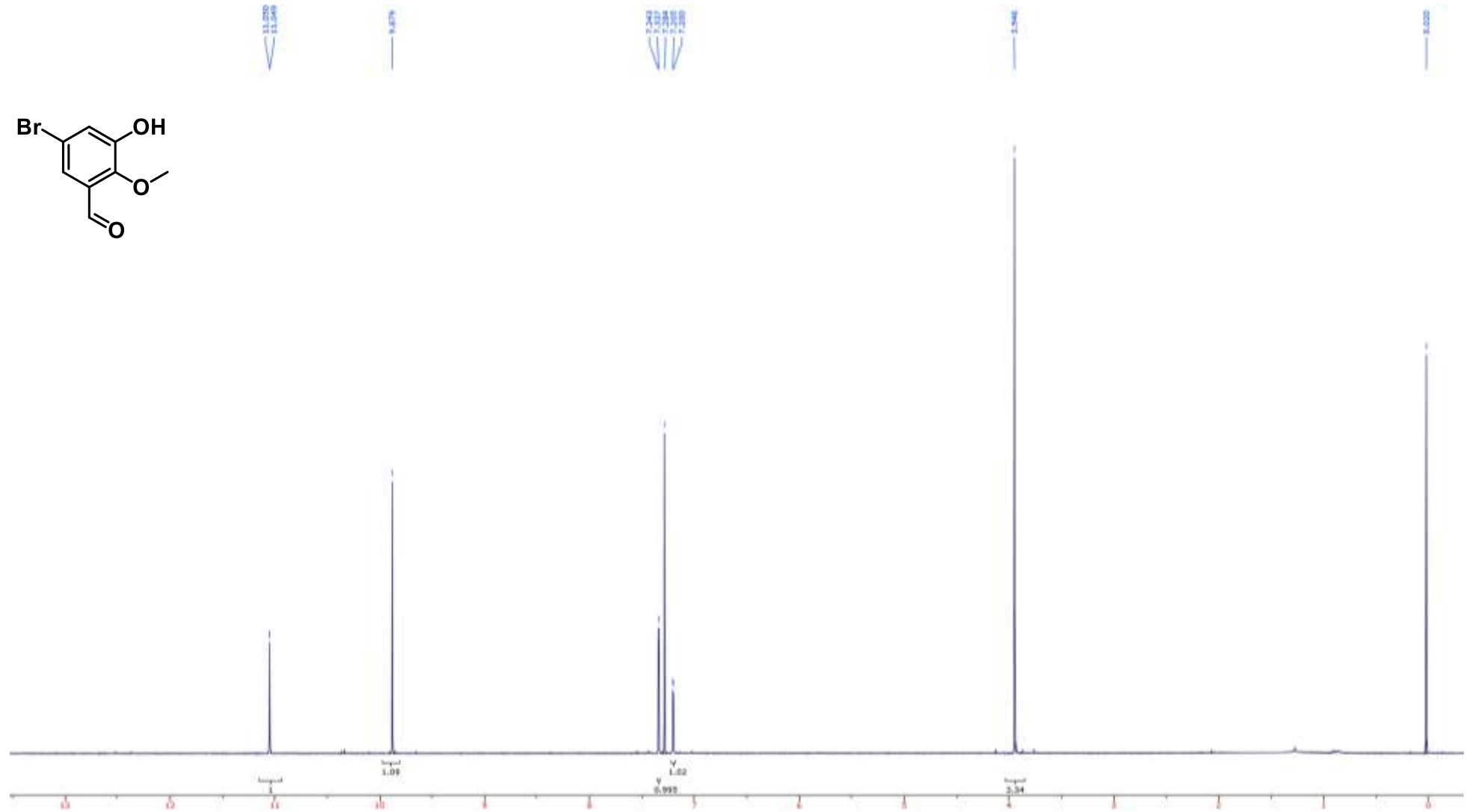
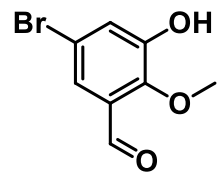
Compound **36** ^1H NMR (400 MHz, d_6 -DMSO)



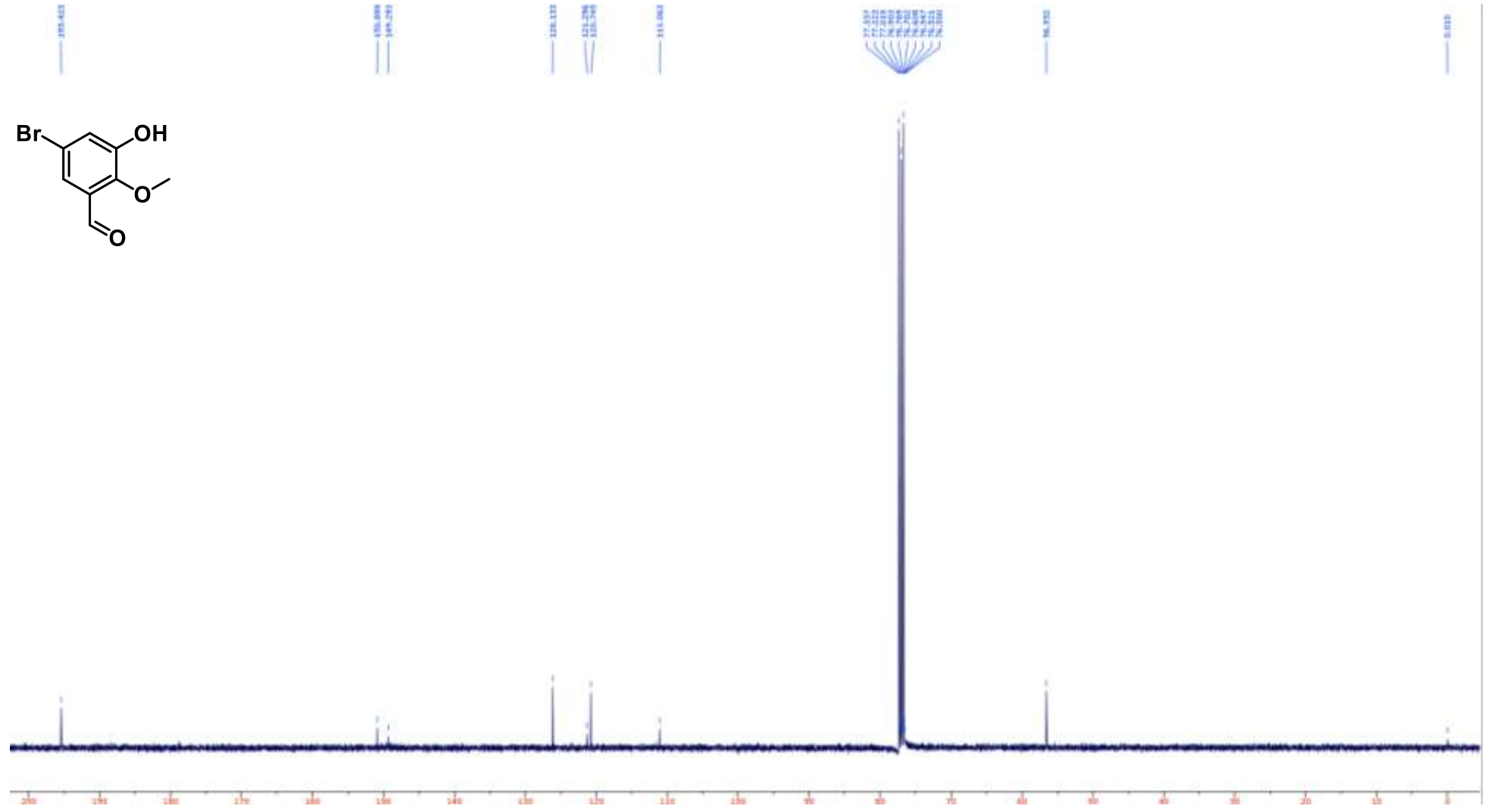
Compound **36** ^{13}C NMR (100 MHz, d_6 -DMSO)



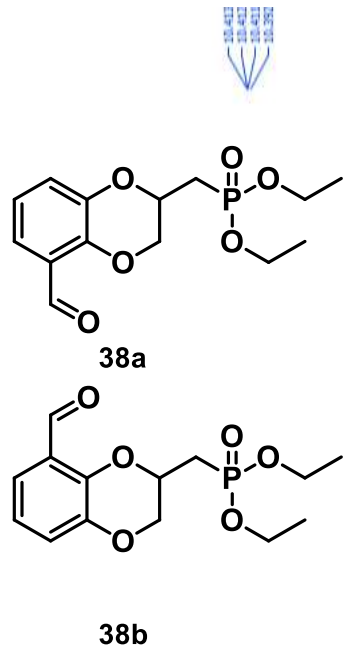
Compound **37** ^1H NMR (400 MHz, CDCl_3)



Compound **37** ^{13}C NMR (100 MHz, CDCl_3)



Compound **38** ^1H NMR (400 MHz, CDCl_3)

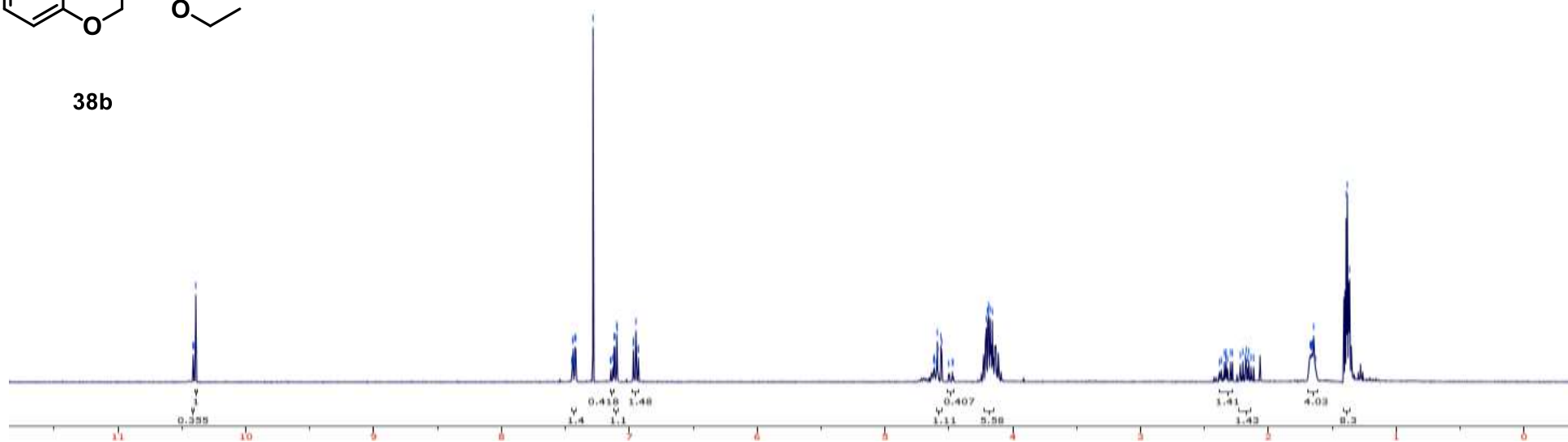


10.412
10.411
10.410
10.392

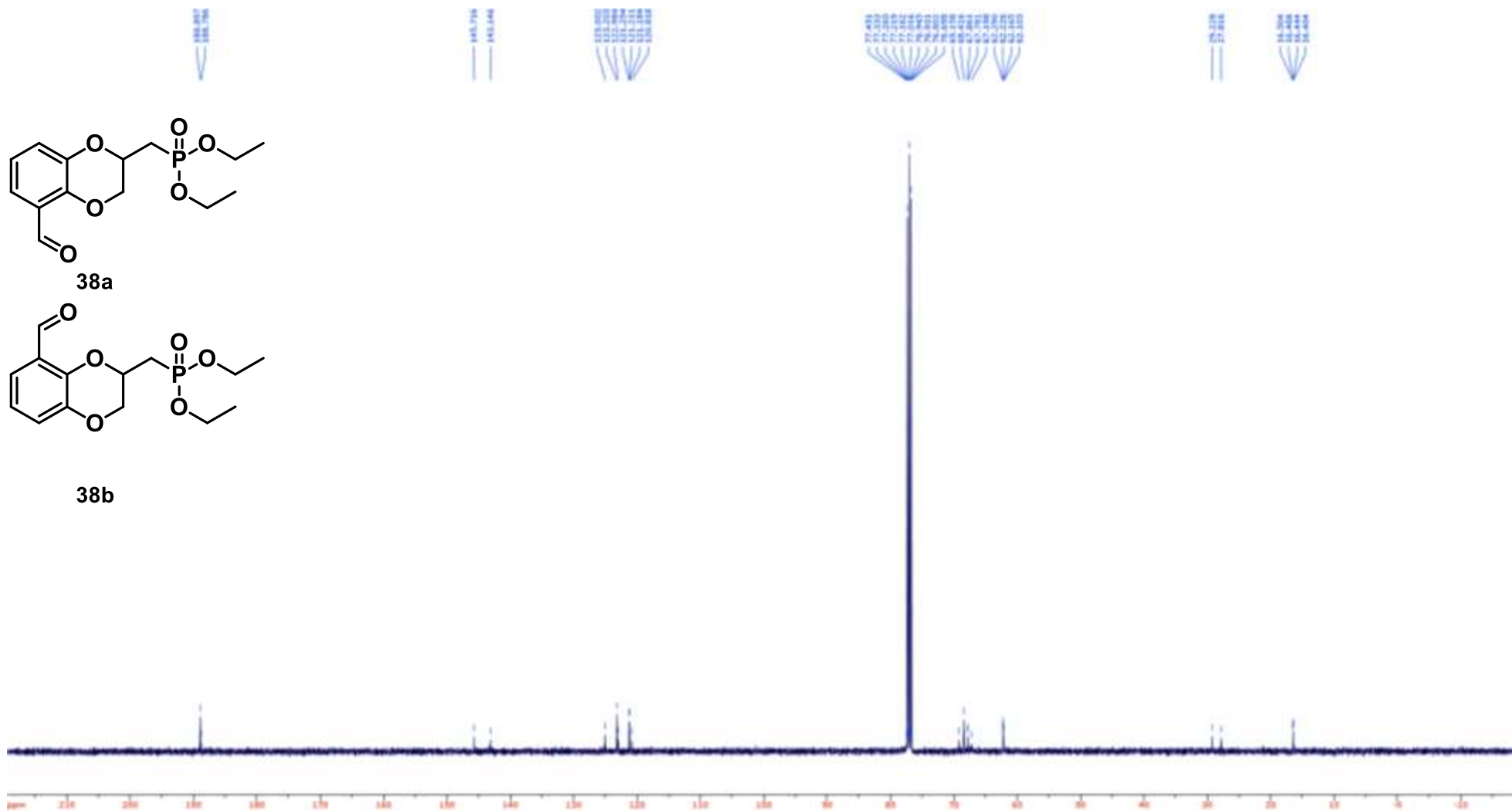
7.7621
7.7615
7.7435
7.631
7.627
7.624
7.584
7.580
7.347
7.343
7.227
7.222
7.118
7.114
7.088
7.084
6.969
6.965
6.929
6.925

4.6218
4.6113
4.5995
4.5955
4.4950
4.4925
4.492
4.5261
4.501
4.472
4.4685
4.468
4.436
4.435
4.409
4.4089
4.3277
4.325

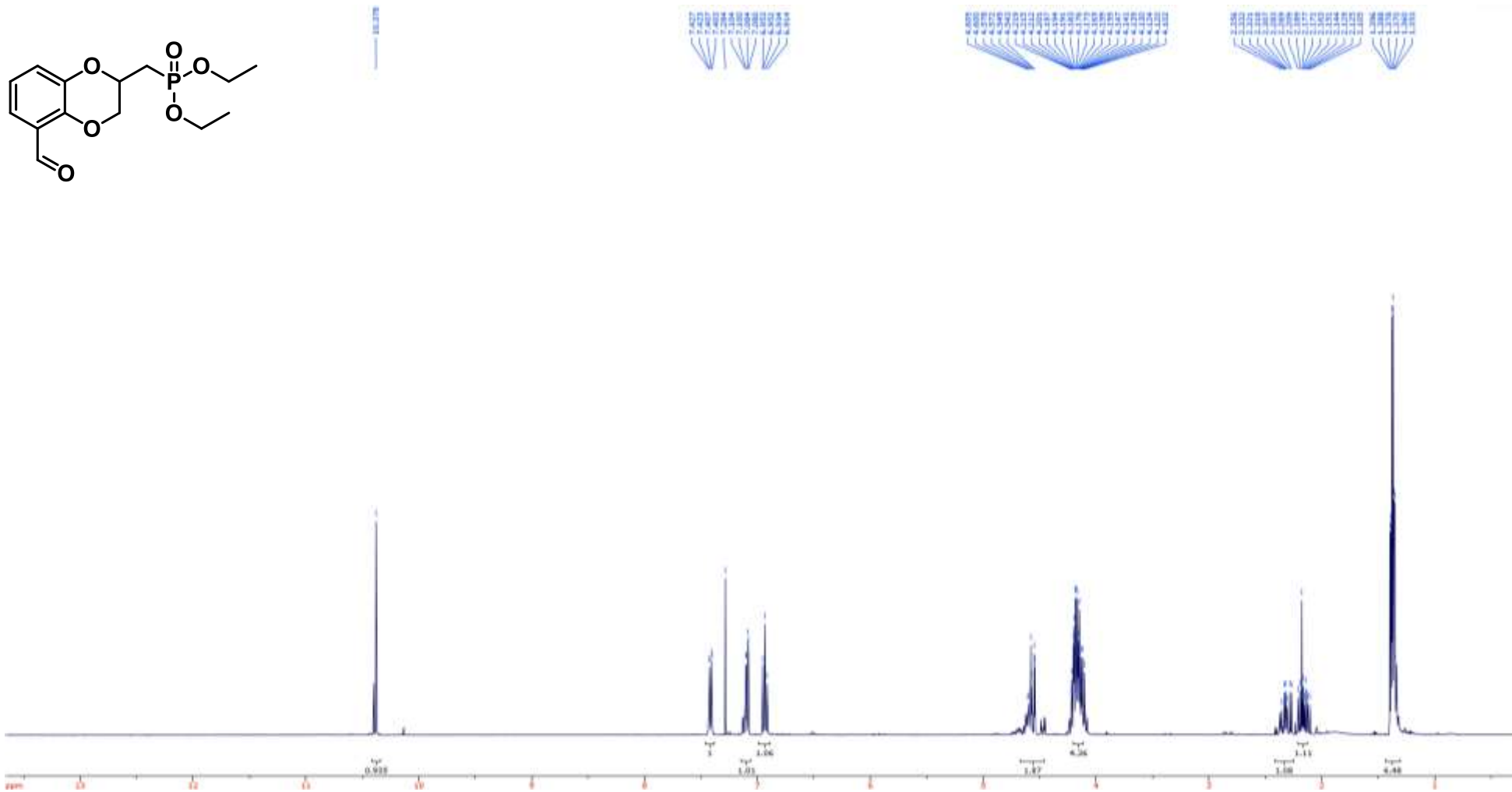
2.2823
2.2822
2.2846
2.2332
2.2330
2.2219
2.2205
2.2204
2.2151
2.2199
2.2181
2.2179
2.2122
2.2121
2.2154
2.2125
2.2115
1.671
1.670
1.6643
1.668
1.668
1.6663
1.662
1.662
1.654
1.645
1.645
1.620
1.390
1.392
1.392



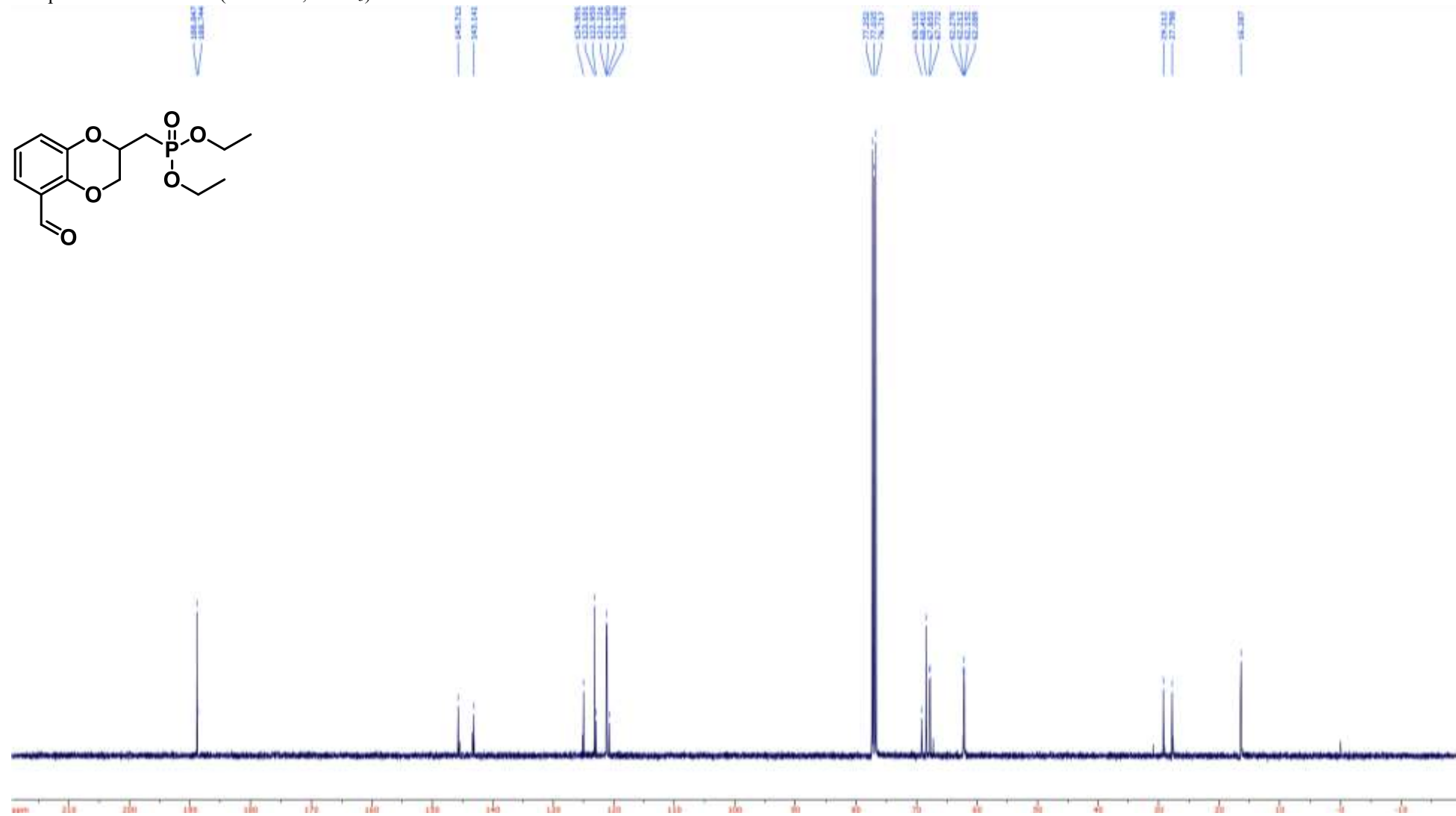
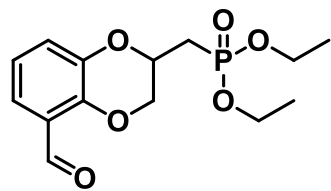
Compound **38** ^{13}C NMR (100 MHz, CDCl_3)



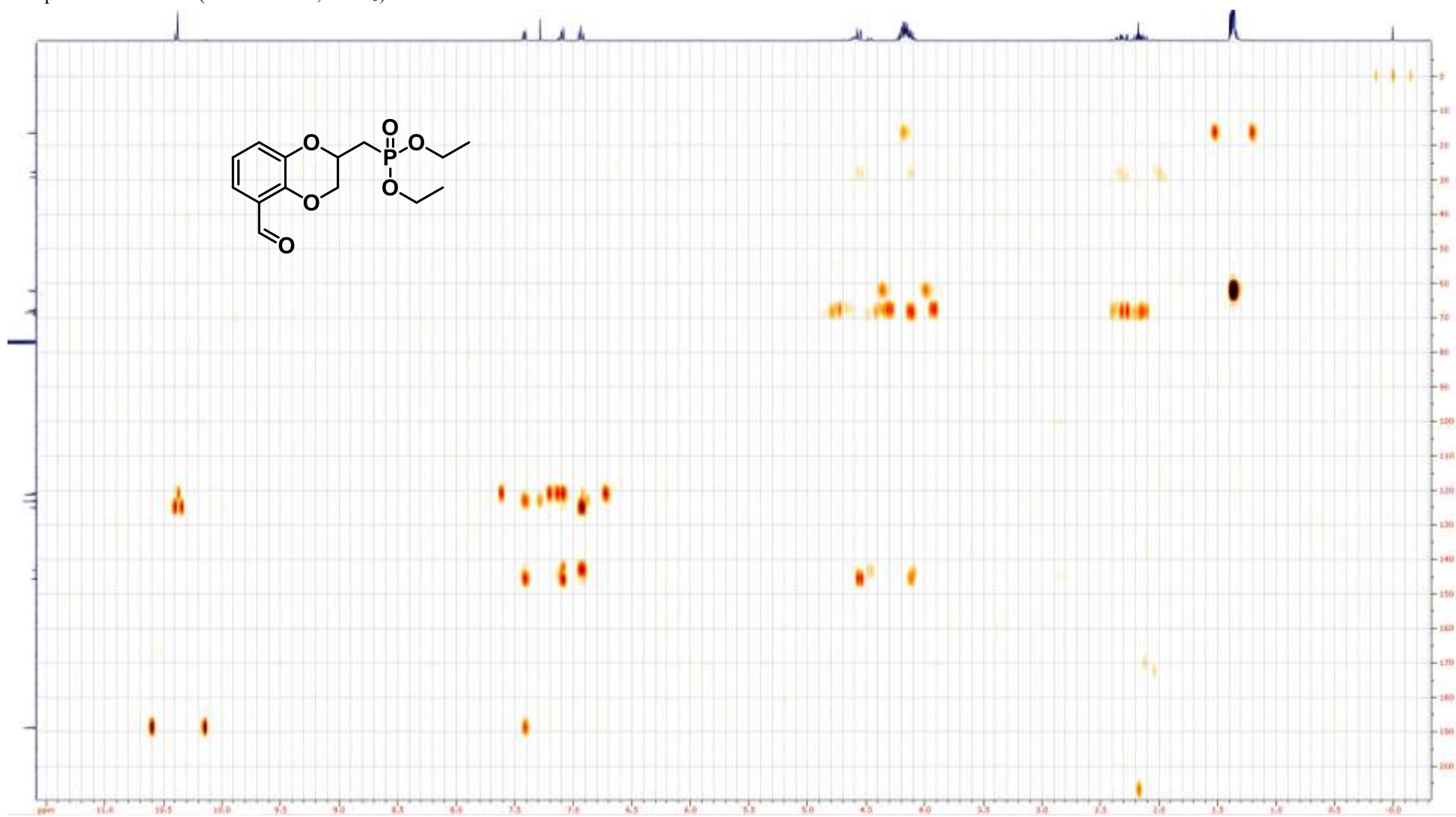
Compound **38a** ^1H NMR (400 MHz, CDCl_3)



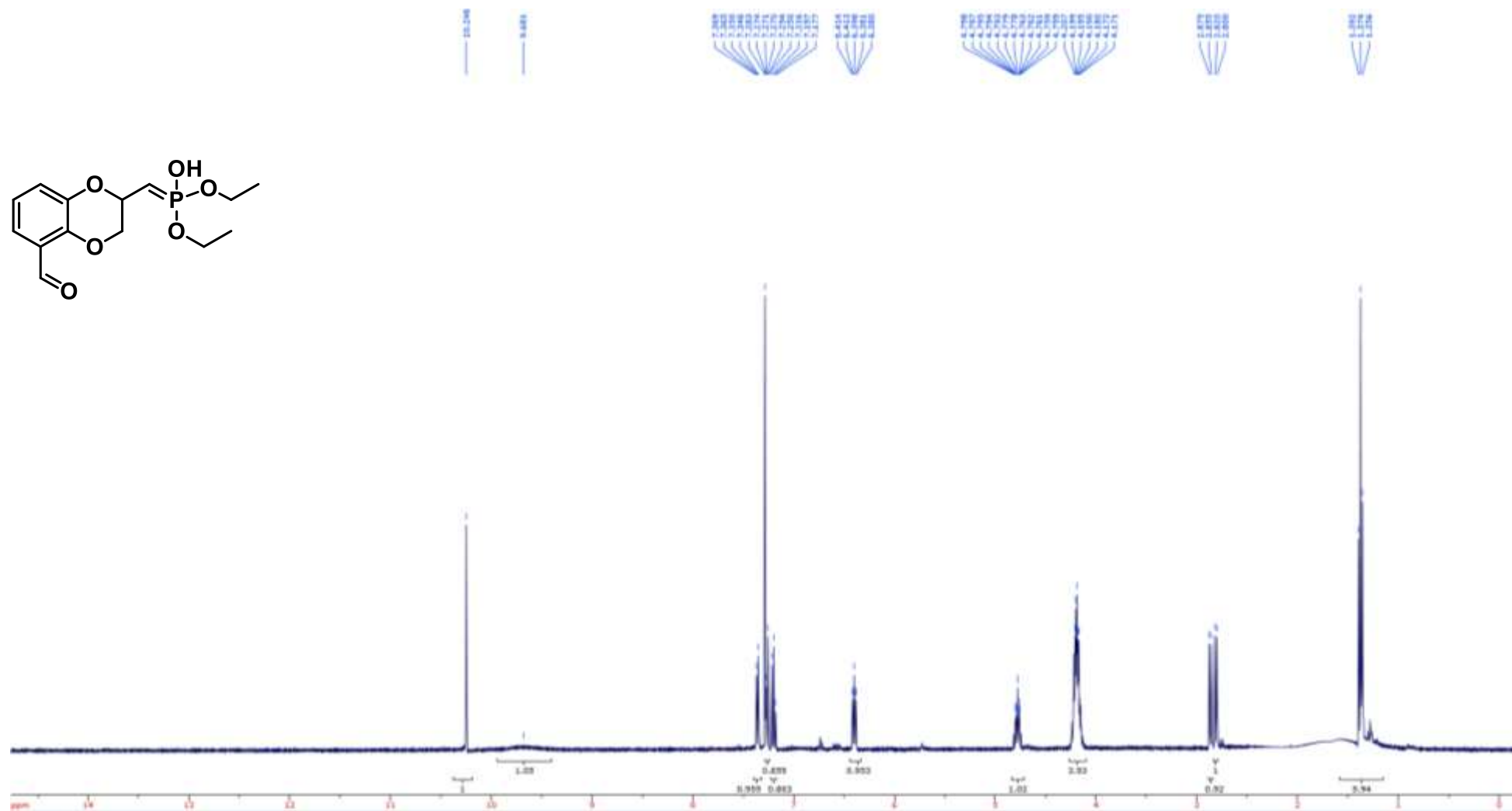
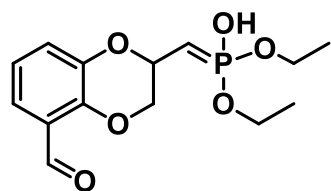
Compound **38a** ^{13}C NMR (100 MHz, CDCl_3)



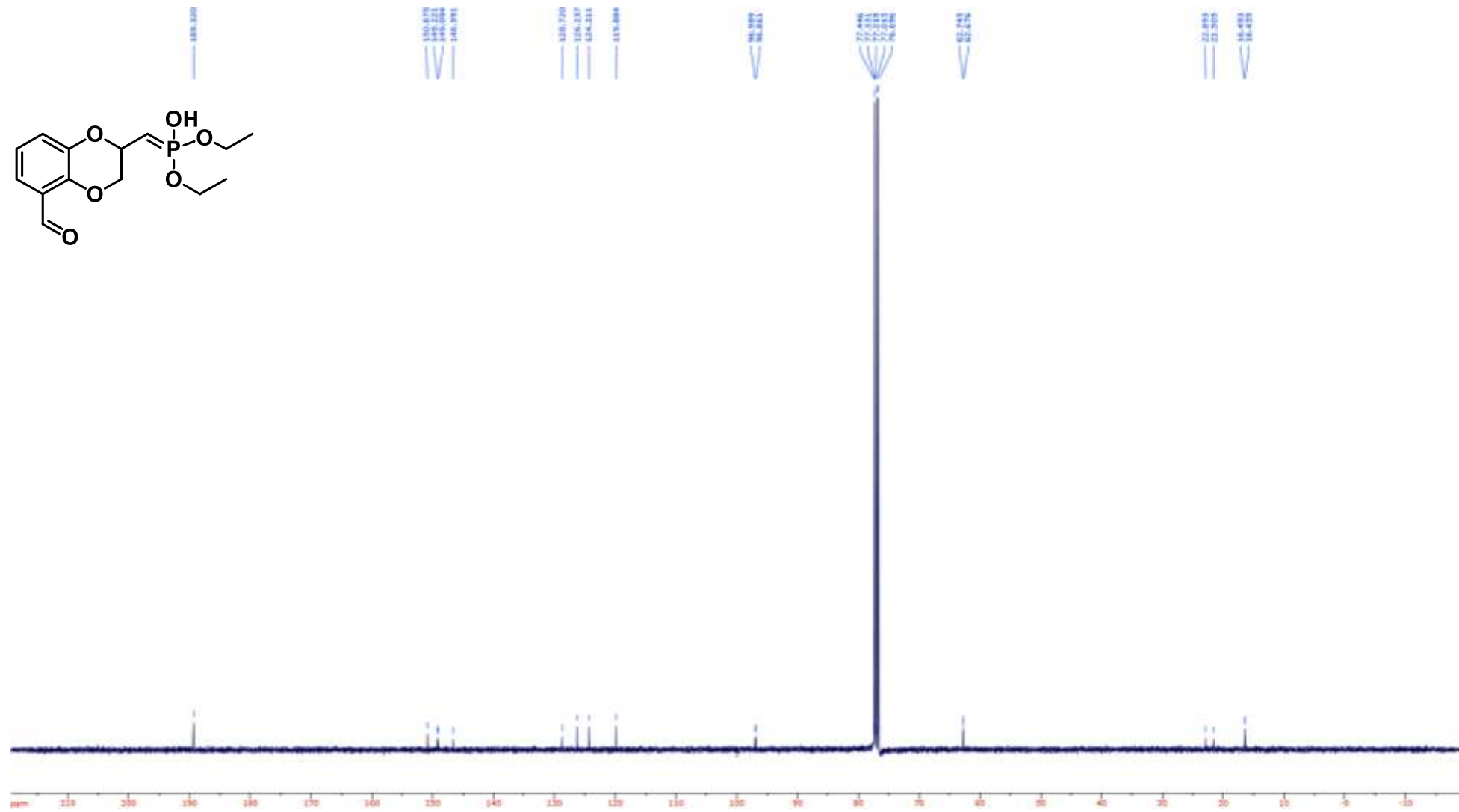
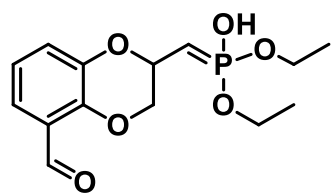
Compound **38a** HMBC (400/100 MHz, CDCl₃)



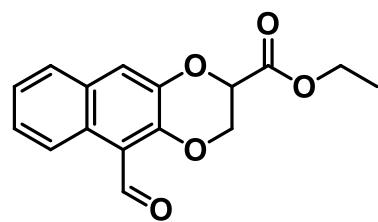
Compound **39** ^1H NMR (400 MHz, CDCl_3)



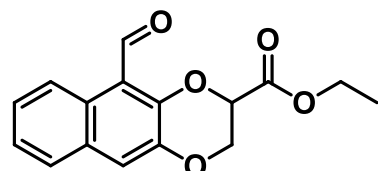
Compound **39** ^{13}C NMR (100 MHz, CDCl_3)



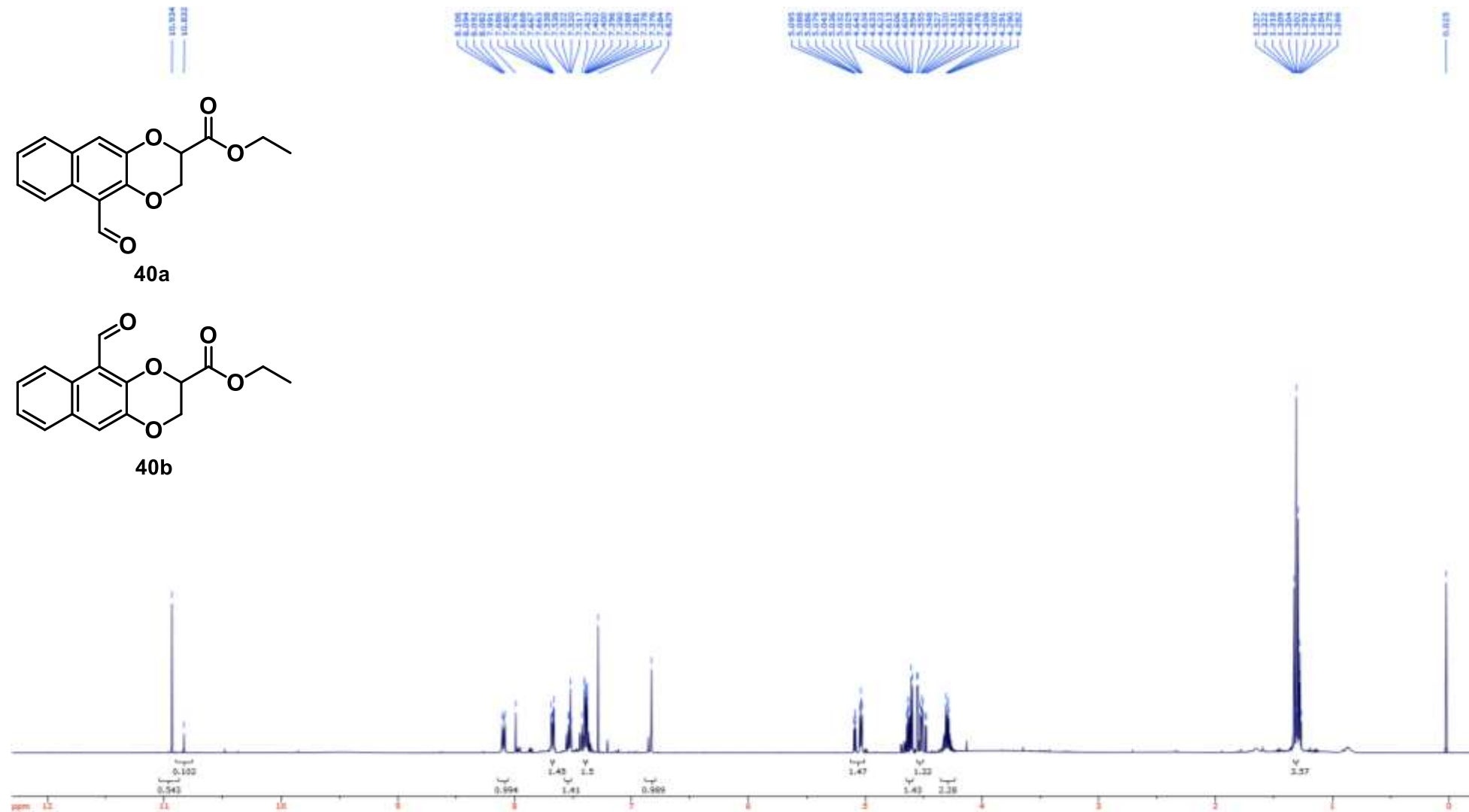
Compound **40** ^1H NMR (400 MHz, CDCl_3)



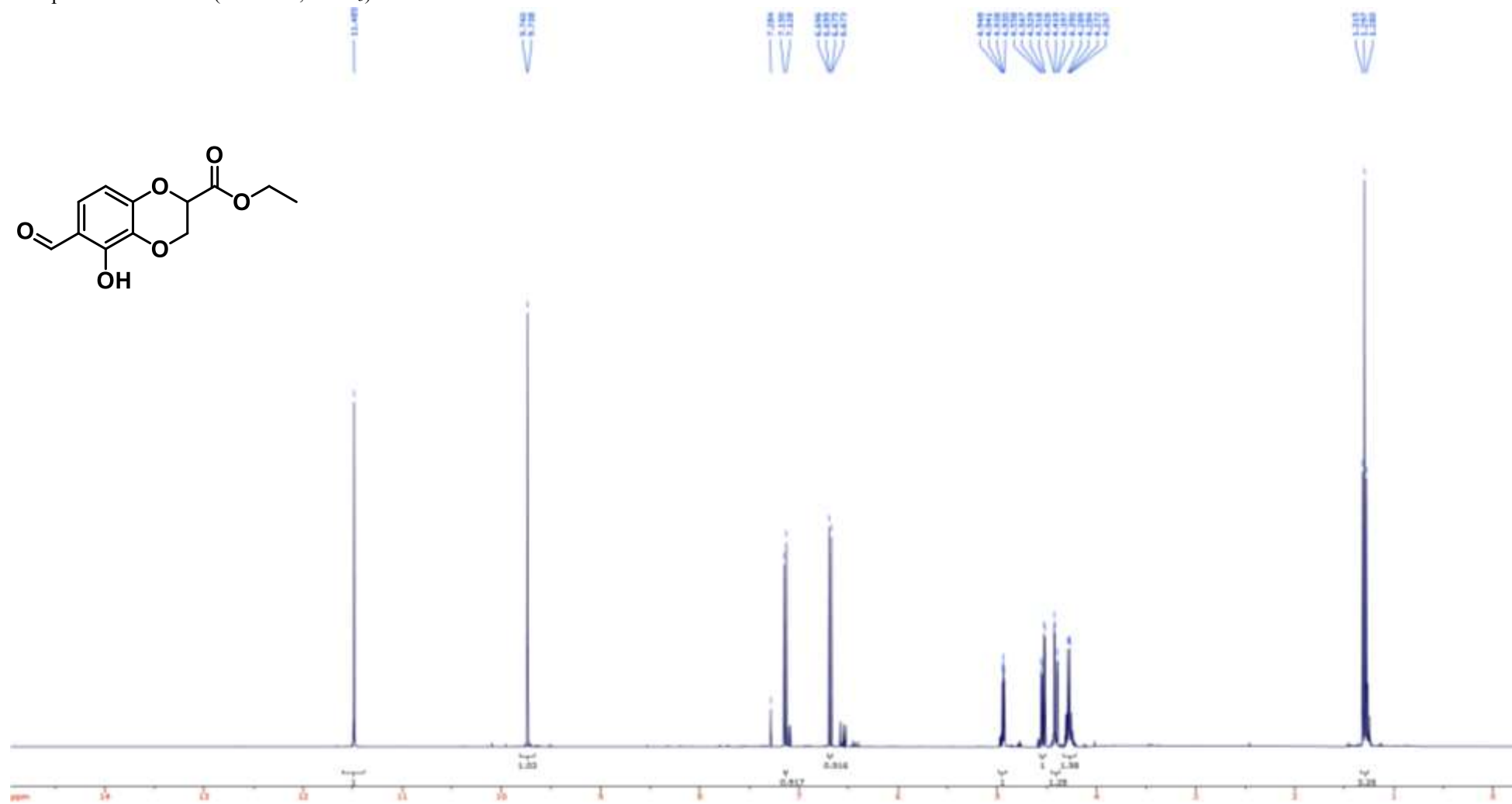
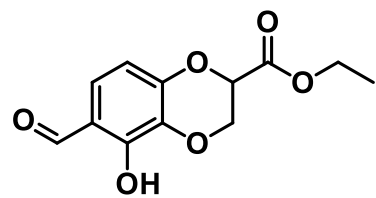
40a



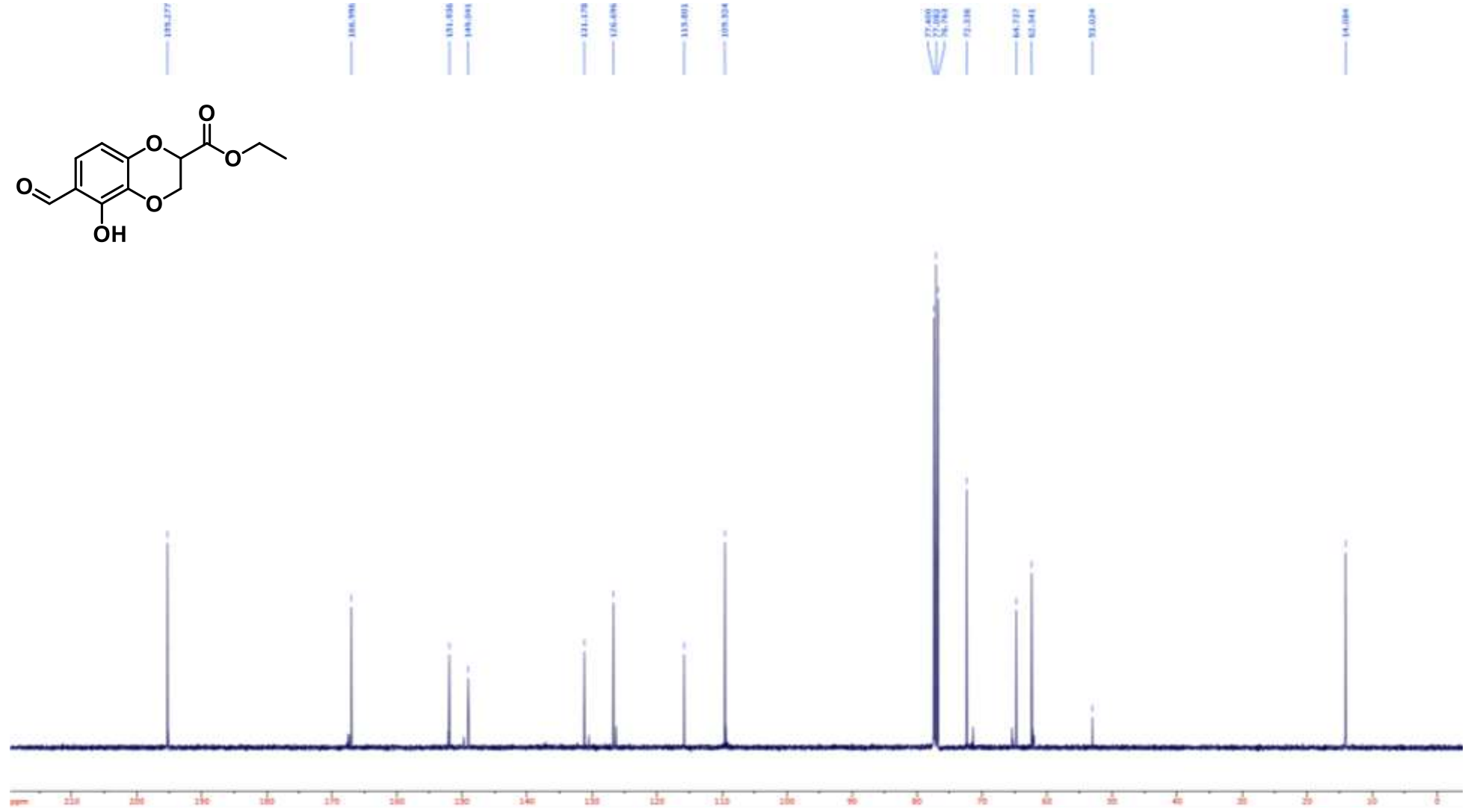
40b



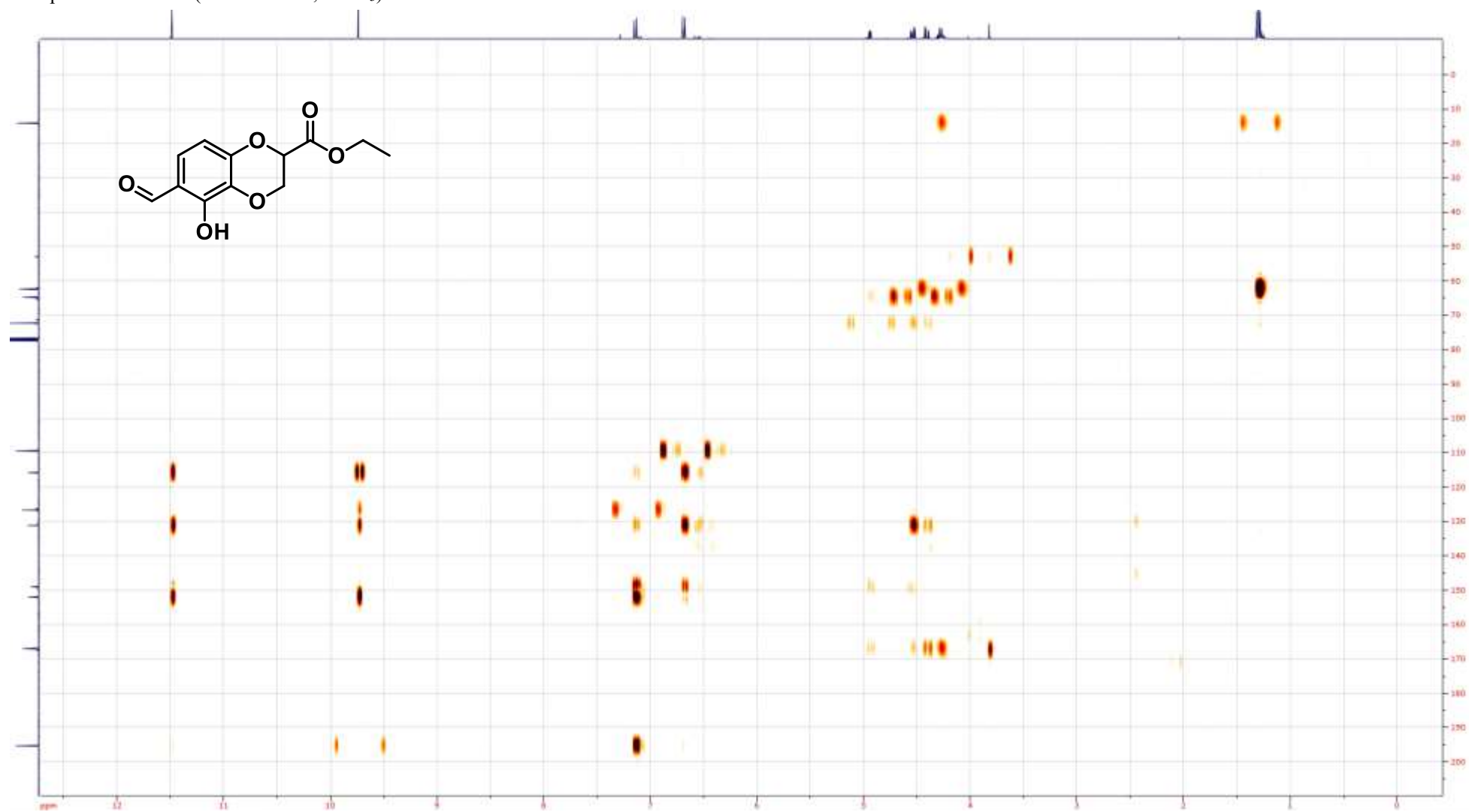
Compound **41** ^1H NMR (400 MHz, CDCl_3)



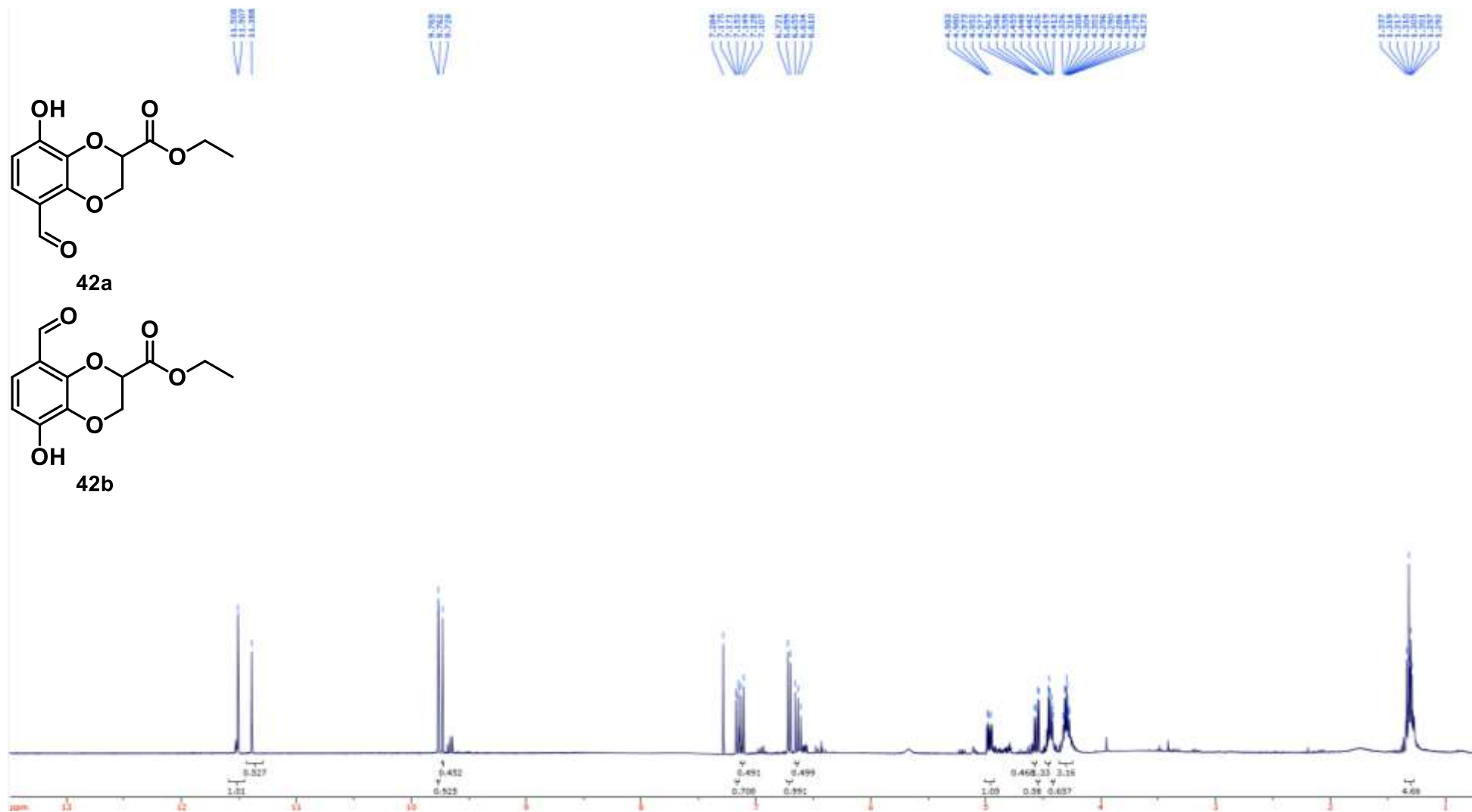
Compound **41** ^{13}C NMR (100 MHz, CDCl_3)



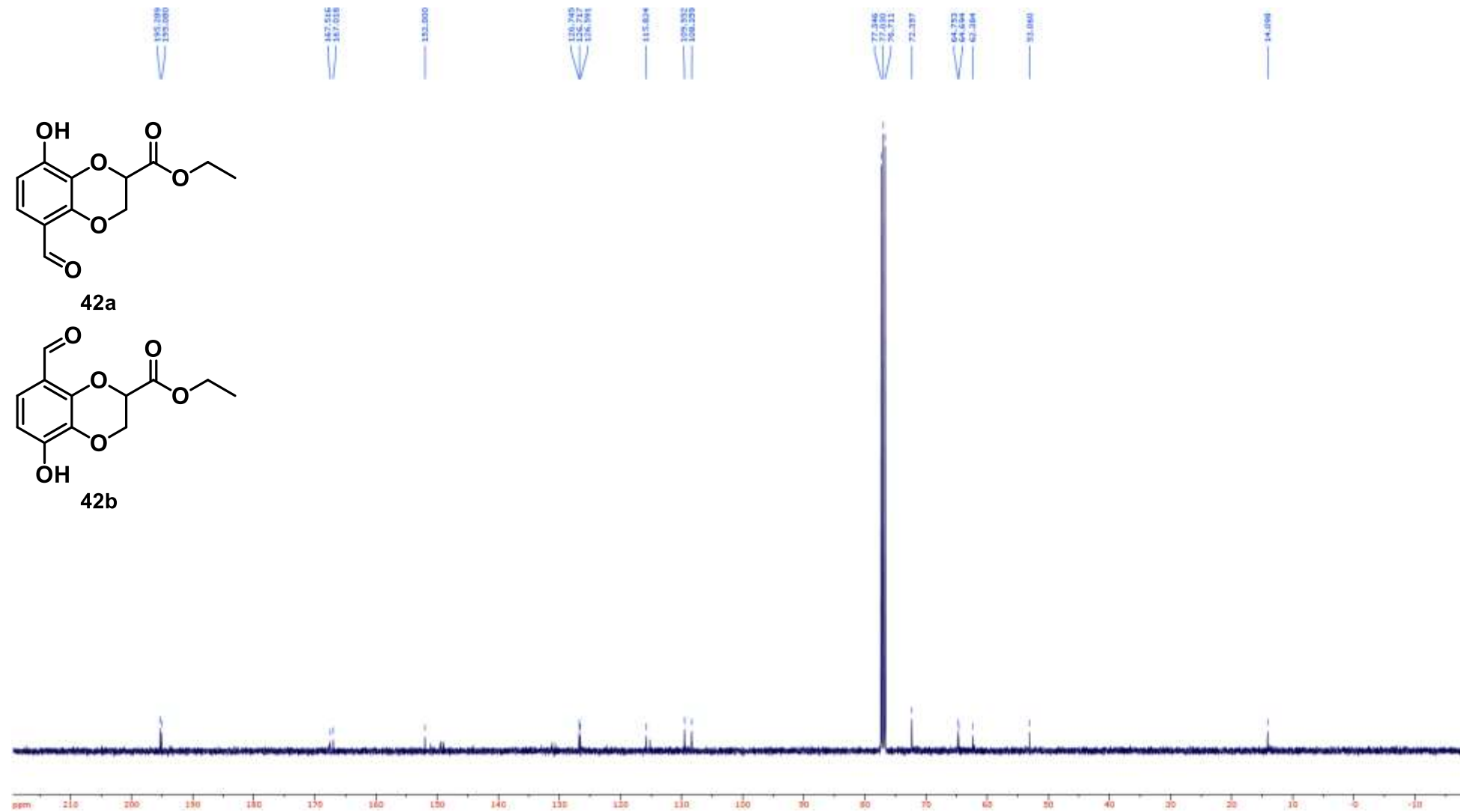
Compound **41** HMBC (400/100 MHz, CDCl₃)



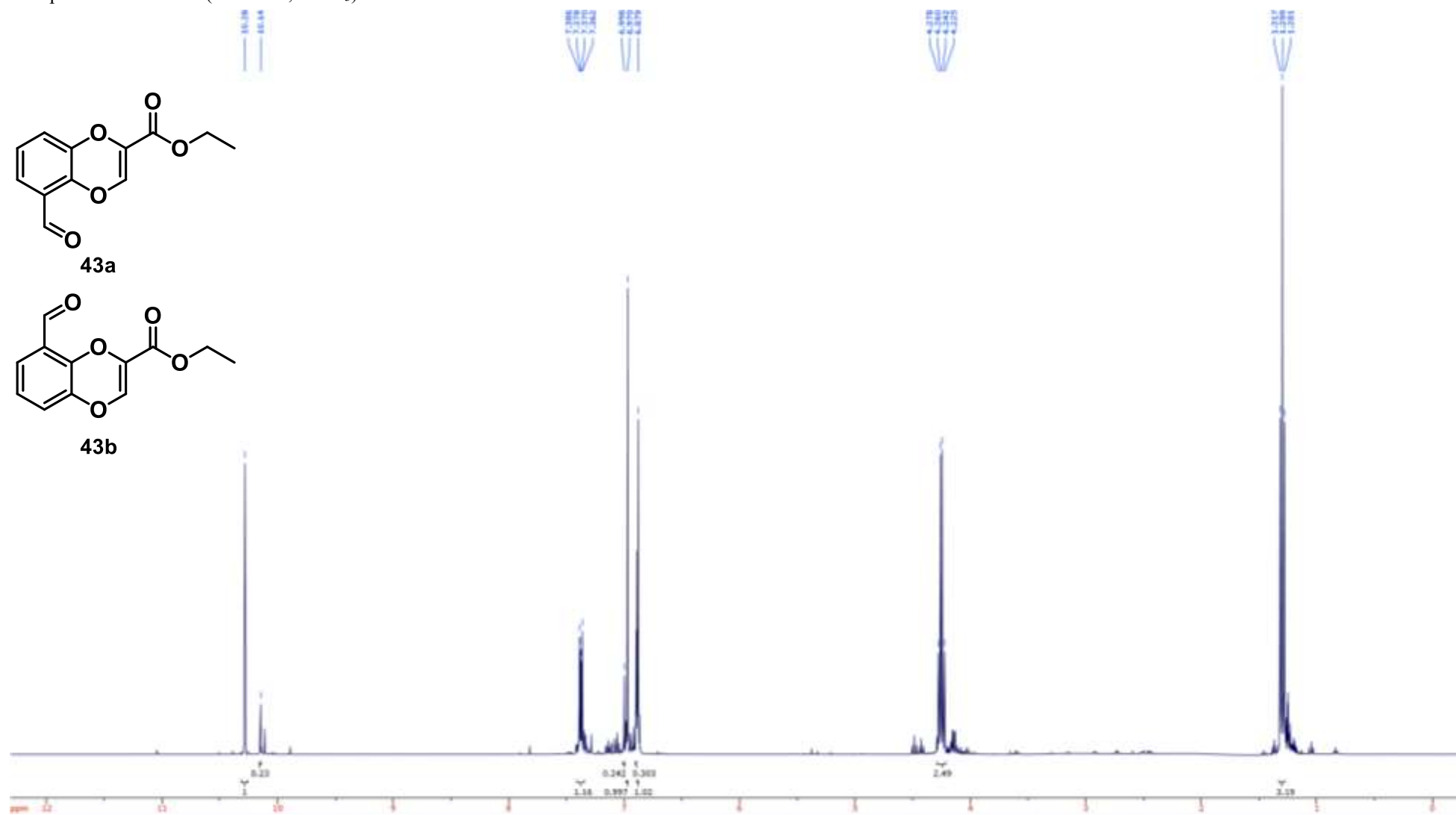
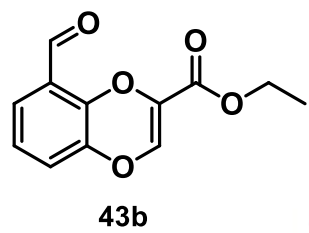
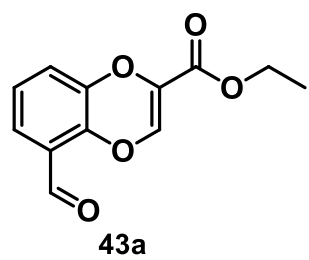
Compound **42** ^1H NMR (400 MHz, CDCl_3)



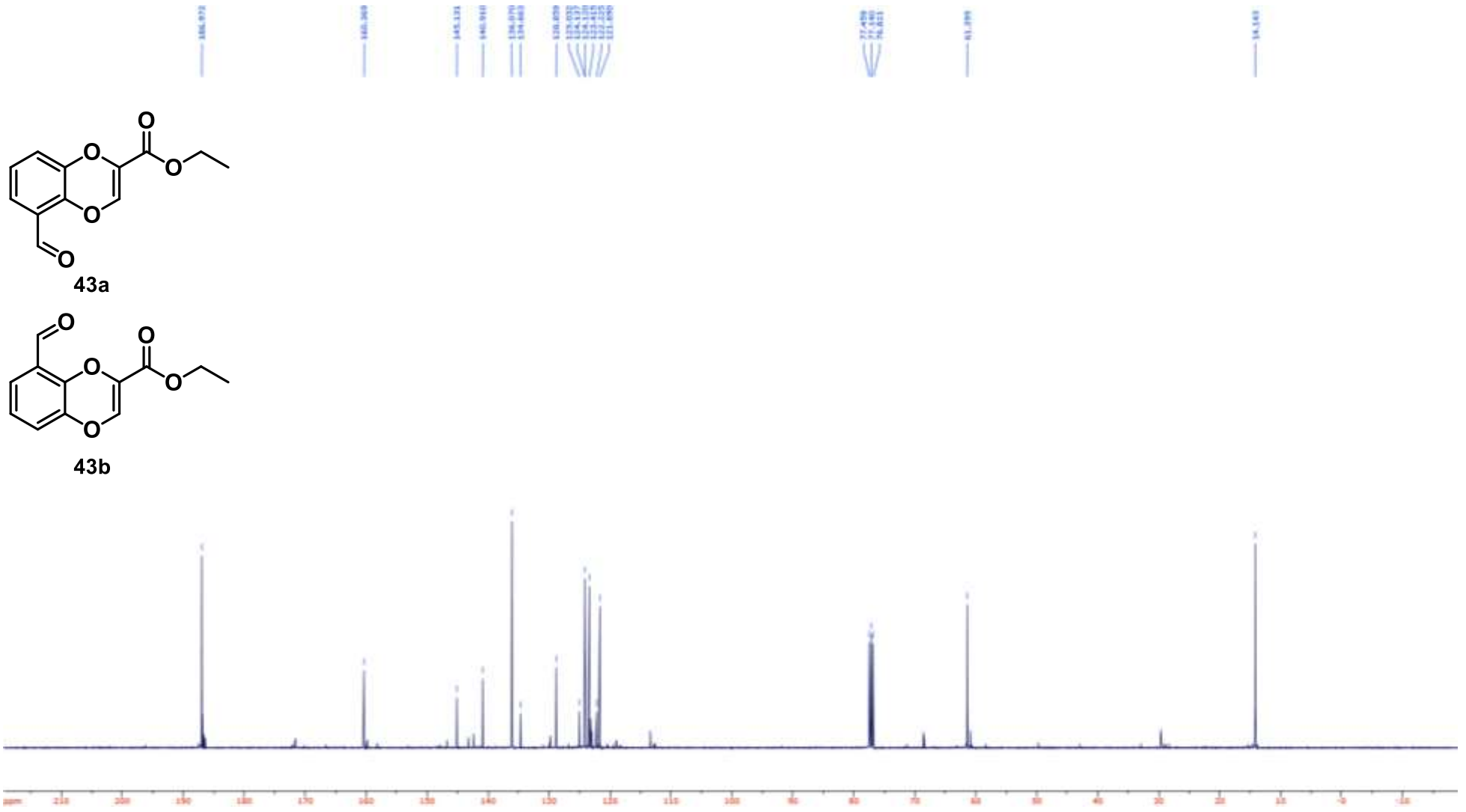
Compound **42** ^{13}C NMR (100 MHz, CDCl_3)



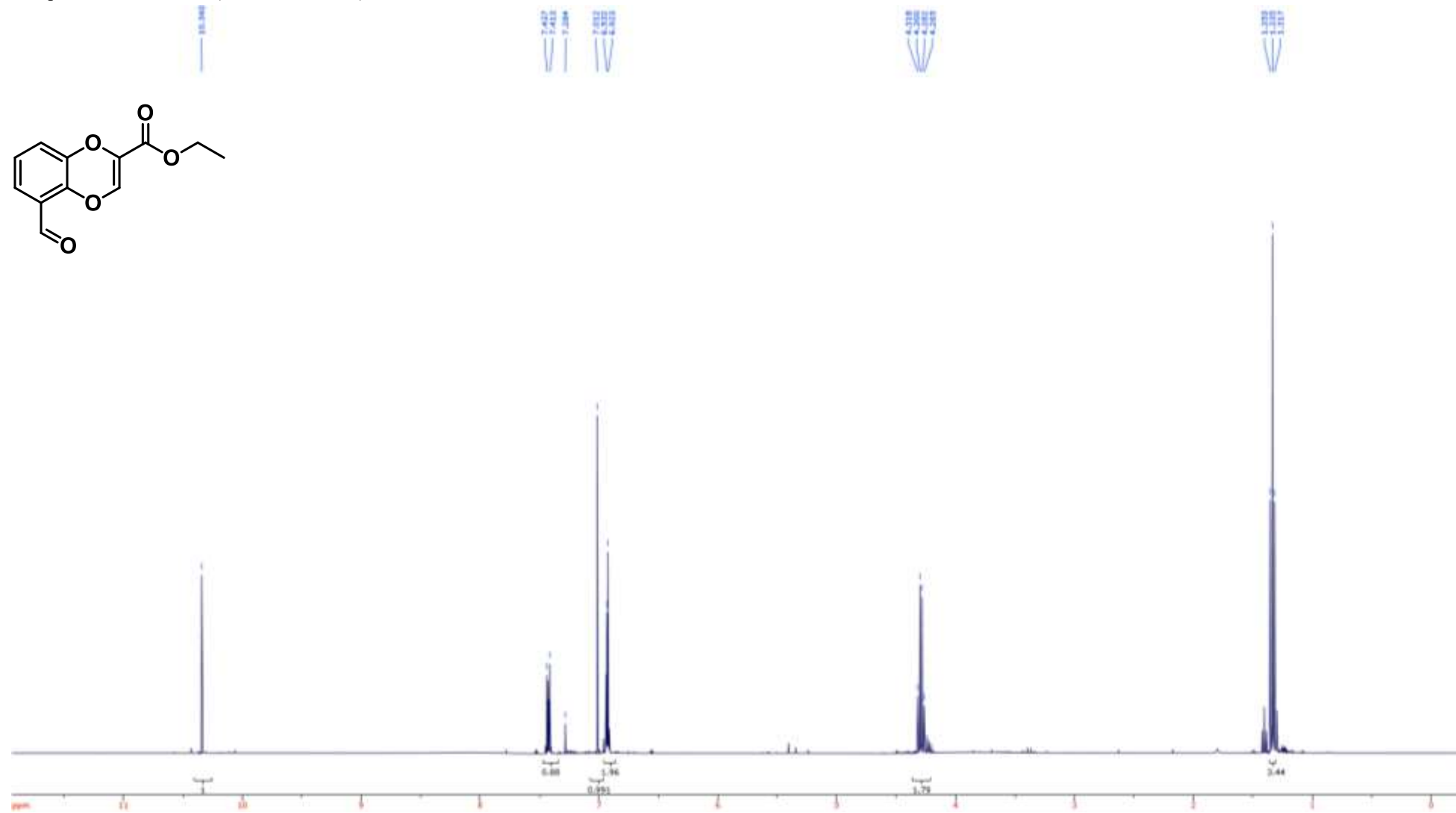
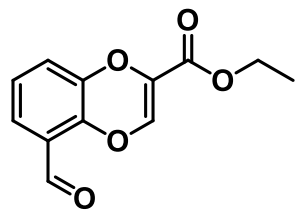
Compound **43** ^1H NMR (400 MHz, CDCl_3)



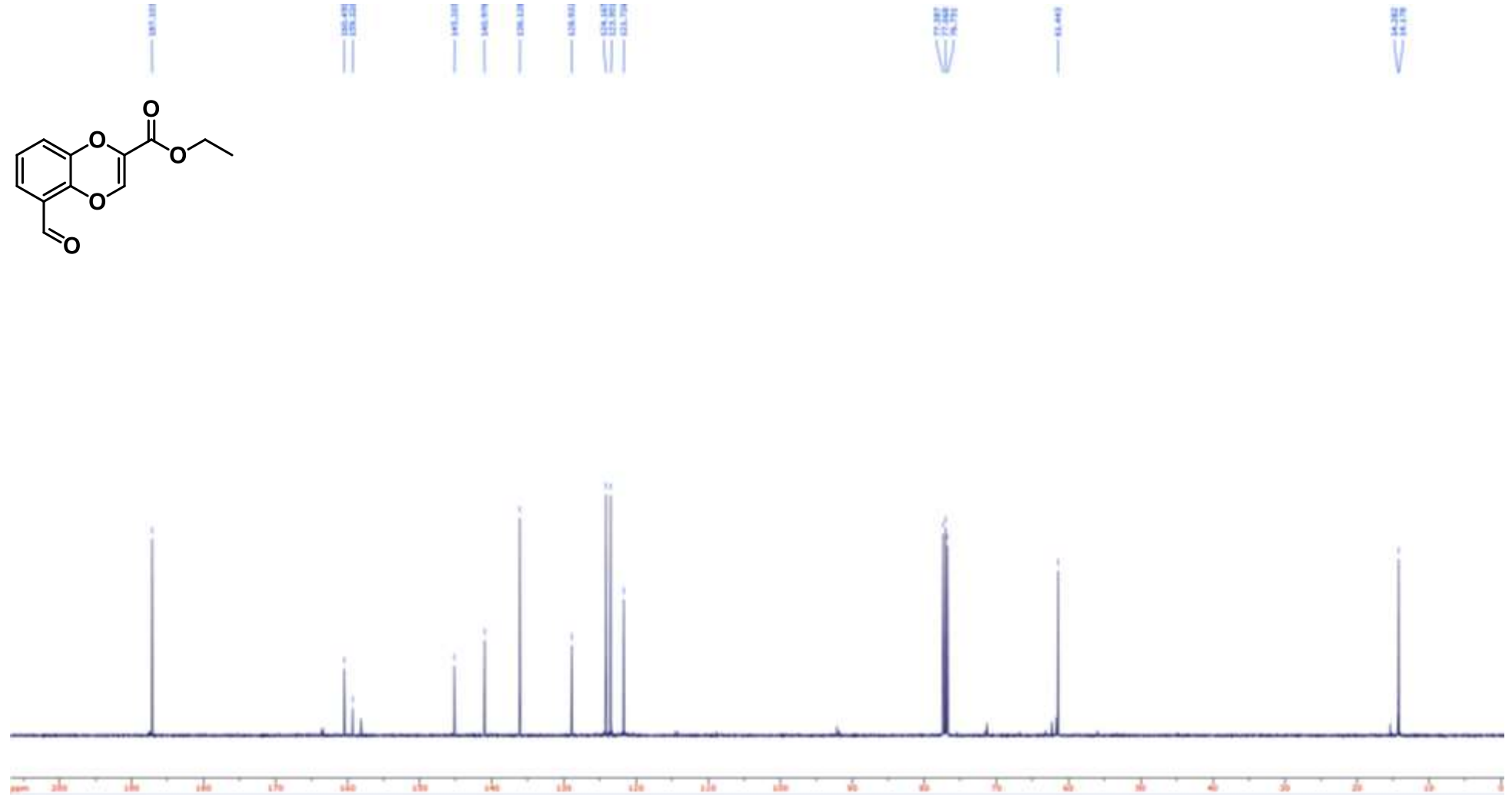
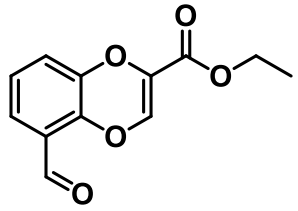
Compound **43** ^{13}C NMR (100 MHz, CDCl_3)



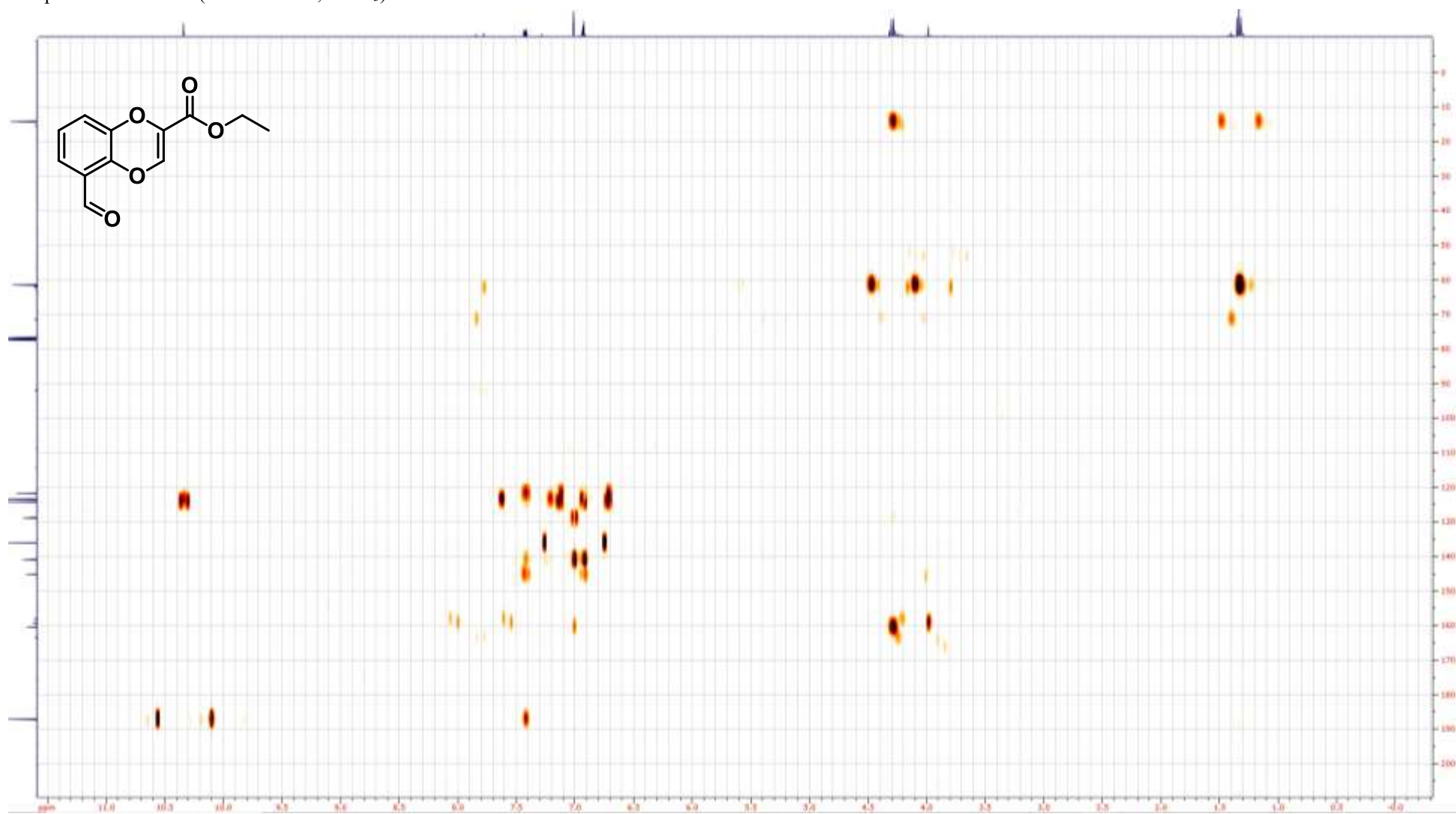
Compound **43a** ^1H NMR (400 MHz, CDCl_3)



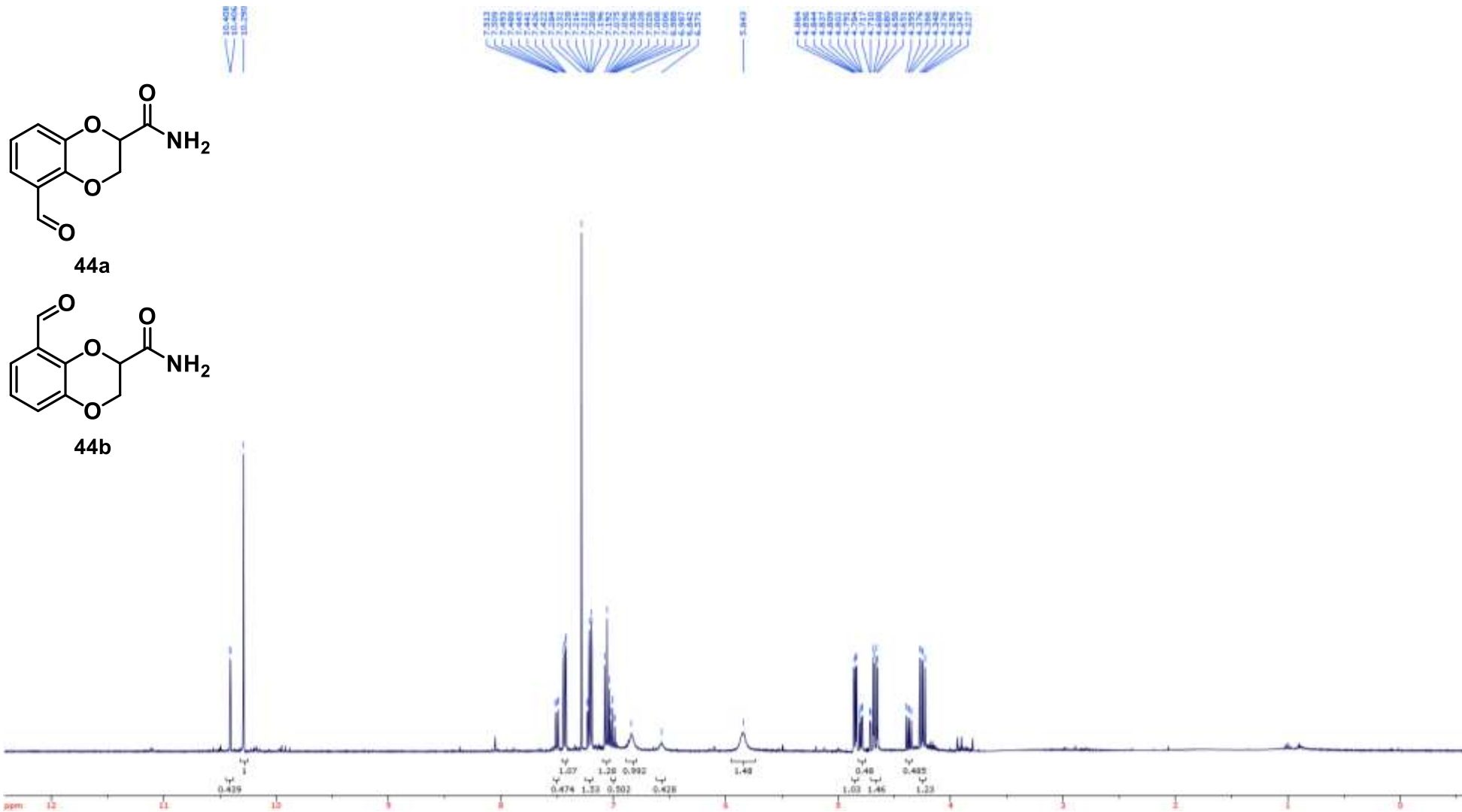
Compound **43a** ^{13}C NMR (100 MHz, CDCl_3)



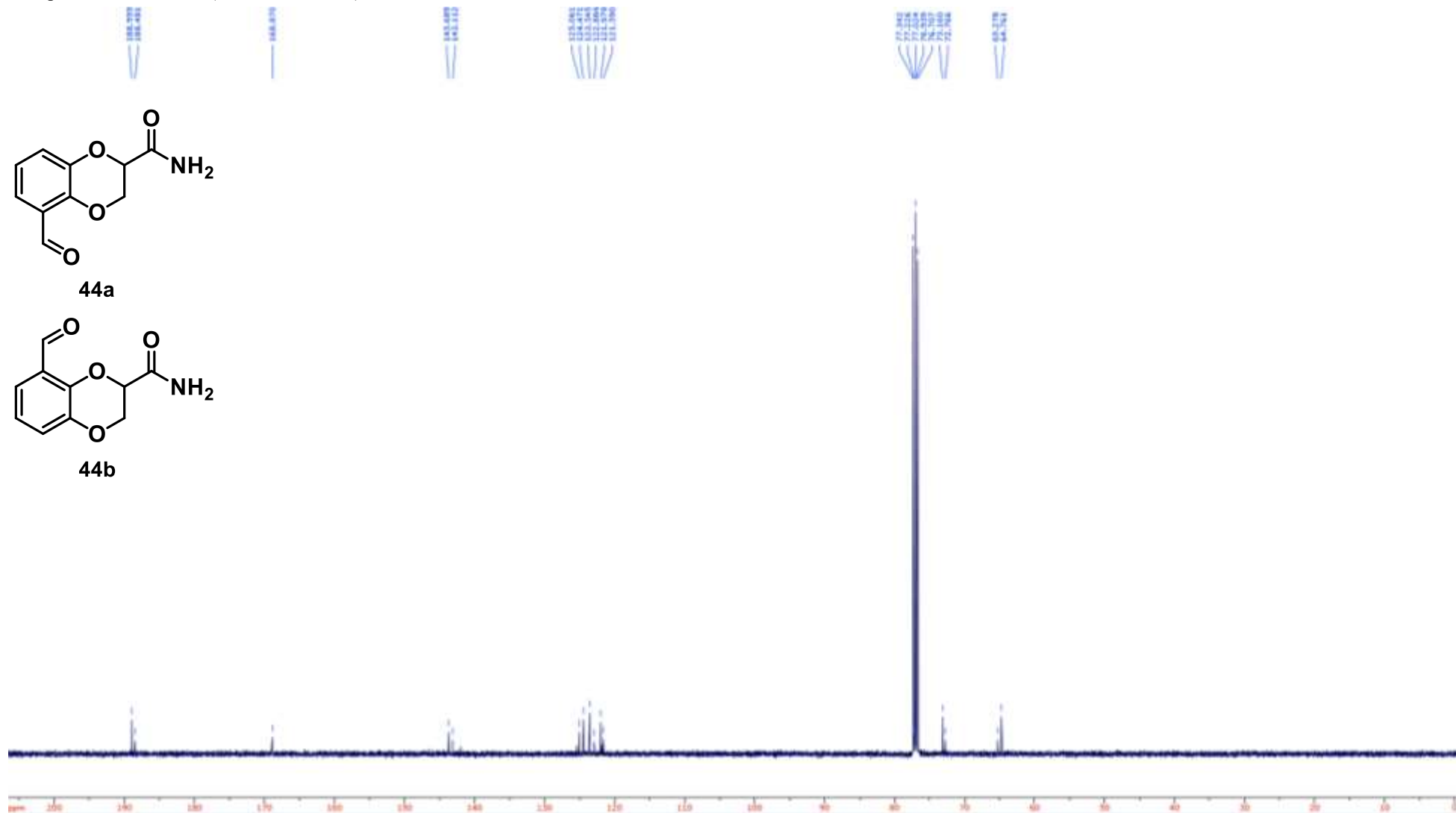
Compound **43a** HMBC (400/100 MHz, CDCl₃)



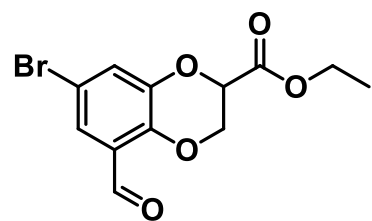
Compound **44** ^1H NMR (400 MHz, CDCl_3)



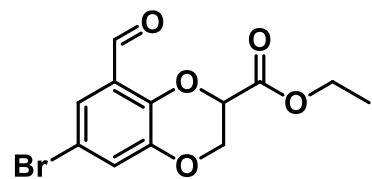
Compound **44** ^{13}C NMR (100 MHz, CDCl_3)



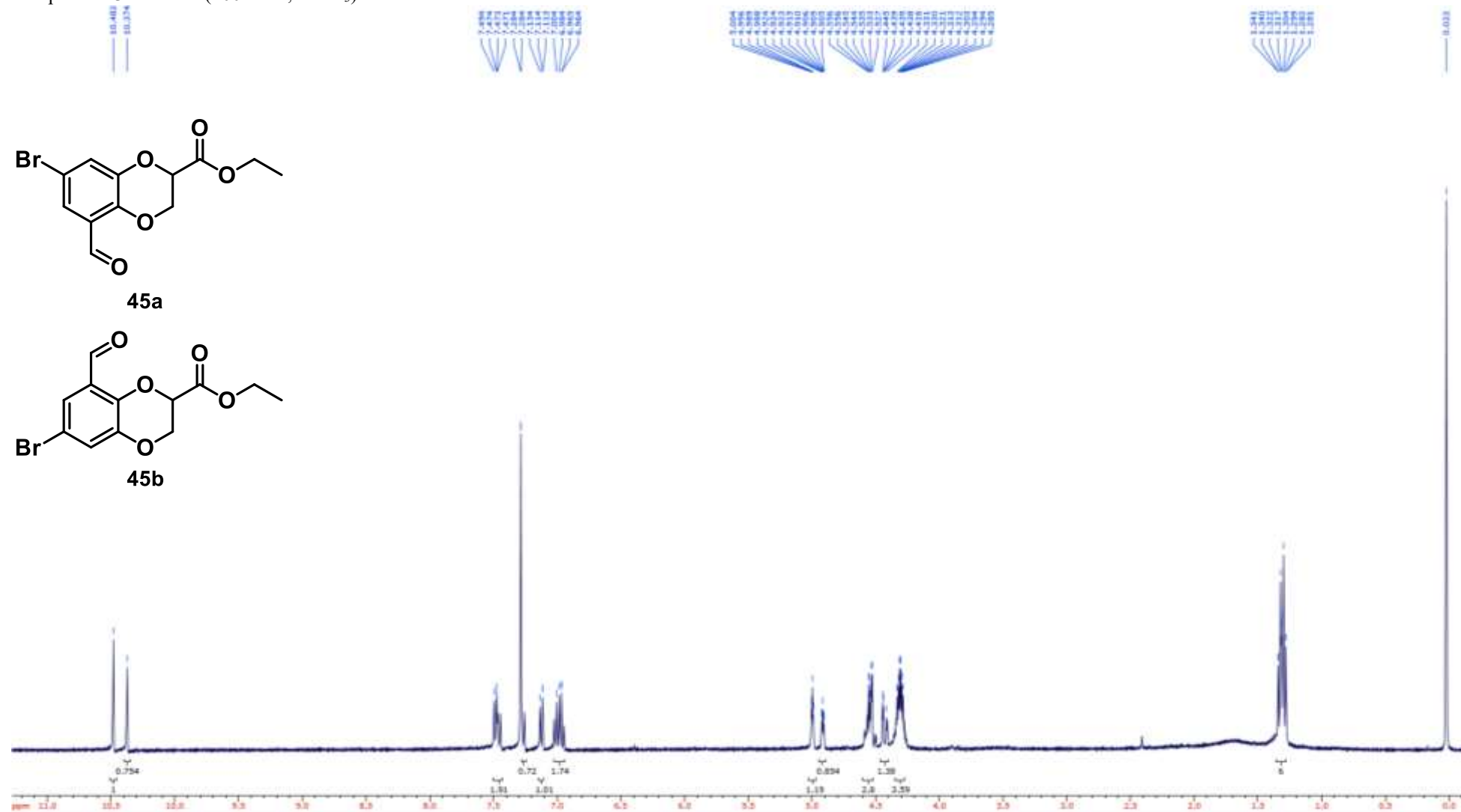
Compound **45** ^1H NMR (400 MHz, CDCl_3)



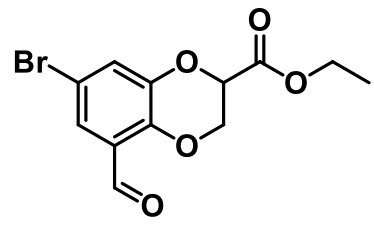
45a



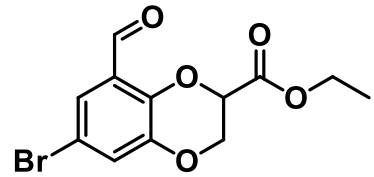
45b



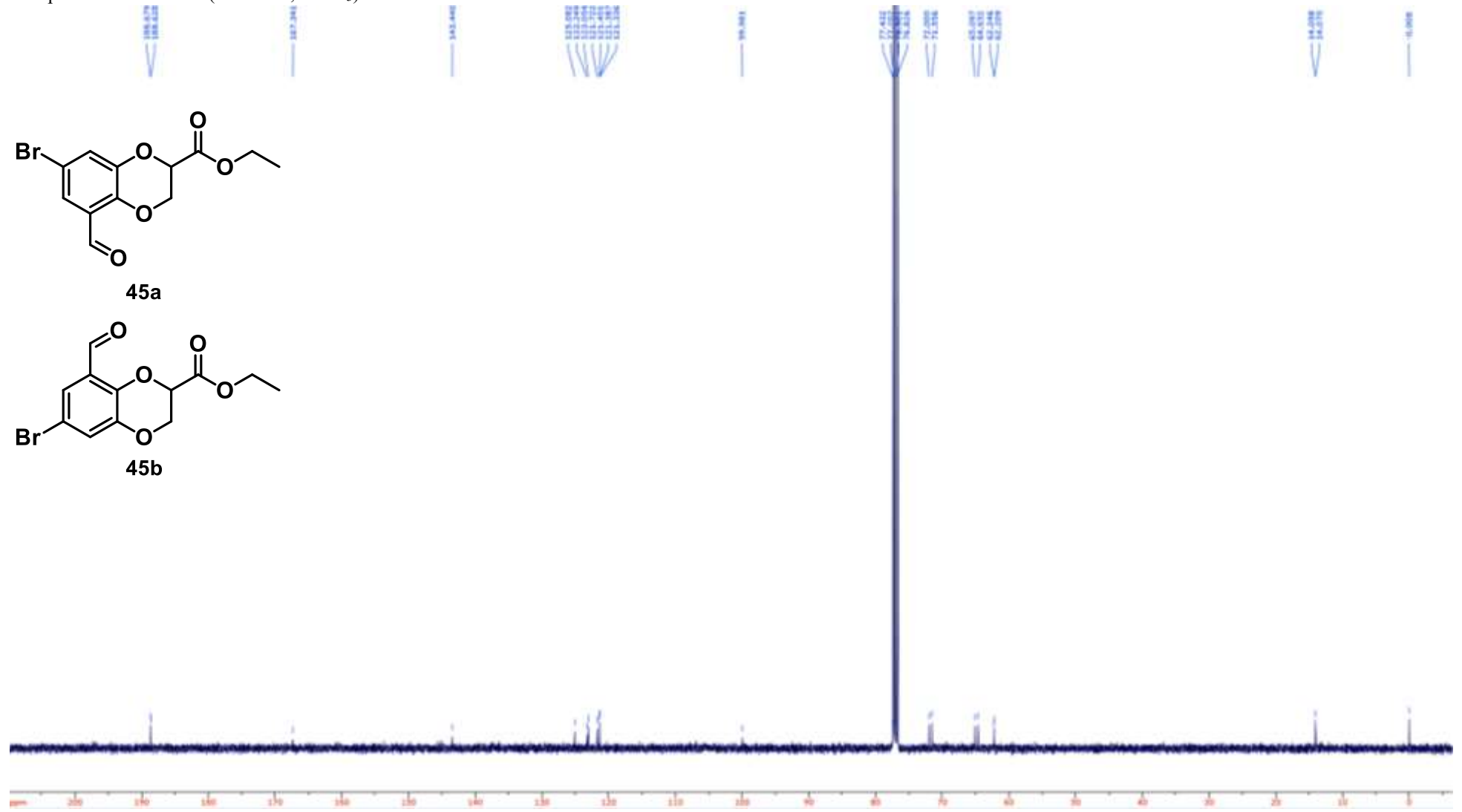
Compound **45** ^{13}C NMR (100 MHz, CDCl_3)



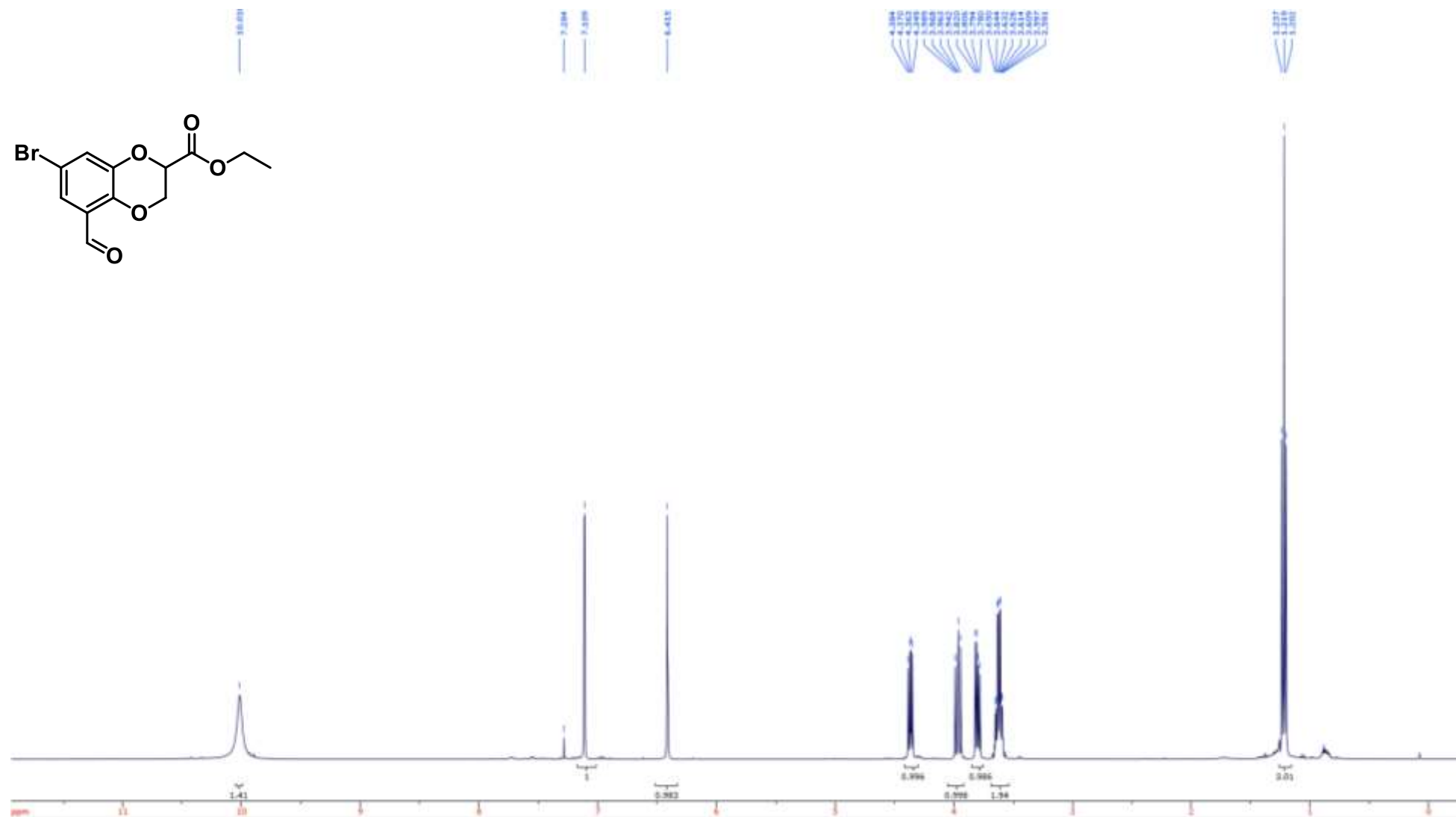
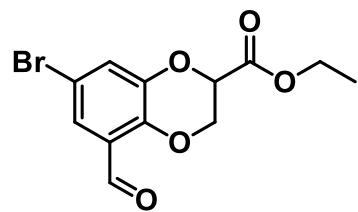
45a



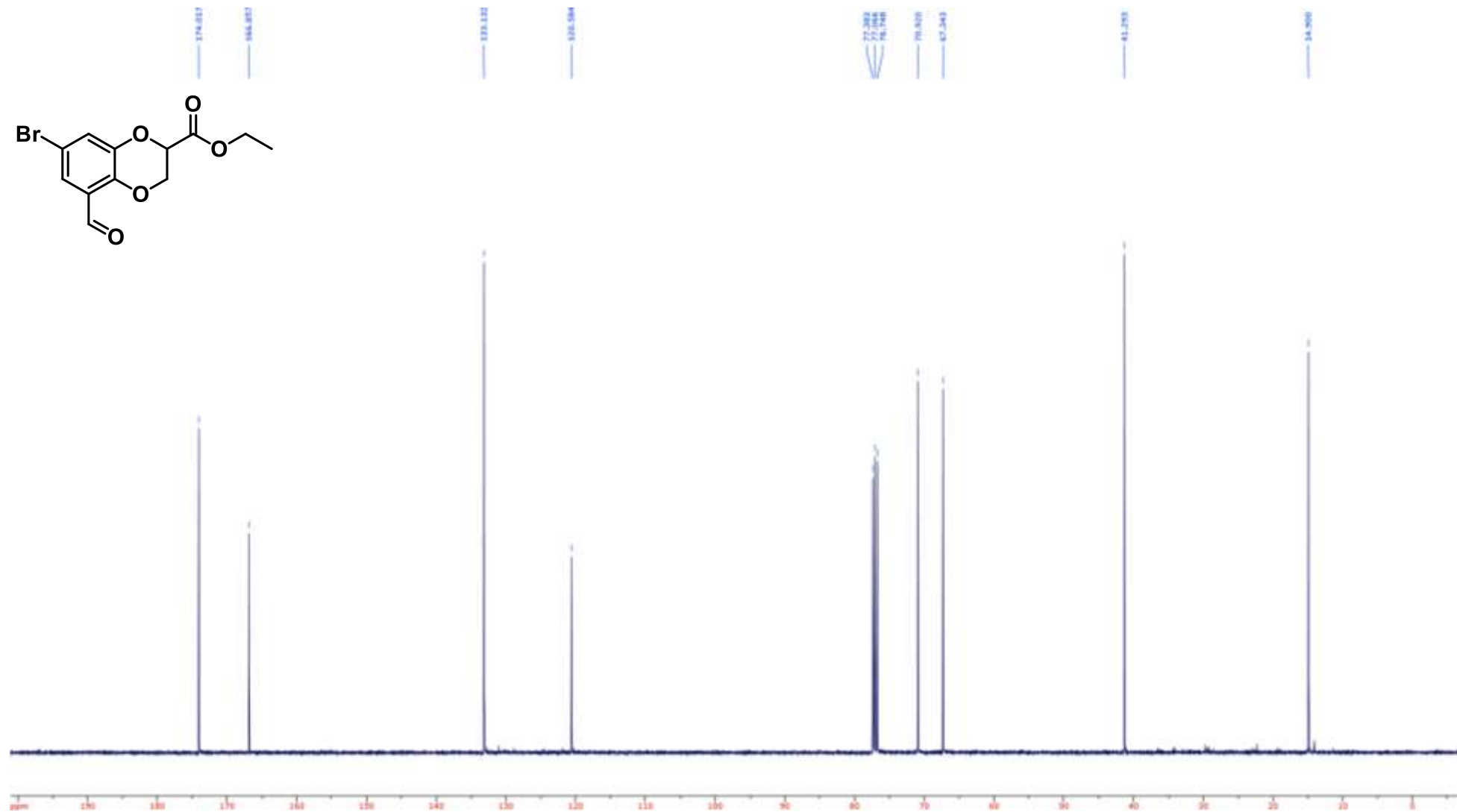
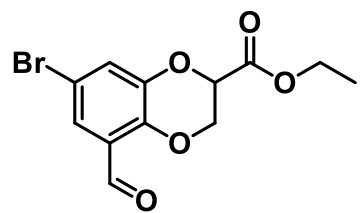
45b



Compound **45a** ^1H NMR (400 MHz, CDCl_3)



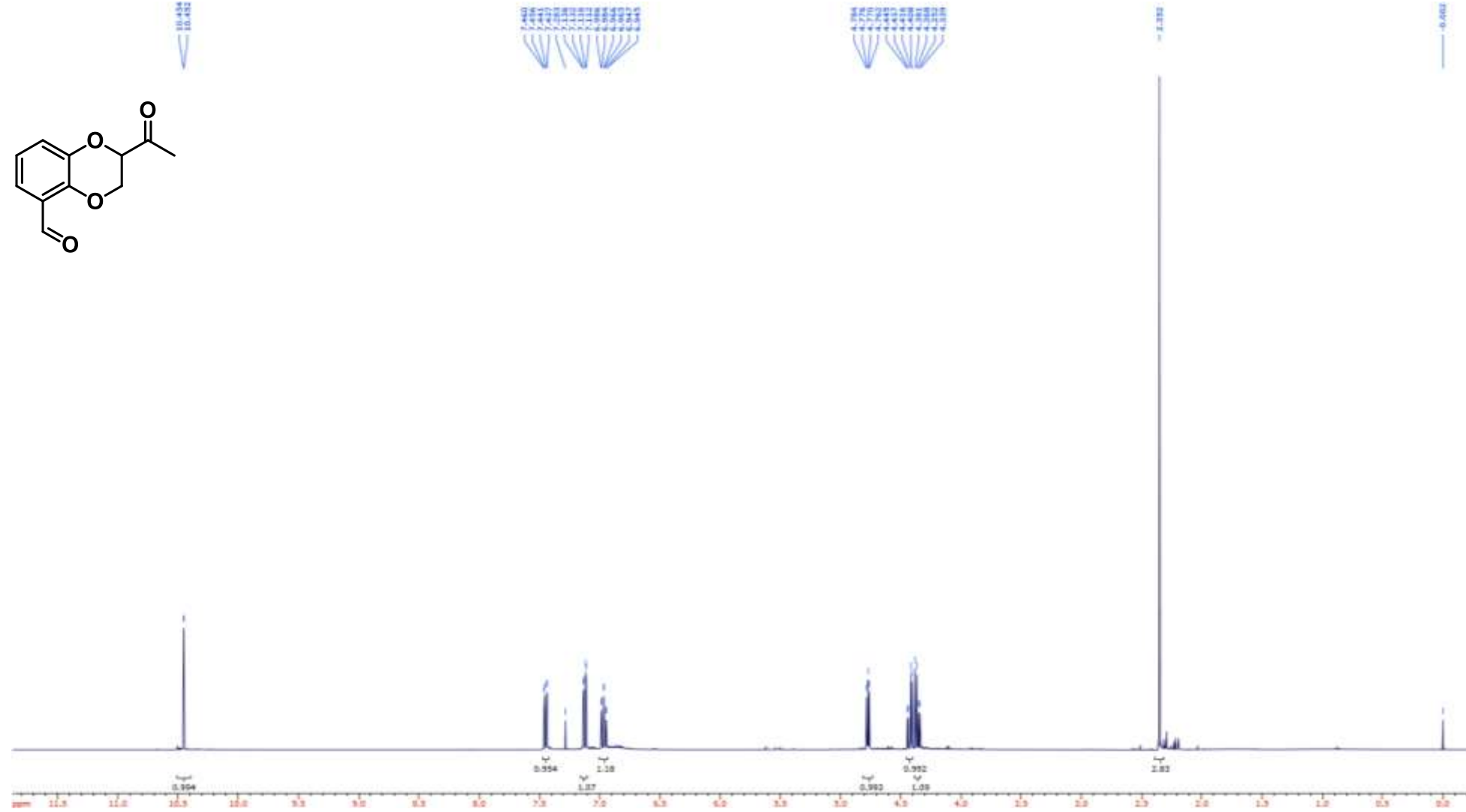
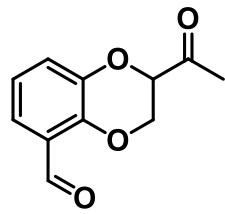
Compound **45a** ^{13}C NMR (100 MHz, CDCl_3)



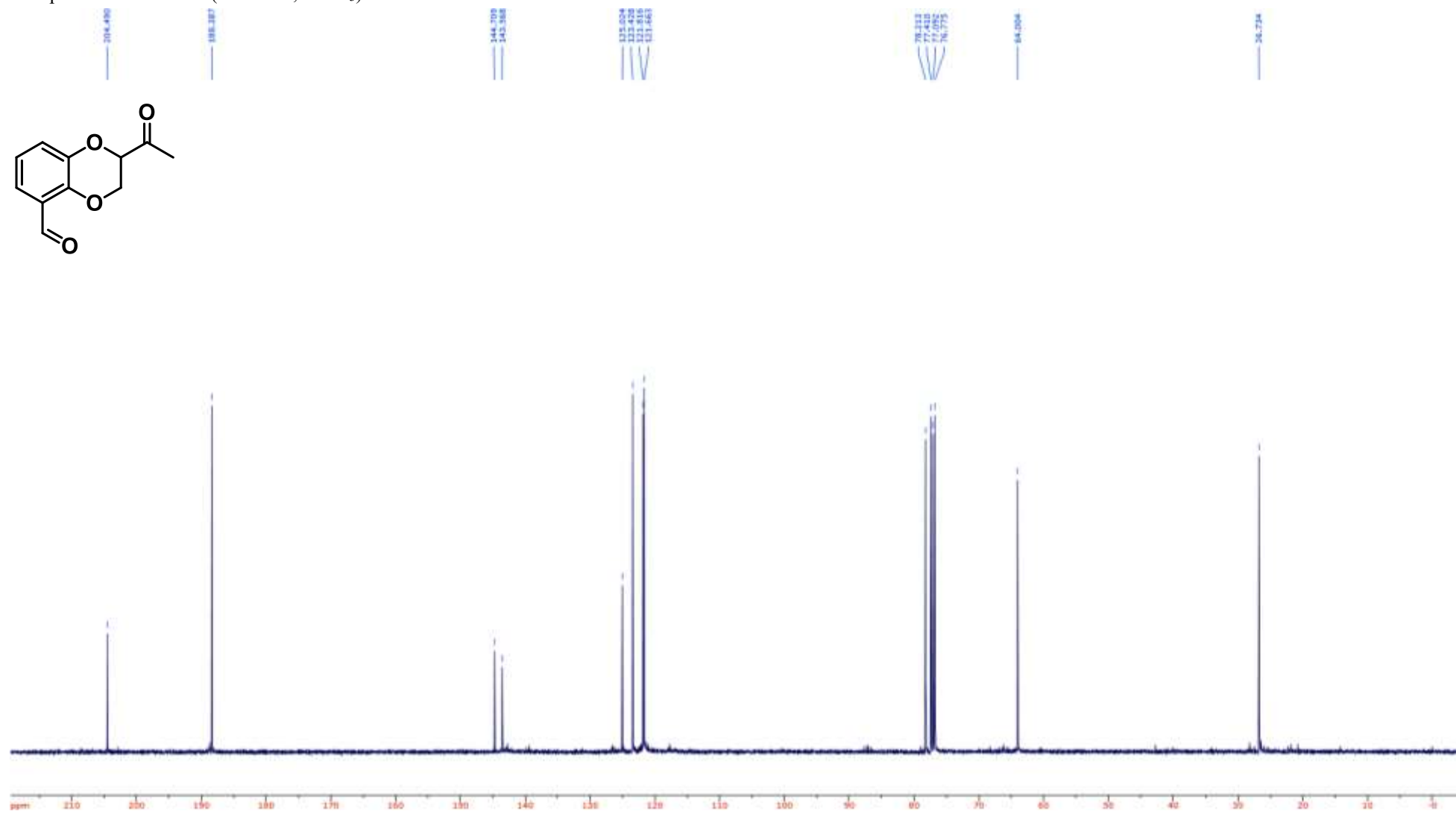
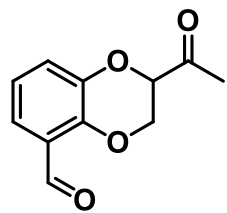
Compound **45a** HMBC (400/100 MHz, CDCl₃)



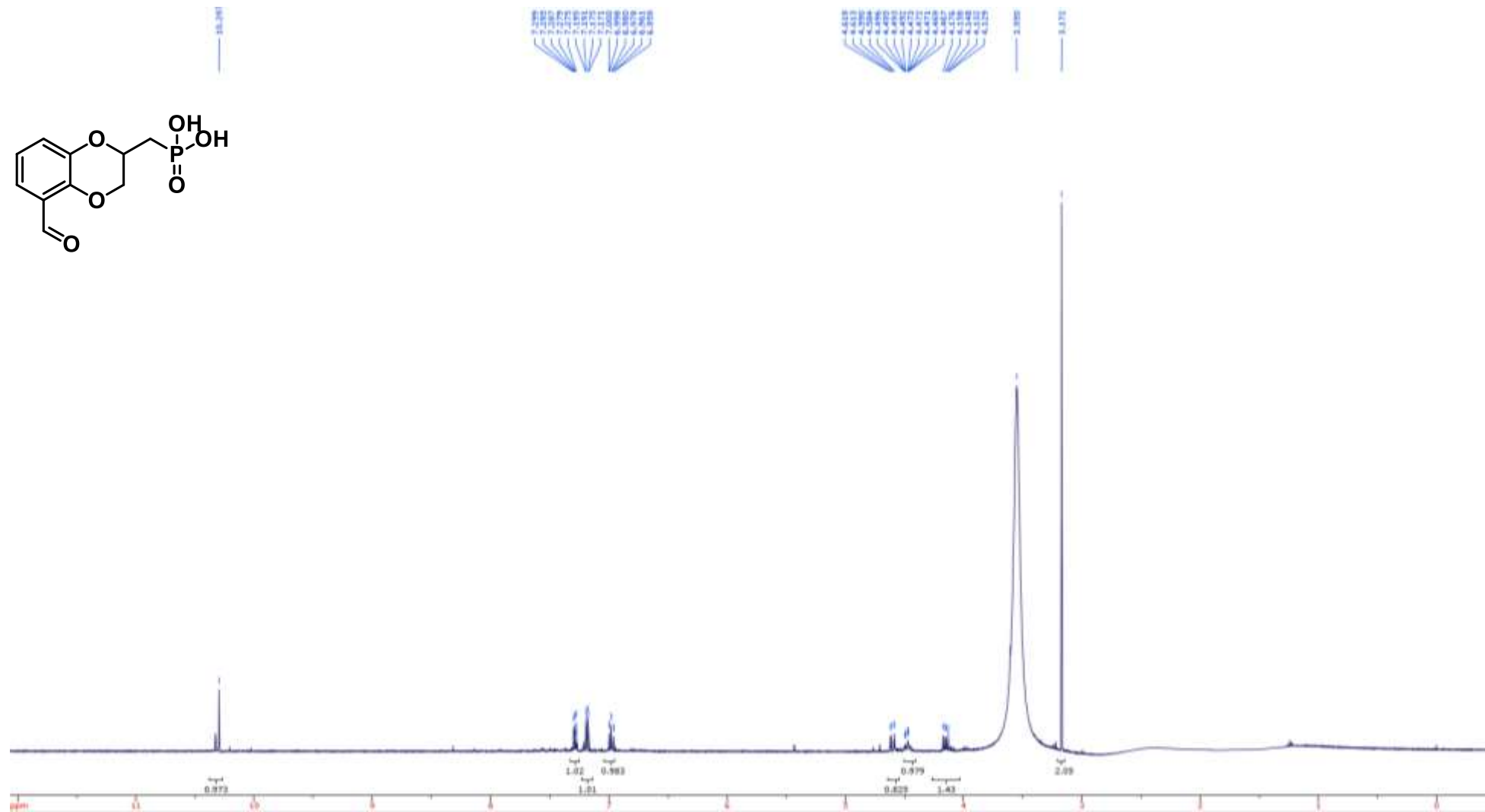
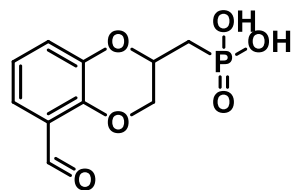
Compound **46** ^1H NMR (400 MHz, CDCl_3)



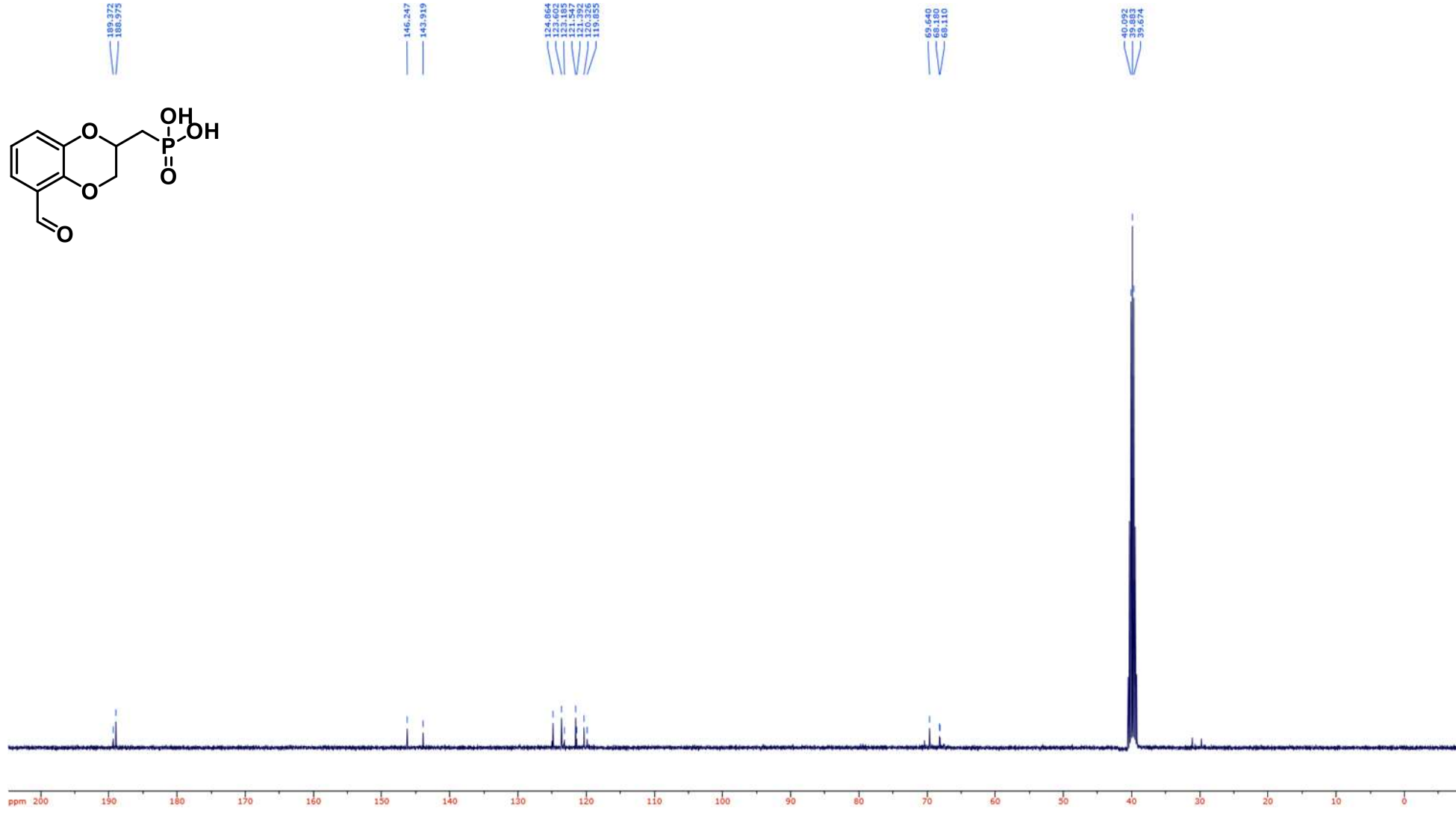
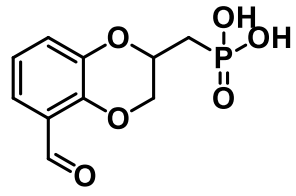
Compound **46** ^{13}C NMR (100 MHz, CDCl_3)



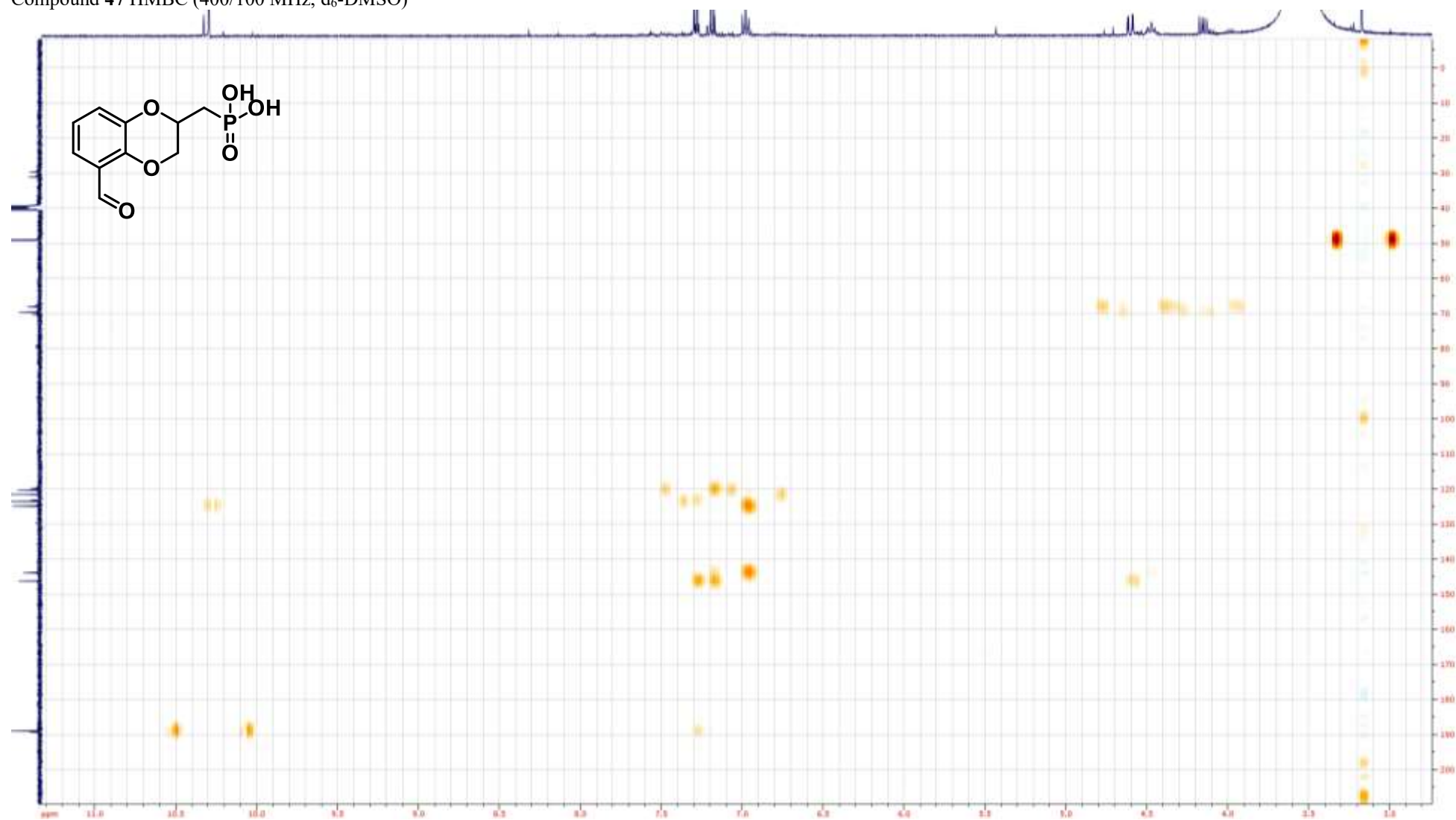
Compound 47 ^1H NMR (400 MHz, $\text{d}_6\text{-DMSO}$)



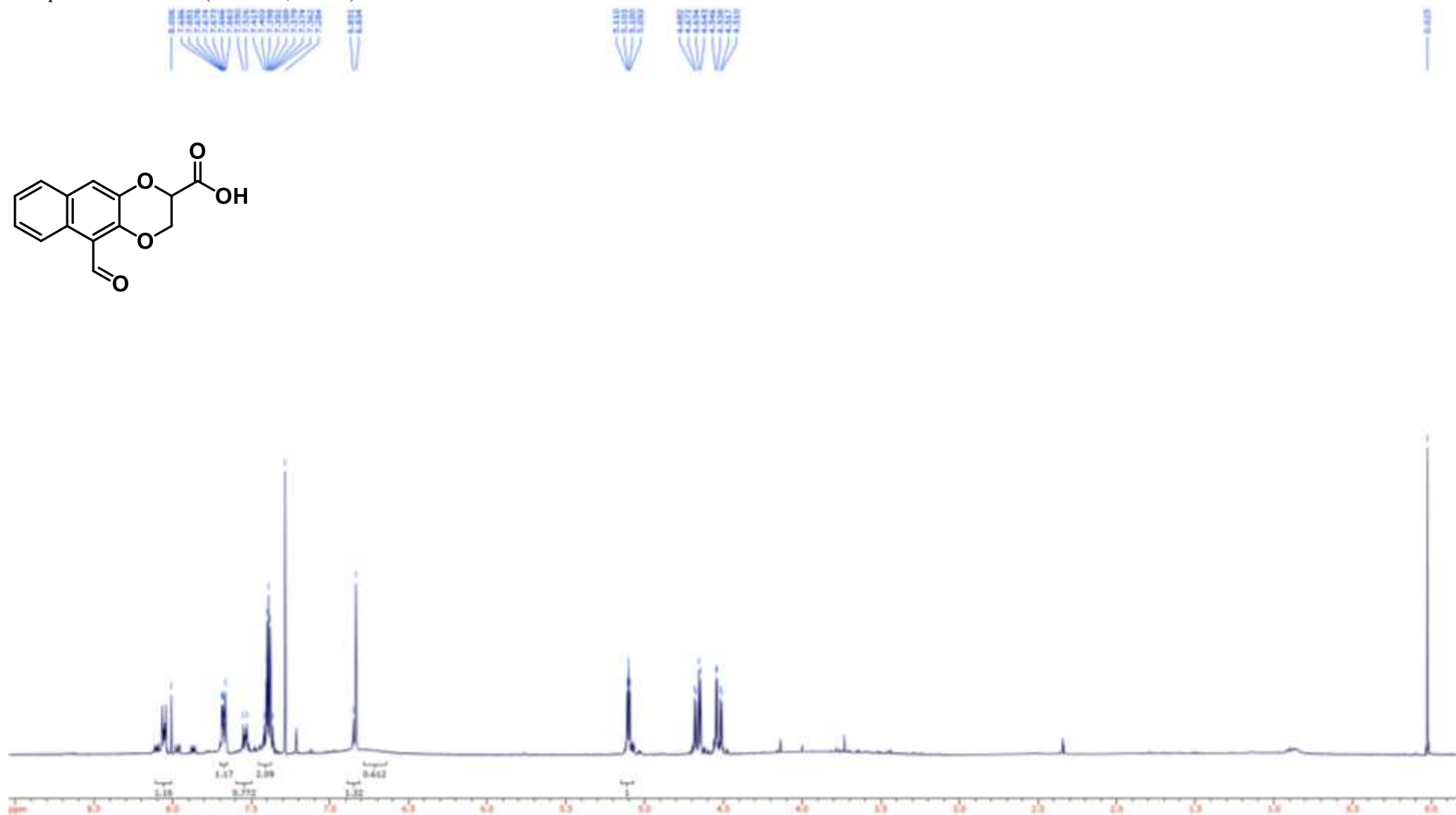
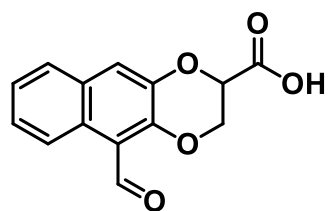
Compound **47** ^{13}C NMR (100 MHz, $\text{d}_6\text{-DMSO}$)



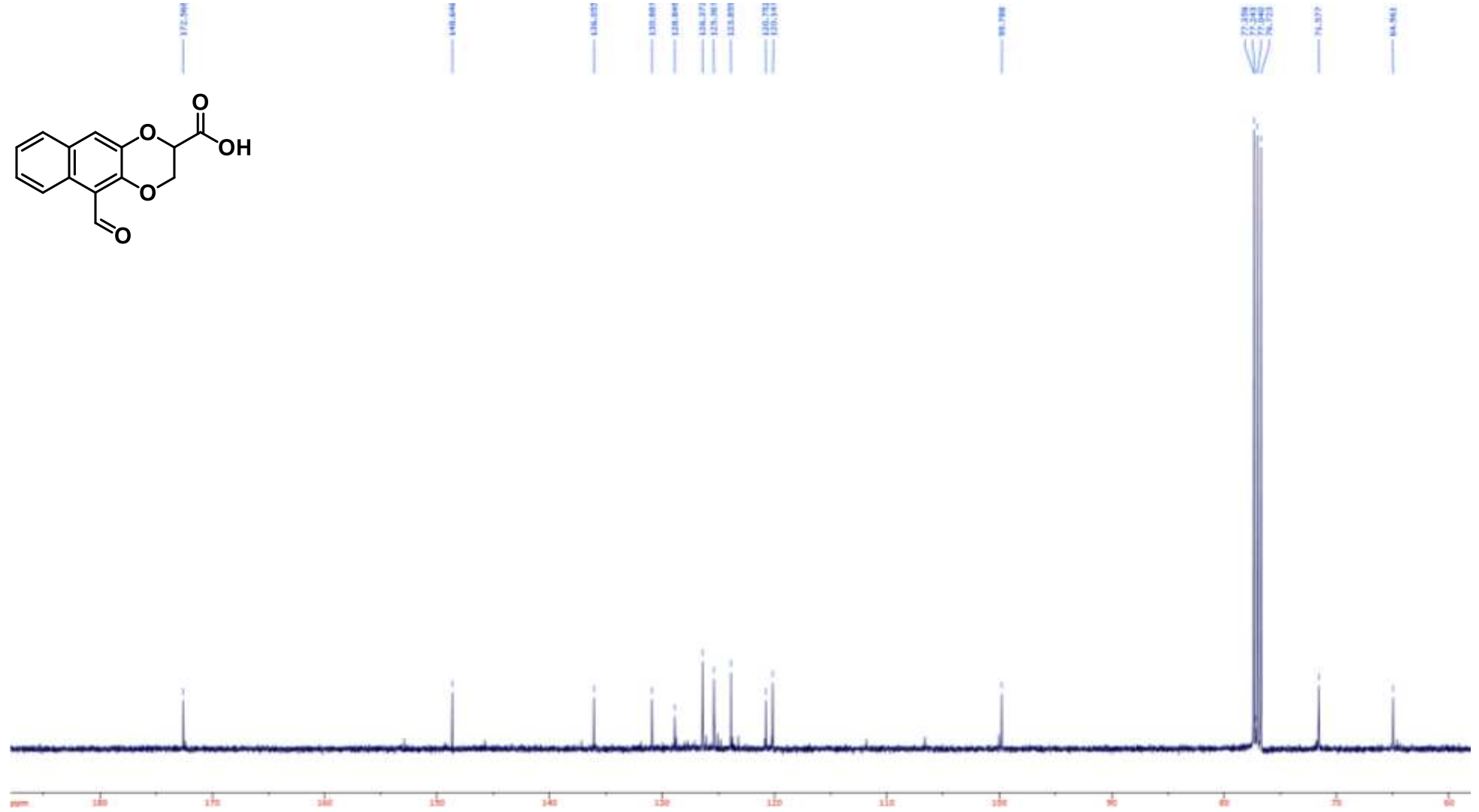
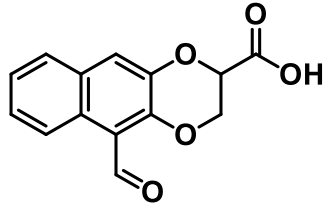
Compound 47 HMBC (400/100 MHz, d₆-DMSO)



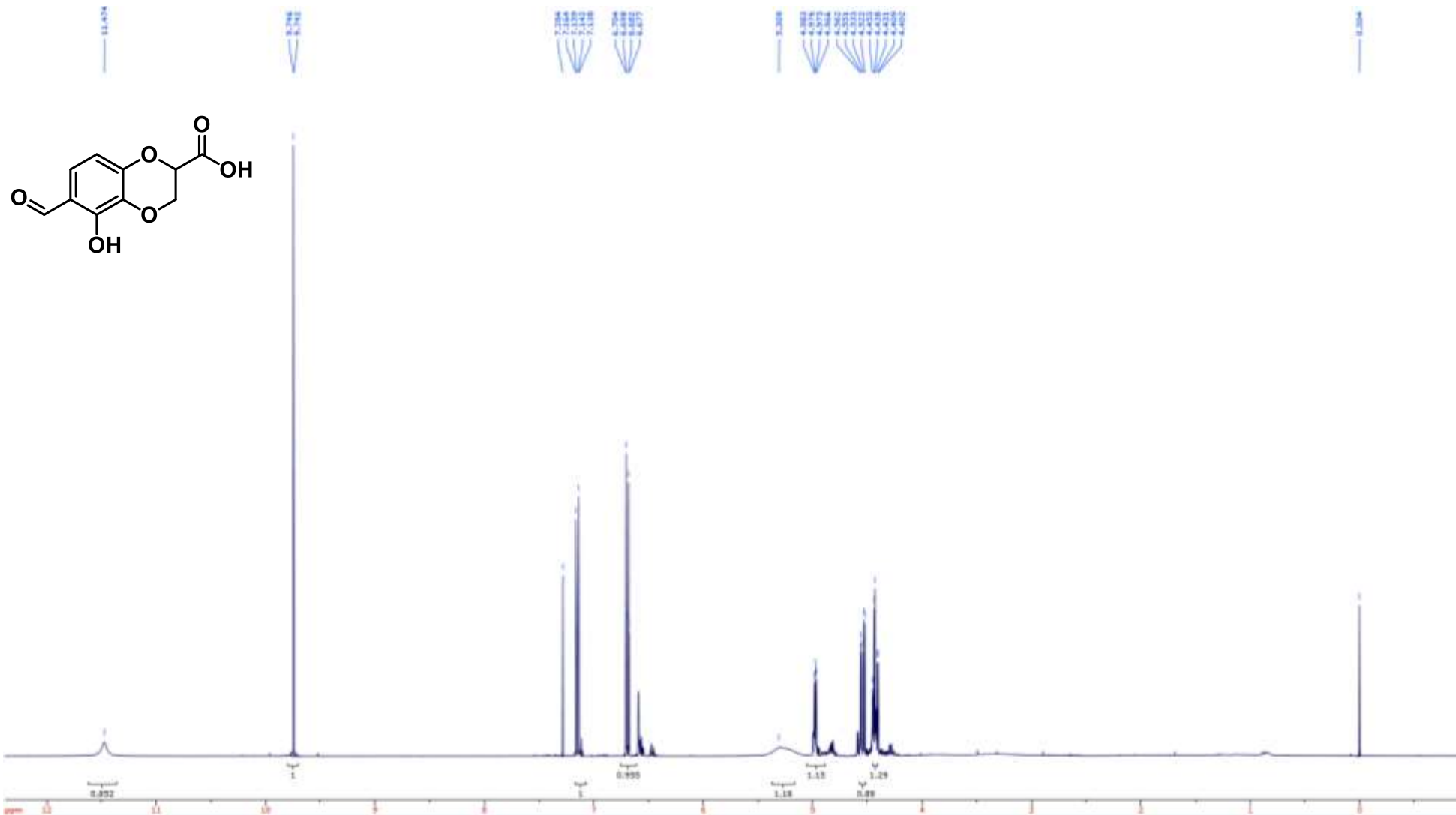
Compound **48** ^1H NMR (400 MHz, CDCl_3)



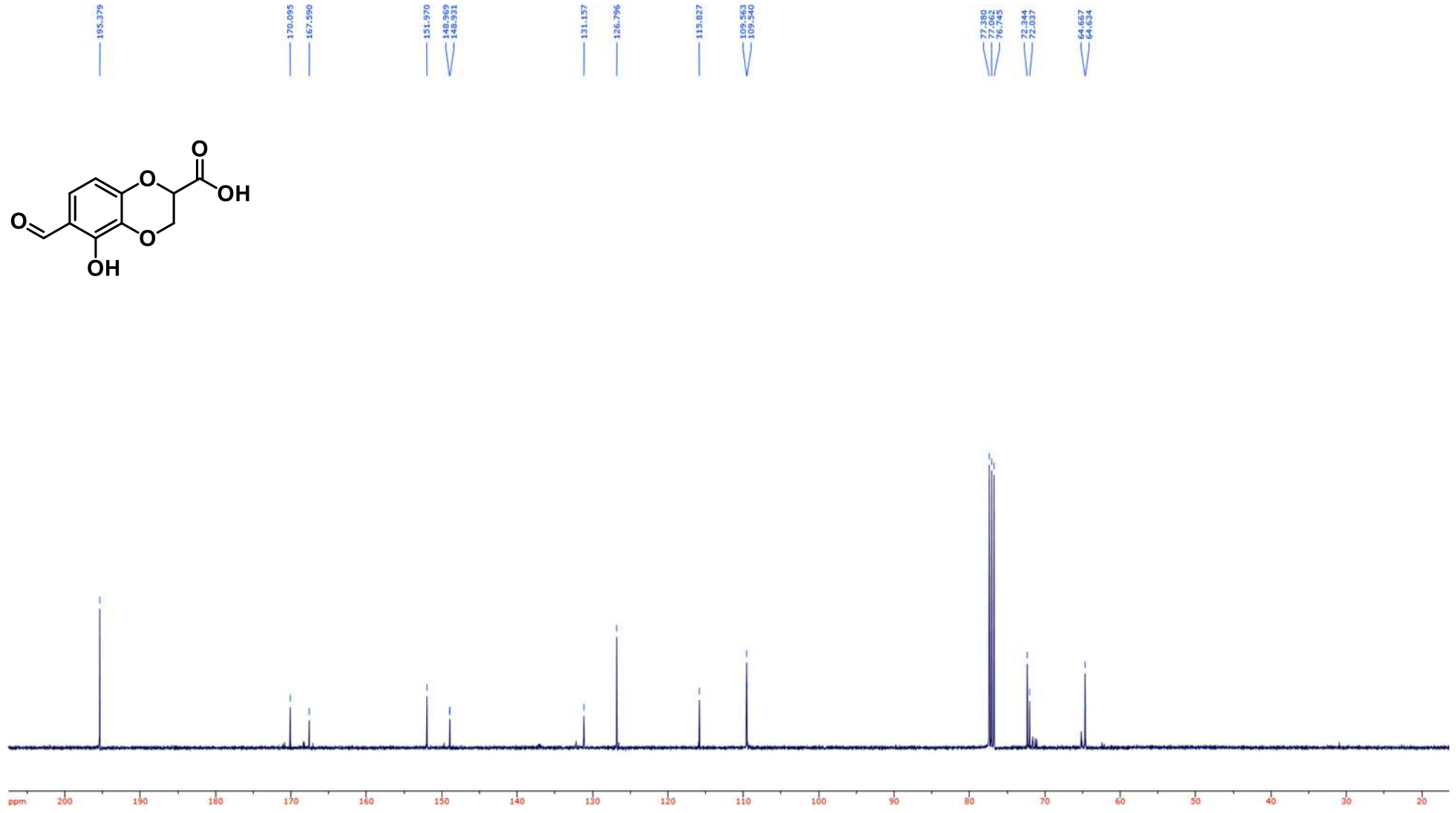
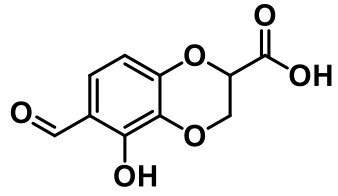
Compound **48** ^{13}C NMR (100 MHz, CDCl_3)



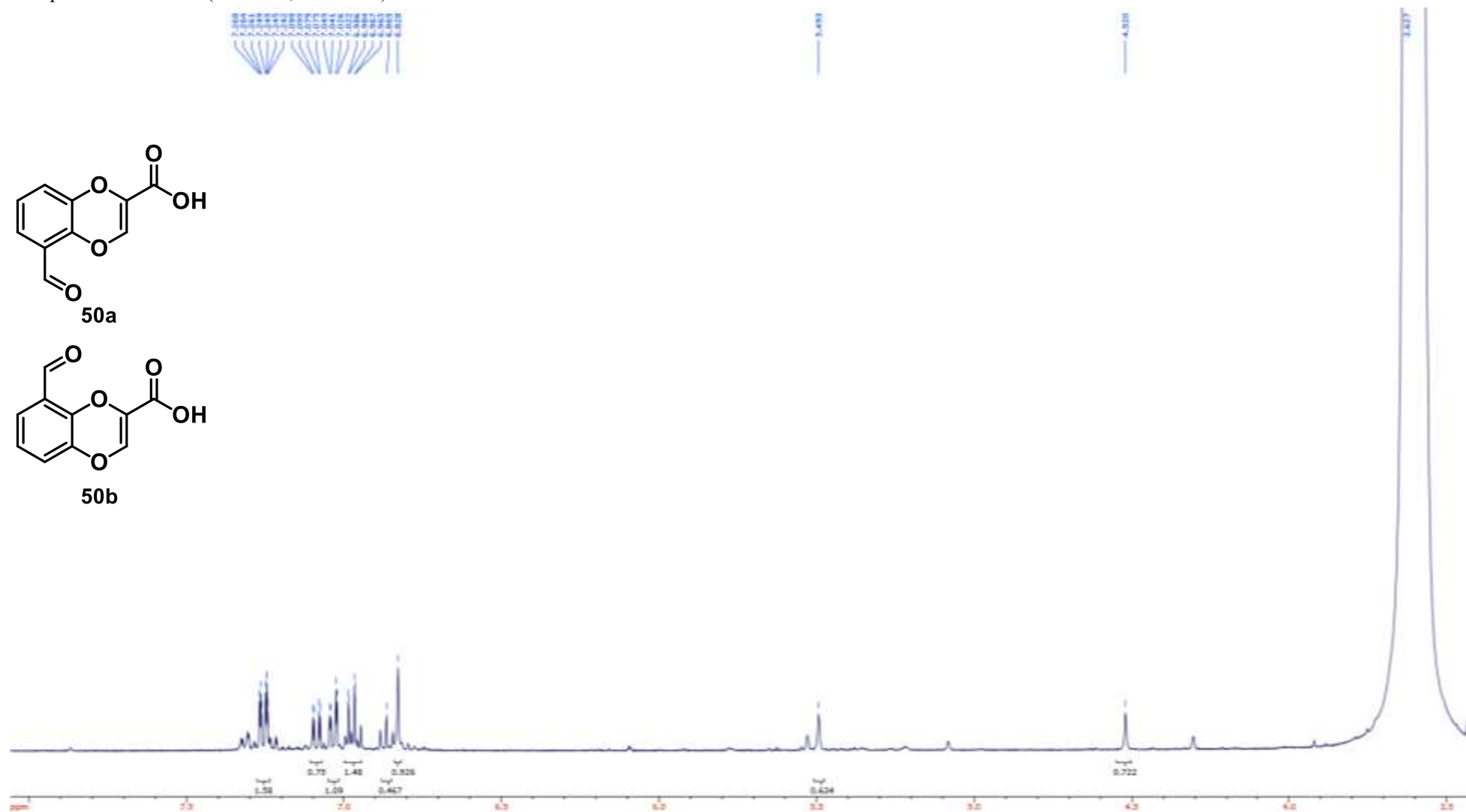
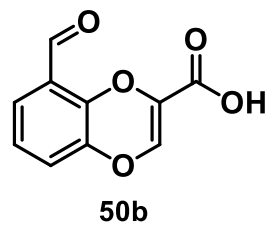
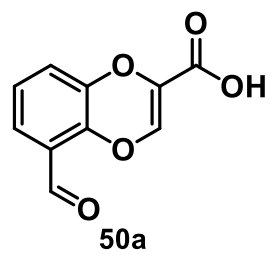
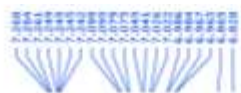
Compound **49** ^1H NMR (400 MHz, CDCl_3)



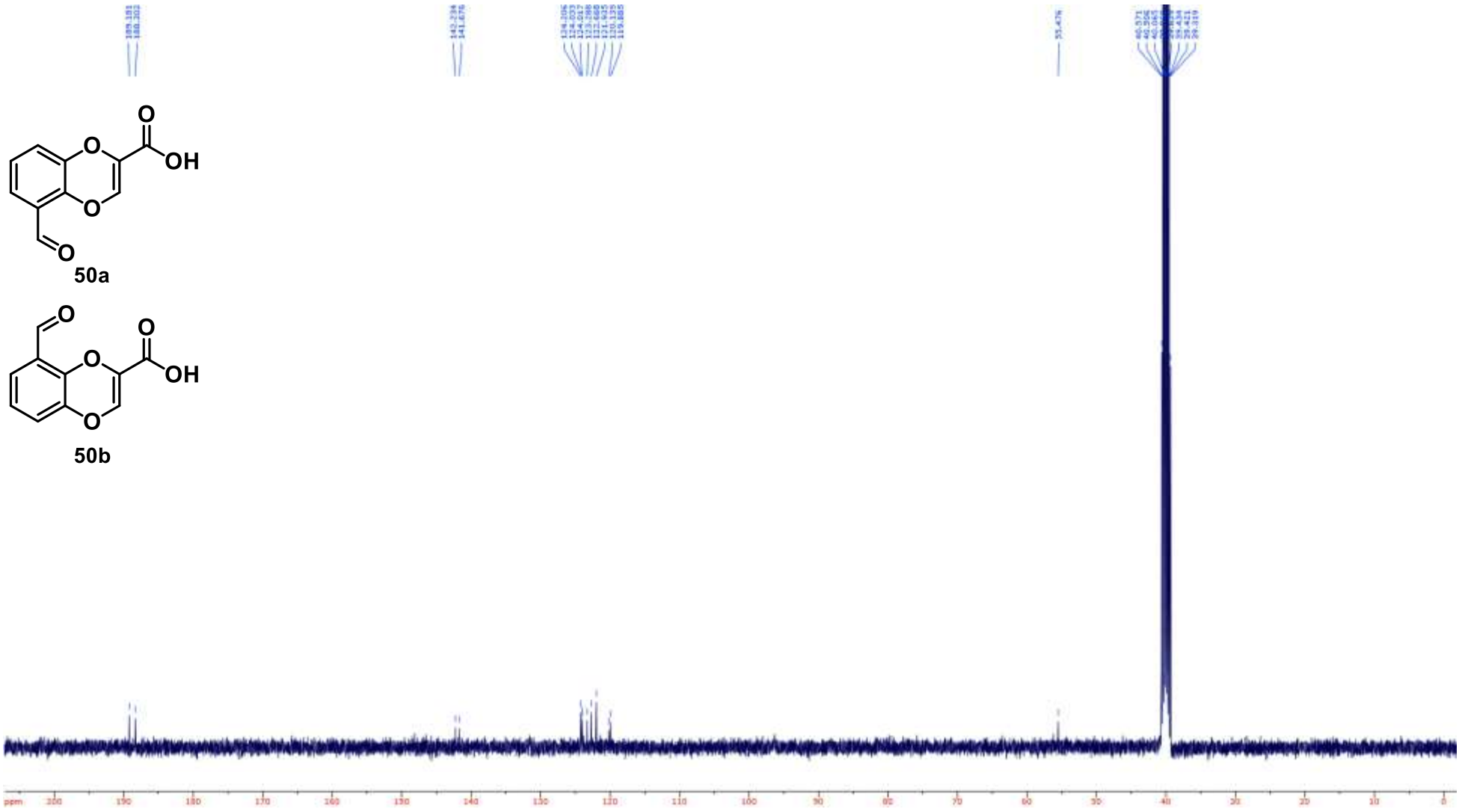
Compound **49** ^{13}C NMR (100 MHz, CDCl_3)



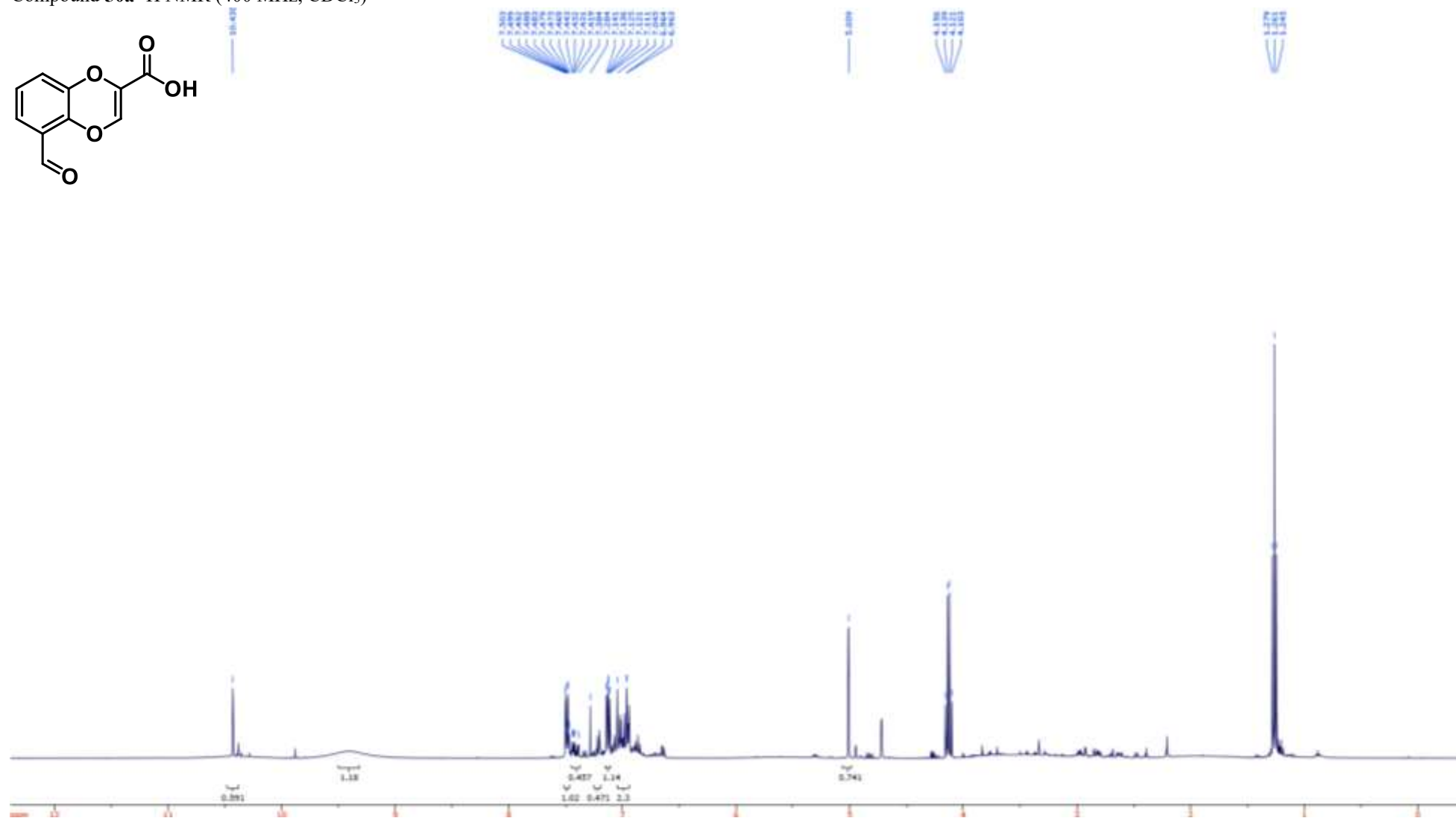
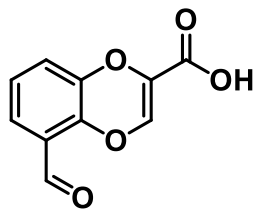
Compound **50** ^1H NMR (400 MHz, $\text{d}_6\text{-DMSO}$)



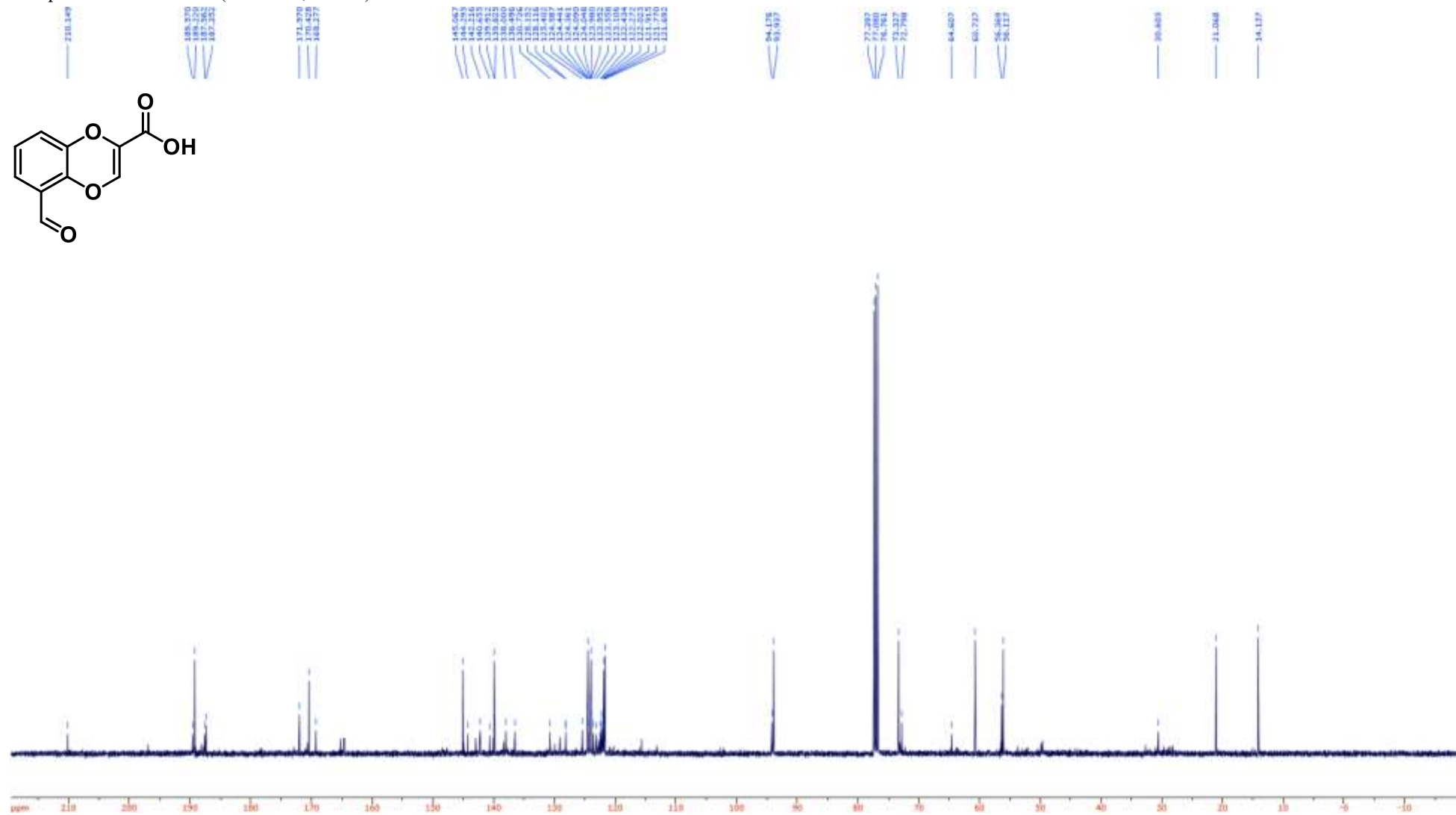
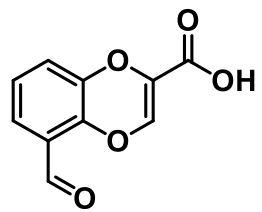
Compound **50** ^{13}C NMR (100 MHz, $\text{d}_6\text{-DMSO}$)



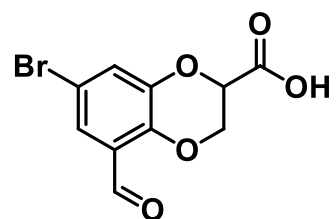
Compound **50a** ^1H NMR (400 MHz, CDCl_3)



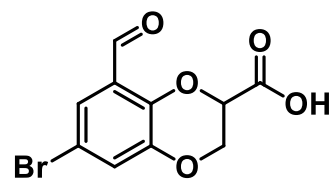
Compound **50a** ^{13}C NMR (100 MHz, CDCl_3)



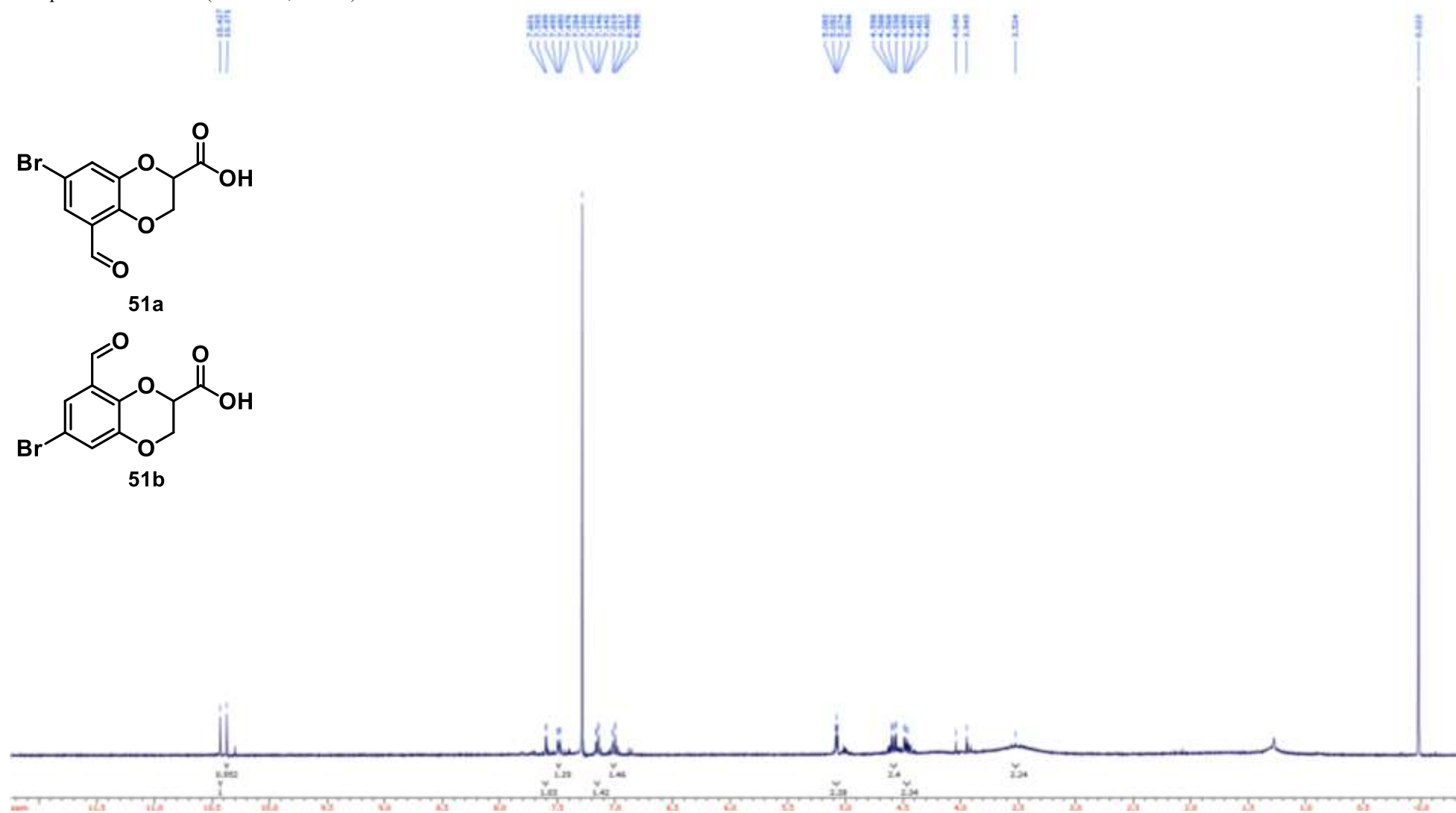
Compound **51** ^1H NMR (400 MHz, CDCl_3)



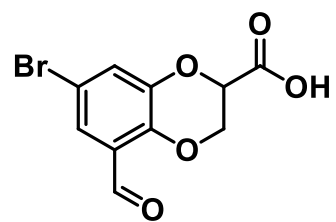
51a



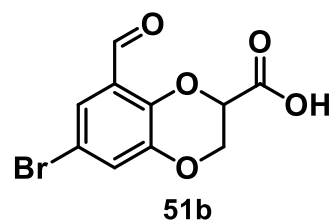
51b



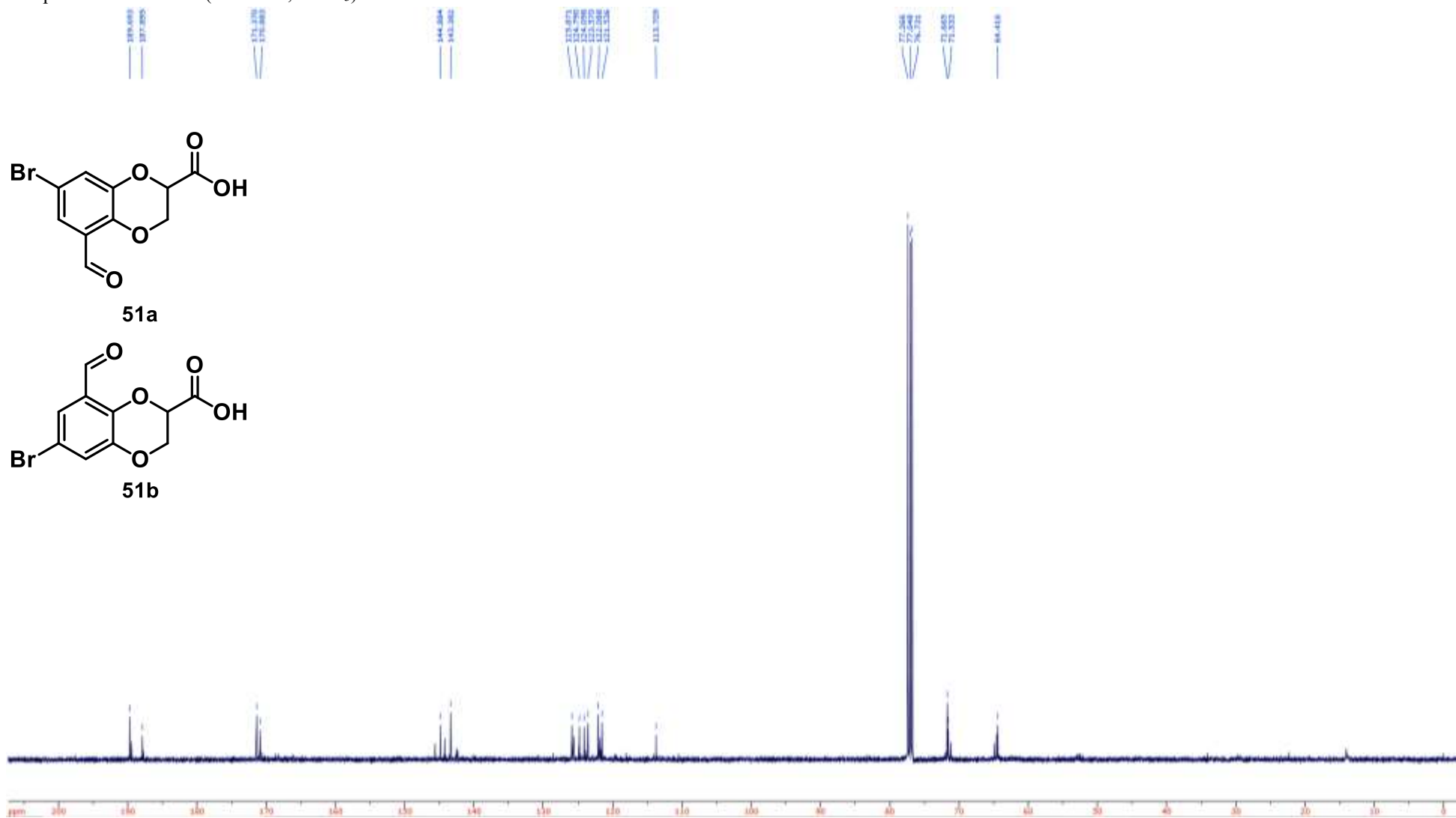
Compound **51** ¹³C NMR (100 MHz, CDCl₃)



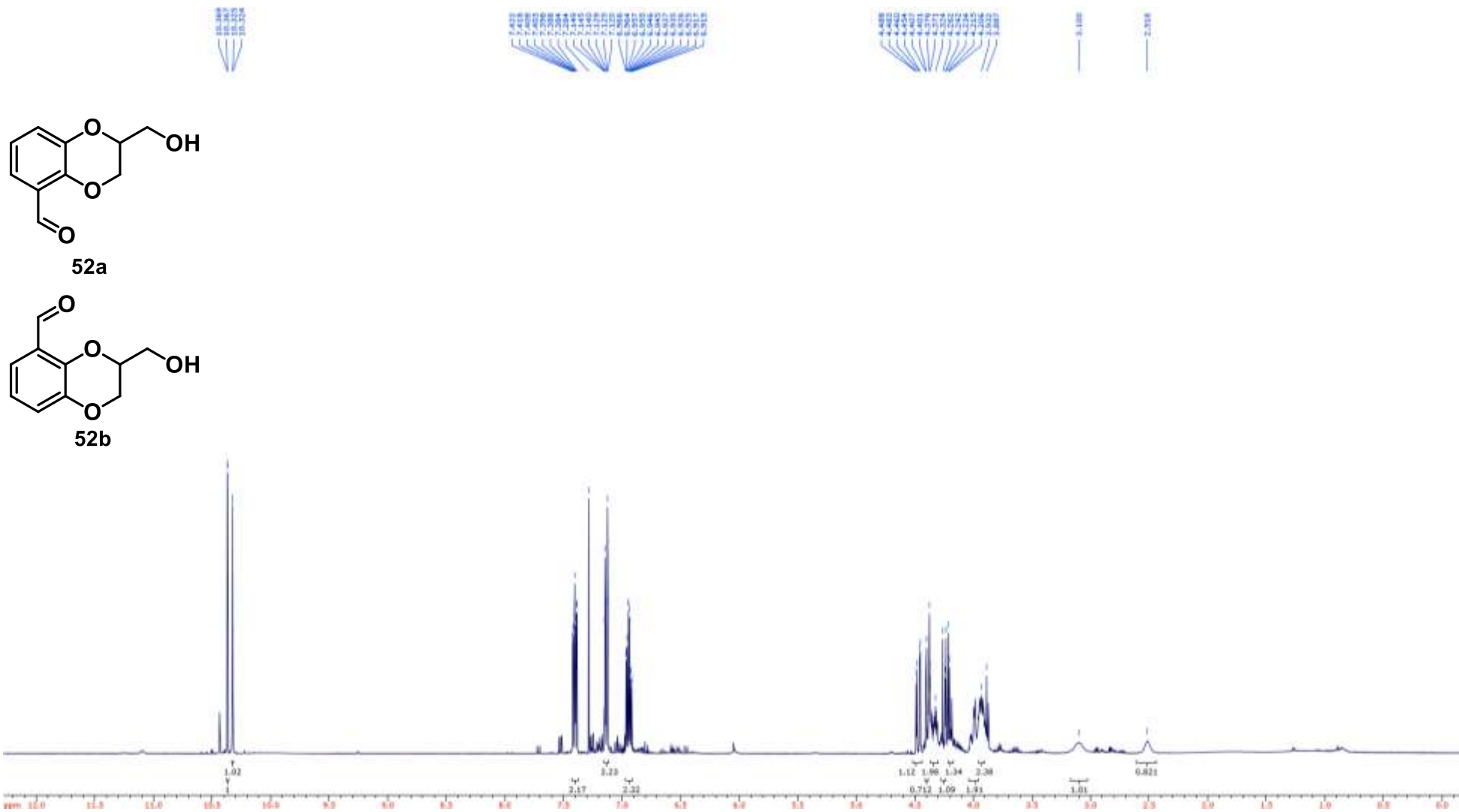
51a



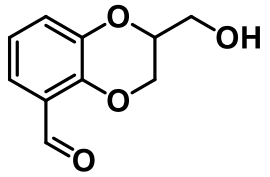
51b



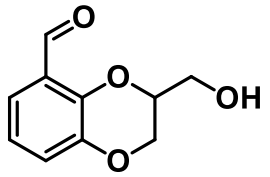
Compound **52** ^1H NMR (400 MHz, CDCl_3)



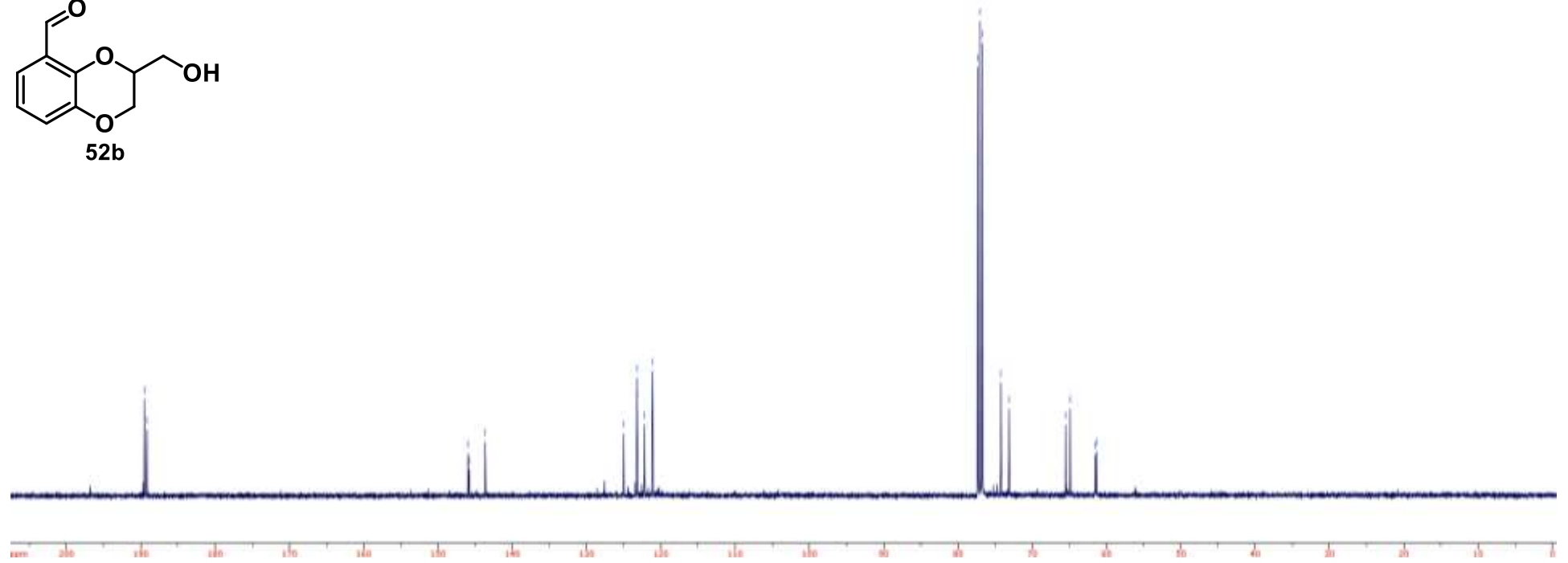
Compound **52** ^{13}C NMR (100 MHz, CDCl_3)



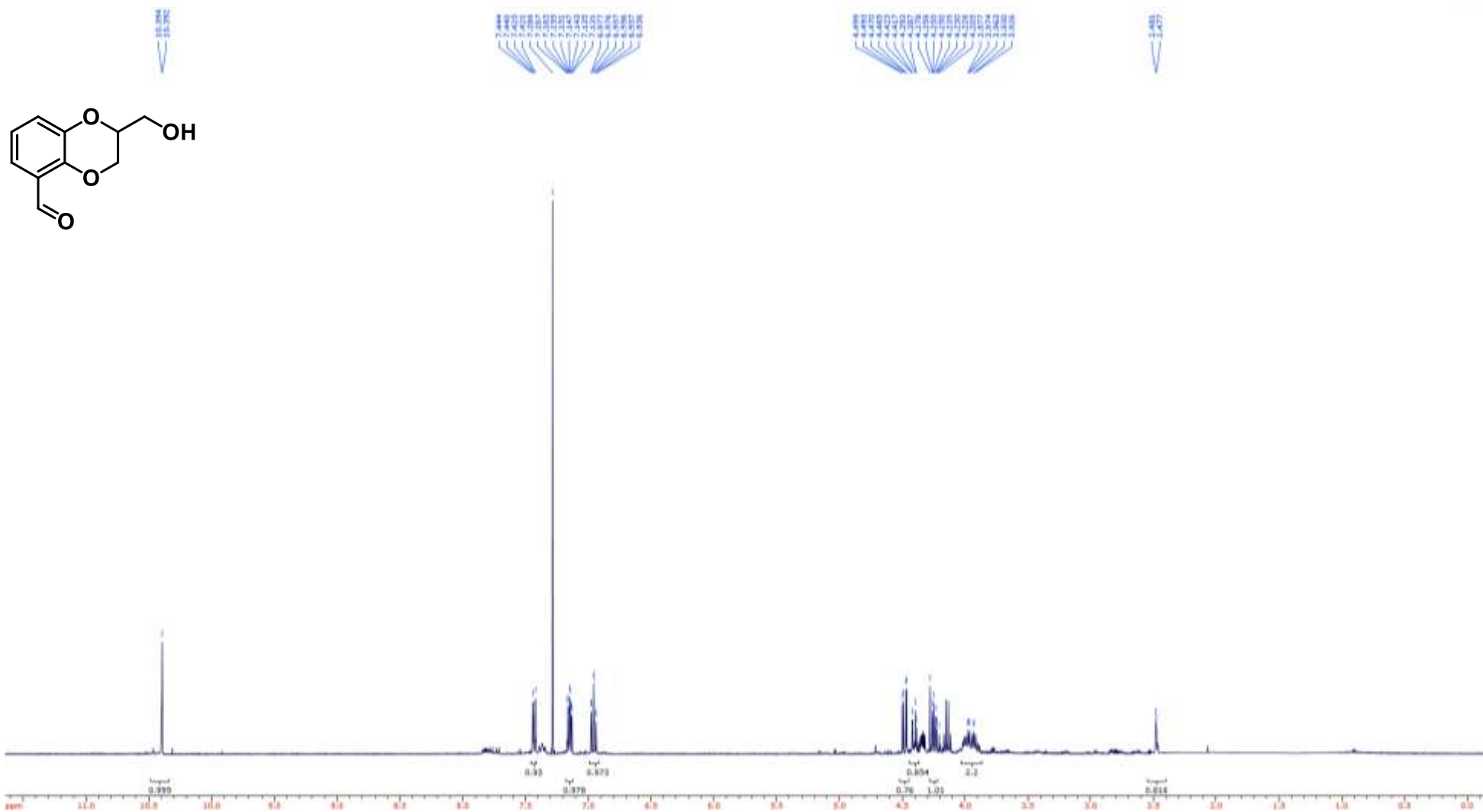
52a



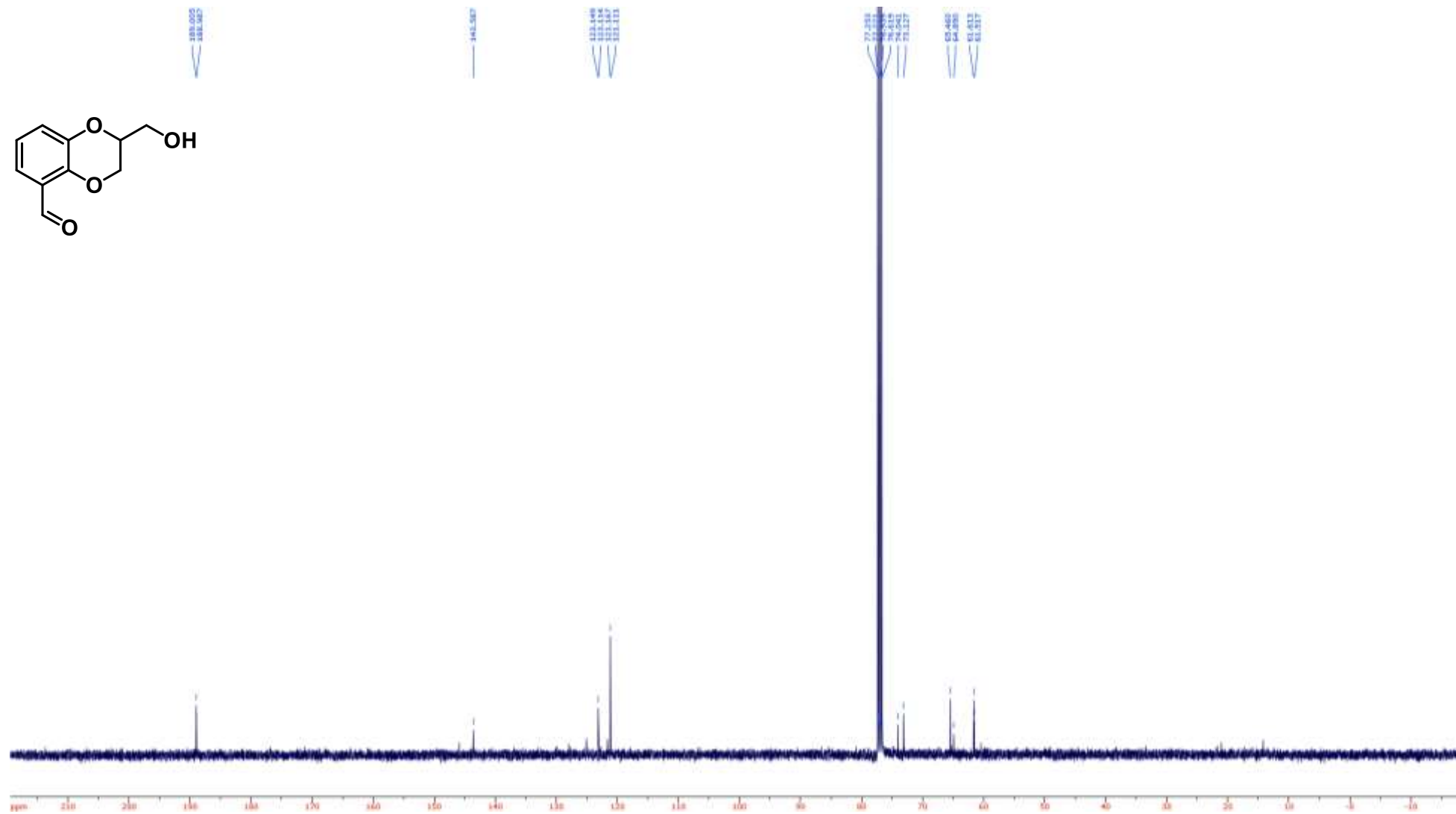
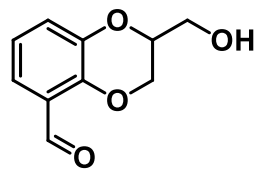
52b



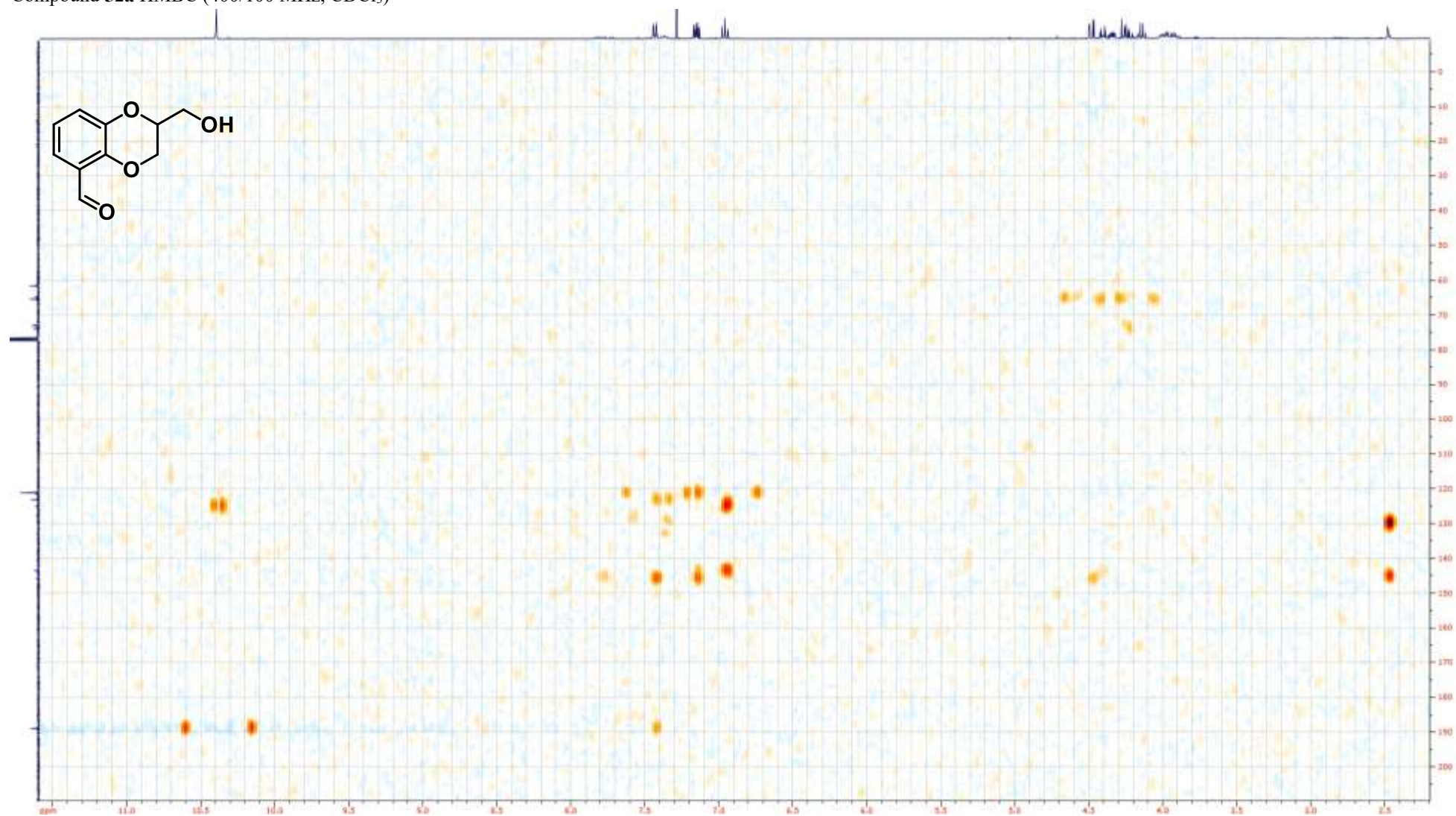
Compound **52a** ^1H NMR (400 MHz, CDCl_3)



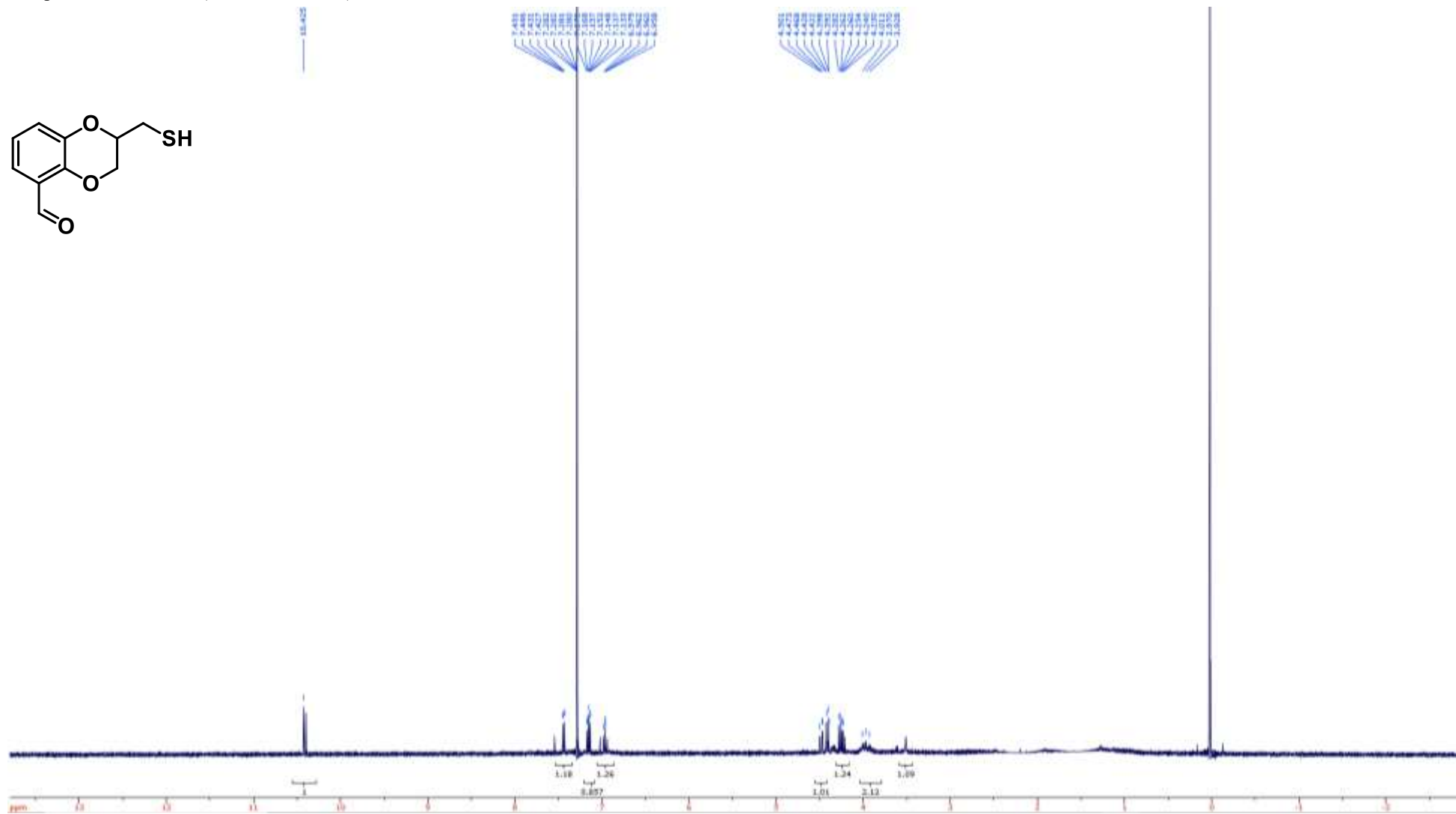
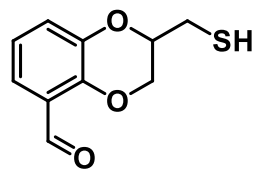
Compound **52a** ^{13}C NMR (100 MHz, CDCl_3)



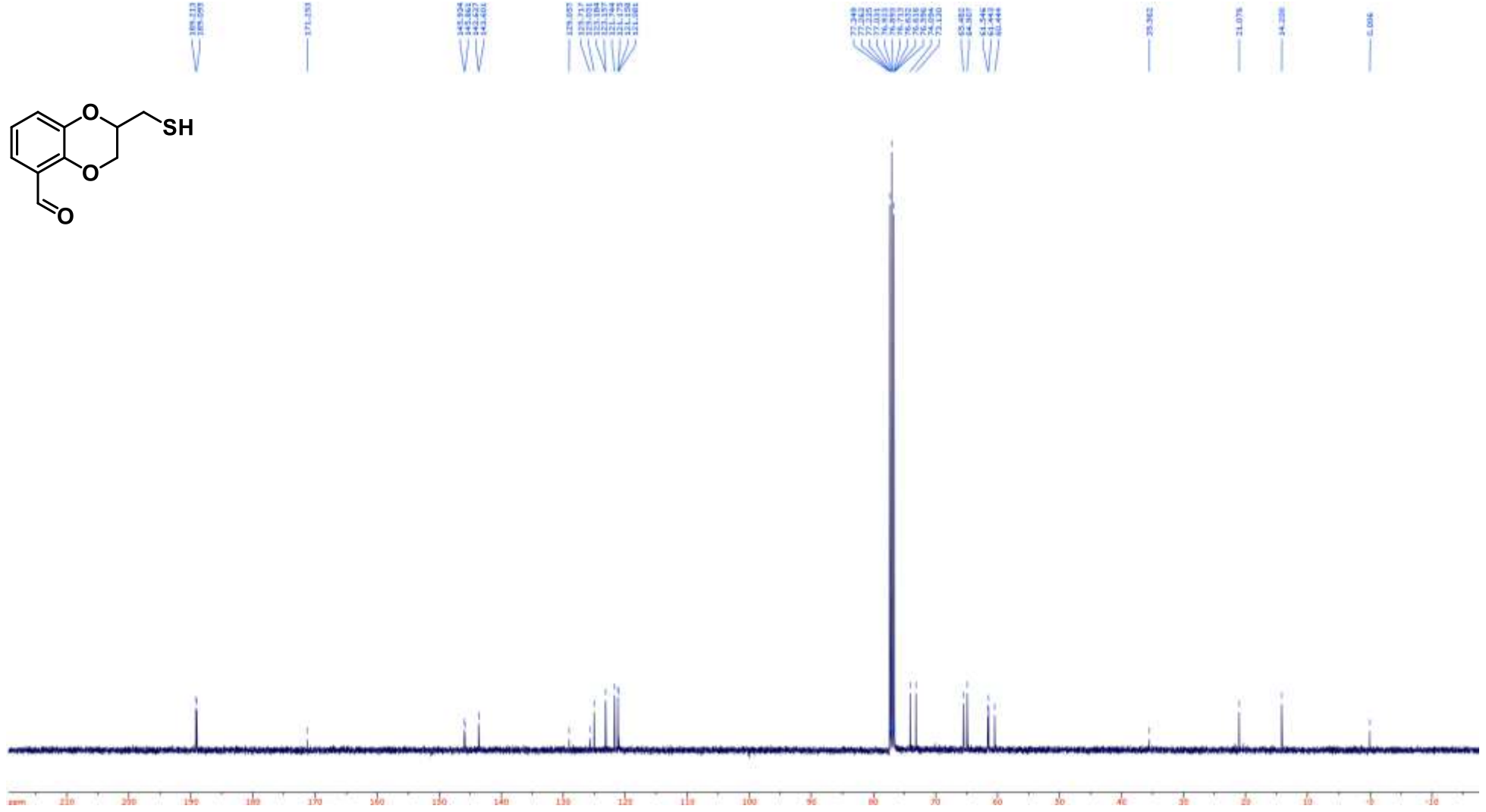
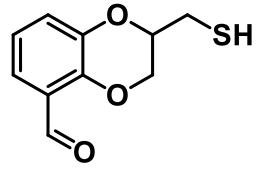
Compound **52a** HMBC (400/100 MHz, CDCl₃)



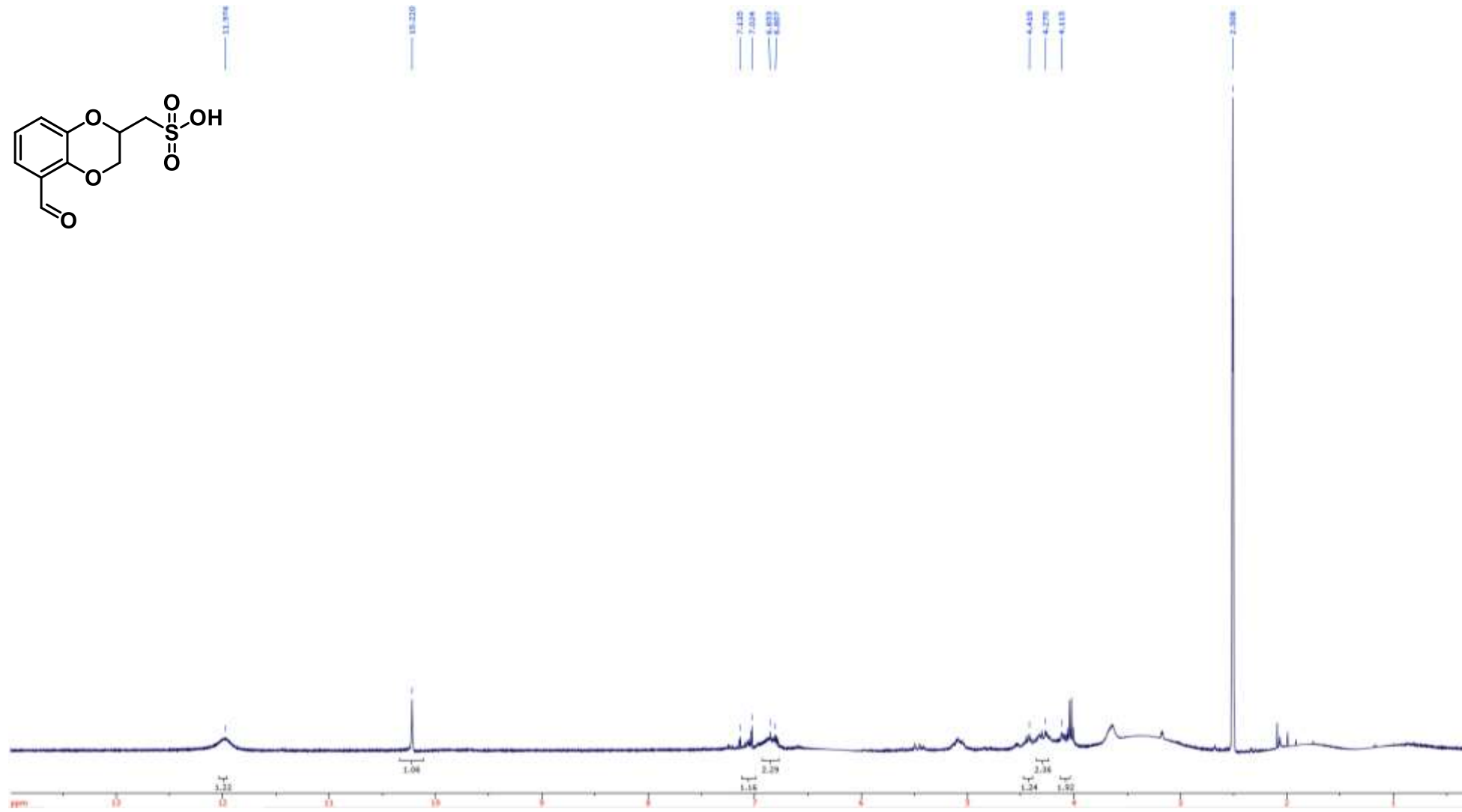
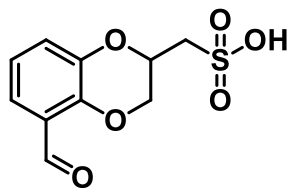
Compound **53** ^1H NMR (400 MHz, CDCl_3)



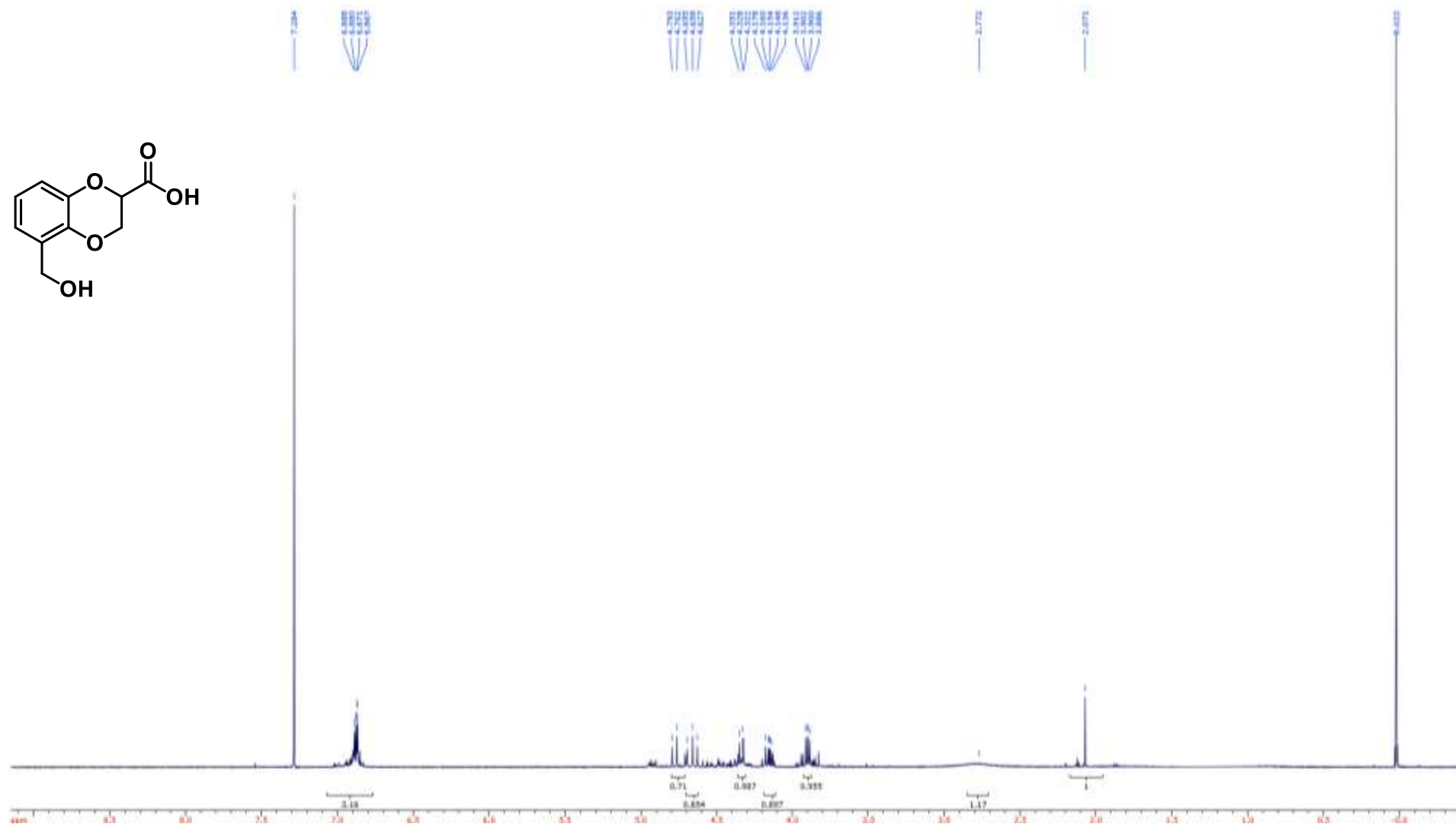
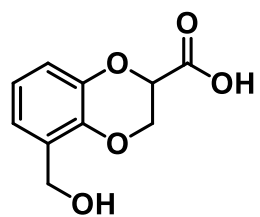
Compound **53** ^{13}C NMR (100 MHz, CDCl_3)



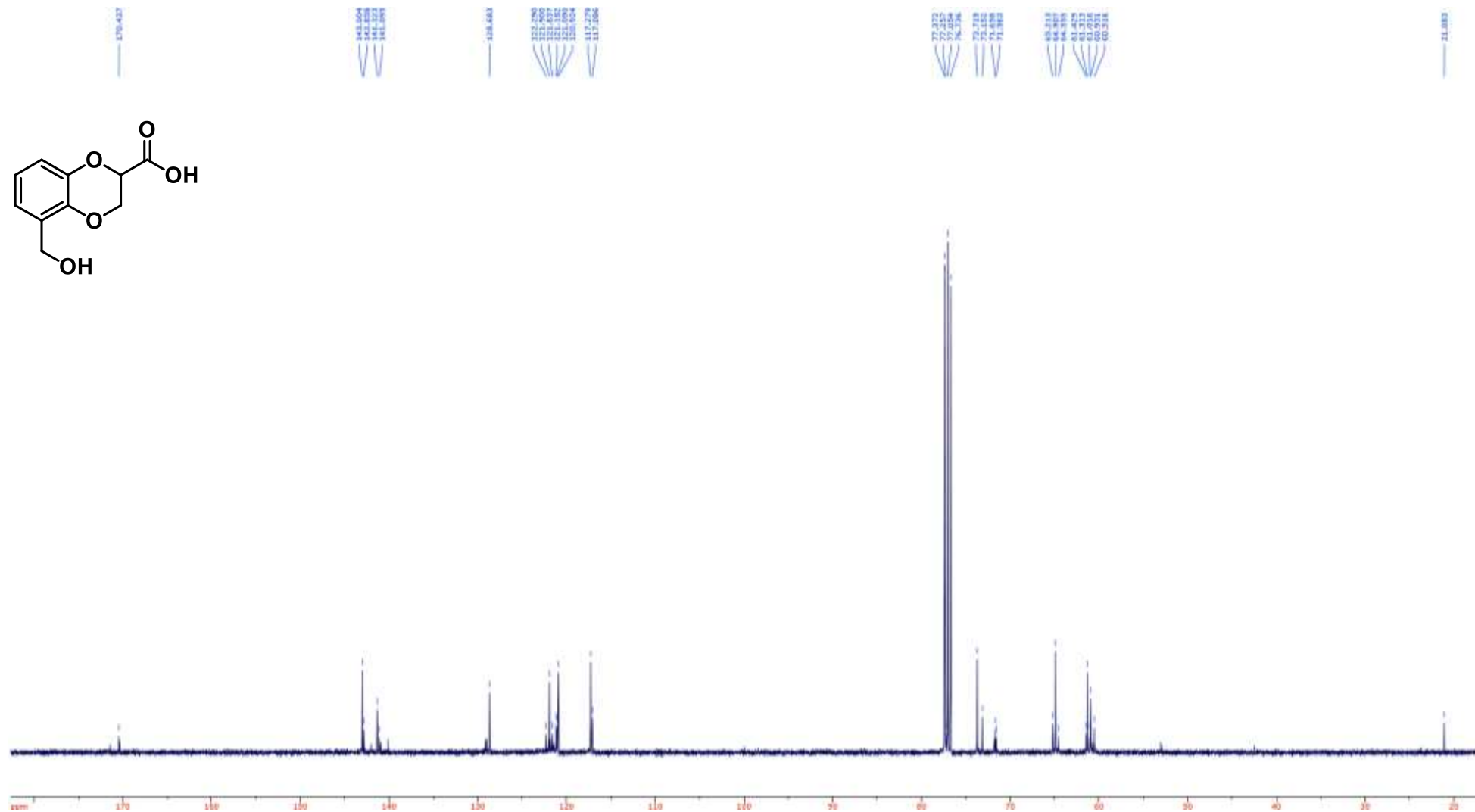
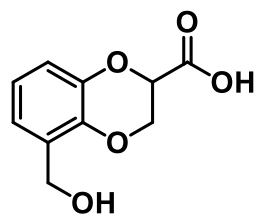
Compound **54** ^1H NMR (400 MHz, CDCl_3)



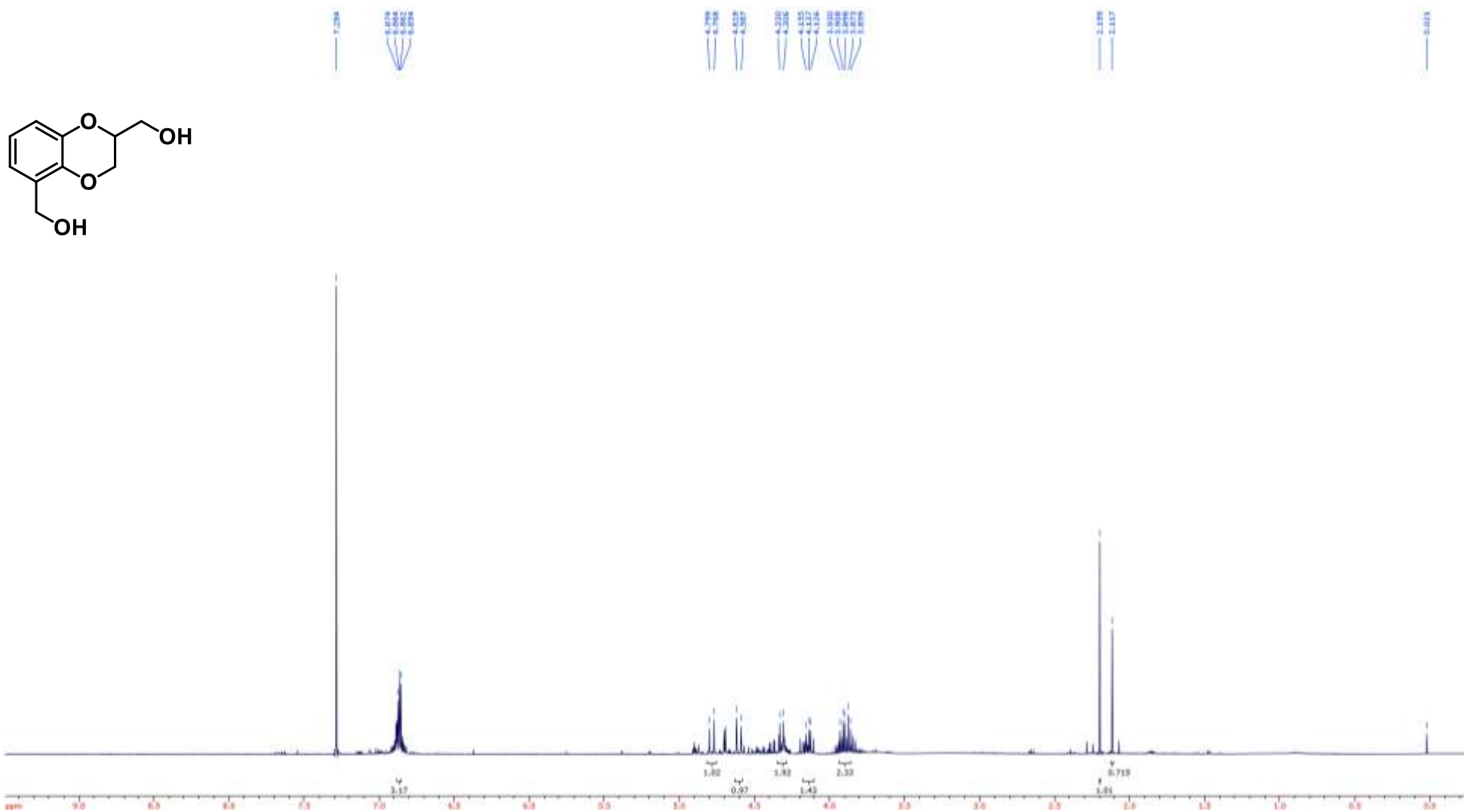
Compound **55** ^1H NMR (400 MHz, CDCl_3)



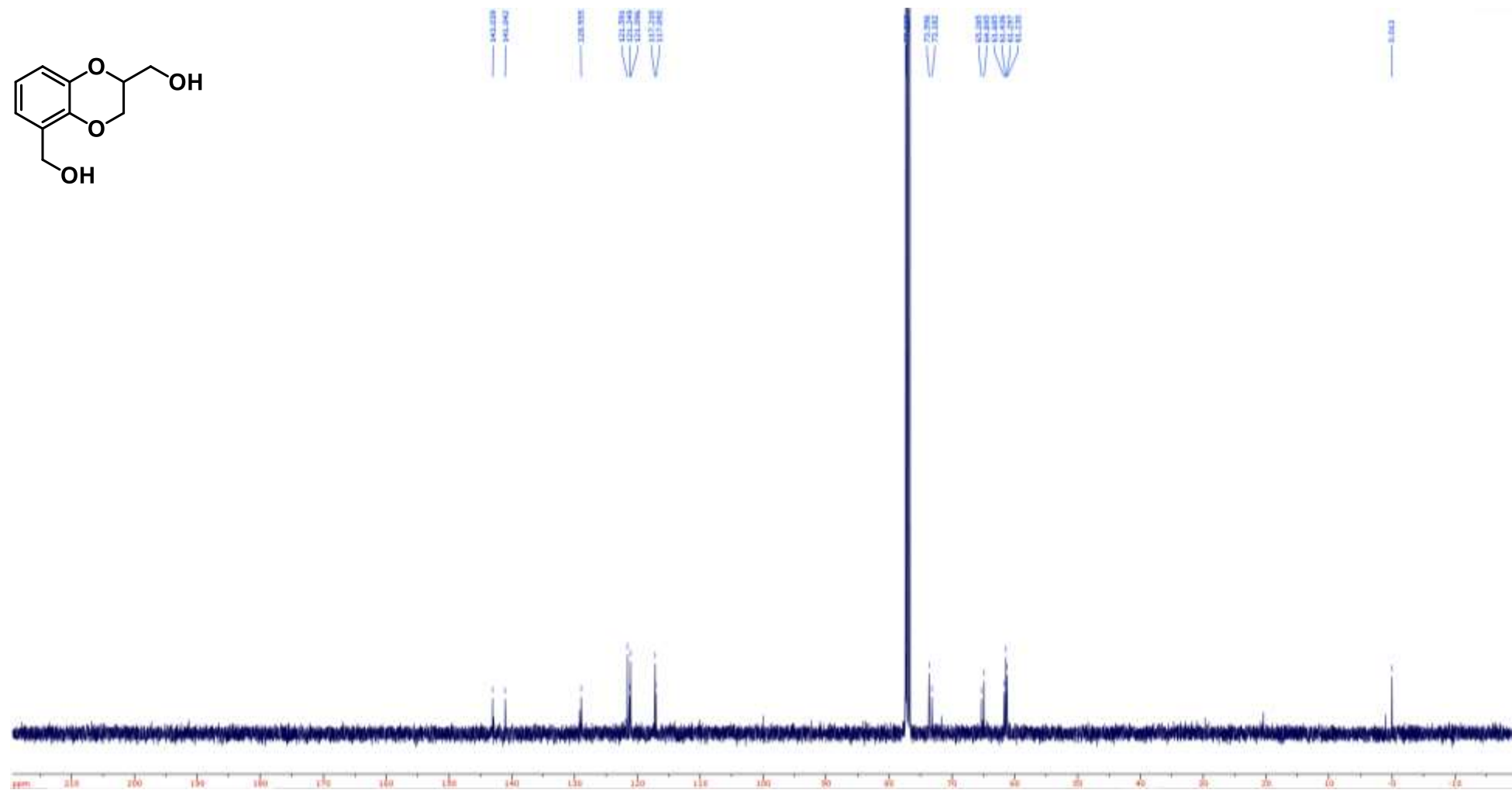
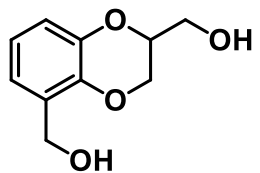
Compound **55** ^{13}C NMR (100 MHz, CDCl_3)



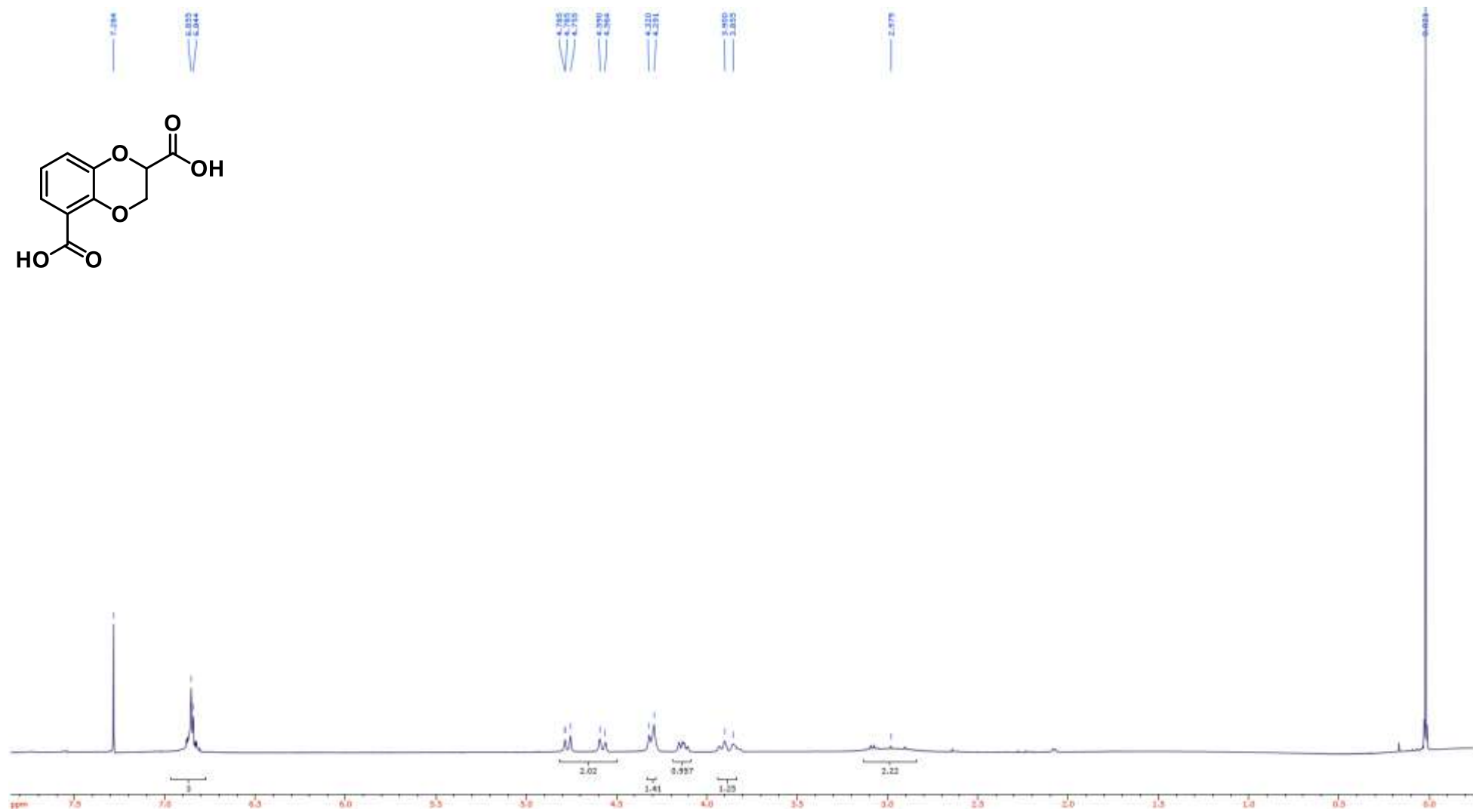
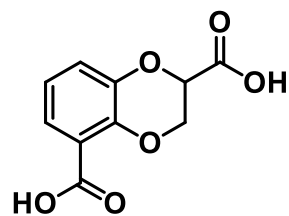
Compound **56** ^1H NMR (400 MHz, CDCl_3)



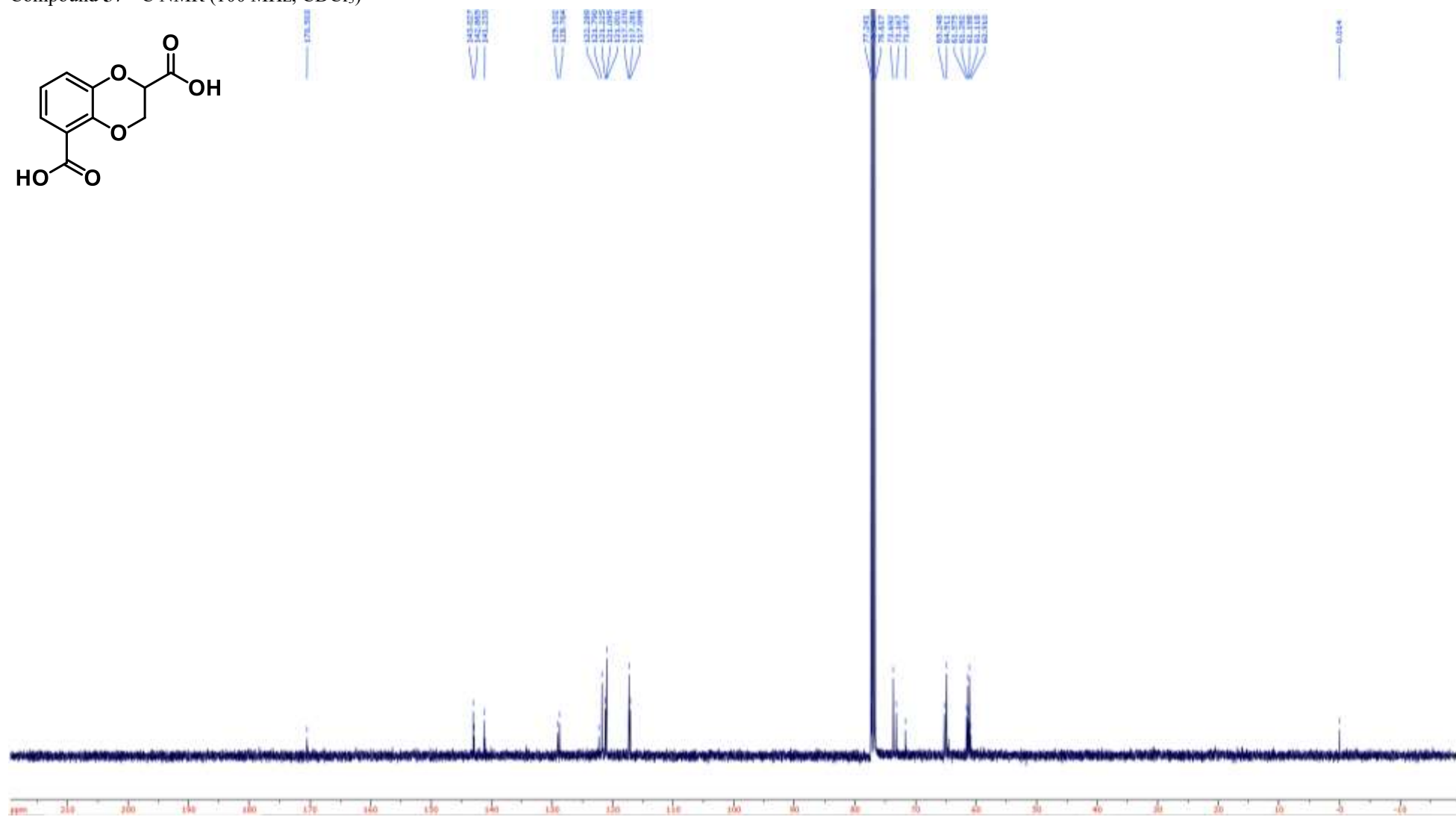
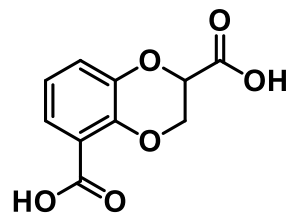
Compound **56** ^{13}C NMR (100 MHz, CDCl_3)



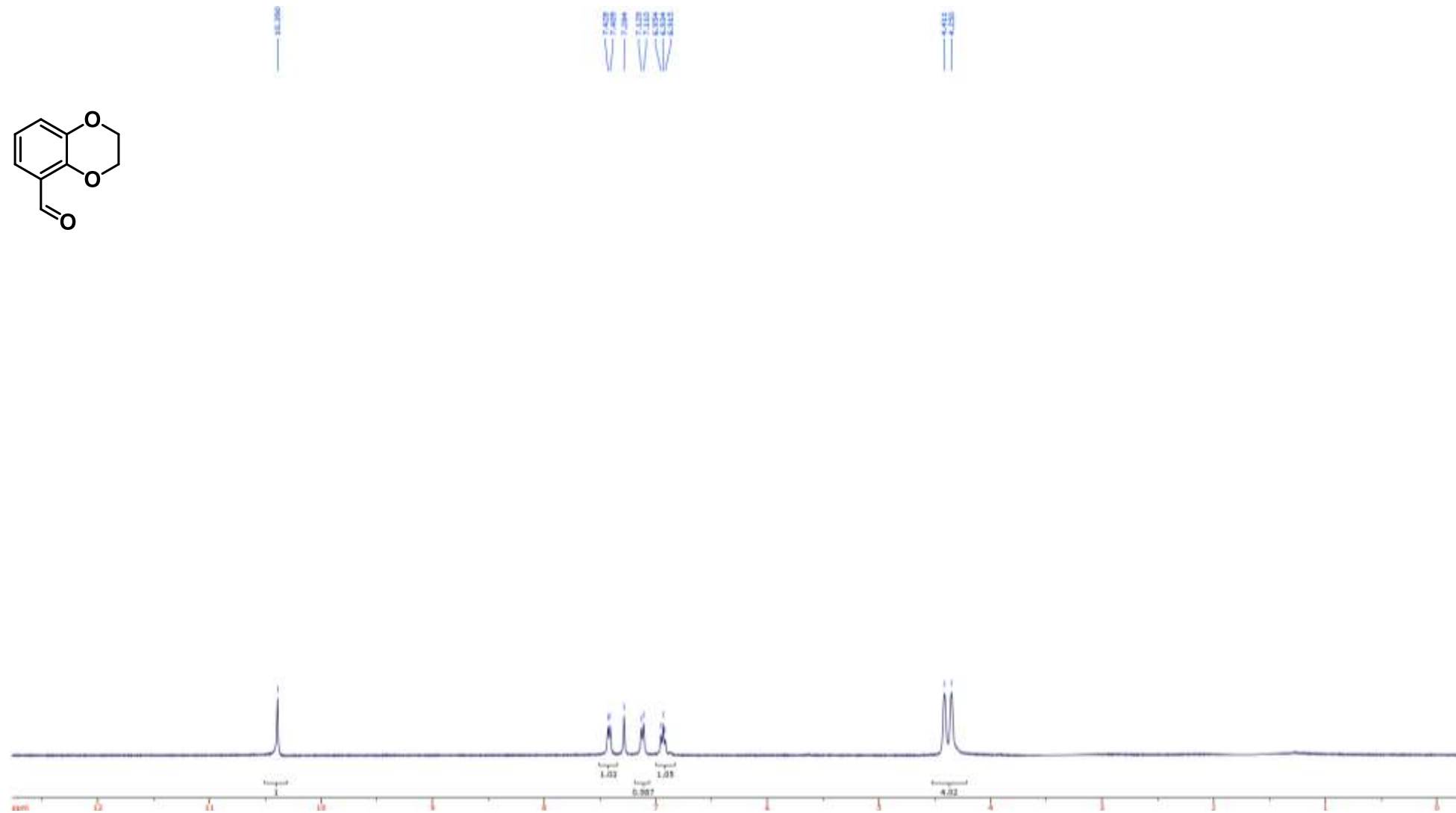
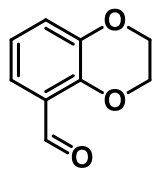
Compound **57** ^1H NMR (400 MHz, CDCl_3)



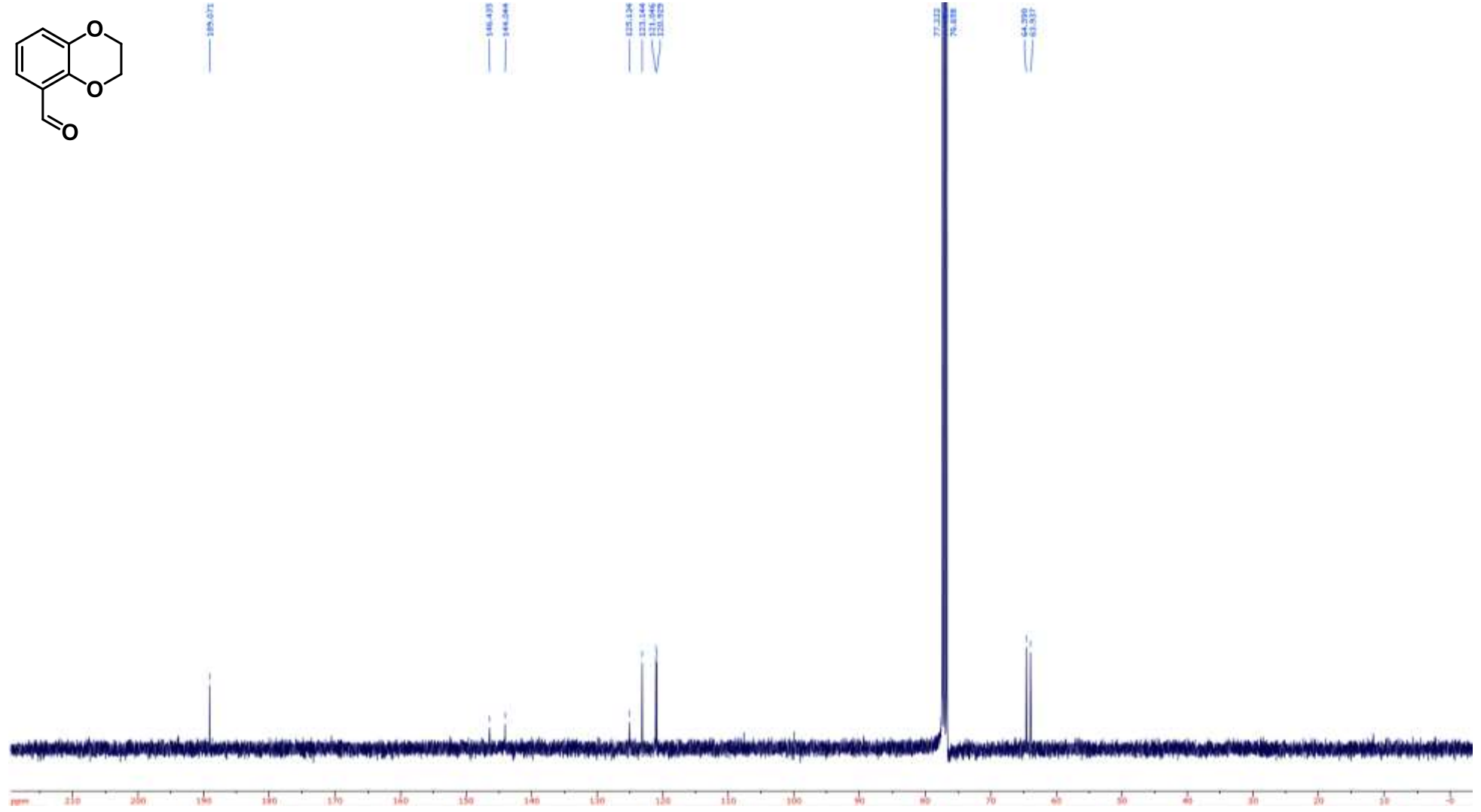
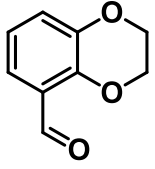
Compound **57** ^{13}C NMR (100 MHz, CDCl_3)



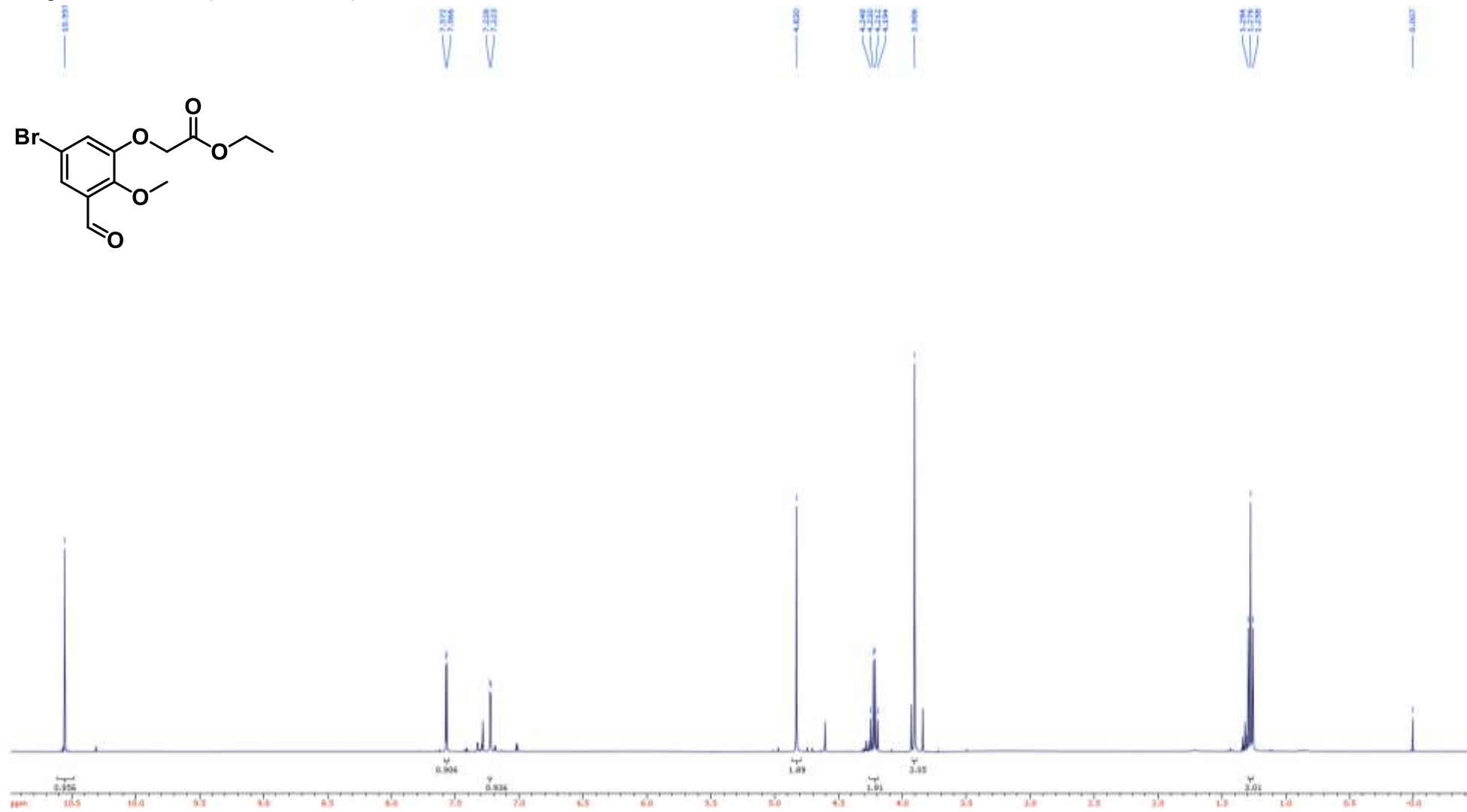
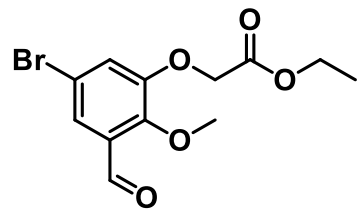
Compound **58** ^1H NMR (400 MHz, CDCl_3)



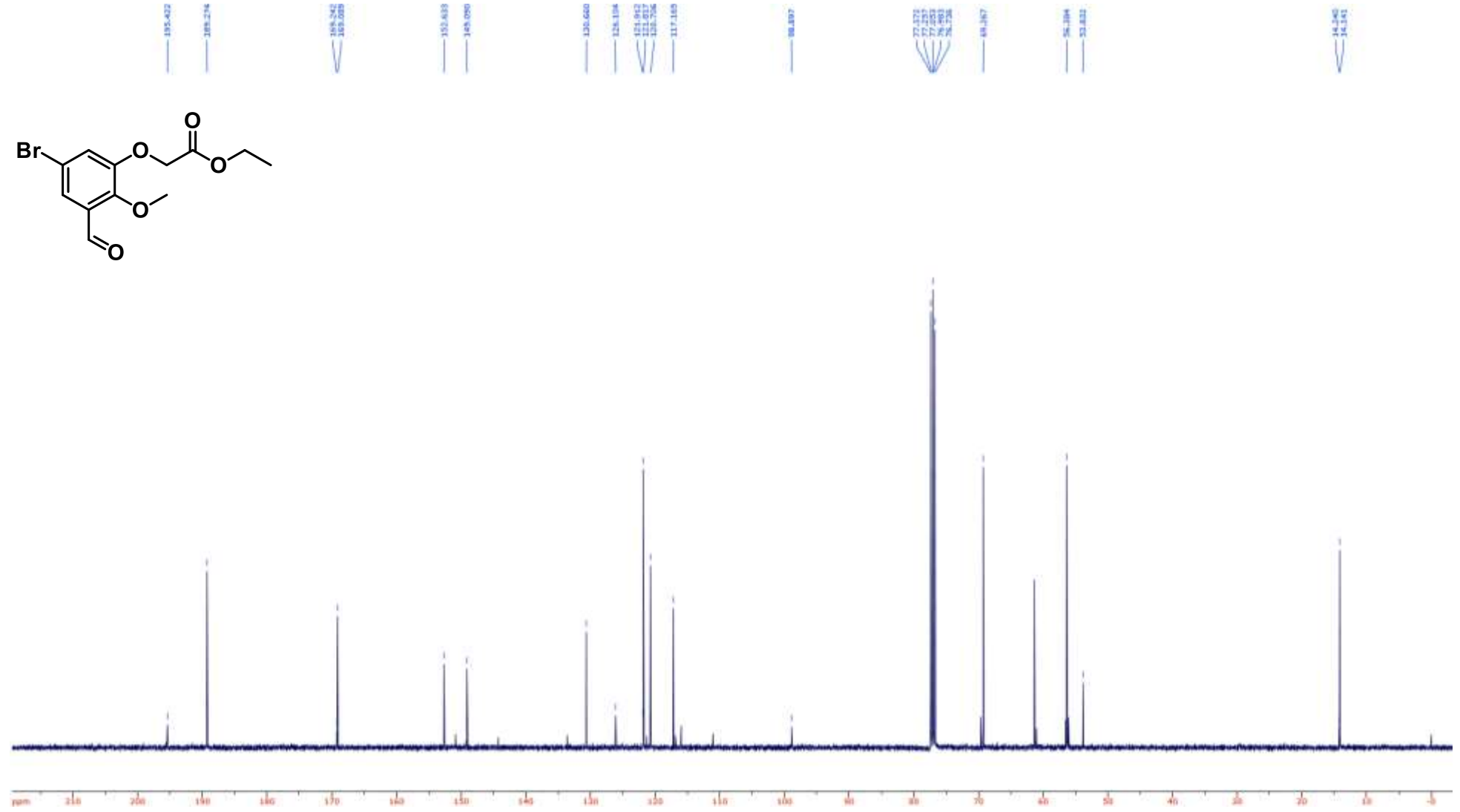
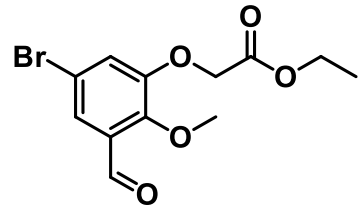
Compound **58** ^{13}C NMR (100 MHz, CDCl_3)



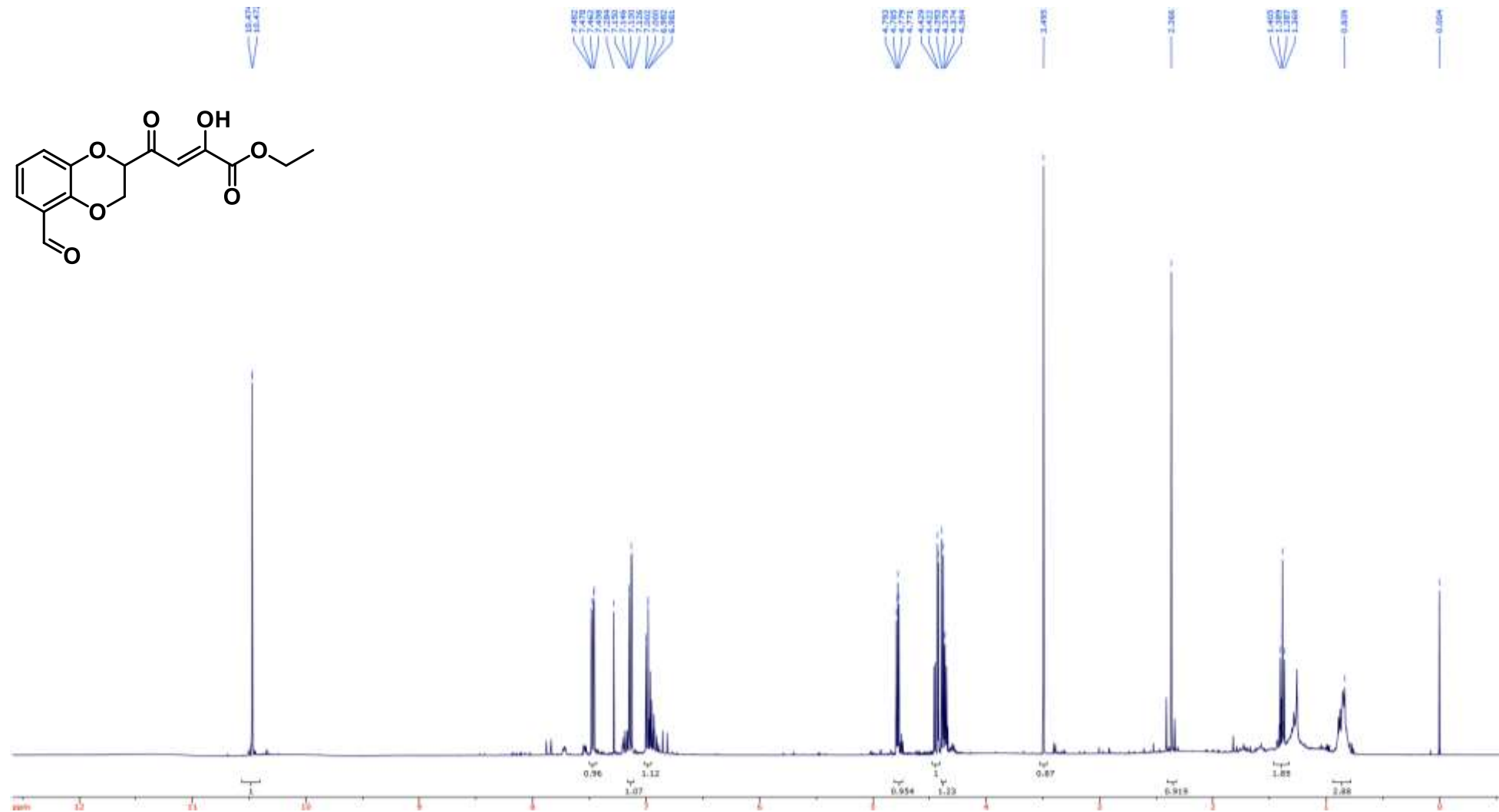
Compound **59** ^1H NMR (400 MHz, CDCl_3)



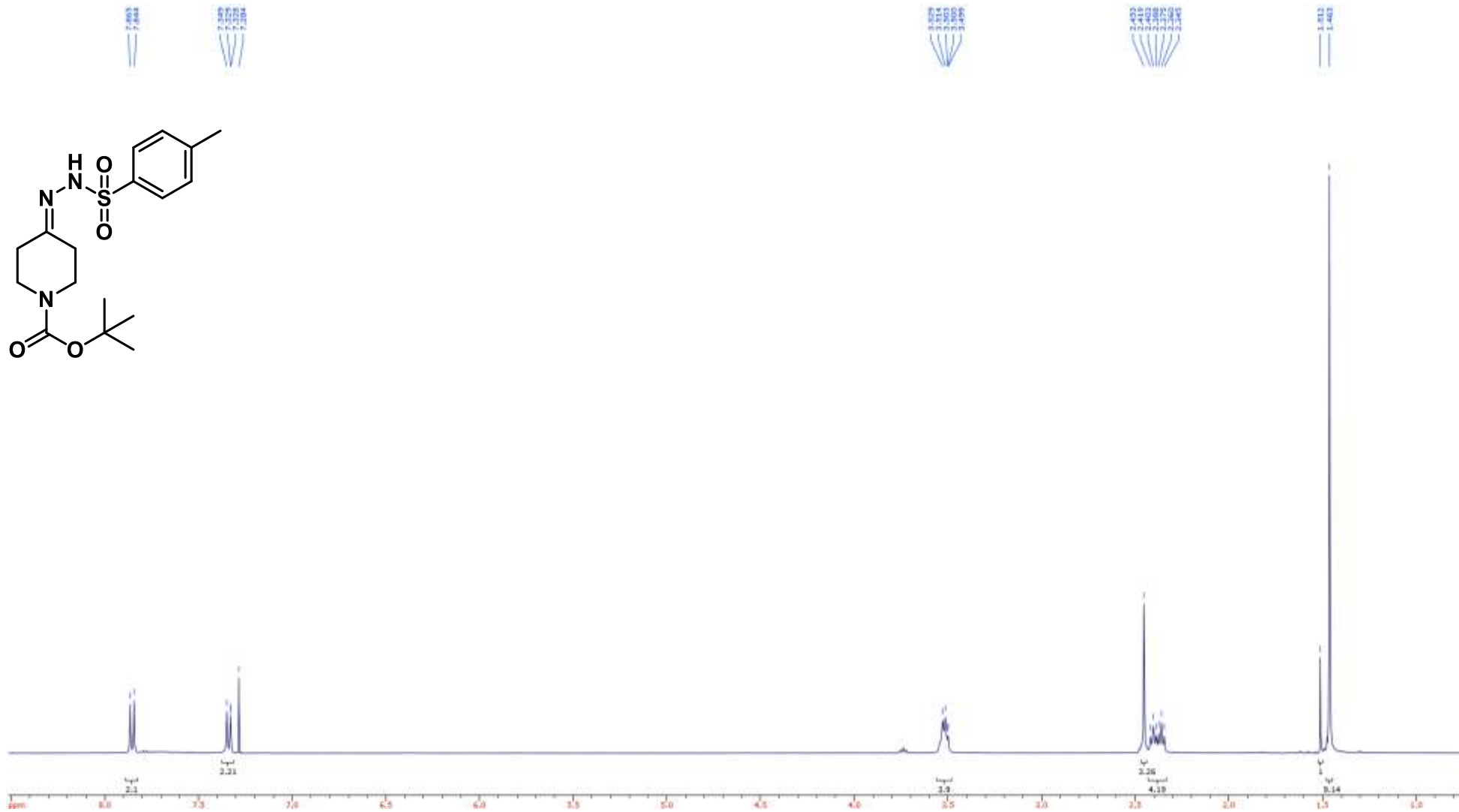
Compound **59** ^{13}C NMR (100 MHz, CDCl_3)



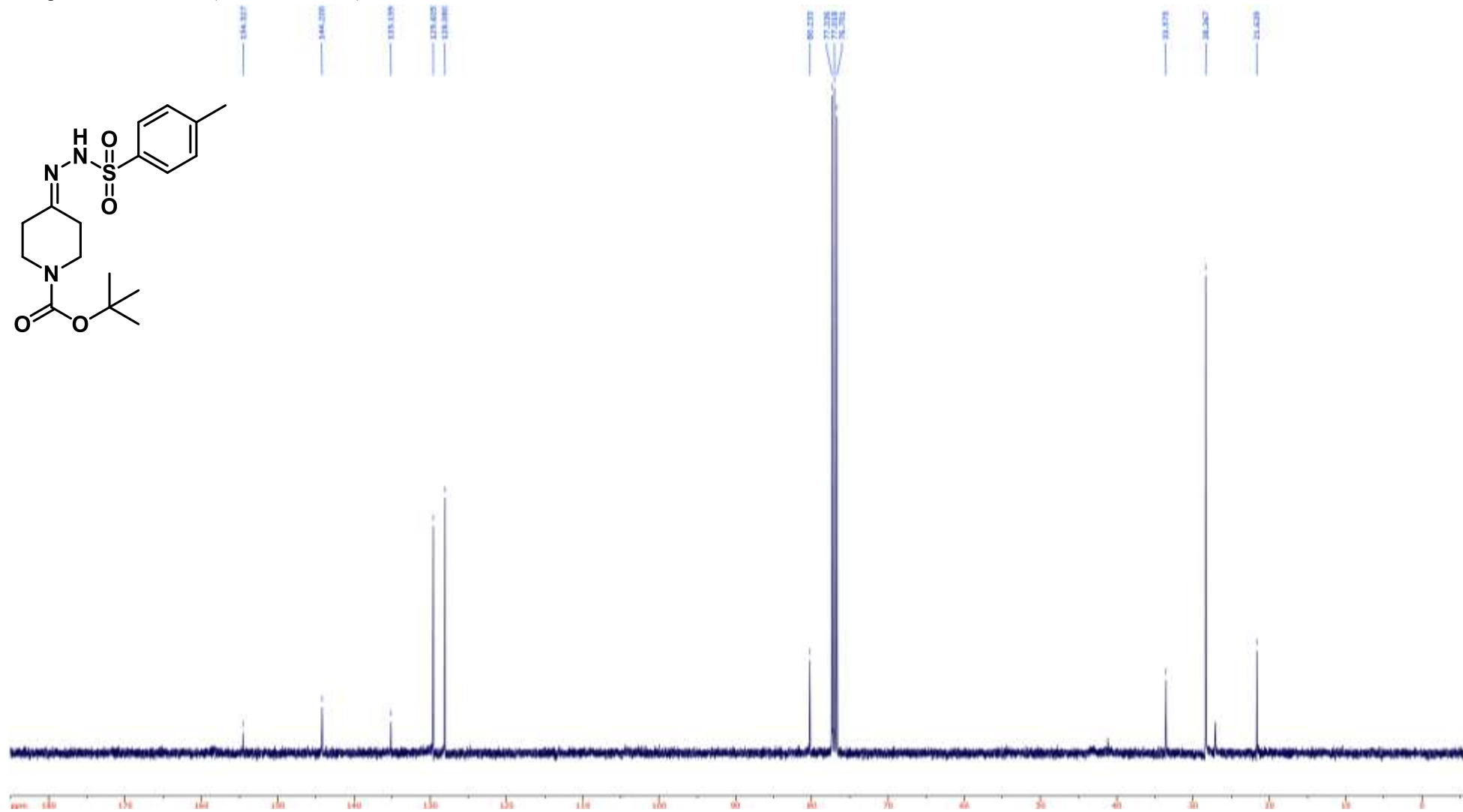
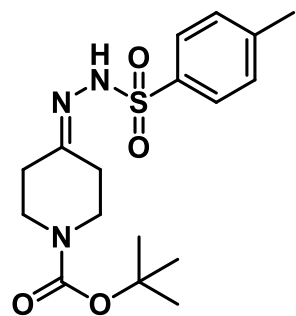
Compound **60** ^1H NMR (400 MHz, CDCl_3)



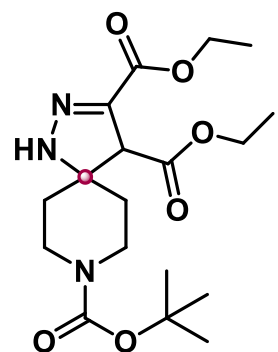
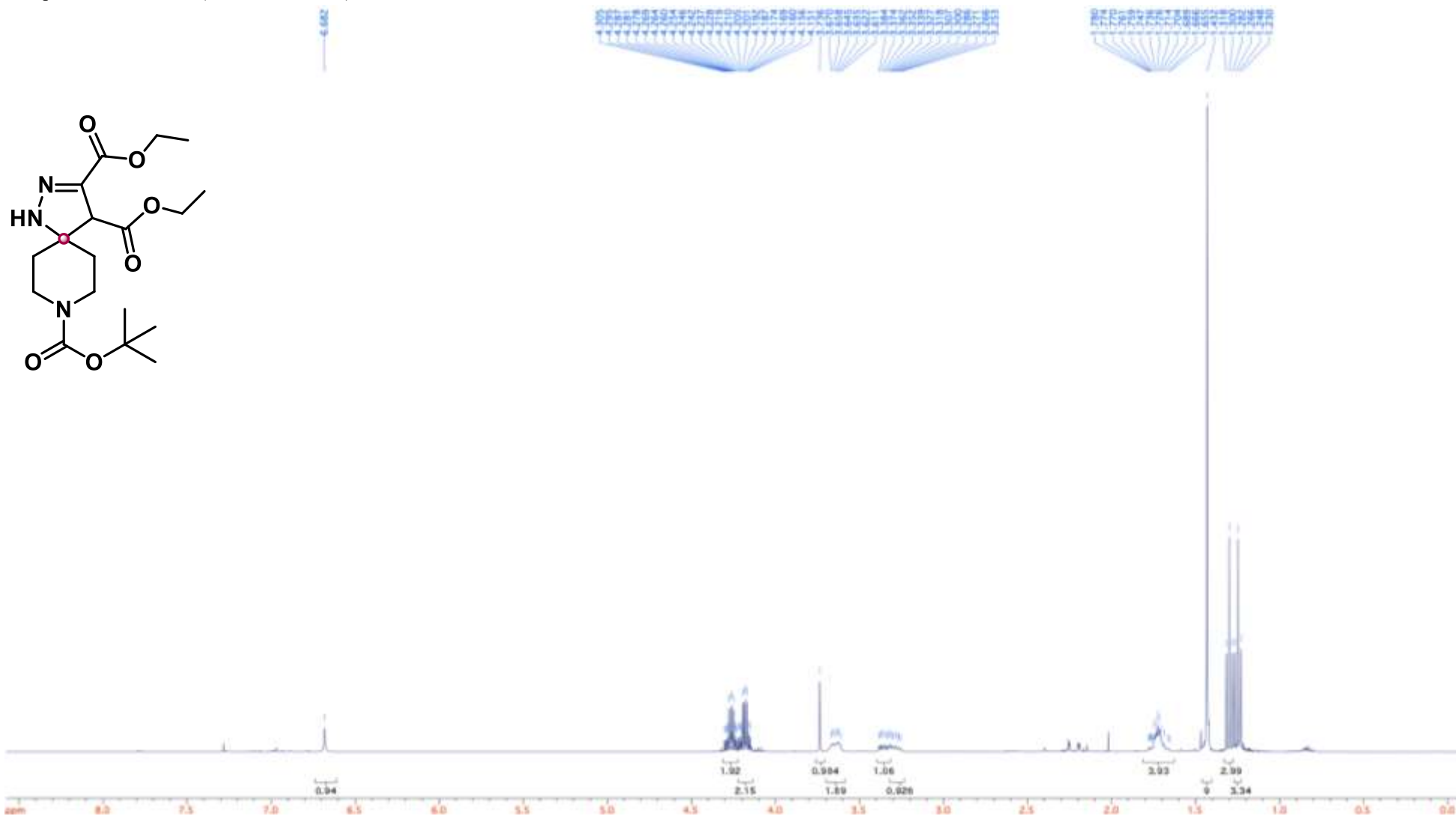
Compound **61** ^1H NMR (400 MHz, CDCl_3)



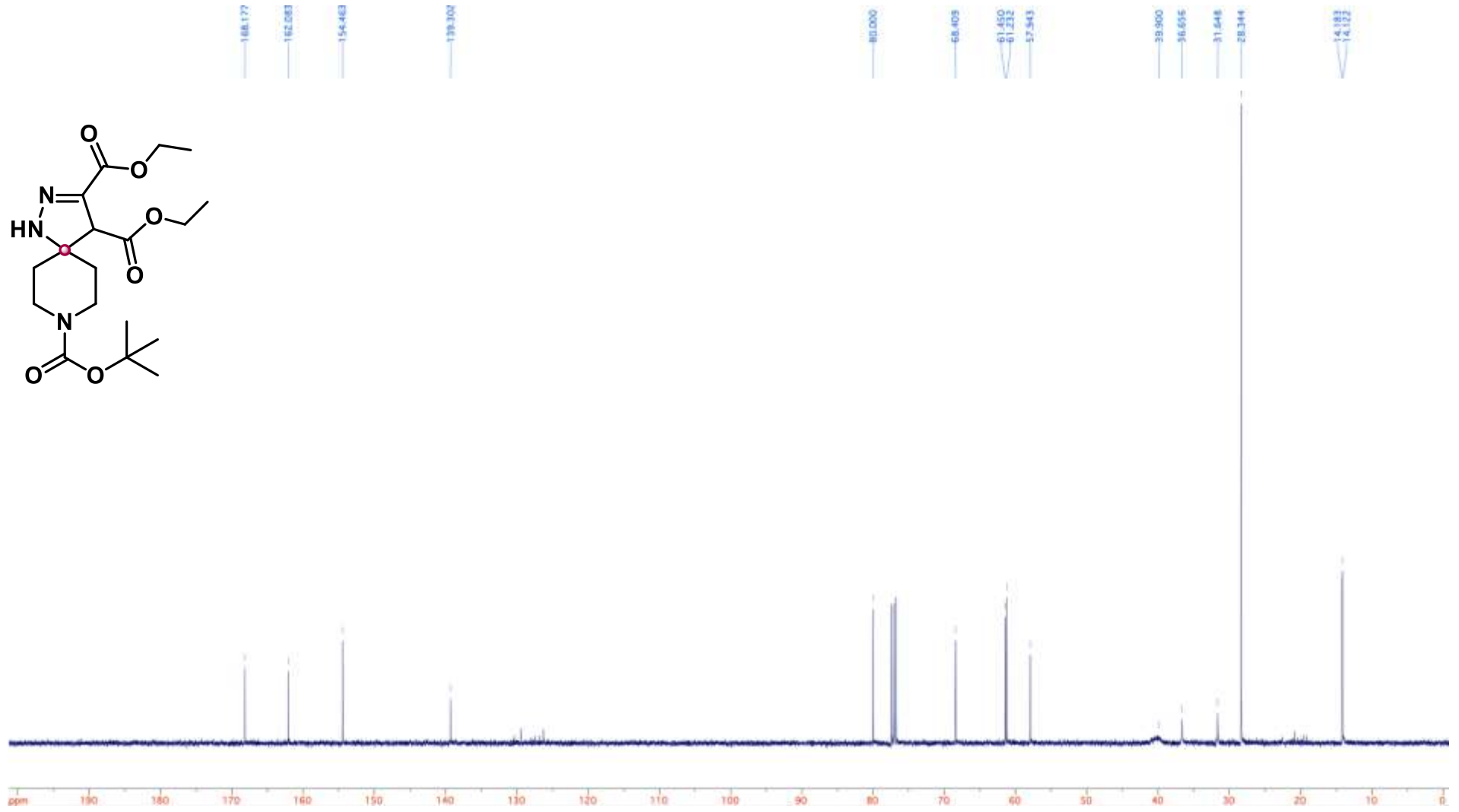
Compound **61** ^{13}C NMR (100 MHz, CDCl_3)



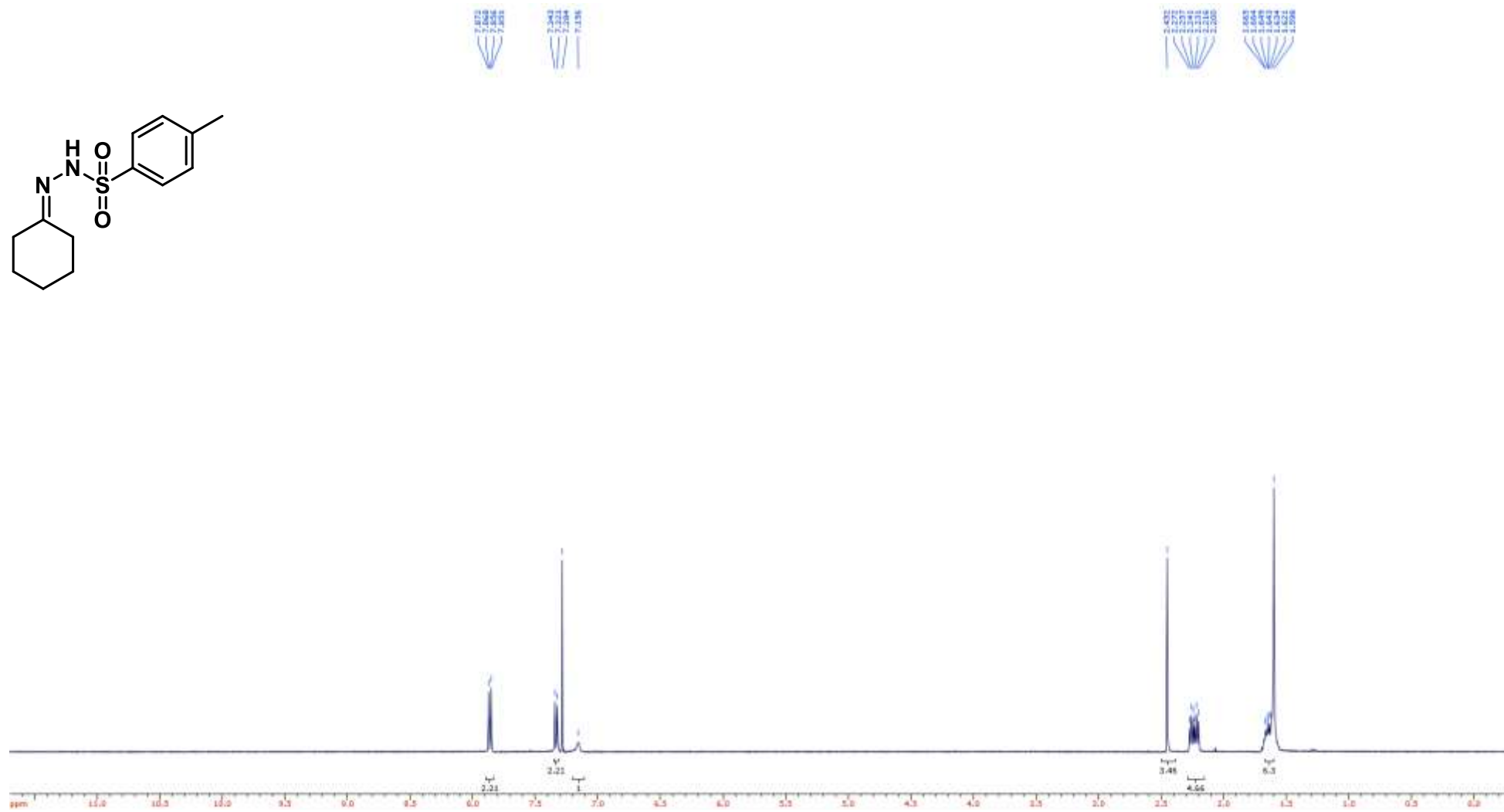
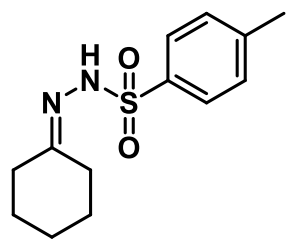
Compound **62** ^1H NMR (400 MHz, CDCl_3)



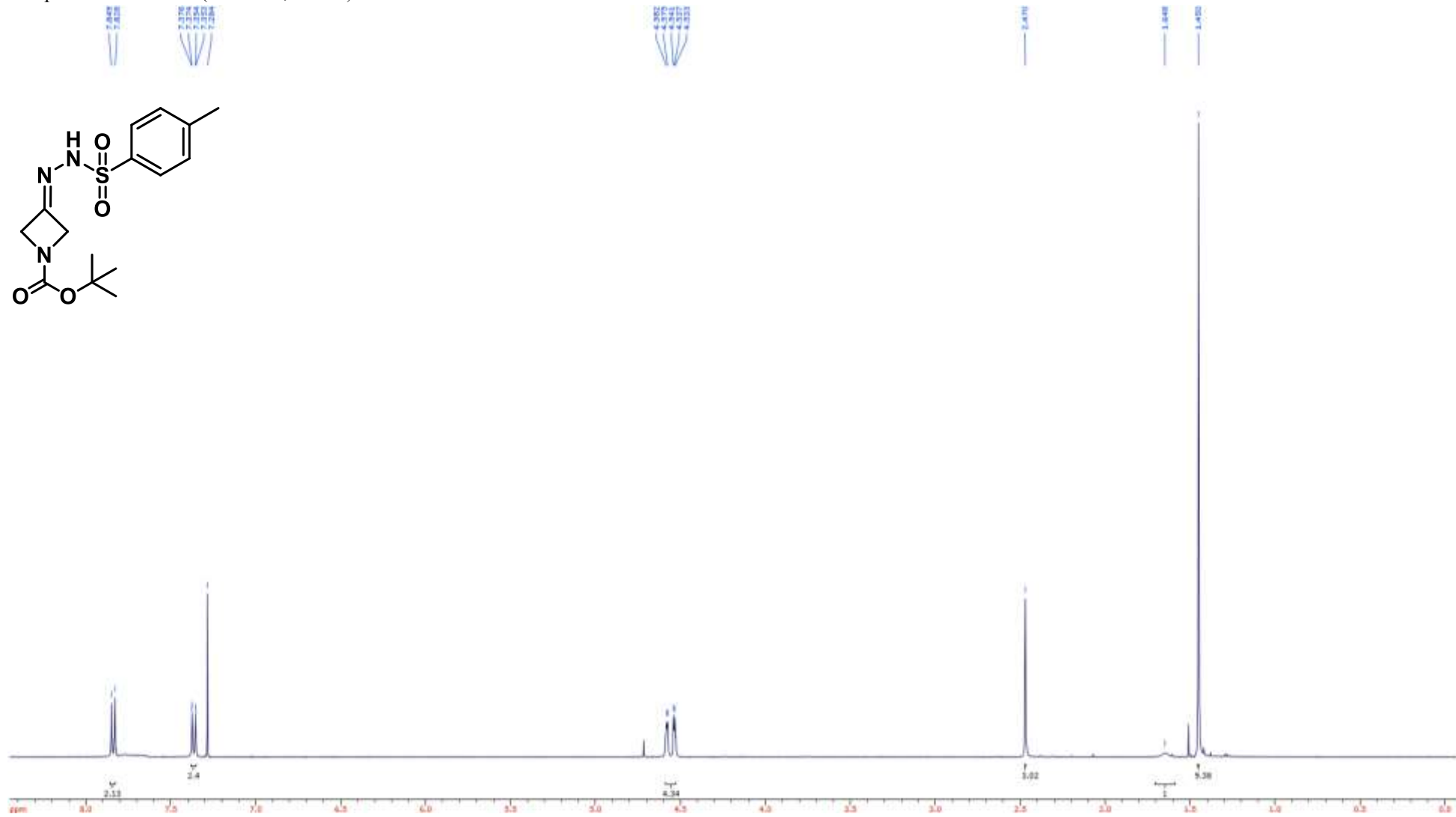
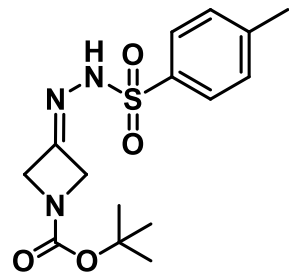
Compound **62** ^{13}C NMR (100 MHz, CDCl_3)



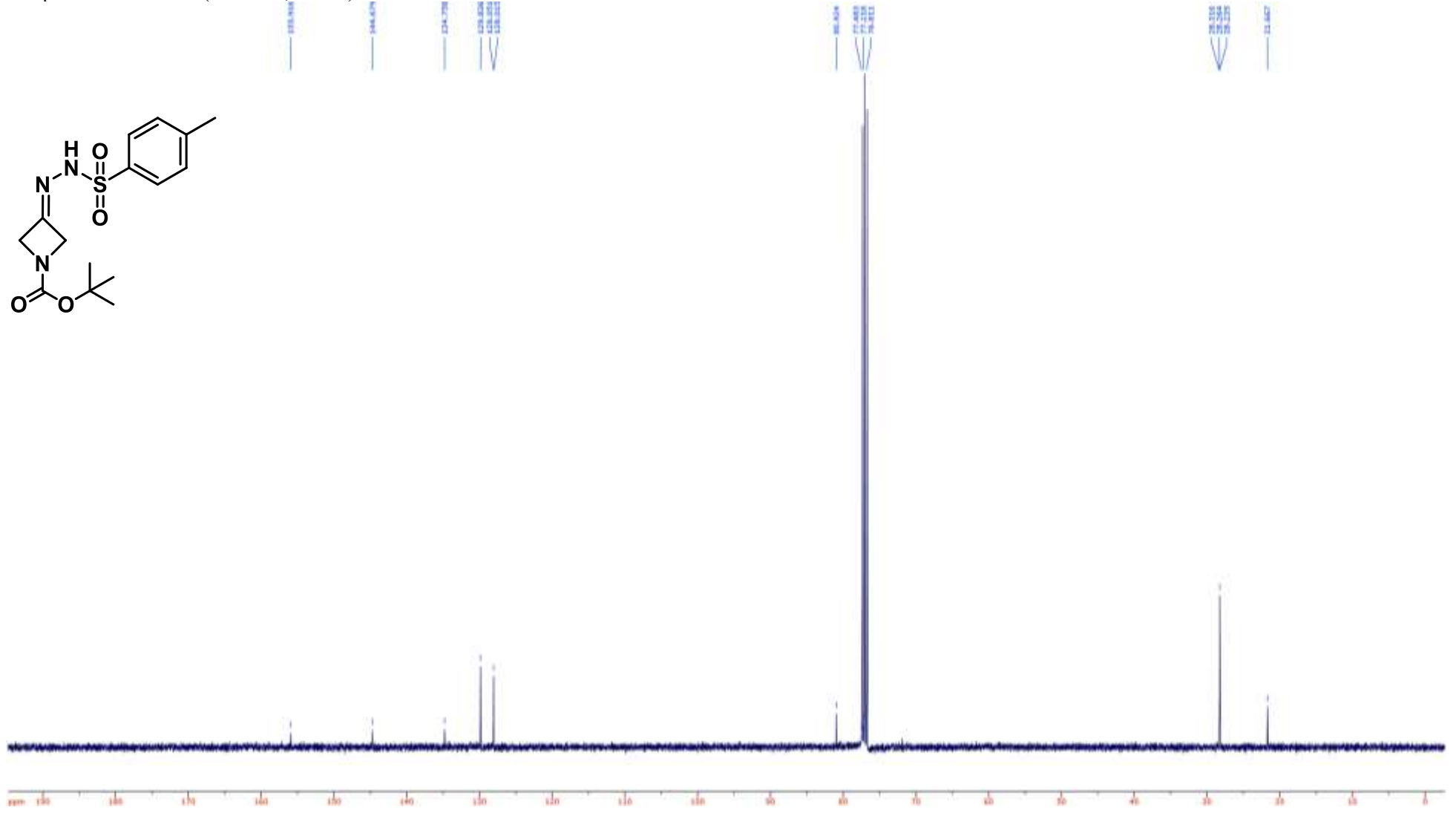
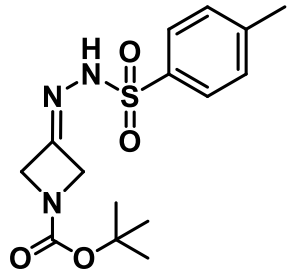
Compound **63** ^1H NMR (400 MHz, CDCl_3)



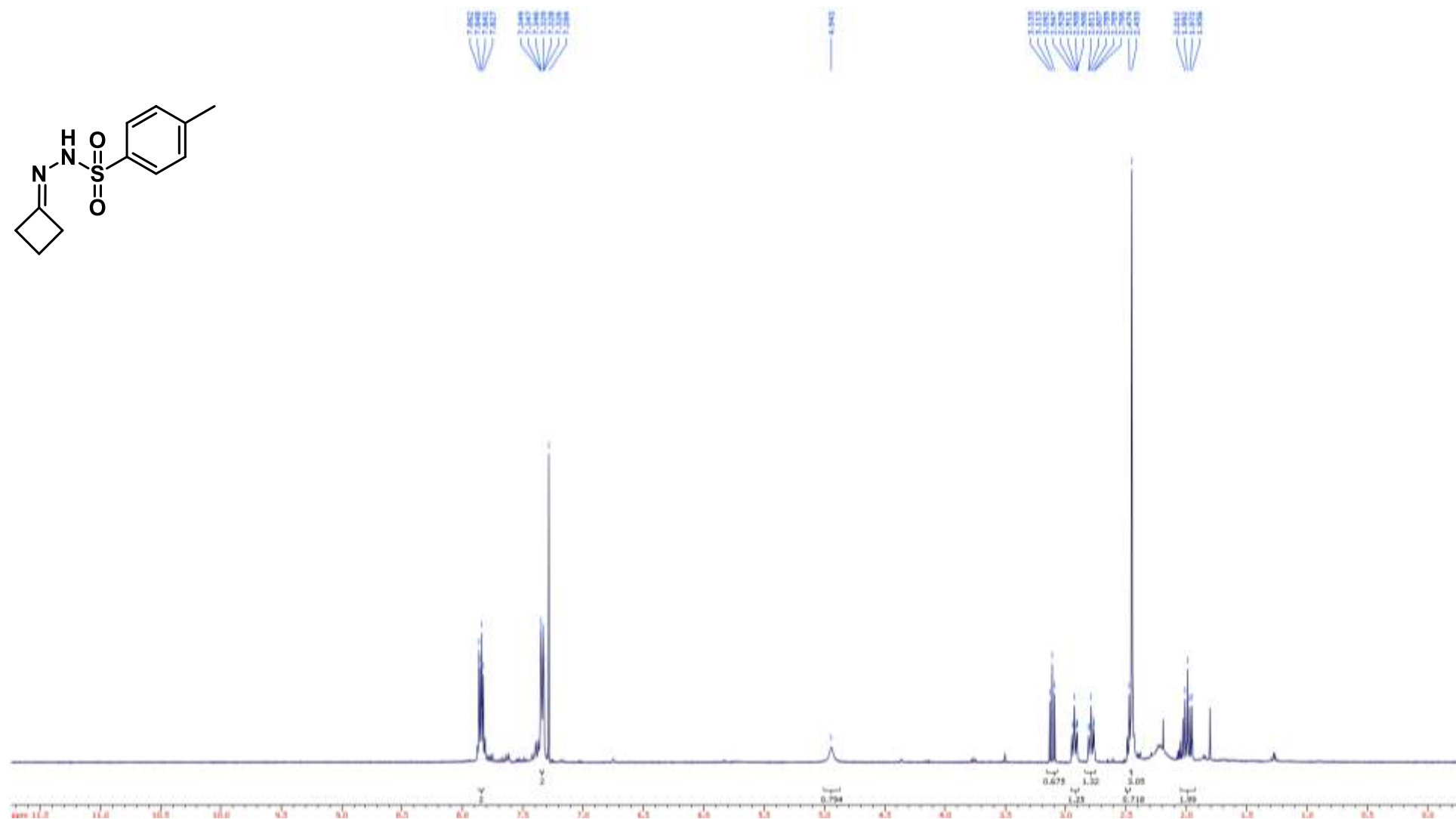
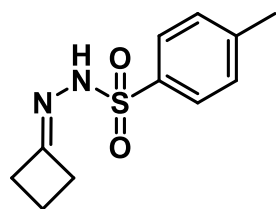
Compound **64** ^1H NMR (400 MHz, CDCl_3)



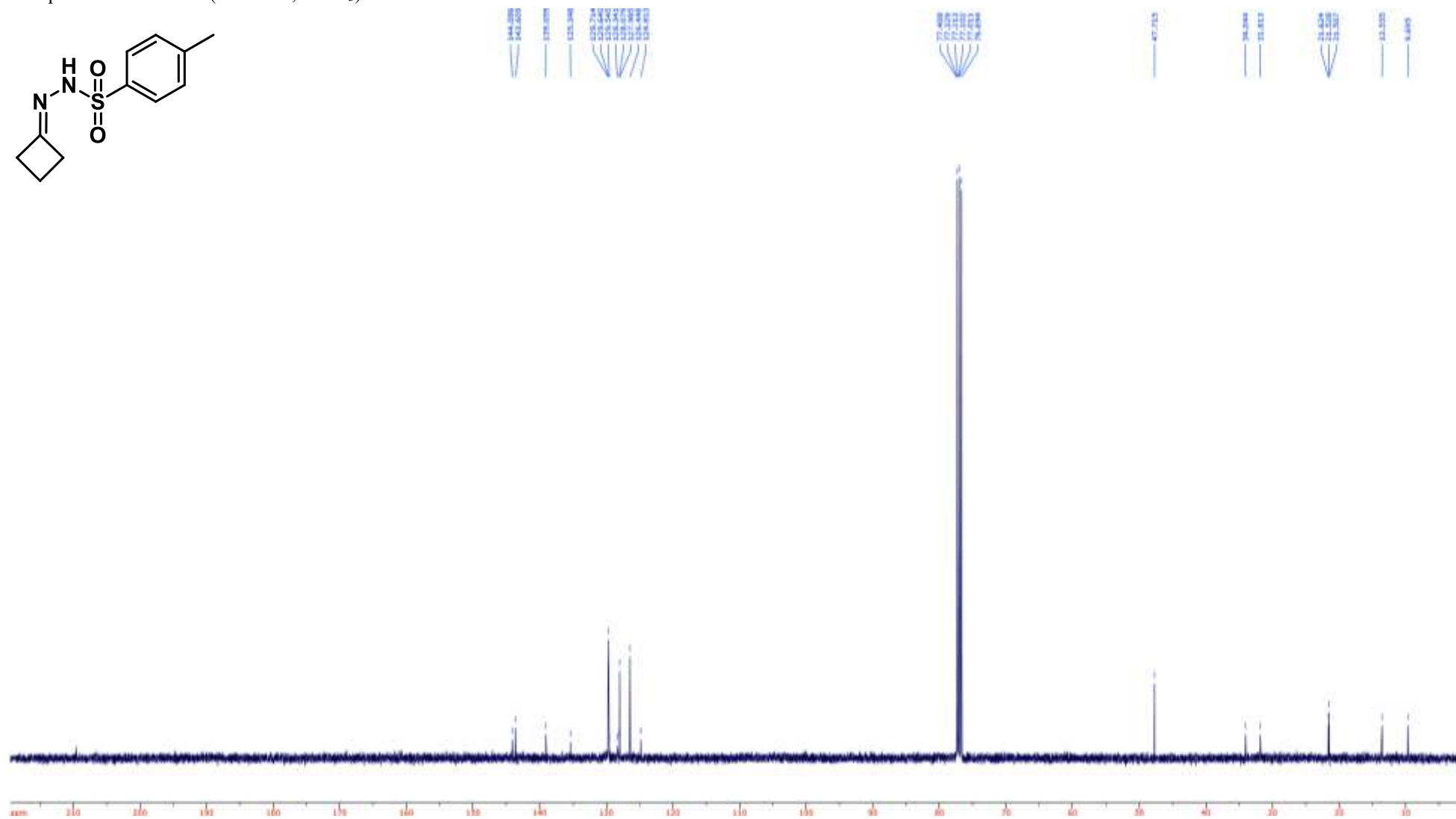
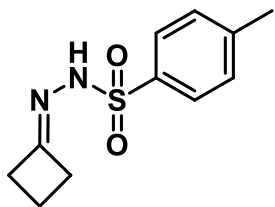
Compound **64** ^{13}C NMR (100 MHz, CDCl_3)



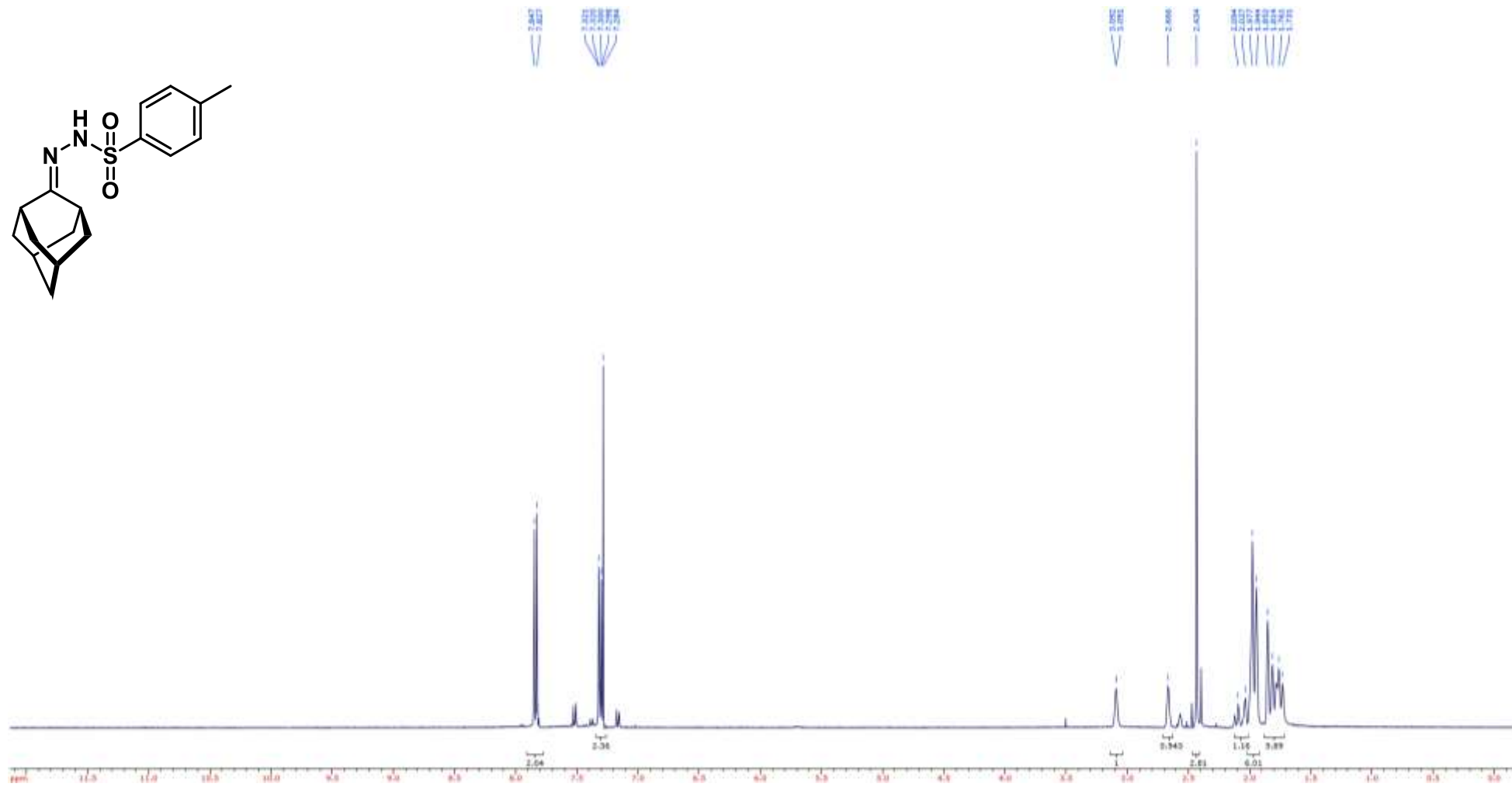
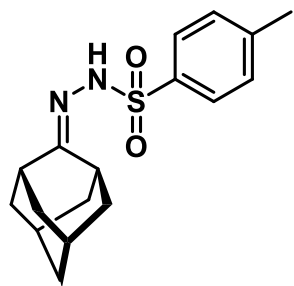
Compound **65** ^1H NMR (400 MHz, CDCl_3)



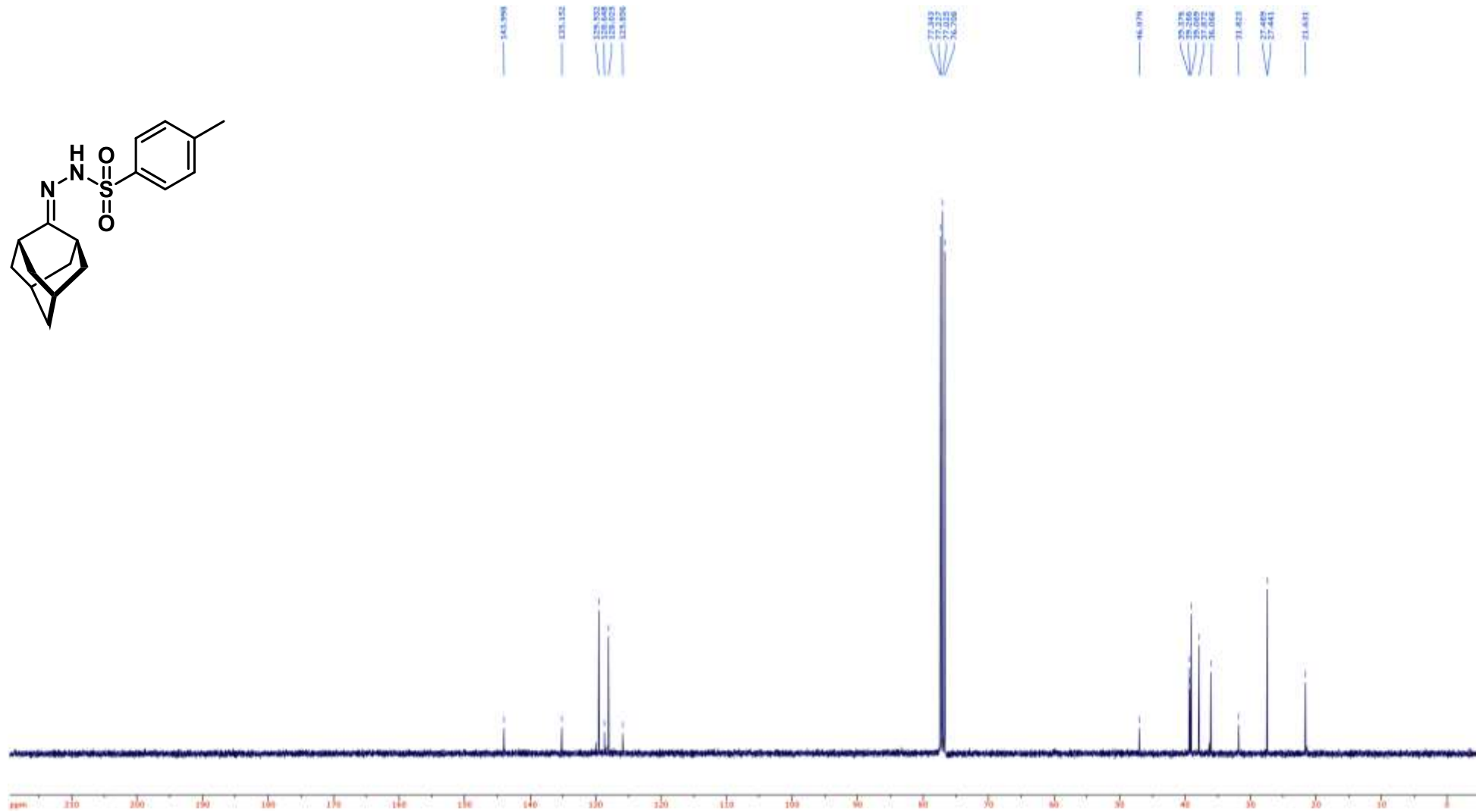
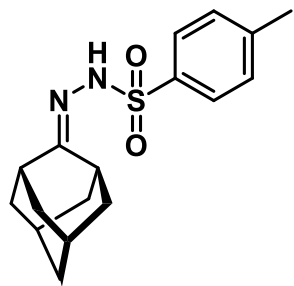
Compound **65** ^{13}C NMR (100 MHz, CDCl_3)



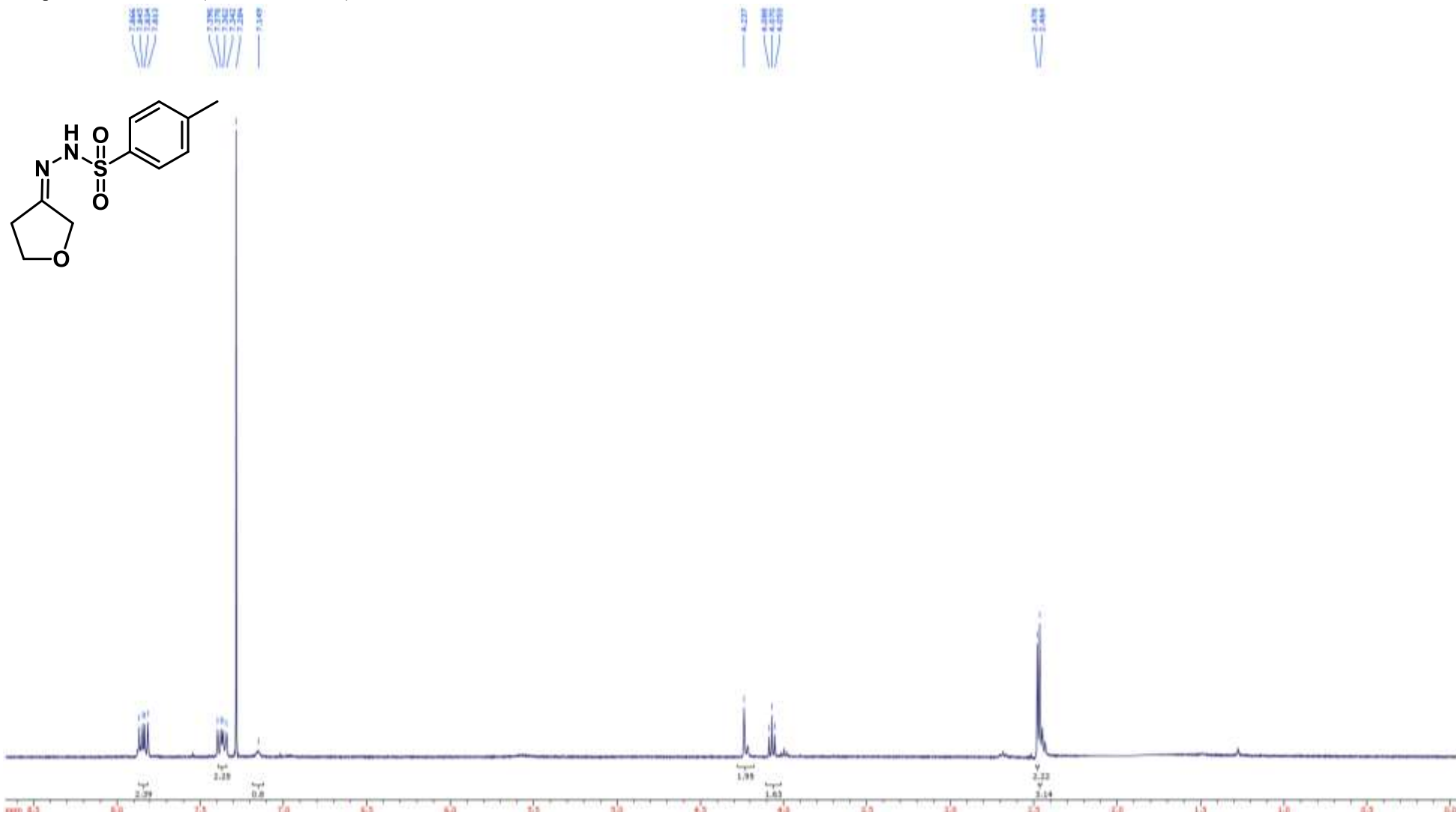
Compound **66** ^1H NMR (400 MHz, CDCl_3)



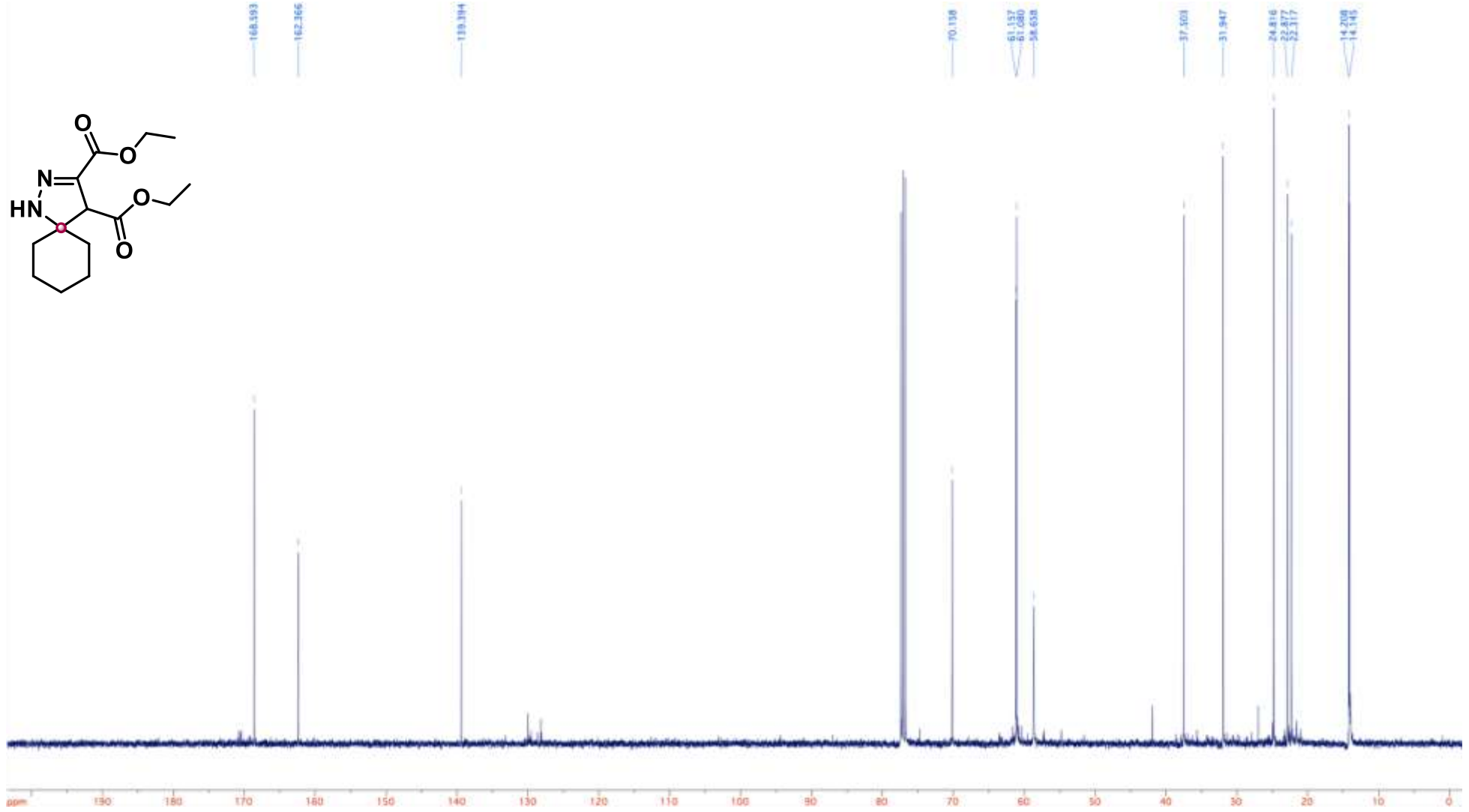
Compound **66** ^{13}C NMR (100 MHz, CDCl_3)



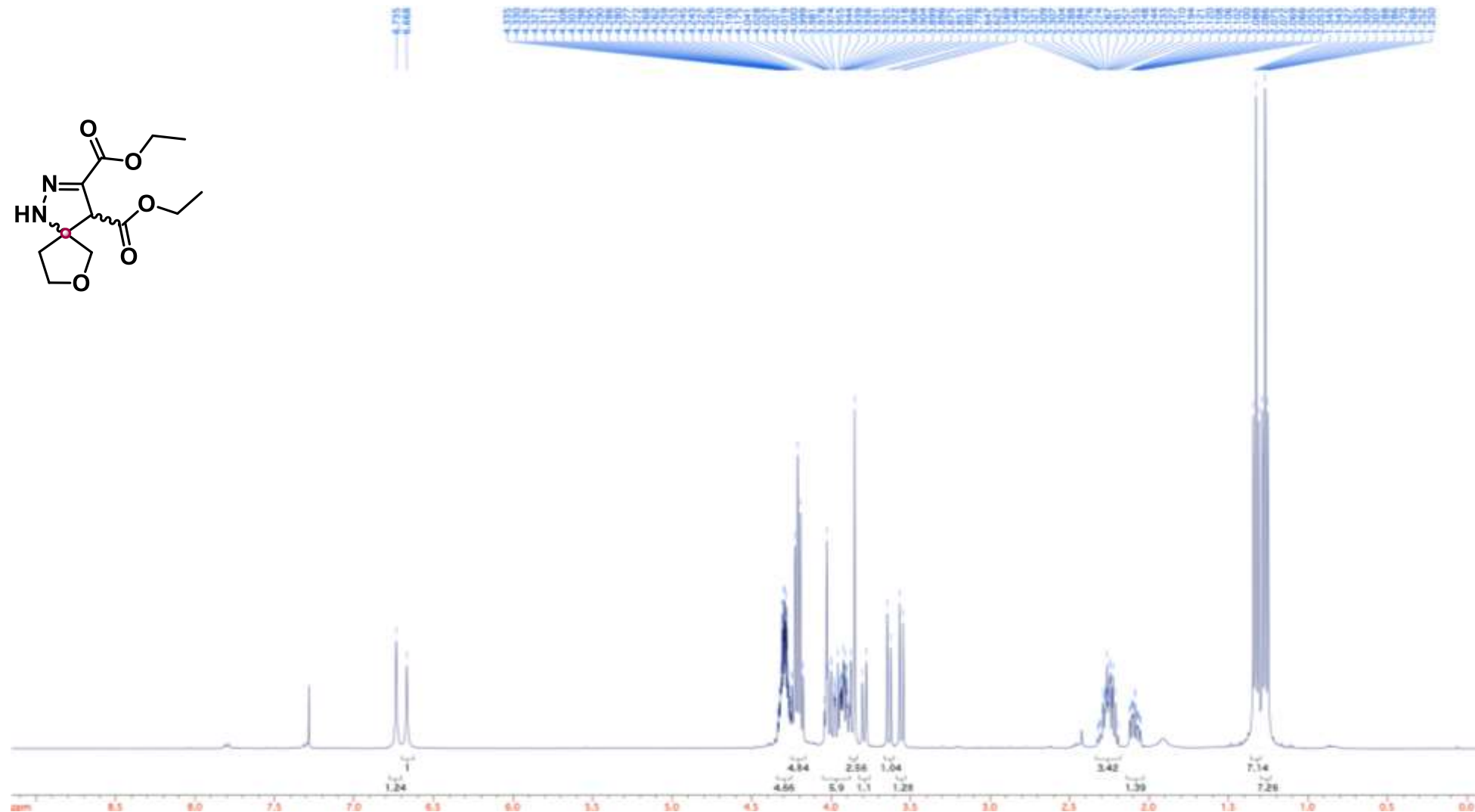
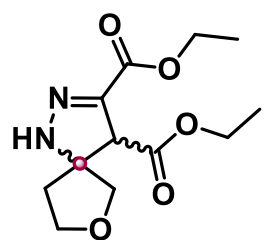
Compound 67 ^1H NMR (400 MHz, CDCl_3)



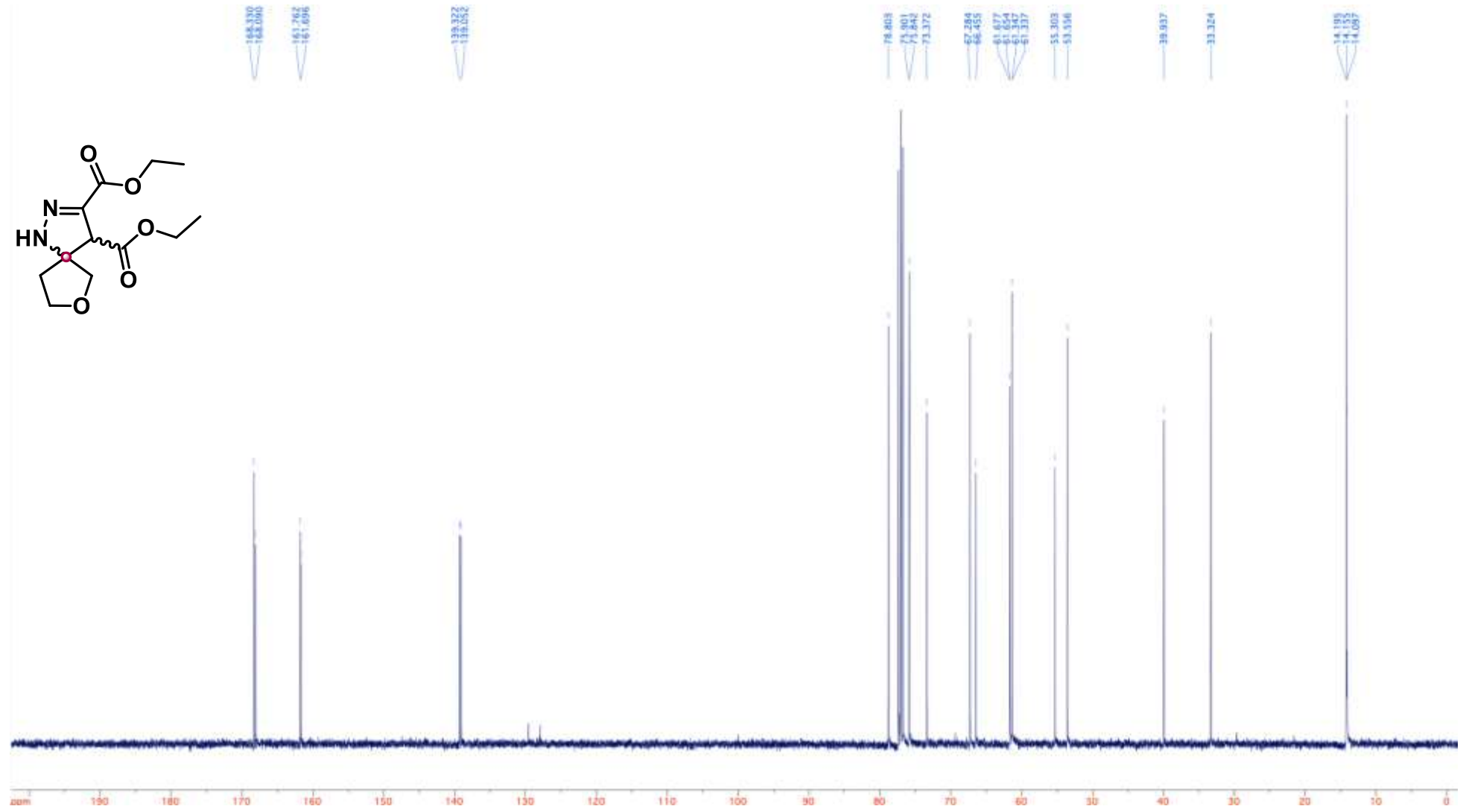
Compound **69** ^{13}C NMR (100 MHz, CDCl_3)



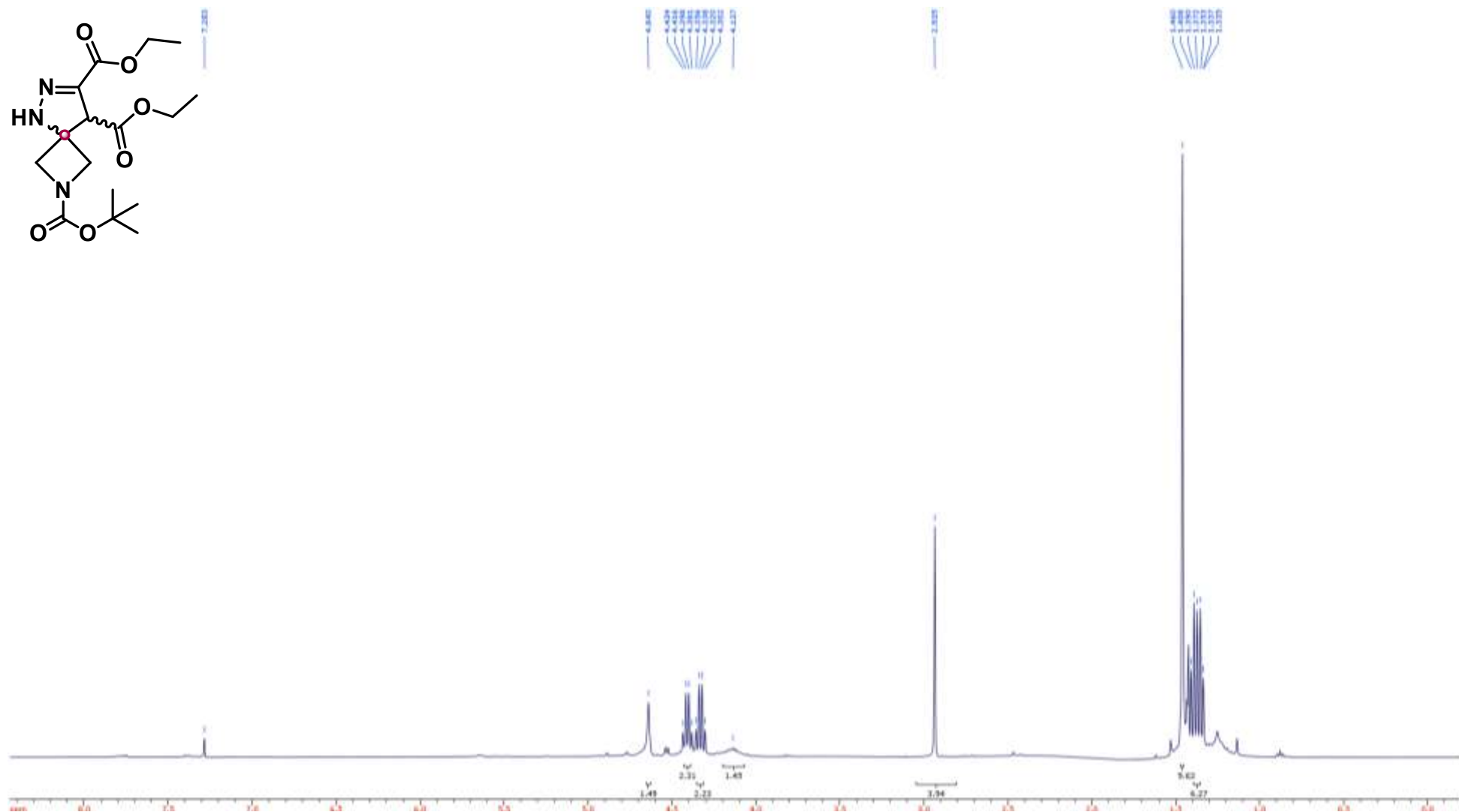
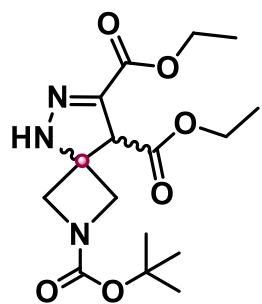
Compound **70** ^1H NMR (400 MHz, CDCl_3)



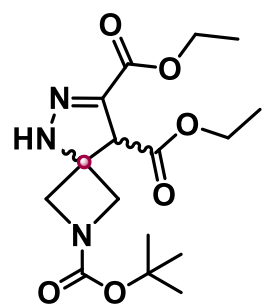
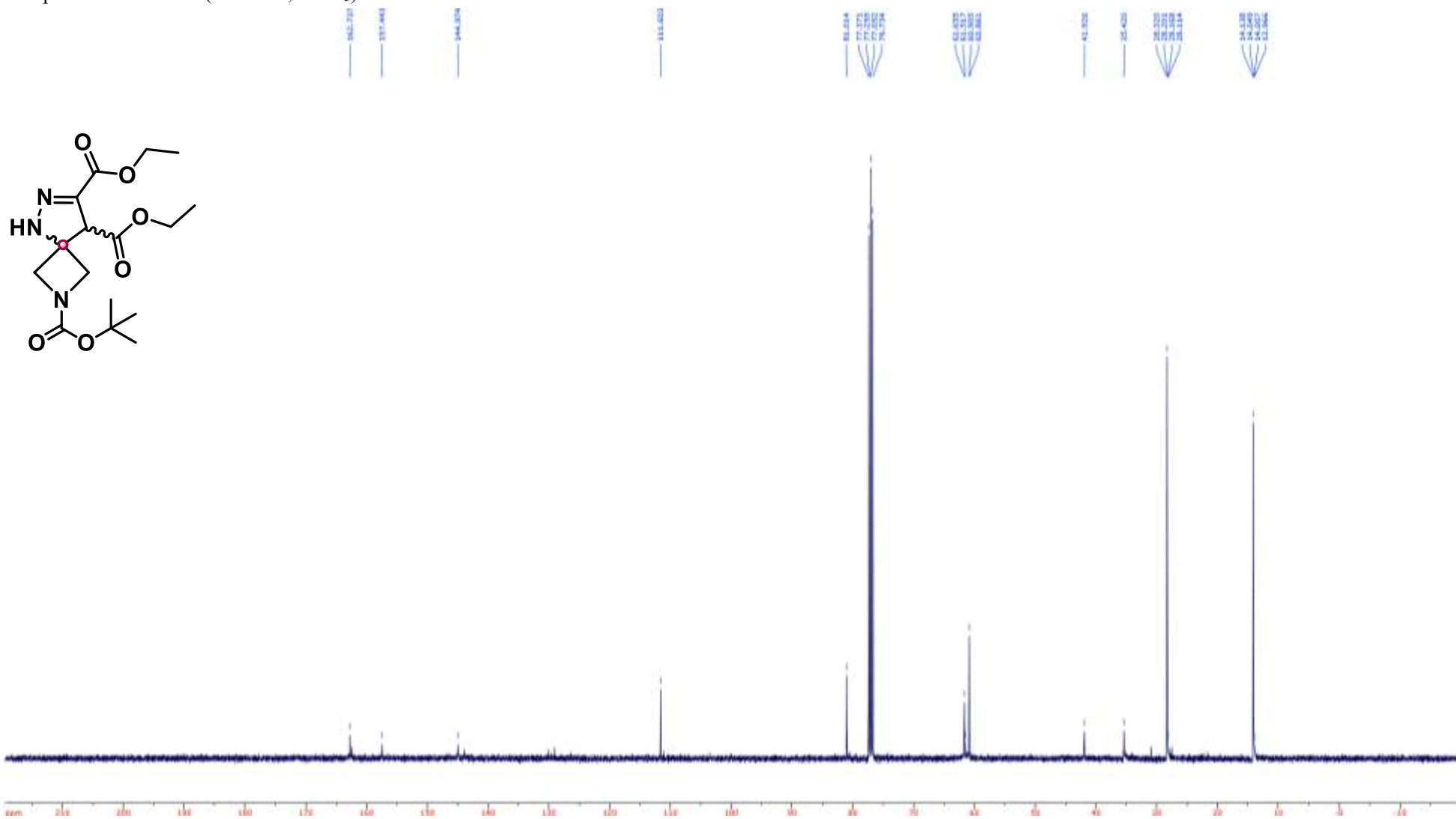
Compound **70** ^{13}C NMR (100 MHz, CDCl_3)



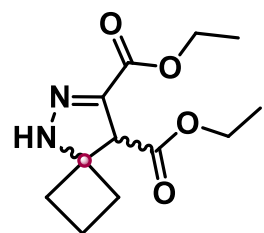
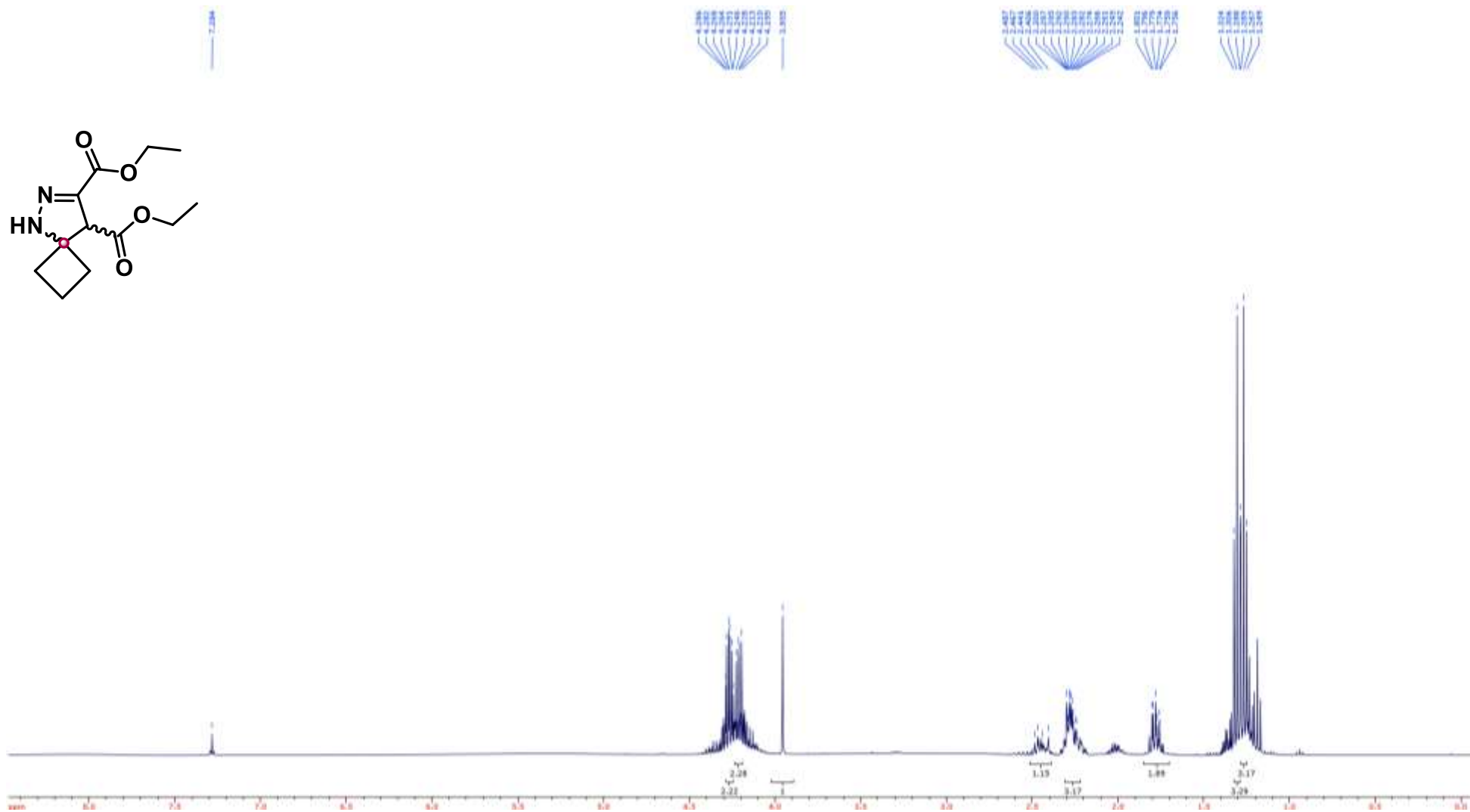
Compound 71 ^1H NMR (400 MHz, CDCl_3)



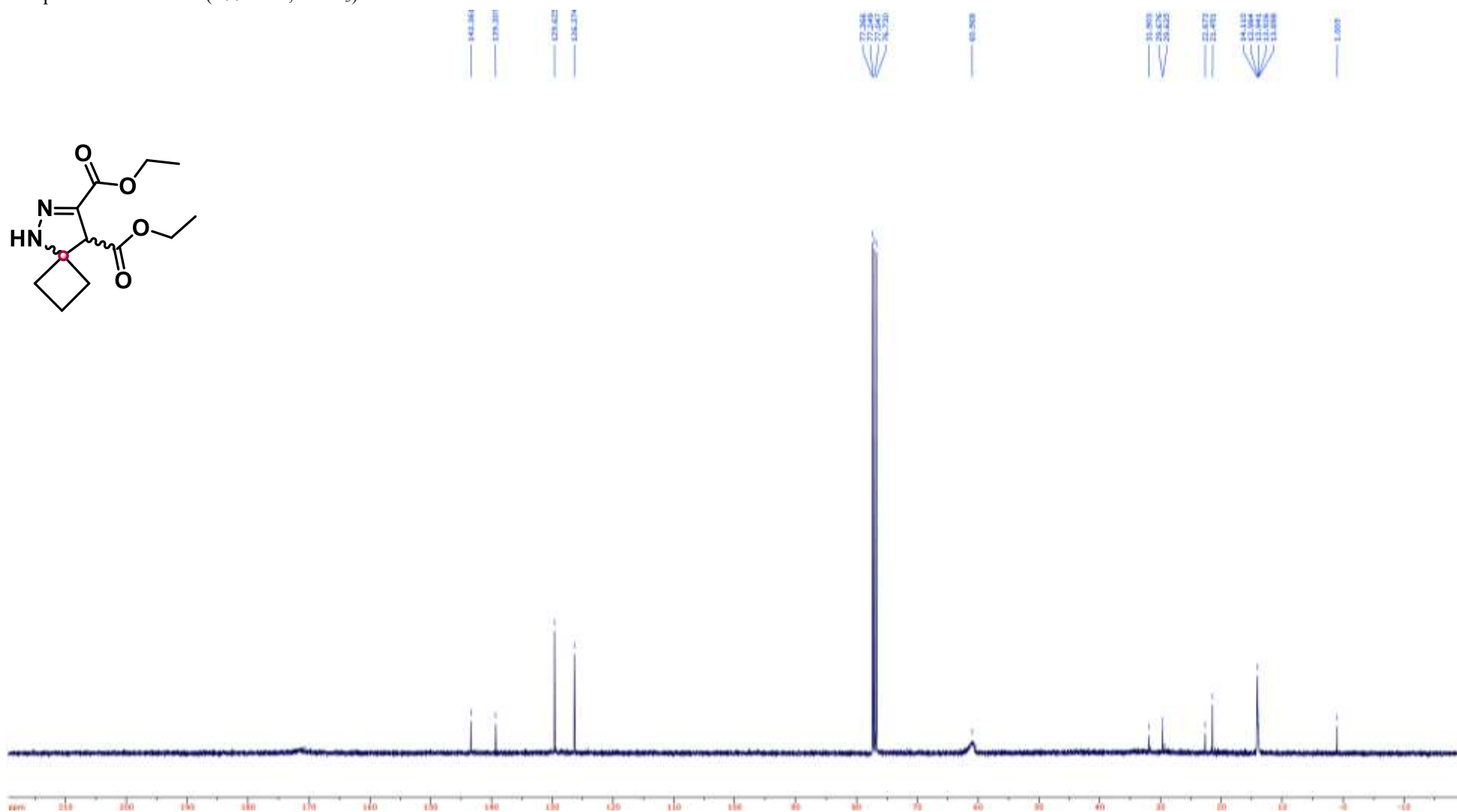
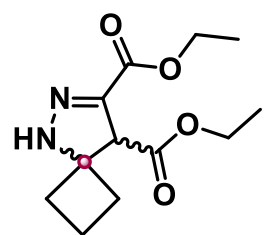
Compound **71** ^{13}C NMR (100 MHz, CDCl_3)



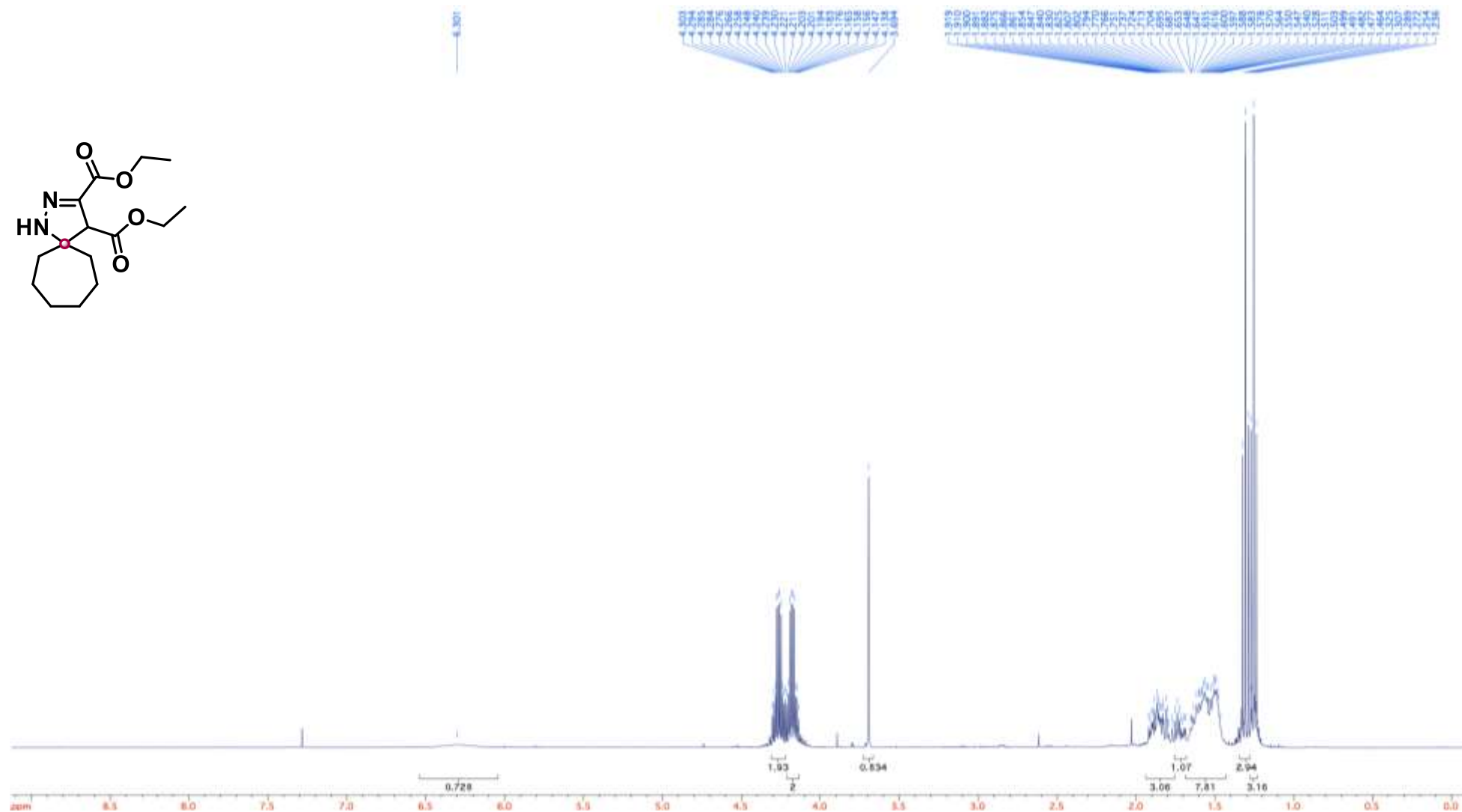
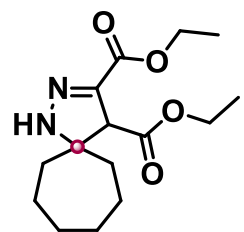
Compound 72 ^1H NMR (400 MHz, CDCl_3)



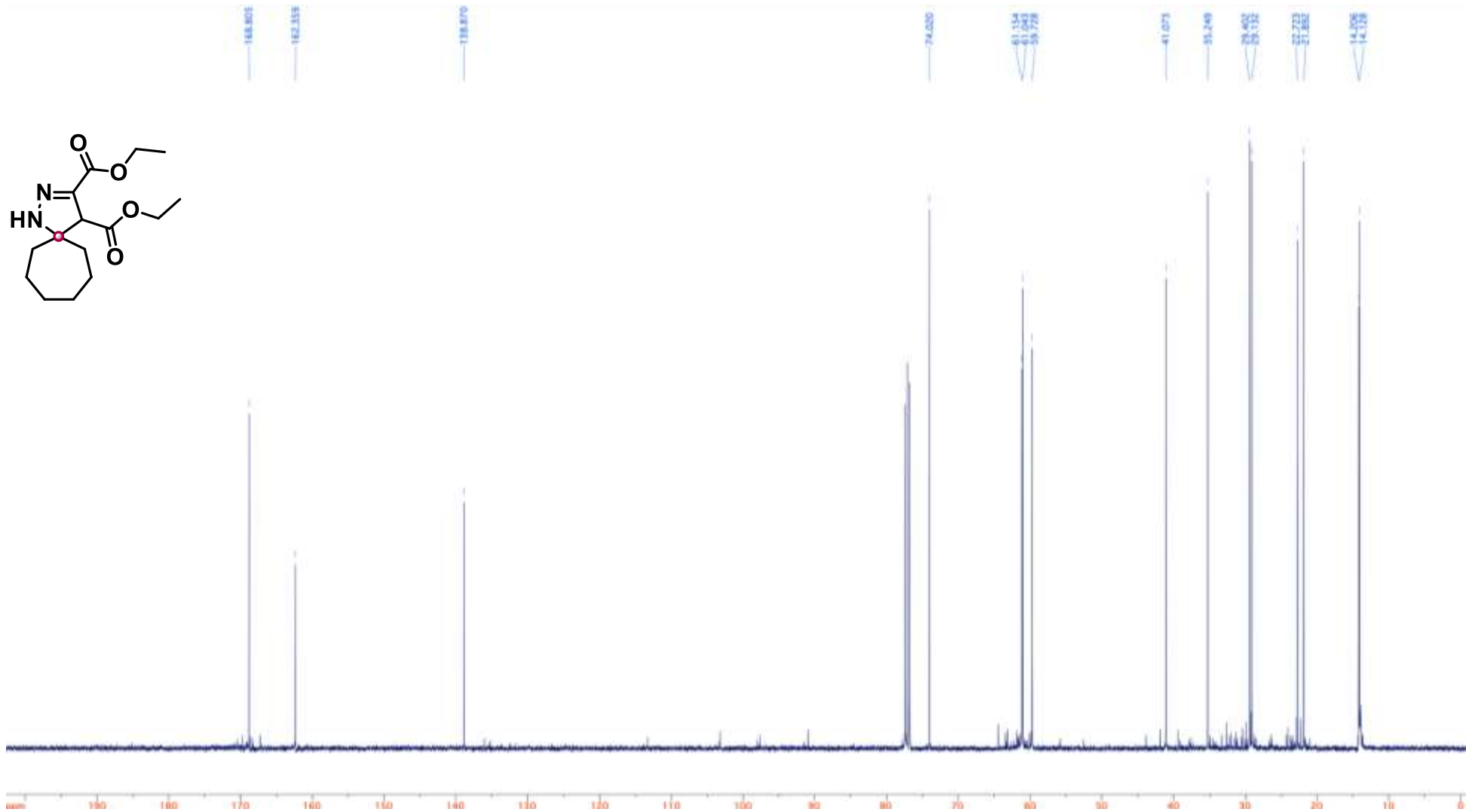
Compound **72** ^{13}C NMR (100 MHz, CDCl_3)



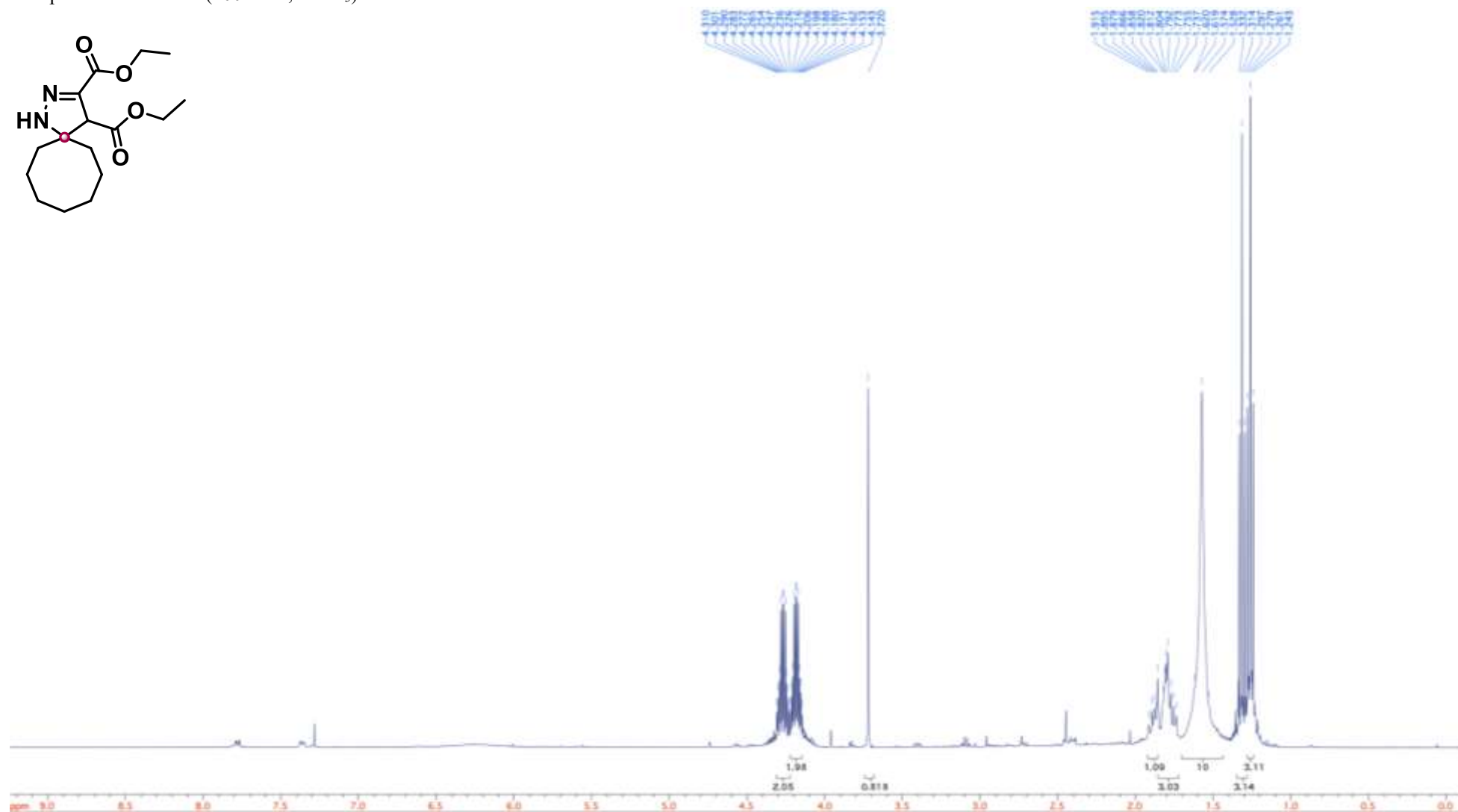
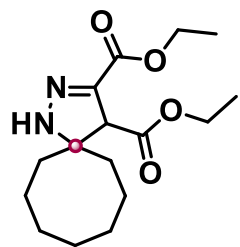
Compound 73 ^1H NMR (400 MHz, CDCl_3)



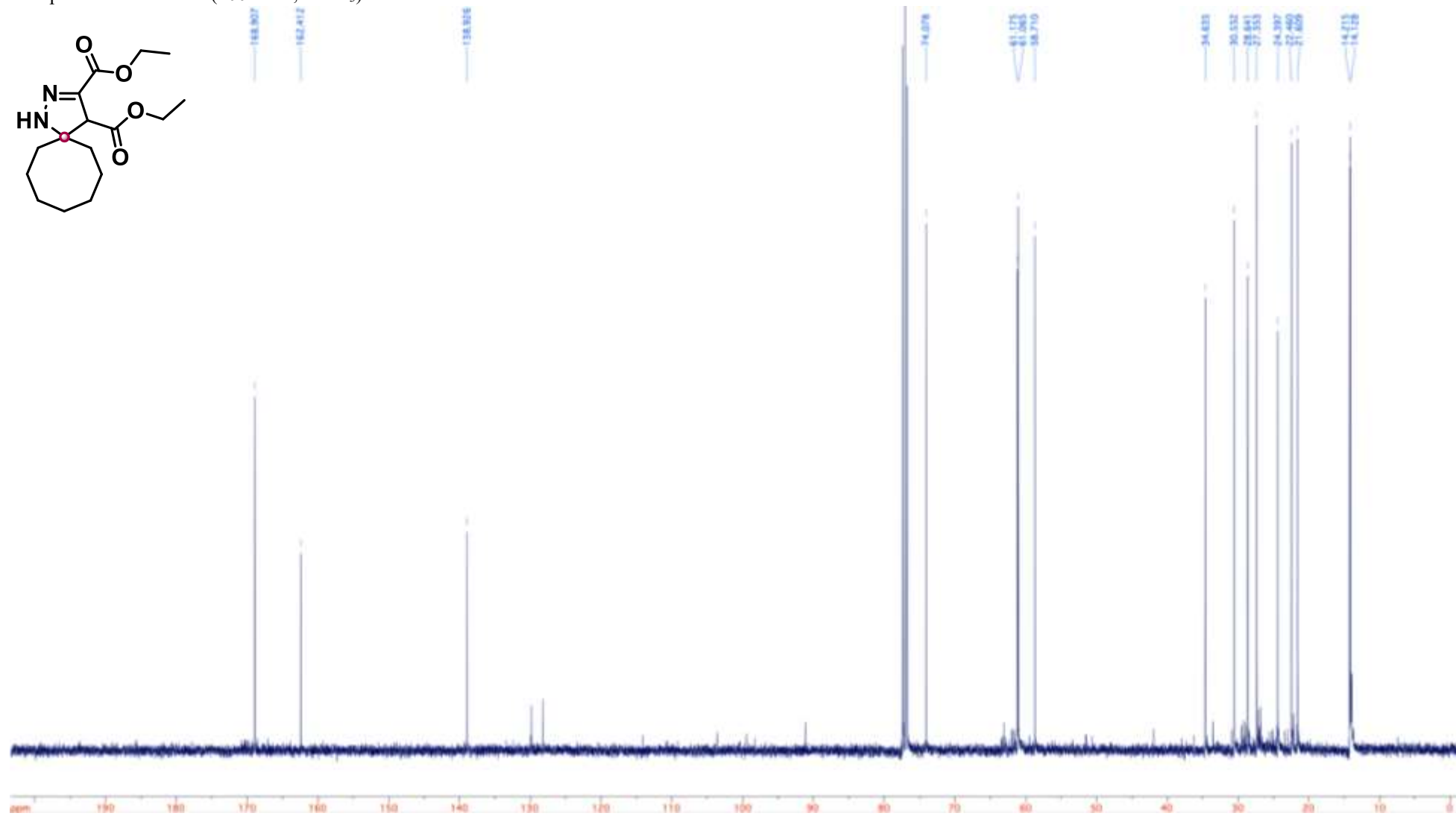
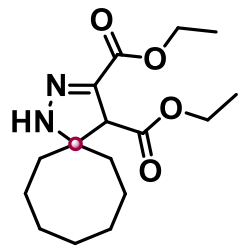
Compound **73** ^{13}C NMR (100 MHz, CDCl_3)



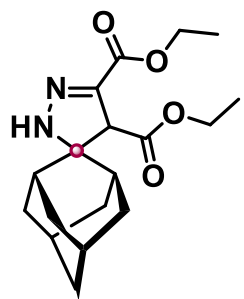
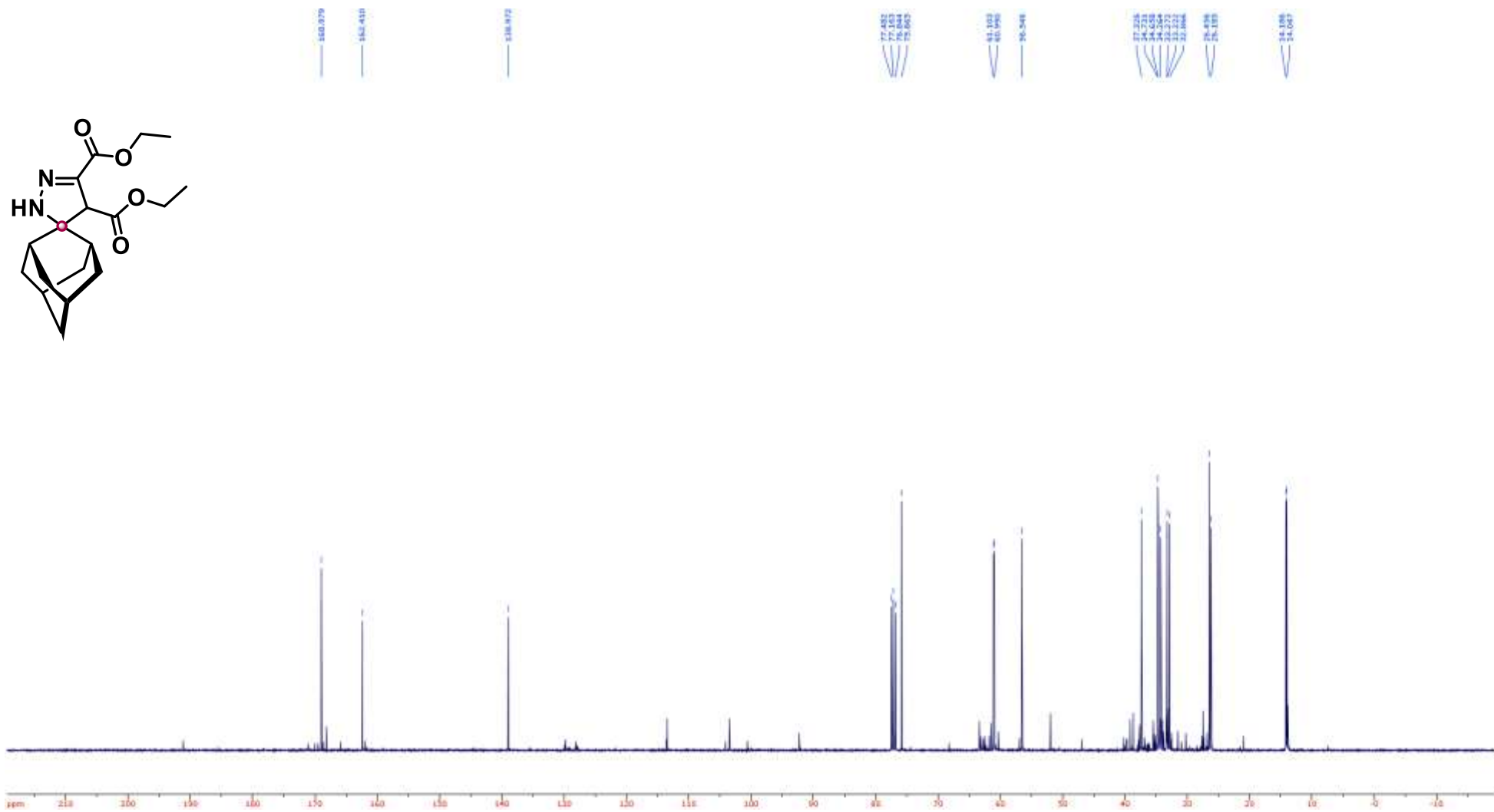
Compound 74 ^1H NMR (400 MHz, CDCl_3)



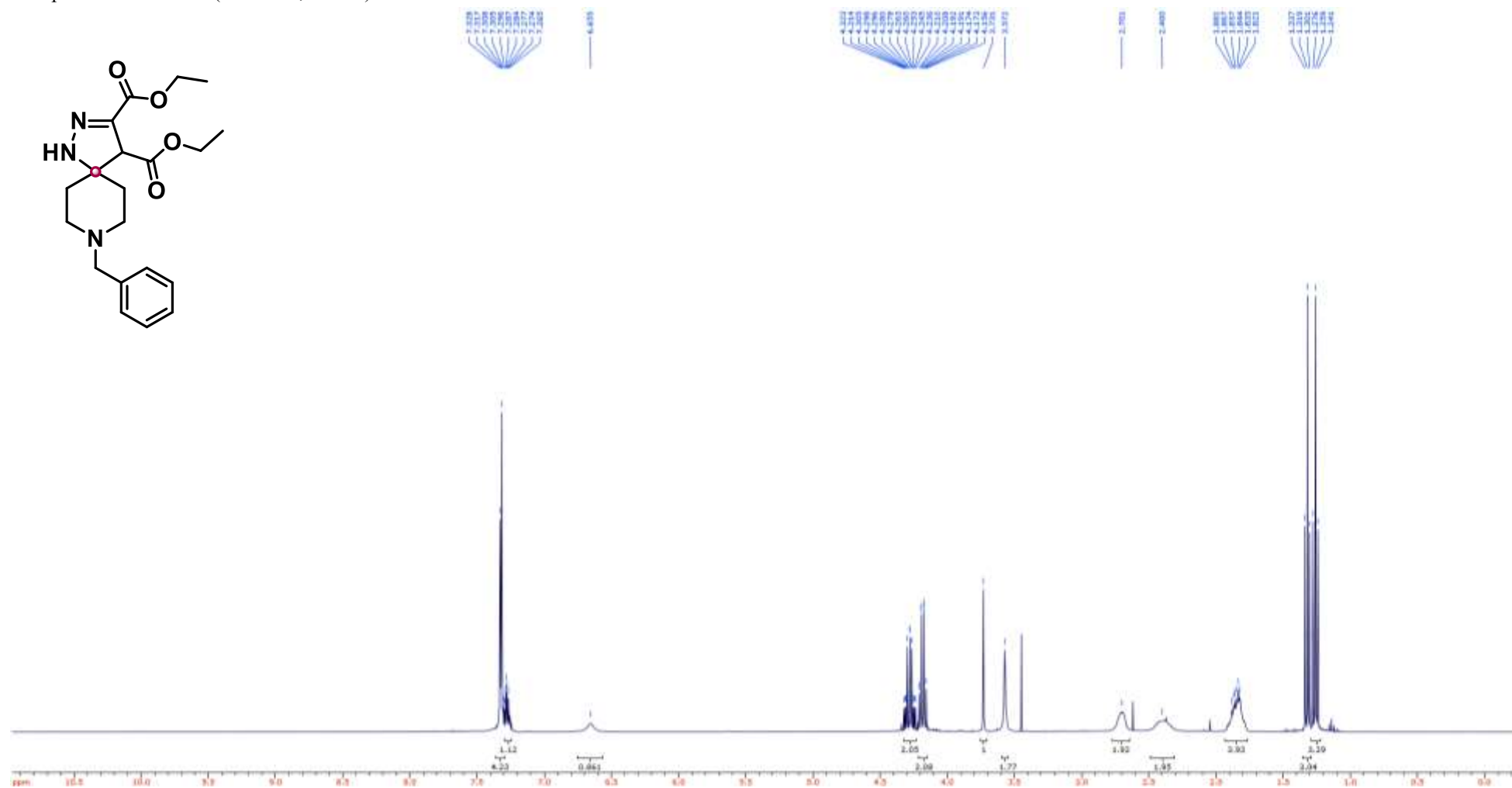
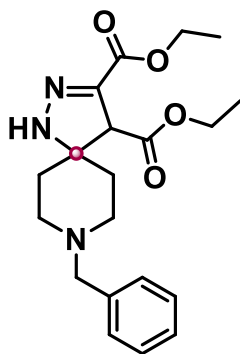
Compound 74 ^{13}C NMR (100 MHz, CDCl_3)



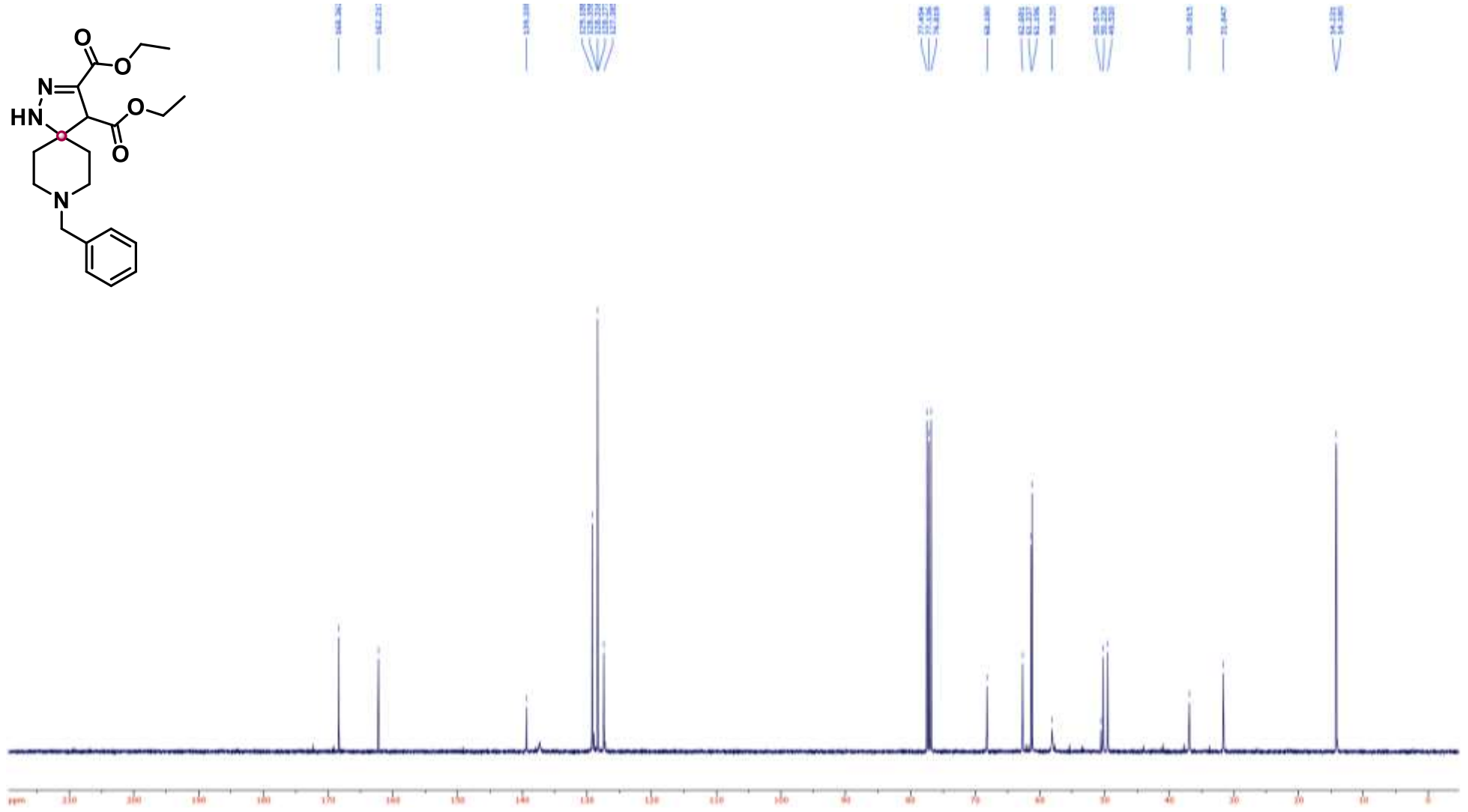
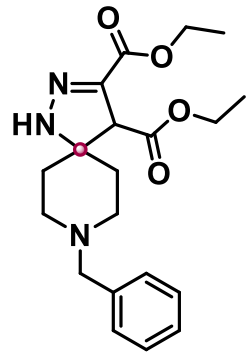
Compound **75** ^{13}C NMR (100 MHz, CDCl_3)



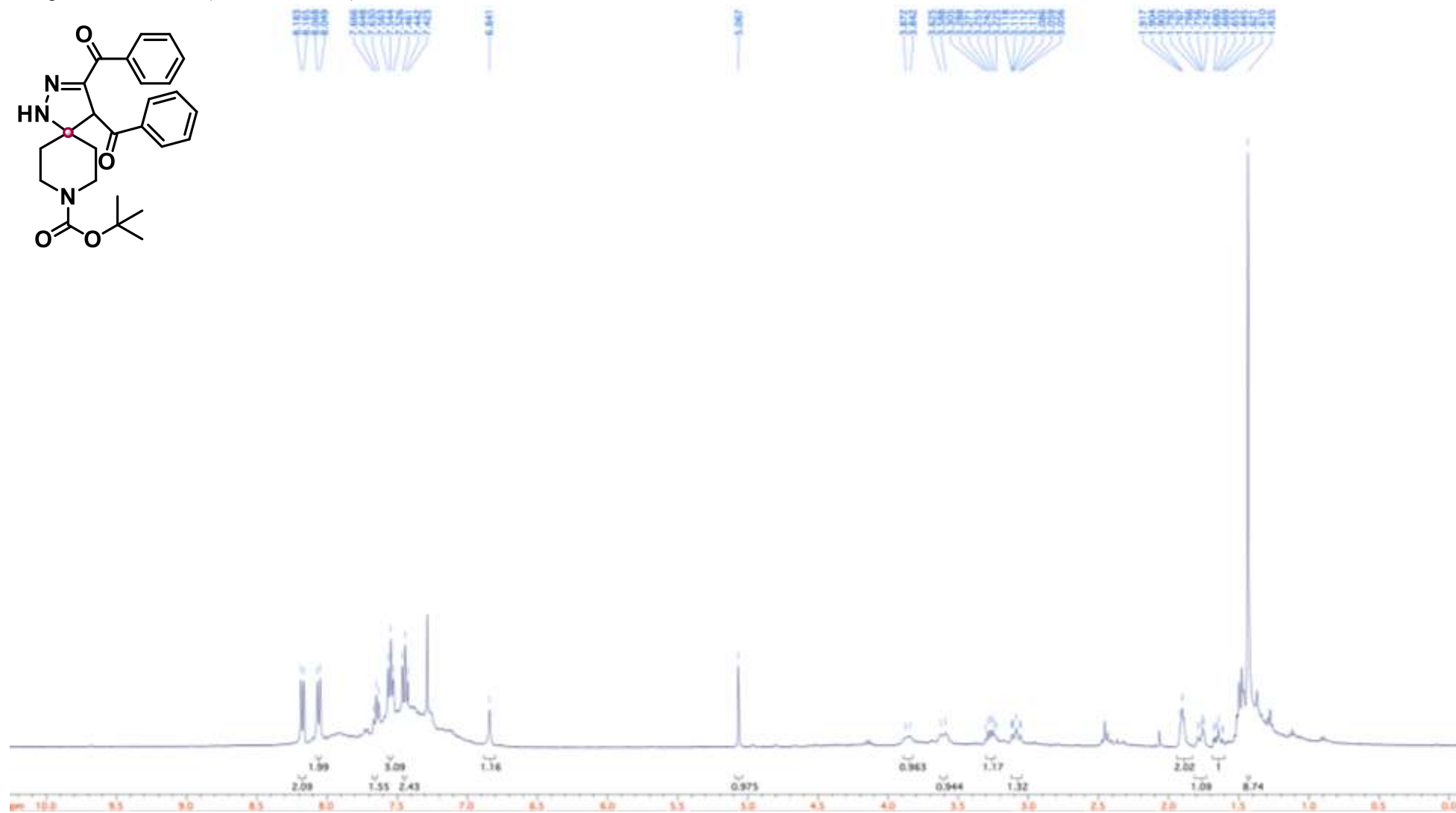
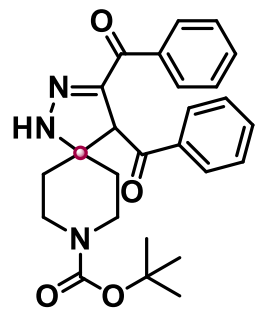
Compound 76 ^1H NMR (400 MHz, CDCl_3)



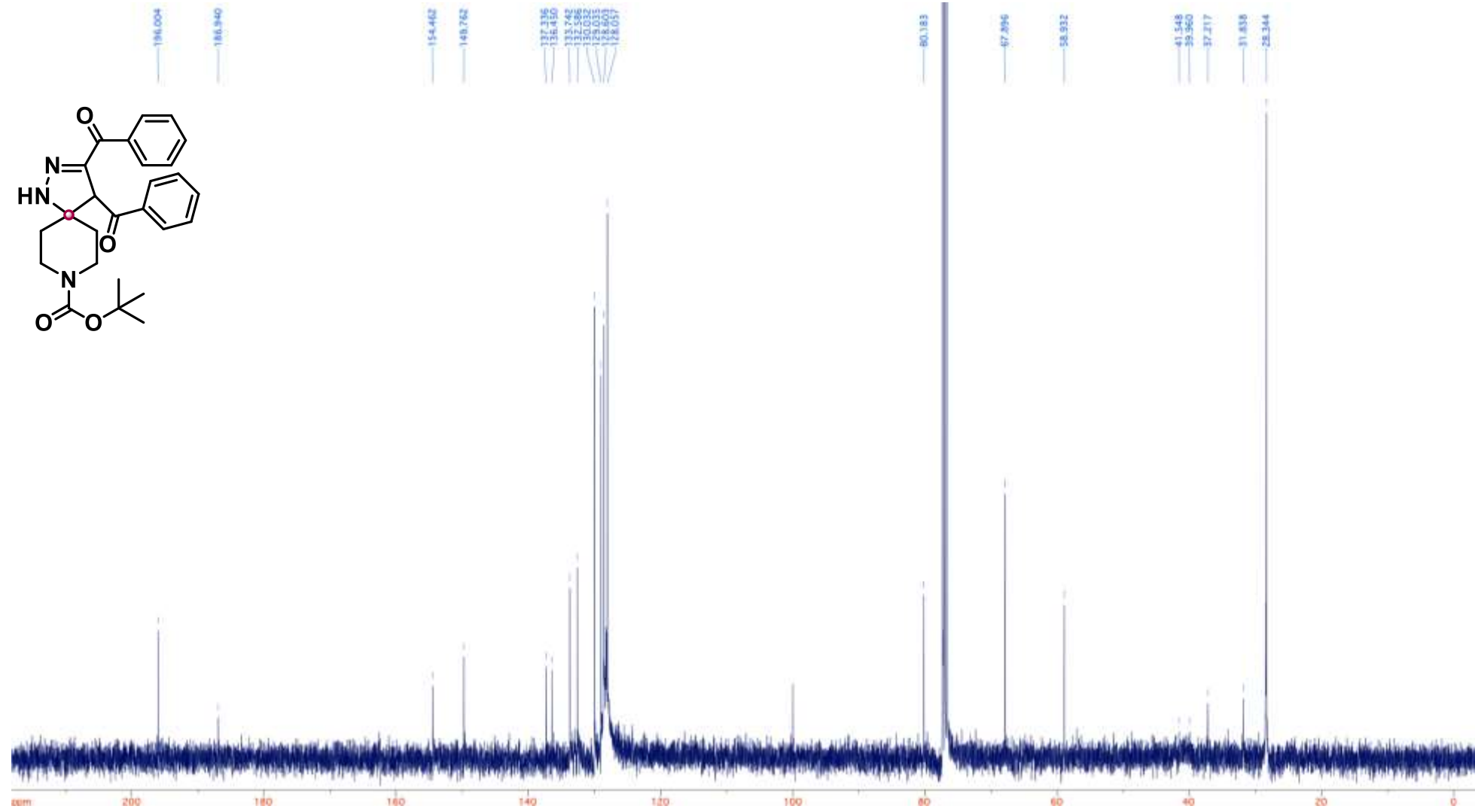
Compound 76 ^{13}C NMR (100 MHz, CDCl_3)



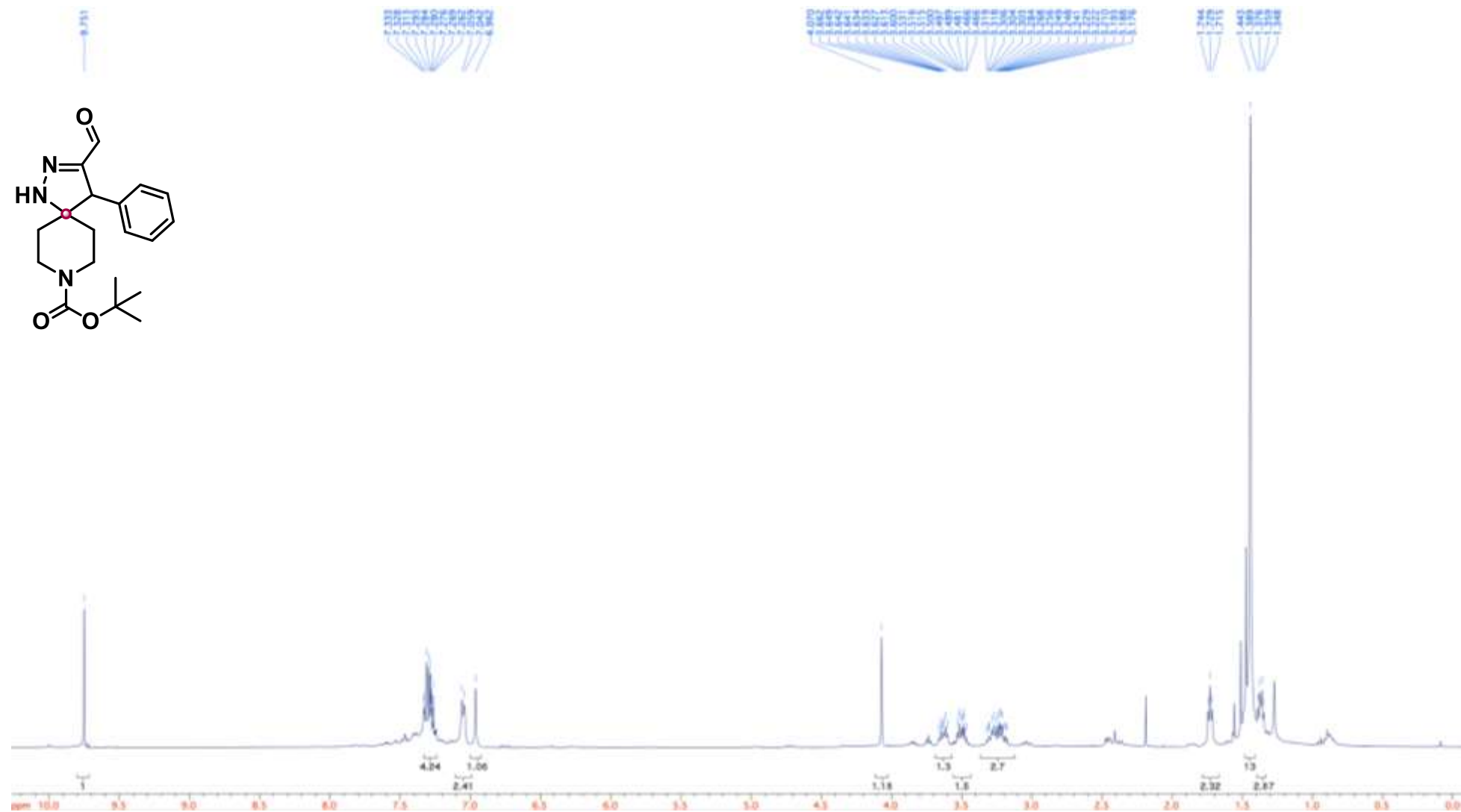
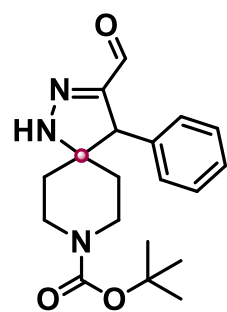
Compound **78** ^1H NMR (400 MHz, CDCl_3)



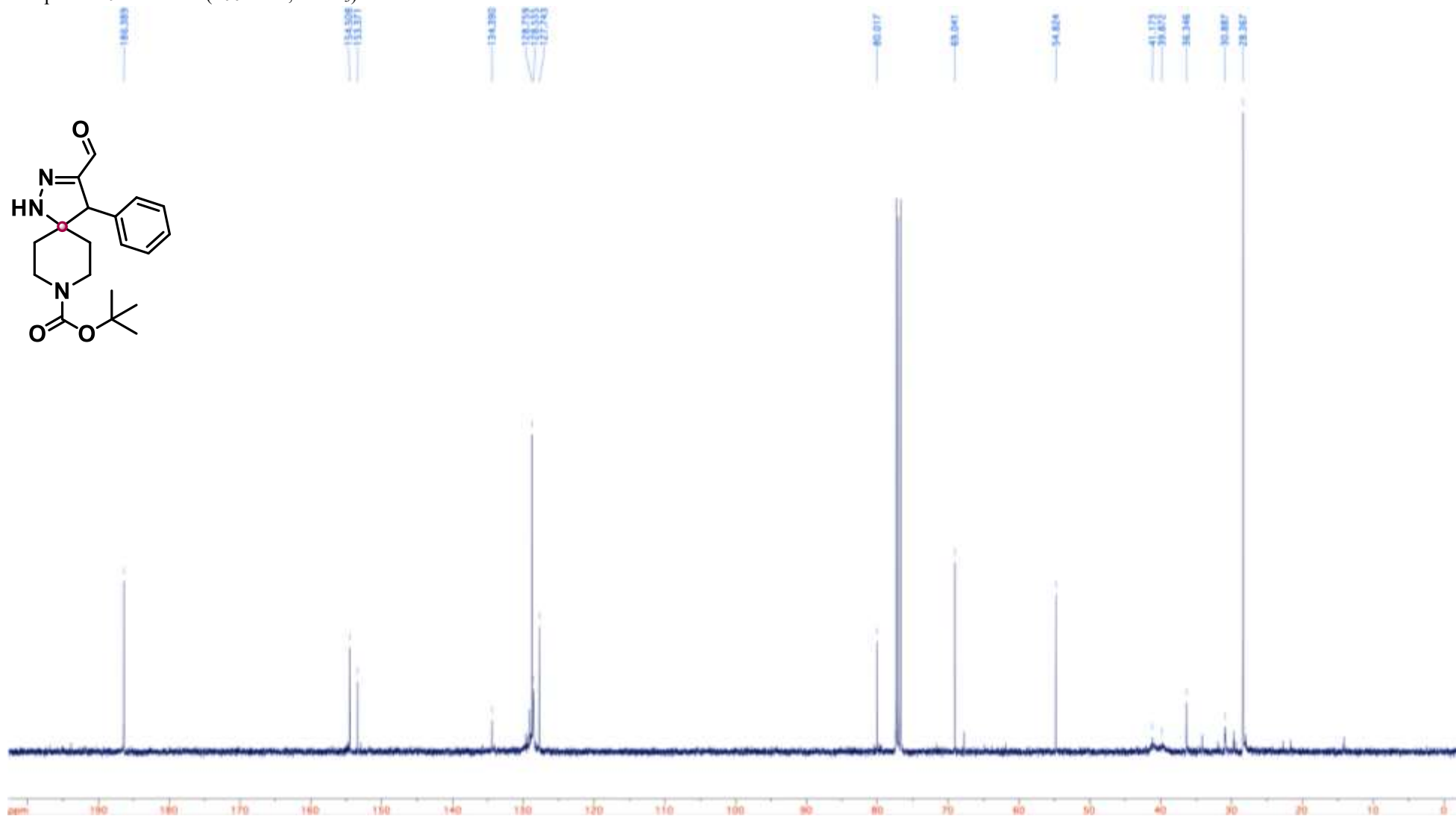
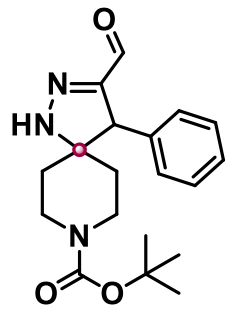
Compound **78** ^{13}C NMR (100 MHz, CDCl_3)



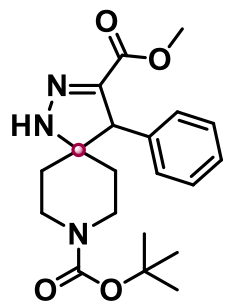
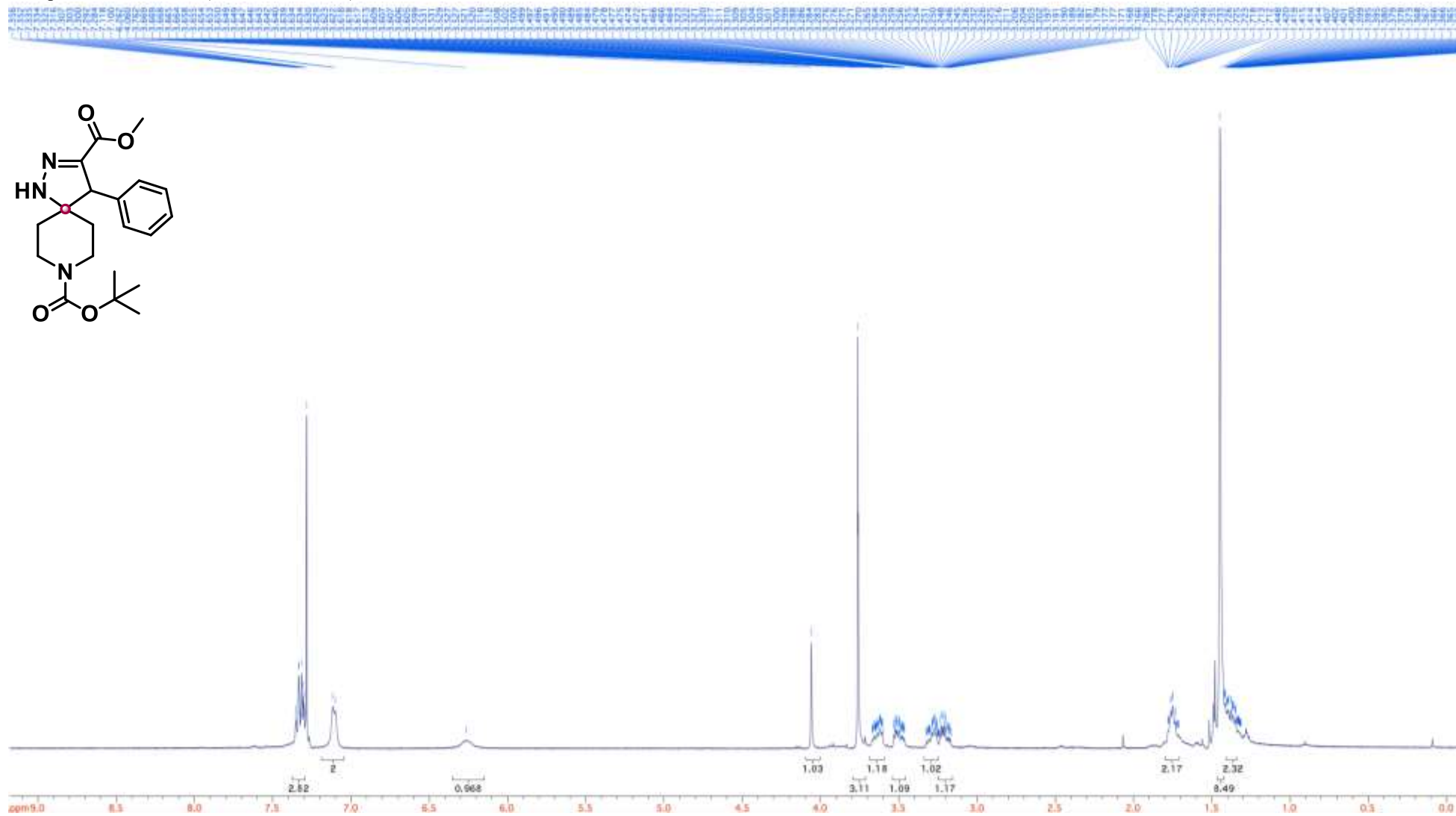
Compound **79** ^1H NMR (400 MHz, CDCl_3)



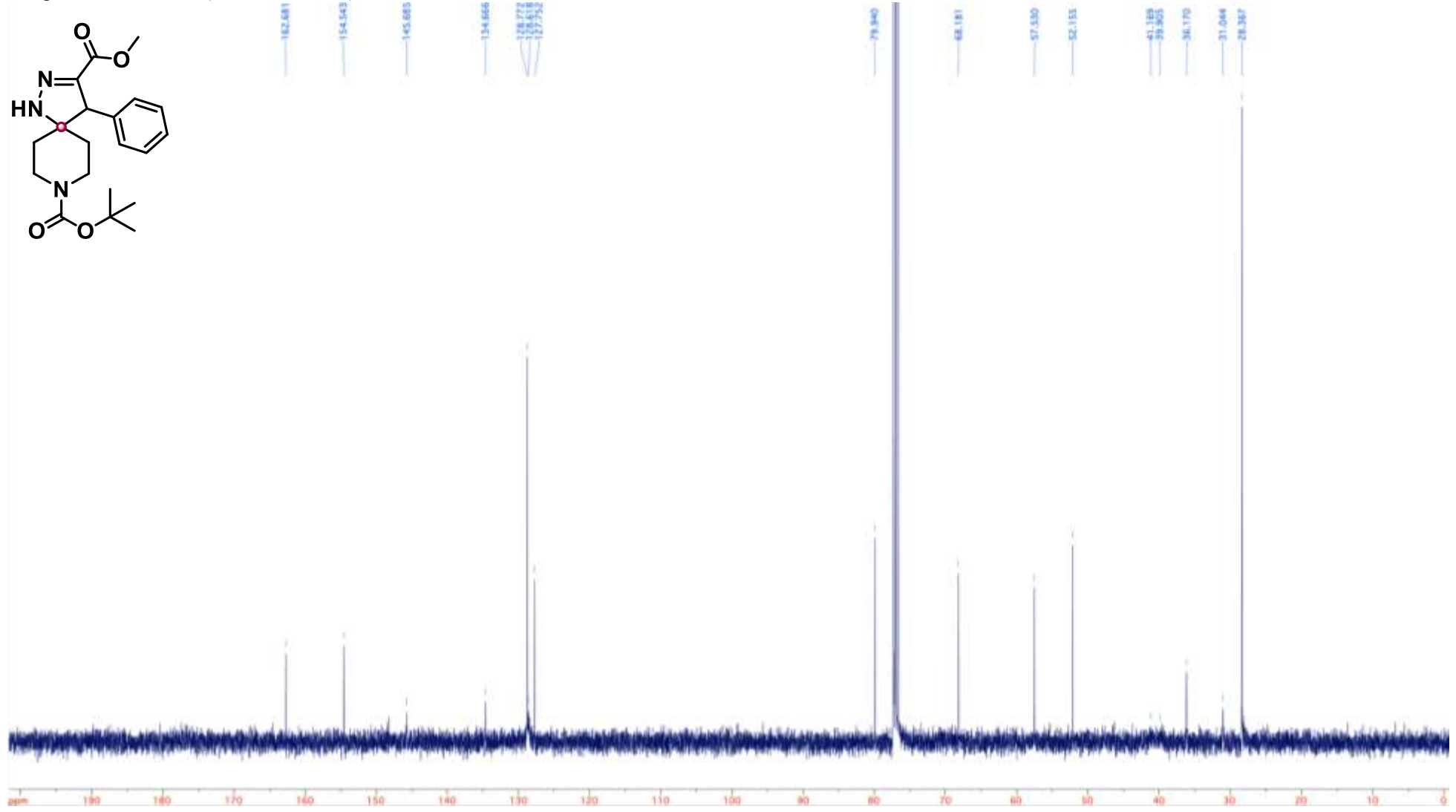
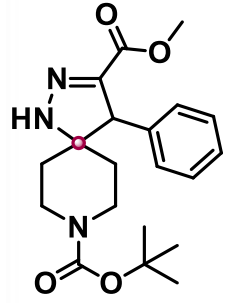
Compound **79** ^{13}C NMR (100 MHz, CDCl_3)



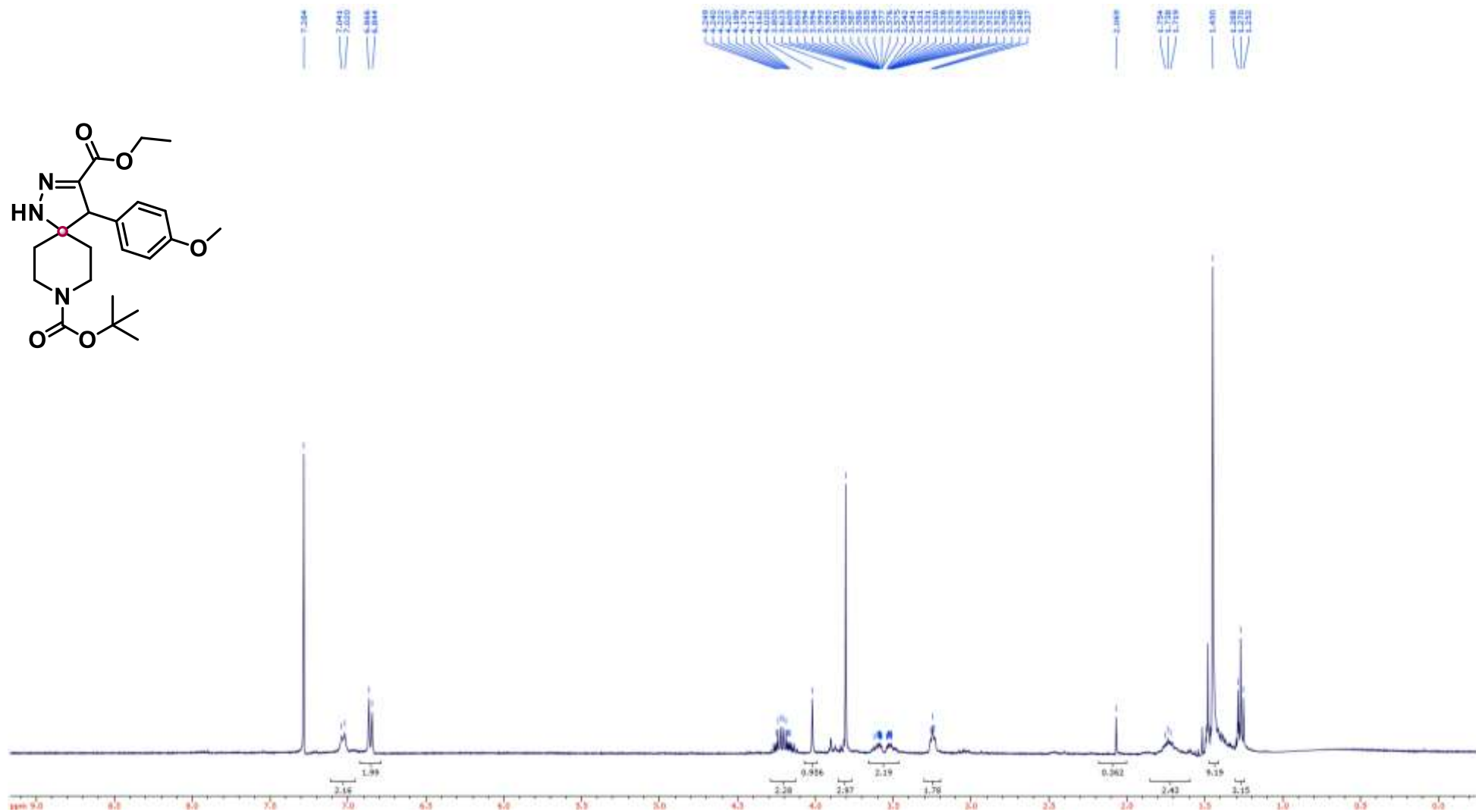
Compound **80** ^1H NMR (400 MHz, CDCl_3)



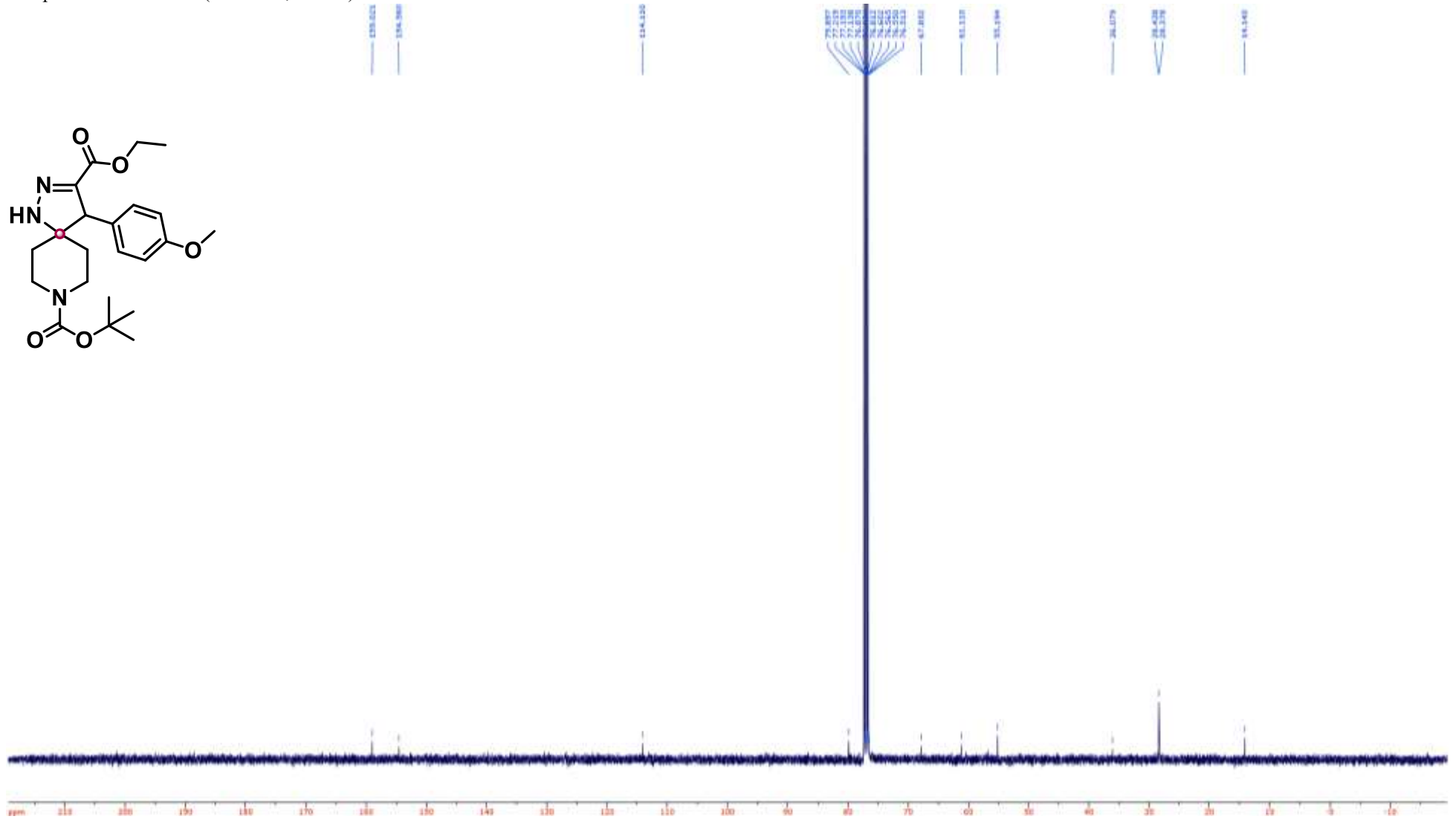
Compound **80** ^{13}C NMR (100 MHz, CDCl_3)



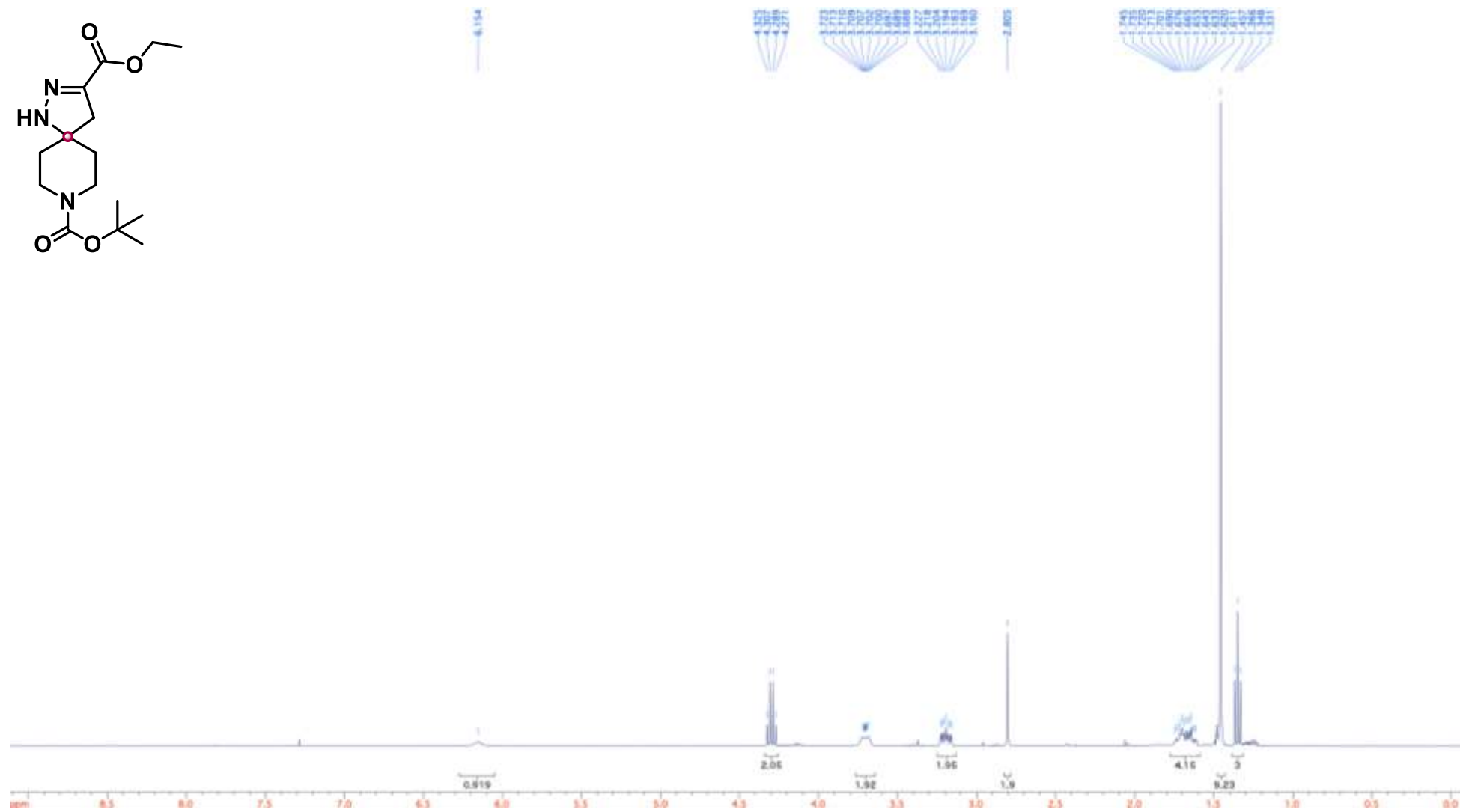
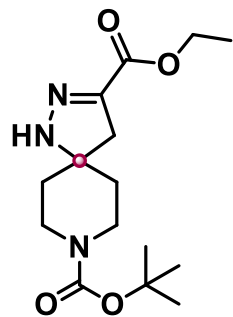
Compound **81** ^1H NMR (400 MHz, CDCl_3)



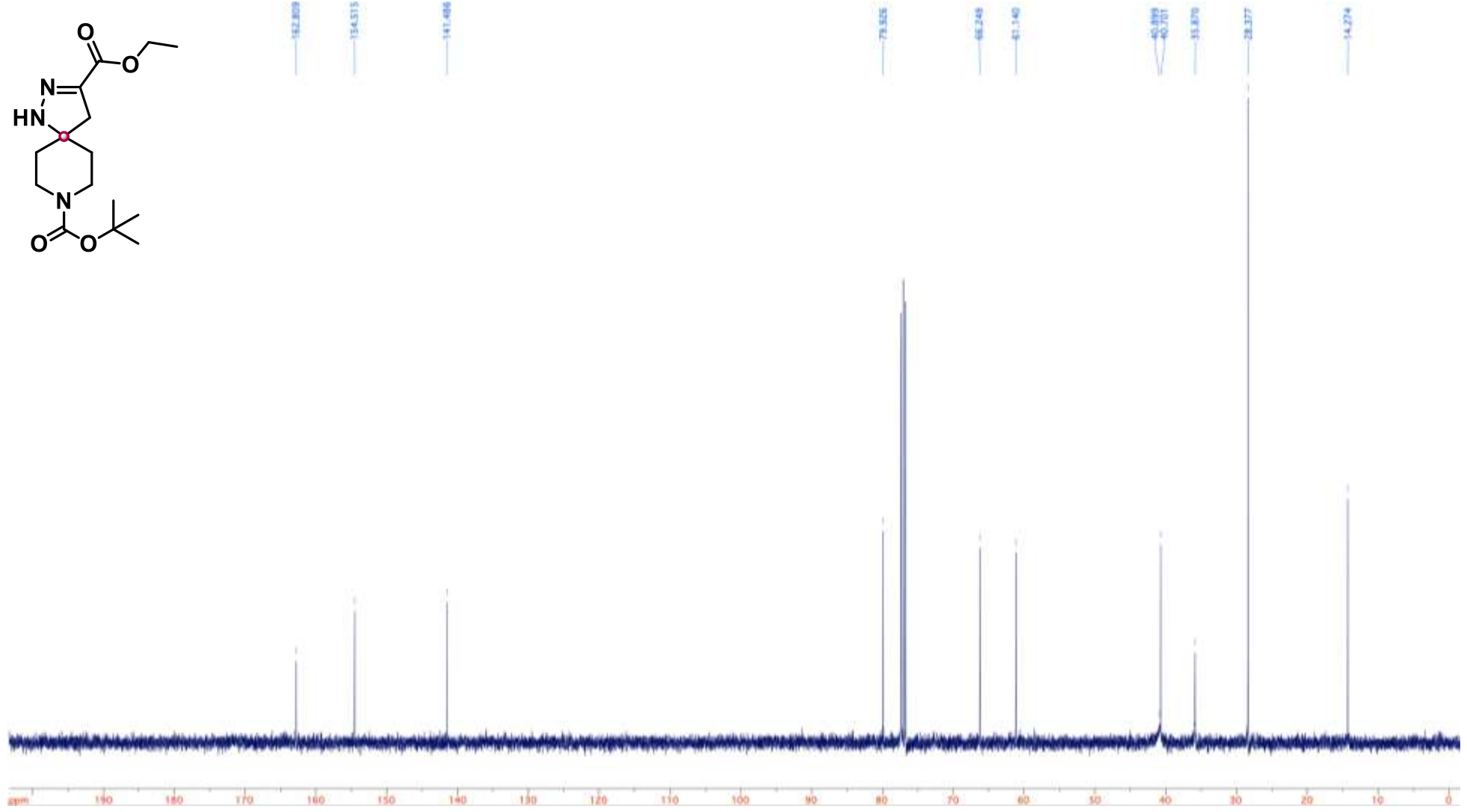
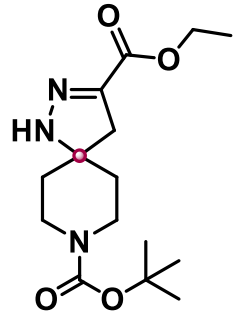
Compound **81** ^{13}C NMR (100 MHz, CDCl_3)



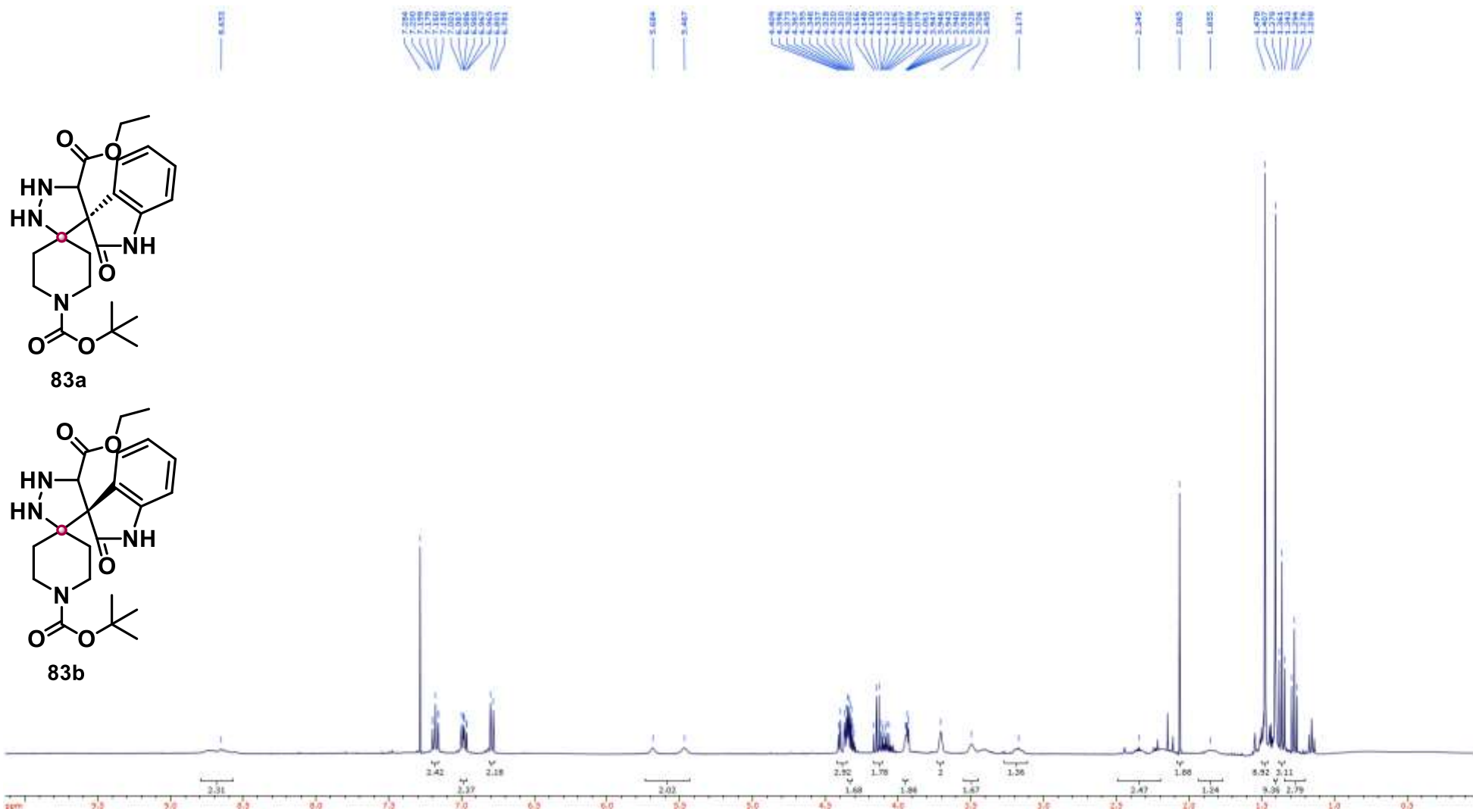
Compound **82** ^1H NMR (400 MHz, CDCl_3)



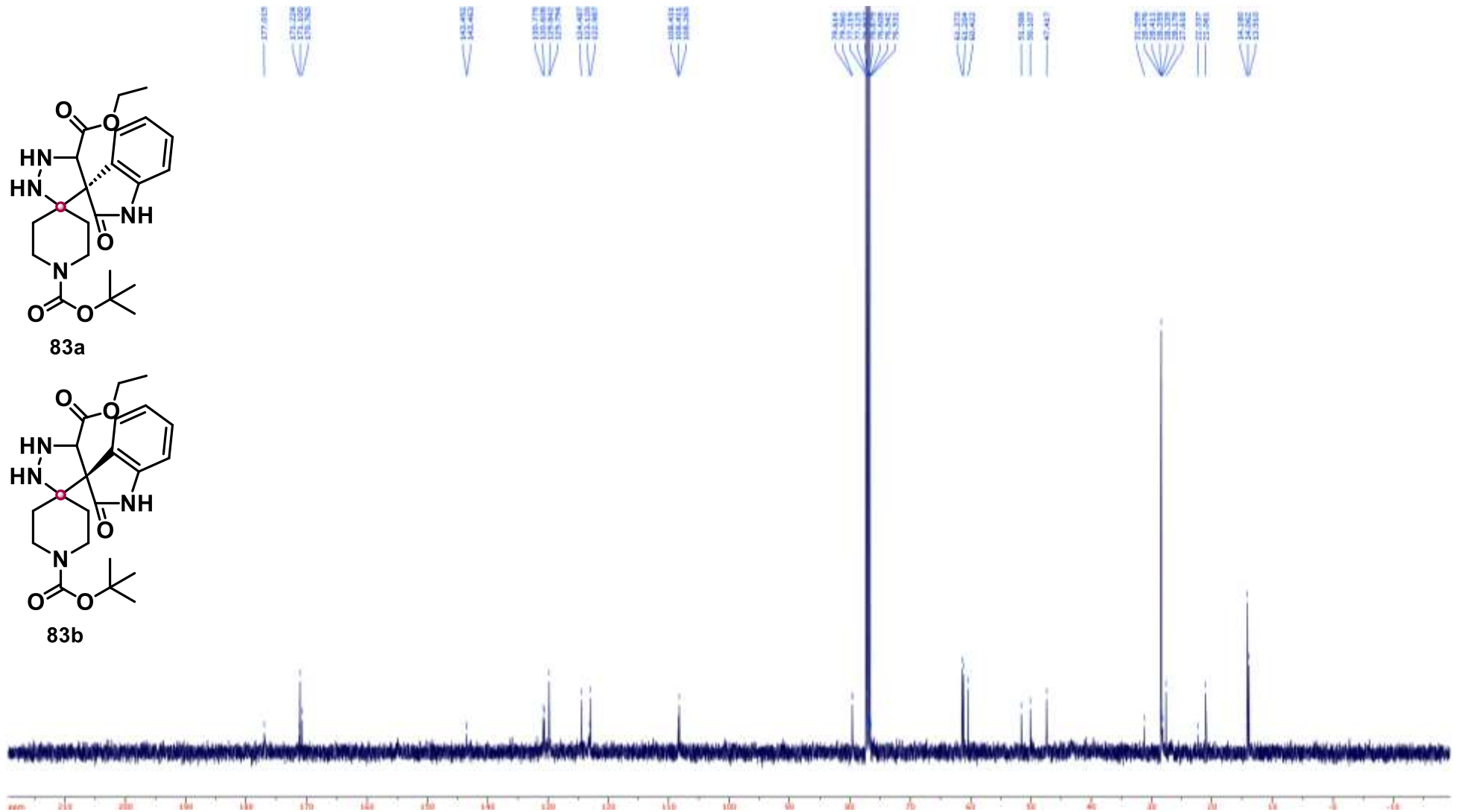
Compound **82** ^{13}C NMR (100 MHz, CDCl_3)



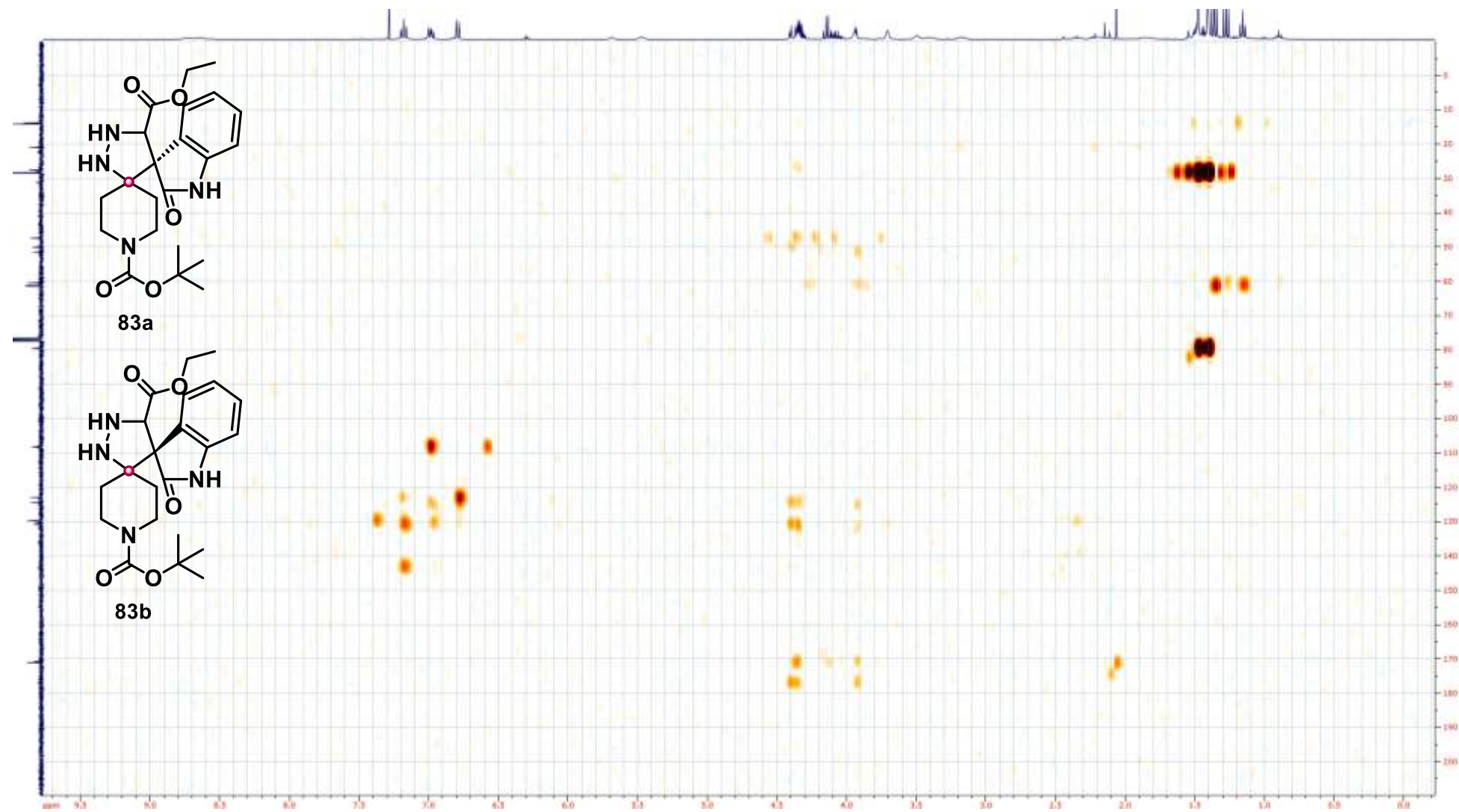
Compound **83** ^1H NMR (400 MHz, CDCl_3)



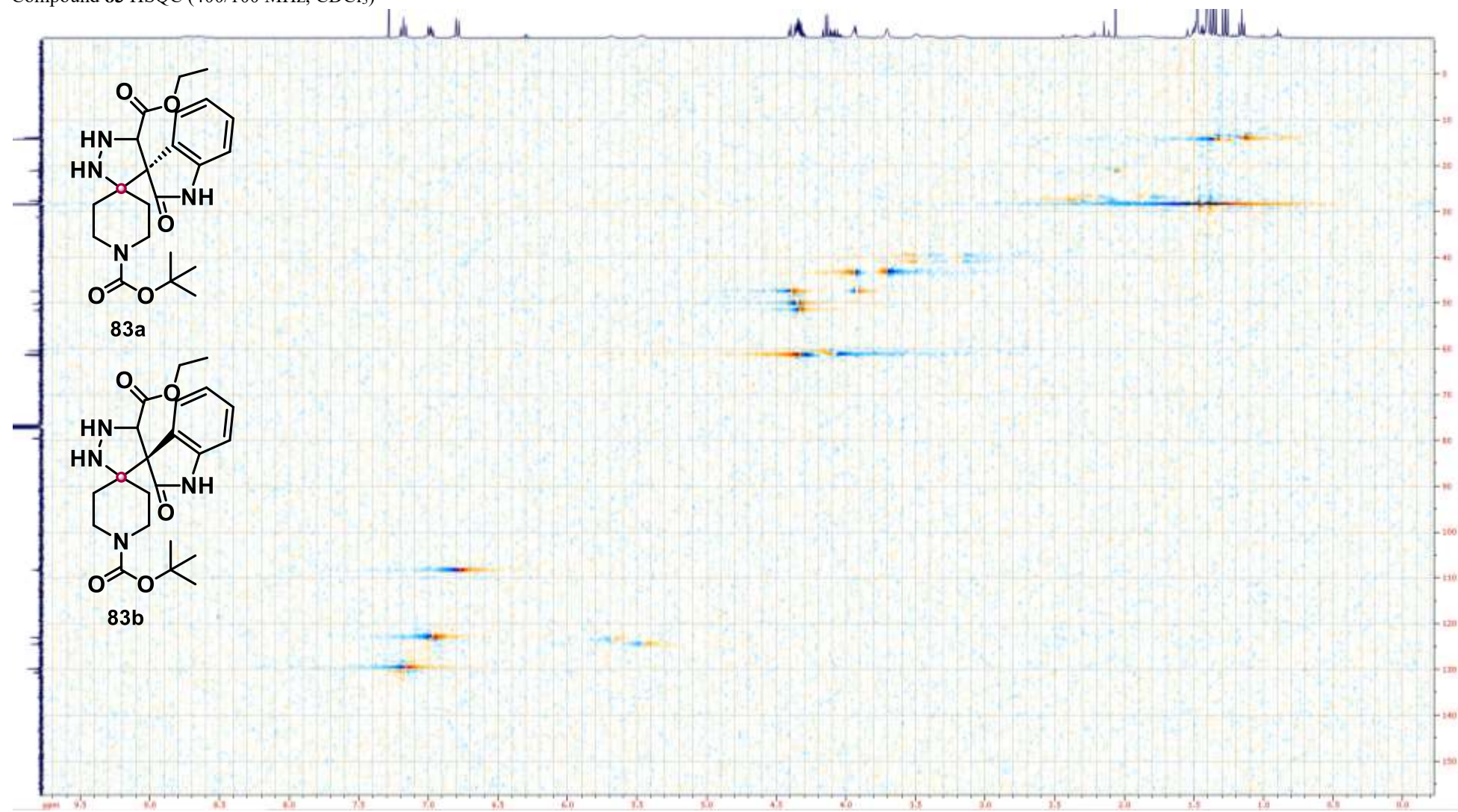
Compound **83** ^{13}C NMR (100 MHz, CDCl_3)



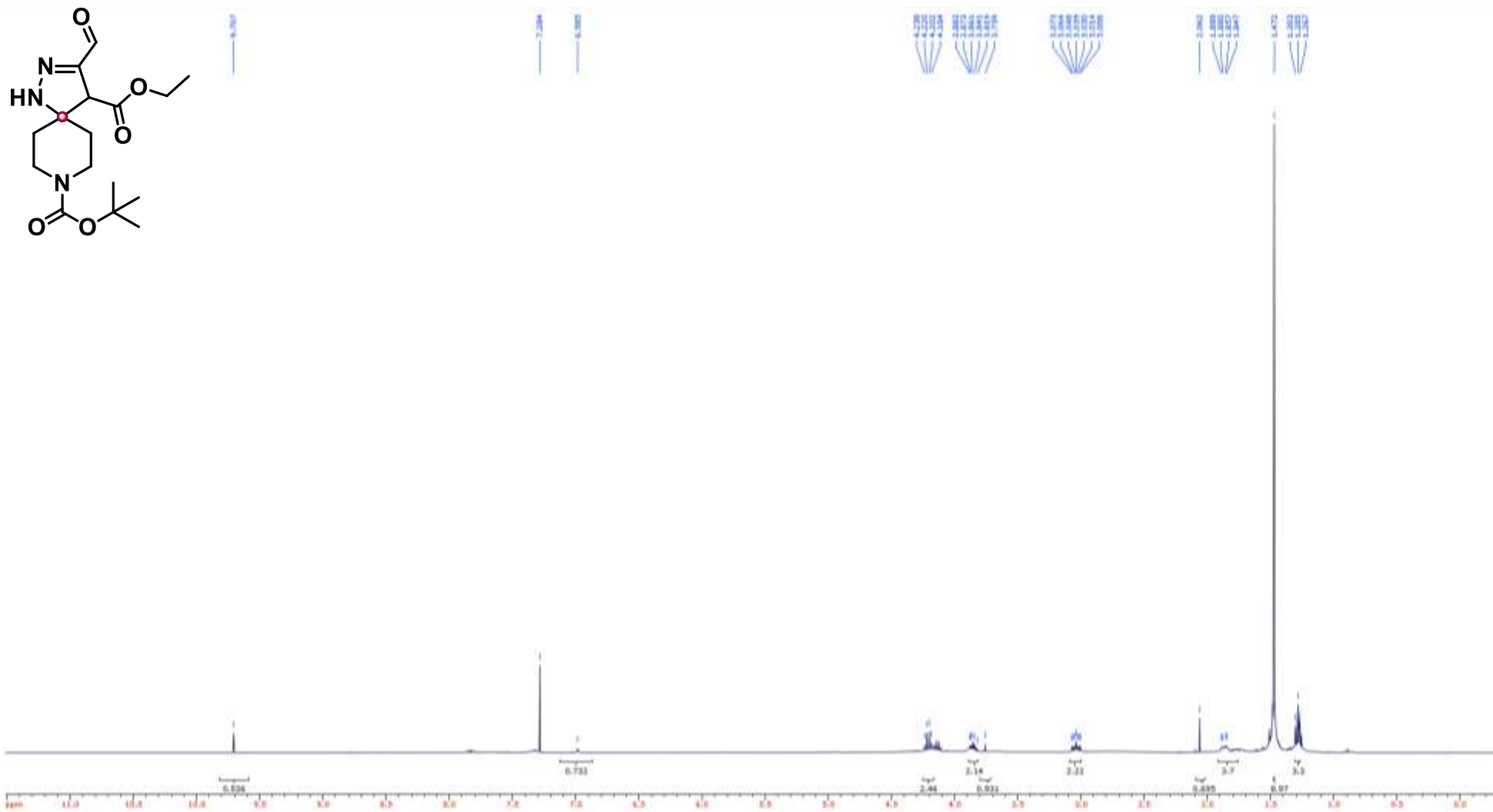
Compound **83** HMBC (400/100 MHz, CDCl₃)



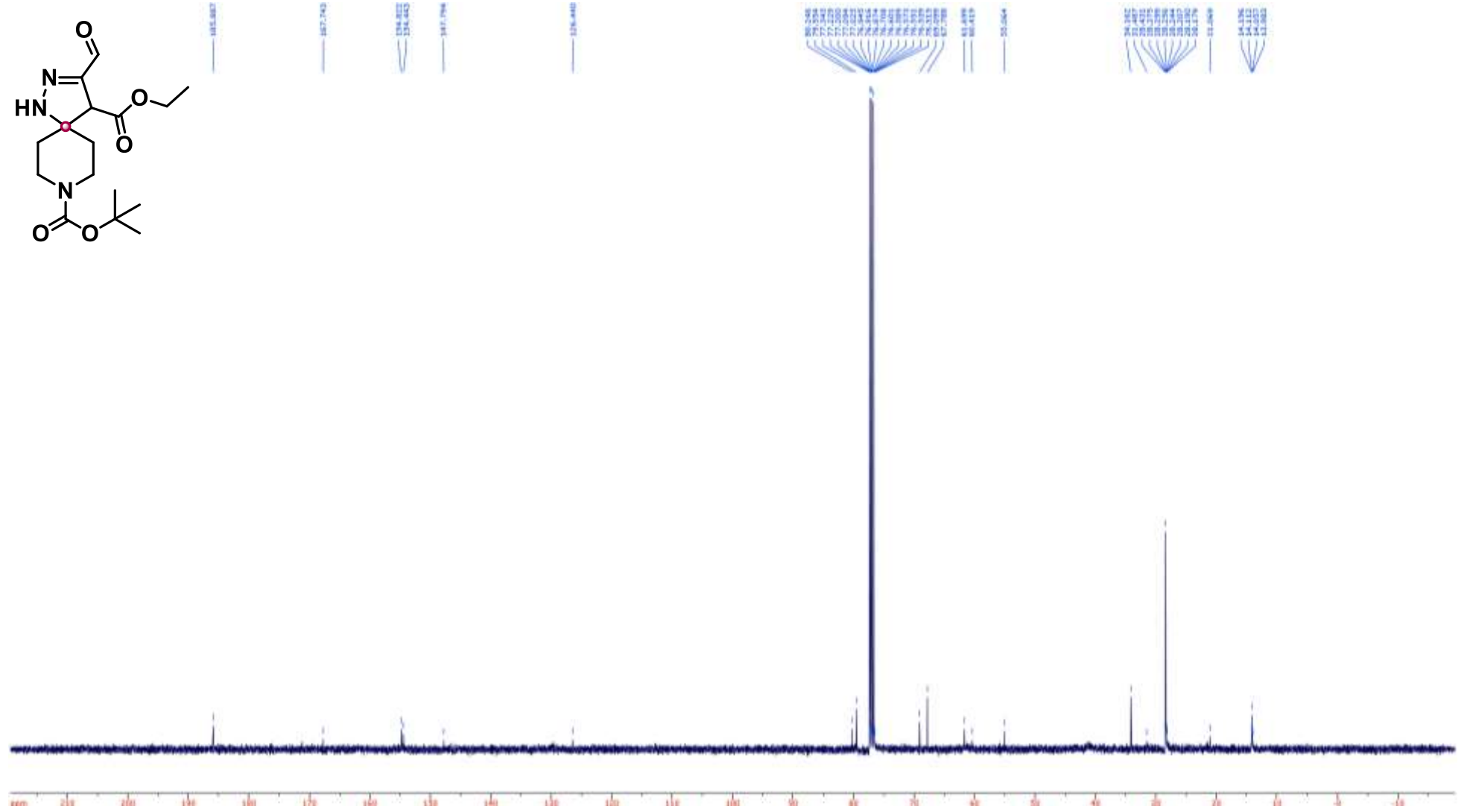
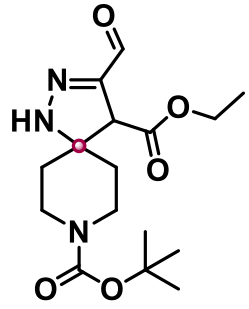
Compound **83** HSQC (400/100 MHz, CDCl₃)



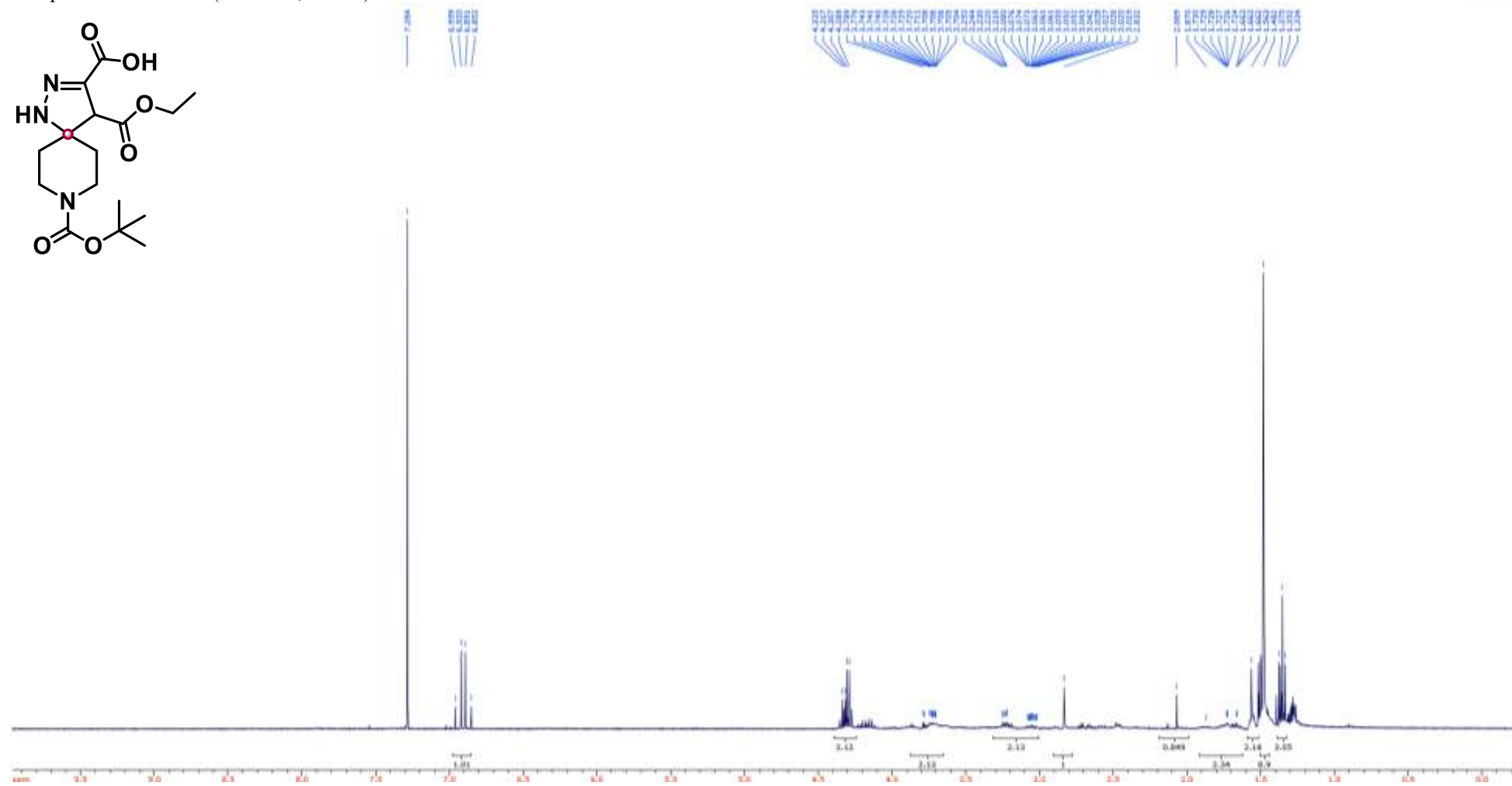
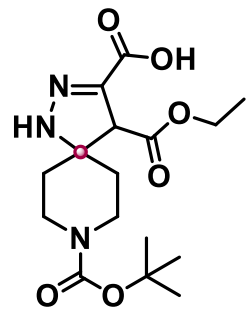
Compound **84** ^1H NMR (400 MHz, CDCl_3)



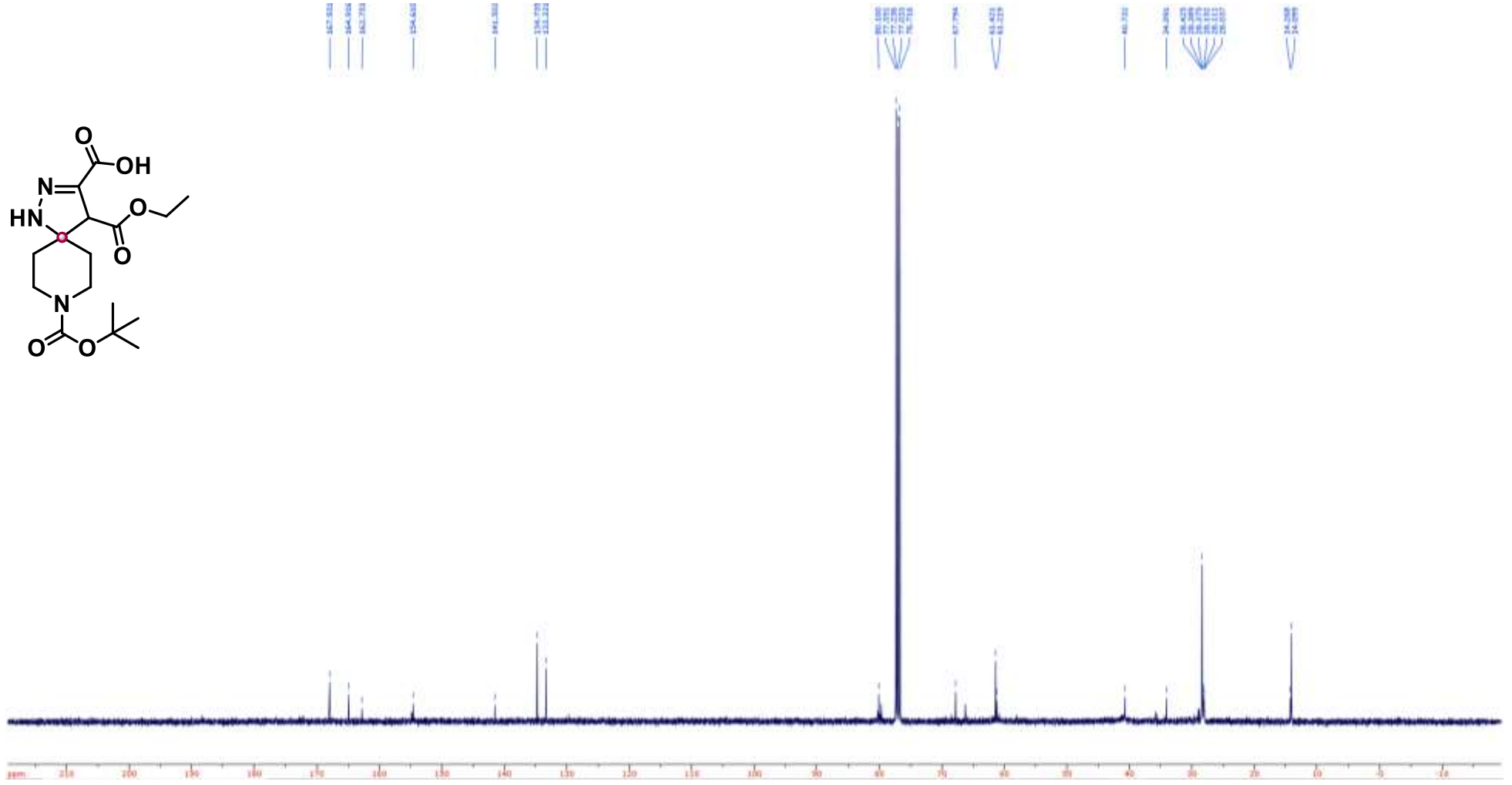
Compound **84** ^{13}C NMR (100 MHz, CDCl_3)



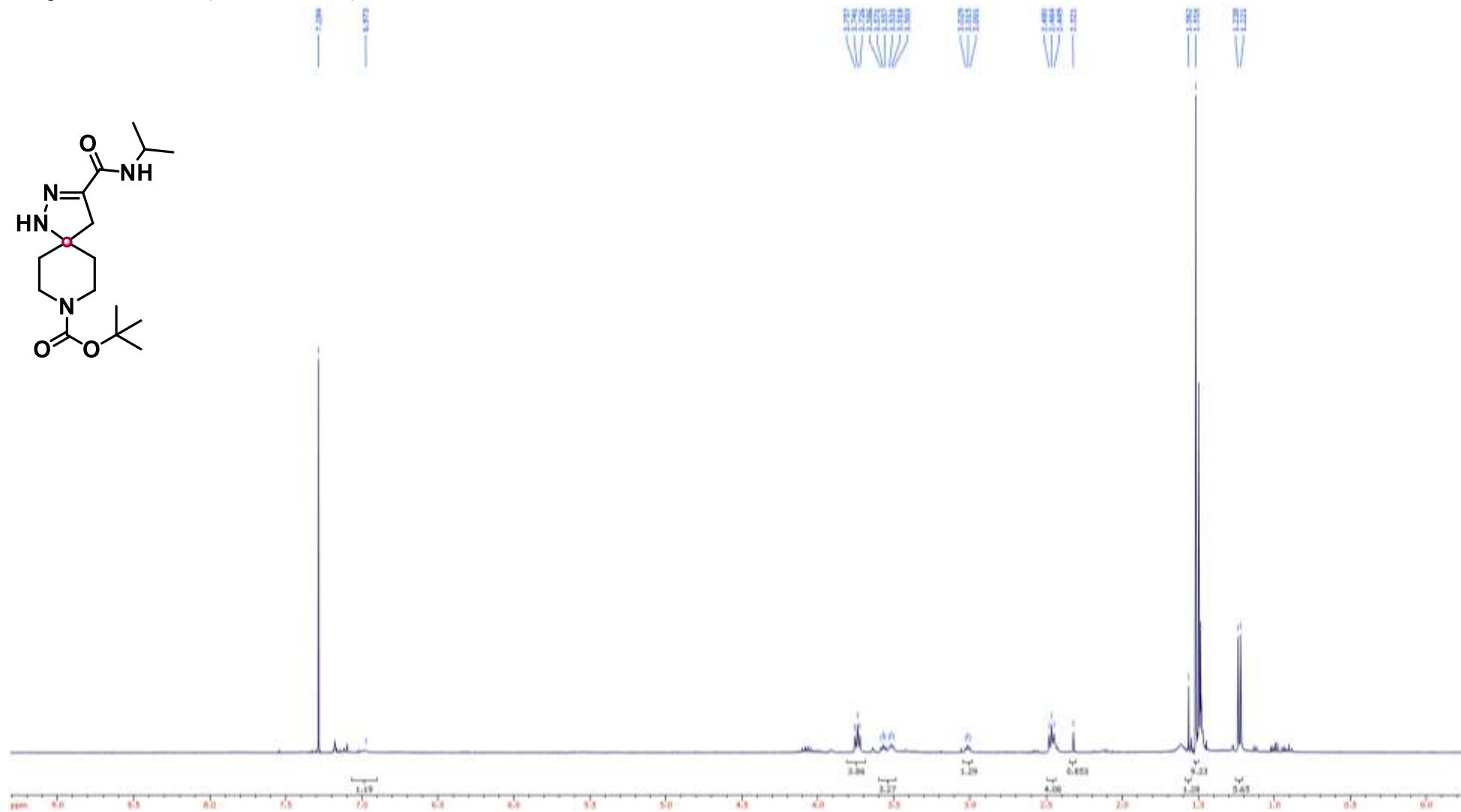
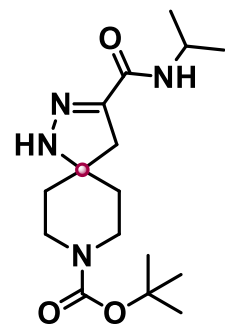
Compound **85** ^1H NMR (400 MHz, CDCl_3)



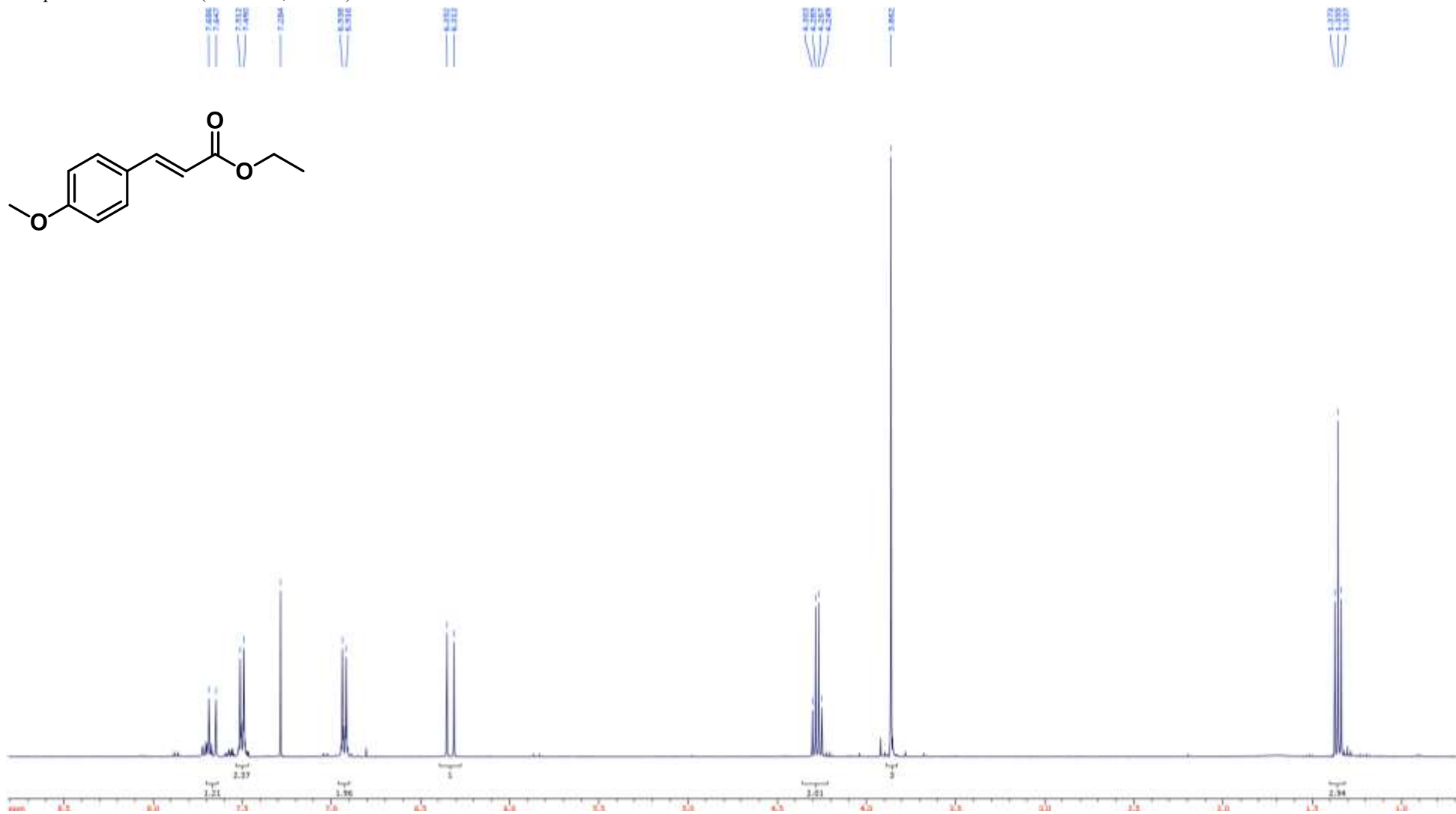
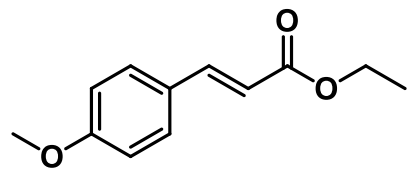
Compound **85** ^{13}C NMR (100 MHz, CDCl_3)



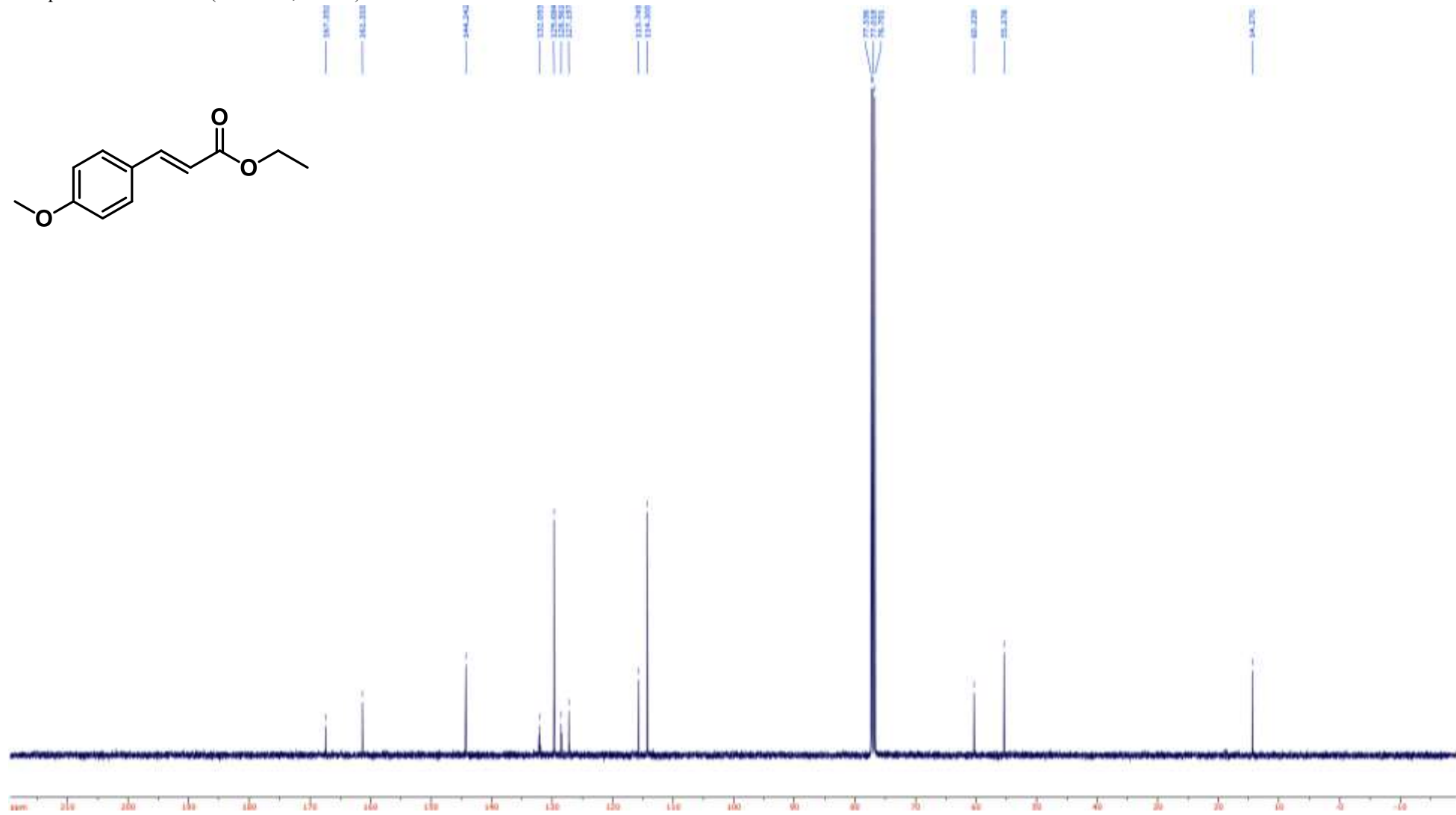
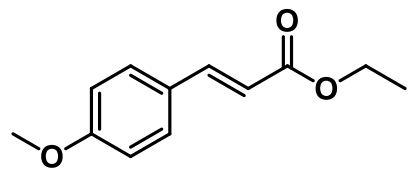
Compound **86** ^1H NMR (400 MHz, CDCl_3)



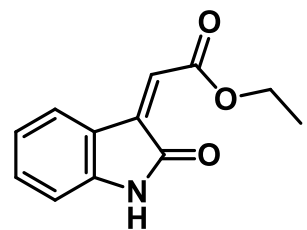
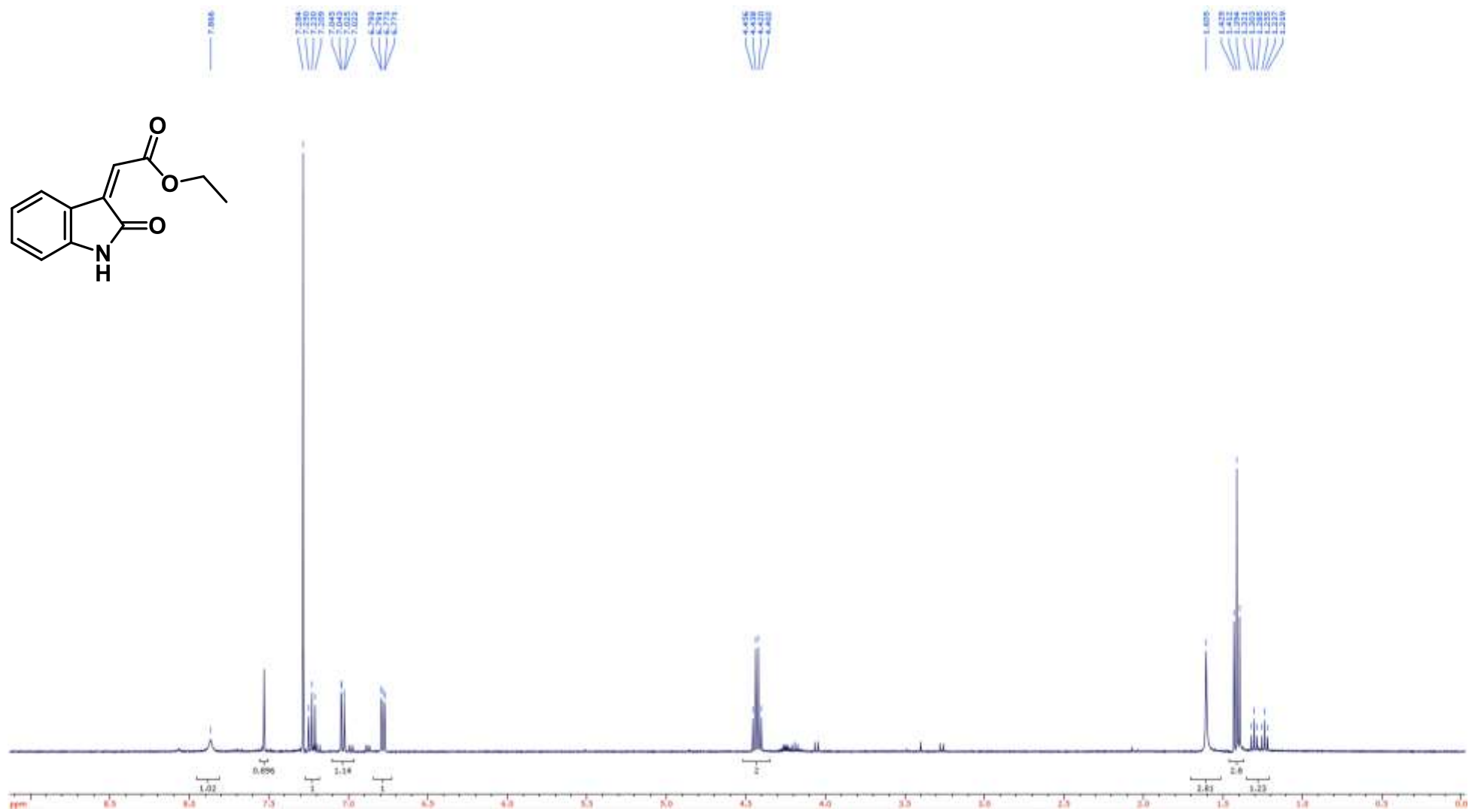
Compound **87** ^1H NMR (400 MHz, CDCl_3)



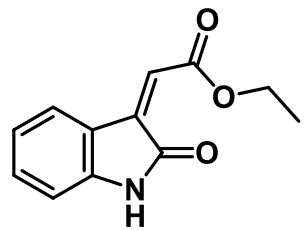
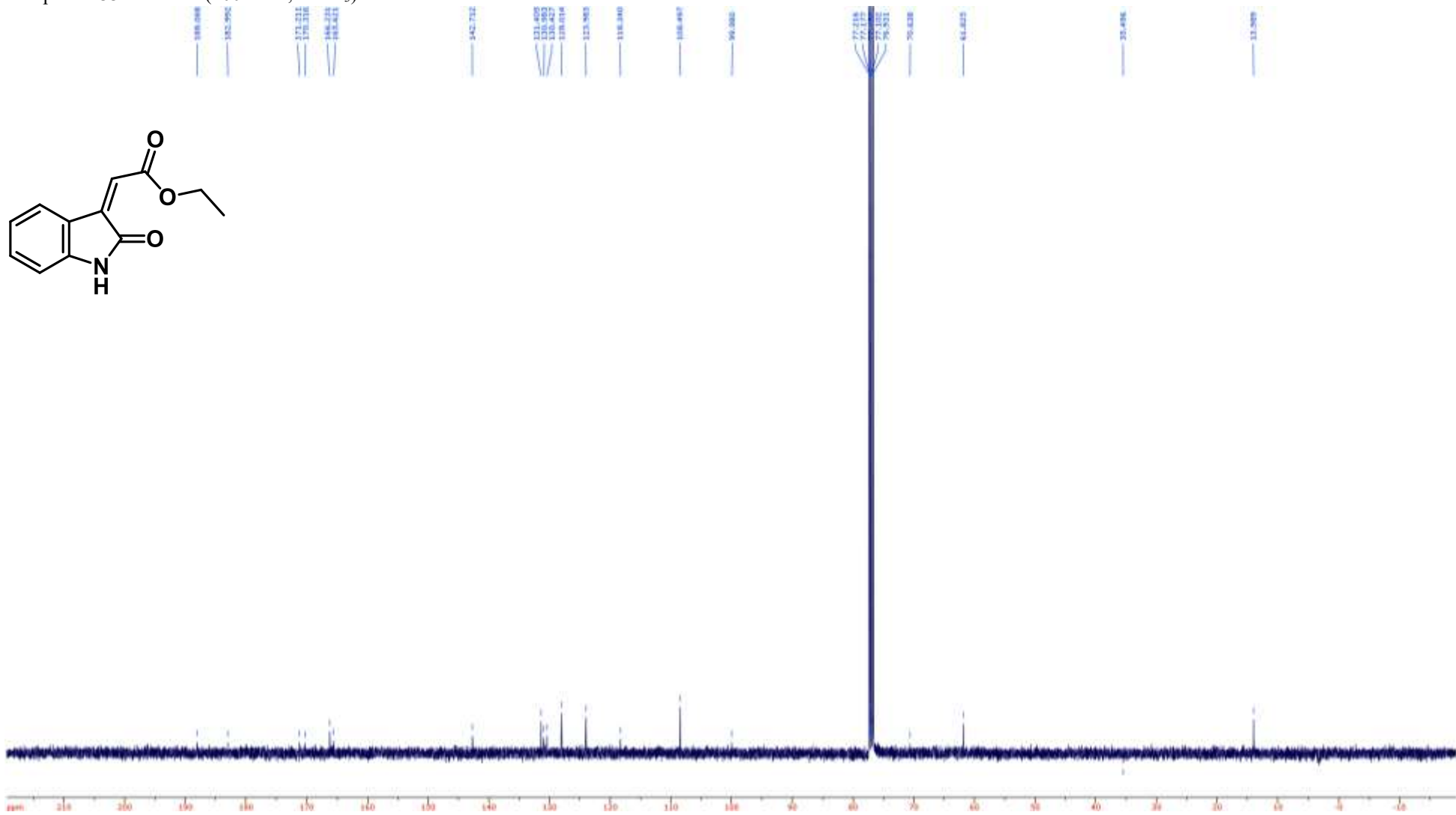
Compound **87** ^{13}C NMR (100 MHz, CDCl_3)



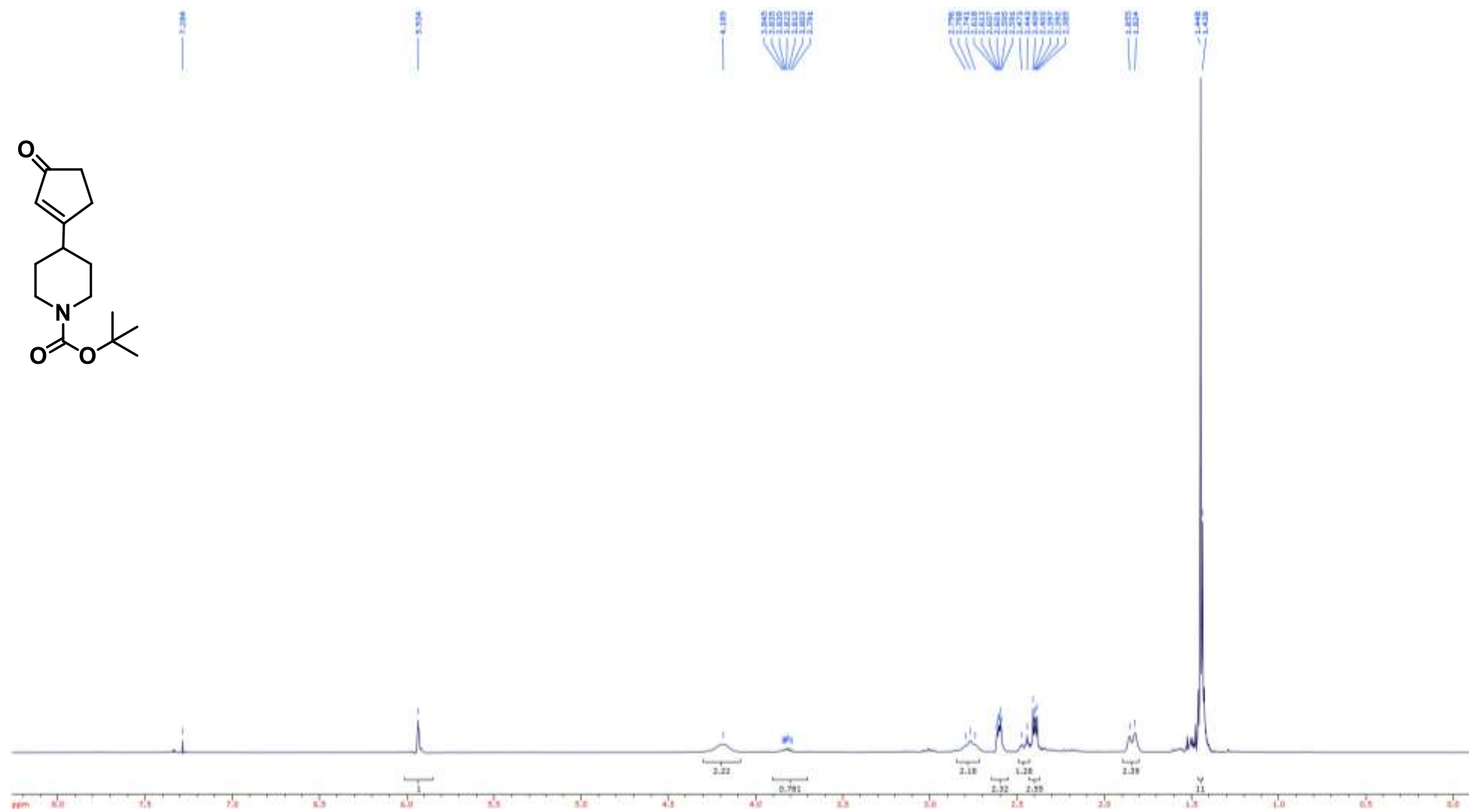
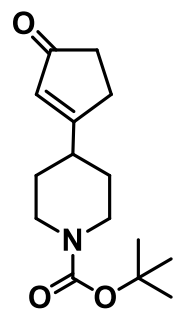
Compound **88** ^1H NMR (400 MHz, CDCl_3)



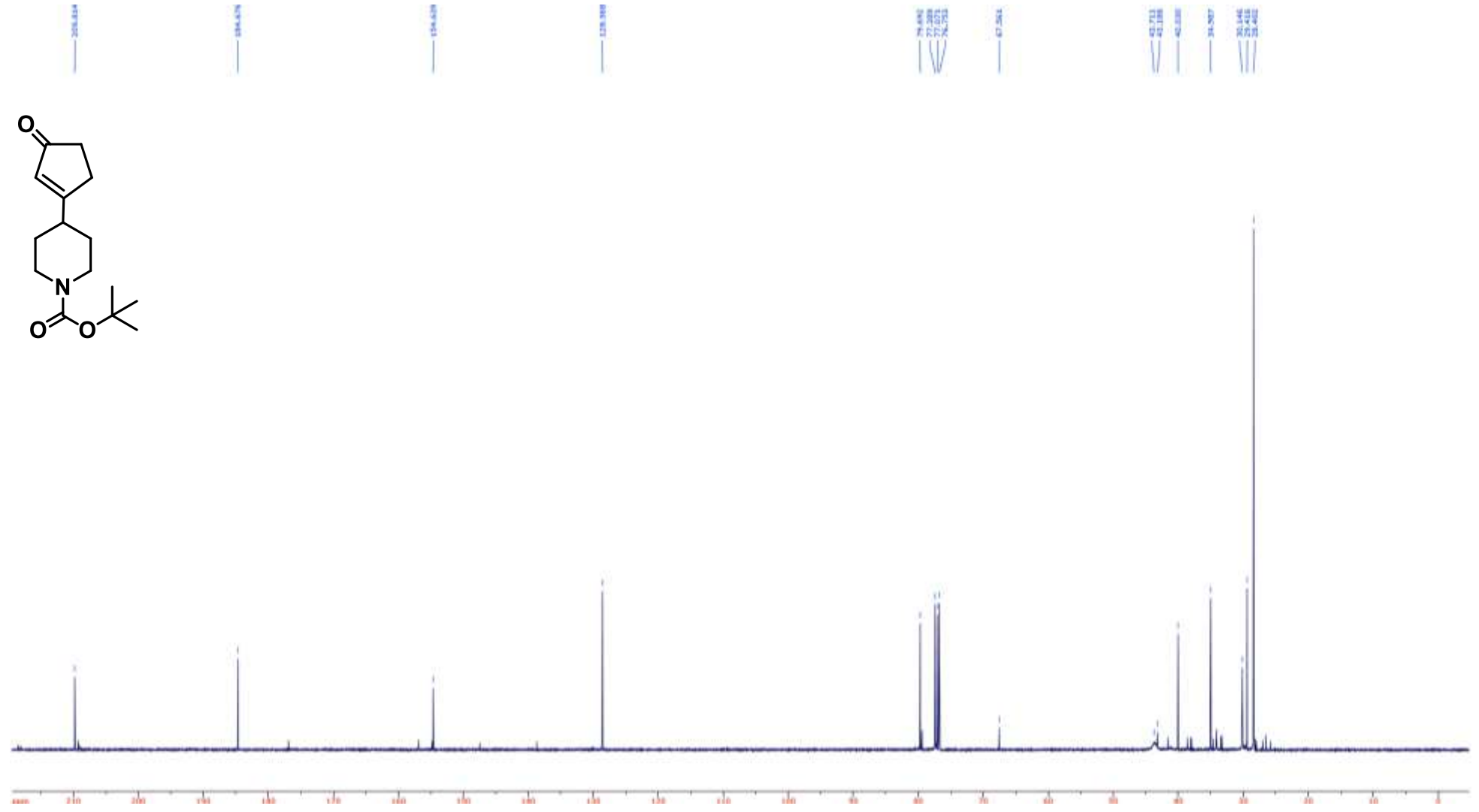
Compound **88** ^{13}C NMR (100 MHz, CDCl_3)



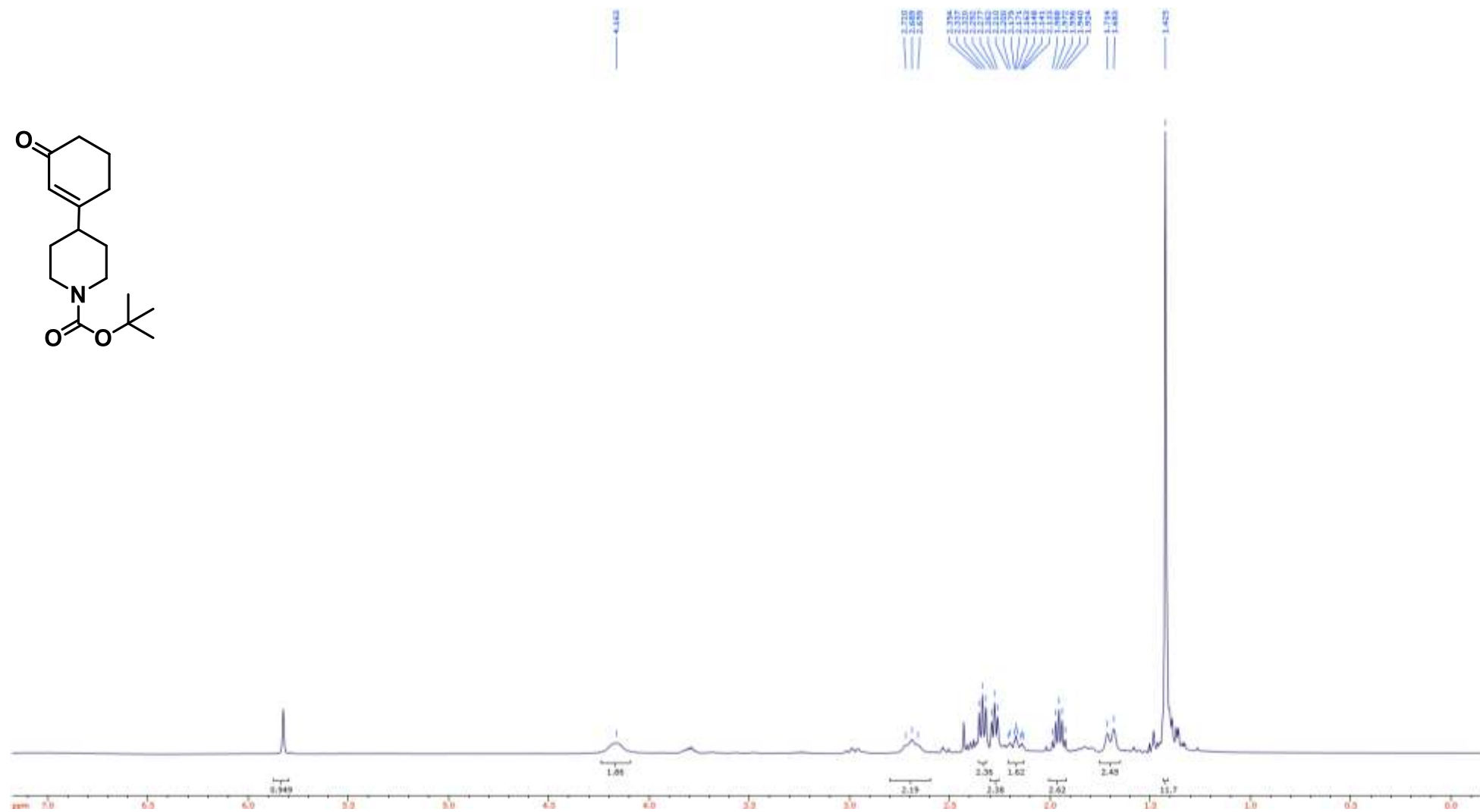
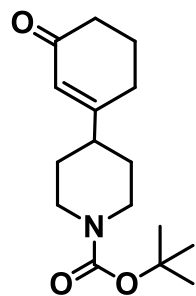
Compound **89** ^1H NMR (400 MHz, CDCl_3)



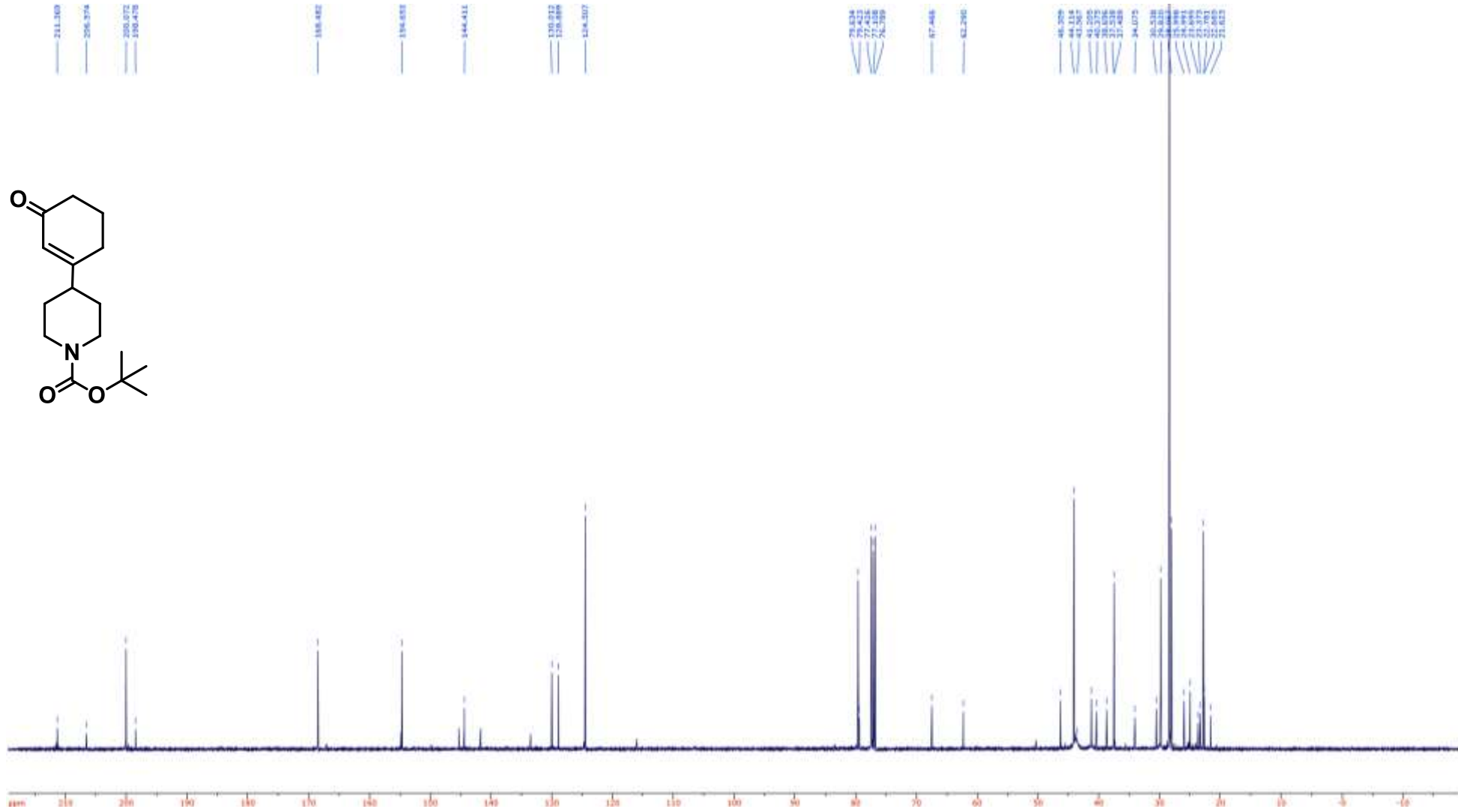
Compound **89** ^{13}C NMR (100 MHz, CDCl_3)



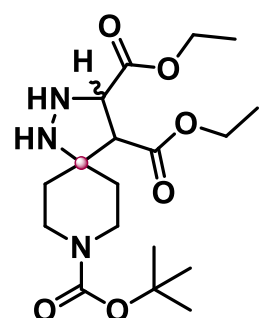
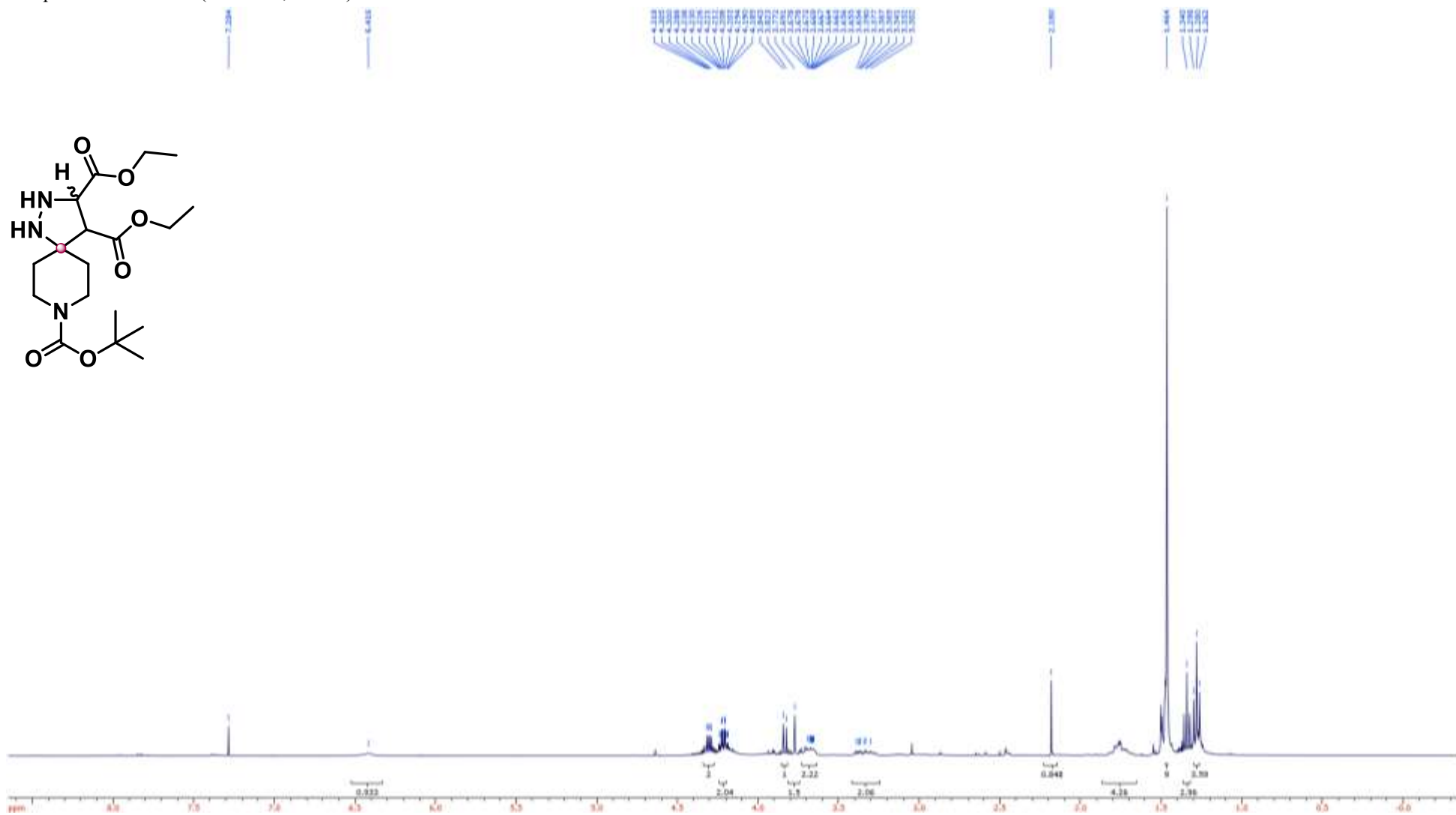
Compound **90** ^1H NMR (400 MHz, CDCl_3)



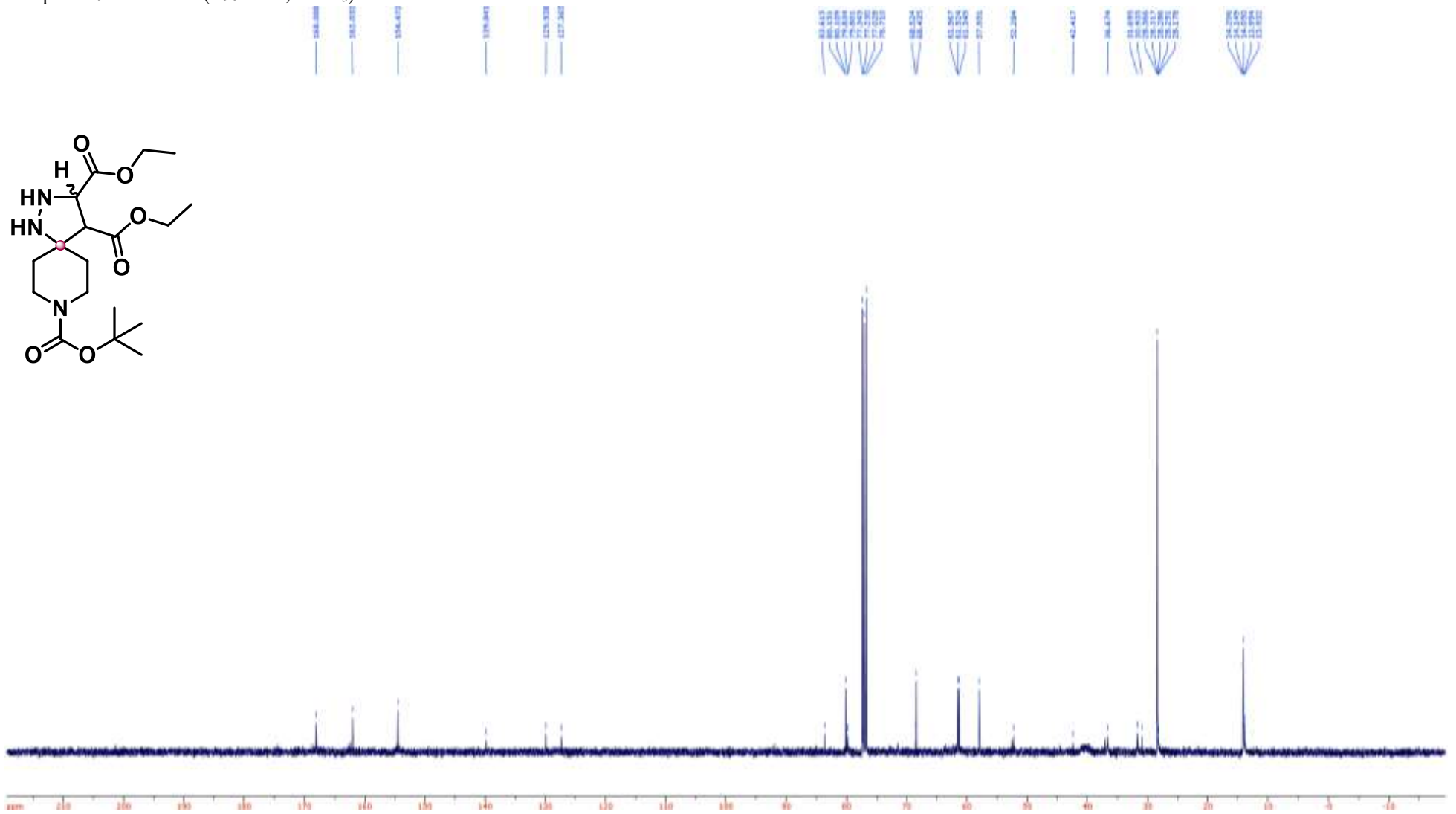
Compound **90** ^{13}C NMR (100 MHz, CDCl_3)



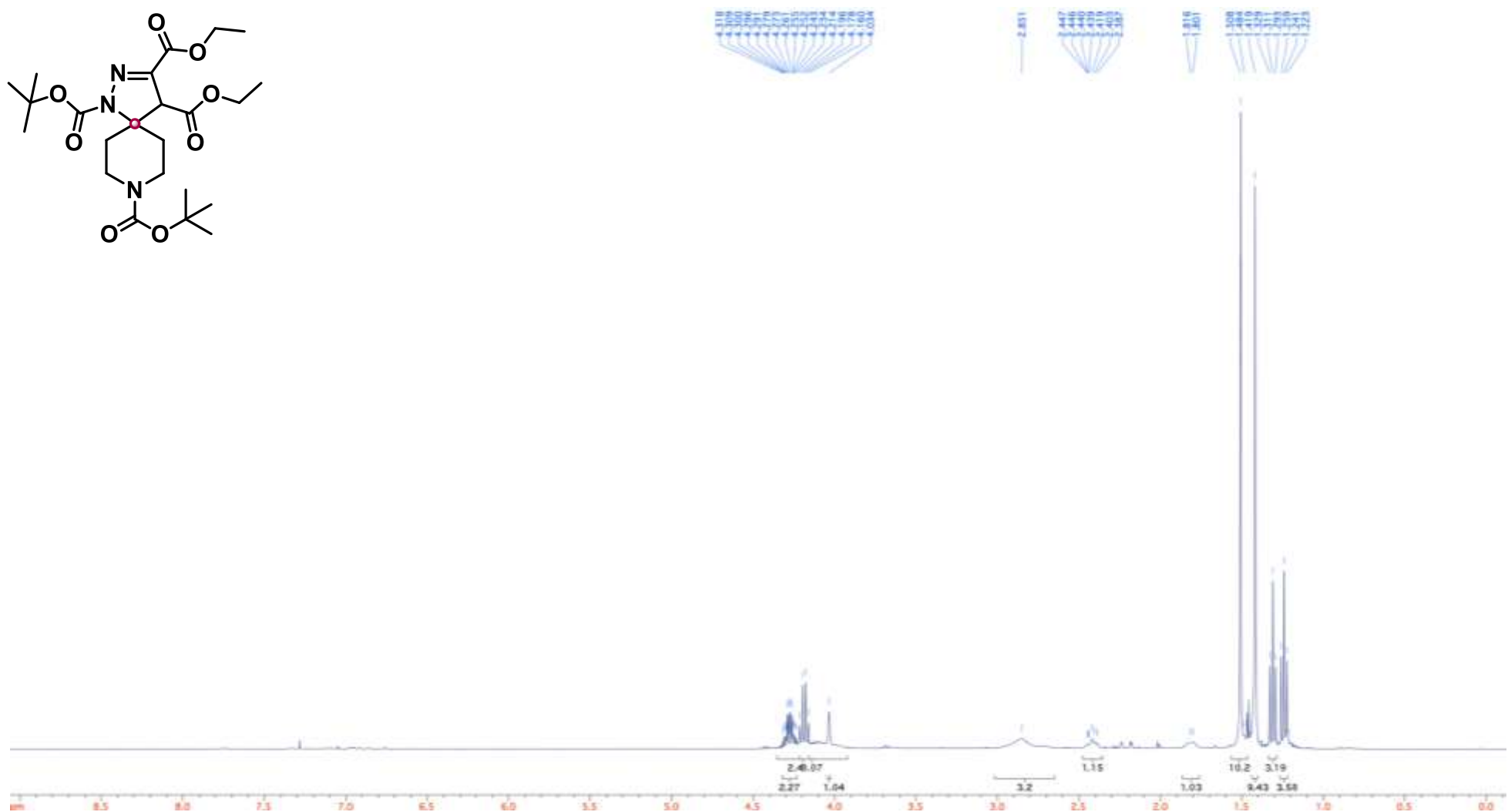
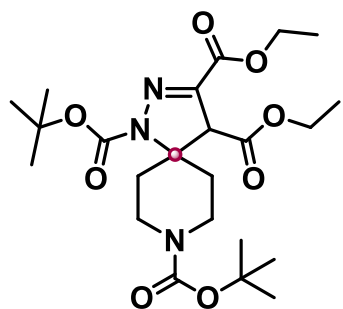
Compound **91** ^1H NMR (400 MHz, CDCl_3)



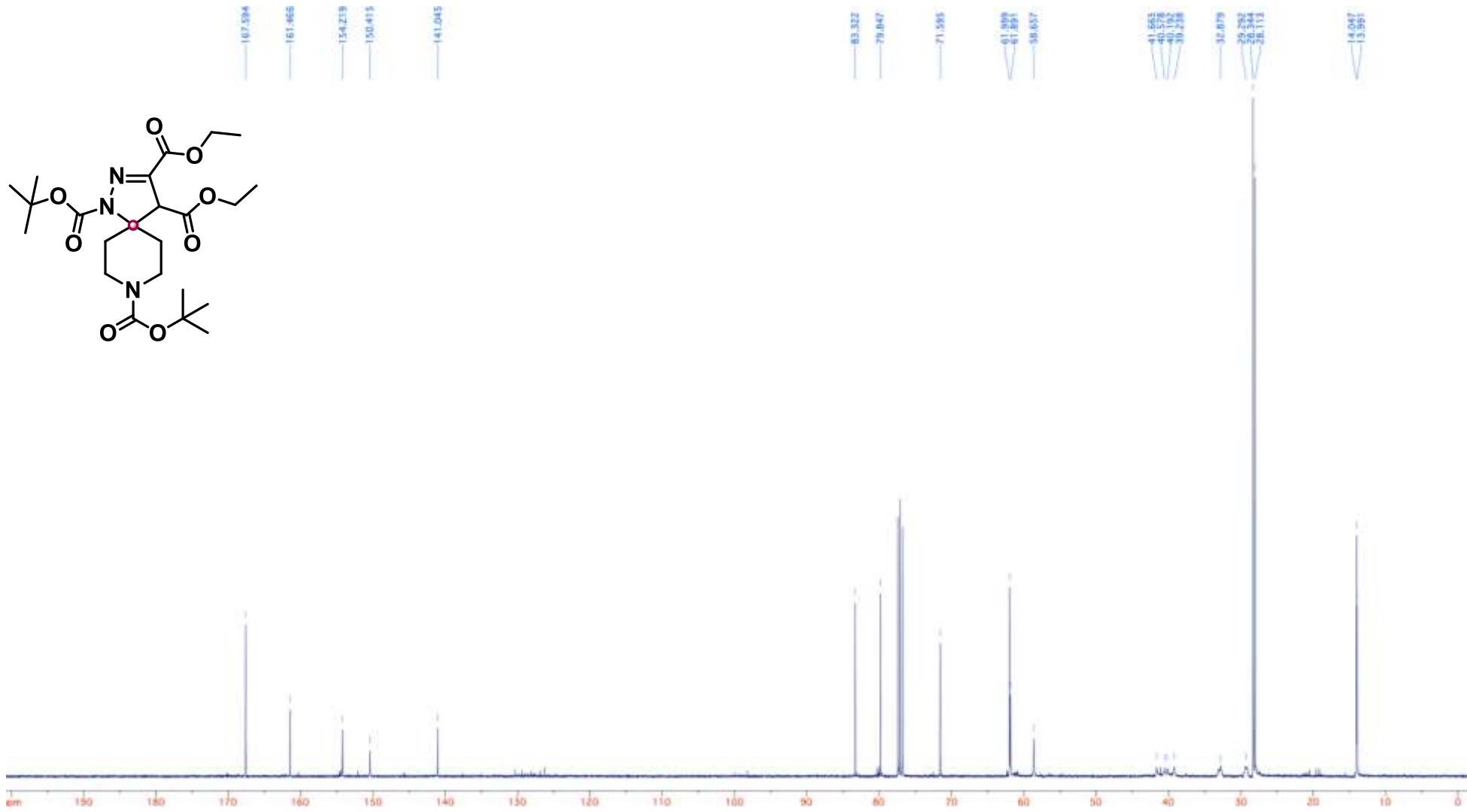
Compound **91** ^{13}C NMR (100 MHz, CDCl_3)



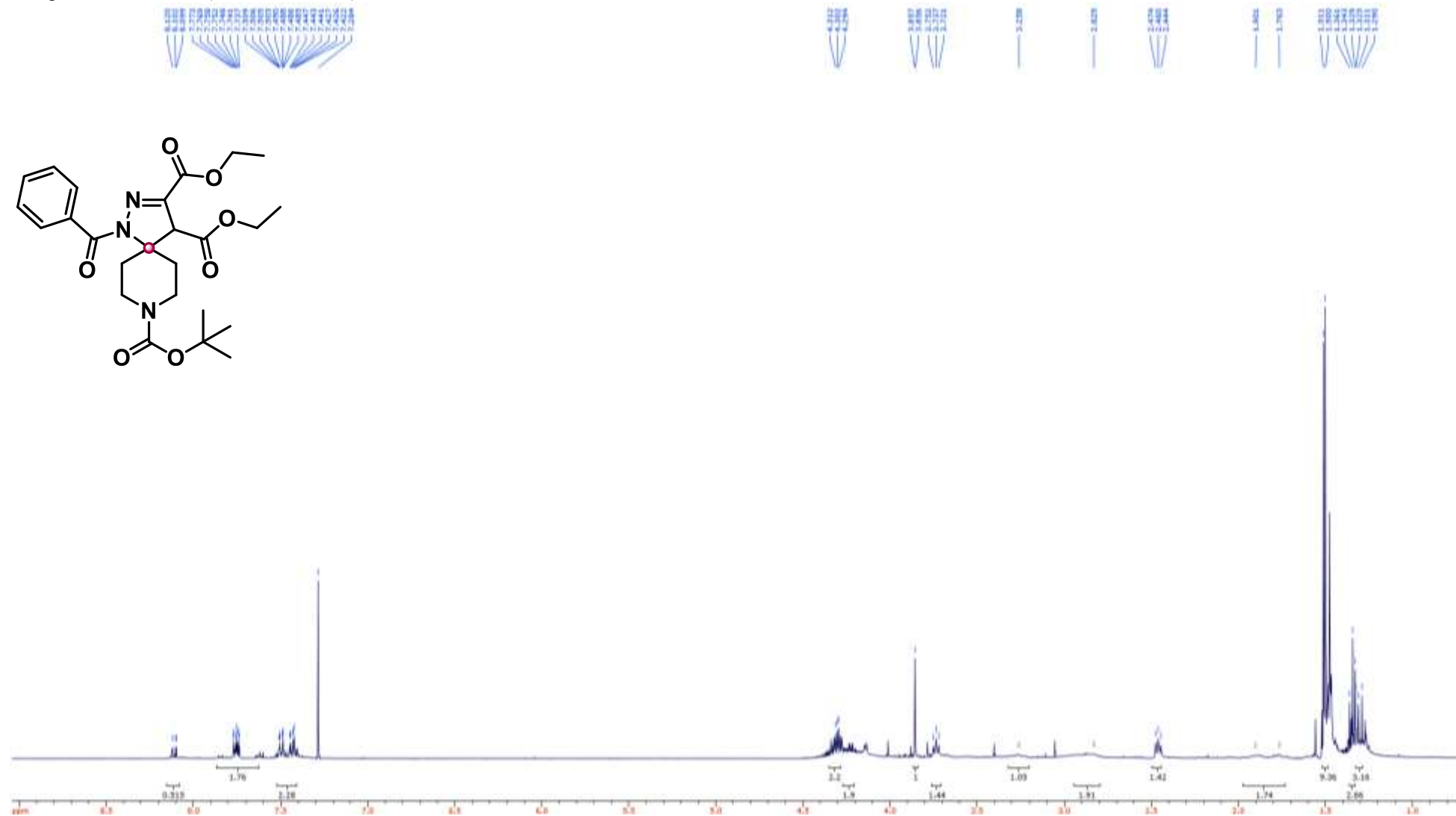
Compound **92** ^1H NMR (400 MHz, CDCl_3)



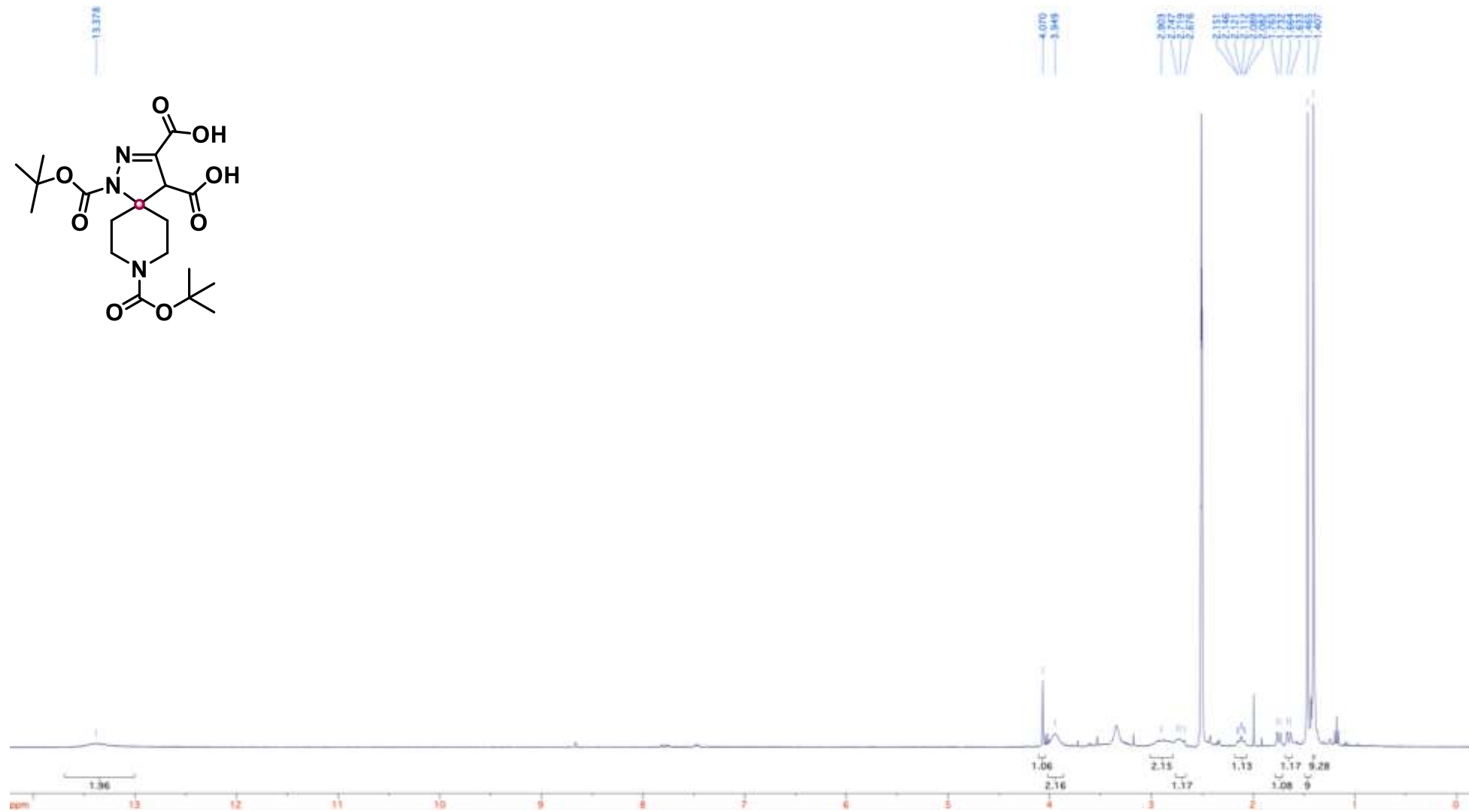
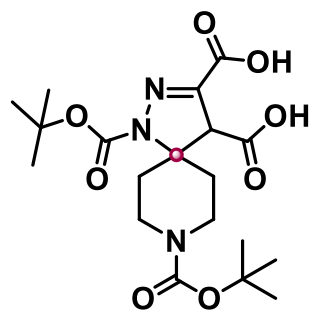
Compound **92** ^{13}C NMR (100 MHz, CDCl_3)



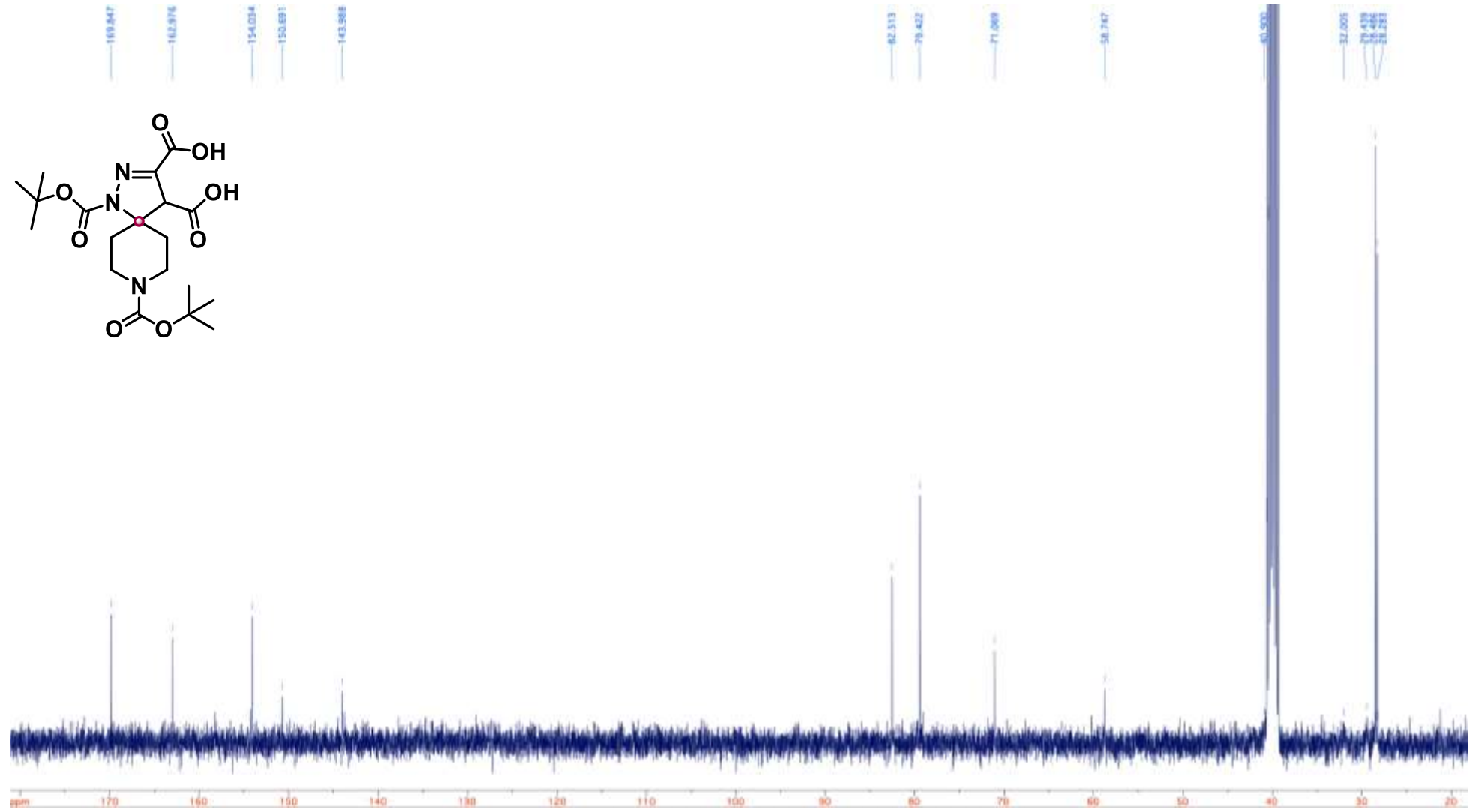
Compound **93** ^1H NMR (400 MHz, CDCl_3)



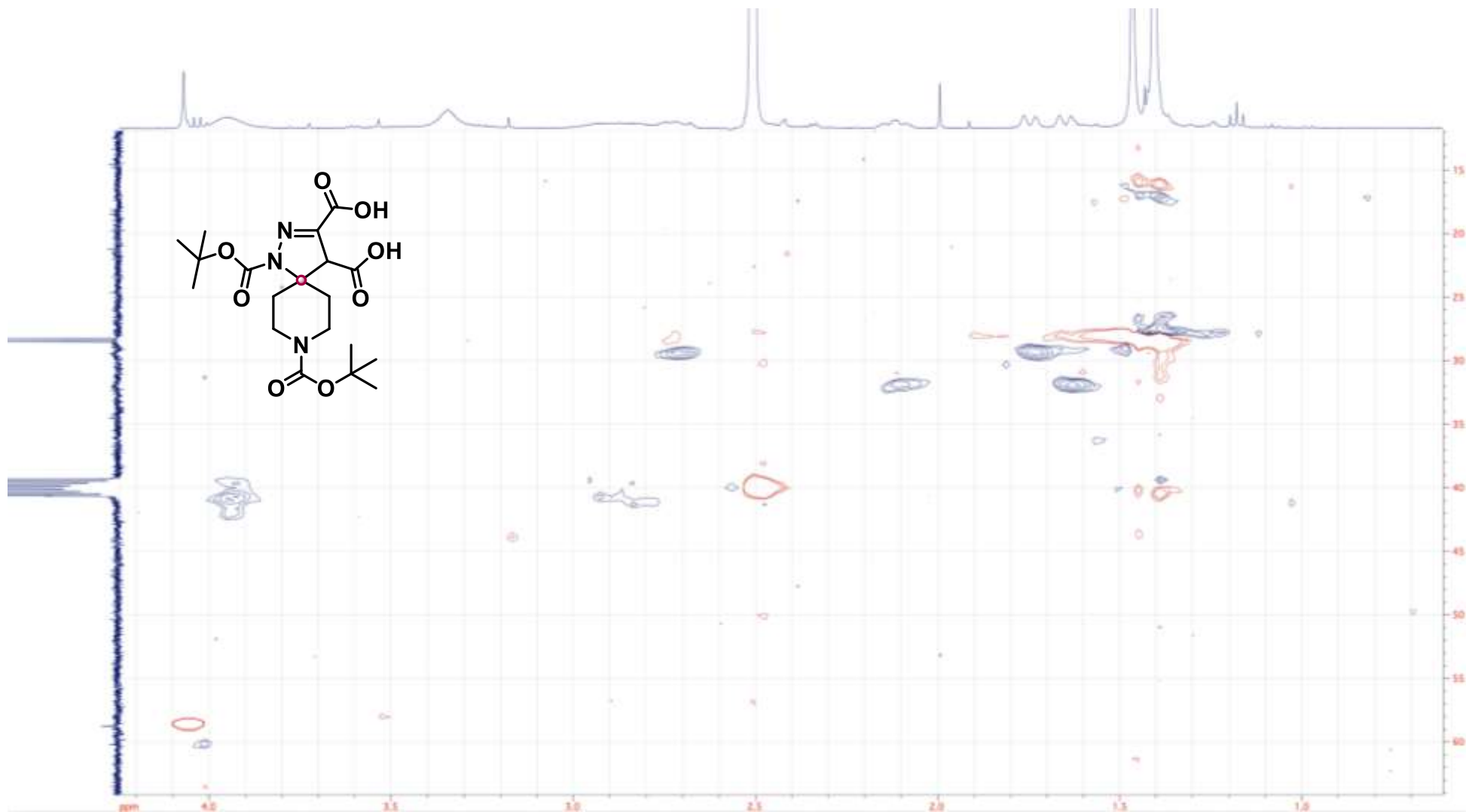
Compound **94** ^1H NMR (400 MHz, d_6 -DMSO)



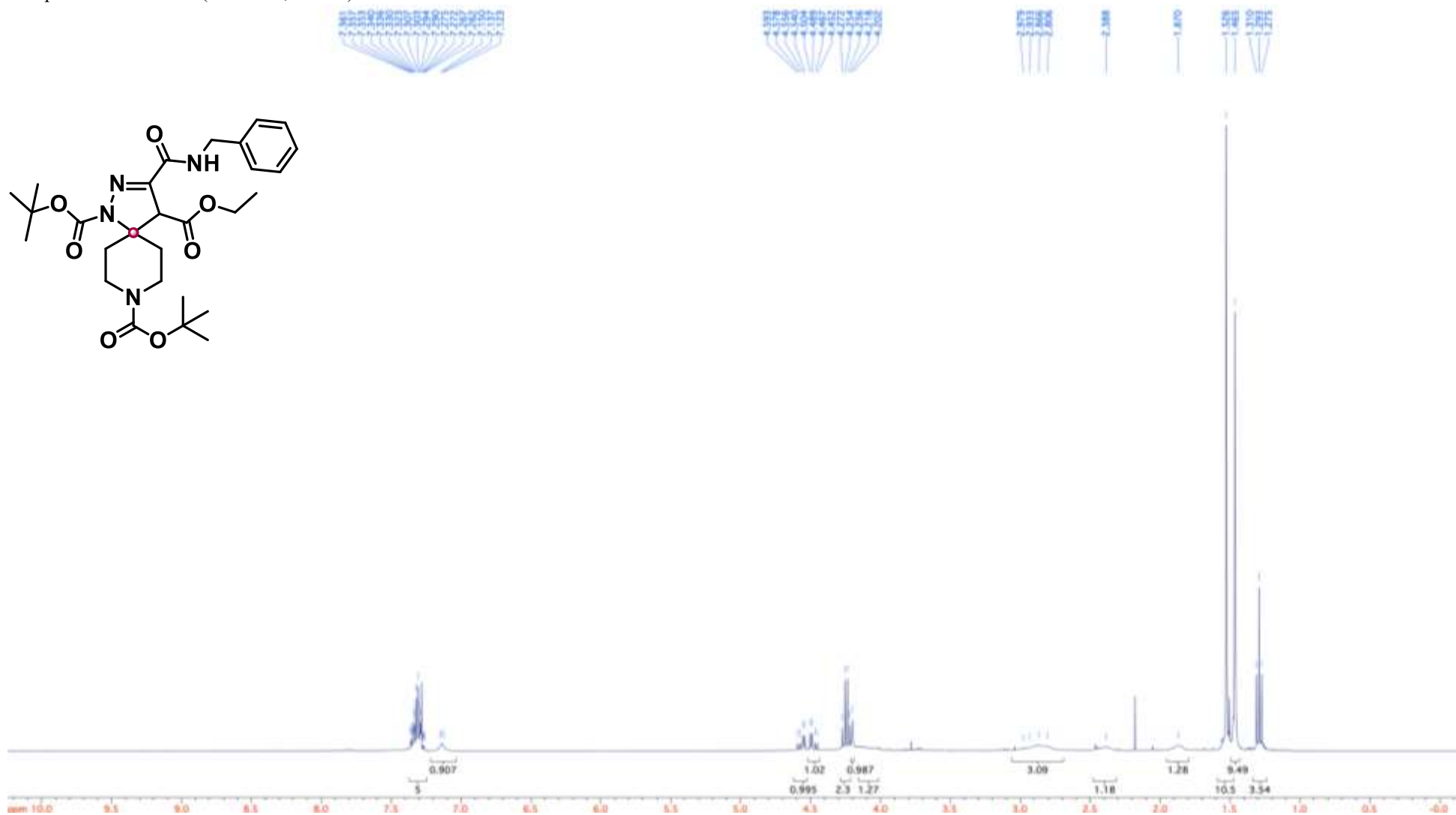
Compound **94** ^{13}C NMR (100 MHz, d_6 -DMSO)



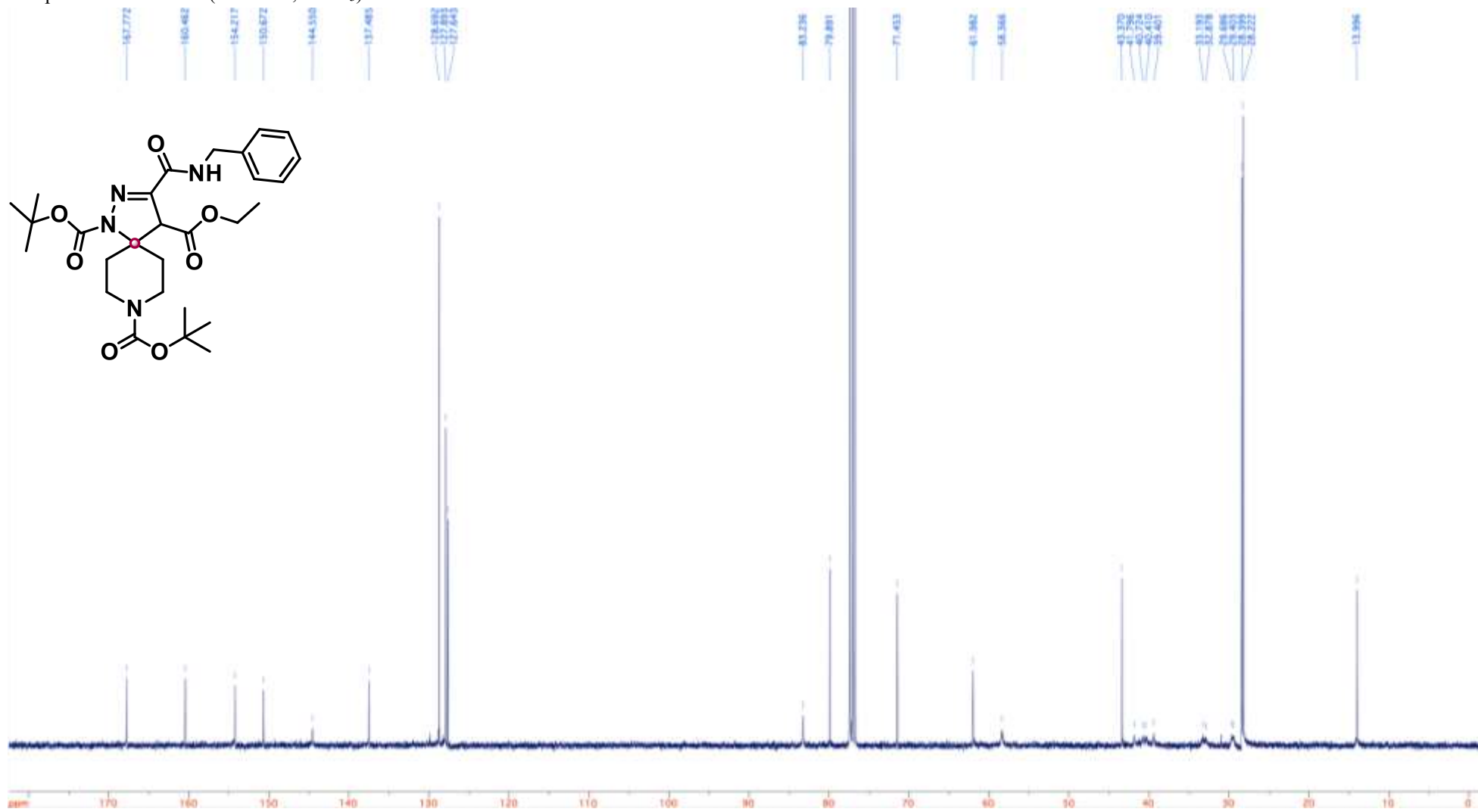
Compound **94** HSQC (400/100 MHz, *d*₆-DMSO)



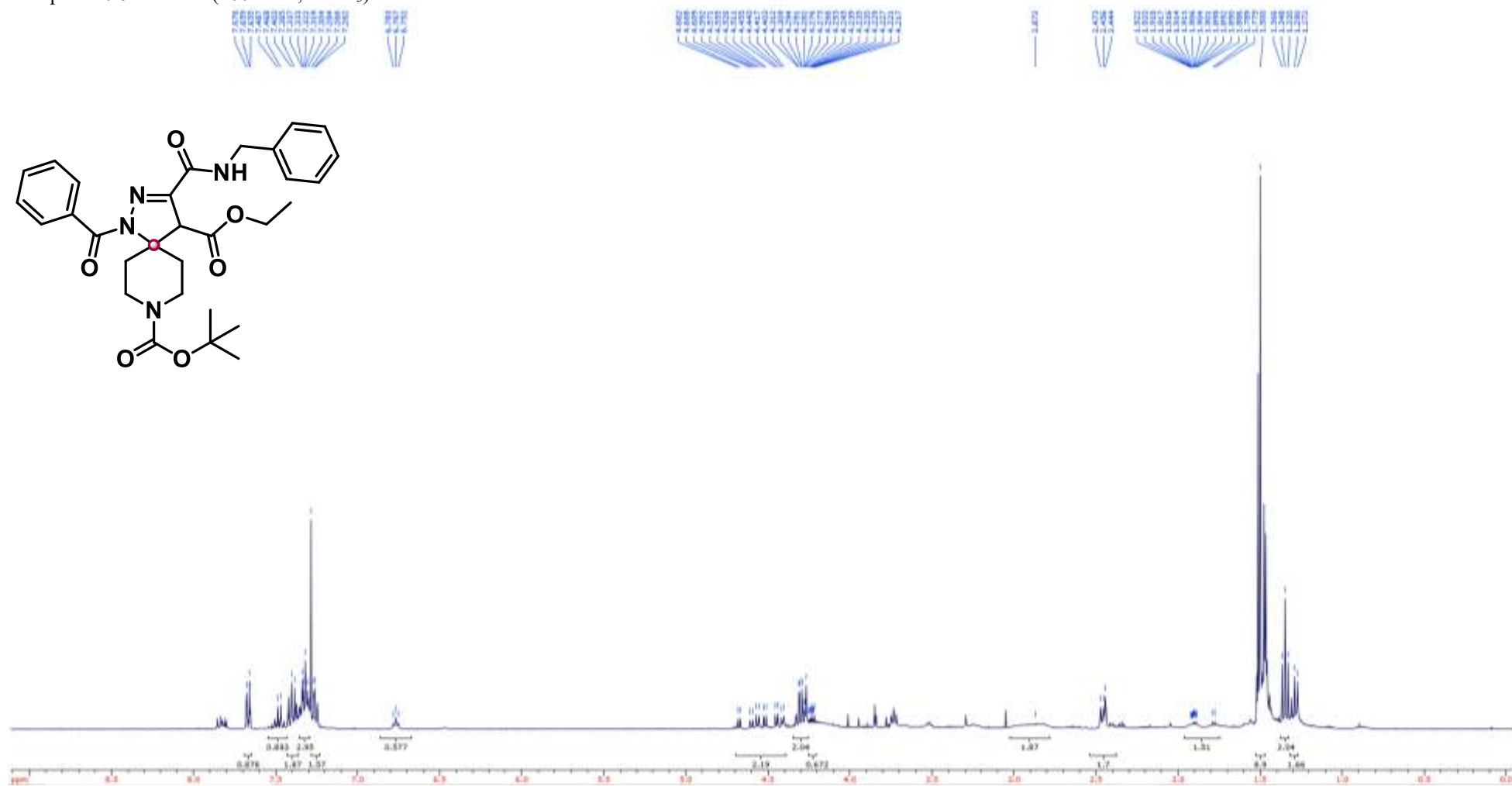
Compound **95** ^1H NMR (400 MHz, CDCl_3)



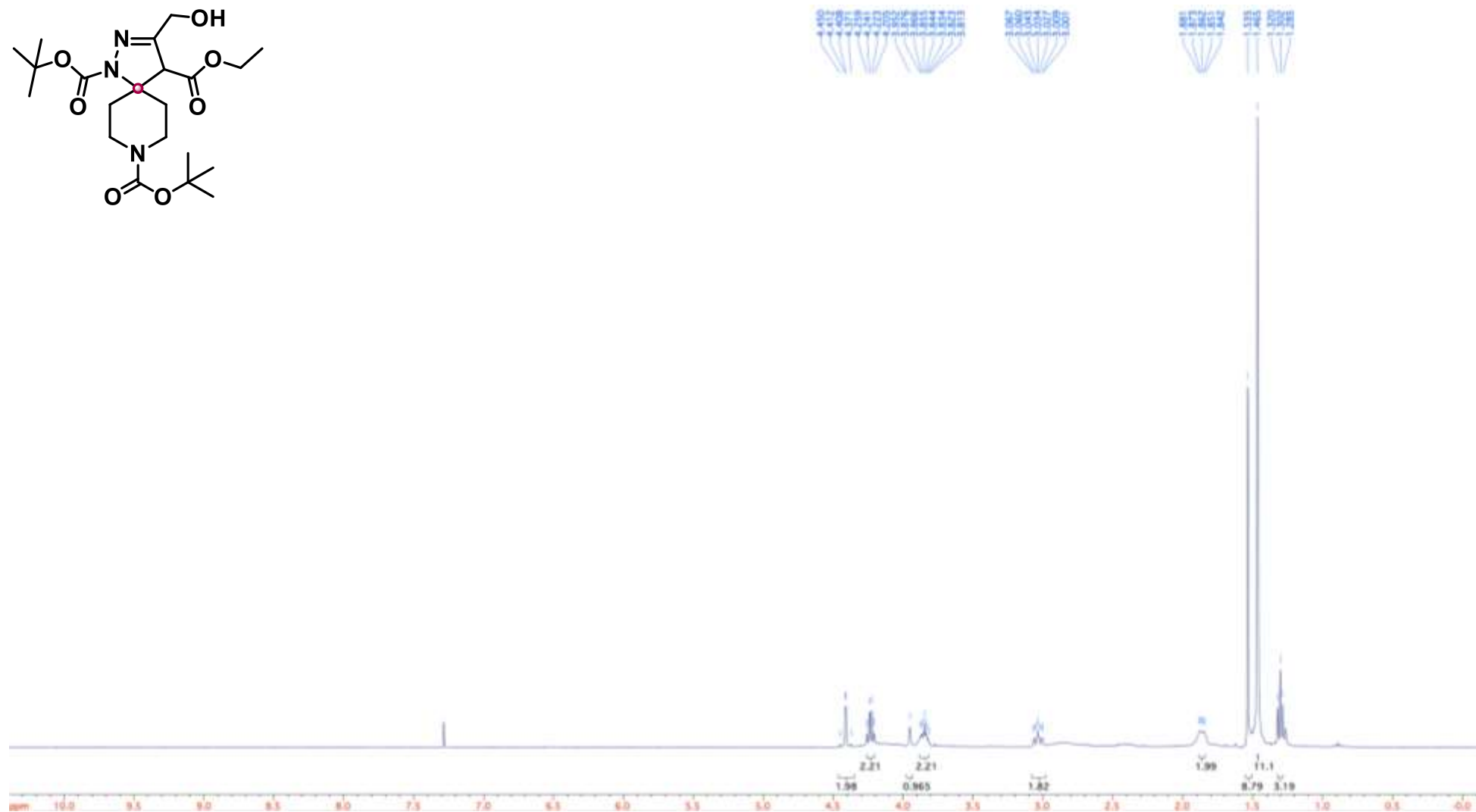
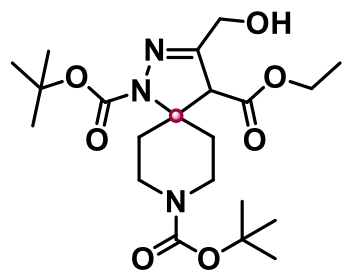
Compound **95** ^{13}C NMR (400 MHz, CDCl_3)



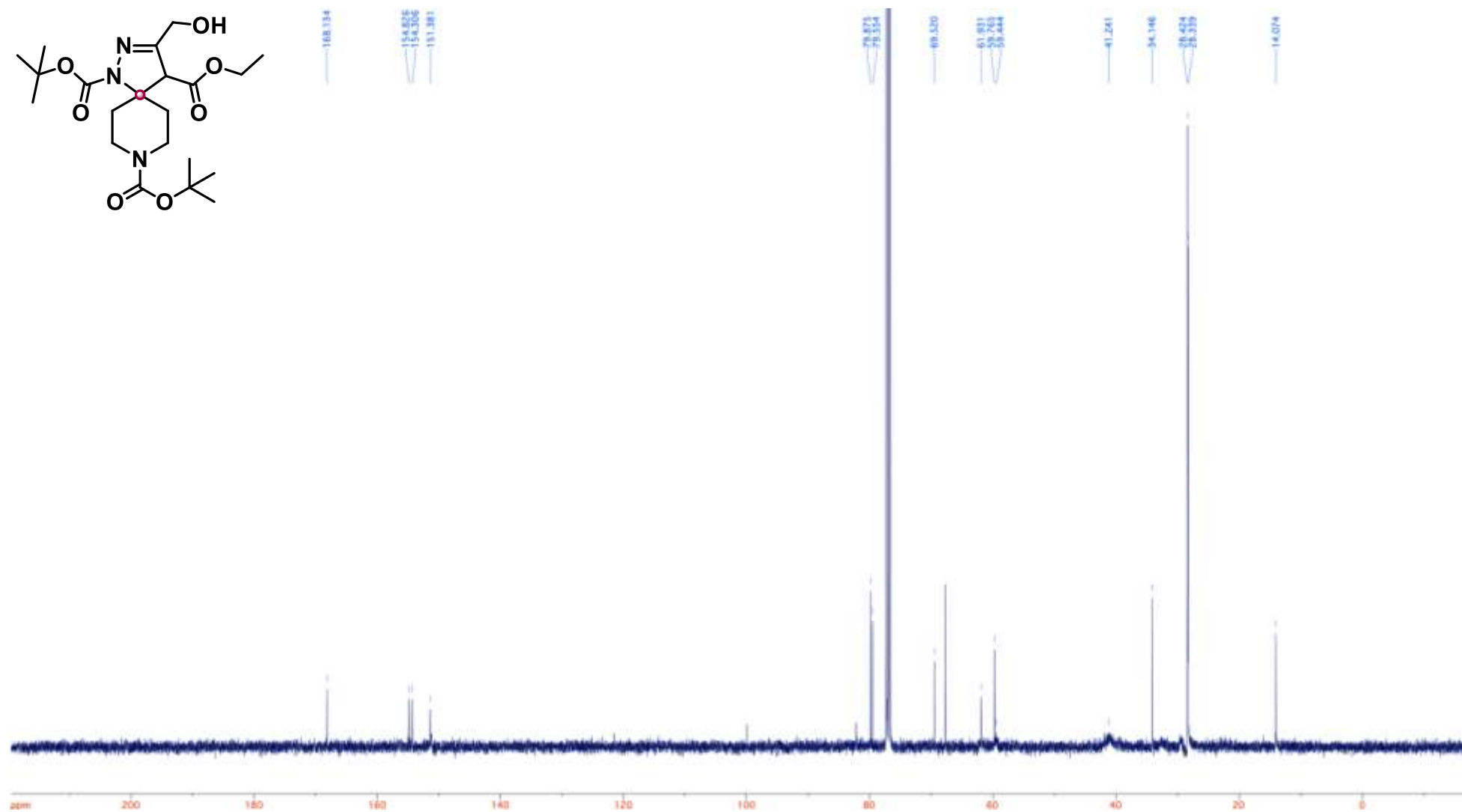
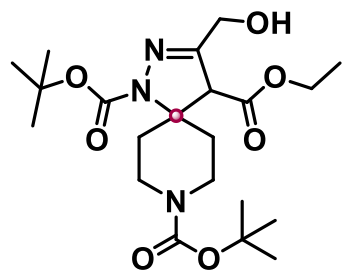
Compound **96** ^1H NMR (400 MHz, CDCl_3)



Compound **97** ^1H NMR (400 MHz, CDCl_3)



Compound **97** ^{13}C NMR (100 MHz, CDCl_3)



6. Appendix references

- 1 J. Montalibet and B. P. Kennedy, *Biochem. Pharmacol.*, 2004, **68**, 1807-1814 (DOI:10.1016/j.bcp.2004.06.024).
- 2 L. K. Harris, S. M. Frumm and A. C. Bishop, *Anal. Biochem.*, 2013, **435**, 99-105 (DOI:10.1016/j.ab.2012.12.025).
- 3 B. Yee, S. Tsuyumu and B. G. Adams, *Biochem. Biophys. Res. Commun.*, 1972, **49**, 1336-1342 (DOI:10.1016/0006-291X(72)90613-4).
- 4 I. Sadowska-Bartosz, A. Pączka, M. Mołoń and G. Bartosz, *FEMS yeast research*, 2013, **13**, 820-830 (DOI:10.1111/1567-1364.12091).
- 5 T. L. Wootton and D. M. Allwood, *OBC*, 2022, **2**, 2255-226 (DOI:10.1039/d2ob00093h).
- 6 D. M. Allwood, D. C. Blakemore, A. D. Brown and S. V. Ley, *J. Org. Chem.*, 2014, **79**, 328-338 (DOI:10.1021/jo402526z).
- 7 R. R. Merchant, D. M. Allwood, D. C. Blakemore and S. V. Ley, *J. Org. Chem.*, 2014, **79**, 8800-8811 (DOI:10.1021/jo501624t).
- 8 D. M. Allwood, D. C. Blakemore and S. V. Ley, *Org. Lett.*, 2014, **16**, 3064-3067 (DOI:10.1021/ol5011714).